Edited by Martin Kaupp,
Michael Bühl, Vladimir G. Malkin

WILEY-VCH

Calculation of NMR and EPR Parameters

Theory and Applications

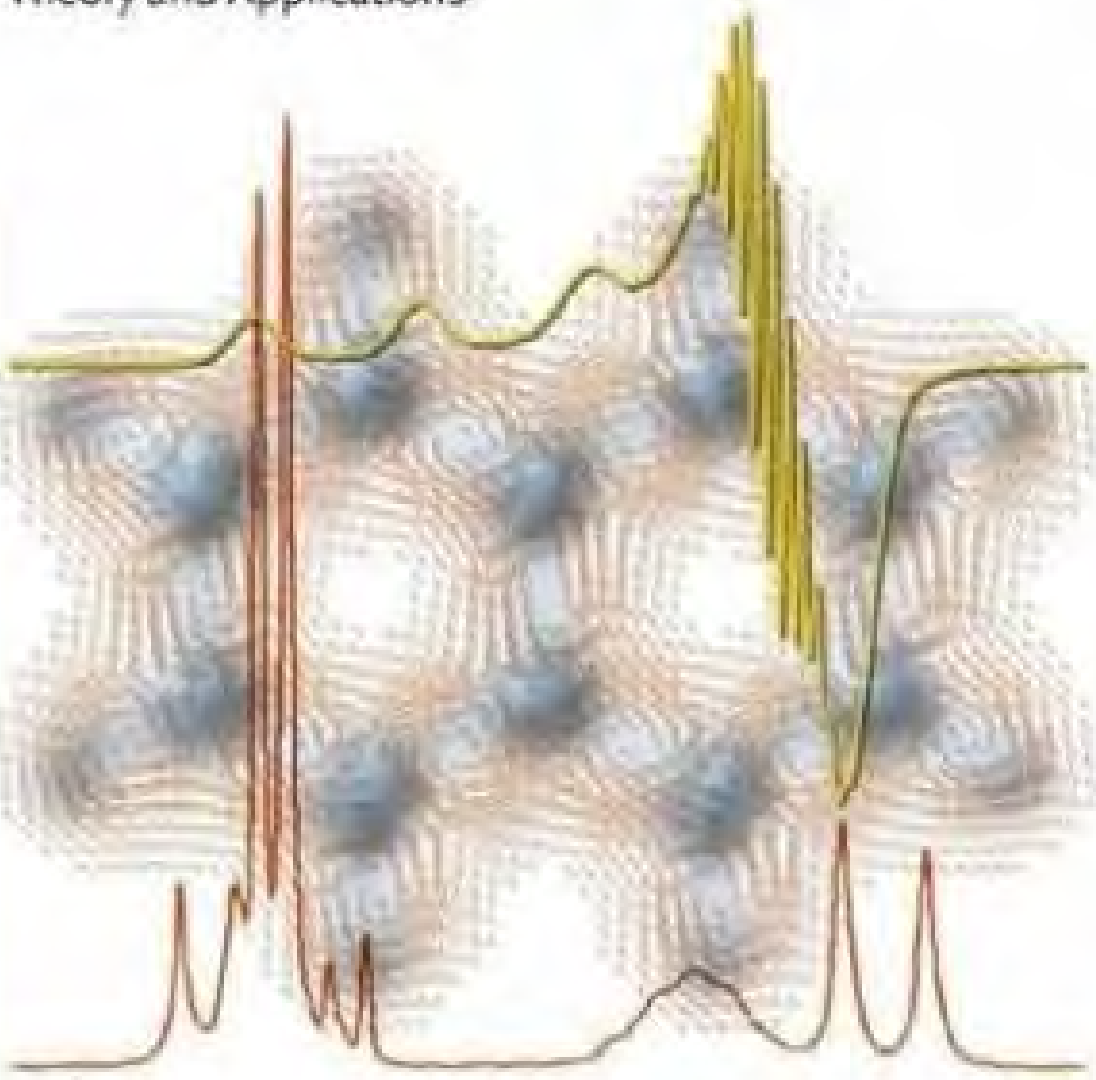

Martin Kaupp, Michael Bühl,
Vladimir G. Malkin
Calculation of NMR and EPR Parameters

Calculation of NMR and EPR Parameters. Theory and Applications.
Edited by Martin Kaupp, Michael Bühl, Vladimir G. Malkin
Copyright © 2004 WILEY-VCH Verlag GmbH & Co. KGaA, Weinheim
ISBN: 3-527-30779-6

Further Titles of Interest:

J. Gasteiger (Ed.)

Handbook of Chemoinformatics

From Data to Knowledge

4 Volumes

2003, ISBN 3-527-30680-3

Ch. Schorn

NMR Spectroscopy: Data Acquisition

2nd Edition

2004, ISBN 3-527-31070-3

F. Gerson, W. Huber

Electron Spin Resonance Spectroscopy of Organic Radicals

2003, ISBN 3-527-30275-1

O. Zerbe (Ed.)

BioNMR in Drug Research

2003, ISBN 3-527-30465-7

P. Carloni, F. Alber (Eds.)

Quantum Medicinal Chemistry

2003, ISBN 3-527-30456-8

D. M. Grant, R. K. Harris (Eds.)

Encyclopedia of Nuclear Magnetic Resonance

9 Volumes

2002, ISBN 0-470-84784-0

Martin Kaupp, Michael Bühl, Vladimir G. Malkin

Calculation of NMR and EPR Parameters

Theory and Applications

WILEY-VCH Verlag GmbH & Co. KGaA

Editors

Prof. Dr. Martin Kaupp
Institute of Inorganic Chemistry
University of Würzburg
Am Hubland
97074 Würzburg
Germany

Priv. Doz. Dr. Michael Bühl
Max-Planck-Institute for Coal Research
Kaiser-Wilhelm-Platz 1
45470 Mülheim an der Ruhr
Germany

Dr. Vladimir G. Malkin, DrSc.
Institute of Inorganic Chemistry
Slovak Academy of Sciences
Dubravska cesta 9
SK-84536 Bratislava
Slovak Republic

This book was carefully produced. Nevertheless, editors, authors and publisher do not warrant the information contained therein to be free of errors. Readers are advised to keep in mind that statements, data, illustrations, procedural details or other items may inadvertently be inaccurate.

Library of Congress Card No. applied for

British Library Cataloguing-in-Publication Data
A catalogue record for this book is available from the British Library.

Bibliographic information published by

Die Deutsche Bibliothek
Die Deutsche Bibliothek lists this publication in the Deutsche Nationalbibliografie; detailed bibliographic data is available in the Internet at <http://dnb.ddb.de>.

© 2004 WILEY-VCH Verlag GmbH & Co. KGaA, Weinheim

All rights reserved (including those of translation into other languages). No part of this book may be reproduced in any form – nor transmitted or translated into machine language without written permission from the publishers. Registered names, trademarks, etc. used in this book, even when not specifically marked as such, are not to be considered unprotected by law.

Printed in the Federal Republic of Germany.

Printed on acid-free paper.

Typesetting Kühn & Weyh, Satz und Medien, Freiburg
Printing betz-druck GmbH, Darmstadt
Bookbinding Buchbinderei J. Schäffer GmbH & Co. KG, Grünstadt

ISBN 3-527-30779-6

Contents

Foreword *XIII*

List of Contributors *XV*

Part A Introductory Chapters

1 Introduction: The Quantum Chemical Calculation of NMR and EPR Parameters *3*
Martin Kaupp, Michael Bühl, and Vladimir G. Malkin

2 Theory of NMR parameters. From Ramsey to Relativity, 1953 to 1983 *7*
Pekka Pyykkö
2.1 Introduction *7*
2.2 Spin–Spin Coupling *9*
2.3 Chemical Shifts *11*
2.4 General Aspects *13*
2.5 From 1983 to 2003 *15*

3 Historical Aspects of EPR Parameter Calculations *21*
Frank Neese and Markéta L. Munzarová

4 The Effective Spin Hamiltonian Concept from a Quantum Chemical Perspective *33*
Gerald H. Lushington

5 Fundamentals of Nonrelativistic and Relativistic Theory of NMR and EPR Parameters *43*
Werner Kutzelnigg
5.1 Introduction *43*
5.2 Classical Theory of the Interaction of a Charged Particle with an Electromagnetic Field *44*
5.3 Quantum Mechanical Hamiltonians in a Time-Independent Electromagnetic Field *50*

Calculation of NMR and EPR Parameters. Theory and Applications.
Edited by Martin Kaupp, Michael Bühl, Vladimir G. Malkin
Copyright © 2004 WILEY-VCH Verlag GmbH & Co. KGaA, Weinheim
ISBN: 3-527-30779-6

5.4 Perturbation Theory of Magnetic Effects *58*
5.5 Non-Relativistic Theory of EPR and NMR Parameters *62*
5.6 Relativistic Theory of Magnetic Properties *69*
5.7 The Leading Relativistic Corrections *72*
5.8 Concluding Remarks *81*

Part B NMR Parameters, Methodological Aspects

6 Chemical Shifts with Hartree–Fock and Density Functional Methods *85*
Christoph van Wüllen
6.1 Introduction *85*
6.2 Linear Response and the Gauge Origin Problem *88*
6.3 Determination of the First-Order Orbitals *90*
6.4 Distributed Gauge Origins, IGLO and GIAO Approaches *92*
6.5 Distributed Gauge Origins in Real Space, a "Continuous Set of Gauge Transformations" *96*
6.6 Beyond Pure Density Functional Theory *97*
6.7 Conclusions *99*

7 Spin–Spin Coupling Constants with HF and DFT Methods *101*
Trygve Helgaker and Magdalena Pecul
7.1 Introduction *101*
7.2 The Calculation of Indirect Nuclear Spin–Spin Coupling Constants *102*
7.3 Examples of Applications *115*
7.4 Conclusions *119*

8 Electron-Correlated Methods for the Calculation of NMR Chemical Shifts *123*
Jürgen Gauss and John F. Stanton
8.1 Introduction *123*
8.2 Theoretical Background *125*
8.3 Electron-Correlated Treatment of NMR Chemical Shifts *132*
8.4 Special developments *133*
8.5 Numerical Results *134*
8.6 Summary and Outlook *136*

9 Semiempirical Methods for the Calculation of NMR Chemical Shifts *141*
Thomas Heine and Gotthard Seifert
9.1 Introduction *141*
9.2 Methods *142*
9.3 Representative Applications *147*
9.4 Concluding Remarks: Limitations of Semiempirical Methods for the Calculation of NMR Parameters *151*

10 Ro-Vibrational Corrections to NMR Parameters *153*
Torgeir A. Ruden and Kenneth Ruud
10.1 Introduction *153*
10.2 Perturbation Theory *154*
10.3 Other Approaches for Calculating Vibrationally Averaged NMR Properties *163*
10.4 Examples of Vibrational Contributions to NMR Properties *164*
10.5 Summary *171*

11 Molecular Dynamics and NMR Parameter Calculations *175*
Debra J. Searles and Hanspeter Huber
11.1 Introduction *175*
11.2 Methods *176*
11.3 Examples *182*
11.4 Summary and Conclusions *187*

12 Use of Continuum Solvent Models in Magnetic Resonance Parameter Calculations *191*
Ilaria Ciofini
12.1 Introduction *191*
12.2 General Features of Continuum Models *192*
12.3 Applications of Continuum Models to the Prediction of NMR Parameters *197*
12.4 Applications of Continuum Models to the Prediction of EPR Parameters *201*
12.5 Conclusions *205*

13 Perturbational and ECP Calculation of Relativistic Effects in NMR Shielding and Spin–Spin Coupling *209*
Juha Vaara, Pekka Manninen, and Perttu Lantto
13.1 Introduction *209*
13.2 Nuclear Shielding and Spin–Spin Coupling *210*
13.3 Electronic Hamiltonian *211*
13.4 Non-Relativistic Contributions *212*
13.5 Relativistic Kinematics and the Spin–Zeeman Effect *213*
13.6 Spin–Orbit Coupling *216*
13.7 Relativistic Corrections to Shielding and Coupling *217*
13.8 Conclusions *223*

14 Calculation of Heavy-Nucleus Chemical Shifts. Relativistic All-Electron Methods *227*
Jochen Autschbach
14.1 Introduction *227*
14.2 Methodological Aspects *229*

14.3 Computational Results 234
14.4 Summary 244

15 Relativistic Calculations of Spin–Spin Coupling Constants of Heavy Nuclei 249
Jochen Autschbach and Tom Ziegler
15.1 Introduction 249
15.2 Methodological Aspects 251
15.3 Computational Results 253
15.4 Summary 262

16 Calculations of Magnetic Resonance Parameters in Solids and Liquids Using Periodic Boundary Conditions 265
Chris J. Pickard and Francesco Mauri
16.1 Introduction 265
16.2 Cluster Approaches to Extended Systems 265
16.3 The Limitations of the Cluster Approach 266
16.4 Infinite Crystals, Periodic Boundary Conditions 267
16.5 Magnetic Resonance Parameters within Periodic Boundary Conditions 267
16.6 Applications of the Planewave-GIPAW Method 272
16.7 Work in Progress and Future Challenges 275
16.8 Conclusion 276

17 Calculation of Nuclear Quadrupole Coupling Constants 279
Peter Schwerdtfeger, Markus Pernpointner, and Witold Nazarewicz
17.1 Introduction 279
17.2 Nuclear Quadrupole Moments 282
17.3 Field Gradients from Ab Initio Calculations 285
17.4 Field Gradients from Density Functional Calculations 288

18 Interpretation of NMR Chemical Shifts 293
Martin Kaupp
18.1 Introduction 293
18.2 Nonrelativistic Case 295
18.3 Relativistic Effects 302
18.4 Concluding Remarks 305

19 Interpretation of Indirect Nuclear Spin–Spin Coupling Constants 307
Olga L. Malkina
19.1 Introduction 307
19.2 The Dirac Vector Model of Spin–Spin Coupling 309
19.3 Decomposition into Individual Contributions 310
19.4 Visualization of Coupling by Real-Space Functions 318
19.5 Conclusions 323

20 First-Principles Calculations of Paramagnetic NMR Shifts *325*
Seongho Moon and Serguei Patchkovskii
20.1 Introduction *325*
20.2 Paramagnetic Shielding Tensor: The General Case Treatment *326*
20.3 Paramagnetic Shielding for an Isolated Kramers Doublet State *330*
20.4 Practical Applications *333*
20.5 Conclusions *337*

Part C NMR Parameters, Applications

21 NMR Parameters in Proteins and Nucleic Acids *341*
David A. Case
21.1 Introduction *341*
21.2 Chemical Shifts, Classical Models *342*
21.3 Chemical Shifts Calculations on Polypeptides and Proteins *345*
21.4 Chemical Shifts in Nucleic Acids *346*
21.5 Indirect Spin–Spin Couplings in Biomolecules *347*
21.6 Conclusions *349*

22 Characterizing Two-Bond NMR ^{13}C–^{15}N, ^{15}N–^{15}N, and ^{19}F–^{15}N Spin–Spin Coupling Constants across Hydrogen Bonds Using Ab Initio EOM-CCSD Calculations *353*
Janet E. Del Bene
22.1 Introduction *353*
22.2 Methods *354*
22.3 Discussion *355*
22.4 Concluding Remarks *369*

23 Calculation of NMR Parameters in Carbocation Chemistry *371*
Hans-Ullrich Siehl and Valerije Vrček
23.1 Introduction *371*
23.2 Alkyl and Cycloalkyl Cations *372*
23.3 Bicyclic and Polycyclic Carbocations *379*
23.4 Vinyl Cations *382*
23.5 π-Stabilized Carbocations *384*
23.6 Heteroatom Stabilized Carbocations *388*
23.7 Conclusions *391*

24 Aromaticity Indices from Magnetic Shieldings *395*
Zhongfang Chen, Thomas Heine, Paul v. R. Schleyer, and Dage Sundholm
24.1 Introduction *395*
24.2 An Overview of Aromaticity Indices Based on Magnetic Shielding *395*
24.3 Applications *401*
24.4 Outlook *405*

25 Fullerenes *409*
Thomas Heine
25.1 Introduction *409*
25.2 Efficient Computation of NMR Parameters of Fullerenes and Their Derivatives *410*
25.3 Classical IPR Fullerenes *411*
25.4 ^{13}C NMR Spectra of Isomeric Fullerene Addition Compounds *413*
25.5 Endohedral Fullerenes *414*
25.6 Fullerene Dimers and Dimer-like Compounds *416*
25.7 Solid State NMR of Fullerenes *418*
25.8 Summary and Perspectives *418*

26 NMR of Transition Metal Compounds *421*
Michael Bühl
26.1 Introduction *421*
26.2 Ligand Chemical Shifts *422*
26.3 Metal Chemical Shifts *424*
26.4 Spin–Spin Coupling Constants *427*
26.5 Miscellaneous *428*
26.6 Conclusion and Outlook *429*

27 Characterization of NMR Tensors via Experiment and Theory *433*
Roderick E. Wasylishen
27.1 Introduction *433*
27.2 Magnetic Shielding and Chemical Shifts *434*
27.3 Nuclear Spin–Spin Coupling *439*
27.4 NMR Spectra of Quadrupolar Nuclei in Solids *443*
27.5 Conclusions *444*

28 Calculations of Nuclear Magnetic Resonance Parameters in Zeolites *449*
Annick Goursot and Dorothée Berthomieu
28.1 Introduction *449*
28.2 Theoretical Methods *451*
28.3 NMR of Framework Elements: Structure Characterization *453*
28.4 ^{1}H NMR: Acidity and Proton Transfer *455*
28.5 NMR Studies of Guest Molecules in Zeolites: in situ NMR *457*
28.6 Conclusions *459*

Part D EPR Parameters, Methodological Aspects

29 DFT Calculations of EPR Hyperfine Coupling Tensors *463*
Markéta L. Munzarová
29.1 Introduction *463*
29.2 Theoretical Background *464*

29.3 The Performance of the Model *467*
29.4 Concluding Remarks *479*

30 Ab Initio Post-Hartree–Fock Calculations of Hyperfine Coupling Tensors and Their Comparison with DFT Approaches *483*
Bernd Engels
30.1 Introduction *483*
30.2 Problems Appearing in MR-CI Computations of A_{iso} *485*
30.3 Error Cancellations in Computations of A_{iso} with DFT *489*
30.4 Concluding Remarks *491*

31 Alternative Fermi Contact Operators for EPR and NMR *493*
Vitaly A. Rassolov and Daniel M. Chipman
31.1 Introduction *493*
31.2 Derivation of New Alternative Operators *494*
31.3 Formal Properties of Short-Range Alternative Operators *496*
31.4 EPR Calculations *499*
31.5 NMR Calculations *501*
31.6 Conclusions *503*

32 Calculation of EPR g-Tensors with Density Functional Theory *505*
Serguei Patchkovskii and Georg Schreckenbach
32.1 Introduction *505*
32.2 The Physical Origin of the g-Tensor *506*
32.3 DFT Expressions for g-Tensors of Isolated Molecules *508*
32.4 Numerical Performance of the DFT Approaches *519*
32.5 Summary and Outlook *530*

33 Ab Initio Calculations of g-Tensors *533*
Gerald H. Lushington

34 Zero-Field Splitting *541*
Frank Neese
34.1 Introduction *541*
34.2 Zero-Field Splittings in EPR Spectroscopy *542*
34.3 Theory of Zero-Field Splittings *552*
34.4 Calculation of Zero-Field Splittings *557*
34.5 Conclusions *561*

Part E EPR Parameters, Applications

35 Computation of Hyperfine Coupling Tensors to Complement EPR Experiments *567*
Fuqiang Ban, James W. Gauld, and Russell J. Boyd
35.1 Introduction *567*

35.2 Insight Gained from a Conventional Ab Initio Approach *568*
35.3 Benchmark Results Using Conventional Methods on Static Gas-phase Structures *568*
35.4 The Performance of Contracted Pople Basis Sets for Small Radicals Consisting Only of First-Row Atoms *570*
35.5 Density Functional Theory: An Alternative to a Conventional Ab Initio Approach *571*
35.6 Consideration of Environmental Effects *572*
35.7 Illustration of the Applications of DFT Methods to Biological Radicals *574*
35.8 Summary *578*

36 Applications to EPR in Bioinorganic Chemistry *581*
Frank Neese
36.1 Introduction *581*
36.2 Biological Metal Sites *582*
36.3 Concluding Remark *589*

Index *593*

Foreword

It is difficult to overemphasize the importance of magnetic resonance techniques in chemistry. Experimental spectra can usually be successfully interpreted empirically, but more difficult cases require a prediction based on the electronic structure. In the last 25 years the calculation of magnetic resonance parameters from first principles has become a powerful research tool that can significantly enhance the utility of magnetic resonance techniques when empirical interpretations are insufficient. This can be crucial even for NMR spectra of organic molecules, where the interpretations are the simplest and where empirical material has been collected for half a century. Examples can be found in such diverse fields as the identification of new fullerenes, the use of calculated chemical shifts as probes of peptide conformation, and the study of hydrogen bonding. Calculations play an even more important role in the inorganic and organometallic fields, where empirical interpretations are far more difficult. The ability to calculate NMR and EPR parameters also increases the efficacy of electronic structure calculations. Computed energies of different structures are often too close to allow a unique identification of the stable isomer. Calculated NMR spectra, however, are often significantly different, so that even simple calculations can lead to unambiguous identification in such cases.

The unprecedented improvement in the cost-effectiveness ratio of computers (about six orders of magnitude over the last 20 years), and the continuing fast pace of development, together with improved computational techniques, will certainly make the calculation of NMR and EPR parameters more routine and more widespread in the future.

This book, then, is particularly timely, edited as it is by three researchers of the younger generation who have themselves played an important role in the development and application of theoretical techniques. The author list includes many of the original developers of improved theoretical methods, as well as a number of leaders in chemical applications, offering a comprehensive coverage of the field.

The calculation of NMR and EPR parameters is less straightforward than the calculation of most other molecular properties. Understanding the source of these difficulties led ultimately to their successful solution. In the theory of NMR chemical shifts, for instance, Hameka has clarified many of the concepts, paving the way to Ditchfield's seminal work on Gauge-Independent (later Gauge-Including) Atomic Orbitals (GIAOs). However, computers and programs in the early seventies were

Calculation of NMR and EPR Parameters. Theory and Applications.
Edited by Martin Kaupp, Michael Bühl, Vladimir G. Malkin
Copyright © 2004 WILEY-VCH Verlag GmbH & Co. KGaA, Weinheim
ISBN: 3-527-30779-6

not yet ready for calculations on chemically relevant larger molecules. A renaissance in NMR chemical shift calculations began around a decade later, with the Individual Gauge for Localized Orbitals (IGLO) method developed by Kutzelnigg and coworkers, with a parallel development by Hansen and Bouman. It took a few more years to show that the currently preferred GIAO method can achieve similar computational efficiency.

The calculation of hyperfine coupling parameters suffers from two major difficulties. Firstly, electron correlation is important, particularly when the direct effect – due to the spin density of the unpaired orbital – vanishes for reasons of symmetry. Much of our understanding of this problem is due to Davidson's analysis. The other problem is high basis set sensitivity, due to the local nature of the interaction. A possible solution for Gaussian basis sets was calculated early on by Meyer; alternative methods are discussed in the present volume.

The calculation of spin-spin coupling constants has a long history but until very recently has received less attention than NMR shieldings, and therefore a summary of recent progress in the field is particularly welcome. Another timely topic, both for chemical shifts and for spin-spin couplings, is the effect of relativity. Because of its importance in inorganic chemistry, this has been in the forefront of recent theoretical work, and is well covered in several chapters. The calculation of electric field gradients, necessary for predicting nuclear quadrupole coupling constants, complements the calculation of NMR parameters. Some other recent topics of high interest include the theory of NMR in paramagnetic systems, and the calculation of EPR *g*-tensors and zero-field splittings. The interpretation of resonance parameters in terms of chemical concepts, although necessarily a somewhat arbitrary procedure, is important for the chemical community; its inclusion here fills a void.

The book covers a wide range of methods, from semi-empirical through density functional to highly accurate correlated wave functions where vibrational corrections become important. The chapter on extended systems will no doubt help bridge the gap between the chemistry and the physics communities in this area. The introductory chapters, written by distinguished scholars, will be particularly useful for anybody entering the field. Finally, the application chapters provide broad coverage, and will be a valuable guide to future work.

In summary, this book promises to become the standard reference for the calculation of NMR and EPR parameters, and will undoubtedly stimulate research in this fascinating and important field.

Peter Pulay Jan. 2004

Department of Chemistry and Biochemistry
Fulbright College of Arts and Sciences
University of Arkansas, Fayetteville, Arkansas

List of Contributors

Jochen Autschbach
Department of Chemistry
University of Buffalo
State University of New York
312 Natural Sciences Complex
Buffalo, NY 14260-3000
USA

Fuqiang Ban
Department of Chemistry
Dalhousie University, Halifax
Nova Scotia
Canada B3H 4J3

Russell J. Boyd
Department of Chemistry
& Biochemistry
University of Windsor
Windsor, Ontario
Canada N9B 3P4

Dorothée Berthomieu
UMR 5618 CNRS, ENSCM
8 rue de l'Ecole Normale
34296 Montpellier Cédex 5
France

Michael Bühl
Max-Planck-Institute
for Coal Research
Kaiser-Wilhelm-Platz 1
45470 Mülheim an der Ruhr
Germany

David A. Case
Department of Molecular Biology
The Scripps Research Institute
La Jolla, CA 92037
USA

Zhongfang Chen
Computational Chemistry Annex
The University of Georgia
Athens, GA 30602-2525
USA

Daniel M. Chipman
Radiation Laboratory
University of Notre Dame
Notre Dame, IN 46556
USA

Ilaria Ciofini
Laboratoire d'Electrochimie
et Chimie Analytique
CNRS-UMR7575
Ecole Nationale Supérieure
de Chimie de Paris
11, Rue P. et M. Curie
75231 Paris
France

Janet E. Del Bene
Department of Chemistry
Youngstown State University
Youngstown, Ohio 44555
USA

Calculation of NMR and EPR Parameters. Theory and Applications.
Edited by Martin Kaupp, Michael Bühl, Vladimir G. Malkin
Copyright © 2004 WILEY-VCH Verlag GmbH & Co. KGaA, Weinheim
ISBN: 3-527-30779-6

Bernd Engels
Institute of Organic Chemistry
University of Würzburg
Am Hubland
97074 Würzburg
Germany

James W. Gauld
Department of Chemistry
& Biochemistry
University of Windsor
Windsor, Ontario N9B 3P4
Canada

Jürgen Gauss
Institute of Physical Chemistry
University of Mainz
55099 Mainz
Germany

Annick Goursot
UMR 5618 CNRS, ENSCM,
8 rue de l'Ecole Normale
34296 Montpellier Cédex 5
France

Thomas Heine
Institute of Physical Chemistry and
Electrochemistry
Technical University of Dresden
Mommsenstraße 13
01062 Dresden
Germany

Trygve Helgaker
Department of Chemistry
University of Oslo
P.O. Box 1033 Blindern
0315 Oslo
Norway

Hanspeter Huber
Department of Chemistry
The University of Basel
Klingelbergstr. 80
4056 Basel
Switzerland

Martin Kaupp
Institute of Inorganic Chemistry
University of Würzburg
Am Hubland
97074 Würzburg
Germany

Werner Kutzelnigg
Department of Theoretical Chemistry
Ruhr-University Bochum
44780 Bochum
Germany

Perttu Lantto
Department of Physical Sciences
P.O. Box 2000
90014 University of Oulu
Finland

Gerald H. Lushington
University of Kansas Molecular
Graphics and Modeling Laboratory
1251 Wescoe Hall Dr.
Lawrence, KS 66045
USA

Vladimir G. Malkin
Institute of Inorganic Chemistry
Slovak Academy of Sciences
Dubravska cesta 9
SK-84536 Bratislava
Slovak Republic

Olga L. Malkina
Institute of Inorganic Chemistry
Slovak Academy of Sciences
Dubravska cesta 9
SK-84536 Bratislava
Slovak Republic

Pekka Manninen
Department of Chemistry
P.O. Box 55 (A.I. Virtasen aukio 1)
00014 University of Helsinki
Finland

Francesco Mauri
Laboratoire de Minéralogie-Cristallogr. de Paris
Université Pierre et Marie Curie
tour 16, case 115
4 Place Jussieu
75252 Paris, Cedex 05
France

Seongho Moon
Department of Molecular Biology
The Scripps Research Institute
10550 North Torrey Pines Road
La Jolla, California 92037
USA

Markéta L. Munzarová
National Centre
for Biomolecular Research
Faculty of Sciences
Kotlárská 2
61137 Brno
Czech Republic

Witold Nazarewicz
Department of Physics and Astronomy
University of Tennessee
401 Nielsen Physics Building
Knoxville, Tennessee 37996-1200
USA

Frank Neese
Max-Planck-Institute of Bioinorganic Chemistry
Postfach 10 13 65
45470 Mülheim an der Ruhr
Germany

Serguei Patchkovskii
Steacie Institute for Molecular Sciences
National Research Council
of Canada, 100
Sussex Drive
Ottawa, Ontario K1A 0R6
Canada

Magdalena Pecul
Department of Chemistry
University of Warsaw
Pasteura 1
02-093 Warsaw
Poland

Markus Pernpointner
Faculty of Chemistry
Institute of Physical Chemistry
Ruprecht-Karls-University of Heidelberg
Im Neuenheimer Feld 229
69120 Heidelberg
Germany

Chris J. Pickard
University of Cambridge
Cavendish Laboratory, TCM Group
Madingley Rd.
Cambridge, CB3 OHE
Great Britain

Pekka Pyykkö
Department of Chemistry
P.O. Box 55 (A.I. Virtasen aukio 1)
00014 University of Helsinki
Finland

Vitaly A. Rassolov
Department of Chemistry and Biochemistry
University of South Carolina
691 Sumter Street
Columbia, SC 29208
USA

Torgeir A. Ruden
Department of Chemistry
University of Oslo
P.O. Box 1033 Blindern
0315 Oslo
Norway

Kenneth Ruud
Department of Chemistry
University of Tromsø
9037 Tromsø
Norway

Paul von Rague Schleyer
University of Georgia
Department of Chemistry
Athens, GA 30602-2556
USA

Georg Schreckenbach
University of Manitoba
Winnipeg, Manitoba, R3T 2N2
Canada

Peter Schwerdtfeger
Department of Chemistry
The University of Auckland
Private Bag 92109, Auckland
New Zealand

Debra J. Searles
School of Science
Griffith University
Brisbane, Qld 4111
Australia

Gotthard Seifert
Institute of Physical Chemistry and
Electrochemistry
Technical University of Dresden
Mommsenstr. 13
01062 Dresden
Germany

Hans-Ullrich Siehl
Department of Organic Chemistry I
University of Ulm
89069 Ulm
Germany

John F. Stanton
Institute for Theoretical Chemistry
Departments of Chemistry
and Biochemistry
The University of Texas at Austin
Austin, TX 78712
USA

Dage Sundholm
Department of Chemistry
P.O. Box 55 (A.I. Virtasen aukio 1)
00014 University of Helsinki
Finland

Juha Vaara
Department of Chemistry
P.O. Box 55 (A.I. Virtasen aukio 1)
00014 University of Helsinki
Finland

Christoph van Wüllen
Technical University Berlin, Sekr. C3
Straße des 17. Juni 135
10623 Berlin
Germany

Valerije Vrcek
Faculty of Pharmacy and Biochemistry
University of Zagreb
A. Kovacica 1
10000 Zagreb
Croatia

Roderick E. Wasylishen
Department of Chemistry
Gunning/Lemieux Chemistry Centre
University of Alberta
Edmonton, Alberta T6G 2G2
Canada

Tom Ziegler
Department of Chemistry
University of Calgary
Calgary, Alberta T2N-1N4
Canada

Part A
Introductory Chapters

Calculation of NMR and EPR Parameters. Theory and Applications.
Edited by Martin Kaupp, Michael Bühl, Vladimir G. Malkin
Copyright © 2004 WILEY-VCH Verlag GmbH & Co. KGaA, Weinheim
ISBN: 3-527-30779-6

1
Introduction: The Quantum Chemical Calculation of NMR and EPR Parameters

Martin Kaupp, Michael Bühl, and Vladimir G. Malkin

It is hard to overestimate the impact of magnetic resonance spectroscopy on modern chemistry. NMR in particular is one of the most important analytical tools, and many an area in natural and life sciences has benefited tremendously from it. The widespread application of NMR and its complement for paramagnetic species, EPR, has entailed an increasing demand for a reliable theoretical treatment of the underlying spectroscopic parameters. Quantum chemical theory has now matured to an extent that it can significantly enhance the information that can be extracted from the spectra, thereby widening the interpretative and analytical power of the respective spectroscopical method.

While early theoretical approaches aimed exclusively at simple, qualitative models, the past decades have seen increasingly quantitative treatments, in particular by ab initio and density functional methods. Progress in this field has been tremendous, starting from the pioneering work of Kutzelnigg and others in the 1980s on chemical shifts. Meanwhile, many more NMR and EPR parameters are in the focus of quantum chemical study, including nuclear spin–spin coupling, nuclear quadrupole coupling, EPR hyperfine coupling, electronic *g*-tensors, zero-field splittings, and paramagnetic NMR parameters. Many of the developed quantum chemical methods have found their way into routine application to questions in chemistry, biology, and solid-state physics. This has widened the group of researchers involved in this kind of work. For example, chemical-shift calculations by quantum chemical methods are not only part of the repertoire of the quantum chemist but are increasingly used also by experimentalists to interpret their measurements. The same holds, e.g., for hyperfine coupling constants in EPR spectroscopy. Other properties, like spin–spin coupling constants and *g*-tensors are on their way to becoming more routine applications. At the same time, further methodological developments widen the range of possible applications, e.g. by including dynamical or solvent effects, or relativistic and electron correlation contributions in more and more detail. Last but not least, the detailed interpretation of the computed MR parameters leads to a direct link from experiment to the electronic structure of molecules, liquids or solids.

The variety of methods available has started to become bewildering to the non-initiated, and even experts on one aspect of MR parameters may not be equally informed about others. There have been reviews on various aspects of the quantum

Calculation of NMR and EPR Parameters. Theory and Applications.
Edited by Martin Kaupp, Michael Bühl, Vladimir G. Malkin
Copyright © 2004 WILEY-VCH Verlag GmbH & Co. KGaA, Weinheim
ISBN: 3-527-30779-6

chemical calculation of magnetic resonance parameters [1], as well as a few proceedings that have emerged from international conferences dedicated to the subject [2]. The basic aspects are also beginning to find their way into standard textbooks of theoretical and computational chemistry [3]. However, to keep an overview of the entire field has become more and more difficult, and the access to information on a particular question related to methodological aspects or practical application is no longer a trivial exercise. There is thus a need for a concise yet reasonably comprehensive treatment which collects the expertise in the various subfields of the quantum chemical calculation of MR parameters and which makes this information available to a wider audience, ranging from theory experts via EPR/NMR experimentalists in academia and industry to graduate or advanced undergraduate students in chemistry and the neighboring disciplines.

It is the purpose of this book to provide such a broad overview. Experts in the various subfields give concise reviews on the most important aspects of methodology and on representative applications, in order to provide easy access to the further literature in the field. Since many of the topics are the subject of active research and development, the book affords also a snapshot of the state-of-the-art in this multifaceted field.

The separation between methodology and applications in the various chapters is not a complete one. That is, most of the methodological chapters may include some examples of applications, and the application chapters may contain brief methodological sections. In this way, the close connection between theoretical development and important fields of application becomes clear to the reader. While we have tried to cover a wide range of topics and subfields, it is impossible to include each and every aspect of the theory of magnetic resonance. In particular, we have concentrated on quantum chemical methods. Some of the older, more approximate models, such as ligand field theory are thus not covered to the same extent as the more quantitative methodologies developed during the past decades. With small exceptions, we also deliberately do not attempt to cover the theory of the spectroscopic measurement, which is available in many NMR and EPR textbooks.

The book is organized as follows: Historical developments and fundamentals of the theory of NMR and EPR parameters are sketched in Chapters 2–5. The methodology of nonrelativistic computation of NMR parameters is detailed in Chapters 6–11, followed by reviews of how to treat effects of thermal motion and solvents on these parameters (Chapters 12–14). Chapters 15–17 give an overview of the relativistic extensions of the theory of NMR chemical shifts and spin–spin coupling constants, and interpretative tools are scrutinized in Chapters 18 and 19. An account of the theory of NMR chemical shifts of paramagnetic compounds (Chapter 20) concludes the predominantly methodological aspects of NMR parameters. Chapters 21–28 are devoted to illustrative applications of NMR computations in various areas of chemistry. The methodology of calculating EPR parameters is developed in Chapters 29–34, and applications to systems of biological interest are covered in Chapters 35 and 36.

References

1 See the introductions of the respective chapters of this book and the literature cited therein.

2 a) *Nuclear Magnetic Shielding and Molecular Structure*, ed. J. A. Tossell, NATO ASI Series Vol. C 386, Kluwer, Dordrecht 1993; b) Special Issue on Quantum Chemical Calculations of NMR and EPR Parameters, eds. M. Kaupp, V.G. Malkin, *J. Comput. Chem.* **1999**, *20*, 1199–1327; c) *Modeling NMR Chemical Shifts*, eds. J. C. Facelli, A. C. de Dios, ACS Symposium Series Vol. 732, American Chemical Society, Washington DC 1999.

3 E.g., a) P. W. Atkins, R. S. Friedman, *Molecular Quantum Mechanics*, 3rd edition, Oxford University Press, Oxford 1997; b) F. Jensen, *Introduction to Computational Chemistry*, Wiley, New York 1998.

2
Theory of NMR parameters. From Ramsey to Relativity, 1953 to 1983

Pekka Pyykkö

The history of NMR, like any history, has no real beginning.

E. D. Becker, C. L. Fisk and C. L. Khetrapal [1].

2.1
Introduction

In NMR spectroscopy, the observed nuclei are shielded from the full external magnetic field, **B**, by the electron shell. Two nuclear magnetic moments can also be pairwise coupled by a magnetic polarization of the electron system. The connection between the corresponding NMR spin–spin coupling tensor, **J**, and shielding tensor, $\boldsymbol{\sigma}$ of a molecule with its non-relativistic electronic wavefunction was found by Norman F. Ramsey [2–7] in 1950–53. For a review see Ref. 8. During the following three decades, a fair amount of qualitative understanding and semiempirical results were accumulated. Even a number of good, by the standard of the time, ab initio calculations were published as early as in the middle 1960s. This body of work is now often forgotten and we here try to rescue it from oblivion. Some useful reviews on the subject are quoted in Table 2.1. We refer to them for full coverage. Only some highlights or broad trends will be mentioned here. An independent historical account is given by Hameka [9]. Several recent articles on this general topic can be found in Volumes 7 and 9 of the Encyclopedia of NMR [1].

Calculation of NMR and EPR Parameters. Theory and Applications.
Edited by Martin Kaupp, Michael Bühl, Vladimir G. Malkin
Copyright © 2004 WILEY-VCH Verlag GmbH & Co. KGaA, Weinheim
ISBN: 3-527-30779-6

Table 2.1. Some reviews covering the theoretical calculations of NMR parameters in 1953–83.

Year	Author	Ref.	Topic
1960	Karplus	[83]	Review on 'weak interactions'.
1965	Barfield and Grant	[84]	Spin–spin coupling.
1965	Hameka	[85]	Book. Includes magnetic properties.
1966	Lipscomb	[86]	Chemical shifts.
1966	Musher	[87]	Theory of chemical shifts.
1967	Davies	[88]	Magnetic properties of molecules. Book.
1967	Letcher and Van Wazer	[89]	^{31}P shifts.
1967	O'Reilly	[90]	Chemical shift calculations.
1968	Memory	[91]	Theory of magnetic-resonance parameters. Book.
1969	Pyykkö	[92]	Spin–spin coupling until 1968.
1971	Emsley and Phillips	[93]	Fluorine chemical shifts.
1971	Murrell	[94]	Spin–spin coupling.
1972–76	Grinter	[95]	Spin–spin coupling[a].
1972	Lipscomb	[38]	Review. Includes chemical shifts.
1972–74	Raynes	[96]	Nuclear shielding[a].
1974	Das	[97]	Relativistic theory of electrons. Includes solid-state nuclear spin–spin coupling. Book.
1974	Ditchfield and Ellis	[98]	^{13}C shifts.
1975	Mallion	[99]	Nuclear shielding[a].
1976	Ditchfield	[100]	Nuclear shielding[a].
1976	Ellis and Ditchfield	[101]	^{13}C coupling constants.
1977	Kowalewski	[102]	Spin–spin coupling 1969–75.
1977–78	Pachler	[103]	Nuclear spin–spin coupling[a].
1978	Raynes	[104]	Theoretical and physical aspects of nuclear shielding[a].
1978	Webb	[105]	Theory of NMR parameters.
1979–80	Pachler and Chalmers	[106]	Nuclear spin–spin coupling[a].
1979	Raynes	[107]	Theoretical and physical aspects of nuclear shielding[a].
1980	Ando and Asakura	[108]	Shielding and stereochemistry of synthetic polymers.
1980–93	Jameson et al.	[109]	Shieldings[a]. Theoretical, physical and inorganic aspects.
1982	Kowalewski	[110, 111]	Spin–spin coupling 1977–81.
1983	Ando and Webb	[112]	Theory of NMR parameters. Book.
1983	Kowalewski	[113]	Spin–spin coupling[a].
1986	Jameson and Osten	[65]	Isotope effects on shielding.
1987	Jameson	[114]	Spin–spin coupling.
1987	Jameson and Mason	[115]	Chemical shifts.

a Annual reviews, mostly June to May.

2.2
Spin–Spin Coupling

2.2.1
Successive Approximations

After Ramsey's theories, the next step was taken by McConnell [10], who related long-distance ^{n}J (AB) coupling constants to the bond-order between atoms A and B. As in Ramsey's own numerical estimates, an effective-energy-denominator, ΔE, and the closure approximation were used for the second-order terms:

$$\sum_{n\neq 0} \frac{|\, n\rangle\langle n\,|}{E_0 - E_n} \simeq \frac{1}{\Delta E}. \tag{2.1}$$

On the semiempirical side, valence bond (VB) models were popular for a while. The *Karplus relation* between three-bond coupling constants, ^{3}J(HH) and the dihedral angle, ϕ, was one classical VB result. The original example [11] was ethane; the applicability of the result was discussed later by Karplus [12]. The influence of the hybridization and the s-character on ^{1}J(CH) and ^{2}J(HH) coupling constants was studied by Juan and Gutowsky [13] as a function of the substituents. Similarly, Karplus and Grant [14] related the J to hybridization and charge distribution in chemical bonds.

Pople and Santry [15] avoided the average energy approximation at semiempirical level by introducing, instead of the bond-order, the quantity

$$\pi_{AB} = 4 \sum_{I}^{\text{occ}} \sum_{J}^{\text{unocc}} (E_I - E_J)^{-1} C_{IA} C_{IB} C_{JA} C_{JB}. \tag{2.2}$$

Here I and J are molecular orbitals while A and B are atoms, or s-type basis orbitals on them. This level is called 'sum-over-states' (SOS) perturbation theory.

2.2.2
FPT

Instead of perturbation theory or response theory, such as 'coupled-Hartree–Fock' (CHF), one can use a numerical approach by introducing finite values for one nuclear moment. This 'finite perturbation theory' (FPT) approach was first used at INDO (Intermediate neglect of differential overlap) level for the Fermi-contact part of J by Pople et al. [16–18]. A popular textbook on this level of theory was that by Pople and Beveridge [19]. A comparison between SOS and FPT for J of H_2 was carried out by Ditchfield et al. [20].

2.2.3
Ab Initio Calculations

The available wavefunctions for H_2 were used for J calculations by Ishiguro [21] and by Das and Bersohn [22]. Kato and Saika [23] calculated the J of the HF molecule at a Hartree-Fock SOS level. For further examples, see the reviews in Tab. 2.1 and Tab. 2.2.

Table 2.2. Some early ab initio results. Shieldings, σ, in ppm. Coupling constants, J, in Hz. For experimental results, and the convergence of modern calculations towards them, see Helgaker et al. [116].

Molecule	Property	Year	Value	Ref.
HF	σ (F)	1964	404.65	36
		1964	378.1	37
		1974	411.7	39
		1975	400.34	76
			410.6[a]	
	σ (H)	1964	28.11	36
		1964	27.48	37
		1974	30.61	39
		1975	27.00	76
			28.5(2)[a]	
	J(HF)	1967	621	23
			500(20)[a]	
ClF	σ (F)	1972	700[b]	
			667[a,b]	

a Experimental value.
b See Table 5.12. of Ref. [38].

2.2.4
Relativistic Effects

Relativistic effects, especially for s orbitals if their contribution is dominant, can be most simply estimated through multiplicative correction factors for the atomic magnetic dipole hyperfine matrix elements (see [24, 25] and references therein). It should be emphasized that the changes are large: Relativistic effects increase the s-orbital matrix element by a factor of roughly 3 for a heavy element ($Z \geq 80$). For J(HgHg) coupling constants, the relativistic increase is an order of magnitude.

A more fundamental way is to formulate a relativistic analog of Ramsey's theory by introducing the magnetic vector potentials

$$\mathbf{A}_A(\mathbf{r}) = \frac{\boldsymbol{\mu}_A \times \mathbf{r}_A}{r_A^3}, \tag{2.3}$$

for the two nuclei A and B in the perturbation

$$H' = c\boldsymbol{\alpha} \cdot (\mathbf{A}_A + \mathbf{A}_B), \tag{2.4}$$

in second-order perturbation theory with four-component (Dirac) wavefunctions, and by selecting the terms, bilinear in μ_A and μ_B [26]. Here $\boldsymbol{\alpha}$ is a Dirac matrix. The implementations in that paper consisted of a simple molecular orbital model only, but gave already the prediction that relativistic effects should increase the relative anisotropy of the **J**. A later SOS implementation by Pyykkö and Wiesenfeld [27], combining atomic Dirac–Fock hyperfine integrals and relativistic extended Hückel (REX) molecular orbitals, localized this increase to a phase-factor difference between $s_{1/2}$ and $p_{1/2}$ orbitals. While the s–s combination gives a diagonal (K, K, K), the $s_{1/2}$–$p_{1/2}$ combination gives a diagonal (K, -K, -K). The same paper gave insight to problems, like the decrease and sign change of ^1J(EH) in H_2E molecules, E = O–Te. Furthermore, the paper led to a partial revision of the symmetry rules [28] for **J**-tensors in molecules with various symmetries by Buckingham et al. [29]. If nothing else holds in a rough semiempirical calculation, symmetry will.

2.2.5
Self-Coupling Effects

For s-electrons, a relativistic treatment is imperative [30] and the finite result arises from the finite nuclear size. For non-spherical nuclear sites, a second-order magnetic hyperfine interaction gives a small 'pseudoquadrupole' interaction [31–33].

2.3
Chemical Shifts

2.3.1
Ab Initio Calculations

What would now be known as 'coupled Hartree-Fock' or response methods, were effectively introduced to ab initio calculations by the group of Lipscomb [34–36]. Induced current densities were plotted. The results could be contrasted to the uncoupled ones by Karplus and Kolker [37], especially on the spin–rotation constant. The diatomic molecules H_2, Li_2, N_2, F_2, LiH, HF and LiF were treated using a Slater basis. Although GIAOs (see Section 2.4) were not yet used, these papers are still worth quoting. For a review, see Lipscomb [38]. Ditchfield [39] reported GTO results for a large data set including polyatomic molecules. For some examples on the results, compared to experiment or modern calculations, see Tab. 2.2. A remarkable example is the large upfield shift of F in the ClF molecule, attributed to a small $\pi^*_{HOMO} - \sigma^*_{LUMO}$ gap [40].

2.3.2 Semiempirical Models

Jameson and Gutowsky [41] related the chemical shift ranges of elements to their $<1/r^3>$ expectation values. Simple orbital models gave insight to the shifts of acetylene, simple hydrides [42, 43], carbonyls [44] and other ^{13}C shifts [45]. Karplus and Das [46] discussed ^{19}F shifts in fluorobenzenes in terms of localized contributions and related σ to the electric field gradient, q.

2.3.3 Crystal-Field-Type Theories

Griffith and Orgel [47] related the NMR shifts of the cobaltic, d^6 S=0 ^{59}Co signals to the crystal-field splitting, $\mathbf{\Delta}$. Buckingham and Stephens [48, 49] developed a theory for the temperature-independent paramagnetic shifts of protons in transition-metal hydrides.

2.3.4 Heavy-Atom Shifts

A heavy halogen, X, can induce large upfield shifts on NMR nuclei, bound to them. Some examples are molecules like ^1HX or $X^{13}CH_3$. These shifts are known as *heavy-atom chemical shifts*. Smaller shifts of either sign can occur further out. The first person to realize that this effect was due to spin–orbit effects, was Nakagawa [50], who used third-order perturbation theory. The work appeared in Japanese in a domestic conference report. The first papers in English [51, 52] also used a third-order-PT approach at semiempirical level. The entire series of halogen-substituted methanes was studied by Cheremisin and Schastnev [53]. A notable example was the observed ^{13}C shift of 290 ppm (from methane) in CI_4. Volodicheva and Rebane [54] discussed the HX series. The semiquantitative insight from these papers remains valid. No ab initio (nor DFT) studies on this topic appeared during the period considered.

2.3.5 Lanthanide Shift Reagents

These were introduced experimentally in 1969 by Hinckley (see Ref. [1], pp. 41–43). A theory was worked out for the contact part by Golding [55] and for the pseudocontact part by Bleaney [56]. A more general form of the latter theory, with explicit sums over the full crystal-field levels at a given temperature, was published by Golding and Pyykkö [57].

2.3.6
Relativistic Theory

At Dirac level, one can again introduce the sum of the two magnetic vector potentials, the first term now coming from the external magnetic field:

$$\mathbf{A}(\mathbf{r}) = \frac{1}{2}\mathbf{B} \times \mathbf{r} + \frac{\boldsymbol{\mu} \times \mathbf{r}}{r^3}, \tag{2.5}$$

In second-order perturbation theory, the energy terms bilinear in **B** and μ will then correspond to the NMR shielding. This idea was published in 1983 independently by Pyper [58], Pyykkö [59] and Zhang and Webb [60]. It was already noted that the 'diamagnetic' shielding term of Ramsey arises approximately from the positron-like intermediate states. For the shielding, this is a large term.

2.3.7
Absolute Shielding Scales

A connection between the paramagnetic shielding term and the spin-rotation constants was found by Ramsey [61]. For a later review, see Flygare [62] and further references in Ref. [8].

2.3.8
Symmetry of the Shielding Tensor

The rules, connecting the site symmetry of the NMR nucleus to the number of independent components of the $\boldsymbol{\sigma}$ tensor, were published by Buckingham and Malm [63].

2.3.9
Isotope Shifts in the Shielding

These were first discussed by Gutowsky [64]. For a review, see Jameson and Osten [65].

2.4
General Aspects

2.4.1
Gauge-Including Atomic Orbitals

These are also called gauge-independent atomic orbitals and were originally suggested by London [66] in a theory of magnetic susceptibilities. He quotes large anisotropies for bismuth, graphite and aromatic compounds. These orbitals were introduced for NMR shifts by Pople [42, 43]. Their first ab initio applications on an NMR

shift seems to be the H_2 work by Hameka [67]. For later work, see Zeroka and Hameka [68]. STOs were still used. The names 'gauge invariant atomic orbital' [69] or 'eichinvariante Atomfunktion' [70] were used in susceptibility calculations in 1959 by him. The acronym GIAO was introduced in 1962 by Hameka [71]. Pople [44] suggested in 1962 the name 'gauge-dependent atomic orbital'.

For the shielding problem (or susceptibilities), the question is, from which *gauge origin* one should take the first term in Eq. (2.55). If one uses a basis of GIAOs,

$$\chi_\nu = \phi_\nu \exp(-\frac{ie}{\hbar c}\mathbf{A}_i \cdot \mathbf{r}), \tag{2.6}$$

for each atomic orbital ϕ_ν at centre i, with the $\mathbf{A}_i$ counted from a common origin, the results will then be independent of that origin. This requirement will exist in relativistic and non-relativistic theories alike.

As the partition of the shielding into diamagnetic and paramagnetic terms depends on the gauge origin, it is in certain cases possible to reduce the latter one to zero, as suggested by Rebane [72]. It can be emphasized that their sum is constant at the basis-set limit [73] in the CHF approximation (called by physicists the 'random-phase approximation', RPA) [74, 75].

The first devices for an efficient implementation of the GIAO ideas appeared at the end of the title period. Following earlier discussions on optimal gauge origin [76, 77], Kutzelnigg [78] introduced the 'individual gauge for localized orbitals' (IGLO) approach at CHF level. It was applied on simple polyatomic molecules using a Gaussian basis [79]. In retrospect the faster basis-set convergence will be an even greater advance than the actual gauge invariance.

When calculating spin–spin-coupling tensors, a logical gauge origin for each hyperfine matrix element is the nucleus in question and this has so far been considered to be an adequate choice.

2.4.2 Basis Sets

The earliest ab initio calculations of NMR parameters were performed using Slater orbitals, which may partially explain their success. Following the general move towards Gaussian orbitals, these orbitals were also adopted for the present purpose. A detailed study on the STO-nG expansions of an STO in Gaussians for the present properties was reported by Ditchfield et al. [39, 80]. Among the earliest GTO calculations were those by Lazzeretti for both $\boldsymbol{\sigma}$ [81] and $\mathbf{J}$ [82].

2.4.3 Note on Dimensions

For historical continuity, we have used Gauss-cgs units. For their conversion to SI units, see Ref. [8].

2.5 From 1983 to 2003

The developments since 1983 and the current situation will be reviewed in the chapters in this book.

Acknowledgment

The work by P.P. is supported by The Academy of Finland. This paper was written during the tenure of a Humboldt Research Prize at Erlangen.

References

1 E. D. Becker, C. L. Fisk, C. L. Khetrapal, The development of NMR, in *Encyclopedia of NMR*, eds. D. M. Grant, R. K. Harris, Vol. 1, Wiley, Chichester, **1995**.
2 N. F. Ramsey, The internal diamagnetic field correction in measurements of the proton magnetic moment, *Phys. Rev.* **1959**, *77*, 567.
3 N. F. Ramsey, Magnetic shielding in molecules, *Phys. Rev.* **1950**, *78*, 699–703.
4 N. F. Ramsey, Dependence of magnetic shielding of nuclei upon molecular orientation, *Phys. Rev.* **1951**, *83*, 540–541.
5 N. F. Ramsey, Chemical effects in nuclear magnetic resonance and in dimagnetic susceptibility, *Phys. Rev.* **1956**, *86*, 243–246.
6 N. F. Ramsey, E. M. Purcell, Interactions between nuclear spins in molecules, *Phys. Rev.* **1952**, *85*, 143–144.
7 N. F. Ramsey, Electron coupled interactions between nuclear spins in molecules, *Phys. Rev.* **1953**, *91*, 303.
8 P. Pyykkö, Perspective on Norman Ramsey's theories of NMR chemical shifts and nuclear spin–spin coupling, *Phys. Rev.* **1950**, *77*, 567 to *Phys. Rev.* **1953**, *91*, 303. *Theor. Chem. Acc.* **2000**, *103*, 214–216.
9 H. F. Hameka, Theoretical studies of Molecular Magnetism, in *Reviews of Modern Quantum Chemistry*, World Scientific, Singapore, **2002**, pp. 1237–1246.
10 H. M. McConnell, MO approximation to electron coupled interaction between nuclear spins, *J. Chem. Phys.* **1956**, *24*, 460–467.
11 M. Karplus, Contact electron–spin coupling of nuclear magnetic moments, *J. Chem. Phys.* **1959**, *30*, 11–15.
12 M. Karplus, Vicinal proton coupling in nuclear magnetic resonance, *J. Am. Chem. Soc.* **1963**, *85*, 2870–2871.
13 C. Juan, H. S. Gutowsky, VB studies of the dependence upon substitutions of C^{13}-H and Si^{29}-H coupling, *J. Chem. Phys.* **1962**, *37*, 2198–2208.
14 M. Karplus, D. M. Grant, A criterion for orbital hybridization and charge distribution in chemical bonds, *Proc. Natl. Acad. Sci. U. S.* **1959**, *45*, 1269–1273.
15 J. A. Pople, D. P. Santry, MO theory of nuclear spin–spin coupling constants. *Mol. Phys.* **1964**, *8*, 1–18.
16 J. A. Pople, J. W. McIver, N. S. Ostlund, Finite perturbation theory for nuclear spin coupling constants, *Chem. Phys. Lett.* **1967**, *1*, 465–466.
17 J. A. Pople, J. W. McIver, N. S. Ostlund, Self-consistent perturbation theory. I. Finite perturbation theory, *J. Chem. Phys.* **1968**, *49*, 2960–2964.
18 J. A. Pople, J. W. McIver, N. S. Ostlund, Self-consistent perturbation theory. II. Nuclear-spin coupling constants, *J. Chem. Phys.* **1968**, *49*, 2965–2970.
19 J. A. Pople, D. L. Beveridge, *Approximate Molecular Orbital Theory*. McGraw-Hill, New York, **1970**.
20 R. Ditchfield, N. S. Ostlund, J. N. Murrell et al., Comparison of the sum-over-states and finite perturbation theories of electrical polarizability and nuclear spin–spin coupling, *Mol. Phys.* **1970**, *18*, 433–440.
21 E. Ishiguro, Electron-coupled interaction between nuclear spins in HD molecule, *Phys. Rev.* **1955**, *111*, 203–208.

22 T. P. Das, R. Bersohn, Electric and magnetic properties of the hydrogen molecule, *Phys. Rev.* **1956**, *115*, 879–910.

23 Y. Kato, A. Saika, Perturbational calculations of the nuclear spin–spin coupling constant for the hydrogen fluoride molecule, *J. Chem. Phys.* **1967**, *46*, 1975–1981.

24 P. Pyykkö, E. Pajanne, Improved relativistic corrections to the Fermi-contact hyperfine Hamiltonian., *Phys. Lett. A* **1971**, *35*, 53–54, errata: *Phys. Lett A* **1972**, *38*, 218.

25 P. Pyykkö, E. Pajanne, M. Inokuti, Hydrogen-like relativistic corrections for electric and magnetic hyperfine integrals, *Int. J. Quantum Chem.* **1973**, *7*, 785–806.

26 P. Pyykkö, Relativistic theory of nuclear spin–spin coupling in molecules, *Chem. Phys.* **1977**, *22*, 289–296.

27 P. Pyykkö, L. Wiesenfeld, Relativistically parameterized extended Hückel calculations. IV. Nuclear spin–spin coupling tensors for main group elements, *Mol. Phys.* **1981**, *43*, 557–580.

28 A. D. Buckingham, I. Love, Theory of the anisotropy of nuclear spin coupling, *J. Mag. Reson.* **1970**, *2*, 338–351.

29 A. D. Buckingham, P. Pyykkö, J.-B. Robert et al., Symmetry rules for the indirect nuclear spin–spin coupling constants revisited, *Mol. Phys.* **1982**, *46*, 177–182.

30 E. Latvamaa, L. Kurittu, P. Pyykkö et al., On second-order magnetic hyperfine interactions in one-electron atoms: connections between the Schrödinger, Dirac and quantum electrodynamical perturbation calculations, *J. Phys. B* **1973**, *6*, 591–600.

31 N. F. Ramsey, Pseudo-quadrupole effect for nuclei in molecules, *Phys. Rev.* **1953**, *89*, 527.

32 P. Pyykkö, On nuclear pseudoquadrupole interactions in metals, *J. Phys. F: Metal Phys.* **1971**, *1*, 479–481.

33 H. B. Jansen, P. Pyykkö, Calculation of the bromine nuclear pseudoquadrupole coupling constant in the LiBr molecule using a density-of-states function deduced from overlap integrals, *in Methods and Structure of Quantum Science*, eds. J.-L. Calais, O. Goscinski, J. Linderberg et al., Plenum Press, New York, **1976**, pp. 409–416.

34 R. M. Stevens, R. M. Pitzer, W. N. Lipscomb, Perturbed Hartree–Fock calculations. I. Magnetic susceptibility and shielding of the LiH molecule, *J. Chem. Phys.* **1963**, *38*, 550–560.

35 R. M. Stevens, W. N. Lipscomb, Perturbed Hartree-Fock calculations. II. Further results for diatomic lithium hydride, *J. Chem. Phys.* **1964**, *40*, 2238–2247.

36 R. M. Stevens, W. N. Lipscomb, Perturbed Hartree–Fock calculations. III. Polarizability and magnetic properties of the HF molecule. *J. Chem. Phys.* **1964**, *41*, 184–194.

37 H. J. Kolker, M. Karplus, Theory of nuclear magnetic shielding in diatomic molecules, *J. Chem. Phys.* **1964**, *41*, 1259–1266.

38 W. N. Lipscomb, Molcular properties, in *Theoretical Chemistry. MTP International Review of Science, Vol. 1*, ed. W. Byers Brown, Butterworths, London, **1972**, 167–196.

39 R. Ditchfield, Self-consistent perturbation theory of diamagnetism. I. A gauge-invariant LCAO method for N.M.R. chemical shifts. *Mol. Phys.* **1974**, *27*, 789–807.

40 C. D. Cornwell, Interpretation of the chemical shift of CIF, *J. Chem. Phys.* **1966**, *44*, 874–880.

41 C. J. Jameson, H. S. Gutowsky, Calculation of chemical shifts. I. General formulation and the *Z* dependence, *J. Chem. Phys.* **1960**, *40*, 1714–1724.

42 J. A. Pople, The theory of chemical shifts in nuclear magnetic resonance. I. Induced current densities, *Proc. R. Soc., London* **1957**, *239*, 541–549.

43 J. A. Pople, The theory of chemical shifts in nuclear magnetic resonance. II. Interpretation of proton shifts, *Proc. R. Soc., London* **1957**, *239*, 550–556.

44 J. A. Pople, The theory of chemical shifts, *Discuss. Faraday Soc.* **1962**, *34*, 7–14.

45 J. A. Pople, The theory of carbon shifts, in N.M.R., *Mol. Phys.* **1964**, *7*, 301–306.

46 M. Karplus, T. P. Das, Theory of localized contributions to the chemical shift. Application to fluorobenzenes, *J. Chem. Phys.* **1961**, *34*, 1683–1692.

47 J. S. Griffith, L. E. Orgel, The residual paramagnetism and nuclear magnetic resonance spectra of cobaltic compounds, *Trans. Faraday Soc.* **1957**, *53*, 601–606.

48 A. D. Buckingham, P. J. Stephens, Proton chemical shifts in the nuclear magnetic resonance spectra of transition metal hydrides: Octahedral complexes, *J. Chem. Soc.* **1964**, 2747–2759.

49 A. D. Buckingham, P. J. Stephens, Proton chemical shifts in the nuclear magnetic resonance spectra of transition metal hydrides: Square-planar platinum(II) complexes., *J. Chem. Soc.* **1964**, 4583–4587.

50 N. Nakagawa, S. Sinada, S. Obinata, Heavy-atom-derived spin polarization shifts, (in Japanese), *The 6th NMR Symposium, Kyoto*, **1967**, pp. 8–12.

51 Y. Nomura, Y. Takeuchi, N. Nakagawa, Substituent effects in aromatic proton NMR spectra. III (1). Substituent effects caused by halogens, *Tetrahedron Lett.* **1969**, 639–642.

52 I. Morishima, K. Endo, T. Yonezawa, Effect of the heavy atom on the nuclear shielding constant. I. The proton chemical shifts in hydrogen halides, *J. Chem. Phys.* **1973**, *59*, 3356–3364.

53 A. A. Cheremisin, P. V. Schastnev, Effects of spin-orbital interactions on ^{13}C NMR chemical shifts in halogen-substituted methanes, *J. Magn. Reson.* **1980**, 459–468.

54 M. I. Volodicheva, T. K. Rebane, Effect of spin-orbit coupling on magnetic shielding of proton in hydrogen halides, *Teor. Eksp. Khim. (USSR)* **1978**, *14 (4)*, 447–455.

55 R. M. Golding, M. P. Halton, A theoretical study of the ^{14}N and ^{17}O N.M.R. shifts in lanthanide complexes, *Austr. J. Chem.* **1972**, *25*, 2577–2581.

56 B. Bleaney, Nuclear magnetic resonance shifts in solution due to lanthanide ions, *J. Magn. Reson.* **1972**, *8*, 91–100.

57 R. M. Golding, P. Pyykkö, On the theory of pseudocontact NMR shifts due to lanthanide complexes, *Mol. Phys.* **1973**, *26*, 1389–1396.

58 N. C. Pyper, The relativistic theory of the chemical shift, *Chem. Phys. Lett.* **1983**, *96*, 204–210.

59 P. Pyykkö, On the relativistic theory of NMR chemical shifts, *Chem. Phys.* **1983**, *74*, 1–7.

60 Z. C. Zhang, G. A. Webb, On the relativistic molecular orbital theory of diamagnetism and NMR chemical shifts, *J. Mol. Struct. (Theochem)* **1983**, *104*, 439–444.

61 N. F. Ramsey, Spin interactions of accelerated nuclei in molecules, *Phys. Rev.* **1953**, *90*, 232.

62 W. H. Flygare, Magnetic interactions in molecules and an analysis of molecular electronic distribution from magnetic parameters, *Chem. Rev.* **1974**, *74*, 653–687.

63 A. D. Buckingham, S. M. Malm, Asymmetry in the nuclear magnetic shielding tensor, *Mol. Phys.* **1971**, *22*, 1127–1130.

64 H. S. Gutowsky, Isotope effects in high resolution NMR spectroscopy, *J. Chem. Phys.* **1959**, *31*, 1683–1684.

65 C. J. Jameson, H. J. Osten, Theoretical aspects of isotope effects on nuclear shielding, *Annu. Rep. NMR Spectrosc.* **1986**, *17*, 1–78.

66 F. London, Théorie quantique des courants interatomiques dans les combinaisons aromatiques, *J. Phys., Radium* **1937**, *8*, 397–409.

67 H. F. Hameka, On the nuclear magnetic shielding in the hydrogen molecule, *Mol. Phys.* **1958**, *1*, 203–215.

68 D. Zeroka, H. F. Hameka, Calculation of magnetic shielding constants of diatomic molecules. I. General theory, *J. Chem. Phys.* **1966**, *45*, 300–311.

69 H. F. Hameka, Calculation of the magnetic susceptibility of methane, *Physica* **1959**, *25*, 626–630.

70 H. F. Hameka, Berechnung der magnetischen Eigenschaften des Wasserstoffmoleküls, *Z. Naturforsch. A* **1959**, *14*, 599–602.

71 H. F. Hameka, Theory of magnetic properties of molcules with particular emphasis on the hydrogen molecule, *Rev. Mod. Phys.* **1962**, *34*, 87–101.

72 T. K. Rebane, A variational principle for the calculation of a correction, quadratic with respect to the magnetic field intensity to the electronic of a molecule, *Zh. Eksp. Teor. Fiz.* **1960**, *38*, 938–965, transl. to English in *Sov. Phys. JETP* **1960**, *11*, 694–695.

73 S. T. Epstein, The Variation Method in Quantum Chemistry. *Academic Press, New York*, **1974**, see G. Schreckenbach, *Theor. Chem. Acc.* **2002**, *108*, 246–253 for recent comments.

74 S. T. Epstein, Gauge invariance of the Hartree–Fock approximation, *J. Chem. Phys.* **1965**, *42*, 2897–2898.

75 D. L. Lin, Gauge properties of the Hartree–Fock and random-phase approximations. *Phys. Rev. A* **1977**, *16*, 600–605.

76 A. J. Sadlej, A new solution for the gauge origin problem, *Chem. Phys. Lett.* **1975**, *36*, 129–133.

77 R. Yaris, On the choice of gauge for approximate quantum mechanical wavefunctions, *Chem. Phys. Lett.* **1976**, *38*, 460–462.

78 W. Kutzelnigg, Theory of magnetic susceptibilities and NMR chemical shifts in terms of localized quantities, *Isr. J. Chem.* **1980**, *19*, 193–200.

79 M. Schindler, W. Kutzelnigg, Theory of magnetic susceptibilities and NMR chemical shifts in terms of localized quantities. II. Application to some molecules, *J. Chem. Phys.* **1982**, *76*, 1919–1933.

80 R. Ditchfield, D. P. Miller, J. A. Pople, Self-consistent molecular-orbital methods. VII. Convergence of Gaussian expansions of Slater-type atomic orbitals in calculations of first- and second-order properties, *J. Chem. Phys.* **1970**, *53*, 613–619.

81 P. Lazzeretti, R. Zanasi, Calculations of proton magnetic shielding constants in polyatomic molecules, *J. Chem. Phys.* **1978**, *68*, 832–839.

82 P. Lazzeretti, Calculation of nuclear spin–spin coupling constants in methanol molecule, *J. Chem. Phys.* **1979**, *71*, 2514–2521.

83 M. Karplus, Weak interactions in molecular quantum mechanics, *Rev. Mod. Phys.* **1960**, *32*, 455–460.

84 M. Bartfield, D. M. Grant, Theory of nuclear spin–spin coupling, *Adv. Magn. Reson.* **1965**, *1*, 149–193.

85 H. F. Hameka, *Advanced Quantum Chemistry*, Addison Wesley, **1965**.

86 W. N. Lipscomb, The chemical shift and other second-order magnetic and electric properties of small molecules, *Adv. Magn. Reson.* **1966**, *2*, 137–176.

87 J. I. Musher, Theory of the chemical shift, *Adv. Magn. Reson.* **1966**, *2*, 177–224.

88 D. W. Davies, *The Theory of Electric and Magnetic Properties of Molecules*, Wiley, London, **1964**.

89 J. H. Letcher, J. R. Van Wazer, Quantum mechanical theory of P^{31} chemical shifts, in *P^{31} Nuclear Magnetic Resonance*, eds. M. Grayson, E. J. Griffith, Vol. 5, Interscience, New York, **1964**, pp. 75–167.

90 D. E. O'Reilly, Chemical shift calculations, *Progr. NMR Spectrosc.*, **1967**, *2*, 1–61.

91 J. D. Memory, *Quantum Theory of Magnetic Resonance Parameters*, McGraw-Hill, New York, **1968**.

92 P. Pyykkö, Quantum theory of electron coupled nuclear spin–spin interactions in molecules and solids, Umpublished internal report, Aarhus University, **1969** (194 references).

93 J. W. Emsley, L. Phillips, Fluorine chemical shifts. *Progr. NMR Spectrosc.* **1971**, *7*, 1–113.

94 J. N. Murrel, The theory of nuclear spin–spin soupling in high resolution NMR spectroscopy, *Progr. NMR Spectrosc.* **1971**, *6*, 1–60.

95 R. Grinter, Nuclear spin–spin coupling, in *Specialist Periodical Reports, Nuclear Magnetic Resonance*, The Chemical Society, London, **1972**, Vol. 1, pp. 51–113, also **1973–1976**, Vol. 2–5.

96 W. T. Raynes, Theoretical and physical aspects of nuclear shielding, *in Specialist Periodical Reports, Nuclear Magnetic Resonance*, The Chemical Society, London, **1972**, Vol. 1, pp. 1–50, also, **1973**, **1974**, Vol. 2, 3.

97 T. P. Das, *Relativistic, Quantum Mechanics of Electrons*, Harper and Row, New York, **1974**.

98 R. Ditchfield, P. D. Ellis, Theory of ^{13}C chemical shifts, in *Topics in Carbon-13 NMR Spectroscopy*, ed. G. C. Levy, Vol. 1, Wiley, New York, **1974**, pp. 1–51.

99 R. B. Mallion, Nuclear shielding, in *Specialist Periodical Reports, Nuclear Magnetic Resonance*, The Chemical Society, London, **1975**, Vol. 4, pp. 1–66.

100 R. Ditchfield, Nuclear shielding, *Specialist Periodical Reports, Nuclear Magnetic Resonance*, The Chemical Society, London, **1976**, Vol. 5, pp. 1–54.

101 P. D. Ellis, R. Ditchfield, Theory of indirect nuclear spin–spin coupling constants with applications to carbon-13 NMR, in *Topics in Carbon-13 NMR Spectroscopy*, ed. G. C. Levy, Wiley, New York, **1976**, Vol. 2, pp. 434–476.

102 J. Kowalewski, Calculations of nuclear spin–spin coupling constants. *Progr. NMR Spectrosc.* **1977**, *11*, 1–78.

103 K. G. R. Pachler, Nuclear spin–spin coupling, *Specialist Periodical Reports, Nuclear Magnetic Resonance*, The Chemical Society, London, **1977**, Vol. 6, also, **1978**, Vol. 4, pp. 73–124.

104 W. T. Raynes, Theoretical and physical aspects of nuclear shielding, *Specialist Periodical Reports, Nuclear Magnetic Resonance*, The Chemical Society, London, **1978**, Vol. 7, pp. 1–25.

105 G. A. Webb, Background theory of NMR parameters, in *NMR and the Periodic Table*, eds. R. K. Harris, B. E. Mann, Academic Press, London, **1978**, pp. 49–89.

106 K. G. R. Pachler, A. A. Chalmers, Nuclear spin–spin coupling, *Specialist Periodical Reports, Nuclear Magnetic Resonance*, The Chemical Society, London, **1979**, Vol. 8; later review **1980**, Vol. 9.

107 W. T. Raynes, Theoretical and physical aspects, of nuclear shielding, *Specialist Periodical Reports, Nuclear Magnetic Resonance,* The Chemical Society, London, **1979**, Vol. 8, pp. 1–19.

108 I. Ando, T. Asakura, NMR chemical shift calculations and stereochemical structures of synthetic polymers, *Annu. Rep. NMR Spectrosc.* **1980**, *10A*, 81–131.

109 C. J. Jameson, J. Mason, Theoretical, physical, and inorganic aspects of chemical shifts, *Specialist Periodical Reports, Nuclear Magnetic Resonance*, The Chemical Society, London, **1980**, Vol. 9, pp. 1–24, later reviews by Jameson in Vol. 10–22, **1981–93**.

110 J. Kowalewski, Calculations of nuclear spin–spin coupling constants, *Annu. Rep. NMR Spectrosc.* **1982**, *12*, 81–176.

111 J. Kowalewski, Theoretical aspects of nuclear spin–spin coupling, *Specialist Periodical Reports, Nuclear Magnetic Resonance*, Royal Society of Chemistry, London, **1982**, Vol. 11, pp. 55–70.

112 I. Ando, G. A. Webb, *Theory of NMR Parameters*, Academic Press, London, **1983**.

113 J. Kowalewski, Theoretical aspects of nuclear spin–spin coupling, *Specialist Periodical Reports, Nuclear Magnetic Resonance*, The Chemical Society, London, **1983**, Vol. 12, pp. 52–67.

114 C. J. Jameson, Spin–spin coupling, in *Multinuclear NMR*, ed. J. Mason, Plenum Press, London, **1987**, pp. 89–131.

115 C. J. Jameson, J. Mason, The chemical shift, in *Multinuclear NMR*, ed. J. Mason, Plenum Press, London, **1987**, pp. 51–88.

116 T. Helgaker, M. Jaszunski, K. Ruud, Ab initio methods for the calculation of NMR shielding and indirect spin–spin coupling constants, *Chem. Rev.* **1999**, *99*, 293–352.

3
Historical Aspects of EPR Parameter Calculations

Frank Neese and Markéta L. Munzarová

The field of theoretical calculations of EPR spin-Hamiltonian parameters was developed in close correspondence with the progress in the experimental technique. Indeed, many of the scientists who made seminal early contributions to the theory of EPR parameters were also involved in experimental studies. It is therefore necessary to briefly describe the history of the EPR method itself before it is possible to understand how the theoretical approaches evolved. The first magnetic resonance experiment was carried out by Zavoisky in Russia in 1945 [1]. At this time he observed resonance lines from $CuCl_2{\cdot}2H_2O$ at a frequency of 133 MHz! Intellectually, this experiment might have been expected for about 10 years based on the studies of Van Vleck in Oxford [2] on molecular magnetism and the group led by Gorter [3] in the Netherlands. However, rapid experimental progress only became possible after World War II due to the development of microwave technology in military based laboratories. In the following years EPR spectroscopy progressed quickly but was a domain of physicists studying transition metal ions in crystals. It is therefore not surprising that the first observation of hyperfine structure in 1949 by Penrose [4] was on a complex of the Cu(II) ion which splits an EPR resonance into four lines due to its nuclear spin of I=3/2. In the early 1950s organic chemists studying aromatic π-radicals became interested in EPR. In 1953 Weissman [5] observed for the first time the EPR spectrum of such a radical and correctly attributed the rich structure observed to the proton hyperfine coupling (HFC) (the first inorganic, transition metal free radical EPR was also seen by Weissman and co-workers in $(SO_3)_2(NO)^{2-}$ in 1952 [6]). In 1953 an important observation was made by Owen and Stevens who for the first time observed the hyperfine structure due to the coordinating ligands in $IrCl_6^{2-}$ [7]. Subsequently EPR evolved in basically three communities which were studying organic radicals and biradicals, open shell transition metal ions, and small inorganic radicals in the gas phase or by matrix isolation techniques respectively. Between the years 1960 and 1980 continuous wave (CW) EPR was developed into a routine technique for the study of paramagnetic molecules with commercial spectrometers being available from several companies. The first spin echo in EPR was observed by Blume in 1958 [8] and in the 1960s pulse techniques were developed mainly in the Bell laboratories in the group of Mims [9–13]. However, it was not until the 1980s that the electronics became sufficiently fast and sufficiently cheap for the pulse techniques to become more widespread (for reviews see [14, 15]).

Calculation of NMR and EPR Parameters. Theory and Applications.
Edited by Martin Kaupp, Michael Bühl, Vladimir G. Malkin
Copyright © 2004 WILEY-VCH Verlag GmbH & Co. KGaA, Weinheim
ISBN: 3-527-30779-6

Already in 1956 the first electron-nuclear double resonance experiment (ENDOR) was conducted by Feher [16, 17] but this technique, despite its considerable power, also took a long time to become more conventionally used. The main technological advances, starting in the early 1980s, were (i) the extensive development of pulse techniques which opened the way for the first 2D-EPR experiment in 1986 [18] and (ii) the construction of spectrometers which operated at higher and higher microwave frequencies and consequently also higher magnetic fields [19–22]. Today these techniques are still improving at a rather rapid pace. Due to these developments it became possible to record EPR spectra with unprecedented resolution. First, one can now sensitively and accurately measure very small isotropic and anisotropic HFCs as well as quadrupole couplings of magnetic nuclei which are very weakly coupled to the electronic spin. Secondly, it is possible to observe resonances from systems with much larger interactions (zero-field splittings (ZFSs), Kramers and non-Kramers systems, exchange coupled systems) which previously could not be studied by EPR techniques. Thirdly, due to the emergence of high-field spectrometers, *g*-tensors can be measured to much higher accuracy than possible previously. Together with these technological advances the systems studied by EPR techniques became ever more complex. In biochemistry, radicals in low-symmetry protein environments with specific hydrogen bonding interactions, mono- and polynuclear metal active sites in metalloproteins, and shortlived charge-separated states in photosynthesis [23] are all accessible to detailed EPR studies nowadays. In solid state and materials sciences paramagnetic defects and metals or radicals in zeolites currently receive much attention. All these developments now require theoreticians to catch up with the technological developments and provide new quantum chemical methods which make it possible to develop the information content of EPR spectra to their full potential.

The small interactions observed in EPR spectra ($<\sim$1–25 cm^{-1}) have been theoretically understood since the early days of quantum mechanics, long before the invention of the EPR technique itself. Indeed, the observation of hyperfine structure in atomic spectra led Pauli in 1924 to postulate the existence of a spin angular momentum [24] based on the famous Stern–Gerlach experiment [25], of which EPR can be considered a fascinating extension. The spin also came as a natural consequence from the Dirac equation which describes the relativistic motion of a single electron [26]. A generalization to more than one electron was developed by Breit [27–29]. In 1957 Bethe and Salpeter wrote an influential monograph that summarized almost all of the microscopic terms in the Hamiltonian that are necessary to understand the phenomena observed in EPR spectra [30]. An important addition was made by Fermi in 1930 who found the important 'Fermi contact interaction' in the spectra of alkali metals with a single valence electron [31]. Although Fermi started his derivation from the Dirac equation, the relativistic nature of the contact term is under dispute since the HFC can be obtained from classical arguments if a magnetic moment for the electron is assumed [32]. A deep discussion has been given by Kutzelnigg who concludes that the isotropic HFC is not an intrinsically relativistic effect and that the δ-function term in the Hamiltonian arises as an artifact of trying to use first order perturbation theory in terms of two component spinors instead of the four

component Dirac spinors to describe the interaction [33]. In addition, it is not widely known that the delta-function notation in the Fermi contact operator was actually introduced much later by Abragam and Pryce [34, 35]. Furthermore, the 1930s witnessed the development of two theoretical frameworks that later served as a basis for the understanding of EPR spectra for many decades. These two theories are the Hückel molecular orbital (HMO) theory of organic π-systems published in 1937 [36] and the crystal field theory (CFT) of transition metal electronic structure developed by Bethe [37] and Van Vleck [38] in the early 1930s and brought into chemistry by Hartmann and co-workers in the early 1950s [39–41].

With the emergence of EPR experiments in 1945 it quickly became evident that the route from the fundamental theory to the actual data was too long, especially if complicated open shell ions in low symmetry environments were studied. A simpler, less fundamental but phenomenologically correct description of the EPR experiment was therefore urgently needed in order to reduce the complexity of the data analysis. The emergence of such a method, the effective spin-Hamiltonian (SH), in the early 1950s must be considered a major intellectual achievement with far reaching consequences for the development of EPR and NMR spectroscopy. The principal idea of the SH is to write down an effective Hamiltonian that only contains spin degrees of freedom together with a few well defined numerical parameters (SH parameters) that are obtained from fitting to the experimental data. Since the spin-only Schrödinger equation is easily solved exactly (or at least numerically with a computer) the experimentalists could now focus their efforts on designing new experiments and plan, describe and analyze them in the framework of the effective SH. Thus, recourse to the much more complicated underlying physics is not necessary. It is not even necessary that the spin entering the SH is the "true" spin of the system. For example, in Kramers systems with large ZFSs one can describe the individual Kramer's doublets by an effective $S=1/2$ SH. The spin in the SH is therefore usually referred to as the "fictitious spin" and the important concept involved in SHs is that they describe the properties of a reasonably well isolated set of states correctly (most frequently an orbitally non-degenerate spin-multiplet with $2S+1$ components). However, spin-only type problems were considered long before the formulation of the SH concept. Most prominently, Breit and Rabi in 1931 obtained a closed form solution of the eigenvalues and eigenvectors of a spin system with an isotropic g-value and an isotropic hyperfine tensor [42] (for more details on the SH concept see Chapter 4 by Lushington).

Thus, in the early 1950s the field of 'theoretical EPR spectroscopy' was reduced to the prediction of a small set of SH parameters. Indeed, Griffith wrote in his famous book "The Spin Hamiltonian is a convenient resting place during the long trek from fundamental theory to the squiggles of an oscilloscope" and it is "the last outpost in our land of theoretical physics" [43]. In the early 1950s it was impossible to seriously consider the solution of the many electron Born–Oppenheimer (BO) problem together with the many small (mainly relativistic) effects that are necessary to understand EPR spectroscopy. It is therefore evident that the first formulation of the theories for SH parameters had to be formulated in the languages of the theories applicable to the *classes of substances* of interest that were available at the time. Conse-

quently, the first development of the SH by Pryce [44, 45] and Abragam and Pryce [34, 35, 46, 47] used perturbation theory in the framework of CFT. A lucid theoretical study is due to Griffith and was published in 1960, some ten years after the introduction of the SH [48]. These workers already arrived at all the terms that are considered essential for the parametrization of EPR experiments today:

1. The *g*-matrix which parametrizes the Zeeman splittings due to the interaction of the total electronic magnetic dipole moment with an external magnetic field (0–10 cm^{-1}).
2. The hyperfine tensor which parametrizes the interactions between the total electronic spin and the nuclear spins (< 1 cm^{-1}).
3. The zero-field splitting which parametrizes the interactions that lift the degeneracy of the $2S+1$ components of a spin multiplet with total spin S (0–25 cm^{-1}).
4. The quadrupole interaction which parametrizes the interaction of the nuclear quadrupole moment (with spin $I > 1/2$) with the total electric field gradient at the nucleus (< 0.01 cm^{-1}).
5. The nuclear Zeeman interaction which describes the Zeeman splitting due to the nuclear magnetic dipoles interacting with an external magnetic field (< 10^{-3} cm^{-1}).

Slightly later the SH was supplemented by appropriate terms to describe exchange and dipolar interactions between interacting spin systems, probably the most detailed presentation is due to Bencini and Gatteschi [49]. In retrospect it may be considered fortunate that these early theories applied to *classes of substances* (transition metal complexes, organic π-radicals) rather than being formulated in an abstract way that can only be implemented numerically and applied to *individual molecules* (see Primas [50] for an in-depth discussion of this point). Thus, the simplified theories can be carried through analytically and lead to closed form solutions that give much insight into the EPR properties of many related molecules.

The inadequacy of CFT to cope quantitatively with the EPR spectra of transition metal ions was understood rather quickly. It was not possible to use pure metal d-orbitals together with constants such as the free-ion spin–orbit coupling (SOC) constant in order to satisfactorily reproduce the experimental findings. Stevens [51], Abragam and Pryce [34, 35], Owen and Thornley [52], and others attributed this to the effects of covalent bonding, which serve to 'dilute' the metal d-orbitals with ligand orbitals. Predominantly this effect was incorporated into the theory by a simple downscaling of the free-ion parameters that enter the Abragam and Pryce SH (see Ref. [52] for a more detailed discussion). The most striking demonstration of the metal–ligand covalency was, of course, the observation of the ligand hyperfine structure (referred to as the 'superhyperfine structure' in the EPR literature) which proved that there is a finite probability of finding an unpaired spin density at the position of the ligand nuclei [7]. Given the strong dominance of the 'effective dilution' ideas it is remarkable that already in 1958 Maki and McGarvey developed a molecular orbital (MO) approach to the EPR spectra of square planar Cu(II) complexes that contained the metal–ligand bonding explicitly [53, 54]. While the original theory

underwent several modifications and improvements [55, 56], it still forms the cornerstone of the qualitative understanding of transition metal EPR. McGarvey's approach, which may be considered to be greatly ahead of its time, is fully described in his review from 1966 [57].

Another difficulty that arose with the CFT was that the values of the central metal HFCs could not be understood without invoking a strongly negative isotropic contribution. The origin of this term was difficult to understand since the metal d-orbitals have no finite probability density at the nucleus. Abragam and Pryce found a solution to this problem in 1951 and attributed the isotropic HFC to unpaired s-electron spin density that came about by configuration interaction (CI) of the ground term with excited terms from the $nd^n(n+1)s^0 \rightarrow nd^{n-1}(n+1)s^1$ configuration [34, 35]. This formulation failed to quantitatively reproduce the isotropic HFCs and Abragam and Pryce therefore introduced a phenomenological term $-P_d\kappa$ into the spin Hamiltonian where $P_d = g_e g_N \beta_e \beta_N \langle r^{-3} \rangle_d$ is considered to be a constant of the free ion. From today's perspective, a CI treatment is perhaps the most satisfying way to describe the small admixtures that give rise to the s-orbital spin densities. However, in order to achieve quantitative results one has to thoroughly correlate the core electrons as well as the admixing $nd^{n-1}(n+1)s^1$ configurations, which implies the use of large and flexible basis sets and probably at least triple excitations from the leading $nd^n(n+1)s^0$ configuration. A much simpler solution is to introduce the s-orbital spin density via the spin-polarization model in a spin-unrestricted self-consistent field framework [58]. In the early 1960s it became possible to obtain accurate unrestricted Hartree–Fock (UHF) solutions for the free atoms and ions and this method was extensively applied by Watson, Freeman and co-workers to understand the isotropic HFCs as a consequence of the core level spin polarization [59, 60]. It attests to their considerable insight that the ideas voiced by Watson and Freeman still stand almost unchanged today and serve as a basis for the qualitative understanding of the isotropic metal nucleus HFC [59, 60].

In conclusion, the Abragam and Pryce SH, together with an empirical correction for the isotropic metal HFC has served well as a basis for the understanding of transition metal EPR spectra for several decades. The most comprehensive descriptions are found in the classic texts of Griffiths [43] and Abragam and Bleaney [61].

A related problem with the interpretation of the HFCs was encountered in the π-radical EPR community at the very beginnings of free radical EPR spectroscopy. The observed HFCs were correctly attributed to the ring protons which, however, lie in a nodal plane of the spin-carrying MO. Thus, based on simple MO theory, there should not be any spin density at the positions of the protons and consequently there should be no isotropic HFC. The solution to this problem was found independently and simultaneously by Weissman [62], McConnell and Chesnut [63–65], Jarret [66] and Bersohn [67] in 1956. The proton spin density was explained along the lines of VB theory adopting the σ-π exchange interaction concept, as well as by means of MO theory considering the admixture of excited configurations involving the C–H bond into the ground-state Slater determinant. Both approaches lead to the conclusion that the spin density at the protons is proportional to the spin density at the adjacent carbon but is negative. This proportionality became known as the

famous McConnell equation [63–65]. In addition, it soon became obvious that the spin polarization of the C–H bond also generates spin density at the carbon nucleus, which led to the formulation of the Karplus–Fraenkel equation [68].

The McConnell relation enabled workers to predict proton HFCs from simple HMO calculations with good to reasonable accuracy and, conversely, was used to test HMO theory by experimentally 'mapping' out the spin density at the various ring carbons from measured EPR spectra of the corresponding radical anions or cations. However, it was recognized almost immediately that Hückel theory could not account for observations such as negative spin populations of carbons at nodes of nonbonding singly occupied orbitals, and the McConnell equation has been extended in various forms [65, 69]. Another important relation was the $\cos(\theta)^2$ proportionality between the isotropic HFC and the angle of a proton that is bound in the C_β position relative to an aromatic radical [70], which is widely used in biochemical studies of, e.g., tyrosyl radicals [71].

The earliest calculations of the spin populations used the CI method starting either from HMO or more elaborate orbitals. An alternative approach is due to McLachlan who incorporated concepts of spin polarization into the HMO theory and thereby obtained a much simpler, insightful, and very successful theory [72, 73]. An important contribution to the field was made in 1967 by Pople and co-workers who invented the first semiempirical CNDO and INDO molecular orbital approaches. The Hartree–Fock method was well known at this time but application to molecules of the size of organic π-radicals was still not in sight. Using a simple parameterization, Pople and co-workers showed that the UHF-INDO method successfully accounted for the isotropic HFCs of many radicals [74, 75]. A good review from this time is due to Beveridge [76]. For a widely used and successful variant see also Plato et al. [77]. This finding caused considerable optimism about the performance of the more rigorous spin-unrestricted Hartree–Fock (UHF) method. However, when these calculations became feasible in the 1970s the results for the prediction of isotropic HFCs were mainly disappointing [78, 79].

For a long time this difficulty 'defined' theoretical EPR spectroscopy and first principle quantum chemical calculations of other EPR parameters were barely considered. For example a review from 1991 titled 'Theoretical Approaches to ESR Spectroscopy' by Feller and Davidson [80] is almost entirely devoted to the isotropic HFCs. The dominance of the isotropic HFC in computational quantum chemistry has several reasons. Quantum chemistry in the form of the HF method has, until recently, been much more successful for organic molecules than for transition metal complexes. In addition, the EPR spectra of organic radicals were typically recorded in fluid solution where any anisotropy in the *g*-matrices or hyperfine interactions is averaged out due to rapid molecular tumbling. Thus, anisotropic HFCs or *g*-values were seldom measured. Where comparison between theory and experiment was possible the anisotropic (dipolar) HFC was found easy to calculate [81], which made extensive method development for this quantity unnecessary. The *g*-tensor, on the other hand, shows very small deviations from the free electron *g*-value in organic radicals. These were difficult to measure and were usually not considered in the quantum chemical analysis. (Perhaps also because it is a second order property

which does not easily follow as an expectation value over the ground state UHF wavefunction, as is the case for the isotropic HFC.) The smallness of the *g*-shifts is a consequence of the small angular momentum in the electronic ground state, which in turn is due to the small SOC constants of the light atoms which most organic radicals are made of. This is a sharp distinction from transition metal complexes which carry much more angular momentum in their electronic ground states. Historically, the division between the organic and inorganic fields became so strong in the 1970s that many workers distinguished "electron spin resonance" (ESR) as EPR applied to organic radicals with little angular momentum contributions while "electron paramagnetic resonance" (EPR) was used in conjunction with the same technique applied to transition metal complexes with significant angular momentum (see e.g. Ref. [82] for a discussion).

In computational quantum chemistry the period from 1970 onwards has seen numerous studies of the isotropic HFCs in organic molecules, with ever increasing sophistication in the treatment of electron correlation, vibronic and environmental effects. It became evident that only the most accurate *ab initio* methods in conjunction with large and flexible basis sets give quantitative agreement with experiment and thus accurate studies were restricted to atoms and very small molecules (see e.g. Bauschlicher for a high level study on the nitrogen atom that nicely illustrates the computational challenges [83]). A good review is provided for example by Engels et al. [81]. The field gained significant momentum when density functional theory (DFT) became available in the early 1990s [84–86]. It quickly became clear that DFT methods give isotropic HFCs of many radicals that are as good as high-level MRCI or CCSD(T) results, provided that an appropriate functional is used [81]. However, the DFT computed HFCs come very close to the most accurate *ab initio* data only in cases where the HF configuration dominates. Where large MRCI calculations with many (30–100) reference determinants are required to get highly accurate data, DFT also fails, and predicts HFCs with a quality in between CISD and QCISD(T) or CCSD(T) [87]. A particular challenge for DFT isotropic HFCs is represented by certain transition metal complexes [88, 89].

Despite the preoccupation of computational quantum chemistry with isotropic HFCs the theory of the SH has made significant progress since the Abragam and Pryce days. The first rigorous derivation of the SH that we are aware of dates back to 1965 and is due to McWeeny [90]. Starting from the microscopic Breit–Pauli terms as described by Bethe and Salpeter, McWeeny combined the ideas of effective Hamiltonians due to Löwdin and himself and the formulation of matrix elements in terms of reduced density matrices (RDMs). He arrived at a rigorous and convenient sum-over-states (SOS) theory that remains, perhaps, unsurpassed today. Illuminating descriptions of his approach are given in McWeeny's monographs 'Spins in Chemistry' [91] and 'Methods of Molecular Quantum Mechanics' [92]. The difficulty with any SOS theory is that there appears to be an infinite number of many electron wavefunctions (or their reduced one- and two-particle densities and transition densities) and that computational implementation is difficult and of unsure convergence. Nevertheless, McWeeny's treatment was also acknowledged by Harriman [82] who wrote a fulminant monograph on EPR parameters in 1978 which gives an in-depth analysis of the relativistic origins of all terms in the SH.

This work must be considered the most thorough, consistent and complete treatment of the subject that is in existence.

Despite the availability of such general formulations more attention was paid by the community to methods that were immediately applicable within the emerging MO framework. In the case of the *g*-tensor, the best-known work is due to Stone who derived a gauge invariant formula starting from a single Slater determinant representation of the ground state as well as of the excited states that enter his SOS *g*-tensor theory [93]. Stone's theory was extended by a number of workers, most prominently Atkins and Jamieson who derived results correct to third order in perturbation theory [94], and by Moss and Perry who extended the theory to orbitally degenerate ground states [95]. Stones's theory was widely used to interpret *g*-tensors of organic radicals and also in conjunction with the extended Hückel method for transition metal complexes in the early 1970s [96, 97]. The first *ab initio* calculation of the *g*-tensor is probably due to Moores and McWeeny in 1973 [98] which was reasonably successful but used very small basis sets and adopted a number of computationally convenient simplifications. For around the next 20 years there are scattered reports of *ab initio* and semiempirical calculations of *g*-values, notably finite perturbation theory calculations [99, 100] and a Green's functions approach [101] but there was apparently relatively little activity in the field. However, in the mid 1990s Lushington and Grein revived the field of *ab initio g*-tensor calculations [102–105]. They first reported ROHF level SOS calculations and later extended their work to the more accurate MR-CI methodology. These calculations are probably the most accurate which are available today. However, even the MR-CI method does not rigorously solve the gauge problem or the uncertain convergence of the SOS expansion when truncated after the lowest few excited states. Therefore Vahtras and co-workers have taken the route via linear response theory and developed a successful multi-configuration linear response approach to *g*-tensors [106–110].

Due to the overwhelming success of DFT in chemistry the more recent developments in the theory of the *g*-tensor have mainly concentrated on DFT approaches. Perhaps due to the lack of an explicit representation of excited states, the DFT development has taken a somewhat different route than the *ab initio* methods. The approaches formulated so far are in line with the analytical derivative techniques that have been extremely successful in quantum chemistry starting from the early 1960s [111–114]. These methods also dominate the closely related field of NMR parameter predictions at both the correlated *ab initio* and DFT levels [115–118]. Following some attempts to compute *g*-values at the scattered-wave Xα-level [119] one of the earliest reports of DFT methods to compute SH *g*-tensors dates back to 1980. It is due to Geurts et al. who used the Hartree–Fock–Slater method and uncoupled self-consistent field perturbation theory to compute the *g*-tensor and the HFCs in [Cu(dithiocarbamate)$_2$], since then a prototypical example [120]. However, despite the success of these calculations they have not been widely used and the field was revived only in the late 1990s when several groups started to develop DFT methods for the prediction of *g*-values [121–127]. Two principal lines of development have been followed: one is due to the use of double perturbation theory starting from standard, nonrelativistic Kohn–Sham solutions [121–125]. The second approach is to solve

some form of spin–orbit coupled DFT equations and then to use first-order perturbation theory to compute the magnetic field effects [126, 127]. We note in passing that a closely related but less well-known theoretical field is the prediction of the SOC contributions to the HFC which give rise to a non-traceless tensor. It already appears in the Abragam and Pryce SH but the first MO method is due to Keijzers and DeBoer in the extended Hückel framework [128]. These contributions are well known to be large for metal- and heavier ligand nuclei. Their computation within the DFT framework became possible only recently [89, 129].

All of these recent developments in the theory of *g*-tensors and HFCs were certainly, to some extent, inspired by the progress in the experimental methods described above. The theoretical DFT methods have presently almost matured from a technical point of view and are being implemented into major quantum chemical packages. They are also easily applied to large molecules and their combination with the popular linear-scaling [130] and embedding [131] procedures will certainly be feasible in the near future. However, while the DFT methods appear to be fairly successful for organic radicals, the field of transition metal complexes is still somewhat problematic. Progress from the fundamental point of view and also from highly correlated *ab initio* approaches appears to be needed.

In conclusion, it is probably fair to say that the principal effects that dominate EPR spectra are well understood. Apparently there is no lack in basic qualitative understanding but there are still shortcomings in the quantitative accuracy of the quantum chemical predictions. In the case of HFCs the main challenge is to cope with the complicated physics of the Fermi contact term. While high accuracy can be achieved for this property with the best available ab initio approaches, more insight is needed in order to devise simpler and more efficient ab initio and DFT methods to predict this property (see Chapter 30 by Engels, Chapter 29 by Munzarova and Chapter 31 by Chipman and Rassolov). Concerning the *g*-tensor, the developments appear to be progressing well although it is presently not entirely clear how to systematically improve the accuracy of the existing DFT approaches for transition metal complexes (see Chapter 33 by Lushington and Chapter 32 by Schreckenbach and Patchkovskii). The theory of the ZFS is in its infancy and requires much more development before quantitative accuracy can be achieved (see Chapter 34 by Neese). Quadrupole couplings appear to be reasonably well predicted by current DFT approaches (see Chapter 17 by Schwerdtfeger). It appears that the progress in the field of EPR parameter prediction has somewhat lagged behind the progress in the experimental methods and the closely related field of NMR parameter predictions. This is probably related to the much smaller user community in EPR compared to that in NMR. However, it should also be realized that the systems studied by EPR spectroscopy often have extremely complicated electronic structures and a single Hartree–Fock determinant is almost never a good starting point. This is clearly different in the NMR field which is dominated by closed-shell molecules. Nonetheless, significant momentum has recently been gained in the EPR field and more and more research groups are becoming interested in the development of new methods for the prediction of EPR parameters and in their application. One may therefore be

optimistic and expect that rapid progress will be made in quantum chemical prediction of EPR parameters in the near future.

Acknowledgements

MLM gratefully acknowledges financial support by the grant LN00A016 from the Ministry of Education of the Czech Republic. FN gratefully acknowledges financial support from the Deutsche Forschungsgemeinschaft within the priority program "Molecular Magnetism" (SPP 1137).

References

1 E. Zavoisky, *J. Phys. USSR* **1945**, *9*, 211.
2 J. H. Van Vleck, *The Theory of Electric and Magnetic Susceptibilities*, Oxford University Press, Oxford **1932**.
3 C. J. Gorter, *Paramagnetic Relaxation*, Elsevier, Amsterdam **1947**.
4 R. P. Penrose, *Nature* **1949**, *196*, 992.
5 S. I. Weissman, J. Townsend, D. E. Paul et al., *J. Chem. Phys.* **1953**, *21*, 2227.
6 G. E. Pake, J. Townsend, S. I. Weissman, *Phys. Rev.* **1952**, *85*, 682.
7 J. Owen, K. H. W. Stevens, *Nature* (*London*) **1953**, *171*, 836.
8 R. J. Blume, *Phys. Rev.* **1958**, *109*, 1867.
9 W. B. Mims, K. Nassau, J. D. McGee, *Phys. Rev.* **1961**, *123*, 2059.
10 W. B. Mims, *Phys. Rev. A* **1964**, *133*, 835.
11 W. B. Mims, *Proc. R. Soc. London* **1965**, *283*, 452.
12 W. B. Mims, *Phys. Rev. B* **1972**, *5*, 2409.
13 E. R. Davies, *Phys. Lett. A* **1974**, *47*, 1.
14 W. B. Mims, J. Peisach, in *Advanced EPR: Applications in Biology and Biochemistry*, ed. A. J. Hoff, Elsevier, Amsterdam **1989**, p. 1.
15 A. Schweiger, G. Jeschke, *Principles of Pulse Electron Paramagnetic Resonance*, Oxford University Press, Oxford **2001**.
16 G. Feher, *Phys. Rev.* **1956**, *103*, 834.
17 G. Feher, *Phys. Rev.* **1959**, *114*, 1219.
18 J. Gorcester, J. H. Free, *J. Chem. Phys.* **1986**, *85*, 5375.
19 O. A. Grinberg, A. A. Dubinski, Y. S. Lebedev, *Russ. Chem. Rev.* **1983**, *52*, 850.
20 E. Haindl, K. Möbius, H. Oloff, *Z. Naturforsch. A* **1985**, *40*, 169.
21 D. E. Budil, K. A. Earle, W. B. Lynch et al., in *Advanced EPR: Applications in Biology and Biochemistry*, ed. A. J. Hoff, Elsevier, Amsterdam **1989**, p. 307.
22 R. T. Weber, J. A. J. M. Disselhorst, L. J. OPrevo et al., *J. Magn. Reson.* **1989**, *81*, 129.
23 W. Lubitz, *Phys. Chem. Chem. Phys.* **2002**, *4*, 5539.
24 W. Pauli, *Z. Phys.* **1927**, *43*, 601.
25 W. Gerlach, O. Stern, *Z. Phys.* **1922**, *9*, 349.
26 P. A. M. Dirac, *The Principles of Quantum Mechanics*, Clarendon Press, Oxford 1930.
27 G. Breit, *Phys. Rev.* **1929**, *34*, 553.
28 G. Breit, *Phys. Rev.* **1930**, *36*, 363.
29 G. Breit, *Phys. Rev.* **1932**, *39*, 616.
30 H. A. Bethe, E. E. Salpeter, *Quantum Mechanics of One- and Two-Electron Atoms*, Academic Press, New York 1957.
31 E. Fermi, *Z. Phys.* **1930**, *60*, 320.
32 N. F. Ramsey, *Molecular Beams*, Oxford University Press, Oxford **1956**.
33 W. Kutzelnigg, *Theor. Chim. Acta* **1988**, *73*, 173.
34 A. Abragam, M. H. L. Pryce, *Proc. R. Soc. London, Ser.A* **1951**, *205*, 131.
35 A. Abragam, M. H. L. Pryce, *Proc. R. Soc. London, Ser.A* **1951**, *206*, 173.
36 E. Hückel, *Z. Elektrochem.* **1937**, *43*, 752.
37 H. A. Bethe, *Ann. Phys.* **1929**, *3*, 135.
38 J. H. Van Vleck, *J. Chem. Phys.* **1935**, *3*, 807.
39 H. Hartmann, H. L. Schläfer, *Z. Phys.* **1951**, *197*, 115.
40 H. Hartmann, H. L. Schläfer, *Z. Naturforsch.A* **1951**, *6*, 751.
41 F. E. Ilse, H. Hartmann, *Z. Phys.* **1951**, *197*, 239.
42 G. Breit, I. I. Rabi, *Phys. Rev.* **1931**, *38*, 2082.

43 J. S. Griffith, *The Theory of Transition Metal Ions.*, Cambridge University Press, Cambridge **1964**.
44 M. H. L. Pryce, *Phys. Rev.* **1950**, *80*, 1107.
45 M. H. L. Pryce, *Proc. Phys. Soc. A* **1950**, *63*, 25.
46 A. Abragam, M. H. L. Pryce, *Proc. Phys. Soc. A* **1950**, *63*, 409.
47 A. Abragam, J. Horowitz, M. H. L. Pryce, *Proc. R. Soc. London Ser. A* **1955**, *230*, 169.
48 J. S. Griffith, *Mol. Phys.* **1960**, *3*, 79.
49 A. Bencini, D. Gatteschi, *EPR of Exchange Coupled Systems*, Springer, Heidelberg **1990**.
50 H. Primas, *Chemistry, Quantum Mechanics and Reductionism*, Springer, Berlin **1981**.
51 K. H. W. Stevens, *Proc. R. Soc. London, Ser. A* **1953**, *219*, 542.
52 J. Owen, J. H. M. Thornley, *Rep. Prog. Phys.* **1966**, *29*, 675.
53 A. H. Maki, B. R. McGarvey, *J. Chem. Phys* **1958**, *29*, 35.
54 A. H. Maki, B. R. McGarvey, *J. Chem. Phys.* **1958**, *29*, 31.
55 J. Ammeter, G. Rist, H. H. Günthard, *J. Chem. Phys.* **1972**, *57*, 3852.
56 D. W. Smith, *J. Chem. Soc. A* **1970**, 3108.
57 B. R. McGarvey, *Transition Met. Chem.* **1966**, *3*, 89.
58 J. A. Pople, R. K. Nesbet, *J. Chem. Phys.* **1954**, *22*, 571.
59 R. E. Watson, A. J. Freeman, *Phys. Rev.* **1961**, *123*, 2027.
60 A. J. Freeman, R. E. Watson, in *Magnetism. Vol. II*, eds. G. T. Rado, H. Suhl, Academic Press, New York **1965**, p. 167.
61 A. Abragam, B. Bleaney, *Electron Paramagnetic Resonance of Transition Ions*, Clarendon Press, Oxford **1970**.
62 S. I. Weissman, *J. Chem. Phys.* **1956**, *25*, 890.
63 H. M. McConnell, *J. Chem. Phys.* **1956**, *24*, 764.
64 H. M. McConnell, *J. Chem. Phys.* **1958**, *28*, 1188.
65 H. M. McConnell, D. B. Chesnut, *J. Chem. Phys.* **1958**, *28*, 107.
66 H. S. Jarret, *J. Chem. Phys.* **1956**, *25*, 1289.
67 R. Bersohn, *J. Chem. Phys.* **1956**, *24*, 1066.
68 M. Karplus, G. K. Fraenkel, *J. Chem. Phys.* **1961**, *35*, 1312.
69 A. D. McLachlan, H. H. Dearman, R. Lefebvre, *J. Chem. Phys.* **1960**, *33*, 65.
70 C. Heller, H. M. McConnell, *J. Chem. Phys.* **1960**, *32*, 1535.
71 G. T. Babcock, M. Espe, C. Hoganson et al., *Acta Chem. Scand.* **1997**, *51*, 533.
72 A. D. McLachlan, *Mol. Phys.* **1959**, *2*, 271.
73 A. D. McLachlan, *Mol. Phys.* **1960**, *3*, 233.
74 J. A. Pople, D. L. Beveridge, P. A. Dobosh, *J. Chem. Phys.* **1967**, *47*, 2026.
75 D. L. Beveridge, J. W. McIver, *J. Chem. Phys.* **1970**, *54*, 4681.
76 D. L. Beveridge, in *Semiempirical Methods of Electronic Structure Calculation. Part B: Applications*, ed. G. A. Segal, Plenum Press, New York **1976**, p. 163.
77 M. Plato, K. Möbius, W. Lubitz, in *Chlorophylls*, ed. H. Scheer, CRC Press, Boca Raton **1991**, p. 1015.
78 D. M. Chipman, *J. Chem. Phys.* **1979**, *71*, 761.
79 D. M. Chipman, *J. Chem. Phys.* **1983**, *78*, 4785.
80 D. Feller, E. R. Davidson, in *Molecular Spectroscopy, Electronic Structure and Intramolecular Interactions*, ed. Z. B. Maksic, Springer, Berlin **1991**, p. 429.
81 B. Engels, L. A. Eriksson, S. Lunell, *Adv. Quant. Chem.* **1996**, *27*, 297.
82 J. E. Harriman, *Theoretical Foundations of Electron Spin Resonance*, Academic Press, New York **1978**.
83 C. W. Bauschlicher, *J. Chem. Phys.* **1990**, *92*, 518.
84 N. Ishii, T. Shimizu, *Phys. Rev. A* **1993**, *48*, 1691.
85 V. Barone, C. Adamo, N. Russo, *Chem. Phys. Lett.* **1995**, *212*, 5.
86 V. G. Malkin, O. L. Malkina, L. A. Eriksson et al., in *Modern Density Functional Theory: A Tool for Chemistry*, eds. J. M. Seminario, P. Politzer, Elsevier, Amsterdam **1994**.
87 L. A. Eriksson, in *Density-functional Methods in Chemistry and Materials Science*, ed. M. Springborg, John Wiley & Sons, New York **1997**, p. 125.
88 M. L. Munzarová, M. Kaupp, *J. Phys. Chem. A*, **1999**, *103*, 9966.
89 F. Neese, *J. Chem. Phys.* **2003**, *117*, 3939.
90 R. McWeeny, *J. Chem. Phys.* **1965**, *42*, 1717.
91 R. McWeeny, *Spins in Chemistry*, Academic Press, New York **1970**.
92 R. McWeeny, *Methods of Molecular Quantum Mechanics*, Academic Press, London **1992**.
93 A. J. Stone, *Proc. R. Soc. London, Ser. A* **1963**, *271*, 424.
94 P. W. Atkins, A. M. Jamieson, *Mol. Phys.* **1967**, *14*, 425.

95 R. E. Moss, A. J. Perry, *Mol. Phys.* **1971**, *22*, 789.
96 C. P. Keijzers, H. J. M. De Vries, A. van der Avoird, *Inorg. Chem.* **1971**, *11*, 1338.
97 C. P. Keijzers, E. De Boer, *Mol. Phys.* **1974**, *29*, 1007.
98 W. H. Moores, R. McWeeny, *Proc. R. Soc. London, Ser. A* **1973**, *332*, 365.
99 M. Ishii, K. Morihashi, O. Kikuchi, *J. Mol. Struct. (Theochem)* **1991**, *235*, 39.
100 S. A. Mustaev, V. G. Malkin, P. V. Schastnev, *J. Struct. Chem.* **1987**, *28*, 41.
101 E. Dalgaard, J. Linderberg, *Int. J. Quant. Chem. Symp.* **1975**, *9*, 269.
102 G. H. Lushington, P. Bündgen, F. Grein, *Int. J. Quant. Chem.* **1995**, *55*, 377.
103 G. H. Lushington, F. Grein, *Theor. Chim. Acta* **1996**, *93*, 259.
104 G. H. Lushington, F. Grein, *Int. J. Quant. Chem.: Quant. Chem. Symp.* **1996**, *30*, 467.
105 G. H. Lushington, F. Grein, *J. Chem. Phys.* **1997**, *106*, 3292.
106 O. Vahtras, B. Minaev, H. Ågren, *Chem. Phys. Lett.* **1997**, *281*, 186.
107 M. Engström, B. Minaev, O. Vahtras et al., *Chem. Phys. Lett.* **1998**, *237*, 149.
108 M. Engström, O. Vahtras, H. Ågren, *Chem. Phys. Lett.* **1999**, *243*, 263.
109 M. Engström, F. Himo, H. Ågren, *Chem. Phys. Lett.* **2000**, *319*, 191.
110 M. Engström, R. Owenius, O. Vahtras, *Chem. Phys. Lett.* **2001**, *338*, 407.
111 L. C. Allen, *Phys. Rev.* **1960**, *118*, 67.
112 R. M. Stevens, R. M. Pitzer, W. N. Lipscomb, *J. Chem. Phys.* **1963**, *38*, 550.
113 J. Gerrat, I. M. Mills, *J. Chem. Phys.* **1968**, *49*, 1719.
114 J. A. Pople, R. Krishnan, H. B. Schlegel et al., *Int. J. Quant. Chem.: Quant. Chem. Symp.* **1979**, *13*, 225.
115 J. A. E. Tossell, *Nuclear Magnetic Shieldings and Molecular Structure*, Kluwer, Dordrecht **1993**.
116 W. Kutzelnigg, U. Fleischer, M. Schindler, in *NMR Basic Principles and Progress, Vol. 23*, eds. P. Diehl, E. Fluck, H. Günther et al., Springer, Heidelberg **1990**.
117 J. Gauss, J. F. Stanton, *J. Chem. Phys.* **1996**, *104*, 2574.
118 M. Kaupp, V. G. Malkin, O. L. Malkina, in *Encyclopedia of Computational Chemistry*, ed. P. v. R. Schleyer, Wiley, Chichester **1998**.
119 D. A. Case, M. Karplus, *J. Am. Chem. Soc.* **1977**, *99*, 6182.
120 P. J. M. Geurts, P. C. P. Bouten, A. van der Avoird, *J. Chem. Phys.* **1980**, *73*, 1306.
121 G. Schreckenbach, T. Ziegler, *J. Phys. Chem. A.* **1997**, *101*, 3388.
122 G. Schreckenbach, T. Ziegler, *Theor. Chem. Acc.* **1998**, *99*, 71.
123 S. Patchkovskii, T. Ziegler, *J. Phys. Chem. A.* **2001**, *105*, 5490.
124 O. L. Malkina, J. Vaara, B. Schimmelpfenning et al., *J. Am. Chem. Soc.* **2000**, *122*, 9206.
125 F. Neese, *J. Chem. Phys.* **2001**, 11080.
126 E. van Lenthe, P. E. S. Wormer, A. van der Avoird, *J. Chem. Phys.* **1997**, *107*, 2488.
127 K. M. Neyman, D. I. Ganyushin, A. V. Matveev et al., *J. Phys. Chem. A* **2002**, *106*, 5022.
128 C. P. Keijzers, E. DeBoer, *J. Chem. Phys.* **1972**, *57*, 1277.
129 E. van Lenthe, A. van der Avoird, E. S. Wormer, *J. Chem. Phys.* **1998**, *108*, 4783.
130 G. E. Scuseria, *J. Phys. Chem. A* **1999**, *103*, 4782.
131 J. Gao, *Rev. Comput. Chem.* **1996**, *7, 119*.

4
The Effective Spin Hamiltonian Concept from a Quantum Chemical Perspective

Gerald H. Lushington

Spin Hamiltonians are fundamental to the understanding of experimental magnetic resonance spectroscopy, providing formalisms in which to systematically assemble spectral data. Spin Hamiltonians are equally vital to the theoretical development of quantum mechanical methods for computing such resonance effects. The actual expressions employed for experimental data assembly and theoretical prediction often appear rather dissimilar, reflecting the different means by which quantification of the Hamiltonian is accomplished. Ultimately, however, both syntactical forms correspond to identical physical effects and thus have a one-to-one correspondence. The goal of this chapter is to describe this correspondence in a way that will aid readers from either scientific field in interpreting the various expressions presented throughout the rest of this book.

The voluminous data generated from nuclear magnetic resonance (NMR) and electron paramagnetic resonance (EPR) spectra are generally reported as constructs called effective spin Hamiltonians. By analogy with quantum mechanical representations of magnetic resonance phenomena, such effects can be conceptually described by effective operators acting on effective spin state functions to divulge state energies, thus conveniently and intuitively relating observed peaks to their physical origin. These effective spin Hamiltonians should not be confused with true quantum mechanical spin Hamiltonians. The former are composed of parametric matrices fitted to observed data, while the latter are sums of differential operators determined from relativistic quantum mechanical interpretations of particle mechanics and electromagnetic interactions. In order to compute NMR and EPR parameters, theoreticians frequently must translate between the two different frameworks, using true quantum mechanical Hamiltonians to quantify physical effects underlying the magnetic resonance, and then employing an effective Hamiltonian in order to meaningfully report their results.

In most molecular spectroscopic techniques, observed electromagnetic absorptions or emissions correspond to transitions or oscillations between different energy eigenstates of the molecule. Typical NMR and EPR experiments detect the conditions under which a molecule undergoes transitions between different nuclear spin and/or electron spin states between which energetic degeneracy has been removed by a fixed strength external magnetic field $\vec{B}$. A molecule with N nuclei can be described by a spatial electronic wave function Ψ, an electronic spin state defined by

Calculation of NMR and EPR Parameters. Theory and Applications.
Edited by Martin Kaupp, Michael Bühl, Vladimir G. Malkin
Copyright © 2004 WILEY-VCH Verlag GmbH & Co. KGaA, Weinheim
ISBN: 3-527-30779-6

the quantum number m_S, and a nuclear spin state defined by quantum numbers $m_1....m_N$. This allows us to summarize a spin transition symbolically as follows:

$$\Phi^a = \left|\Psi, m_S^a, m_1^a....m_N^a\right\rangle \quad \Leftrightarrow \quad \Phi^b = \left|\Psi, m_S^b, m_1^b....m_N^b\right\rangle \tag{4.1}$$

wherein a and b index the two spin states between which a transition occurs. One should note that Eq. (4.1) makes a reasonable assumption that Ψ remains relatively stable during the transition: an approximation that will be implicit throughout the rest of this chapter.

As should be expected for effects adhering to quantum mechanical conditions, the transition probabilities are at a maximum when the energy of incident radiation is exactly equal to the energetic separation of the two states between which resonance is occurring. The spectral peak corresponding to the transition in Eq. (4.1), therefore, should be centered around a frequency equivalent to the following energy:

$$\Delta E^{ab} = E(\Phi^b) - E(\Phi^a) = E(m_S^b, m_1^b, ..., m_N^b) - E(m_S^a, m_1^a, ..., m_N^a) \tag{4.2}$$

Theoretical prediction and characterization of such transitions is accomplished via expressions that can account for and represent the excitation energies. This is generally done by constructing a spin Hamiltonian $\hat{H}_S$ capable of extracting energies (relative to the zero-field total electronic energy) for each spin state via expectation value equations:

$$\begin{aligned} \left\langle \Phi^a \middle| \hat{H}_S \middle| \Phi^a \right\rangle &= \left\langle m_S^a m_1^a....m_N^a \middle| \hat{H}_S \middle| m_S^a, m_1^a....m_N^a \right\rangle \\ &= E(m_S^a, m_1^a, ..., m_N^a) \end{aligned} \tag{4.3}$$

It is possible to relate both experimental and theoretical spectroscopic formulations in terms of Eq. (4.3), however $\hat{H}_S$ generally takes on a different meaning depending on the context in which it is being used. In cases where Eq. (4.3) is employed as a means for computationally predicting a spectrum, $\hat{H}_S$ entails a set of "quantum mechanical" operators representing relevant physical effects influencing the transition energy. This differs fundamentally from the scenario where $\hat{H}_S$ "effectively parametrizes" the relationship between the system's state variables and its experimentally observed transitions. This is the main difference between the notion of "quantum mechanical" and "effective" spin Hamiltonians. Nonetheless, both forms do represent the same basis of magnetic resonant transitions: oscillations between electronic and nuclear spin magnetic dipoles under the influence of an external magnetic field $\vec{B}$. Both thus incorporate all pair-wise interactions arising from each constituent magnetic dipole such as that associated with the electron spin $\vec{S}$, the following collection of nuclear spins:

$$\vec{I} = \sum_{C=1}^{N} \vec{I}_C \tag{4.4}$$

and electron orbital angular momentum $\vec{L}$, each interacting with each other and with $\vec{B}$. These couplings lead to the fully general spin Hamiltonian:

$$\begin{aligned}\hat{H}_S &= \hat{H}(S,S) + \hat{H}(S,I) + \hat{H}(S,L) + \hat{H}(S,B) + \hat{H}(I,I) + \hat{H}(I,L) + \hat{H}(I,B) \\ &+ \hat{H}(L,L) + \hat{H}(L,B) \end{aligned} \tag{4.5}$$

In most magnetic resonance experiments, $\vec{L}$ has only a small effect on spin transitions relative to $\vec{B}$; thus one often simplifies $\hat{H}_S$ to the following form:

$$\hat{H}_S = \hat{H}(S,S) + \hat{H}(S,I) + \hat{H}(S,B) + \hat{H}(I,I) + \hat{H}(I,B) \tag{4.6}$$

In the case of effective representations of Eq. (4.6), all contributions of $\vec{L}$ to the resonance condition are readily incorporated into the parameters defining the above spin–spin and spin–field terms. The quantum mechanical analog to this procedure is to account for the effect of $\vec{L}$ not within $\hat{H}_S$ itself, but by incorporating it into a modified spatial wave function, Ψ_L. This wave function may be determined either by solving the Schrödinger equation via a spatial Hamiltonian augmented with operators representing the $\vec{L}$-dependent interactions:

$$(\hat{H}_0 + \hat{H}_L)\Psi_L = (E_0 + E_L)\Psi_L; \qquad \hat{H}_L = \hat{H}(L,S) + \hat{H}(L,I) + \hat{H}(L,L) + \hat{H}(L,B) \tag{4.7}$$

or by accounting for these terms via perturbation theory:

$$\langle \Psi_L| = \langle \Psi_0| + \sum_i c_{i0}(L,B,S)\langle \Psi_i|; \qquad c_{i0}(L,B,S) = \langle \Psi_0|\hat{H}_L|\Psi_i\rangle \tag{4.8}$$

where $\hat{H}_0$ is the conventional electronic (i.e., non-magnetic) Hamiltonian, Ψ_0 and E_0 are its eigenvector and eigenvalue respectively, and i is an index over the system's excited state manifold. Regardless of whether Ψ_L is assembled via Eq. (4.7) or via Eq. (4.8), one may extract its spin state energies via:

$$\langle \Phi_L^a|\hat{H}_S|\Phi_L^a\rangle = E(\Psi_L, m_S^a, m_1^a, ..., m_N^a) \tag{4.9}$$

So what does $\hat{H}_S$ look like? In the absence of external perturbations, one can compute the classical interaction energy between two magnetic dipoles, or between a dipole and a uniform external magnetic field, as a simple scalar product. We might envision rewriting $\hat{H}_S$ as:

$$\hat{H}_S = C_{SS}\vec{S}\cdot\vec{S} + C_{SI}\vec{S}\cdot\vec{I} + C_{SB}\vec{S}\cdot\vec{B} + C_{II}\vec{I}\cdot\vec{I} + C_{IB}\vec{I}\cdot\vec{B} \tag{4.10}$$

where the constants C parametrize the dependence of transition energy on the different dipole–dipole interactions for a given molecule. This expression is valid as written for systems with spherical symmetry (e.g., isolated atoms). In anisotropic cases such as molecules, aspherical electronic charge distribution and nonzero orbital angular momentum can induce directional dependence in the various interactions relevant to magnetic resonance. In order to accommodate such anisotropy, one generally replaces the simple scalar product representation with a matrix multiplication scheme of the form:

$$\hat{H}(U,V) = K_{UV}\,\vec{U}\cdot\overleftrightarrow{T}_{UV}\cdot\vec{V} \tag{4.11}$$

wherein $\vec{U}$ and $\vec{V}$ are two arbitrary dipoles, K_{UV} is a universal constant (independent of molecule type, but unique for the specific interaction), and $\overleftrightarrow{T}_{UV}$ is a 3 × 3 Cartesian matrix providing a full characterization of the directional dependence of the interaction for the given anisotropic molecule. $\overleftrightarrow{T}_{UV}$ can be expanded as follows:

$$\overleftrightarrow{T}_{UV} = \begin{vmatrix} T_{UV}^{xx} & T_{UV}^{xy} & T_{UV}^{xz} \\ T_{UV}^{yx} & T_{UV}^{yy} & T_{UV}^{yz} \\ T_{UV}^{zx} & T_{UV}^{zy} & T_{UV}^{zz} \end{vmatrix} \tag{4.12}$$

where T_{UV}^{xy}, for example, is a scalar that parametrizes the energetic contribution arising from the interaction of the x-component of $\vec{U}$ with the y-component of $\vec{V}$. For cases where $\vec{U}$ and $\vec{V}$ are the same quantity (e.g., as for $\hat{H}(S,S)$ or $\hat{H}(I,I)$), $\overleftrightarrow{T}_{UV}$ fits the algebraic definition of a tensor. In cases of inequivalent vectors ($\vec{U} \neq \vec{V}$), it is no longer technically correct to call $\overleftrightarrow{T}_{UV}$ a tensor [1], but all such dipolar interaction matrices have traditionally still been referred to as tensors, so the convention will be perpetuated herein.

The exact form in which one reports an effective $\hat{H}_S$ for different experiments is based on conventions that have evolved within the different spectroscopic communities. As the NMR and EPR communities tend to deal with molecules exposed to significantly different physical conditions (e.g., different magnetic field strength, transition timescale, etc.), it should come as little surprise that the two groups generally use rather different looking effective spin Hamiltonians. In the case of NMR, one frequently sees the spin Hamiltonian written as something of the following form [2]:

$$\hat{H}_S(NMR) = -\sum_{C=1}^{N}\hbar\gamma_C\vec{B}\cdot(\overleftrightarrow{1}-\overleftrightarrow{\sigma}_C)\cdot\vec{I}_C + \frac{\hbar^2}{2}\sum_{C=1}^{N}\sum_{\substack{D=1\\D\neq C}}^{N}\gamma_C\gamma_D\vec{I}_C\cdot(\overleftrightarrow{D}_{CD}+\overleftrightarrow{J}_{CD})\cdot\vec{I}_D \tag{4.13}$$

where $\hbar\gamma_C$ arises from the standard nuclear magnetic dipole definition ($\vec{\mu}_C = \hbar\gamma_C\vec{I}_C$), $\overleftrightarrow{1}$ is a unitary tensor, $\overleftrightarrow{\sigma}_C$ is the nuclear shielding tensor, and $\overleftrightarrow{D}_{CD}$ and $\overleftrightarrow{J}_{CD}$ are the classical dipolar and indirect nuclear spin–spin (J-) coupling tensors respectively. $\overleftrightarrow{\sigma}_C$ describes the peak's shape and shift (or the center of a split-peak pattern) for resonances arising from each of the resonant nuclei, while $\overleftrightarrow{D}_{CD}$ and $\overleftrightarrow{J}_{CD}$, relevant for all molecules with more than one nucleus with a nonzero dipole, parametrize the magnitude of peak splitting that may arise from the coupling of each pair of nuclei with a nonzero magnetic dipole.

The NMR effective spin Hamiltonian in Eq. (4.13) is a pragmatic generalization that satisfactorily addresses the relevant interactions present in most NMR spectra. There are scenarios, however, when additional terms must be added. When paramagnetic systems are studied via NMR, for example, one often observes additional effects (e.g., the Knight shift [3]) enabled by coupling between electron and nuclear spin magnetic dipoles, as can be summarized by the following operator:

$$\hat{H}(S,I) = \sum_{C=1}^{N} \vec{S} \cdot \overleftrightarrow{A}_C \cdot \vec{I}_C \tag{4.14}$$

(where $\overleftrightarrow{A}_C$ is the hyperfine coupling tensor for center C) that must then be incorporated into $\hat{H}_S(NMR)$. Electron spin–orbit effects can also affect NMR spectra but, as per Eq. (4.7) and Eq. (4.8), these effects are generally accounted for outside of $\hat{H}_S$.

Molecules containing high spin nuclear magnetic dipoles (e.g., $|\vec{I}_C| > ½$) constitute another special case in NMR because additional important resonance effects may arise from electrostatic considerations. High spin nuclei possess an intrinsic electric quadrupole moment in addition to their magnetic dipole; thus the different projections of nuclear spin, $m_C = |I_C|, |I_C\text{-}1|,\ldots,\text{-}|I_C|$, are energetically split by the presence of the various electrostatic charges (both electronic and nuclear) in their vicinity, leading to potential resonance conditions [5] that can be parametrized by the following operator:

$$\hat{H}_Q(I,I) = \sum_{\substack{C=1 \\ |I_C|\geq 1}}^{N} \vec{I}_C \cdot \overleftrightarrow{Q}_{CC} \cdot \vec{I}_C \tag{4.15}$$

where $\overleftrightarrow{Q}$ is the nuclear quadrupole coupling tensor. Resonances between nuclear quadrupole moments are, to a very good approximation, independent of external magnetic field, but as different field strengths shift the various magnetic dipole energies it can be possible to observe both magnetic dipole and nuclear quadrupole resonance within the same spectrum. In such cases, $\hat{H}_S(NMR)$ should include $\hat{H}_Q(I,I)$. However, most choices of field strength lead to magnetic dipole and electric quadrupole spectra that are significantly separated, thus the latter is often studied as a distinct phenomenon. In this case Eq. (4.15) becomes its own effective Hamiltonian governing the effect known as nuclear quadrupole resonance (NQR).

The basic and most common effective spin Hamiltonian used for analyzing EPR spectra is something of the form:

$$\hat{H}_S(EPR) = \mu_B \vec{S} \cdot \overleftrightarrow{g} \cdot \vec{B} + \sum_{C=1}^{N} \vec{S} \cdot \overleftrightarrow{A}_C \cdot \vec{I}_C \tag{4.16}$$

where the first term details the so-called electronic Zeeman effect that governs the position of peaks (or split-peak patterns) within EPR spectra, and the second term is the same quantity used to parametrize Knight shifts in NMR spectra, but manifests itself in EPR spectra as the hyperfine splitting term.

Similarities between $\hat{H}_S(EPR)$ as written above and $\hat{H}_S(NMR)$ (as per Eq. (4.13)) may not be immediately obvious, but there are several functional analogies that may be drawn between the two. Both contain two primary terms, one of which governs spectral splitting and the other spectral shift. Also, the *g*-tensor, $\overleftrightarrow{g}$, that parametrizes the electronic Zeeman effect, is frequently reported in the literature in the following form:

$$\overleftrightarrow{g} = g_e \overleftrightarrow{1} + (\Delta\overleftrightarrow{g}) \tag{4.17}$$

which emphasizes a similarity to $\overleftrightarrow{\sigma}_C$, and conveys the fact that *g*-tensors relate spatially dependent shifts (induced by various perturbations in bound atomic and molecule environments) relative to a basic reference, in this case the free electron *g*-value, g_e. Equation (4.16) is also akin to Eq. (4.13) in terms of incompleteness. While the basic $\hat{H}_S(NMR)$ expression omitted potentially relevant terms relating to hyperfine coupling and nuclear quadrupole coupling, the EPR effective spin Hamiltonian above is also lacking a fully general account of the interactions. In all cases of high spin paramagnetism ($|\vec{S}| > ½$), for example, one must augment Eq. (4.16), with the zero-field splitting term:

$$\hat{H}(S,S) = \vec{S} \cdot \overleftrightarrow{D} \cdot \vec{S} \tag{4.18}$$

arising from the magnetic dipolar interactions between the multiple unpaired electrons in the system (note that the zero-field splitting tensor, $\overleftrightarrow{D}$, should not be confused with the classical dipolar nuclear spin–spin coupling tensor in Eq. (4.13). Additional spin–spin coupling effects such as the Heisenberg Hamiltonian for quantum coherence studies, and the long-range spin-dipolar interaction (a common solvent effect) have also been observed. As was the case for NMR studies of paramagnetic cases, electron spin–orbit coupling has a significant impact on the relevant state energies in EPR, but once again, $\hat{H}(S,L)$ is generally represented within Ψ_L and not in the effective spin Hamiltonian.

Although most molecules studied via EPR have non-zero nuclear magnetic moments, the magnetic dipole associated with a spinning nucleus is only of the order of 1/2000 the strength of an electron spin magnetic dipole; thus chemical shift and nuclear spin–spin coupling interactions are typically found on a different energy scale compared to those of the electronic Zeeman or hyperfine interactions. Thus, while detailed formulations have been developed to accommodate cases where nuclear spins must be quantified [6], it is often reasonable to neglect $\hat{H}(I,B)$ and $\hat{H}(I,I)$ terms within $\hat{H}_S(EPR)$. Several practical exceptions deserve mention, however. Electron nuclear double resonance (ENDOR) spectroscopy, for example, resolves effects arising from both electronic and nuclear spin resonance; a fascinating innovation accomplished by monitoring the effect on EPR hyperfine intensities (for a system whose electron Zeeman transitions have been saturated with high powered microwave radiation) that result from driving the NMR transitions via a sweep of high-intensity radio frequencies [7]. ENDOR effectively combines the resolution and nuclear selectivity of NMR with the inherent sensitivity of EPR, allowing for highly detailed characterization of structural attributes and dynamic effects. ENDOR experiments are typically not used to resolve extremely fine features such as nuclear spin–spin coupling constants, but do combine chemical shift and electric quadrupole terms with the standard $\hat{H}_S(EPR)$, to yield:

$$\hat{H}_S(ENDOR) = \mu_B \vec{S} \cdot \overleftrightarrow{g} \cdot \vec{B} + \sum_{C=1}^{N} \vec{S} \cdot \overleftrightarrow{A}_C \cdot \vec{I}_C - \sum_{C=1}^{N} \hbar \gamma_C \vec{B} \cdot (\overleftrightarrow{1} - \overleftrightarrow{g}_C) \cdot \vec{I}_C + \sum_{\substack{C=1 \\ |I_C| \geq 1}}^{N} \vec{I}_C \cdot \overleftrightarrow{Q}_{CC} \cdot \vec{I}_C \tag{4.19}$$

where $\overleftrightarrow{g}_C$ is equal to the $\overleftrightarrow{\sigma}_C$ tensor of NMR, reflecting one of several minor syntactical differences between NMR and EPR. The above $\hat{H}_S$ also governs two related techniques called dynamic nuclear polarization (DNP) and electron spin echo envelope modulation (ESEEM). Experimentally, DNP is highly analogous to ENDOR, except that instead of driving the NMR transitions to enhance hyperfine resolution, one drives the EPR transitions to enhance NMR sensitivity [8]. Meanwhile, ESEEM measures modulations in spin echoes produced by a short series of microwave pulses, permitting detection of electronic hyperfine and nuclear quadrupole resonance effects [9].

At this point we have catalogued and described a number of effective spin Hamiltonians of relevance to the NMR and EPR communities. In each case, the basic expressions contain parametric tensors that relate inter-state energetics as a function of effective spin operators that represent various spin states of atoms or molecules. Analysis of experimental magnetic resonance spectra is one way to parametrize these various tensors, but in this book we are primarily concerned with theoretical means for doing so. This can be accomplished by tying together the concept of a true quantum mechanical spin Hamiltonian with that of an effective one.

Each of the spin Hamiltonians listed in Eqs. (4.13)–(4.16), (4.18) and (4.19) is applicable to either the effective parametric or the quantum mechanical forms, and is constructed to describe all interactions among the various magnetic dipoles that can change state during a magnetic resonance experiment. As we shall see in the following chapter by Kutzelnigg, all of the constituent magnetic interactions can be represented by operators arising from relativistic quantum mechanics. From the Breit–Pauli equation (a many-electron extrapolation of the Dirac equation [10]), one can thus equate $\hat{H}(U, V)$ with a sum of all relativistic operators exhibiting bilinear dependence on $\vec{U}$ and $\vec{V}$.

To quickly illustrate how one would go about predicting magnetic resonance spectra, consider the case of the electronic Zeeman effect. In this case one must examine the Breit–Pauli Hamiltonian and select all terms with bilinear dependence on $\vec{S}$ and $\vec{B}$. This leads to the construction of a quantum mechanical spin Hamiltonian as follows:

$$\hat{H}_S^{QM}(Zeeman) = \hat{H}_o(S, B) + \hat{H}_{RMC}(S, B) + \hat{H}_{1e}(S, B) + \hat{H}_{2e}(S, B) \tag{4.20}$$

In this expression, the zeroth-order approximation arises as the following operator:

$$\hat{H}_0(S, B) = g_e \mu_B \sum_i \vec{S}_i \cdot \vec{B} \tag{4.21}$$

(wherein the index i refers to electrons), the second term:

$$\hat{H}_{RMC}(S,B) = -g_e\mu_B \frac{\hbar^2}{m^2 c^c} \sum_i \vec{S}_i \cdot \vec{B} \tag{4.22}$$

is the relativistic mass correction to the spin Zeeman term (wherein m is the mass of an electron and c is the speed of light), and:

$$\hat{H}_{1e}(S,B) = -g_e\mu_B \frac{e^2}{4mc^2} \sum_C \sum_i \frac{Z_C}{r_{iC}^3} [(\vec{S}_i \cdot \vec{B})(\vec{r}_{iC} \cdot \vec{r}_{iG}) - (\vec{S}_i \cdot \vec{r}_{iG})(\vec{r}_{iC} \cdot \vec{B})] \tag{4.23}$$

$$\hat{H}_{2e}(S,B) = g_e\mu_B \frac{e^2}{4mc^2} \sum_i \sum_j \frac{1}{r_{ij}^3} \left\{ [(\vec{S}_i + 2\vec{S}_j) \cdot \vec{B}](\vec{r}_{ij} \cdot \vec{r}_{iG}) - [(\vec{S}_i + 2\vec{S}_j) \cdot \vec{r}_{iG}](\vec{r}_{ij} \cdot \vec{B}) \right\} \tag{4.24}$$

are called the one- and two-electron spin-orbit Zeeman gauge corrections respectively (wherein the index G refers to the gauge origin of the system). Given this full Hamiltonian $\hat{H}_S^{QM}(Zeeman)$, and an electronic wavefunction Ψ_L that has been perturbed by the orbital Zeeman operator:

$$\hat{H}(L,B) = -\frac{\mu_B}{\hbar} \sum_i \vec{L}_{iG} \cdot \vec{B} \tag{4.25}$$

and both the one- and two-electron spin–orbit coupling operators:

$$\hat{H}_{1e}(S,L) = \frac{g_e\mu_B^2}{\hbar} \sum_C \sum_i \frac{Z_C}{r_{iC}} \vec{S}_i \cdot \vec{L}_{iC} \tag{4.26}$$

$$\hat{H}_{2e}(S,L) = -\frac{g_e\mu_B^2}{\hbar} \sum_i \sum_j \frac{i}{r_{ij}} (\vec{S}_i + 2\vec{S}_j) \cdot \vec{L}_{ij} \tag{4.27}$$

one may derive the full slate of electronic Zeeman transitions by an expectation value expression such as is given in Eq. (4.9). In order to translate this quantum mechanical prediction into an effective spin Hamiltonian parametrization for the electronic Zeeman effect (i.e., the first term of Eq. (4.16)), one need only equate the expectation value expression of the quantum mechanical Hamiltonian with that of the effective spin Hamiltonian, and note that elements of the g-tensor $\overleftrightarrow{g}$ simply correspond to:

$$g^{xy} = \frac{1}{\mu_B} \frac{\partial^2 \left\langle \hat{H}_S(EPR) \right\rangle}{\partial B_x \partial S_y} = \frac{1}{\mu_B} \frac{\partial^2 \langle \Phi_L | H^{QM}(S,B) | \Phi_L \rangle}{\partial B_x \partial S_y} \tag{4.28}$$

A detailed description of exactly how Eq. (4.28) is implemented is beyond the scope of this chapter, but an excellent formulation is given elsewhere [11]. All of the other interaction terms listed within the other spin Hamiltonians given by Eqs. (4.13)–(4.16), (4.18) and (4.19) may be quantum mechanically parametrized in an analogous fashion.

Finally, one should note that, in Eqs. (4.8) and (4.9), $|\Phi_L\rangle$ is written as a perturbative sum-over-states expansion that incorporates the effect of orbital response to the external magnetic field. This would normally imply the use of double perturbation theory to evaluate Eq. (4.28); a strategy that the rest of this book will reveal to have been widely used to compute NMR and EPR parameters. Other chapters will also show that other successful methods have also been formulated based on direct incorporation of magnetic response phenomena into the spatial wave function. Equation (4.28) is valid as written for either form of $|\Phi_L\rangle$, however, thus providing a point of comparison for the two approaches.

References

1 A. Abragam, B. Bleaney, *Electron Paramagnetic Resonance of Transition Metal Ions*, Clarendon Press, Oxford **1970**.

2 A. Abragam, *The Principles of Nuclear Magnetic Resonance*, Oxford University Press, Oxford **1961**.

3 J. Owen, M. Browne, W.D. Knight et al., *Phys. Rev.* **1956**, *102*, 1501; W.D. Knight, *Philos. Mag., B* **1999**, *79*, 1231.

4 J. Vaara, K. Ruud, O. Vahtras, *J. Chem. Phys.* **1999**, *111*, 2900 and references therein.

5 H. Kruger, *Z. Phys.* **1951**, *130*, 371.

6 B. Bleaney, *Philos. Mag.* **1951**, *42*, 441.

7 G. Feher, *Phys. Rev.* **1956**, *103*, 834.

8 M. Abraham, M.H. McCausland, F.N.H. Robinson, *Phys. Rev. Lett.* **1959**, *2*, 449–451.

9 L.G. Rowan, E.L. Hahn, W.B. Mims, *Phys. Rev. A*, **1964**, *137*, 61.

10 R.E. Moss, *Advanced Molecular Quantum Mechanics*, Chapman and Hall, London **1973**.

11 J.E. Harriman, *Theoretical Foundations of Electron Spin Resonance*, Academic Press, New York **1978**.

5
Fundamentals of Nonrelativistic and Relativistic Theory of NMR and EPR Parameters

Werner Kutzelnigg

5.1
Introduction

The theory of NMR and EPR parameters is essentially the quantum theory of an atom or a molecule in magnetic fields of different origin, namely an external homogeneous field, and that created by the magnetic moment of a nucleus.

First-order effects, which are *linear* in the field strength, vanish for *non-degenerate states*, and take account of a splitting of degenerate levels, giving rise to the *Zeeman effect*, which is directly observable in EPR, and is accompanied by the *hyperfine interaction*. These first-order properties are also responsible for *temperature-dependent* paramagnetism and mainly responsible for *nuclear magnetic shielding in degenerate states*.

Second-order properties, which are *quadratic* in the field strength include *magnetizability* (magnetic susceptibility), *nuclear magnetic shielding* (mainly for non-degenerate states) and the related *NMR chemical shift*, as well as (indirect) *nuclear spin coupling*. Second-order properties can be rationalized with the argument that one field induces a current density, that interacts with the other field.

In order to fully appreciate the theory of atoms or molecules in a magnetic field, the recapitulation of some basic aspects of electrodynamics and classical mechanics is recommended. We insist particularly on one aspect hardly mentioned in textbooks, namely that mechanics is Galilei-invariant, whereas electrodynamics is Lorentz invariant. Consistent combinations of the two theories are either that of mechanics with the *non-relativistic limit* (*nrl*) of electrodynamics, or that of full electrodynamics with the Lorentz invariant generalization of mechanics, i.e. the *special theory of relativity*.

In quantizing the classical theory one must, in either case, consider that electrons have to be described by *spinor* wavefunctions. This leads, in the relativistic regime, to the Dirac equation, and, in the *nrl*, to the *Lévy-Leblond equation*, which differs from the Schrödinger equation mainly in the presence of a term which describes the interaction of spin with an external magnetic field.

This spin-dependent term is important for first-order properties, but it contributes neither to the magnetic susceptibility, nor to the nuclear magnetic shielding for non-degenerate states in the *nrl*. It does contribute to the (indirect) nuclear spin

Calculation of NMR and EPR Parameters. Theory and Applications.
Edited by Martin Kaupp, Michael Bühl, Vladimir G. Malkin
Copyright © 2004 WILEY-VCH Verlag GmbH & Co. KGaA, Weinheim
ISBN: 3-527-30779-6

coupling, even in the *nrl*, and to the relativistic corrections to nuclear magnetic shielding (there in combination with the spin–orbit interaction). Relativistic effects are qualitatively different for degenerate states with the degeneracy split by spin–orbit interaction and for non-degenerate or simply spin-degenerate states.

A systematic theory of magnetic properties and their relativistic corrections is possible in terms of *direct perturbation theory*. In a fully relativistic theory a problem arises with the identification of the counterpart of the *diamagnetic contribution* to second-order properties in non-relativistic theory. The popular interpretation of the sum over negative-energy states in a sum-over-states expression becomes obsolete, if one realizes, that by means of a simple unitary transformation of the Dirac operator a counterpart of the diamagnetic term appears naturally.

We concentrate our attention on one-electron systems, because most relevant features arise already for these, since the interaction with magnetic fields is described by *one-electron operators*. So the generalization to many-electron systems is rather obvious. One-electron systems are atypical only in the respect that they cannot be in a *non-degenerate* state, at variance with the majority of ground states of molecules of interest.

5.2 Classical Theory of the Interaction of a Charged Particle with an Electromagnetic Field

5.2.1 The Maxwell Equations in the Vacuum

The Maxwell equations [1,2]

$$\text{div } \vec{E} = a\,\varrho \tag{5.1}$$

$$\text{div } \vec{B} = 0 \tag{5.2}$$

$$\text{rot } \vec{E} = -b\,\dot{\vec{B}} \tag{5.3}$$

$$\text{rot } \vec{B} = \frac{a}{bc^2}\,\vec{j} + \frac{1}{bc^2}\,\dot{\vec{E}} \tag{5.4}$$

relate the *electric* ($\vec{E}$) and *magnetic* ($\vec{B}$) field strengths to the *charge density* (ϱ) and the *current density* ($\vec{j}$). In a vacuum one needs, unlike in the presence of media, only *one* electric and *one* magnetic field. It is, in this context, legitimate to refer to $\vec{B}$ as the *magnetic field strength*, although some authors prefer, for historical reasons, the names *magnetic flux density* or *magnetic induction* for $\vec{B}$ and reserve the name magnetic field strength for the $\vec{H}$ field (that will never appear in this text). In Eqs. (5.1 to 5.4) c is the velocity of light, while the constants a and b depend on the chosen system of units, as indicated in Table 5.1.

To describe the motion of a charged particle in an electromagnetic field we also need the expression of the *force* acting on a point particle of charge q and velocity $\vec{v}$. It consists of the *Coulomb* force (due to $\vec{E}$) and the *Lorentz* force (due to $\vec{B}$).

Table 5.1 The constants a and b of the Maxwell equations for various systems of units

	el. stat.	el. mag.	Gauß	SI
a	4π	$4\pi c^2$	4π	$\frac{1}{\varepsilon_0}$
b	1	1	$\frac{1}{c}$	1
f	1	1	1	1

$$\vec{k} = fq(\vec{E} + b\,\vec{v} \times \vec{B}) \tag{5.5}$$

The parameter f also depends on the chosen system of units. However, since it is equal to 1 for all proposed systems, we shall henceforth ignore f.

5.2.2 The Electrodynamic Potentials

A partial solution of the Maxwell equations (5.1 to 5.4) is possible, if one realizes that Eq. (5.2) implies that $\vec{B}$ can be written as the curl (rot) of a vector field $\vec{A}$, called *vector potential*.

$$\vec{B} = \mathrm{rot}\vec{A} \tag{5.6}$$

While $\vec{A}$ determines $\vec{B}$ uniquely, the converse is not true. One may add grad λ of an arbitrary scalar function λ (called *gauge* function) to $\vec{A}$, without changing the validity of Eq. (5.6). In fact $\vec{A}'$, defined as

$$\vec{A}' = \vec{A} + \mathrm{grad}\lambda;\ \mathrm{rot}\vec{A}' = \mathrm{rot}\vec{A} + \mathrm{rot}\ (\mathrm{grad}\lambda) = \mathrm{rot}\vec{A} \tag{5.7}$$

is *equivalent* to $\vec{A}$ (i.e. corresponds to the same $\vec{B}$). One says $\vec{A}$ and $\vec{A}'$ differ in the *gauge of the vector potential*. If we insert Eq. (5.6) into Eq. (5.3)

$$\mathrm{rot}\ \vec{E} = -b\,\dot{\vec{B}} = -b\ \mathrm{rot}\ \dot{\vec{A}};\ \mathrm{rot}\ (\vec{E} + b\,\dot{\vec{A}}) = 0 \tag{5.8}$$

we find that $\vec{E} + b\,\dot{\vec{A}}$ can be expressed as the gradient of a scalar potential Φ:

$$\vec{E} + b\,\dot{\vec{A}} = -\mathrm{grad}\ \Phi \tag{5.9}$$

Φ is determined except for an arbitrary additive constant, i.e. Φ' given by

$$\Phi' = \Phi + const. \tag{5.10}$$

is *equivalent* to Φ (in the same sense as $\vec{A}'$ is equivalent to $\vec{A}$). We can now express $\vec{E}$ and $\vec{B}$ in Eq. (5.1) and Eq. (5.4) in terms of $\vec{A}$ and Φ, using

$$\text{rot}\ (\text{rot}\vec{A}) = -\Delta\vec{A} + \text{grad}\ \text{div}\vec{A} \tag{5.11}$$

Instead of the *four* Maxwell equations (5.1 to 5.4) for $\vec{E}$ and $\vec{B}$ we now have *two* equations for Φ and $\vec{A}$. Rather than giving the general expressions, we consider two special choices of the gauge of $\vec{A}$. It is no loss of generality to require that

$$\text{div}\ \vec{A} = 0 \tag{5.12}$$

One refers to this choice as *Coulomb gauge*. The equations satisfied by Φ and $\vec{A}$ are then

$$\Delta\Phi = -a\ \varrho \tag{5.13}$$

$$-\Delta\vec{A} + \frac{1}{c^2}\ddot{\vec{A}} + \frac{1}{bc^2}\ \text{grad}\ \dot{\Phi} = \frac{a}{bc^2}\ \vec{j} \tag{5.14}$$

The name *Coulomb* gauge alludes to the fact that Φ satisfies a *Poisson equation* like does the *Coulomb* potential in electrostatics. An alternative is the *Lorentz gauge*

$$\text{div}\vec{A} + \frac{1}{bc^2}\dot{\Phi} = 0 \tag{5.15}$$

The counterparts of Eqs. (5.13 and 5.14) are then

$$-\Delta\Phi + \frac{1}{c^2}\ddot{\Phi} = a\varrho \tag{5.16}$$

$$-\Delta\vec{A} + \frac{1}{c^2}\ddot{\vec{A}} = \frac{a}{bc^2}\ \vec{j} \tag{5.17}$$

If Φ and $\vec{A}$ are *time-independent*, the two gauges are indistinguishable.
In the absence of ϱ and $\vec{j}$, Eqs. (5.16) and (5.17) are *wave equations* describing the propagation of an electromagnetic wave.

5.2.3
Lagrangean of a Charged Particle in an Electromagnetic Field

We start from the expression (5.5) for the *force on a point particle* with charge q. This force is (unless $\vec{B} = 0$) *not* the gradient of a potential. However it can be derived from a *kinetic potential* U, according to the prescription:

$$k_\alpha = -\frac{\partial U}{\partial\alpha} + \frac{\mathrm{d}}{\mathrm{d}t}\frac{\partial U}{\partial\dot{\alpha}};\ \alpha = x, y, z \tag{5.18}$$

In the present case we have

$$U = q(\Phi - b\ \vec{v}\cdot\vec{A}) \tag{5.19}$$

If a force can be derived from a kinetic potential U in the sense of Eq. (5.18), one can define a *Lagrangean*

$$L = T - U;\ \ T = \frac{1}{2} m(\dot{\vec{r}})^2 \tag{5.20}$$

with T the kinetic energy. The equations of motion are then

$$\frac{\partial L}{\partial \alpha} - \frac{\mathrm{d}}{\mathrm{d}t}\frac{\partial L}{\partial \dot{\alpha}} = 0;\ \ \alpha = x, y, z \tag{5.21}$$

They are the *Euler Lagrange equations* corresponding to *Hamilton's* variational principle

$$\int_{t_1}^{t_2} L\ \mathrm{d}t = \text{Extr.} \tag{5.22}$$

It is then further possible to define the momenta p_α, canonically conjugated to the coordinates α as

$$p_\alpha = \frac{\partial L}{\partial \dot{\alpha}};\ \ \alpha = x, y, z \tag{5.23}$$

and the Hamiltonian

$$H = \sum_\alpha \dot{\alpha} p_\alpha - L \tag{5.24}$$

While the Lagrangean L is a function of the position $\vec{r}$ and the velocity $\dot{\vec{r}}$ of the particle, the Hamiltonian H is a function of the position $\vec{r}$ and the momentum $\vec{p} = (p_x, p_y, p_z)$. The change of variables from L to H is a special case of a *Legendre transformation*.

The equations of motion in the Hamiltonian form are

$$\frac{\partial H}{\partial p_\alpha} = \dot{\alpha};\ \ \frac{\partial H}{\partial \alpha} = -\dot{p}_\alpha;\ \ \alpha = x, y, z \tag{5.25}$$

In our case the *canonical momenta* are

$$p_\alpha = \frac{\partial L}{\partial \dot{\alpha}} = m\ \dot{\alpha} + b\ q\ A_\alpha;\ \ \vec{p} = m\ \vec{v} + b\ q\vec{A} \tag{5.26}$$

and the Hamiltonian is

$$H = \vec{v}\vec{p} - L = \frac{1}{2m}(\vec{p} - b\ q\ \vec{A})^2 + q\ \Phi = \frac{1}{2m}\vec{\pi}^2 + q\ \Phi \tag{5.27}$$

with $\vec{\pi}$ the *kinematic momentum* complementary to the *canonic momentum* $\vec{p}$

$$\vec{\pi} = \vec{p} - b\ q\ \vec{A} = m\vec{v} \tag{5.28}$$

Although the Hamiltonian contains $\vec{A}$, and depends hence on the gauge of $\vec{A}$, the Hamiltonian equations of motion are independent of the gauge and depend only on $\vec{B}$ and $\vec{E}$. If the electromagnetic fields are time-independent, the Hamiltonian H is constant and equal to the energy E, which is then a *constant of motion*.

5.2.4 The Non-Relativistic Limit of Electrodynamics

Two serious objections against the above given derivation of the *Lagrangean* and the *Hamiltonian* can be raised. Both are hardly mentioned in textbooks, and are related to some *incompatibility* between classical mechanics and electrodynamics.

1. Mechanics is Galilei-invariant, electrodynamics is Lorentz-invariant.
2. While classical mechanics is conveniently formulated for point particles, point charges are unacceptable in electrodynamics.

Two coordinate systems are called *inertial systems*, if they move with respect to each other with a constant velocity $\vec{u}_{12}$. The *relativity principle* requires that physical laws are the same in all *inertial systems*, and that physical quantities must transform according to some transformation law between two inertial systems.

There are two main relativity principles and associated transformations:

a) The *Galilei transformation*. Its main feature is that velocities are simply added as vectors. If a particle has the velocity $\vec{v}_1$ in system 1, it has the velocity

$$\vec{v}_2 = \vec{v}_1 + \vec{u}_{12} \tag{5.29}$$

in system 2. The *time t* is the same in the two systems. Under a Galilei transformation *distances in space* like $|\vec{r}_1 - \vec{r}_2|$ are invariant. There is *no* upper bound for velocities.

b) The *Lorentz transformation*. Its main characteristic is a maximal speed c, which is the same in all inertial systems. Not only points $\vec{r}$ in space, but also the time t differs in two inertial systems. Under a Lorentz transformation *distances in the four-dimensional Minkowski space* like $\{|\vec{r}_1 - \vec{r}_2|^2 - c^2|t_1 - t_2|^2\}$ are invariant. If $\vec{v}$ is some characteristic velocity, the physical laws can be expanded in powers of $\beta = |\vec{v}|/c$. The Galilei transformation is the limit for $\beta \to 0$ of the Lorentz transformation.

Since classical mechanics transforms under the Galilei transformation and electrodynamics under the Lorentz transformation, they must not be combined naively. One rather has two choices. One is to follow Einstein on his way to the *special theory of relativity*, and to modify classical mechanics, such that it becomes Lorentz invariant (see Section 5.2.5). The other way is to search for the non-relativistic limit (*nrl*) of electrodynamics, before one combines it with mechanics. This will then lead to a consistent theory for particles which move sufficiently slowly.

In our formulation Eqs. (5.1) to (5.4) of the Maxwell equations the *nrl* is already prepared. In fact in the limit $c^{-2} \to 0$ the r.h.s. of Eq. (5.4) vanishes, i.e. Eq. (5.4) has to be replaced by Eq. (5.30)

$$\text{rot } \vec{B} = 0 \tag{5.30}$$

while Eqs. (5.1) to (5.3) remain unaffected. We must, of course, regard the constants a and b as independent of c, even if for some systems of units they formally contain

c. In the *nrl* so constructed we ignore the magnetic field created by an electric current or a moving charge, as well as the *displacement current*. These must be regarded as *relativistic effects*. The induction of an electric field by a moving magnetic field survives in the *nrl*. Since also the Lorentz force remains present in the *nrl*, we can in the *nrl* construct a Lagrangean and a *Hamiltonian* for the movement of a particle in an electromagnetic field. This is not the only possibility to define a *nrl* of electrodynamics, but it is most convenient for our purposes. It agrees with the *nrl* of electrodynamics studied by Lévy-Leblond [3].

Under these conditions the derivation of *L* and *H* given in the previous subsection gets an a *posteriori* justification. The kinetic potential U given by Eq. (5.19) is Galilei-invariant, if *B* and *E* satisfy the *nrl* of the Maxwell equations. In this limit the electrodynamical potentials satisfy

$$\Delta\Phi = -a\varrho;\ \Delta\vec{A} = 0 \tag{5.31}$$

In the *nrl* there is *no* propagation of electromagnetic waves

To take the *nrl* of electrodynamics becomes particularly important, if we consider the motion of *several* charged particles, which interact through electric and magnetic forces. In rigorous (i.e. Lorentz-invariant) electrodynamics there is a magnetic interaction in addition to the electric interaction and both interactions are *retarded*. Then *it is not possible* to define a many-particle Hamiltonian. This is only the case in the *nrl*, where only the non-retarded (static) Coulomb interaction survives. It is consistent to consider magnetic and retardation effects only together with relativistic corrections to the kinematics, which are also of $O(c^{-2})$. Then one gets the many-particle Hamiltonian:

$$H = \sum_i \left\{ \frac{1}{2m} (\vec{p}_i - b\ q_i \vec{A}_i)^2 + q_i \Phi_i \right\} + \sum_{i<j} a\ q_i q_j \frac{1}{4\pi |\vec{r}_i - \vec{r}_j|} \tag{5.32}$$

The second incompatibility of classical mechanics and electrodynamics is related to the fact that in classical mechanics one idealizes moving particles as point masses, while electrodynamics does not tolerate point charges, because the energy of the field created by a point particle is infinite. This is serious because this energy behaves as an inert mass, which would then be infinite too. If one regards the observed mass of the electron as *entirely* due to its electric field, it must have a radius of the order of the *classical* or *Thomson* radius [1]

$$r_{cl} = \frac{ae^2}{4\pi mc^2} = 2.82\ 10^{-15} m \tag{5.33}$$

Otherwise (i.e. if the electron also has a *mechanical mass*), its radius must be larger than r_{cl}. A compromise view is that the electron has a finite radius, but that this is so small that the validity of point mass mechanics remains unaffected. This problem does not disappear when we switch to quantum mechanics. The infinite mass of a point charge does, in fact, play a role in quantum electrodynamics (QED), where a finite observable mass is achieved by so-called *mass renormalization*.

5.2.5
Lorentz-Invariant Generalization of Classical Mechanics

To create a Lorentz invariant Lagrangean for the motion of a relativistic charged particle, we need a Lorentz invariant expression for the Lagrangean L_0 in the absence of a field, which yields in the *nrl* the non-relativistic kinetic energy (except for an additive constant). It turns out that this must be chosen as:

$$L_0 = -mc^2\sqrt{1-\beta^2} = -mc^2 + \frac{m}{2}v^2 + O\left(\frac{v^4}{c^2}\right) \tag{5.34}$$

which corresponds to a Lorentz invariant generalization of Hamilton's variation principle Eq. (5.22). The kinetic potential U Eq. (5.19) is already Lorentz invariant, provided that Φ and $\vec{A}$ satisfy Eqs. (5.13 and 5.14) or Eqs. (5.16 and 5.17). Hence the Lagrangean in the presence of an electromagnetic field is

$$L = -mc^2\sqrt{1-\beta^2} - q\,\Phi + bq\,\vec{A}\vec{v} \tag{5.35}$$

Inserting this L into the Lagrange equations of motion makes these Lorentz invariant and hence relativistically correct. We can construct the canonical momenta

$$p_\alpha = \frac{\partial L}{\partial \dot{\alpha}} = \frac{mv_\alpha}{\sqrt{1-\beta^2}} + bq\,A_\alpha;\ \vec{p} = \frac{m\vec{v}}{\sqrt{1-\beta^2}} + bq\,\vec{A} \tag{5.36}$$

A Legendre transformation leads to the Hamiltonian

$$H = \vec{p}\cdot\vec{v} - L = c\sqrt{(\vec{p} - bq\,\vec{A})^2 + m^2c^2} + q\Phi \tag{5.37}$$

If $\frac{\partial H}{\partial t} = 0$, $H = E$ is a constant of motion, and we get the *relativistic energy law*

$$(E - q\,\Phi)^2 = c^2(\vec{p} - b\,q\,\vec{A})^2 + m^2c^4 = c^2\vec{\pi}^2 + m^2c^4 \tag{5.38}$$

Unfortunately, the concept of the Lagrangean or the Hamiltonian for a relativistic particle moving in an external electromagnetic field *cannot be generalized to n-particle systems*, not even to $n = 2$.

5.3
Quantum Mechanical Hamiltonians in a Time-Independent Electromagnetic Field

5.3.1
The Many-Electron Schrödinger Hamiltonian

We obtain the non-relativistic n-electron Hamiltonian from its classical counterpart Eq. (5.32), if we insert the Coulomb potential due to point charges and replace the momentum $\vec{p}$ by the momentum operator $\hat{\vec{p}}$. We assume that $\vec{A}$ is time-independent, and that Φ is only due to the Coulomb interaction of electrons and nuclei. We

ignore the nuclear repulsion, which, for fixed geometry, is a constant. i and j count electrons.

$$H = \sum_j h(j) + \sum_{i<j} \frac{a}{4\pi} \frac{e^2}{|\vec{r}_i - \vec{r}_j|} \tag{5.39}$$

$$h(j) = \frac{1}{2m} [\, \hat{\vec{p}}_j + b|e|\vec{A}(j)]^2 + V(j) \tag{5.40}$$

$$\vec{p}_j = -i\,\hbar\nabla_j \tag{5.41}$$

$$V(j) = |e|\Phi(j);\ \ \Phi(j) = -\sum_\mu \frac{aZ_\mu|e|}{4\pi|\vec{r}_\mu - \vec{r}_j|} \tag{5.42}$$

This Hamiltonian is only valid for spin-free particles. Otherwise a spin-dependent term must be added, to which we come later (Section 5.3.11).

5.3.2 Atomic Units

By introducing *atomic units* one gets rid of all fundamental constants. Two systems of atomic units have been suggested [2]. For the *Hartree system* [4] one starts from the Gaussian system ($b = \frac{1}{c}, a = 4\pi$) with three basic units, and measures then all quantities of the dimension of mass, electric charge and action in units of $m, |e|$ and $\hbar$.

For the *SI-based system of atomic units* [5] one starts from the SI system ($b = 1, a = \frac{1}{\varepsilon_0}$) with three basic units, and then measures all quantities of the dimension of mass, electric charge, action, and constant of dielectricity of the vacuum in units of $m, |e|,\ \hbar$, and $4\pi\varepsilon_0$.

In both systems of atomic units $\frac{a}{4\pi} = 1$, hence we get the same Hamiltonian, except for the terms which contain b, which differs in the two systems. It is convenient to keep b. One has so a formulation that is valid for both systems. Moreover b can be used as a formal perturbation parameter, which measures the strength of the magnetic field. The Hamiltonian Eq. (5.39) becomes so

$$H = \sum_j h(j) + \sum_{i<j} \frac{1}{|\vec{r}_i - \vec{r}_j|} \tag{5.43}$$

$$h(j) = \frac{1}{2}[-i\nabla_j + b\vec{A}(j)]^2 + V(j) \tag{5.44}$$

$$V(j) = -\sum_\mu \frac{Z_\mu}{|\vec{r}_\mu - \vec{r}_j|} \tag{5.45}$$

Tacitly one uses another basic unit, namely the *mol*. Hence atomic units, can, depending on the case, either refer to a single atom or molecule, or to a *mol*. Molecular and molar properties need not be distinguished at the level of atomic units.

5.3.3 Reformulation of the Hamiltonian

Using the Coulomb gauge Eq. (5.12) $h(j)$ can be reformulated to

$$\begin{aligned} h(j) &= \frac{1}{2}[-i\nabla_j + b\vec{A}(j)]^2 + V(j) \\ &= h_0(j) - \frac{1}{2}ib[\nabla_j\vec{A}(j) + \vec{A}(j)\nabla_j] + \frac{1}{2}b^2\vec{A}^2(j) \\ &= h_0(j) + b\vec{A}(j)\vec{p}_j + \frac{1}{2}b^2\vec{A}^2(j); \end{aligned}$$

$$h_0(j) = -\frac{1}{2}\nabla_j^2 + V(j) \tag{5.46}$$

There is one term *linear*, one *quadratic* in $\vec{A}$ (or b). This Hamiltonian is still preliminary, because the term representing the interaction of the electron spin with the magnetic field is missing (see Section 5.3.11).

It should be mentioned that the *Coulomb gauge* Eq. (5.12) does not determine $\vec{A}_k$ uniquely. It is still possible to add to $\vec{A}_k$ the gradient of a *gauge function* λ

$$\mathrm{div}(\vec{A} + \mathrm{grad}\lambda) = \mathrm{div}\ \mathrm{grad}\lambda = \Delta\lambda = 0 \tag{5.47}$$

provided that λ satisfies the *Laplace equation* $\Delta\lambda = 0$

5.3.4 Gauge Transformation, Non-Relativistic

Let us apply a unitary transformation with $\lambda = \lambda(\vec{r})$, $\Delta\lambda = 0$, to the Hamiltonian (5.43):

$$\tilde{H} = e^{-ib\Lambda}He^{ib\Lambda} = \sum_j \tilde{h}(j) + \sum_{i<j}\frac{1}{|\vec{r}_i - \vec{r}_j|};\ \Lambda = \sum_j \lambda(\vec{r}_j) \tag{5.48}$$

$$\begin{aligned} \tilde{h} &= e^{-ib\lambda}he^{ib\lambda} = h + ib[h,\lambda] - \frac{b^2}{2}[[h,\lambda],\lambda] + \ldots \\ &= h - \frac{ib}{2}[\nabla^2,\lambda] + \frac{b^2}{4}[[\nabla^2,\lambda],\lambda] + b^2[\vec{A}\nabla,\lambda] \\ &= h_0 + b\tilde{\vec{A}}\vec{p} + \frac{b^2}{2}\tilde{\vec{A}}^2 \end{aligned} \tag{5.49}$$

$$\tilde{\vec{A}} = \vec{A} + \mathrm{grad}\lambda;\ \tilde{H}\tilde{\Psi} = E\tilde{\Psi};\ \tilde{\Psi} = e^{-ib\Lambda}\Psi \tag{5.50}$$

This unitary transformation changes the Hamiltonian and its eigenfunctions, but does not affect its eigenvalues. The transformed Hamiltonian differs from the origi-

nal one only in a change of the gauge of the vector potential. A change of the gauge is hence equivalent to a unitary *gauge transformation* of the Hamiltonian.

5.3.5
Homogeneous External Magnetic Field

For a homogeneous magnetic field the field strength $\vec{B}_0$ is the same at any point $\vec{r}$ of space. A possible choice of the corresponding vector potential $\vec{A}_0$ is (we use the subscript 0 for an *external* homogeneous field):

$$\begin{aligned}\vec{A}_0 &= \frac{1}{2}\vec{B}_0 \times (\vec{r} - \vec{R}) = \frac{1}{2}\vec{B}_0 \times \vec{r} - \frac{1}{2}\vec{B}_0 \times \vec{R} \\ &= \frac{1}{2}\vec{B}_0 \times \vec{r} + \mathrm{grad}\lambda;\ \lambda = -\frac{1}{2}(\vec{B}_0 \times \vec{R}) \cdot \vec{r}\end{aligned} \tag{5.51}$$

with the *gauge origin* $\vec{R}$ fixed, but otherwise arbitrary. A change of gauge origin $\vec{R}$ is a special kind of gauge transformation.

Choosing $\vec{R} = 0$ the one-electron part of the Hamiltonian can be rewritten as:

$$\begin{aligned}h &= -\frac{1}{2}\nabla^2 + \frac{b}{2}(\vec{B}_0 \times \vec{r}) \cdot \vec{p} + \frac{1}{8}b^2(\vec{B}_0 \times \vec{r})^2 \\ &= -\frac{1}{2}\nabla^2 + \frac{b}{2}\vec{B}_0 \cdot \vec{l} + \frac{1}{8}b^2 r^2 B_0^2 \sin^2(\vec{r}, \vec{B}_0)\end{aligned} \tag{5.52}$$

Here l is the angular momentum with respect to the gauge origin.

While in atoms the position of the nucleus is a *natural* gauge origin, there is usually *no* natural gauge origin in molecules.

5.3.6
Field of a Magnetic Point Dipole

The vector potential $\vec{A}_k$ created by the magnetic moment of a nucleus, described by a magnetic point dipole $\vec{\mu}_k$ at position $\vec{\rho}_k$ is (the subscript k counts nuclei):

$$\vec{A}_k = d\frac{\vec{\mu}_k \times (\vec{r} - \vec{\rho}_k)}{|\vec{r} - \vec{\rho}_k|^3};\ d = \frac{a}{4\pi b^2 c^2} \tag{5.53}$$

For this field there is a *natural gauge origin* at the position of the nucleus, and there is, unlike for a homogeneous field, no need to consider other possible gauge origins. The constant d, which depends on the chosen system of units, is equal to $\frac{\mu_0}{4\pi}$ in the SI system, to 1 in the Hartree system, and to c^{-2} in the SI-based system of atomic units. The nuclear magnetic dipole moment $\vec{\mu}_k$ is the expectation value, with respect to the *nuclear spin wavefunction*, of the nuclear magnetic dipole moment operator

$$\hat{\vec{\mu}}_k = \gamma_k \vec{S}_k \tag{5.54}$$

where $\vec{S}_k$ is the operator of the nuclear spin, and the factor γ_k contains the *nuclear gyromagnetic* factor, as well as the ratio between the *nuclear* and the electronic *magneton* (i.e. essentially that between electronic and nuclear mass).

In constructing the corresponding field strength $\vec{B}_k$ from $\vec{A}_k$, one must realize, that the derivatives implicit in 'rot' must be taken in the *distribution sense* [7], hence there is an extra term involving a *delta function*. For $\vec{\rho}_k = 0$ we get

$$\vec{B}_k = \mathrm{rot}\vec{A}_k = d\frac{r^2\vec{\mu}_k - 3(\vec{\mu}_k\cdot\vec{r})\vec{r}}{r^5} + d\frac{r^2\vec{\mu}_k - (\vec{\mu}_k\cdot\vec{r})\vec{r}}{r^4}\delta(r) \tag{5.55}$$

The *delta 'function'* term (which simulates the boundary term of an integration by parts [7]) is only meaningful in the non-relativistic context, where the wavefunction is regular at the position of a nucleus. There is *no delta function* term in an *exact relativistic theory* for point nuclei, where the wavefunction has a weak singularity at the position of a nucleus, and where the integrals over negative powers of r do not diverge. The situation is more subtle, and hardly understood, in practical relativistic calculations with regularized wavefunctions.

5.3.7 The Dirac Operator

A relativistic electron in a (time-independent) electromagnetic field is described by the Dirac operator D and the time-independent Dirac equation:

$$D = \beta mc^2 + c\vec{\alpha}\cdot(\hat{\vec{p}} + b|e|\vec{A}) + V \tag{5.56}$$

$$\vec{\alpha} = (\alpha_x, \alpha_y, \alpha_z) \tag{5.57}$$

$$D\psi = W\psi = (E + mc^2)\psi \tag{5.58}$$

ψ is a *four-component (bispinor)* wavefunction, $\beta, \alpha_x, \alpha_y, \alpha_z$ are four-by-four matrices (5.67), called *Dirac matrices*, which satisfy the anticommutation relations

$$[\alpha_p, \alpha_q]_+ = \alpha_p\alpha_q + \alpha_q\alpha_p = 2\delta_{pq} \tag{5.59}$$

$$[\alpha_p, \beta]_+ = \alpha_p\beta + \beta\alpha_p = 0 \tag{5.60}$$

$$[\beta, \beta]_+ = 2\beta^2 = 2 \tag{5.61}$$

The energy eigenvalue W can be positive (describing an electron) or negative (describing a positron). We are only interested in electronic states.

Unlike in the non-relativistic theory it is not possible to construct the Dirac operator by *direct quantization* of the relativistic non-quantal Hamiltonian (5.37). The reason for this is not, as originally believed, that the naively quantized Hamiltonian

(5.37), containing a square root, is ill-behaved. The point is that electrons are particles with spin $\frac{1}{2}$ and must hence be described by *spinors*, i.e. by mathematical entities, that have a particular transformation behavior under the group of Lorentz transformations. This requires that the wavefunction consists of four components. A relation to the relativistic non-quantized theory exists insofar, as the Dirac operator is consistent with the relativistic energy relation (5.38). From Eq. (5.56) and the anticommutation relations we get

$$\beta mc^2 + c\vec{\alpha} \cdot (\vec{p} + b|e|\vec{A}) = D - V \tag{5.62}$$

$$(\beta mc^2 + c\vec{\alpha} \cdot [\vec{p} + b|e|\vec{A}])^2 = (D - V)^2 \tag{5.63}$$

$$m^2c^4 + c^2(\vec{p} + b|e|\vec{A})^2 = (D - V)^2 \tag{5.64}$$

There is another difference to the non-relativistic case. In relativistic theory, a many-electron Hamiltonian is not defined, not even classically. Therefore an exact relativistic *n*-electron Hamiltonian *is not available*. One can only use approximate Hamiltonians. In the simplest approximation one replaces the electron interaction by its *nrl*, i.e. the static Coulomb interaction. In a more refined approach one uses the Breit interaction, which takes care of magnetic and retardation effects to the leading order in v^2/c^2. A virtually exact, but extremely complicated, theory is possible by means of quantum electrodynamics (QED). It has hardly been applied beyond atoms with 3 or 4 electrons.

Fortunately the magnetic properties, that we study here, are one-electron properties. We can therefore understand the essential points by referring to a one-electron theory.

Having realized that an electron must be described by a spinor wavefunction, the question arises whether this is also the case in a non-relativistic theory. Lévy-Leblond [3] was probably the first to point out that the Galilei group has, like the Lorentz group, *spinor representations*. The search for a Galilei invariant field theory for a particle with *rest mass m* and *spin* $\frac{1}{2}$ led automatically to the Lévy-Leblond equation. We follow here a different route and derive the Lévy-Leblond equation as the *nrl* of the Dirac equation. This provides an easy access to the perturbation theory of relativistic effects.

5.3.8
Atomic Units, Relativistic

We prefer to use the *Hartree* or the *SI-based atomic unit* system even in the relativistic context. Then we must express the velocity of light *c* in *atomic units of velocity*, where it gets the value $\alpha^{-1} \approx 137$, i.e. the inverse of the fine structure constant α. It is unfortunate that the letter α is used both for the fine structure constant and the Dirac matrices. We keep *c* in the meaning of α^{-1}. Then the Dirac operator for an electron in a magnetic field reads

$$D = D_0 + bD_1;\ D_0 = \beta c^2 + c\vec{\alpha}\cdot\vec{p} + V;\ D_1 = c\vec{\alpha}\cdot\vec{A} \tag{5.65}$$

Alternatively, one may use so-called *natural* (or relativistic) units. Starting from the Gaussian system, one measures masses, velocities, and action in units of m, c, and $\hbar$. Then $|e|$ must be measured in these units, where it has the value $\alpha \approx \frac{1}{137}$, and is then called the *coupling constant*.

5.3.9
Gauge Transformation, Relativistic

Like in non-relativistic theory, a gauge transformation of the Dirac Hamiltonian corresponds to a change of the gauge of $\vec{A}$. It is even simpler.

$$\tilde{D} = e^{-ib\lambda} D e^{ib\lambda} = D + ib[D,\lambda] - \frac{b^2}{2}[[D,\lambda],\lambda] + \ldots = D_0 + bc\alpha\cdot\tilde{\vec{A}}$$

$$\tilde{\vec{A}} = \vec{A} + \ \mathrm{grad}\lambda;\ \tilde{D}\tilde{\psi} = W\tilde{\psi};\ \tilde{\psi} = e^{-ib\lambda}\psi \tag{5.66}$$

5.3.10
Block Form of the Dirac Equation

We decompose the four-component spinor ψ into two two-component spinors φ and χ. Then the 4 by 4-matrices α_q and β can be written as blocks consisting of 2 by 2-matrices:

$$\psi = \begin{pmatrix}\varphi\\ \chi\end{pmatrix};\ \beta = \begin{pmatrix}1 & 0\\ 0 & -1\end{pmatrix};\ \alpha_q = \begin{pmatrix}0 & \sigma_q\\ \sigma_q & 0\end{pmatrix};\ \vec{\alpha} = \begin{pmatrix}0 & \vec{\sigma}\\ \vec{\sigma} & 0\end{pmatrix} \tag{5.67}$$

with $\vec{\sigma}$ the vector of the three 2 by 2 Pauli matrices

$$\vec{\sigma} = (\sigma_x, \sigma_y, \sigma_z) \tag{5.68}$$

$$\sigma_x = \begin{pmatrix}0 & 1\\ 1 & 0\end{pmatrix};\ \sigma_y = \begin{pmatrix}0 & -i\\ i & 0\end{pmatrix};\ \sigma_z = \begin{pmatrix}1 & 0\\ 0 & -1\end{pmatrix} \tag{5.69}$$

The Dirac equation then becomes in block form,

$$(D - c^2)\psi = \begin{pmatrix}V & c\vec{\sigma}(\vec{p}+b\vec{A})\\ c\vec{\sigma}(\vec{p}+b\vec{A}) & V-2c^2\end{pmatrix}\begin{pmatrix}\varphi\\ \chi\end{pmatrix} = E\begin{pmatrix}\varphi\\ \chi\end{pmatrix} \tag{5.70}$$

φ and χ are two-component spinors. We call φ the upper (or 'large') component, χ the lower (or 'small') component. The names 'large' and 'small' refer to the fact that for *electronic states* φ is large and χ smaller of the order $O(c^{-1})$. For positronic states the role of φ and χ is inverted.

Note that unlike the non-relativistic Hamiltonian, the Dirac operator contains only a term *linear* in b and *no quadratic* one.

5.3.11
The Lévy-Leblond Equation

Let us limit our interest to *electronic* states (for which $W = mc^2 + E > 0$). Let us express the Dirac equation in terms of φ and $\bar{\chi} = c\chi$, such that the components φ and $\bar{\chi}$ are of the same order in powers of c^{-1}. We get

$$\psi = \begin{pmatrix} \varphi \\ \chi \end{pmatrix} \rightarrow \bar{\psi} = \begin{pmatrix} \varphi \\ \bar{\chi} \end{pmatrix} = \begin{pmatrix} \varphi \\ c\ \ \chi \end{pmatrix} \tag{5.71}$$

$$(D - c^2)\psi = E\psi \rightarrow \bar{D}\bar{\psi} = ES\bar{\psi} \tag{5.72}$$

$$\begin{pmatrix} V & \vec{\sigma}\ \ (\vec{p}+b\vec{A}) \\ \vec{\sigma}(\vec{p}+b\vec{A}) & \frac{V}{c^2}-2 \end{pmatrix} \begin{pmatrix} \varphi \\ \bar{\chi} \end{pmatrix} = E \begin{pmatrix} 1 & 0 \\ 0 & \frac{1}{c^2} \end{pmatrix} \begin{pmatrix} \varphi \\ \bar{\chi} \end{pmatrix} \tag{5.73}$$

(For negative-energy states a different change of the metric has to be taken). It is straightforward to perform in Eqs. (5.72) and (5.73) the limit $c^{-2} \rightarrow 0$.

$$D_{LL}\psi_{LL} = E_{LL}S_0\psi_{LL} \tag{5.74}$$

$$\begin{pmatrix} V & \vec{\sigma}(\vec{p}+b\vec{A}) \\ \vec{\sigma}(\vec{p}+b\vec{A}) & -2 \end{pmatrix} \begin{pmatrix} \varphi_{LL} \\ \chi_{LL} \end{pmatrix} = E_{LL} \begin{pmatrix} 1 & 0 \\ 0 & 0 \end{pmatrix} \begin{pmatrix} \varphi_{LL} \\ \chi_{LL} \end{pmatrix} \tag{5.75}$$

Eqs. (5.74) or (5.75) are known as the Lévy-Leblond equation in the presence of a magnetic field with E_{LL} the corresponding eigenvalue. It can be multiplied out to:

$$V\varphi_{LL} + \vec{\sigma} \cdot (\vec{p} + b\ \vec{A})\chi_{LL} = E_{LL}\varphi_{LL} \tag{5.76}$$

$$\vec{\sigma} \cdot (\vec{p} + b\ \vec{A})\varphi_{LL} - 2\chi_{LL} = 0 \tag{5.77}$$

Eq. (5.77) can be solved for χ_{LL}, and the result can be inserted into Eq. (5.76)

$$\chi_{LL} = \frac{1}{2}\vec{\sigma} \cdot (\vec{p} + b\ \vec{A})\varphi_{LL} \tag{5.78}$$

$$E_{LL}\varphi_{LL} = V\varphi_{LL} + \frac{1}{2}[\vec{\sigma} \cdot (\vec{p} + b\ \vec{A})]^2\varphi_{LL} = \{H_0 + bH_1 + b^2H_2\}\varphi_{LL} \tag{5.79}$$

$$H_0 = \frac{1}{2}\hat{p}^2 + V;\ \ H_1 = [\vec{A} \cdot \vec{p} + \frac{1}{2}\vec{\sigma} \cdot \vec{B}];\ \ H_2 = \frac{1}{2}(\vec{A})^2 \tag{5.80}$$

We arrive thus at the *Pauli equation*, i.e. the Schrödinger equation plus a spin-dependent term for the *upper* part φ_{LL} of the Lévy-Leblond bispinor ψ_{LL}. The spin-depen-

dent term arises here naturally, while starting from the Schrödinger equation it has to be added in an ad hoc way. In deriving (5.79) use has been made of some identities, that involve $\vec{\sigma}$.

$$(\vec{\sigma}\vec{a}) \cdot (\vec{\sigma}\vec{b}) = \vec{a} \cdot \vec{b} + i\vec{\sigma} \cdot (\vec{a} \times \vec{b}) \tag{5.81}$$

$$\vec{\sigma} \cdot (\vec{a} \times \vec{p}) + \vec{\sigma} \cdot (\vec{p} \times \vec{a}) = \vec{\sigma} \cdot (\vec{a} \times \vec{p}) - \vec{\sigma} \cdot (\vec{a} \times \vec{p}) - i\vec{\sigma} \cdot (\mathrm{rot}\ \vec{a})$$

$$= -i\ \vec{\sigma} \cdot (\mathrm{rot}\ \vec{a}) \tag{5.82}$$

For the special case of an external homogeneous magnetic field $\vec{B}_0$ we get

$$H_{10} = \vec{A}_0 \cdot \vec{p} + \frac{1}{2}\vec{\sigma} \cdot \vec{B}_0 = \frac{1}{2}\vec{B}_0 \cdot \left\{ (\vec{r} - \vec{R}) \times \vec{p} \right\} + \frac{1}{2}\vec{\sigma} \cdot \vec{B}_0$$

$$= \frac{1}{2}\vec{B}_0 \cdot \vec{l} + \frac{1}{2}\vec{B}_0 \cdot \vec{\sigma} = \frac{1}{2}\ \vec{B}_0 \cdot (\vec{l} + 2\vec{s});\ \vec{s} = \frac{1}{2}\vec{\sigma};\ H_{20} = \frac{1}{2}\vec{A}_0^2 \tag{5.83}$$

$\vec{l}$ is the angular momentum operator with respect to the origin $\vec{R}$ and $\vec{s}$ the spin operator. Noting that $\vec{s}$ satisfies the same commutation relations as $\vec{l} = \vec{r} \times \vec{p}$,

$$[l_x, l_y] = i\ l_z;\ cycl.;\ [s_x, s_y] = i\ s_z;\ cycl \tag{5.84}$$

and hence represents an angular momentum, one obtains a *gyromagnetic* ratio $g = 2$ for the spin relative to the orbital angular momentum. The quantity $\frac{b}{2}$ plays the role of the *Bohr magneton*. If one uses atomic units, there is no need to introduce the Bohr magneton. For the counterpart of Eq. (5.83) for the field $\vec{B}_k$ due to a nuclear magnetic moment we shall use the notation H_{01}

$$H_{01} = \vec{A}_k \cdot \vec{p} + \frac{1}{2}\vec{\sigma} \cdot \vec{B}_k = d\frac{\vec{\mu}_k \cdot \vec{l}_k}{|\vec{r} - \vec{\rho}_k|^3} + \frac{1}{2}\vec{\sigma} \cdot \vec{B}_k;\ \vec{l}_k = (\vec{r} - \vec{\rho}_k) \times \vec{p} \tag{5.85}$$

with A_k and B_k defined by Eqs. (5.53) and (5.55). The terms bilinear in two fields are

$$H_{11} = \vec{A}_0 \cdot \vec{A}_k;\ H_{011} = \vec{A}_k \cdot \vec{A}_l \tag{5.86}$$

5.4 Perturbation Theory of Magnetic Effects

5.4.1 First- and Second-Order Properties

Consider a Hamiltonian H, that depends analytically on a parameter λ, and assume that the eigenvalue E and the eigenfunction ψ can be expanded in powers of λ as well. The k^{th} derivative of E with respect to λ is then a k^{th}-order property.

$$H = H_0 + \lambda H_1 + \lambda^2 H_2 + \ldots \tag{5.87}$$

$$E = E_0 + \lambda E_1 + \lambda^2 E_2 + \lambda^3 E_3 + \ldots \tag{5.88}$$

$$\psi = \psi_0 + \lambda \psi_1 + \lambda^2 \psi_2 + \lambda^3 \psi_3 + \ldots \tag{5.89}$$

$$\left(\frac{\partial E}{\partial \lambda}\right)_{\lambda=0} = E_1; \left(\frac{\partial^2 E}{\partial \lambda^2}\right)_{\lambda=0} = 2E_2 \tag{5.90}$$

The standard method to evaluate properties is *perturbation theory*. One obtains

$$E_1 = \langle \psi_0 | H_1 | \psi_0 \rangle \tag{5.91}$$

$$E_2 = \langle \psi_0 | H_2 | \psi_0 \rangle + \langle \psi_0 | H_1 | \psi_1 \rangle; \text{etc.} \tag{5.92}$$

with ψ_1 solution of

$$(H_0 - E_0)\psi_1 + (H_1 - E_1)\psi_0 = 0 \tag{5.93}$$

In the somewhat old-fashioned *sum-over-states* formulation of perturbation theory one expands ψ_1 in terms of the eigenstates ϕ_p of H_0 with eigenvalues ε_p ($\psi_0 = \phi_0$; $\varepsilon_0 = E_0$) and gets

$$E_2 = \sum_{p>0} \frac{|\langle \phi_0 | H_1 - E_1 | \phi_p \rangle|^2}{\varepsilon_0 - \varepsilon_p} \tag{5.94}$$

The Hamiltonian can depend on two or more parameters, e.g.

$$H = H_0 + \kappa H_{10} + \lambda H_{01} + \kappa^2 H_{20} + \kappa\lambda H_{11} + \ldots$$

$$E = E_0 + \kappa E_{10} + \lambda E_{01} + \kappa^2 E_{20}$$

$$+ \lambda^2 E_{02} + \kappa\lambda E_{11} + \ldots \tag{5.95}$$

$$\left(\frac{\partial E}{\partial \kappa}\right)_{(\kappa=0,\lambda=0)} = E_{10}; \left(\frac{\partial E}{\partial \lambda}\right)_{(\kappa=0,\lambda=0)} = E_{01}$$

$$\left(\frac{\partial^2 E}{\partial \kappa \partial \lambda}\right)_{(\kappa=0,\lambda=0)} = E_{11}; \ldots \tag{5.96}$$

Such *mixed* properties are evaluated by means of *double (or multiple) perturbation theory*. For a mixed second order property E_{11} one gets e.g.

$$E_{11} = \langle\psi_0|H_{11}|\psi_0\rangle + 2\mathrm{Re}\langle\psi_0|H_{10}|\psi_{01}\rangle = \langle\psi_0|H_{11}|\psi_0\rangle + 2\mathrm{Re}\langle\psi_0|H_{01}|\psi_{10}\rangle \quad (5.97)$$

That E_{11} can be expressed either in terms of ψ_{01} or ψ_{10} is a manifestation of Dalgarno's exchange theorem [6]. The two perturbation parameters κ and λ can e.g. refer to two different fields or to two Cartesian components of the same field. In the sum-over-states formulation we get:

$$E_{11} = \langle\psi_0|H_{11}|\psi_0\rangle + \sum_{p>0} \frac{\langle\phi_0|H_{10} - E_{10}|\phi_p\rangle\langle\phi_p|H_{01} - E_{01}|\phi_0\rangle}{\varepsilon_0 - \varepsilon_p} \quad (5.98)$$

It is rather common that an eigenvalue of H_0, i.e. in the absence of the perturbation, is degenerate, but that this degeneracy is removed by the perturbation. Then one must apply *degenerate perturbation theory*. This means one has first to find the *perturbation-adapted* unperturbed states. This can often be achieved in terms of symmetry arguments, namely if the perturbation lowers the symmetry. The Hamiltonian of an atom in a magnetic field is no longer invariant with respect to arbitrary rotations, but only with respect to rotations about the field axis, hence only m_s and m_l (in the relativistic regime only m_j) are good quantum numbers, and no longer l, s or j. If symmetry does not determine the *perturbation-adapted* unperturbed states uniquely, one must first construct the matrix representation of H_1 in the basis of the zeroth order degenerate states and then diagonalize this matrix, before one can evaluate higher-order perturbation corrections.

5.4.2 Magnetic Properties

We now explicitly consider the components of the magnetic field strength of a homogeneous external magnetic field

$$\vec{B}_0 = (B_{0x}, B_{0y}, B_{0z}) \quad (5.99)$$

and those of the magnetic moment of the k^{th} nucleus

$$\vec{\mu}_k = \{\mu_{kx}, \mu_{ky}, \mu_{kz}\} \quad (5.100)$$

as the perturbation parameters. We are especially interested in the components of the electronic magnetic moment

$$m_\alpha = -\left(\frac{\partial E}{\partial B_{0\alpha}}\right)_{B_{0\alpha}=0} ; \ \vec{m} = (m_x, m_y, m_z) \quad (5.101)$$

and the *magnetizability tensor*

$$\chi_{\alpha\beta} = -\left(\frac{\partial^2 E}{\partial B_{0\alpha}\partial B_{0\beta}}\right)_{B_{0\alpha}=0, B_{0\beta}=0} ; \qquad \underline{\underline{\chi}} = \begin{pmatrix} \chi_{xx} & \chi_{xy} & \chi_{xz} \\ \chi_{yx} & \chi_{yy} & \chi_{yz} \\ \chi_{zx} & \chi_{zy} & \chi_{zz} \end{pmatrix} \quad (5.102)$$

This tensor is symmetric, i.e. $\chi_{\alpha\beta} = \chi_{\beta\alpha}$. While the term *magnetizability* refers to a single atom or molecule, the corresponding bulk property (*per mol*) is the *magnetic susceptibility*. In appropriate atomic units they have the same value. An example of an asymmetric tensor is that of the *NMR shielding*

$$\sigma_{\alpha\beta}^{(k)} = \frac{\partial^2 E}{\partial \mu_{k\alpha} \partial B_{0\beta}}; \; \underline{\underline{\sigma}}^{(k)} = \begin{pmatrix} \sigma_{xx}^{(k)} & \sigma_{x\gamma}^{(k)} & \sigma_{xz}^{(k)} \\ \sigma_{\gamma x}^{(k)} & \sigma_{\gamma\gamma}^{(k)} & \sigma_{\gamma z}^{(k)} \\ \sigma_{zx}^{(k)} & \sigma_{z\gamma}^{(k)} & \sigma_{zz}^{(k)} \end{pmatrix} \tag{5.103}$$

and that of the nuclear spin coupling

$$J_{\alpha\beta}^{(k,l)} = \frac{\partial^2 E}{\partial \mu_{k\alpha} \partial \mu_{l\beta}}; \; \underline{\underline{J}}^{(k,l)} = \begin{pmatrix} J_{xx}^{(k,l)} & J_{x\gamma}^{(k,l)} & J_{xz}^{(k,l)} \\ J_{\gamma x}^{(k,l)} & J_{\gamma\gamma}^{(k,l)} & J_{\gamma z}^{(k,l)} \\ J_{zx}^{(k,l)} & J_{z\gamma}^{(k,l)} & J_{zz}^{(k,l)} \end{pmatrix} \tag{5.104}$$

Often one is mainly interested in the isotropic parts of these tensors e.g.

$$\sigma^{(k)} = \frac{1}{3}\{\sigma_{xx}^{(k)} + \sigma_{\gamma\gamma}^{(k)} + \sigma_{zz}^{(k)}\} \tag{5.105}$$

Note the minus sign in Eq. (5.102), such that $\chi > 0$ for paramagnetism and $\chi < 0$ for diamagnetism. This convention is counterintuitive, and therefore not always respected.

The climax in the confusion about sign conventions is that for *nuclear magnetic shieldings*, which refer to a bare nucleus, the sign is chosen opposite to that for *chemical shifts*, relative to a *standard* for the respective nucleus, see Eq. (5.128).

For a systematic notation for magnetic properties we add two to four subscripts to E. The first subscript always refers to orders in c^{-1}, and increases in steps of 2. So $E_{0\ldots}$ always means *non-relativistic*, while $E_{2\ldots}$ means the *leading relativistic correction*. The second label counts orders in the *external* homogeneous magnetic field $\vec{B}_0$, the third (and possibly the fourth) label orders in a nuclear magnetic moment $\vec{\mu}_k$ or $\vec{\mu}_l$. Since $\vec{B}_0$ and $\vec{\mu}_k$ are vectors, and we want to avoid extra labels for the Cartesian coordinates, we contract the corresponding tensors (that represent the properties) with $\vec{B}_0$ and/or $\vec{\mu}_k$, to arrive at scalar expressions, e.g.

$$bE_{010} = -\vec{m}\vec{B}_0 = -\sum_\alpha m_\alpha B_{0\alpha}; \; m_\alpha = -\frac{\partial E}{\partial B_{0\alpha}}; \; \alpha = x, \gamma, z \tag{5.106}$$

$$b^2 E_{020} = -\frac{1}{2}\sum_{\alpha\beta} B_{0\alpha}\chi_{\alpha\beta}B_{0\beta} \tag{5.107}$$

$$b^2 dE_{011} = \sum_{\alpha\beta} \mu_{k\alpha}\sigma_{\alpha\beta}B_{0\beta} \tag{5.108}$$

The factor b for E_{010}, bd for E_{001}, b^2 for E_{020}, or b^2d for E_{011} is *not* included in the definition of E_{01} etc., but it enters the expressions for χ, σ etc. This convention is convenient, but by no means compulsory.

5.5 Non-Relativistic Theory of EPR and NMR Parameters

5.5.1 First-Order Properties

If we consider one-electron states, we must, in principle, always deal with *degenerate perturbation theory*, because a state for an odd number of electrons is always *Kramers degenerate*, and this degeneracy is split by the magnetic field. Fortunately, at least in the *nrl*, i.e. in the absence of spin–orbit interaction, the perturbation-adapted unperturbed states are fully determined by symmetry, e.g. for an asymmetric molecule simply by the eigenvalue M_S of S_z. Then a first order property can simply be evaluated as the expectation value Eq. (5.91) of the perturbation operator H_1 with the unperturbed wavefunction with appropriate spin. For a *non-degenerate state* (which is only possible for an even number of electrons) E_1 vanishes, because H_1, see Eq. (5.80), is a *pseudoscalar one-electron operator*, both for $H_1 = H_{10}$ Eq. (5.83) and $H_1 = H_{01}$ Eq. (5.85). For an n-electron system we get

$$E_1 = \sum_{\nu} n_\nu \langle \phi_0^{(\nu)} | H_1 | \phi_0^{(\nu)} \rangle \tag{5.109}$$

with n_ν the occupation number of the ν^{th} unperturbed natural spin orbital $\phi_0^{(\nu)}$. Within the Hartree–Fock approximation n_ν can only be equal to 1 or 0. For a state with *only double occupancy*, the contributions of orbitals occupied with α or β spin just cancel.

There is a competition between the splitting of the zeroth order degeneracy by H_1, i.e. the magnetic field, and by spin–orbit interaction. Since the latter is a relativistic effect, (see 5.7.3), we can, in the non-relativistic context, only study states, that are not affected by spin–orbit interaction, i.e. atomic states with $S = 0$ and/or $L = 0$, states of linear molecules with $S = 0$ and/or $\Lambda = 0$, and states of arbitrary molecules with only spin degeneracy.

5.5.2 The Zeeman Effect

Let us now, for the sake of simplicity, only consider one-electron states. For a homogeneous field we get in view of Eq. (5.83) for a perturbation-adapted state

$$E_{010} = \langle \varphi_0 | H_{10} | \varphi_0 \rangle = \frac{1}{2} \langle \varphi_0 | \vec{B}_0 \cdot (\vec{l} + 2\vec{s}) | \varphi_0 \rangle; \; bE_{010} = -\vec{m} \cdot \vec{B}_0 \tag{5.110}$$

Here $\vec{m}$ is the (permanent) electronic *magnetic* moment of the perturbation-adapted state. E_{010} describes the *Zeeman shift* of the considered state. In the case of a doublet state the difference in E_{010} between the two components is called the *Zeeman splitting*. Direct transitions between Zeeman levels are observed in the EPR spectrum.

If the degeneracy is due to spin, and there is no orbital angular momentum, the Zeeman shift is given by the contribution (for $\vec{B}_0$ in z-direction, which is also the quantization axis for the spin)

$$bE_{010}(m_s) = \frac{b}{2}\langle\varphi^{(0)}|\vec{B}_0 \cdot 2\vec{s}|\varphi^{(0)}\rangle = -\frac{1}{2}gB_{0z}m_s \tag{5.111}$$

with $g = 2$. For a one-electron atom in an eigenstate of l^2 and l_z, but averaged over spin, we get

$$bE_{010}(m_l) = -\frac{1}{2}gB_{0z}m_l \tag{5.112}$$

with $g = 1$. For a highly symmetric molecule in a spatially degenerate state, that is not eigenstate of l^2 and l_z one gets a similar result with g between 0 and 1.

The value $g = 2$ holds in the non-relativistic regime for spin degeneracy in the absence of orbital degeneracy. Deviations from the *spin-only value* $g = 2$ occur on one hand as a result of relativistic corrections (mainly spin–orbit coupling), see Section 5.7.3, on the other hand because even for a free electron there are QED corrections to the g-factor.

If one considers an *ensemble* of atoms or molecules in a degenerate state, at a certain temperature T, rather than a single atom or molecule, in a magnetic field, one has to deal with a Boltzmann distribution over the Zeeman levels E_m. The energy shift ΔE is then

$$\Delta E = \frac{\sum_m bE_m \exp(-bE_m/kT)}{\sum_m \exp(-bE_m/kT)} = -\frac{b^2}{kT}\sum_m E_m^2 + O(b^3);\ E_m = E_{010}(m) \tag{5.113}$$

where the sum goes over all Zeeman levels, counted by the quantum number m. The term linear in b cancels, and the leading contribution to ΔE is *quadratic* in b (or $\vec{B}_0$) and proportional to $1/T$. One refers to this as ordinary (or temperature-dependent) *paramagnetism*.

5.5.3
Hyperfine Splitting; Fermi Contact Interaction

If $\vec{B}_k$ is the magnetic field created by the k^{th} nucleus, Eq. (5.110) becomes (see Eq. (5.85))

$$E_{001} = \langle\varphi_0|H_{01}|\varphi_0\rangle = \langle\varphi_0|\vec{A}_k \cdot \vec{p} + \frac{1}{2}\vec{\sigma} \cdot \vec{B}_k|\varphi_0\rangle \tag{5.114}$$

with $\vec{B}_k$ given by Eq. (5.55) (including the δ function term). Let us assume that there is only *spin degeneracy*, i.e. that the spin-independent perturbation $\vec{A}_k \cdot \vec{p}$ does not contribute. If we note that both $\vec{\sigma}$ and $\vec{\mu}_k$ are quantized in the direction of the external magnetic field, and that the relative orientation of the molecule and the nuclear spin is statistical, we have to average Eq. (5.114) over these orientations. Then the only term that survives in Eq. (5.114) is that due the totally symmetric part of $\vec{\sigma} \cdot \vec{B}_k$, i.e.

$$\langle\varphi_0|\vec{\sigma}\cdot\vec{B}_k|\varphi_0\rangle_{av} = \frac{2}{3}\langle\varphi_0|\frac{\vec{\sigma}\vec{\mu}_k}{r^2}\delta(r)|\varphi_0\rangle = \frac{2}{3}\int|\varphi_0|^2\frac{\vec{\sigma}\vec{\mu}_k}{r^2}\delta(r)\mathrm{d}\tau$$

$$= \frac{2}{3}\int|\varphi_0|^2\vec{\sigma}\vec{\mu}_k\delta(r)\mathrm{d}\Omega\ \mathrm{d}r = \frac{8\pi}{3}|\varphi_0(0)|^2\vec{\sigma}\vec{\mu}_k \tag{5.115}$$

This is known as *Fermi contact term* and is responsible for the hyperfine splitting of the EPR spectra.

A more satisfactory derivation of this term is obtained, if one does not start from the Pauli Hamiltonian as in Eq. (5.114), but directly from the Levy-Léblond operator Eq. (5.74). Then one has to evaluate, directly from $\vec{A}_k$ rather than $\vec{B}_k$,

$$E_{001} = \mathrm{Re}\langle\varphi_0|\vec{\sigma}\vec{A}_k|\chi_0\rangle = \frac{1}{4}\langle\varphi_0|(\vec{\sigma}\vec{A}_k)(\vec{\sigma}\vec{p})|\varphi_0\rangle + \frac{1}{4}\langle\vec{\sigma}\vec{p}\ \varphi_0|\vec{\sigma}\vec{A}_k\ \varphi_0\rangle \tag{5.116}$$

This leads to Eq. (5.114), including the δ-function term, if one applies the *turn-over rule* to $\vec{\sigma}\cdot\vec{p}$. This rule is based on an *integration by parts*, and is only valid, if the integrand has no singularities at the boundaries [7]. Since here the integrand is singular at $r = 0$, there is a *boundary term*, of which one must take care, and this gives exactly rise to the Fermi contact interaction. This has been discussed in more detail elsewhere [7]. It requires that the *test function* φ_0^2 is sufficiently regular.

The Fermi contact term also dominates the *nuclear magnetic shielding for degenerate (paramagnetic) atoms or molecules*. In fact, as discussed in connection with the (temperature-dependent) paramagnetism one must consider a Boltzmann distribution of the electronic magnetic moments in the external field. For each orientation there is a Fermi contact interaction with the magnetic field of the nucleus. One gets an expression like Eq. (5.113), just with the factor bE_m in front of the exponential replaced by the corresponding hyperfine shift $bdE_{001}(m)$. More details on NMR spectra of paramagnetic molecules are found in Chapter 20 by Moon and Patchkovski in this book.

5.5.4
Second-Order Properties

'Diagonal' or 'mixed' second-order properties of a one-electron state are of the general form Eq. (5.92) or Eq. (5.97) respectively, with H_{10} and H_{20} given by Eq. (5.83), H_{01} by Eq. (5.85), and H_{11} or H_{011} by Eq. (5.86). The first-order perturbation function needed in Eq. (5.92) or Eq. (5.97) is the response to the 'other field' and obtained as the solution of an equation of the type

$$(H_0 - E_0)\varphi_{01} + \left\{\vec{A}\vec{p} + \frac{1}{2}\vec{\sigma}\vec{B}\right\}\varphi_0 - E_{01}\varphi_0 = 0 \tag{5.117}$$

Due to the fact that the Hamiltonian Eq. (5.80) contains two spin-independent terms, one linear and one quadratic in b, and a spin-dependent term linear in b, there are three contributions to any second-order property, called *diamagnetic, para-*

magnetic, and spin-dependent. For the two latter contributions there are two alternative expressions in the sense of the Dalgarno exchange theorem, depending on which field is treated as the 'first' and which as the 'second' field.

For an *n*-electron system, one must sum over expressions like (5.92) or (5.97) multiplied by the occupation numbers, like in Eq. (5.109). Moreover the first-order response functions like φ_{01} are not obtained from the inhomogeneous differential equation (5.93), but e.g. by the slightly more complicated equations of coupled-Hartree–Fock or coupled MC-SCF theory [11,14], where H_0 is replaced by the *Fock operator*, and where also some coupling terms arise. For the discussion of the general features, this does, however, not matter much.

We shall mainly be interested in closed shell states, which are non-degenerate, and for which first-order effects vanish.

5.5.5 Role of the Spin-Dependent Term

The first-order perturbation operator contains a spin-dependent term $\frac{1}{2}\vec{\sigma}\vec{B}$, that has only a selective effect on second-order properties. Let us look at the sum-over states formulation Eqs. (5.94) and (5.98) and insert Eq. (5.83) and/or Eq. (5.85). Then the sum of the paramagnetic contribution and the spin-dependent term is

$$\sum_{p>0} \frac{\langle\phi_0|\vec{A}_k\vec{p} + \frac{1}{2}\vec{\sigma}\vec{B}_k|\phi_p\rangle\langle\phi_p|\vec{A}_l\vec{p} + \frac{1}{2}\vec{\sigma}\vec{B}_l|\phi_0\rangle}{\varepsilon_0 - \varepsilon_p} \tag{5.118}$$

If $k = l = 0$, i.e. if we consider the *magnetizability*, both spin-dependent matrix elements vanish

$$\langle\phi_0|\frac{1}{2}\vec{\sigma}\vec{B}_0|\phi_p\rangle = 0 \tag{5.119}$$

because $\vec{B}_0$ is constant (independent of $\vec{r}$), and ϕ_p is orthogonal to ϕ_0. The spin-dependent term $\frac{1}{2}\vec{\sigma}\vec{B}_0$ does not contribute at all to the magnetizability.

If only say $k = 0$, i.e. if we consider *nuclear magnetic shielding*, the matrix element (5.119) still vanishes, but the corresponding one

$$\langle\phi_0|\frac{1}{2}\vec{\sigma}\vec{B}_k|\phi_p\rangle \tag{5.120}$$

does not, since $\vec{B}_k$ is *not* independent of $\vec{r}$. However, the contributions to (5.118) with $\vec{A}_k\vec{p}$ in one matrix element and $\vec{\sigma}\vec{B}_l$ in the other (or vice versa), summed over the occupied one-particle states ϕ_0, compensate each other for a *closed shell state*, because the contributions with α and β spin have opposite sign. For an *open-shell n*-electron state there is no full compensation, but for this a temperature-dependent shielding dominates anyway, see Section 5.5.2. There will be a spin-dependent net effect even for a closed shell state, when we come to relativistic corrections (Section 5.7.5).

If, finally, both fields are due to nuclei, i.e. if we describe *nuclear spin coupling*, neither of the matrix elements (5.120) vanishes, and the contribution to (5.118)

$$\frac{1}{4}\sum_{p>0}\frac{\langle\phi_0|\vec{\sigma}\vec{B}_k|\phi_p\rangle\langle\phi_p|\vec{\sigma}\vec{B}_l|\phi_0\rangle}{\varepsilon_0-\varepsilon_p} \tag{5.121}$$

does not vanish, and often even dominates the nuclear spin–spin coupling.

It is customary (see Section 5.3.6) to further subdivide $\vec{\sigma}\vec{B}_k$, according to Eq. (5.55) into a *Fermi contact* and a *spin-dipole* term. This decomposition is somewhat artificial, since it results from an integration by parts, and since in a rigorous relativistic theory there is no Fermi contact term. However, in practice often the Fermi contact term dominates and deserves special attention.

5.5.6
Magnetizability (Magnetic Susceptibility)

For both fields $\vec{B}_0$ homogeneous (and identical) the spin-dependent contribution to H_{10} can be ignored (see Section 5.5.5). In view of (5.51, 5.52) we get for one electron:

$$E_{02}=\frac{1}{2}\langle\varphi_0|A_0^2|\varphi_0\rangle+\frac{1}{2}\langle\varphi_0|\vec{B}_0\cdot\vec{l}|\varphi_{01}\rangle;\ b^2E_{02}=-\frac{1}{2}\vec{B}\underline{\underline{\chi}}\vec{B} \tag{5.122}$$

E_{02} consists of a diamagnetic (or *Langevin*) term E_{02}^d and a (temperature-independent) paramagnetic (or *van-Vleck*) term E_{02}^p. The latter must be distinguished from the ordinary or temperature-dependent paramagnetism (see Section 5.5.2).

One can generally show that, for a ground state,

$$E_{02}^d=\frac{1}{2}\langle\varphi_0|A_0^2|\varphi_0\rangle\geq 0;\ E_{02}^p=\frac{1}{2}\langle\varphi_0|\vec{B}_0\cdot\vec{l}|\varphi_{01}\rangle\leq 0 \tag{5.123}$$

The first inequality holds, because $A_0^2\geq 0$, while the second one is easily checked from the sum-over states formula Eq. (5.94).

For an atom, choosing the gauge origin at the nucleus, E_{02}^p vanishes, because, for a field in the z-direction, φ_0 is the eigenfunction of l_z, and φ_{01} is orthogonal to φ_0. One then gets (χ is then, of course, isotropic).

$$E_{02}=\frac{1}{12}B_0^2\langle r^2\rangle;\ \chi=-\frac{1}{6}b^2\langle r^2\rangle \tag{5.124}$$

In the special case of the ground state of H-like ions this means $E_{02}=\frac{1}{4Z^2};\ \chi=-\frac{b^2}{2Z^2}$.

5.5.7
The Gauge-Origin Problem

Not only is the energy E of an atom or a molecule in a magnetic field invariant under a change of the gauge of the vector potential (Section 5.3.4), but this also holds for all derivatives of the energy with respect to components of the field strength. In particular E_{02} is gauge invariant. However the diamagnetic and paramagnetic contributions E_{02}^d and E_{02}^p to E_{02} depend individually on the gauge. One sees easily e.g. that A_0^2 with A_0 constructed according to Eq. (5.51) does depend on the gauge origin $\vec{R}$.

$$A_0^2 = \frac{1}{4}\ B_0^2(\vec{r} - \vec{R})^2 - \frac{1}{4}[\vec{B}_0 \cdot (\vec{r} - \vec{R})]^2 \tag{5.125}$$

This dependence is compensated by the $\vec{R}$-dependence of the paramagnetic term. In fact a shift of the gauge origin from 0 to $\vec{R}$ changes φ_{01} according to

$$\varphi_{01} \rightarrow \varphi_{01} - ib\lambda\varphi_0;\ \lambda = \frac{1}{2}(\vec{B}_0 \times \vec{R}) \cdot \vec{r} \tag{5.126}$$

but this is only realized if the chosen basis is able to account for this change of φ_{01} [12]. In practice there is therefore only an incomplete cancellation of $\vec{R}$-dependent terms. This can make approximate calculations very inaccurate, and it is imperative to take account of an optimal gauge. There is a *natural* gauge origin for *atoms* at the position of the nucleus. However, there is no natural gauge origin for molecules. It has turned out that for molecules it is recommended not to choose a single gauge origin, but gauge origins distributed over the molecule. The best-known representatives of distributed gauges are (a) the use of *gauge-including orbitals* (GIAO) or *London orbitals* as basis for the expansion of wavefunctions [8, 9, 10], and (b) the IGLO (*individual gauge for localized orbitals*) method, in which a different gauge origin is used for different localized orbitals [11, 12, 13]. The IGLO method can be rationalized in terms of a *nonlocal* generalization of a gauge transformation [14]. More about the gauge-origin problem is found in Chapter 6 by van Wüllen.

5.5.8
Nuclear Magnetic Shielding; NMR Chemical Shift

We now consider two magnetic fields, an external homogeneous one $\vec{B}_0$, and $\vec{B}_k$ of the k^{th} nucleus. The one-electron contribution to the mixed second-order energy, which is responsible for the nuclear magnetic shielding is then

$$E_{011} = \langle\varphi_0|\vec{A}_k \cdot \vec{A}_0|\varphi_0\rangle + \mathrm{Re}\langle\varphi_0|2\vec{A}_k \cdot \vec{p} + \vec{\sigma} \cdot \vec{B}_k|\varphi_{010}\rangle \tag{5.127}$$

where φ_{010} is identical with the φ_{01} as determined by Eq. (5.117). The diamagnetic term $E_{011}^d = \langle\varphi_0|\vec{A}_k \cdot \vec{A}_0|\varphi_0\rangle$ is now referred to as the *Lamb term*, while the paramagnetic term $E_{011}^d = 2\ \langle\varphi_0|\vec{A}_k \cdot \vec{p}|\varphi_{010}\rangle$ is called the *Ramsey term*. The sum of the spin-dependent contribution $\langle\varphi_0|\vec{\sigma} \cdot \vec{B}_k|\varphi_{010}\rangle$ (over the occupied spin orbitals) vanishes for a non-degenerate *n*-electron state and can hence be ignored.

In Eq. (5.127) we have chosen the first-order perturbation function φ_{010} with *respect to the external field* $\vec{B}_0$. This is not only recommended because then one has a *single* φ_{010} for all possible nuclei, but also because the singularity of the field due to a nucleus may create difficulties for the construction of φ_{001}.

At variance with the formal expression E_{011} (5.127), the shift tensor $\underline{\underline{\sigma}}^{(k)}$, related to it via Eq. (5.108), does contain a factor b^2d. This happens to be equal to $c^{-2} = \alpha^2$ for *both* systems of atomic units. The question whether this implies that nuclear magnetic shielding must be regarded as a *relativistic effect*, is nevertheless rather futile. The factor b^2d arises entirely from factors by which *external* perturbations are multi-

plied. Otherwise the theory is entirely based on a *non-relativistic Hamiltonian*. There are no effects of relativistic kinematics involved. One may only argue that relativistic corrections to the *nrl* of electrodynamics play a role (since any magnetic moment has its origin in a current). In this respect there is a fundamental difference to, say, spin–orbit interaction, which cannot be described correctly without taking care of relativistic kinematics [2].

The NMR shielding comes out as a *dimensionless* quantity, because it is the ratio between the *indirect* interaction of the nuclei with the external field, mediated by the electrons, and the *direct interaction*, which is simply $\vec{B} \cdot \vec{\mu}$ in either system of atomic units.

The full shielding tensors $\underline{\underline{\sigma}}^{(k)}$ (for more details see Chapter 27 by Wasylishen) have been studied less than their isotropic parts $\sigma^{(k)}$ or the *chemical shifts* $\delta^{(k)}$, which are defined relative to a *standard* $\sigma^{(k)}_{std}$ for the respective nucleus.

$$\delta^{(k)} = \sigma^{(k)}_{std} - \sigma^{(k)} \tag{5.128}$$

The theoretical calculation of chemical shifts was, for a long time, plagued by the gauge-origin problem (see Section 5.5.7). With *distributed gauge methods*, like GIAO or IGLO this problem has been solved (see Section 5.5.7).

For an atom, choosing the gauge origin at the nucleus, one gets $E^p_{011} = 0$, for the same reason as $E^p_{02} = 0$ (see Section 5.5.6). One then arrives at

$$E_{011} = \frac{1}{3}|\vec{B}_0||\vec{\mu}_k|\langle r^{-1}\rangle;\ \sigma = \frac{1}{3}b^2 d\langle r^{-1}\rangle = \frac{1}{3}\alpha^2\langle r^{-1}\rangle \tag{5.129}$$

In the special case of the ground state of H-like ions this means $\sigma = \frac{1}{3}\alpha^2 Z$. The NMR chemical shift is probably one of the best examples for a fruitful cooperation between theory and experiment. Details can be found in many reviews [12, 13, 14], and in several chapters in this book. Readers interested in the history, especially in the fundamental work of Ramsey [15] are referred to the paper by Pyykkö [16] and to Chapter 2 by Pyykkö.

5.5.9
Nuclear Spin-Coupling

We now come to the case where both perturbing magnetic fields are due to nuclei. We can start from essentially the same expression for a mixed second-order property as before, cf. Eq. (5.127).

$$E_{0011} = \langle\varphi_0|\vec{A}_k \cdot \vec{A}_l|\varphi_0\rangle + \mathrm{Re}\langle\varphi_0|2\vec{A}_k \cdot \vec{p} + \vec{\sigma} \cdot \vec{B}_k|\varphi_{0001}\rangle \tag{5.130}$$

with φ_{0001} essentially determined from the counterpart of Eq. (5.117). The main difference to magnetizability and nuclear magnetic shielding is, that now the spin-dependent terms in the perturbation operator cannot be ignored (see Section 5.5.5).

While in the case of magnetizability and NMR shielding we had to consider one diamagnetic and one paramagnetic term, we have now again one diamagnetic term,

but four paramagnetic ones. This results from the decomposition of H_{01} into a spin-independent and a spin-dependent term, and a further decomposition of the latter into a *spin-dipolar* and a *Fermi-contact* term (see Section 5.5.5). In the sum-over-states expression (5.121) there is (at least for closed-shell states) one contribution, where both factors contain a spin-independent term, and three more for spin-dependent terms of the same or different kind.

If one rationalizes the sum-over-states formula in terms of *n-electron states*, then for a closed-shell reference state, the operator $\vec{A}_k \cdot \vec{p}$ only couples to excited *singlet* states, and the operator $\vec{B} \cdot \vec{\sigma}$ to excited *triplet* states. The formal appearance of contributions with singlet vs. triplet *intermediate states* may suggest that many electron effects are involved. However, what matters is whether we deal with a spin-dependent or a spin-independent operator, and they play a different role, even for one-electron states.

There is also a direct magnetic interaction between the nuclear magnetic moments, that is independent of the electronic wavefunction. This interaction is important in solids with a fixed orientation between molecules, but it levels out e.g. in solution.

While for the calculation of the NMR shielding, one does not need to know the numerical value of $\vec{\mu}_k$ (or rather the factor γ_k, which relates $\vec{\mu}_k$ to the nuclear spin Eq. (5.54) (this determines, of course, the unshielded resonance frequency), in order to relate the computed spin coupling tensors to the experimentally observed ones, the γ_k values need to be known.

There is only one aspect in which nuclear spin coupling is simpler than the other second-order properties, namely that there is no gauge-origin problem.

Let us finally mention that even the case $k = l$ is physically meaningful, not as a coupling between two nuclear spins, but as a higher-order effect involving the magnetic moment of a single nucleus. However, the E_{002} evaluated in this philosophy, *diverges* [7]. A finite result is only obtained if one abandons the model of a point dipole and accounts for an extended nucleus. Replacement of a point dipole by an extended dipole has, however, no noticeable effect in those cases where no divergence arises.

5.6
Relativistic Theory of Magnetic Properties

5.6.1
Perturbation Theory of a Dirac Electron in a Magnetic Field

Let us start from the Dirac equation (5.58) and (5.70) for an electron in a magnetic field with vector potential $\vec{A}$ and expand the Dirac operator according to Eq. (5.65), the (four-component) wavefunction ψ and the energy W (which includes the rest mass contribution c^2) in powers of b.

$$W = W_0 + b\ W_1 + b^2\ W_2 + \ldots;\ \psi = \psi_0 + b\ \psi_1 + b^2\ \psi_2 + \ldots \tag{5.131}$$

$$D_0 = \begin{pmatrix} V & c\vec{\sigma}\vec{p} \\ c\vec{\sigma}\vec{p} & V-2c^2 \end{pmatrix};\ D_1 = \begin{pmatrix} 0 & \vec{\sigma}\vec{A} \\ c\vec{\sigma}\vec{A} & 0 \end{pmatrix} \tag{5.132}$$

Now we use only one label, which counts *orders in the magnetic perturbation*. Hence, formally, we only consider a single perturbation, but the generalization to more than one magnetic field is straightforward. The zeroth and first order wavefunctions are $\psi_0 = (\varphi_0, \chi_0)$ and $\psi_1 = (\varphi_1, \chi_1)$ respectively. For the counterparts W_1 and W_2 of the non-relativistic first- and second-order properties E_1 and E_2 we get

$$W_1 = \langle \psi_0 | D_1 | \psi_0 \rangle = 2c\mathrm{Re}\langle \varphi_0 | \vec{\sigma} \cdot \vec{A} | \chi_0 \rangle \tag{5.133}$$

$$W_2 = \mathrm{Re}\langle \psi_0 | D_1 | \psi_1 \rangle = c\mathrm{Re}\{\langle \varphi_0 | \vec{\sigma} \cdot \vec{A} | \chi_1 \rangle + \langle \varphi_1 | \vec{\sigma} \cdot \vec{A} | \chi_0 \rangle\} \tag{5.134}$$

with ψ_0 and ψ_1 solutions of

$$(D_0 - W_0)\psi_0 = (D_0 - E_0 - c^2)\psi_0 = 0 \tag{5.135}$$

$$(D_0 - W_0)\psi_1 = -(D_1 - W_1)\psi_0;\ \langle \psi_0 | \psi_1 \rangle = 0 \tag{5.136}$$

Note that W_0 contains the rest mass contribution c^2. The normalization condition contained in Eq. (5.136) is convenient, because it removes W_1 from the expression for W_2.

Like in the non-relativistic case we observe that D_1 is a *pseudoscalar* operator and hence W_1 vanishes for non-degenerate (n-electron) states. For degenerate states W_1 describes the Zeeman splitting, provided that $\vec{A}_0$ represents a homogeneous external field. For $\vec{A}_k$ due to a nucleus, W_1 is the relativistic generalization of the hyperfine interaction.

W_2 consists of a *single* term, that formally resembles the paramagnetic contribution E_{02}^p to E_{02} in non-relativistic theory, while there is no direct counterpart of E_{02}^d. It is somewhat puzzling that W_2 does, unlike in the non-relativistic theory, *not* appear as the sum of a diamagnetic and a paramagnetic contribution. Such a decomposition can be achieved, in a somewhat artificial way, in evaluating W_2 by means of the sum-over states formulation [17,18,19]

$$W_2 = \sum_q \frac{|\langle \psi_0 | D_1 | \psi_{q0} \rangle|^2}{W_0 - W_{q0}} \tag{5.137}$$

Unlike the non-relativistic Hamiltonian, the Dirac operator has both positive-energy and negative-energy eigenstates. While the partial sum over the former to W_2 looks like the obvious relativistic generalization of the paramagnetic contribution, the partial sum over negative energy states does not have a direct non-relativistic counterpart. On the other hand this partial sum can (for the ground state ($q = 0$)) be estimated as:

$$W_2^{neg} = \sum_{q, W_{q0}<0} \frac{|\langle\psi_0|D_1|\psi_{q0}\rangle|^2}{W_0 - W_{q0}} \leq \sum_{k, W_{q0}<0} \frac{|\langle\psi_0|D_1|\psi_{q0}\rangle|^2}{W_0 + c^2} \leq \frac{\langle\psi_0|D_1^2|\psi_0\rangle}{W_0 + c^2}$$

$$= \frac{\langle\psi_0|c^2A^2|\psi_0\rangle}{W_0 + c^2} = \langle\psi_0|A^2|\psi_0\rangle[1 + \frac{W_0}{c^2}]^{-1} \tag{5.138}$$

$$\approx \frac{1}{2}\langle\psi_0|A^2|\psi_0\rangle \tag{5.139}$$

In the limit $2c^2 \to 0$ this approaches the non-relativistic E_{02}^d.

The interpretation of diamagnetism as due to negative-energy states is, although formally plausible, unsatisfactory for various rather serious reasons [20]. Let us only mention two of them

1. This would mean to recur to a *different mechanism* in the relativistic and the non-relativistic context, with a discontinuity in the non-relativistic limit. In this limit there are *no* negative-energy states.
2. The sum-over-states formalism involving negative-energy states is tedious and inelegant, if it is performed in a *brute-force* way. It is unreliable and hard to correct if one tries to *approximate this sum by a closure approximation*.

5.6.2 Unitary Transformation of the Dirac Operator

There is a much more convincing way to arrive at a decomposition of W_2 into a diamagnetic and a paramagnetic contribution, namely via a unitary transformation of D [20] that *removes the off-diagonal operator* $c\vec{\alpha}\cdot\vec{A}$ to the leading order in b.

$$\tilde{D} = \exp\{-b\tau\}D\exp\{b\tau\} = D_0 + b\tilde{D}_1 + b^2\tilde{D}_2 + O(b^3) \tag{5.140}$$

$$\tau = -\frac{1}{2c}\beta\vec{\alpha}\cdot\vec{A} = -\tau^\dagger \tag{5.141}$$

$$\tilde{D}_1 = D_1 + [D_0, \tau] = \frac{1}{2}\beta[\vec{\alpha}\cdot\vec{p}, \vec{\alpha}\cdot\vec{A}]_+ = \beta\{\vec{A}\cdot\vec{p} + \frac{1}{2}\vec{\sigma}\cdot\vec{B}\} = \beta H_1 \tag{5.142}$$

$$\tilde{D}_2 = [D_1, \tau] + \frac{1}{2}[[D_0, \tau], \tau] = \frac{1}{2}\beta A^2 - \frac{1}{4c}[H_1, \vec{\alpha}\cdot\vec{A}]_+ \tag{5.143}$$

where we have used

$$\beta\vec{\alpha} = -\vec{\alpha}\beta;\ \ (\vec{\alpha}\cdot\vec{a})(\vec{\alpha}\cdot\vec{b}) = \vec{a}\cdot\vec{b} + i\vec{\sigma}\cdot(\vec{a}\times\vec{b});\ \ \nabla\vec{A} = 0;\ \ \vec{B} = \mathrm{rot}\vec{A} \tag{5.144}$$

$\tilde{D}_1$ differs from the non-relativistic H_1 (5.80) mainly in the fact that it acts on four-component spinors. For W_1 and W_2 we now get

$$W_1 = \langle \psi_0 | \tilde{D}_1 | \psi_0 \rangle = \langle \varphi_0 | H_1 | \varphi_0 \rangle - \langle \chi_0 | H_1 | \chi_0 \rangle \tag{5.145}$$

$$W_2 = W_2^p + W_2^{d1} + W_2^{d2} \tag{5.146}$$

$$\begin{aligned} W_2^p &= \mathrm{Re}\langle \psi_0 | \tilde{D}_1 - W_1 | \tilde{\psi}_1 \rangle \\ &= \mathrm{Re}\{\langle \varphi_0 | H_1 - W_1 | \tilde{\varphi}_1 \rangle - \langle \chi_0 | H_1 + W_1 | \tilde{\chi}_1 \rangle\} \end{aligned} \tag{5.147}$$

$$W_2^{d1} = \frac{1}{2}\langle \psi_0 | \beta A^2 | \psi_0 \rangle = \frac{1}{2}\langle \varphi_0 | A^2 | \varphi_0 \rangle - \frac{1}{2}\langle \chi_0 | A^2 | \chi_0 \rangle \tag{5.148}$$

$$W_2^{d2} = -\frac{1}{2c}\mathrm{Re}\langle \varphi_0 | [H_1, \vec{\sigma} \cdot \vec{A}]_+ | \chi_0 \rangle \tag{5.149}$$

The first-order wavefunction $\tilde{\psi}_1$ is obtained from

$$(D_0 - W_0)\tilde{\psi}_1 = -(\tilde{D}_1 - W_1)\psi_0; \ \langle \psi_0 | \tilde{\psi}_1 \rangle = 0 \tag{5.150}$$

While the energy (i.e. the W_k) as well as ψ_0 are unaffected by the transformation from D to $\tilde{D}$, the relation between $\tilde{\psi}_1$ and ψ_1 is

$$\tilde{\psi}_1 = \psi_1 + \frac{1}{2c}\beta\vec{\alpha} \cdot \vec{A}\psi_0 \tag{5.151}$$

The expressions Eq. (5.147) to (5.149) [20] were first derived by Szmytkowski [21] making use of the Gordon decomposition of the induced current density.

For the ground state of H-like ions one can easily evaluate W_{10} or W_{01}, i.e the relativistic Zeeman splitting and hyperfine interaction either from Eq. (5.133) or Eq. (5.145). If one uses Eq. (5.145) for W_{01}, one must ignore the *delta-function* term, which becomes meaningless in this context. One gets

$$W_{10} = \frac{2m_s}{3}(1 + 2\sqrt{1 - \alpha^2 Z^2}); \ W_{01} = \frac{8Z^3 m_s}{3}\{2\alpha^2 Z^2 + \sqrt{1 - \alpha^2 Z^2} - 2\}^{-1} \tag{5.152}$$

Closed expressions are also available for the energy quantities related to the magnetizability (W_{20}) [30], and the NMR shielding (W_{11}) [31], but they are too complicated to be reproduced here. We come, in Section (5.7.5), to their expansion in powers of α^2.

5.7 The Leading Relativistic Corrections

5.7.1 Direct Perturbation Theory (DPT)

We can sketch the basic ideas of *direct perturbation theory* (DPT) of relativistic effects only briefly, for details the reader is referred to a recent review [2] and the original literature [20, 22, 23, 24, 25]. We start from the Dirac equation with modified metric

(5.72) in block form (5.73). While in sec. 5.3.11 we only considered the limit $c^{-2} \to 0$, we now expand (5.72) or (5.73) in powers of both c^{-2} and b as perturbation parameters. We therefore write (see Eqs. (5.71) and (5.72))

$$0 = (D_{00} + c^{-2} D_{20} + bD_{01} - ES_0 - Ec^{-2} S_2)\bar{\psi} \tag{5.153}$$

$$D_{00} = \begin{pmatrix} V & \vec{\sigma}\cdot\vec{p} \\ \vec{\sigma}\cdot\vec{p} & -2 \end{pmatrix}; D_{20} = \begin{pmatrix} 0 & 0 \\ 0 & V \end{pmatrix}; D_{01} = \begin{pmatrix} 0 & \vec{\sigma}\cdot\vec{A} \\ \vec{\sigma}\cdot\vec{A} & 0 \end{pmatrix} \tag{5.154}$$

$$S_0 = \begin{pmatrix} 1 & 0 \\ 0 & 0 \end{pmatrix}; S_2 = \begin{pmatrix} 0 & 0 \\ 0 & 1 \end{pmatrix} \tag{5.155}$$

$$E = \sum_{k,l} c^{-k} b^l E_{kl};\ \bar{\psi} = \sum_{k,l} c^{-k} b^l \psi_{kl} \tag{5.156}$$

The first subscript counts orders in c^{-1} (only even orders are present), the second subscript orders in b. Like in Sec. 5.6 we consider formally a single magnetic perturbation, but the generalization to more perturbations is straightforward.

The lowest-order equations are:

$$(D_{00} - E_{00} S_0)\psi_{00} = 0 \tag{5.157}$$

$$(D_{00} - E_{00} S_0)\psi_{20} + (D_{20} - E_{20} S_0 - E_{00} S_2)\psi_{00} = 0 \tag{5.158}$$

$$(D_{00} - E_{00} S_0)\psi_{01} + (D_{01} - E_{01} S_0)\psi_{00} = 0 \tag{5.159}$$

$$(D_{00} - E_{00} S_0)\psi_{02} + (D_{01} - E_{01} S_0)\psi_{01} - E_{02} S_0 \psi_{00} = 0 \tag{5.160}$$

$$\begin{aligned}&(D_{00} - E_{00} S_0)\psi_{21} + (D_{20} - E_{20} S_0 - E_{00} S_2)\psi_{01} \\ &+ (D_{01} - E_{01} S_0)\psi_{20} - (E_{21} S_0 + E_{01} S_2)\psi_{00} = 0\end{aligned} \tag{5.161}$$

All these equations can, of course, be written in block form like Eq. (5.75). The solutions are not unique and we can impose a *normalization condition*. The *unitary normalization*

$$1 = \langle \psi_{00} | S_0 | \psi_{00} \rangle = \langle \varphi_{00} | \varphi_{00} \rangle \tag{5.162}$$

$$\begin{aligned}0 &= \langle \psi_{20} | S_0 | \psi_{00} \rangle + \langle \psi_{00} | S_0 | \psi_{20} \rangle + \langle \psi_{00} | S_2 | \psi_{00} \rangle \\ &= \langle \varphi_{20} | \varphi_{00} \rangle + \langle \varphi_{00} | \varphi_{20} \rangle + \langle \chi_{00} | \chi_{00} \rangle\end{aligned} \tag{5.163}$$

$$0 = \langle \psi_{01} | S_0 | \psi_{00} \rangle + \langle \psi_{01} | S_0 | \psi_{01} \rangle = \langle \varphi_{01} | \varphi_{00} \rangle + \langle \varphi_{00} | \varphi_{01} \rangle \tag{5.164}$$

is recommended. From scalar multiplication of Eq. (5.157) by (5.161) from the left by ψ_{00} one gets

$$E_{20} = E_{20}\langle\psi_{00}|S_0|\psi_{00}\rangle = \langle\psi_{00}|D_{20} - E_{00}S_2|\psi_{00}\rangle = \langle\chi_{00}|V - E_{00}|\chi_{00}\rangle \tag{5.165}$$

$$E_{01} = E_{01}\langle\psi_{00}|S_0|\psi_{00}\rangle = \langle\psi_{00}|D_{01}|\psi_{00}\rangle = 2\mathrm{Re}\langle\varphi_{00}|\vec{\sigma}\cdot\vec{A}|\chi_{00}\rangle \tag{5.166}$$

$$\begin{aligned} E_{02} &= \langle\psi_{00}|D_{01} - E_{01}S_0|\psi_{01}\rangle \\ &= \mathrm{Re}\{\langle\varphi_{00}|\vec{\sigma}\cdot\vec{A}|\chi_{01}\rangle + \langle\varphi_{01}|\vec{\sigma}\cdot\vec{A}|\chi_{00}\rangle\} - E_{01}\mathrm{Re}\langle\varphi_{00}|\varphi_{01}\rangle \end{aligned} \tag{5.167}$$

$$\begin{aligned} E_{21} &= \langle\psi_{00}|D_{20} - E_{20}S_0 - E_{00}S_2|\psi_{01}\rangle + \langle\psi_{00}|D_{01} - E_{01}S_0|\psi_{20}\rangle \\ &\quad -E_{01}\langle\psi_{00}|S_2|\psi_{00}\rangle \end{aligned} \tag{5.168}$$

In analogy one obtains expressions for E_{40}, E_{22}, etc., which can be further simplified, using identities based on Eq. (5.157) to (5.161).

5.7.2 The Leading Relativistic Corrections to the Energy

Although our interest is in the relativistic corrections to *properties*, we have to say a few words on the relativistic corrections to the *energy*. The zeroth-order equation (5.157) is in block form

$$\begin{pmatrix} V & \vec{\sigma}\vec{p} \\ \vec{\sigma}\vec{p} & -2 \end{pmatrix}\begin{pmatrix} \varphi_{00} \\ \chi_{00} \end{pmatrix} = E_{00}\begin{pmatrix} 1 & 0 \\ 0 & 0 \end{pmatrix}\begin{pmatrix} \varphi_{00} \\ \chi_{00} \end{pmatrix} \tag{5.169}$$

or equivalently

$$(H_0 - E_{00})\varphi_{00} = 0;\ \chi_{00} = \frac{1}{2}\vec{\sigma}\cdot\vec{p}\varphi_{00};\ H_0 = V + \frac{1}{2}p^2 \tag{5.170}$$

From (5.165) the leading relativistic correction to the energy is

$$\begin{aligned} E_{20} &= \langle\chi_{00}|V - E_{00}|\chi_{00}\rangle = \frac{1}{4}\langle\vec{\sigma}\cdot\vec{p}\varphi_{00}|V - E_{00}|\vec{\sigma}\cdot\vec{p}\varphi_{00}\rangle \\ &= \frac{1}{4}\langle\varphi_{00}|\vec{\sigma}\vec{p}(H_0 - E_{00} - T)\vec{\sigma}\vec{p}|\varphi_{00}\rangle \\ &= \frac{1}{4}\langle\varphi_{00}|\vec{\sigma}\vec{p}[H_0, \vec{\sigma}\vec{p}]|\varphi_{00}\rangle + \frac{1}{2}\langle\varphi_0|T(H_0 - E_{00})|\varphi_{00}\rangle - \frac{1}{2}\langle\varphi_{00}|T^2|\varphi_{00}\rangle \end{aligned} \tag{5.171}$$

with T the operator of the kinetic energy. E_{20} can be interpreted as the sum of four terms, with both (5.173) and (5.174) coming from the the first term in the last line of (5.171):

$$-\frac{1}{2}\langle\varphi_{00}|T^2|\varphi_{00}\rangle = \textit{mass–velocity} \tag{5.172}$$

$$\frac{1}{8}\langle\varphi_{00}|\nabla^2 V|\varphi_{00}\rangle = \textit{Darwin term} \tag{5.173}$$

$$\frac{1}{4}\langle\varphi_{00}|\vec{\sigma}\cdot(\nabla V\times\vec{p})|\varphi_{00}\rangle = \textit{spin–orbit term} \tag{5.174}$$

$$\frac{1}{2}\langle\varphi_{00}|T(H_0-E_{00})|\varphi_{00}\rangle = \textit{correction term} \tag{5.175}$$

It is a matter of convention whether or not one includes the factor c^{-2} in the definition of these relativistic corrections. The first two of these terms represent *scalar* or *spin-independent* corrections, the third term is *spin-dependent* and responsible for the *spin–orbit interaction*, while the last term is a correction, that vanishes, if the non-relativistic problem is solved exactly, and is therefore often ignored.

The spin–orbit interaction operator H_{so} can, for V a central potential (i.e. for an atom) be rewritten as

$$H_{so} = \frac{1}{4}\vec{\sigma}\cdot(\nabla V\times\vec{p}) = \frac{1}{4r}\frac{dV}{dr}\vec{\sigma}\cdot(\vec{r}\times\vec{p}) = \frac{1}{4r}\frac{dV}{dr}\vec{\sigma}\cdot\vec{l} \tag{5.176}$$

While a non-degenerate state is only affected by *scalar* relativistic corrections, there is a splitting of degenerate states via spin–orbit interaction. For a relativistic (one-electron) atom only $\vec{j}=\vec{l}+\vec{s}$, and no longer $\vec{l}$ and $\vec{s}$ separately commute with the Dirac Hamiltonian. The *spin–orbit term* couples the orbital and spin angular momenta $\vec{l}$ and $\vec{s}$ to a total angular momentum $\vec{j}$.

Therefore, to account for relativistic corrections to a state that is degenerate in the *nrl*, one must apply *degenerate perturbation theory*. Rather than to consider the relativistic correction to the energy of a single state, one must use an effective Hamiltonian in the basis of the zeroth-order degenerate states [20],

$$L_{ij}^{(2,0)} = \frac{1}{4}\langle\vec{\sigma}\vec{p}\;\varphi_i^{(00)}|V-\frac{1}{2}(\varepsilon_i+\varepsilon_j)|\vec{\sigma}\vec{p}\;\varphi_j^{(00)}\rangle \tag{5.177}$$

and diagonalize this to get the perturbation-adapted states and the leading relativistic corrections to the energy. This is a generalization of Eq. (5.171).

For higher-order corrections one needs e.g. ψ_{20}, that is determined from Eq. (5.158) or in component form

$$(V-E_{00})\varphi_{20}+\vec{\sigma}\vec{p}\chi_{20}-E_{20}\varphi_{00}=0 \tag{5.178}$$

$$\vec{\sigma}\vec{p}\varphi_{20}-2\chi_{20}+(V-E_{00})\chi_{00}=0 \tag{5.179}$$

with the solution

$$(H_0-E_{00})\varphi_{20} = -\left\{\frac{1}{4}\vec{\sigma}\vec{p}(V-E_{00})\vec{\sigma}\vec{p}-E_{20}\right\}\varphi_{00} \tag{5.180}$$

$$\chi_{20} = \frac{1}{2}\left\{ \vec{\sigma}\vec{p}\varphi_{20} + (V - E_{00})\chi_{00} \right\} \tag{5.181}$$

There are also relativistic corrections to the electron interaction. These have two origins. The Coulomb interaction gives rise to two-electron contributions to the spin–orbit interaction, which mainly shield the one-electron spin–orbit interaction to some extent. If one includes the Breit interaction between the electrons, one takes care of spin–other-orbit interaction, and electron-spin–spin interaction. There are also scalar two-electron terms, and finally so-called radiative (QED) corrections. The fact that we cannot comment on these additional terms, does not mean that they are generally unimportant. For more details see e.g. ref. [2].

5.7.3
The Relativistic Corrections to First-Order Properties in the *Absence* of Zeroth-Order Spin–Orbit Splitting

For relativistic corrections to properties one can apply DPT as sketched in Section 5.7.1 and evaluate the correction to first-order properties [24] from Eq. (5.168) or rather from one of the two alternative expressions typical for double perturbation theory [6]:

$$\begin{aligned} E_{21} &= 2\mathrm{Re}\langle\psi_{00}|D_{20} - E_{20}S_0 - E_{00}S_2|\psi_{01}\rangle - E_{01}\langle\psi_{00}|S_2|\psi_{00}\rangle \\ &= 2\mathrm{Re}\langle\psi_{00}|D_{01} - E_{01}S_0|\psi_{20}\rangle - E_{01}\langle\psi_{00}|S_2|\psi_{00}\rangle = 2\langle\psi_{00}|D_{01}|\psi_{00}\rangle \end{aligned} \tag{5.182}$$

Alternatively one can apply DPT to the *transformed* Dirac operator of Section 5.6.2, where one gets [20]:

$$\begin{aligned} E_{21} &= \langle\psi_{00}|\tilde{D}_{21} - E_{01}S_2|\psi_{00}\rangle + 2\mathrm{Re}\langle\psi_{00}|D_{20} - E_{20}S_0 - E_{00}S_2|\tilde{\psi}_{01}\rangle \\ &= -\langle\chi_{00}|H_1 + E_{01}|\chi_{00}\rangle + 2\mathrm{Re}\langle\chi_{00}|V - E_{00}|\tilde{\chi}_{01}\rangle \end{aligned} \tag{5.183}$$

$$\begin{aligned} E_{21} &= \langle\psi_{00}|\tilde{D}_{21} - E_{01}S_2|\psi_{00}\rangle + 2\mathrm{Re}\langle\psi_{00}|\tilde{D}_{01} - E_{01}S_0|\psi_{20}\rangle \\ &= -\langle\chi_{00}|H_1|\chi_{00}\rangle + 2\mathrm{Re}\langle\varphi_{00}|H_1|\varphi_{20}\rangle \end{aligned} \tag{5.184}$$

$$\tilde{D}_{01} = \begin{pmatrix} H_1 & 0 \\ 0 & 0 \end{pmatrix}; \tilde{D}_{02} = \begin{pmatrix} \frac{1}{2}A^2 & 0 \\ 0 & 0 \end{pmatrix}; \tilde{D}_{21} = \begin{pmatrix} 0 & 0 \\ 0 & -H_1 \end{pmatrix}$$

$$\tilde{D}_{22} = \begin{pmatrix} 0 & ß & ß - \frac{1}{4}[H_1, \vec{\sigma}\cdot\vec{A}]_+ \\ -\frac{1}{4}[H_1, \vec{\sigma}\cdot\vec{A}]_+ & & -\frac{1}{2}A^2 \end{pmatrix} \tag{5.185}$$

with H_1 the non-relativistic perturbation operator (5.80), see (5.142).

Both expressions (5.183) and (5.184) are valid in the unitary normalization (5.164). They are related to each other by the Dalgarno exchange theorem. The term

common to both expressions does not contain a perturbation correction to the wavefunction, somewhat like the diamagnetic contribution to non-relativistic second-order properties (Section 5.5.4).

Concerning the relativistic corrections to magnetic properties, one must distinguish between states the degeneracy of which in the *nrl* is *split by spin–orbit interaction* even in the absence of a magnetic field, and states without a spin–orbit splitting. For the latter one can directly evaluate the leading relativistic corrections to the Zeeman splitting or the hyperfine interaction. There are various equivalent formulations, of which the expressions (5.183, 5.184) are particularly compact [20].

For atoms (without spin–orbit interaction) in a homogeneous field $\vec{B}_0$, (5.183) or (5.184) simplify to

$$E_{21} = -\langle \chi_{00} | H_1 + E_{01} | \chi_{00} \rangle \tag{5.186}$$

For the ground state of H-like ions the Zeeman splitting is

$$2b\{1 - \frac{\alpha^2 Z^2}{3} - \frac{\alpha^4 Z^4}{12} + O(\alpha^6 Z^6)\} \tag{5.187}$$

The deviation from the *spin-only* value $bg = 2b$ results from the fact that the relativistic wavefunction is no longer an eigenfunction of s_z. In the present case this is manifest in the *small component* χ_{00}, which is a $1p_{\frac{1}{2}}$ function with $g = \frac{2}{3}$ (see Section 5.7.4). Note that this can be regarded as an effect of spin–orbit interaction, although we would not have got this effect if we had simply added a spin–orbit term H_{so} to the non-relativistic Hamiltonian.

For the evaluation of the relativistic correction to the *hyperfine splitting* the counterpart of the expressions (5.183, 5.184) cannot be used, because although the sum of the two terms is regular, they diverge individually, and a controlled cancellation of the diverging terms is nontrivial. There is no problem with the expression [24]

$$E_{201} = 2\mathrm{Re}\{\langle \varphi_{200} | \vec{\sigma} \cdot \vec{A}_k | \chi_{000} \rangle + \langle \chi_{200} | \vec{\sigma} \cdot \vec{A}_k | \varphi_{000} \rangle\} \tag{5.188}$$

based on Eq. (5.182). For the hyperfine splitting of the ground state of H-like ions one gets

$$bd\{\frac{4Z^3}{3} + 2\alpha^2 Z^5 + \frac{17}{6}\alpha^4 Z^7 + O(\alpha^6 Z^9)\} \tag{5.189}$$

A numerical study of such relativistic corrections was published by Hennum et al. [26].

Generally the relativistic correction is not isotropic, i.e. the magnetic moment of a molecule is not necessarily parallel to the direction of the field. Then the g-factor has to be replaced by a g-tensor.

In order to describe experiments correctly, one must not forget that due to *quantum electrodynamic* (QED) corrections even the g-factor of a *free electron* is not exactly equal to 2, but rather $g = 2.0023193 \approx 2 + \alpha/\pi$ [27]. This QED correction must simply be added to the corrections which result from relativistic effects.

5.7.4
The Relativistic Corrections to First-Order Properties in the *Presence* of Zeroth-Order Spin–Orbit Splitting

For a state, which is degenerate in the *nrl*, the splitting due to relativity in the absence of a magnetic field, must usually be taken account of, before one switches on the field. For an atomic state (we consider one-electron states) this means that it can no longer be classified in terms of its quantum numbers l, m_l, s, m_s, but only in terms of j, m_j, while in the presence of a magnetic field only m_j remains. The Zeeman splitting in the *nrl* is then determined by the g value of the Landé formula.

For the projection of the total magnetic moment $\vec{m} = \vec{l} + 2\vec{s}$ on the total angular momentum $\vec{j} = \vec{l} + \vec{s}$ we get

$$\frac{\langle \vec{m}\cdot\vec{j}\rangle}{\langle \vec{j}\cdot\vec{j}\rangle} = 1 + \frac{\langle \vec{s}\cdot\vec{j}\rangle}{\langle \vec{j}\cdot\vec{j}\rangle} = 1 + \frac{\langle \vec{s}\cdot\vec{l}\rangle + \langle \vec{s}\cdot\vec{s}\rangle}{\langle \vec{j}\cdot\vec{j}\rangle} = 1 + \frac{\frac{1}{2}\langle \vec{j}^{\,2} - \vec{l}^{\,2} - \vec{s}^{\,2}\rangle + \langle \vec{s}^{\,2}\rangle}{j(j+1)}$$
$$= 1 + \frac{j(j+1) - l(l+1) + s(s+1)}{2j(j+1)} = g \tag{5.190}$$

$$E_{01}(m_j) = \frac{b}{2}\; g\; m_j\; B_{0z} \tag{5.191}$$

In a second step we can, for the m_j states evaluate the relativistic corrections as in Section 5.7.3. This procedure only works for sufficiently weak magnetic fields, such that the Zeeman splitting is small with respect to the spin–orbit splitting. If both splittings have comparable magnitude, we must apply *quasidegenerate* perturbation theory, i.e. take all states with the same l and s together as the basis of a matrix representation of both relativistic corrections and interaction with the magnetic field. The matrix elements then have a power series expansion in both perturbation parameters, but the eigenvalues of this matrix (to be evaluated for actual values of the parameters) are not analytic in the two parameters (with some exceptions like atomic states with $m_j = j = l + \frac{1}{2}$) . Then we are in the regime of the *anomalous Zeeman effect*.

A special case of spin–orbit splitting in molecules (where also electron spin–spin interaction plays a role) is the *zero-field splitting* of *triplet* states (and states of higher spin multiplicities). Here for molecules of sufficiently low symmetry the three-fold degeneracy in the *nrl* is split into three components with the magnetic moments in the direction of the three Cartesian axes in a molecule-fixed system. If one applies a magnetic field, there is a competition between the Zeeman splitting and the zero-field splitting, much like in the anomalous Zeeman effect.

5.7.5
The Leading Relativistic Corrections to Second-Order Properties

The relativistic corrections like E_{220} and E_{211} to second-order properties can be evaluated by means of multiple direct perturbation theory in a straightforward way, but the resulting expressions are rather lengthy [24] and not easily interpreted. Again we

have the choice between DPT applied to the original Dirac equation [24] as sketched in Section 5.7.1, and DPT applied to the transformed Dirac operator [20]. In the first case one needs the first-order correction $\psi_{01} = (\varphi_{01}, \chi_{01})$ of the wavefunction due to the magnetic perturbation, obtained from Eq. (5.159), which after straightforward manipulations leads to

$$(H_0 - E_{00})\varphi_{01} + H_1\varphi_{00} = 0;\ \chi_{01} = \frac{1}{2}\vec{\sigma}\vec{p}\varphi_{01} + \frac{1}{2}\vec{\sigma}\vec{A}\varphi_{00};\ \langle\varphi_{00}|\varphi_{01}\rangle = 0 \tag{5.192}$$

In the second case one has to replace Eq. (5.159) by

$$(D_{00} - E_{00}S_0)\tilde{\psi}_{01} + (\tilde{D}_{01} - E_{01}S_0)\psi_{00} = 0 \tag{5.193}$$

and get $\tilde{\psi}_{01} = (\tilde{\varphi}_{01}, \tilde{\chi}_{01})$ from

$$(H_0 - E_0)\tilde{\varphi}_{01} + H_1\varphi_{00} = 0;\ \tilde{\chi}_{01} = \frac{1}{2}\vec{\sigma}\cdot\vec{p}\tilde{\varphi}_{01};\ \langle\varphi_{00}|\tilde{\varphi}_{01}\rangle = 0 \tag{5.194}$$

One finds that $\varphi_{01} = \tilde{\varphi}_{01}$, and that this even agrees with the non-relativistic φ_{01}, but that $\chi_{01} \neq \tilde{\chi}_{01}$.

For our purposes a formulation based on the transformed Dirac operator is recommended [20] in which E_{22} is, in analogy to the decomposition (5.146) of W_2, decomposed into one paramagnetic and two diamagnetic parts.

$$E_{22} = E_{22}^{d1} + E_{22}^{d2} + E_{22}^{p} \tag{5.195}$$

$$E_{22}^{d1} = \mathrm{Re}\langle\varphi_{00}|A_0^2|\varphi_{20}\rangle - \frac{1}{2}\langle\chi_{00}|A_0^2|\chi_{00}\rangle \tag{5.196}$$

$$E_{22}^{d2} = -\frac{1}{2}\mathrm{Re}\langle\varphi_{00}|[H_1, \vec{\sigma}\cdot\vec{A}_0]_+|\chi_{00}\rangle \tag{5.197}$$

$$\begin{aligned} E_{22}^{p} &= \langle\tilde{\chi}_{01}|V - E_{00}|\tilde{\chi}_{01}\rangle - E_{20}\langle\tilde{\varphi}_{01}|\tilde{\varphi}_{01}\rangle \\ &\quad -2\mathrm{Re}\langle\chi_{00}|H_1 + E_{01}|\tilde{\chi}_{01}\rangle + 2\mathrm{Re}\langle\varphi_{20}|H_1 - E_{01}|\tilde{\varphi}_{01}\rangle \end{aligned} \tag{5.198}$$

We note that in view of Eq. (5.119) the spin-dependent part of H_1 does *not* contribute to E_{22}^p. In the special case of the ground state of H-like systems $\varphi_{01} = 0,\ \tilde{\chi}_{01} = 0$, and hence $E_{22}^p = 0$, i.e. the paramagnetic term does not only vanish in the *nrl*, its leading relativistic correction vanishes as well, relativistic effects enter to higher order in $Z^2\alpha^2$ only [29]. We get

$$\chi = -b^2\{\frac{1}{2Z^2} - \frac{2}{3}\alpha^2 + 0.09516Z^2\alpha^4 + O(Z^4\alpha^6)\} \tag{5.199}$$

The correction $-\frac{2}{3}$ has a contribution of $-\frac{13}{24}$ from E_{22}^{d1} and $-\frac{1}{8}$ from E_{22}^{d2}.

The counterpart of (5.195) for a mixed second-order property, such as nuclear magnetic shielding (or nuclear spin coupling) is

$$E_{211} = E_{211}^{d1} + E_{211}^{d2} + E_{211}^{p} \tag{5.200}$$

$$E_{211}^{d1} = 2\mathrm{Re}\langle\varphi_{000}|\vec{A}_k \cdot \vec{A}_l|\varphi_{200}\rangle - \langle\chi_{000}|\vec{A}_k \cdot \vec{A}_l|\chi_{000}\rangle \tag{5.201}$$

$$E_{211}^{d2} = -\frac{1}{2}\mathrm{Re}\langle\varphi_{000}|[H_{10}, \vec{\sigma}\cdot\vec{A}_l]_+ + [H_{01}, \vec{\sigma}\cdot\vec{A}_k]_+|\chi_{000}\rangle \tag{5.202}$$

$$\begin{aligned} E_{211}^{p} = {} & \langle\tilde{\chi}_{010}|V - E_0|\tilde{\chi}_{001}\rangle - \langle\tilde{\chi}_{001}|V - E_0|\tilde{\chi}_{010}\rangle - 2\mathrm{Re}E_{20}\langle\tilde{\varphi}_{010}|\tilde{\varphi}_{001}\rangle \\ & -2\mathrm{Re}\langle\chi_{000}|H_{10} + E_{010}|\tilde{\chi}_{001}\rangle - 2\mathrm{Re}\langle\chi_{000}|H_{01} + E_{001}|\tilde{\chi}_{010}\rangle \\ & +2\mathrm{Re}\langle\varphi_{200}|H_{10} - E_{010}|\tilde{\varphi}_{001}\rangle + 2\mathrm{Re}\langle\varphi_{200}|H_{01} - E_{001}|\tilde{\varphi}_{010}\rangle \end{aligned} \tag{5.203}$$

Now we can argue that the spin-dependent contributions to $\tilde{\varphi}_{010}$ and $\tilde{\chi}_{010}$ vanish, but that those to $\tilde{\varphi}_{001}$ and $\tilde{\chi}_{001}$ don't. These can, together with spin-dependent parts in φ_{200} yield non-vanishing net contributions to E_{211}^{p}, even for a closed-shell state. In a sum-over-states formulation these contributions look like

$$\sum_{p>0,q>0} \frac{\langle\phi_0|H_{so}|\phi_p\rangle\langle\phi_p|H_{10} - E_{10}|\phi_q\rangle\langle\phi_q|\vec{\sigma}_k \cdot \vec{B}_k|\phi_0\rangle}{(\varepsilon_0 - \varepsilon_p)(\varepsilon_0 - \varepsilon_q)} \tag{5.204}$$

where H_{so} is the spin–orbit interaction operator, and $\vec{\sigma}_k \cdot \vec{B}_k$ essentially the Fermi-contact term. Such an expression was first proposed by Namura et al. [28] in a somewhat ad hoc study of spin–orbit effects on nuclear magnetic shielding.

For the ground state of H-like ions one gets [29]:

$$\sigma = \alpha^2\{\frac{Z}{3} + \frac{97}{108}Z^3\alpha^2 + \frac{289}{216}Z^5\alpha^4 + O(Z^7\alpha^6)\} \tag{5.205}$$

The correction $\frac{97}{108}$ has a contribution of 0 from E_{211}^{d1} and $-\frac{1}{3}$ from E_{211}^{d2}, $\frac{4}{3}$ and $-\frac{11}{108}$ come from the term $-2\mathrm{Re}\langle\chi_0|H_{10} + E_{010}|\tilde{\chi}_{001}\rangle$ with $\tilde{\chi}_{001}$ a $p_{\frac{1}{2}}$ and a $p_{\frac{3}{2}}$ function respectively. One can interpret the last term as a spin–orbit effect. For the relativistic correction to nuclear spin–spin coupling, the formal expressions are quite similar, but there is a large number of terms. Now there is even a coupling between spin-dependent and spin-independent terms mediated by spin–orbit interaction. Chapters 13, 14 and 15 treat relativistic effects on NMR parameters.

5.7.6
Second-Order [O(c^4)] Relativistic Corrections

These have been evaluated [24], but cannot be documented here.

5.8 Concluding Remarks

We could only cover a few aspects of the theory of atoms and molecules in a magnetic field. We have always assumed that the magnetic fields are so small that they are sufficiently well described by the leading order of perturbation theory in the field strength. This is usually realized for the external fields used in NMR or EPR experiments, as well as for those due to the nuclei. Higher orders in the field strength do not cause serious difficulties, but are usually not required. The theory of atoms or molecules in *very strong magnetic fields* [32], where interesting new phenomena arise, is beyond the scope of this review. We have always made the *clamped-nuclei* approximation for molecules in a fixed geometry. We could not discuss the Born–Oppenheimer approximation in the presence of magnetic fields [33], which has non-trivial aspects. We have further, not commented on the effect of magnetic fields on vibrational and rotational motions (as studied in microwave spectra), nor on the effect of zero-point vibrations or thermal averaging on magnetic properties. Something on these aspects is found in Chapters 10 and 11.

In this review we were explicitly concerned with one-electron systems. Since magnetic perturbations are described by one-electron operators, most results are transferable to many-electron systems. For these the standard approach is *coupled Hartree–Fock*. To account for effects of *non-dynamic* electron correlation *coupled MC-SCF* is appropriate. The IGLO method for the evaluation of nuclear magnetic shielding, in which different gauge origins are used for different localized molecular orbitals, has been formulated both in the coupled Hartree–Fock [11] and the coupled-MC-SCF context [14]. To take care of the dynamic electron correlation, a MP2 (Møller–Plesset of second order) [34] and a CC (coupled-cluster) theory [35] of magnetic properties have also been formulated. A cheap way to account for some correlation effects is DFT in the presence of magnetic fields [36] and Chapter 6. While non-relativistic coupled Hartree–Fock calculations based on IGLO or GIAO have become routine, both sophisticated treatments of electron correlation and of relativistic effects are still quite challenging.

Some results, mainly on relativistic effects, are published here for the first time. The bibliography of this review consists mainly of references *for further reading*. We have not attempted to document the history. For this see Ref. [16] and Chapters 2 and 3.

Acknowledgement

The author thanks Ch. van Wüllen, V. Staemmler, R. Franke, and I. Malkina for valuable comments.

References

1 J. D. Jackson, *Classical Electrodynamics*, 2nd edition, Wiley, New York **1975**.
2 W. Kutzelnigg, Perturbation Theory of Relativistic Effects, in *Relativistic Electronic Structure Theory. Part I. Fundamentals*, ed. P. Schwerdtfeger, Elsevier, Amsterdam **2002**.
3 J. M. Lévy-Leblond, *Commun. Math. Phys.* **1967**, *6*, 286; J. M. Lévy-Leblond, *Riv. Nuovo Cimento* **1974**, *4*, 909.
4 D. R. Hartree, *Proc. Cambridge Phil. Soc.* **1926**, *245*, 89.
5 D. H. Whiffen, *Pure Appl. Chem.* **1978**, *50*, 75.
6 A. Dalgarno, A. L. Stewart, *Proc. Roy. Soc. London, Ser. A* **1956**, *238*, 269, 276.
7 W. Kutzelnigg, *Theoret. Chim. Acta* **1988**, *73*, 173.
8 F. London, *J. Phys. Radium* **1937**, *8*, 397.
9 J. A. Pople, *Proc. Roy. Soc. London, Ser. A* **1957**, *239*, 541.
10 R. N. Ditchfield, *Mol. Phys.* **1974**, *27*, 789.
11 W. Kutzelnigg, *Isr. J. Chem.* **1980**, *19*, 193; M. Schindler, W. Kutzelnigg, *J. Chem. Phys.* **1982**, *76*, 1919.
12 W. Kutzelnigg, U. Fleischer, M. Schindler, *NMR, Basic Principles and Progress*, **1990**, *23*, 165.
13 U. Fleischer, C. van Wüllen, W. Kutzelnigg, Ab initio calculation of NMR chemical shifts in *Encyclopedia of Computational Chemistry*, ed. P.v.R. Schleyer et al., Wiley, New York **1998**.
14 Ch. van Wüllen, W. Kutzelnigg, in *METECC-95*, p.243–280, ed. E. Clementi, G. Corongiu, STEF, Cagliari, **1995**; Ch. van Wüllen, W. Kutzelnigg, *J. Chem. Phys.* **1996**, *104*, 2330.
15 N. F. Ramsey, *Phys. Rev.* **1950**, *77*, 567; N. F. Ramsey, *Phys. Rev.* **1953**, *83*, 540; N. F. Ramsey, *Phys. Rev.* **1953**, *91*, 303.
16 P. Pyykkö, *Theoret. Chim. Acc* **2000**, *103*, 214.
17 M. M. Sternheim, *Phys. Rev.* **1962**, *128*, 676.
18 P. Pyykkö, *Chem. Phys.* **1977**, *22*, 289; *Chem. Phys.* **1983**, *74*, 1.
19 G. A. Aucar, T. Saue, L.Visscher, H. A. Jensen, *J. Chem. Phys.* **1999**, *110*, 6208.
20 W. Kutzelnigg, *Phys. Rev. A* **2003**, *67*, 032109.
21 R. Szmytkowski, *Phys. Rev. A* **2002**, *65*, 032112.
22 W. Kutzelnigg, *Z. Phys.* **1989**, *11*, 15; W. Kutzelnigg, *Z. Phys.* **1990**, *15*, 27.
23 W. Kutzelnigg, *Phys. Rev. A* **2003**, *67*, 032109.
24 W. Kutzelnigg, *J. Comput. Chem.* **1999**, *20*, 1199.
25 A. Rutkowski, *J. Phys. B* **1986** *149*, 3419, 3434.
26 A. C. Hennum, W. M. Klopper, T. Helgaker *J. Chem. Phys.* **2001**, *115*, 7356.
27 C. Itzykson, J.-B. Zuber, *Quantum Field Theory*, McGraw-Hill, New York **1980**.
28 Y. Namura,Y. Takeuchi, N. Nakagawa, *Tetrahedron Lett.* **1969**, 639.
29 W. Kutzelnigg, M. Dahlbeck, unpublished results.
30 R. Szmytkowski, *J. Phys. B.* **2002**, *35*, 1379.
31 N. C. Pyper, Z. C. Zhang, *Mol. Phys.* **1999**, *97*, 391.
32 P. Schmelcher, L. S. Cederbaum, in *Strong Magnetic Fields: Techniques and Experiments*, eds. F. Herlach, N. Miura. Vol. 2, World Scientific, Singapore **2003**.
33 P. Schmelcher, L. S.Cederbaum, U. Kappes, in *Conceptual Trends in Quantum Chemistry*, eds. E.S. Kryachko, J. L. Calais, pp. 1–51, Kluwer, Dordrecht **1994**.
34 J. Gauss, Chem. *Phys. Lett.* **1992**, *191*, 614.
35 J. Gauss, J. F. Stanton, *J. Chem. Phys.* **1996**, *104*, 2574.
36 V. G. Malkin, O. L. Malkina, M. E. Casida et al., *J. Am. Chem. Soc.* **1994**, *116*, 5898.

Part B
NMR Parameters, Methodological Aspects

Calculation of NMR and EPR Parameters. Theory and Applications.
Edited by Martin Kaupp, Michael Bühl, Vladimir G. Malkin
Copyright © 2004 WILEY-VCH Verlag GmbH & Co. KGaA, Weinheim
ISBN: 3-527-30779-6

6
Chemical Shifts with Hartree–Fock and Density Functional Methods

Christoph van Wüllen

6.1
Introduction

What is actually measured in a nuclear magnetic resonance (NMR) experiment is a local magnetic field strength [1, 2]. As far as chemical shifts are concerned, the magnetic nucleus itself merely acts as a probe (measuring device): the orientation of its magnetic moment is quantised which leads to discrete energy levels. Transitions between these energy levels can be induced by electromagnetic waves in the radio frequency range. The energy differences which can thus be measured are proportional to the local magnetic field strength at the nucleus. While the local magnetic field can be computed at any position by quantum chemical calculations, only its value at the position of the nuclei can thus be measured. The local magnetic field is a superposition of the external magnetic field $\vec{B}_{ext}$ and the magnetic field $\vec{B}_{ind}$ induced by the currents in the molecule.

$$\vec{B}_{loc}(\vec{r}) = \vec{B}_{ext}(\vec{r}) + \vec{B}_{ind}(\vec{r}) \tag{6.1}$$

In this chapter we only consider homogeneous external magnetic fields for which $\vec{B}_{ext}$ is position-independent. According to the Biot–Savart law, a current density $\vec{j}(\vec{r})$ induces, at position $\vec{s}$, a magnetic field

$$\vec{B}_{ind}(\vec{s}) = -\frac{1}{c^2}\int \frac{\vec{j}(\vec{r}) \times (\vec{r}-\vec{s})}{|\vec{r}-\vec{s}|^3}\,\mathrm{d}\vec{r} \tag{6.2}$$

SI-based atomic units (Hartree) [3] are used throughout this chapter, and c is the speed of light (in atomic units, $c \approx 137$). The pre-factor $1/c^2$ arises since, in atomic units, $4\pi\varepsilon_0 = 1$ and the vacuum permeability μ_0 has thus the numerical value $4\pi/c^2$. A more detailed discussion of electromagnetic units is given in this volume in Chapter 5 by Kutzelnigg on the fundamentals of the calculation of magnetic properties.

We will only consider closed-shell molecules for which the current density $\vec{j}(\vec{r})$ vanishes in the absence of external magnetic fields. If such a molecule is put into a homogeneous external magnetic field $\vec{B}_{ext}$, this field induces within the molecule a non-vanishing current density. Once this induced current density has been calcu-

Calculation of NMR and EPR Parameters. Theory and Applications.
Edited by Martin Kaupp, Michael Bühl, Vladimir G. Malkin
Copyright © 2004 WILEY-VCH Verlag GmbH & Co. KGaA, Weinheim
ISBN: 3-527-30779-6

lated, $\vec{B}_{ind}$ can be computed via Eq. (6.2). One defines the magnetic shielding constant $\mathring{A}$ as the negative ratio between the external and the induced field

$$\vec{B}_{ind}(\vec{s}) = -\sigma(\vec{s})\,\vec{B}_{ext} \tag{6.3}$$

For closed-shell atoms, $\vec{B}_{ind}$ is anti-parallel to $\vec{B}_{ext}$ at the position of the nucleus and thus weakens $\vec{B}_{ext}$, hence the name magnetic shielding. In general, $\vec{B}_{ind}$ is not parallel to $\vec{B}_{ext}$, such that the (position-dependent) shielding constant $\mathring{A}$ is a non-symmetric tensor. In practice one cannot directly measure the magnetic shielding because the magnetic field strength and the nuclear magnetic moments are not known to ppm accuracy. Instead the difference between the magnetic shielding of a reference compound and the probe is measured, and this difference is called the chemical shift. We will only refer to the magnetic shielding constant since this is the quantity that is calculated first and then converted to the chemical shift in an obvious way.

To calculate chemical shifts which can be measured in an NMR experiment, one only needs the magnetic shielding constants at the positions of the magnetic nuclei. Magnetic shielding constants at other positions, also called "nucleus independent chemical shifts" (NICS) [4] can be calculated but there is no experimental device to measure them. They however are useful for discussion of the electronic structure. For example, the magnetic shielding in the centre of aromatic rings gives information on the induced current density and thus on the aromaticity of the molecule in question [4, 5] (see also Chapter 24 by Heine et al.).

To evaluate the current density $\vec{j}(\vec{r})$ we have to perform, in principle, a Hartree–Fock or density functional calculation in the presence of the external magnetic field $\vec{B}_{ext}$. If $\hat{H}^{(0)}$ is the molecular Hamiltonian in the absence of magnetic fields, the field-dependent Hamiltonian is obtained if we replace the operator for the linear momentum, $\vec{p}$, by $\vec{p} + \vec{A}_{ext}$where $\vec{A}_{ext}$ is the vector potential describing the external magnetic field. One can always choose vector potentials which are divergence free, thus we have

$$div\,\vec{A}_{ext} = \vec{\nabla}\vec{A}_{ext} = 0, \mathring{A}curl\,\vec{A}_{ext} = \vec{\nabla} \times \vec{A}_{ext} = \vec{B}_{ext} \tag{6.4}$$

and after a little algebra one obtains

$$\hat{H} = \hat{H}^{(0)} + \vec{A}_{ext}\vec{p} + \frac{1}{2}\vec{A}_{ext}^2 \tag{6.5}$$

Unfortunately, there are still many choices for $\vec{A}_{ext}$ for a given magnetic field. One possible class of such choices is

$$\vec{A}_{ext} = \frac{1}{2}\vec{B}_{ext} \times \left(\vec{r} - \vec{R}\right) \tag{6.6}$$

but there are many others. In Eq. (6.6), $\vec{R}$ is the so-called gauge origin which can be chosen arbitrarily. Inserting Eq. (6.6) into Eq. (6.5) finally gives the magnetic-field dependent Hamiltonian

$$\hat{H}\left(\vec{B}_{ext},\vec{R}\right)=\hat{H}(0)+\frac{1}{2}\left(\left(\vec{r}-\vec{R}\right)\times\vec{p}\right)\vec{B}_{ext}+\frac{1}{8}\left(\vec{B}_{ext}\times\left(\vec{r}-\vec{R}\right)\right)^{2} \tag{6.7}$$

which depends not only on the magnetic field but also on the choice of the gauge origin $\vec{R}$. The current density can be computed from the wave function which is a single Slater determinant in the Hartree–Fock approach. In the density functional case, the wave function of the non-interacting Kohn–Sham reference system is also a Slater determinant which makes the density functional computational procedure very similar to the Hartree–Fock case although the computed objects have a different meaning. We only consider closed-shell systems described by a single $2n$-electron Slater determinant Ψ built from n doubly occupied orbitals φ_k. Note that this closed-shell structure is not destroyed by (weak) magnetic fields. The (charge) current density is then given by

$$\vec{j}=i\sum_{k=1}^{n}\left\{\varphi_k^{*}\vec{\nabla}\varphi_k-\left(\vec{\nabla}\varphi_k^{*}\right)\varphi_k\right\}-2\vec{A}_{ext}\sum_{k=1}^{n}\varphi_k^{*}\varphi_k \tag{6.8}$$

Note that we have included the (negative) unit charge of the electron in the definition of the current density and that the occupation number (2.0) of the occupied orbitals is included in Eq. (6.8) and all that follows. Although $\vec{A}_{ext}$ depends on the choice of the gauge origin, $\vec{j}(\vec{r})$ (and any other quantum mechanical observable) does not, at least if the Hartree–Fock (or Kohn–Sham) equations are solved exactly. To verify this, we note that Hamiltonians $\hat{H}\left(\vec{B}_{ext},\vec{R}\right)$ from Eq. (6.7) for different choices of $\vec{R}$ are related by a *gauge transformation*

$$\begin{aligned}
&\vec{A}_{ext}\mapsto\vec{A}_{ext}-\vec{\nabla}\Lambda(\vec{r})\\
&\Lambda(\vec{r})=\frac{1}{2}\left(\vec{B}_{ext}\times\vec{R}'\right)\vec{r}\\
&\hat{H}\left(\vec{B}_{ext},\vec{R}+\vec{R}'\right)=\exp(i\Lambda)\hat{H}\left(\vec{B}_{ext},\vec{R}\right)\exp(-i\Lambda)\\
&=\hat{H}\left(\vec{B}_{ext},\vec{R}\right)-i\left[\hat{H}\left(\vec{B}_{ext},\vec{R}\right),\Lambda\right]-\frac{1}{2}\left[\left[\hat{H}\left(\vec{B}_{ext},\vec{R}\right),\Lambda\right],\Lambda\right]
\end{aligned} \tag{6.9}$$

Likewise, if $\varphi_k\left(\vec{B}_{ext},\vec{R}\right)$ are the Hartree–Fock (or Kohn–Sham) orbitals for the Hamiltonian $\hat{H}\left(\vec{B}_{ext},\vec{R}\right)$, the orbitals for the Hamiltonian with shifted gauge origin are given by

$$\varphi_k\left(\vec{B}_{ext},\vec{R}+\vec{R}'\right)=\exp(i\Lambda)\varphi_k\left(\vec{B}_{ext},\vec{R}\right) \tag{6.10}$$

It is left as an (instructive) exercise to show that the current density, Eq. (6.8) is the same for both gauge origins. Note however that unless $\vec{B}_{ext}=0$, the orbitals themselves depend *strongly* on the chosen gauge origin.

6.2 Linear Response and the Gauge Origin Problem

For magnetic field strengths available in the experimental set-up (up to about 20 T), the induced current density in closed-shell molecules is, to a good approximation, linear in the strength of the field, and terms of second and higher order in the magnetic field strength are rather small. In this regime, the magnetic shielding constant is independent of the strength of the external field. It is therefore well justified to perform calculations in the limit $\vec{B}_{ext} \to 0$. Therefore we can use static linear response theory (perturbation theory) to evaluate the induced current density. We thus expand the one-particle Hamiltonian and the Hartree–Fock (or Kohn–Sham) orbitals as

$$\begin{aligned} \hat{h} &= \hat{h}^{(0)} + i\hat{h}^{(1)} + O\left(B_{ext}^2\right) \\ \varphi_k &= \varphi_k^{(0)} + i\varphi_k^{(1)} + O\left(B_{ext}^2\right) \end{aligned} \tag{6.11}$$

where $\varphi_k^{(0)}$ are the Hartree–Fock orbitals in the absence of external magnetic fields, and $i\varphi_k^{(1)}$ the first-order response of the orbitals when switching on the magnetic field. The orthonormality condition for the field-dependent orbitals yields the condition

$$\left\langle \varphi_k^{(0)} \,\middle|\, \varphi_l^{(1)} \right\rangle - \left\langle \varphi_k^{(1)} \,\middle|\, \varphi_l^{(0)} \right\rangle = 0 \tag{6.12}$$

For closed-shell systems, the $\varphi_k^{(0)}$ can always be chosen real, and it will become clear later that, in this case, the first-order change of the orbitals is purely imaginary such that the $\varphi_k^{(1)}$ are real as well. The (real) current density vanishes if there is no external magnetic field,

$$\vec{j} = \vec{j}^{(1)} + O\left(B_{ext}^2\right) \tag{6.13}$$

its linear response to the magnetic field is

$$\vec{j}^{(1)} = 2\sum_{k=1}^{n} \left\{ \varphi_k^{(1)} \vec{\nabla} \varphi_k^{(0)} - \varphi_k^{(0)} \vec{\nabla} \varphi_k^{(1)} \right\} - 2\vec{A}_{ext} \sum_{k=1}^{n} \varphi_k^{(0)} \varphi_k^{(0)} \tag{6.14}$$

and consists of two terms: the first term, called the paramagnetic part of the current density, involves the linear response of the orbitals, while the second term, the diamagnetic part, can be evaluated without knowing $\varphi_k^{(1)}$. This separation is not unique: under a gauge transformation (Eqs. (6.9) and (6.10)), the first-order orbitals and the paramagnetic and diamagnetic parts of the first-order current density change as

$$\begin{aligned}
&\varphi_k^{(1)} \mapsto \varphi_k^{(1)} + \Lambda\varphi_k^{(0)} \\
&\vec{j}_{para}^{(1)} \mapsto \vec{j}_{para}^{(1)} - 2\vec{\nabla}\Lambda \sum_{k=1}^{n} \varphi_k^{(0)}\varphi_k^{(0)} \\
&\vec{j}_{dia}^{(1)} \mapsto \vec{j}_{dia}^{(1)} + 2\vec{\nabla}\Lambda \sum_{k=1}^{n} \varphi_k^{(0)}\varphi_k^{(0)}
\end{aligned} \tag{6.15}$$

while, of course, the sum of the paramagnetic and diamagnetic parts does not depend on the gauge origin if the Hartree–Fock equations are solved exactly. Note that both terms get very large in absolute value if the gauge origin is far away from the system.

This situation changes if the orbitals are expanded in a finite basis set. It may happen that $\varphi_k^{(1)}$ can reasonably be expanded in the given basis set for specific choices of the gauge origin while other choices only allow a poor representation of $\varphi_k^{(1)}$. For a closed-shell atom for example, the $\varphi_k^{(1)}$ vanish for symmetry reasons if the gauge origin is located at the position of the nucleus. Therefore $\vec{j}^{(1)}$ and the magnetic shielding at the nuclear position is easily calculated

$$\vec{j}^{(1)}(\vec{r}) = -2\vec{A}_{ext}\sum_{k=1}^{n}\varphi_k^{(0)}\varphi_k^{(0)} = -\left(\vec{B}_{ext}\times\vec{r}\right)\sum_{k=1}^{n}\varphi_k^{(0)}\varphi_k^{(0)} \tag{6.16}$$

$$\vec{B}_{ind}(0) = \frac{1}{c^2}\sum_{k=1}^{n}\left\langle\varphi_k^{(0)}\right|\frac{\left(\vec{B}_{ext}\times\vec{r}\right)\times\vec{r}}{r^3}\left|\varphi_k^{(0)}\right\rangle = -\frac{2\vec{B}_{ext}}{3c^2}\sum_{k=1}^{n}\left\langle\varphi_k^{(0)}\right|\frac{1}{r}\left|\varphi_k^{(0)}\right\rangle$$

and we see that the nuclear shielding tensor σ is diagonal ($\vec{B}_{ind}$ is antiparallel to $\vec{B}_{ext}$ at the position of the nucleus), the diagonal value being $1/3c^2$ times the expectation value of r^{-1} (this result was first obtained by Lamb [1]). If the gauge origin is now shifted to $\vec{R}$, the first-order orbitals become, according to Eq. (6.14)

$$\varphi_k^{(1)} = \Lambda\varphi_k^{(0)} = \frac{1}{2}\left(\vec{B}_{ext}\times\vec{R}\right)\vec{r}\varphi_k^{(0)} \tag{6.17}$$

The heart of the gauge origin problem is that the $\varphi_k^{(1)}$ *cannot be expanded* in basis sets conventionally used for atomic and molecular calculations. For example, if $\varphi_k^{(0)}$ is a 2p orbital of a neon atom, then $\varphi_k^{(1)}$ requires a set of d functions which is as large as the p set ("fully polarised" basis sets). In practice, a calculation on a small molecule like methane requires several polarisation functions on each atom, and even then a non-negligible gauge dependence remains. In Table 6.1, the isotropic shielding constants (mean value of the diagonal elements of the σ tensor) at the position of a hydrogen nucleus in the methane molecule are given. Three different gauge origins were used: at the position of the carbon nucleus, at the position of the hydrogen nucleus whose shielding is calculated, and at the position of one of the other three hydrogen atoms.

Four different basis sets were used: first, an unpolarised triple zeta basis set (TZ) from Ref. [6], the same basis set augmented by three sets of polarisation functions

Table 6.1 Isotropic hydrogen magnetic shielding constants for methane. [a)]

Basis Set	Common Gauge Origin at			IGLO	GIAO
	C atom	same H	other H		
TZ	28.58	62.01	17.43	32.48	32.57
TZ +3P	30.97	41.22	27.56	31.29	31.35
TZ-dec +3P	30.98	32.07	30.62	31.20	31.34
Extended	31.23	31.26	31.22	31.24	31.25

a) Absolute magnetic shielding constants in ppm. Hartee–Fock calculations with a common gauge origin and with the IGLO and GIAO variants of distributed gauge origins. See text for a description of the basis sets.

(TZ +3P), the TZ+3P basis set but further decontracting the p functions on carbon from 411 to 21111 (TZ-dec +3P), and an extended uncontracted basis set (19s19p19d4f for carbon, 10s10p4d for hydrogen) in which the s, p, and d basis functions for carbon and the s and p basis functions for hydrogen have the same (even-tempered) exponents. The extended basis set is close to "full polarisation", which means that $\vec{r}\,\varphi_k^{(0)}$ can decently be expanded in the basis sets for all occupied Hartree–Fock orbitals. From the data in Table 6.1 we can deduce how basis sets must be constructed to allow a decent approximation of the first-order orbitals in a magnetic field: First, all atoms should have polarisation functions. Furthermore, further decontraction of the 2p orbital reduced the gauge dependence significantly because this allows for a better polarisation of the s orbitals. But even for the TZ-dec+3P basis set, the gauge dependence of the hydrogen shift is much too large, given that the experimental hydrogen shielding scale has a width of about 10 ppm. For larger molecules with more than a few non-hydrogen atoms it is virtually impossible to obtain a result close to the basis set limit with *any* choice of the gauge origin. The practical problem is not the fact that the results depend on the choice of the gauge origin, but that there is no choice for the gauge origin which gives reasonably converged results with basis sets that can routinely be used.

6.3 Determination of the First-Order Orbitals

Before we address the problem of how to circumvent the gauge origin problem, let us recall how the first-order orbitals $\varphi_k^{(1)}$ are determined. In a basis set Hartree–Fock or density functional calculation, there are, besides the occupied orbitals φ_k, also the unoccupied orbitals φ_a. We will use the indices *k, l, m* for occupied and *a, b, c* for unoccupied (virtual) orbitals. The combined set of occupied and unoccupied orbitals form an orthonormal basis of the linear hull of the basis functions. The number of unoccupied orbitals, N_{virt}, is of course the difference between the basis set size N_{bas} and the number of occupied orbitals. For practical reasons, we will expand both occupied and virtual $\varphi_p^{(1)}$ in the orbitals of the field-free calculation:

$$\varphi_p^{(1)} = \sum_{q=1}^{N_{bas}} Y_{qp} \varphi_q^{(0)} \tag{6.18}$$

The requirement that the field-dependent orbitals are orthogonal for all values of the magnetic field strength gives the additional constraint $Y_{pq} = Y_{qp}$. This implies that only Y_{pq} with one index referring to occupied and the other to virtual orbitals contributes to the first-order current, so only these need be computed.

The stationarity condition for the Hartree–Fock energy requires that matrix elements of the Fock operator between occupied and unoccupied orbitals vanish:

$$0 = F_{ak} = \langle \varphi_a | \hat{h} \left| \varphi_k \right\rangle + 2 \sum_{l=1}^{n} \left(\varphi_l \varphi_l \middle| \varphi_a \varphi_k \right) - \sum_{l=1}^{n} \left(\varphi_a \varphi_l \middle| \varphi_l \varphi_k \right) \tag{6.19}$$

Here we have used the Mulliken notation for the two-electron integrals, and $\hat{h}$ is the one-particle Hamiltonian. In the Kohn–Sham density functional method, the "Fock" matrix elements look similar, the last term being replaced by the matrix elements of the exchange-correlation potential. The first-order orbitals $\varphi_k^{(1)}$ are determined from the condition that the first-order change of all the F_{ak} vanishes, that is, the stationarity condition is required to hold for all values of the magnetic field strength. For the first-order (in the magnetic field strength) change of the Fock matrix elements one gets after some algebra

$$\begin{aligned} F_{ak} &= F_{ak}^{(0)} + i F_{ak}^{(1)} + O\left(B_{ext}^2\right) \\ F_{ak}^{(1)} &= \left\langle \varphi_a^{(0)} \middle| \hat{h}^{(1)} \middle| \varphi_k^{(0)} \right\rangle + \sum_{l=1}^{n} \sum_{b=n+1}^{N_{bas}} H_{ak,bl} Y_{bl} \end{aligned} \tag{6.20}$$

with the magnetic Hessian

$$H_{ak,bl} = \delta_{lk} F_{ab}^{(0)} - \delta_{ab} F_{lk}^{(0)} + \left(\varphi_a^{(0)} \varphi_b^{(0)} \middle| \varphi_l^{(0)} \varphi_k^{(0)} \right) - \left(\varphi_a^{(0)} \varphi_l^{(0)} \middle| \varphi_b^{(0)} \varphi_k^{(0)} \right) \tag{6.21}$$

The equation to determine the Y_{ak} , which reads $F_{ak}^{(1)} = 0$, is thus

$$\left\langle \varphi_a^{(0)} \middle| \hat{h}^{(1)} \middle| \varphi_k^{(0)} \right\rangle + \sum_{l=1}^{n} \sum_{b=n+1}^{N_{bas}} H_{ak,bl} Y_{bl} = 0 \tag{6.22}$$

with the first-order Hamiltonian $i\hat{h}^{(1)}$

$$\hat{h}^{(1)} = -i \frac{1}{2} \left(\left(\vec{r} - \vec{R} \right) \times \vec{p} \right) \vec{B}_{ext} = -\frac{1}{2} \left(\left(\vec{r} - \vec{R} \right) \times \vec{\nabla} \right) \vec{B}_{ext} \tag{6.23}$$

In the Hartree–Fock case, the linear system Eq. (6.22) is called *the coupled Hartree–Fock* equation, first used for the determination of magnetic shielding constants in Ref. [7]. The name alludes to the fact that Eq. (6.22) has to be solved iteratively for larger systems. An obvious simplification arises for the Hessian if the orbitals are canonical, i.e. if the Fock matrix is diagonal. This also speeds up the convergence of

the iterative solution of Eq. (6.22) since the Hessian is more diagonal dominant in this case. In density functional calculations, again the last two terms of the Hessian vanish, which makes the solution of the linear system trivial for canonical orbitals. In this case, one obtains the coefficients of the first-order orbitals and the first-order current density as

$$Y_{ak} = -\frac{\left\langle \varphi_a^{(0)} \middle| \hat{h}^{(1)} \middle| \varphi_k^{(0)} \right\rangle}{F_{aa}^{(0)} - F_{kk}^{(0)}} = \frac{\left\langle \varphi_a^{(0)} \middle| \frac{1}{2}\left(\left(\vec{r}-\vec{R}\right)\times\vec{\nabla}\right) \vec{B}_{ext} \middle| \varphi_k^{(0)} \right\rangle}{F_{aa}^{(0)} - F_{kk}^{(0)}} \tag{6.24}$$

$$\vec{j}^{(1)} = 2\sum_{k=1}^{n}\sum_{a=n+1}^{N_{bas}} Y_{ak}\left\{\varphi_a^{(0)}\vec{\nabla}\varphi_k^{(0)} - \varphi_k^{(0)}\vec{\nabla}\varphi_a^{(0)}\right\} - \left(\vec{B}_{ext}\times\left(\vec{r}-\vec{R}\right)\right)\sum_{k=1}^{n}\varphi_k^{(0)}\varphi_k^{(0)} \tag{6.25}$$

This is why, in the density functional case, Eq. (6.24) is sometimes called the *uncoupled DFT* equation. Equations (6.24) and (6.25) are also called a sum-over-states (SOS) formula. In many chemical shift calculations based on density functional theory, one goes beyond uncoupled DFT. This can be done by including current-dependent terms in the exchange-correlation energy (which is discussed in Section 6.6) or by using so-called hybrid functionals that include "exact exchange" expressions.

Hybrid functionals such as B3LYP are very popular nowadays. Here the exchange-correlation energy is a functional of the electron density (as in the density functional case) augmented by the Hartree–Fock expression for the exchange energy scaled down to (typically) 20%. The calculation of chemical shifts with such functionals proceeds exactly as in the Hartree–Fock case but with the last two terms of Eq. (6.21) scaled down accordingly.

6.4 Distributed Gauge Origins, IGLO and GIAO Approaches

Because of the problems associated with a common gauge origin for a large molecule, all practical methods for the calculation of chemical shifts introduce the concept of *distributed* gauge origins which spread over the molecule. To illustrate this concept, we consider an ensemble of closed-shell atoms well apart (such that their densities do not overlap). We choose $\vec{R} = 0$ as the gauge origin. The current density in the vicinity of atom A at position $\vec{R}_A$ is not affected by the presence of the other atoms and reads, according to Eq. (6.16)

$$\vec{j}^{(1)}(\vec{r}) = -\left(\vec{B}_{ext}\times\left(\vec{r}-\vec{R}_A\right)\right)\sum_{k=1}^{n}\varphi_k^{(0)}\varphi_k^{(0)} \quad \text{(in the vicinity of atom A)} \tag{6.26}$$

If the orbitals $\varphi_k^{(0)}$ are chosen localised on the atoms, and if we let $\vec{R}_k$ be the charge centre of orbital $\varphi_k^{(0)}$, then for the orbitals localised on atom A, $\vec{R}_k \approx \vec{R}_A$ and we get

$$\vec{j}^{(1)}(\vec{r}) \approx -\sum_{k=1}^{n}\left(\vec{B}_{ext}\times\left(\vec{r}-\vec{R}_k\right)\right)\varphi_k^{(0)}\varphi_k^{(0)}$$
$$=\sum_{k=1}^{n}\left(\vec{B}_{ext}\times\vec{R}_k\right)\varphi_k^{(0)}\varphi_k^{(0)}-\left(\vec{B}_{ext}\times\vec{r}\right)\sum_{k=1}^{n}\varphi_k^{(0)}\varphi_k^{(0)} \tag{6.27}$$

Note that while Eq. (6.26) only holds in the vicinity of atom A, Eq. (6.27) is valid everywhere. We have thus expressed the first-order current as a sum of local diamagnetic orbital contributions, in which we have assigned *individual gauge origins* $\vec{R}_k$ *to the localised orbitals* $\varphi_k^{(0)}$ (first line of Eq. (6.27)). Since the last term of the second line of Eq. (6.27) is identified as the diamagnetic part (for gauge origin $\vec{R}=0$) of the first-order current, we have (an approximation to) the paramagnetic current and thus to the first-order orbitals (for that gauge origin)

$$\vec{j}^{(1)}_{para}(\vec{r}) \approx \sum_{k=1}^{n}\left(\vec{B}_{ext}\times\vec{R}_k\right)\varphi_k^{(0)}\varphi_k^{(0)} = 2\sum_{k=1}^{n}\vec{\nabla}\Lambda_k\varphi_k^{(0)}\varphi_k^{(0)},\ \Lambda_k(\vec{r})=\frac{1}{2}\left(\vec{B}_{ext}\times\vec{R}_k\right)\vec{r}$$
$$\phi_k^{(1)}(\vec{r}) \approx -\Lambda_k(\vec{r})\varphi_k^{(0)}(\vec{r}) \tag{6.28}$$

The nature of the physical system thus gives us some information on the first-order orbitals, and this information should of course be exploited in our calculations. We can thus, for any molecular system, use the ansatz

$$\phi_k^{(1)}(\vec{r}) = -\Lambda_k(\vec{r})\varphi_k^{(0)}(\vec{r}) + \tilde{\phi}_k^{(1)}(\vec{r}) \tag{6.29}$$

in which the first-order orbital is written as a sum of the gauge term and the yet unknown "rest" $\tilde{\phi}_k^{(1)}(\vec{r})$ which has to be expanded in the basis set. If the orbitals are localised with charge centre $\vec{R}_k$ and the gauge factors Λ_k chosen according to Eq. (6.28), we can expect that the "rest" $\tilde{\varphi}_k^{(1)}$ is much smaller than the full first-order orbital $\varphi_k^{(1)}$, which leads to reduced errors if it is expanded in the finite basis set. In other words, the gauge term $-\Lambda_k\varphi_k^{(0)}$ contains most of that part of $\varphi_k^{(1)}$ which cannot be expanded in the basis set. Using Eq. (6.29), the first-order current and the induced magnetic field at position $\vec{s}$ read

$$\vec{j}^{(1)} = 2\sum_{k=1}^{n}\left\{\tilde{\varphi}_k^{(1)}\vec{\nabla}\varphi_k^{(0)} - \varphi_k^{(0)}\vec{\nabla}\tilde{\varphi}_k^{(1)}\right\} - \sum_{k=1}^{n}\left(\vec{B}_{ext}\times\left(\vec{r}-\vec{R}_k\right)\right)\varphi_k^{(0)}\varphi_k^{(0)} \tag{6.30}$$

$$\vec{B}_{ind}(\vec{s}) = \frac{4}{c^2}\sum_{k=1}^{n}\left\langle\tilde{\varphi}_k^{(1)}\right|\frac{(\vec{r}-\vec{s})\times\vec{\nabla}}{|\vec{r}-\vec{s}|^3}\left|\varphi_k^{(0)}\right\rangle$$
$$+\frac{1}{c^2}\sum_{k=1}^{n}\left\langle\varphi_k^{(0)}\right|\frac{\left(\vec{B}_{ext}\times\left(\vec{r}-\vec{R}_k\right)\right)\times(\vec{r}-\vec{s})}{|\vec{r}-\vec{s}|^3}\left|\varphi_k^{(0)}\right\rangle \tag{6.31}$$

and again involve local diamagnetic contributions (from the localised orbitals with their individual gauge origins).

The use of localised orbitals has some disadvantages: the coupled Hartree–Fock equations converge faster if the magnetic Hessian is expressed in terms of canonical orbitals (see Section 6.3), and in the density functional case, the sum-over-states formula Eqs. (6.24) and (6.25)) can only be used with canonical orbitals. While the original formulation of the IGLO method [8, 9] works as described above, modern implementations of IGLO [10] transform everything back to canonical orbitals once the ansatz Eq. (6.29) has been made: First one localises the orbitals, that is, one calculates the transformation matrix U from the canonical orbitals $\varphi_k^{(0)}$ to the localised orbitals $\varphi_k^{(L,0)}$:

$$\varphi_k^{(L,0)} = \sum_{l=1}^{n} U_{lk}\varphi_l^{(0)}, \;\; \varphi_k^{(0)} = \sum_{l=1}^{n} U_{kl}\varphi_l^{(L,0)} \tag{6.32}$$

Since the localised orbitals also form an orthonormal set, the matrix U is orthogonal. Next one applies the ansatz Eq. (6.29) to the expansion of the canonical orbitals in terms of localised orbitals:

$$\phi_k^{(1)}(\vec{r}) = -\sum_{l=1}^{n} U_{kl}\Lambda_l(\vec{r})\varphi_l^{(L,0)}(\vec{r}) + \tilde{\phi}_k^{(1)}(\vec{r}) = -\sum_{l,m=1}^{n} U_{ml}U_{kl}\Lambda_l(\vec{r})\varphi_m^{(0)}(\vec{r}) + \tilde{\phi}_k^{(1)}(\vec{r}) \tag{6.33}$$

If one calculates $\vec{j}^{(1)}$ from these first-order orbitals one gets

$$\vec{j}^{(1)} = 2\sum_{k=1}^{n}\left\{\tilde{\varphi}_k^{(1)}\vec{\nabla}\varphi_k^{(0)} - \varphi_k^{(0)}\vec{\nabla}\tilde{\varphi}_k^{(1)}\right\} - \sum_{k=1}^{n}\left(\vec{B}_{ext}\times\left(\vec{r}-\vec{R}_k\right)\right)\varphi_k^{(L,0)}\varphi_k^{(L,0)} \tag{6.34}$$

which is equivalent to Eq. (6.30) in the sense that the diamagnetic part is given as a sum of local contributions. Note that the final results obtained in the two variants of IGLO do not differ.

The IGLO concept has been used in conjunction with the Hartree–Fock [8] and multi-configuration Hartree–Fock [9] methods and within density functional calculations of magnetic shielding constants [11–15]. It was the first solution to the gauge origin problem which produced a large body of accurate computational data and has therefore been a milestone in the quantum chemical computation of magnetic shielding constants. However there are also some disadvantages which stem from the necessity to use (at least in an intermediate way) localised orbitals:

1. Orbital localisation is not always uniquely defined. This means that for a given basis set and molecular geometry, the magnetic shielding constants also depend on the particular choice of localised orbitals.
2. If the charge centres of the localised orbitals have a lower symmetry than the molecular framework itself, then different magnetic shielding constants may be obtained at symmetry-equivalent positions. In a linear molecule like HCl for example, the localisation of the L shell yields four sp^3 hybrids, and the two

components of the shielding tensors perpendicular to the molecular axis need not be the same. Likewise, the localised orbitals of the cyclopentadienyl anion will not reflect the fivefold symmetry and different magnetic shielding constants are computed for the five carbon atoms.

3. Not all computational methods allow for orbital localisation. Localised orbitals for multi-configuration Hartree–Fock wave functions can only be constructed in the CASSCF case, and even then a full-valence CAS is required in most cases to get reasonably localised orbitals.

These problems are absent if one introduces the distributed gauge origins at the level of basis functions (instead of molecular orbitals). This leads to the GIAO (gauge including atomic orbitals) method, first used within the coupled Hartree–Fock scheme by Ditchfield [17]. The GIAO approach only works with localised, atom-centred basis functions but apart from this requirement, GIAO can be combined with wave functions of any type. To understand how GIAO works we again start from Eq. (6.28) but expand the orbitals into N_{bas} basis functions χ_μ:

$$\varphi_k^{(0)} = \sum_{\mu=1}^{N_{bas}} C_{\mu k}\, \chi_\mu \tag{6.35}$$

In complete analogy to Eqs. (6.29) and (6.33) one makes the GIAO ansatz

$$\phi_k^{(1)}(\vec{r}) \approx -\sum_{\mu=1}^{N_{bas}} C_{\mu k} \Lambda_\mu(\vec{r}) \chi_\mu(\vec{r}) + \tilde{\phi}_k^{(1)}(\vec{r}),\ \Lambda_\mu(\vec{r}) = \frac{1}{2}\left(\vec{B}_{ext} \times \vec{R}_\mu\right) \vec{r} \tag{6.36}$$

with $\vec{R}_\mu$ being the centre of the basis function χ_μ, that is the position of the nucleus which carries that particular basis function. A comparison of Eqs. (6.33) and (6.36) reveals the formal analogy between IGLO and GIAO. In the GIAO ansatz Eq. (6.36) the first-order current density becomes

$$\begin{aligned}\vec{j}^{(1)} &= 2\sum_{k=1}^{n} \tilde{\varphi}_k^{(1)} \vec{\nabla} \varphi_k^{(0)} - \varphi_k^{(0)} \vec{\nabla} \tilde{\varphi}_k^{(1)} \\ &+ \sum_{k=1}^{n} \sum_{\mu,\nu=1}^{N_{bas}} C_{\mu k} C_{\nu k} \left(\Lambda_\nu - \Lambda_\mu\right) \left(\chi_\mu \vec{\nabla} \chi_\nu - \chi_\nu \vec{\nabla} \chi_\mu\right) \\ &+ \sum_{k=1}^{n} \sum_{\mu,\nu=1}^{N_{bas}} C_{\mu k} C_{\nu k} \left(\vec{B}_{ext} \times \left(\vec{r} - \frac{1}{2}\left(\vec{R}_\mu + \vec{R}_\nu\right)\right)\right) \chi_\mu \chi_\nu\end{aligned} \tag{6.37}$$

Similar to the IGLO case, we have a local diamagnetic contribution with individual gauge origins for basis functions (third term), a paramagnetic contribution which is calculated from the $\tilde{\varphi}_k^{(1)}$ (first term) and an additional term which vanishes in our example of well-separated closed-shell atoms (two basis functions either share the same centre or they do not overlap). This second term is absent in the IGLO variant because of the orthogonality of the localised molecular orbitals. Early applications of the GIAO concept were hampered by the fact that the calculation of the two-electron integrals involving the gauge term was very slow. It was the main advantage of the IGLO method that such integrals could be avoided [8]. It was only much later that

GIAO became more popular than IGLO, when modern techniques were used to evaluate the integrals [18].

It is beyond the scope of this chapter to derive the working equations for the GIAO and IGLO methods, and to explain the additional approximations involved in existing implementations of IGLO. Both methods are rather successful, as can be seen from Table 6.1: the magnetic shielding constants obtained both with IGLO and GIAO converge spectacularly faster to the basis set limit than calculations based on a common gauge origin, no matter where it is. As a rule of thumb, basis sets of triple to quadruple zeta quality with two to three sets of polarisation functions give results close to the basis set limit.

6.5 Distributed Gauge Origins in Real Space, a "Continuous Set of Gauge Transformations"

While most chemical shift calculations today are based either on the IGLO or GIAO concept of distributed gauge origins, another method has been proposed which works quite differently: Eq. (6.2) shows that the induced magnetic field can be computed as a three-dimensional integral involving the current density. Let us assume we would evaluate this integral by numerical quadrature. Then we would compute the current density at a large set of grid points and then perform the integration. It is perfectly legitimate to restart the computation of $\vec{j}^1(\vec{r})$ at each grid point, using a gauge origin which is most appropriate for computing $\vec{j}^1(\vec{r})$ at that specific location. Although this is not a gauge transformation in a mathematical sense, this procedure has been termed "continuous set of gauge transformations" (CSGT) [19]. Formally one might consider the computed first-order current as a function of two variables: the position $\vec{r}$ in space where the current is computed and the location $\vec{R}(\vec{r})$ of the gauge origin, which might depend on $\vec{r}$. At first glance it seems highly inefficient to compute the first-order orbitals at thousands of grid points, each time using a different gauge origin. However, since the $\varphi_k^{(1)}$ are determined from a set of *linear* equations, one only needs to solve two sets of coupled Hartree–Fock equations from which the first-order orbitals are easily computed for any gauge origin [19]. First applications used the choice $\vec{R}(\vec{r}) = \vec{r}$. In this case, the diamagnetic part of the first-order current formally vanishes. In the original work, the integrals involving $\vec{j}^1(\vec{r})$ were evaluated by numerical quadrature, but it was shown later that in the case $\vec{R}(\vec{r}) = \vec{r}$ the integrals can be done analytically [20] and that the working equations are equivalent to a method proposed earlier by Geertsen [21] within a propagator formalism. It is generally a good idea to keep the diamagnetic contributions small, since then the more difficult paramagnetic contributions will also be small in absolute value. However $\vec{R}(\vec{r}) = \vec{r}$ is not the optimal choice. This has been deduced from numerical results in Ref. [19] and also follows from a theoretical analysis in Ref. [22]. It can clearly be understood that, from the picture of the gauge origin problem laid out in Section 6.2, in the case of separated closed-shell atoms, the best choice for $\vec{R}(\vec{r})$ is the position of the nearest nucleus. Such a shift of the gauge origin has been used together with the CSGT method [19, 23] and is similar to what had been

termed "individual gauge for atoms in molecules" (IGAIM) [24]. From the data presented in Ref. [23] a reasonable convergence towards the basis set limit can be concluded, similar to (but not outperforming) the GIAO method. It has also been suggested to determine $\vec{R}(\vec{r})$ such that the paramagnetic part of $\vec{j}^1(\vec{r})$ (at least the components perpendicular to the external magnetic field) vanish [25]. Although this looks attractive since the paramagnetic terms are the "difficult" ones, the results were not convincing.

6.6 Beyond Pure Density Functional Theory

In the density functional framework, the density, and thus the exchange-correlation energy, is not changed through first order in the magnetic field strength. On the one hand, this fundamental difference to the Hartree–Fock case leads to a very simple computational procedure for the calculation of the first-order current, namely the sum-over-states formula Eqs. (6.24) and (6.25). On the other hand, it looks physically incorrect that there is no first-order change of the exchange-correlation potential although this follows, in the last analysis, from the Hohenberg–Kohn theorem. This theorem has been formulated for an electronic system in an arbitrary external potential but does not consider magnetic fields. In this case, the density as the basic variable is not enough, there must be an additional variable that depends on the current density. Such a (non-relativistic) current density functional theory has been formulated by Vignale and Rasolt [26–28]. The problem is that, in contrast to the relativistic case, the wave function does not determine the current density, which also depends on the external vector potential through its diamagnetic part. The paramagnetic part alone is not gauge invariant, but a gauge invariant variable $\vec{\nu}$ can be obtained by defining

$$\vec{\nu} = -i \sum_{k=1}^{n} \vec{\nabla} \times \frac{\varphi_k^* \vec{\nabla} \varphi_k - \left(\vec{\nabla} \varphi_k^*\right) \varphi_k}{\rho} \tag{6.38}$$

A local (in ρ and $\vec{\nu}$) exchange-correlation functional has been proposed in Refs. [26, 28]. Equations using such a functional in IGLO and GIAO chemical shift calculations have been given in Ref. [29], and the first implementation (using the GIAO framework) has been reported in Ref. [30]. The outcome was rather disappointing. Table 6.2 reports results of density functional calculations of the magnetic shielding at the fluorine nucleus in the F_2 molecule. This molecule is a hard test case: the HOMO–LUMO (π and σ^*) energy difference is rather small at the density functional level, and this is mainly responsible for the overestimation of the paramagnetic contributions to the shielding [31] in (uncoupled) density functional calculations. Including current-dependent terms in the exchange-correlation functional does not cure this situation: in fact, including current-dependent terms has less effect than changes in the basis set or using different exchange-correlation functionals.

Table 6.2 Density functional results for the (absolute) magnetic shielding in F_2.

Method	Exchange-Correlation functional				
	LDA	BP	PW91	BLYP	B3LYP
Uncoupled DFT GIAO	–283 [a]	–284 [f]		–272 a)	
	–308 [f]				
CDFT GIAO	–293 [a]			–281 [a]	
SIC DFT GIAO	–278 [f]				
Uncoupled DFT IGLO	–272 [b]	–251 [b]	–245 [d]		
Coupled DFT IGLO	–216 [c]	–198 [c]			
SOS DFT IGLO			–203 [d]		
Hybrid DFT LORG					–252 [e]
WAH-DFT LORG					–186 [e]

a) Ref. [30], **b)** Ref. [11], **c)** Ref. [12], **d)** Ref. [13], **e)** Ref. [38], **f)** Ref. [39], calculated at DFT-optimised geometry. The experimental r_e-value is –193 ppm [16].

Malkin, Malkina and Salahub have developed a quite different strategy to improve upon uncoupled density functional calculations: based on a comparison of the Hartree–Fock and density functional equations, they introduced additional terms in the molecular Hessian which resulted in a rather complicated numerical scheme ("coupled DFT IGLO"). However, as can be seen from Table 6.2, in problematic cases like the fluorine molecule, the results were greatly improved. Since this method is much more expensive than uncoupled DFT, and since it is not invariant against orbital rotations within the occupied space, it was soon replaced by the so-called "sum over states" (SOS) density functional method. Here one starts from Eq. (6.24) but introduces corrections to the "energy denominators" $F^{(0)}_{aa} - F^{(0)}_{kk}$, that is, one replaces

$$F^{(0)}_{aa} - F^{(0)}_{kk} \;\rightarrow\; F^{(0)}_{aa} - F^{(0)}_{kk} + \Delta_{ak} \tag{6.39}$$

where the motivation for the correction again comes from a comparison with the Hartree–Fock case. The resulting procedure is computationally as inexpensive as uncoupled DFT, but improves the results substantially (see Tab. 6.2). This method has been applied in numerous cases and has been shown to be rather useful. Note that the substitution Eq. (6.39) destroys the gauge invariance of the first-order current [29], but this is more a theoretical than a practical drawback [32, 33].

Using hybrid exchange-correlation functionals including "exact exchange" (such as the popular B3LYP functional) one implicitly includes current-dependent terms in the exchange energy. For typical molecules containing only main-group elements, B3LYP chemical shifts are not consistently better than results obtained from pure density functionals [14, 23, 34]. For example, the B3LYP result for F_2 (see Tab. 6.2) is no improvement over the results from pure density functionals. Other hybrid functionals have been tested with about the same success [35]. Note that for chemical shifts of most transition metal atoms, the situation seems to be quite different and

B3LYP is a substantial improvement over pure density functional methods [36, 37], see also Chapter 26 by Bühl on transition metal compounds.

While the Malkin correction addresses the energy denominators in the sum-over-states formula Eq. (6.24), Wilson et al. (WAH) have argued that it is also the shape of the Kohn–Sham orbitals that need to be improved. They suggested a procedure in which the occupied and virtual orbitals $\varphi_k^{(0)}, Å\varphi_a^{(0)}$ and orbital energies $F_{aa}^{(0)}, ÅF_{kk}^{(0)}$ are obtained from a hybrid functional density functional calculation and then plugged into the sum-over-states formula Eq. (6.24). The amount of exact exchange had to be reduced from 0.20 to 0.05 in the B3LYP functional, and the final results depend critically on this parameter. This procedure also yields greatly improved magnetic shielding constants, but shares with Malkin's method that it breaks gauge invariance [14]. The major deficiency in the exchange-correlation potential comes from the improper cancellation of self-interaction in the Coulomb and exchange energy. Therefore a self-interaction-corrected (SIC) version of density functional theory has also been tested in magnetic shielding calculations [39, 40]. The method is somewhat problematic since the energy and all properties derived from it depend on the particular choice of the occupied orbitals. For the fluorine molecule (see Tab. 6.2) at least, no improvement can be observed. Note that the magnetic shielding constants from Ref. [39] have been obtained at the equilibrium distance at density functional level and will be about 30 ppm larger (i.e., smaller in absolute value) if one repeats the calculation at the experimental equilibrium distance.

Originally it was believed that the neglect of the current-dependent contributions to the exchange-correlation energy is the reason for the unsatisfactory results from uncoupled density functional calculations. But now it is generally accepted that a pure density functional should be able to give accurate magnetic shielding constants, provided that it is tailored to the calculation of magnetic properties [34, 38].

6.7 Conclusions

The most important ingredient in a Hartree-Fock or density functional calculation of magnetic shielding constants is the introduction of distributed gauge origins. In contrast to the success of density functional theory for the calculation of molecular structures and energetics, it does not provide a systematic improvement over Hartree–Fock for the calculation of magnetic shielding. "Emperical" corrections like the recipe of Malkin et al. or the suggestion of Wilson et al. dramatically improve the density functional results although they break gauge invariance, which is a fundamental property of the theory. It seems that we will still have to wait some time for a rigorous density functional method which gives good magnetic shielding constants.

References

1 W. E. Lamb Jr., *Phys. Rev.* **1941**, *60*, 817.
2 N. F. Ramsey, *Phys. Rev.* **1950**, *78*, 699.
3 D. H. Whiffen, *Pure Appl. Chem.* **1978**, *50*, 75.
4 P. v. R. Schleyer, C. Maerker, A. Dransfeld et al., *J. Am. Chem. Soc.* **1996**, *118*, 6317.
5 J. A. N. F. Gomes , R. B. Mallion, *Chem. Rev.* **2001**, *101*, 1349.
6 A. Schäfer, H. Horn, R. Ahlrichs, *J. Chem Phys.* **1992**, *97*, 2571.
7 R. M. Stephens, R. M. Pitzer, W. N. Lipscomb, *J. Chem Phys.* **1963**, *38*, 550.
8 M. Schindler, W. Kutzelnigg, *J. Chem Phys.* **1982**, *76*, 1919.
9 C. van Wüllen, W. Kutzelnigg, *J. Chem Phys.* **1996**, *104*, 2330.
10 C. van Wüllen, W. Kutzelnigg, in *Methods and Techniques in Computational Chemistry: METECC-95*, eds. E. Clementi and G. Corongiu, STEF, Cagliari **1995**.
11 V. G. Malkin, O. L. Malkina, D. R. Salahub, *Chem. Phys. Lett.* **1993**, *204*, 80.
12 V. G. Malkin, O. L. Malkina, D. R. Salahub, *Chem. Phys. Lett.* **1993**, *204*, 87.
13 V. G. Malkin, O. L. Malkina, M. E. Casida et al., *J. Am. Chem. Soc.* **1994**, *116*, 5989.
14 C. van Wüllen, *Phys. Chem. Chem. Phys.* **2000**, *2*, 2137.
15 L. Olsson, D. Cremer, *J. Chem Phys.* **1996**, *105*, 8995.
16 C. J. Jameson, A. K. Jameson, P. M. Burrell, *J. Chem Phys.* **1980**, *73*, 6013.
17 R. Ditchfield, *J. Chem Phys.* **1972**, *56*, 5688.
18 K. Wolinski, J. F. Hinton, P. Pulay, *J. Am. Chem. Soc.* **1990**, *112*, 8251.
19 T. A. Keith, R. W. F. Bader, *Chem. Phys. Lett.* **1993**, *210*, 223.
20 P. Lazzeretti, M. Malagoli, R. Zanasi, *Chem. Phys. Lett.* **1994**, *220*, 299.
21 J. Geertsen, *Chem. Phys. Lett.* **1991**, *179*, 479.
22 S. Coriani, P. Lazzeretti, M. Malgoli et al., *Theor. Chim. Acta* **1994**, *89*, 181.
23 J. R. Cheeseman, G. W. Trucks, T. A. Keith et al., *J. Chem Phys.* **1996**, *104*, 5497.
24 T. A. Keith, R. W. F. Bader, *Chem. Phys. Lett.* **1992**, *194*, 1.
25 R. Zanasi, P. Lazzeretti, M. Malagoli et al., *J. Chem Phys.* **1995**, *102*, 7150.
26 G. Vingale, M. Rasolt, *Phys. Rev. Lett.* **1987**, *59*, 2360; Erratum *Phys. Rev. Lett.* **1989**, *62*, 115.
27 G. Vingale, M. Rasolt, *Phys. Rev. B* **1988**, *37*, 10685.
28 G. Vingale, M. Rasolt, D. J. W. Geldart, *Phys. Rev. B* **1988**, *37*, 2502.
29 C. van Wüllen, *J. Chem Phys.* **1995**, *102*, 2806.
30 A. M. Lee, N. C. Handy, S. M. Colwell, *J. Chem Phys.* **1995**, *103*, 10095.
31 G. Schreckenbach , T. Ziegler, *J. Phys. Chem.* **1995**, *99*, 606.
32 V. G. Malkin, O. L. Malkina, D. R. Salahub, *J. Chem Phys.* **1996**, *104*, 1163.
33 C. van Wüllen, *J. Chem Phys.* **1996**, *104*, 1165.
34 P. J. Wilson, R. D. Amos, N. C. Handy, *Mol. Phys.* **1999**, *97*, 757.
35 C. Adamo, V. Barone, *Chem. Phys. Lett.* **1998**, *298*, 113.
36 M. Bühl, *Chem. Phys. Lett.* **1997**, *267*, 251.
37 M. Bühl, M. Kaupp, O. L. Malkina et al., *J. Comput. Chem.* **1999**, *20*, 91.
38 P. J. Wilson, R. D. Amos, N. C. Handy, *Chem. Phys. Lett.* **1999**, *312*, 475.
39 S. Patchkovskii, J. Autschbach, T. Ziegler, *J. Chem Phys.* **2001**, *115*, 26.
40 S. Patchkovskii, T. Ziegler, *J. Phys. Chem. A* **2002**, *106*, 1088.

7
Spin–Spin Coupling Constants with HF and DFT Methods

Trygve Helgaker and Magdalena Pecul

7.1
Introduction

Nuclear magnetic resonance (NMR) spectroscopy constitutes an extremely useful tool for the determination of molecular electronic structure and molecular conformation. Apart from the shielding constants, the indirect nuclear spin–spin coupling constants represent the most important source of structural information of high-resolution NMR. First, the magnitude of the indirect spin–spin coupling constants depends on the electron distribution between the coupled nuclei, providing valuable information on chemical bonding. Second, since the indirect spin–spin coupling constants are highly sensitive to the molecular geometry, they are extensively used in conformational studies [1–5]. In both cases, quantum-chemical calculations of indirect spin–spin constants can play an important role in the interpretation of the measured coupling constants in terms of the electronic and geometric structure [6,7].

Nowadays, the need for inexpensive computational techniques capable of reliably predicting spin–spin coupling constants stems from arguably the most important application area of high-resolution NMR spectroscopy: the elucidation of the native structures of biopolymers, in which the indirect spin–spin coupling constants play a crucial role. Vicinal (three-bond) coupling constants, in particular, have for a long time been used to determine dihedral angles [1,2]. One-bond coupling constants (especially those of carbon and nitrogen), geminal (two-bond) coupling constants, and even long-range proton–proton coupling constants have also found widespread use in molecular-structure elucidations [4,5,8–10]. Very recently, the discovery of coupling constants transmitted through hydrogen bonds has made the spin–spin couplings even more useful for the determination of the high-order structures of biopolymers [11–17].

Realistic models of biomolecules are necessarily of substantial size, thus the need for fast-scaling computational methods for spin–spin coupling constant calculations by means of ab initio theory. Unfortunately, the accurate calculation of indirect nuclear spin–spin coupling constants has proved to be significantly more difficult than that of the other NMR parameters, such as the nuclear magnetic shielding constants and the nuclear quadrupole coupling constants. First, in nonrelativistic the-

Calculation of NMR and EPR Parameters. Theory and Applications.
Edited by Martin Kaupp, Michael Bühl, Vladimir G. Malkin
Copyright © 2004 WILEY-VCH Verlag GmbH & Co. KGaA, Weinheim
ISBN: 3-527-30779-6

ory, there are several distinct mechanisms contributing to the spin–spin coupling constants [18]: the diamagnetic spin–orbit (DSO) term, the paramagnetic spin–orbit (PSO) term, the spin–dipole (SD) term, and the Fermi-contact (FC) term. Although, in most cases, the FC term dominates the isotropic coupling, none of the contributions can be a priori neglected, increasing the programming and computational efforts. Next, the FC and SD terms involve triplet perturbations, requiring a flexible description of the molecular electronic structure. Finally, for an accurate calculation of the FC contribution, it is necessary to provide a good description of the electron density at the nuclei, something which is difficult to achieve by means of Gaussian orbitals, which are used in most ab initio calculations. Clearly, therefore, the routine calculation of indirect nuclear spin–spin coupling constants for large systems such as biomolecules presents a formidable challenge for computational chemistry. Although the spin–spin coupling constants of small molecular systems can be calculated by a number of methods, including high-level coupled-cluster theory with the inclusion of connected triple excitations [19], the only methods currently capable of routinely treating systems containing more than 10 to 20 atoms are those provided by density-functional theory (DFT).

The present chapter is intended as an introduction to the calculation of indirect nuclear spin–spin coupling constants by means of self-consistent field (SCF) theories, that is, by Hartree–Fock theory and, in particular, by Kohn–Sham DFT. First, in Section 7.2, we provide some theoretical background for the calculation of spin–spin coupling constants; next, in Section 7.3, we briefly review the application of DFT to the calculation of these constants.

7.2
The Calculation of Indirect Nuclear Spin–Spin Coupling Constants

The elements of the reduced indirect nuclear spin–spin coupling tensor $\mathbf{K}_{KL}$ of nuclei K and L can be identified as the mixed second derivatives of the total electronic energy E ($\mathbf{M}_1$, $\mathbf{M}_2$, . . .) of the molecular system with respect to the magnetic moments $\mathbf{M}_K$ and $\mathbf{M}_L$ of nuclei K and L:

$$\mathbf{K}_{KL} = \left. \frac{\mathrm{d}^2 E(\mathbf{M}_1, \mathbf{M}_2, \cdots)}{\mathrm{d}\mathbf{M}_K \mathrm{d}\mathbf{M}_L} \right|_{\mathbf{M}_K = \mathbf{M}_L = \cdots = \mathbf{0}}, \tag{7.1}$$

where we have ignored the direct (through-space) contribution to the coupling tensor $\mathbf{D}_{KL}$, which arises from purely nuclear–nuclear interactions and does not contribute to the electronic energy E ($\mathbf{M}_1$, $\mathbf{M}_2$, . . .). Usually, the indirect nuclear spin–spin interactions are expressed not in terms of the reduced coupling tensor $\mathbf{K}_{KL}$ of Eq. (7.1) but rather in terms of the indirect nuclear spin–spin coupling tensor

$$\mathbf{J}_{KL} = h \frac{\gamma_K}{2\pi} \frac{\gamma_L}{2\pi} \mathbf{K}_{KL}, \tag{7.2}$$

where γ_K and γ_L are the magnetogyric ratios of the two nuclei. For freely tumbling molecules in the gas or liquid phases such as those observed in high-resolution NMR, only the isotropic part of the indirect coupling tensor is observed:

$$J_{KL} = \frac{1}{3}\mathrm{Tr}\,\mathbf{J}_{KL}. \tag{7.3}$$

Since $\mathbf{D}_{KL}$ is traceless, there is no direct contribution to the coupling in such cases.

7.2.1 Ramsey's Nonrelativistic Theory of Nuclear Spin–Spin Coupling Constants

Since the nuclear spin–spin coupling tensors may be expressed as second derivatives of the electronic energy, they may be calculated using standard second-order response theory, within a relativistic or nonrelativistic framework. In the nonrelativistic closed-shell case, treated here, it is instructive to consider the equivalent sum-over-states expression of second-order perturbation theory, first presented by Ramsey in 1953 [18]:

$$\mathbf{K}_{KL} = \left\langle 0\middle|\mathbf{h}_{KL}^{\mathrm{DSO}}\middle|0\right\rangle - 2\sum_{n_\mathrm{S}\neq 0}\frac{\left\langle 0\middle|\mathbf{h}_K^{\mathrm{PSO}}\middle|n_\mathrm{S}\right\rangle\left\langle n_\mathrm{S}\middle|(\mathbf{h}_L^{\mathrm{PSO}})^{\mathrm{T}}\middle|0\right\rangle}{E_{n_\mathrm{S}} - E_0}$$

$$-2\sum_{n_\mathrm{T}}\frac{\left\langle 0\middle|\mathbf{h}_K^{\mathrm{FC}} + \mathbf{h}_K^{\mathrm{SD}}\middle|n_\mathrm{T}\right\rangle\left\langle n_\mathrm{T}\middle|(\mathbf{h}_L^{\mathrm{FC}})^{\mathrm{T}} + (\mathbf{h}_L^{\mathrm{SD}})^{\mathrm{T}}\middle|0\right\rangle}{E_{n_\mathrm{T}} - E_0}. \tag{7.4}$$

We have here introduced the diamagnetic spin–orbit (DSO), paramagnetic spin–orbit (PSO), Fermi-contact (FC), and spin–dipole (SD) operators (in atomic units)

$$\mathbf{h}_{KL}^{\mathrm{DSO}} = \alpha^4\sum_i\frac{\mathbf{r}_{iK}^{\mathrm{T}}\mathbf{r}_{iL}\mathbf{I}_3 - \mathbf{r}_{iK}\mathbf{r}_{iL}^{\mathrm{T}}}{r_{iK}^3 r_{iL}^3}, \tag{7.5}$$

$$\mathbf{h}_K^{\mathrm{PSO}} = -\mathrm{i}\alpha^2\sum_i\frac{\mathbf{r}_{iK}\times\nabla_i}{r_{iK}^3}, \tag{7.6}$$

$$\mathbf{h}_K^{\mathrm{FC}} = \frac{8\pi\alpha^2}{3}\sum_i\delta(\mathbf{r}_{iK})\mathbf{s}_i, \tag{7.7}$$

$$\mathbf{h}_K^{\mathrm{SD}} = \alpha^2\sum_i\frac{3\mathbf{r}_{iK}^{\mathrm{T}}\mathbf{s}_i\,\mathbf{r}_{iK} - r_{iK}^2\mathbf{s}_i}{r_{iK}^5}, \tag{7.8}$$

where $\alpha \approx 1/137$ is the fine-structure constant, $\mathbf{r}_{iK}$ is the position of electron i relative to nucleus K, $\mathbf{I}_3$ is the three-by-three unit matrix, $\delta(\mathbf{r}_{iK})$ is the Dirac delta function, and $\mathbf{s}_i$ is the spin of electron i. In the reduced coupling tensor Eq. (7.4), the first summation is over all excited singlet states $|n_\mathrm{S}\rangle$ with energy E_{n_S} and the second summation is over all triplet states $|n_\mathrm{T}\rangle$ with energy E_{n_T}; in the one-electron operators Eqs. (7.5)–(7.8), the summations are over all electrons. In all expressions, superscript T denotes vector transposition.

We first note that all four operators Eqs. (7.5)–(7.8) are local with respect to the positions of the nuclei, making the spin–spin couplings small for large internuclear separations. The FC operator, in particular, is extreme in this respect, since only the electrons at the nuclei contribute to the coupling. Moreover, whereas the DSO and PSO operators in Eqs. (7.5) and (7.6) are singlet operators, coupling the nuclear magnetic moments to the orbital motion of the electrons, the FC and SD operators in Eqs. (7.7) and (7.8) are triplet operators, coupling the nuclear moments to the spin of the electrons. In nonrelativistic theory, therefore, there is a clear physical distinction between, on the one hand, the orbital contribution to the indirect spin–spin coupling tensor (mediated by the DSO and PSO operators) and, on the other hand, the spin contributions (mediated by the FC and SD operators).

Among the different mechanisms contributing to the indirect spin–spin coupling, by far the most important is the FC mechanism. Formally, its importance stems from the large prefactor of $8\pi/3$ in the FC operator Eq. (7.7), ensuring that the pure FC and mixed FC–SD contributions to the spin–spin coupling tensor usually dominate, in particular, for one-bond couplings. However, since the FC operator is purely isotropic and the SD operator is purely anisotropic, there are no mixed FC–SD contributions to isotropic coupling constants (as measured in isotropic liquids and gases) and, likewise, no pure FC contributions to anisotropic coupling constants (as measured in liquid crystals and solids). In short, whereas isotropic coupling constants are typically dominated by the pure FC contribution, anisotropic coupling constants are typically dominated by the mixed FC–SD contribution; the remaining DSO, PSO, and pure SD contributions are usually less important, at least for one-bond couplings. Nevertheless, none of the contributions can be a priori neglected, since each may become important in special cases. In the HF molecule, for example, the FC and PSO contributions are both large and of the same sign; a substantial PSO contribution is also characteristic of fluorine couplings in other molecules [20, 21]. The N_2 molecule is also atypical in this respect: the PSO contribution is about twice as large as the FC contribution, while the SD contribution is about as large as the PSO contribution but of opposite sign.

We finally note that the indirect nuclear spin–spin coupling constants depend sensitively on the molecular geometry, in particular, the FC contribution, which may change dramatically with small changes in the geometry. For example, in some cases, the usually dominant FC contribution may change sign or become very small at certain geometries. Clearly, in calculations of the spin–spin couplings, the molecular geometry must be chosen with great care. By the same token, the vibrational corrections to the indirect spin–spin coupling constants may be very large (10% or more). Therefore, for a meaningful comparison with experiment, these corrections should be evaluated.

7.2.2
The Calculation of Indirect Spin–Spin Coupling Tensors by Response Theory

The paramagnetic contributions to the reduced spin–spin coupling tensor involve, in Ramsey's theory Eq. (7.4), the summation over a complete set of excited states. In

practice, these states are inaccessible to us and the sum-over-states terms are calculated differently, using linear response theory. In this theory, the response of the electronic system is obtained from the solution of a set of linear equations, one equation for each independent perturbation. In the following, we give a brief summary of the calculation of indirect spin–spin coupling constants by response theory. For a more general introduction to the application of response theory to the calculation of NMR parameters, in particular, to the calculation of nuclear shielding tensors and indirect nuclear spin–spin coupling tensors, we refer to the recent review by Helgaker, Jaszuński, and Ruud [6].

7.2.2.1 Parametrization of the One-Electron Density Matrix

In SCF theory, we work in terms of a determinantal wavefunction constructed from a set of N orthonormal spin orbitals $\phi_I(\mathbf{x})$, where $\mathbf{x}$ denotes collectively the spatial coordinates $\mathbf{r}$ and the spin coordinate s of the electron. In Hartree–Fock theory, this wavefunction represents our approximation to the true N-electron ground-state wavefunction; in Kohn–Sham theory, it corresponds to a noninteracting reference state, whose electron density represents the true ground-state density of the system.

From the occupied spin orbitals, we may calculate the electron spin density of the electronic system in the following manner:

$$\rho(\mathbf{x}) = \sum_I \phi_I^*(\mathbf{x})\phi_I(\mathbf{x}). \tag{7.9}$$

As we perturb the system by introducing a set of nuclear magnetic moments, collectively denoted by $\mathbf{M}$, the corresponding determinantal wavefunction changes. The resulting perturbed electron density may then be calculated as

$$\rho(\mathbf{x};\kappa) = \sum_{PQ} D_{PQ}(\kappa)\phi_P^*(\mathbf{x})\phi_Q(\mathbf{x}), \tag{7.10}$$

where the summation is now over all pairs of spin orbitals (not just over those that are occupied in the unperturbed system) and where the $D_{PQ}(\kappa)$ are the elements of the one-electron density matrix, parametrized in an exponential manner:

$$\mathbf{D}(\kappa) = \exp\begin{pmatrix} \mathbf{0} & -\kappa^\dagger \\ \kappa & \mathbf{0} \end{pmatrix} \begin{pmatrix} \mathbf{I}_N & \mathbf{0} \\ \mathbf{0} & \mathbf{0} \end{pmatrix} \exp\begin{pmatrix} \mathbf{0} & \kappa^\dagger \\ -\kappa & \mathbf{0} \end{pmatrix}. \tag{7.11}$$

Here the dimension of the unit matrix $\mathbf{I}_N$ is equal to the number of occupied spin orbitals N, while the dimension of the rectangular matrix κ is equal to $V \times N$, where V is the number of unoccupied spin orbitals. By freely choosing the real and imaginary parts of κ,

$$\kappa_{AI} = {}^{\mathrm{R}}\kappa_{AI} + \mathrm{i}\,{}^{\mathrm{I}}\kappa_{AI}, \tag{7.12}$$

we can generate any valid spin density matrix $\mathbf{D}(\kappa)$ and spin density $\rho(\mathbf{x};\kappa)$ from Eq. (7.11) [22]. In the above and the following equations, we use the convention that capital letters I and J denote occupied spin orbitals, A and B denote unoccupied spin orbitals, while P, Q, R, and S are used for general (occupied or unoccupied) spin orbitals.

To calculate molecular properties such as the indirect nuclear spin–spin coupling constants, it is necessary to determine the first and second derivatives of the density matrix with respect to the real and imaginary components of κ. Expanding the density matrix Eq. (7.11) to second order in κ and differentiating, we obtain

$$\frac{\partial D_{PQ}}{\partial^{\mathrm{R}}\kappa_{AI}} = \delta_{PA}\delta_{QI} + \delta_{PI}\delta_{QA}, \tag{7.13}$$

$$\frac{\partial D_{PQ}}{\partial^{\mathrm{I}}\kappa_{AI}} = \mathrm{i}\Big(\delta_{PA}\delta_{QI} - \delta_{PI}\delta_{QA}\Big), \tag{7.14}$$

$$\frac{\partial^2 D_{PQ}}{\partial^{\mathrm{R/I}}\kappa_{AI}\partial^{\mathrm{R/I}}\kappa_{BJ}} = \delta_{IJ}\Big(\delta_{PA}\delta_{QB} + \delta_{PB}\delta_{QA}\Big) - \delta_{AB}\Big(\delta_{PI}\delta_{QJ} + \delta_{PJ}\delta_{QI}\Big), \tag{7.15}$$

$$\frac{\partial^2 D_{PQ}}{\partial^{\mathrm{I}}\kappa_{AI}\partial^{\mathrm{R}}\kappa_{BJ}} = \mathrm{i}\,\delta_{IJ}\Big(\delta_{PA}\delta_{QB} - \delta_{PB}\delta_{QA}\Big) + \mathrm{i}\,\delta_{AB}\Big(\delta_{PI}\delta_{QJ} - \delta_{PJ}\delta_{QI}\Big). \tag{7.16}$$

We note that these expressions are valid only at $\kappa = \mathbf{0}$, which is sufficient for the calculation of properties at $\mathbf{M} = \mathbf{0}$.

7.2.2.2 The Electronic Energy

From κ and hence $\mathbf{D}(\kappa)$ and $\rho(\mathbf{x};\kappa)$, we can calculate all other properties in SCF theory. In particular, to calculate the total electronic energy, we first introduce the one- and two-electron integrals:

$$\begin{aligned} h_{PQ}(\mathbf{M}) = &-\frac{1}{2}\int \phi_P^*(\mathbf{x})\nabla^2\phi_Q(\mathbf{x})\,\mathrm{d}\mathbf{x} - \sum_K Z_K \int \phi_P^*(\mathbf{x}) r_K^{-1}\phi_Q(\mathbf{x})\,\mathrm{d}\mathbf{x} \\ &+ \sum_K \mathbf{M}_K^{\mathrm{T}} \int \phi_P^*(\mathbf{x})\Big(\mathbf{h}_K^{\mathrm{PSO}} + \mathbf{h}_K^{\mathrm{FC}} + \mathbf{h}_K^{\mathrm{SD}}\Big)\phi_Q(\mathbf{x})\,\mathrm{d}\mathbf{x} \\ &+ \frac{1}{2}\sum_{KL} \mathbf{M}_K^{\mathrm{T}} \int \phi_P^*(\mathbf{x})\mathbf{h}_{KL}^{\mathrm{DSO}}\phi_Q(\mathbf{x})\,\mathrm{d}\mathbf{x}\,\mathbf{M}_L, \end{aligned} \tag{7.17}$$

$$g_{PQRS} = \int\int \phi_P^*(\mathbf{x}_1)\phi_Q(\mathbf{x}_1) r_{12}^{-1} \phi_R^*(\mathbf{x}_2)\phi_S(\mathbf{x}_2)\,\mathrm{d}\mathbf{x}_1\,\mathrm{d}\mathbf{x}_2. \tag{7.18}$$

where the PSO, FC, and SD operators are given in Eqs. (7.5)–(7.8) (but with no summation over electrons), and where Z_K and $\mathbf{M}_K$ are, respectively, the charge and the magnetic moment of nucleus K. From these integrals, we may calculate the Kohn–Sham energy as

$$E(\mathbf{M};\kappa) = \sum_{PQ} D_{PQ}(\kappa) h_{PQ}(\mathbf{M}) + \frac{1}{2}\sum_{PQRS} D_{PQ}(\kappa) D_{RS}(\kappa) g_{PQRS}$$

$$-\frac{1}{2}\gamma \sum_{PQRS} D_{PS}(\kappa) D_{RQ}(\kappa)\, g_{PQRS} + E_{\mathrm{XC}}\left[\rho(\mathbf{x};\kappa)\right] + h_{\mathrm{nuc}}, \tag{7.19}$$

The exchange–correlation energy $E_{\mathrm{XC}}[\rho(\mathbf{x};\kappa)]$ is a functional of the electron spin density $\rho(\mathbf{x};\kappa)$. In the local-density approximation (LDA), $E_{\mathrm{XC}}[\rho(\mathbf{x};\kappa)]$ is local in the density; in the generalized gradient approximation (GGA), it is local in the density gradient as well:

$$E_{\mathrm{XC}}[\rho(\mathbf{x};\kappa)] = \int f\left(\rho(\mathbf{x};\kappa), \zeta(\mathbf{x};\kappa)\right) \mathrm{d}\mathbf{x}, \tag{7.20}$$

where

$$\zeta(\mathbf{x};\kappa) = \nabla\rho(\mathbf{x};\kappa) \cdot \nabla\rho(\mathbf{x};\kappa). \tag{7.21}$$

In hybrid DFT, some proportion γ of the exact exchange is added to the Kohn–Sham energy; in pure DFT, $\gamma = 0$. In Hartree–Fock theory, $\gamma = 1$ and there is no contribution from the exchange–correlation functional $E_{\mathrm{XC}}[\rho(\mathbf{x};\kappa)] = 0$.

For the optimized electronic state, the energy is stationary with respect to variations in the elements of κ:

$$\frac{\partial E(\mathbf{M};\kappa)}{\partial \kappa_{AI}} = 0. \tag{7.22}$$

Introducing the Kohn–Sham matrix

$$F_{PQ} = h_{PQ} + \sum_{J}\left(g_{PQJJ} - \gamma g_{PJJQ}\right) + \int \left(\frac{\partial f}{\partial \rho}\phi_P \phi_Q + 2\frac{\partial f}{\partial \zeta}\nabla\rho \cdot \nabla\phi_P \phi_Q\right)\mathrm{d}\mathbf{x} \tag{7.23}$$

where we have assumed that the exchange–correlation functional is local in the density $\rho(\mathbf{x})$ and in the gradient norm $\zeta(\mathbf{x})$, we may calculate these derivatives as

$$\frac{\partial E(\mathbf{M};\kappa)}{\partial \kappa_{AI}} = 2F_{AI}. \tag{7.24}$$

Thus, for a variationally optimized SCF state, the Kohn–Sham matrix is block diagonal $F_{AI} = 0$. In canonical Kohn–Sham theory, the Kohn–Sham matrix is chosen to

be diagonal at convergence, with diagonal elements corresponding to the orbital energies

$$F_{PQ} = \delta_{PQ}\varepsilon_P. \tag{7.25}$$

In the following, we shall assume doubly occupied real canonical orbitals for the unperturbed system.

7.2.2.3 Linear Response Theory

Let us now consider how the energy changes as we perturb the system by introducing a set of nuclear magnetic moments **M**. In SCF theory, we then assume that, for all values of **M**, the electronic energy remains fully optimized with respect to κ so that the energy satisfies the stationary condition

$$\left.\frac{\partial E(\mathbf{M};\kappa)}{\partial \kappa}\right|_{\kappa=\kappa_{\text{opt}}} = 0 \tag{7.26}$$

for all values of **M**. In this expression, κ_{opt} represents the optimized value of the variational parameters. For $\mathbf{M} = \mathbf{0}$, we have chosen $\kappa_{\text{opt}} = \mathbf{0}$; for $\mathbf{M} \neq \mathbf{0}$, it follows that $\kappa_{\text{opt}} \neq \mathbf{0}$. In the following, we tacitly assume that all derivatives are taken at $\mathbf{M} = \mathbf{0}$ with $\kappa = \mathbf{0}$ and suppress the arguments to $E(\mathbf{M};\kappa)$ for brevity.

Taking the total derivative of the optimized energy with respect to $\mathbf{M}_K$, using the chain rule, and invoking the stationary condition Eq. (7.26), we obtain:

$$\frac{\mathrm{d}E}{\mathrm{d}\mathbf{M}_K} = \frac{\partial E}{\partial \mathbf{M}_K} + \frac{\partial E}{\partial \kappa}\frac{\partial \kappa}{\partial \mathbf{M}_K} = \frac{\partial E}{\partial \mathbf{M}_K}. \tag{7.27}$$

Further differentiation with respect to $\mathbf{M}_L$ and use of the chain rule give the following expression for the reduced spin–spin coupling constant:

$$\mathbf{K}_{KL} = \frac{\partial^2 E}{\partial \mathbf{M}_K \partial \mathbf{M}_L} + \frac{\partial^2 E}{\partial \mathbf{M}_K \partial \kappa}\frac{\partial \kappa}{\partial \mathbf{M}_L}, \tag{7.28}$$

where $\partial\kappa/\partial\mathbf{M}_L$ represents the response of the wavefunction to the nuclear magnetic moment $\mathbf{M}_L$. To determine $\partial\kappa/\partial\mathbf{M}_L$, we take the total derivative of the variational condition Eq. (7.26) with respect to $\mathbf{M}_L$ and obtain the first-order response equations:

$$\frac{\partial^2 E}{\partial \kappa^2}\frac{\partial \kappa}{\partial \mathbf{M}_L} = -\frac{\partial^2 E}{\partial \kappa \partial \mathbf{M}_L}. \tag{7.29}$$

For the calculation of the indirect nuclear spin–spin coupling constants by linear response theory, Eqs. (7.28) and (7.29) constitute the central equations.

In the following, we first discuss the evaluation of the electronic Hessian $\partial^2 E/\partial\kappa^2$ in Section 7.2.2.4. Next, in Section 7.2.2.5, we consider the solution of the linear response equations Eq. (7.29) and, in particular, the evaluation of their right-hand sides $\partial^2 E/\partial\kappa\partial\mathbf{M}_L$. Finally, in Section 7.2.2.6, we consider the evaluation of the reduced spin–spin coupling constants according to Eq. (7.28).

7.2.2.4 The Electronic Hessian

In the previous subsection, we introduced the electronic Hessian in the spin-orbital representation, whose elements are given by:

$$G_{AI,BJ} = \frac{\partial^2 E}{\partial\kappa_{AI}\partial\kappa_{BJ}}. \tag{7.30}$$

These elements may be evaluated in the spin-orbital basis, by applying the rules in Eqs. (7.13)–(7.16). However, it is more convenient to work not directly in terms of κ_{AI} but rather in terms of the real and imaginary components of the singlet and triplet rotation parameters, here given in Cartesian form:

$$\begin{aligned}
{}^{\mathrm{R/I}}\kappa^{0}_{ai} &= {}^{\mathrm{R/I}}\kappa_{a\alpha,i\alpha} + {}^{\mathrm{R/I}}\kappa_{a\beta,i\beta}, & {}^{\mathrm{R/I}}\kappa^{\mathrm{z}}_{ai} &= {}^{\mathrm{R/I}}\kappa_{a\alpha,i\alpha} - {}^{\mathrm{R/I}}\kappa_{a\beta,i\beta},\\
{}^{\mathrm{R/I}}\kappa^{\mathrm{x}}_{ai} &= {}^{\mathrm{R/I}}\kappa_{a\alpha,i\beta} + {}^{\mathrm{R/I}}\kappa_{\alpha\beta,i\alpha}, & {}^{\mathrm{R/I}}\kappa^{\mathrm{y}}_{ai} &= {}^{\mathrm{I/R}}\kappa_{a\alpha,i\beta} - {}^{\mathrm{I/R}}\kappa_{\alpha\beta,i\alpha}.
\end{aligned} \tag{7.31}$$

In this representation, the Hessian of a closed-shell electronic state becomes block diagonal, with no coupling between elements belonging to the different rotational classes. Lower-case subscripts are here used for orbitals, to distinguish these from spin orbitals.

To determine the Hessian, we assume that the exchange–correlation functional depends locally on the density and on the spin density along the spin-quantization axis (here the z axis)

$$\rho_{\mathrm{s}}(\mathbf{r}) = \sum_{pq} D_{p\alpha q\alpha}\phi_{p\alpha}(\mathbf{r})\phi_{q\alpha}(\mathbf{r}) + \sum_{pq} D_{p\beta q\beta}\phi_{p\beta}(\mathbf{r})\phi_{q\beta}(\mathbf{r}), \tag{7.32}$$

$$\rho_{\mathrm{t}}(\mathbf{r}) = \sum_{pq} D_{p\alpha q\alpha}\phi_{p\alpha}(\mathbf{r})\phi_{q\alpha}(\mathbf{r}) - \sum_{pq} D_{p\beta q\beta}\phi_{p\beta}(\mathbf{r})\phi_{q\beta}(\mathbf{r}), \tag{7.33}$$

and possibly on their gradient scalar products

$$\zeta_{\mathrm{ss}}(\mathbf{r}) = \nabla\rho_{\mathrm{s}}(\mathbf{r})\cdot\nabla\rho_{\mathrm{s}}(\mathbf{r}),\ \zeta_{\mathrm{st}}(\mathbf{r}) = \nabla\rho_{\mathrm{s}}(\mathbf{r})\cdot\nabla\rho_{\mathrm{t}}(\mathbf{r}),\ \ \zeta_{\mathrm{tt}}(\mathbf{r}) = \nabla\rho_{\mathrm{t}}(\mathbf{r})\cdot\nabla\rho_{\mathrm{t}}(\mathbf{r}), \tag{7.34}$$

in the following manner:

$$E_{\mathrm{XC}}[\rho(\mathbf{x})] = \int f\big(\rho_{\mathrm{s}}(\mathbf{r}),\rho_{\mathrm{t}}(\mathbf{r}),\zeta_{\mathrm{ss}}(\mathbf{r}),\zeta_{\mathrm{st}}(\mathbf{r}),\zeta_{\mathrm{tt}}(\mathbf{r})\big)\mathrm{d}\mathbf{r}. \tag{7.35}$$

Taking the second derivatives of the electronic energy Eq. (7.19) with respect to the ${}^{R}\kappa^{0}_{ai}$ and with respect to the ${}^{R}\kappa^{z}_{ai}$, we then find that the elements of the Hessian for real singlet rotations ${}^{RR}\mathbf{G}^{ss}$ and for real triplet rotations ${}^{RR}\mathbf{G}^{tt}$ may be written in the form:

$$
\begin{aligned}
{}^{RR}G^{uu}_{ai,bj} &= \delta_{ij}\delta_{ab}\left(\varepsilon_a - \varepsilon_i\right) + 4\delta_{su}\, g_{aibj} - \gamma\left(g_{abij} + g_{ajib}\right) + \int \frac{\partial^2 f}{\partial \rho_u^2}\, \phi_a\phi_i\phi_b\phi_j \, \mathrm{d}\mathbf{r} \\
&+ 2\int \frac{\partial f}{\partial \zeta_{uu}} \left(\nabla\phi_a\phi_i\right)\cdot\left(\nabla\phi_b\phi_j\right)\mathrm{d}\mathbf{r} + \int \frac{\partial^2 f}{\partial \zeta_{su}^2}\left(\nabla\rho_s\cdot\nabla\phi_a\phi_i\right)\left(\nabla\rho_s\cdot\nabla\phi_b\phi_j\right)\mathrm{d}\mathbf{r} \\
&+ \int \frac{\partial^2 f}{\partial \rho_u \partial \zeta_{su}}\left[\left(\nabla\rho_s\cdot\nabla\phi_a\phi_i\right)\phi_b\phi_j + \phi_a\phi_i\left(\nabla\rho_s\cdot\nabla\phi_b\phi_j\right)\right]\mathrm{d}\mathbf{r},
\end{aligned}
\tag{7.36}
$$

where the second, two-electron Coulomb term is present only in the singlet case (u = s). The exchange–correlation contributions are in the singlet case calculated from the derivatives of $f(\rho_s, \rho_t, \zeta_{ss}, \zeta_{st}, \zeta_{tt})$ with respect to ρ_s and ζ_{ss}; in the triplet case, they are obtained from the derivatives with respect to ρ_t, ζ_{st}, and ζ_{tt}. In LDA, only the first, second, and fourth terms in Eq. (7.36) contribute to the Hessian; in GGA, all terms contribute. In Ref. [23], the singlet and triplet Hessians are given in a slightly different form.

For closed-shell systems, the triplet Hessians are the same in all three Cartesian directions, as follows from general considerations involving the Wigner–Eckart theorem. We may therefore calculate the triplet Hessians in the x and y directions (obtained by differentiation with respect to the ${}^{R}\kappa^{x}_{ai}$ and the ${}^{R}\kappa^{y}_{ai}$, respectively) according to Eq. (7.36), but with the densities Eqs. (7.32)–(7.34) set up with spin quantization along the x and y axes, respectively. However, we note that, in order for the equivalence of the three triplet Hessians to arise naturally, the exchange–correlation functional must be defined in a more general manner than in Eq. (7.35), depending on all four components of the spin density $\rho(\mathbf{x})$ and its gradient scalar products. The present approach is adequate, provided the three Cartesian directions are treated separately.

With respect to imaginary rotations, the electronic Hessian takes the same, simple form in the singlet and triplet cases:

$$
{}^{II}G^{uu}_{ai,bj} = \delta_{ij}\delta_{ab}(\varepsilon_a - \varepsilon_i) - \gamma\left(g_{abij} - g_{ajib}\right). \tag{7.37}
$$

We note, in particular, that there are no contributions from the exchange–correlation functional except through the orbital energies. Also, in pure DFT ($\gamma = 0$), the imaginary Hessian Eq. (7.37) becomes diagonal, whereas the real Hessian Eq. (7.36) is always nondiagonal. In LDA and GGA, therefore, imaginary perturbations, for example, first-order perturbations involving the orbital motion of the electrons, are easily treated.

7.2.2.5 The Response Equations

To obtain the responses of the wavefunction to the perturbations in Eq. (7.29), we need to evaluate the elements of the right-hand sides:

$$\mathbf{R}_{L,AI} = \frac{\partial^2 E}{\partial \kappa_{AI} \partial \mathbf{M}_L}. \tag{7.38}$$

In principle, we need only solve three response equations for each nucleus, one for each Cartesian component of $\mathbf{M}_L$. However, to take advantage of the symmetries of the operators that contribute to the right-hand sides, we decompose $\mathbf{R}_{L,AI}$ as follows:

$$\mathbf{R}_{L,AI} = \mathbf{R}^{\mathrm{PSO}}_{L,AI} + \mathbf{R}^{\mathrm{FC}}_{L,AI} + \mathbf{R}^{\mathrm{SD}}_{L,AI}. \tag{7.39}$$

From Eqs. (7.6)–(7.8), we recall that $\mathbf{h}^{\mathrm{PSO}}_L$ is an imaginary singlet operator, whereas $\mathbf{h}^{\mathrm{FC}}_K$ and $\mathbf{h}^{\mathrm{SD}}_K$ are isotropic and anisotropic triplet operators, respectively. We begin by considering the contribution from the PSO operator to $\mathbf{R}_{L,AI}$.

Differentiating the electronic energy Eq. (7.19) with respect to $\mathbf{M}_L$ and κ_{AI}, we obtain:

$$\mathbf{R}^{\mathrm{PSO}}_{L,AI} = \sum_{PQ} \frac{\partial D_{PQ}}{\partial \kappa_{AI}} \left\langle \phi_P \middle| \mathbf{h}^{\mathrm{PSO}}_L \middle| \phi_Q \right\rangle. \tag{7.40}$$

Because of the special symmetries of $\mathbf{h}^{\mathrm{PSO}}_L$, only derivatives with respect to imaginary singlet rotations ${}^{\mathrm{I}}_{0}\kappa_{ai}$ in Eq. (7.31) give nonzero contributions to the right-hand side:

$$\mathbf{R}^{\mathrm{PSO}}_{L,ai} = \sum_{PQ} \frac{\partial D_{PQ}}{\partial {}^{\mathrm{I}}_{0}\kappa_{ai}} \left\langle \phi_P \middle| \mathbf{h}^{\mathrm{PSO}}_L \middle| \phi_Q \right\rangle = 2\alpha^2 \int \phi_a(\mathbf{r}) r_L^{-3} \mathbf{r}_L \times \nabla \phi_i(\mathbf{r})\, \mathrm{d}\mathbf{r}. \tag{7.41}$$

Thus, to calculate the response of the wavefunction to this operator, we need only solve linear equations involving imaginary singlet rotations:

$$\sum_{bj} {}^{\mathrm{II}}G^{\mathrm{ss}}_{ai,bj} \lambda^{\mathrm{PSO}}_{L,bj} = -\mathbf{R}^{\mathrm{PSO}}_{L,ai}. \tag{7.42}$$

In pure DFT, ${}^{\mathrm{II}}\mathbf{G}^{\mathrm{ss}}$ is diagonal and $\lambda^{\mathrm{PSO}}_{L,bj}$ is obtained directly, in a noniterative manner. Conversely, in Hartree–Fock theory and in hybrid DFT, the presence of exact exchange makes the Hessian nondiagonal. The three components $\lambda^{\mathrm{PSO}}_{L,bj}$ are then calculated iteratively, using some direct method that avoids the explicit construction of ${}^{\mathrm{II}}\mathbf{G}^{\mathrm{ss}}$.

From the isotropy of the triplet $\mathbf{h}^{\mathrm{FC}}_L$ operator, we find that the expectation value of each Cartesian component $[\mathbf{R}^{\mathrm{FC}}_L]_\mu$ (μ = x,y,z), when differentiated with respect to the corresponding Cartesian component ${}^{\mathrm{R}}\kappa^{\mu}_{ai}$, gives rise to the same right–hand element:

$$R^{\mathrm{FC}}_{L,ai} = \sum_{PQ} \frac{\partial D_{PQ}}{\partial {}^{R}\kappa^{\mu}_{ai}} \left\langle \phi_P \middle| \left[\mathbf{h}^{\mathrm{FC}}_{L}\right]_{\mu} \middle| \phi_Q \right\rangle = \frac{8\pi\alpha^2}{3} \phi_a(\mathbf{q}_L)\phi_i(\mathbf{q}_L), \tag{7.43}$$

where $\mathbf{q}_L$ is the position of nucleus L. All other derivatives vanish. Since, in addition, the Hessian is the same for the three Cartesian components, we need only solve one set of equations to obtain the FC response:

$$\sum_{bj} {}^{\mathrm{RR}}G^{\mathrm{tt}}_{ai,bj} \lambda^{\mathrm{FC}}_{L,bj} = -R^{\mathrm{FC}}_{L,ai}. \tag{7.44}$$

By contrast, the anisotropic SD operator requires more effort. As seen from Eq. (7.8), each Cartesian component of $\mathbf{R}^{\mathrm{SD}}_{L,ai}$ contains one contribution from each of the three Cartesian components of the spin operators $\mathbf{s}_i$. Because of the different symmetries of these components, they are treated separately, giving rise to a total of nine SD right-hand sides for each nucleus:

$$\mathbf{R}^{\mathrm{SD}}_{L,ai} = \alpha^2 \int \phi_a(\mathbf{r}) r_L^{-5} \left(3\mathbf{r}_L\mathbf{r}_L^{\mathrm{T}} - r_L^2\mathbf{I}_3\right)\phi_i(\mathbf{r})\,\mathrm{d}\mathbf{r}. \tag{7.45}$$

However, since the three-by-three $\mathbf{R}^{\mathrm{SD}}_{L,ai}$ matrix is symmetric and since the same Hessian is used for each component, there are only six distinct SD response equations to be solved:

$$\sum_{bj} {}^{\mathrm{RR}}G^{\mathrm{tt}}_{ai,bj} \lambda^{\mathrm{SD}}_{L,bj} = -\mathbf{R}^{\mathrm{SD}}_{L,ai}. \tag{7.46}$$

Unlike the imaginary Hessian ${}^{\mathrm{II}}\mathbf{G}^{\mathrm{ss}}$ in Eq. (7.42), the real Hessian ${}^{\mathrm{RR}}\mathbf{G}^{\mathrm{tt}}$ in Eqs. (7.44) and (7.46) is nondiagonal. To obtain the triplet responses $\lambda^{\mathrm{FC}}_{L,bj}$ and $\lambda^{\mathrm{SD}}_{L,bj}$, we must therefore solve a total of seven sets of linear equations for each nucleus L.

7.2.2.6 Evaluation of the Spin–Spin Coupling Tensors

Having obtained the response of the system to the magnetic nuclei $\mathbf{M}_L$ by solving ten response equations for each nucleus Eqs. (7.42), (7.44), and (7.46), the calculation of the indirect spin–spin coupling tensors is trivial. We first note that, according to Eq. (7.28), the static contribution to the reduced spin–spin coupling tensor corresponds to an expectation value of the DSO operator in Eq. (7.5):

$$\mathbf{K}^{\mathrm{DSO}}_{KL} = \frac{\partial^2 E}{\partial\mathbf{M}_K\partial\mathbf{M}_L} = 2\alpha^4 \sum_i \int \phi_i(\mathbf{r}) r_K^{-3} r_L^{-3} \left(\mathbf{r}_K^{\mathrm{T}}\mathbf{r}_L\mathbf{I}_3 - \mathbf{r}_K\mathbf{r}_L^{\mathrm{T}}\right)\phi_i(\mathbf{r})\,\mathrm{d}\mathbf{r}, \tag{7.47}$$

where the summation is over all occupied orbitals $\phi_i(\mathbf{r})$. Because of the rather complicated structure of the DSO integral, this term is usually evaluated by numerical quadrature.

Having calculated the static contribution Eq. (7.47) as well as the responses Eqs. (7.42), (7.44) and (7.46), we may now assemble the total reduced coupling tensor

$$\mathbf{K}_{KL} = \mathbf{K}_{KL}^{\mathrm{DSO}} + \sum_{ai} \lambda_{ai,K}^{\mathrm{PSO}} \left(\mathbf{R}_{ai,L}^{\mathrm{PSO}}\right)^{\mathrm{T}} + \mathbf{I}_3 \sum_{ai} \lambda_{ai,K}^{\mathrm{FC}} R_{ai,L}^{\mathrm{FC}} + \sum_{ai} \lambda_{ai,K}^{\mathrm{SD}} \mathbf{R}_{ai,L}^{\mathrm{SD}}$$

$$+ \sum_{ai} \lambda_{ai,K}^{\mathrm{FC}} \mathbf{R}_{ai,L}^{\mathrm{SD}} + \sum_{ai} \mathbf{R}_{ai,K}^{\mathrm{SD}} \lambda_{ai,L}^{\mathrm{FC}}, \tag{7.48}$$

where we recall that, whereas $\mathbf{R}_{ai,L}^{\mathrm{PSO}}$ is a three-dimensional column vector and $R_{ai,L}^{\mathrm{FC}}$ is a scalar, $\mathbf{R}_{ai,L}^{\mathrm{SD}}$ is a three-by-three symmetric matrix. Since $\mathbf{R}_{ai,L}^{\mathrm{SD}}$ is traceless, we obtain for the coupling constant K_{KL} between nuclei K and L:

$$K_{KL} = \frac{1}{3} \mathrm{Tr}\, \mathbf{K}_{KL}^{\mathrm{DSO}} + \frac{1}{3} \sum_{ai} \left(\lambda_{ai,K}^{\mathrm{PSO}}\right)^{\mathrm{T}} \mathbf{R}_{ai,L}^{\mathrm{PSO}} + \sum_{ai} \lambda_{ai,K}^{\mathrm{FC}} R_{ai,L}^{\mathrm{FC}} + \frac{1}{3} \mathrm{Tr} \sum_{ai} \lambda_{ai,K}^{\mathrm{SD}} \mathbf{R}_{ai,L}^{\mathrm{SD}}, \tag{7.49}$$

with no coupling between the FC and SD perturbations. We finally note that, to obtain all couplings to a given nucleus L, we need to solve the response equations only for that nucleus; for the remaining nuclei $K \neq L$, it is sufficient to calculate their right-hand sides. However, if all couplings among all nuclei are required, then we must solve a total of $10n$ linear equations, where n is the number of magnetic nuclei in the molecule.

7.2.2.7 Finite Perturbation Theory

Up to now, we have considered the fully analytical approach to the calculation of nuclear spin–spin coupling constants according to Eqs. (7.28) and (7.29). Alternatively, the spin–spin coupling constants may be calculated by finite perturbation theory (FPT), a mixed numerical–analytical scheme developed by Pople and coworkers in the late 1960s [24, 25]. From Eq. (7.27), we note that, for example, the FC contribution to the spin–spin coupling constants can be expressed as

$$\mathbf{K}_{KL}^{\mathrm{FC}} = \sum_{PQ} \frac{\mathrm{d}D_{PQ}}{\mathrm{d}\mathbf{M}_K} \int \phi_P(\mathbf{x}) \mathbf{h}_L^{\mathrm{FC}} \phi_Q(\mathbf{x})\, \mathrm{d}\mathbf{x} \tag{7.50}$$

In this summation, the first factor is an element of the total derivative of the one-electron density matrix with respect to $\mathbf{M}_K$. In FPT, the perturbed density matrix is calculated by finite difference, requiring the optimization of the electronic wavefunction in the presence of the nuclear magnetic moment $\mathbf{M}_K$ (made artificially

large to avoid problems with finite precision). The FPT method is easy to implement (but requires a spin-unrestricted code), see also Chapter 19 by O. Malkina. However, it is less efficient and more susceptible to numerical errors than the fully analytical approach. We also note that, in principle, the spin–spin coupling constants may be evaluated by a fully numerical approach, obtaining the second derivatives by finite difference of the electronic energy. However, this approach is inefficient and rarely used.

Finally, we note that, in SCF theory, the nuclear spin–spin coupling constants may also be calculated in a more approximate manner, using the sum-over-states (SOS) approach. In this approach, the numerators and denominators of the paramagnetic terms in Ramsey's expression Eq. (7.4) are approximated so as to enable an evaluation of the nuclear spin–spin coupling constants without solving linear equations. We note, however, that the SOS approach often works poorly for the dominant FC contribution.

7.2.3
SCF Implementations of Spin–Spin Coupling Constants

Today, a number of quantum-chemistry packages offer the capability of carrying out spin–spin coupling calculations at the Hartree–Fock level, using response theory. Probably, the first purely analytical approach at the Hartree–Fock level is that by Ditchfield and Snyder from 1972 [26]. We also note the multiconfigurational SCF (MCSCF) implementation of Vahtras et al., which includes Hartree–Fock theory as a special case [27]. For a historical overview of the early development of methods for the calculation of spin–spin coupling constants at the semi-empirical and ab initio levels of theory, see the review by Kowalewski from 1977 [28]; for a more recent review with emphasis on ab initio theory, see Ref. [6]. For a more general historical review of the theory of NMR parameters, see Chapter 2 by P. Pyykkö.

The first successful (and still very popular) implementation of Kohn–Sham theory for the calculation of indirect nuclear spin–spin coupling constants is that of Malkin, Malkina, and Salahub from 1994 [29–31], at the LDA and GGA levels. In their implementation, the FC term is calculated by FPT and the SD term is omitted, although the important SD–FC contribution to the spin–spin coupling anisotropy is obtained by FPT. The PSO term is approximated by using the SOS approach.

Another early DFT implementation of indirect nuclear spin–spin coupling constants is that at the LDA level of Dickson and Ziegler from 1996 [32], also with the neglect of the SD contribution. Relying on Slater rather than Gaussian atomic orbitals, it avoids the problem of representing the nuclear cusp, so crucial to the accurate description of the FC interaction. Their approach has subsequently been made analytical at the GGA level, and also extended to account for relativity by means of the zeroth-order regular approximation (ZORA) [33, 34], see Chapter 15 by Autschbach and Ziegler.

The first fully analytical DFT implementations of indirect nuclear spin–spin couplings, including all four terms in Ramsey's theory, are those presented in 2000 by

Sychrovský, Gräfenstein, and Cremer [35] and by Helgaker, Watson, and Handy [36]. Both implementations include hybrid DFT, as well as LDA and GGA.

7.3 Examples of Applications

From the discussion in Section 7.2, it is clear that the calculation of indirect nuclear spin–spin coupling constants is very similar in Hartree–Fock and Kohn–Sham theories, differing only in their treatment of exchange and correlation. Moreover, both theories can be applied to a wide variety of molecular systems; for instance, unlike the correlated ab initio methods developed for the calculation of spin–spin coupling constants, they can easily be extended to large systems by invoking linear-scaling techniques. However, as we shall see in the present section, the quality of the calculated Hartree–Fock and Kohn–Sham indirect spin–spin coupling constants is very different. Whereas the Hartree–Fock model is erratic and often produces physically meaningless spin–spin coupling constants, the Kohn–Sham method consistently produces results of high quality, although some problematic areas remain.

7.3.1 Hartree–Fock Theory

It is well known that Hartree–Fock theory yields triplet excitation energies that are too low, especially for molecules with multiple bonds, such as C_2H_2, and C_2H_4. This phenomenon, called triplet instability, manifests itself also in calculations of spin–spin coupling constants, since the usually leading FC term stems from the triplet perturbation. A more complete discussion of triplet instability is provided in Ref. [37].

Because of triplet-instability problems, the Hartree–Fock model is rarely used nowadays for calculating indirect nuclear spin–spin coupling constants. Applications of Hartree–Fock theory are therefore only briefly discussed here. As a rule of thumb, the Hartree–Fock one- and three-bond coupling constants of organic and simple inorganic molecules without multiple bonds are usually correct with respect to the sign but are overestimated by at least 20% to 30%, see the coupling constants of HF, H_2O, NH_3, CH_4, C_2H_6, or CH_3NH_2 in Table 7.1. The geminal coupling constants, such as the tabulated $^2J_{HH}$ couplings of H_2O, NH_3, or CH_4, and $^2J_{CH}$ of C_2H_6, are even more strongly overestimated. Finally, for molecules such as CO, HCN, C_2H_2, and C_2H_4 in Table 7.1, the Hartree–Fock model gives nonsensical results.

Although, in special cases, some information can be extracted from the spin–spin coupling constants calculated at the Hartree–Fock level, the use of this model for the calculation of such constants should be discouraged. Indeed, more reliable results are often obtained by means of semi-empirical approximations to the Hartree–Fock model [38, 39], such as the extended Hückel approximation [40] and the intermediate neglect of differential overlap (INDO) approximation [24, 25]. The semi-empirical approaches to the calculation of NMR parameters are reviewed by Heine and Seifert in Chapter 9.

Table 7.1 Calculated[a] and experimental[b] indirect nuclear spin–spin coupling constants (Hz). The vibrational correction has been calculated at the B3LYP/HIII-su3 level [58], with exception of FHF^-, for which all results have been obtained with the aug-cc-pVDZ-su1 basis

		J^{HF}_{eq}	J^{LDA}_{eq}	J^{BLYP}_{eq}	J^{B3LYP}_{eq}	J^{CAS}_{eq}	J^{RAS}_{eq}	J^{SOPPA}_{eq}	J^{CCSD}_{eq}	J^{CC3}_{eq}	J^{B3LYP}_{vib}	J^{exp}_{tot}
HF	$^1J_{HF}$	668.9	395.9	390.0	416.6	542.6	544.2	529.4	521.6	521.5	–38.0	500
CO	$^1J_{CO}$	–5.5	26.8	22.8	18.4	11.5	16.1	18.6	15.7	15.3	0.7	16.4
$^{14}N^{15}N$	$^1J_{NN}$	–15.4	–2.9	4.1	2.9	0.5	0.8	2.1	1.8	1.8	0.1	1.8
FHF^-	$^2J_{FF}$	656.8	–175.3	–112.6	24.9		358.1	239.8	438.6		–26.9	≈247
	$^1J_{HF}$	181.0	17.0	0.4	38.4		126.5	104.5	81.6		17.1	107.0
H_2O	$^1J_{OH}$	–103.8	–65.7	–72.6	–75.9	–83.9	–76.7	–80.6	–78.9	–78.5	5.4	–80.6
	$^2J_{HH}$	–22.8	–3.3	–11.1	–7.5	–9.6	–7.8	–8.8	–7.8	–7.4	0.9	–7.3
$HC^{15}N$	$^1J_{CN}$	–10.3	–7.6	–12.2	–19.2		–19.8		–18.2	–17.9	2.0	–18.5
	$^1J_{CH}$	224.4	224.2	284.6	283.5		258.9		245.8	242.1	5.1	267.3
	$^2J_{NH}$	–35.4	–6.2	–5.8	–7.8		–6.8		–7.7	–7.7	0.8	–7.4
$^{14}NH_3$	$^1J_{NH}$	53.3	35.6	43.1	45.7	42.3	43.6	44.3	41.8		–0.3	43.8
	$^2J_{HH}$	–22.7	–4.6	–8.0	–10.1	–9.8	–11.3	–11.3	–12.1		0.7	–9.6
CH_4	$^1J_{CH}$	156.6	100.2	133.3	132.6	116.7	120.6	122.3			5.3	125.3
	$^2J_{HH}$	–27.1	–7.3	–12.5	–13.3	–13.2	–13.2	–14.0			–0.7	–12.8
C_2H_2	$^1J_{CC}$	424.8	176.8	201.0	205.1	187.7	184.7	190.0			–10.0	174.8
	$^1J_{CH}$	420.8	215.6	276.8	271.9	238.5	244.3	254.9			4.6	247.6
	$^2J_{CH}$	–59.5	48.9	57.2	56.0	47.0	53.1	51.7			–3.0	50.1
	$^3J_{HH}$	89.7	6.5	10.3	10.6	12.1	10.9	11.3			–0.1	9.6
C_2H_4	$^1J_{CC}$	1270.2	50.6	68.6	74.7	75.7	68.8	70.3	70.1		0.9	67.6
	$^1J_{CH}$	754.5	128.5	167.2	165.3	155.7	151.6	157.2	153.2		5.1	156.3
	$^2J_{CH}$	–572.0	1.3	0.1	–1.3	–5.8	–1.6	–3.1	–3.0		–1.2	–2.4
	$^2J_{HH}$	–344.2	4.8	5.3	2.9	–2.4	1.1	1.0	0.4		0.3	2.3
	$^3J_{cis}$	360.4	9.9	13.0	13.5	12.4	11.5	11.8	11.6		1.2	11.7
	$^3J_{trans}$	400.0	14.6	20.3	20.7	18.4	17.8	18.4	17.8		2.3	19.0
C_2H_6	$^1J_{CC}$	60.6	18.6	29.5	32.6		38.4		34.1			34.5
	$^1J_{CH}$	149.1	94.0	122.7	122.6		120.3		114.1			125.2
	$^2J_{CH}$	–11.3	–1.2	–2.2	–3.0		–5.5		–4.4			–4.7
	$^2J_{HH}$	–24.1	–6.5	–10.4	–11.3		–14.4		–12.1			
	$^3J^{ave}_{HH}$	9.6	6.0	8.0	7.8		7.3		6.7			8.0
$CH_3{}^{15}NH_2$	$^1J_{CN}$	–15.3	1.9	–0.3	–2.3		–6.5		–5.1			–4.5±0.5
	$^1J_{CH}$	159.2	98.5	129.4	129.5		128.3		120.9			132.5±0.2
	$^1J_{NH}$	–78.1	–52.3	–62.4	–63.3		–65.0		–61.7			–65.0±0.2
	$^2J_{CH}$	–9.9	–0.1	–1.1	–1.9		–4.4		–3.3			
	$^2J_{NH}$	0.5	–1.7	–2.3	–3.0		–0.7		–0.9			–1.0±0.1
	$^2J_{HCH}$	–22.7	–5.7	–9.1	–10.1		–13.3		–11.1			
	$^2J_{HNH}$	–20.9	–3.6	–6.2	–7.6		–10.8		–9.3			
	$^3J^{ave}_{HH}$	8.2	5.40	7.2	6.9		6.3		5.8			7.1±0.1

a For references to the literature theoretical data, see Refs. [36, 46, 58]. CAS = complete active space, RAS = restricted active space, SOPPA = second-order polarization propagator approximation. The Hartree–Fock and Kohn–Sham results have been obtained by the authors, as have the results for FHF^-.

b For references to the literature experimental data, see Refs. [15, 36, 46, 58].

7.3.2 Density-Functional Theory

In recent years, DFT has been extensively applied to the calculation of indirect nuclear spin–spin coupling constants, for a variety of systems. The discussion given below is by no means complete. Rather, we focus on some typical application areas of DFT and point to the remaining problems. Some less routine applications of DFT to the calculation of spin–spin coupling constants such as the calculation of vibrational, solvent, and relativistic corrections are also outlined.

7.3.2.1 Calculations on Large Systems

We begin our discussion with calculations on models of biologically active compounds. One of the most important concepts in structural chemistry is the Karplus relation, which relates vicinal coupling constants to dihedral angles [1, 2]. DFT has been applied to the study of this relation as well as to other conformational studies in models of biomolecules [31, 41–44]. Thus, the conformational dependence of the spin–spin coupling constants has been studied by means of DFT in carbohydrates (methyl-β-D-xylopyranoside [31] and methyl-α-D-xylopyranoside [43]) and in dipeptides (cyclo(L-Pro-L-Pro) [44]). The DFT method has also been used to investigate the effects of hydrogen-bond formation and of pyrimidine- and purine-ring conformation on the one- and two-bond spin–spin coupling constants in nucleic base pairs [45]. Many examples of modeling the angular dependence of spin–spin coupling constants by means of DFT are found in Ref. [42]. We note that the DFT results for the vicinal $^3J_{HH}$ coupling constants should be quite reliable since it has been shown that, for such couplings in ethane, methylamine, methanol [46] and for glycolaldehyde [41], the three-parameter Becke–Lee–Yang–Parr (B3LYP) functional [47, 48] provides an accuracy comparable to that of the coupled-cluster singles-and-doubles (CCSD) model.

Hydrogen-bond-transmitted nuclear spin–spin coupling constants offer another interesting subject for theoretical investigations. Indeed, soon after their observation in proteins and in nucleic acids, these coupling constants were successfully calculated, by means of DFT, in nucleic base pairs and in protein models [49]; calculations on the 16-atom model of the Watson–Crick guanine–cytosine pair were reported in Ref. [8]. DFT calculations of intermolecular coupling constants in biopolymer models have also been carried out for cyclic [50] and linear [51] formamidine dimers, for an acetylethylamine–imidazole complex [52], for the DNA triplets T · A–T and C^+ · G–C [53], for nucleotide-type complexes between $Mg[PO_4(CH_3)]$ and $[PO_4(CH_3)_2]^-$, and for several amino acids [54]. The calculated ^1H, ^{15}N, ^{13}C, and ^{31}P coupling constants agree at least semi-quantitatively with experiment and have proved helpful in structural studies. A comparison of the intermolecular spin–spin coupling constants calculated by means of DFT on the one hand and by means of the MCSCF and CCSD methods on the other hand indicates that the conclusions drawn from the calculations mentioned above should be correct [55]. A comprehensive review of the calculations of this type of coupling constants is provided by Pecul

and Sadlej in Ref. [56], while J. E. DelBene in Chapter 22 describes CCSD calculations of them.

DFT has been also applied to the calculation of spin–spin coupling constants in large inorganic systems. Perhaps the largest, in terms of the number of basis functions, DFT calculation of the full set of indirect nuclear spin–spin coupling constants carried out to date is that for fullerene C_{60} [57]. Examples of relativistic DFT calculations of spin–spin coupling constants in inorganic molecules are discussed by Autschbach and Ziegler in Chapter 15.

7.3.2.2 Vibrational, Environmental and Relativistic Effects

Since the indirect spin–spin coupling constants depend critically on the molecular geometry, the vibrational corrections to them are often substantial. Unfortunately, the inclusion of vibrational corrections is very expensive, requiring the calculation of the couplings for a large set of molecular geometries. Until recently, therefore, such corrections have only been calculated for rather small systems [6]. However, with the recent emergence of inexpensive but accurate DFT techniques, the calculation of such corrections has become feasible also for larger molecules. Such studies have recently been undertaken [58] and some of the calculated vibrational corrections to spin–spin coupling constants are shown in Table 7.1. Clearly, since the corrections typically constitute 5% of the total coupling (and sometimes more than 10%), their inclusion is needed for a meaningful comparison with experiment (in highly accurate work) and also for benchmarking the performance of less accurate methods. We note that, in many cases, the best agreement with experiment is currently obtained by combining highly accurate equilibrium spin–spin coupling constants evaluated at the coupled-cluster level with DFT vibrational corrections. The subject is more fully discussed by Ruden and Ruud in Chapter 10.

DFT has also been used to calculate indirect spin–spin coupling constants in the condensed phase, taking into account the influence of the environment. For example, the coupling constants in a liquid environment described by the polarizable continuum model (PCM) have recently been calculated for benzene [59]. Although a direct comparison with experiment is difficult, this approach appears to offer a reliable and relatively inexpensive way to account for solvation, as is necessary for a fully quantitative comparison with liquid-phase measurements. The PCM and explicit-solvent DFT models have also been used to study the effects of hydration on the spin–spin coupling constants in nucleic base pairs [32]. The description of solvation by either method improves the agreement between calculated and experimental values of the coupling constants. A more complete discussion of solvent effects is provided by Ciofini in Chapter 12.

Since the indirect nuclear spin–spin coupling constants depend critically on the description of the electronic density at the nuclei, they are sensitive to relativistic effects. In the ZORA approach of Autschbach and Ziegler, such effects are included [33, 34]. However, since their approach is discussed elsewhere in this volume (Chapter 15), we only mention here that it has been successfully applied to the calculation of several types of heavy-atom couplings [60–62].

7.3.2.3 Problems

The accumulated computational experience with DFT shows that, with the present standard exchange–correlation functionals, the most urgent problem is the accuracy of the calculated spin–spin constants for electron-rich atoms, as first observed by Malkin et al. for fluorine couplings [30]. In general, the DFT description of the FC contribution to the spin–spin coupling constants deteriorates with increasing number of lone pairs on the coupled atoms. This behavior has been observed for one-bond coupling constants in simple inorganic molecules such as HF [30, 36, 63, 64], for fluorine couplings transmitted through many bonds in organic molecules [20, 21], and for hydrogen-bond-transmitted fluorine couplings [15, 55]. Examples of this behavior are found in Table 7.1, where the coupling constants of HF and FHF^- are significantly underestimated by DFT. To a lesser extent, the same problem occurs for oxygen [46, 55], although we note that, for $^1J_{OH}$ of H_2O in Table 7.1, the B3LYP result is only slightly less accurate than the CCSD and restricted active-space SCF (RASSCF) results. The use of DFT to calculate coupling constants of fluorine and other halogens is therefore discouraged unless the couplings are dominated by the PSO term, as is often true for fluorine–fluorine coupling constants [20, 21, 61].

Extensive studies of the suitability of the different exchange–correlation functionals for spin–spin calculations have not been carried out yet. However, the experience accumulated so far suggests that hybrid functionals such as the B3LYP functional are the best ones for spin–spin calculations [36, 64], see Table 7.1. The good performance of the B3LYP functional has been demonstrated not only for isotropic spin–spin coupling constants but also for anisotropic components of the coupling tensors [64].

7.4 Conclusions

We have reviewed the non-empirical calculation of indirect nuclear spin–spin coupling constants by SCF theories, in particular, by means of Hartree–Fock and Kohn–Sham theories. While both methods are relatively inexpensive and can be applied to large systems, the Kohn–Sham method provides coupling constants that are far superior to those rendered by Hartree–Fock theory. Whereas the Hartree–Fock model is unreliable, often providing results that bear little resemblance to the true coupling constants, the Kohn–Sham DFT method produces spin–spin coupling constants whose accuracy often rivals that of highly correlated ab initio methods. Nevertheless, some problem areas persist, in particular for the spin–spin couplings to electron-rich atoms such as the fluorine atom. These problems may be solved with the introduction of better exchange–correlation functionals but, for the moment, their presence prevents Kohn–Sham theory from emerging as a fully quantitative predictive method for calculations of indirect nuclear spin–spin coupling constants.

Acknowledgment

TH acknowledges support from the Program for Supercomputing (nn1118k) and MP acknowledges support from the 3 TO9A 121 16 KBN Grant.

References

1 M. Karplus, *J. Chem. Phys.* **1959**, *30*, 11.
2 M. Karplus, *J. Am. Chem. Soc.* **1963**, *85*, 2870.
3 M. J. Minch, *Concepts Magn. Reson.* **1994**, *6*, 41.
4 N. Juranic, P. K. Ilich, S. Macura, *J. Am. Chem. Soc.* **1995**, *117*, 405.
5 W. T. Thomas, *Prog. NMR. Spectrosc.* **1997**, *30*, 183.
6 T. Helgaker, M. Jaszuński, K. Ruud, *Chem. Rev.* **1999**, *99*, 293.
7 J. Vaara, J. Jokisaari, R. E. Wasylishen et al., *Prog. NMR. Spectrosc.* **2002**, *41*, 233.
8 A. J. Dingley, J. E. Masse, R. D. Peterson et al., *J. Am. Chem. Soc.* **1999**, *121*, 6019.
9 L. B. Krivdin, G. A. Kalabin, *Prog. NMR. Spectrosc.* **1989**, *21*, 293.
10 S. S. Wijmenga, B. N. M. van Buuren, *Prog. NMR. Spectrosc.* **1998**, *32*, 287.
11 F. Cordier, S. Grzesiek, *J. Am. Chem. Soc.* **1999**, *121*, 1601.
12 A. J. Dingley, S. Grzesiek, *J. Am. Chem. Soc.* **1998**, *120*, 8293.
13 P. R. Blake, J. B. Park, M. W. W. Adams et al., *J. Am. Chem. Soc.* **1992**, *114*, 4931.
14 G. Cornilescu, B. E. Ramirez, M. K. Frank et al., *J. Am. Chem. Soc.* **1999**, *121*, 6275.
15 I. G. Shenderovich, S. H. Smirnov, G. S. Denisov et al., *Ber. Bunsen-Ges. Phys. Chem.* **1998**, *102*, 422.
16 K. Pervushin, A. Ono, C. Fernandez et al., *Proc Natl. Acad. Sci. USA* **1998**, *95*, 14147.
17 A. J. Dingley, F. Cordier, S. Grzesiek, *Concepts Magn. Reson.* **2001**, *13*, 103.
18 N. F. Ramsey, *Phys. Rev.* **1953**, *91*, 303.
19 A. A. Auer, J. Gauss, *J. Chem. Phys.* **2001**, *115*, 1619.
20 J. E. Peralta, V. Barone, R. H. Contreras, *J. Am. Chem. Soc.* **2001**, *123*, 9162.
21 V. Barone, J. E. Peralta, R. H. Contreras et al., *J. Phys. Chem. A*, **2002**, *106*, 5607.
22 T. Helgaker, P. Jørgensen, J. Olsen, *Molecular Electronic-Structure Theory*, Wiley, Chichester, **2000**.
23 R. Bauernschmitt, R. Ahlrichs, *Chem. Phys. Lett.* **1996**, *256*, 454.
24 J. A. Pople, J. W. McIver, Jr., N. S. Ostlund, *J. Chem. Phys.* **1968**, *49*, 2960.
25 J. A. Pople, J. W. McIver, Jr., N. S. Ostlund, *J. Chem. Phys.* **1968**, *49*, 2965.
26 R. Ditchfield, L. C. Snyder, *J. Chem. Phys.* **1972**, *56*, 5823.
27 O. Vahtras, H. Ågren, P. Jørgensen et al., *J. Chem. Phys.* **1992**, *96*, 6120.
28 J. Kowalewski, *Prog. NMR. Spectrosc.* **1977**, *11*, 1.
29 V. G. Malkin, O. L. Malkina, D. R. Salahub, *Chem. Phys. Lett.* **1994**, *221*, 91.
30 O. L. Malkina, D. R. Salahub, V. G. Malkin, *J. Chem. Phys.* **1996**, *105*, 8793.
31 M. Hricovini, O. L. Malkina, F. Bizik et al., *J. Phys. Chem. A.* **1997**, *101*, 9756.
32 R. M. Dickson, T. Ziegler, *J. Phys. Chem.* **1996**, *100*, 5286.
33 J. Autschbach, T. Ziegler, *J. Chem. Phys.* **2000**, *113*, 936.
34 J. Autschbach, T. Ziegler, *J. Chem. Phys.* **2000**, *113*, 9410.
35 V. Sychrovský, J. Gräfenstein, D. Cremer, *J. Chem. Phys.* **2000**, *113*, 3530.
36 T. Helgaker, M. Watson, N. C. Handy, *J. Chem. Phys.* **2000**, *113*, 9402.
37 H. Fukui, *Prog. NMR. Spectrosc.* **1999**, *35*, 267.
38 G. E. Maciel, J. W. McIver, Jr., N. S. Ostlund et al., *J. Am. Chem. Soc.* **1970**, *92*, 1.
39 G. E. Maciel, J. W. McIver, Jr., N. S. Ostlund et al, *J. Am. Chem. Soc.* **1970**, *92*, 11.
40 F. A. A. M. De Leeuw, C. A. G. Haasnoot, C. Altona, *J. Am. Chem. Soc.* **1984**, *106*, 2299.
41 T. Ratajczyk, M. Pecul, J. Sadlej et al., *J. Phys. Chem. A*, submitted.
42 R. H. Contreras, J. E. Peralta, *Prog. NMR. Spectrosc.* **2000**, *37*, 321.
43 O. L. Malkina, M. Hricovini, F. Bizik et al., *J. Phys. Chem. A* **2001**, *105*, 9188.
44 P. Bouř, V. Sychrovský, P. Malon et al., *J. Phys. Chem. A* **2002**, *106*, 7321.

45 V. Sychrovský, J. Vacek, P. Hobza et al., *J. Phys. Chem. B* **2002**, *106*, 10242.
46 M. Pecul, T. Helgaker, *Int. J. Mol. Sci.* **2003**, *4*, 143.
47 A. D. Becke, *J. Chem. Phys.* **1993**, *98*, 5648.
48 P. J. Stephens, F. J. Devlin, C. F. Chabalowski et al., *J. Phys. Chem.* **1994**, *98*, 11623.
49 C. Scheurer, R. Brüschweiler, *J. Am. Chem. Soc.* **1999**, *121*, 8661.
50 H. Benedict, I. G. Shenderovich, O. L. Malkina et al., *J. Am. Chem. Soc.* **2000**, *112*, 1979.
51 A. Bagno, *Chem. Eur. J.* **2001**, *6*, 2925.
52 T. Heinz, O. Moreira, K. Pervushin, *Helvetica Chimica Acta* **2002**, *85*, 3984.
53 M. Barfield, A. J. Dingley, J. Feigon et al., *J. Am. Chem. Soc.* **2001**, *123*, 4014.
54 J. Czernek, R. Brüschweiler, *J. Am. Chem. Soc.* **2001**, *123*, 11079.
55 M. Pecul, J. Sadlej, T. Helgaker, *Chem. Phys. Lett.* **2003**, *372*, 476.
56 M. Pecul, J. Sadlej, in Computational Chemistry: Reviews of Current Trends, Ab Initio Calculations of the Intermolecular Nuclear Spin–Spin Coupling Constants, in press.
57 M. Jaszuński, K. Ruud, T. Helgaker, *Mol. Phys.* **2003**, *101*, 1997.
58 T. A. Ruden, O. B. Lutnæs, T. Helgaker et al., *J. Chem. Phys.* **2003**, *118*, 9572.
59 K. Ruud, L. Frediani, R. Cammi et al., *Int. J. Mol. Sci.* **2003**, *4*, 119.
60 J. Autschbach, C. D. Igna, T. Ziegler, *J. Am. Chem. Soc.* **2003**, *125*, 1028.
61 D. L. Bryce, R. E. Wasylishen, J. Autschbach et al., *J. Am. Chem. Soc.* **2002**, *124*, 4894.
62 D. L. Bryce, R. E. Washylishen, *Inorg. Chem.* **2002**, *41*, 3091.
63 S. Patchovskii, J. Autschbach, T. Ziegler, *J. Chem. Phys.* **2001**, *115*, 26.
64 P. Lantto, J. Vaara, T. Helgaker, *J. Chem. Phys.* **2002**, *117*, 5998.

8
Electron-Correlated Methods for the Calculation of NMR Chemical Shifts

Jürgen Gauss and John F. Stanton

8.1
Introduction

Consideration of electron correlation is essential for the accurate prediction of nuclear magnetic shielding constants and the related nuclear magnetic resonance (NMR) chemical shifts. However, this was not fully realized for some time, since Hartree–Fock self-consistent-field (HF-SCF) calculations have been quite useful for the prediction of *relative* shifts [1] where error cancellation plays a major role. Accordingly, methods for including electron correlation effects in NMR chemical shift calculations have been developed only within the last decade [2–5]. For obvious reasons, the initial focus in the development of reliable methods for the prediction of NMR chemical shifts focused on the gauge-origin problem [6] which was a serious obstacle for quite some time and is the source of the observed slow basis-set convergence. The gauge-origin problem is nowadays routinely handled with the so-called local gauge-origin schemes [7–12]. At least for molecular calculations with atom-centered basis functions, the gauge-including atomic orbital (GIAO) approach [7–10] represents the preferred choice and has become something of a *de facto* standard. Another complication that slowed development of electron-correlated calculations of NMR chemical shifts is that the nuclear magnetic shielding tensor is a second-order property. Calculation of NMR chemical shifts thus requires evaluation of a second derivative of the energy (or of some related sum-over-states expressions) [4, 5]. However, because the involved perturbations transform the real wavefunction of the unperturbed molecule into complex field-dependent wavefunctions, magnetic properties, unlike electric properties and other second-order quantities such as harmonic force constants, cannot be computed easily using numerical differentiation techniques. Hence, development of analytic differentiation schemes [13] was necessary and represented the main bottleneck in the development of correlated schemes for the calculation of chemical shifts.

Although predated by some early developments based on the use of a single, common gauge-origin [14–16], the field of electron-correlated calculations of NMR chemical shifts started with the work of Bouman and Hansen [17]. Their scheme known as the second-order localized orbital/local origin (SOLO) approach is based on the localized orbitals/local origin (LORG) scheme [12] to handle the gauge-origin

Calculation of NMR and EPR Parameters. Theory and Applications.
Edited by Martin Kaupp, Michael Bühl, Vladimir G. Malkin
Copyright © 2004 WILEY-VCH Verlag GmbH & Co. KGaA, Weinheim
ISBN: 3-527-30779-6

problem and the second-order polarization propagator approximation (SOPPA) [18] for the inclusion of electron correlation. However, numerical results obtained with this approach were less than satisfactory and SOLO is now rarely used. The more successful schemes have been developed within the framework of GIAOs and analytic derivative theory and this is the basis for the standard tools now used to compute NMR chemical shifts. The initial implementation of the GIAO approach within second-order Møller–Plesset (MP2) perturbation theory [19, 20] was used almost immediately to resolve outstanding problems in (car)borane and carbocation chemistry [21, 22]. The GIAO approach was soon thereafter extended to higher orders of perturbation theory (MP3, MP4) [23, 24], various coupled-cluster (CC) models [24–29], as well as to multi-configurational SCF (MCSCF) wavefunctions [30]. The development culminated in the recent implementation of a GIAO scheme within the full CC singles, doubles, triples (CCSDT) model [29]. Parallel to these developments in the GIAO framework, a multi-configurational (MC) extension of the individual gauge for localized approach (IGLO) [11] has also been reported [31–33]. More recently, MCSCF and SOPPA calculations using the continuous set of gauge transformation (CSGT) method [34, 35] to deal with the gauge problem have been presented [36].

It should be mentioned that the use of density-functional theory (DFT) to compute NMR chemical shifts has turned out to be a pragmatic alternative to sophisticated electron-correlated approaches (see Ref. [37] as well as Chapter 6 by van Wüllen). However, since these schemes involve an *implicit* rather than *explicit* treatment of electron correlation, they will not be discussed further here. Nevertheless, it is appropriate to note that highly accurate CC calculations (preferably at the CCSD(T) level) have been used as the standard benchmark results to calibrate the performance of DFT methods for computing this important chemical property.

The current chapter gives a brief overview of the field of NMR chemical shift calculations, with specific attention to how explicit treatment of electron correlation is included. For this purpose, we sketch the required background (definition of the shielding tensor, local gauge-origins, electron-correlated methods, analytic second derivatives; see Section 2), list the methods available for the computation of chemical shifts and comment on their advantages and disadvantages (Section 3), describe a few special developments (*e.g.*, integral-direct approaches and local-correlation schemes for the treatment of larger molecules; Section 4), and cite some numerical results which demonstrate the usefulness of these methods (Section 5). An outlook and discussion of future developments in this otherwise rather mature area of quantum chemistry concludes this chapter.

8.2 Theoretical Background

8.2.1 The Shielding Tensor

Elements of the chemical shielding tensor σ that governs the magnitude of the observed NMR chemical shift of the Nth nucleus in a molecule can be expressed as the second-order response to the external magnetic field $\mathbf{B}$ (B_x, B_y, and B_z) and components of the corresponding nuclear magnetic moment $\boldsymbol{m}^N$ (m_x^N, m_y^N, and m_z^N). This means that the tensor elements can be computed as the corresponding second derivatives of the electronic energy

$$\sigma_{ij} = \left(\frac{\mathrm{d}E_{\text{electronic}}}{\mathrm{d}B_j \mathrm{d}m_i^N} \right)_{\mathbf{B},\mathbf{m}^N=0} \tag{8.1}$$

In an exact theory, this is precisely equivalent to the sum-over-states expression

$$\sigma_{ij} = \left\langle \Psi_0 \left| \frac{\partial^2 H}{\partial B_j \partial m_i^N} \right| \Psi_0 \right\rangle + \sum_I \frac{\langle \Psi_0 | \partial H / \partial B_j | \Psi_I \rangle \langle \Psi_I | \partial H / \partial m_i^N | \Psi_0 \rangle}{E_0 - E_I} \tag{8.2}$$

where Ψ_0 and E_0 denote the wavefunction and energy of the (unperturbed) electronic ground state. The sum runs over all excited states Ψ_I with energies E_I and $\partial H/\partial B_j$, $\partial H/\partial m_i^N$, and $\partial^2 H/\partial B_j \partial m_i^N$ denotes the differentiated Hamiltonian (see Eqs. (8.3) to (8.6)).

To evaluate the derivative (or the corresponding sum-over-states expression), it is necessary to specify the Hamiltonian for a molecule in an external magnetic field. This Hamiltonian can be given in the following form

$$\begin{aligned} H = H_0 &+ \sum_{j=x,y,z} \frac{\partial H}{\partial B_j} B_j + \sum_N \sum_{i=x,y,z} \frac{\partial H}{\partial m_i^N} m_i^N \\ &+ \sum_N \sum_{i=x,y,z} \sum_{j=x,y,z} \frac{\partial^2 H}{\partial B_j \partial m_i^N} B_j m_i^N + \ldots . \end{aligned} \tag{8.3}$$

H_0 is the usual field-free, non-relativistic Hamiltonian of a molecule and the perturbation contributions are given by

$$\frac{\partial H}{\partial B_j} = \sum_k \frac{1}{2} \Big((\mathbf{r}(k) - \mathbf{R}_O) \times \mathbf{p}(k) \Big)_j \tag{8.4}$$

$$\frac{\partial H}{\partial m_i^N} = \sum_k \alpha^2 \frac{\left(\left(\mathbf{r}(k) - \mathbf{R}^N\right) \times \mathbf{p}(k)\right)_i}{\left|\mathbf{r}(k) - \mathbf{R}^N\right|^3} \tag{8.5}$$

$$\frac{\partial^2 H}{\partial B_j m_i^N} = \sum_k \frac{\alpha^2}{2} \frac{(\mathbf{r}(k) - \mathbf{R}_O) \cdot (\mathbf{r}(k) - \mathbf{R}^N)\delta_{ij} - (\mathbf{r}(k) - \mathbf{R}_O)_i (\mathbf{r}(k) - \mathbf{R}^N)_j}{|\mathbf{r}(k) - \mathbf{R}^N|^3.} \tag{8.6}$$

where $\mathbf{r}(k)$ and $\mathbf{p}(k)$ are the position and momentum operators for the kth electron, $\mathbf{R}_O$ the gauge origin, $\mathbf{R}^N$ the position of the Nth nucleus, and α is the fine-structure constant.

8.2.2
Gauge-Origin Dependence and Local Gauge-Origin Methods

Use of a common gauge origin in NMR chemical shift calculations, i.e., of

$$\mathbf{B} = \nabla \times \mathbf{A} \tag{8.7}$$

with the vector potential

$$\mathbf{A}(\mathbf{r}) = \frac{1}{2}\mathbf{B} \times (\mathbf{r} - \mathbf{R}_O) \tag{8.8}$$

together with an arbitrary gauge-origin $\mathbf{R}_O$, leads to unsatisfactory results in the sense that the computed shieldings depend (often strongly) on the chosen gauge origin, and is the source of agonizingly slow basis-set convergence in the calculations.

While a detailed discussion of the gauge-origin problem is beyond the scope of this contribution (see Chapter 6 by van Wüllen), it should be noted that standard approaches intended for the routine calculation of NMR chemical shifts all use one of a small number of local gauge-origin approaches. While the individual gauge for localized orbital (IGLO) approach [11] (the use of localized occupied molecular orbitals together with individual gauge-origins chosen for each occupied orbital at its corresponding centroid) remains popular for calculations at the HF-SCF level, the gauge-including atomic orbital (GIAO) approach [7–10] (the use of local gauge origins for atomic orbitals) has become the overwhelmingly most popular choice for electron-correlated calculations. This is due to the fact that the GIAO approach does not impose any restriction on the molecular orbitals used and therefore is easier to apply in conjunction with treatments of electron correlation. For example, Møller–Plesset perturbation theory is usually formulated in terms of delocalized canonical orbitals and not in terms of localized orbitals as required for the IGLO and closely

related LORG [12] treatments. The GIAO approach is usually not described as a 'local gauge-origin' method but rather in the sense that the calculations are performed with the following field-dependent basis functions, viz.

$$\chi_\mu(\mathbf{B}) = \exp\left(-\frac{i}{2}\left(\mathbf{B} \times (\mathbf{R}_\mu - \mathbf{R}_O) \cdot \mathbf{r}\right)\right)\chi_\mu \tag{8.9}$$

instead of the usual field-independent functions (Gaussians) χ_μ centered at $\mathbf{R}_\mu$. This reformulation facilitates the treatment of shielding tensors in an energy-derivative formalism (see, for example, Ref. [38]) together with perturbation-dependent basis functions, which build upon well-known treatments for the analytic evaluation of forces on nuclei and harmonic force constants [13].

Nevertheless, it should be noted that the use of "local gauge-origin" approaches does *not* actually resolve the gauge problem. Rather, they provide a means to generate unambiguous and unique results (due to the choice of a well-defined set of local gauge origins) and can be shown to ensure rapid basis-set convergence. For some electron-correlated approaches, specifically the non-variational MP and CC schemes, gauge-invariance is not even preserved in the basis-set limit since these methods do not satisfy the hypervirial theorem [39]. However, this issue can be ignored in the calculation of NMR chemical shifts, but might prove relevant for other magnetic properties [40].

It is also appropriate at this point to mention the continuous set of gauge-transformation (CSGT) approach of Keith and Bader [34] (which is equivalent to the continuous transformation of origin of the current density (CTOCD-DZ) scheme of Lazzeretti et al. [35]). However, calculations reported so far indicate that the basis-set convergence of this method for avoiding the gauge-origin problem is inferior to that found with the GIAO approach [36]. Hence, we believe it unlikely to have a major impact on the field in the future.

8.2.3
Electron Correlation Treatments

Over the years, many approaches for the treatment of electron correlation have been developed [41]. In the following, we will briefly summarize those which are currently relevant for the calculation of NMR chemical shifts. The corresponding schemes can be classified as to whether they are based on a single Slater determinant (in most cases, but not necessarily, the HF-SCF wavefunction) or a multi-configurational (MC) ansatz and to whether electron correlation is treated via variational methods such as configuration interaction (CI) or nonvariational approaches based on perturbation or CC theory. The MC approaches are thought to be needed for the description of so-called static correlation effects (in the limit that they are very large); dynamical correlation is best treated via the so-called single-reference approaches. For (closed-shell) molecules at their equilibrium geometry, usually what is of interest in NMR chemical shift calculations, static correlation effects are often

less important so that it is not surprising that the single-reference approaches are more commonly used in this area of quantum chemical applications.

Amongst the single-reference approaches, second-order Møller–Plesset perturbation theory (MP2, also known as second-order many-body perturbation theory [MBPT(2)]) is the most popular approach for the low-level treatment of electron correlation [42, 43]. It is the least expensive and the conceptually simplest correlation treatment and can therefore be applied to very large molecules. The domain of applicability for MP2 has been significantly extended by the use of integral-direct implementations [44], exploitation of local-correlation schemes [45] and the use of resolution-of-identity (RI) techniques [46]. Higher-orders of MP perturbation theory (MP3, MP4, etc.) are less useful, and consequently less popular. Third order (MP3) is nowadays considered to be essentially useless, since results obtained at this level are usually inferior to MP2, a phenomenon that arises from the characteristically oscillatory convergence of perturbation theory. MP4 offers some improvement (inclusion of triple excitations), but has also been found to be of limited use. MP5 and MP6 are also available, but far too expensive for routine application [47].

Quantitative treatments of electron correlation are best achieved and accessed in a systematic way by the coupled-cluster approaches [48], which are based on an exponential ansatz for the wavefunction and involve infinite-order summations of many classes of perturbation theory diagrams. In particular, the CC singles and doubles (CCSD) approximation [49] and CCSD augmented by a perturbative treatment of triple excitations, CCSD(T) [50] are routinely applied. In comparison to those schemes, the full CC singles, doubles, triples (CCSDT) model [51] and augmented CCSDT approaches that feature corrections for quadruple and even higher excitations [52] are currently too expensive for routine application, but it can be expected that they will be used more commonly in the future. Variational CI methods [53] were very popular in the seventies, but the problem of size-consistency (the quality of the correlation treatment degrades systematically as the size of the system under consideration increases) and the not-unrelated superiority of results obtained with corresponding CC approaches (i.e., CCSD in comparison with CISD) have significantly diminished the use of single-reference CI techniques in quantum chemical applications.

MC approaches [54–56] are based on the MCSCF method, which involves the optimization of molecular orbitals within a restricted subspace of electronic occupations and provides a means to treat static electron correlation effects if the “active space” is appropriately chosen. Dynamical correlation effects can be treated within this framework via perturbation theory (the essentially identical CASPT2 and MR-MP2 methods) [55] or in a more complete manner via configuration interaction (MR-CI). However, there is still a lack of size-consistency in MR-CI, and this has led to the development of some interesting approaches that are loosely based on ideas similar to those underlying coupled-cluster theory. Perhaps most prominent among these are the MR averaged coupled-pair-functional (MR-ACPF) [57] and MR average quadratic coupled-cluster (MR-AQCC) [58] methods.

8.2.4
Analytic Second Derivatives

The calculation of the shielding tensor in GIAO-based electron-correlated methods is based on the energy derivative formula (see Eq. (8.1)) together with the Hamiltonian given in Eqs. (8.4) to (8.6). Hence, these calculations are based on "analytic derivative theory" [13] which was first used by Stephens, Pitzer and Lipscomb [59] for magnetic properties (within common gauge-origin calculations) and in its more general form originates from the classic work of Pulay [60]. The formulation of computationally efficient expressions for second derivatives exploits two fundamental considerations. First, it is important to realize that analytic computation of first derivatives does not require any perturbed wavefunction parameters [13]. While it is trivial to demonstrate this for a variational approach such as HF-SCF or MCSCF, it also holds for non-variational approaches such as perturbation theory and CC. However, an additional perturbation-independent linear equation must be solved in the latter class of methods, the solution of which can be shown to account for the first-order response of the wavefunction using the interchange theorem of perturbation theory [61]. Within the context of orbital response contributions, this is known as the *Z*-vector method of Handy and Schaefer [62] while recovery of effects associated with relaxation of the cluster amplitudes in CC theory leads to the so-called Λ equations [63]. Overall, for any method, the corresponding expression for first derivatives corresponding to one-electron perturbations can be written as [64]

$$\frac{\partial E}{\partial x} = \sum_{\mu\nu} D_{\mu\nu} \frac{\partial h_{\mu\nu}}{\partial x} \tag{8.10}$$

where $D_{\mu\nu}$ are elements of the corresponding (effective) one-particle density matrix, $\partial h_{\mu\nu}/\partial x$ elements of the perturbed one-electron Hamiltonian matrix, and the indices μ and ν refer to the atomic orbital basis functions. The density matrix $D_{\mu\nu}$ is constructed in HF-SCF theory from the MO coefficients. In perturbation theory, it is augmented by contributions from the excitation amplitudes and the *Z*-vector equations, in CC theory from the cluster amplitudes, the *Z*-vector equations and the solution to the Λ equation, and finally in CI from the CI coefficients and the *Z*-vector contribution. On the other hand, in MCSCF theory, knowledge of the MO coefficients and configuration expansion coefficient suffices. Gradients in MR-CI and MR-MP theory again require consideration of a Z-vector contribution to account for the orbital response since the energy is no longer stationary with respect to rotations that mix different orbital spaces. The second issue is that it is not clear a priori in what order (with respect to the perturbations) the energy should be differentiated when the perturbations belong to distinct classes. This is of course the case for the nuclear magnetic shielding (see above) [19]; this ambiguity is important because the first differentiation as outlined above does not introduce any dependence on perturbed wavefunction parameters, while the second necessarily does. Thus, it is advantageous to perform the initial differentiation with respect to m_i^N and subsequent differentiation with respect to B_j. This results in an expression that requires

perturbed wavefunction parameters only for the magnetic field components (of which there are three), while differentiating first with respect to B_j and then with respect to m_i^N yields expressions that involve the perturbed wavefunction for all [three times the number of atoms N_{atoms}] components of the nuclear magnetic moments. As the cost for the determination of the first-order wavefunction for each perturbation is more or less similar (at least in the scaling with the size of the system) to the cost required for the computation of the unperturbed wavefunction, it is clear that the first choice is the preferred one. Use of a symmetrized expression is less desirable than either of the options considered above since perturbed wavefunction parameters would be needed for *all* ($3N_{atoms}$+3) perturbations. The best strategy is consequently to compute shieldings via the following "asymmetric" second derivative expression [19]

$$\frac{\partial^2 E}{\partial B_j \partial m_i^N} = \sum_{\mu\nu} D_{\mu\nu} \frac{\partial^2 h_{\mu\nu}}{\partial B_j \partial m_i^N} + \sum_{\mu\nu} \frac{\partial D_{\mu\nu}}{\partial B_j} \frac{\partial h_{\mu\nu}}{\partial m_i^N} \tag{8.11}$$

On the basis of Eq. (8.11), the cost for the calculation of shieldings is thus about 6 (MP2, CCSD) to 9 (CCSD(T)) times that of a corresponding gradient calculation, where it is assumed that calculation of the perturbed wavefunction parameters costs about two to three times as much as the solution of the equations for the unperturbed parameters.

It should be emphasized that Eq. (8.11) holds also for the use of GIAOs, as the first differentiation (with respect to m_i^N, a perturbation on which the basis functions do not depend) involves just a one-electron perturbation and the two-electron perturbation is only introduced in the second step. The same is not true if the differentiations are carried out in the opposite order.

Apart from MCSCF, which is formally similar to the simple HF-SCF method, implementations of electron-correlated schemes for the calculation of shieldings have two prominent features [20, 24, 26]:

1. Steps required for the calculation of unperturbed wavefunction parameters. Those steps include one- and two-electron integral evaluation, solution of HF-SCF equations, AO to MO integral transformation, and if necessary, solution of equations for cluster amplitudes/CI coefficients, for Λ amplitudes, as well as the computation of the unperturbed one- and two-particle density matrices. These steps are all that is needed to compute the "diamagnetic" contribution to the shielding which involves just the unperturbed density matrix.
2. Steps required for the calculation of the perturbed wavefunction parameters. These steps are best, but not necessarily, (see, for example, Ref. [65]) carried out within an outer loop over the components of the magnetic field. For each component, the one- and two-electron integral derivatives (the latter are needed only when GIAOs are used) are computed, the coupled-perturbed HF (CPHF) equations for the determination of the perturbed MO coefficients are

solved, the perturbed integrals transformed into the MO basis, the equations for the perturbed wavefunction parameters (cluster amplitudes, CI coefficients and/or Λ amplitudes) are solved, and the perturbed density matrices are computed. These steps yield then, as a final result, the so-called paramagnetic contribution to the shielding. However, note that these terms should not be taken too literally in practical GIAO-based computations, as there is a great deal of ambiguity. For a more in-depth discussion of their meaning within the GIAO framework, see, for example, Ref. [66].

Disk space requirements, which can be a limiting factor in many large-scale correlated calculations, are roughly a factor of two greater for a shielding calculation than for corresponding gradient calculations. The CPU timings are roughly 3 to 9 times that for a gradient calculation with the exact ratio depending on the method. It simplifies the implementation and computations somewhat that electron-correlated shielding calculations do not require a transformation of the two-particle density matrix from the MO to the AO basis. For further technical details concerning the implementation of electron-correlated schemes, we refer the reader to the original work [20, 24, 26, 30].

8.2.5 Polarization-Propagator Approaches

For the HF-SCF ansatz, an alternative and equivalent formulation is given by the sum-over-states expression with the ground-state wavefunction given by the HF state and the excited states determined via the random-phase approximation (RPA). The sum-over-states expression can also be used as a starting point for the introduction of electron correlation. Using a perturbation expansion starting with the HF wavefunction as zeroth-order state and considering all contributions to the sum-over-states expressions, (transition moments and excitation energies) up to second-order in the so-called electron–electron interaction (often termed the "fluctuation potential") yields what is known as second-order PPA (SOPPA) [18]. This ansatz has been successfully used for excitation energies [67] and, for example, indirect spin–spin coupling constants [68], but is somewhat less satisfactory for nuclear shieldings. Also, there is not a strict one-to-one correspondence between a specific ground state wavefunction and properties calculated with the SOPPA method, so that it cannot be properly considered as an MP2 treatment of the second-order property. Another unpleasant aspect is that the electron-correlation contribution to the diamagnetic term, given by a simple expectation value, cannot be as easily treated as the paramagnetic contribution.

Some effort has been made to improve SOPPA by using the converged doubles amplitudes from CCSD calculations instead of the corresponding first-order (MP2) approximations [69]. There are somewhat unappealing theoretical aspects of this method (for example, the singles amplitudes from CCSD are completely ignored so that the weight of the doubly-excited determinants is not properly approximated by

just the double-excitation amplitudes), but it does seem to provide a generally systematic improvement over the original SOPPA method.

A further problem with SOPPA and SOPPA(CCSD) is that implementations are currently available only for one-electron perturbations and these can of course not be used with GIAOs. Besides the unsatisfactory common gauge-origin scheme, SOPPA implementations are available within the LORG treatment (the SOLO approach of Bouman and Hansen [17]) and more recently within the CSGT scheme mentioned earlier in this work [36]. However we do not believe that these methods will play a major role in future calculations of NMR chemical shifts.

8.3
Electron-Correlated Treatment of NMR Chemical Shifts

Figure 8.1 gives an overview summarizing currently available schemes for the calculation of nuclear magnetic shielding constants at electron-correlated levels (again with the caveat that we are not discussing DFT-based approaches in this review). It is seen that such schemes are available within the GIAO framework for a wide selection of methods that ranges from MP2 to various CC levels up to CCSDT. For all other schemes to deal with the gauge problem, the state-of-the-art is far behind this standard; application of IGLO is so far restricted to MCSCF, while LORG has only been used in connection with the SOPPA scheme. The CSGT method has been implemented within SOPPA and MCSCF.

From a practical point of view, the most important methods are probably GIAO-MP2, GIAO-CCSD(T), and GIAO-MCSCF. GIAO-MP2 (which has an N^5 scaling of the computational cost; N stands here for the number of AOs) offers an, in many

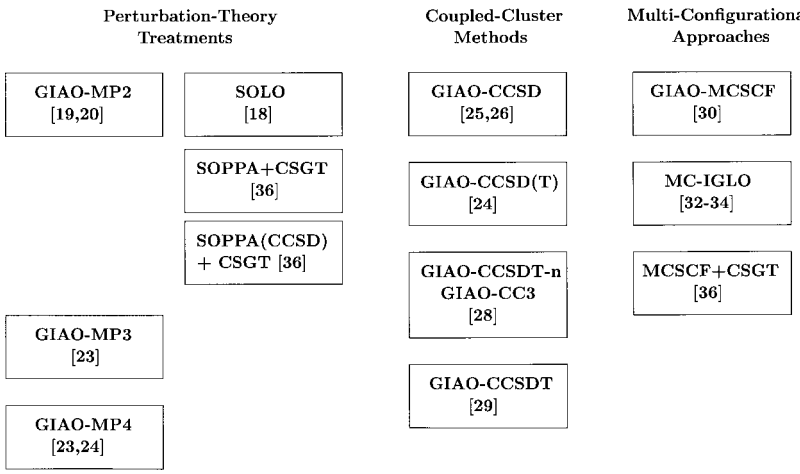

Figure 8.1 Overview of quantum chemical methods for electron-correlated calculation of NMR chemical shifts using schemes to handle explicitly the gauge-origin problem.

cases, reasonable and often excellent treatment of electron correlation effects and is a clear improvement over HF-SCF. Its applicability (discussed below) extends to molecules with roughly 50–70 atoms treated by more than 600 basis functions. The GIAO-CCSD(T) approach (N^7 scaling) allows a near-quantitative treatment of electron correlation and is the method of choice when MP2 is not sufficient. Due to the increased CPU demands of GIAO-CCSD(T) relative to the corresponding MP2 calculation, it can only be applied to small to medium-sized systems (up to 10 to 15 atoms) described by up to 400 basis functions. GIAO-CCSDT calculations (with a N^8 scaling) are of some interest for benchmarking, but otherwise clearly too expensive to date for routine application. For cases with strong static correlation, GIAO-MCSCF offers an interesting alternative, although, except for very small molecules in which the active space configuration expansion begins to approach the full CI space, no quantitative treatment can be expected. The cost of these calculations depends strongly on the size of the chosen active space with respect to which it is factorial in nature. Hence, the range of applicability for large-scale and accurate MCSCF calculations is limited.

For the routine use of the electron-correlated schemes for NMR shifts, only the ACESII (Austin-Mainz version) [70] includes all of the GIAO-MP and GIAO-CC schemes. The GIAO-MP2 method is also available in Turbomole [71] and Gaussian [72]. GIAO-MCSCF and SOPPA calculations can be carried out with the Dalton package [73], while methods based on IGLO and LORG are found only in somewhat less accessible packages.

8.4 Special developments

One of the main focuses of current methodological developments in quantum chemistry is the treatment of large molecules. Hence, there is a clear need also to extend the applicability of the conventional electron-correlated schemes. While corresponding developments (i.e., integral-direct techniques, linear-scaling, local correlation, resolution-of-identity approaches) have been pursued, the bulk of these have focused only on energy calculations. For NMR chemical shifts, it is only at the GIAO-MP2 level where some of these ideas have been applied [65, 74, 75].

An integral-direct implementation of GIAO-MP2 [65, 74] was developed and included in the Turbomole program package [71], which enables calculations with up to several hundred basis functions. The efficient use of point-group symmetry (if present) further enhances the applicability [65] which is limited only by CPU requirements. The usefulness of this technique is illustrated by calculations on $Al_4(C_5H_5)_4$ (D_{2d} symmetry) and B_4(t-Bu)$_4$ (T_d) with more than 600 basis functions [65].

To reduce the CPU time in GIAO-MP2 calculations, exploratory work has been done within the framework of local correlation. Initial results obtained for a GIAO-local-MP2 (GIAO-LMP2) scheme with a pilot code are encouraging [75]. It is

expected that an optimal implementation will further extend the range of applicability of the existing GIAO-MP2 schemes.

8.5 Numerical Results

The purpose of the current chapter is clearly not the in-depth discussion of the application of electron-correlated NMR chemical shift calculations to chemical problems. However, a brief discussion of some numerical results is nevertheless warranted in order to demonstrate the performance of the discussed approaches and to show the improvements over HF-SCF when electron correlation is considered.

We first consider N_2 for which correlation effects are significant. Figure 8.2 displays the deviation of the shielding constants computed at different levels of theory in comparison with the corresponding experimental value. It is seen that MP2 overestimates the correlation contribution by nearly 20 ppm, while MP3 underestimates it by 15 ppm. MP4 again overestimates the correlation corrections, in particular when triple excitations are included. On the other hand, the CC results are very accurate and lend credence to the idea that near quantitative accuracy can be achieved with these methods. The observed "oscillatory behavior" of perturbation theory appears here and is characteristic, although there are also cases (for example, BH [77]) which exhibit monotonic convergence. Other electron correlated methods do not perform as well for N_2. SOPPA calculations [78] significantly underestimate

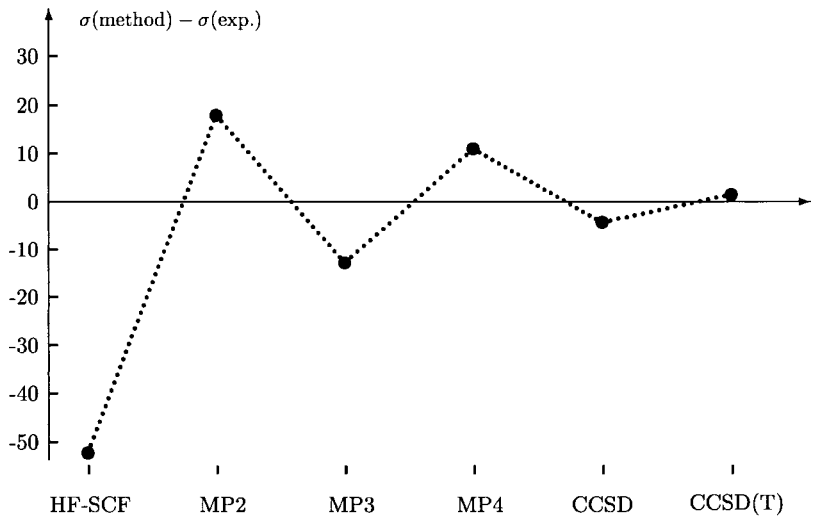

Figure 8.2 ^{15}N shielding constant of N_2 calculated at different levels of theory in comparison to the corresponding experimental equilibrium value (computational results from Ref. [24], experimental value from Ref. [76]).

correlation effects (the values are in the range of –72 to –82 ppm as opposed to the correct value of ca. –55 ppm); results obtained with MCSCF [30, 32] exhibit a strong dependence on the chosen active space.

A more comprehensive comparison of the different methods is given in Tab. 8.1 where shielding constants for HF, H_2O, NH_3, CH_4, CO, and F_2 are summarized. The results support our previous conclusions: oscillatory behavior is seen when perturbation theory is used, while CCSD(T) agrees satisfactorily with experiment in all cases. The GIAO-MCSCF results in Tab. 8.1 show that this approach works best for simple cases such as HF and H_2O, while less satisfactory results are found for the other molecules. In particular, the GIAO-MCSCF treatment of F_2 features an alarmingly slow convergence with respect to the chosen active space [30]. On the other hand, there are cases where static correlation is important and where MCSCF methods thus are appropriate. One example is the ozone molecule (see Tab. 8.2), where HF-SCF and MP calculations are an unmitigated disaster. However, MCSCF calculations (MC-IGLO and GIAO-MCSCF) yield qualitatively correct descriptions [31, 79] in satisfactory agreement with experiment [80, 81] even though it should be noted that the highest-level CC treatments are at least as good for this pathological example.

There are some recent review articles [5, 4, 83] which further discuss applications of electron-correlated calculations of NMR chemical shifts to problems in inorganic and organic chemistry. To this, we would like to add that a recent benchmark study of ^{13}C shieldings demonstrates that CCSD(T) calculations using large basis sets together with consideration of vibrational corrections enable the prediction of gas-phase shieldings with an accuracy of about 1 to 2 ppm [82]. This study is perhaps

Table 8.1 Comparison of nuclear magnetic shielding constants (in ppm) calculated at HF-SCF, MP2, MP3, MP4, CCSD, CCSD(T), and MCSCF levels of theory using the GIAO ansatz.[a]

Molecule	Nucleus	HF-SCF	MP2	MP3	MP4	CCSD	CCSD(T)	MCSCF	exp. σ_e[b]
HF	^{19}F	413.6	424.2	417.8	419.9	418.1	418.6	419.6	420.0 ± 1.0
	^{1}H	28.4	28.9	29.1	29.2	29.1	29.2	28.5	28.90 ± 0.01
H_2O	^{17}O	328.1	346.1	336.7	339.7	336.9	337.9	335.3	357.6 ± 17.2
	^{1}H	30.7	30.7	30.9	30.9	30.9	30.9	30.2	
NH_3	^{15}N	262.3	276.5	270.1	271.8	269.7	270.7		273.3 ± 0.3
	^{1}H	31.7	31.4	31.6	31.6	31.6	31.6		
CH_4	^{13}C	194.8	201.0	198.8	199.5	198.7	199.1	198.2	198.4 ± 0.9
	^{1}H	31.7	31.4	31.5	31.5	31.5	31.5	31.3	
CO	^{13}C	–25.5	10.6	–4.2	12.7	0.8	5.6	8.2	3.29 ± 0.9
	^{17}O	–87.7	–46.5	–68.3	–44.0	–56.0	–52.9	–38.9	–38.7 ± 17.2
F_2	^{19}F	–167.9	–170.0	–176.9	–180.7	–171.1	–186.5	–136.6	–196.0 ± 1.0

a HF-SCF, MP2, CCSD, CCSD(T) results from Ref. [24], MP3 results from Ref. [23], MP4 results from Ref. [5], and MCSCF results from Ref. [30].

b Experimental equilibrium values for HF, CO, and F_2 derived from σ_0 values and rovibrational corrections given in Ref. [76], σ_e values for H_2O, NH_3, and CH_4 as compiled in Ref. [24].

Table 8.2 Comparison of computed and experimental ^{17}O nuclear magnetic shielding constants (in ppm) of ozone.

Metod	$O_{terminal}$	$O_{central}$	Ref.
IGLO-HF	–2814	–2929	[31]
GIAO-HF	–2862	–2768	[24]
MC-IGLO	–1153	–658	[31]
GIAO-MCSCF	–1126	–703	[79]
GIAO-MP2	+1248	+2875	[24]
GIAO-CCSD	–1403	–968	[24]
GIAO-CCSD(T)	–1183	–724	[24]
GIAO-CCSDT-1	–927	–415	[29]
GIAO-CCSDT	–1261	–775	[29]
Exp.	–1290	–724	[80]
	–1289 ± 170	–625 ± 240	[81]

the most detailed and extensive set of calibrations yet performed for NMR chemical shift calculations based on CC theory.

8.6 Summary and Outlook

The last ten years have witnessed the growth of electron-correlated NMR chemical shift calculations from infancy to the point at which the field can be regarded as mature. Several types of methods are available, featuring different treatments of the gauge-origin problem and ways in which correlation effects are included. These methods have also been complemented somewhat by DFT schemes that, although plagued by some still unresolved formal difficulties, have proven to be quite popular and useful for practitioners of quantum chemistry.

Now that the basic methods are developed and their ability to predict NMR spectra is fairly well-established, it seems clear that GIAO-MP2 is a useful approach for medium-sized molecules, with GIAO-CCSD(T) calculations necessitated only when very high accuracy is desired or there are significant non-dynamical correlation effects present. In the latter case, GIAO-MCSCF represents an equally attractive alternative. For large molecules, DFT methods currently are the preferred choice. It is certain that the next decade of methodological development in this area will focus on extending the range of applicability of GIAO-MP2 and GIAO-CCSD(T) approaches further. To some degree, the foundations for this work have already been laid, and an efficient implementation of GIAO-LMP2 should probably be made in the next few years. It will then be possible to carry out electron-correlated calculations of NMR chemical shifts for large molecules, an opportunity that will almost certainly lead to biological application of the approach. Another path to be explored is the use of resolution-of-identity (RI) techniques within GIAO-MP2.

However, the development of other highly accurate approaches will not stop. It would be particularly worthwhile to consider GIAO-based NMR calculations within MR-MP and MR-CI (or the related ACPF/AQCC methods) for the treatment of very difficult cases. These include transition metal systems and singlet biradicals. In the former area, the incorporation of relativistic effects within a GIAO-based electron-correlated scheme will also be useful and probably important in order to achieve a high level of accuracy.

References

1 W. Kutzelnigg, U. Fleischer, M. Schindler, in *NMR Basic Principles and Progress*, Eds. P. Diehl, E. Fluck, H. Günther et al., Springer, Berlin, **1990**, Vol. *23*, p. 165.

2 J. Gauss, *Ber. Bunsen-Ges. Phys. Chem.* **1995**, *99*, 1001.

3 U. Fleischer, W. Kutzelnigg, C. v. Wüllen, in *Encyclopedia of Computational Chemistry*, Eds. P.v.R. Schleyer, N.L. Allinger, T. Clark et al., Wiley, Chichester, **1998**, p. 1827.

4 T. Helgaker, M. Jaszunski, K. Ruud, *Chem. Rev.* **1999**, *99*, 293.

5 J. Gauss, J.F. Stanton, *Adv. Chem. Phys.* **2002**, *123*, 355.

6 See, for example, S.T. Epstein, *J. Chem. Phys.* **1965**, *42*, 2897.

7 F. London, *J. Phys. Radium* **1937**, *8*, 397.

8 H. Hameka, *Mol. Phys.* **1958**, *1*, 203; H. Hameka, *Z. Naturforsch. A* **1959**, *14*, 599.

9 R. Ditchfield, *J. Chem. Phys.* **1972**, *56*, 5688; R. Ditchfield, *Mol. Phys.* **1974**, *27*, 789.

10 K. Wolinski, J.F. Hinton, P. Pulay, *J. Am. Chem. Soc.* **1990**, *112*, 8251.

11 W. Kutzelnigg, *Isr. J. Chem.* **1980**, *19*, 193; M. Schindler, W. Kutzelnigg, *J. Chem. Phys.* **1982**, *76*, 1919.

12 A.E. Hansen, T.D. Bouman, *J. Chem. Phys.* **1985**, *82*, 5036.

13 See, for example, P. Pulay, in *Modern Electronic Structure Theory, Part II*, Ed. D.R. Yarkony, World Scientific, Singapore **1995**, p. 1191; J.F. Stanton, J. Gauss, *Int. Rev. Phys. Chem.* **2000**, *19*, 61.

14 J. Oddershede, J. Geertsen, *J. Chem. Phys.* **1990**, *92*, 6036; I. Paiderova, J. Komasa, J. Oddershede, *Mol. Phys.* **1991**, *72*, 559.

15 M. Jaszunski, A. Rizzo, D.L. Yeager, *Chem. Phys.* **1989**, *136*, 385.

16 It should be noted that Cybulski and Bishop (S.M. Cybulski, D.M. Bishop, *Chem. Phys. Lett.* **1996**, *250*, 471; S.M. Cybulski, D.M. Bishop, *J. Chem. Phys.* **1996**, *106*, 4082) developed common gauge-origin methods for the calculation of nuclear magnetic shieldings at MP2, MP3 and linear CCD level. However, with the (actually earlier!) availability of local gauge-origin methods at the same levels of theory, these developments are obsolete and do not play a major role.

17 T.D. Bouman, A.E. Hansen, *Chem. Phys. Lett.* **1990**, *175*, 292.

18 J. Oddershede, P. Jørgensen, D.L. Yeager, *Comput. Phys. Rep.* **1984**, *2*, 33.

19 J. Gauss, *Chem. Phys. Lett.* **1992**, *191*, 614.

20 J. Gauss, *J. Chem. Phys.* **1993**, *99*, 3629.

21 See, for example, M. Bühl, J. Gauss, M. Hofmann et al., *J. Am. Chem. Soc.* **1993**, *115*, 12385; P.v.R. Schleyer, J. Gauss, M. Bühl et al., *J. Chem. Soc. Chem. Commun.* **1993**, 1766.

22 See, for example, S. Sieber, P.v.R. Schleyer, J. Gauss, *J. Am. Chem. Soc.* **1993**, *115*, 6987; H.-U. Siehl, T. Müller, J. Gauss et al., *J. Am. Chem. Soc.* **1994**, *116*, 6384; P. Buzek, P.v.R. Schleyer, H. Vancik et al., *Angew. Chem.*, **1994**, *104*, 470.

23 J. Gauss, *Chem. Phys. Lett.* **1994**, *229*, 198.

24 J. Gauss, J.F. Stanton, *J. Chem. Phys.* **1996**, *104*, 2574.

25 J. Gauss, J.F. Stanton, *J. Chem. Phys.* **1995**, *102*, 251.

26 J. Gauss, J.F. Stanton, *J. Chem. Phys.* **1995**, *103*, 3561.

27 O. Christiansen, J. Gauss, J.F. Stanton, *Chem. Phys. Lett.* **1997**, *266*, 53.

28 J. Gauss and J.F. Stanton, *Phys. Chem. Chem. Phys.* **2000**, *2*, 2047.

29 J. Gauss, *J. Chem. Phys.* **2002**, *116*, 4773.

30 K. Ruud, T. Helgaker, R. Kobayashi et al.

31 W. Kutzelnigg, C. v. Wüllen, U. Fleischer et al., in *Nuclear Magnetic Shieldings and Molecu-*

lar Structure, Ed. J.A. Tossell, NATO ASI Series C 386, Kluwer, Dordrecht **1993**, p. 141.
32 C.v. Wüllen, W. Kutzelnigg, *Chem. Phys. Lett.* **1993**, *205*, 563.
33 C.v. Wüllen, W. Kutzelnigg, *J. Chem. Phys.* **1996**, *104*, 2330.
34 T.A. Keith, R.F.W. Bader, *Chem. Phys. Lett.* **1993**, *210*, 223.
35 P. Lazzeretti, M. Malagoli, R. Zanasi, *Chem. Phys. Lett.* **1994**, *220*, 299.
36 A. Ligabue, S.P.A. Sauer, P. Lazzeretti, *J. Chem. Phys.* **2003**, *118*, 6830.
37 For a review, see M. Bühl, M. Kaupp, O.L. Malkina et al., *J. Comp. Chem.* **1999**, *20*, 91.
38 T. Helgaker, P. Jørgensen, *J. Chem. Phys.* **1991**, *95*, 2595.
39 T.B. Pedersen, H. Koch, *Chem. Phys. Lett.* **1998**, *293*, 251 and *J. Chem. Phys.* **1994**, *100*, 8178.
40 T.B. Pedersen, H. Koch, C. Hättig, *J. Chem. Phys.* **1999**, *110*, 8318.
41 See, for example, review articles in *Modern Electronic Structure Theory*, Ed. D.R. Yarkony, World Scientific, Singapore **1995** and in *Encyclopedia of Computational Chemistry*, Eds. P.v.R. Schleyer, N.L. Allinger, T. Clark et al., Wiley, Chichester **1998**.
42 C. Møller, M.S. Plesset, *Phys. Rev.* **1934**, *46*, 618.
43 For a recent review on Møller–Plesset perturbation theory, see D. Cremer, in *Encyclopedia of Computational Chemistry*, Eds. P.v.R. Schleyer, N.L. Allinger, T. Clark et al., Wiley, Chichester **1998**, p. 1706.
44 J. Almlöf, S. Saebø, *Chem. Phys. Lett.* **1989**, *154*, 83; M. Head-Gordon, J.A. Pople, M.J. Frisch, *Chem. Phys. Lett.* **1988**, *153*, 503.
45 P. Pulay, *Chem. Phys. Lett.* **1983** *100*, 151; P. Pulay, S. Saebø, *Theor. Chim. Acta* **1986** *69*, 357; S. Saebø, P. Pulay, *J. Chem. Phys.* **1987** *86*, 914; M. Schütz, G. Hetzer, H.-J. Werner, *J. Chem. Phys.* **1999**, *111*, 5691.
46 O. Vahtras, J. Almlöf, M.W. Feyereisen, *Chem. Phys. Lett.* **1993**, *213*, 514; F. Weigend, M. Häser, *Theor. Chim. Acta* **1997** *97*, 331; F. Weigend, M. Häser, H. Patzelt et al., *Chem. Phys. Lett.* **1998**, *294*, 143.
47 S.A Kucharski, R.J. Bartlett, *Chem. Phys. Lett.* **1995**, *237*, 264; D. Cremer, Y. He, *J. Phys. Chem.* **1996**, *100*, 6173.
48 For a recent review, see J. Gauss, in *Encyclopedia of Computational Chemistry*, Eds. P.v.R. Schleyer, N.L. Allinger, T. Clark et al., Wiley, Chichester **1998**, p. 615.
49 G.D. Purvis, R.J. Bartlett, *J. Chem. Phys.* **1982**, *76*, 1910.
50 K. Raghavachari, G.W. Trucks, J.A. Pople et al., *Chem. Phys. Lett.* **1989**, *157*, 479.
51 J. Noga, R.J. Bartlett, *J. Chem. Phys.* **1987**, *86*, 7041; Erratum **1988**, *89*, 3401; G.E. Scuseria, H.F. Schaefer, *Chem. Phys. Lett.* **1988**, *152*, 382.
52 M. Kállay, P.R. Surjan, *J. Chem. Phys.* **2000**, *113*, 1359; S. Hirata, M. Nooijen, R.J. Bartlett, *Chem. Phys. Lett.* **2000**, *326*, 255; J. Olsen, *J. Chem. Phys.* **2000**, *113*, 7140.
53 For a review, see I. Shavitt, in *The Electronic Structure of Atoms and Molecules*, Ed. H.F. Schaefer, Addison-Wesley, Reading, Massachusetts **1972**, p. 189.
54 For reviews, see H.-J. Werner, in *Ab Initio Methods in Quantum Chemistry*, Ed. K.P. Lawley, Wiley, New York **1987**, Part II, p. 1; R. Shepard, in *Ab Initio Methods in Quantum Chemistry*, Ed. K.P. Lawley, Wiley, New York **1987**, Part II, p. 62; B.O. Roos, in *Ab Initio Methods in Quantum Chemistry*, Ed. K.P. Lawley, Wiley, New York **1987**, Part II, p. 399.
55 For a review see B.O. Roos, K. Andersson, in *Modern Electronic Structure Theory, Part I*, Ed. D.R. Yarkony, World Scientific, Singapore **1995**, p. 55.
56 For a review see P. G. Szalay, in *Modern Ideas in Coupled-Cluster Methods*, Ed. R.J. Bartlett, World Scientific, Singapore **1997**, p. 81.
57 R. Gdanitz, R. Ahlrichs, *Chem. Phys. Lett.* **1988**, *143*, 413.
58 P. G. Szalay, R. J. Bartlett, *Chem. Phys. Lett.* **1993**, *214*, 481.
59 R.M. Stephens, R.M. Pitzer, W.N. Lipscomb, *J. Chem. Phys.* **1963**, *38*, 550.
60 P. Pulay, *Mol. Phys.* **1969**, *17*, 197.
61 See, for example, R.M. Sternheimer, H.M. Foley, *Phys. Rev.* **1952** *92*, 1460; A.M. Dalgarno; A.L. Stewart, *Proc. Roy. Soc.* **1958**, *A 247*, 245.
62 N.C. Handy, H.F. Schaefer, *J. Chem. Phys.* **1984**, *81*, 5031.
63 L. Adamowicz, W.D. Laidig, R.J. Bartlett, *Int. J. Quant. Chem. Symp.* **1984**, *18*, 245.
64 J.E. Rice, R.D. Amos, *Chem. Phys. Lett.* **1985**, *122*, 585.
65 M. Kollwitz, M. Häser, J. Gauss, *J. Chem. Phys.* **1998**, *108*, 8295.

66 J. Gauss, K. Ruud, T. Helgaker, *J. Chem. Phys.* **1996**, *105*, 2804.

67 See, for example, M.J. Packer, E.K. Dalskov, T. Enevoldsen et al., *J. Chem. Phys.* **1996**, *105*, 5886.

68 See, for example, T. Enevoldsen, J. Oddershede, S.P.A. Sauer, *Theor. Chem. Acc.* **1998**, *100*, 275.

69 S.P.A. Sauer, *J. Phys. B* **1997**, *30*, 3773.

70 ACESII: J.F. Stanton et al., The University of Texas at Austin and Universität Mainz, **2003**.

71 TURBOMOLE (Version 5.6): R. Ahlrichs et al., Universität Karlsruhe, **2002**.

72 GAUSSIAN 03: M.J. Frisch et al., Gaussian Inc., Pittsburgh, PA, **2003**.

73 DALTON (Release 1.2): T. Helgaker et al., University of Oslo, **2001**.

74 M. Kollwitz, J. Gauss, *Chem. Phys. Lett.* **1996**, *260*, 639.

75 J. Gauss, H.-J. Werner, *Phys. Chem. Chem. Phys.* **2000**, *2*, 2083.

76 D. Sundholm, J. Gauss, A. Schäfer, *J. Chem. Phys.* **1996**, *105*, 11051.

77 J. Gauss, K. Ruud, *Int. J. Quantum Chem. Symp.* **1995**, *29*, 437.

78 S.P.A Sauer, I. Paiderova, J. Oddershede, *Mol. Phys.* **1994**, *81*, 87.

79 S. Coriani, M. Jaszunski, A. Rizzo, K. Ruud, *Chem. Phys. Lett.* **1998**, *287*, 677.

80 I.J. Solomon, J.N. Keith, A.J. Kacmarek, J.K. Raney, *J. Am. Chem. Soc.* **1968**, *90*, 5408.

81 E.A. Cohen, K.W.H. Hillig, H.M. Pickett, *J. Mol. Struct.* **1995**, *352–353*, 273.

82 A.A. Auer, J. Gauss, J.F. Stanton, *J. Chem. Phys.* **2003**, *118*, 10407.

83 M. Bühl, in *Encyclopedia of Computational Chemistry*, Eds. P.v.R. Schleyer, N.L. Allinger, T. Clark et al., Wiley, Chichester **1998**, p. 1835.

9
Semiempirical Methods for the Calculation of NMR Chemical Shifts

Thomas Heine and Gotthard Seifert

9.1
Introduction

Various methods for the calculation of the nuclear magnetic shielding have been developed and applied since the fundamental formulation of the theory by Ramsey [1]. Originally, most of the methods for "ab initio" or "first principle" treatments of NMR parameters in molecules were based on the Hartree–Fock (HF) formalism in connection with perturbation theory to consider the external magnetic field. Linear combination of atomic orbitals (LCAO) "ab initio" calculations with large basis sets have been performed within the coupled HF perturbation theory (CHF) (see e.g. Ref. [2]). The effect of electron correlation was studied and NMR schemes were developed for many post-HF methods (for review, see Ref. [3]).

Significant improvements for the calculation of the NMR parameters could be achieved by the GIAO (gauge including atomic orbitals, originally called "gauge invariant atomic orbitals" or "London orbitals") approach from Ditchfield [4], as well as by the method of individual gauge for localised orbitals (IGLO) from Kutzelnigg and Schindler [5]. Since the early 90s, both methods (see, for example, for IGLO [6, 7], for GIAO [8, 9]) have been also successfully applied within density-functional theory (DFT) and the local density approximation (LDA) or the generalised gradient approximation (GGA) – for reviews see e.g. Refs. [10, 11]. However, it has been pointed out already by Bieger et al. [12] that the calculation of the nuclear magnetic shielding cannot strictly be justified within DFT, as the presence of the magnetic field requires an extension. This extension is given by the CDFT (current density functional theory) [13].

The application of semiempirical quantum chemical methods for NMR calculations goes back to the 1960s. After studies with simple model wavefunctions, already back in the 1950s, the semiempirical NDO (neglect of differential overlap) methods [14] were used in connection with an uncoupled Hartree-Fock perturbation treatment (UCHF) [15]. This is also known as the "sum-over-states" (SOS) method [16]. Combinations of the complete NDO (CNDO) and intermediate NDO (INDO) method with GIAOs were also developed and applied [17, 18], as well as combinations with the method of individual gauge transformations [19, 20].

Calculation of NMR and EPR Parameters. Theory and Applications.
Edited by Martin Kaupp, Michael Bühl, Vladimir G. Malkin
Copyright © 2004 WILEY-VCH Verlag GmbH & Co. KGaA, Weinheim
ISBN: 3-527-30779-6

Most widely used was a rather crude model for estimations of nuclear magnetic shieldings, the so called "ΔE" model. This model can formally be derived from the UCHF treatment, where the energy denominator in the perturbation expansion with the virtual orbitals is just replaced by an "averaged" energy denominator (ΔE). Though it is a very strong approximation, it was successfully applied for qualitative interpretations of chemical shifts, see e.g. Ref. [21]. It can give simple relations between chemical shifts and corresponding charges of atoms obtained from quantum chemical calculations, but it also makes clear that there are generally no simple correlations between chemical shifts and charges, for example.

After a short description of the basics for calculating nuclear magnetic shielding in (closed shell) molecules, the "sum-over-states" (SOS) as well as the "ΔE" model are described briefly. As examples of modern semiempirical schemes the GIAO-MNDO (modified NDO) [18, 22] and the IGLO-DFTB [23] methods are discussed. The capabilities of these methods are illustrated by a few representative applications. Finally, concluding remarks concerning the outlook and limitations of semiempirical calculations of nuclear magnetic shieldings are given. We will not discuss here the manifold of models, which are not based on quantum chemical calculations.

9.2 Methods

9.2.1 General Considerations

The nuclear magnetic shielding tensor ($\boldsymbol{\sigma}^k \leftrightarrow \sigma^k_{\alpha\beta}$) describes the induced field ($\vec{B}_{\mathrm{ind}}$) at a nucleus k in presence of an external field ($\vec{B}_0$):

$$(\vec{B}_{\mathrm{ind}})_\alpha = -\sum_\beta \sigma^k_{\alpha\beta} (\vec{B}_0)_\beta \tag{9.1}$$

Biot-Savart's law gives the relation between the induced field and the current density in a molecule (Gaussian units):

$$\vec{B}_{\mathrm{ind}} = \frac{1}{c} \int \frac{\vec{J} \times \vec{r}_k}{r_k^3} d^3 r \tag{9.2}$$

The current density ($\vec{J}$) is given by the electronic wavefunction:

$$\vec{J} = \frac{i}{2} \left[(\nabla \Psi^*) \Psi - \Psi^* (\nabla \Psi) \right] - \frac{1}{c} \vec{A} \Psi^* \Psi. \tag{9.3}$$

$\vec{A}$ is the vector potential of the external magnetic field. According to the definition of the shielding tensor as a linear response property, only terms in first order of $\vec{B}_0$ are needed in a Taylor series of J:

$$J(\vec{B}_0) = \vec{J}^0 + \vec{B}_0 \frac{\partial \vec{J}}{\partial \vec{B}_0} + \ldots \tag{9.4}$$

$\vec{J}^0$, the current density in the absence of an external magnetic field, is zero for molecules with no permanent magnetic moment. The first order current density is then given by:

$$\vec{B}_0 J^1 = \frac{i}{2}\left[(\nabla\Psi^0)\Psi^1 - \Psi^1(\nabla\Psi^0)\right] - \frac{1}{c}\vec{A}\Psi^0\Psi^0. \tag{9.5}$$

I.e., the first order current density $\left(\vec{B}_0 J^1 \equiv \frac{\partial \vec{J}}{\partial \vec{B}_0}\right)$ with the first order perturbed wave function (Ψ^1), has to be considered in *Biot-Savart's* law for calculations of nuclear magnetic shielding tensors. Within a Coulombic gauge for the vector potential ($\vec{A} = 1/2(\vec{B} \times \vec{r})$), one obtains finally for the shielding tensor at nucleus k:

$$\boldsymbol{\sigma} = \frac{1}{2c^2}\left\langle \Psi^0 \left| \frac{\vec{r}\,\vec{r}_k\, \boldsymbol{I} - \vec{r}_k \otimes \vec{r}}{r_k^3} \right| \Psi^0 \right\rangle - \frac{2}{c}\left\langle \Psi^0 \left| \frac{\vec{L}}{r_k^3} \right| \vec{\Psi}^1 \right\rangle \tag{9.6}$$

The first term is the so-called diamagnetic contribution ($\boldsymbol{\sigma}^{dia}$) of the shielding tensor, whereas the second term is called the paramagnetic term ($\boldsymbol{\sigma}^{para}$). Expanding the perturbed wavefunction (Ψ^1) in terms of the excited states of the unperturbed wavefunction (Ψ_n^0) one obtains:

$$\boldsymbol{\sigma}^{para} = -\frac{1}{c}\sum_{n\neq 0} \frac{1}{E_n - E_0}\left\langle \Psi_n^0 \left| \frac{\vec{L}}{r_k^3} \right| \Psi_0^0 \right\rangle \left\langle \Psi_0^0 \left| \vec{L} \right| \Psi_n^0 \right\rangle, \tag{9.7}$$

where E_0 and E_n are the ground state and the excited state energies, respectively, and $\vec{L}$ is the angular momentum operator. The diamagnetic term remains unchanged because it depends only on the unperturbed wavefunction. This is the "classical" representation of the nuclear magnetic shielding tensor in diamagnetic molecules as already derived by Ramsey [1]. It is also the basis of most of the semiempirical treatments of (nuclear) magnetic shieldings in molecules.

9.2.2
The SOS and the "ΔE" Model

Using a simple molecular orbital (MO – ψ_i) expansion for the wave functions (Ψ_n), and an LCAO representation of the MOs ($\psi_i = \sum_\mu c_\mu^i \phi_\mu$), the nuclear magnetic shielding tensor may be written as:

$$\boldsymbol{\sigma} = \frac{1}{2c^2}\sum_i^{occ}\sum_{\mu\nu} c_\mu^i c_\nu^i \left\langle \phi_\mu \left| \frac{\vec{r}\,\vec{r}_k \boldsymbol{I} - \vec{r}_k \otimes \vec{r}}{r_k^3} \right| \phi_\nu \right\rangle -$$

$$-\frac{2}{c^2}\sum_{i}^{occ}\sum_{l}^{unocc}(\varepsilon_i-\varepsilon_l)^{-1}\sum_{\mu<\nu}\sum_{\lambda<\eta}\left(c_\mu^l c_\nu^i - c_\mu^i c_\nu^l\right)\left(c_\lambda^l c_\eta^i - c_\lambda^i c_\eta^l\right)\cdot$$

$$\cdot\left\langle \phi_\mu\left|\frac{\vec{L}}{r_k^3}\right|\phi_\nu\right\rangle\left\langle \phi_\lambda\left|\vec{L}\right|\phi_\eta\right\rangle \tag{9.8}$$

The summation includes occupied ("occ") and unoccupied ("unocc") MOs and is often called the "sum-over-states" (SOS) method [16]. A very crude estimation of the nuclear magnetic shielding tensor is possible, if the summation over the occupied and unoccupied MOs in the paramagnetic term is replaced by an averaged energy denominator (ΔE) [24]:

$$\boldsymbol{\sigma}^{para} = -\frac{2}{c^2}\,\frac{1}{\Delta E}\sum_{i}^{occ}\sum_{\mu\nu}c_\mu^i c_\nu^i\left\langle \phi_\mu\left|\frac{\vec{L}\cdot\vec{L}}{r_k^3}\right|\phi_\nu\right\rangle \tag{9.9}$$

The diamagnetic term remains again unchanged. Often, ΔE is correlated with the HOMO–LUMO gap, or experimental excitation energies, or just taken as a fixed empirical parameter. In this approximation, the paramagnetic term also contains only contributions from occupied MOs.

9.2.3
The CHF Equations within Semiempirical Schemes, GIAO-MNDO

After some early trials [17] and several attempts in between [25–28] to apply the GIAO treatment within the semiempirical NDO methods, recently Patchkovskii and Thiel [18, 22] proposed a combination of the MNDO method with GIAOs. In this method, GIAOs [4] have been introduced to ensure gauge invariance

$$\varphi_\mu(\vec{r}) = \phi_\mu(\vec{r})\,exp\left(-\frac{i}{2c}\left(\vec{B}\times\vec{R}_\mu\right)^\dagger\vec{r}\right), \tag{9.10}$$

where ϕ_μ is a real atomic basis function (e.g., Slater function or Gaussian), centered at a position $\vec{R}_\mu$. The shielding is expressed as the second derivative of the energy with respect to the magnetic field and the magnetic moment of the nucleus, which leads to the CHF equations within the MNDO approximation (for details, see Ref. [22]). The wavefunction perturbed in $\vec{B}$ is expressed using first-order perturbation theory in an expansion of unoccupied states. The phase factors of the GIAOs cancel for all one- and two-center two-electron integrals within the MNDO approximation. The magnetic field enters the one-electron Fock matrix contribution in the CHF equations, which has the form

$$F_{\mu\nu}^{\alpha,a} = H_{\mu\nu}^{a0} = \frac{\partial}{\partial \vec{B}_a} \left\langle \varphi_\mu \left| \hat{h}^{00} + \vec{B}_a \hat{h}^{a0} \right| \varphi_\nu \right\rangle \Big|_{\vec{B}=0}$$

$$= \left\langle \phi_\mu \left| \hat{h}^{a0} \right| \phi_\nu \right\rangle - \frac{i}{2c} \left\langle \left(\vec{r} \times \vec{R}_\mu \right)_a \phi_\mu \left| \hat{h}^{00} \right| \phi_\nu \right\rangle$$

$$+ \frac{i}{2c} \left\langle \phi_\mu \left| \hat{h}^{00} \right| \left(\vec{r} \times \vec{R}_\mu \right)_a \phi_\nu \right\rangle \tag{9.11}$$

which is notably simpler than in ab initio theory. NDO-type approximations further simplify this expression to

$$H_{\mu\nu}^{a0} = \frac{1}{2c} \Bigg\{ \left(\vec{R}_\mu \times \vec{R}_\nu \right) H_{\mu\nu}^{\mathrm{MNDO}}$$

$$+ \left(\vec{R}_\mu - \vec{R}_\nu \right) \times \left(\beta_{\mu\nu}^{\mathrm{N}} \left\langle \phi_\mu \left| \vec{r} - \vec{R}_\nu \right| \phi_\nu \right\rangle \right)$$

$$- \frac{1}{2} \left\langle \phi_\mu \left| \hat{L}^{R_\nu} \right| \phi_\nu \right\rangle + \frac{1}{2} \left\langle \phi_\nu \left| \hat{L}^{R_\mu} \right| \phi_\mu \right\rangle \Bigg\}_a . \tag{9.12}$$

The equivalent expression (except for having $\beta_{\mu\nu}^{\mathrm{N}} = \beta_{\mu\nu}$ as a parameter which can be varied independently) was used previously in INDO [25] and MNDO [26] studies of the shielding tensors. An earlier INDO study [27] used a similar expression, but omitted the second term, while an uncoupled MNDO study [28] retained only the two last terms.

Finally, the GIAO-MNDO equations can be written as (gauge-independent) dia- and paramagnetic contributions:

$$\sigma_{ab}^{dia} = \sum_{\mu\nu} H_{\mu\nu}^{ab(d)} P_{\mu\nu} \tag{9.13}$$

$$\sigma_{ab}^{para} = \sum_{\mu\nu} H_{\mu\nu}^{ab(p)} P_{\mu\nu} + \sum_{\mu\nu} H_{\mu\nu}^{0b} P_{\mu\nu}^{a0} , \tag{9.14}$$

$$H_{\mu\nu}^{0b} = -\frac{1}{c} \left\langle \phi_\mu \left| \frac{\hat{L}_b^R}{\left| \vec{r} - \vec{R} \right|^3} \right| \phi_\nu \right\rangle , \tag{9.15}$$

$$H_{\mu\nu}^{ab(p)} = -\frac{1}{2c} \left(\vec{R}_\mu \times \vec{R}_\nu \right)_a H_{\mu\nu}^{0b} , \tag{9.16}$$

$$H_{\mu\nu}^{ab(d)} = \frac{1}{2c^2} \Bigg\{ \left\langle \phi_\mu \left| \left(\left(\vec{r} - \vec{R}_\mu \right) \times \left(\vec{R}_\nu - \vec{R}_\mu \right) \right)_a \frac{\hat{L}_b^R}{\left| \vec{r} - \vec{R} \right|^3} \right| \phi_\nu \right\rangle$$

$$+ \left\langle \phi_\mu \left| \frac{\delta_{ab} (\vec{r} - \vec{R}_\nu)^\dagger (\vec{r} - \vec{R}) - (\vec{r} - \vec{R}_\nu)_b (\vec{r} - \vec{R})_a}{\left| \vec{r} - \vec{R} \right|^3} \right| \phi_\nu \right\rangle \Bigg\} , \tag{9.17}$$

where $\vec{R}$ is the position of the nucleus (or point in space) at which the shielding tensor is evaluated. These equations completely define the NMR shielding tensor within the MNDO approximation.

GIAO-MNDO parameters have been created for H, C, N, and O, and tested for an extensive set of molecules [18, 22]. Linear correlation with experimental data gave correlation coefficients of 0.994 for ^{13}C NMR parameters. In the parametrisation of Patchkovskii and Thiel, which uses nine parameters for four elements, the RMS value for ^{13}C NMR chemical shift is 12.6 ppm (out of a test set of 94 molecules) [22], which is considerably lower than in earlier GIAO-MNDO treatments. However, individual differences of 50 ppm have been observed for some sp^3 carbons, and these errors can become larger than 100 ppm for shifts in the high upfield region. The performance of ^{17}O and ^{15}N shifts is similar, but for ^{1}H shifts the results can be improved to an individual error of ~3 ppm if three-center integrals are taken into account in the MNDO treatment [22].

9.2.4
IGLO-DFTB, a Semiempirical Method within the CDFT

The density-functional based non-orthogonal tight-binding (DFTB) method [29, 30] is an approximation to DFT. The DFTB method is based on an LCAO Ansatz for the Kohn–Sham molecular orbitals. The expansion coefficients c_ν^i are found by solving the secular problem

$$\sum_\mu c_\mu^i \left(H_{\mu\nu} - \varepsilon_i S_{\mu\nu}\right) = 0 \quad \text{for all } \nu \tag{9.18}$$

which is expressed in terms of the Kohn–Sham matrix elements $H_{\mu\nu}=\langle\phi_\mu|\hat{T}+V_{\text{eff}}|\phi_\nu\rangle$ and overlap matrix elements $S_{\mu\nu}=\langle\phi_\mu|\phi_\nu\rangle$. The effective potential V_{eff} is approximated as a superposition of atomic contributions, each determined by an LDA–DFT calculation on a fictitious spherical pseudo-atom subjected to an additional potential $(r/r_0)^n$. The valence wavefunctions and the effective potential are both taken from the pseudo-atomic calculation. It is only necessary to consider two-center elements of the Kohn–Sham matrix [29]

$$H_{\mu\nu} = \begin{cases} \langle\phi_\mu|\hat{T} + V_j + V_k|\phi_\nu\rangle & \text{for } j \neq k \\ \varepsilon_\mu & \text{for } \mu = \nu \\ o & \text{otherwise,} \end{cases} \tag{9.19}$$

containing the effective potentials V_j, V_k of the atoms j and k that carry functions ϕ_μ and ϕ_ν. In the case of $j = k$, the one-particle energies of the free atom ε_μ are used, giving the correct reference energy in the dissociation limit. Restriction to two-center terms leads to a Kohn–Sham matrix similar to empirically parametrised non-orthogonal tight-binding schemes, but all parameters are obtained here consistently from LDA–DFT calculations.

In the present IGLO-DFTB implementation, the atomic orbitals and the atomic electron density are expanded in a set of contracted Gaussian-type orbitals (CGTO), which are computed in a modified version of the program package deMon [31], but this way the GTO-DFTB method can be implemented in any conventional wave-function-based package for property calculations in quantum chemistry.

So far, it has been applied with the deMon-NMR package [6,7], which uses the IGLO method [5]. This choice has the advantage of reducing the gauge dependence and the paramagnetic contributions, thereby minimising the sensitivity to basis sets in the final computed result. As in present DFT-NMR treatments, IGLO-DFTB is an uncoupled theory. For the computation of the shielding tensor the deMon-NMR package [6] is used. Localised molecular orbitals were constructed with the iterative Foster–Boys procedure [32] which gives a relatively strong localisation. In the IGLO-DFTB method, only valence orbitals are treated. Fullerenes with their half-full valence shells are favourable cases as their virtual spaces usually span all necessary symmetries of the perturbed molecular orbitals [33].

Chemical shifts are calculated from the calculated shieldings of the fullerene site and C_{60} and then transformed to δ_{TMS} values. The same technique is applied in ab initio computations of chemical shifts of fullerenes to remove a systematic error (see Chapter 25 by Heine).

The raw calculated ^{13}C NMR spectra span too large a range of shifts in comparison to experiment. This feature arises from an overestimation of the spread of the paramagnetic parts of the shieldings. We therefore apply an empirical correction, multiplying the paramagnetic part of all shieldings by a constant scaling factor. This is equivalent to making a correction of the energies of the unoccupied molecular orbitals. It is well known that approximate DFT treatments, including many LDA and GGA functionals, give poor energies for unoccupied orbitals [34] and more-or-less sophisticated correction schemes have been proposed [7]. The simple multiplicative factor chosen here is 0.7, as this gives a reasonable value for the sp^2–sp^3 difference in the C_{60} dimer.

9.3 Representative Applications

A major field of recent application of semi-empirical methods for the evaluation of NMR parameters have been fullerenes and their derivatives (see also Chapter 25). These are relatively large molecules (60 and more atoms, hence 240 and more basis functions in a minimal basis treatment), and usually several isomers needed to be treated. Two questions have been addressed in the literature using these methods: Nucleus-independent chemical shifts [35] of the centers of organic rings [36] and fullerenes [37], and the computation of ^{13}C NMR chemical shifts of fullerenes and their derivatives [23, 38–40].

9.3.1
NICS of Organic Molecules

GIAO-MNDO was used to compute the NICS for a wide range of organic molecules, including [*n*]-annulenes, polycyclic hydrocarbons, heterocycles, cage molecules, fullerenes, and pericyclic transition states [36]. In general, there was reasonable agreement with NICS data from ab initio and density functional calculations, which is visualised in Fig. 9.1.

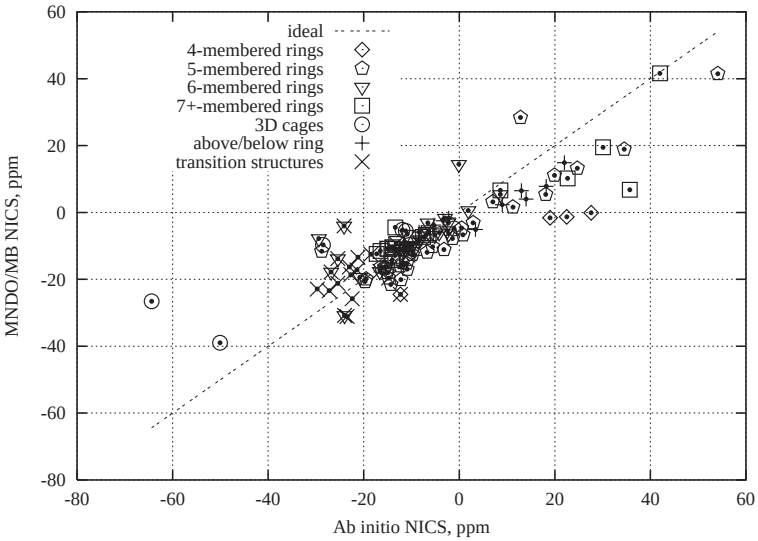

Figure 9.1 Correlation between MNDO and ab initio NICS values (data from Ref. [36]). This figure has been kindly provided by Dr. Serguei Patchkovskii.

The semiempirical NICS values tend to be smaller in absolute value than their ab initio counterparts, but they often show similar trends. The aromatic or antiaromatic character of a given system can normally be assigned correctly on the basis of the MNDO NICS values.

9.3.2
Endohedral NICS Values in Fullerenes

NICS values in the centers of fullerenes have been discussed as a useful criterion for the aromaticity of fullerenes [41]. The NICS values at cage centers are essentially equal to the experimentally accessible ^{3}He endohedral shift, which is one possibility for the characterisation of fullerenes using a single index (for a review, see Ref. [42]). Chen and Thiel [37] evaluated endohedral NICS values for a large series of fullerenes, including small fullerenes C_{20} to C_{50}, and fullerenes with isolated pentagons

C_{60} to C_{102}. In these computations, the geometry of the cages has been computed by MNDO and B3LYP/6-31G* levels. The endohedral NICS values have been evaluated using the GIAO-MNDO and using GIAO-CHF/3-21G for the higher, and GIAO-CHF/6-31G* for the lower fullerenes. Thus, the influence of the computational level of the geometry and of the shielding computation on the chemical shift can be evaluated.

The results are compared in Fig. 9.2. It can clearly be seen that the correlation between MNDO and CHF shifts is much better for the higher than for the lower fullerenes. Two possibilities can explain this result: (i) the MNDO method works better for the higher fullerenes due to their larger HOMO–LUMO gap and higher stability, and/or (ii) this fact is due to the relatively small 3-21G basis set, which has only one s and one p function more than the minimal MNDO basis itself, which was used for the CHF computations for the higher fullerenes.

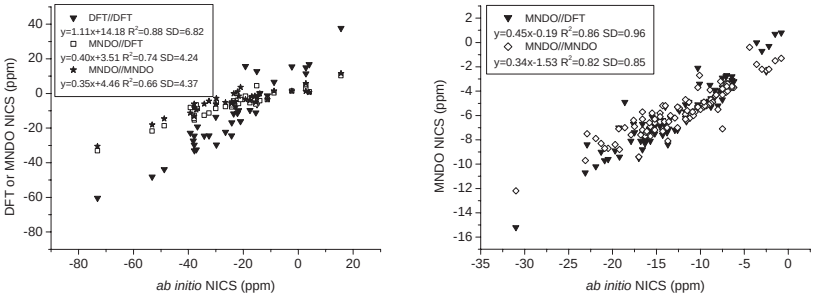

Figure 9.2 Scatter plot of semiempirical/DFT vs. ab initio NICS values (in ppm), (a) for higher, (b) for smaller fullerenes. These plots have been kindly provided by Dr. Z. Chen.

9.3.3
C_{119}, an Odd-Numbered Fullerene

Fullerenes contain even numbers of trivalent, sp^2-like atoms [43]. However, McElvany et al. [44] observed additional odd-numbered species C_{119}, C_{129} and C_{139} by mass spectroscopy, which are expected to be dimeric structures of C_{60} and C_{70} fullerenes, where several sp^3-like bridging atoms link the two moieties with overall loss of one atom [45]. These molecules can be produced e.g. by reacting fullerenes with ozone [44] or by thermolysis of $C_{120}O$ at 550–600 °C with a yield of ~1 % [46]. The C_{119} species has a single predominant isomer for which the ^{13}C NMR spectrum was recorded by Gromov et al. [46]. The observed pattern is compatible with an isomer of C_2 symmetry with two signals in the sp^3 carbon region accounting for three (2+1) atoms.

In agreement with other calculations, the DFTB method finds the isomer **A** (C_2) to be favoured energetically by ~1.9 eV among eight plausible candidates for the structure of C_{119} [39]. The calculated ^{13}C NMR chemical shifts [39] are compatible with the experimental spectrum, and identify this isomer as the species obtained

experimentally by Gromov et al. [46]. The structures and ^{13}C NMR data are shown in Fig. 9.3.

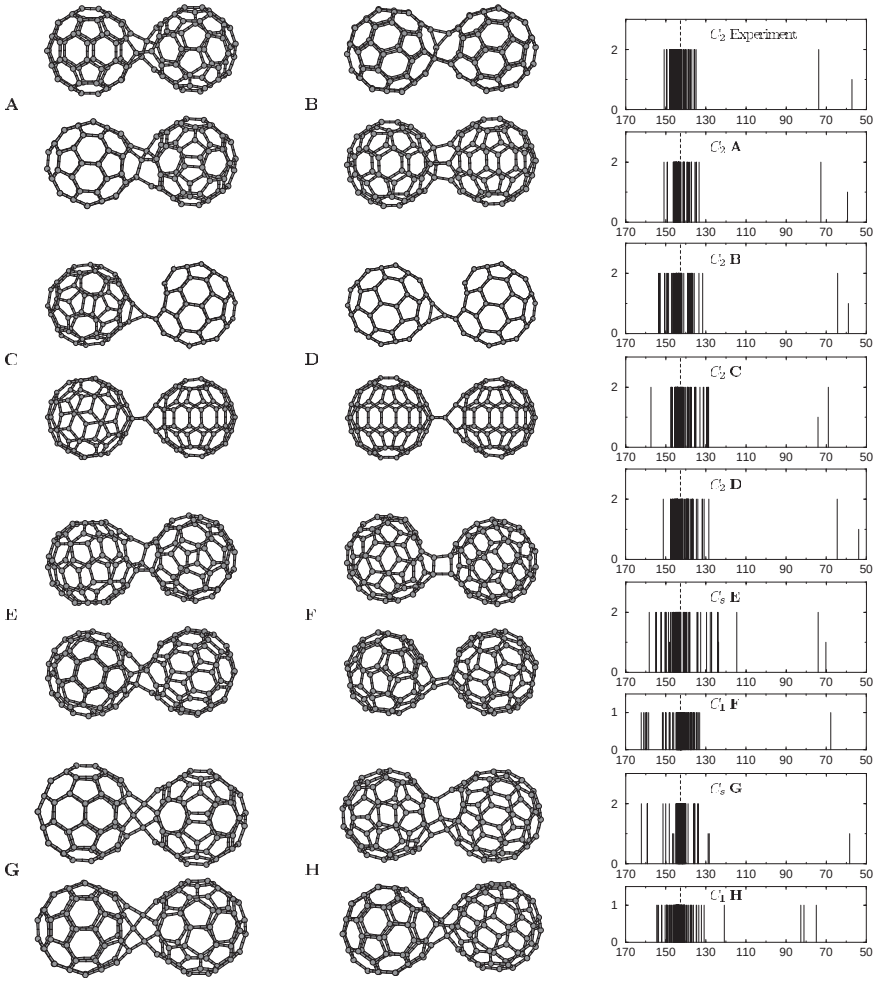

Figure 9.3 Structures (top and side view) and ^{13}C NMR patterns of proposed C_{119} isomers are displayed on the left, the idealised experimental [46] (top) and computed ^{13}C NMR patterns on the right side. Displayed data is taken from Ref. [39]. NMR chemical shifts are given in ppm with respect to TMS.

9.4 Concluding Remarks: Limitations of Semi-Empirical Methods for the Calculation of NMR Parameters

In all present implementations NMR parameters are computed as a sum represented by a diamagnetic and a paramagnetic part. The diamagnetic part is simply an expectation value, while the paramagnetic part is calculated over an expansion series of unoccupied molecular orbitals. While the diamagnetic part can be calculated at satisfactory accuracy in semi-empirical methods, the paramagnetic part suffers the limitations of the expansion series by the fact that a minimal valence basis is used. In semi-empirical methods it is not straightforward to go towards a basis set limit, as the change of basis will influence the parametrisation of the method itself. In addition to the well-known removal of gauge dependence it is therefore absolutely necessary to reduce the paramagnetic contribution by an efficient gauge transformation, as for example IGLO or GIAO.

For the same reasons, those applications work best for semiempirical methods which have either a small paramagnetic contribution (for example which are nearly spherical symmetric, such as noble gases), or large systems with a large number of virtual basis functions, which may compensate for the drawback of the minimal basis to some extent. Similar comments can be made for ab initio methods employing small basis sets, and the quality of semi-empirical results for fullerenes are competitive with CHF-computations at the 3-21G level (see the fullerene dimer discussion in Chapter 25.).

With the success of density-functional theory, the availability of inexpensive and performant computational hardware and the development of highly efficient algorithms for quantum-chemistry software, the importance of semi-empirical methods within quantum chemistry has been strongly reduced. Still, these types of methods have their niche, for example for orienting computations, evaluation of trends, comparison of many isomers and computation of very large molecules.

This conclusion may have been given for any other type of structure, energy or property computation with semi-empirical methods. However, generally for NMR computations only one single point calculation is necessary, and in most cases this is a feasible task, even though it may take a long computing time.

Acknowledgements

We thank Dr. Serguei Patchkovskii for many fruitful discussions. The Deutsche Forschungsgemeinschaft is acknowledged for financial support.

References

1 N. F. Ramsey, *Phys. Rev.* **1950**, *78*, 699; *Physica* **1951**, *17*, 303; *Phys. Rev.* **1952**, *86*, 243.
2 W. N. Lipscomb, *Adv. Magn. Reson.* **1966**, *2*, 137.
3 J. Gauss, J. F. Stanton, *Adv. Chem. Phys.* **2002**, *123*, 355.
4 R. Ditchfield, *J. Chem. Phys.* **1972**, *56*, 5688.
5 W. Kutzelnigg, *Isr. J. Chem.* **1980**, *19*, 193; M. Schindler, W. Kutzelnigg, *J. Chem. Phys.* **1982**, *76*, 1919.
6 V. G. Malkin, O. L. Malkina, D. R. Salahub, *Chem. Phys. Lett.* **1993**, *204*, 80, 87.
7 V. G. Malkin, O. L. Malkina, M. E. Casida et al., *J. Am. Chem. Soc.* **1994**, *116*, 5898.
8 K. Friedrich, G. Seifert, G. Großmann, *Z. Phys.* **1990**, *D17*, 45.
9 G. Schreckenbach, T. Ziegler, *J. Chem. Phys.* **1995**, *99*, 606.
10 M. Bühl, M. Kaupp, O. L. Malkina et al., *J. Comput. Chem.* **1999**, *20*, 91.
11 G. Schreckenbach, T. Ziegler, *Theor. Chem. Acc.* **1998**, *99*, 71.
12 W. Bieger, G. Seifert, H. Eschrig et al., *Chem. Phys. Lett.* **1985**, *115*, 275.
13 A. K. Rajagopal, J. Callaway, *Phys. Rev. B* **1973**, *7*, 1912; H. Eschrig, G. Seifert, P. Ziesche, *Solid. State Commun.* **1985**, *56*, 777.
14 J. A. Pople, G. A. Segal, *J. Chem. Phys.* **1965**, *43*, S129.
15 A. Dalgarno, *Adv. Phys.* **1962**, *11*, 281; M. Karplus, H. J. Kolker, *J. Chem. Phys.* **1964**, *41*, 1259.
16 A. Velenik, R. M. Lynden-Bell, *Mol. Phys.* **1970**, *19*, 371.
17 W. R. Bley, *Mol. Phys.* **1971**, *16*, 303; *Mol. Phys.* **1971**, *20*, 491.
18 S. Patchkovskii, W. Thiel, *J. Comput. Chem.* **1999**, *20*, 1220.
19 H. Schmiedel, *Phys. Stat Solidii B* **1975**, *67*, K27.
20 K. Salzer, *Ann. Phys. (Leipzig)* **1979**, *36*, 91.
21 G. Engelhardt, R. Radeglia, H. Jancke et al., *Org. Magn. Reson.* **1973**, *5*, 561.
22 S. Patchkovskii, PhD Thesis, University of Zürich, Zürich **1997**.
23 T. Heine, G. Seifert, P. W. Fowler et al., *J. Phys. Chem. A* **1999**, *103*, 8738.
24 M. Karplus, J. A. Pople, *J. Chem. Phys.* **1963**, *38*, 2803; C. J. Jameson, H. S. Gutowsky, *J. Chem. Phys.* **1964**, *40*, 1714.
25 A.R. Garber, P.D. Ellis, K. Seidman et al., *J. Magn. Reson.* **1979**, *34*, 1.
26 X. You, W. Wu, *Magn. Reson. Chem.* **1987**, *25*, 860.
27 P.D. Ellis, G.E. Maciel, J.W. McIver Jr., *J. Am. Chem. Soc.* **1972**, *94*, 4069; *J. Am. Chem. Soc.* **1973**, *95*, 5857.
28 D.I. Sheibe, Yu.K. Grishin, V.M. Mamaev et al., *Organomet. Chem. USSR*, **1990**, *3*, 182.
29 G. Seifert, D. Porezag, T. Frauenheim, *Int. J. Quantum Chem.* **1996**, *58*, 185.
30 D. Porezag, T. Frauenheim, T. Köhler et al., *Phys. Rev. B* **1995**, *51*, 12947.
31 A. M. Köster, G. Geudtner, A. Goursot et al., deMon, NRC Ottawa **2002**.
32 J. M. Foster, S. F. Boys, *Rev. Mod. Phys.* **1960**, *32*, 296, 303, 305.
33 P. W. Fowler, P. Lazzeretti, R. Zanasi, *Chem. Phys. Lett.* **1990**, *165*, 79.
34 A. Savin, C. J. Umrigar, X. Gonze, *Chem. Phys. Lett.* **1998**, *288*, 391.
35 P. v. R. Schleyer, C. Maerker, A. Dransfeld et al., *J. Am. Chem. Soc.* **1996**, *118*, 6317.
36 S. Patchkovskii, W. Thiel, *J. Mol. Model.* **2000**, *6*, 67.
37 Z. Chen, W. Thiel, *Chem. Phys. Lett.* **2003**, *367*, 15.
38 T. Heine, M. Bühl, P. W. Fowler et al., *Chem. Phys. Lett.* **2000**, *316*, 373.
39 T. Heine, F. Zerbetto, G. Seifert et al., *J. Phys. Chem. A* **2000**, *104*, 3865.
40 T. Heine, F. Zerbetto, G. Seifert et al., *J. Phys. Chem. A* **2001**, *105*, 1140.
41 M. Bühl, *Chem. Eur. J.* **1998**, *4*, 734.
42 M. Bühl, A. Hirsch, *Chem. Rev.* **2001**, *101*, 153.
43 P. W. Fowler, D. E. Manolopoulos, *An Atlas of Fullerenes*, Clarendon Press, Oxford **1995**.
44 R. S. W. McElvany, J. H. Callahan, L. D. Lamb et al., *Science* **1993**, *260*, 1632.
45 S. Lebedkin, H. Rietschel, G. B. Adams et al., *J. Chem. Phys.* **1999**, *24*, 11768.
46 A. Gromov, S. Ballenweg, S. Giesa et al., *Chem. Phys. Lett.* **1997**, *267*, 460.

10
Ro-Vibrational Corrections to NMR Parameters

Torgeir A. Ruden and Kenneth Ruud

10.1
Introduction

In order to compare theoretical results with accurate experimental observations, it is important to account for the motion of the nuclear framework. Nuclear shieldings and indirect spin–spin coupling constants often show a strong dependence on the molecular geometry, and studies have demonstrated that the effects of molecular motion may change NMR properties by more than 10 % [1]. Furthermore, secondary isotope effects observed in NMR and the temperature dependence of nuclear shielding and indirect spin–spin coupling tensors are usually determined by the ro-vibrational part of the molecular wavefunction alone, necessitating the consideration of ro-vibrational contributions to these properties. In calculations comparing relative chemical shifts, however, the errors introduced in the calculation when neglecting ro-vibrational corrections are often somewhat reduced compared to the case of absolute shieldings, since the ro-vibrational corrections often go in the same direction. Exceptions to this rule, such as for instance the fluorine shieldings in difluorobenzene [2], do exist, however, making it difficult to determine a priori whether the neglect of ro-vibrational corrections will increase or reduce the difference with respect to experimental relative chemical shifts.

There are numerous methods for calculating ro-vibrationally averaged molecular properties, which are all well developed and documented [3–7]. In this chapter we will focus on the use of second-order perturbation theory for calculating ro-vibrational contributions to NMR properties. To date this is the approach most widely used for calculating ro-vibrational contributions to polyatomic molecules for these properties, and other approaches will therefore only be discussed briefly.

In the following we will first describe the calculation of zero-point vibrational contributions to NMR properties within the perturbational approach, before briefly discussing strategies for calculating secondary isotope effects and the temperature dependence of the properties within the perturbation formalism. In this formalism the expressions used to calculate ro-vibrationally averaged molecular properties vary, depending on the reference geometry used [8–11], the choice of coordinates [12] and on the presence of additional electric or magnetic fields [13, 14]. We will thus outline

Calculation of NMR and EPR Parameters. Theory and Applications.
Edited by Martin Kaupp, Michael Bühl, Vladimir G. Malkin
Copyright © 2004 WILEY-VCH Verlag GmbH & Co. KGaA, Weinheim
ISBN: 3-527-30779-6

a general perturbation theory approach, pointing out differences between various methods where appropriate.

Other approaches for calculating vibrational contributions are then briefly discussed, before we conclude by giving a few examples of the results that can be obtained, and their importance in comparison to the electronic contributions.

10.2 Perturbation Theory

In this section, the use of perturbation theory for calculating ro-vibrationally averaged properties will be discussed. We first discuss the calculation of zero-point vibrational effects on the properties, and then discuss isotope and temperature effects.

10.2.1 Zero-Point Vibrational Contributions

The nuclear framework of a molecule is moving even at 0 K, leading to what is commonly referred to as zero-point vibrational corrections (ZPVC) to molecular properties. In order to account for these effects we need to evaluate (using here the nuclear shielding tensor σ as an example)

$$\langle \sigma \rangle = \frac{\langle \Psi | \sigma_{\mathrm{el}}(\mathbf{R}_K) | \Psi \rangle}{\langle \Psi | \Psi \rangle} \tag{10.1}$$

where σ_{el} is the electronic contribution to the nuclear shielding tensor $\sigma(\mathbf{R}_K)$, and where we have explicitly indicated the dependence of the shielding tensor on the molecular geometry. Ψ is the vibrational ground state wavefunction. Expanding the nuclear wavefunction in a perturbation expansion, we may write Eq. (10.1) as

$$\langle \sigma \rangle = \sum_{n=0}^{\infty} \left\langle \sigma^{(n)} \right\rangle = \sum_{n=0}^{\infty} \sum_{k=0}^{n} \left[\left\langle \lambda^k \Psi^{(k)} \middle| \sigma_{\mathrm{el}} \middle| \lambda^{n-k} \Psi^{(n-k)} \right\rangle \right]$$

$$\times \left[1 + \sum_{l,m=1}^{\infty} (-1)^m \left(\left\langle \lambda^l \Psi^{(l)} \middle| \lambda^l \Psi^{(l)} \right\rangle \right)^m \right] \tag{10.2}$$

where $\langle \sigma^{(n)} \rangle$ is the nth order contribution to the vibrationally averaged shielding tensor considered. In Eq. (10.2) we have also expanded the normalization of the wavefunction in a Taylor expansion around the unperturbed wavefunction $\Psi^{(0)}$. It is worth noticing that the perturbation expansion only changes the normalization of $\Psi^{(0)}$ to second or higher orders in λ. Since we in the following will only consider perturbation corrections to the vibrational wavefunction to first order, we will ignore the contributions arising from the reorthonormalization.

In order to proceed, a zeroth-order nuclear Hamiltonian is needed, and this is commonly chosen to be the regular harmonic oscillator Hamiltonian [15]

$$H^{(0)} = \frac{1}{2}\sum_K \left(P_K^2 + \omega_K^2 Q_K^2\right) \tag{10.3}$$

where Q_K is the normal coordinate K with a harmonic frequency $\omega_K = \sqrt{F_{KK}} = \frac{d^2E}{dQ_K^2}$, with E being the electronic energy of the molecule. P_K is the momentum operator for the same normal coordinate.

The unperturbed ground state vibrational wavefunction can be written as a product of harmonic oscillator wavefunctions in the different normal coordinates

$$\Psi^{(0)}(\mathbf{Q}) = \Phi_0(\mathbf{Q}) = \prod_K \phi_K^0(Q_K) \tag{11.4}$$

where ϕ_K^n is the nth excited harmonic-oscillator state of the Kth vibrational normal mode.

The anharmonicity of the potential energy surface is treated as perturbations to this reference Hamiltonian, the nth order Hamiltonian in the perturbation expansion being

$$H^{(1)} = \sum_K F_K Q_K + \frac{1}{6}\sum_{KLM} F_{KLM} Q_K Q_L Q_M \tag{10.5}$$

$$H^{(n)} = \frac{1}{(n+2)!}\sum_{KLMN\cdots} F_{KLMN\cdots} Q_K Q_L Q_M Q_N \cdots, \; n \geq 2 \tag{10.6}$$

where $F_{KLMN\cdots}$ is the ith derivative of the electronic energy with respect to the normal coordinates Q_K, Q_L, Q_M, $Q_N \cdots$ at some reference geometry.

The first-order correction to the ground-state vibrational wavefunction is expanded in the full set of virtual excitations from $\Psi^{(0)}(\mathbf{Q})$. Assuming a fourth-order Taylor expansion of the potential energy surface, the only contributions to the first-order perturbed wavefunction are from single and triple excitations [8, 10]

$$\Psi^{(1)}(\mathbf{Q}) = \sum_K \left[a_K^1 \Phi_K^1(\mathbf{Q}) + a_K^3 \Phi_K^3(\mathbf{Q})\right] + \sum_{K\neq L} b_{KL}^{21} \Phi_{KL}^{21}(\mathbf{Q}) + \sum_{K\neq L\neq M} c_{KLM}^{111} \Phi_{KLM}^{111}(\mathbf{Q}) \tag{10.7}$$

where $\Phi_{KLM}^{klm}(\mathbf{Q})$, for example, has been obtained from $\Phi_0(\mathbf{Q})$ by exciting the Kth, Lth, and Mth modes to the kth, lth, and mth harmonic-oscillator states, respectively. The expansion coefficients in Eq. (10.7) are given by [10]

$$a_K^1 = -\frac{1}{\sqrt{2}\omega_K^{3/2}}\left(F_K + \frac{1}{4}\sum_L \frac{F_{KLL}}{\omega_L}\right) \tag{10.8}$$

$$a_K^3 = -\frac{\sqrt{3}}{36\omega_K{}^{5/2}} F_{KKK} \tag{10.9}$$

$$b_{KL}^{21} = -\frac{F_{KKL}}{4\omega_K\sqrt{\omega_L}(2\omega_K + \omega_L)} \tag{10.10}$$

$$c_{KLM}^{111} = -\frac{F_{KLM}}{12\sqrt{2\omega_K\omega_L\omega_M}(\omega_K + \omega_L + \omega_M)} \tag{10.11}$$

and can be calculated using the gradient (F_K), the harmonic frequency ($\omega_K = \sqrt{F_{KK}}$) and cubic force-field (F_{KLM}).

In a similar manner as for the vibrational force field, we expand the shielding tensor in a Taylor series in normal coordinates around some reference geometry

$$\sigma(\mathbf{Q}) = \sigma_0 + \sigma_1 + \sigma_2 \cdots = \sigma_{\text{ref}} + \sum_K \frac{\mathrm{d}\sigma}{\mathrm{d}Q_K} Q_K + \frac{1}{2}\sum_{K\neq L} \frac{\mathrm{d}^2\sigma}{\mathrm{d}Q_K \mathrm{d}Q_L} Q_K Q_L \cdots \tag{10.12}$$

We can now order the contributions to the ZPVC according to the order in λ of the vibrational wavefunction as defined in Eq. (10.2). For the unperturbed wavefunction, the only non-vanishing terms are those of even order in Eq. (10.12) [8]

$$\left\langle \sigma^{(0)} \right\rangle = \left\langle \Psi^{(0)} | \sigma_0 + \sigma_2 \cdots | \Psi^{(0)} \right\rangle \tag{10.13}$$

The first two contributions can be calculated as [8, 10]

$$\left\langle \Psi^{(0)} \middle| \sigma_0 \middle| \Psi^{(0)} \right\rangle = \sigma \tag{10.14}$$

$$\left\langle \Psi^{(0)} | \sigma_2 | \Psi^{(0)} \right\rangle = \frac{1}{4}\sum_K \frac{1}{\omega_K} \frac{\mathrm{d}^2\sigma}{\mathrm{d}Q_K^2} \tag{10.15}$$

The contributions to first order in λ only contain terms of odd orders in Eq. (10.12) [8]

$$\left\langle \sigma^{(1)} \right\rangle = 2\left\langle \Psi^{(0)} | \sigma_1 + \sigma_3 \cdots | \Psi^{(1)} \right\rangle \tag{10.16}$$

where the two leading terms can be calculated as [8, 10]

$$\left\langle \Psi^{(0)} | \sigma_1 | \Psi^{(1)} \right\rangle = \sqrt{2} \sum_K \frac{\mathrm{d}\sigma}{\mathrm{d}Q_K} \frac{a_K^1}{\sqrt{\omega_K}} \tag{10.17}$$

$$\begin{aligned}\left\langle \Psi^{(0)} | \sigma_3 | \Psi^{(1)} \right\rangle = {} & \frac{1}{6}\sqrt{\frac{3}{2}} \sum_K \frac{\mathrm{d}^3\sigma}{\mathrm{d}Q_K^3} \left(\frac{\sqrt{3}a_K^1 + \sqrt{2}a_K^3}{\omega_K^{3/2}} \right) \\ & + \frac{1}{4} \sum_{K \neq L} \frac{\mathrm{d}^3\sigma}{\mathrm{d}Q_K^2 \mathrm{d}Q_L} \left(\frac{\sqrt{2}a_K^1 + 2b_{KL}^{21}}{\omega_K \sqrt{\omega_L}} \right) \\ & + \frac{1}{6\sqrt{2}} \sum_{K \neq L \neq M} \frac{\mathrm{d}^3\sigma}{\mathrm{d}Q_K \mathrm{d}Q_L \mathrm{d}Q_M} \frac{c_{KLM}^{111}}{\sqrt{\omega_K \omega_L \omega_M}}\end{aligned} \tag{10.18}$$

Although higher-order terms have been investigated for diatomic molecules [3, 16], most calculations include only the three terms

$$\langle \sigma \rangle = \left\langle \Psi^{(0)} | \sigma_0 | \Psi^{(0)} \right\rangle + \left\langle \Psi^{(0)} | \sigma_2 | \Psi^{(0)} \right\rangle + 2\left\langle \Psi^{(0)} | \sigma_1 | \Psi^{(1)} \right\rangle \tag{10.19}$$

which may alternatively be written in the form

$$\langle \sigma \rangle = \sigma + \sum_K \frac{\mathrm{d}\sigma}{\mathrm{d}Q_K} \langle Q_K \rangle + \frac{1}{2} \sum_K \frac{\mathrm{d}^2\sigma}{\mathrm{d}Q_K^2} \left\langle Q_K^2 \right\rangle \tag{10.20}$$

Still, these terms have been shown to account for more than 90 % of the vibrational contribution to the shielding constants in four diatomic molecules [3].

The discussion has so far been concerned with the expansion of the potential energy and shielding tensor surfaces around an arbitrary molecular geometry. The most obvious choice of expansion point is the equilibrium geometry. At this geometry, the molecular gradient is zero, and Eq. (10.19) can be reduced to [8,9]

$$\langle \sigma \rangle = \sigma_{\mathrm{eq}} + \frac{1}{4} \sum_K \frac{1}{\omega_K} \left[\frac{\mathrm{d}^2\sigma_{\mathrm{eq}}}{\mathrm{d}Q_K^2} - \frac{1}{\omega_K} \frac{\mathrm{d}\sigma_{\mathrm{eq}}}{\mathrm{d}Q_K} \sum_L \frac{F_{KLL}^{\mathrm{eq}}}{\omega_L} \right] \tag{10.21}$$

An alternative expansion point, referred to as *the effective geometry*, can be found by minimizing the energy functional [17]

$$\tilde{E} = V^0 + \left\langle \Psi^{(0)} \middle| H^0 \middle| \Psi^{(0)} \right\rangle \tag{10.22}$$

with respect to the expansion point. The minimization of Eq. (10.22) is equivalent to requiring that [10]

$$F_K^{\text{eff}} + \frac{1}{4}\sum_L \frac{F_{KLL}^{\text{eff}}}{\omega_L} = 0 \tag{10.23}$$

Inserting Eq. (10.23) into Eq. (10.8) shows that all a_K^1 coefficients are zero at this expansion point. In other words, the leading anharmonic contributions in Eq. (10.16) vanish at this geometry, and the vibrationally averaged shielding tensor is then given as [11]

$$\langle \sigma \rangle = \sigma_{\text{eff}} + \frac{1}{4}\sum_K \frac{1}{\omega_K} \frac{\mathrm{d}^2 \sigma_{\text{eff}}}{\mathrm{d}Q_K^2} \tag{10.24}$$

and by comparing with Eq. (10.20) we note that the effective geometry is characterized by having the averaged linear displacements vanish. Since the force field in Eq. (10.24) is calculated at a non-equilibrium geometry, spurious imaginary frequencies may occur [18], and care has to be used in how these are treated. Most often these imaginary frequencies are related to delocalized vibrational motions such as internal rotations of methyl groups. We note that the determination of the effective geometry requires the same information as required in Eq. (10.21), since the effective geometry has to be determined using parts of the cubic force field [10]

$$Q_K^{\text{eff}} = Q_K^{\text{eq}} - \frac{1}{4\omega_K^2} \sum_L \frac{F_{KLL}^{\text{eq}}}{\omega_L} \tag{10.25}$$

This expression is identical to the expression one would obtain for the vibrationally averaged geometry using Eq. (10.19), and thus corresponds to what is often denoted r_z geometries. For diatomic molecules it has been shown that the use of the effective geometry as an expansion point reduces the magnitude of the higher-order anharmonic corrections compared to an expansion around the equilibrium geometry [16]. The importance of the anharmonic corrections does of course, in general, vary, but a study of different molecular properties for four diatomics showed that the use of the effective geometry recovered 98–106% of the exact zero-point vibrational correction, whereas the same span for the use of the equilibrium geometry was 88–101%. The differences between the two approaches are therefore small, although the effective geometry in general had a much smaller deviation from the exact result than the equilibrium geometry.

As we have demonstrated, the calculation of the ZPVCs to a molecular property is in the perturbation approach reduced to the calculation of a series of geometrical derivatives of the molecular energy and the properties. To the best of our knowledge, there are no analytical implementations of the derivatives needed for spin–spin coupling constants or, in the case of nuclear shieldings, analytical implementations of shielding derivatives that also solve the gauge origin dependence. However, there are several ways that such derivatives can be evaluated numerically. One approach is to fit an analytic hypersurface to the properties and energies calculated at different geometries. The derivatives can then be obtained by differentiation of the fitted surface [19–27]. Alternatively, the necessary derivatives may be calculated numerically [28], relying as much as possible on available analytical derivatives [29]. Such an approach can easily be automated, making the calculation of vibrational corrections straightforward, though time consuming. For instance, if we assume that analytical gradients and no property derivatives are available analytically, we will need to carry out $6N-11$ property and gradient calculations, where N is the number of atoms, to get the necessary derivatives. The calculation of zero-point vibrationally averaged NMR properties, and spin–spin coupling constants in particular, will therefore be dominated by the time needed for the calculation of the property derivatives.

10.2.2 Isotope Effects

Whereas the electronic wavefunction in the Born–Oppenheimer approximation is independent of the exact nature of the nuclei, and thus does not depend on the nuclear magnetic moments or the nuclear masses, the NMR parameters are not. Through their dependence on the nuclear magnetic moments, the substitution of, for instance, a hydrogen atom with a deuterium will lead to a large change in the NMR signals observed for this nucleus, known as primary isotope shifts. Although small changes in the chemical shielding of the nucleus will also occur due to the change in the nuclear part of the wavefunction when the mass of the nucleus is altered, these effects are small and not easily extracted due to the large shift in the observed resonance frequency of the nucleus. For the same reason has primary isotope effects on the indirect spin–spin coupling constants not received much attention.

More interesting are the secondary isotope effects, that is, the change in a shielding constant or indirect spin–spin coupling constant due to the change in the mass of a different nucleus, since this effect is solely determined by the vibrational wavefunction of a molecular species. An example of a secondary isotope effect is the change in the proton shielding of water when substituting ^{16}O with ^{17}O. Since the effect is determined by the changes in the vibrational wavefunction only, no differences would be found for two isotopomers if only the contributions from the electronic wavefunction were considered.

It is worth noticing that if we, for instance, substitute one of the protons in water with deuterium, the symmetry of the total electron-nuclear wavefunction is reduced in comparison to the most common isotopomer of water $H_2{}^{16}O$, even though the

electronic part of the wavefunction retains its full C_{2v} symmetry. This has the consequence that elements of the shielding and/or spin–spin coupling tensors that would otherwise vanish due to symmetry may now become accessible to investigation.

In the previous section the ZPVC to the properties was written in terms of derivatives with respect to normal coordinates. This choice of internal coordinates is isotope dependent, and thus not very efficient for studying all isotopomers of a molecule. Since the normal coordinates differ for the different isotopomers, the derivatives will also differ. Consequently, in order to calculate the secondary isotope effect, the complete set of derivatives would have to be calculated for all isotopomers.

One way to avoid this problem in the calculation of property derivatives, which usually are the most expensive derivatives, is to use a set of internal coordinates using the full symmetry of the electronic wavefunction. The normal coordinates of a given isotopomer are related to these internal coordinates through a non-linear equation [30]

$$S_i = \sum_K \mathcal{L}_i^K Q_K + \frac{1}{2}\sum_{KL} \mathcal{L}_i^{KL} Q_K Q_L \tag{10.26}$$

where

$$\mathcal{L}_i^K = \left.\frac{\mathrm{d}S_i}{\mathrm{d}Q_K}\right|_{Q=Q_{\mathrm{eq}}} \tag{10.27}$$

$$\mathcal{L}_i^{KL} = \left.\frac{\mathrm{d}^2 S_i}{\mathrm{d}Q_K \mathrm{d}Q_L}\right|_{Q=Q_{\mathrm{eq}}} \tag{10.28}$$

From this we find that

$$\frac{\mathrm{d}\sigma}{\mathrm{d}Q_K} = \sum_i \frac{\mathrm{d}\sigma}{\mathrm{d}S_i}\mathcal{L}_i^K \tag{10.29}$$

$$\frac{\mathrm{d}^2\sigma}{\mathrm{d}Q_K^2} = \sum_{ij} \frac{\mathrm{d}^2\sigma}{\mathrm{d}S_i \mathrm{d}S_j}\mathcal{L}_i^K \mathcal{L}_j^K + \sum_i \frac{\mathrm{d}\sigma}{\mathrm{d}S_i}\mathcal{L}_i^{KK} \tag{10.30}$$

Inserting these two expressions into Eq. (10.21) we get at the equilibrium geometry

$$\langle\sigma\rangle = \sigma_{\mathrm{eq}} + \frac{1}{4}\sum_{Ki} \frac{1}{\omega_K}\left[\sum_j \frac{\mathrm{d}^2\sigma_{\mathrm{eq}}}{\mathrm{d}S_i \mathrm{d}S_j}\mathcal{L}_i^K \mathcal{L}_j^K + \frac{\mathrm{d}\sigma_{\mathrm{eq}}}{\mathrm{d}S_i}\left(\mathcal{L}_i^{KK} - \frac{\mathcal{L}_i^K}{\omega_K}\sum_L \frac{F_{KLL}^{\mathrm{eq}}}{\omega_L}\right)\right] \tag{10.31}$$

as previously given in Ref. [12].

The secondary isotope effect between two isotopomers, using the normal coordinates Q_K and $Q_{K'}$, can then be given by

$$\Delta\sigma^{\mathrm{sec}} = \frac{1}{4}\sum_{ij}\frac{\mathrm{d}^2\sigma_{\mathrm{eq}}}{\mathrm{d}S_i\mathrm{d}S_j}\left[\sum_K \frac{\mathcal{L}_i^K\mathcal{L}_j^K}{\omega_K} - \sum_{K'}\frac{\mathcal{L}_i^{K'}\mathcal{L}_j^{K'}}{\omega_{K'}}\right]$$

$$+\sum_i \frac{\mathrm{d}\sigma_{\mathrm{eq}}}{\mathrm{d}S_i}\left[\sum_K\left(\frac{\mathcal{L}_i^{KK}}{\omega_K} - \frac{\mathcal{L}_i^K}{\omega_K^2}\sum_L\frac{F_{KLL}^{\mathrm{eq}}}{\omega_L}\right) - \sum_{K'}\left(\frac{\mathcal{L}_i^{K'K'}}{\omega_{K'}} - \frac{\mathcal{L}_i^{K'}}{\omega_{K'}^2}\sum_{L'}\frac{F_{K'L'L'}^{\mathrm{eq}}}{\omega_{L'}}\right)\right] \quad (10.32)$$

where all isotope dependences have been incorporated into the parameters governing the vibrational wavefunction. We therefore note that if the vibrational wavefunctions of two isotopomers do not differ much, the secondary isotope effect will be small.

Note that although these equations make the property derivatives isotope independent, it will no longer suffice to calculate the diagonal elements of the second derivative of the property, the entire second derivative matrix would have to be calculated. Thus, if only a few isotopomers are being studied, the recalculation of the quantities in Eq. (10.21) for each isotopomer would still be the most efficient approach. In order to reuse the property derivatives, we also need to choose an isotope-independent expansion point, such as the equilibrium geometry. Isotope-dependent geometries, such as the effective geometry, change for each isotopomer, and the property derivatives will therefore differ for each isotopomer.

10.2.3
Temperature Effects

The discussion has so far focused on the effects of the zero-point vibrational motion of the nuclear framework on the NMR parameters. Although dominant, these effects cannot account for the observed variations of NMR parameters as the temperature changes. The observed temperature changes are primarily due to two effects: (1) the populations of higher vibrational states, and (2) centrifugal distortion. Of these, the latter is most often dominant at normal temperatures.

Eqs. (10.15) and (10.17) for calculating ZPVCs to the NMR properties can very easily be extended to the vibrational average of a molecular property in an arbitrary vibrational state described by the vibrational quantum numbers ν_K [9]

$$\left\langle \Psi^{(0)}|\sigma_2|\Psi^{(0)}\right\rangle = \frac{1}{2}\sum_K \frac{\left(\nu_K + \frac{1}{2}\right)}{\omega_K}\,\frac{\mathrm{d}^2\sigma}{\mathrm{d}Q_K^2} \quad (10.33)$$

$$\left\langle \Psi^{(0)} | \sigma_1 | \Psi^{(1)} \right\rangle = 2\sqrt{2} \sum_K \frac{\mathrm{d}\sigma}{\mathrm{d}Q_K} \frac{a_K^1 \left(\nu_K + \frac{1}{2} \right)}{\sqrt{\omega_K}} \tag{10.34}$$

In order to estimate the temperature dependence of the property, we assume that the populations of the excited states are determined by a Boltzmann distribution. By averaging over all possible vibrational states using a Boltzmann weighting of the population of the excited states, the vibrationally averaged molecular properties at thermal equilibrium may be calculated as [9, 31]

$$\left\langle \Psi^{(0)} | \sigma_2 | \Psi^{(0)} \right\rangle = \frac{1}{4} \sum_K \frac{1}{\omega_K} \frac{\mathrm{d}^2\sigma}{\mathrm{d}Q_K^2} \coth\left(\frac{\omega_K}{2k_\mathrm{B}T} \right) \tag{10.35}$$

$$\left\langle \Psi^{(0)} | \sigma_1 | \Psi^{(1)} \right\rangle = \sqrt{2} \sum_K \frac{\mathrm{d}\sigma}{\mathrm{d}Q_K} \frac{a_K^1}{\sqrt{\omega_K}} \tag{10.36}$$

where

$$a_K^1 = -\frac{1}{\sqrt{2}\omega_K^{3/2}} \left(F_K + \frac{1}{4} \sum_L \frac{F_{KLL}}{\omega_L} \coth\left(\frac{\omega_L}{2k_\mathrm{B}T} \right) \right) , \tag{10.37}$$

and k_B is the Boltzmann constant.

It is worth noticing that similar modifications can be applied to define an effective geometry at thermal equilibrium

$$Q_K^{\mathrm{eff}} = Q_K^{\mathrm{eq}} - \frac{1}{4\omega_K^2} \sum_L \frac{F_{KLL}^{\mathrm{eq}}}{\omega_L} \coth\left(\frac{\omega_L}{2k_\mathrm{B}T} \right) \tag{10.38}$$

We note that there will be a unique effective geometry *for each temperature* [32]. This is in accordance with the interpretation of the effective geometry as the r_z geometry, which is temperature dependent. Clearly, the approach based on determining the effective geometry becomes computationally more expensive for the study of temperature effects than that based on an expansion around the equilibrium geometry, due to the need for calculating the properties and property derivatives at several geometries. The change in the property when changing the effective geometry is the most important contribution to the temperature dependence of the NMR properties, especially when centrifugal distortions are taken into account [32].

The population of higher rotational states does not in itself change the value of the NMR properties since there is no dependence of the calculated properties on the rotational state. However, the coupling of the rotational and vibrational motion in

what is referred to as centrifugal distortions, that is, the elongation of bonds as the rotational state of the molecule increases, give important contributions to the ro-vibrational corrections.

In evaluating the centrifugal distortions, it is customary to assume that the spacings of the rotational energy levels are much smaller than $k_B T$, allowing for the use of the law of equipartitioning of the energy, leading to the following contribution to the ro-vibrational corrections due to centrifugal distortions [9]

$$\left\langle \Psi^{(0)} | \sigma_1 | \Psi^{(1)} \right\rangle_{\text{centr}} = \frac{k_B T}{2} \sum_K \frac{d\sigma}{dQ_K} \frac{1}{\omega_K^2} \sum_\alpha \frac{a_K^{(\alpha\alpha)}}{I_{\alpha\alpha}} \tag{10.39}$$

In this equation, $I_{\alpha\alpha}$ is the moment-of-inertia tensor at the equilibrium geometry, and $a_K^{\alpha\alpha}$ is the coefficient of expansion of $I_{\alpha\alpha}$ in normal coordinate Q_K [9].

We note that centrifugal corrections will also affect the effective geometries [32]

$$Q_K^{\text{eff}} = Q_K^{\text{eq}} - \frac{1}{4\omega_K^2} \left[\sum_L \frac{F_{KLL}^{\text{eq}}}{\omega_L} \coth\left(\frac{\omega_K}{2k_B T} \right) - 2k_B T \sum_\alpha \frac{a_K^{(\alpha\alpha)}}{I_{\alpha\alpha}} \right] \tag{10.40}$$

10.3 Other Approaches for Calculating Vibrationally Averaged NMR Properties

As previously mentioned, there are other approaches for calculating the vibrational contributions to molecular properties. The list presented here is not meant to be exhaustive, but intended to give the reader a flavor of other approaches in use for calculating vibrationally averaged NMR properties. Although each of these methods have more severe limitations on the size of molecular systems amenable for accurate investigations than the perturbation approach, they also have certain advantages.

In one approach the vibrational contributions to the properties are determined by solving the vibrational differential equation numerically [5, 33–35]. This is usually done either by the Numerov–Cooley method [4, 36] or the finite element method [37]. By calculating the vibrational contributions in this way, the vibrational wavefunction can be determined practically exactly. The accuracy of the vibrationally averaged property is thus determined by the quality of the electronic wavefunction alone. In practice the method is however limited to diatomic molecules, where the potential energy surface is one-dimensional, making the approach not applicable for most molecular systems.

The main limitation in calculating the ro-vibrational contributions to properties in polyatomic molecules using perturbation theory is the type of potential energy surface that can be treated. Perturbation theory will only account for the ro-vibrational motion on single-well potential energy surfaces, or a potential energy surface

where tunneling between the different wells is insignificant. The approach does therefore not account for tunneling effects in the vibrational wavefunction, such as those giving rise to the large H–H scalar quantum exchange spin–spin coupling constants found in some transition metal hydrides [38–43]. Although we will not go into the details of this effect (the interested reader is instead referred to Ref. [44]), it is worth noting that this coupling constant can be viewed as arising from the exchange of protons in the metal hydride complex, and that they often display an exponential increase with increasing temperature.

One way to calculate the ro-vibrational average of a molecular property on all types of potential energy surfaces, is by quantum Monte-Carlo (QMC) simulations on the nuclear framework (see for instance Ref. [6]). Given enough sampling points, the QMC approach will solve the vibrational problem equally well within the limits of accuracy imposed by the electronic structure method used. The disadvantage is that property calculations are needed in a large number of nuclear configurations, typically in the range of about 6000 for small- to medium-sized hydrocarbons [45, 46]. This puts serious constraints on the electronic structure method that can be used in such simulations, thus reducing the overall quality of the results.

Another approach that can be utilized for all types of potential energy surfaces is to use snapshots of molecular dynamics simulations (or the entire dynamics runs) [47–51], so far most commonly used in order to model solvent effects, as such studies will implicitly include the motion of the nuclear framework. However, since there is no representative "unperturbed" reference system, such an approach will, in general, not allow the vibrational contribution to the calculated molecular property to be isolated. The approach furthermore shares the same problem as the QMC approach in that a large number of nuclear configurations may be needed. For more details about molecular dynamics simulations, see Chapter 11 by Searles and Huber.

Let us finally mention that a vibrationally averaged property can also be calculated by deriving the vibrational wavefunction variationally [7] from some model Hamiltonian (see for instance Ref. [52]). These vibrational wavefunctions can in turn be used to calculate the vibrational average of some property as an expectation value, for instance for shielding or spin–spin coupling constants [53, 54].

10.4 Examples of Vibrational Contributions to NMR Properties

We finally give a few illustrative examples of the importance of including vibrational corrections in the calculation of NMR properties. Our purpose is not to give an exhaustive description of available investigations in the literature, but rather to give illustrations of the importance of ro-vibrational corrections in accurate calculations of nuclear shieldings and indirect spin–spin coupling constants. We also hope that the reader will get an impression of the quality of the calculated results that can be obtained for temperature effects and isotope shifts.

10.4.1
Nuclear Magnetic Shielding Constants

The most comprehensive and accurate studies of ro-vibrational corrections to diatomic molecules have been presented by Sundholm, Gauss and Schäfer [33, 55]. They presented highly accurate CCSD(T) calculations for the nuclear shieldings of five diatomic molecules, calculating the ro-vibrational corrections numerically. Although the vibrational corrections to these molecules have been studied in several other investigations, we consider the results of Sundholm et al. to be the most accurate presented to date, and therefore focus our discussion on their results.

The results from their investigations are collected in Tab. 10.1. From this table we see that the zero-point vibrational corrections vary from about –0.35 ppm for protons, to more than –30 ppm for the fluorine nucleus in F_2. For F_2, the ZPVC accounts for almost 15% of the vibrationally averaged shielding. The changes in the shieldings when increasing the temperature from 0 K to 300 K is approximately an order of magnitude smaller than the zero-point vibrational corrections.

Table 10.1. Absolute shieldings, zero-point vibrational corrections, and temperature corrections calculated at the CCSD(T) level for selected diatomic molecules. Results taken from Ref. [33]. All results reported in ppm.

Molecule	Nucleus	σ_0	σ_{ZPV}	$\sigma_{T=300\ K}-\sigma_{ZPV}$	$<\sigma>_{300\ K}$	Experiment
$^1H_2$	H	26.667	–0.355	–0.014	26.298	26.363(4)
$^1H^{19}F$	H	29.01	–0.323	–0.035	28.48	28.5(2)
$^1H^{19}F$	F	419.68	–10.00	–0.42	409.2	410(6)
$^{13}C^{16}O$	C	5.29	–2.24	–0.15	2.9	1.0(12)
$^{12}C^{17}O$	O	–53.5	–5.73	–0.35	–59.3(20)	–42.3(172)
$^{15}N_2$	N	–58.7	–4.03	–0.24	–62.7(10)	–61.6
$^{19}F_2$	F	–197.53	–30.87	–4.69	–225.5	–232.8(60)

Let us briefly discuss the results for $C^{17}O$ in Tab. 10.1 in some more detail. The result for this molecule differs significantly from the experimental estimate, although within the rather generous experimental error bar. Since $C^{17}O$ is the basis for the absolute shielding scale of oxygen, Sundholm et al. proposed a new absolute shielding scale for ^{17}O of –59.34±2 ppm for the oxygen shielding in $C^{17}O$ based on their accurate calculations.

This value was corroborated by RASSCF calculations by Vaara et al. on the water molecule [56]. Since the electron correlation problem is much simpler in water than in CO, the absolute shielding in water is an attractive alternative for establishing an absolute shielding scale for oxygen. The ro-vibrational corrections were however calculated using perturbation theory. By using the absolute shielding constant calculated for the oxygen nucleus in water and the experimental chemical shift between water and carbon monoxide, they proposed an absolute shielding constant for $C^{17}O$ of –62.3±1.4 ppm. This result was in turn corroborated by a recent reinvestigation of

the spin–rotation constant of $C^{17}O$ [57], which leads to an absolute oxygen shielding constant for $C^{17}O$ of –62.7±0.6 ppm [58].

In an investigation of more than 40 different organic molecules [18], it was found that the ZPVCs to the proton shieldings were transferable between molecules, depending only on the functional nature of the carbon to which the protons were attached. We have collected the transferable ZPVCs reported in Ref. [18] in Tab. 10.2. The reason for this transferability of the proton ZPVCs can be traced to the local nature of the vibrational motion of the proton, which only affects other nuclei to a very limited extent during their vibrational motions. Similar transferability of the zero-point vibrational corrections was not observed for the shielding constants of other nuclei such as carbon [2, 18, 59] or fluorine [2].

Table 10.2. Transferable zero-point vibrational corrections to proton shieldings attached to different functional groups as given in Refs. [3, 18]. All results reported in ppm.

Molecule	Average ZPV to σ^H
Methane	–0.59
$-CR_2\mathbf{H}$	–0.70±0.11
$=CR\mathbf{H}$	–0.46±0.13
$\equiv C\mathbf{H}$	–0.76±0.01
H-CRO	–0.55±0.06
RO-**H**	0.48±0.13
RN-$\mathbf{H}_2$	–0.18±0.03
RCOO-**H**	–0.49±0.06
Ar-**H**	–0.39±0.06

Turning to isotope shifts we will discuss only briefly recent calculations on water [56, 60] and the series of molecules CX_2 (X=O,S,Se,Te). For water, several highly accurate calculations of the isotope shifts have been presented, and a few of these are collected and compared to experimental observations in Tab. 10.3. As can be seen, good agreement is observed for most of these isotope shifts, which has to be considered impressive considering the small magnitude of some of these isotope shifts such as for instance the shifts due to oxygen isotopic substitution, changing the proton shielding by only 1–2 ppb. There are, however, fairly large differences between the different theoretical results despite the fact that both calculations used MCSCF wavefunctions with only slightly different active spaces. The reasons for these discrepancies remain unclear, though the fact that Ref. [56] used a computed force field, whereas Ref. [60] used an experimentally derived force field may be one important source of these observed differences.

In cases where relativistic effects become important, and in particular spin–orbit effects (see Chapter 13 by Vaara, Manninen and Lantto and Chapter 14 by Autschbach), the vibrational corrections may also be affected. The most striking example of this is the proton shieldings in hydrogen bromide and hydrogen iodide [61, 62]. At the non-relativistic level, the zero-point vibrational correction in hydrogen iodide is

calculated to be –0.26 ppm, whereas the inclusion of the spin–orbit contribution *reverses the sign* of the vibrational correction, leading to a ZPVC of +0.99 ppm. The reason for this dramatic change in the ZPVC is the coupling of the magnetic moment to the external magnetic field through the spin–orbit and Fermi contact operators, and this contribution shows a very strong and oppositely directed geometry dependence compared to the non-relativistic contributions to the shielding. The importance of spin–orbit contributions to the geometry dependence of nuclear shieldings was also nicely illustrated for the series of molecules CX_2 (X=O,S,Se,Te), where it was possible to reproduce the experimentally observed secondary isotope shifts on carbon only when spin–orbit contributions were included in the calculations [63, 64].

Table 10.3. Isotope shifts in water measured for the oxygen relative to $H_2{}^{17}O$, and for the proton shieldings relative to $H_2{}^{16}O$. All results reported in ppb.

Method	Ref.	$HD^{17}O$ σ_O	$D_2{}^{17}O$ σ_O	$HD^{16}O$ σ_H	H_2O σ_H
MCSCF	[56]	1600	3180	43	2
MCSCF	[60]	1360	2700	39	2
Exp. (cyclohexane)	[86]	1550(50)	3090(50)		
Exp. (gas phase)	[87]		4040(350)		
Exp. (nitromethane)	[88]	1386(1)	2764(1)		
Exp. (liquid)	[89]		3080(200)		
Exp. (acetone)	[90]			30(3)	
Exp. (liquid)	[91]				2
Exp. (nitromethane)	[92]				1.1(1)

The field of temperature effects on shieldings in polyatomic molecules in the gas phase was pioneered, experimentally as well as theoretically, by Jameson and coworkers in the early 90s [65–68]. Considering the crudeness of the theoretical methods used in these early works (both in terms of the basis sets that could be used as well as the fact that most of the calculations were done at the Hartree–Fock level), the agreement between the theoretical and experimental results is very good. We would in particular like to point out the analysis of NH_3 and PH_3, where it was demonstrated that the non-local inversion mode of the ammonia molecule had to be modeled explicitly rather than by using a perturbation expansion in order to be able to reproduce the experimentally observed temperature dependence of the isotope shifts. In contrast, a perturbation analysis proved sufficient in the case of PH_3 due to the much higher barrier to inversion in this molecule. Unfortunately, little attention has been paid to the use of the temperature dependence of nuclear shieldings as a means to understand intermolecular interactions and the details of the ro-vibrational wavefunction since these early works.

10.4.2
Indirect Spin–Spin Coupling Constants

Theoretical investigations of the ro-vibrational contributions to indirect spin–spin coupling constants, including secondary isotope effects, have been investigated in a number of studies. These effects have usually been calculated using either the second-order polarization propagator approach (SOPPA) [19–22, 24, 69, 70] or MCSCF linear response theory [71–73].

Lately, DFT has also been shown to give good estimates of the zero-point vibrational contribution to spin–spin coupling constants [1]. Due to the low cost of DFT calculations, it has been possible to extend the size of the molecules, making it possible to investigate vibrational contributions to indirect spin–spin coupling constants for molecules consisting of 10–15 atoms.

Although investigations for larger molecules are beginning to appear [1, 74], most studies of ro-vibrational contributions to indirect spin–spin coupling constants have been carried out on somewhat smaller molecules. For these molecules, the difference between theory and experiment is often no larger than the ro-vibrational contributions, and the inclusion of these effects reduces the discrepancy between theory and experiment significantly [1, 75].

As an example of this we have listed the single point calculations, ro-vibrational contributions and experimental results for three small molecules in Tab. 10.4. The single-point calculations are all calculated using a RASSCF type wavefunction [75–77], whereas the ZPVC ΔJ_{ZPV} are calculated from Eq. (10.21) using DFT [1]. The temperature effects for C_2H_2 [22] and CH_4 [78] are calculated at the SOPPA(CCSD) level of theory, using isotope-independent versions of Eq. (10.35), (10.36) and (10.39). For HF, the temperature effect is calculated using a RASSCF type wavefunction from a somewhat different set of equations [72, 79].

Table 10.4. Different contributions to the ro-vibrational averaged indirect nuclear spin–spin coupling constants (Hz); $J_{T=300} = J_{\mathrm{eq}} + \Delta J_{\mathrm{ZPV}} + \Delta J_{T=300\ \mathrm{K}}$

	Ref.	$^1H^{19}F$	Ref.	$^{13}C_2{}^1H_2$				Ref.	$^{13}C^1H_4$	
		$^1J_{H,F}$		$^1J_{C,C}$	$^1J_{C,H}$	$^2J_{C,H}$	$^3J_{H,H}$		$^1J_{C,H}$	$^2J^*_{H,H}$
J_{eq}	[76]	544.2	[75]	184.7	244.3	53.1	10.9	[77]	120.6	–13.2
ΔJ_{ZPV}	[1]	–37.7	[1]	–9.3	4.7	–2.8	–0.1	[1]	5.3	–0.7
$\Delta J_{T=300\ \mathrm{K}}$	[72]	–2.8	[22]	1.0	0.0	0.5	0.1	[78]	0.1	0.0
$J_{T=300}$		503.7		176.4	249.0	50.8	10.9		126.0	–13.9
$J_{\mathrm{Exp.}}$	[80]	500	[93]	174.8	247.6	50.1	9.6	[24]	125.3	–12.8[a]

a Experimental $^2J^*_{\mathrm{HH}}$ found from $^2J_{\mathrm{HD}}$ using $^2J^*_{\mathrm{HH}} = \frac{\gamma_H}{\gamma_D}{}^2J_{\mathrm{HD}}$

Considering the values found for the ZPVCs in Tab. 10.4, it is clear that inclusion of these effects may change the indirect spin–spin coupling constants significantly. The results in this table suggest that the ZPVC may be as large as 7% of the equilibrium value, and it has in fact been shown that it may be larger than 10% for some smaller coupling constants [1,74]. The importance of including vibrational effects is

particularly evident for the $^1J_{HF}$ coupling constant in HF. Although estimates for the ZPVC of this coupling constant vary, calculations and experimental results indicate that this contribution is somewhere between 25 and 40 Hz [1, 72, 80].

Comparison of the ZPVCs with the temperature effects suggests that changing the temperature from 0 to 300 K changes the ro-vibrational contribution by 10–15% [19–22, 24, 69, 70], as illustrated in Tab. 10.4. The only exception is the $^2J_{CH}$ coupling constant in C_2H_2 where the temperature effect is found to be as large as the ZPVC. However, the ZPVC is almost negligible for this coupling constant. For the temperature effects, the largest change in the indirect spin–spin coupling constant is found for the $^1J_{HF}$ coupling constant in HF, where the coupling constant changes by 2.8 Hz when the temperature is increased from 0 to 300 K.

Comparing the calculated total value of the spin–spin coupling constant, $J_{T=300} = J_{eq} + \Delta J_{ZPV} + \Delta J_{T=300\,K}$, with experiment, we see that all numbers are within a few Hz of the experimental values. The importance of including nuclear motion is obvious when comparing this discrepancy with the magnitude of the ro-vibrational corrections which may be as large as 30 Hz.

As an example of calculations of ZPVCs for larger molecules, the results for benzene [1] are listed in Tab. 10.5. The best calculated results using both MCSCF [81] and DFT [1] are also listed in this table, together with a set of experimental results [81, 82]. As seen, the inclusion of ZPVC does not improve the agreement between the single point calculations and experiment. Based on the quality of the DFT ZPVC [1] to the indirect spin–spin coupling constants, better single point results for benzene are clearly needed.

Table 10.5. Indirect nuclear spin-spin coupling constants of benzene (Hz). DFT results are collected from Ref. [1], while the MCSCF results are found in Ref. [81]. Experimental results are found in Ref. [81], except for the HH-couplings which are collected from Ref. [82].

	$J_{eq}^{B3LYP\ a}$	$J_{eq}^{MCSCF\ b}$	$\Delta J_{ZPV}^{B3LYP\ a}$	$J_{tot}{}^{c}$
$^1J_{C,C}$	60.0	70.9	–0.1	56.0
$^2J_{C,C}$	–1.8	–5.0	–0.8	–2.5
$^3J_{C,C}$	11.2	19.1	0.7	10.1
$^1J_{C,H}$	166.3	176.7	4.8	158.6
$^2J_{C,H}$	2.0	–7.4	–0.4	1.0
$^3J_{C,H}$	8.0	11.7	0.5	7.5
$^4J_{C,H}$	–1.2	–1.3	–0.3	–1.3
$^3J_{H,H}$	8.7		0.5	7.5
$^4J_{H,H}$	1.3		0.2	1.4
$^5J_{H,H}$	0.8		0.1	0.7

a Ref. [1].
b Ref. [81].
c Ref. [81], and Ref. [82] for the HH coupling constants.

There have recently been several theoretical studies published concerning secondary isotope effects using the SOPPA(CCSD) approach [19–22, 24, 69, 70]. There have

also been many experimental studies in this area, which have been reviewed several times [83–85].

When discussing secondary isotope effects, it is useful to distinguish between isotopic substitution of hydrogen and of heavier elements. The effects of isotopic substitution in heavier elements is exemplified in Tab. 10.6, where both theoretical and experimental changes in the ro-vibrational contributions are given for $H^{13}C^{13}CH$ relative to $H^{12}C^{13}CH$ at 300 K [22]. We note that the secondary isotope effects involving the substitution of heavier elements are very small. The small magnitude of the secondary isotope effects is due to the relatively small change in the nuclear mass, which again implies that the nuclear wavefunction does not change much. Since the error bars in the experimental results are of the same magnitude as the secondary isotope effects [22], no conclusions as to the quality of the theoretical results can be drawn based on a comparison for these isotopomers.

Table. 10.6. Secondary isotope effects, ΔJ^{sec}, in $H^{13}C^{13}CH$ relative to $H^{12}C^{13}CH$ at 300 K. The total ro-vibrational contributions, $J^{ro\text{-}vib}$, are also listed (Hz) [22].

	$J^{ro\text{-}vib}$	ΔJ^{sec}	
		Calc.	Exp.
^1J(C,H)	4.866	–0.001	–0.013
^2J(C,H)	–3.703	0.019	0.016
^3J(H,H)	–1.272	0.001	0.009

Isotopic substitution of hydrogen, however, changes the nuclear wavefunction significantly. As illustrated for the $^1J_{C,H}$ coupling constant in methane, see Tab. 10.7, substitution of hydrogen might change the ro-vibrational contribution to the indirect spin–spin coupling constants by up to 25%. However this is not always the case, as illustrated for $^2J_{H,D}$ in Tab. 10.7. For this coupling constant the secondary isotope effect is almost negligible compared to the ro-vibrational contribution. A comparison of the SOPPA(CCSD) calculations and the experimental results for $^1J_{C,H}$ suggests that this theoretical approach can calculate the secondary isotope effect quite accurately. The theoretical and experimental results differ by about 10%.

Table 10.7. Secondary isotope effects at 300 K, ΔJ^{sec} , in ^1J(C,H) and ^2J(H,D) relative to $^{13}CH_4$ and $^{13}CH_3D$ respectively. The total ro-vibrational contributions, $J^{ro\text{-}vib}$, are listed (Hz) [20].

	$^1J^{ro\text{-}vib}_{C,H}$	$\Delta^1J^{sec}_{C,H}$		$^2J^{ro\text{-}vib}_{H,D}$	$\Delta^2J^{sec}_{H,D}$
		Calc[a]	Exp.[b]		Calc. [a]
$^{13}CH_3D$	4.737	–0.397	–0.356	–0.688	
$^{13}CH_2D_2$	4.343	–0.791		–0.689	–0.001
$^{13}CHD_3$	3.956	–1.179	–1.046	–0.687	0.001

a Ref. [20]. **b** Ref. [31].

It is worth noting that the calculations published so far suggest that secondary isotope effects are almost unaffected by temperature changes [22], and almost all of the secondary isotope effects can therefore be estimated by considering the ZPVC only.

10.5 Summary

We have in this chapter briefly reviewed the perturbation theory approach for calculating ro-vibrational corrections to NMR parameters at an arbitrary expansion point. Emphasis has been put on describing the computational considerations that have to be made in the choice of expansion point and coordinate system for the perturbation expansion. We have also given a few examples of theoretical calculations of zero-point vibrational corrections, isotope shifts and temperature effects on the nuclear magnetic shielding constants and indirect spin–spin coupling constants. We have demonstrated that modern ab initio calculations of NMR parameters have reached such a high level of accuracy that the effects of the motion of the nuclear framework cannot be ignored when comparing with highly accurate experimental observations.

Acknowledgement

This work has received support from the Norwegian Research Council through a Strategic University Program in Quantum Chemistry (Grant No 154011/420).

References

1 T. A. Ruden, O. B. Lutnæs, T. Helgaker et al., *J. Chem. Phys.* **2003**, *118*, 9572.
2 P.-O. Åstrand, K. Ruud, *Phys. Chem. Chem. Phys.* **2003**, *5*, 501.
3 K. Ruud, P.-O. Åstrand, P. R. Taylor, *Int. J. Comput. Methods. Sci Eng.* **2003**, *3*, 7.
4 C. E. Clifford, D. J. Malik, *J. Chem. Phys.* **1987**, *87*, 2806.
5 D. Sundholm, J. Gauss, R. Ahlrichs, *Chem. Phys. Lett.* **1995**, *243*, 264.
6 M. C. Böhm, J. Schulte, R. Ramiréz, *Int. J. Quantum Chem.* **2002**, *86*, 280.
7 H. Wei, T. Carrington, *J. Chem. Phys.* **1992**, *97*, 3029.
8 C. W. Kern, R. L. Matcha, *J. Chem. Phys.* **1968**, *49*, 2081.
9 M. Toyama, T. Oka, Y. Morino, *J. Mol. Spectrosc.* **1964**, *13*, 193.
10 P.-O. Åstrand, K. Ruud, P. R. Taylor, *J. Chem. Phys.* **2000**, *112*, 2655.
11 K. Ruud, P.-O. Åstrand, P. R. Taylor, *J. Chem. Phys.* **2000**, *112*, 2668.
12 W. T. Raynes, J. Geertsen, J. Oddershede, *Int. J. Quantum Chem.* **1994**, *52*, 153.
13 V. E. Ingamells, M. G. Papadopolous, A. J. Sadlej, *J. Chem. Phys.* **2000**, *112*, 1645.
14 V. E. Ingamells, M. G. Papadopolous, A. J. Sadlej, *Chem. Phys.* **2000**, *260*, 1.
15 E. B. Wilson Jr, J. C. Decius, P. C. Cross, *Molecular Vibrations*, McGraw-Hill, New York **1955**.
16 P.-O. Åstrand, K. Ruud, D. Sundholm, *Theor. Chem. Acc.* **2000**, *103*, 365.
17 P.-O. Åstrand, G. Karlström, A. Engdahl et al., *J. Chem. Phys.* **1995**, *102*, 3534.

18 K. Ruud, P.-O. Åstrand, P. R. Taylor, *J. Am. Chem. Soc.* **2001**, *123*, 4826.
19 R. D. Wigglesworth, W. T. Raynes, S. P. A. Sauer et al., *Mol. Phys.* **1998**, *94*, 851.
20 R. D. Wigglesworth, W. T. Raynes, S. P. A. Sauer et al., *Mol. Phys.* **1997**, *92*, 77.
21 S. P. A. Sauer, W. T. Raynes, R. A. Nicholls, *J. Chem. Phys.* **2001**, *115*, 5994.
22 R. D. Wigglesworth, W. T. Raynes, S. Kirpekar et al., *J. Chem. Phys.* **2000**, *112*, 3735, Erratum, *J. Chem. Phys.* **2001**, *114*, 9192.
23 S. P. A. Sauer, C. K. Møller, H. Koch et al., *Chem. Phys.* **1998**, *238*, 385.
24 B. Bennett, W. T. Raynes, W. Anderson, *Spectrochim. Acta Part A* **1989**, *45*, 821.
25 A. J. Russell, M. A. Spackman, *Mol. Phys.* **1995**, *84*, 1239.
26 A. J. Russell, M. A. Spackman, *Mol. Phys.* **1996**, *88*, 1109.
27 A. J. Russell, M. A. Spackman, *Mol. Phys.* **1997**, *90*, 251.
28 L. Råde, B. Westergren, *Mathematics Handbook for Science and Engineering*, 4th edition, Springer, Berlin **1999**.
29 T. A. Ruden, P. R. Taylor, T. Helgaker, *J. Chem. Phys.* **2003**, *119*, 1951.
30 A. R. Hoy, I. M. Mills, G. Strey, *Mol. Phys.* **1972**, *24*, 1265.
31 B. Bennett, W. T. Raynes, C. W. Anderson, *Spectrochim. Acta Part. A* **1989**, *45*, 821.
32 K. Ruud, J. Lounila, J. Vaara, unpublished results.
33 D. Sundholm, J. Gauss, A. Schäfer, *J. Chem. Phys.* **1996**, *105*, 11051.
34 J. Gauss, D. Sundholm, *Mol. Phys.* **1997**, *91*, 449.
35 V. E. Ingamells, M. G. Papadopoulos, A. J. Sadlej, *Chem. Phys. Lett.* **2000**, *316*, 541.
36 J. W. Cooley, *Math. Comput.* **1961**, *15*, 363.
37 O. Zienkiewicz, *The Finite Element Method*, McGraw-Hill, London **1977**.
38 T. Arliguie, B. Chaudret, J. Devillers et al., *C. R. Acad. Sci. Paris*, **1987**, *305II*, 1523.
39 A. Antinolo, B. Chaudret, G. Commenges et al., *J. Chem. Soc., Chem. Commun.* **1988**, 1210.
40 K. W. Zilm, D. M. Heinekey, D. M. Millar et al., *J. Am. Chem. Soc.* **1989**, *111*, 3089.
41 D. H. Jones, J. A Labinger, D. P. Weitekamp, *J. Am. Chem. Soc.* **1989**, *111*, 3087.
42 E. M. Hiller, R. A. Harris, *J. Chem. Phys.* **1994**, *100*, 2522.
43 S. Szymański, *J. Chem. Phys.* **1996**, *104*, 8216; Erratum, *J. Chem. Phys.* **1997**, *106*, 3430.
44 F. Maseras, A. Lledós, E. Clot et al., *Chem. Rev.* **2000**, *100*, 601.
45 M. C. Böhm, R. Ramiréz, J. Schulte, *Chem. Phys.* **1998**, *227*, 271.
46 M. C. Böhm, J. Schulte, E. Hernández et al., *Chem. Phys.* **2001**, *264*, 371.
47 V. G. Malkin, O. L. Malkina, G. Steinebrunner et al., *Chem. Eur. J.* **1996**, *2*, 452.
48 M. Cossi, O. Crescenzi, *J. Chem. Phys.* **2003**, *118*, 8863.
49 B. Mennucci, J. M. Martinez, J. Tomasi, *J. Phys. Chem. A* **2001**, *105*, 7287.
50 B. G. Pfommer, F. Mauri, S. G. Louie, *J. Am. Chem. Soc.* **2000**, *122*, 123.
51 Q. Cui, M. Karplus, *J. Phys. Chem. B* **2000**, *104*, 3721.
52 D. J. Diestler, V. McKoy, *Mol. Phys.* **1997**, *92*, 430.
53 J. E. Del Bene, M. J. T. Jordan, S. A. Perera et al., *J. Phys. Chem. A* **2001**, *105*, 8399.
54 M. J. T. Jordan, J. S. S. Toh, J. E. Del Bene, *Chem. Phys. Lett.* **2001**, *346*, 288.
55 D. Sundholm, J. Gauss, *Mol. Phys.* **1997**, *92*, 1007.
56 J. Vaara, J. Lounila, K. Ruud, T. Helgaker, *J. Chem. Phys.* **1998**, *109*, 8388.
57 G. Cazzoli, L. Dore, C. Puzzarini et al., *Phys. Chem. Chem. Phys.* **2002**, *4*, 3575.
58 R. E. Wasylishen, D. E. Bryce, *J. Chem. Phys.* **2003**, *117*, 10061.
59 A. A. Auer, J. Gauss, J. F. Stanton, *J. Chem. Phys.* **2003**, *118*, 10407.
60 R. D. Wigglesworth, W. T. Raynes, S. P. A. Sauer et al., *Mol. Phys.* **1999**, *96*, 1595.
61 B. Minaev, J. Vaara, K. Ruud et al., *Chem. Phys. Lett.* **1998**, *295*, 455.
62 B. Cromp, T. Carrington Jr., D. R. Salahub et al., *J. Chem. Phys.* **1999**, *110*, 7153.
63 J. Lounila, J. Vaara, Y. Hiltunen et al., *J. Chem. Phys.* **1997**, *107*, 1350.
64 P. Lantto, J. Vaara, A. M. Kantola et al., *J. Am. Chem. Soc.* **2002**, *124*, 2762.
65 C. J. Jameson, A. K. Jameson, S. M. Cohen et al., *J. Chem. Phys.* **1981**, *74*, 1608.
66 C. J. Jameson, A. C. de Dios, A. K. Jameson, *J. Chem. Phys.* **1991**, *95*, 9042.
67 C. J. Jameson, A. C. de Dios, A. K. Jameson, *J. Chem. Phys.* **1991**, *95*, 1069.
68 C. J. Jameson, *Chem. Rev.* **1991**, *91*, 1375.
69 J. Oddershede, J. Geertsen, G. E. Scuseria, *J. Phys. Chem.* **1988**, *92*, 3056.

70 S. P. A. Sauer, C. K. Møller, H. Koch et al., *Chem. Phys.* **1998**, *238*, 385.
71 O. Vahtras, H. Ågren, P. Jørgensen et al., *J. Chem. Phys.* **1992**, *96*, 6120.
72 P.-O. Åstrand, K. Ruud, K. V. Mikkelsen et al., *J. Chem. Phys.* **1999**, *110*, 9463.
73 J. Casanueva, J. San Fabián, E. Díez et al., *J. Mol. Struct.* **2001**, *565*, 449.
74 T. A. Ruden, T. Helgaker, M. Jaszuński, *Chem. Phys.* **2003**, *296*, 53.
75 M. Jaszuński, K. Ruud, *Chem. Phys. Lett.* **2001**, *336*, 473.
76 J. San Fabián, J. Casanueva, E. San Fabián et al., *J. Chem. Phys.* **2000**, *112*, 4143.
77 J. Guilleme, J. San Fabián, *J. Chem. Phys.* **1998**, *109*, 8168.
78 T. Enevoldsen, J. Oddershede, S. P. A. Sauer, *Theor. Chim. Acta* **1998**, *100*, 275.
79 P.-O. Åstrand, K. V. Mikkelsen, *J. Chem. Phys.* **1996**, *104*, 648.
80 S. M. Bass, R. L. DeLeon, J. S. Muenter, *J. Chem. Phys.* **1987**, *86*, 4305.
81 J. Kaski, J. Vaara, J. Jokisaari, *J. Am. Chem. Soc.* **1996**, *118*, 8879.
82 R. Laatikainen, J. Ratilainen, R. Sebastian et al., *J. Am. Chem. Soc.* **1995**, *117*, 11006.
83 C. J. Jameson, H.-J Osten, *J. Am. Chem. Soc.* **1986**, *108*, 2497.
84 N. M. Sergeyev, in *NMR Basic Principles, Progress*, Vol. 22, p. 31, Springer, Berlin **1990**.
85 C. J. Jameson, *Encyclopedia of NMR*, Wiley, Chichester **1996**, p. 2638.
86 R. E. Wasylishen, J. O. Friedrich, *Can. J. Chem.* **1987**, *65*, 2238.
87 W. T. Raynes, *Mol. Phys.* **1983**, *49*, 443.
88 N. M. Sergeyev, N. D. Sergeyeva, W. T. Raynes, *J. Magn. Reson.* **1999**, *137*, 311.
89 O. Lutz, H. Oehler, *Z. Naturforsch. A* **1977**, *32*, 131.
90 J. R. Holmes, D. Kivelson, W. C. Drinkard, *J. Chem. Phys.* **1962**, *37*, 150.
91 B. Sredni, S. Pinchas, *J. Magn. Reson.* **1972**, *7*, 289.
92 N. D. Sergeyeva, J. P. Jacobsen, N. M. Sergeyev, *J. Chem. Soc., Chem. Commun.* **1998**, 1355.
93 K. Jackowski, M. Wilczek, M. Pecul et al., *J. Phys. Chem. A* **2000**, *104*, 9806.

11
Molecular Dynamics and NMR Parameter Calculations

Debra J. Searles and Hanspeter Huber

11.1
Introduction

Although in some cases the gas phase NMR parameters may be close to those of a molecule in its solvent, in cases where there are strong interactions between the solvent and the molecule studied, this is not the case. This is particularly important in solutions such as aqueous solutions where the solvent is polar, and hydrogen bonding may occur. The calculation of NMR parameters for liquids has only become possible in the last 15 years. Most accurate calculations of this type involve the use of fluid simulations to provide typical fluid configurations, in conjunction with a quantum chemical calculation to determine the NMR parameter of interest. Although fluid simulations and reasonably accurate quantum mechanical calculations of molecules were possible well before this time, the complication that delayed the development of the calculation of these properties was the necessity for considering intermolecular interactions in the quantum mechanical calculations when fluids are treated. This generally requires much larger basis sets with polarisation functions and diffuse functions and inclusion of electron correlation must be at a higher level. (see Ref. [1]).

Today it is possible to calculate NMR properties of liquids which are of similar accuracy to experiment for electric field gradients (EFGs) and chemical shifts for liquids composed of small molecules. Apart from direct predictive capacities, the advantage of determining these parameters using molecular dynamics simulations in conjunction with quantum mechanical calculations is that the simulations give us a clear picture of the microscopic structure of the fluid and may be able to lead to models of the fluid and response of NMR properties to liquid state conditions.

In this chapter we will outline the current approaches in which simulations are combined with quantum mechanical calculations to determine NMR properties, and highlight some important investigations that have been carried out. An overview of work in this field until approximately the end of 2000 is included in our chapter in *Encyclopedia of Nuclear Magnetic Resonance: A Supplement* [2], and we will refer to that review for details of work discussed there. Another important review in this field [3] discusses ab initio methods for the calculation of solvent effects on the NMR shielding and spin–spin coupling. For more detailed discussions on the use of

Calculation of NMR and EPR Parameters. Theory and Applications.
Edited by Martin Kaupp, Michael Bühl, Vladimir G. Malkin
Copyright © 2004 WILEY-VCH Verlag GmbH & Co. KGaA, Weinheim
ISBN: 3-527-30779-6

extended systems and continuum solvent models, the reader is referred to Chapter 16 by Mauri and Pickard and Chapter 12 by Ciofini.

Molecular dynamics (MD) simulation is a well established technique for the study of liquids and provides a means of determining structural and dynamic properties and understanding the structure of the fluid and dynamics in fluids on a molecular level. It can be combined with ab initio quantum chemical calculations to determine NMR parameters. Molecular dynamics simulations involve modeling a liquid by treating each molecule or atom as a particle. An initial configuration of the liquid is generated and the forces on each atom (or molecule) are calculated. In the usual 'classical' MD simulations, a force field is determined from a potential energy hypersurface (that is developed using empirical methods, quantum mechanical methods, or a combination of these before the simulation is commenced). The forces are then used in Newton's equations of motion to update the configuration. This process is repeated to generate a trajectory (a contiguous set of configurations) for the fluid. Usually, the microcanonical ensemble is explored by the trajectory, however other ensembles can be modeled by modification of the equations of motion [4]. Two extensions of the classical MD simulations that incorporate the quantum mechanics more thoroughly are the Born–Oppenheimer (BO) MD simulations where the forces at each timestep are calculated quantum mechanically and the classical Newtonian equations of motion are solved, and the ab initio Car–Parrinello (CP) MD simulations, where quantum mechanical calculations are performed at each step of the simulation to solve the Car–Parrinello equations of motion [5].

In Section 11.2 we summarize the methods that are currently employed to determine NMR properties of liquids. In Section 11.3 we discuss the NMR parameters that have been calculated using quantum mechanical methods in conjunction with molecular dynamics simulations, highlighting important recent developments and examples of systems that have been studied. The most thoroughly investigated system is liquid water due to the importance of this system and the significant difference in the properties of the gas phase water monomer and the liquid water systems. A comparison of results obtained for liquid water using different methods will therefore be presented in Section 11.3.

11.2 Methods

11.2.1 The Cluster Method [2, 3]

In the cluster method, quantum chemical calculations are carried out on an ensemble of supermolecules, which are clusters of molecules representing the molecule of interest surrounded by solvent. In order to ensure that the ensemble of supermolecules properly represents the liquid, the clusters are generated using Monte Carlo (MC) simulations or from single configurations ('snapshots') of a classical simulation trajectory formed using molecular dynamics (MD) simulations [4]. In the clus-

ter method, a molecule is randomly selected from the molecules in the MC or MD liquid snapshot, and the configuration of molecules near the central molecule is used to form the cluster. The cluster method is illustrated in Fig. 11.1.

Generally, in order to adequately model a bulk liquid, and thus to obtain clusters of the correct structure, the MC or MD simulations involve hundreds or thousands of molecules in periodic boundary conditions [4]. However, for calculations of NMR parameters, it has been shown that the clusters extracted from this bulk liquid as input for the quantum mechanical calculations can be considerably smaller [6]. The size of the cluster will vary with the size of the molecule, the solvent, the parameter to be calculated and the accuracy required. For determination of the deuterium QCC in water, clusters of five molecules were found to be adequate [6], whereas for chemical shifts in water more than 13 molecules may be necessary [7]. Naturally, the precision of the calculation is improved with the number of clusters considered, and the number of clusters included must consider a reasonable balance between the time required for the calculation and the thoroughness of sampling of the liquid state ensemble.

In CPMD or BOMD simulations, at each step of a simulation an ab initio calculation is carried out using all the molecules in the unit cell. These potentially provide a more realistic model of the system, however the time required for the calculations is considerably longer and therefore smaller unit cells must be used and simulation times are inevitably much shorter, limiting the sampling of the liquid state phase space. Use of density functional theory (DFT) has made simulations of small systems feasible using these methods. Clusters of molecules can be generated using these simulations in the same way that they are generated using classical simulations, and the properties can be calculated.

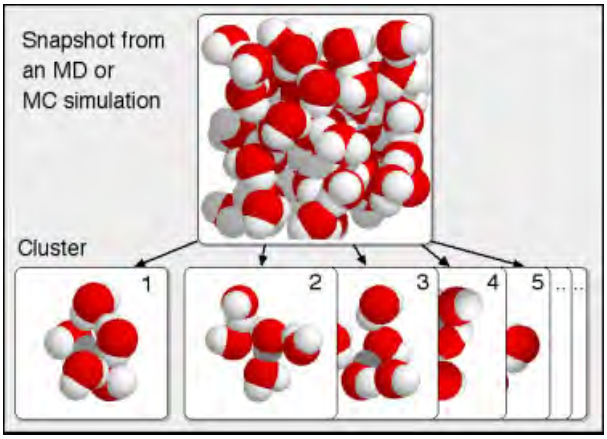

Figure 11.1 In the cluster method one (as in the figure) or more snapshots from a simulation are used to extract clusters around atoms of interest. Here clusters of size five are selected around water protons of interest (dark proton in the center of the clusters) to calculate the proton chemical shielding. Each cluster is treated as a supermolecule in a quantum chemical calculation and the average is obtained to yield the chemical shielding in the liquid.

The limitations of CPMD simulations are demonstrated by Bühl and co-workers [8] where, for a highly charged system ($[Fe(CN)_6]^{4-}$), CPMD simulations were unable to produce reliable results for the ^{57}Fe chemical shift due to interactions between periodic images of the ion in the simulations, which produced unreasonable structures. This problem is unavoidable using CPMD due to the restricted system size that can currently be considered (in Ref. [8] a complex ion surrounded by 44 water molecules was simulated). To circumvent this problem, simulations of a droplet of 449 water molecules surrounding the complex ion were carried out. In order to reduce the computational effort required, while allowing study of a sufficiently large system that boundary effects would be negligible could be studied, the BOMD simulations embedded a molecular mechanics calculation on the water molecules in a quantum mechanical treatment of the complex ion. This method enabled accurate determination of the ^{57}Fe chemical shift [8, 9] in solution.

In some cases, the main effect of the solvent molecules on the molecular property is due to electrostatic effects [10] and such a solvent in the cluster can be modeled as a simple distribution of charges (an electrostatic model). However, in general, the full electronic effects should be considered using a quantum chemical calculation. In order to optimize the results obtained for NMR properties of fluids, the quantum chemical calculations on the clusters can be designed explicitly for the problem to be solved. In the calculation of local properties, such as an electric field gradient EFG or a chemical shift, a very accurate basis set is required close to the location of interest, smaller basis sets in the next region and only small basis sets far away. This scheme was developed under the name "basis sets of high local quality" in the early eighties [2].

If clusters are selected randomly from MC or MD configurations the method can only be used to obtain static properties like chemical shifts or nuclear quadrupole coupling constants (NQCCs). However it is also possible to select clusters as a time sequence from one molecular trajectory, so that time-dependent properties like the relaxation time can be calculated, although with limited statistical accuracy (see e.g. Ref. [11]).

The cluster method was developed in the early 1990s and since then has been used to calculate various liquid state properties. Algorithms have been developed to calculate properties including vibrations [12], NQCCs [6], chemical shifts [13], spin–spin couplings [14], electronic spectra [15], and EPR hyperfine couplings [16]. These algorithms have been applied extensively since these early papers and extended to study a wide range of liquids. In this chapter we will discuss the calculation of chemical shifts, NQCCs, EFGs and relaxation times and spin–spin coupling using the cluster method.

11.2.2 Use of Property Surfaces

The cluster method described above requires a quantum mechanical calculation to be carried out for each cluster that is generated. An alternative method involves the use of quantum mechanical calculations to generate a function that represents the

dependence of the property on the configuration of the cluster *before* the simulation is carried out. This is analogous to the generation of a potential energy function or hypersurface from a grid of potential energy data, that allows the potential energy of a molecule or supermolecule with any configuration to be determined. The property surface is then incorporated into the simulation program and is used to determine the property as the simulation proceeds. Use of an a priori calculated property surface is particularly important in the determination of properties that involve integration of time-correlation functions, for example the quadrupolar relaxation time [17, 18] , which requires the property to be determined at each step of a simulation and a simulation period that is sufficient for the time-correlation function to decay to zero. It would be prohibitive to carry out such a calculation if it was necessary to perform quantum mechanical calculations at every step of the simulation (typically many thousands) in order to accurately determine the time-correlation function. Use of this method is most suitable for properties that are only dependent on a few structural parameters, which is usually the case if the property is pair-additive: that is, the property of a molecule in the liquid is well represented by a sum of the effect of each individual solvent molecule [19]. In these cases, construction of the surface is not prohibitive. If the property is pair-additive, a dimer property surface is sufficient to calculate the property of any liquid state configuration. Pair-additive property surfaces have been shown to be excellent for calculation of EFGs [20] and chemical shifts [21] in water where pair-additivity is not a good approximation for the potential energy surface. This means that accurate and precise calculation of relaxation times can be carried out, which would be impossible using the cluster method (Section 11.2.1).

11.2.3
Periodic Treatments of NMR Properties (see Chapter 16)

If CP or BO MD methods are used it is reasonable to calculate properties, such as NMR parameters, simultaneously incorporating the periodicity of the system into the property calculations. Although it would also be possible to do this when conventional, classical simulations are carried out, the property calculations would be very time-consuming compared to the simulations and therefore impractical. The periodicity can be implemented for the calculation of NMR properties in various ways, as discussed below. The advantage of these methods is that cluster size is not limited but, as discussed in Section 11.2.1, a disadvantage is that the time required for the calculations is considerably longer. As well as smaller unit cells and shorter simulation times, less rigorous methods can be used in the quantum mechanical calculation of both the force field and the property of interest.

A number of different methods have been used to deal with the periodic boundary conditions in the determination of the NMR properties of liquids. The simplest method is to explicitly include a finite number of periodic images of the cell [22]. This is clearly very computationally demanding and the number of images that can be considered is restricted. In order to address this in Ref. [22] the water molecules were treated as point charges. This is not always a good approximation [23].

Perhaps the first proposal for calculation of NMR properties of condensed matter using methods that fully account for the periodicity of the system was the Mauri–Pfrommer–Louie (MPL) method [24–26]. This approach is discussed in Chapter 16.

Putrino, Sebastiani and Parrinello [27] suggested an alternative method where variational density functional perturbation theory is used in conjunction with advanced gradient correction formulae to determine vibrational modes, Raman scattering and chemical shifts. This method has also been applied to calculate the chemical shifts of a biomolecule [28]. More recently Parrinello and co-workers have developed a method in which exponentially decaying Wannier orbitals [29, 30] are used, the localised nature of which reduces the computation time. Rather than expanding the magnetic field as a periodic function (as in the MPL method), a periodic position operator is defined. These methods have been used to determine chemical shifts in liquid water [30].

11.2.4
Continuum Methods (see Chapter 12)

In this approach, the solvent is treated using continuum models or a reaction field. It is the method that is commonly incorporated in quantum chemical packages to model solvent effects. Figure 11.2 illustrates how the system is modeled in this scheme. The molecule of interest is assumed to reside in a "cavity", with a continuum of fluid existing around the cavity which interacts with the molecular electric field via a reaction field. The reaction field thus models the long-range electrostatic and inductive interactions between the solvent and the solute. The method can be improved by including solvent molecules in the cavity [2, 3, 31–33], and has been modified to treat the intermolecular field using a perturbation theory [34, 35]. These methods have been discussed in detail by Helgaker et al. [3], in Section XIII D.

Zhan and Chipman [36] showed that if a reaction field is employed, use of a surface polarisation term to represent the electrostatic potential produced by the solvent polarisation is not generally adequate, and that inclusion of volume polarization effects is important.

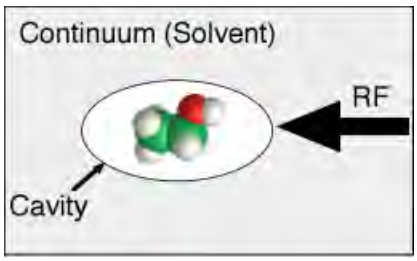

Figure 11.2 The continuum or reaction field methods place the solute molecule in a cavity and treat the solvent as a continuum, which reacts on the molecular electric field by a reaction field (RF). The cavity might be a sphere, an ellipsoid as shown in the figure, or a more complicated shape following the surface of the molecule. One of the problems of these methods for the calculation of NMR properties seems to be the extreme sensitivity of the latter to the (empirical) size of the cavity.

A growing amount of evidence suggests that reaction-field type methods are insufficient to examine the effects of solvents, and that the solvent molecules need to be explicitly taken into account [37, 38]. The explicit inclusion of solvent molecules has been shown to be particularly important when hydrogen-bridged systems are considered [38]. As more solvent molecules are included, this method approaches the cluster method discussed above.

Nymand et al. [34] have determined the chemical shifts of water. The polarisable continuum model (PCM) has been used to determine the chemical shifts of CH_3CN and CH_3NO_2 in water [39], diazines in various solvents [38] and the ^{17}O shift of *N*-methylformamide in aqueous solution [40].

11.2.5 Other Methods

Hirata and co-workers [41, 42] have developed a method known as the reference interaction site model combined with a self-consistent field calculations approach (RISM-SCF approach) where the solvent and solute are both treated at the atomic level. This method only takes into account the effect of electrostatic interactions on the electronic structure of the solute, and disregards the electron overlap. It is suggested [42] that the neglect of the intermolecular overlap of the electrons may be responsible for the lack of quantitative agreement and this is confirmed using a molecular cluster model. Hirata and co-workers intend including this effect in an extended theory [42].

Two methods that do not involve liquid simulations, but can be used to predict chemical shifts of liquids are the quantum cluster equilibrium (QCE) method [2, 43] and the Boltzmann averaging method [44]. We discuss them briefly here, and present some results obtained using these methods in Section 11.3

The QCE method uses quantum statistical thermodynamics to determine the clusters that should be present, and the probability that they would be observed in the liquid state canonical ensemble at the required temperature, pressure and composition [45]. The cluster populations obtained are then used to determine an expectation value of the properties of interest, such as the chemical shifts and the NQCC [43].

The Boltzmann averaging method is similar to the QCE method, but involves determination of the energy and NMR property of interest as a function of the structure of the molecule, fitting an analytical function to the data. The expectation value for the NMR property is obtained for the canonical ensemble by directly substituting these functions and carrying out a numerical integration. Swalina et al. [44] discuss the Boltzmann averaging method, and use it in a study of the temperature dependence of chemical shifts of an isolated molecule. They compare the results with a MD study. To simplify generation of the potential energy and chemical shift functions, only the torsional variations are considered by Swalina et al. In their MD study the energy was obtained from an empirical potential and the shifts were averaged from 20,000 snapshots of the gas phase molecule, however they obtain poor

results using this method due to the use of a poor torsional potential to generate the force fields. The Boltzmann method is probably limited to a few degrees of freedom, whereas the MD method is more general and easily extended to include solvent effects (i.e. the cluster method). The Boltzmann method applied in a discrete way (summing over clusters rather than generating a function and integrating) is equivalent to the QCE method. The Boltzmann averaging method can also be readily extended to study solvent effects [44].

11.2.6 Combinations of Methods

It seems natural that the best and most widely applicable approach may come from combining a number of different methods. The combination of cluster methods and continuum methods has been mentioned in Section 11.2.3 as a way of improving the continuum methods. However, combination of the methods may not always be straightforward. Mennucci et al. [32] found that results obtained from a cluster method calculation on acetonitrile in chloroform were more accurate than those obtained when the same clusters were treated in combination with a continuum calculation. It is unclear whether the pure cluster calculations were fortuitously close to the experimental result, or if the way in which the approaches were combined was inadequate. The convergence of results obtained by the cluster method alone and then with a combination of the cluster method and a continuum method has been tested by Barone et al. [40] who found that the number of clusters required for convergence of the ^{17}O shift of *N*-methylformamide in aqueous solution is considerably reduced when the combined method is used. It is expected that the convergence will be sensitive to the system studied.

11.3 Examples

11.3.1 Chemical Shifts

The first paper that we are aware of that described the determination of the change in the chemical shift as clusters are formed using ab initio calculations was by Jackowski [46] who looked at ^{13}C and ^{15}N chemical shifts in acetonitrile and compared them with the gas-to-liquid change in the chemical shift determined experimentally. In 1993, Svishchev and Kusalik [47] carried out the first calculation of a liquid state NMR parameter that used MD simulations in order to generate the configurations. In that work liquid water was considered.

Most of the calculations of the chemical shift in the late 1990s were on water at ambient conditions. A summary of the results of that work is given in Ref. [2] and will not be repeated here. However, Tab. 11.1 shows the results that were presented

there together with more recent results that are discussed below. Care should be taken in consideration of the difference in the experimental chemical shift for liquid water and gaseous water due to the difficulty of referencing the two values to the same scale.

Table 11.1 Difference between the proton and ^{17}O chemical shifts of water in the gas and liquid phases.

Reference	Difference between gas and liquid phase chemical shift		Method
	proton	^{17}O	
Hirata et al. (2000) [41]	–1.81	+23.0	RISM-SCF approach (see Section 2.8.2.5); using empirical potential
Hirata et al. (2001) [42]	–1.821		RISM-SCF approach (see Section 2.8.2.5); using empirical potential
Mikkelsen et al. (1996) [31]	–0.95	+9.4	Continuum Method
Mikkelsen et al. (1996) [31]	–3.97	–16.4	Continuum Method; containing first solvation shell in cavity
Nymand and Åstrand (1997) [35]	–3.04	–7.39	Continuum Method including perturbation theory
Chesnut and Rusiloski (1994) [13]	–2.3±1.6	–20.3±9.6	Cluster Method; CFF-91 force field; HF-GIAO method for shift calculations
Cui and Karplus (2000) [48]	–2.5	–27.6	Cluster Method; 100 clusters; QM/MM method with rigid TIP3P potential; DFT calculations on the B3LYP/6-311G(d,p) level
Cui and Karplus (2000) [48]	–2.9	–22.3	Cluster Method; 100 clusters; QM/MM method with flexible TIP3P potential; DFT calculations on the B3LYP/6-311G(d,p) level
Cui and Karplus (2000) [48]	–2.8	–32.0	Cluster Method; 10 clusters; QM/MM with rigid TIP3P potential; DFT calculations on the B3LYP/6-311++G(d,p) level
Malkin et al. (1996) [7]	–2.8±0.3	–44.8±2.3	Cluster Method; 10 clusters of 9 molecules; flexible TIP3P potential; SOS-DFPT with an IGLO-III basis set
Malkin et al. (1996) [7]	–3.0±0.3	–46.6±4.4	Cluster Method; 10 clusters of 9 molecules; Bopp et al. potential [49]; SOS-DFPT with an IGLO-III basis set
Malkin et al. (1996) [7]	–3.4±0.4	–36.8±2.7	Cluster Method; 10 clusters of 9 molecules; MYCL potential [50]; SOS-DFPT with an IGLO-III basis set
Pfrommer et al. (2000) [26]	–5.8±0.1	–36.6±0.5	Periodic Boundary Method; CPMD; BLYP functional; 32 molecules in PBCs
Sebastiani and Parrinello (2001) [29]	–4.1	–30	Periodic Boundary Method; CPMD with Wannier orbitals; 32 molecules in PBCs; 9 ps trajectory

Reference	Difference between gas and liquid phase chemical shift		Method
	proton	^{17}O	
Sebastiani and Parrinello (2002) [30]	–5.1		Periodic Boundary Method; CPMD with Wannier orbitals; 32 molecules in PBCs; 9 ps trajectory (different trajectory to that in [29])
Ludwig (2002) [43]	–4.35		QCE method; up to 8 molecules per cluster
Experiment: proton: [51, 52]; ^{17}O: [53, 54]	–4.3	–36.1	Experiment

The most recent results by Sebastiani and Parrinello use CPMD simulations, fully accounting for the periodicity [29, 30] (see Tab. 11.1). The variational perturbation that is employed was described in Ref. [27]. In their recent work Sebastiani and Parrinello applied the variation perturbation method with Wannier orbitals (localized) to liquid water at standard conditions, with 32 molecules per cell, and employing the BLYP density functional. They obtained good agreement with experiment for H but poor agreement for O, which is attributed to use of a pseudopotential within the frozen core approximation. However, the possibility of an error in the experimental results should not be dismissed. In Ref. [30], H liquid-gas shifts in two supercritical states are also considered (0.73 g cm^{-3}, 653 K and 0.32 g cm^{-3}, 647 K).

New results for liquid water have also been obtained using the QCE method [43]. Results for ammonia, hydrogen sulfide and phosphine were also obtained. Excellent agreement with experiment is obtained for water (note that in their Fig. 7, the proton chemical shift in water is compared with a much older experimental value and better agreement is obtained with the later experimental value of –4.3 ppm [51, 52]), fair agreement is obtained for ammonia (–1.29 ppm cf. experimental: –1.05 ppm) and poor agreement with experiment is obtained for hydrogen sulfide (–0.25 ppm cf. experimental: –1.50 ppm) and phosphine (0.04 ppm cf. experimental: –0.78 ppm).

Chemical shift anisotropies have been determined by Cui and Karplus [48] who find that the change in the oxygen chemical shift anisotropy in going from gas to liquid is just 0.2 and –3.2 ppm, using the rigid and flexible water model, respectively, and the change in the hydrogen chemical shift anisotropy is 6.0 and 7.7 ppm, respectively.

In the past three years, the types of solutions for which chemical shift calculations have been carried out has been extended.

Bühl and co-workers have carried out a number of calculations of chemical shifts of transition metal ions and complex ions in solution [8, 9, 22, 23]. Transition metal nuclei are known to exhibit large ranges of chemical shift, and therefore it is of interest to study the changes in chemical shift due in solution. Bühl and Parrinello [22] carried out CPMD simulations of three vanadium complexes with 28 to 30 mole-

cules in a periodic cell, and calculated the chemical shifts for snapshots of a trajectory of 1 ps duration. Periodic boundary conditions were not used in the chemical shift calculations, however the water molecules in the unit cell and six adjacent boxes were represented as point charges. Temperature and solvent shifts were calculated. Effects of the order of 30 ppm were observed due to solvation; these are small relative to the absolute chemical shifts (~600 ppm) and the range of vanadium chemical shifts. The calculated chemical shifts of the solutions differed from the experimental values by up to ~150 ppm, and although the relative experimental shift of $[H_2VO_4]^-$ and $[VO_2(OH_2)_4]^+$ in aqueous solution is well reproduced (15 ppm (expt) and 18 ppm (calc)), the experimental and calculated chemical shifts of $[VO(O_2)_2(OH_2)]^-$ in solution relative to $[H_2VO_4]^-$ and $[VO_2(OH_2)_4]^+$ differ. The experimental chemical shift of $[VO(O_2)_2(OH_2)]^-$ in solution is larger than either $[H_2VO_4]^-$ or $[VO_2(OH_2)_4]^+$, but the calculated value is smaller. No explanation was found for this, however the authors suggest that better functionals are needed. Point charges were used to represent the water molecules and were shown to be adequate. Although the authors assume, or show qualitatively by the radial distribution function, that the equilibration was long enough to yield at least an equilibrium first solvation shell, it could be possible that the typical equilibration time of 0.5 ps and sampling over 1 to 2 ps is too short for equilibration between vibrational and other degrees of freedom (typically 10 ps in water), and for organising and sampling of the possible water-complex structures.

Bühl et al. [8, 9, 23] carried out a similar study on anionic Fe complexes in solution (see Section 11.2.1). However, in this case an explicit treatment of the water molecules was found to be necessary (a point charge representation of the water was inadequate). A recent study by Bühl of the ^{55}Mn and ^{17}O chemical shifts of MnO_4^- in water [23] followed a similar scheme. The periodic simulation cell included 30 water molecules, and clusters containing 10 water molecules were sampled and used in the chemical shift calculations (periodicity was not treated in the chemical shift calculations). As with Fe anions, it was found necessary to include the water molecules explicitly. Negligible shifts in the chemical shift of ^{55}Mn were observed, but a shift of 31 ppm was observed for ^{17}O.

In 2001, a biological problem was solved using a chemical shift calculation [55, 56]. The problem was treated using CPMD [55]. An experimental study has shown that two different ^{13}C peaks appear from the carboxylic groups of the two aspartyl residues next to the central hydroxy group in the pepstatin A/HIV-1 protease complex. The structure suggested by the experimentalists turns out to be unstable in a CP simulation and the structure to which it evolves does not have two significantly different ^{13}C resonances. Hence a new diprotonated structure is suggested, which is the most stable diprotonated form and gives reasonable agreement with the experimental shifts as well as with the isotopic shifts.

Casanovas et al. [57] compared calculations and experimental determinations of chemical shifts of the carbon atoms in *p*-menthane-3,9-diols. In this work, the two most populated conformations of the molecules were determined using molecular dynamics simulations and the arrangement of the solvent was obtained. Calculations of the chemical shifts were carried out on these clusters with 3 solvent mole-

cules in most cases and up to 16 solvent molecules in some cases. A more rigorous (and time-consuming) result could be obtained by considering an ensemble of configurations rather than just the most stable conformations, however, as seen in this work, the changes in the carbon chemical shifts are very small. Nevertheless, studies of the chemical shifts of flexible molecules in solution would be of importance when the chemical shifts vary greatly.

In the last few years, during development of better computational routes to solution phase properties, the N chemical shifts in acetonitrile and pyridine were determined by Mennucci et al. [32] and the ^{17}O shift of *N*-methylformamide in aqueous solution was determined by Barone et al. [40]

11.3.2 Electric Field Gradients and Relaxation

Early work on the calculation of the EFGs and quadrupole relaxation focused on the study of monatomic ions and atoms where the EFG is produced solely by the solvent (see Ref. [2]). The earliest calculations were on the EFG at the nucleus of configurations of Li^+, Na^+ and Cl^- in solution that were determined using Monte Carlo simulations [58, 59] and in 1984 the work was extended to MD simulations, yielding relaxation times from first principles for the first time [60].

The deuterium NQCC of liquid water is an interesting candidate for study since both the molecular structure and intermolecular interactions have significant influence on the EFG. In addition, the strong intermolecular interactions in hydrogen bonded liquid water mean that the influence of neighboring molecules in the cluster will be important. Now, good agreement between the calculated and experimental values of the D and ^{17}O NQCC in liquid water is obtained. These results are discussed in detail in Ref. [2].

As well as liquid water, systems including liquid CO_2 [61] (^{17}O NQCC), liquid ammonia [62] (^{14}N and deuterium NQCC), methanol in carbon tetrachloride [63] (hydroxy-deuterium NQCC of methanol), dimethyl sulfoxide in water [64, 65] (deuterium NQCC) have been determined using the cluster method (for further discussion of these systems, see Ref. [2]).

Recently QCE calculations have been carried out [43] to determine the difference between the liquid and gas-phase deuterium NQCC in water, ammonia (calculated: –14 kHz; experimental: –15 kHz to –28 kHz) (Note: the gas values given in Ref. [43] are incorrect (see Ref. [66]) and should be 260 kHz), hydrogen sulfide and phosphine. For hydrogen sulfide and phosphine the calculated shifts are only a few kHz and can probably not be detected experimentally.

More recently work has been carried out in order to determine the quadrupolar relaxation in liquid water and in a mixture of water and dimethyl sulfoxide [17, 18]. It was not obvious that the EFG at the deuterium nucleus in water would be well represented by the pair-additive approximation, especially since pair-additivity is a poor assumption for the potential, however it was recently shown that the EFGs at deuterium nuclei in liquid water are highly pair additive [20]. Again, the use of pair-additivity results in substantial computer time savings in the quantum chemical cal-

culation of the EFGs, and hence their NQCCs, for nuclei in liquid systems using the so-called cluster approach. It also permits the simulation of quadrupolar relaxation times from EFG hypersurfaces obtained within the pair-additive approximation [17, 18].

11.3.3
Spin–Spin Coupling and Magnetic Susceptibility

There has been relatively little work on spin–spin coupling and magnetic susceptibility in liquid systems. (see Ref. [2]). We are aware of only two recent papers in this field.

Autschbach and Ziegler [37] have recently carried out quantum mechanical calculations of ^{195}Pt and ^{199}Hg spin–spin couplings in a series of coordination compounds with an increasing number of solvent molecules. Convergence towards the liquid values is observed, as well as reasonable semi-quantitative agreement with experiment. Charge donation of the solvent to the coordinated heavy atom and into the heavy atom–ligand bonds suggests that explicit inclusion of solvent molecules is important. It is anticipated that the coordination number of these heavy atoms in solution is high since better agreement with experiment is obtained with clusters containing a larger number of solvent molecules [37]. This work does not properly sample the liquid solution configuration (only a single optimised geometry is considered for the clusters) however, due to the agreement with experiment that they obtain, Autschbach and Ziegler suggest that this might not be required.

The magnetic susceptibility of normal and supercritical water has been calculated by Sebastiani and Parrinello using CPMD simulations and incorporating the periodicity of the system in the property calculations [30]. An approach to determine the magnetic susceptibility of a periodic system was also presented by Mauri and Louie [24], although solids were considered rather than liquids.

11.4
Summary and Conclusions

The methods described above have been applied to a wide range of systems. The continuum methods are the most widely used schemes as they are readily implemented and give results relatively quickly and automatically, however they are not generally very accurate. In order to get good results, the microscopic features need to be built into them, making them more and more like a cluster method and removing the advantage of a seamless implementation.

The cluster method has been widely used with both classical simulations and CPMD or BOMD simulations to generate the trajectories. The cluster method using classical simulations gives good results for the systems studied, is straightforward to implement, can be applied to a wide range of systems and the calculation of the NMR property can be carried out using a high level of quantum mechanical theory. CPMD simulations are necessary in some cases in order to properly model the solu-

tion, however these simulations are still extremely time-consuming and therefore only relatively small systems can be studied for short periods of time. Furthermore, it is necessary to use DFT, which may not be sufficiently accurate for some systems. Nevertheless, the number of systems treated using this method has increased considerably over the past few years.

Acknowledgements

This work is part of the project 2000-066530.01 of the Schweizerischer Nationalfonds zur Förderung der Wissenschaften. We thank the Australian Research Council for support of this work.

References

1 H. Huber, A. J. Dyson, B. Kirchner, *Chem. Soc. Rev.* **1999**, *28*, 121.
2 D. J. Searles, H. Huber, in *Encyclopedia of Nuclear Magnetic Resonance: Supplementary Volume*, John Wiley & Sons, **2002**, p. 215, and references therein.
3 T. Helgaker, M. Jaszunski, K. Ruud, *Chem. Rev.* **1999**, *99*, 293.
4 M. P. Allen, D. J. Tildesley, *Computer Simulation of Liquids*, Clarendon Press, Oxford **1987**.
5 K. Laasonen, M. Sprik, M. Parrinello et al., *J. Chem. Phys.* **1993**, *99*, 9080.
6 R. Eggenberger, S. Gerber, H. Huber et al., *J. Chem. Phys.* **1992**, *97*, 5898.
7 V. G. Malkin, O. L. Malkina, G. Steinebrunner et al., *Chem. Eur. J.* **1996**, *2*, 452.
8 M. Bühl, F. T. Mauschick, *Phys. Chem. Chem. Phys.* **2002**, *4*, 5508.
9 M. Bühl, F. T. Mauschick, F. Terstegen et al., *Angew. Chem. Int. Ed. Engl.* **2002**, *41*, 2312.
10 J. Vaara, J. Jokisaari, T. T. Rantala et al., *Mol. Phys.* **1994**, *82*, 13.
11 C. Scheurer, N. R. Skrynnikov, S. F. Lienin et al., *J. Am. Chem. Soc.* **1999**, *121*, 4242.
12 K. Hermansson, S. Knuts, J. Lindgren, *J. Chem. Phys.* **1991**, *95*, 7486.
13 D. B. Chesnut, B. E. Rusiloski, *J. Mol. Struct. (Theochem)* **1994**, *314*, 19.
14 D. A. Case, C. Scheurer, R. Brüschweiler, *J. Am. Chem. Soc.* **2000**, *122*, 10390.
15 K. Coutinho, S. Canuto, *J. Mol. Struct. (Theochem)* **1993**, *106*, 99.
16 H. Takase, O. Kikuchi, *Chem. Phys.* **1994**, *181*, 57.
17 E. H. Hardy, M. G. Müller, P. S. Vogt et al., *J. Chem. Phys.* **2003**, *119*, 6184.
18 M. G. Müller, E. H. Hardy, P. S. Vogt et al., in preparation.
19 A. Halkier, B. Kirchner, H. Huber et al., *Chem. Phys.* **2000**, *253*, 183.
20 M. G. Müller, B. Kirchner, P. S. Vogt et al., *Chem. Phys. Lett.* **2001**, *346*, 160.
21 M. G. Müller and H. Huber, *Collect. Czech. Chem. Commun.*, accepted.
22 M. Bühl, M. Parrinello, *Chem. Eur. J.* **2001**, *7*, 4487.
23 M. Bühl, *J. Phys. Chem. A* **2002**, *106*, 10505.
24 F. Mauri, S. G. Louie, *Phys. Rev. Lett.* **1996**, *76*, 4246.
25 F. Mauri, B. G. Pfrommer, S. G. Louie, *Phys. Rev. Lett.* **1996**, *77*, 5300.
26 B. G. Pfrommer, F. Mauri, S. G. Louie, *J. Am. Chem. Soc.* **2000**, *122*, 123.
27 A. Putrino, D. Sebastiani, M. Parrinello, *J. Chem. Phys.* **2000**, *113*, 7102.
28 D. Sebastiani, G. Goward, I. Schnell et al., *Comput. Phys. Commun.* **2002**, *147*, 707.
29 D. Sebastiani, M. Parrinello, *J. Phys. Chem. A* **2001**, *105*, 1951.
30 D. Sebastiani, M. Parrinello, *Chem.Phys. Chem.* **2002**, *3*, 675.
31 K. V. Mikkelsen, K. Ruud, T. Helgaker, *Chem. Phys. Lett.* **1996**, *253*, 443.

32 B. Mennucci, J. M. Martinez, J. Tomasi, *J. Phys. Chem. A* **2001**, *105*, 7287.
33 K. V. Mikkelsen, K. Ruud, T. Helgaker, *J. Comput. Chem.* **1999**, *20*, 1281.
34 T. M. Nymand, P.-O. Åstrand, K. V. Mikkelsen, *J. Phys. Chem. B* **1997**, *101*, 4105.
35 T. M. Nymand, P.-O. Åstrand, *J. Chem. Phys.* **1997**, *106*, 8332.
36 C.-G. Zhan, D. M. Chipman, *J. Chem. Phys.* **1999**, *110*, 1611.
37 J. Autschbach, T. Ziegler, *J. Am. Chem. Soc.* **2001**, *123*, 3341.
38 B. Mennucci, *J. Am. Chem. Soc.* **2002**, *124*, 1506.
39 R. Cammi, B. Mennucci, J. Tomasi, *J. Chem. Phys.* **1999**, *110*, 7627.
40 V. Barone, O. Crescenzi, R. Improta, *Quant. Struct.-Act. Relat.* **2002**, *21*, 105.
41 T. Yamazaki, H. Sato, F. Hirata, *Chem. Phys. Lett.* **2000**, *325*, 668.
42 T. Yamazaki, H. Sato, F. Hirata, *J. Chem. Phys.* **2001**, *115*, 8949.
43 R. Ludwig, *Phys. Chem. Chem. Phys.* **2002**, *4*, 5481.
44 C. W. Swalina, E. P. O'Brien, G. Moyna, *Magn. Reson. Chem.* **2002**, *40*, 195.
45 F. Weinhold, *J. Chem. Phys.* **1998**, *109*, 367.
46 K. Jackowski, *Chem. Phys. Lett.* **1992**, *194*, 167.
47 I. M. Svishchev, P. G. Kusalik, *J. Am. Chem. Soc.* **1993**, *115*, 8270.
48 Q. Cui, M. Karplus, *J. Phys. Chem. B* **2000**, *104*, 3721.
49 P. Bopp, G. Jancsó, K. Heinzinger, *Chem. Phys. Lett.* **1983**, *98*, 129.
50 G. C. Lie, E. Clementi, *Phys. Rev. A* **1986**, *33*, 2679.
51 J. C. Hindman, *J. Chem. Phys.* **1966**, *44*, 4582.
52 W. T. Raynes, *Nucl. Magn. Reson.* **1978**, *7*, 1.
53 W. T. Raynes, *Mol. Phys.* **1983**, *49*, 443.
54 A. E. Florin, M. Alei, *J. Phys. Chem.* **1967**, *47*, 4268.
55 S. Piana, D. Sebastiani, P. Carloni et al., *J. Am. Chem. Soc.* **2001**, *123*, 8730.
56 P. Carloni, U. Rothlisberger, M. Parrinello, *Acc. Chem. Res.* **2002**, *35*, 455.
57 J. Casanovas, A. M. Namba, S. Leon et al., *J. Org. Chem.* **2001**, *66*, 3775.
58 S. Engström, B. Jönsson, *Mol. Phys.* **1981**, *43*, 1235.
59 S. Engström, B. Jönsson, B. Jönsson, *J. Magn. Reson.* **1982**, *50*, 1.
60 S. Engström, B. Jönsson, R. W. Impey, *J. Chem. Phys.* **1984**, *80*, 5481.
61 M. Holz, R. Haselmeier, A. J. Dyson et al., *Phys. Chem. Chem. Phys.* **2000**, *2*, 1717.
62 A. Laaksonen, R. E. Wasylishen, *Z. Naturforsch. A* **1995**, *50*, 137.
63 P. J. Merkling, M. D. Zeidler, P. A. Bopp, *J. Mol. Liq.* **2000**, *85*, 57.
64 B. Kirchner, D. J. Searles, A. J. Dyson et al., *J. Am. Chem. Soc.* **2000**, *122*, 5379.
65 H. Huber, B. Kirchner, D. J. Searles, *J. Mol. Liq.* **2002**, *97–98*, 71.
66 H. Huber, *J. Chem. Phys.* **1985**, *83*, 4591.

12
Use of Continuum Solvent Models in Magnetic Resonance Parameter Calculations

Ilaria Ciofini

12.1
Introduction

Several physicochemical molecular properties such as structure, vibrational frequencies and UV–vis transitions, depend strongly on the chemical surroundings. In fact, environmental effects can hardly be neglected in order to get a realistic model of many chemical processes. Generally speaking, the surrounding medium influences the system under investigation in two ways: (i) it induces structural modifications (indirect effect); and (ii) for a given structure, it modifies the electron density distribution (direct effect).

NMR and EPR measurements, especially at high fields, are extremely sensitive to both indirect and direct effects. Therefore it is not surprising that they have been used as a probe of the intra- and inter-molecular interactions of systems in different chemical environments, especially in the case of biologically relevant species [1–4]. Since the NMR and EPR spectroscopic parameters depend explicitly on the accurate description of the density/spin density, a full quantum chemical (QM) model of the molecule itself (the solute, M) and of its interaction with the solvent (S) is mandatory.

Here, we will focus on simplified, yet reliable, methods based on the continuum model of a solvent taking into account, when necessary, their coupling with other computational approaches in order to simulate both bulk and short-range (specific) solute–solvent interactions.

The first continuum models were elaborated at the beginning of the last century [5–9] and their success relies on their simplicity and their straightforward link to physical concepts. Nevertheless current continuum models have developed much from the first simplified schemes. An extensive review of continuum models up to the most recent developments and applications can be found in several papers [10–15]. The basic idea of all continuum models is the partitioning of the solution into two subunits: the solute (M) and the solvent (S). The solute (M) is described fully at a microscopic (here quantum) level. The solvent, on the other hand, is incorporated as a continuum medium (a *continuous* electric field, the so-called *reaction field*), representing a statistical average over all solvent degrees of freedom at thermal equilibrium. The main solute–solvent interaction is electrostatic although recent

Calculation of NMR and EPR Parameters. Theory and Applications.
Edited by Martin Kaupp, Michael Bühl, Vladimir G. Malkin
Copyright © 2004 WILEY-VCH Verlag GmbH & Co. KGaA, Weinheim
ISBN: 3-527-30779-6

developments of continuum models include also non-electrostatic terms [16]. Continuum models have been successfully applied to analyse the influence of the environment on reaction rates/thermodynamics and/or to study its influence on selected observables of local, macroscopic and time-dependent nature [12, 17–20]. Nevertheless, the development of formalisms for the ab initio calculation of magnetic field dependent properties in solution has only quite recently received attention [21–25]. As a consequence, relatively few ab initio (Hartree–Fock, post-Hartree–Fock and density functional theory) calculations of magnetic resonance parameters can be found in the literature [21–36], an exception being the prediction of hyperfine coupling constants [37–39].

12.2 General Features of Continuum Models

Let us consider a solute molecule M (or a solute–solvent molecular aggregate, M–S_n) surrounded by a solvent. The solute is adjusted inside a cavity of the solvent: the first step in all continuum models (except for those without an explicit representation of the solvent [40], not considered here) is to define the size and shape of the solute cavity. Inside the cavity the solvent dielectric constant is equal to one, while, outside it, the dielectric constant is set to the solvent bulk value. The shape and size of the cavity can influence significantly the computed observable and they remain an adjustable degree of freedom for all the models. The cavity should include all (in reality most) of the solute electronic distribution but, at the same time, should not be too large in order to avoid damping of solvent effects. These facts are particularly important for charged, zwitterionic and radical species [41] as well as for the simulation of NMR parameters [24,34]. The fraction of solute charge density lying outside the cavity is usually referred to as "escaped charge". Recently, particular attention has been devoted to the development of methods that minimise the escaped charge [42]. The most commonly used cavity shapes are of three types: (i) regularly shaped cavities (spheres, ellipsoids, cylinders); (ii) molecular cavities defined as the overlap of regular shapes (spheres) centred on each atom [43] or group of atoms [44]; (iii) molecular cavities defined as the region of space surrounded by an arbitrary isodensity surface [45]. When using molecular shape cavities, additional spheres can be added out of the nuclear position [44]. Originally the radius of each atom-centred sphere was taken as Bondi's Van der Waals radius [46] increased by 20% [43]. Molecular cavities defined by an isodensity surface are advantageous since only one parameter, the isodensity value, is needed to define them. However, they seem to lead to erratic behavior when dealing with charged systems [47].

The solute–solvent interaction can be considered as a pertubation ($V_{M\text{-}S}$) of the molecular Hamiltonian (H_0) describing the isolated solute. The overall Hamiltonian (H) is given by:

$$\hat{H}(r, R, g_s) = \hat{H}_0(r, R) + \hat{V}_{M-S}(r, R, g_s) \tag{12.1}$$

where r are the electronic and R the nuclear coordinates of the solute and g_s is a thermally averaged distribution function of the solvent molecules. Solving the Schrödinger equation:

$$\hat{H}\ \Psi = \left[\hat{H}_0 + \hat{V}_{M-S}\right]\ \Psi = E\ \Psi \tag{12.2}$$

one gets the description of the solute in the presence of the solvent reaction field.

Within a classical treatment, the work (free energy, ΔG_{ele}) necessary to bring the solute M from the gas phase to solution, considering only electrostatic solute–solvent interactions, $\hat{V}^{ele}_{M-S}$, and the solute nuclear and electronic charge density, ρ^{e+n}_M, unchanged by the solvation process, is given by [48]:

$$\Delta G_{ele} = \frac{W_{ele}}{2} = \frac{\langle\ \Psi|\hat{V}^{ele}_{M-S}|\ \Psi\rangle}{2} = \frac{\int_{inside\ cav}\rho^{e+n}_M(r)\ \Phi_\sigma\ (r)dr^3}{2} \tag{12.3}$$

where Φ_σ is the electric potential generated by the polarised dielectric. Inclusion of non-electrostatic solute–solvent interactions (such as repulsion, dispersion and cavitation energies) can be found in Ref. [16].

Since Φ_σ depends on ρ^{e+n}_M which in turn depends on Φ_σ the problem to be solved is non-linear. First one has to get ρ^{e+n}_M and then solve an electrostatic problem in order to define Φ_σ. The electrostatic problem is solved using the Poisson equation that expresses the electrostatic potential as a function of the density distribution of the solute and the dielectric constant of the medium. In a compact form we can write [14]:

$$\begin{cases} -\nabla^2\Phi_\sigma = 4\pi\rho^{e+n}_M & \text{inside the cavity} \\ L\Phi_\sigma = 0 & \text{outside the cavity} \\ [\Phi_\sigma] = 0 & \text{on the cavity surface} \\ [\partial_L\Phi_\sigma] = 0 & \text{on the cavity surface} \end{cases} \tag{12.4}$$

where $[\Phi_\sigma]$ and $[\partial_L\Phi_\sigma]$ are the boundary conditions for the potential and its gradient, stating that the potential on the outside and inside of the surface and the electric field perpendicular to the surface must be equaly. The $L\Phi_\sigma$ term has a different analytical form for different types of medium. In particular in the case of a linear infinite isotropic dielectric using the Poisson equation, $L\Phi_\sigma$ is given by:

$$L\Phi_\sigma\ = -\varepsilon\nabla^2\Phi_\sigma \tag{12.5}$$

The Poisson equation is valid under the condition of zero ionic strength. In the case of an ionic solution the Poisson–Boltzmann (PB) equation, in its linearised form, valid at low ionic strength, is normally used. Formalisms for the treatment of ionic and anisotropic dielectrics have been fully developed [49].

Several approaches have been used to model both the quantum chemical (get ρ^{e+n}_M) and the electrostatic problem (define Φ_σ). Tomasi and Persico [10] grouped them into 5 classes: (1) the multipole expansion (MEP), (2) the apparent surface charge (ASC), (3) the image charge (IC), (4) the finite difference (FD), (5) the finite elements (FE) methods. Additionally we mention the methods based on the general-

ised Born approximation (GB) [50]. Here we will concentrate only on MEP and ASC methods, the most commonly used to compute NMR and EPR parameters.

Multipole expansion methods (MEP) are used in connection with regular shape cavities (spheres or ellipsoids). The total nuclear and electronic density of the solute (ρ_M^{e+n}) can be expanded into molecular multipole moments of order ℓ (M_ℓ^m). These multipole moments will interact with the reaction field (that is the electrostatic potential describing the solvent) which is also expanded in terms of multipoles (M_ℓ^m). Following the notation of Rivail and Rinaldi [51] and using the Kirkwood–Onsager model [7, 8] valid for a spherical cavity, the work necessary to bring the solute from the gas phase to solution can be expressed as:

$$\Delta G_{ele} = \frac{1}{2}\sum_{\ell=0}^{\infty}\sum_{m'=-\ell}^{\ell}\sum_{\ell'=0}^{\infty}\sum_{m'-\ell}^{\ell} M_\ell^m f_{\ell\ell'}^{mm'} M_{\ell'}^{m'} \tag{12.6}$$

where f are reaction field factors dependent on the solvent dielectric constant and cavity radius. In actual calculations of magnetic properties, the expansion is truncated to $\ell = 10$ [22]. Generalisation of this model to the use of an ellipsoidal cavity has been made by Rivail and coworkers [52].

Most of the continuum methods using molecular shape cavities solve the electrostatic problem using the apparent surface method. In this method, the electrostatic potential (Φ_o) is described via an apparent charge distribution spread over the surface of the cavity. This method, mainly developed by Tomasi and co-workers [43], is usually referred to as the polarisable continuum model (PCM) or as the MST (Miertuš –Scrocco–Tomasi) method. In this framework the irregular surface of the molecular cavity is projected onto spherical polygons divided into tesserae, and the apparent surface charge distribution is discretised as a sum of point charges placed at the centre of each tessera [53]. The apparent surface charges are partitioned into two sets depending on the source that generated them (electrons or nuclei) following the procedure proposed by Sakurai [54]. The integral equation on a volume is therefore transformed to a finite summation on surface elements. Several implementations of PCM are available nowadays depending on how the electrostatic problem is solved (such as C-PCM [55], IEF-PCM [56], QINT-PCM [57], iterative PCM [58]). Beside PCM, other ASC methods to be mentioned are Klamt's COSMO (from which the C-PCM is derived) [59], Chipman's SS(V)PE [60] and Foresman's ICPM/SCIPCM [45] methods.

The solution of the Schrödinger equation in the presence of the solvent reaction field (Eq. (12.1)) is equivalent to the minimisation of the free energy functional G:

$$G = \langle \Psi | \hat{H} - \frac{1}{2}\hat{V}_{M-S} | \Psi \rangle \tag{12.7}$$

At the Hartree–Fock level, within the PCM framework, we have:

$$\begin{aligned} G &= \langle \Psi | \hat{H} - \frac{1}{2}\hat{V}_{M-S} | \Psi \rangle = tr\mathbf{P}\tilde{\mathbf{h}} + \frac{1}{2}tr\mathbf{P}\tilde{\mathbf{G}} + V_{nn} + \frac{1}{2}U_{nn} \\ \tilde{\mathbf{h}} &= \mathbf{h} + \frac{1}{2}(\mathbf{j} + \mathbf{y}) \\ \tilde{\mathbf{G}} &= \mathbf{G}(\mathbf{P}) + \mathbf{X}_{ele}(\mathbf{P}) \end{aligned} \tag{12.8}$$

In Eq. (12.8) only electrostatic (**j**, **y**, $\mathbf{X}_{ele,}$ U_{nn}) solute–solvent interactions have been considered. **P** is the solute density matrix, **h** and **G** are the standard one and two electron matrices for the isolated solute while V_{nn} and U_{nn} are the solute–solute and solute–solvent nuclear repulsion energy. The matrices **j**, **y** (monoelectronic) and $\mathbf{X}_{ele}$ (bielectronic) represent the contribution to the potential due to the electrostatic solute–solvent interactions and they depend explicitly on the apparent charges spread over the surface cavity. Since the apparent charges depend on solute charge density distribution the solution is obtained by solving iteratively the modified Fock equation:

$$\begin{aligned} \tilde{\mathbf{F}}\mathbf{C} &= \mathbf{S}\mathbf{C}\varepsilon \\ \tilde{\mathbf{F}} &= \tilde{\mathbf{h}} + \tilde{\mathbf{G}} \end{aligned} \tag{12.9}$$

12.2.1 NMR and EPR Parameters within the Framework of Continuum Models

Early attempts to compute magnetic properties using continuum models are due to Rivail [61], Webb [62] and Bishop [63]. More recently Mikkelsen has developed a multiconfigurational-self consistent field multipolar reaction field method (MC-SCF MEP) to compute a wide range of magnetic properties including nuclear magnetic shielding, electric field gradient and spin–spin coupling [22,29]. In these treatments the solvent is included as a reaction field via the MEP approach and spherical cavities are used. The solvent contribution to the total energy in the presence of a homogeneous magnetic field (equilibrium solvent response) can be written as:

$$E_{sol}(\mathbf{B}) = \sum_{\ell m} g_\ell \left(\langle T_{\ell m} \rangle \right)^2 \tag{12.10}$$

where $\langle T_{\ell m} \rangle$are the solute electronic and nuclear charge moment and g_ℓ depends on the dielectric constant of the solvent (ε), on the cavity size (R_{cav}) and on the order of the multipole-moment expansion parameter (ℓ) as [22]:

$$g_\ell = -\frac{1}{2} R_{cav}^{-(2\ell+1)} \frac{(\ell+1)(\varepsilon+1)}{\ell+(\ell+1)\varepsilon} \tag{12.11}$$

The solvent contribution to any second order properties (such as for instance nuclear magnetic shielding) can then be expressed as:

$$\frac{\partial E_{sol}(\mathbf{B})}{\partial\alpha\partial\beta} = 2\sum_{\ell m} g_\ell \langle T_{\ell m} \rangle \frac{\partial^2 \langle T_{\ell m} \rangle}{\partial\alpha\partial\beta} + 2\sum_{\ell m} g_\ell \frac{\partial \langle T_{\ell m} \rangle}{\partial\alpha} \frac{\partial \langle T_{\ell m} \rangle}{\partial\beta} \tag{12.12}$$

The calculation of paramagnetic and diamagnetic spin–orbit contributions (PSO and DSO) as well as the evaluation of spin dipole (SD) and Fermi contact (FC) contributions to spin–spin coupling constants in the presence of the solvent reaction field, using the linear response function of the solvated molecule, have been also implemented [22]. Gauge invariant atomic orbitals (GIAO) [64] are used to avoid gauge dependence. Following Cammi's recent implementation of a MCSCF-PCM scheme [19], the evaluation of indirect spin–spin coupling constants at the MCSCF-

PCM level have become possible, although for the moment only HF/DFT results have been published [66].

Concerning the use of ASC methods, Cammi developed [21] a formalism to evaluate nuclear shieldings at Hartree–Fock (HF) and density functional theory (DFT) level using molecular shape cavities within the framework of PCM. Using the general expression for the second derivatives of G with respect to any arbitrary parameters [65], we can write (here the superscript indicates the variable with respect to which the derivation is performed):

$$\frac{\partial^2 G}{\partial\alpha\partial\beta} = tr\mathbf{P}\tilde{\mathbf{h}}^{\alpha,\beta} + \frac{1}{2}tr\mathbf{P}\tilde{\mathbf{G}}^{\alpha,\beta}(\mathbf{P}) - tr\mathbf{S}^{\alpha,\beta}\mathbf{W} + \tilde{V}_{\mathrm{nn}}^{\alpha\beta} + tr\mathbf{P}^{\beta}\tilde{\mathbf{h}}^{\alpha} + tr\mathbf{P}^{\beta}\tilde{\mathbf{G}}^{\alpha}(\mathbf{P}) - tr\mathbf{S}^{\alpha}\mathbf{W}^{\beta} \tag{12.13}$$

where:

$$\begin{aligned} &\mathbf{W} = \mathbf{P}\tilde{\mathbf{F}}\mathbf{P} \\ &\tilde{\mathbf{F}}(\beta) = \tilde{\mathbf{h}}^{\beta} + \tilde{\mathbf{G}}^{\beta}(\mathbf{P}) \end{aligned} \tag{12.14}$$

Setting $\alpha = B_i$ and $\beta = \mu_j^X$ we get the nuclear magnetic shielding:

$$\sigma_{ij}^X = \frac{\partial^2 G}{\partial B_i \partial \mu_j^X} = tr\left[\mathbf{P}\tilde{\mathbf{h}}^{B_i,\mu_j^X} + \mathbf{P}^{B_i}\tilde{\mathbf{h}}^{\mu_j^X}\right] \tag{12.15}$$

where $\tilde{\mathbf{h}}^{\mu_j^X}$ and $\tilde{\mathbf{h}}^{B_i,\mu_j^X}$ are the first derivative of the one-electron Hamiltonian with respect to the nuclear magnetic moment and its second derivative with respect to the nuclear magnetic moment and magnetic field, respectively. Explicit solvent effects are included only via the derivative of the density matrix with respect to the magnetic field ($\mathbf{P}^{B_i}$) that is obtained by solving coupled-perturbed HF or Kohn–Sham equations. In order to avoid gauge dependence, both GIAO [64] and continuous set of gauge transformation (CSGT) [67] formalisms have been implemented [21].

Both MEP and ASC implementations take into account only solute–solvent electrostatic contributions to the magnetic properties.

With regard to the prediction of EPR parameters in solution, the calculation of isotropic hyperfine coupling constants (Fermi contact term, a_N) is straightforward as the expectation value using the wavefunction computed in the presence of the solvent reaction field.

Finally, the only attempt to compute electronic g-tensors in the presence of a solvent reaction field is very recent [68]. In this case the wavefunctions obtained from C-PCM [55,59] calculations were used within the framework of sum-over-states density functional perturbation theory (SOS-DFPT) [69] to compute g-shifts.

12.3
Applications of Continuum Models to the Prediction of NMR Parameters

The most recent ab initio calculations of NMR parameters in the presence of a solvent reaction field can be grouped into two classes corresponding to two different implementations: (i) the DALTON [70] one using the multipole expansion method (and more recently PCM [66]) in conjunction with a MC-SCF or HF procedure; (ii) the GAUSSIAN [71] one using ASC approaches in conjunction with DFT or HF methods. Additionally, calculations of ^{15}N shieldings by Chipman based on the SS(V)PE method [24] and the seminal work of Cremer on ^{11}B and ^{15}N shieldings using IGLO/PCM [25] should also be mentioned.

Examples of calculations of solvent effects on spin–spin coupling constants can be found in the literature due to the work of Mikkelsen [29,72], Pecul [28], Ruud [66] and of Contreras [73] and coworkers, the latter evaluating solvent effects only on the Fermi contact term.

Concerning nuclear magnetic shielding calculations, most of the studies focused on the solvent effect on ^{15}N shieldings since this nucleus appears to be extremely sensitive to the nature of the solvent [74]. Nevertheless, papers concerning solvent induced shifts on other nuclei (such as C [22,28], S [72], Se [29] or O [36]) can be found. The effect of solvent cavity and escaped charge on the computed shielding using ASC methods has been analysed carefully by Zhan and Chipman [24] and, to a lesser extent, by Mennucci and coworkers [34]. In particular it turns out that, using PCM, non-electrostatic solute–solvent interactions can be artificially simulated using a larger molecular cavity, allowing better agreement with the experimental data, especially in the case of a non-polar, non-protic solvent. A corresponding analysis for MEP methods highlights small cavity size effects that follow the same trends [22].

Here we will focus only on the prediction of solvent induced nuclear magnetic resonance shifts ($-\Delta\delta$) rather than on the prediction of the absolute nuclear magnetic shielding in solution (σ). If we consider Buckingham partitioning of solvent contributions to shielding [75], most of the ab initio studies focus only on the electrostatic solute–solvent interaction ($-\Delta\delta_E$).

An almost direct comparison between solvent effect on nuclear shielding computed at a MEP and PCM level is possible in the case of tetrazole derivatives. 1-methyl-1,2,3,4 tetrazole and 1-methyl-1,2,3,5-tetrazole (Fig. 12.1) were studied both at a MCSCF-MEP (GIAO) [30] and at a DFT-PCM (CSGT/hybrid) level [32].

Both methods reproduce correctly the overall solvent effect, that is a shielding effect on the pyridine type nitrogen atoms with increase in solvent polarity and an opposite effect (de-shielding) for the pyrrole-type nitrogen atoms. The DFT-PCM

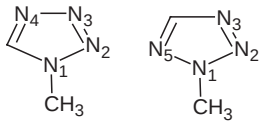

<1-2-3-4> <1-2-3-5>

Figure 12.1 Structure of 1-methyl-1,2,3,4 tetrazole (<1,2,3,4>) and 1-methyl-1,2,3,5 tetrazole (<1,2,3,5>).

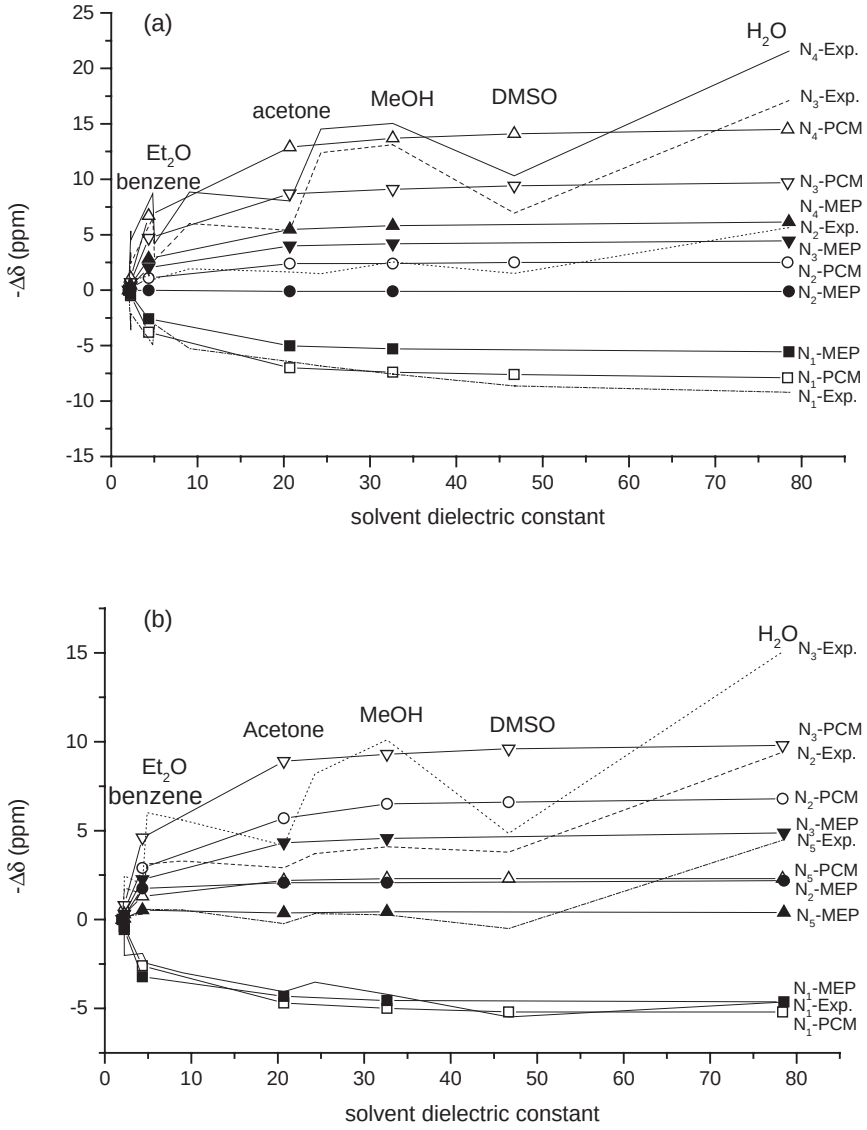

Figure 12.2 Computed [30,32] and experimental [76] solvent to cyclohexane ^{15}N nuclear magnetic shielding shifts ($-\Delta\delta^{15}N$); in ppm) as a function of solvent dielectric constant for <1,2,3,4> (a) and <1,2,3,5> (b). Computed values: Square $\delta\sigma(N_1)$; circle $-\Delta\delta(N_2)$; down-triangle $-\Delta\delta(N_3)$; up-triangle $-\Delta\delta(N_4)$ (a)/$-\Delta\delta(N_5)$ (b). Open marks=PCM-B3LYP/CSGT/6-311++G(2d,2p) calculations [32]; full marks=MEP-MCSCF/GIAO/H-II calculations [30]. Experimental data from ref. [76]. MP2/6-311G(2d,2p) in vacuum optimised structures for MCSCF calculations and PCM/B3LYP/6-311++G(2d,2p) PCM optimised structure for DFT calculations were used.

method predicts larger solvent shifts, in better agreement with the experimental data (see Fig. 12.2a and b).

Furthermore, while the N_2 and N_5 shieldings are predicted to be practically unaffected by the solvent at the MCSCF-MEP level, they show a smooth dependence on solvent at the DFT-PCM level, in better agreement with the experimental data. It should be stressed in this context that the calculations have been performed using different structures and basis sets. A comparison of the computed [30,32] and experimental [76] solvent shifts highlights that the main discrepancy between both DFT-PCM and MCSCF-MEP trends with respect to the experimental data are related to the presence of specific solute–solvent interactions, such as for H-bonding solvents. The importance of direct solute–solvent interactions in the prediction of nuclear shielding, already stressed by Pecul and Sadlej [28], received particular attention due to the works of Mennucci and co-workers [34, 35]. Two possible computational procedures were investigated to simulate ^{15}N solvent shifts in a low to medium polar and protic solvent (chloroform, $CHCl_3$) [34] and in a highly polar and protic solvent (water) [35]. Since hydrogen bonding in $CHCl_3$ is rather weak, a realistic simulation of the solute and solvent first solvation sphere is obtained by considering a dynamic situation, that is an ensemble of different structures sampled via a classical molecular dynamics simulation (using both rigid and flexible solute and solvent models). In particular, two sets of clusters including the solute (CH_3CN or pyridine, C_5H_5N) and the first solvation sphere (defined as all $CHCl_3$ molecules having a N_{solute}–H_{CHCl3} distance smaller than a given cut-off value) were taken from snapshots of microcanonical classical MD simulations. These clusters were then used to compute the shielding in vacuum or in a continuum. The calculations on clusters were performed using a multilayer (ONIOM) approach. In particular the solute was taken into account at a hybrid DFT level and the explicit solvent molecules at a HF level.

The calculations showed (Table 12.1) that in the case of pyridine the addition of the solvent reaction field both to the isolated solute and to the clusters drives the computed ^{15}N nuclear shielding solvent shift towards the experimental values. On the other hand, for CH_3CN the ^{15}N solvent shift is well reproduced using a supermolecular (cluster) approach while an overestimation (practically a doubling) of solvent shifts is computed when adding the solvent reaction field to both the isolated

Table 12.1 Experimental [a] and computed [b] nitrogen isotropic solvent shifts for $CHCl_3$ ($-\Delta\delta$(N); in ppm) of acetonitrile and pyridine.

	PCM[c]	Cluster[d]	Cluster+PCM[e]	Exp.[a]
Acetonitrile	–17.72	–5.32	–16.78	–6.2
Pyridine	–13.97	–8.42	–15.70	–14.1

a Ref. [74]. **b** Ref. [34]. **c** IEF-PCM result [56]. **d** Average values computed from calculations on MD snapshot clusters using an ONIOM approach (B3LYP/6-311+G(d, p) for the solute and HF/STO3G for solvent explicit molecules). **e** Clusters (d) embedded in IEF-PCM [56].

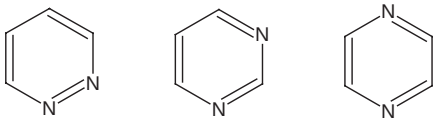

Figure 12.3 Structure of 1,2-diazine (pyridazine), 1,3-diazine (pyrimidine) and 1,4-diazine (pyrazine).

solute and the clusters. The latter calculations show that the screening of the first solvation sphere is, in this case, still insufficient. In the case of more polar and protic solvents, such as water, the hydrogen bonding network is stronger. Instead of a dynamic picture such as the MD snapshots, the local structure of the solute is well reproduced by the minima obtained by optimising the structure of a supermolecular cluster that includes the first solvent coordination sphere of the nitrogen atoms. Therefore in the analysis of the ^{15}N solvent shift from cyclohexane to water for pyridazine, pyrimidine and pyrazine (Fig. 12.3), Mennucci [35] took into account direct water to diazine interactions by inclusion of up to two solvating water molecules, and added the bulk solvent effects by PCM.

The results show that PCM alone cannot reproduce the effect of strong H bonding (in particular the polarisation effect due to direct solute–solvent interaction rather than the indirect, structural, effect) and that the inclusion of the first solvation sphere of N is mandatory. The use of decomposition of the shielding in terms

Table 12.2 Experimental [a] and computed [b] nitrogen isotropic NMR cyclohexane to water shifts ($-\Delta\delta_{cyc}$(N); in ppm) of M (M=pyridazine, pyrimidine and pyrazine).

	PCM	M-1w	M-1w +PCM	M-2w	M-2w +PCM	Exp.
Pyridazine						
$-\Delta\delta^N$	12.71 (19.43)[c]	25.44	41.92	35.30/17.16[d]	49.43 /41.91[d]	41.55
Pyrimidine						
$-\Delta\delta^N$	3.60 (6.35)[c]	13.62	19.36	12.70	15.93	16.84
Pyrazine						
$-\Delta\delta$	2.33 (5.28)[c]	18.46	24.57	12.97	18.55	16.85

a Ref. [77]. **b** At B3LYP/GIAO/6-311+G(d,p)) level of theory from Ref. [35]. **c** Cavity computed using atomic Van der Waals radii scaled by 1.2; all other data refer to computations performed with Van der Waals radii scaled by 1.4. **d** The two values correspond to the two non-equivalent N atoms. PCM refers to computations performed using the IEF-PCM implementation [56]. M-1w and M-2w refer to calculations performed in vacuum clusters made of solute and 1 and 2 water molecules respectively; M-1w+ PCM and M-2w+PCM refer to calculations performed for the solute + water clusters in the presence of the solvent reaction field. The corresponding optimised structures were used.

of diamagnetic and paramagnetic contributions, of Pople's model for the local paramagnetic contribution and of NBO analysis, highlights the removal of density from the N lone pair (n) due to H-bonding interactions. This reduces the absolute (deshielding) paramagnetic contribution due to n–π* contributions, thus providing the observed net increase in the total nuclear shielding when going from non-protic to protic solvents, the diamagnetic contribution remaining constant. At the same time, the computed increase in the n–π* transition energy [35] when going from vacuum to solvated systems could play the same role in reducing the paramagnetic contribution. The inclusion of bulk effects using a continuum model amplifies H bonding effects, makes the diazine–water interaction stronger and increases the agreement between the computed and experimental solvent shifts (Table 12.2).

Similar procedures, a coupling of MD and continuum models, were used by Barone and Cossi [36] to analyse the ^{17}O nuclear magnetic resonance solvent shift within the DFT/PCM framework.

12.4
Applications of Continuum Models to the Prediction of EPR Parameters

The continuum model, in particular PCM eventually combined with supermolecular approaches, has been successfully applied to understand and predict the isotropic hyperfine coupling constants (hcc, a_N) of organic radicals in solution. Particular attention has been devoted to biologically relevant radicals. Recent and extensive reviews on this topic and, more generally, on the simulation of biological systems in condensed phases, can be found in the literature [37, 39]. Since a_N depends on the spin density distribution at the nuclei, local structural deformation (such as direct solute–solvent interactions but also large amplitude vibrations) can influence significantly the hcc values. A realistic simulation of hcc should include, when necessary, not only the bulk effect but also direct solute–solvent interactions and thermal averaging on large amplitude modes (LAM). To summarise the *state of the art,* we will take as an example the work of Adamo and co-workers [78] concerning the calculation of the isotropic hyperfine coupling constants of the free radicals derived from H addition to cytosine. These radicals, namely the 5yl, 6yl and N3H (Fig. 12.4),

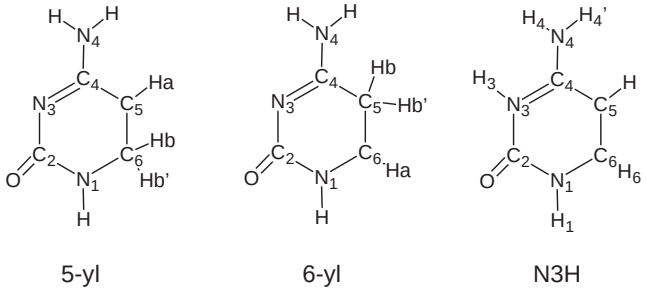

Figure 12.4 Structure and numbering of the three radical species arising from H addition to cytosine (5-yl, 6-yl and N3H).

Table 12.3 Isotropic hyperfine coupling constants (in G) [78].

	Vacuum	C-PCM	C-PCM + <LAM>$_{298\ K}$	Exp.
		6yl		
H_a	–15.0	–15.6	–18.5	±18.6[a] (±18.6)[b] –18.7[c]
H_b	14.6	16.1	37.7	±40.0 (±37.5)
H_b'	48.0	50.7	37.7	±40.0 (±37.5)
		5yl		
H_a	–17.4	–17.9	–18.5	±16.7 [a](±17.2)[b] –18.4[c]
H_b	51.3	54.7	52.1	±55 (±48.8)
H_b'	50.0	47.5	52.1	±55 (±48.8)
		N3H		
H_4	21.0	20.2	16.7	–1.6
H_4'	–1.1	–1.2	–1.0	–1.6
H_6	–15.5	–15.7	–15.7	–13.5
H_3	–0.2	0.0	–0.7	–2.0

All values computed at UB3LYP level using optimised UB3LYP/6-311G(d,p) geometries. Vacuum and C-PCM stand for calculations perfomed in vacuum or solvent reaction field (C-PCM [55]) using a EPR-II basis. C-PCM +<LAM>$_{298\ K/vacuum}$ are results taking into account both solvent and vibrational (<LAM>) contributions to hcc obtained after vibrational averaging along the puckering normal mode at 298 K in vacuum using a EPR-II basis. EPR-II basis set from Ref. [79]. **a** Frozen aqueous solution measurements at 77 K from Ref. [80]. **b** Crystal measurements at 298 K from Ref. [81]. **c** Crystal measurements at 10 K from Ref. [82].

show a puckered optimised structure, their planar form being a first order saddle point.

The computed hcc of the three species are reported in Table 12.3.

If we focus on the 6yl radical, experimentally the two H_b show equivalent hcc (±40 G in frozen aqueous solution; ±37.5 G in the crystal). Nevertheless, they are predicted to be strongly non-equivalent when using the equilibrium, puckered, geometry (50.7 G and 16.1 G at the B3LYP/EPR-II/C-PCM level) and equivalent for a planar (transition state) conformation (38.0 G). Considering the potential energy curve along the large amplitude (LAM) normal mode responsible for C6 inversion, that is the puckering mode, two minima separated by a 2 kJ mol^{-1} barrier are found. Neglecting the coupling with the other modes, it is possible to evaluate the vibrational states along this path. From Fig. 12.5, it is clear that the low-lying vibrational states are delocalised between the two minima and, as a consequence, as a function of the temperature the radical can have, on average, a practically planar conformation.

Taking into account a vibrational averaging of the hcc following the LAM, led to the evaluation of an equivalent vibrationally averaged hcc value for the two H_b of 37.7 G, in good agreement with experimental data. A more detailed discussion for the other two adducts (5yl and N3H) can be found in the original paper [78]. Exam-

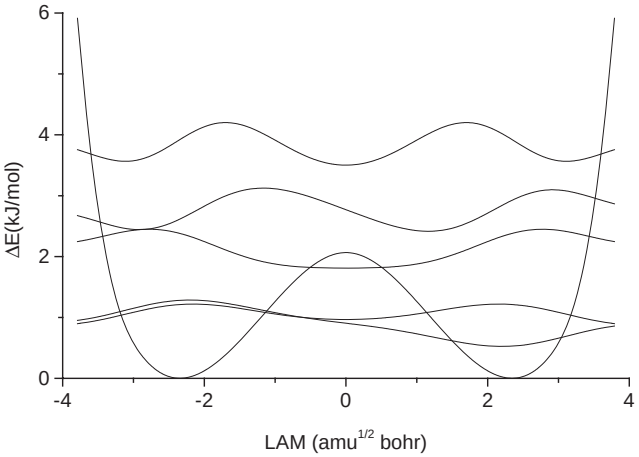

Figure 12.5 Computed potential energy surface and lower lying vibrational levels for ring puckering mode of 6-yl [78] (provided by C. Adamo).

ples of the importance of direct solute–solvent interaction in the evaluation of hcc can be found in Ref. [37,39].

Regarding the calculation of *g*-tensors in conjunction with continuum solvent models, only one example is available [68], and it makes use of SOS-DFPT [69] for the calculation of *g*-shifts in semiquinones. Since it is well known that the largest *g*-tensor component in semiquinones (Fig. 12.6), g_x, is very sensitive to interactions with the environment [3, 4], these systems were taken as test cases for several theo-

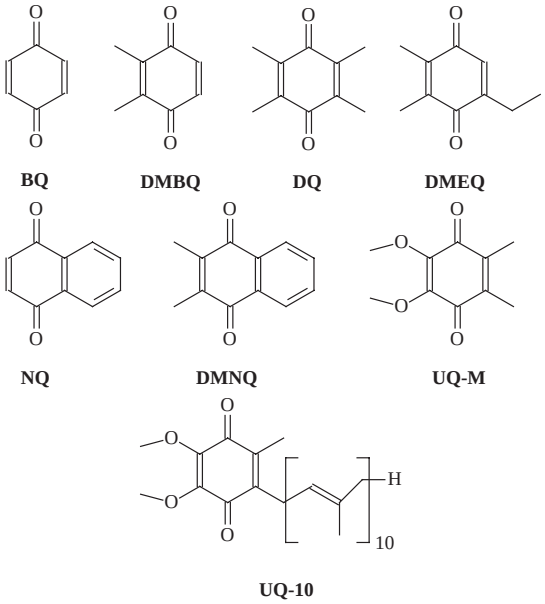

Figure 12.6 Structure of selected quinone derivatives: BQ = 1,4-benzoquinone, DMBQ = 2,3-dimethyl-1,4-benzoquinone, DMEQ = 2,3-dimethyl-5-ethyl-1,4-benzoquinone, DQ = 2,3,4,6-tetramethyl-1,4-benzoquinone, NQ = 1,4-naphthoquinone, DMNQ = 2,3-dimethyl-1,4-naphthoquinone, UQ-M = 2,3-dimethoxy-1,4-benzoquinone, UQ-10 = 2,3-dimethoxy –5-methyl-6-decaprenyl-4-benzoquinone.

Table 12.4 Computed *g*-shift components (in ppm) for semiquinone radical anions.[a]

	Δg_{iso}	Δg_x	Δg_y	Δg_z
$BQ^{-\bullet}$	3190	6530	3065	–20
$BQ^{-\bullet}{}_{PCM/THF}$	3091	6285	3012	–23
$BQ^{-\bullet}{}_{PCM/Acetonitrile}$	3076	6247	3004	–24
$BQ^{-\bullet}{}_{PCM/DMSO}$	3083	6265	3007	–24
$BQ^{-\bullet}{}_{PCM/H_2O}$	2987	6024	2964	–27
$[BQ(H_2O)_4]^{-\bullet}$	2608	4889	2935	+2
$[BQ(H_2O)_4]^{-\bullet}{}_{PCM/H_2O}$	2557	4787	2906	–23
Exp[b]	2350	4130	2940	–30
$DMBQ^{-\bullet}$	3061	6131	3057	–3
$DMBQ^{-\bullet}{}_{PCM/THF}$	2997	5989	3008	–5
$DMBQ^{-\bullet}{}_{PCM/Acetonitrile}$	2987	5968	3000	–5
$DMBQ^{-\bullet}{}_{PCM/DMSO}$	2989	5973	3000	–5
$DMBQ^{-\bullet}{}_{PCM/H_2O}$	2912	5784	2957	–8
$[DMBQ(H_2O)_4]^{-\bullet}$	2509	4716	2817	–30
$[DMBQ(H_2O)_4]^{-\bullet}{}_{PCM/H2O}$	2421	4545	2784	–67
Exp[b]	2240	3870	2900	–60
$NQ^{-\bullet}$	2850	5627	2898	25
$NQ^{-\bullet}{}_{PCM/THF}$	2795	5428	2973	24
$NQ^{-\bullet}{}_{PCM/Acetonitrile}$	2750	5388	2840	24
$NQ^{-\bullet}{}_{PCM/DMSO}$	2750	5387	2840	24
$NQ^{-\bullet}{}_{PCM/H2O}$	2656	5161	2786	22
$[NQ(H_2O)_4]^{-\bullet}$	2259	4145	2630	1
$[NQ(H_2O)_4]^{-\bullet}{}_{PCM/H2O}$	2177	3959	2578	–6
Exp[b]	2060	3500	2730	–40

a All values were computed at BP86/DZVP level using the corresponding optimised; C-PCM [55] was used as continuum solvent model [68]. **b** Ref. [3].

retical studies aimed at understanding the role of both specific solute–solvent and electrostatic interactions [83].

The results obtained when computing the *g*-tensor in vacuum, using a supermolecular approach, using a continuum model, or coupling a supermolecular approach with the continuum, are summarised in Table 12.4 for three selected molecules, namely BQ, DMBQ and NQ (refer to Fig. 12.6).

Generally, the inclusion of solvent as a continuum correctly drives the g_x towards the experimental values for all semiquinone derivatives while substituent effects on the *g*-tensors are computed to be of the same magnitude as in gas-phase calculations [83]. In particular, a decrease in g_x due to delocalisation of spin density into the condensed benzene ring or hyperconjugative effects of methyl groups is found, both in the gas phase and in solution, when going from BQ to NQ and DMBQ respectively. By comparison of computed *g*-values for the same semiquinone derivative in different solvents, a non-linear dependence of *g* on solvent dielectric constant is found,

Table 12.5 HOMO and SOMO β orbital energies (ε_{HOMO}, ε_{SOMO}) of $BQ^{-\bullet}$ in different environments and decomposition of the HOMO→SOMO contribution to g_x in terms of SO and OZ matrix elements. $<OZ>_{H\to S}$ and $<SO>_{H\to S}$ are in 10^{-4} eV T^{-1} and 10^4 eV respectively.

	$BQ^{-\bullet}$	$BQ^{-\bullet}_{THF}$	$BQ^{-\bullet}_{DMSO}$	$BQ^{-\bullet}_{ACETO}$	$BQ^{-\bullet}_{H2O}$	$[BQ(H_2O)_4]^{-\bullet}$
ε_{HOMO} (au)	–0.027	–0.157	–0.174	–0.173	–0.192	–0.095
ε_{SOMO} (au)	0.038	–0.090	–0.107	–0.106	–0.123	–0.024
$\Delta\varepsilon$ *(eV)*	1.79	1.83	1.84	1.84	1.87	1.97
$<SO>_{H\to S}$	49.80	49.22	49.14	49.11	48.40	43.02
$<OZ>_{H\to S}$	0.61	0.61	0.61	0.61	0.60	0.49

the larger the shifts the higher the solvent polarity. Nevertheless the continuum alone is not able to reproduce the direct hydrogen-bonding semiquinone–water interactions, and the absolute effect on g_x is only ca. 200–300 ppm, roughly 10% of the overall effect obtained upon adding explicitly four water molecules. The best performance is found when adding the PCM model to the supermolecular cluster. This further reduces Δg_x by another few hundred ppm and brings it closer to experiment.

Within the framework of SOS-DFPT [69], the decomposition of the leading $\Delta g_{SO/OZ}$ contribution of BQ^- in terms of single excitations allowed the HOMO–SOMO gap excitation to be defined as the major contributor to the g_x-shift (here we refer to the highest doubly occupied molecular orbital as HOMO and to the singly occupied molecular orbital as SOMO).

The analysis of the different contributions to $\Delta g_{x\ (SO/OZ)}$ for the HOMO–SOMO excitation when going from vacuum, to PCM, to cluster approaches (Table 12.5) highlights the main solvent effects.

In solution, the HOMO–SOMO gap increases and the spin density on oxygen decreases with increase in solvent polarity. Addition of explicit water molecules enhances both effects, thus leading to an overall reduction of g_x.

12.5 Conclusions

With the recent developments of continuum solvent approaches, the modelling of a wider class of chemical problems in solution becomes affordable at an ab initio level, at a computational cost comparable to gas phase calculations. Concerning magnetic properties, the delicate interplay between long-range (electrostatic) and short-range (van der Waals or direct) solute–solvent interactions must be correctly taken into account in order to get a realistic picture. In this respect the recent advances in continuum models provide a cheap but rigorous tool, not only due to their coupling with molecular dynamics, multi-layer or supermolecular approaches, but also to the recent developments focused on the description of non-isotropic media such as liquid crystals [84].

Acknowledgements

The author gratefully acknowledges Prof. Vincenzo Barone, Prof. Carlo Adamo, Prof. Henry Chermette and Prof. Martin Kaupp for helpful comments and discussions, Dr. Orlando Crescenzi and Prof. V. Barone for providing pre-prints, Dr M. Ruiz-Lopez for providing reprints and Pio Bättig for help in bibliographic research. A grant from CNRS ("Projet Jeune Equipes") is acknowledged.

References

1 C. J. Jameson, A. C. de Dios, in *Molecular Magnetic Shielding and Molecular Structure*, ed. J. A. Tossell, Kluwer, Dordrecht **1999**, p. 95; W. T. Raynes, A. D. Buckingham, H. J. Bernestein, *J. Phys. Chem.* **1962**, *36*, 3481.
2 R. Calvo, E. C. Abresch, R. Bittl et al., *J. Am. Chem. Soc.* **2000**, *122*, 7327.
3 F. MacMillan, F. Lendzian, W. Lubitz, *Magn. Reson. Chem.* **1995**, *33*, 81; F. MacMillan, J. Hanley, L. van der Weerd et al., *Biochemistry* **1997**, *36*, 9297.
4 W. Lubitz, G. Feher, *Appl. Magn. Reson.* **1999**, *17*, 1; H. Levanon, K. Möbius, *Annu. Rev. Biophys. Biomol. Struct.* **1997**, *26*, 495; J. A. Pedersen, *EPR Spectra from Natural and Synthetic Quinones and Quinoids*, CRC Press, Boca Raton, FL **1985**.
5 M. Z. Born, *Phys.* **1920**, *1*, 45.
6 R. P. Bell, *Trans. Faraday Soc.* **1931**, *27*, 797.
7 J. G. Kirkwood, *Chem. Phys.* **1934**, *2*, 351.
8 L. Onsager, *J. Am. Chem. Soc.* **1936**, *58*, 1486.
9 P. Debye, E. Hückel, *Phys. Z.* **1923**, *24*, 185.
10 J. Tomasi, M. Persico, *Chem. Rev.* **1994**, *94*, 2027.
11 J.-L. Rivail, D. Rinaldi, in *Computational Chemistry, Review of Current Trends*, ed. J. Leszczynki, World Scientific, New York **1995**, p. 139; C. J. Cramer, D. G. Truhlar, in *Reviews in Computational Chemistry*, eds. K. B. Lipkowitz, D. B. Boyd, VCH, New York **1995**, Vol. 6, p.1; C. J. Cramer, D. G. Truhlar, in *Solvent Effects and Chemical Reactivity*, eds. O. Tapia, J. Bertran, Kluwer, Dordrecht **1996**, p. 1.
12 C. J. Cramer, D. G. Truhlar, *Chem. Rev.* **1999**, *99*, 2160.
13 J. Tomasi, B. Mennucci, R. Cammi et al., in *Theoretical Aspects of Biochemical Reactivity*, eds. G. Náray-Szabo, A. Warshel, Kluwer, Dordrecht **1997**, p. 1.
14 C. Amovilli, V. Barone, R. Cammi et al., *Adv. Quant. Chem.* **1998**, *32*, 227.
15 J. Tomasi, R. Cammi, B. Mennucci et al., *Phys. Chem. Chem. Phys.* **2002**, *4*, 5697.
16 C. Amovilli, B. Mennucci, *J. Chem, Phys. B* **1997**, *101*, 1051; R. A. Pierotti, *Chem. Rev.* **1976**, *76*, 717; P. Claverie, *Perspect. Quantum Chem. Biochem.* **1978**, *2*, 69; C. Colominas, F. J. Luque, J. Texidó et al., *Chem. Phys.* **1999**, *240*, 253; F. M. Floris, J. Tomasi, J. L. Pascual-Ahuir, *J. Comput. Chem.* **1991**, *12*, 784; J. Tomasi, B. Mennucci, E. Cancès, *J. Mol. Struct. (Theochem)* **1999**, *211*, 464.
17 R. Cammi, C. Cappelli, S. Corni et al., *J. Phys. Chem. A* **2000**, *104*, 9874; C. Cappelli, S. Corni, J. Tomasi, *J. Phys. Chem. A* **2002**, *106*, 6426, J. Tomasi, R. Cammi, J. R. Cheeseman et al., *J. Phys. Chem. A* **2002**, *106*, 6102.
18 K. V. Mikkelsen, P. Jørgensen, J.H. J. A. Jensen, *J. Chem. Phys.* **1994**, *100*, 6597.
19 M. Cossi, V. Barone, *J. Phys. Chem. A* **2000**, *104*, 10614; C. Cappelli, S. Corni, J. Tomasi, *J. Chem. Phys.* **2001**, *115*, 5531; R. Cammi, J. Tomasi, *Int. J. Quant. Chem.* **1996**, *60*, 297; R. Cammi, L. Frediani, B. Mennucci et al., *J. Chem. Phys.* **2002**, *117*, 13.
20 M. Cossi, V. Barone, M. A. Robb, *J. Chem. Phys.* **1999**, *111*, 5295; P. A. Nielsen, P.-O. Norby, T. Liljefors et al., *J. Am. Chem. Soc.* **2000**, *122*, 3151; R. Improta, C. Benzi, V. Barone, *J. Am. Chem. Soc.* **2001**, *123*, 12568;
21 R. Cammi, *J. Chem. Phys.* **1998**, *109*, 3185; R. Cammi, B. Mennucci, J. Tomasi, *J. Chem. Phys.* **1999**, *110*, 7627.
22 K. V. Mikkelsen, P. Jørgensen, K. Ruud et al., *J. Chem. Phys.* **1997**, *106*, 1170.
23 K. V. Mikkelsen, K. Ruud, T. Helgaker, *Chem. Phys. Lett.* **1996**, *253*, 443.
24 C.-G. Zhan, D. M. Chipman, *J. Chem. Phys.* **1999**, *110*, 1611.

25 D. Cremer, L. Olsson, F. Reichel et al., *Isr. J. Chem.* **1993**, *33*, 369.
26 P.-O. Åstrand, K. V. Mikkelsen, K. Ruud et al., *J. Phys. Chem.* **1996**, *100*, 19771.
27 D. B. Chesnut, B. E. Rusiloski, *J. Mol. Struct. (Theochem)* **1994**, *314*, 12.
28 M. Pecul, J. Sadlej, *Chem. Phys.* **1998**, *234*, 111; M. Pecul, J. Sadlej, *Chem. Phys. Lett.* **1999**, *308*, 486; M. Pecul, J. Sadlej, *Chem. Phys.* **2000**, *255*, 137.
29 P.-O. Åstrand, K. V. Mikkelsen, P. Jørgensen et al., *J. Phys. Chem.* **1998**, *108*, 2528.
30 M. Jaszunski, K. V. Mikkelsen, A. Rizzo et al., *J. Phys. Chem. A* **2000**, *104*, 146.
31 T. Yamazaki, H. Sato, F. Hirata, *Chem. Phys. Lett.* **2000**, *325*, 668.
32 M. N. Manalo, A. C. de Dios, R. Cammi, *J. Phys. Chem. A* **2000**, *104*, 9600.
33 T. Vreven, B. Mennucci, C. O. da Silva et al., *J. Chem. Phys.* **2001**, *115*, 62.
34 B. Mennucci, J. M. Martínez, J. Tomasi, *J. Chem. Phys.* **2001**, *105*, 7287.
35 B. Mennucci, *J. Am. Chem. Soc.* **2002**, *124*, 1506.
36 V. Barone, O. Crescenzi, R. Improta, *Quant. Struct.-Act. Relat.* **2002**, *21*, 105; M. Cossi, O. Crescenzi, *J. Chem. Phys.*, in press.
37 C. Adamo, M. Cossi, N. Rega et al. in *Theoretical Biochemistry- Process and Properties of Biological Systems, Theoretical and Computational Chemistry*, ed. L. A. Eriksson, Elsevier, Amsterdam **2001**, Vol. 9, 467.
38 C. Adamo, A. di Matteo, P. Rey et al., *J. Phys. Chem. A* **1999**, *103*, 3481; C. Adamo, R. Subra, A. di Matteo et al., *J. Chem. Phys.* **1998**, *109*, 10244; G. A. A. Saracino, A. Tedeschi, G. d'Errico et al., *J. Chem, Phys. A* **2002**, *106*, 10700; S. Naumov, J. Reinhold, D. Beckert, *Phys. Chem. Chem. Phys.* **2003**, *5*, 64.
39 R. Improta, V. Barone, *Chem. Rev.*, submitted.
40 R. Constanciel, *Theor. Chim. Acta* **1986**, *69*, 505.
41 R. Bonaccorsi, P. Palla, J. Tomasi, *J. Am. Chem. Soc.* **1984**, *106*, 1945.
42 E. Cancès, B. Mennucci, *J. Chem. Phys.* **2001**, *115*, 6130; M. Cossi, N. Rega, G. Scalmani et al., *J. Chem. Phys.* **2001**, *114*, 5691; D. M. Chipman, *J. Chem. Phys.* **1999**, *110*, 8012; D. M. Chipman, *J. Chem. Phys.* **2000**, *112*, 5558.
43 S. Miertuš, E. Scrocco, J. Tomasi, *Chem. Phys.***1981**, *55*, 117; R. Cammi, J. Tomasi, *J. Comput. Chem.* **1995**, *16*, 1449.
44 V. Barone, M. Cossi, *J. Phys. Chem. A* **1998**, *102*, 1995.
45 J. B. Foresman, T. A. Keith, K.B. Wiberg et al., *J. Phys. Chem.* **1996**, *100*, 16098.
46 A. Bondi, *J. Chem. Phys.* **1964**, *68*, 441.
47 M. Cossi, V. Barone, R. Cammi et al., *Chem. Phys. Lett.* **1996**, *255*, 327.
48 C. J. F. Böttcher, *Theory of Electric Polarisation*, Elsevier, Amsterdam **1952**.
49 M. Cossi, V. Barone, B. Mennucci et al., *Chem. Phys.Lett.* **1998**, *286*, 253; B. Mennucci, M. Cossi, J. Tomasi, *J. Chem. Phys.* **1995**, *102*, 6837.
50 C. J. Cramer, D. G. Truhlar, *J. Am. Chem. Soc.* **1991**, *113*, 8305.
51 D. Rinaldi, J.-L. Rivail, *Theor. Chim. Acta* **1973**, *32*, 57.
52 D. Rinaldi, M.F. Ruiz Lopez , J.-L. Rivail, *J. Chem. Phys.* **1983**, *78*, 834; V. Dillet, D. Rinaldi, J. G. Ángyán et al., *Chem. Phys. Lett.* **1993**, *202*, 18.
53 J. L. Pascual-Ahuir, E. Silla, *J. Comput. Chem.* **1990**, *11*, 1047; E. Silla, I. Tuñón, J. L. Pascual-Ahuir, *J. Comput. Chem.* **1991**, *12*, 1077; J. L. Pascual-Ahuir, I. Tuñón, E. Silla, *J. Comput. Chem.* **1994**, *15*, 1127; C. S. Pomelli, J. Tomasi, *Theor. Chem. Acc.* **1998**, *99*, 34.
54 H. Hoshi, M. Sakurai, Y. Iroue et al., *J. Chem. Phys.* **1987**, *87*, 1107; T. Fukurui, M. Sakurai, Y. Inoue, *J. Comp.Chem.* **1993**, *16*, 378.
55 V. Barone, M. Cossi, *J. Chem. Phys. A* **1998**, *102*, 1995.
56 E. Cancès, B. Mennucci, J. Tomasi, *J. Chem. Phys.* **1997**, *107*, 3032; B. Mennucci, E. Cancès, J. Tomasi, *J. Phys. Chem. B* **1997**, *101*, 10506.
57 C. Pomelli, J. Tomasi, *Theor. Chim. Acc.* **1997**, *96*, 39.
58 C. S. Pomelli, J. Tomasi, V. Barone, *Theor. Chem. Acc.* **2001**, *22*, 1262.
59 A. Klamt, G. Schüürman, *J. Chem. Soc., Perkins Trans.*2 **1993**, 799.
60 C.-G. Zhan, J. Bentley, D. M. Chipman, *J. Chem. Phys.* **1998**, *108*, 117.
61 M. F. Ruiz-Lopez, R. Rinaldi, J. L Rivail et al., *J. Magn. Reson. Synop.* **1982**, *12*, 320.
62 J. Webb, *Magn. Reson.* **1985**, *63*, 354.
63 D. M. Bishop, S. M. Cybulski, *J. Magn. Reson. Ser. A* **1994**, *107*, 99.
64 F. London, *Naturwissenschaften* **1937**, *15*, 187; R. Ditchfield, *J. Chem. Phys.* **1972**, *56*, 5688; K. Woliński, J. F. Hinton, P. Pulay, *J. Am. Chem. Soc.* **1990**, *112*, 8251.

65 R. Cammi, J. Tomasi, *J. Chem. Phys.* **1994**, *101*, 3888.

66 K. Ruud, L. Frediani, R. Cammi et al., *Int. J. Mol. Sci.* **2003**, *4*, 119.

67 T. A. Keith, R. F. W. Bader, *Chem. Phys. Lett.* **1993**, *210*, 223.

68 I. Ciofini, R. Reviakine, A. Arbouznikov et al., *Theor. Chem. Acc.*, in press.

69 O. Malkina, J. Vaara, B. Schimmelpfennig et al., *J. Am. Chem. Soc.* **2000**, *122*, 9206; M. Kaupp, in *EPR Spectroscopy of Free Radicals in Solids. Trends in Methods and Applications*, eds. A. Lund, M. Shiotani, Kluwer, Dordrecht **2003**.

70 T. Helgaker, H.J.A. Jensen, P. Jørgensen et al., *Dalton, A Molecular Electronic Structure Program, Release 1.2*, **2001**.

71 M. J. Frisch, G. W. Trucks, H. B. Schlegel et al., *Gaussian Development Version*, Gaussian, Inc., Pittsburgh PA **2002**.

72 K. V. Mikkelsen, K. Ruud, T. Helgaker, *J. Comput. Chem.* **1999**, *20*, 1281.

73 D. G. Zaccari, J. P. Snyder, J. E. Peralta et al., *Mol. Phys.* **2002**, *100*, 705; D. G. Zaccari, V. Barone, J. E. Peralta et al., *Int. J. Mol. Sci.* **2003**, *4*, 93.

74 M. Witanowski, L. Stefaniak, G. A. Webb, in *Annual Report on NMR Spectroscopy*, ed. G. A. Webb, Academic Press, London **1993**, Vol. 25.

75 A. D. Buckingham, *Can. J. Chem.* **1960**, *38*, 300; A. D. Buckingham, T. Schaefer, W. G. Schneider, *J. Chem. Phys.* **1960**, *32*, 1227.

76 M. Witanowski, Z. Biedrzycka, W. Sicinska et al., *J. Magn. Reson.* **1997**, *124*, 127; M. Witanowski, Z. Biedrzycka, W. Sicinska et al., *J. Magn. Reson.* **1998**, *131*, 54.

77 M. Witanowski, W. Sicinska, S. Biernat et al., *J. Magn. Reson.* **1991**, *91*, 289.

78 C. Adamo, M. Heitzmann, F. Meilleur et al., *J. Am. Chem. Soc.* **2001**, *123*, 7113.

79 V. Barone, in *Recent Advances in Density Functional Methods Part I*, ed. D. P. Chong, World Scientific, Singapore **1996**.

80 E. Westhof, Y. Lyon, A. van der Vorst, *Int. J. Radiat. Biol.* **1997**, *32*, 499.

81 E. Westhof, *Int. J. Radiat. Biol.* **1973**, *23*, 389.

82 E. Sagstuen, E. Hole, W. H. Nelson et al., *J. Phys. Chem.* **1992**, *92*, 8269.

83 M. Kaupp, C. Remenyi, J. Vaara et al., *J. Am. Chem. Soc.* **2002**, *124*, 2709; M. Kaupp, *Biochemistry* **2002**, *40*, 2895; M. Engström, O. Vahtras, H. Ågren, *Chem. Phys.* **1999**, *243*, 263; K. M. Neyman, D. I. Ganyushin, Ž. Rinkevičius et al., *Int. J. Quant. Chem.* **2002**, *90*, 1404.

84 B. Mennucci, R. Cammi, *Int. J. Quant. Chem.*, in press.

13
Perturbational and ECP Calculation of Relativistic Effects in NMR Shielding and Spin–Spin Coupling

Juha Vaara, Pekka Manninen and Perttu Lantto

13.1
Introduction

The consequences of special relativity are important for the spectral parameters of nuclear magnetic resonance (NMR) spectroscopy in systems containing heavy elements [1, 2]. Relativity has to be taken into account when electronic velocities are no longer small compared to the speed of light, for example near heavy nuclei. The NMR observables, the nuclear shielding tensor $\boldsymbol{\sigma}$ and spin–spin coupling tensor $\mathbf{J}$, receive large contributions from the atomic core region and hence are subject to pronounced relativistic effects. After pioneering papers featuring formalism and semi-empirical calculations [3], Aucar and Oddershede [4], Ishikawa et al. [5], Quiney et al. [6], and Visscher et al. [7] introduced ab initio methods in fully relativistic four-component Dirac–Hartree–Fock (DHF) calculations of the NMR parameters. Romero and Aucar incorporated quantum electrodynamical effects into the DHF framework [8].

The high computational cost of the DHF-based methods motivates the development of approximate relativistic methods. Both perturbational approaches based on a non-relativistic (NR) reference state as well as the Breit–Pauli molecular Hamiltonian, H_{BP} [9–11], and variationally stable one- and two-component methods have been applied for $\boldsymbol{\sigma}$ and $\mathbf{J}$ [2]. The zeroth-order regular approximation (ZORA) [12] and the Douglas–Kroll–Hess (DKH) transformation [13] belong to the latter category. These approaches are discussed in other chapters of this book (see for instance Chapters 6–8). The fact that all methods based on the transformed Dirac Hamiltonian are subject to picture change effects [14], implies substantial programming effort to obtain property integrals, particularly in the ZORA and DKH methods. In contrast, the perturbational approach based on H_{BP} is supported by numerous quantum chemical implementations of the relevant integrals. Furthermore, relativistic corrections based on H_{BP} lend themselves easily to interpretations in terms of the familiar NR concepts, and provide an interpolation step between the NR and Dirac regimes. As H_{BP} is not variationally stable [15], its singular operators should only be used up to first order, or leading relativistic effects, with only one such operator at a time in expressions featuring multiple perturbations [7, 16]. Direct perturbation theory (DPT) [17] avoids the singularities of H_{BP}, and has been outlined for magnetic

Calculation of NMR and EPR Parameters. Theory and Applications.
Edited by Martin Kaupp, Michael Bühl, Vladimir G. Malkin
Copyright © 2004 WILEY-VCH Verlag GmbH & Co. KGaA, Weinheim
ISBN: 3-527-30779-6

properties [18, 19]. We are not aware of practical computational implementations of DPT to NMR properties yet.

In this chapter, we give a systematic survey of all the leading-order relativistic one-electron terms in $\boldsymbol{\sigma}$ and $\mathbf{J}$ resulting from perturbation theory (PT) based on the (Breit–)Pauli Hamiltonian. Additionally, we cover the two-electron spin–orbit (SO) interactions. We start from a two-component positive-energy Hamiltonian [20] for a molecule bearing two nuclear magnetic dipole moments placed in an external magnetic field, and show the resulting contributions to $\boldsymbol{\sigma}$ and $\mathbf{J}$ at various orders of PT. In doing so, the normal procedure of taking into account the electron spin symmetry as well as time-reversal invariance of the resulting energy terms, is applied. We mention briefly some of the important papers and results for the terms. We limit ourselves to closed-shell, diamagnetic molecules.

13.2
Nuclear Shielding and Spin–Spin Coupling

$\boldsymbol{\sigma}_K$ couples a nuclear magnetic moment $\boldsymbol{\mu}_K = \gamma_K \mathbf{I}_K$ to the external magnetic field $\mathbf{B}_0$, whereas $\mathbf{J}_{KL}$ couples the moments of two nuclei, via the electron system. Here, γ_K is the gyromagnetic ratio of nucleus K. The Cartesian $\varepsilon\tau$ components of the tensors are

$$\sigma_{K,\varepsilon\tau} = \frac{1}{\gamma_K} \frac{\partial^2 E(\mathbf{I}_K, \mathbf{B}_0)}{\partial I_{K,\varepsilon} \partial B_{0,\tau}}\bigg|_{\mathbf{I}_K=\mathbf{0},\mathbf{B}_0=\mathbf{0}} ; \quad J_{KL,\varepsilon\tau} = \frac{1}{2\pi} \frac{\partial^2 E(\mathbf{I}_K, \mathbf{I}_L)}{\partial I_{K,\varepsilon} \partial I_{L,\tau}}\bigg|_{\mathbf{I}_K=\mathbf{0},\mathbf{I}_L=\mathbf{0}} \tag{13.1}$$

where E is the perturbed electronic energy of the molecule. E involves the field-dependent momentum $\boldsymbol{\pi} = \mathbf{p} + \mathbf{A}$, where $\mathbf{A} = \mathbf{A}_0 + \mathbf{A}_K + \mathbf{A}_L$ is the sum of the vector potentials of $\mathbf{B}_0$ in the Coulomb gauge, $\nabla \cdot \mathbf{A} = 0$, as well as the field caused by the point-like magnetic dipole moments of nuclei K and L, with

$$\mathbf{A}_0(\mathbf{r}_i) = \frac{1}{2}\mathbf{B}_0 \times \mathbf{r}_{iO}; \quad \mathbf{A}_K(\mathbf{r}_i) = \alpha^2 \gamma_K \frac{\mathbf{I}_K \times \mathbf{r}_{iK}}{r_{iK}^3}. \tag{13.2}$$

In Eqs. (13.2), $\mathbf{r}_{iO} = \mathbf{r}_i - \mathbf{R}_O$ where $\mathbf{r}_i$ is the location of electron i and O refers to the gauge origin, $\mathbf{r}_{iK} = \mathbf{r}_i - \mathbf{R}_K$ where $\mathbf{R}_K$ is the location of K, and α is the fine structure constant. The different contributions to $\boldsymbol{\sigma}_K$ follow from combining the obtained $\mathbf{I}_K$ and $\mathbf{B}_0$-dependent energy terms in different orders of PT. Correspondingly, energy terms depending on both $\mathbf{I}_K$ and $\mathbf{I}_L$ contribute to $\mathbf{J}_{KL}$. In the present SI-based atomic unit system, the NR expressions of $\boldsymbol{\sigma}$ and $\mathbf{J}$ appear as $\mathcal{O}(\alpha^2)$ and $\mathcal{O}(\alpha^4)$, respectively, whereas the leading-order relativistic terms appear two powers of α higher.

13.3 Electronic Hamiltonian

The two-component, positive-energy Hamiltonian that we consider can be written as $H = H_{\mathrm{ne}} + H_{\mathrm{kin}}^{\mathrm{NR}} + H_{\mathrm{kin}}^{\mathrm{R}} + H^{\mathrm{Dar(1)}} + H^{\mathrm{SO}}$ [20], where H_{ne} is the NR nuclear attraction potential,

$$H_{\mathrm{kin}}^{\mathrm{NR}} = \frac{1}{2}\sum_i \left(\pi_i^2 + \mathrm{i}\vec{\sigma}_i \cdot \boldsymbol{\pi}_i \times \boldsymbol{\pi}_i\right) \tag{13.3}$$

describes the NR kinematics and the spin-Zeeman interaction ($\vec{\sigma}$ is a vector of the Pauli spin matrices),

$$H_{\mathrm{kin}}^{\mathrm{R}} = -\frac{1}{8}\alpha^2 \sum_i \left(\pi_i^2 + \mathrm{i}\vec{\sigma}_i \cdot \boldsymbol{\pi}_i \times \boldsymbol{\pi}_i\right)^2 \tag{13.4}$$

provides a relativistic correction to the previous term, and

$$H^{\mathrm{Dar(1)}} = \frac{1}{2}\pi\alpha^2 \sum_N Z_N \sum_i \delta(\mathbf{r}_{iN}) \tag{13.5}$$

is the relativistic one-electron Darwin term, where Z_N is the charge of nucleus N. Finally, the relativistic SO term

$$H^{\mathrm{SO}} = H^{\mathrm{SO(1)}} + H^{\mathrm{SO(2)}} \tag{13.6}$$

$$H^{\mathrm{SO(1)}} = \frac{1}{4}\alpha^2 \sum_N Z_N \sum_i \frac{\vec{\sigma}_i \cdot (\mathbf{r}_{iN} \times \boldsymbol{\pi}_i)}{r_{iN}^3} \tag{13.7}$$

$$H^{\mathrm{SO(2)}} = -\frac{1}{4}\alpha^2 \sum_{ij}{}' \frac{\left(\vec{\sigma}_i + 2\vec{\sigma}_j\right) \cdot \mathbf{r}_{ij} \times \boldsymbol{\pi}_i}{r_{ij}^3} \tag{13.8}$$

consists of both one- and two-electron contributions. The latter is, besides the NR Coulomb repulsion between the electrons, $\frac{1}{2}\sum_{ij}{}' \frac{1}{r_{ij}}$, which is included in the optimisation of the reference state, the only two-electron term that we consider. For the other two-electron operators in H_{BP}, we refer to Refs. [9–11].

13.4 Non-Relativistic Contributions

The operators appearing in the NR theory of $\boldsymbol{\sigma}$ and $\mathbf{J}$ arise from Eq. (13.3), the NR kinematic term

$$\frac{1}{2}\sum_i \pi_i^2 \approx H^{\mathrm{KE}} + H_{B_0}^{\mathrm{OZ}} + H_K^{\mathrm{PSO}} + H_L^{\mathrm{PSO}} + H_{KB_0}^{\mathrm{DS}} + H_{LB_0}^{\mathrm{DS}} + H_{KL}^{\mathrm{DSO}} \tag{13.9}$$

and the NR spin–Zeeman term

$$\frac{1}{2}i\sum_i \vec{\sigma}_i \cdot (\boldsymbol{\pi}_i \times \boldsymbol{\pi}_i) = \frac{1}{2}\sum_i \vec{\sigma}_i \cdot \mathbf{B}_i = H_{B_0}^{\mathrm{SZ}} + H_K^{\mathrm{FC}} + H_L^{\mathrm{FC}} + H_K^{\mathrm{SD}} + H_L^{\mathrm{SD}}. \tag{13.10}$$

$H^{\mathrm{KE}} = -\frac{1}{2}\sum_i \nabla_i^2$ is the NR kinetic energy, and

$$H_{B_0}^{\mathrm{OZ}} = \frac{1}{2}\sum_\varepsilon B_{0,\varepsilon}\sum_i \ell_{iO,\varepsilon}; \quad H_K^{\mathrm{PSO}} = \alpha^2\gamma_K\sum_\varepsilon I_{K,\varepsilon}\sum_i \frac{\ell_{iK,\varepsilon}}{r_{iK}^3} \tag{13.11}$$

$$H_{KB_0}^{\mathrm{DS}} = \frac{1}{2}\alpha^2\gamma_K\sum_{\varepsilon\tau} I_{K,\varepsilon}B_{0,\tau}\sum_i \frac{\delta_{\varepsilon\tau}(\mathbf{r}_{iO}\cdot\mathbf{r}_{iK}) - r_{iO,\varepsilon}r_{iK,\tau}}{r_{iK}^3} \tag{13.12}$$

$$H_{KL}^{\mathrm{DSO}} = \frac{1}{2}\alpha^4\gamma_K\gamma_L\sum_{\varepsilon\tau} I_{K,\varepsilon}I_{L,\tau}\sum_i \frac{\delta_{\varepsilon\tau}(\mathbf{r}_{iL}\cdot\mathbf{r}_{iK}) - r_{iL,\varepsilon}r_{iK,\tau}}{r_{iK}^3 r_{iL}^3}. \tag{13.13}$$

In these formulae, $\boldsymbol{\ell}_{iO} = -\,\mathrm{i}\mathbf{r}_{iO}\times\nabla_i$ and $\boldsymbol{\ell}_{iK} = -\,\mathrm{i}\mathbf{r}_{iK}\times\nabla_i$ are the orbital angular momenta with respect to O and K, respectively. The abbreviations denote the orbital Zeeman (OZ) interaction, paramagnetic nuclear spin–electron orbit (PSO) interaction, and diamagnetic nuclear spin–electron orbit interactions, DS and DSO. We have omitted from Eq. (13.9) the terms quadratic in either B_0 or I_K.

In Eq. (13.10), the total magnetic field $\mathbf{B}_i$ contains the external field as well as the contact and dipolar fields from K and L [21] and

$$H_{B_0}^{\mathrm{SZ}} = \frac{1}{2}g_e\sum_\varepsilon B_{0,\varepsilon}\sum_i s_{i,\varepsilon} \tag{13.14}$$

$$H_K^{\mathrm{FC}} = \frac{4\pi}{3}\alpha^2 g_e\gamma_K\sum_\varepsilon I_{K,\varepsilon}\sum_i \delta(\mathbf{r}_{iK})s_{i,\varepsilon} \tag{13.15}$$

$$H_K^{\mathrm{SD}} = \frac{1}{2}\alpha^2 g_e\gamma_K\sum_{\nu\varepsilon} I_{K,\varepsilon}\sum_i s_{i,\nu}\frac{3r_{iK,\nu}r_{iK,\varepsilon} - \delta_{\nu\varepsilon}r_{iK}^2}{r_{iK}^5} \tag{13.16}$$

are the spin–Zeeman (SZ), Fermi contact (FC), and spin-dipole (SD) operators, in this order. We have used $\mathbf{s}_i = \frac{1}{2}\vec{\boldsymbol{\sigma}}_i$ for the electron spin operator. The experimental free-electron *g*-value, $g_e = 2.002319$ has been introduced semi-empirically in Eqs. (13.14–13.16) and in the following, instead of $g_e = 2$ as in the Dirac theory.

The NR contributions to $\boldsymbol{\sigma}$ and $\mathbf{J}$ resulting from these operators are listed in Tab. 13.1. Ref. [23] and the chapters of this book provide comprehensive reviews on the quantum chemical calculation of the NR terms.

Table 13.1 Non-relativistic contributions to nuclear magnetic shielding and spin-spin coupling tensors, $\boldsymbol{\sigma}$ and $\mathbf{J}$, respectively.

	First-order terms, $\langle A \rangle$			Second-order terms, $\langle\langle A;B \rangle\rangle_0$[a]			Interm.	Tensor[b]
Property	Symbol	A	Tensor[b]	Symbol	A and B		states[c]	
$\boldsymbol{\sigma}_K$	d	$H^{\mathrm{DS}}_{KB_o}$	0,2,1	p	H^{PSO}_K	and $H^{\mathrm{OZ}}_{B_o}$	singlet	0,2,1
$\mathbf{J}_{KL}$	DSO	H^{DSO}_{KL}	0,2,1	PSO	H^{PSO}_K	and H^{PSO}_L	singlet	0,2,1
				FC	H^{FC}_K	and H^{FC}_L	triplet	0
				SD	H^{SD}_K	and H^{SD}_L	triplet	0,2,1
				SD/FC	H^{SD}_K	and H^{FC}_L ($K \leftrightarrow L$)[d]	triplet	2

a) Linear response notation corresponding to a standard second-order PT expression involving the time-independent operators A and B [22].

b) Contributions to tensorial ranks: 0 corresponds to the isotropic shielding or spin–spin coupling constant, $T = 1/3\ (T_{xx} + T_{yy} + T_{zz})$, where $\mathbf{T}$ is either $\boldsymbol{\sigma}_K$ or $\mathbf{J}_{KL}$, 2 to the anisotropic but symmetric contributions $T^S_{\varepsilon\tau} = 1/2\ (T_{\varepsilon\tau} + T_{\tau\varepsilon}) - T\delta_{\varepsilon\tau}$ and 1 to the anisotropic and antisymmetric contributions $T^A_{\varepsilon\tau} = 1/2\ (T_{\varepsilon\tau} - T_{\tau\varepsilon})$.

c) Spin symmetry of the intermediate states when the ground state is a singlet.

d) Contributions from both perturbations of nuclear indices K and L.

13.5 Relativistic Kinematics and the Spin–Zeeman Effect

Relativistic terms in $\boldsymbol{\sigma}$ and $\mathbf{J}$ arise when considering the terms (13.4), (13.5), (13.7) and (13.8) in the Hamiltonian. In Eq. (13.4), $\boldsymbol{\pi}_i^2$ and $\mathrm{i}\vec{\boldsymbol{\sigma}}_i \cdot \boldsymbol{\pi}_i \times \boldsymbol{\pi}_i$ do not commute for spatially non-uniform magnetic fields (such as those due to the nuclei), and thus

$$H^{\mathrm{R}}_{\mathrm{kin}} = -\frac{1}{8}\alpha^2 \sum_i \boldsymbol{\pi}_i^4 - \frac{1}{8}\alpha^2 \mathrm{i} \sum_i \left[\boldsymbol{\pi}_i^2, \vec{\boldsymbol{\sigma}}_i \cdot \boldsymbol{\pi}_i \times \boldsymbol{\pi}_i\right]_+ + \frac{1}{8}\alpha^2 \sum_i (\vec{\boldsymbol{\sigma}}_i \cdot \boldsymbol{\pi}_i \times \boldsymbol{\pi}_i)^2, \tag{13.17}$$

where the anticommutator of the operators A and B is denoted $[A, B]_+ = AB + BA$. Expanding the first term gives rise to

$$-\frac{1}{8}\alpha^2\sum_i \pi^4 \approx H^{\mathrm{mv}} + H_{B_0}^{\mathrm{OZ-KE}} + H_K^{\mathrm{PSO-KE}} + H_L^{\mathrm{PSO-KE}} + H_{KB_0}^{\mathrm{DS-KE}} +$$

$$H_{LB_0}^{\mathrm{DS-KE}} + H_{KL}^{\mathrm{DSO-KE}} + H_{KB_0}^{\mathrm{PSO-OZ}} + H_{LB_0}^{\mathrm{PSO-OZ}} + H_{KL}^{\mathrm{PSO-PSO}}, \tag{13.18}$$

where

$$H^{\mathrm{mv}} = -\frac{1}{8}\alpha^2\sum_i \nabla_i^4 \tag{13.19}$$

$$H_{B_0}^{\mathrm{OZ-KE}} = \frac{1}{4}\alpha^2\sum_\varepsilon B_{0,\varepsilon}\sum_i \ell_{iO,\varepsilon}\nabla_i^2 \tag{13.20}$$

$$H_K^{\mathrm{PSO-KE}} = \frac{1}{4}\alpha^4\gamma_K\sum_\varepsilon I_{K,\varepsilon}\sum_i \left[\nabla_i^2, \frac{\ell_{iK,\varepsilon}}{r_{iK}^3}\right]_+ \tag{13.21}$$

$$H_{KB_0}^{\mathrm{DS-KE}} = \frac{1}{8}\alpha^4\gamma_K\sum_{\varepsilon\tau} I_{K,\varepsilon}B_{0,\tau}\sum_i \left[\nabla_i^2, \frac{\delta_{\varepsilon\tau}(\mathbf{r}_{iO}\cdot\mathbf{r}_{iK}) - r_{iO,\varepsilon}r_{iK,\tau}}{r_{iK}^3}\right]_+ \tag{13.22}$$

$$H_{KL}^{\mathrm{DSO-KE}} = \frac{1}{8}\alpha^6\gamma_K\gamma_L\sum_{\varepsilon\tau} I_{K,\varepsilon}I_{L,\tau}\sum_i \left[\nabla_i^2, \frac{\delta_{\varepsilon\tau}(\mathbf{r}_{iL}\cdot\mathbf{r}_{iK}) - r_{iL,\varepsilon}r_{iK,\tau}}{r_{iK}^3 r_{iL}^3}\right]_+ \tag{13.23}$$

$$H_{KB_0}^{\mathrm{PSO-OZ}} = \frac{1}{4}\alpha^4\gamma_K\sum_{\varepsilon\tau} I_{K,\varepsilon}B_{0,\tau}\sum_i \left[\frac{\ell_{iK,\varepsilon}}{r_{iK}^3}, \ell_{iO,\tau}\right]_+ \tag{13.24}$$

$$H_{KL}^{\mathrm{PSO-PSO}} = \frac{1}{2}\alpha^6\gamma_K\gamma_L\sum_{\varepsilon\tau} I_{K,\varepsilon}I_{L,\tau}\sum_i \left[\frac{\ell_{iK,\varepsilon}}{r_{iK}^3}, \frac{\ell_{iL,\tau}}{r_{iL}^3}\right]_+ \tag{13.25}$$

are the mass-velocity (mv) Hamiltonian, kinetic energy corrections to the NR Zeeman and orbital hyperfine operators (OZ-KE, PSO-KE, DS-KE and DSO-KE), and two new cross-terms between the NR terms, PSO-OZ and PSO-PSO. We have omitted terms higher than quadratic in the vector potential, and also those where B_0, I_K or I_L appear to second power.

The electron-spin dependent second term in Eq. (13.17) becomes

$$-\frac{1}{8}\alpha^2 \mathrm{i}\sum_i \left[\pi_i^2, \vec{\sigma}_i \cdot \boldsymbol{\pi}_i \times \boldsymbol{\pi}_i\right]_+ = -\frac{1}{8}\alpha^2 \sum_i \left[\pi_i^2, \vec{\sigma}_i \cdot \mathbf{B}_i\right]_+$$
$$\approx H_{B_0}^{\mathrm{SZ-KE}} + H_K^{\mathrm{FC-KE}} + H_L^{\mathrm{FC-KE}} + H_K^{\mathrm{SD-KE}} + H_L^{\mathrm{SD-KE}} \tag{13.26}$$

where

$$H_{B_0}^{\mathrm{SZ-KE}} = \frac{1}{4}\alpha^2 g_e \sum_\varepsilon B_{0,\varepsilon} \sum_i s_{i,\varepsilon} \nabla_i^2 \tag{13.27}$$

$$H_K^{\mathrm{FC-KE}} = \frac{\pi}{3}\alpha^4 g_e \gamma_K \sum_\varepsilon I_{K,\varepsilon} \sum_i s_{i,\varepsilon} \left[\nabla_i^2, \delta(\mathbf{r}_{iK})\right]_+ \tag{13.28}$$

$$H_K^{\mathrm{SD-KE}} = \frac{1}{8}\alpha^4 g_e \gamma_K \sum_{\varepsilon\tau} I_{K,\tau} \sum_i s_{i,\varepsilon} \left[\nabla_i^2, \frac{3 r_{iK,\varepsilon} r_{iK,\tau} - \delta_{\varepsilon\tau} r_{iK}^2}{r_{iK}^5}\right]_+ \tag{13.29}$$

are the kinetic energy corrections to the spin–Zeeman (SZ-KE) and the Fermi-contact and spin-dipole hyperfine operators, FC-KE and SD-KE, respectively. We have omitted terms as before, and additionally the terms of the $\alpha^4 I_K B_0$ or $\alpha^6 I_K I_L$ forms, but which contain an electron spin dependence. The latter do not contribute to the leading-order relativistic terms in $\boldsymbol{\sigma}$ or $\mathbf{J}$ in closed-shell systems.

The last term arising from $H_{\mathrm{kin}}^{\mathrm{R}}$ is

$$\frac{1}{8}\alpha^2 \sum_i (\vec{\sigma}_i \cdot \boldsymbol{\pi}_i \times \boldsymbol{\pi}_i)^2 = -\frac{1}{8}\alpha^2 \sum_i (\vec{\sigma}_i \cdot \mathbf{B}_i)^2$$
$$\approx H_{KB_0}^{\mathrm{con}} + H_{LB_0}^{\mathrm{con}} + H_{KB_0}^{\mathrm{dip}} + H_{LB_0}^{\mathrm{dip}} + H_{KL}^{\mathrm{con-dip}} + H_{KL}^{\mathrm{dip-dip}}, \tag{13.30}$$

where the dependence on electron spin vanishes, i.e. $(\vec{\sigma}_i \cdot \mathbf{B}_i)^2 = B_i^2$, as seen from applying $(\vec{\sigma} \cdot \mathbf{A})(\vec{\sigma} \cdot \mathbf{B}) = \mathbf{A} \cdot \mathbf{B} + \mathrm{i}\vec{\sigma} \cdot \mathbf{A} \times \mathbf{B}$. The remaining, electron spin-independent hyperfine operators arise from cross-terms between the homogeneous external field and the contact and dipolar fields from K and L:

$$H_{KB_0}^{\mathrm{con}} = -\frac{2\pi}{3}\alpha^4 \gamma_K \sum_\varepsilon B_{0,\varepsilon} \sum_i \delta(\mathbf{r}_{iK}) I_{K,\varepsilon} \tag{13.31}$$

$$H_{KB_0}^{\mathrm{dip}} = -\frac{1}{4}\alpha^4 \gamma_K \sum_{\varepsilon\tau} I_{K,\varepsilon} B_{0,\tau} \sum_i \frac{3r_{iK,\varepsilon} r_{iK,\tau} - \delta_{\varepsilon\tau} r_{iK}^2}{r_{iK}^5} \tag{13.32}$$

$$H_{KL}^{\mathrm{con-dip}} = -\frac{2\pi}{3}\alpha^6 \gamma_K \gamma_L \sum_{\varepsilon\tau} I_{K,\varepsilon} I_{L,\tau} \sum_i \left[\delta(\mathbf{r}_{iK}) \frac{3r_{iL,\varepsilon} r_{iL,\tau} - \delta_{\varepsilon\tau} r_{iL}^2}{r_{iL}^5} \right.$$

$$\left. + \delta(\mathbf{r}_{iL}) \frac{3r_{iK,\varepsilon} r_{iK,\tau} - \delta_{\varepsilon\tau} r_{iK}^2}{r_{iK}^5} \right] \tag{13.33}$$

$$H_{KL}^{\mathrm{dip-dip}} = -\frac{1}{4}\alpha^6 \gamma_K \gamma_L \sum_{\varepsilon\tau} I_{K,\varepsilon} I_{L,\tau} \sum_i \frac{1}{r_{iK}^5 r_{iL}^5} \left[9r_{iK,\varepsilon} r_{iL,\tau} (\mathbf{r}_{iK} \cdot \mathbf{r}_{iL}) \right.$$

$$\left. - 3r_{iK,\varepsilon} r_{iK,\tau} r_{iL}^2 - 3r_{iL,\varepsilon} r_{iL,\tau} r_{iK}^2 + \delta_{\varepsilon\tau} r_{iK}^2 r_{iL}^2 \right] \tag{13.34}$$

The corresponding "con-con" cross term, proportional to the product of the contact fields of two nuclei that do not coincide, vanishes everywhere in space.

13.6 Spin–Orbit Coupling

The one- and two-electron SO Hamiltonians become

$$H^{\mathrm{SO}(n)} = h^{\mathrm{SO}(n)} + H_{B_0}^{\mathrm{SO}(n)} + H_K^{\mathrm{SO}(n)} + H_L^{\mathrm{SO}(n)}, \tag{13.35}$$

where the field-independent and -dependent SO interactions are

$$h^{\mathrm{SO}(1)} = \frac{1}{4}\alpha^2 g_e \sum_N Z_N \sum_\nu \sum_i s_{i,\nu} \frac{\ell_{iN,\nu}}{r_{iN}^3} \tag{13.36}$$

$$h^{\mathrm{SO}(2)} = -\frac{1}{4}\alpha^2 g_e \sum_\nu {\sum_{ij}}' \left(s_{i,\nu} + 2s_{j,\nu} \right) \frac{\ell_{ij,\nu}}{r_{ij}^3} \tag{13.37}$$

$$H_{B_0}^{\mathrm{SO}(1)} = \frac{1}{8}\alpha^2 g_e \sum_N Z_N \sum_{\nu\varepsilon} B_{0,\varepsilon} \sum_i s_{i,\nu} \frac{\delta_{\nu\varepsilon}\left(\mathbf{r}_{iO}\cdot\mathbf{r}_{iN}\right) - r_{iO,\nu} r_{iN,\varepsilon}}{r_{iN}^3} \tag{13.38}$$

$$H_{B_0}^{\mathrm{SO}(2)} = -\frac{1}{8}\alpha^2 g_e \sum_{\nu\varepsilon} B_{0,\varepsilon} \sum_{ij}{}' \left(s_{i,\nu} + 2s_{j,\nu}\right) \frac{\delta_{\nu\varepsilon}\left(\mathbf{r}_{iO}\cdot\mathbf{r}_{ij}\right) - r_{iO,\nu} r_{ij,\varepsilon}}{r_{ij}^3} \tag{13.39}$$

$$H_K^{\mathrm{SO}(1)} = \frac{1}{4}\alpha^4 g_e \gamma_K \sum_N Z_N \sum_{\nu\varepsilon} I_{K,\varepsilon} \sum_i s_{i,\nu} \frac{\delta_{\nu\varepsilon}\left(\mathbf{r}_{iK}\cdot\mathbf{r}_{iN}\right) - r_{iK,\nu} r_{iN,\varepsilon}}{r_{iK}^3 r_{iN}^3} \tag{13.40}$$

$$H_K^{\mathrm{SO}(2)} = -\frac{1}{4}\alpha^4 g_e \gamma_K \sum_{\nu\varepsilon} I_{K,\varepsilon} \sum_{ij}{}' \left(s_{i,\nu} + 2s_{j,\nu}\right) \frac{\delta_{\nu\varepsilon}\left(\mathbf{r}_{iK}\cdot\mathbf{r}_{ij}\right) - r_{iK,\nu} r_{ij,\varepsilon}}{r_{iK}^3 r_{ij}^3} \tag{13.41}$$

13.7 Relativistic Corrections to Shielding and Coupling

We have summarised in Tab. 13.2 and 13.3 the leading-order relativistic contributions to $\boldsymbol{\sigma}$ and $\mathbf{J}$, resulting from the previous perturbation operators acting upon a NR spin- and field-free reference state. Numerical results for some of the terms are listed in Tab. 13.4 for $\boldsymbol{\sigma}$ in the HI molecule and in Tab. 13.5 for $\mathbf{J}$ in H_2Te. Most of the leading-order corrections are included for $\boldsymbol{\sigma}$ in Tab. 13.4, and even the missing ones are not expected to pose problems in the perturbation calculation. In contrast, the coupling contributions featuring the FC and mv or Dar(1) operators simultaneously, diverge upon increasing the size of the basis set. Hence, the present approach has much more limited potential for couplings than for shieldings. In the latter case, no such divergent terms occur.

The development of the perturbational method for including relativistic effects into calculations of NMR parameters, based on H_{BP}, began when the SO coupling effects (the SO-I terms) were noted to be an important factor for $\boldsymbol{\sigma}$ [30–33] of light nuclei in systems containing heavy atoms. A transparent interpretation of this effect was given in Ref. [34]. Cheremisin and Schastnev [33] as well as Fukui et al. [20] introduced the SO-II effect due to the magnetic field dependence of the SO Hamiltonian. It should be noted that the FC-I and FC-II as well as the SD-I and SD-II terms are not individually gauge invariant, but the sums of the corresponding third- and second-order effects are [20]. With the gauge origin sensibly placed close to the center of charge of the molecule, the SO-I term dominates the relativistic effects on the

shieldings of light nuclei (Tab. 13.4). The SO-II term appears with a sign opposite to that of the SO-I [20,35] and is numerically larger for the heavy nuclei themselves.

Table 13.2 Leading-order, $\mathcal{O}(\alpha^4)$, relativistic contributions to the nuclear magnetic shielding tensor $\boldsymbol{\sigma}$.[a]

First-order terms, $\langle \boldsymbol{A} \rangle$

Symbol	A	Tensor	Type[b]
con.	$H^{\mathrm{con}}_{KB_0}$	0	Act.
dip	$H^{\mathrm{dip}}_{KB_0}$	2	Act.
d-ke	$H^{\mathrm{DS-KE}}_{KB_0}$	0,2,1	Act., HAHA?[c]
p-OZ	$H^{\mathrm{PSO-OZ}}_{KB_0}$	0,2,1	Act., HAHA?[c]

Second-order terms, $\langle\langle \boldsymbol{A; B} \rangle\rangle_{\boldsymbol{0}}$

Symbol	A and B	Interm. states	Tensor	Type
p-ke/OZ	$H^{\mathrm{PSO-KE}}_{K}$ and $H^{\mathrm{OZ}}_{B_0}$	singlet	0,2,1	Act.
p/OZ-KE	H^{PSO}_{K} and $H^{\mathrm{OZ-KE}}_{B_0}$	singlet	0,2,1	Act.
d/mv	$H^{\mathrm{DS}}_{KB_0}$ and H^{mv}	singlet	0,2,1	Pass.
d/Dar	$H^{\mathrm{DS}}_{KB_0}$ and $H^{\mathrm{Dar(1)}}$	singlet	0,2,1	Pass.
FC/SZ-KE	H^{FC}_{K} and $H^{\mathrm{SZ-KE}}_{B_0}$	triplet	0	Act., HAHA
SD/SZ-KE	H^{SD}_{K} and $H^{\mathrm{SZ-KE}}_{B_0}$	triplet	2	Act.
FC-II	H^{FC}_{K} and $H^{\mathrm{SO(1\&2)}}_{B_0}$	triplet	0,2,1	Act., HAHA
SD-II	H^{SD}_{K} and $H^{\mathrm{SO(1\&2)}}_{B_0}$	triplet	0,2,1	Act.

Third-order terms, $\langle\langle \boldsymbol{A; B, C} \rangle\rangle_{\boldsymbol{0,0}}$ [d]

Symbol	A, B and C	Interm. states	Tensor	Type
p/mv	H^{PSO}_{K}, $H^{\mathrm{OZ}}_{B_0}$ and H^{mv}	singlet	0,2,1	Pass.
p/Dar	H^{PSO}_{K}, $H^{\mathrm{OZ}}_{B_0}$ and $H^{\mathrm{Dar(1)}}$	singlet	0,2,1	Pass.
FC-I	H^{FC}_{K}, $H^{\mathrm{OZ}}_{B_0}$ and $h^{\mathrm{SO(1\&2)}}$	triplet and singlet[e]	0,2,1	Pass., HALA
SD-I	H^{SD}_{K}, $H^{\mathrm{OZ}}_{B_0}$ and $h^{\mathrm{SO(1\&2)}}$	triplet and singlet[e]	0,2,1	Pass., HALA

a) See footnotes in Tab. 13.1
b) Classification into passive/active as well as into HAHA/HALA (if known) categories.
c) The results of Ref. [24] point to the HAHA character.
d) Quadratic response notation corresponding to standard third-order PT expression involving the time-independent operators A,B and C [22].
e) Both triplet and singlet intermediate states contribute.

Table 13.3 Leading order, $\mathcal{O}(\alpha^6)$, relativistic contributions to the spin-spin coupling tensor $\mathbf{J}$.[a]

First-order terms, $\langle \boldsymbol{A} \rangle$

Symbol	A	Tensor	Type
con-dip	$H_{KL}^{\text{con–dip}}$	2	Act.
dip-dip	$H_{KL}^{\text{dip–dip}}$	0,2,1	Act.
DSO-KE	$H_{KL}^{\text{DSO–KE}}$	0,2,1	Act.
PSO-PSO	$H_{KL}^{\text{PSO–PSO}}$	0,2,1	Act.

Second-order terms, $\langle\langle \boldsymbol{A; B} \rangle\rangle_{\mathbf{0}}$

Symbol	A and B	Interm. states	Tensor	Type
DSO/mv	H_{KL}^{DSO} and H^{mv}	singlet	0,2,1	Pass.
DSO/Dar	H_{KL}^{DSO} and $H^{\text{Dar(1)}}$	singlet	0,2,1	Pass.
PSO/PSO-KE	H_{K}^{PSO} and $H_{L}^{\text{PSO–KE}}$ ($K \leftrightarrow L$)	singlet	0,2,1	Act.
FC/FC-KE	H_{K}^{FC} and $H_{L}^{\text{FC–KE}}$ ($K \leftrightarrow L$)	triplet	0	Act.
FC/SD-KE	H_{K}^{FC} and $H_{L}^{\text{SD–KE}}$ ($K \leftrightarrow L$)	triplet	2	Act.
SD/FC-KE	H_{K}^{SD} and $H_{L}^{\text{FC–KE}}$ ($K \leftrightarrow L$)	triplet	2	Act.
SD/SD-KE	H_{K}^{SD} and $H_{L}^{\text{SD–KE}}$ ($K \leftrightarrow L$)	triplet	0,2,1	Act.
FC/SO	H_{K}^{FC} and $H_{L}^{\text{SO(1\&2)}}$ ($K \leftrightarrow L$)	triplet	0,2,1	Act.
SD/SO	H_{K}^{SD} and $H_{L}^{\text{SO(1\&2)}}$ ($K \leftrightarrow L$)	triplet	0,2,1	Act.

Third-order terms, $\langle\langle \boldsymbol{A; B, C} \rangle\rangle_{\mathbf{0,0}}$

Symbol	A, B and C	Interm. states	Tensor	Type
PSO/mv	H_{K}^{PSO}, H_{L}^{PSO} and H^{mv}	singlet	0,2,1	Pass.
PSO/Dar	H_{K}^{PSO}, H_{L}^{PSO} and $H^{\text{Dar(1)}}$	singlet	0,2,1	Pass.
FC/mv	H_{K}^{FC}, H_{L}^{FC} and H^{mv}	triplet and singlet	0	Pass.
SD/mv	H_{K}^{SD}, H_{L}^{SD} and H^{mv}	triplet and singlet	0,2,1	Pass.
FC/Dar	H_{K}^{FC}, H_{L}^{FC} and $H^{\text{Dar(1)}}$	triplet and singlet	0	Pass.
SD/Dar	H_{K}^{SD}, H_{L}^{SD} and $H^{\text{Dar(1)}}$	triplet and singlet	0,2,1	Pass.
SD/FC/mv	H_{K}^{SD}, H_{L}^{FC} and H^{mv} ($K \leftrightarrow L$)	triplet and singlet	2	Pass.
FC/PSO	H_{K}^{FC}, H_{L}^{PSO} and $h^{\text{SO(1\&2)}}$ ($K \leftrightarrow L$)	triplet and singlet	0,2,1	Pass.
SD/PSO	H_{K}^{SD}, H_{L}^{PSO} and $h^{\text{SO(1\&2)}}$ ($K \leftrightarrow L$)	triplet and singlet	0, 2, 1	Pass.

a) See footnotes in Tab. 13.1 and 13.2.

Table 13.4 Numerical results for the non-relativistic as well as the leading-order relativistic nuclear magnetic shielding constants of ^{1}H and ^{127}I in the HI molecule.[a]

		NR[b]			Passive SR effects			
Nucleus	**Theory**	***d***	***p***	**GIAO**	***d*/mv**	***d*/Dar**	***p*/mv**	***p*/Dar**
I	SCF	5507.76	–951.65	4556.04	889.86	–474.46	–386.51	126.54
	CASSCF	5507.85	–845.85	4661.91	889.85	–474.45	–317.48	85.41
H	SCF	19.84	12.40	31.45	0.336	–0.570	0.293	–0.241
	CASSCF	20.52	11.85	31.57	0.233	–0.463	0.159	–0.128
		Active non-SO			**Passive SO effects**			
		con	**FC/SZ-KE**	**p/OZ-KE**	**FC-I(1)**	**SD-I(1)**	**FC-I(2)**	**SD-I(2)**
I	SCF	–623.14	1931.08	143.00	107.90	46.13	–10.35	–5.11
	CASSCF	–623.14	1931.01	142.97	86.85	13.75	–8.45	–3.03
H	SCF	–0.002	–0.019	–0.002	18.601	0.585	–1.245	0.548
	CASSCF	–0.002	–0.013	–0.002	11.876	0.343	–0.836	–0.029
		Active SO						
		FC-II(1)	**SD-II(1)**		**Total**	**DHF[c]**	**Exp.**	
I	SCF	–330.40	43.38		6013.96	6768.4		
	CASSCF	–330.35	43.33		6098.17			
H	SCF	0.020	0.000		49.754	47.98		
	CASSCF	0.014	0.000		42.719		43.86[d]	

a) In ppm. Uncontracted basis sets: I [22*s*18*p*17*d*2*f*] and H [8*s*3*p*1*d*], SCF and complete active space SCF calculations with 8 electrons correlated in 13 orbitals. The DALTON program [25] has been used. For further details, refer to Ref. [26].

b) Dia- and paramagnetic terms from a common gauge origin (at I) calculation. The GIAO NR results (used also in the "Total" column) include both dia- and paramagnetic contributions.

c) Ref. [7]. The result for HI is probably overestimated due to the sc. diamagnetic approximation. See the discussion in Ref. [26].

d) Ref. [27].

The contribution of the full (one- and two-electron) field-free SO operator differs only by a few percent from the results obtained with the one-electron SO operator only, for heavy nuclei [36, 37]. The computationally very efficient, one-electron/one-center mean-field approximation to the one- and two-electron SO operator [38] using the AMFI software [39], has been adopted for these calculations [37]. The SO-I contributions were found to be strongly dependent on internuclear distances [40, 41], and to cause dramatic effects on the experimentally observable secondary isotope effects on $\boldsymbol{\sigma}$ [42].

The first applications of SO-I corrections to **J** were discussed in Refs. [16, 43, 44]. While these studies demonstrated the need to consider also the electron spin-free, scalar relativistic (SR) effects when at least one of the coupled nuclei is a heavy one, the SO terms may be sufficient for couplings between light nuclei in heavy atom systems [43]. The FC/SO and SD/SO terms, introduced in [43], are even formally not available for couplings to heavy centres as the SO hyperfine integral in $H_K^{\mathrm{SO}(1)}$ diverges in these cases [43].

Table 13.5 Numerical results for the non-relativistic as well as leading order relativistic $^1J_{HTe}$ and $^2J_{HH}$ spin-spin coupling constants in the H_2Te molecule.[a]

		NR			
Coupling	**Theory**	**DSO**	**PSO**	**SD**	**FC**
HTe	SCF	0.02	–26.79	7.46	–272.94
	CASSCF	0.01	–28.77	1.80	–254.13
HH	SCF	–1.22	1.00	0.00	–21.85
CASSCF		–1.20	1.00	0.02	–18.71

		Passive SR effects					
Coupling	**Theory**	**DSO/mv**	**DSO/Dar**	**PSO/mv**	**PSO/Dar**	**SD/mv**	**SD/Dar**
HTe	SCF	0.0042	–0.0082	–15.5277	–0.1142	7.1704	–1.7753
	CASSCF	0.0036	–0.0071	–16.4871	0.1888	2.1495	–0.5477
HH	SCF	0.0123	–0.0009	0.0787	–0.0513	–0.0087	0.0092
	CASSCF	0.0122	–0.0087	0.0917	–0.0596	–0.0137	0.0112

		Passive SO effects				Active SO effects	
Coupling	**Theory**	**FC-I(1)**	**SD-I(1)**	**FC-I(2)**	**SD-I(2)**	**FC-II(1)**	**SD-II(1)**
HTe	SCF	73.7599	–1.7334	–0.3133	0.1352		
	CASSCF	54.3049	–2.1624	–0.3623	0.1191		
HH	SCF	1.9836	0.0304	–0.1245	–0.0023	0.00142	–0.00016
	CASSCF	1.4090	0.0171	–0.0895	–0.0014	0.00050	–0.00015

		Total						
Coupling	**Theory**	**NR**	**SR**	**SO**	**SR+SO**	**Total**	**DHF[28]**	**Exp. [29]**
HTe	SCF	–292.25	–10.25	71.85	61.60	–230.65	92.21	
	CASSCF	–281.09	–14.70	51.90	37.20	–243.89		–59±2
HH	SCF	–22.07	0.03	1.89	1.92	–20.15	–23.45	
	CASSCF	–18.89	0.03	1.34	1.37	–17.53		

a) In Hz. See footnote *a* in Tab. 13.4.

The contributions to $\boldsymbol{\sigma}$ arising from the cross-coupling of the relativistic correction to the electronic spin–Zeeman interaction (SZ-KE) and the spin-dependent FC and SD hyperfine interactions, were found in Ref. [20]. These contributions, of which the FC/SZ-KE term was later numerically found by Visscher et al. [7] to be the dominant one for heavy nuclei (see also Tab. 13.4), cannot straightforwardly be characterised either as SO or SR effects. The FC/SZ-KE contribution is also very insensitive both to the chemical environment and electron correlation effects, as pointed out in Refs. [26, 45, 46]. Melo et al. [45] presented a comprehensive formal survey of the leading-order corrections to $\boldsymbol{\sigma}$ arising from H_{BP}, and the relation of this level of theory to the four-component framework including vacuum polarization effects.

Numerically probably the most complete study of $\boldsymbol{\sigma}$ so far was carried out in Ref. [26], where reproduction of the DHF data of similar quality to that with the ZORA and DKH methods, was achieved for hydrogen chalcogenides, hydrogen halides and noble gas atoms. Relativistic effects were classified into two categories in Ref. [26].

The "active" terms feature relativistic perturbations referring explicitly to the degrees of freedom in the effective NMR spin Hamiltonian, the nuclear spins **I** and/or the external magnetic field $\mathbf{B}_0$. The "passive" perturbations do not contain **I** or $\mathbf{B}_0$, and affect the NMR parameters through relativistic modification of the wave function only. Bouten et al. [24] earlier referred to exactly the same classification with their "direct" and "indirect" effects, respectively. The SO-I effect on either $\boldsymbol{\sigma}$ or **J** is an example of a passive effect, where the **I**- and $\mathbf{B}_0$-independent part of the SO interaction induces spin polarisation to the closed-shell reference state, and the magnetic perturbations take the NR form. The FC/SZ-KE contribution to $\boldsymbol{\sigma}$ exemplifies an active effect, as reference to $\mathbf{B}_0$ is carried by the relativistic SZ-KE operator itself. The class of active, **I**-dependent SR effects was not included in the calculations of Ref. [26].

A further useful categorisation of shielding effects is into heavy-atom influence on the heavy atom (HAHA) and heavy-atom effects on the light atoms (HALA) [47]. Mechanisms belonging to the HAHA type mainly affect the NMR observables of the same nucleus in which the relativistic effect originates. The HALA effects are, in turn, mediated to the light nuclei from the heavy atoms. While the FC/SZ-KE term in $\boldsymbol{\sigma}$ is responsible for the majority of the HAHA effect [26, 46], the SO-I mechanism has both HAHA and HALA character. Obviously this classification is not as well-defined as the one into active and passive effects.

In its most rigorous form, perturbational relativity means inclusion of both the relativistic as well as magnetic perturbations on equal footing, with the reference state optimised using ab initio or density-functional theory (DFT) methods and a NR spin- and external field-free Hamiltonian. Such "fully perturbational" studies have been carried out in Refs. [7, 26, 35, 36, 40, 42, 45, 46] for $\boldsymbol{\sigma}$ and in Refs. [16, 43, 44] for **J**, at various ab initio levels. Nakatsuji et al. [48] used finite perturbation theory (FPT) for the SO-I contributions to $\boldsymbol{\sigma}$. Malkin et al. [49] applied FPT by including the FC interaction as a finite perturbation, in their DFT calculations of the SO-I shielding term.

DFT studies based on SR effective core potentials (ECPs) were pioneered by Kaupp et al. [50, 51] as well as Bacskay et al. [52]. There, the relativistic effects are included in formally NR self-consistent valence-only calculations, through the ECP parameters that are optimised in relativistic atomic calculations. The ECP technique indirectly allows inclusion of relativistic effects beyond leading order, but it has been limited to only the NMR parameters of the light centres of the system, those for which no ECPs are used (see, however, Ref. [53]). Nakatsuji et al. [54] (at the SCF level) and Vaara et al. [55] supplemented the ECP method with perturbational SO effects on $\boldsymbol{\sigma}$. It is in the ECP framework where the present SO corrections to **J** are expected to have their main application potential. ECPs intrinsically allow only for the passive relativistic effects to be included. A comparison of ab initio all-electron and DFT ECP calculations for ^{1}H shielding in HI is given in Tab. 13.6.

The limitation to passive relativistic effects applies also to the optimisation of the reference state including the SR mv and Dar(1) operators together with a relativistic frozen core [62, 63], later including perturbational SO-I terms [64]. Ref. [24] extended the method with the active SR effects on $\boldsymbol{\sigma}$. HAHA effects and, hence, $\boldsymbol{\sigma}$ in the abso-

Table 13.6 Comparison of ab initio all-electron and DFT effective core potential results for the ^{1}H nuclear magnetic shielding constant in the HI molecule.[a]

Theory	NR	Pass. SR	Act. non-SO
SCF	31.57	–0.156	–0.021
CASSCF	31.64	–0.164	–0.017
DFT/LDA		30.12[b]	
DFT/PW91		30.47[b]	
DFT/BP86		30.69[b]	
DFT/P86		30.73[b]	

	Passive SO		Active SO		
	Total FC[c]	Total SD[c]	FC-II(1)	SD-II(1)	Total
SCF	16.332	0.284	0.019	0.000	48.03
CASSCF	11.115	0.220	0.014	0.000	42.91
DFT/LDA	9.602	–	0.008	–	39.73
DFT/PW91	10.314	–	0.008	–	40.79
DFT/BP86	11.643	–	0.009	–	42.34
DFT/P86	12.062	–	0.010	–	42.80

a) In ppm. See text for definitions of acronyms. All calculations with a common gauge origin at the I nucleus. All-electron SCF and CASSCF calculations as in footnote *a* of Tab. 13.4, apart from the following contracted basis: I [20*s*16*p*14*d*/14*s*13*p*12*d*] and H [6*s*2*p*/4*s*2*p*]. DFT ECP calculations with the method of Ref. [55] using the de Mon-NMR-EPR program [56] with the SR and SO ECPs and [6*s*6*p*2*d*/4*s*4*p*2*d*] valence basis sets [57] for iodine, and the [6*s*2*p*/4*s*2*p*] set for H. SO contributions from H obtained using the AMFI program [39]. The different functionals used are local density approximation (LDA) and three generalised gradient approximations: Perdew–Wang91 (PW91) [58], Becke–Perdew (BP86) [59, 60], and Perdew86 (P86) [61]. The de Mon-NMR-EPR implementation does not include the SD terms in the SO contributions.
b) The ECP calculation includes the passive SR effects.
c) Total FC = FC-I(1) + FC-I(2), Total SD = SD-I(1) + SD-I(2).

lute sense are incompletely recovered by the frozen core method, whereas the situation is better for the relative chemical shifts.

13.8 Conclusions

We have presented the approach of perturbational calculation of the leading-order relativistic effects on the spectral parameters of NMR spectroscopy, the nuclear shielding tensor $\boldsymbol{\sigma}$ and indirect spin–spin coupling tensor $\mathbf{J}$, based on a non-relativistic (NR) spin- and external field-free, ab initio or density-functional reference state. In this method, relativistic effects are incorporated by using the relativistic as well as magnetic interaction operators, based on the (Breit–)Pauli Hamiltonian, as perturba-

tions on equal footing. A classification into passive and active relativistic effects has been presented, where the former feature modification of the NR expressions by relativistic field- and nuclear spin-free operators, taken up to first order. In the active effects, the relativistic perturbation operators are also considered up to first order only, but contain an explicit functional dependence on the external magnetic field and/or the nuclear magnetic moment. We mainly discussed the one-electron perturbation operators, but also considered the two-electron spin–orbit (SO) operator. It turns out that the complete set of leading one-electron corrections to $\boldsymbol{\sigma}$ can be obtained perturbationally, whereas the leading corrections to $\mathbf{J}$ feature divergent terms due to the simultaneous occurrence of multiple singular operators in some of the perturbation-theoretical expressions. An approach based on effective core potentials (ECPs) can be used for the NMR parameters of the light atomic centers only, for which no ECPs are used. The ECP technique allows a variationally stable inclusion of the spin-free passive relativistic effects from the cores of the ECP centres, in the formally NR valence calculation, but the SO effects can be added perturbationally. We gave a brief survey of the literature concerning the different relativistic terms.

Acknowledgements

The fruitful cooperation with Profs. Martin Kaupp (Würzburg) and Kenneth Ruud (Tromsø) has significantly benefitted our research in this field. JV is Academy Fellow of the Academy of Finland, and on leave from the NMR Research Group, Department of Physical Sciences, University of Oulu, Finland. He is further supported by the Magnus Ehrnrooth Fund as well as the Vilho, Yrjö and Kalle Väisälä Foundation. PM is supported by the Jenny and Antti Wihuri and Magnus Ehrnrooth Funds as well as the Chancellor of the University of Helsinki. PL thanks the Finnish Cultural Foundation, the Pohjois-Pohjanmaa Fund of the Finnish Cultural Foundation, the Tauno Tönninki Foundation and the Magnus Ehrnrooth Fund for financial support. The computational resources were partially provided by the Center for Scientific Computing, Espoo, Finland.

References

1 P. Pyykkö, *Adv. Quantum Chem.* **1978**, *11*, 353; *Chem. Rev.* **1988**, *88*, 563.
2 J. Autschbach, T. Ziegler, in *Encyclopedia of Nuclear Magnetic Resonance, Vol. 9: Advances in NMR*, eds. D. M. Grant, R. K. Harris, Wiley, Chichester **2002**, p. 306.
3 P. Pyykkö, *Chem. Phys.* **1977**, *22*, 289; **1983**, *74*, 1; Z. C. Zhang, G. A. Webb, *J. Mol. Struct. (THEOCHEM)* **1983**, *104*, 439; N. C. Pyper, *Chem. Phys. Lett.* **1983**, *96*, 204; P. Pyykkö, A. Görling, N. Rösch, *Mol. Phys.* **1987**, *61*, 195.
4 G. A. Aucar, J. Oddershede, *Int. J. Quantum Chem.* **1993**, *47*, 425.
5 Y. Ishikawa, T. Nakajima, M. Hada et al., *Chem. Phys. Lett.* **1998**, *283*, 119.
6 H. M. Quiney, H. Skaane, I. P. Grant, *Chem. Phys. Lett.* **1998**, *290*, 473.
7 L. Visscher, T. Enevoldsen, T. Saue et al., *J. Comput. Chem.* **1999**, *20*, 1262.
8 R. H. Romero, G. A. Aucar, *Phys. Rev. A* **2002**, *65*, 053411; *Int. J. Mol. Sci.* **2002**, *3*, 1.

9 R. E. Moss, *Advanced Molecular Quantum Mechanics*, Chapman & Hall, London **1973**.
10 R. McWeeny, *Methods of Molecular Quantum Mechanics*, 2nd Edition, Academic Press, London **1992**.
11 J. E. Harriman, *Theoretical Foundations of Electron Spin Resonance*, Academic Press, New York **1978**.
12 S. K. Wolff, T. Ziegler, E. van Lenthe et al., *J. Chem. Phys.* **1999**, *110*, 7689; J. Autschbach, T. Ziegler, *J. Chem. Phys.* **2000**, *113*, 936; **2000**, *113*, 9410; H. Fukui, T. Baba, *J. Chem. Phys.* **2002**, *117*, 7836.
13 C. C. Ballard, M. Hada, H. Kaneko et al., *Chem. Phys. Lett.* **1996**, *254*, 170; R. Fukuda, M. Hada, H. Nakatsuji, *J. Chem. Phys.* **2003**, *118*, 1015; **2003**, *118*, 1027; H. Fukui, T. Baba, *J. Chem. Phys.* **1998**, *108*, 3854; T. Baba, H. Fukui, *J. Chem. Phys.* **1999**, *110*, 131.
14 M. Barysz, A. J. Sadlej, *Theor. Chim. Acta* **1997**, *97*, 260; V. Kellö, A. J. Sadlej, *Int. J. Quantum Chem.* **1998**, *68*, 159.
15 W. Kutzelnigg, *Z. Phys. D* **1990**, *15*, 27.
16 S. Kirpekar, H. J. Aa. Jensen, J. Oddershede, *Theor. Chim. Acta* **1997**, *95*, 35.
17 See, e.g. W. Kutzelnigg, in *Relativistic Electronic Structure Theory. Part 1. Fundamentals*, ed. P. Schwerdtfeger, Elsevier, Amsterdam **2002**, p. 664.
18 W. Kutzelnigg, *J. Comput. Chem.* **1999**, *20*, 1199.
19 A. C. Hennum, W. Klopper, T. Helgaker, *J. Chem. Phys.* **2001**, *115*, 7356.
20 H. Fukui, T. Baba, H. Inomata, *J. Chem. Phys.* **1996**, *105*, 3175; **1997**, *106*, 2987.
21 W. Kutzelnigg, *Theor. Chim. Acta* **1988**, *73*, 173.
22 J. Olsen, P. Jørgensen, *J. Chem. Phys.* **1985**, *82*, 3235; in *Modern Electronic Structure Theory, Part II*, ed. D. R. Yarkony, World Scientific, Singapore **1995**, p. 857.
23 T. Helgaker, M. Jaszuński, K. Ruud, *Chem. Rev.* **1999**, *99*, 293.
24 R. Bouten, E. J. Baerends, E. van Lenthe et al., *J. Phys. Chem. A* **2000**, *104*, 5600.
25 T. Helgaker, H. J. Aa. Jensen, P. Jørgensen et al., DALTON, a molecular electronic structure program, Release 1.2.1, **2001**.
26 P. Manninen, P. Lantto, J. Vaara et al., *J. Chem. Phys.* **2003**, *119*, 2623.
27 W. G. Schneider, H. J. Bernstein, J. A. Pople, *J. Chem. Phys.* **1958**, *28*, 601.
28 S. S. Gómez, R. H. Romero, G. A. Aucar, *J. Chem. Phys.* **2002**, *117*, 7942.
29 C. Glidewell, D. W. H. Rankin, G. M. Sheldrick, *Trans. Faraday Soc.* **1969**, *65*, 1409.
30 N. Nagakawa, S. Shinada, S. Obinata, The 6th NMR Symposium, Kyoto, **1967** (unpublished); Y. Nomura, Y. Takeuchi, N. Nagakawa, *Tetrahedron Lett.* **1969**, *8*, 639.
31 I. Morishima, K. Endo, T. Yonezawa, *J. Chem. Phys.* **1973**, *59*, 3356.
32 M. I. Volodicheva, T. K. Rebane, *Teor. Éksp. Khim.* **1978**, *14*, 447 [*Theor. Exp. Chem. (USSR)* **1979**, *14*, 348].
33 A. A. Cheremisin, P. V. Schastnev, *J. Magn. Reson.* **1980**, *40*, 459.
34 M. Kaupp, O. L. Malkina, V. G. Malkin et al., *Chem.-Eur. J.* **1998**, *4*, 118.
35 J. Vaara, K. Ruud, O. Vahtras, *J. Chem. Phys.* **1999**, *111*, 2900.
36 J. Vaara, K. Ruud, O. Vahtras et al., *J. Chem. Phys.* **1998**, *109*, 1212.
37 O. L. Malkina, B. Schimmelpfennig, M. Kaupp et al., *Chem. Phys. Lett.* **1998**, *296*, 93.
38 B. A. Hess, C. M. Marian, U. Wahlgren et al., *Chem. Phys. Lett.* **1996**, *251*, 365.
39 B. Schimmelpfennig, Atomic and Molecular Mean-field Integral program (AMFI), Stockholms Universitet, **1996**.
40 B. Minaev, J. Vaara, K. Ruud et al., *Chem. Phys. Lett.* **1998**, *295*, 455.
41 B. Cromp, T. Carrington, Jr., D. R. Salahub et al., *J. Chem. Phys.* **1999**, *110*, 7153.
42 P. Lantto, J. Vaara, A. Kantola et al., *J. Am. Chem. Soc.* **2002**, *124*, 2762.
43 J. Vaara, K. Ruud, O. Vahtras, *J. Comput. Chem.* **1999**, *20*, 1314.
44 S. Kirpekar, S. P. A. Sauer, *Theor. Chem. Acc.* **1999**, *103*, 146.
45 J. I. Melo, M. C. Ruiz de Azua, C. G. Giribet et al., *J. Chem. Phys.* **2003**, *118*, 471.
46 S. S. Gómez, R. H. Romero, G. A. Aucar, *Chem. Phys. Lett.* **2003**, *367*, 265.
47 U. Edlund, T. Lejon, P. Pyykkö et al., *J. Am. Chem. Soc.* **1987**, *109*, 5982.
48 H. Nakatsuji, H. Takashima, M. Hada, *Chem. Phys. Lett.* **1995**, *233*, 95; H. Nakatsuji, M. Hada, T. Tejima et al., *Chem. Phys. Lett.* **1996**, *249*, 284.
49 V. G. Malkin, O. L. Malkina, D. R. Salahub, *Chem. Phys. Lett.* **1996**, *261*, 335.
50 M. Kaupp, V. G. Malkin, O. L. Malkina et al., *J. Am. Chem. Soc.* **1995**, *117*, 1851; **1995**, *117*, 8492; *Chem. Phys. Lett.* **1995**, *235*, 382.

51 M. Kaupp, Habilitationsschrift, Universität Stuttgart, **1996**.

52 G. B. Bacskay, I. Bytheway, N. S. Hush, *J. Am. Chem. Soc.* **1996**, *118*, 3753.

53 J. R. Yates, C. J. Pickard, M. C. Payne et al., *J. Chem. Phys.* **2003**, *118*, 5746.

54 H. Nakatsuji, T. Nakajima, M. Hada et al., *Chem. Phys. Lett.* **1995**, *247*, 418; H. Kaneko, M. Hada, T. Nakajima et al., *Chem. Phys. Lett.* **1996**, *261*, 1.

55 J. Vaara, O. L. Malkina, H. Stoll et al., *J. Chem. Phys.* **2001**, *114*, 61.

56 D. R. Salahub, R. Fournier, P. Mlynarski et al., in *Density Functional Methods in Chemistry*, eds. J. Labanowski, J. Andzelm, Springer, New York **1991**; A. St-Amant, D. R. Salahub, *Chem. Phys. Lett.* **1990**, *169*, 387. V. G. Malkin, O. L. Malkina, L. A. Eriksson et al., in *Modern Density Functional Theory: A Tool for Chemistry; Theoretical and Computational Chemistry*, Vol. 2, eds. J. M. Seminario, P. Politzer, Elsevier, Amsterdam **1995**.

57 M. Dolg, Ph.D. Thesis, Universität Stuttgart, **1989**; A. Bergner, M. Dolg, W. Küchle et al., *Mol. Phys.* **1993**, *80*, 1431; M. Kaupp, P. v. R. Schleyer, H. Stoll et al., *J. Am. Chem. Soc.* **1991**, *113*, 6012.

58 J. P. Perdew, Y. Wang, *Phys. Rev. B* **1992**, *45*, 13244; J. P. Perdew, J. A. Chevary, S. H. Vosko et al., *Phys. Rev. B* **1992**, *46*, 6671.

59 A. D. Becke, *Phys. Rev. A* **1988**, *38*, 3098.

60 J. P. Perdew, *Phys. Rev. B* **1986**, *33*, 8822.

61 J. P. Perdew, Y. Wang, *Phys. Rev. B* **1986**, *33*, 8800.

62 G. Schreckenbach, T. Ziegler, *Int. J. Quantum Chem.* **1996**, *60*, 753.

63 G. Schreckenbach, T. Ziegler, *Int. J. Quantum Chem.* **1997**, *61*, 899.

64 S. K. Wolff, T. Ziegler, *J. Chem. Phys.* **1998**, *109*, 895.

14
Calculation of Heavy-Nucleus Chemical Shifts. Relativistic All-Electron Methods

Jochen Autschbach

14.1
Introduction

Among those magnetic molecular properties that are currently accessible to computations the nuclear magnetic shielding is of outstanding importance in virtually all fields of chemical research as well as related disciplines. Thus, since the time that the quantum mechanical treatment of molecules became computationally feasible on a larger scale, methodology has been developed and applied in order to calculate nuclear shieldings and NMR chemical shifts in an attempt to rationalize the mechanisms that determine the observed signs, magnitudes, and trends among different nuclei and/or molecules. The last decades have also seen an increasing interest in the relativistic computation of nuclear shieldings in molecules containing heavy atoms (see Sections 14.2 and 14.3 for references). "Heavy" is not always well defined in the context of computational chemistry, but trivially some of the heaviest stable NMR nuclei such as ^{195}Pt, ^{199}Hg, ^{205}Tl, or ^{207}Pb must be considered as such. It is now textbook knowledge that for molecules containing these and other heavy elements a relativistic theoretical formalism is necessary. Of course it depends on the intended accuracy of the computational results, and in this respect on the very property that is computed, whether a nonrelativistic formalism is sufficient or not for its theoretical description. One might agree that the use of a relativistic theory is imperative when the nonrelativistic formalism is not able to reproduce the observables at least semi-quantitatively. To this end, there appears to be a general consent about "relativistic effects" becoming highly important for the structure and bonding of molecules containing at least one atom with a nuclear charge Z larger than about 54 (Xe). This rule-of-thumb refers to the currently achievable accuracy of standard quantum chemical methodology. By "standard" is meant here currently popular and well established ab initio or density functional methods such as Hartree–Fock, MP*n*, or DFT with hybrid or non-hybrid functionals that are applicable to not just the smallest molecules. Molecular properties such as heavy-nucleus shieldings that depend on the electronic structure in the very vicinity of the nuclei often require a relativistic treatment even at much smaller nuclear charges, but certainly for the heavy nuclei of the 6th row of the periodic table. Also, when a much higher accuracy of the computations is required than that currently offered by standard quantum

Calculation of NMR and EPR Parameters. Theory and Applications.
Edited by Martin Kaupp, Michael Bühl, Vladimir G. Malkin
Copyright © 2004 WILEY-VCH Verlag GmbH & Co. KGaA, Weinheim
ISBN: 3-527-30779-6

chemical methods a relativistic formalism is necessary even for lighter elements, along with an accurate treatment of the electron correlation.

This chapter is concerned with the inclusion of relativistic effects into NMR computations in a direct manner, i.e. as part of the Hamiltonian that describes the kinematics of the electrons. Typically in such calculations all electrons are treated at a specific relativistic level, though sometimes core orbitals are not variationally treated but are transferred from atomic computations (frozen-core). Such an approach is opposite to a pseudopotential formalism by which relativistic effects in the outer core and valence shells can be accounted for in an indirect manner through the potential of the inner (i.e. core) electrons. In the literature a distinction between HALA effects on NMR parameters [1], i.e. the effect of the presence of a heavy atom (HA) on the nuclear shielding of a light neighbor atom (LA), and HAHA effects [2], which are the relativistic effects on the heavy atom's own shielding, is frequently made. The use of effective core potentials (ECPs) is usually computationally very efficient, they can be very accurate [3], and they are readily employed for a study of HALA effects. However, the computational codes currently in use in conjunction with ECPs would need to be modified in order to account for the presence of the pseudopotential for the computation of the heavy atom shielding. The wavefunction/orbitals obtained from a direct all-electron relativistic computation can be directly employed for the purpose of NMR calculations, including heavy atom shieldings, provided the NMR operators have been implemented in the NMR code in a consistent manner (see Section 14.2 for further comments on this issue). In the following, emphasis will be put on HAHA effects, for which a variety of all-electron relativistic formalisms have been developed and applied. Some interesting HALA effects will also be discussed. Chapter 15 by Autschbach and Ziegler also focuses on coupling constants involving at least one heavy nucleus. For the description of HALA effects, both a relativistic ECP on the heavy atom and an all-electron method should be equally successful. The former approach in the framework of NMR computations is described in Chapter 13 by Vaara et al. A somewhat intermediate status have perturbational computations of order c^{-2} of only the spin–orbit coupling induced effects on nuclear shieldings, which are briefly discussed here, and in more detail in Chapter 13. They are generally very successful for the treatment of HALA but not for that of HAHA effects. See also Chapter 18 by Kaupp. Previously, relativistic NMR calculations have been reviewed in Ref. [4], together with all-electron methods, covering the literature up to early 2001.

This chapter is organized as follows: In Section 14.2 some of the underlying methodology by which relativistic computations of NMR parameters are currently carried out is outlined. Emphasis will be put on the similarities between the different methods rather than presenting individual explicit expressions or technical details. In Section 14.3 applications of the theory to nuclear shieldings in diamagnetic heavy element compounds are described, with an emphasis on heavy nucleus chemical shifts for which experimental data are available for comparison. Ab initio and DFT computations are reviewed here; for an overview of semi-empirical calculations see Chapter 9 by Heine et al. A few examples of shielding anisotropies are also presented, though for a more detailed account the reader is referred to Chapter 27

by Wasylishen. Section 14.4 contains some concluding remarks. Throughout this chapter and Chapter 15 Hartree atomic units with $e=1$, $m_e=1$, $h=2\pi$, $4\pi\varepsilon_0=1$, $c=137.03599976(50)$ are employed. Thus prefactors containing $e, m_e, 4\pi\varepsilon_0$ and $\hbar = h/(2\pi)$ are generally omitted, whereas the speed of light, c, is explicitly included. Equations referring to magnetic properties have been converted from SI to atomic units. The fine structure constant α is in atomic units equal to c^{-1}. The latter occurs in the equations indicating the relative magnitude of the hyperfine terms in the Hamiltonian as compared to relativistic corrections of $\mathcal{O}(c^{-2})$ and the nonrelativistic terms $\mathcal{O}(c^0)$. No details regarding gauge corrections and the GIAO [5, 6] or IGLO [7] methods will be presented since they are discussed in detail in Chapter 6 by van Wüllen and recent review articles [8, 9]. Further, shielding surfaces, ro-vibrational corrections, and isotope effects, are discussed in Chapter 10 by Ruud. Open-shell systems are the subject of Chapter 20 by Patchkovskii and are not considered here.

14.2 Methodological Aspects

For a general introduction on the shielding tensor and the chemical shift the reader is referred to Chapter 6 by van Wüllen. See also Chapter 5 by Kutzelnigg for further details on the relativistic NMR formalism.

As in the nonrelativistic theory, within the framework of quantum mechanical double perturbation theory [10], the shielding nuclear magnetic tensor is given as [11, 12]

$$\boldsymbol{\sigma}_A = \left.\frac{\partial^2 E}{\partial \boldsymbol{B}\partial \boldsymbol{\mu}_A}\right|_{\boldsymbol{B}=0,\boldsymbol{\mu}_A=0} \tag{14.1}$$

Here, $\boldsymbol{\mu}_A$ is the magnetic moment due to the nuclear spin, and $\boldsymbol{B}$ is the external magnetic field. E is the total *relativistic* molecular energy not including the nuclear Zeeman term $\boldsymbol{\mu}_A \cdot \boldsymbol{B}$. In Eq. (14.1) a possible (supposedly negligible [13]) $\boldsymbol{B}$-field dependence of $\boldsymbol{\sigma}_A$ is not included. Taking the derivative of E in Eq. (14.1) analytically involves the analytic derivatives of the wavefunction Ψ (or Kohn–Sham orbitals φ_i in density functional theory DFT [14]) with respect to either $\boldsymbol{B}$ or $\boldsymbol{\mu}_A$, i.e. $\Psi^{(1,0)} = (\partial\Psi/\partial\boldsymbol{B})|_{\boldsymbol{\mu}_A=0,\boldsymbol{B}=0}$ or $\Psi^{(0,1)} = (\partial\Psi/\partial\boldsymbol{\mu}_A)|_{\boldsymbol{\mu}_A=0,\boldsymbol{B}=0}$. Alternatively, finite-field approaches are not uncommon in which the calculation of Ψ is carried out twice, with and without the presence of $\hat{H}^{(1,0)}$ or $\hat{H}^{(0,1)}$ times a small number, and $\Psi^{(1,0)}$ or $\Psi^{(0,1)}$ is then approximated by a finite difference instead of the true derivative. Further one needs to know the magnetic perturbation operators $\hat{H}^{(1,0)} = (\partial\hat{H}/\partial\boldsymbol{B})|_{\boldsymbol{\mu}_A=0,\boldsymbol{B}=0}$, $\hat{H}^{(0,1)} = (\partial\hat{H}/\partial\boldsymbol{\mu}_A)|_{\boldsymbol{\mu}_A=0,\boldsymbol{B}=0}$ and $\hat{H}^{(1,1)} = (\partial^2\hat{H}/\partial\boldsymbol{B}\partial\boldsymbol{\mu}_A)|_{\boldsymbol{\mu}_A=0,\boldsymbol{B}=0}$. Contributions to $\boldsymbol{\sigma}_A$ from $\hat{H}^{(1,1)}$ are commonly referred to as the diamagnetic contribution, whereas those from $\hat{H}^{(1,0)}$ and $\hat{H}^{(0,1)}$ are the paramagnetic ones.

It is decided when deriving the NMR perturbation operators and computing the unperturbed wavefunction (orbitals) and energy from a specific expression for $\hat{H}$ whether either a nonrelativistic formalism or a relativistic one (and which particular

form) is specified. Alternatively, one can also formulate relativistic corrections to $\boldsymbol{\sigma}_A$ in the form of a third (and higher) derivatives of E in the form

$$\Delta^{\mathrm{rel}}\boldsymbol{\sigma}_A = c^{-2} \cdot \left.\frac{\partial^3 E}{\partial \boldsymbol{B}\partial \boldsymbol{\mu}_A \partial c^{-2}}\right|_{c\to\infty,\boldsymbol{\mu}_A=0,\boldsymbol{B}=0} + \mathcal{O}(c^{-4}). \tag{14.2}$$

The powers of c^{-2} serve as convenient small perturbation parameters within the relativistic theory. Though perturbational approaches can be advantageous for interpretational purposes (clear separation of leading (c^{-2}) and higher order (c^{-4}, c^{-6} . . .) relativistic corrections) it should be kept in mind that for the heaviest NMR nuclei the relativistic effects on $\boldsymbol{\sigma}$ can be huge and will not be fully covered by the terms linear in c^{-2}. This gives variational relativistic methods an advantage of relative conceptual simplicity over higher order relativistic perturbational approaches when computing $\boldsymbol{\sigma}_A$ for a heavy nucleus or its neighbor atoms.

It is of importance that the perturbation operators $\hat{H}^{(1,0)}$, $\hat{H}^{(0,1)}$, and $\hat{H}^{(1,1)}$ are derived within the same relativistic formalism that is used to determine the unperturbed quantities $E^{(0,0)}$ and $\Psi^{(0,0)}$ (or $\varphi_i^{(0,0)}$) in order to avoid inconsistencies and concomitant errors. Due to the complexity of relativistic computations of nuclear shieldings, simplified "mixed" approaches have occasionally been devised and are still in use. However, the results need to be viewed with some care and have been criticized, e.g., in Ref. [15]. The errors being introduced by using "alien" operators within relativistic formalisms are sometimes referred to as picture change effects [16]. To illustrate the problem, it is known that relativistic atomic s and $p_{1/2}$ wavefunctions / orbitals logarithmically diverge at point-like nuclei (see literature cited in Ref. [17]). In the nonrelativistic theory the Fermi-contact (FC) operator samples the value of the orbitals at the point-nuclei. This nonrelativistic operator should thus yield infinity in conjunction with relativistic wavefunctions/orbitals that diverge at the nucleus in the limit of a complete basis. Because, typically in molecular computations, basis functions are employed that stay finite at the nuclei, by choice of the basis set any value for the matrix elements of the nonrelativistic FC operator can be obtained in a relativistic calculation. The quasi-relativistic generalizations of the FC operator, as well as the four-component formalism, avoid these divergences at point-nuclei but usually sample the vicinity of the nuclei together with the spatial K-shell instead [18–21] (see also Chapter 31 by Chipman et al.). In a more realistic calculation with a finite nucleus no such divergences should occur; nevertheless the perturbation operators must be chosen consistently with the unperturbed solution. In order to account for a non-point like nuclear dipole, the Gaussian nuclear model [22] is frequently employed in NMR computations.[1)]

1) It is worthwhile to mention that the combination of a point-like magnetic dipole with a point-nuclear charge within an *approximate* (i.e. quasi-) relativistic calculation is, due to the combination of the generalized FC operators the diverging wavefunctions / orbitals, perhaps not applicable to systems in which a nucleus has a charge greater than approximately 118. This has been shown, e.g., for the elimination of the small component (ESC) scheme [23] and the ZORA [24].

Concerns regarding infinite matrix elements also hold for certain singular operators if they are used in variational calculations. This can be problematic for the already mentioned finite-field approaches or variational relativistic computations employing variationally unstable operators. This is not to be confused with the aforementioned picture change errors, though variational collapse can indeed result from the inconsistent use of operators within relativistic formalisms.

In the early 1980s several articles were published dealing with the four-component relativistic formalism for nuclear shieldings in molecules [25–27], which was subsequently reviewed in Ref. [28]. By that time it had already been recognized that spin–orbit coupling due to a heavy halogen atom must be responsible for the well-known large proton and ^{13}C upfield shifts in their neighborhood [29–32]. However, scalar relativistic effects and/or a consistent four-component formalism for molecular applications had not been widely discussed. The perturbation operators in the four-component Dirac picture are

$$\hat{H}_u^{(1,0)} = -\frac{c}{2}[\boldsymbol{\alpha} \times \boldsymbol{r}]_u \tag{14.3a}$$

$$\hat{H}_u^{(0,1)} = -\frac{1}{c}\left[\boldsymbol{\alpha} \times \frac{\boldsymbol{r}_A}{r_A^3}\right]_u \tag{14.3b}$$

for the $u \in \{x, y, z\}$ component of the perturbing nuclear spin vector. Here, $\boldsymbol{\alpha}$ is the 3-vector of the 4×4 Dirac matrices. These two operators have to be seen as the four-component generalizations of the orbital-Zeeman (OZ) and the paramagnetic orbital (OP) terms of Ramsey's nonrelativistic theory [33] for nuclear shieldings. They also implicitly include, due to their action on a four–component wavefunction / orbitals, the contributions from the spin-dependent Fermi-contact (FC) and spin-dipole (SD) terms of the nonrelativistic theory as well as the spin–Zeeman term. There is no explicit analog for the diamagnetic shielding (DS) operator in the four-component picture. This apparent discrepancy has been numerically analyzed in Ref. [34] (for the case of the diamagnetic spin–spin coupling), and the diamagnetic part has been traced back to contributions from "negative energy" eigenfunctions of the Dirac operator that usually enter the equation for the shielding tensor via the magnetically perturbed wavefunction. This has previously been pointed out in Ref. [35] and also in Refs. [26, 27] (see also Chapter 2 by Pyykkö). The topic has been recently discussed in detail by Kutzelnigg [36], where the reader can also find remarks about kinetic balance in the presence of a magnetic field, an issue prevalent in four-component relativistic computations using basis sets. Schemes have been devised in order to decompose the shielding tensor of a four-component method in terms of more familiar paramagnetic and diamagnetic contributions (the so-called Gordon-decomposition [25, 36, 37]) in order to facilitate interpretations. Table 14.1 lists a comparison of the operators that enter the expression for the shielding tensor in different relativistic theories. Recently, the formalism for the inclusion of QED self-energy corrections for the relativistic computation of NMR observables has been investigated [38]. QED effects on atomic hyperfine integrals have been discussed in Ref. [39] through their inclusion via model potentials.

Table 14.1 Comparison of one-electron operators that contribute to the nuclear shielding in Eq. (14.1) in different relativistic formulations and in the nonrelativistic limit, and a selection of literatur references that list explicit expressions

Nonrelativistic	**Two-component (Quasirelativistic) DKH2, ZORA, ...**	**Relativistic Perturbational Schemes**	**Four-component "Fully Relativistic"**
diamagnetic shielding (DS)	diamagnetic shielding (DS[a])	nonrelativistic terms DS, OZ, OP	Eqs. (14.3a, 14.3b) corresponding to OZ, OP, FC, SD
orbital Zeeman (OZ)	orbital Zeeman (OZ[a])	if spin–orbit coupling included: FC and SD yield shielding contributions	DS implicity included in shielding tensor
paramagnetic orbital (OP)	paramagnetic orbital (OP[a])		
Fermi-contact (FC) (zero contrib.[b])	Fermi contact (FC[a])	plus many additional operators $\mathcal{O}(c^{-2})$, $\mathcal{O}(c^{-4})$	
spin-dipole (SD) (zero contrib.[b])	spin-dipole (SD[a])		
Refs. [8, 9, 11, 12] & many others	Refs. [18, 19, 23], [15, 51–55]	Refs. [29–32, 40–45], [36, 56]	Refs. [25–27], [46–50]

a) Two-component relativistic generalization of the respective operator.
b) Contributions due to FC and SD term from spin-up and spin-down orbitals in nonrelativistic or scalar relativistic scheme cancel exactly.

Fully relativistic four-component computations on molecules are even today not routinely carried out. Indeed, it has taken until the late 1990s for the first four-component Hartree–Fock computations of nuclear shielding in molecules to be reported in the literature [37, 47, 57]. In contrast, atomic four-component NMR computations have been discussed and carried out much earlier [58–61]. However the accurate determination of atomic nuclear shieldings with large basis sets is still a computational challenge (see, e.g., a recent publication by Vaara and Pyykkö [62]). From early on, attempts have been made to compute nuclear shieldings by means of approximate two-component relativistic Hamiltonians instead. Most familiar to most readers is perhaps the (Breit–) Pauli Hamiltonian [18, 63, 64] which is obtained from the two-component relativistic Hamiltonian as a perturbation of order c^{-2}. Its use in molecular computations is generally restricted to a perturbational approach in order c^{-2} because of its highly singular behavior [65, 66] and its variational instability. Nonetheless, variational computations have been carried out with the Pauli operator because by using large frozen cores and very restricted basis sets in the core region of the heavy nuclei one can keep the variational instability somewhat "under control" (meaning the instability does not show up because of basis set restrictions). The field-free one-electron Pauli Hamiltonian has the form

$$\hat{h}^{\text{Pauli}} = -\frac{\hat{\boldsymbol{p}}^4}{8c^2} - \frac{(\hat{\boldsymbol{p}}^2 V_N)}{8c^2} + \frac{i}{2c^2}\hat{\boldsymbol{S}}\left[(\hat{\boldsymbol{p}}V_N)\times\hat{\boldsymbol{p}}\right], \tag{14.4}$$

where $\hat{\boldsymbol{S}} = \boldsymbol{\sigma}_s/2$ is the one-electron spin-operator, V_N the nuclear potential. The last term in Eq. (14.4) is the one-electron Pauli spin–orbit (SO) operator. There are also two-electron SO operators arising in two-component relativistic theories, the use of which in NMR calculations has been discussed, for example, in Refs. [41, 48, 67]. Upon considering the presence of the external magnetic field and the nuclear spins, a rather large number of relativistic magnetic perturbation operators in addition to the nonrelativistic ones are obtained from Eq. (14.4) that are explicitly listed for instance in Refs. [40, 43, 45, 56, 68]. These, and a number of additional, operators are obtained when the minimal substitution is correctly applied in the Dirac Hamiltonian before the transformation to two-component form [45, 56].

An alternative, nonsingular, perturbational relativistic approach is facilitated by the "direct" four-component relativistic perturbation theory (DPT) [17, 69–72]. The inclusion of magnetic interactions in the DPT formalism has been discussed in detail by Kutzelnigg [44]. The implementation of the resulting hyperfine integrals has recently been outlined [73]. Applications to nuclear shieldings for heavy atomic systems are not known to the author at the time of writing this chapter.

Besides the four-component theory and perturbational Hamiltonians there are currently two rather popular variationally stable two-component methods in use that have both been successfully applied to nuclear shieldings in molecules. One is Hess' version [74, 75] of the second-order Douglas–Kroll [76] transformation (DKH2), the other is the zeroth-order regular approximation (ZORA) [77]. Both methods contain relativistic effects to higher order than c^{-2}, but are still approximations to the exact two-component relativistic Hamiltonian which is not explicitly known. It has been demonstrated that for a variety of molecular properties (energies, geometries, and vibrational frequencies) which are determined by the valence shell orbitals and their relativistic corrections, the DKH2 and the ZORA method yield very similar results [78]. This is not necessarily to be expected for nuclear shieldings as well because they depend on the electronic structure very close to the nuclei. For core-orbital energies, DKH2 yields better approximations to the four-component results than (unscaled) ZORA, though regarding the orbital shapes this is not necessarily the case [17, 77, 79]. For chemical shifts, the two methods seem to perform comparably well, which is likely due to the fact that most contributions from the core orbitals cancel when the chemical shift is evaluated.[2)] The perturbation operators

2) It is important in this context to distinguish between the core orbitals vs. valence orbitals and their contributions to the shielding tensor, and the spatial contributions to the integrals that determine the shielding tensor. Generally speaking, the diamagnetic shielding stems mainly from the core orbitals and the spatial core regions, whereas at least large parts of the paramagnetic shielding and the SO contributions are determined by the core tails of the valence orbitals. For this reason, most of the diamagnetic shielding cancels regarding the chemical shift whereas the paramagnetic and SO terms are heavily dependent on the chemical environment.

that arise from the two methodologies can be found in the references listed in Tab. 14.1. They can be viewed as regularized analogs of the nonrelativistic operators additionally including kinematic factors that become important in the vicinity of the nuclei and/or for large momenta of the electrons. Therefore the nonrelativistic terminology will also be used here for these operators (see Tab. 14.1). Because of the computational efficiency of DKH2, ZORA, and other possible variational two-component methods, it can be expected that they will strongly contribute to the body of computational data on heavy-nucleus shielding tensors in molecules in the near future. However, there is also an increasing number of recent four-component results, as will be seen in the next section.

Apart from acronyms already specified, use of the following abbreviations is made from now on: SO = spin–orbit coupling (one and/or two-electron terms), vPSO, vPSC, vPauli for variational Pauli SO only, scalar only, and scalar + SO, respectively. Similarly, pPSO, pPSC, pPauli denote perturbational relativistic calculations $\mathcal{O}(c^{-2})$. DKH2-vPSO is an example for a "mixed approach". HF = Hartree–Fock. HF-Dirac = four-component Hartree–Fock. MCSCF = multiconfigurational self-consistent field.

14.3 Computational Results

14.3.1 Proton Chemical Shifts in Hydrogen Halides

Perhaps the most prominent examples for relativistic effects on NMR properties are the proton and ^{13}C shielding constants in the neighborhood of heavy halogens. Among these, the series HX, X = F, Cl, Br, I is the best studied example. Table 14.2 lists some of the computational data for HX that have been published over the last three decades. Because of the ideal benchmark character of the HX series (small molecules, large relativistic effects, experimental data available), new relativistic methodologies are frequently tested with these molecules. As can be seen, some of the data have been published very recently, testifying to the continuing, even increasing, interest in new efficient and accurate methodology by which to treat NMR properties of heavy atomic systems. The discrepancy between the two different 1999 four-component HF results is probably due to the use of an insufficiently flexible basis set in the case of Ref. [37]. For comments on the similarity between HF-ZORA and DFT-ZORA in Tab. 14.2 see below where the shifts of the heavy atom X are discussed.

Table 14.2. Proton chemical shifts in HX, X=Cl, Br, I

$-\delta_{^1H}$[a] X=	Cl		Br		I	
Method/Year	**nrel**[c]	**rel**	**nrel**	**rel**	**nrel**	**rel**
semiemp. pPSO/1973 [30]	8.02	8.24	11.24	13.85	13.08	20.92
semiemp.pPSO/1978 [31]	2.1	2.7	5.75	10.0	3.22	16.8
REX/1987 [1]		0.45		3.35		11.01
HF vPSO/1995 [80]	2.43	3.17	2.57	7.72	3.07	18.93
HF DKH2-vPSO/1996 [81]	1.92	2.69	2.36	7.87	0.04	19.93
DFT pPSO/1996[d] [82]	1.68	2.31	1.23	5.34	1.61	13.24
DFT vPSC/1997 [83]	1.4	1.5	1.7	1.8	2.1	2.3
MCSCF pPSO/1998 [41]	1.98	2.57	2.19	6.04	2.74	14.68
DFT vPauli/1998 [84]		1.43		5.34		11.79
HF scalar DKH2/1999 [85]	2.08	2.17	2.39	3.06	2.62	4.95
HF Dirac / 1999 [47]	2.39	3.13	2.82	8.21	3.32	20.11
HF Dirac / 1999 [37]		2.68		4.91		10.71
DFT SO-ECP / 2001 [86]	1.68	2.39	1.21	6.42	1.61	14.87
DFT ZORA / 2002 [4]	1.57	2.45	1.84	5.31	2.19	13.6
HF ZORA / 2002 [52]	2.28	2.57	2.64	4.86	2.83	13.49
HF DKH2 / 2002 [52, 53]	2.28	3.20	2.64	8.23	2.83	20.26
HF DKH2 / 2003 [55]	2.45	3.22	2.65	8.81	3.06	21.38
HF pPauli / 2003 [56]	2.25	3.18	2.42	8.33	3.06	21.85
MCSCF pPauli / 2003 [56]	1.98	2.66	2.19	6.14	2.73	14.61
exp (±0.02)[b]		2.58		6.43		15.34

a) In ppm, with respect to HF, all values ×(–1).
b) Experimental values as quoted in Ref. [84]. Uncertainty due to the experimental value for HF (measured w.r.t. CH_4).
c) Nonrelativistic values listed if reported in reference.
d) Preliminary results were published in 1995 in Ref. [87].

14.3.2
HALA Effects Due to Spin–Orbit Coupling

Computational studies of the proton shieldings in HX date back to the 1970s, when a perturbation approach employing the SO part of the Pauli operator together with LCAO wavefunctions was used [30]. It had been realized already in the late 1960s [29] that spin–orbit coupling must be responsible for the increasing shielding of the proton along the series; an assertion that could not be proven by computational results at that time, but is evident from Tab. 14.2. This is the prime example for a HALA effect induced by spin–orbit coupling at the heavy atom. Because scalar relativistic effects play virtually no role for the proton shielding in HX (and also the ^{13}C shielding in $CH_{4-n}X_n$, the SO effects of which were first computationally studied in Ref. [32] by the semiempirical INDO method) much of the effort of implementing first-principles relativistic nuclear shielding calculations has for a long time focused on the inclusion of spin–orbit coupling at a perturbational level. The results

obtained for HX and other systems have provided justification for this approach. It has been, among other results, established beyond doubt that the so-called "normal halogen dependence" (NHD), i.e. an increased shielding for light neighbor nuclei of X along the series X = F, Cl, Br, I, is a SO-induced relativistic effect. An interpretation of this trend has been made in almost all publications dealing with such computations. See, for example, the references in Tab. 14.2, and also Chapter 18 by Kaupp and Ref. [88]. Ref. [84] gives an explanation of the somewhat unintuitive trend for ^{13}C shifts in 5d transition metal carbonyl complexes. Extremely large SO effects have been reported for σ_P in the PX_4^+ series, which has been attributed to the strong s-character of the P-X bonds (Ref. [89], DFT-pPSO). If the SO contributions are quenched, as appears typical for early transition metal halides, the so-called "inverse halogen dependence" (IHD) is observed in experiments and reproduced by computations (for instance for Nb hexahalides and Ti tetrahalides, Ref. [90], HF-vPSO). Because the SO contributions to the nuclear shielding are mainly caused by SO-induced cross terms between the OZ and the FC term (Tab. 14.1), there is an analogy to the FC term of nuclear spin–spin coupling. This analogy had also already been proposed in 1969 [29]. Recently, numerical evidence on the Karplus-curve-like dependence of SO–induced shielding on dihedral angles, closely following the one for the ^3J(H–I) spin–spin coupling constants, could be provided for iodoethane [91] (DFT-pPSO). Many other studies [8, 32, 41, 80, 82, 84, 86, 89, 92–97] of SO contributions to light nucleus shieldings have been carried out and interpretations have been made. Interesting cases are the series $CCl_{4-n}I_n$, $CBr_{4-n}I_n$, $CH_{4-n}I_n$, and $CH_{4-n}Br_n$, that were recently studied with respect to their "nonlinear NHD" [95]. The reader is referred to Ref. [4] and Chapter 13 by Vaara et al. for more complete overviews on the methodology, as well as Chapter 18 by Kaupp.

14.3.3
Halide Shielding Constants in Hydrogen Halides as an Example of HAHA Effects

Because of the historical development, scalar relativistic effects on nuclear shielding were only studied much later, in particular when it became essential to include them in order to study shielding constants of the heavy nuclei themselves. As previously mentioned, scalar relativistic HALA effects can easily be studied with a non-relativistic NMR code by employing relativistic ECPs. Spin–orbit ECPs can also be employed for this purpose [86, 92, 95, 98] which gives additional access to the often dominant spin–orbit–induced HALA effects. An example is listed in Tab. 14.2 for comparison. In the following, we will focus on heavy atom shieldings and the HAHA effects.

Table 14.3 lists the shielding constants for the heavy nucleus X in the HX series. Note the publication dates ≥ 1996 as compared to Tab. 14.2. Scalar relativistic contributions are seen to be of high importance for the shielding of the heavy nucleus in HX, with an increase of roughly $Z^{3.5}$ according to Fukui et al. [15]. This result appears to be typical since a similar trend has been obtained from Dirac–Fock computations on group 15 and 16 hydrides, for which a dependence of the relativistic contributions on the heavy-nucleus shielding $\sim Z^{3.2}$ was reported [50]. Manninen et

al. found a Z^3–dependence for a pPauli treatment [56]. There are some recent Hartree–Fock reference data available for σ_X in HX for a comparison of various relativistic methods. The results are also listed in Tab. 14.3. Unfortunately, due to the approximations and the different basis sets that have been applied no definite conclusions can be drawn at this time about the performance of the various methods. The comparison of the 1998 data [41] as well as the 2003 data [56] between Hartree–Fock and the correlated MCSCF methods suggests that σ_X is moderately affected by electron correlation. In Ref. [45] it was found by a perturbational relativistic approach employing both Hartree–Fock and a correlated wavefunction (SOPPA = second-order polarization propagator approach) that some of the relativistic corrections on σ_X in HX and CH_3X are virtually unaffected by electron correlation. This would lead to the conclusion that indeed rather similar σ_X (within ~100 ppm) can be expected for HX from relativistic correlated ab initio and Hartree–Fock computations including both scalar and spin–orbit coupling effects. If this is true then the

Table 14.3 Halide nuclear shielding constants σ_X in HX, X = F, Cl, Br, I.

σ_X X=		F		Cl		Br		I	
Method/Year	Ref.	nrel	rel	nrel	rel	nrel	rel	nrel	rel
HF pPSO / 1996	[40, 68]	413.6	412.0	952.0	941.7	2652.6	2562.3	4562.8	4272.4
HF pPSO / 1998	[41][a]	413.6	414.0	946.8	949.5	2633.9	2666.7	4551.7	4686.8
MCSCF pPSO / 1998	[41][a]	422.5	422.8	968.6	970.5	2682.0	2704.5	4654.5	4743.0
MCSCF pPSO / 1999	[42][b]	422.5	421.3	968.6	960.0	2682.0	2624.6	4654.5	4469.6
HF Dirac / 1998	[48]	418.1	409.5	961.2	1027.7				
HF Dirac / 1999	[47]	414.3	423.3	957.0	1020.1	2634.2	3224.6	4541.4	6768.4
HF scalar DKH2 / 1999	[85]	413.5	415.8	950.1	969.1	2643.2	2863.8	4538.2	5714.2
HF DKH2 / 2002[c]	[52, 53]	413.5	422.3	949.9	1014.7	2641.3	3401.2	4539.8	8843.8
HF ZORA / 2002	[52]	413.5	416.4	949.9	970.1	2641.3	2851.0	4539.8	5487.3
DFT ZORA / 2003[d]		412.8	414.9	940.3	957.3	2574.2	2801.5	4431.7	5478.6
HF DKH2 / 2003	[55]	416.8	423.4	957.5	1018.9	2634.9	3164.9	4540.4	6508.5
HF pPauli / 2003	[56]	413.6	422.7	946.8	1009.5	2633.9	3222.8	4556.0	6652.5
MCSCF pPauli / 2003	[56]	422.5	431.5	968.6	1030.9	2682.1	3265.5	4661.9	6732.8
expt.[e]			410±6		952		2617		4510

a) Neglecting contributions due to the minimal substitution $\hat{\boldsymbol{p}} \rightarrow \hat{\boldsymbol{\pi}}$ in the Pauli-SO operator (4).

b) Including contributions due to the minimal substitution $\hat{\boldsymbol{p}} \rightarrow \hat{\boldsymbol{\pi}}$ in the Pauli-SO operator (4).

c) Employing nonrelativistic operators regrading the $\boldsymbol{\mu}_A$ and $\boldsymbol{B}$ perturbations.

d) ZORA-DFT data computed for this work, BP86 functional, same basis set used as for computation of DFT-ZORA proton shifts in Tab. 14. 2 (QZ4P, [99]), Ref. [4].

e) Experimental data as compiled in Ref. [41]. Estimates based on a combination of computed diamagnetic shielding constants and experimentally determined spin–rotation constants, employing the nonrelativistic relation between spin–rotation constant and the paramagnetic shielding tensor [100].

Hartree–Fock and the DFT values should also be comparable, which suggests that the rather good agreement between Fukui's HF-ZORA results and the DFT-ZORA values is to some extent meaningful. On the other hand, some approximations (such as neglecting the electronic Coulomb potential in the ZORA one-electron operator, and others) have been made in Ref. [52] but not in the DFT-ZORA implementation, therefore differences should be expected. There is also a similarity between the HF-ZORA and the DFT-ZORA results for the proton shifts in Tab. 14.2 which is difficult to understand because HF-ZORA can be expected to yield results similar to the other relativistic Hartree–Fock data (about 20 ppm for HI), whereas DFT-ZORA should, and does, give similar results to the DFT-SO-ECP method. These are significantly smaller due to the inclusion of electron correlation.

A direct comparison of the DKH2 data of Ref. [52] (Fukui and Baba, 2002) with those from Ref. [55] (Fukuda et al., 2003) cannot be made since in Ref. [52] the use of the nonrelativistic magnetic perturbation operators [53] represents a severe approximation. Surprisingly, the "QR-0" approximation to the DKH2 approach that has also been implemented by Fukuda et al. in Ref. [55], and which was described as corresponding to the very same approximation of using the nonrelativistic operators, yields consistently *smaller* shielding constants than the full DKH2 results [54, 55]. The authors refer to their method for technical and methodological reasons as GIAO-FP-QR-GUHF (which perhaps represents a new landmark for the length of quantum chemical acronyms) indicating that the perturbed wavefunction $(\partial\Psi/\partial\boldsymbol{B})|_{\boldsymbol{\mu}_A=0,\boldsymbol{B}=0}$ is obtained by a finite perturbation technique. It is not clear whether the discrepancy is due to such technical issues or related to different basis sets. Very good agreement is obtained between the HF-DKH2 results by Fukuda et al. [55] and the four-component HF results by Visscher et al. [47] in Tab. 14.3. Further, very good agreement between DKH2 and four-component Hartree–Fock for nuclear shielding constants of rare gas atoms has been reported in Ref. [54]. The DKH2 shieldings for the rare gas atoms are also very similar to the near basis-set limit Dirac-HF results of Ref. [62]. At the same time, in an earlier study of H_2Y, Y = O, S, Se, Te, large differences between DKH2 and Dirac-HF were reported for σ_{Te} [57]. From the data of Tab. 14.3 one can conclude that (1) for the heavy nucleus shielding in HX the scalar relativistic effects are much larger and positive as compared to the negative, i.e. deshielding, sum of the SO contributions, and, (2) that it is at present not completely clear how different relativistic approaches perform in comparison, though, tentatively, it seems as if the ZORA approach tends to yield smaller absolute shieldings (but not necessarily chemical shifts, see below) than four-component HF or the existing DKH2 implementations.

14.3.4
H_2Y and YH_3

Further recent four-component HF benchmark results for light and heavy-nucleus shielding constants in small molecules can be found, for instance, in Refs. [57] (H_2Y, Y = O, S, Se, Te; also HF-DKH2), or [50] (H_2Y, Y = O, S, Se, Te, Po, and YH_3, Y = N, P, As, Sb, Bi; no comparison with experimental data). The H_2Y series was also

studied by a pPSO approach in Ref. [42] where a comparison with experimental data has been made. The experimental estimate of 4954 ppm for σ_{Te} in $H_2{}^{125}Te$ was underestimated by more than 1000 ppm in the computations (HF and MCSCF), likely due to the missing scalar relativistic effects. The SO contributions were –233 ppm. In comparison, in Ref. [50], the total relativistic change for σ_{Te} was reported as +1963 ppm (Dirac-HF). Again, the correlation effects on the heavy-nucleus shielding in Ref. [42] were found to be only modest.

14.3.5
Mercury Shielding Constants: Scalar, Spin–Orbit, Correlation, and Solvent Effects

Apart from the HX and H_2Y series and the rare gas atoms there are not very many computations with different methodology available that have been applied to the same heavy nucleus shieldings. An exception is the case of mercury. A comparison between ZORA-DFT and DKH2-HF is made for δ_{Hg} in the series HgX_2 and MeHgX (X = Cl, Br, I, Me = CH_3) in Tab. 14.4. Due to a possible strong influence of electron correlation on the shielding tensor in general, it is difficult to rate the quality of the results in terms of relativistic and correlation contributions. The findings of Refs. [45, 56] and the data of Tab. 14.3 do not yet permit general conclusions about the importance of correlation for heavy-nucleus shieldings in general, though there is an increasing body of data for heavy-nucleus shieldings for which the correlation effects are on the one hand not negligible, on the other hand comparatively small when taking the magnitude of the relativistic corrections as well as the accuracy of the computations in comparison with experimental data into consideration. In con-

Table 14.4 ^{199}Hg chemical shifts for HgX_2 and MeHgX, X = Cl, Br, I, Me = CH_3, without and including the spin–orbit–induced terms in the shielding tensor. Chemical shifts with respect to $HgMe_2$. All values multiplied by (–1).

Molecule	DFT ZORA[a,b]		HF DKH2[a,c]			Expt.[b]
	no SO	incl. SO	nrel	no SO	incl. SO	
HgMeCl	922.1	942.6	561.8	1002.1	485.2	861
HgMeBr	840.3	1068.2	538.9	863.8	953.3	915
HgMeI	500.8	1024.9	354.4	555.1	1411.1	1097
$HgCl_2$	1368.7	1555.9	859.0	1408.2	1168.7	1519
$HgBr_2$	1484.3	2684.4	1063.3	1561.0	3462.1	2213
HgI_2	1029.2	3506.0	567.0	863.3	4779.4	3447

a) calculated from the reported data in the respective publication. "no SO" refers to relativistic shielding constants calculated from a two-component spin-orbit coupled wavefunction / Kohn–Sham orbitals from which the FC and SD spin–orbit contributions to σ_{Hg} have been subtracted. These values are similar, but not identical, to those that would be obtained from scalar relativistic computations (see Ref. [101] for some scalar ZORA data for HgMeX).

b) Ref. [19].

c) Ref. [55].

trast, besides the usual pathological [102] cases N_2, CO, O_3, CH_2N_2, etc., "relativistic" examples have been investigated (CX_3^+, Ref. [94], DFT-pPSO and nonrel. MP2) where large correlation effects on the shielding tensor of a light nucleus were found. The basis sets that were applied for the different computations in Tab. 14.4 are not directly comparable, which also makes an assessment somewhat difficult. It has been previously noted that "cross terms" between scalar and SO contributions to σ_{Hg} are very important [103], which means that the SO-induced change of σ_{Hg} strongly depends on the well-known scalar relativistic change of the Hg–ligand bonds [104] (i.e. the amount of Hg s/d hybridization). The results in Tab. 14.4 (and Tab. 14.3) indicate that for a proper evaluation of shieldings of heavy nuclei in a molecule both scalar and spin–orbit relativistic effects are of high importance, since the experimental trends for σ_{Hg} are only reproduced when the SO contributions are included.

In Ref. [103], the HgX_2 systems had previously been studied by a mixed HF-DKH2/vPSO approach, and a systematical overestimation of the Hg chemical shifts with respect to experiment when using a flexible basis set had been attributed to a missing treatment of two-electron spin–orbit terms. $HgMe_2$ data were not reported in this work, but assuming an exact result for $HgCl_2$, chemical shifts of –3191 and –4130 would have been obtained for $HgBr_2$ and HgI_2 with respect to $HgMe_2$. From Tab. 14.4, however, it can be seen that the HF-DKH2 approach by the same authors which includes two-electron SO terms at the Breit–Pauli level, yields even larger shifts for these compounds. Previous experience with the two-electron SO contributions indicates that their *relative* importance decreases in comparison to the one-electron SO contributions when the nuclear charges become larger [41, 48, 67, 105]. Interestingly, the computational results from the ZORA-DFT and the HF-DKH2 methods in Tab. 14.4 excluding the SO contributions agree much better with each other, whereas the SO contributions are much larger for HF-DKH2. It is important to note that the absolute shielding values reported in Refs. [19, 55] for the reference compound $HgMe_2$ differ by almost 5000 ppm (8020 and 12772 ppm, respectively), also due to the SO contributions. However this difference is cancelled to a large extent when the chemical shifts are evaluated. Previously, the authors of Ref. [55] had reported an even larger HF-DKH2 mercury shielding of 15128 ppm for the $HgMe_2$ reference, but still obtained (very small) chemical shifts for $Hg(SiH_3)_2$ and $Hg(GeH_3)_2$, in good agreement with experimental data. It is therefore likely that the differences are due to core-contributions that hardly affect the chemical shifts.

When comparing to experimental data it is important to consider solvent effects, as was explicitly demonstrated by Wolff et al. [19]. Solvent–induced changes of up to 10^3 ppm for δ_{Hg} were found experimentally for HgI_2, and values of similar magnitude in the computations in Ref. [19]. These are cases where the solvent strongly coordinates to the heavy atom. Unfortunately, the inclusion of solvent molecules causes the systems to be rather big for relativistic computations, therefore no broad study regarding solvent effects on heavy-atom shieldings is currently available.

14.3.6
Tellurium Absolute Shielding Constants and Chemical Shifts

Another comparison between HF and DFT has recently been made for ^{125}Te shieldings. In Ref. [51], a HF-DKH2 approach has been applied by Hada et al. to a subset of Te compounds that were previously studied by Ruiz-Morales et al. [106,107] with the vPSC method of Ref. [83]. In Ref. [106], because of the rather good agreement with experimental data the authors concluded that spin–orbit corrections are not vital for the evaluation of Te chemical shifts, and thus reasonable predictions can be made by a scalar approach alone. Indeed, the HF-DKH2 results of Ref. [51] confirm that the SO contributions to the chemical shifts are only modest, though not negligible. However, this seems to be due to a cancellation between different compounds when evaluating the chemical shift, as large SO contributions to the shielding were reported $\sim 2 \cdot 10^3$ ppm). A similar quality of agreement with experimental chemical shifts was obtained in both studies. However, the absolute experimental Te shielding scale correction of –945 ppm proposed by Ruiz-Morales et al. has been questioned by Hada et al. because their calculated absolute shieldings agree better with the original shielding scale of Ref. [108]. Taking into consideration the large possible differences between computed shielding constants that were mentioned above, it is obvious that further studies are necessary in order to settle this question. Moreover, it is at present not clear whether the usual procedure to generate experimental absolute shielding scales from measurements of spin–rotation constants along with computations of the diamagnetic shielding tensor can also be applied in the relativistic case.

Chemical shifts for Te and Se have also been studied very recently by a scalar relativistic ZORA pseudopotential plane-wave DFT code [109, 110]. In contrast to other methodology cited in this paper, the nonrelativistic approach adopted in Ref. [109] is able to treat extended periodic systems. It deals explicitly with the presence of the pseudopotential by a method devised by Van de Walle and Blöchl [111]. See also Chapter 16 by Pickard and Mauri. In Ref. [110] the authors have adapted the procedure to the scalar ZORA operator. The results for ^{125}Te absolute shieldings are in agreement with the vPSC frozen-core DFT results of Ruiz-Morales et al. [106], taking into account that different density functionals have been employed (PBE [112] in Ref. [110] vs. BP [113, 114] in Ref. [106]) and that the basis sets and many technical aspects of the codes are very different. The largest disagreement of 276 ppm between the two approaches was found for $(TeCF_2)_2$, with the ZORA results being closer to the "experimental" shielding value of 1066 ppm proposed in Ref. [106]. The scalar relativistic increase of σ_{Te} was of the order of 300 ppm for all six samples. For the ^{77}Se shieldings calculated in Ref. [110] a mean absolute error of 63 ppm (5 samples) with respect to (revised) experimental shieldings has been obtained with the scalar ZORA DFT method. Relativistic effects on σ_{Se} were less than 100 ppm and positive in all cases.

14.3.7
W, Pt, Pb, and U Shielding Constants, and Computations on Larger Systems

Some data for comparison are further available ror ^{183}W chemical shifts. With respect to the reference WO_4^{2-}, the tungsten shifts in $W(CO)_6$, WF_6, and WCl_6 were calculated with DFT-vPauli and DFT-ZORA as –3306, –107, 1773 and –3876, –630, 1932 ppm, respectively [115]. The experimental values are –3446, –1121, 2181 ppm for the series, as compiled in Ref. [115]. The scalar variational Pauli (vPSC) DFT approach had previously predicted a chemical shift of –3703 ppm for $W(CO)_6$, with modest relativistic corrections of +372 ppm. Tungsten shieldings have also been computed by a mixed HF-DKH2/vPSO approach in Ref. [116] for WO_4^{2-}, WF_6, and WCl_6, using a number of different basis sets. The "basis set C" data yielded tungsten chemical shifts of –1135 and 2686 ppm for WF_6 and WCl_6, respectively (nonrelativistic: –1795 and 2266 ppm). Overall, in Ref. [115] the DFT-ZORA method was found to yield a mean error of approximately 3% of the chemical shift range of 7000 ppm for a larger number of tungsten complexes. The DFT-vPauli resulted in a mean error of about 6% for these systems. In the same paper, DFT-ZORA was found to produce a similar accuracy for a number of ^{207}Pb shifts (4% of the shift range), whereas DFT-vPauli resulted in a mean error of 16%. A very large spin–orbit–induced chemical shift change of –8000 ppm has been predicted for PbI_4 in this work.

Because of the efficiency of the Kohn–Sham DFT approach to take electron correlation, at least approximately, into consideration, most of the relativistic NMR investigations of heavy-nucleus shieldings in larger systems have so far been carried out with DFT codes either based on the Pauli operator (Eq. (14.4)) or the ZORA operator. The methodologies have been developed by Ziegler and coworkers [19, 43, 83, 84]. A comparison of the ZORA-DFT and the variational Pauli-DFT methods for the metal shieldings in group 6 to 8 tetraoxo-metallates has been made by Bouten et al. [43]. It has been concluded that the ZORA method yields superior results over the variational Pauli approach, which corroborates the previous findings in Ref. [115] for tungsten and lead complexes. The tetraoxo-metallates have previously been used as a benchmark set for the DFT computation of ^{17}O shielding constants in transition metal systems [83, 117]. Unfortunately, in Ref. [43] the oxygen shieldings have not been reported for comparison.

A density functional study by Schreckenbach et al. for ^{235}U as well as ligand shieldings in uranium compounds [19, 118, 119], has not consistently come to the conclusion that the ZORA approach always performs better for these compounds than vPauli. ECPs were also applied in Ref. [118]. Regarding the chemical shifts of light ligands, it was found that while the nonhybrid density functionals could not reproduce the trends for the ^{19}F-shift in the $UF_{6-n}Cl_n$ series [118] they were successful in reproducing those for $UF_{5-n}(OCH_3)_n$, $n = 1$–4 [119]. Also, the trends for the ^{17}O-shifts in uranyl complexes could be reproduced, with ZORA performing best though still underestimating the oxygen shifts by about 10%. For the $UF_{6-n}Cl_n$ series, an ECP approach with the B3LYP hybrid functional could reproduce the trends for the ^{19}F shifts, however the magnitudes of the shifts were systematically overestimated. A chemical shift range of at least 21,000 ppm for ^{235}U has been predicted,

however so far no experimental data are available. Regarding the U-shieldings, it could be demonstrated that the trends for the ^{235}U shielding constants among the set of 23 complexes that were studied are determined by the average energy gap between the HOMO U-5f$_{xyz}$ and the seven lowest lying virtual MOs (U-5f with antibonding ligand contributions), whereas the HOMO–LUMO gap itself does not explain the trends [119]. The latter is often used in interpretations of NMR parameters, since in an orbital-based formalism (HF, DFT) the inverses of occupied-virtual orbital energy differences directly enter the expressions for the shielding tensor via finding the perturbed orbitals in the presence of the external field. See also Ref. [4] for further details.

That the orbital energy differences are not always the only guide for an interpretation of NMR chemical shifts has also been pointed out in a DFT-ZORA study of ^{195}Pt shifts in 23 Pt complexes [120]. The matrix elements entering the shielding tensor expression need to be considered as well. For the latter, sometimes a qualitative estimate can already be sufficient to rationalize the trends, which has been backed up by a detailed numerical analysis in Ref. [120]. Many of the complexes studied in this paper exhibit a pronounced NHD for δ_{Pt}. However, unlike the cases of HX, CH_3X etc. the platinum NHD was demontrated to be caused by trends both for the paramagnetic shielding as well as for the usually dominant SO contributions. An explanation relying on the HSAB concept was worked out in order to rationalize the unexpected trend for the paramagnetic contribution.

14.3.8
Shielding Anisotropies

Besides the isotropic shielding σ_A, the anisotropy $\Delta\sigma_A$ also carries a lot of vital information about the geometric and electronic structure around nucleus *A*. In many of the already cited publications, theoretical values for $\Delta\sigma_A$ have been reported, and frequently very large relativistic effects have been found. A heavy atom example for which experimental data are available is presented in Tab. 14.5 for $\Delta\sigma$ of ^{199}Hg in methyl-mercury halides and $HgMe_2$. As in the case of the already discussed isotropic shieldings, the experimentally observed trends along the series X = Cl, Br, I are only reproduced in the computations if spin-orbit coupling is considered. Interestingly, as in the case of the chemical shifts, the shielding anisotropies for the two different computational approaches DFT-ZORA vs. HF-DKH2 *without* the SO contributions are rather similar, but change drastically when SO contributions are included, due to their different signs. With both methods, the experimental trends are correctly reproduced, however the DFT-ZORA results significantly overestimate $\Delta\sigma$, whereas it is strongly underestimated in the HF-DKH2 calculations. Whether the reason lies in the relativistic approach, or is due to electron correlation, is yet unclear. It is also likely that environmental effects due to the liquid crystal solvents that were employed in order to determine the experimental data would need to be explicitly considered in the computations. This is strongly indicated by the previously mentioned computational study of Hg chemical shifts by Wolff et al. [19].

Table 14.5 ^{199}Hg chemical shifts anisotropies $\Delta\sigma$ for MeHgX, X = Cl, Br, I, Me = CH_3, without and including the spin-orbit-induced terms in the shielding tensor.

Molecule	DFT ZORA[b,c]			HF DKH2[a,d]		expt.[e]	expt.[c]
	no SO	incl. SO	nrel	no SO	incl. SO[d]		
HgMe	6462	7857	4473.3	5877.0	4843.6	7325±55	7355±55
HgMeCl	5179	6319	3677.5	4913.1	4258.0	5535±80	5430±40
HgMeBr	5322	6168	3718.6	5121.3	3570.0	5455±100	5140±90
HgMeI	5763	6071	4000.0	5574.4	2731.1	5480±300	4840±70

a) See footnote a of Tab. 14.4. For this reason, the values here differ somewhat from the scalar relativistic results reported in Ref. [101].
b) Method „C" of Ref. [101] referring to DFT-ZORA computations with the same basis set employed as in Ref. [19] (Tab. 14.4) for comparison. Shielding anisotropies with an extended basis (Method „B" in Ref. [101]) were consistently larger by 600 to 1000 ppm.
c) Ref. [101].
d) Ref. [55].
e) Ref. [121].

Other examples for which relativistic corrections to shielding anisotropies, often also for a heavy nucleus, have been reported are HX (X = F, Cl, Br, I) [15, 40–42, 47, 52, 53, 85], H_2Y (Y = O, S, Se, Te [, Po]) [42, 50], YH_3 (Y = N, P, As, Sb, Bi) [50], CH_3X (X = F, Cl, Br, I) [41, 42]

14.4 Summary

It is now possible by various computational methods to compute nuclear shieldings and NMR chemical shifts for molecules containing heavy elements from first-principles theory, even for heavy nuclei. Some of the developments are quite recent and have not yet been extended for a correlated relativistic ab initio treatment. For the inclusion of electron correlation DFT can already be employed. For the investigation of heavy-nucleus shieldings, both scalar and SO relativistic effects need to be considered. The available body of computational data indicates, in comparison with experimental results, that in many cases the trends that are obtained for heavy atomic systems are dominated by spin–orbit coupling, whereas scalar relativistic effects are of high importance in order to obtain the correct magnitudes of heavy-atom chemical shifts. Developments are still ongoing in several laboratories worldwide in order to improve and extend the present methodologies, and to provide further case studies.

Acknowledgements

The author acknowledges financial support in form of an „Emmy Noether" fellowship by the Deutsche Forschungsgemeinschaft (DFG) and thanks professors B. A. Hess and P. Pyykkö for discussions. He is grateful to G. Schreckenbach, P. Lantto, M. Bühl, J. Vaara and P. Pyykkö for preprints of upcoming manuscripts.

References

1 P. Pyykkö, A. Görling, N. Rösch, *Mol. Phys.* **1987**, *61*, 195–205.
2 U. Edlund, T. Lejon, P. Pyykkö et al., *J. Am. Chem. Soc.* **1987**, *109*, 5982–5985.
3 P. Schwertdtfeger, J. R. Brown, J. K. Laerdahl et al., *J. Chem. Phys.* **2000**, *113*, 7110–7118.
4 J. Autschbach, T. Ziegler, Relativistic Computation of NMR Shieldings and Spin–spin Coupling Constants, in *Encyclopedia of Nuclear Magnetic Resonance*, Vol. 9, eds. D. M. Grant, R. K. Harris, Wiley, Chichester **2002**.
5 R. Ditchfield, *Mol. Phys.* **1974**, *27*, 789–807.
6 G. Schreckenbach, *Theor. Chem. Acc.* **2002**, *108*, 246–253.
7 W. Kutzelnigg, *Isr. J. Chem.* **1980**, *19*, 193–200.
8 T. Helgaker, M. Jaszuński, K. Ruud, *Chem. Rev.* **1999**, *99*, 293–352.
9 U. Fleischer, C. van Wüllen, W. Kutzelnigg, NMR Chemical Shift Computation: Ab initio, in *Encyclopedia of Computational Chemistry*, ed. von Ragué Schleyer, P., John Wiley & Sons, Chichester **1998**.
10 S. T. Epstein, *The Variation Method in Quantum Chemistry*, Academic Press, New York **1974**.
11 D. B. Chesnut, *Annu. Rep. NMR Spectrosc.* **1995**, *29*, 71–122.
12 D. B. Chesnut, The ab initio Computation of Nuclear Magnetic Resonance Chemical shielding, in *Reviews in Computational Chemistry*, Vol. 8, eds. K. B. Lipkowitz, D. B. Boyd, VCH, New York **1996**.
13 K. Endo, K. Yamamoto, *J. Phys. Soc. Jpn.* **1995**, *64*, 4053–4054.
14 R. G. Parr, W. Yang, *Density Functional Theory of Atoms and Molecules*, Oxford University Press, New York **1989**.
15 H. Fukui, T. Baba, *J. Chem. Phys.* **1998**, *108*, 3854–3862.
16 W. H. E. Schwarz, Fundamentals of Relativistic Effects in Chemistry, in *The Concept of the Chemical Bond*, Vol. 2, ed. Masic, Z. B., Springer, Berlin **1990**.
17 J. Autschbach, W. H. E. Schwarz, *Theor. Chem. Acc.* **2000**, *104*, 82–88.
18 J. E. Harriman, *Theoretical Foundations of Electron Spin Resonance*, Academic Press, New York **1978**.
19 S. K. Wolff, T. Ziegler, E. van Lenthe et al., *J. Chem. Phys.* **1999**, *110*, 7689–7698.
20 T. Enevoldsen, L. Visscher, T. Saue et al., *J. Chem. Phys.* **2000**, *112*, 3493–3498.
21 J. Autschbach, T. Ziegler, *J. Chem. Phys.* **2000**, *113*, 936–947.
22 L. Visscher, K. Dyall, *At. Data Nucl. Data Tables* **1997**, *67*, 207–224.
23 S. Blügel, H. Akai, R. Zeller et al., *Phys. Rev. B* **1987**, *35*, 3271; H. Akai, M. Akai, S. Blügel et al., *Prog. Theor. Phys. Suppl.* **1990**, *101*, 11–77.
24 J. Autschbach, unpublished, results.
25 N. C. Pyper, *Chem. Phys. Lett.* **1983**, *96*, 204–210; N. C. Pyper, *Chem. Phys. Lett.* **1983**, *96*, 211–217.
26 P. Pyykkö, *Chem. Phys.* **1983**, *74*, 1–7.
27 Z. C. Zhang, G. A. Webb, *J. Mol. Struct.* **1983**, *104*, 439–444.
28 C. J. Jameson, *Nucl. Magn. Reson.* **1984**, *13*, 1–20.
29 Y. Nomura, Y. Takeuchi, N. Nakagawa, *Tetrahedron Lett.* **1969**, *8*, 639–642.
30 I. Morishima, K. Endo, T. Yonezawa, *J. Chem. Phys.* **1973**, *59*, 3356–3364.
31 M. I. Volodicheva, T. K. Rebane, *Teor. Éksp. Khim. (Engl. Ed. Theor. Exp. Chemistry)* **1978**, *14*, 348–354.
32 A. A. Cheremisin, P. V. Schastnev, *J. Magn. Reson.* **1980**, *40*, 459–468.
33 N. F. Ramsey, *Phys. Rev.* **1950**, *78*, 699–703; N. F. Ramsey, *Phys. Rev.* **1952**, *86*, 243–246.
34 G. A.Aucar, T. Saue, L. Visscher et al., *J. Chem. Phys.* **1999**, *110*, 6208–6218.
35 H. M. Quiney, H. Skaane, I. P. Grant, *Chem. Phys. Lett.* **1998**, *290*, 473–480.
36 W. Kutzelnigg, *Phys. Rev. A* **2003**, *67*, 032109–12.

37 M. Hada, Y. Ishikawa, J. Nakatani et al., *Chem. Phys. Lett.* **1999**, *310*, 342–346.
38 R. H. Romero, G. A. Aucar, *Int. J. Mol. Sci.* **2002**, *3*, 914–930.
39 P. Pyykkö, L.-B. Zhao, *J. Phys. B* **2003**, *39*, 1469–1478.
40 H. Fukui, T. Baba, H. Inomata, *J. Chem. Phys.* **1996**, *105*, 3175–3186.
41 J. Vaara, K. Ruud, O. Vahtras et al., *J. Chem. Phys.* **1998**, *109*, 1212–1222.
42 J. Vaara, K. Ruud, O. Vahtras, *J. Chem. Phys.* **1999**, *111*, 2900–2908.
43 R. Bouten, E. J. Baerends, E. van Lenthe et al., *J. Chem. Phys.* **2000**, *104*, 5600–5611.
44 W. Kutzelnigg, *J. Comput. Chem.* **1999**, *20*, 1199–1219.
45 J. I. Melo, M. C. Ruiz de Azua, C. G. Giribet et al., *J. Chem. Phys.* **2003**, *118*, 471–486.
46 G. A. Aucar, J. Oddershede, *Int. J. Quantum Chem.* **1993**, *47*, 425–435.
47 L. Visscher, T. Enevoldsen, T. Saue et al., *J. Comput, Chem.* **1999**, *20*, 1262–1273.
48 Y. Ishikawa, T. Nakajima, M. Hada et al., *Chem. Phys. Lett.* **1998**, *283*, 119–124.
49 I. P. Grant, H. M. Quiney, *Int. J. Quantum Chem.* **2000**, *80*, 283–297.
50 S. S. Gomez, R. H. Romero, G. A. Aucar, *J. Chem. Phys.* **2002**, *117*, 7942–7946.
51 M. Hada, J. Wan, R. Fukuda et al., *J. Comput. Chem.* **2001**, *22*, 1502–1508.
52 H. Fukui, T. Baba, *J. Chem. Phys.* **2002**, *117*, 7836–7844.
53 T. Baba, H. Fukui, *Mol. Phys.* **2002**, *100*, 623–633.
54 R. Fukuda, M. Hada, H. Nakatsuji, *J. Chem. Phys.* **2003**, *118*, 1015–1026.
55 R. Fukuda, M. Hada, H. Nakatsuji, *J. Chem. Phys.* **2003**, *118*, 1027–1035.
56 P. Manninen, P. Lantto, J. Vaara, *J. Chem. Phys.* **2003**, *119*, 2623–2637.
57 M. Hada, R. Fukuda, H. Nakatsuji, *Chem. Phys. Lett.* **2000**, *321*, 452–458.
58 S. H. Lin, *Mol. Phys.* **1967**, *12*, 91–93.
59 R. A. Hegstrom, *Phys. Rev.* **1969**, *184*, 17–22.
60 F. D. Feiock, W. Johnson, *Phys. Rev.* **1969**, *187*, 39–50.
61 D. Kolb, W. R. Johnson, P. Shorer, *Phys. Rev. A* **1982**, *26*, 19–31.
62 J. Vaara, P. Pyykkö, *J. Chem. Phys.* **2003**, *118*, 2973–2976.
63 W. Pauli, Die allgemeinen Prinzipien der Wellenmechanik, in *Handbuch der Physik*, Vol. 5; Springer, Berlin **1958**.
64 R. E. Moss, *Advanced Molecular Quantum Mechanics*, Chapman and Hall, London **1973**.
65 R. E. Moss, H. P. Trivedi, *Mol. Phys.* **1979**, *38*, 1611–1619.
66 J. D. Morrison, R. E. Moss, *Mol. Phys.* **1980**, *41*, 491–507.
67 O. L. Malkina, B. Schimmelpfennig, M. Kaupp et al., *Chem. Phys. Lett.* **1998**, *296*, 93–104.
68 H. Fukui, T. Baba, H. Inomata, *J. Chem. Phys.* **1997**, *106*, 2987.
69 G. L. Sewell, *Proc. Cambridge Phil. Soc.* **1949**, *45*, 631.
70 R. A. Moore, *Can. J. Phys.* **1975**, *53*, 1240; R. A. Moore, *Can. J. Phys.* **1975**, *53*, 1247; R. A. Moore, *Can. J. Phys.* **1975**, *53*, 1251.
71 A. Rutkowski, *J. Phys. B* **1986**, *19*, 149–158; A. Rutkowski, *J. Phys. B* **1986**, *19*, 3431–3441; A. Rutowski, *J. Phys. B* **1986**, *19*, 3443–3455.
72 W. Kutzelnigg, *Z. Phys. D.* **1989**, *11*, 15–28; W. Kutzelnigg, *Z. Phys. D.* **1990**, *15*, 27–50; W. Kutzelnigg, E. Ottschofski, R. Franke, *J. Chem. Phys.* **1995**, *102*, 1740.
73 A. C. Hennum, W. Klopper, T. Helgaker, *J. Chem. Phys.* **2001**, *115*, 7356–7363.
74 B. A. Hess, Relativistic Theory and Applications, in *Encyclopedia of Computational Chemistry*; ed. P. von Ragué Schleyer, John Wiley & Sons, Chichester **1998**; B. A. Hess, *Phys. Rev. A* **1986**, *33*, 3742–3748; A. Wolf, M. Reiher, B. A. Hess, *J. Chem. Phys.* **2002**, *117*, 9215–9226.
75 M. Barysz, A. J. Sadlej, *J. Mol. Struct. (THEOCHEM)* **2001**, *573*, 181–200.
76 M. Douglas, N. M. Kroll, *Ann. Phys. (N.Y.)* **1974**, *82*, 89.
77 E. van Lenthe, E. J. Baerends, J. G. Snijders, *J. Chem. Phys.* **1993**, *99*, 4597–4610; E. van Lenthe, Thesis, Vrije Universiteit Amsterdam, Netherlands, **1996**; K. Dyall, E. van Lenthe, *J. Chem. Phys.* **1999**, *111*, 1366–1372.
78 G. Hong, M. Dolg, L. Li, *Chem. Phys. Lett.* **2001**, *334*, 396–402.
79 K. Molzberger, W. H. E. Schwarz, *Theor. Chim. Acta* **1996**, *94*, 213–222.
80 H. Nakatsuji, H. Takashima, M. Hada, *Chem. Phys. Lett.* **1995**, *233*, 95–101.
81 C. B. Ballard, M. Hada, H. Kaneko et al., *Chem. Phys. Lett.* **1996**, *254*, 170–178.
82 V. G. Malkin, O. L. Malkina, D. R. Salahub, *Chem. Phys. Lett.* **1996**, *261*, 335–345.
83 G. Schreckenbach, T. Ziegler, *Int. J. Quantum Chem.* **1997**, *61*, 899–918.

84 S. K. Wolff, T. Ziegler, *J. Chem. Phys.* **1998**, *109*, 895–905.
85 T. Baba, H. Fukui, *J. Chem. Phys.* **1999**, *110*, 131–137.
86 J. Vaara, O. L. Malkina, H. Stoll et al., *J. Chem. Phys.* **2001**, *114*, 61–71.
87 V. G.Malkin, O. L. Malkina, L. A. Eriksson et al., The Calculation of NMR and ESR Spectroscopy Parameters using Density Functional Theory, in *Modern Density Functional Theory: A Tool for Chemistry*, Vol. 2, eds. J. M. Seminario, P. Politzer, Elsevier, Amsterdam **1995**.
88 M. Kaupp, Relativistic Effects on NMR Chemical Shifts, in *Relativistic Electronic Structure Theory*, Vol 2, eds. P. Schwerdtfeger, Elsevier, Amsterdam **2003**, in press.
89 M. Kaupp, C. Aubauer, G. Engelhardt et al., *J. Chem Phys.* **1999**, *100*, 3897–3902.
90 H. Nakatsuji, Z.-M. Hu, T. Nakajima, *Chem. Phys. Lett.* **1997**, *275*, 429–436.
91 M. Kaupp, O. L. Malkina, V. G. Malkin et al., *Chem. Eur. J.* **1998**, *4*, 118–126.
92 H. Nakatsuji, T. Nakajima, M. Hada et al., *Chem. Phys. Lett.* **1995**, *247*, 418–424.
93 K. Endo, K. Yamamoto, H. Okada, *Bull. Chem. Soc. Jpn.* **1995**, *68*, 3341–3345.
94 M. Kaupp, O. L. Malkina, V. G. Malkin, *Chem. Phys. Lett.* **1997**, *265*, 55–59.
95 S. Fukawa, M. Hada, R. Fukuda et al., *J. Comput. Chem.* **2001**, *22*, 528–536.
96 M. Kaupp, V. G. Malkin, O. L. Malkina, NMR of Transition Metal Compounds, in *Encyclopedia of Computitional Chemistry*, ed. P. von Ragué Schleyer, John Wiley & Sons, Chichester **1998**.
97 M. Bühl, M. Kaupp, O. L. Malkina et al., *J. Comput. Chem.* **1998**, *20*, 91–105.
98 H. Nakatsuji, M. Hada, T. Nakajima et al., *Chem. Phys. Lett.* **1996**, *249*, 284–289.
99 "Amsterdam Density Functional Program", Theoretical Chemistry, Vrije Universiteit, Amsterdam URL: http://www.scm.com.
100 W. H. Flygare, *Chem. Rev.* **1974**, *74*, 653–687.
101 J. Jokisaari, S. Järvinen, J. Autschbach et al., *J. Phys. Chem. A* **2002**, *106*, 9313–9318.
102 C. J. Jameson, A. C. de Dios, Theoretical and Physical Aspects of Nuclear Shielding, in *Nuclear Magnetic Resonance, a Specialist Periodical Report*, Vol. 31, ed. G. A. Webb, Royal Society of Chemistry, Cambridge **2002**.
103 H. Nakatsuji, M. Hada, H. Kaneko et al., *Chem. Phys. Lett.* **1996**, *255*, 195–202.
104 P. Pyykkö, *Chem. Rev.* **1988**, *88*, 563–594.
105 S. Okada, M. Shinada, O. Matsuoka, *J. Chem. Phys.* **1990**, *93*, 5013–5019.
106 Y. Ruiz–Morales, G. Schreckenbach, T. Ziegler, *J. Phys. Chem. A* **1997**, *101*, 4121–4127.
107 G. Schreckenbach, T. Ziegler, *Theor. Chem. Acc.* **1998**, *99*, 71–82.
108 C. J. Jameson, A. K. Jameson, *Chem. Phys. Lett.* **1987**, *135*, 254–259.
109 C. J. Pickard, F. Mauri, *Phys. Rev. B* **2001**, *63*, 245101–13.
110 J. R. Yates, C. J. Pickard, M. C. Payne et al., *J. Chem. Phys.* **2003**, *118*, 5746–5753.
111 C. G. Van de Walle, P. E. Blöchl, *Phys. Rev. B* **1993**, *47*, 4244–4235.
112 J. P. Perdew, K. Burke, M. Ernzerhof, *Phys. Rev. Lett.* **1996**, *77*, 3865–3868.
113 A. D. Becke, *Phys. Rev. A* **1988**, *38*, 3098–3100.
114 J. P. Perdew, *Phys. Rev. B* **1986**, *33*, 8822–8824.
115 A. Rodriguez-Fortea, P. Alemany, T. Ziegler, *J. Phys. Chem. A* **1999**, *103*, 8288–8294.
116 M. Hada, H. Kaneko, H. Nakatsuji, *Chem. Phys. Lett.* **1996**, *261*, 7–12.
117 M. Kaupp, V. G. Malkin, O. L. Malkina et al., *J. Am. Chem. Soc.* **1995**, *117*, 1851–1852; Erratum, *J. Am. Chem. Soc.* **1995**, *117*, 8492.
118 G. Schreckenbach, S. K. Wolff, T. Ziegler, *J. Phys. Chem. A* **2000**, *104*, 8244–8255.
119 G. Schreckenbach, *Inorg. Chem.* **2002**, *41*, 6560–6572.
120 T. M. Gilbert, T. Ziegler, *J. Phys. Chem. A* **1999**, *103*, 7535–7543.
121 J. D. Kennedy, W. McFarlane, *J. Chem. Soc., Faraday Trans. 2* **1976**, *72*, 1653–1660.

15
Relativistic Calculations of Spin–Spin Coupling Constants of Heavy Nuclei

Jochen Autschbach and Tom Ziegler

15.1
Introduction

In theoretical and computational chemistry, two important observables of the NMR experiment are subject both to routine applications and ongoing methodological developments: nuclear shielding and indirect spin–spin coupling constants. The former are the subject of the preceding chapter in this book by one of us (Chapter 14 by Autschbach). There, the reader will also find an introduction to relativistic computations of NMR observables that apply to nuclear shieldings and nuclear spin–spin coupling constants alike. The latter, and in particular the recent research activities devoted to the relativistic computation of spin–spin coupling constants involving heavy nuclei in molecules, are the subject of the present chapter. A combined review on relativistic NMR computations, with references up to early 2001, has been previously published by us in Ref. [1]. See also a recent review article on spin–spin coupling tensors by Vaara et al. [2].

While the number of publications devoted to nonrelativistic nuclear shielding computations for molecules range in the thousands, computations of heavy atom shieldings or spin–spin coupling constants are still comparatively rare. The computation of nuclear spin–spin coupling constants has generally received far less attention than nuclear shieldings [3–6], and this is even more so for couplings involving a heavy nucleus because of the necessary relativistic theoretical approach [1]. At the same time, a wealth of information can be extracted from the coupling constants that often requires an investigation and analysis both by experimental and theoretical tools. For instance coupling constants between heavy metals in di- or oligonuclear transition metal complexes have long been of interest to experimentalists and theoreticians alike. Partially, this might be due to the very large coupling constants that are frequently observed. The "world record" is currently held by a crown-ether complex of Hg_2^{2+} with 284 kHz for ^1J(Hg–Hg) [7].

The past decade has seen a strong increase in scientific work devoted to spin–spin coupling constants computations. However, at the time of writing (Spring 2003) there are still not many computational implementations available that can treat nuclear spin–spin coupling constants relativistically. Furthermore, some of the available relativistic methodology is so far restricted to semiempirical theories, or is not

Calculation of NMR and EPR Parameters. Theory and Applications.
Edited by Martin Kaupp, Michael Bühl, Vladimir G. Malkin
Copyright © 2004 WILEY-VCH Verlag GmbH & Co. KGaA, Weinheim
ISBN: 3-527-30779-6

capable of treating with scalar relativistic effects. Following the historical development in computational NMR, attempts have been made to recover the relativistic effects on spin–spin coupling constants by a perturbational treatment of spin-orbit coupling alone. However, when a coupling constant involving a heavy nucleus is of interest, this approach is not accurate enough because of the often dominant, sometimes huge, scalar relativistic effects (see Section 15.3). At the same time spin–spin coupling constants are quite sensitive to the electronic structure, perhaps even more than nuclear shieldings. It is one of the reasons why they are such universal chemical probes, however it also requires an inclusion of electron correlation in the computations. This is perhaps why why currently a two-component relativistic method based on density functional theory (DFT) developed in 2000 by the present authors has recently been described as "for practical problems the most applicable of the presently available methods [. . ., for heavy atomic systems] with potential for large systems as well" (Vaara et al., Ref. [2]). It must be noted, though, that the DFT approach, as facilitated by currently well established functionals, is not without shortcomings and the previous quotation thus emphasizes the general applicability of the available computer code, not necessarily its performance regarding specific "problematic", in particular small light atomic, systems. It can be expected that in the near future efficient codes based on different relativistic methods will become available which will allow for a more diverse comparison of computational results.

In Section 15.2 we will briefly outline some of the theoretical details underlying the computation of nuclear spin–spin coupling constants. Because of the large overlap with the methodology for the calculation of nuclear magnetic shielding tensors, we refer the reader to Chapter 14 regarding common features and the general scope of the article, the usage of units, etc. In Section 15.3 we present computational results from calculations of coupling constants involving at least one heavy atom. Regarding the treatment of the heavy-atom (HA) effects on couplings between light atoms (LA) in a molecule (a so-called HALA effect) the same considerations apply as for nuclear shieldings, namely that they can be treated equally well by effective core potentials (ECPs) or direct relativistic methods. For the former, and light-nucleus coupling constants, an otherwise nonrelativistic NMR code is sufficient. ECP approaches are discussed in the Chapter 13 by Vaara et al. We have thus decided not to elaborate on such applications here since the sometimes spectacular effects of relativity on heavy-nucleus coupling constants (HAHA effects) appear more appropriate for the scope of this paper. For recent reviews on the computation of spin–spin coupling constants including nonrelativistic methods see, e.g. Refs. [2, 6]. We restrict ourselves here to a discussion of the indirect coupling between nuclear spins which is mediated by the electronic systems in a molecule, and refer the reader to Ref. [8] as well as to Chapter 27 by Wasylishen for details about the direct dipolar "through space" coupling. The dipolar coupling vanishes for quickly rotating molecules, as is the case for measurements in solution or in the gas phase.

15.2 Methodological Aspects

The spin Hamiltonian that describes the interaction between the spin magnetic moments $\boldsymbol{\mu}_A$ and $\boldsymbol{\mu}_B$ of two nuclei A, B in a molecule is

$$H = \boldsymbol{\mu}_A \mathbf{K}_{AB} \boldsymbol{\mu}_B. \tag{15.1}$$

In formal agreement with Eq. (15.1) the indirect *nuclear spin–spin coupling tensor* K_{AB} is quantum-chemically calculated from the molecular energy E by double perturbation theory as

$$\mathbf{K}_{AB} = \left. \frac{\partial^2 E}{\partial \boldsymbol{\mu}_A \partial \boldsymbol{\mu}_B} \right|_{\boldsymbol{\mu}_A=0, \boldsymbol{\mu}_B=0}. \tag{15.2}$$

The rotational average of $\mathbf{K}$, the isotropic coupling constant, will be denoted by K. K is given in SI units of $\mathrm{T}^2\,\mathrm{J}^{-1}$ or $\mathrm{kg\,m^{-2}\,A^{-2}\,s^{-2}}$, with typical magnitudes of 10^{19} to 10^{23}. The relation to the J coupling constants (in Hz) of the NMR experiment is

$$J_{AB} = \frac{\hbar}{2\pi} \gamma_A \gamma_B K_{AB} \tag{15.3}$$

where the γ_a and γ_B are the magneto-gyric ratios of the nuclei.

Eq. (15.2) refers to a general *relativistic* energy expression, from which the desired couplings can then also be evaluated for heavy nuclei. The magnetic perturbation operators that enter the expressions for the nuclear spin–spin coupling tensor are collected in Tab. 15.1. The nonrelativistic formalism for indirect spin–spin coupling

Table. 15.1 Comparison of one-electron operators that contribute to the indirect nuclear spin–spin coupling constant in Eq. (15.2), in different relativistic formulations and in the nonrelativistic limit, and a selection of literature references that lists explicit expressions.

Nonrelativistic	Two-component (Quasirelativistic) DKH2, ZORA,...	Relativistic Perturbational Schemes	Four-component ("Fully Relativistic")
diamagnetic orbital (OD)	diamagnetic orbital (OD)[a]	nonrelativistic terms OD, OP, FC, SD	Eq (15.4) corresponding to OP, FC, SD
paramagnetic orbital (OP)	paramagnetic orbital (OP)[a]	if spin–orbit coupling included: FC/SD and OP yield additional	
Fermi-contact (FC)	Fermi-contact (FC)[a]	cross contributions plus many additional	OD implicitly included in coupling tensor
spin-dipole (SD)	spin-dipole (SD)[a]	operators $O(c^{-2})$, $O(c^{-4})$	
Refs. [1–5, 9] and many others	Refs. [10–13]	Refs. [14–19]	Refs. [20–28]

a) Two-component relativistic generalization of the respective operator.

constants is described in Chapter 7 by Helgaker et al. In contrast to the nuclear shielding, already at the nonrelativistic or scalar quasi-relativistic level the electron–spin dependent FC and SD terms yield nonzero contributions to the spin–spin coupling constant. In fact, the FC mechanism is often the most important one, though counter examples are known in which the OP mechanism is dominant or where the usually negligible SD–term yields sizeable contributions [4, 13, 29, 30]. In the presence of spin–orbit coupling, i.e. in two-component relativistic methods, additional cross terms between FC and OP, and between SD and OP, respectively, occur that are zero otherwise. The explanation and interpretation closely follows the one for the spin–orbit induced cross terms between FC/SD and the orbital–Zeeman (OZ) operators for the nuclear shielding. It is based upon the fact that a magnetic field (here due to the paramagnetic orbital current density induced by one of the nuclear spins, instead of an external field) causes a spin-density in the molecule which is detected by the FC term at the other nucleus.

In the four-component Dirac formalism, only the perturbation operator

$$\hat{H}_u^{(0,1)} = -\frac{1}{c}\left[\boldsymbol{\alpha} \times \frac{\boldsymbol{r}_A}{r_A^3}\right]_u \tag{15.4}$$

(for the $u \in \{x, y, z\}$ component of the spin-vector of each nucleus A) is responsible for the nuclear spin–spin coupling constants. The electron-spin dependent contributions as well as the relativistic spin–orbit cross terms are implicitly included due to the operators' action on the four-component wavefunction/orbitals. The FC, SD, OP, and OD, operators are obtained from Eq. (15.4) upon transformation to a two-component form in the nonrelativistic limit [1]. There is no explicit diamagnetic term present in the four-component formalism. The respective contributions to the coupling tensor were in a numerical study explicitly traced back to positronic states that were, in addition to the electronic states, used as a basis set for the perturbed wavefunctions [25]. This topic has also been discussed earlier in Ref. [31–33] regarding the diamagnetic shielding term, and recently in detail by Kutzelnigg [34].

Generally, only orbitals that have sufficiently large values close to *both* nuclei A, B contribute to K_{AB}. These are the valence orbitals, in particular those that contribute to chemical bonds between A and B. In this sense[1)], just as chemical shifts, the spin–spin coupling constant are "valence shell properties", and for their accurate computation only the valence (sometimes also the outer core-)orbitals have to be correctly described. The perturbation operators are large in spatial regions close to the nuclei (see also Chapter 31 by Rassolov and Chipman). For instance the FC-operator acts nonrelativistically *at* the (point) nucleus, in two-component formalisms within the K-shell of an atom. The latter is also true for the four-component hyperfine integrals. This means that the tails of the valence orbitals must be very accurately modeled, which usually demands atom-centered basis functions with high exponents, in particular for a Gaussian basis. In a relativistic calculation, the

1) We refer to the somewhat ambiguous partitioning of the electron density into core and valence contributions from orthogonal orbitals.

demands on the basis set in the near-nuclear region are even higher because of the large relativistic increase of the orbital densities and the concomitant effects on the hyperfine integrals. In particular the FC-mechanism is very strongly influenced, as most of the examples in Section 15.3 will demonstrate.

For further details on relativistic methodology for spin–spin coupling constant computations we refer to Ref. [1]. Generally, there is a variety of different approaches available which allow for relativistic calculations of heavy-atomic molecules, and a subsequent calculation of nuclear spin–spin coupling constants by double-perturbation theory by Eq. (15.2). Currently, spin–spin coupling calculations based on the four-component formalism are restricted to Hartree–Fock (HF) or Hückel theory which imposes severe limitations on the accuracy, and in the Hartree–Fock–Dirac (HF–Dirac) case on the size of the systems that can be treated efficiently. Four-component DFT methodology of spin–spin coupling constants will probably become available in the near future and greatly enhance the predictive power of four-component methods with respect to experimental data. However, the expense of such methods is still likely to limit the molecules that can be studied to small models or benchmark systems. Approximate (quasirelativistic) two-component relativistic methods have been developed to overcome these limitations, based on the Pauli-operator or parts of it, or the so-called zeroth-order regular approximation. Literature references for these methodologies will be cited in the next section.

The following acronyms and abbreviations will be used in the next section in order to designate various methodological approaches for spin–spin coupling computations. SO = spin–orbit, or spin–orbit coupling. vPSO, vPSC, vPauli for variational Pauli SO only, scalar only, and scalar + SO, respectively. Similarly, pPSO, pPSC, pPauli denote perturbational relativistic calculations $\mathcal{O}(c^{-2})$. ZORA = zeroth-order regular approximation. HF = Hartree–Fock. HF-Dirac = four-component Hartree–Fock. MCSCF = multiconfigurational self-consistent field. REX = relativistic (four-component) extended Hückel theory.

15.3 Computational Results

15.3.1 Relativistic Scaling Factors

Relativistic effects on hyperfine splittings were considered already in 1930 in theoretical work. It has been noted in Ref. [35] that an approximate treatment earlier worked out by Fermi (which implicitly leads to the FC operator, Tab. 15.1) must be modified. Inspired by Ref. [35], relativistic scaling factors (RSFs) to atomic hyperfine integrals that are obtained from a comparison of the respective relativistic and non-relativistic values from atomic calculations have subsequently been used for the theoretical prediction of nuclear spin–spin coupling constants in heavy-atomic molecules. This semiempirical approach was in particular put forward by Pyykkö and coworkers in 1973 [36] (see also Ref. [37]). Such RSFs, or hyperfine integrals

obtained from relativistic atomic computations, are still in use, mainly in semiempirical codes in order to determine spin–spin coupling constants [38–42]. They were also applied by Malkina et al. [43] on top of a nonrelativistic DFT-calculation of J(Sn–H) in SnH_4. Good agreement with the experimental value was obtained after inclusion of the scaling factor of 1.348. A somewhat related procedure has been proposed in Ref. [44] where scalar relativistic values for the orbitals at the nuclei obtained from vPSC atomic calculations (employing frozen cores) have been used to scale the matrix elements of the FC operator in nonrelativistic molecular computations.

The use of RSFs has turned out not to be extremely successful in the prediction of chemical trends that occur for series of related molecules. Also, they do not cover HALA effects, i.e. relativistic effects on coupling constants between light atoms L′ and L″ in the neighborhood of a heavy nucleus. Nonetheless, they can be very useful in order to estimate the magnitude of the relativistic effects that can be expected for coupling constants involving heavy nuclei that are dominated by the FC contribution. For instance, for the Hg 6s orbital, a RSF of about 2.44 has been proposed [36]. When the bonding between Hg and a ligand atom L is mostly determined by the Hg 6s, a relativistic change of K(Hg–L) by roughly a factor of 3 must be expected. For K(Hg–Hg), a change by an order of magnitude might occur. For molecules in which strong relativistic effects on bonding are present, where the FC term is not the only important contribution to the coupling constant and/or where electronic spin–orbit coupling is large, or if HALA effects are of interest, a more consistent treatment of relativistic effects on nuclear spin–spin coupling constants in first-principles calculations is necessary.

15.3.2
Semiempirical Methods

In Ref. [41] a large number of heavy nucleus coupling constants were studied semiempirically (AM1, PM3, MNDO), based on the use of RSFs (see also Ref. [23]). Among others, the systems YH_4, YMe_4, YCl_4, $R_3Y–YR_3$, and YH_3^- (Y = C, Si, Sn, Pb), were investigated. In some cases good agreement with experimental results was obtained, but the PM3 model in particular appeared to be rather problematic. This situation has subsequently been analyzed [42] and could be partially attributed to so-called triplet instabilities [3]. We refer to Chapter 9 by Heine et al. for further information on semiempirical methodologies.

While discussing semiempirical approaches, the large body of results obtained by the “relativistic extended Hückel” (REX) method should not go unnoticed. See, for instance, Refs. [21, 22, 45] just to name a few key publications, and Tab. 15.2 for an example. Due to the inherent inaccuracies related to the Hückel approximation we do not discuss the results here in detail. However, we point out that many qualitative trends are reproduced by such calculations which can greatly facilitate a deeper understanding of the outcome of more accurate, but also more complicated, methods.

Table 15.2 Some calculated reduced indirect coupling constants in the H_2Y series, Y=O, S, Se, Te, in $T^2\,J^{-1}$

Coupling	expt.[a]	MCSCF+pPSO[c]			Dirac–HF[d]	Dirac–HF[e]		REX[f]	
		nr. HF[b]	nrel	rel	rel	nrel	rel	nrel	rel
O-H	48.3	62.9	51.4	51.3	57.8	63.7	63.1		36.6
S-H		42.9	40.2	39.8	41.6	45.5	45.1		28.5
Se-H	27.6	48.9	48.9	44.8	25.1	46.1	25.2	14.1	2.6
Te-H	±15	77.2	74.2	60.4	–24.2	86.0	–21.9	–16	–98
Po-H						73.7	–1481		

a) A subset of experimental data compiled in Ref. [18]. The conversion factors for $J \rightarrow K$ from Ref. [18] have been used to convert experimental values to reduced coupling constants K.
b) Hartree–Fock data additionally reported in Ref. [18].
c) Ref. [18].
d) Ref. [25].
e) Ref. [28].
f) Ref. [21].

15.3.3 Four-Component Methods

The four-component formalism was worked out already in 1977 by Pyykkö [20], and a "proof of concept" was provided in the form of a LCAO calculation of K(Hg–C) in dimethyl-mercury. The results are very typical for Hg–ligand coupling constants, with a relativistic increase in the isotropic coupling by a factor of 2.7, mainly due to scalar relativistic effects. Contributions caused by SO coupling were almost negligible. The coupling anisotropy ΔK was found to increase by a factor of 3.3, with a larger contribution due to SO coupling. The final results did somewhat depend on the choice of the hyperfine integrals and were reported as 1524 to $1327 \cdot 10^{19}\,T^2\,J^{-1}$ (nrel: 571.7, expt.: 1264) for K(Hg–C) and 535.4 to $456.7 \cdot 10^{19}\,T^2\,J^{-1}$ (nrel: 164.5, expt.: 599) for ΔK, in reasonable agreement with the experimental values. These relativistic effects should be compared to the celebrated large relativistic bond-length contraction of AuH which is 10% in magnitude. The comparison clearly demonstrates the high importance of treating relativistic effects when calculating nuclear spin–spin coupling constants. Even for rather light elements such as Ge, the relativistic change of K(Ge–L) is of the order of 10% [26] whereas, at present computational accuracies, relativistic geometry effects are usually neglibible for such compounds.

More recently, four-component formalisms for the computation of spin–spin coupling constants have been discussed in detail in the framework of molecular electronic structure theory [23], and HF–Dirac applications to small molecules have been reported [24–26, 28]. These data provide valuable benchmarks for the magnitude of relativistic effects on spin–spin coupling constants, and for alternative implementations or more accurate ab initio computations which can be expected in the future. They also demonstrate that electron correlation is of high importance for a reliable determination of these properties, since the HF–Dirac level of theory is, in

many cases, inadequate when a comparison with experimental data is attempted. This has been shown, for example, by Visscher et al. in Ref. [26] for K(Y–H) in YH_4 (Y = C, Si, Ge, Sn, Pb), where reasonable agreement with experiment could only be achieved after the HF–Dirac results were scaled by respective ratios of the nonrelativistic correlated SOPPA (second-order polarization propagator approach) and HF values. For PbH_4, this ratio amounts to 0.76. At the same time, the Pb–H coupling constant increased at the HF level by a factor of approximately 2.56.

Besides the YH_4 series, another frequently studied benchmark case is the series H_2Y (Y = O, S, Se, Te (, Po)). A selection of computed coupling constants is listed in Tab. 15.2. It can be seen that the Y–H coupling is strongly influenced by relativistic effects when the chalcogen atom becomes heavier. Obviously for Te (and Po) very large scalar relativistic effects dominate, whereas the SO contributions to K(Y–H) in the series are also important but much smaller. The authors of Ref. [25] have also pointed out that the HF–Dirac level of theory does not allow for a direct comparison with experimental data. Apart from missing contributions due to electron correlation, this has been attributed to triplet instabilities which typically plague the calculations of spin–spin coupling constants within the HF approach already at the nonrelativistic level of theory [3].

In addition to the H_2Y series, in Ref. [28] the group-15 hydrides were also studied by four-component HF theory, and similar trends were obtained. The nuclear shielding tensors were also calculated. Further four-component HF data were reported for K(H–X) in the HX diatomics (X = F, Cl, Br, I) [24], and very large relativistic effects were found for instance for HI: nrel = –13.0, rel = $-113 \cdot 10^{19}\,T^2\,J^{-1}$. The SO corrections to the HX coupling constants were also individually calculated by the MCSCF-pPSO approach in Ref. [18], and as in the H_2Y case found to be rather small as compared to the large scalar relativistic contributions.

15.3.4
Electron Correlation

Electron correlation contributions to K(Y–H) in H_2Y at the nonrelativistic level were demonstrated to be sizeable in Ref. [18] (compare Tab. 15.2), but more pronounced for the lighter molecules. An estimate of the correlation contribution of about –24% to K(Pb–H) in PbH_4 has already been mentioned above. Very strong correlation effects have been found for the H–H coupling constants in the H_2Y series, and in particular for H_2O. It should be noted that the K(H–H) are determined here by large contributions from the OD, the OP, and the FC/SD terms with different signs and are thus very sensitive to subtle changes in the electronic structure. Upon inclusion of SO relativistic contributions to K(H–H) in the H_2Y systems good agreement with experiment could be achieved with the correlated MCSCF+pPSO approach. The authors of Ref. [18] have thus concluded that the SO terms are the dominating relativistic contributions to such coupling constants. That is: for a description of HALA effects the perturbational inclusion of spin–orbit coupling was considered as sufficient.

The K(H–H) for the heavier systems in the YH_4 series were found to be very strongly affected by relativistic effects, for example 0.1 (nrel.) vs. 0.8 (rel.) $\cdot\, 10^{19}\,T^2\,J^{-1}$

for SnH_4 and 0.18 vs. $3.62 \cdot 10^{19}\,T^2\,J^{-1}$ for PbH_4. Whether these are also dominated just by the SO effects is unclear. An important question here is that of possible cross terms between relativity and electron correlation in the coupling constants. To our knowledge, this problem has not yet been addressed explicitly in a computational study.

15.3.5 Perturbational Methods

Perturbational approaches that follow the development of relativistic chemical shifts calculations have also been applied to spin–spin coupling constants. By this we mean a perturbational inclusion of the Pauli SO operator in the coupling constant calculation which has been proven to cover most of the HALA effects on chemical shifts in many cases (see Ref. [1], Chapter 14 and Chapter 13). One example has already been mentioned: the MSCSF-pPSO method listed in Tab. 15.2. In Ref. [16] (see also Ref. [15]) Kirpekar et al. have applied a similar approach to K(Pb–H) and K(H–H) in PbH_4, with unsatisfactory results regarding a comparison with experimental data for the former. An estimate for the experimental K(Pb–H) in PbH_4, extrapolated from $PbMe_3H$ and $PbMe_2H_2$ (Me = CH_3) is $112 \cdot 10^{20}\,T^2\,J^{-1}$. At the correlated MCSCF level, a nonrelativistic result of 56.2, and a relativistic one of $48.3 \cdot 10^{20}\,T^2\,J^{-1}$ have been obtained for K(Pb–H) in Ref. [16]. In comparison, the scaled HF-Dirac result of Ref. [26] is $138.3 \cdot 10^{20}\,T^2\,J^{-1}$ (unscaled: 181.9) . The negative relativistic correction obtained by Kirpekar et al. represents the SO induced contributions (mostly FC-OP cross-terms) similar to those obtained in Ref. [18] for H_2Y, whereas the obviously most important scalar relativistic corrections could not be obtained from this approach. At the same time, a reduction of the FC term by about 20% due to electron correlation has been reported, along with very large correlation effects on the FC term of the H–H coupling constant. The situation for the YH_4 systems is thus very similar to the H_2Y series listed in Tab. 15.2. The body of available data up to early 2000 has indicated that spin–orbit corrections to heavy-atom coupling constants are likely to be of minor importance, which was explicitly pointed out in Ref. [26] for the PbH_4 example.

Unfortunately, the pPauli approach (i.e. including scalar relativistic terms) has been found not to be applicable to nuclear spin–spin coupling constants, because of the combination of highly singular perturbation operators [46]. Applications of a nonsingular four-component relativistic perturbation theory ("Direct perturbation theory" DPT [47–51]) to the calculation of spin–spin coupling constants in molecules have not yet been carried out, though a route for the calculation of the respective matrix elements of the magnetic perturbations that show up in the formalism [17] has recently been discussed [19].

15.3.6
Two-Component ZORA–DFT Calculations

Currently, the work-horse of computational chemistry is density functional theory (DFT). The present authors have in 2000 implemented a two-component relativistic DFT approach for the computation of nuclear spin–spin coupling constants, based on the variationally stable ZORA one-electron Hamiltonian [12, 13]. Because DFT includes, to some extent (limited by the approximations that were applied to derive the functional) the important electron correlation effects, it allows for a semi-quantitative, sometimes quantitative, comparison with experimental data in many cases. The coupled perturbed Kohn–Sham approach is apparently also much more robust towards the triplet instability problem. Regarding the influence of the ZORA approximation to relativity, we are not aware of any published results obtained from a four-component DFT treatment which would allow for a systematic comparison. A recent study has shown, however, that the FC-type hyperfine integrals obtained from ZORA calculations on heavy atoms are within a few per mil of the Dirac values for valence s–orbitals [52]. For the innermost core-orbitals in heavy atoms large errors are obtained due to the deviations between ZORA and Dirac, but since these orbitals do not contribute to the coupling tensor the ZORA approach to the calculation of spin–spin coupling constants can be regarded as very accurate. Van Lenthe et al. have previously come to similar conclusions regarding EPR hyperfine splittings [53].

The well studied case of PbH_4 and its methyl derivates has been used [13] to verify the sign and magnitude of the SO corrections to *K*(Pb–H) reported by Kirpekar et al. in Ref. [16] as well as the magnitude of the correlation contributions (about –20 to –25% by comparison to the HF–Dirac results of Ref. [26]). Good agreement with experiment could be achieved, with calculated DFT-ZORA values for the one-bond *K*(Pb–H) in PbH_4, $PbMe_2H_2$, and $PbMe_3H$ of 122, 98.3, and $89.1 \cdot 10^{20}\,T^2\,J^{-1}$, respectively (expt.: 112, 98.7, and 92.3). Figure 15.1 displays an overview of the accuracy that has been obtained for a number of heavy-metal-ligand one-bond coupling constants.

The DFT-ZORA approach has during the last three years been applied to a number of heavy atom spin–spin coupling constants (i) in order to provide benchmark results and demonstrate the reproducibility of experimentally observed trends by computations, and to investigate (ii) the magnitude of scalar and spin–orbit relativistic corrections, (iii) *environmental effects*, and (iv) *periodic trends*.

Starting with point (ii), in the light of the previously mentioned results regarding the magnitude of spin–orbit coupling effects on nuclear spin–spin coupling constants, it has been somewhat surprising that in the case of Tl–X (X = F, Cl, Br, I) coupling constants SO effects constitute the most important contributions when the halogen atom becomes heavier [13, 55]. The FC-OP cross-term is the largest individual contribution, for example, to *K*(Tl–I). For the series TlF, TlCl, TlBr, and TlI, the computed results in Ref. [13] were (ZORA, BP functional) –138.8, –128.8, –131.6, and $-114.9 \cdot 10^{20}\,T^2\,J^{-1}$ in scalar relativistic calculations, but –203.4, –218.5, –315.3, and $-381.8 \cdot 10^{20}\,T^2\,J^{-1}$ including the SO effects. The experimental values are –202,

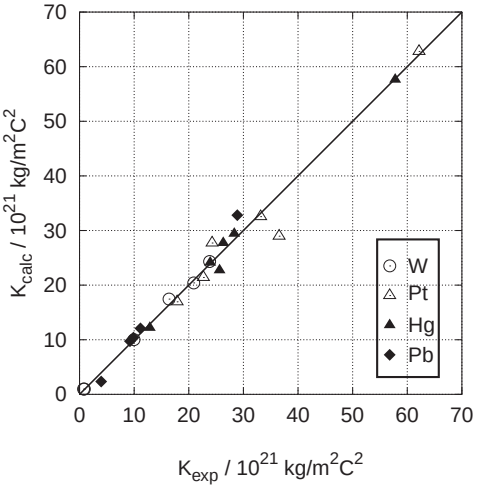

Figure 15.1 One-bond metal–ligand reduced nuclear spin–spin coupling constants (absolute values) for metal complexes obtained from scalar relativistic DFT-ZORA computations and compared to experimental values. Data taken from Refs. [54, 12]. The line is not a fit but indicates ideal agreement with experiment. The different markers indicate different heavy metals. For not octahedrally or tetrahedrally coordinated metal centers, the first coordination shell has been completed with solvent molecules, as described in Ref. [54].

–224, –361, and $-474 \cdot 10^{20}\,T^2\,J^{-1}$, respectively (as compiled in Ref. [29]). The deviations between theory and experiment for TlBr and TlI have tentatively been attributed to deficiencies in the applied functionals. For many coupling constants that were investigated so far, SO effects were indeed small to negligible, but if heavy p-block elements are involved and both the FC and the OP term are large (as is the case for TlX) this might not be the case.

The periodic trends of K and ΔK of TlX and other diatomics have been analyzed in detail by Bryce and Wasylishen [29] based on experimental data and nonrelativistic MCSCF computations for light atomic systems. A subsequent DFT-ZORA study [30] has been devoted to the periodic trends of K(X–Y) in interhalogen diatomics. A linear increase of the magnitude of K(X–Y) and ΔK with $Z_X \cdot Z_Y$ has been found, along with satisfactory agreement between theory and experiment. For these systems again the FC term is not the dominating contribution, but rather the OP term, and for the heavier systems SO effects on K become very important. A general tendency in the p-block of the periodic table appears to be an increase in the relative anisotropy, $\Delta K/K$, for increasing nuclear charges, along with an increasing magnitude of K. The increase in the relative anisotropy has qualitatively been analyzed by Pyykkö and Wiesenfeld [21] based upon REX theory.

Regarding environmental effects, the influence of coordination of solvent molecules to a heavy metal center has been studied in Refs. [55, 56]. Sometimes very large positive shifts of the FC term to one-bond metal–ligand coupling constants were reported in Ref. [55]. For instance, K(Hg–C) in $Hg(CN)_2$ increased from 425.5

to $560.7 \cdot 10^{19}\,T^2\,J^{-1}$ (nrel.: 237.9, expt.: 577.8) upon coordination by four methanol molecules, which has been analyzed and explained by a small donation of charge from the solvent into the metal–ligand σ bonds. Similar effects were found for square planar Pt complexes. A general trend is that the solvent shift is more pronounced for stronger nucleophilic solvents and increases with the number of coordinating solvent molecules.

An interesting example is $[(NC)_5Pt\text{-}Tl(CN)]^-$, for which in scalar relativistic DFT-ZORA computations the Pt–Tl coupling constant of $J = 19$ kHz increased to 43 kHz upon coordination of the Tl center by four water molecules [56] (nrel.: 5.4 kHz, expt. value in aqueous solution is 57 kHz). At the same time, water complexation creates a rather unintuitive pattern of the Tl–C one- and two-bond coupling constants. The enormous relativistic increase of the coupling between the two heavy metals could be expected based on the magnitude of the RSFs for the 6s shells. This and related systems have also been theoretically studied in Refs. [57, 58]. In the latter work (model systems with CN^- replaced by H^-), the unusually short Pt–Tl distance of approx. 2.6 Å and certain experimental conclusions about the Pt and Tl oxidation states [59] could be explained, and in agreement with the theoretical NMR analysis [56] it was found that the bonds along the C–Pt–Tl–C axis are highly delocalized.

The DFT-ZORA method has been applied to coupling tensors in various halogen and xenon fluorides by Bryce and Wasylishen [60]. Spin–spin coupling constants and also chemical shifts in a number of covalent Xe compounds and van der Waals complexes have further been studied by Bagno and Saielli [61] who reported good agreement between theoretical and experimental values. Excellent agreement of the computational results with experimental data has been reported in Ref. [60], provided both scalar and SO effects were considered and reliable geometries were employed in the computations. An interpretation of the results was given in terms of the dependence of the OP term on the number of valence shell lone pairs, and the dependence of the FC/SD terms on bond distances. For some apparently closely related systems (such as XF_6^+ and XF_6^-) the X–F coupling constants were found to be of opposite sign (with their magnitudes in very good agreement with experimental values). This indicates a serious potential trap when interpreting trends in experimental results for which the sign is unknown.

Recent work has been devoted to heavy metal–metal coupling constants in dinuclear metal complexes [62, 63]. The case of Pt–Pt couplings, investigated in Ref. [63], is discussed by Bühl in Chapter 26. In Ref. [62] the extremely large coupling constants between Hg and Hg in complexes containing Hg_2^{2+} and Hg_3^{2+} have been investigated. Similar to the somewhat unintuitive case of K(Pt–Pt), it was found that *coordination* and *polarization* of a metal–metal fragment explain the magnitude of the metal–metal coupling constants. The coordination can thereby be due to ligands or solvent molecules. Unlike the previously studied systems in which only one metal center could be coordinated by the solvent [55, 56], here solvent or ligand coordination of both metals of a metal–metal fragment reduces its coupling constant in the systems investigated so far. This can be rationalized by a simple argument based on Hückel theory [62]. For the complex of Hg_2^{2+} with the crown ethers 18-crown-6 and 15-crown-5, very good agreement with the experimental ^1J(Hg–Hg) of 284 kHz

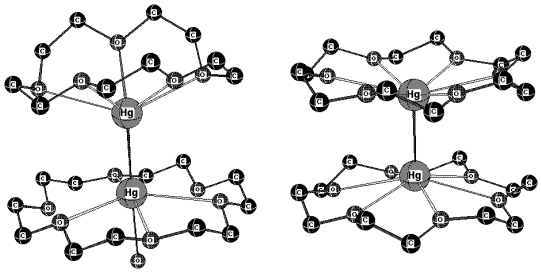

J^{expt}(Hg-Hg) = 284 kHz

J^{calc} (Hg-Hg) = 278 kHz J^{calc} (Hg-Hg) = 599 kHz

Figure 15.2 Reduced Hg–Hg coupling constants (^{199}Hg) for crown ether complexes of Hg_2^{2+}, from Ref. [62]. Computations based on the scalar DFT-ZORA approach. The left complex (mixed 18-crown-6 and 15-crown-5) has been computed based on the crystal structure of Ref. [7], the right one (both 18-crown-6) based on an optimized geometry

(^{199}Hg) [7] could be achieved. This is currently the largest experimentally determined coupling constant. The calculated scalar DFT-ZORA result is 278 kHz, missing SO corrections were estimated to be of the order of –10% or smaller (see Fig. 15.2 for an illustration). At the same time, the coupling constant in the (hypothetical) free Hg_2^{2+} is likely to be around 0.9 MHz, indicating that the upper limit for Hg–Hg coupling constants has not yet been reached in experiments. However, a system such as the Hg_2(18-crown-6)$_2$ complex in Fig. 15.2 for which we have calculated a coupling constant of 0.6 MHz does not allow an easy NMR detection of J(Hg–Hg) due to its symmetry. A polarization of the Hg_2^{2+} fragment due to an unsymmetric environment would, however, reduce the coupling. In the same work the one-bond and the two-bond Hg–Hg coupling constant in Hg_3^{2+} have been calculated. ^2J(Hg–Hg) has been estimated to be much larger than the one-bond coupling, in agreement with a qualitative argument based on Hückel theory as well as REX calculations [5, 64]. Again, environmental effects, here from the solvent SO_2, were found to be very pronounced. In such, and probably many other metal–metal bonded systems, relativistic effects on spin–spin coupling constants serve as a strong "magnifying glass" for the study of the influence of coordination on the metal–metal bond.

15.3.7
Coupling Anisotropies

Anisotropies ΔK have not yet been extensively discussed in the literature for spin–spin coupling involving heavy nuclei. A number of examples in the references that were cited so far are Me_3XY (X = C, Si, Sn, Pb; Y = F, Cl; semi-empirical study Ref. [40]), TlX and XF (X = F, Cl, Br, I; DFT-ZORA, Ref. [13]), XY (DFT-ZORA, Ref. [30]), HX (HF-Dirac, Ref. [24]); MCSCF-pPSO, Ref. [18]), H_2Y (Y = O, S, Se, Te; HF–Dirac,

Ref. [28]; MCSCF-pPSO Ref. [18]), Xe and halogen fluorides (DFT-ZORA, Ref. [60]). We refer to the recent overview by Vaara et al. [2] and to Chapter 27 by Wasylishen for further examples and details.

15.4 Summary

Spin–spin coupling constants and tensors are very difficult to calculate accurately, even nonrelativistically for light atomic systems. In addition to this, scalar relativistic effects on nuclear spin–spin coupling constants can be spectacularly large when a heavy nucleus is involved, which makes a relativistic treatment imperative when experimental results are to be reproduced or interpreted. When heavy p-block elements are involved, and scalar or nonrelativistic calculations predict sizeable contributions from both the FC and the OP terms, spin–orbit coupling coupling effects are also likely to be of high importance for the coupling constant. Recent computational studies have further indicated that environmental effects can contribute strongly to the experimentally observed coupling constants, and should thus be considered in interpretations and computational models.

A number of computer codes are available for the study of heavy atomic spin–spin coupling constants, based on four-component theory, or employing different relativistic approximations or RSFs, with underlying semiempirical, DFT, or ab initio methodology. Because of the strong sensitivity of spin–spin coupling constants it is advisable to use high-quality computational models whenever possible.

Acknowledgments

J. A. acknowledges financial support in form on “Emmy Noether” fellowship by the Deutsche Forschungsgemeinschaft (DFG) and thanks professor P. Pyykkö for comments on the manuscript. T. Z. acknowledges a Canada Research Chair from the Canadian government. We are also grateful for financial support from the National Science and Engineering Research Council of Canada (NSERC) for the work on ZORA spin–spin coupling constants.

References

1 J. Autschbach, T. Ziegler, Relativistic Computation of NMR Shieldings and Spin–spin Coupling Constants, in *Encyclopedia of Nuclear Magnetic Resonance*, Vol. 9, eds. D. M. Grant, R. K. Harris, John Wiley & Sons, Chichester **2002**.

2 J. Vaara, J. Jokisaari, R. E. Wasylishen et al., *Prog. Nucl. Magn. Reson. Spectros.* **2002**, *41*, 233–304.

3 T. Helgaker, M. Jaszuński, K. Ruud, *Chem. Rev.* **1999**, *99*, 293–352.

4 J. Kowalewski, *Annu. Rep. NMR Spectrosc.* **1982**, *12*, 81–176.

5 R. H. Contreras, J. C. Facelli, *Annu. Rep. NMR Spectrosc.* **1993**, *27*, 255–356.
6 R. H. Contreras, J. E. Peralta, C. G. Giribet, *Annu. Rep. NMR Spectrosc.* **2000**, *41*, 55–184.
7 R. Malleier, H. Kopacka, W. Schuh et al., *Chem. Commun.* **2001**, 51–52.
8 R. Wasylishen, Dipolar and Indirect Coupling Tensors in Solids, in *Encyclopedia of Nuclear Magnetic Resonance*, eds. D. M. Grant, R. K. Harris, John Wiley & Sons, Chichester, **1996**.
9 N. F. Ramsey, *Phys. Rev.* **1953**, *91*, 303.
10 J. E. Harriman, *Theoretical Foundations of Electron Spin Resonance*, Academic Press: New York **1978**.
11 S. Blügel, H. Akai, R. Zeller et al., *Phys. Rev. B* **1987**, *35*, 3271.
12 J. Autschbach, T. Ziegler, *J. Chem. Phys.* **2000**, *113*, 936–947.
13 J. Autschbach, T. Ziegler, *J. Chem. Phys.* **2000**, *113*, 9410–9418.
14 H. Fukui, T. Baba, H. Inomata, *J. Chem. Phys.* **1996**, *105*, 3175–3186.
15 S. Kirpekar, H. J. A. Jensen, J. Oddershede, *Theor. Chim. Acta* **1997**, *95*, 35.
16 S. Kirpekar, S. P. A. Sauer, *Theor. Chem. Acc.* **1999**, *103*, 146–153.
17 W. Kutzelnigg, *J. Comput. Chem.* **1999**, *20*, 1199–1219.
18 J. Vaara, K. Ruud, O. Vahtras, *J. Comput. Chem.* **1999**, *20*, 1314–1327.
19 A. C. Hennum, W. Klopper, T. Helgaker, *J. Chem. Phys.* **2001**, *115*, 7356–7363.
20 P. Pyykkö, *Chem. Phys.* **1977**, *22*, 289–296.
21 P. Pyykkö, L. Wiesenfeld, *Mol. Phys.* **1981**, *43*, 557–580.
22 N. Rösch, P. Pyykkö, *Mol. Phys.* **1986**, *57*, 193–200.
23 G. A. Aucar, J. Oddershede, *Int. J. Quantum Chem.* **1993**, *47*, 425–435.
24 L. Visscher, T. Enevoldsen, T. Saue et al., *J. Comput. Chem.* **1999**, *20*, 1262–1273.
25 G. A. Aucar, T. Saue, L. Visscher et al., *J. Chem. Phys.* **1999**, *110*, 6208–6218.
26 T. Enevoldsen. L. Visscher, T. Sauer et al., *J. Chem. Phys.* **2000**, *112*, 3493–3498.
27 R. H. Romero, G. A. Aucar, *Phys. Rev. A.* **2002**, *65*, 053411.
28 S. S. Gomez, R. H. Romero, G. A. Aucar, *J. Chem. Phys.* **2002**, *117*, 7942–7946.
29 D. L. Bryce, R. E. Wasylishen, *J. Am. Chem. Soc.* **2000**, *122*, 3197–3205.
30 D. L. Bryce, R. E. Wasylishen, J. Autschbach et al., *J. Am. Chem. Soc.* **2002**, *124*, 4894–4900.
31 H. M. Quiney, H. Skaane, I. P. Grant, *Chem. Phys. Lett.* **1998**, *290*, 473–480.
32 P. Pyykkö, *Chem. Phys.* **1983**, *74*, 1–7.
33 Z. C. Zhang, G. A. Webb, *J. Mol. Struct.* **1983**, *104*, 439–444.
34 W. Kutzelnigg, *Phys. Rev. A* **2003**, *67*, 032109–12.
35 G. Breit, *Phys. Rev.* **1930**, *35*, 1447–1451.
36 P. Pyykkö, E. Pajanne, M. Inokuti, *Int. J. Quantum Chem.* **1973**, *7*, 785–806.
37 D. K. Dalling, H. S. Gutowsky, *J. Chem. Phys.* **1971**, *55*, 4959.
38 G. A. Aucar, R. H. Contreras, *J. Magn. Reson.* **1991**, *93*, 413–418.
39 G. A. Aucar, E. Botek, S. Gómez et al., *J. Organomet. Chem.* **1996**, *524*, 1–7.
40 J. A. Gonzaléz, G. A. Aucar, M. C. Ruiz de Azúa et al., *Int. J. Quantum Chem.* **1997**, *61*, 823–833.
41 R. M. Lobayan, G. A. Aucar, *J. Mol. Struct.* **1998**, *452*, 1–11.
42 R. M. Lobayan, G. A. Aucar, *J. Mol. Struct.* **1998**, *452*, 13–23.
43 O. L. Malkina, D. R. Salahub, V. G. Malkin, *J. Chem. Phys.* **1996**, *105*, 8793–8800.
44 J. Khandogin, T. Ziegler, *J. Phys. Chem. A* **2000**, *104*, 113–120.
45 P. Pyykkö, *J. Organomet. Chem.* **1982**, *232*, 21–32.
46 P. Manninen, P. Lantto, J. Vaara, *J. Chem. Phys.* **2003**, *119*, 2623–2637.
47 G. L. Sewell, *Proc. Cambridge Phil. Soc.* **1949**, *45*, 631.
48 R. A. Moore, *Can. J. Phys.* **1975**, *53*, 1240; R. A. Moore, *Can. J. Phys.* **1975**, *53*, 1247; R. A. Moore, *Can. J. Phys.* **1975**, *53*, 1251.
49 A. Rutkowski, *J. Phys. B* **1986**, *19*, 149–158; A. Rutkowski, *J. Phys. B* **1986**, *19*, 3431–3441; A. Rutkowski, *J. Phys. B*, **1986**, *19*, 3443–3455.
50 W. Kutzelnigg, *Z. Phys. D.* **1989**, *11*, 15–28; W. Kutzelnigg, *Z. Phys. D.* **1990**, *15*, 27–50; W. Kutzelnigg, E. Ottschofski, R. Franke, *J. Chem. Phys.* **1995**, *102*, 1740.
51 J. Autschbach, W. H. E. Schwarz, *Theor. Chem. Acc.* **2000**, *104*, 82–88.
52 J. Autschbach, *Theor. Chem. Acc.* **2004**, *112*, 52–57.
53 E. van Lenthe, A. van der Avoird, P. E. S. Wormer, *J. Chem. Phys.* **1998**, *108*, 4783–4796.
54 J. Autschbach, T. Ziegler, *J. Chem. Phys.* **2002**, *116*, 891–896.

55 J. Autschbach, T. Ziegler, *J. Am. Chem. Soc.* **2001**, *123*, 3341–3349.

56 J. Autschbach, T. Ziegler, *J. Am. Chem. Soc.* **2001**, *123*, 5320–5324.

57 M. R. Russo, N. Kaltsoyannis, *Inorg. Chim. Acta* **2001**, *312*, 221–225.

58 P. Pyykkö, M. Patzschke, M., *Faraday Discuss.* **2002**, *124*, 41–51.

59 M. Maliarik, K. Berg, J. Glaser et al., *Inorg. Chem.* **1998**, *37*, 2910–2919.

60 D. L. Bryce, R. E. Wasylishen, *Inorg. Chem.*, **2002**, *41*, 3091–3101.

61 A. Bagno, G. Saielli, *Chem. Eur. J.* **2003**, *9*, 1486–1495.

62 J. Autschbach, C. D. Igna, T. Ziegler, *J. Am. Chem. Soc.* **2003**, *125*, 4937–4942.

63 J. Autschbach, C. D. Igna, T. Ziegler, *J. Am. Chem. Soc.* **2003**, *125*, 1028–1032.

64 P. Pyykkö, unpublished REX results for Hg_3^{2+}.

16
Calculations of Magnetic Resonance Parameters in Solids and Liquids Using Periodic Boundary Conditions

Chris J. Pickard and Francesco Mauri

16.1
Introduction

Whether you are interested in molecular or condensed phases of matter, in all but the ideal "gas phase" you are drawn to consider large numbers of atoms and molecules in extended regions of space. All "quantum chemical" theoretical techniques for the prediction of magnetic resonance parameters naturally treat the situation of single, small, collections of atoms or molecules.

In this chapter we will describe methods, originating in the solid state physics community, that allow predictions of magnetic resonance parameters to be made for extended, infinite, collections of atoms: specifically in the crystalline state, but through the super-cell approximation, also in aperiodic systems.

These methods are based on density functional theory (DFT), and the plane-wave pseudopotential method, a technique which has become ubiquitous in the first principles study of complex materials [1, 2], or the linearized augmented plane wave (LAPW) [3] method for the calculation of electric field gradients [4].

16.2
Cluster Approaches to Extended Systems

In reality, all crystals or liquids must come to an end and the infinitely periodic crystal is an idealization. It is therefore natural to attempt to describe them as very large molecules. Such a strategy is known as the "cluster" approximation, and in the absence of a theory for the calculation of magnetic resonance parameters in truly infinite systems, it is the only approach that can be taken. It is an approximation because only relatively small clusters can be tackled with modern computational techniques (certainly small as compared to macroscopic crystals).

For the reasons described in more detail below, the size of the cluster chosen to approximate the solid can be critical, as is, if the cluster is to be as small as possible, the precise choice of the cluster, and "termination" of the dangling bonds produced on cutting the cluster from the infinite solid (for a covalent solid) or how the electrostatics are dealt with (for an ionic solid).

Calculation of NMR and EPR Parameters. Theory and Applications.
Edited by Martin Kaupp, Michael Bühl, Vladimir G. Malkin
Copyright © 2004 WILEY-VCH Verlag GmbH & Co. KGaA, Weinheim
ISBN: 3-527-30779-6

Despite these limitations, the growing importance of MAS NMR as an experimental tool for the determination of the atomistic properties of solids has prompted many theoretical investigations using the necessary cluster approximation and existing approaches to the calculation of magnetic resonance parameters. For example, Tossell and co-workers pioneered the application of the cluster approximation to the calculation of ^{29}Si and ^{17}O NMR parameters in silicates [5–8]. These calculations exhibited trends that correlate well with experimental data, and have been useful in the quantification of structural distributions in silicate glasses.

16.3 The Limitations of the Cluster Approach

There would be little need to develop new methods to calculate magnetic resonance parameters specifically in the solid state if we could be confident that it is well described by existing techniques and in all situations. However, there are at least two phenomena that cast doubt on this assumption. They may be characterized as (i) quantum mechanical and (ii) electrostatic effects.

As a consequence of the quantum mechanical uncertainty principle, electrons are delocalized. The perturbation of a system at a given point gives rise to a variation in the electronic properties up to some distance from the site of the perturbation. For example, in a cluster or a nanocrystal the HOMO–LUMO gap can be considerably larger than the gap in the bulk material, due to quantum confinement effects (see for example Ref. [9]). The presence of a surface in a cluster changes the NMR parameters for atoms that are not part of the surface [10]. In an insulator, the change in the electronic properties due to the presence of a surface decays exponentially with the distance from the surface, with a typical decay length. This decay length is of the order of that of the maximally localized Wannier or Boys orbitals of the same system, typically from a few Ångstroms to a few nanometers. The more covalent a system is (or the greater the dispersion of the electronic bands) the greater the decay length. We would therefore expect that in semiconducting systems the decay length will be much larger than in an ionic oxide. Consequently the size of a cluster required to eliminate the quantum effects related to the presence of the surface for the calculation of the NMR parameters is larger for semiconductors than for oxides. Since the quantum effect decays exponentially, it is straightforward to verify the convergence of these effects with cluster size.

The electrostatic effects are possibly even more important for the calculation of magnetic resonance parameters in the solid state, because in certain situations their range of influence can be very much greater. Again, there is a qualitative difference between extended and finite systems. In nature, so as to minimize the energy, the surfaces of macroscopic crystals have a surface charge which is fixed by the condition that the macroscopic electric field (the averages of the field over each unit cell) is zero. Thus, if we want to model a real crystal we must ensure that the average electric field per unit cell is zero. This condition is guaranteed by the use of periodic boundary conditions for the potential, but is not reproduced in a finite approxima-

tion to the same solid if the model cluster is not large enough. This deviation of the electric field with respect to its bulk value can affect the NMR parameters. Given the long range nature of the electrostatic interaction, the electric field does not converge exponentially to the bulk value with cluster size, but rather by a power law. In certain cases the zero average electric field over the unit cell can only be obtained if electrons are transferred from one part of the surface to another. This transfer can only occur in very large clusters. The electrostatic effects are more important for ionic systems and for the NMR parameters of highly polarisable atoms (such as oxygen). Electrostatic effects could, in principle, be corrected by computing the NMR parameters for a cluster in an applied external electric field. The external electric field would be chosen in such a way that the average electric field in a periodic unit cell is zero. However this approach would require, at a minimum, the inclusion in the cluster of at least one crystalline unit cell.

16.4
Infinite Crystals, Periodic Boundary Conditions

Crystals, with translational symmetry, are an important class of extended systems, one on which much of solid state physics had focused in the past. In the process, techniques have been developed that allow theories to be developed and experimental observations to be rationalized. The lattice translational symmetry can be exploited, via periodic boundary conditions, so that the electronic structure can itself be rationalized in terms of a new quantum number, the **k**-vector, or crystal momentum.

While these theoretical techniques formally apply only to perfect crystals, it is common practice to approximate aperiodic systems as crystals with large, or "super" cells. These cells are chosen to be large enough that the effects of the approximation are minimized while capturing the physics of the aperiodic structure. This supercell technique can be applied to isolated molecules (allowing comparison with quantum chemical approaches), defects in solids, surfaces and surface chemistry, and the amorphous or liquid states.

16.5
Magnetic Resonance Parameters within Periodic Boundary Conditions

An effective approach to the calculation of magnetic resonance properties of extended systems is to consider a truly infinite model, allowing for the possibility of an extended electronic structure. We now describe the technical problems, and solutions to those problems, that constitute a useful, truly crystalline approach.

16.5.1
Magnetic Perturbation in Extended Systems

Until the work of Mauri, Pfrommer and Louie [11, 12] no theory existed for the first-principles or ab inito prediction of magnetic resonance parameters in extended systems, forcing all attempts to perform calculations to support solid state MAS NMR experiments to rely on the cluster approximation and existing finite system approaches. The reason for this was that the magnetic resonance parameters, calculated as a perturbative response to an applied uniform magnetic field, require expectation values of the position operator to be evaluated. But these expectation values are not defined for an extended system, since the position operator cannot be represented under periodic boundary conditions. As a result, traditional approaches are inappropriate for the treatment of extended systems.

The approach taken by Mauri et al. [11, 12] is to obtain the magnetic response to a uniform field as the long-wavelength limit of a periodically modulated field, and in addition, to remove the numerical instability introduced in this limit using a sum rule.

More recently, Sebastiani and Parrinello [13] have developed an alternative approach. The magnetic perturbation is evaluated in terms of localized Wannier functions (the localized occupied orbitals). The localized nature of the Wannier functions allows the use of the position operator in the perturbation Hamiltonian.

Both these approaches should be thought of all-electron approaches, while they have been used extensively in combination with pseudopotentials without any attempt to remove the error introduced by their use. For this reason, while several useful applications have emerged, [10, 14–20] the use of the two methods has been restricted to the calculation of chemical shifts of the light elements (hydrogen, carbon, and nitrogen). The pseudopotential error for hydrogen is minimal because it has no core electrons. For the elements of the Li–F period, the pseudisation only weakly affects the 2p channel, which, for these atoms, dominates the dependence of the chemical shifts on the chemical environment. Thus the uncorrected pseudopotential results are in reasonable agreement with those obtained without pseudopotentials (for example the pseudopotential error on the relative chemical shift of carbon is of the order of 20% [24]). For the elements of the other periods the pseudopotential error is much larger than the relative chemical shifts [24].

The ability to deal with the heavier elements and to provide a more accurate description of the light elements requires an explicit treatment of the complications introduced by making the pseudopotential approximation.

16.5.2
All-Electron Magnetic Response with Pseudopotentials

Apart from the early and isolated attempt of Ridard et al. [21], it had been widely expected within the quantum chemical community that any theory for the calculation of NMR chemical shifts for nuclei described with a pseudopotential would fail due to the non-rigid nature of the core contributions to the total chemical shift [22].

However, a careful separation of core and valence contributions that ensures that they are individually gauge-invariant, by Gregor et al. [23], demonstrated that this is not the case and that the core contributions are rigid. This suggested that a pseudopotential based theory of NMR might, in fact, exist.

However, the calculation of NMR chemical shifts within a pseudopotential approach requires the solution of two distinct problems. (i) The description of the coupling of electrons to the uniform magnetic fields within a pseudopotential Hamiltonian. Indeed, despite the widespread use of nonlocal pseudopotentials in electronic structure calculations, until recently it was unclear how nonlocal Hamiltonians should be coupled to magnetic fields. (ii) The description of the induced currents within the pseudisation region. The pseudopotential approximation explicitly neglects the form of the electronic wavefunctions near the nucleus. The pseudowavefunctions are chosen to be as smooth as possible in the core region, and the correct nodal structure of the wavefunctions is lost. This leads to a good approximation for the calculation of total energies and properties for which the matrix elements are dominated by the regions outside the core, but prevents a direct calculation of the properties, such as the electric-field-gradients or the NMR chemical shifts, that depend critically on the details of the wavefunctions in the core region. In particular, the NMR chemical shifts require an accurate description of the induced currents near the nuclei.

To solve these two problems Pickard and Mauri have introduced the gauge including projector augmented wave (GIPAW) method [24], which is an extension of Blöchl's projector augmented wave (PAW) method [25]. The PAW method provides an extremely useful framework for the unification of all-electron (full-potential) linearized augmented plane-wave [3] and pseudopotential approaches. Indeed, it it has become clear that PAW offers a general approach to the calculation of all-electron properties from pseudopotential based schemes.

In the presence of a magnetic field, the PAW approach is not invariant on spatial translation or gauge origin transformation (even if the wavefunctions are defined in the full Hilbert space). In the GIPAW method the translational invariance is restored by introducing into the PAW procedure magnetic-field-dependent phase-factors similar to those used in the gauge including atomic orbital (GIAO) method [26].

In Ref. [24], the chemical shifts obtained using the GIPAW method have been validated by comparison with those computed using the individual gauges for atoms in molecules (IGAIM) [27] as implemented in GAUSSIAN94. The comparison was performed on a set of small molecules (CH_4, CH_3F, C_6H_6, TMS, SiH_3F, Si_2H_4, SiH_4, CO, CF_4, SiF_4, PF_3, P_2, P_4). Both types of calculation were performed within the local density approximation (LDA) of DFT. High-quality basis sets [28] (cc-pCVQZ for C, O, F, Si and P and cc-pVQZ for H) were used in the GAUSSIAN94 calculation. In the GIPAW calculation the $1s^2$ orbitals were considered as core states for C, O, and F and the $1s^22s^22p^6$ orbitals for Si and P. The molecules were placed in $6000\,a_0^3$ supercells, and the wavefunctions were expanded in plane-waves with a 100 Ry cut-off. In Fig. 16.1 we present the data in Table 1 of Ref. [24] in graphical form, a comparison between the GIPAW results and those calculated in the IGAIM

approach. In the upper panel we report the GIPAW results obtained by addressing only the first of the two problems stated above: the correct pseudo-Hamiltonian is used but the effect of pseudisation on the currents in the core region is neglected. In the lower panel, we report the GIPAW results obtained both using the correct pseudo-Hamiltonian and reconstructing the all-electron currents in the core region. The absence of reconstruction leads to meaningful results only for H and possibly first row elements such as C. With the reconstruction of the current the agreement between the GIPAW and IGAIM approaches is practically perfect for all elements.

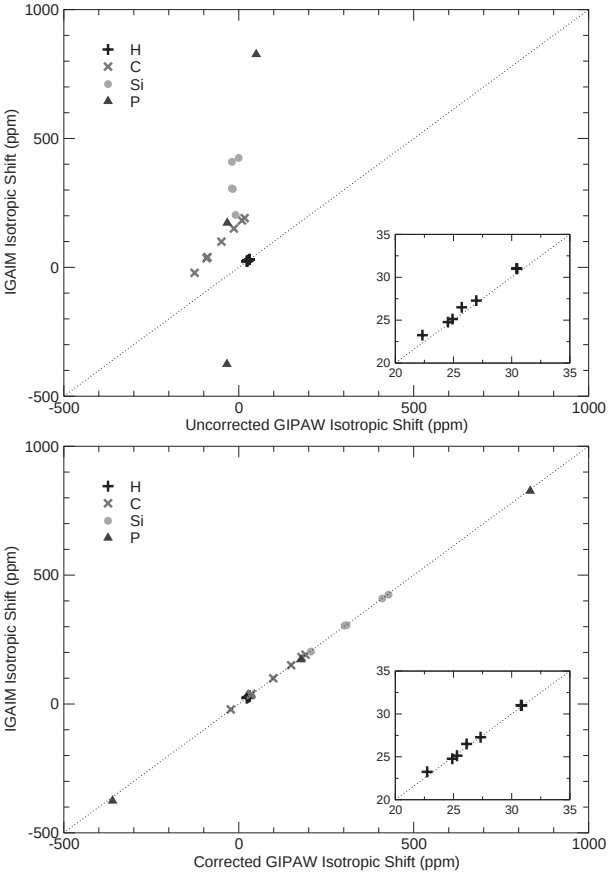

Figure 16.1 A comparison of the GIPAW (*x* axis) and IGAIM (*y* axis) approaches for the isotropic chemical shifts of a selection of small molecules. In the upper panel the GIPAW results have been obtained without correcting the induced current in the core region. In the lower panel the all-electron current in the core region is reconstructed. The dashed lines indicate a perfect agreement.

16.5.3 The Plane-Wave Basis Set

Where local orbital basis sets dominate quantum chemistry, the plane wave basis set is widely used in the solid state physics community. While many basis functions are required to describe each electronic band, the simplicity of the basis, along with the use of fast Fourier transforms, ensures that a computational penalty is not paid. Importantly, the quality of the plane-wave basis set is determined by a single parameter, the cut-off energy. This enables convergence with basis set size to be simply monitored, and full convergence to be achieved at moderate computational cost. For example, the GIPAW calculation of the NMR parameters of the ferrierite zeolite,

Table 16.1 Comparison of the NMR nuclear shielding constants obtained with GIPAW using the single gauge method (defined as the "molecular method" in [24]) and the CSGT method (defined as the "molecular sum rule method" in [24]). The GIPAW-LDA calculations were performed using a plane-wave cut off of 100 Ry and in a 6000 a_0^3 simulation cell.

Molecule	Single Gauge	CSGT	Molecule	Single Gauge	CSGT
^{1}H			C_6H_6	36.13	36.14
CH_4	30.75	30.76	CF_4	34.62	34.30
CH_3F	26.02	26.01	TMS	179.17	179.19
C_6H_6	22.69	22.69	^{29}Si		
TMS	30.76	30.76	SiF_4	410.12	409.85
SiH_3F	25.40	25.40	SiH_3F	308.27	308.23
Si_2H_4	24.92	24.93	Si_2H_4	206.50	206.49
SiH_4	27.57	27.58	SiH_4	427.95	427.95
^{13}C			TMS	302.61	302.61
CO	–22.92	–22.90	^{31}P		
CH_4	191.08	191.09	PF_3	177.90	177.70
CH_3F	98.53	98.52	P_2	–360.97	–360.97
CH_3NH_2	149.61	149.62	P_4	832.87	832.87

which contains 108 atoms in the unit cell, requires 10 h on 16 processors of an IBM Power4 (1.3 GHz) computer. [29] In this calculation the error on the absolute chemical shifts due to the use of pseudopotentials and a plane-wave basis set is as small as that obtained within the IGAIM approach with a cc-pCVTZ basis set (see Table 3 of Ref. [29]). In addition, the sum rules [23, 24] that ensure the invariance of the chemical shifts with respect to the vector-potential gauge are well satisfied by plane-wave basis sets of even modest size. Thus, in contrast to calculations performed with atomic or Gaussian basis sets, with plane-waves, the chemical shifts obtained with the single gauge for the vector potential coincide with those obtained with the continuous set of gauge transformations (CSGT) [30] method as shown in Table 16.1. The numbers in this Table have been extracted from Table II of Ref. [24]. Finally, the plane-wave basis set does not suffer from any basis set superposition error, nor is there any bias in the basis set towards either localized or diffuse electronic states.

16.5.4
Electric Field Gradients and the Quadrupolar Coupling Constants

In addition to the NMR chemical shift tensors, for nuclei with spin greater than one half the quadrupolar coupling constants make an important contribution to magnetic resonance spectra. These coupling constants can be related to the electric field gradients at the nuclei. In principle, the electric field, and hence its gradient, is available as a result of any first principles electronic structure calculation. Indeed, it is a quantity that has been frequently calculated in the solid state using the full potential linear augmented wave method [4]. But, again, the pseudopotential approach does not automatically provide the correct form of the wavefunctions at the nuclei. There have been several approaches developed to account for this, including the work of Meyer et al. [31] which reconstructs the all electron wavefunctions in the core region by solving the Kohn–Sham equations using appropriate boundary equations, and that of Trail and Bird [32] who pursue an embedding potential and Green function-based approach. In addition, and consistently with our GIPAW approach for the other magnetic resonance parameters, the efficient PAW reconstruction scheme has been shown to work well by Petrilli et al. and more recently by Profeta et al. [29, 33].

16.5.5
Relativistic Effects through ZORA

As measurements of the magnetic resonance parameters of nuclei beyond the second period are of increasing interest, it is important that accurate theoretical techniques are available to predict and interpret these experimental results. The GIPAW approach has been extended to produce a method for the efficient calculation of NMR shielding tensors for the heavy elements [34]. Scalar relativistic effects, neglecting the spin–orbit coupling, are introduced by means of the zeroth-order regular approximation (ZORA) approach to the Dirac equation [35]. Using this method, a relativistic calculation on, for example, TeH_2 has roughly the same computational cost as a non-relativistic calculation on OH_2, due to the removal of electronic degrees of freedom by the use of pseudopotentials. This opens up the possibility of calculating the chemical shielding of heavy atom nuclei in molecular and periodic systems containing several hundred atoms.

16.6
Applications of the Planewave-GIPAW Method

To demonstrate the range of applicability, and usefulness, of the planewave-GIPAW method, two applications are discussed in the following.

16.6.1
The Atomic Structure of Icosahedral B_4C Boron Carbide

The first application of the GIPAW method was to elucidate the atomic structure of icosahedral boron carbide, where both X-ray and neutron techniques had failed to locate the carbon atoms in the B_4C structure [36]. Combining total energy calculations for a number of candidate structures, with the calculated ^{11}B and ^{13}C NMR chemical shifts, and comparing with available experimentally measured shifts (which had been only partly interpreted), it was possible not only to determine the location of the C atoms in the structure, but also to extract the density of defects in the structure, and the defect structure itself. The icosahedral boron carbide structure is shown in Fig. 16.2, and four of the possible structures that were considered are described as follows: (i) the *chain* model with one CCC chain and one B_{12} icosahedron in the unit cell, (ii) the *polar* model with one CBC chain and one $B_{11}C$ icosahedron, the C atom being substituted into a polar site, (iii) the *equatorial* model, with one CBC chain and one $B_{11}C$ icosahedron, the C atom being substituted into an equatorial site, and (iv) the *bipolar* model with two C atoms in the same icosahedron on polar sites, none on a second and two CBC chains, in a 30 atom unit cell.

Total energy DFT calculations found the polar model to be the most stable, with the bipolar model the next most stable. Tables 16.2 and 16.3 respectively report the experimental and theoretical ^{13}C NMR chemical shift data, from which it is possible to conclude that 95% of the icosahedra have the C atom in the polar site, 2.5% have two C atoms in polar sites, and 2.5% contain no C. In addition, all chains were

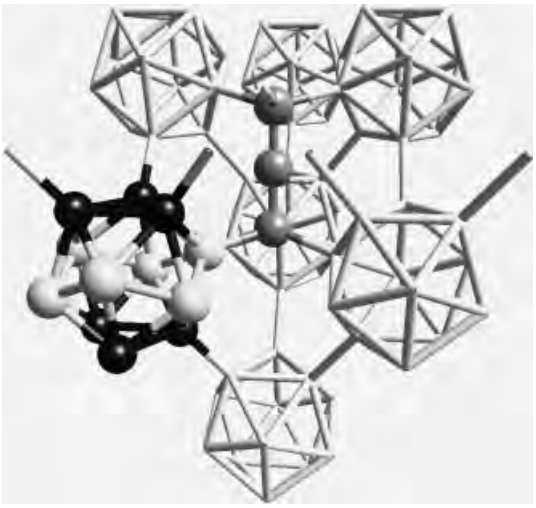

Figure 16.2 Atomic structure of B_4C. The black atoms are on the so-called *polar* sites, bonded to neighboring icosahedra. The white atoms form a puckered hexagon and are in *equatorial* sites. The gray atoms form the *chain*, to which the *equatorial* atoms are bonded.

Table. 16.2 B_4C: experimental ^{13}C NMR chemical shifts, δ_{TMS}, and the corresponding peak intensities. Note that the weak resonance at 101.3 ppm is visible only in the best resolved spectrum [40].

δ_{TMS}[a]	Intensity[a]	δ_{TMS}[b]	Intensity[b]	δ_{TMS}[c]	SIntensity[c]
13±15	66.7%	–0.6	75.6%	1.0	66.9%
85±10	33.3%	79	24.4%	81.9	31.4%
				101.3	1.7%

a) Ref. [41]
b) Ref. [42]
c) Ref. [40]

Table 16.3 Theoretical ^{13}C NMR chemical shift, δ_{TMS}, for the four models. The shifts are calculated using the planewave-GIPAW method and referenced by fixing the claculated ^{13}C δ_{TMS} value of $(B_{11}CH_{12})^-$ to the experimental one. For full computational details see Ref. [36].

	Structural Model			
Carbon Site	***Polar***	***Bi-Polar***	***Equatiorial***	***Chain***
chain-end	–3.9	–1.7	0.8	19.9
chain-end	1.3	–1.1	9.9	19.9
polar	81.6	100.8		
polar		104.0		
equatorial			79.1	
chain-center				233.8

found to be CBC. This study demonstrated that the first principles calculation of NMR chemical shifts and total energies in the solid state is a powerful complement to experimental measurements, bringing value to existing experimental data that might otherwise not be fully exploited.

16.6.2
Assignment of the Zeolite Ferrierite Spectrum

^{17}O NMR parameters, both the chemical shifts and the quadrupolar coupling constants, were calculated for a variety of SiO_2 polymorphs [29]. The use of plane-waves permitted fully converged calculations to be performed on structures containing up to 144 atoms in the unit cell. The calculated NMR parameters of cristobalite, quartz, coesite and zeolite faujasite were found to be in excellent agreement with experimental data, demonstrating that density functional theory is able to reproduce, with high accuracy, the ^{17}O NMR parameters in SiO_2 systems. This precision, absent in previous studies [37], was used to assign the spectrum of the zeolite ferrierite (see Fig. 16.3). The data calculated for the range of SiO_2 polymorphs were used to confirm that there is no simple correlation between the chemical shift and quadrupolar coupling constant and the Si–O–Si angle, emphasizing the importance of predictive theories.

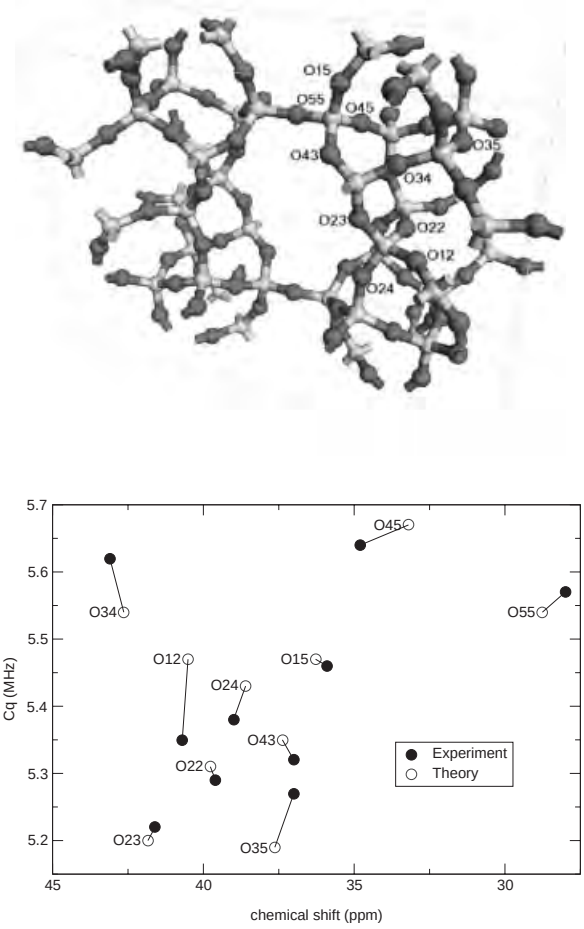

Figure 16.3 Each ^{17}O site in the ferrierite structure is represented by a point whose coordinates are its quadrupolar coupling constant (C_q) and chemical shift (δ) parameters. The theoretical chemical shifts are translated so that their mean values coincide with the experimental ones. The assignment of the experimental spectrum is performed by minimizing in the C_q and δ space the total distance between experimental and theoretical points.

16.7 Work in Progress and Future Challenges

In addition to the calculation of NMR chemical shifts, the GIPAW method has been successfully used for the description of the EPR g-tensor for defects in solids [38]. There is an ongoing effort to apply the GIPAW approach to the calculation of other magnetic response properties, in particular of the NMR spin–spin coupling constants, and the chemical and Knight shifts in metallic solids.

Other possible future developments would include the extension of the ZORA method to treat relativistic effects beyond the scalar approximation specifically the spin–orbit interaction that can dominate for the very heavy elements (see Chapters 13 by Vaara et al. and 14 by Autschbach).

Concerning the technical improvements of the GIPAW method, the possibility to use Vanderbilt ultrasoft-pseudopotentials [39], in which the wavefunction-norm is not conserved, would result in a considerable gain in computational efficiency. In particular, Vanderbilt pseudopotentials permit a much smaller plane-wave basis set to be used for the so-called *hard* elements (the first row elements, the transition metals and the 4f and 5f elements). The current implementation of the GIPAW method is based on norm-conserving pseudopotentials. However, there is work in progress to generalize the GIPAW method to handle the relaxation of the norm-conservation constraint.

Finally, the implementation of the GIPAW method currently makes use of DFT and plane-wave basis sets. However, in the GIPAW formalism, the wavefunctions could be just as well expanded in terms of Gaussian or atomic orbitals basis sets. In particular, the GIPAW method may be equally well applied to traditional quantum chemical approaches for the calculation of magnetic resonance parameters. This would allow the available techniques which describe electrons at a level beyond density functional theory to be used to efficiently study the heavy elements.

16.8 Conclusion

It is now possible to compute NMR chemical shifts in extended solids using DFT and periodic boundary conditions [11–13] In addition, the GIPAW approach [24] reconciles the prediction of highly accurate absolute chemical shifts with the use of pseudopotentials and plane-wave basis sets. The strength of the GIPAW method lies in its range of applicability throughout the periodic table and in crystals or aperiodic systems through the super-cell approximation, its relative computational efficiency, and its scaling on massively parallel computers. The plane-wave pseudopotential method is the first principles technique which may most convincingly be called "black box". As a result, we expect that experimental magnetic resonance practitioners will soon be able to perform first principle calculations alongside their experiments for systems containing several hundred inequivalent atoms.

References

1 M. C. Payne, M. P. Teter, D. C. Allan et al., *Rev. of Mod. Phys.* **1992**, *64*, 1045–1097.
2 V. Milman, B. Winkler, J. A. White, et al., *Int. J. Quantum Chem.* **2000**, *77*, 895–910.
3 P. Blaha, K. Schwarz, P. Sorantin et al., *Comput. Phys. Commun.* **1990**, *59*, 399.
4 K. Schwarz, C. Ambrosch-Draxl, P. Blaha, *Phys. Rev. B* **1990**, *42*, 2051–2061.
5 J. A. Tossel, P. Lazzaretti, *Chem. Phys.* **1984**, *112*, 205–212.
6 J. A. Tossel, P. Lazzaretti, *Phys. Chem. Miner.* **1988**, *15*, 564–569.
7 J. A. Tossel, *J. Non-Cryst. Solids* **1990**, *120*, 13–19.
8 C. G. Lindsay, J. A. Tossell, *Phys. Chem. Miner.* **1991**, *18*, 191–198.
9 A. J. Williamson, J. C. Grossman, R. Q. Hood et al., *Phys. Rev. Lett.* **2002**, *89*, 196803.
10 F. Mauri, B. G. Pfrommer, S. G. Louie, *Phys. Rev. B.* **1999**, *60*, 2941.
11 F. Mauri, G. Louie, *Phys. Rev. Lett.* **1996**, *76*, 4246–4249.
12 F. Mauri, B. G. Pfrommer, S. G. Louie, *Phys. Rev. Lett.* **1996**, *77*, 5300–5303.
13 D. Sebastiani and M. Parrinello, *J. Phys. Chem. A* **2001**, *105*, 1951–1958.
14 F. Mauri, B. G. Pfrommer, S. G. Louie, *Phys. Rev. Lett.* **1997**, *79*, 2340.
15 Y.-G. Yoon, B. G. Pfrommer, F. Mauri et al., *Phys. Rev. Lett.* **1998**, *80*, 3388.
16 B. G. Pfrommer, F. Mauri, S. G. Louie, *J. Am. Chem. Soc.* **2000**, *122*, 123–129.
17 F. Buda, P. Giannozzi, F. Mauri, *J. Phys. Chem.* **2000**, *104*, 9048.
18 D. Sebastiani, M. Parrinello, *Chem. Phys. Chem.* **2002**, *3*, 675.
19 G. R. Goward, M. F. H. Schuster, D. Sebastiani et al., *J. Chem. Phys. B* **2002**, *106*, 9322.
20. D. Sebastiani, G. Goward, I. Schnell et al., *J. Mol. Struct. (THEOCHEM)* **2003**, *625*, 283–288.
21 J. Ridard, B. Levy, Ph. Millie, *Mol. Phys.* **1978**, *36*, 1025.
22 W. Kutzelnigg, U. Fleischer, M. Schindler, in *NMR Basic Principles and Progress*, Springer-Verlag, Berlin **1990**, Vol. 23, pp. 165–262.
23 T. Gregor, F. Mauri, R. Car, *J. Chem. Phys.* **1999**, *111*, 1815–1822.
24 C. J. Pickard, F. Mauri, *Phys. Rev. B* **2001**, *63*, 245101.
25 P. E. Blöchl, *Phys. Rev. B* **1994**, *50*, 17953–17979.
26 R. Ditchfield, *J. Chem. Phys.* **1972**, *56*, 5688.
27 J. R. Cheeseman, G. W. Trucks, T. A. Keith et al., *J. Chem. Phys.* **1996**, *104*, 5497.
28 D. Woon, T. H. Dunning, Jr., *J. Chem. Phys.* **1995**, *103*, 4572. The cc-pCVQZ basis sets for third-row elements were obtained by personal communication from T. H. Dunning, Jr., K. Peterson.
29 M. Profeta, F. Mauri, J. Pickard, *J. Am. Chem. Soc.* **2003**, *125*, 541–548.
30 T. A. Keith, F. W. Bader, *Chem. Phys. Lett.* **1993**, *210*, 223.
31 B. Meyer, K. Hummler, C. Elsässer et al., *J. Phys. Condensed Matter* **1995**, *7*, 9201–9217.
32 J. R. Trail, D. M. Bird, *Phys. Rev. B* **1999**, *60*, 7863–7874.
33 H. M. Petrilli, P. E. Blöchl, P. Blaha et al., *Phys. Rev. B.* **1998**, *57*, 14690–14697.
34 J. Yates, C. J. Pickard, M. C. Payne et al., *J. Chem. Phys.* **2003**, *118*, 5746–5753.
35 R. Bouten, E. J. Baerends, E. van Lenthe et al., *J. Phys. Chem. A* **2000**, *104*, 5600–5611.
36 F. Mauri, N. Vast, J. Pickard, *Phys. Rev. Lett.* **2001**, *87*, 085506.
37 L. M. Bull, B. Bussemer, T. Anupold, J. Sauer et al., *J. Am. Chem. Soc.* **2000**, *124*, 4948–4958.
38 C. J. Pickard and F. Mauri, *Phys. Rev. Lett.* **2002**, *88*, 086403.
39 D. Vanderbilt, *Phys. Rev. B* **1990**, *41*, 7892–7895.
40 R. J. Kirkpatrick, T. Aselage, B. L. Phillips et al., *Boron Rich Solids, Conf. Proc.* **1991**, *231*, 261.
41 T. M. Duncun, *J. Am. Chem. Soc.* **1984**, *106*, 2270.
42 T. Harazono, Y. Hiroyama, Tokuko Watanabe, *Bull. Chem. Soc. Jpn.* **1996**, *69*, 2419.

17
Calculation of Nuclear Quadrupole Coupling Constants

Peter Schwerdtfeger, Markus Pernpointner, and Witold Nazarewicz

17.1
Introduction

The interpretation of quadrupole-split or quadrupole-relaxed NMR spectra will include the coupling of the nuclear spin with the electric field gradient caused by the quadrupolar deformation of the nucleus [1–4]. About three quarters of the magnetically active nuclei ($I > 0$) have a nonzero (spectroscopic) quadrupole moment (NQM); these are the nuclei with $I > 1/2$. The phenomenon of nuclear deformation has a long and interesting history. As early as 1924 it was suggested by Pauli [5] that the hyperfine structure of atomic and molecular energy levels resulted from the electromagnetic interaction with nonspherical atomic nuclei. Ten years later, nuclear quadrupole coupling (NQC) was observed by Schüler and Schmidt for the electronic spectrum of ^{151}Eu and ^{153}Eu [6]. In 1936, Casimir developed theoretical foundations of the electron–nucleus coupling due to the nonspherical distribution of nuclear charge [2]. The fact that nuclei need not be spherical was then emphasized by Bohr in his classic paper on the nuclear liquid-drop model [7]. In 1939 Kellog et al. observed nuclear quadrupole coupling for the first time in molecules (D_2 and HD) using molecular beam magnetic resonance [8, 9]. NQC in nuclear quadrupole resonance (NQR) spectroscopy was first observed by Dehmelt and Krüger in 1950 [10], and in the same year in NMR spectroscopy by Pound [11]. Pound also published a thorough theoretical analysis of the nuclear quadrupole coupling he observed in solid-state NMR. Later in 1953 Bloembergen and Rowland [12, 13] showed that the intensity of the nuclear magnetic resonance signal in copper decreased rapidly when a small amount of solute was introduced, which was correctly interpreted in 1960 by Kohn and Vosko [14]. Already in 1961 a number of NQMs were derived by Das and Pomerantz using NMR spectroscopy together with calculations for the electric field gradients (EFG) of Be, Sc, Re, La, Mg, Co, Zn, and Cd [15]. An early review was given by Cohen and Reif [16]. The precise determination of nuclear quadrupole moments, and electric field gradients in atoms, molecules and the solid state, is still a very active area in quantum chemistry and physics, and will be reviewed in this chapter.

Calculation of NMR and EPR Parameters. Theory and Applications.
Edited by Martin Kaupp, Michael Bühl, Vladimir G. Malkin
Copyright © 2004 WILEY-VCH Verlag GmbH & Co. KGaA, Weinheim
ISBN: 3-527-30779-6

We briefly repeat some of the more fundamental aspects of nuclear quadrupole coupling in NMR spectroscopy which will be helpful for further discussions. The interaction energy of a nuclear charge distribution ρ_c with a potential V is

$$E = \int \rho_C(\vec{r}) V(\vec{r})\, \mathrm{d}\vec{r} \tag{17.1}$$

which, after a Taylor expansion of the potential $V(\vec{r})$ around the origin gives as the most important term the quadrupole energy[1)]

$$E_2 = \frac{1}{6}\sum_{\alpha,\beta} (V^{\alpha\beta} Q^{\alpha\beta} + V^{\alpha\beta}\delta_{\alpha\beta} \int r^2 \rho_c(\vec{r})\, \mathrm{d}\vec{r}) \tag{17.2}$$

with

$$Q^{\alpha\beta} = \int (3x_\alpha x_\beta - \delta_{\alpha\beta} r^2)\, \rho_c(\vec{r})\mathrm{d}\vec{r} \tag{17.3}$$

Here $Q^{\alpha\beta}$ is the expectation value over the NQM (second rank) tensor operator, and $V^{\alpha\beta}$ is the EFG tensor. To high accuracy, the Poisson term can be neglected in NMR spectroscopy, and the Laplace equation can be applied instead for the field gradient tensor [17] (for a detailed discussion, see Ref. 18). Equation (17.2) therefore becomes,

$$E_2 = \frac{1}{6}\sum_{\alpha,\beta} V^{\alpha\beta} Q^{\alpha\beta} \tag{17.4}$$

and we have $\mathrm{tr}(V^{\alpha\beta}) = 0$. With the use of the Wigner–Eckart theorem, the quadrupolar Hamiltonian (now for N nuclei) can be written in the following form ($I > 1/2$) [19]

$$\hat{H}_{NQC} = \sum_i \frac{eQ_i}{6I_i(2I_i-1)} \sum_{\alpha,\beta}^{3} \hat{V}_i^{\alpha\beta} \left\{ \frac{3}{2}\left[\hat{I}_i^\alpha, \hat{I}_i^\beta\right]_+ + \delta_{\alpha\beta}\hat{\vec{I}}_i^2 \right\} \tag{17.5}$$

where eQ_i is the spectroscopic nuclear quadrupole moment, I_i the nuclear spin quantum number and $\hat{I}_i^\alpha$ the nuclear spin operator, and $\hat{V}_i^{\alpha\beta}$ is the electric field gradient tensor of nucleus i where $\alpha,\beta = x, y,$ or z.

Strong magnetic fields applied in NMR spectroscopy lead to large Zeeman splittings of the nuclear levels. As a rule, the Larmor frequency is higher than the quadrupolar coupling frequency, and the quadrupolar interaction can be treated perturbatively in first and second order [20]. This is in contrast to nuclear quadrupole resonance (NQR) spectroscopy where the quadrupolar-split nuclear energy levels are used for the resonance and weak magnetic fields are applied. Suppose that the principal axis system for the electric field gradient is (x,y,z), that is $V^{\alpha\beta} = 0$ for $\alpha \neq \beta$ and the $(V^{\alpha\beta})$ tensor is diagonal. If we apply a strong magnetic field H_0 along a new z'-axis with the quadrupolar nucleus placed at the origin, the Hamiltonian for an

1) Because of parity symmetry the odd electric contributions vanish and the monopole term leads only to a constant shift in the spectrum.

axially symmetric field (V^{xx}=V^{yy} ⇒ asymmetry parameter $\eta = (V^{xx} - V^{yy})/V^{zz}$ with $|V^{xx}| \le |V^{yy}| \le |V^{zz}|$) becomes

$$\hat{H} = -\hbar\gamma_n H_0 \hat{I}_{z'} + \frac{e^2 qQ}{4I(2I-1)}\left(3\hat{I}_{z'}^2 - \hat{\vec{I}}^2\right) \tag{17.6}$$

and $V^{zz} = +q$, $V^{xx} = V^{yy} = -1/2q$. q is simply called the electric field gradient (EFG) (note: another sign convention is often used originating from the field being defined as $\vec{F} = -\text{grad}\ V$. The matrix elements are evaluated straightforwardly and we obtain for the energy levels

$$E_m = -\hbar m\gamma_n H_0 + \frac{e^2 qQ}{8I(2I-1)}(3\cos^2\theta - 1)(3m^2 - I(I+1)) \tag{17.7}$$

The nuclear quadrupole coupling constant ν_{NQCC} for a specific nucleus is usually given in MHz, $\nu_{NQCC}[\text{MHz}] = 234.9647Q[\text{barn}]q[\text{a.u.}]$. Equation (17.7) shows that levels with equal $|m|$ values (e.g. $m = \pm\frac{1}{2}$ and $m = \pm\frac{2}{3}$ for $I = \frac{3}{2}$) are shifted by the same amount. Hence for $I = \frac{3}{2}$ the absorption peak splits into a symmetric triplet with the central absorption line unshifted (this, however, changes in higher-order perturbation theory) [3]. The line splitting also depends on the asymmetry parameter if $\eta \neq 0$ ($0 \le \eta \le 1$; see Ref. 21 for more details). From this splitting the nuclear quadrupole coupling constant (and, in principle, the asymmetry parameter η) can be derived.

A nuclear quadrupole moment leads to rapid spin–lattice and spin–spin relaxation giving rather broad lines. Thus, for nuclei with large nuclear quadrupole moments, high resolution work often becomes difficult if not impossible. It is therefore of no surprise that the influence of higher moments like the nuclear hexadecapole moment (NHDM) has not yet been observed [18]; even so there have been a number of claims in the past including methods like NQR [22, 23]. In the latest NMR experiment, Liao and Harbison reported no evidence for nuclear hexadecapole coupling in the ^{127}I nucleus of CdI [24]. For heavier nuclei with larger deformations, such effects are estimated to be in the mHz region of the spectrum. It remains therefore questionable whether such tiny effects can be detected by NMR spectroscopy. We mention, however, that third-order quadrupolar effects have been observed very recently in an NMR spectrum of andalusite at 11.7 T using two-dimensional magic-angle spinning, which gave 2.5 kHz for an aluminum site with a quadrupolar coupling frequency of 2.3 MHz [25].

Another small effect is the dependence of the NQCC on the applied magnetic field. The presence of an external magnetic field $\vec{B}$ will alter the wavefunction and therefore change the EFG at each atomic center. A Taylor expansion with respect to the magnetic field yields the first- and second-order response properties described by third- ($V^{\alpha\beta\gamma} = \partial^2 V^{\alpha\beta}/\partial B_\gamma$) and fourth- ($V^{\alpha\beta\gamma\delta} = \partial^2 V^{\alpha\beta}/\partial B_\gamma \partial B_\delta$) rank tensors [26]. The quadratic term has been observed recently by Meersmann and Haake [27] for the ^{131}Xe (I = 3/2) NMR spectrum in isotropic media ($V^{\alpha\beta}$ = 0 at 0 T) in strong magnetic fields between 7 and 17 T, and theoretically verified and analyzed by Vaara and Pyykkö [28]. The quadratic splitting for ^{131}Xe is about 15 mHz T^{-2}, while the higher quartic term is very small and can be neglected [28].

17.2 Nuclear Quadrupole Moments

The knowledge of accurate NQMs for specific isotopes is important for the interpretation of high-precision NMR spectra. Currently the most accurate way to obtain the nuclear quadrupole moment Q is indirectly by high-resolution spectroscopy to derive the nuclear quadrupole coupling constant e^2qQ in Eq. (17.6) together with very precise calculations for the electric field gradient tensor $V^{\alpha\beta}$. This can be achieved from either atomic experiments (electronic or muonic transitions in atoms); from rotational spectroscopy of linear molecules or from magnetic resonance or Mössbauer spectroscopy. Nuclear quadrupole moments can be obtained experimentally by a variety of methods, including electron scattering, inelastic hadron scattering, Coulomb excitation, hyperfine effects in muonic atoms, and hyperfine techniques [29]. An updated account of the most recent nuclear quadrupole moments has been given recently by Pyykkö [30]. NQMs can also be obtained from nuclear structure calculations, which we briefly outline in the following.

The electric NQM is a measure of the extent to which the nuclear charge distribution deviates from spherical symmetry. The spectroscopic moment Q appearing in Eq. (17.6) is defined by [31,32]

$$Q = \langle I, M = I | \hat{Q} | I, M = I \rangle \tag{17.8}$$

where the operator $\hat{Q}$ is written as

$$\hat{Q} = \sqrt{\frac{16\pi}{5}} \sum_{i=1}^{A} e_i r_i^2 Y_{20}(\Omega_i) \tag{17.9}$$

In Eq. (17.9), e_i denotes the electric charge of the ith nucleon. For free nucleons, $e_p = e$ and $e_n = 0$. The moment defined in Eq. (17.8) is the laboratory-system quadrupole moment. It should not be confused with the *intrinsic* quadrupole moment (or the quadrupole moment in the body-fixed system defined in terms of the principal axes of the quadrupole tensor). If the nucleus is well deformed (i.e., the intrinsic system can be defined), the spectroscopic moment can be expressed in terms of the intrinsic moments by the standard transformation to the body-fixed frame [32]. For instance, the relation between Q and the (static) intrinsic quadrupole moment of the axial nucleus, Q_0, is given by

$$Q = \frac{3\langle K^2 \rangle - I(I+1)}{(I+1)(2I+3)} Q_0 \tag{17.10}$$

where K is the projection of the nuclear spin on the intrinsic nuclear axis. If Coriolis coupling is present (or the nuclear shape is triaxial), the quantum number K is strongly mixed, and proper care should be taken when calculating $\langle K^2 \rangle$ [18,33]. In many cases, however, for well-deformed axial nuclei, the quantum number K is very nearly conserved. For $K = I$ (which usually applies to the ground state of a deformed odd–A or an odd–odd nucleus), one gets,

$$Q = \frac{I(2I-1)}{(I+1)(2I+3)} Q_0 \tag{17.11}$$

One has to keep in mind, however, that for weakly deformed or transitional nuclei, the concept of a body-fixed system (and that of the intrinsic quadrupole moment) cannot be applied, and the connection between Q and the intrinsic nuclear shape cannot be made.

The intrinsic quadrupole moment Q_0 is usually calculated directly from the charge density ρ_c,

$$Q = \sqrt{\frac{16\pi}{5}} \int \rho_c(\vec{r}) r^2 Y_{20}(\Omega) \mathrm{d}\vec{r} \tag{17.12}$$

Often, quadrupole moments are parametrized in terms of deformation parameters. If the nuclear surface is defined through the multipole expansion,

$$R(\Omega;\bar{\alpha}) = C(\bar{\alpha}) r_o A^{1/3} \left[1 + \sum_{\lambda=1}^{\lambda_{\max}} \sum_{\mu=-\lambda}^{\lambda} \alpha_{\lambda\mu} Y_{\lambda\mu}(\Omega) \right] \tag{17.13}$$

where $(\bar{\alpha})$ denotes the set of deformation parameters $\alpha_{\lambda\mu}$ and $C(\bar{\alpha})$ is the volume-conserving factor. For the shapes axially symmetric with respect to the z-axis, all deformation parameters with $\mu \neq 0$ disappear. The remaining deformation parameters $\alpha_{\lambda 0}$ are usually called β_λ, i.e. $\beta_\lambda = \alpha_{\lambda 0}$. For small deformations, one can neglect second-order contributions and Q_0 can be written as

$$Q_0 = \frac{3Ze(r_o A^{1/3})^2}{\sqrt{5\pi}} \beta_2 \tag{17.14}$$

There are other definitions of nuclear deformations used in nuclear calculations. For a comprehensive review of various parametrizations of nuclear shape see Ref. 29.

Theoretical methods to calculate the NQM can be divided into two groups. In the models of the first group (e.g., ab initio approaches and the nuclear shell model) the nuclear many-body wavefunction is explicitly defined in the laboratory frame. Thus, no intrinsic frame is introduced and it is not necessary to specify any nuclear shape or deformation. The second group consists of mean-field models utilizing the concept of intrinsic frame in which the notion of shape deformation appears naturally.

17.2.1
Ab Initio Nuclear Structure Calculations

Ab initio quantum Monte Carlo calculations can be carried out for relatively light nuclei with $A \leq 16$. They involve the use of bare, non-relativistic two- and three-nucleon interactions in the Schrödinger equation. Recent calculations have shown that nuclear structure indeed develops from the underlying nucleon–nucleon and three-nucleon forces, and that the properties of light nuclei are reproduced satisfactorily [34, 35]. Ab initio calculations for few-nucleon systems have also been carried out within the framework of the no-core shell model. Here, an effective Hamiltonian is derived from the bare force between nucleons, and all protons and neutrons are

active. In addition to two-body effective interactions, three- or higher-body effective interactions as well as real three-body interactions can be utilized [36–38].

17.2.2 Laboratory-System Models

The nuclear shell model involves the use of an effective Hamiltonian within a restricted model space. This effective interaction can, in principle, be derived from the bare interaction. Shell-model techniques can then be applied to this effective Hamiltonian to calculate the structure of the nucleus of interest. The dimensions of the shell-model matrices grow very fast with the number of active orbitals. Therefore, in the heavy region, it is only for nuclei with a few particles outside closed shells that it has been possible to perform large-scale shell-model calculations. Recently, with major computational advances, both in the traditional shell-model methodology and in the use of Monte Carlo methods, the nuclear shell-model approach has been successfully applied to the description of moderately heavy nuclei ($A \sim 60$). Since the number of active nucleons is limited (contrary to the no-core shell model mentioned above), the coupling to other shells is taken care of by effective interactions and charges. The effective charges take into account polarization effects due to the nucleons disregarded in actual calculations. Consequently, in the shell-model framework, the values of e_p and e_n appearing in Eq. (17.9) deviate from the bare charges. The recent shell-model calculations of quadrupole moments can be found in, e.g., Refs. [39–42] (diagonalization shell-model), [43–45] (Monte-Carlo shell-model), and [46, 47] (variational shell-model).

17.2.3 Mean-Field Models

The mean-field models for nuclear structure have been reviewed in Refs. [48, 49]. In the self-consistent Hartree–Fock+BCS (HF) and Hartree–Fock–Bogolyubov (HFB) methods, nucleons are described as nonrelativistic particles moving independently in a common average field. The dependence of energy on various nucleonic densities and currents is defined through the energy functional to which the variational principle is applied. The self-consistent mean fields depend on the effective forces acting between nucleons. The commonly used forces used in the HFB calculations are zero-range Skyrme and finite-range Gogny forces. In the relativistic mean-field (RMF) models, nucleons are described as independent Dirac particles moving in local isoscalar–scalar, isoscalar–vector, and isovector–vector mean fields usually associated with σ, ω, and ρ mesons, respectively. These couple to the corresponding local densities of the nucleons which are bilinear covariants of the Dirac spinors.

There is a world of different parametrizations for HFB as well as RMF. They agree well for stable nuclei but can yield differing predictions in extrapolations. For a particular choice of the effective force and proton and neutron numbers, the resulting self-consistent mean field may be spherical or deformed [50]. The intrinsic quadrupole moment is directly obtained from the charge density at the self-consis-

tent minimum. The systematic self-consistent calculations of quadrupole moments and equilibrium deformations across the periodic table can be found in Refs. [51–54] (HF + BCS), [55–57](HFB), and [58,59] (RMF). Nuclear deformations can also be calculated in the non-self-consistent macroscopic–microscopic (shell-correction) method [60]. The main assumption of this approach is that the total energy of a nucleus can be composed into the macroscopic energy (usually replaced by the phenomenological liquid-drop or droplet model expression) and the shell-correction term calculated using the deformed independent-particle model (usually approximated through Woods–Saxon, folded-Yukawa, or Nilsson average potentials). The relationship between the macroscopic–microscopic method and the HF approach is given by the so-called Strutinsky energy theorem [61]. There exist many tables of nuclear deformations calculated within this method [29]. Commonly used are the tabulations by Möller and collaborators [62] (using the finite-range droplet macroscopic energy and the folded-Yukawa microscopic model) and the extended Thomas–Fermi+Strutinsky Integral (ETFSI) model [63] (in which the macroscopic energy is given by the fourth-order extended Thomas–Fermi approximation, and the shell correction is obtained from the same Skyrme interaction as in the macroscopic part). Other calculations are limited to particular regions of the chart of the nuclides [64–67].

17.3 Field Gradients from Ab Initio Calculations

The field gradient operator for the electronic Eq. (17.15) and nuclear Eq. (17.16) contribution at the center $\vec{R}_X$

$$V_{el}^{\alpha\beta}\left(\vec{r}_i;\vec{R}_X\right) = -\frac{3\left(\vec{r}_i-\vec{R}_X\right)_\alpha\left(\vec{r}_i-\vec{R}_X\right)_\beta - \left|\vec{r}_i-\vec{R}_X\right|^2\delta_{\alpha\beta}}{\left|\vec{r}_i-\vec{R}_X\right|^5} \tag{17.15}$$

and

$$V_{nuc}^{\alpha\beta}\left(\vec{R}_X\right) = \sum_{Y\neq X} Z_Y \frac{3\left(\vec{R}_Y-\vec{R}_X\right)_\alpha\left(\vec{R}_Y-\vec{R}_X\right)_\beta - \left|\vec{R}_Y-\vec{R}_X\right|^2\delta_{\alpha\beta}}{\left|\vec{R}_Y-\vec{R}_X\right|^5} \tag{17.16}$$

behaves inversely proportional to the third power of the distance from the point of reference and is therefore considered a core-property (Note again the sign definition: a positive unit charge on the z-axis at distance R will create a field gradient $q = +2/R^3$). The letters α, β denote the Cartesian components x,y,z and X,Y,Z of the electronic or nuclear coordinates. This operator clearly emphasizes the inner regions of the electronic wavefunction, where, in the case of heavier nuclei, the electrons reach high velocities necessitating a relativistic treatment in order to obtain accurate EFG results [68, 69]. The nuclear contribution Eq. (17.16) exhibiting the same functional behavior is merely an additive constant for a given molecular geometry or lattice structure. In atoms, the (traceless) EFG tensor is non-zero only in the presence of

open valence shells with $l > 0$ ($j > 1/2$) destroying spherical symmetry. Molecular EFGs arise due to the nonspherical electronic density distribution, except for systems possessing cubic symmetry (octahedral or tetrahedral site). The measurement of the NQCC is therefore a very sensitive and efficient method for detecting symmetry breaking effects, e.g. Jahn–Teller or other distortions, disordered materials, impurities, or defects in the solid state [70–75]. Note however, that in cubic or spherical open-shell systems, spin–orbit effects can still create an EFG along the angular-momentum axis [76–78].

In the nonrelativistic (NR) case (Hartree–Fock or Kohn–Sham DFT) the matrix element of $\hat{V}_{el}^{\alpha\beta}$ is directly obtained from the expectation value

$$V^{\alpha\beta}\left(\vec{R}_X\right) = \sum_i \left\langle \varphi_i(\vec{r}) \middle| \hat{V}_{el}^{\alpha\beta}\left(\vec{r};\vec{R}_X\right) \middle| \varphi_i(\vec{r}) \right\rangle + V_{nuc}^{\alpha\beta}\left(\vec{R}_X\right) \tag{17.17}$$

with $\varphi_i(\vec{r}_i)$ being the molecular orbitals. At the correlated level, the construction of the one-particle density matrix is required [79–81]. Accurate nonrelativistic correlated EFG calculations for molecules containing a few light atoms are now done routinely [82]. Due to the limited availability of analytic gradients for relativistic correlated methods, Sadlej and Kellö developed a finite field method using $\lambda V_{el}^{\alpha\beta}(\vec{R}_X)$ as a perturbation in the SCF procedure [83]. This is equivalent to calculating the response of the molecular orbitals via the coupled-perturbed Dirac–Hartree–Fock (DHF) equations starting from an unperturbed set of MOs. This set of modified orbitals then enters the four-index transformation yielding the MO-integrals necessary for the correlated calculations. Vibrational corrections have to be considered as well [84].

The most rigorous way including relativity from the beginning is the many-electron Dirac–Coulomb–Hartree–Fock (DC-HF) approach. In its 'no pair' form [85], where a projection on the positive-energy spinor space is carried out, this form of the Hamiltonian has proven to perform very well and is nowadays routinely applied in four-component calculations including electron correlation treatment. QED corrections can be added as well, which in first order leads to the Dirac–Coulomb–Breit operator being available in numerical atomic structure codes [86] and partially (as the Gaunt term) also in molecular DHF codes [87]. So far, not many genuine four-component EFG results are available, which is mainly due to the large computational effort these calculations require and to the availability of accurate one-component approximation schemes. However, the inclusion of property operators, in combination with relativistic approximation schemes, bears some complications known as the picture-change error [83, 88, 89]. If the EFG results are not governed by large spin–orbit coupling effects, a variationally stable scalar-relativistic method such as the Douglas–Kroll (DK) approximation [90, 91] can be applied. In general, the direct application of Eq. (17.17) in one- or two-component relativistic schemes neglects the unitary transformation of the EFG operator from the original Dirac to the Schrödinger picture. Such picture change errors can be very large for core properties like the EFG [89, 92]. In the case of the EFG operator, this transformation becomes quite complicated and was just recently performed by Malkin et al. [93]. The error is tolerable for light systems but EFG results become totally erroneous for molecules con-

taining heavy atoms. An alternative approach has therefore been devised based on modeling the quadrupole moment perturbation via point charges (the PCNQM model), leading to accurate DK EFG values [94, 95].

Four-component MP2 and coupled cluster (CCSD(T)) calculations of the EFG at the halogen centers in the corresponding hydrogen halides were performed recently by Visscher et al. [96]. We compare their results with nonrelativistic and scalar-relativistic (DK) EFGs obtained by Kellö and Sadlej [97] at the ab initio level and to DFT results obtained by Malkin et al. [93] (Tab. 17.1). The importance of scalar relativistic effects, especially for the heavier elements, is evident. The picture change error is rather large (1 a.u. for the iodine EFG; compare DK-HF using Eq. (17.17) with picture change-free results listed in Table 17.1). Spin–orbit effects are difficult to estimate since the scalar relativistic and four-component relativistic calculations use different basis sets. Nevertheless, the data listed by Visscher et al. indicate that they further diminish the EFG on the halide center [96].

Table 17.1 Four-component CCSD(T) EFGs q at the halogen center for the HX molecules [96] compared to the scalar relativistic calculations by Kellö and Sadlej [97] and to DFT results obtained by Malkin et al. [93].

	HCl	HBr	HI
NR-HF	3.464	6.998	9.726
DK-HF/Eq. (17.17)	3.540	7.806	12.657
DK-HF	3.511	7.520	11.683
DC-HF	3.666	7.625	11.648
NR-CCSD(T)	3.410	6.720	9.104
DK-CCSD(T)	3.481	7.489	11.819
DC-CCSD(T)	3.377	7.035	10.751
NR-DFT-PW86	3.506	7.000	9.512
DK-DFT-PW86	3.548	7.442	11.108

The influence of the Gaunt term of the Breit interaction was investigated for the halogen EFG in hydrogen halides, and the corresponding changes amounted to (in a.u.) -1×10^{-3} for F, -7×10^{-3} for Cl, and -22×10^{-3} for Br [98]. In the case of molecules containing heavy atoms such as TlH, these contributions influenced the EFG even more where inclusion of the Gaunt operator led to an EFG increase of +0.125 a. u. [99].

External fields and field gradients influence the field gradient at the nucleus under consideration and therefore the resulting nuclear quadrupole coupling. From an expansion of the EFG in terms of such perturbations, the Sternheimer shielding/antishielding (depending on the sign) [100–103] and the EFG polarizabilities can be obtained [104, 105]. Detailed studies of intermolecular influences on the EFG can be found in Ref. [106] based on a derivative Hartree–Fock calculation, and multiconfiguration SCF results of generalized shielding factors also became available in the meantime [107]. A more recent study by Coriani et al. is concerned with electric

field effects on molecular EFGs at the coupled-cluster level [108]. We note that such EFG responses have not yet been measured.

17.4 Field Gradients from Density Functional Calculations

In the early days of computational chemistry and physics, density functional theory (DFT) was the most popular method for the calculation of EFGs in atoms, molecules, or the solid state [109]. Today DFT is routinely used for EFG calculations in molecules or the solid state [110–117]. It is clear that DFT is specially suited for larger molecules, such as biological systems, because of the low computational cost compared to wavefunction-based procedures [118, 119]. Since the EFG is a typical core property there was no reason to assume that DFT would not perform well. Indeed, a comparison between B3LYP and MP4 for the deuterium NQCC for 25 molecules shows only minute differences between both methods [110], and in general for main group elements, DFT seems to perform extremely well [120, 121], except perhaps for electric field responses to EFGs where B3LYP yields results less reliable than Hartree–Fock [122]. Table 17.1 shows DFT results obtained by Malkin et al. [93] in good agreement with the relativistic coupled-cluster results.

The situation changes dramatically for a number of transition-metal-containing compounds. For example, current DFT is not able to correctly describe the electron density distribution in CuCl [123]. Here the polarization of the Cu(3d) core by the electronegative chlorine atom has to be correctly described to obtain accurate electric properties such as the dipole moment or the electric field gradient on either center. For example, the CuCl dipole moment varies considerably between the different DFT approximations, i.e., 4.14 D for HFS, 4.38 D for LDA, 4.30 D for BLYP, and 4.87 D for B3LYP (the DK-CCSD(T) value is 5.32 D). Slight variations in the charge distributions obviously affect the EFG, i.e., q(Cu) is +0.67 a.u. for HFS, +0.50 a.u for LDA, +0.54 a.u. for BLYP, and +0.15 a.u. for B3LYP [123] (–0.34 a.u. (!) at the DK-CCSD(T) level; the experimental value is –0.31(2) a.u. [124]). The chlorine EFG is similarly affected, although to a lesser extent. These results have been confirmed recently by Baerends and co-workers, who also obtained large errors in DFT EFG calculations for other copper halides and the halides of silver using the zeroth-order regular approximation (ZORA) to the Dirac equation [125]. The situation does not differ much for iron compounds. For q(Fe) in ferrocene, DFT calculations give 1.36 a.u. for both HFS and LDA, 1.43 a.u. for BLYP, and 1.85 a.u. for B3LYP (1.50 a.u. at the CCSD(T) level) [39, 126]. Problems therefore arise for the accurate determination of the ^{57}Fe NQM [39, 127]. This is not to say that DFT does not perform well for all transition metal compounds, as good agreement between theory and experiment has been achieved in calculations using the Vienna solid-state DFT code [128–133]. The accurate determination of EFGs from DFT for transition-element-containing compounds remains nevertheless an open question which has to be addressed in the near future.

Acknowledgment

One of the authors (MP) gratefully acknowledges financial support from the Deutsche Forschungsgemeinschaft. PS thanks Tim Bastow (CSIRO, Clayton Soth, Australia) and Pekka Pyykkö (Helsinki) for interesting discussions. This work was supported in part by the U.S. Department of Energy under Contract Nos. DE-FG02-96ER40963 (University of Tennessee) and DE-AC05-00OR22725 with UT-Battelle, LLC (Oak Ridge National Laboratory).

References

1 J. A. S. Smith, *Chem. Soc. Rev.* **1986**, *15*, 225.
2 H. B. G. Casimir, *On the Interaction Between Atomic Nuclei and Electrons*, Prize Essay, Teyler's Tweede, Harlem [II:2], **1936**.
3 A. J. Varga, in *Encyclopedia of Nuclear Magnetic Resonance*, Vol.1–9, Wiley, New York **2002**, p. 3869.
4 A. Abragam, *Principles of Nuclear Magnetism*, Clarendon Press, Oxford **1961**.
5 W. Pauli, *Naturwiss.* **1924**, *12*, 741.
6 H. Schüler, T. Schmidt, *Z. Phys.* **1935**, *94*, 457.
7 N. Bohr, *Nature* **1936**, *137*, 344.
8 J. M. B. Kellog, I. I. Rabi, N. F. Ramsey et al., *Phys. Rev.* **1936**, *55*, 318.
9 J. M. B. Kellog, I. I. Rabi, N. F. Ramsey et al., *Phys. Rev.* **1940**, *57*, 677.
10 H.-G. Dehmelt, H. Krüger, *Naturwiss.* **1950**, *37*, 111.
11 R. V. Pound, *Phys. Rev.* **1950**, *79*, 685.
12 N. Bloembergen, T. J. Rowland, *Acta Metall.* **1953**, *1*, 731.
13 T. J. Rowland, *Phys. Rev.* **1960**, *119*, 900.
14 W. Kohn, S. H. Vosko, *Phys. Rev.* **1960**, *119*, 912.
15 T. P. Das, M. Pomerantz, *Phys. Rev.* **1961**, *123*, 2070.
16 M. H. Cohen, F. Reif, *Solid State Physics* **1957**, *5*, 321.
17 C. P. Slichter, *Principles of Magnetic Resonance*, ed. P. Fulde, Springer Series in Solid-State Sciences, Vol. 1, Springer, New York **1990**.
18 J. Thyssen, P. Schwerdtfeger, M. Bender et al., *Phys. Rev. A* **2001**, *63*, 022505.
19 P. P. Man, in *Encyclopedia of Nuclear Magnetic Resonance*, Vol.1–9, Wiley, New York **2002**, p. 3838.
20 Z. Gan, *J. Chem. Phys.* **2001**, *114*, 10845.
21 E. A. C. Lucken, *Nuclear Quadrupole Coupling Constants*, Academic Press, New York **1969**.
22 H. Goutou, *J. Magn. Reson.* **1983**, *54*, 36.
23 G. K. Semin, A. M. Raevsky, S. I. Gushin, *Chem. Phys. Lett.* **1985**, *121*, 214.
24 M.-Y. Liao, G. S. Harbison, *J. Chem. Phys.* **1994**, *100*, 1895.
25 Z. Gan, P. Srinivasan, J. R. Quine et al., *Chem. Phys. Lett.* **2003**, *367*, 163.
26 B. Filsinger, P. Gutsche, U. Haeberlen et al., *J. Magn. Reson.* **1997**, *125*, 280-290.
27 T. Meersmann, M. Hauke, *Phys. Rev. Lett.* **1998**, *81*, 1211.
28 J. Vaara, P. Pyykkö, *Phys. Rev. Lett.* **2001**, *86*, 3268.
29 W. Nazarewicz, I. Ragnarsson, in *Handbook of Nuclear Properties*, eds. D. N. Poenaru, W. Greiner, Clarendon Press, Oxford **1996**, p. 80.
30 P. Pyykkö, *Mol. Phys.* **2001**, *99*, 1617.
31 A. Bohr, B.R. Mottelson, *Nuclear Structure*, Vol. I, Benjamin, New York **1969**.
32 A. Bohr, B.R. Mottelson, *Nuclear Structure*, Vol.II , Benjamin, New York **1975**.
33 I. Ragnarsson, P.B. Semmes, *Hyperfine Interact.* **1988**, *43*, 425.
34 R. B. Wiringa, S. C. Pieper, J. Carlson et al., *Phys. Rev. C* **2000**, *62*, 014001.
35 S. C. Pieper, V. R. Pandharipande, R. B. Wiringa et al., *Phys. Rev. C* **2001**, *64*, 014001.
36 P. Navratil, J.P. Vary, B.R.Barrett, *Phys. Rev. Lett.* **2000**, *84*, 5728.
37 E. Caurier, P. Navratil, W. E. Ormand et al., *Phys. Rev. C* **2002**, *66*, 024314.
38 B. R. Barrett, P. Navratil, J. P. Vary, *Nucl. Phys. A* **2002**, *704*, 254c.
39 G. Martínez-Pinedo, P. Schwerdtfeger, E. Caurier et al., *Phys. Rev. Lett.* **2001**, *87*, 062701.
40 E. Caurier, F. Nowacki, A. Poves, *Nucl. Phys. A* **2001**, *693*, 374.

41 E. Caurier, F. Nowacki, A. Poves, *Eur. Phys. J. A* **2002**, *15*, 145.
42 E. Caurier, G. Martinez-Pinedo, *Nucl. Phys. A* **2002**, *704*, 60c.
43 N. Shimizu, T. Otsuka, T. Mizusaki et al., *Nucl. Phys. A* **2002**, *704*, 244c.
44 T. Otsuka, Y. Utsuno, R. Fujimoto et al., *Eur. Phys. J. A* **2002**, *15*, 151.
45 M. Honma, B. A. Brown, T. Mizusaki et al., *Nucl. Phys. A* **2002**, *704*, 134c.
46 A. Petrovici, K. W. Schmid, A. Faessler, *Nucl. Phys. A* **2000**, *665*, 333.
47 A. Petrovici, K. W. Schmid, A. Faessler, *Nucl. Phys. A* **2002**, *710*, 246.
48 S. Åberg, H. Flocard, W. Nazarewicz, *Annu. Rev. Nucl. Part. Sci.* **1990**, *40*, 439.
49 M. Bender, P.-H. Heenen, P.-G. Reinhard, *Rev. Mod. Phys.* **2003**, *75*, 121.
50 W. Nazarewicz, *Nucl. Phys. A* **1994**, *574*, 27c.
51 N. Tajima, S. Takahara, N. Onishi, *Nucl. Phys. A* **1996**, *603*, 23.
52 N. Tajima, *Prog. Theor. Phys. (Kyoto), Suppl.* **2001**, *142*, 265; http://serv.apphy.fukui-u.ac.jp/~tajima/isnd/isnd.html
53 F. Tondeur, S. Goriely, J. M. Pearson, *Phys. Rev. C* **2000**, *62*, 024308.
54 S. Goriely, J. M. Pearson, F. Tondeur, *At. Data Nucl. Data Tables* **2001**, *77*, 311. http://www-astro.ulb.ac.be/Html/hfbcs1.html
55 M. Samyn, S. Goriely, P.-H. Heenen et al., *Nucl. Phys. A* **2001**, *700*, 142.
56 S. Goriely, M. Samyn, P. H. Heenen et al., *Phys. Rev. C* **2002**, *66*, 024326; http://www-astro.ulb.ac.be/Html/hfb2.html
57 J. Dobaczewski, W. Nazarewicz, M. V. Stoitsov, *Eur. Phys. J. A* **2002**, *15*, 21.
58 G. A. Lalazissis, S. Raman, P. Ring, *At. Data Nucl. Data Tables* **1999**, *71*, 1.
59 K. Rutz, M. Bender, P.-G. Reinhard et al., *Nucl. Phys. A* **1998**, *634*, 67.
60 M. Brack, J. Damgaard, A. S. Jensen et al., *Rev. Mod. Phys.* **1972**, *44*, 320.
61 V. M. Strutinsky, *Nucl. Phys. A* **1974**, *218*, 169.
62 P. Möller, J. R. Nix, W. D. Myers et al., *At. Data Nucl. Data Tables* **1995**, *59*, 185; http://t2.lanl.gov/data/astro/molnix96/molnix.html
63 Y. Aboussir, J. M. Pearson, A. K. Dutta et al., *At. Data Nucl. Data Tables* **1995**, *61*, 127; http://www-astro.ulb.ac.be/Html/etfsi2.html
64 S. Hofmann, W. Nazarewicz, *Nucl. Phys. A* **1994**, *573*, 356.
65 W. Nazarewicz, *Progr. Part. Nucl. Phys.* **1992**, *28*, 307
66 W. Nazarewicz, M. A. Riley, J. D. Garrett, *Nucl. Phys. A* **1990**, *512*, 61.
67 R.R.Chasman, *Z.Phys. A* **1991**, *339*, 111.
68 V. Kellö, A. J. Sadlej, *Chem. Phys. Lett.* **1990**, *174*, 641.
69 P. Pyykkö, M. Seth, *Theor. Chem. Acta* **1997**, *96*, 92.
70 G. Seewald, E. Hagn, E. Zech et al., *Phys. Rev. B* **2002**, *66*, 174401.
71 G. Le Caer, R. A. Brand, *J. Phys.: Condens. Matter* **1998**, *10*, 10715.
72 T. P. Das, P. C. Schmidt, *Z. Naturforsch. A* **1986**, *41*, 47.
73 H. Watanabe, *At. Data Nucl. Data Tables* **1990**, *46*, 285.
74 L. A. Errico, G. Fabricius, M. Renteria, *Hyperfine Interact.* **2002**, *136/137*, 749.
75 P. J. Bray, *Encyclopedia of Nuclear Magnetic Resonance*, Vol.1–9, Wiley, New York **2002**, p.3848.
76 K. Raghunathan, J. Andriessen, S. N. Ray et al., *Phys. Rev. Lett.* **1980**, *44*, 312.
77 J. M. Hirsch, G. H. Zimmermann III, D. J. Larson et al., *Phys. Rev. A.* **1977**, *16*, 484.
78 D. van Ormondt, *J. Phys. C* **1978**, *11*, 203.
79 Y. Yamaguchi, Y. Osamura, J. D. Goddard et al., *A New Dimension to Quantum Chemistry. Analytic Derivative Methods in Ab Initio Molecular Electronic Structure Theory*, Oxford University Press, Oxford **1994**.
80 P. Jørgensen, J. Simons, *J. Chem. Phys.* **1983**, *79*, 334.
81 A. Halkier, H. Koch, O. Christiansen et al., *J. Chem. Phys.* **1997**, *107*, 849.
82 J. Vojtík, L. Cespiva, J. Savrda et al., *J. Mol. Spectrosc.* **1990**, *142*, 279.
83 V. Kellö, A. J. Sadlej, *Int. J. Quantum Chem.* **1998**, *68*, 159.
84 M. Seth, M. Pernpointner, G. A. Bowmaker et al., *Mol. Phys.* **1999**, *96*, 1767.
85 J. Sucher, *Phys. Rev. A* **1980**, *22*, 348.
86 K. D. Dyall, I. P. Grant, F. A. Parpia et al., *Comput. Phys. Commun.* **1989**, *55*, 425.
87 L. Visscher, O. Visser, P. J. C. Aerts et al., *Comput. Phys. Commun.* **1994**, *81*,120.
88 E. J. Baerends, W. H. E. Schwarz, P. Schwerdtfeger et al., *J. Phys. B: At. Mol. Phys.* **1990**, *23*, 3225.
89 M. Barysz, A. J. Sadlej, *Theor. Chim. Acta* **1997**, *97*, 260.

90 B. Hess, in *Relativistic Electronic Structure Theory. Part 1. Fundamentals*, ed. P. Schwerdtfeger, Elsevier, Amsterdam **2002**.
91 K. G. Dyall, *Int. J. Quantum Chem.* **2000**, *78*, 412.
92 M. Pernpointner, P. Schwerdtfeger, B. A. Hess, *Int. J. Quantum Chem.* **2000**, *76*, 371.
93 I. Malkin, O. L. Malkina, V. G. Malkin, *Chem. Phys. Lett.* **2002**, *361*, 231.
94 M. Pernpointner, M. Seth, P. Schwerdtfeger, *J. Chem. Phys.* **1998**, *108*, 6722.
95 V. Kellö, A. J. Sadlej, *J. Chem. Phys.* **2000**, *112*, 522.
96 L. Visscher, T. Enevoldsen, T. Saue et al., *J. Chem. Phys.* **1998**, 109, 9677.
97 V. Kellö, A. J. Sadlej, *Mol. Phys.* **1996**, *89*, 127.
98 O. Visser, L. Visscher, P. J. C. Aerts et al., *Theor. Chim. Acta* **1992**, 81, 405.
99 M. Pernpointner, *J. Phys. B: At. Mol. Phys.* **2002**, *35*, 383.
100 R. M. Sternheimer, *Phys. Rev.* **1950**, *80*, 102.
101 R. M. Sternheimer, *Phys. Rev.* **1951**, *84*, 244.
102 R. M. Sternheimer, *Phys. Rev.* **1952**, *86*, 316.
103 R. M. Sternheimer, *Phys. Rev.* **1954**, *95*, 736.
104 S. Engström, H. Wennerström, B. Jönsson et al., *Mol. Phys.* **1977**, *34*, 813.
105 P. W. Fowler, P. Lazzeretti, E. Steiner et al., *Chem. Phys.* **1989**, *133*, 221.
106 J. D. Augspurger, C. E. Dykstra, *J. Chem. Phys.* **1993**, *99*, 1828.
107 A. Rizzo, K. Ruud, T. Helgaker et al., *J. Chem. Phys.* **1998**, *109*, 2264.
108 S. Coriana, A. Halkier, P. Jørgensen et al., *J. Chem. Phys.* **2000**, *113*, 1688.
109 N. Bessis, J. Picart, J. P. Desclaux, *Phys. Rev.* **1969**, *187*, 88.
110 W. C. Bailey, *J. Mol. Spectrosc.* **1998**, *190*, 318.
111 W. C. Bailey, *Chem. Phys.* **2000**, *252*, 57.
112 W. C. Bailey, *Chem. Phys. Lett.* **1998**, *292*, 71.
113 M. A. Fedotov, O. L. Malkina, V. G. Malkin, *Chem. Phys. Lett.* **1996**, *258*, 330.
114 W. Tröger, T. Butz, P. Blaha et al., *Hyperfine Interact.* **1993**, *80*, 1109.
115 H. M. Petrilli, P. E. Blöchl, P. Blaha et al., *Phys. Rev. B* **1998**, *57*, 14690.
116 D. Borchers, P. C. Schmidt, A. Weiss, *Z. Naturforsch.A* **1988**, *43*, 643.
117 P. Dufek, P. Blaha, K. Schwarz, *Phys. Rev. Lett.* **1995**, *75*, 3545.
118 R. Ida, G. Wu, *J. Phys. Chem. A* **2002**, *106*, 11234.
119 R. V. Havlin, N. Godbout, R. Salzmann et al., *J. Am. Chem. Soc.* **1998**, *120*, 3144.
120 W. C. Bailey, F. M. Gonzalez, J. Castiglione, *Chem. Phys.* **2000**, *260*, 327.
121 J. N. Latosinska, *Int. J. Quantum Chem.* **2003**, *91*, 284.
122 A. Rizzo, K. Ruud, T. Helgaker et al., *Chem. Phys. Lett.* **2003**, *372*, 377.
123 P. Schwerdtfeger, M. Pernpointner, J. K. Laerdahl, *J. Chem. Phys.* **1999**, *111*, 3357.
124 J. Hoeft, J. J. Lovas, E. Tiemann et al., *Z. Naturforsch. A* **1970**, *25*, 34.
125 E. van Lenthe, E. J. Baerends, *J. Chem. Phys.* **2000**, *112*, 8279.
126 P. Schwerdtfeger, T. Söhnel, M. Pernpointner et al., *J. Chem. Phys.* **2001**, *115*, 5913.
127 F. Hagelberg, T. P. Das, K. C. Mishra, *Phys. Rev. B* **2002**, *65*, 014425.
128 P. Blaha, K. Schwarz, P. H. Dederichs, *Phys. Rev. B* **1988**, 37, 2792.
129 P. Blaha, K. Schwarz, W. Faber et al., *Hyperfine Interact.* **2000**, *126*, 389.
130 T. Soldner, W. Tröger, T. Butz et al., *Z. Naturforsch A* **1998**, *53*, 404.
131 H. M. Petrilli, P. E. Blöchl, P. Blaha et al., *Phys.Rev. B* **1998**, *57*, 14690.
132 N. Ulbrich, W. Tröger, T. Butz et al., *Z. Naturforsch. A* **2000**, *55*, 301.
133 T. J. Bastow, M. I. Burgar, C. Maunders, *Solid State Commun.* **2002**, *122*, 629.

18
Interpretation of NMR Chemical Shifts

Martin Kaupp

18.1
Introduction

To relate the (computed or measured) magnetic shielding tensor for a nucleus in a molecule or solid to the electronic structure of the system in question is by no means a trivial exercise. As is discussed from different viewpoints in several chapters of this book, the chemical shift tensor is a "second-order" or "linear response" property. It reflects the simultaneous perturbation of the wavefunction of the system by the magnetic moment of the nucleus in question, as well as by the external magnetic field. Even the nonrelativistic formalism involves the still relatively straightforward diamagnetic and the more involved paramagnetic contributions to nuclear shielding. In the case of relativistic effects, in particular of spin–orbit coupling, further contributions come into play and complicate matters even more (in a four-component framework, the perturbation formalism looks simpler, but the underlying physics are no less complex).

In view of the wide use of NMR spectroscopy and of the ready availability of NMR chemical shift information in many areas of chemistry, biology and materials science, it is nevertheless mandatory that one attempts to extract all possible relevant information about molecular and electronic structure from nuclear shieldings. Already from the beginnings of NMR history, and certainly after Ramsey published his famous perturbation equations of nuclear shielding [1], the rapidly growing NMR community used chemical shifts as important indicators of molecular and electronic structure (cf. Chapter 2 by Pyykkö). Unfortunately, the absence of reliable quantitative computational methods at the time, combined with the relative complexity of the theoretical expressions, has led to numerous misconceptions. Frequently, handwaving arguments were put forward which emphasized changes in one isolated contribution as the origin of relative chemical shifts, without solid background. Sometimes, decreased nuclear shieldings (that is, larger chemical shifts) were indiscriminately associated with lower atomic charges, i.e. with a removal of (ground-state) electron density from the atom in question. Correlations with charges or electronegativity abound in the literature, in spite of the facts that (i) these may just hold in a narrow range of similar compounds, and (ii) there are crucial examples in which it has been shown that the correlations were in fact completely fortui-

Calculation of NMR and EPR Parameters. Theory and Applications.
Edited by Martin Kaupp, Michael Bühl, Vladimir G. Malkin
Copyright © 2004 WILEY-VCH Verlag GmbH & Co. KGaA, Weinheim
ISBN: 3-527-30779-6

tous. A point in case is the so-called "heavy-atom effects", which in most textbooks and in much of the original literature are explained by inappropriate and often even mutually contradictory models, but which are nowadays agreed to arise predominantly from relativistic spin–orbit contributions (see also Chapter 13 by Vaara, Manninen, and Lantto, and Chapter 14 by Autschbach). While correlations with optical excitation energies are popular, particularly in transition-metal NMR [2], it is well known that the range of these correlations is also limited. They immediately cease to work when (i) several electronic states contribute to a similar extent and chemical modification changes their contributions in different directions, and (ii) when magnetic and electric-dipole symmetry selection rules differ significantly.

The development of more and more sophisticated and reliable quantum chemical methods over the past two decades puts in our hands the necessary tools to compute, with sometimes impressive accuracy, nuclear shielding tensors from first principles, including relativistic effects as well as electron correlation, as is described in detail elsewhere in this book (see Chapter 6 by van Wüllen, Chapter 8 by Gauss and Stanton, Chapter 13 by Vaara, Manninen, and Lantto and Chapter 14 by Autschbach). This should, in principle, allow the extraction of the necessary electronic-structure information from quantitative shielding calculations, provided we have the necessary tools. This does not of course mean that the analysis is less difficult than for more approximate, simpler treatments, on the contrary! However, the additional benefit is to derive qualitative concepts from calculations that are also quantitatively adequate.

In this chapter, we will summarize the ways in which the line from quantitative computation to qualitative insight into chemical shifts may be drawn, and we will illustrate the existing methodology by a few suitable examples. The first part is dedicated to the nonrelativistic formalism and thus to cases where relativistic effects are thought not to be dominant, or where at least the main trends can be understood without relativity. The second part will emphasize relativistic effects, in particular spin–orbit induced changes in chemical shifts, which have recently been the center of increased attention by many workers. A more detailed account of the latter topic is provided elsewhere [3], and relativistic shielding calculations have been reviewed several times from different viewpoints during the past five years [4]. One part of the "nonrelativistic" interpretation work has also been summarized [5]. Here, the underlying theoretical and computational formalism will be kept to the absolutely necessary minimum, and the reader is referred to Chapter 6 by van Wüllen, Chapter 13 by Vaara, Manninen, and Lantto, and Chapter 8 by Gauss and Stanton, for more details.

18.2
Nonrelativistic Case

18.2.1
Formalism of MO-by-MO Analyses

Leaving relativistic effects aside for the moment, the well-known second-order Rayleigh–Schrödinger perturbation theory (PT) formalism of the Ramsey equation (Eqs. (18.1)–(18.3)) for nuclear shieldings is the appropriate starting point of our discussion. What we get is the well-known separation into a diamagnetic term, which is expressed as an expectation value with the ground state wavefunction (Eq. (18.2)) and thus may be computed rather straightforwardly, and the paramagnetic shielding term (Eq. (18.3)), which is expressed conventionally in a sum-over-states form that implies an involvement of electronically excited states.

$$\boldsymbol{\sigma} = \boldsymbol{\sigma}^{\mathbf{d}} + \boldsymbol{\sigma}^{\mathbf{p}} \tag{18.1}$$

$$\sigma^{\mathrm{d}}_{\mathrm{N},uv} = \frac{1}{2c^2}\left\langle \Psi_0 \left| \sum_i \frac{(\mathbf{r}_{i\mathrm{O}}\mathbf{r}_{i\mathrm{N}})\delta_{uv} - r_{i\mathrm{O},v} r_{i\mathrm{N},u}}{r^3_{i\mathrm{N}}} \right| \Psi_0 \right\rangle, \tag{18.2}$$

$$\sigma^{\mathrm{p}}_{\mathrm{N},uv} = \frac{1}{2c^2}\sum_{n\neq 0} \frac{\left\langle \Psi_n \left| \sum_i l_{\mathrm{O}i,v} \right| \Psi_0 \right\rangle \cdot \left\langle \Psi_0 \left| \sum_i l_{\mathrm{N}i,u} r^{-3}_{i\mathrm{N}} \right| \Psi_n \right\rangle}{E_0 - {}^1E_n} + \text{complex conjugate} \tag{18.3}$$

Ψ_0 and Ψ_n denote the singlet ground and nth excited-state wavefunctions, respectively, E_0 and ${}^1E_n$ are the corresponding total energies, $r_{i\mathrm{O}}$ and $r_{i\mathrm{N}}$ the distance of electron i from the origin of the external magnetic vector potential and from the nucleus N, respectively. The angular momentum operator $\boldsymbol{l}_{\mathbf{O}i}$ in the first matrix element in the numerator of Eq. (18.3) represents the interaction of the external field with electron i (orbital Zeeman term, OZ), and $\boldsymbol{l}_{\mathbf{N}i} \cdot r^{-3}_{\mathrm{n}i}$ in the second matrix element corresponds to the interaction of electron i with the nuclear magnetic dipole field (paramagnetic spin–orbit term, PSO).

We keep in mind that this is only one possibility (see below), and that most computational schemes avoid an explicit computation of excited states of the system. Moreover, Eqs. (18.1) – (18.3) refer to a specific common gauge origin. Other choices of gauge origin will change the individual expressions for $\boldsymbol{\sigma}^{\mathbf{d}}$ and $\boldsymbol{\sigma}^{\mathbf{p}}$ (without formally changing the overall shielding). The $\boldsymbol{\sigma}^{\mathbf{d}}$ and $\boldsymbol{\sigma}^{\mathbf{p}}$ terms are thus not individually gauge invariant (cf., e.g. Ref. [5]). This has to be taken into account in any reasonable interpretation of nuclear shieldings. We will refer here to various approaches to the gauge problem, that are discussed in detail (with detailed references) in Chapter 6 by van Wüllen. These are single-gauge origin methods (SGO), "gauge-including atomic orbitals" (GIAO), "individual gauges for localized orbitals" (IGLO), "local-

ized-orbital local origin" (LORG), "continuous-set-of-gauge transformations" (CSGT) or "individual gauges for atoms in molecules" (IGAIM) approaches.

Most practical calculations to date have been carried out at the Hartree–Fock (HF) or Kohn–Sham density-functional (DFT) levels, i.e. with approaches that employ a single Slater determinant (see Chapter 6). This provides a molecular-orbital (MO) framework that is used in most cases to analyze the more difficult $\boldsymbol{\sigma}^{\mathbf{p}}$ term. That is, Eq. (18.3) may be expressed as a double sum over occupied and vacant MOs, Eq. (18.4) ($\boldsymbol{\sigma}^{\mathbf{d}}$ may be expressed as a single sum over occupied MOs):

$$\sigma^{\mathrm{p}}_{\mathrm{N},uv} = \frac{2}{c^2}\sum_{k}^{\mathrm{occ}}\sum_{a}^{\mathrm{vac}} \frac{\left\langle \varphi_k \left| \bar{l}_{\mathbf{O}i,v} \right| \varphi_a \right\rangle \left\langle \varphi_a \left| \bar{l}_{\mathbf{N}i,u} \cdot r_{i\mathrm{N}}^{-3} \right| \varphi_m \right\rangle}{\Delta E_{k\rightarrow a}} + \mathrm{cc} \qquad (18.4)$$

For HF or hybrid-DFT calculations, coupled-perturbed HF or Kohn–Sham (KS) equations have to be analyzed.[1)] A particularly transparent interpretation is found within "pure" DFT treatments, i.e. when the Kohn–Sham potential is multiplicative. This holds for local density (LDA), gradient-corrected (GGA) or meta-GGA functionals, provided that the exchange-correlation functional is not made to depend on the induced current density $\vec{\mathbf{j}}$ (as is the case in almost all applications of these types of functionals to date [6]; see Chapter 6). In this case, the coupling terms vanish, and the energy denominators in Eq. (18.4) simplify further to differences between the energies of occupied and unoccupied KS orbitals, in an "uncoupled DFT" framework (in some treatments, correction terms have been added to the energy denominators for better quantitative accuracy, see e.g. Ref. [7]). In general, any single-determinantal approach allows an analysis of $\boldsymbol{\sigma}^{\mathbf{p}}$ in terms of occupied and vacant MOs.

As a result of this type of MO-by-MO analysis, one may deconstruct both $\boldsymbol{\sigma}^{\mathbf{d}}$ and $\boldsymbol{\sigma}^{\mathbf{p}}$ into contributions from individual occupied MOs, and $\boldsymbol{\sigma}^{\mathbf{p}}$ may be further decomposed into individual terms of Eq. (18.4), i.e. into individual couplings between occupied and vacant MOs. Both OZ and PSO matrix elements in the numerators of Eq. (18.4) involve angular-momentum operators arising from magnetic fields. The PSO term contains an r^{-3} dependence and is thus rather "shortsighted". It is expected to react most sensitively to charge transfer from or to the atom in question (see below). As both operators involve magnetic angular momentum, only couplings that are magnetic-dipole allowed will contribute to $\boldsymbol{\sigma}^{\mathbf{p}}$. The selection rules may be remembered best by a "right-hand mnemonic", in which the thumb and the first two fingers of the right hand specify the directions of the OZ and PSO angular momentum operators, and of the resulting shielding tensor principal component, respectively. Analyses of Eq. (18.4) were already initiated in the early days of NMR theory, originally based on rather approximate treatments, often within an average-energy-denominator approximation (cf. Chapter 9 by Heine and Seifert). Modern HF or DFT shielding calculations are also commonly analyzed within MO-by-MO

1) That is, if we want to express the equation still in a sum-over-states fashion, the energy denominators $\Delta E_{k\rightarrow a}$ and the effective angular momentum operators $\boldsymbol{l}_{\mathbf{O}i}$ and $\boldsymbol{l}_{\mathbf{N}i}$ contain nonlocal exchange contributions.

schemes. The following important points have to be taken into account in such analyses:

1. As pointed out above, $\boldsymbol{\sigma}^{\mathbf{d}}$ and $\boldsymbol{\sigma}^{\mathbf{p}}$ are not individually gauge invariant and will thus have different appearance and magnitude for different types of gauge origin. Also, the individual contributions to $\boldsymbol{\sigma}^{\mathbf{p}}$ in Eq. (18.4) will depend on the gauge origin. This holds for SGO methods (which have the disadvantage of relatively slow basis-set convergence, see Chapter 6) but also for methods with distributed gauges. It has been suggested that methods like the CSGT or IGAIM approaches, that use real-space information to distribute gauges, provide individually gauge invariant $\boldsymbol{\sigma}^{\mathbf{d}}$ and $\boldsymbol{\sigma}^{\mathbf{p}}$ contributions and may thus be interpreted most rewardingly [8]. However, this contrasts with the overall slower basis-set convergence of these approaches compared to, e.g., the GIAO treatment. On the other hand, approaches like GIAO or IGLO that distribute gauge origins based on a partitioning in the Hilbert space spanned by some atomic or molecular orbital basis set, give rise to additional terms in Eq. (18.4). For example, in the GIAO case, additional contributions arise from a rotation among the occupied MOs, which is difficult to interpret chemically. These terms are sometimes summed in $\boldsymbol{\sigma}^{\mathbf{p}}$ and sometimes given separately. Similarly, within the IGLO framework, an additional $\boldsymbol{\sigma}^{\mathbf{p0}}$ term appears that represents the shift of the gauge to the corresponding localized orbital [5]. Provided these additional terms do not change much from one chemical environment to the next, they will not affect relative chemical shifts and may be ignored. Unfortunately this is not always the case, and then one has to deal with this complication.
2. The shielding tensor is furthermore invariant to any unitary transformation within the space of occupied and/or unoccupied MOs. However, the interpretation obtained from Eq. (18.4) will change with such a transformation. Indeed, very different rationalizations for chemical shifts have been provided within different frameworks. In particular, a very different view is obtained in a delocalized, canonical MO (CMO) framework compared to an interpretation in terms of localized MOs (LMOs). Typically, SGO, GIAO, CSGT or IGAIM results have been analyzed in terms of canonical MOs. On the other hand, in IGLO and LORG studies, the appropriate equivalents of Eq. (18.4) are usually obtained as a sum of couplings between localized occupied and canonical unoccupied MOs. While IGLO calculations have usually employed [5] LMOs obtained from the Boys localization scheme [9], more recently [10] DFT-IGLO results have also been obtained with the Pipek–Mezey (PM) localization [11]. Apart from often providing better convergence of the localization procedure, the PM LMOs are more local than Boys LMOs (see also Section 18.2.3). Most recently, Weinhold and coworkers [12] have used an a posteriori MO transformation to express GIAO shielding tensors in terms of contributions from natural bond orbitals (NBO). NBOs are strictly localized MOs, and small delocalization tails show up as additional, sparsely occupied "antibonding" or "Rydberg-type" NBOs. This "natural chemical shielding" analysis

(NCS) allows an even finer decomposition of the shielding contributions to discuss small delocalization effects, such as hyperconjugation. The NBO framework is not unambiguous, however, and depends strongly on the most appropriate NBO "Lewis structure" obtained during the NBO procedure. As any LMO-based approach, NCS fails in more delocalized situations.

This discussion shows, that a bewildering variety of possible MO-by-MO analysis schemes is available. The interpretations obtained from these schemes are bound to differ strongly, and it is most important that a consistent discussion does not mix up arguments across the schemes. Different types of analyses may be used more beneficially in a complementary fashion. Moreover, it should generally be stated clearly which framework has been used in a given analysis, and the model dependence of any of these analyses should be acknowledged. Obviously, the applied analysis method should be chosen appropriately, according to the system of interest: LMO- (or NBO-) based schemes are most appropriate when dealing with well-localized bonding situations, CMO analyses will be advantageous in delocalized cases, such as clusters, transition metal complexes, or extended π-systems. It should also be noted that a connection of the energy denominators in Eq. (18.4) to excitations observed by optical spectroscopy is only possible in the case of CMO-based schemes. If one is interested in σ/π separation for planar or quasiplanar π-systems, a CMO analysis or an LMO analysis with PM LMOs seems most appropriate. A few representative examples are provided in Section 18.2.3.

18.2.2
Real-Space Analyses

As indicated above, a sum-over-states expansion such as the Ramsey equations (18.2)–(18.4) is only one way of expressing the perturbation of the system. A real-space quantity that plays an important role in the interpretation of nuclear shieldings is the induced current density $\vec{\mathbf{j}}$, which may also be separated into a diamagnetic and a paramagnetic part (again, the separation is gauge dependent):

$$\vec{\mathbf{j}} = \vec{\mathbf{j}}_{\mathbf{d}} + \vec{\mathbf{j}}_{\mathbf{p}} = -2\vec{\mathbf{A}}_{\text{ext}}\Psi^*\Psi + i(\Psi^*\vec{\nabla}\Psi - \Psi\vec{\nabla}\Psi^*) \tag{18.5}$$

$\vec{\mathbf{j}}$ is a vector field and thus may be visualized in terms of flux lines, isocontour lines or little arrows indicating the direction and magnitude of $\vec{\mathbf{j}}$ at a given point in space (see cover picture). Current density plots are particularly important in the interpretation of magnetic susceptibilities but are also useful for nuclear shieldings. This is specifically the case for delocalized ring currents in extended π-systems. The interpretation of ring currents in the context of discussions of aromaticity is covered in Chapter 24 by Chen, Heine, Schleyer, and Sundholm and will thus not be elaborated upon here. The same holds for iso-shielding surfaces, i.e. three-dimensional displays of shieldings in space.

A quantity related to $\vec{\mathbf{j}}$ is the shielding density $\vec{\sigma}^{\mathrm{N}}(r)$ introduced by Jameson and Buckingham [13], which is defined by

$$\boldsymbol{\sigma}^{\mathrm{N}}(\mathbf{r}) \cdot \vec{\mathbf{B}} = -\frac{1}{c}\frac{\vec{\mathbf{r}}_{\mathrm{iN}} \times \vec{\mathbf{j}}(r)}{r_{\mathrm{iN}}^3} \tag{18.6}$$

The shielding density provides the shielding constant (more precisely the appropriate tensor components) when integrated over all of space. There has been comparably little further work on $\boldsymbol{\sigma}^{\mathrm{N}}(\mathbf{r})$, possibly because it is demanding to compute analytically. Keith and Bader integrated $\boldsymbol{\sigma}^{\mathrm{N}}(\mathbf{r})$ over atomic basins within the "atoms-in-molecules" framework [14]. They found that almost all changes in the shielding of a given nucleus in different environments arise from the atomic basin of the nucleus in question. This is not very surprising, given the shortsighted nature of the PSO operator (see above). It seems that the potential of these types of real-space functions, "property densities", has not yet been exploited fully, and it is expected that their further scrutiny will provide more insight. Similar real-space approaches have recently been shown to give unprecedented insight into the pathways of indirect nuclear spin–spin coupling [15]. This is discussed in more detail in Chapter 19 by Malkina. The particular advantage of real-space analyses is the independence from orbital transformations.

18.2.3
A Few Application Examples

Immediately after the development of the CHF-IGLO method by Kutzelnigg and coworkers [16], the art of LMO analyses of shielding tensors was demonstrated and used extensively for the understanding of many observations. Before GIAO-based methods became competitive in terms of computational efficiency, for a number of years the IGLO method was almost the only method applied regularly to larger chemical systems. We refer the reader to a basic and widely cited article [5] that does not only show some of the first plots of current densities, but provides also numerous examples for CHF-IGLO-based LMO analyses of shielding tensors for light main group compounds, encompassing shifts of essentially all NMR-active nuclei up to chlorine. Often, the contributions of different MOs have been illustrated by plotting the result of the action of cartesian components of angular momentum operators (cf. Eq. (18.4)) on a given MO or LMO, i.e. the transformed MO $\phi' = \hat{\mathbf{l}}_u \phi$. This corresponds to the right-hand side of one of the matrix elements in Eq. (18.4), either with or without an r^{-3}-factor. Provided that the transformed occupied MO ϕ' overlaps well in space with a vacant MO, the corresponding matrix element will be large (the same holds for the coupling of a transformed vacant with an occupied MO, see below). As an example, Fig. 18.1 uses these types of plots to explain the occurrence of a paramagnetic current in the BH molecule, one of the few small Van-Vleck-paramagnetic closed-shell systems.

A number of important general features were noted in these LMO analyses: (i) The core–shell LMOs on one center make negligible contributions to the shieldings of other atoms in the system. This provides a justification for the subsequent use of effective-core potentials on heavy atoms for the inclusion of scalar relativistic effects

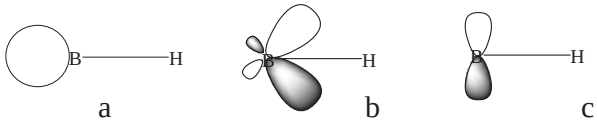

Figure 18.1 LMO-based explanation of the occurrence of a paramagnetic current in BH (adapted from Fig. 6 in Ref. [5]). a) Lone pair ϕ_1 on B (occupied LMO). b) Result of "rotation": $\phi_1' = \mathbf{l_u}\phi_1$ ($\mathbf{l_u}$ represents angular momentum perpendicular to the molecular axis). c) low-lying vacant MO, available to couple with ϕ_1'. As a result of these couplings, a paramagnetic current in the plane is created (and an equivalent one in the molecular plane perpendicular to it).

in the calculation of shieldings of light neighboring atoms [17]. (ii) The 1s-type core–shell contributions at the nucleus of interest are generally transferable from one system to another. In the third and lower periods, the further core–shell LMO contributions were no longer necessarily very well transferable (better transferability of core–shell contributions may be obtained with a different choice of gauge, which has been used to construct a pseudopotential-based scheme [18], see also Chapter 16 by Mauri and Pickard). (iii) The predominant contributions to relative shifts come in any case from the valence orbitals, and both their spatial extent and shape, and their energies matter. Since lone-pair-type LMOs are usually relatively high in energy, they frequently make particularly large contributions to $\boldsymbol{\sigma}^{\mathbf{p}}$, especially if low-lying vacant MOs are present (e.g. from an adjacent multiple bond). (iv) The valence-shell contributions are normally not transferable in the sense of an increment system, as the contribution from a given occupied LMO depends strongly on the availability of low-lying vacant MOs to which the occupied LMO may be coupled by the magnetic operators. A relatively recent application to substituent effects in carbon, silicon, and titanium compounds may serve as a good example for the question of transferability [19].

The initial applications were done mainly within a CHF-IGLO approach. The development of the first DFT-IGLO implementations by Malkin et al. [7] extended the routine applicability of the IGLO approach, and thereby of LMO-based analyses, to systems in which electron correlation effects play a larger role, e.g. to transition metal complexes. However, the usefulness of an LMO-based analysis decreases as one moves to more and more delocalized bonding situations (see above). LMOs based on the PM localization scheme [11] were used for the first time in DFT-IGLO calculations of ^{17}O shieldings in transition metal oxo complexes [10], where they provided a more stable scheme with less dependence of the shieldings on the way the metal core–shells were localized than with the traditional Boys scheme. Apart from these technical advantages, the PM-IGLO scheme also provided useful MO-analyses, e.g., for a set of transition metal carbonyl clusters [20]. A main motivation for the implementation of the "PM-IGLO" scheme was, that in studies of delocalized π-systems, the PM localization, unlike the Boys scheme, provides a separation into σ- and π-LMO contributions [21] (see also Chapter 24). For LMO analyses within a LORG treatment, we refer to Ref. [22].

The analysis of nuclear shieldings in terms of canonical MOs based on DFT-GIAO calculations [23] was pioneered by Ziegler and coworkers, with particular emphasis on transition-metal complexes. As an example we will discuss here the analysis by Ruiz-Morales et al. of the unusually large ^{1}H shieldings in typical transition metal hydrides L_nMH [24]. Already Buckingham and Stevens [25] had proposed a model that involves paramagnetic currents within the incomplete metal d-shell that are "off-center" at the position of the hydrogen nucleus and thereby provide an overall positive shielding contribution to $\boldsymbol{\sigma}(^1\mathrm{H})$ (cf. the related, simpler example of ^{19}F shielding in ClF [5, 8]). This has been confirmed by a DFT-GIAO-based CMO-analysis in [24], as illustrated in Fig. 18.2. The components of the magnetic field perpendicular to the M–H bond induce current loops in the *xz*- and *yz*-planes. The angular momentum operators couple mainly d_π-type metal orbitals to the low-lying vacant d_{σ^*}(M–H) MO, thereby providing large positive contributions to $\sigma_\perp^{\mathbf{P}}$. We note in passing, that in case of the largest "hydridic high-field shifts" known, which range down to chemical shifts of –50 ppm relative to TMS in case of some iridium complexes [2], these $\boldsymbol{\sigma}^{\mathbf{P}}$ contributions are augmented further by sizeable shielding spin–orbit effects [3, 26] (cf. Section 18.3.1).

Similar analyses have been carried out in several cases, e.g. for ^{31}P coordination shifts in some transition metal phosphine complexes [27], or in a recent study of ^{195}Pt shifts [28]. In these studies, illustrations of $\phi' = \mathbf{l}_\mathbf{u}\phi$, as well as discussions of the energy denominators in Eq. (18.4) have played a major role, whereas no detailed decomposition of Eq. (18.4) into individual terms has been provided. This may be partly due to the fact that the GIAO shieldings also involve rotations within the space of the occupied MOs, which are hard to interpret chemically.

In a recent study of ^{29}Si shifts in symmetrically and unsymmetrically substituted disilenes, we have, for this reason, resorted to CMO-analyses within the framework of SGO-based calculations [29], using sufficiently large basis sets. This allowed us to make somewhat more detailed analyses of the individual matrix elements in the numerators of Eq. (18.4). It turned out, e.g., that the energy denominators control largely the magnitude of substituent effects in symmetrically substituted disilenes,

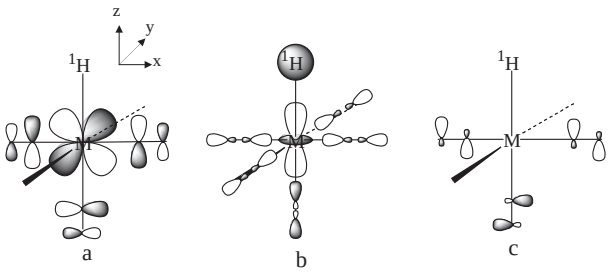

Figure 18.2 Explanation of ^{1}H high-field shifts in transition metal hydrides, based on DFT-GIAO analyses (adapted from Ref. [24]). a) d_π-type HOMO; b) d_{σ^*}-type vacant MO; c) Result of action of angular momentum operator along *y*-direction on d_{σ^*}-type vacant MO. This transformed MO may interact with the d_π-type HOMO. An equivalent interaction results from angular momentum along *x*, and a d_π-type MO in the *yz* plane.

as had been assumed previously [30]. In contrast, the PSO matrix elements in Eq. (18.4) explained the unusually large, characteristic differences between the two silicon nuclei in unsymmetrically substituted disilenes [29]. In the latter case, the same CMOs, and thus the same energy denominators, are involved in the shieldings of both silicon nuclei. Consequently, the spatial extent of the CMOs at the two sites was shown to be the decisive factor. Somewhat less detailed CMO analyses within a CGO scheme have also been carried out in many examples by Nakatsuji and coworkers [31]. An interesting and detailed analysis of the large ^{19}F shielding in ClF and in related compounds has been carried out by Wiberg et al., using the abovementioned simplification of the analysis within the IGAIM approach [8]. Previous arguments about the importance of the phase of the relevant CMOs were thus confirmed, but again a further analysis in terms of energy denominators and matrix elements was not done.

18.3 Relativistic Effects

Everything said up to now has assumed that relativistic effects are negligible. This is frequently not the case. In particular, even for light nuclei, spin–orbit effects due to neighboring heavy atoms may be substantial and are nowadays accepted to be the source of the long-known "heavy-atom effects" on nuclear shieldings (in particular, the so-called "heavy-atom effect on the shielding of the light neighboring atom", HALA; cf. Ref. [32] and Chapters 13 and 14). The inclusion of spin–orbit effects may indeed change the predominant rationalization of relative chemical shifts fundamentally. As the interpretation of relativistic effects on nuclear shieldings has recently been covered in depth elsewhere [3], we will only briefly mention here the main aspects and refer the reader to Ref. [3] for more details.

18.3.1 Spin-Orbit Effects

If we consider spin–orbit (SO) coupling as a further perturbation, SO corrections to chemical shifts are computed within third-order PT (for details, see Chapter 13; in contrast, variational inclusion of spin–orbit coupling in a two- or four-component treatment preserves the second-order PT framework, see Chapter 14). At the Breit–Pauli PT level, the dominant third-order terms may be written in a sum-over-states expansion as:

$$\boldsymbol{\sigma}_{\mathbf{N}}^{\mathbf{SO-I-K}} = \left[\sum_{m,n\neq 0} \frac{\left\langle 0 \middle| \mathbf{H}^{\mathbf{K}} \middle| m_{\mathrm{T}} \right\rangle \left\langle m_{\mathrm{T}} \middle| \mathbf{H}^{\mathbf{SO}} \middle| n_{\mathrm{S}} \right\rangle \left\langle n_{\mathrm{S}} \middle| \mathbf{H}^{\mathbf{B}_0} \middle| 0 \right\rangle}{(E_0 - {}^3E_m)(E_0 - {}^1E_n)} + \text{permutations} \right], \tag{18.7}$$

where $\mathbf{H}^{\mathbf{K}}$ represents hyperfine interactions (predominantly a Fermi-contact term, $\mathbf{H}^{\mathbf{FC}}$), $\mathbf{H}^{\mathbf{SO}}$ the molecular one- and two-electron spin–orbit operators, and $\mathbf{H}^{\mathbf{B}_0}$ the external magnetic field (cf. also Eq. (18.3)). The expression couples both singlet and triplet states, as $\mathbf{H}^{\mathbf{SO}}$ and $\mathbf{H}^{\mathbf{K}}$ involve electronic spin. Other perturbation terms, that arise at the same order in the fine structure constant α as these SO terms, contribute mainly to the absolute shieldings of the heavy nuclei themselves. However, they appear to be negligible for the shieldings of neighboring nuclei, and in general for relative shifts (see Chapter 13).

At first sight, the expressions in Eq. (18.7) look very complicated and difficult to interpret. To this end, a relatively simple analogy to the Fermi-contact mechanism of indirect nuclear spin–spin coupling has been extremely helpful [33]: In the presence of an external magnetic field, spin–orbit coupling near the nucleus of a heavy atom in the system mixes some triplet character into the singlet ground-state wavefunction and thereby causes spin polarization, primarily in the valence shell of the heavy atom. However, the spin polarization is also felt near the NMR-active nuclei in the system (even for light nuclei) and causes an extra contribution to their chemical shifts via hyperfine interactions (mainly via the Fermi-contact term, $\mathbf{H}^{\mathbf{FC}}$). The magnitude of this "spin–orbit chemical shift" may range from very small to almost the entire shielding range of a given nucleus. It may be shielding or deshielding. The value of the abovementioned analogy (cf. schematical displays of this scheme in Refs. [3, 4, 33]) lies in the fact, that the appreciable know-how about the Fermi-contact mechanism of spin–spin coupling (cf. Ref. [2] and Chapter 7 by Helgaker and Pecul, and Chapter 19 by Malkina) holds also to a large extent for the spin–orbit-shifts. This analogy was proven in detail [33], and it has been applied to a wide range of systems and questions [3] (further similarities link the SO shifts to the contact shifts in paramagnetic NMR, cf. Chapter 20 by Moon and Patchkovskii).

Here we just point out some of the main conclusions drawn from these studies:

1. Long-range SO contributions follow the well-known patterns known for spin–spin-couplings, e.g. the damped oscillatory behavior in aromatic systems or a Karplus-type dependence on dihedral angles [33].
2. As for the FC mechanism of spin–spin couplings, the s-character in the bonds from the NMR-active atom to its neighbors (along the bond path to the heavy atom(s)) is decisive for the magnitude of the effect. This explains many well-known observations and trends throughout the periodic table: s-character is large in main-group systems in their maximum oxidation state, and SO-shifts are correspondingly large. This results, e.g., in the well-known normal-halogen dependence (NHD), that is, increasing shielding with increasing atomic number of the halogen substituent bonded to the NMR-active atom, and increasing shielding with increasing number of heavy-atom substituents. The latter trend may be faster than linear, due to the increasing s-character along the same series [3]). In contrast, s-character is small in bonding to main-group atoms in lower oxidation states (the s-character concentrates in nonbonding orbitals) and in complexes of early transition metals. SO-shifts are thus small in these systems. Atoms with particularly large s-

character in bonding, especially hydrogen but also, e.g., mercury, feature an extremely large dependence on SO effects, whereas atoms with low s-character in bonding, like fluorine or oxygen, experience small SO effects on their shieldings [3].

Further insights that are compatible with the perturbation expressions (Eq. (18.7)) but which do not follow directly from the abovementioned analogy are (for heavy-atom substituents directly bonded to the NMR atom):

3. If occupied MOs of π-type character with respect to the bond from the NMR atom to the heavy-atom substituent dominate the interactions in Eq. (18.7), the SO-effects are shielding [3, 34]. This holds, e.g., for heavy halogen or chalcogen substituents (with the former having two, the latter only one π-type nonbonding orbital), or for the t_{2g}-type MOs of octahedral d^6 transition metal complexes [3]. If, in contrast, the predominant interactions involve an occupied MO of σ-character, as for example in the case of the ^{13}C shifts in organomercury or organoindium(I) compounds, the SO-shifts are deshielding.
4. The energy denominators in Eq. (18.7) involve a product of two energy differences. It is thus mandatory for large SO-shifts that the ground and excited states involved (in an MO framework the occupied and vacant MOs) do not differ too much in energy.
5. As the SO-shifts are typically anisotropic, they may also change significantly the anisotropy, and sometimes the orientation, of the overall shielding tensor [3].

These insights derive from calculations at rather disparate levels of theory, ranging from two-component Douglas–Kroll-based Hartree–Fock or ZORA-DFT levels to one-component DFT, either with fully analytical or with partly finite-field PT treatments. Many examples and references may be found in Ref. [3], and we refrain here from going into detail.

18.3.2 Spin-Free (Scalar) Relativistic Effects

The main effect of scalar relativity is a modification of the overall electronic structure of the system. This may affect chemical shifts either via a change of molecular structure or via changes in the wavefunction at a given structure. For example, the relativistic expansion of the d-shell in 5d-metals makes bonds to electronegative ligands in high oxidation states stronger and more ionic, or the contraction of the 6s-shell affects significantly the electronic structure of late transition metals or main-group elements in the 6th period [35]. The interpretation of these scalar relativistic effects depends to some extent on the theoretical framework used (i.e. four-component, two-component, one-component treatments, and perturbational or variational treatments of scalar relativistic effects). We refer to Ref. [3] and to Chapters 13 and 14 for more details.

18.4 Concluding Remarks

The NMR chemical shift tensor is not an easy property to interpret chemically. Simple correlations with only one quantity, like atomic charge or energy denominators, are usually not sufficient for a detailed understanding of shielding trends. An understanding that is a basis for predictive models necessarily has to be derived from a detailed analysis of the relevant perturbation expressions. Only then we may identify the decisive interrelations between electronic structure and spectroscopic observable. We have provided examples of the methods that are commonly used to extract chemical information from computed shielding tensors. In particular, we have attempted to point out the advantages and disadvantages of a given theoretical framework for specific bonding situations and chemical questions. Currently, the detailed MO-by-MO analysis of $\boldsymbol{\sigma}^{\mathbf{d}}$ and $\boldsymbol{\sigma}^{\mathbf{p}}$ at a suitable level, where necessary augmented by an analysis of spin–orbit effects, is the most widely used approach. Real-space analyses, based on current densities or on shielding densities, deserve further study as promising alternative tools.

Acknowledgments

The author is grateful to many past and current collaborators in the area of magnetic resonance parameters. Vladimir G. Malkin and Olga L. Malkina (Bratislava) provided helpful comments on the manuscript. Our own work in this field has been supported by Deutsche Forschungsgemeinschaft and by Fonds der Chemischen Industrie, as well as by the graduate college "Moderne Methoden der magnetischen Resonanz in der Materialforschung" at Universität Stuttgart.

References

1 N. F. Ramsey, *Phys. Rev.* **1950**, *77*, 567; N. F. Ramsey, *Phys. Rev.* **1950**, *78*, 699; N. F. Ramsey, *Phys. Rev.* **1951**, *83*, 540; N. F. Ramsey, *Phys. Rev.* **1952**, *86*, 243.

2 See, e.g.: *Multinuclear NMR*, ed. J. Mason, Plenum Press, New York **1987**, and references cited therein.

3 M. Kaupp, Relativistic Effects on NMR Chemical Shifts, in *Relativistic Quantum Chemistry*, Vol. 2, ed. P. Schwerdtfeger, Elsevier, Amsterdam, in press.

4 See, e.g.: a) M. Kaupp, O. L. Malkina, V. G. Malkin, NMR of Transition Metal Compounds, in *Encyclopedia of Computational Chemistry*, ed. P. v. R. Schleyer, Wiley Interscience, New York **1998**, pp. 1857 ff; b) M. Bühl, M. Kaupp, V. G. Malkin et al., *J. Comput. Chem.* **1999**, *20*, 91; c) G. Schreckenbach, T. Ziegler, *Theor. Chem. Acc.* **1998**, 99, 71; d) J. Autschbach, T. Ziegler, Relativistic Computation of NMR Shieldings and Spin-Spin Coupling Constants, in *Encyclopedia of Nuclear Magnetic Resonance*, Vol. 9, eds. D. M. Grant, R. K. Harris, Wiley, Chichester **2002**, pp. 306–323; e) J. Autschbach, T. Ziegler, *Coord. Chem. Rev.* **2003**, *238*, 83.

5 W. Kutzelnigg, U. Fleischer, M. Schindler, in *NMR-Basic Principles and Progress*, Vol. 23, Springer, Heidelberg **1990**, pp.165–262; see also: W. Kutzelnigg, *J. Mol. Struct. (THEOCHEM)* **1989**, *202*, 11.

6 See, however: A. M. Lee, N. C. Handy, S. M. Colwell, *J. Chem. Phys.* **1995**, *103*, 10095.

7 V. G. Malkin, O. L. Malkina, L. A. Eriksson et al., in *Modern Density Functional Theory: A Tool for Chemistry; Theoretical and Computational Chemistry*, eds. J. M. Seminario, P. Politzer, Vol. 2, Elsevier, Amsterdam **1995**, pp. 273–347; V. G. Malkin, O. L. Malkina, M. E. Casida et al., *J. Am. Chem. Soc.* **1994**, *116*, 5898.

8 See, e.g.: K. B. Wiberg, J. D. Hammer, K. Zilm et al., *J. Phys. Chem. A* **1998**, *102*, 8766.

9 S. F. Boys, in *Quantum Theory of Atoms, Molecules and the Solid State*, ed. P. O. Löwdin, Academic Press, New York **1966**, pp. 253 ff.

10 M. Kaupp, O. L. Malkina, V. G. Malkin, *J. Chem. Phys.* **1997**, *106*, 9201.

11 J. Pipek, P. G. Mezey, *J. Chem. Phys.* **1989**, *90*, 4916.

12 J. A. Bohmann, F. Weinhold, T. C. Farrar, *J. Chem. Phys.* **1997**, *107*, 1173.

13 C. J. Jameson, A. D. Buckingham, *J. Chem. Phys.* **1980**, *73*, 5684; C. J. Jameson, A. D. Buckingham, *J. Phys. Chem.* **1979**, *83*, 3366.

14 T. A. Keith, R. W. F. Bader, *Can. J. Chem.* **1996**, *74*, 185.

15 O. L. Malkina, V. G. Malkin, *Angew. Chemie, Int. Ed. Engl.* **2003**, *42*, 4335.

16 W. Kutzelnigg, *Isr. J. Chem.* **1980**, *27*, 789; M. Schindler, W. Kutzelnigg, *J. Chem. Phys.* **1982**, *76*, 1919.

17 M. Kaupp, V. G. Malkin, O. L. Malkina et al., *J. Am. Chem. Soc.* **1995**, *117*, 1851; **1995**, *117*, 8492.

18 T. Gregor, F. Mauri, R. Car, *J. Chem. Phys.* **1999**, *111*, 1815; C. J. Pickard, F. Mauri, *Phys. Rev. B* **2001**, *63*, 245101.

19 S. Berger, W. Bock, G. Frenking et al., *J. Am. Chem. Soc.* **1995**, *117*, 3820.

20 R. Salzmann, M. Kaupp, M. McMahon et al., *J. Am. Chem. Soc.* **1998**, *120*, 4771.

21 P. v. R. Schleyer, H. Jiao, N. J. R. van Eikema Hommes et al., *J. Am. Chem. Soc.* **1997**, *119*, 12669.

22 A. E. Hansen, T. D. Bouman, in *Nuclear Magnetic Shieldings and Molecular Structure* ed. J. A. Tossell, Kluwer, Dordrecht 1993, pp. 117 ff, and references cited therein.

23 G. Schreckenbach, T. Ziegler, *J. Phys. Chem.* **1995**, *99*, 606.

24 Y. Ruiz-Morales, G. Schreckenbach, T. Ziegler, *Organometallics* **1996**, *15*, 3920.

25 A. D. Buckingham, P. J. Stephens, *J. Chem. Soc.* **1964**, 2747; ibid. **1964**, 4583.

26 P. Lantto, J. Vaara, M. Kaupp, unpublished results.

27 Y. Ruiz-Morales, T. Ziegler, *J. Phys. Chem. A* **1998**, *102*, 3970.

28 T. M. Gilbert, T. Ziegler, *J. Phys. Chem. A* **1999**, *103*, 7535.

29 D. Auer, C. Strohmann, A. V. Arbuznikov et al. *Organometallics* **2003**, *22*, 2442.

30 R. West, J. D. Cavalieri, J. J. Buffy et al., *J. Am. Chem. Soc.* **1997**, *119*, 4972.

31 H. Nakatsuji, in *Nuclear Magnetic Shieldings and Molecular Structure*, ed. J. A. Tossell, Kluwer, Dordrecht **1993**, pp. 263 ff, and references cited therein.

32 P. Pyykkö, A. Görling, N. Rösch, *Mol. Phys.* **1987**, *61*, 195.

33 M. Kaupp, O. L. Malkina, V. G. Malkin et al., *Chem. Eur. J.* **1998**, *4*, 118. This analogy had already been implied early on by Y. Nomura, Y. Takeuchi, N. Nakagawa, *Tetrahedron Lett.* **1969**, *8*, 639.

34 See, e.g. M. Kaupp, O. L. Malkina, V. G. Malkin, *J. Comput. Chem.* **1999**, *20*, 1304, and references therein.

35 See, e.g. P. Pyykkö, *Chem. Rev.* **1988**, *88*, 563.

19
Interpretation of Indirect Nuclear Spin–Spin Coupling Constants

Olga L. Malkina

19.1
Introduction

The high sensitivity of indirect nuclear spin–spin coupling constants to subtle changes in the geometrical and electronic structure makes them an important source of chemical information. However, the extraction of this information is not always straightforward, and couplings often require careful analysis and interpretation. For this reason, measurements of spin–spin coupling have always been accompanied by attempts to rationalize the phenomenon and explain its mechanisms. Numerous reviews are devoted to this topic. In recent years this field has become the subject of even more interest for two major reasons. First, tremendous progress in quantum-chemical calculations of spin–spin couplings allows one to obtain reliable results, even for systems of considerable size, using density functional theory (DFT) (see Chapter 7 by Helgaker and Pecul), to take into account relativistic effects for compounds containing heavier elements (see Chapter 15 by Autschbach and Ziegler), or to get highly accurate data for difficult cases employing post-Hartree–Fock approaches. Theoretical methods have become so reliable that all information needed for the analysis of spin–spin couplings can, in principle, be taken from calculations. Second, the experimental discovery of spin–spin coupling through hydrogen bonds called for new interpretational tools in order to understand its mechanisms (see Chapter 22 by DelBene). Therefore, it is not surprising that in recent years, analysis of spin–spin coupling has become topical again. In this chapter, available tools for the interpretation of spin–spin couplings, including new approaches for the visualization of spin–spin coupling pathways using real-space functions, will be outlined.

In the non-relativistic treatment, there are four contributions to the indirect nuclear spin–spin coupling constant: the Fermi-contact (FC), paramagnetic spin–orbit (PSO), spin-dipolar (SD) and diamagnetic spin–orbit (DSO) terms (see Chapter 7). Splitting the total coupling constant into these four contributions may be considered as a first level of interpretation. The FC term is usually dominant. However, in some cases (such as coupling through a multiple bond) other terms may be as important as the contact term. For example, equation-of-motion-CCSD calculations [1] showed that in the CO molecule, the PSO term is responsible for

Calculation of NMR and EPR Parameters. Theory and Applications.
Edited by Martin Kaupp, Michael Bühl, Vladimir G. Malkin
Copyright © 2004 WILEY-VCH Verlag GmbH & Co. KGaA, Weinheim
ISBN: 3-527-30779-6

about 80% of the total coupling (13.0 of 15.5 Hz) and the DSO contribution is of the same order of magnitude as the FC term (– 4.6 and 7.0 Hz correspondingly). In the N_2 molecule, the PSO contribution is found to be 2.8 Hz, while the FC part is only 0.3 Hz (EOM-CCSD [1]). The PSO term is also known to play an important role in ^1J(H–F) and ^1J(H–Cl) couplings [1, 2]. It can also be significant for two-bond couplings. For example, for ^2J(F–F) in CF_4, the PSO part accounts for about –112 Hz [3]. Another remarkable example is ^1J(M–O) in 3d-oxo-complexes [4], where the PSO term is not only comparable in magnitude with the FC contribution but is actually the leading term defining the trend in the M = V, Cr, Mn series. Khandongin and Ziegler [4] found the PSO term to be extremely important for such couplings, and they analyzed it further by decomposing it into individual contributions from molecular orbitals. It should be noted that the PSO part itself being so carefully examined is a rather rare event. Since the calculation of the PSO contribution is computationally very similar to the calculation of NMR chemical shifts (CS), all techniques available for analysis of CS can be applied to the PSO term (see Chapter 18 by Kaupp). Still, in the overwhelming majority of applications the analysis of spin–spin couplings is restricted to the FC term, as it typically governs the coupling. Approaches based on different perturbation theories for the analysis of this contribution have a long history and are well developed nowadays. In the remainder of the chapter, we will consider only the interpretation of the Fermi-contact term.

Before considering the available tools for analyses of couplings, let us outline possible goals of the interpretation: (1) understanding the underlying physical phenomena; (2) rationalization of the observed trends in a series of compounds, in other words finding the most important factors influencing the coupling; (3) explanation of "unusual" (counterintuitive at first glance) values and dependences; (4) prediction of the sign and magnitude of unknown coupling constants, even without doing direct quantum-chemical calculations; (5) last, but not least, understanding of the coupling pathways, for example, in multiple-ring systems, or answering the old question of whether a particular spin–spin interaction goes "through-bond" or "through-space". It should be mentioned that there is no universally accepted definition of "through-space" coupling despite the topic having been disputed for many years. The term usually refers to anomalously large coupling constants for nuclei many bonds apart but physically close in space [5]. One of the most striking examples of "through-space" interaction is the coupling constant of J(F–F) = 17 Hz found for a pair of spatially proximate fluorines in a polypeptide formally separated by 89 bonds [6].

Analysis of coupling usually assumes the establishment of a connection between the coupling and a set of chemically relevant quantum-mechanical concepts used for the characterization of electronic structure. The most commonly used concepts are localized and canonical molecular orbitals (MO), one-electron energies, bond orders, populations, atomic charges, electronegativities, etc. Although very useful in describing the electronic structure, none of these concepts are observable in the quantum-mechanical sense, and thus their meaning is to an extent somewhat arbitrary. Accordingly, the interpretation (and the obtained conclusions) can depend on the models or concepts employed. It would be preferable to have an approach which

involves little or no arbitrary concepts or approximations. Below we will discuss different theoretical approaches, keeping in mind the previously-formulated goals and the possible "non-uniqueness" of the interpretation.

Historically, the first interpretations were aimed at establishing a physical picture and general understanding of spin–spin interaction rather than quantitative analysis: (i) the Dirac vector model explaining the propagation of spin-polarization (induced by the FC interaction) through a chain of chemical bonds in a molecule [7]; (ii) Pople and Bothner-By's model [8], which allows one to analyze the coupling in terms of individual excitations and s-character of MOs at the nuclei; typically this interpretation is illustrated by energy level diagrams; (iii) the interpretation, suggested by Barfield and Karplus, in terms of so-called "interbond bond orders" characterizing the interaction of a pair of bonds; this analysis was implemented in the framework of the valence-bond (VB) method [9]. Both analyses (ii) and (iii) are based on Ramsey's sum-over-states (SOS) expression [10]. Later, another approach for the calculation of spin–spin couplings, based on finite perturbation theory (FPT) [11], became popular. Within FPT, the Fermi-contact operator on one of the coupled nuclei is included in the Hamiltonian as a perturbation, and the coupling constant is obtained from the spin density at the position of the second coupled nucleus. This gives the background of interpretation of couplings based on the analysis of the spin-density matrix in terms of molecular orbitals (canonical, localized, semilocalized etc.). It should be kept in mind, that methods other than SOS or FPT (i.e. coupled Hartree–Fock, coupled DFT, or linear response) can also provide the basis for interpretation, using either an "SOS-like" expression or a spin-density matrix. A review of all modern approaches for the calculation of spin–spin couplings is beyond the scope of this chapter, the remainder of which will focus on the discussion of possible methods of interpretation and their historical origins. New approaches for visualization of spin–spin coupling by real-space functions will be presented in Section 19.4. Before going to more sophisticated tools for analysis, in Section 19.2 we will briefly outline a simple physical picture of coupling, known as the Dirac vector model.

19.2
The Dirac Vector Model of Spin–Spin Coupling

This model, based on the FC interaction of nuclear and electron spins and Hund's rule, can be found in almost any NMR textbook. The explanation is considered so classical that the names of its authors are often omitted. The Dirac vector model of spin–spin coupling was proposed by Duval and Koide [7] in 1964 in order to account for the appearance of different signs in the long-range couplings in saturated compounds.

Let us consider the coupling of two directly bonded nuclei (M and N) with positive magnetogyric ratios. The Fermi-contact mechanism at M stabilizes the anti-parallel orientation of an electron spin in the proximity of nucleus M. Consequently, the second electron of the bond (possessing the opposite spin according to the Pauli

principle) will have a slightly higher probability of being found near N. In turn, the contact mechanism at N will make the anti-parallel arrangement of the second nuclear spin preferable (with respect to the spin of the nearest electron, and therefore also anti-parallel with respect to the spin of the first nucleus). In this case, the anti-parallel orientation of nuclear spins leads to a lower energy and the Dirac vector model predicts a positive coupling constant.

If the coupled nuclei are separated by a number of bonds, then the electronic interaction in the region of each intervening atom should be taken into account. According to Hund's rule, in these areas the parallel orientation of the electron spins is preferred. Applying the Pauli principle to each bond in the chain connecting two coupled nuclei, one can conclude that coupling through an odd number of bonds should be positive and through an even number of bonds, negative (again assuming positive magnetogyric ratios of both coupled nuclei).

Though the Dirac vector model gives a simple physical picture of how the spin interaction propagates over the pathway connecting two coupled nuclei and greatly aids general understanding of the effect, this model is an oversimplification. It fails to explain the variety of couplings. For example, the positive sign of ^2J(H–H) in formaldehyde is an obvious contradiction of the Dirac vector model, which does not take into account sp^x-hybridization of coupled or intervening atoms. Therefore couplings through multiple bonds are outside the applicability of this model. The Dirac vector model is not able to describe the influence of lone pairs on couplings, and many other experimentally known effects. Furthermore the model was designed to yield a picture of a purely "through-bond" interaction (assuming a well localized Lewis-type electronic structure), and as such it cannot provide any immediate insight on "through-space" coupling. In short, the Dirac vector model is too simple for an adequate interpretation of the complex phenomenon of indirect nuclear spin–spin coupling. More sophisticated quantum-chemical approaches are needed. Among them, the oldest, which still remain very popular, are sum-over-states (SOS) and finite perturbation theory (FPT).

19.3
Decomposition into Individual Contributions

19.3.1
SOS within Linear Combination of Atomic Orbitals (LCAO)

The basis for sum-over-states calculations of spin–spin couplings was developed in 1953 by Ramsey [10]. In 1964, Pople and Santry [12] applied Ramsey's SOS equations to the calculation of coupling constants in the framework of molecular orbital theory, obtaining the following expression for the Fermi-contact contribution to the reduced coupling constant K_{MN}:

$$K_{MN} = -\frac{256\pi^2}{9}\beta^2 \sum_{i}^{occ}\sum_{j}^{vac}\left({}^3\Delta E_{i\to j}\right)^{-1}\left\langle \varphi_i \middle| \delta(r - R_M) \middle| \varphi_j \right\rangle \left\langle \varphi_j \middle| \delta(r - R_N) \middle| \varphi_i \right\rangle \quad (19.1)$$

Here β is the Bohr magneton, δ is the Dirac-delta function, R_M and R_N are the positions of the coupled nuclei. As can be seen from Eq. (19.1), only pairs of molecular orbitals (φ_i and φ_j) having non-zero amplitudes at the positions of both atoms M and N can contribute to the coupling. Also, the magnitude of a particular contribution depends on the energy difference between the ground state singlet and the corresponding excited triplet ($^3\Delta E_{i\to j}$). It turns out that analysis of these two quantities, the amplitudes of molecular orbitals and the energy denominators, can indeed explain many couplings. Eq. (19.1) became a favored basis for interpretation of coupling constants for many years (see, for example, the reviews [13–15]), partly because in simple cases experimentalists are able to estimate the energy denominator and at least the signs of the molecular orbitals at the positions of the coupled nuclei without doing quantum-chemical calculations.

In the LCAO (linear combination of atomic orbitals) approach, Eq. (19.1) can be rewritten as follows:

$$K_{MN} = -\frac{256\pi^2}{9}\beta^2 \sum_{i}^{occ}\sum_{j}^{vac}\left(^3\Delta E_{i\to j}\right)^{-1}\sum_{\lambda\mu\nu\sigma} C_{\lambda i}C_{\mu j}C_{\nu j}C_{\sigma i}\left\langle\chi_\lambda\left|\delta(r-R_M)\right|\chi_\mu\right\rangle \left\langle\chi_\nu\left|\delta(r-R_N)\right|\chi_\sigma\right\rangle \tag{19.2}$$

where $C_{\eta k}$ are molecular orbital coefficients. This expression allows one to interpret the couplings in terms of atomic orbitals χ_η. If one is interested only in the dominant terms, further approximations can be made. The triplet–singlet energy difference can be approximated by the difference of the one-electron energies of the corresponding molecular orbitals. Furthermore, since at the position of a given atom atomic orbitals from other atoms are likely to have small amplitudes, two-center integrals in Eq. (19.2) can be neglected. Taking into account that only s-orbitals have non-zero amplitudes at the position of the atom, we get the following equation[1]:

$$K_{MN} = -\frac{64\pi^2}{9}\beta^2\left\langle s_M\left|\delta\left(r-R_M\right)\right|s_M\right\rangle\left\langle s_N\left|\delta\left(r-R_N\right)\right|s_N\right\rangle\pi_{s_M,s_N} \tag{19.3}$$

$$\pi_{\mu,\nu} = 4\sum_{i}^{occ}\sum_{a}^{vac}\left(\varepsilon_i-\varepsilon_a\right)^{-1}C_{\mu i}C_{\nu a}C_{\mu a}C_{\nu i} \tag{19.4}$$

where $\pi_{\mu,\nu}$ is the so-called "mutual polarizability" of the atomic orbitals χ_μ and χ_ν introduced by Coulson and Longuet-Higgins [16]. In Equations (19.3) and (19.4), the value of K_{MN} is written as the sum of the contributions from the individual $i\to a$ excitations. Those with smaller $(\varepsilon_i-\varepsilon_a)$ differences are the most important ones.

1) In the original paper [12], Pople and Santry employed the INDO (intermediate neglect of differential overlap) method and, thus, only valence atomic orbitals were considered. Therefore, in their work, in order to compensate for the absence of 1s orbitals, they treated contributions from 2s atomic orbitals as fitted parameters.

Usually, there are only a few significant terms in the right-hand side of Eq. (19.4). Therefore for the interpretation it may be enough to analyze just a few excitations (i.e. from bonding to antibonding orbitals). Molecular orbital coefficients in Eq. (19.4) can be positive or negative and, consequently, each contribution can be either positive or negative. The interplay between the values of $(\varepsilon_i - \varepsilon_a)$ and the signs of the MO coefficients determines the coupling.

The magnitude of the coupling is also proportional to the s-densities of the molecular orbitals at the nuclei, that is, to the s-character of the corresponding MOs. Since, in turn, the s-character of the bonds is influenced by the sp^x-hybridization and electronegativity of ligands, the use of the s-character argument can, in principle, explain a variety of couplings in chemically different situations and rationalize the trends observed in series of compounds (which the Dirac vector model cannot do). However, it should be noted that the π electrons (known to play an important role in the spin–spin coupling for unsaturated compounds) do not enter this interpretation directly, though they do affect the electronic distribution in a molecule. Therefore, it is not surprising that it can be difficult to understand spin–spin coupling pathway(s) solely by considering Eqs. (19.3) and (19.4).

19.3.2
Valence-Bond Bond-Order SOS approach

In 1969, Barfield and Karplus [9] suggested the valence-bond bond-order formulation of Ramsey's SOS equations. In this method, the singlet ground state wavefunction is written as a linear combination of linearly independent, nonpolar valence-bond (VB) functions [17] constructed in a special way from atomic orbitals. After a number of approximations, including somewhat less transparent ones than those of Pople and Santry, Barfield and Karplus arrive at the following expression for the FC coupling term:

$$K_{\mathrm{MN}} = \frac{256\pi^2}{9}\beta^2 \ (2\Delta E)^{-1} \sum_{t,u} \chi_t^2(R_{\mathrm{M}}) \ \chi_u^2(R_{\mathrm{N}}) p(t,u) \qquad (19.5)$$

where *p(t,u)* is the Penney–Dirac bond order [18, 19]. In the case of completely localized bonds, *p(t,u)* is equal to one for bonded atoms and zero otherwise. In delocalized systems it can be either positive or negative. In Eq. (19.5), the coupling is decomposed into the sum of contributions from the pairs of atomic orbitals. We see again that only atomic orbitals with nonzero densities at the positions of the coupled atoms can contribute to the FC term.

In order to provide a basis for further analysis, Barfield and Karplus considered the interaction of two bonds in the molecular four-electron fragment and introduced a new quantity characterizing this interaction: "interbond bond orders" (four for each four-electron fragment; see Ref. [9] for more details). It was shown that, within some additional approximations, the interbond bond orders are determined by the formal two-electron exchange integrals associated with the corresponding orbitals. The Penney–Dirac bond orders can be expressed in Taylor series with respect to

interbond bond orders. After neglecting the third- and higher order terms and substituting the Penney–Dirac bond orders by these expansions in Eq. (19.5), one can get the "direct" (first-order terms) and "indirect" contributions (second-order terms). Barfield and Karplus pointed out that the "direct" contributions could be important not only for geminal and vicinal H–H couplings, but also for long-range couplings, if the bonds containing the coupled nuclei are sufficiently close in space (resulting in non-negligible values of the exchange integrals).

The dependence of the interbond bond orders on the exchange integrals was used in an attempt to clarify the dichotomy between "through-space" and "through-bonds" interactions. According to Barfield and Karplus, the exchange interaction between non-bonded orbitals corresponds to a "through-space" mechanism, while the interaction of adjacent orbitals contributes to "through-bonds" coupling. From this point of view, the vicinal ^{3}J(H–H) coupling in ethane represents neither a pure "through-space" nor a pure "through-bonds" interaction.

We see that despite a number of severe approximations the valence-bond bond-order formulation of SOS brings us closer to an understanding of coupling pathways. In fact, valence bond theory was considered [5] as a "great success in qualitatively describing trends in ^{3}J(H–H)". In particular, this theory was able to provide an explanation for the dependence of the vicinal H–H coupling on the dihedral angle (nowadays known as Karplus-type dependence).

Sum-over-states based approaches for the interpretation of spin–spin couplings turned out to be quite successful. The work of Pople and Bothner-By [8] on the systematization and interpretation of geminal H–H couplings is one of the definitive works in this field. Following Pople and Santry [12], energy diagrams were used for the rationalization of ^{31}P couplings in transition metal complexes [14, 15]. The signs of lone-pair effects on spin–spin coupling constants were also explained with the help of energy diagrams [13]. Unfortunately, SOS approaches at both Hartree–Fock (HF) and density functional theory (DFT) levels (i.e. for quantum-chemical methods with moderate computational demand) in many cases cannot quantitatively reproduce experimentally observed values of couplings without an artificial scaling procedure [20, 21]. Therefore, quite often these methods can provide information only for qualitative or semi-quantitative interpretation, and are thus not truly satisfactory from a theoretical point of view.

19.3.3
Single Finite Perturbation Theory (FPT)

Another method for the calculation of the FC contribution was suggested by Pople et al. in 1967 [11]. The idea of the method is as follows. First, the Fermi-contact operator at one of the coupled nuclei is included as a small but finite perturbation in the Hamiltonian. Due to the presence of the spin operator, the perturbation will have different signs for alpha and beta electrons, causing spin-polarization in an otherwise closed-shell system. The Schrödinger equation is then solved self-consistently. The perturbed molecular orbitals thus obtained are used to calculate the expectation value of the second Fermi-contact operator that is essentially the value

of the spin density at the position of the second coupled nucleus. Actually, the values of the spin density can be calculated at the positions of all other nuclei (with the obvious exclusion of the one chosen as the center of the perturbation), and thus only one SCF (self-consistent-field) calculation is required to obtain the couplings of one nucleus with all others. The FPT calculations, being based on a numerical evaluation of the energy derivative, can be sensitive to the value of the perturbation parameter (a description of a more elaborate linear response method can be found in Chapter 7). However, FPT can be easily implemented at different levels of theory and, more importantly, in most cases gives rather reliable results at the DFT level [22]. Therefore, finite perturbation theory can be applied for calculation of couplings in systems of moderately large size, and the information obtained can be used directly for a *quantitative* interpretation of spin–spin couplings.

Since, in the single-FPT framework, the value of the spin–spin coupling constant is expressed as the spin density, all tools available for analyzing the electron density can be applied. A natural way to analyze the spin density (which is simply the difference between alpha- and beta-electron densities) is to decompose it into contributions from canonical or localized molecular orbitals (LMOs). For a localization procedure, different criteria can be used. In fact, the canonical molecular orbitals can be subjected to any unitary transformation. The resulting molecular orbitals will give the same total energy and the same alpha- and beta-electron densities, though the picture in terms of individual contributions can be quite different. The interpretation is not unique and the underlying concepts should always be kept in mind.

The choice of appropriate orbitals for the analysis (LMOs versus canonical MOs) is subjective. Canonical orbitals can be too delocalized, but can be classified by their one-electron energies. For example, Munzarová and Sklenář [23] recently used canonical MOs for the interpretation of three-bond sugar–base couplings in purine and pyrimidine nucleosides. They showed that the difference in the Karplus-type dependences for those nucleosides is connected to the two highest occupied (canonical) molecular orbitals. On the other hand, the localized molecular orbitals are closer to chemical intuition, but they may not be the best choice to describe a phenomenon with a delocalized nature, such as a long-range nuclear spin–spin coupling. Another disadvantage of the localized molecular orbitals is that they cannot be used for energy level diagrams because LMOs are not eigenfunctions of the Hamiltonian.

With the goal of overcoming the shortcomings of the usual LMOs while keeping their advantages regarding chemical interpretation, Wilkens et al. suggested the so-called natural *J*-coupling analysis (NJC) [24] based on natural bond orbitals (NBO) and natural localized molecular orbitals (NLMO) [25]. The starting point for constructing the NBO and NLMO sets is the density matrix rather than canonical molecular orbitals. By construction, both NBOs and NLMOs are complete and orthonormal, and they are connected to canonical MOs by unitary transformations. Normally, NBOs of near double occupancy are well localized and correspond to Lewis-type orbitals commonly used by chemists. The density matrix in the NBO basis is usually slightly non-diagonal. In contrast to NBOs, NLMOs are semilocalized. In the expansion of a particular NLMO in the NBO basis, the coefficient in front of the parent NBO is near unity (and therefore the shape of the NLMO resembles that of

the parent NBO). The sum of other terms (antibonding and/or Rydberg NBOs, both weakly occupied) represents a non-Lewis delocalization tail of the NLMO. The density matrix in the NLMO basis is diagonal. This allows one to rewrite the expression for the FC contribution in the framework of single perturbation theory as the sum of individual NLMO contributions.

The splitting of each NLMO into a linear combination of NBOs gives the decomposition of coupling in terms of NBOs. The contribution arising from the parent NBO is called the Lewis coupling contribution [24]. According to Wilkens et al. [24], the origin of the Lewis contribution lies in steric interaction and its mechanism is analogous to the "direct" coupling mechanism introduced by Barfield and Karplus [9] in the VB method. The contributions coming from antibonding NBOs (and related to "indirect" contributions in VB) are usually smaller. In NJC, they are interpreted as "residual intrabond repolarization" and "interbond spin delocalization" contributions, depending on whether the NBO corresponds to the NLMO's own antibond or not. In the latter case, delocalization contributions reflect either conjugative or hyperconjugative interactions. Typically the hyperconjugative phenomena are more important for *J*-coupling than other delocalization mechanisms. For example, according to the NJC analysis for ^{3}J(H–H) in ethane (*trans* conformation, B3LYP/6-311**), the NLMO contributions from the C–H bonds containing the coupled protons give 14.04 Hz of the total value of 14.72 Hz. Each contribution of 7.02 Hz consists of the Lewis part (+5.52 Hz), the interbond delocalization contribution (+2.63 Hz) corresponding to the hyperconjugative interaction with the C–H antibonding MO of another coupled proton, the repolarization contribution (–0.07 Hz) and the remaining delocalization contributions with the sum of –1.05 Hz. It should be noted that NJC, even in the framework of single FPT, allows (to an extent) energy arguments to be brought out (see Ref. [24] for more details), although no direct connection with the excitation energies can be concluded.

However, in the current implementation [24], the NJC analysis is not able to overcome another deficiency of single FPT: the results of interpretation may depend on which of the coupled nuclei was chosen as a center of perturbation. Wilkens et al. [24] suggested to "restore the physical symmetry of coupling" by averaging individual spin density contributions from two single FPT calculations (with perturbation on the first and then on the second nucleus). This probably still cannot be considered as a full remedy, just as the result of the interplay of two FC operators cannot be replaced by their half sum and the plot of the averaged spin density would not necessarily reflect the coupling pathway.

19.3.4
Some Examples

It should be noted that the use of one perturbation theory for calculation of spin–spin couplings does not prohibit the interpretation of the results with the techniques typical for another one. One can combine different approaches making use of their advantages. Let us consider some instructive examples.

To the best of our knowledge, the first calculation of spin–spin coupling at the post-Hartree–Fock level was done already in 1967 by Armour and Stone [26]. They used the configuration interaction method (CI) to compute the H–H couplings in ethylene. The sum-over-states perturbation theory was employed. Due to very limited computer facilities at that time, the basis set was fairly small by modern standards: it contained only 14 Slater orbitals. The CI calculated values for vicinal couplings (both *cis* and *trans*) were in good agreement with experiment while the geminal constant was some way off. In order to understand the reason for this failure, the authors performed another CI calculation based on localized MOs to find out the nature of important contributions. They rewrote the CI expression for the FC contribution as a perturbation expansion in the electron correlation and analyzed the series in terms of canonical and localized orbitals. Armour and Stone found that (1) the inclusion of correlation is very important; (2) the expansion converges rather slowly; (3) when localized orbitals are used, the expansion converges even more slowly. Still, the transformation to LMOs proved to be useful, because it showed that, for geminal couplings, the most important contributions come from bonding and antibonding C–H orbitals. The plot of these orbitals in the molecular plane demonstrates that the nodal lines of both orbitals pass near the second hydrogen. That means that small changes in the positions of nodes can significantly alter the contributions from these orbitals and even change their sign. This is why the geminal coupling was difficult to calculate.

Bacskay et al. [27] calculated the Fermi-contact term in ^2J(H–D) for molecular hydrogen complexes of Os(II) with various ligands using FPT at the density functional theory level. The calculated results were in reasonable agreement with experiment, in contrast to earlier calculations of Craw et al. performed with Hartree–Fock and MP2 methods using double finite perturbation theory [28]. Strong correlations of the calculated ^2J(H–D) values with the H–D distance and the Os–HD bond strength (defined as the energy associated with the removal of the HD ligand from the complex) were explained on the basis of SOS arguments. In the molecular hydrogen complexes of Os(II), the bonding and antibonding HD orbitals mix with the appropriate metal orbitals, reducing their s-character on H and D. Assuming that the changes in the energy denominator in Eq. (19.1) are small upon complex formation, the value of ^2J(H–D) should correlate with the strength of the metal–dihydrogen interaction, that is, a stronger metal–hydrogen bond should be accompanied by a decreased value of coupling.

Khandogin and Ziegler [4] studied M–C and M–O couplings in transition-metal complexes using the FPT DFT approach for calculations. For the interpretation of the results, they also used the sum-over-states expression for the FC contribution. Though FPT and SOS cannot be expected to give the same answer (for example, compare the SOS-DFT [21] and FPT-DFT [29] performances for various C–C and C–H couplings), for ^1J(M–O) in 3d-transition-metal tetraoxo complexes the results of the two approaches are quite close. This allowed the authors to interpret the results in terms of contributions from individual occupied MOs. The contributions from the two highest occupied orbitals (calculated with SOS) constitute about 90% of the FC value obtained with FPT. The contribution from the lower orbital is posi-

tive and about 2–3 times larger in magnitude than the HOMO (highest occupied molecular orbital) contribution, which is negative. For M–C couplings in 3d-carbonyl complexes, the picture is more complicated. While for $V(CO)_6^-$ and $Co(CO)_4^-$ the contributions from the two highest occupied orbitals sum to nearly the total FC value, for $Fe(CO)_5$ they sum to about 66% and 120% of the equatorial and axial FC couplings respectively.

Another interesting example [30] is a combination of the NBO/NLMO analysis with the SOS-HF calculation for vicinal NMR proton–proton couplings. It should be noted that in order to get quantitative agreement with experimental values, all calculated couplings were scaled according to the fitting procedure of Edison at al. [20]. The individual contributions to ^3J(H–H) were obtained in the following non-trivial way. After reaching SCF convergence, the Fock matrix was transferred to the NBO basis. The relevant off-diagonal elements (for example, those corresponding to a particular bonding–antibonding interaction) were then deleted from the Fock matrix and the new MO coefficients (still in the NBO basis) were found. After transforming the MO coefficients back to the AO basis, the coupling constant was calculated once more. The difference between the values obtained with the complete Fock matrix and with some particular interaction excluded is treated as the contribution from this interaction. It is instructive to compare the results of this analysis with the above-discussed NBO/NLMO analysis of Wilkens et al. [24] for the *trans* ^3J(H–H) coupling in ethane. Esteban et al. [30] did not find explicit Lewis contributions, in contrast to Ref. [24], where they were responsible for about 75% of the total value. According to Wilkens et al., the remaining part of the coupling was due to two bonding–antibonding interactions (of the C–H bonds of coupled protons), which gave about 35%, and a few other interactions with smaller negative contributions. Esteban et al. obtained a very different picture: virtually the entire calculated coupling constant (about 17.6 Hz) arose from only the two bonding–antibonding interactions.[2)] The discrepancy may be connected with the different accuracy of the methods employed (SOS-HF versus FPT-DFT) and with the difference in the concept of the *contribution* itself.

We see that the decomposition of the value of coupling into separate contributions is by no means unique. There is no commonly accepted point of view on the interpretation of even such a well-studied example as vicinal proton–proton coupling in ethane. Is there an alternative way to analyze the coupling without splitting its value into different components which are very much dependent on the underlying concepts? The answer will be provided in the next section.

2) It should be noted that in Ref. [30], these interactions are named as "through-space" rather than hyperconjugative (as defined in Ref. [24]).

19.4
Visualization of Coupling by Real-Space Functions

While all the approaches discussed above rely on decomposition of couplings into contributions from different sorts of orbitals, an alternative way is to look at the distribution of some functions, closely related to the coupling, in 3-D space without further separation. For example, the distribution of the spin density, obtained from FPT (or response theory), can be easily visualized. The plot will show the propagation of the spin-polarization due to the magnetic moment of the perturbed nucleus. Looking at such a picture and judging by the spin density at the positions of all other nuclei, one can immediately estimate the signs and magnitudes of all couplings with that nucleus. For example, Fig. 19.1 shows the distribution of the spin density in benzene with the center of perturbation on one of the hydrogens. Comparison with experiment shows that the signs and relative magnitudes of all couplings with this hydrogen atom are correctly reproduced. However, this kind of picture is not very useful for understanding the pathways of one particular coupling because the plot contains too much information and is not specific for any one coupling.

Another general approach for visualization is to express a given property as a three-dimensional integral. Then the integrand can be considered as a property density, and hence is a real space function that can be visualised. The plot of the property density can show us to what extent different areas of the electronic structure of the molecule are involved in the analyzed property. This general idea was thoroughly

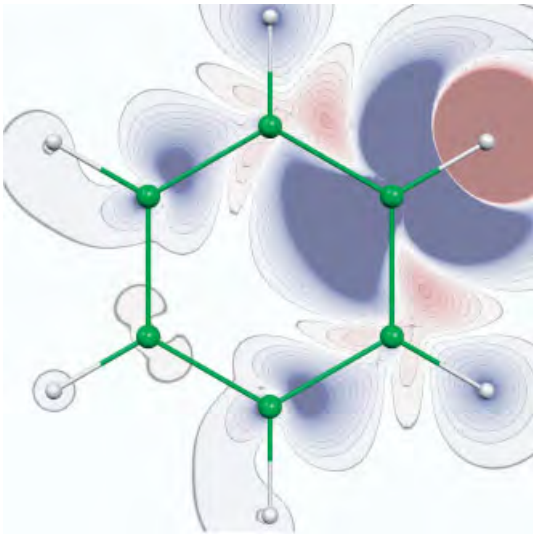

Figure 19.1 Visualization of the spin density in benzene obtained from single FPT with the center of perturbation on the hydrogen at the right upper part of the plot.

discussed by Jameson and Buckingham [31]. Moreover, using the concept of the current density induced by an external magnetic field, Jameson and Buckingham visualized nuclear magnetic shieldings. Quite recently, two different approaches for visualization of spin–spin couplings were suggested: by Soncini and Lazzeretti [32] and by Malkina and Malkin [33].

Besides using the property density, there is another possibility suggested by Malkina and Malkin [33]: namely to visualize the difference between the electron densities obtained for the same molecule but with the two nuclear spins being parallel and antiparallel. Since the electron density is an observable, it is possible, in principle, to measure both densities and thus their difference. This is an advantage in comparison with the visualization of a property density: the latter may be defined using different expressions. Below we will briefly discuss different methods for visualization of coupling.

19.4.1
Visualization Based on the Concept of the Current Density

For constructing a spin–spin coupling density, Soncini and Lazzeretti [32] used the coupled Hartree–Fock (CHF) computational scheme (see Chapter 7). Similar to the approach of Jameson and Buckingham, the concept of the current density, this time induced by the nuclear magnetic dipole, was employed. Although the densities of all four contributions (FC, PSO, DSO and SD) were considered, most attention was paid to the Fermi-contact coupling density dominating for one- and two-bond couplings in CH_4, NH_3, H_2O, and HF. The spin–spin coupling densities were plotted as three-dimensional perspectives and contour maps in the plane 0.2 Bohr above the formal "through-bond" path. The couplings were characterized by the sequence of spike-up and spike-down patterns along the bonds involving the coupled nuclei. Soncini and Lazzeretti rationalized the patterns in the language of the Fermi correlation. Their explanation is in accordance with the Dirac vector model. No molecular orbitals were involved in the interpretation of spin–spin couplings in this work. It was found that the intensities of peaks depended on the electronegativity of the heavier atom.

The visualization approach of Soncini and Lazzeretti appeared only recently and, to the best of our knowledge, it has not been applied yet for different types of couplings (e.g. through multiple bonds) or to distinguish between "through-bond" and "through-space" interactions. The approach is interesting, though its real usefulness still remains to be seen. However, at least one possible shortcoming can be indicated even now. The expression for the coupling density derived in that work [32] is not symmetric with respect to the coupled nuclei: it contains the current density induced only by one of the two interacting magnetic dipoles. Therefore, from the physical point of view, the straightforward picture following from this expression is not completely correct. The authors suggested to symmetrize the integrand by taking the half sum of the two expressions containing different current densities (due to one of the coupled nuclei). It is not clear whether the artificial symmetrization fully restores the correctness of the picture.

19.4.2
Visualization Based on the Double Finite Perturbation Theory

In 1979, for calculation of spin–spin couplings at the CI (configuration interaction) level, Kowalewski et al. [34] proposed an elegant idea in which both coupled nuclei are treated on an equal basis. In this approach, called double finite perturbation theory (DFPT), the FC operators on both coupled nuclei are included in the Hamiltonian simultaneously. The value of the coupling constant is proportional to the bilinear derivative of the total energy with respect to the nuclear magnetic moments, which in DFPT is calculated numerically:

$$J_{MN} = \left.\frac{\partial^2 E(\lambda_M, \lambda_N)}{\partial\lambda_M \partial\lambda_N}\right|_{\lambda_M=\lambda_N=0} \approx \frac{E(\lambda_M, \lambda_N) - E(\lambda_M, -\lambda_N)}{2\lambda_M\lambda_N} \tag{19.6}$$

(here the magnetic moments of the coupled nuclei M and N are considered as perturbation parameters λ_M and λ_N, respectively). In other words, the calculation of one coupling constant requires two SCF steps, for the parallel (λ_M and λ_N of the same sign) and antiparallel (λ_M and λ_N of opposite signs) orientations of the magnetic moments of the interacting nuclei. From the computational point of view, DFPT is less practical than single FPT where one SCF step gives couplings of one nucleus (chosen as a center of perturbation) with all others. However, DFPT is valuable as a basis for interpretation because it faithfully describes the underlying physics: the coupling constant is a probe of the energy splitting between the states with parallel and antiparallel nuclear spins. Moreover, since both Fermi-contact operators are included simultaneously, the picture obtained from DFPT reflects the real *interaction* of the operators and no artificial symmetrization is needed.

If the total energies from both SCF calculations are written as three-dimensional integrals, then the difference of the integrands gives the coupling energy density ε_{MN} (CED) multiplied by a proper coefficient:

$$J_{MN} = \int \frac{\varepsilon(\lambda_M, \lambda_N) - \varepsilon(\lambda_M, -\lambda_N)}{2\lambda_M\lambda_N} dV = \frac{\hbar}{2\pi}\gamma_M\gamma_N \int \varepsilon_{MN}(r) dV \tag{19.7}$$

The integral of CED over space is equal to the reduced coupling constant. Actually, CED is also a property density in the sense used by Jameson and Buckingham [31], though different from the coupling density of Soncini and Lazzeretti [32]. The plot of CED can clearly show the coupling pathways. For example, Fig. 19.2 illustrates the different mechanisms ("through-space" and "through-bond") of ^2J(P–P) in bis(-difluorophosphino)methylamine. In this and the following plots, blue and red colors correspond to positive and negative function values, respectively. The relative importance of different pathways may be judged by intensities and volumes. Figure 19.2 clearly demonstrates that a considerable pathway goes "through space" (the area of the lone pairs of the phosphorus atoms), but the "through-bond" interaction is also important. It is interesting to note that a significant amount of CED is located out-

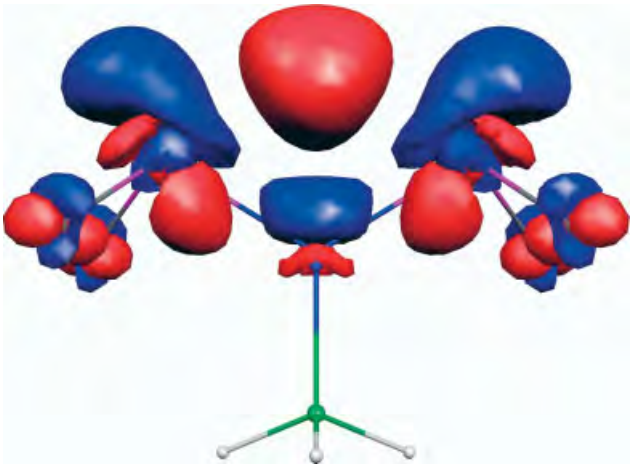

Figure 19.2 Visualization of ^2J(P–P) coupling energy density (CED) in bis(diflurophosphino)methylamine.

side the formal pathways of the interaction (mostly in the area of fluorine lone pairs). It suggests that substitution of fluorine atoms by hydrogens or other atoms/groups without lone pairs may change the value of the P–P coupling noticeably.

Besides CED, DFPT can provide another real-space function, the coupling deformation density (CDD), as a useful tool for the interpretation of spin–spin couplings:

$$\rho_{MN}(r) = \frac{\rho(\lambda_M, \lambda_n, \mathbf{r}) - \rho(\lambda_M, -\lambda_N, \mathbf{r})}{\lambda_M \lambda_N} \tag{19.8}$$

where ρ (λ_M, λ_N, **r**) and ρ (λ_M, $-\lambda_N$, **r**) are the electron densities for parallel and antiparallel orientation of nuclear spins. The topologies of CED and CDD are very similar [33]. Nevertheless, it should be noted that, in contrast to CED, the integral of CDD over space is equal to zero (the integral of CED over space is equal to the reduced coupling constant). As an example of CDD, the paths of the spin–spin interaction for ^5J(H–H) in benzene are presented in Fig. 19.3. From the comparison of Figs. 19.1 and 19.3 one can easily see that the information obtained from single and double FPT is different and somewhat complementary. The latter shows the defined pathways only for one particular coupling but contains no information about other couplings.

The visualization of couplings can thus provide a picture of spin–spin interaction without involving any molecular orbitals or other auxiliary chemical or physical concepts. Furthermore, both CDD and CED allow one to perform further analysis with decomposition of CDD or CED into individual contributions. The space within a molecule can be divided into smaller basins according to Bader's "atoms in molecules" approach [35] or with the help of the electron localization function (ELF) [36]. The integral of CED over a basin will then give the contribution of this particular

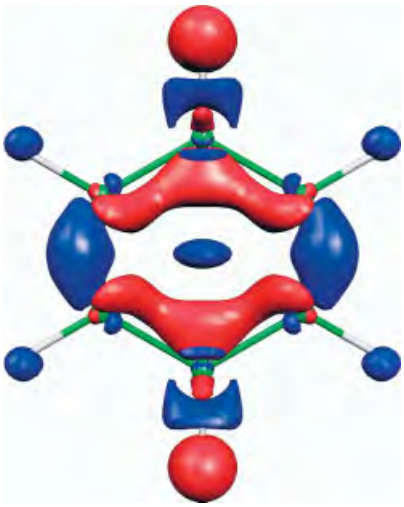

Figure 19.3 Visualization of ^{5}J(H–H) coupling electron deformation density (CDD) in benzene.

basin to the coupling constant. For example, for the *trans* ^{3}J(H–H) in ethane[3)], the CED contributions from the ELF basins are as follows [37]: the carbon core regions together give about +10 Hz and the C–H bonds containing coupled hydrogens have the largest contribution of +68 Hz, while the other four C–H bonds give only 2 Hz. The area of the C–C bond gives a negative contribution of about –65.5 Hz.

CDD, being the difference of two electron densities, can be naturally analyzed in terms of canonical, localized, or any other type of molecular orbitals including NBOs and NLMOs [25]. One possibility is the least squares fit of CDD by a linear combination of the products of pairs of the unperturbed molecular orbitals (both occupied and vacant) that are obtained from the SCF calculation with the unperturbed Hamiltonian. Mathematically, this procedure is simply reduced to the fit of the CDD density matrix by a linear combination of the density matrices corresponding to the products of MOs. Interesting insights are provided by visualization of the *trans* ^{3}J(H–H) coupling in ethane (see Fig. 19.4) – an example where different MO-based analyses lead to different conclusions, as discussed above. The origin of the mismatch in the interpretations is quite obvious, the red lobes which lie between C–C and C–H bonds. Different schemes of localization and analyses would assign them to different bonds, leading to different conclusions. Our new analysis of CDD in terms of pairs of MOs shows, however, that for qualitative interpretation of these areas of the overall CDD picture one has to take into account not only seven bonding and seven antibonding MOs (as one might expect for this molecule) but also seven vacant molecular orbitals lying above the antibonding MOs [38].

3) The plot of CED is not shown here but it is very similar to the CDD picture in Fig. 19.4.

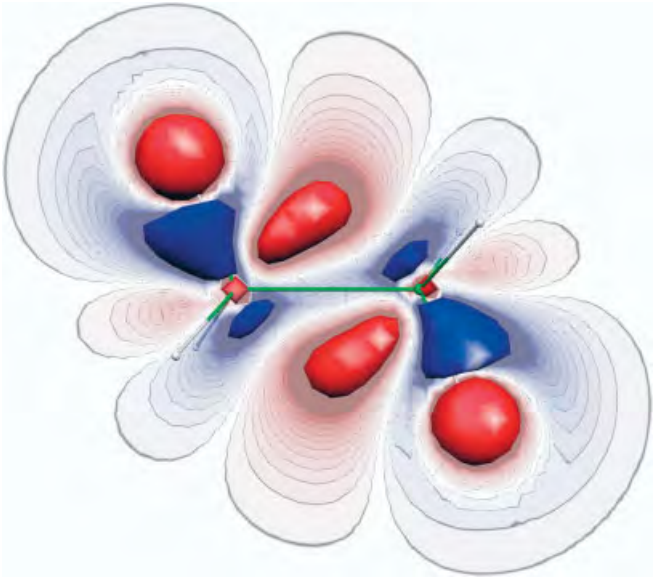

Figure 19.4 Visualization of *trans* ^3J(H–H) coupling electron deformation density (CDD) in ethane.

19.5 Conclusions

Many different tools for the interpretation of spin–spin coupling constants are available. Different perturbation theories used for the analysis have their advantages and disadvantages. The interpretation is not unique and depends on the underlying concepts. Recently developed approaches for the visualization of spin–spin coupling pathways give new insight into the complex phenomenon of spin–spin coupling.

Acknowledgment

The author is very grateful to Vladimir Malkin and Martin Kaupp for numerous and helpful discussions, and for their patience as editors of the book. James Asher is thanked for critical reading of the manuscript. Financial support from the Slovak grant agency VEGA (No. 2/3103/23) is also acknowledged.

References

1 S. A. Perera, H. Sekino, R. J. Bartlett, *J. Chem. Phys.* **1994**, *101*, 2186.
2 J. Geertsen, J. Oddershede, G. E. Scuseria, *Int. J. Quantum Chem. Symp.* **1987**, *21*, 475.
3 O. L. Malkina, unpublished results; DFT with Perdew-86 exchange-correlation functional, IGLO-III basis set.
4 J. Khandogin, T. Ziegler, *Spectrochim. Acta, Part A* **1999**, *55*, 607.
5 R. K. Harris, *Nuclear Magnetic Resonance Spectroscopy*, Pitman, London **1983**.
6 B. J. Kimber, J. Feeney, G. C. K. Roberts et al., *Nature* **1978**, *271*, 184.
7 E. Duval, S. Koide, *Phys. Lett.*, **1964**, *8*, 314.
8 J. A. Pople, A. A. Bothner-By, *J. Chem. Phys.* **1965**, *42*, 1339.
9 M. Barfield, M. Karplus, *J. Amer. Chem. Soc.* **1969**, *91*, 1.
10 N. F. Ramsay, *Phys. Rev.* **1953**, *91*, 303.
11 J. A. Pople, J. W. McIver Jr., N. S. Ostlund, *Chem. Phys. Lett.* **1967**, *1*, 465.
12 J. A. Pople, D. P. Santry, *Mol. Phys.* **1964**, *8*, 1.
13 V. M. S. Gil, W. von Philipsborn, *Magn.Reson. Chem.*, **1989**, *27*, 409.
14 J. G. Verkade, *Coord. Chem. Rev.* **1972/1973**, *9*, 1.
15 P. S. Pregosin, R. W. Kunz, *^{31}P and ^{13}C NMR* of Transition Metal Phosphine Complexes, Springer-Verlag, Berlin **1979**.
16 C. A. Coulson, H. C. Longuet-Higgins, *Proc. R. Soc. London, Ser. A* **1947**, *191*, 39.
17 L. Pauling, *J. Chem. Phys.* **1933**, *1*, 280.
18 W. G. Penney, *Proc. R. Soc. London, Ser. A* **1937**, *158*, 306.
19 D. Clarkson, C. A. Coulson, T. H. Goodwin, *Tetrahedron* **1963**, *19*, 2153.
20 A. S. Edison, J. L. Markley, F. Weinhold, *J. Phys. Chem.* **1993**, *97*, 11657.
21 P. Bouř, M. Buděšínský, *J. Chem. Phys.* **1998**, *110*, 2836.
22 O. L. Malkina, D. R. Salahub, V. G. Malkin, *J. Chem. Phys.* **1996**, *105*, 8793.
23 M. L. Munzarová, V. Sklenář, *J. Am. Chem. Soc.* **2002**, *124*, 10666.
24 S. J. Wilkens, W. M. Westler, J. L. Markley et al., *J. Am. Chem. Soc.* **2001**, *123*, 12026.
25 F. Weinhold, in *Encyclopedia of Computational Chemistry*, eds. P. v. R. Schleyer, N. L. Allinger, P. A. Kollman et al., Wiley, Chichester **1998**, Vol. 3, pp. 1792.
26 E. A. Armour, A. J. Stone, *Proc. R. Soc. London, Ser. A* **1967**, *302*, 25.
27 G. B. Bacskay, I. Bytheway, N. S. Hush, *J. Am. Chem. Soc.* **1996**, *118*, 3753.
28 J. S. Craw, G. B. Bacskay, N. S. Hush, *J. Am. Chem. Soc.* **1994**, *116*, 5937.
29 V. G. Malkin, O. L. Malkina, D. R. Salahub, *Chem. Phys. Lett.* **1994**, *221*, 91.
30 A. L. Esteban, M. P. Galache, F. Mora et al., *J. Phys. Chem. A* **2001**, *105*, 5298.
31 C. J. Jameson, A. D. Buckingham, *J. Chem. Phys.* **1980**, *73*, 5684.
32 A. Soncini, P. Lazzeretti, *J. Chem. Phys.* **2003**, *118*, 7165.
33 O. L. Malkina, V. G. Malkin, *Angew. Chem. Int. Ed. Engl.* **2003**, *42*, 4335.
34 J. Kowalewski, A. Laaksonen, B. Roos et al., *J. Chem. Phys.* **1979**, *71*, 2896.
35 R. F. W. Bader, *Atoms in Molecules – A Quantum Theory*, Oxford University Press, Oxford **1990**.
36 A. Savin, R. Nesper, S. Wengert et al., *Angew. Chem.* **1997**, *109*, 1892.
37 O. L. Malkina, A. Patrakov, M. Kaupp, unpublished results.
38 O. L. Malkina, unpublished results.

20
First-Principles Calculations of Paramagnetic NMR Shifts

Seongho Moon and Serguei Patchkovskii

20.1
Introduction

The importance of nuclear magnetic resonance (NMR) spectroscopy for studies of paramagnetic species, particularly in biomolecules, cannot be overestimated [1–3]. Paramagnetic NMR (PNMR) spectra serve as the source of long-range structural data (available through the pseudocontact shift δ^{PC}) [4–6] and provide a sensitive probe of the magnitudes and signs of the spin density distributions (through the Fermi contact shifts δ^{FC}) [7, 8]. With the continuing experimental advances in the field of paramagnetic NMR [2, 3], its value can only increase in the future.

In the analysis of PNMR spectra, experimental chemical shift is customarily decomposed into three parts: the "reference" (or "orbital") shift δ^{orb}, the Fermi contact shift δ^{FC}, and pseudocontact shift δ^{PC}:

$$\delta = \delta^{orb} + \delta^{FC} + \delta^{PC} \tag{20.1}$$

The reference shift δ^{orb} is analogous to the usual NMR chemical shift in diamagnetic systems (see Chapter 6). This term is approximately temperature-independent and is usually taken to be equal to the chemical shift in a similar diamagnetic environment.

The contact shift δ^{FC} arises from the Fermi contact interaction between the nuclear magnetic moment, and the average spin density at the location of the nucleus. In the simplest case, it is given by [9]:

$$\delta^{FC} = A_{iso} \frac{\bar{g}\beta_e S(S+1)}{g_I \beta_N 3kT} \tag{20.2}$$

In Eq. (20.2), A_{iso} is the isotropic hyperfine coupling constant, $\bar{g}$ is the rotationally averaged electronic g-value, g_I is the nuclear g-value, β_e and β_N are the Bohr and nuclear magnetons, respectively. The multiplicity of the electronic state is given by $(2S+1)$, while kT represents the thermal energy.

The pseudocontact shift δ^{PC} arises due to the long-range dipolar interaction between the induced magnetic moment at the radical site, and the nuclear magnetic moment. In the simplest form, it is given by [10]:

Calculation of NMR and EPR Parameters. Theory and Applications.
Edited by Martin Kaupp, Michael Bühl, Vladimir G. Malkin
Copyright © 2004 WILEY-VCH Verlag GmbH & Co. KGaA, Weinheim
ISBN: 3-527-30779-6

$$\delta^{PC} = \frac{\beta_e^2 S(S+1)}{3kT} \frac{(3\cos^2 \Omega - 1)}{R^3} F(g) \tag{20.3}$$

If the radical centre is taken at the coordinate origin, Ω is the angle between its principal symmetry axis, and the direction to the nucleus of interest. The distance between the induced magnetic moment and the nucleus is given by R. Finally, $F(g)$ is an algebraic function of the g-tensor components, which subsumes the relative magnitudes of various relaxation times. In more complicated situations, the pseudocontact term can also exhibit T^{-2} temperature dependence [11, 12].

Despite the remarkable progress made in the field of the first-principles calculations of NMR parameters (See Ref. [13] and other chapters of this book), the simple, „back of the envelope" equations (20.1)–(20.3) still form the mainstay of both the experimental and theoretical approaches to the paramagnetic NMR shifts. (However, see Refs. [11, 12, 14–20] for some counterexamples.) This is hardly surprising, given that the published paramagnetic NMR expressions are often geared for a specific class of radicals [12, 14–16, 20], and can be rather laborious (but enlightening) in their practical application [14–16].

The aim of this chapter is to show that the development of the first-principles approaches to NMR and EPR parameters (and particularly, the EPR g-tensor and hyperfine A-tensor) has reached the stage, where completely non-empirical prediction of the PNMR chemical shifts is finally becoming possible. The rest of this chapter is organized as follows: Section 20.2 introduces a complete, general expression for the paramagnetic NMR shielding and gives the recipe for practical calculations. In Section 20.3, a special case (spatially non-degenerate Kramers doublet) is considered in more detail. Section 20.4 presents selected numerical results, while Section 20.5 provides the summary and outlines possible future developments.

20.2
Paramagnetic Shielding Tensor: The General Case Treatment

In the theoretical analysis of the open-shell NMR shielding tensor σ_{ab}, it is advantageous to separate the electronic Hamiltonian into four parts:

$$\hat{H} = \hat{H}^o + \hat{H}^B + \hat{H}^\mu + \hat{H}^{\mu,B} \tag{20.4}$$

The field- and nuclear spin-free part $\hat{H}^o$ is given by (atomic units) [21]:

$$\hat{H}^o = \sum_j -\frac{1}{2}\nabla_j^2 - \sum_{j,n} \frac{Z_n}{|\vec{r}_j - \vec{R}_n|} + \sum_{j<k} \frac{1}{|\vec{r}_j - \vec{r}_k|} \tag{20.5}$$

where indices j and k refer to electrons, and index n goes over the (fixed) nuclei, with their charges given by Z_n. In systems with significant spin–orbit (SO) interaction, field free spin–orbit (SO) operators (Eqs. (32.6), (32.8) and (32.9) of Chapter 32) will also appear in $\hat{H}^o$.

The operator $\hat{H}^B$ collects all terms linear in the magnetic field strength $\vec{B}$. At the minimum, it will include the orbital Zeeman and electron spin Zeeman operators [21]:

$$\hat{H}^B = \frac{\alpha}{2}\sum_j \left[(\vec{r}_j \times \hat{\vec{p}}_j)\cdot\vec{B} + g_e \hat{\vec{s}}_j \cdot \vec{B}\right] \tag{20.6}$$

Here, α is the fine structure constant ($\alpha = 2\beta_e = 1/c$ in atomic units, where $c \approx 137.04$ is the speed of light). Operators $\hat{\vec{p}}_j$ and $\hat{\vec{s}}_j$ refer to the momentum and spin of an electron j, respectively. Factor g_e is the free-electron g-value ($g_e \approx 2.0023$). If the SO coupling operators are included in Eq. (20.5), corresponding gauge corrections should appear in Eq. (20.6) as well [21].

The operator $\hat{H}^\mu$ includes the terms linear in the nuclear magnetic moment $\vec{\mu}_I = g_I \beta_N \hat{\vec{I}}$, where $\hat{\vec{I}}$ is the nuclear spin operator. At the least, the dipolar and Fermi contact hyperfine operators should be considered [21]:

$$\hat{H}^\mu = -\frac{\alpha}{2} g_e \sum_j \left(\frac{\hat{\vec{s}}_j \cdot \vec{\mu}_I}{|\vec{r}_j - \vec{R}_\mu|^3} - 3\frac{(\hat{\vec{s}}_j \cdot (\vec{r}_j - \vec{R}_\mu))(\vec{\mu}_I \cdot (\vec{r}_j - \vec{R}_\mu))}{|\vec{r}_j - \vec{R}_\mu|^5} \right) + \frac{4\pi\alpha}{3} g' \sum_j \hat{\vec{s}}_j \cdot \vec{\mu}_I \delta(\vec{r}_j - \vec{R}_\mu) \tag{20.7}$$

where g' is the spin–orbit g-factor ($g' = 2g_e - 2$). Coordinates of the magnetic moment $\vec{\mu}_I$ are given by $\vec{R}_\mu$. Please see Ref. [21] and Chapters 29 and 30 for other relevant contributions to this operator.

Finally, the operator $\hat{H}^{\mu,B}$ includes the terms bilinear in $\vec{B}$ and $\vec{\mu}$. The minimal treatment must include at least the nuclear Zeeman gauge (diamagnetic) correction [21]:

$$\hat{H}^{\mu,B} = \frac{\alpha^2}{2}\sum_j \frac{(\vec{r}_j \cdot (\vec{r}_j - \vec{R}_\mu))(\vec{\mu}_I \cdot \vec{B}) - (\vec{r}_j \cdot \vec{\mu}_I)((\vec{r}_j - \vec{R}_\mu)\cdot\vec{B})}{|\vec{r}_j - \vec{R}_\mu|^3} \tag{20.8}$$

Further, we assume that the total energies of low-lying, thermally accessible electronic states E_k are known at least through the terms linear and bilinear in $\vec{B}$ and $\vec{\mu}$:

$$E_k(B,\mu) = E_k^{(0,0)} + \sum_a E_k^{(a,0)} B_a + \sum_b E_k^{(0,b)} \mu_b + \sum_{a,b} E_k^{(a,b)} B_a \mu_b \tag{20.9}$$

$$E_k^{(a,0)} = \left(\frac{\partial E_k}{\partial B_a}\right)_{\vec{\mu}=\vec{B}=0} \tag{20.10}$$

$$E_k^{(0,b)} = \left(\frac{\partial E_k}{\partial \mu_b}\right)_{\vec{\mu}=\vec{B}=0} \tag{20.11}$$

$$E_k^{(a,b)} = \left(\frac{\partial^2 E_k}{\partial B_a \partial \mu_b}\right)_{\vec{\mu}=\vec{B}=0} \tag{20.12}$$

The means of calculating the derivatives (20.10)–(20.12) are discussed elsewhere [13, 22, 23]. For most systems of practical interest, the second term in Eq. (20.9) is gen-

erally comparable to the thermal energy kT, while the third and the fourth terms are small, compared to both kT, and the second term.

A subtle, but important point is related to the choice of the wavefunctions, used for the evaluation of the derivatives (20.10)–(20.12). The derivatives of E_k with respect to the "small" perturbation $\vec{\mu}$ must be taken for the eigenstates of the Hamiltonian, adapted to the "large" perturbation $\vec{B}$. For example, the total energy E must include the electronic Zeeman operators (Eq. (20.6)) variationally, but the hyperfine terms (Eq. (20.7)) only through the first order [9]. The derivatives $E_k^{(0,b)}$ are then implicitly dependent on the direction of the (formally zero) magnetic field $\vec{B}$ (See Section 20.3 for a practical example).

Assuming that the electronic energy levels are in a thermal equilibrium, the average energy for fixed values of B and μ is given by:

$$\langle E(B,\mu)\rangle = \frac{\sum_k E_k(B,\mu)e^{-W_k(B,\mu)/kT}}{\sum_k e^{-W_k(B,\mu)/kT}} \tag{20.13}$$

Because of the different time scales of the nuclear and electron spin relaxation, the Boltzmann energy factors W_k in Eq. (20.13) are not necessarily identical to E_k. For the moment, it is sufficient to assume that $W_k(B,\mu)$ can be expanded similarly to Eqs. (20.9)–(20.12).

As an example, consider a system of one unpaired electron (S=1/2), and one nuclear magnetic moment (I=1/2). The electron and nuclear spins are coupled to a heat bath, with the relaxation times T_S and T_I, respectively. If $T_S << T_I$ (as is usually the case), equilibrium state populations are determined by the faster process alone [24], and $W_k(B,\mu)$ will show no dependence on the nuclear magnetic moment. In more complicated cases, density matrix methods can be used to calculate equilibrium state populations [25]. Such simulations require detailed knowledge of the relaxation processes in the system, and are therefore beyond the scope of this chapter.

Assuming that the equilibrium implied by Eq. (20.13) is fast on the NMR time scale, the average components of the absolute NMR shielding tensor σ_{ab} are given by:

$$\sigma_{ab} = \left(\frac{\partial^2}{\partial B_a \partial \mu_b}\langle E(B,\mu)\rangle\right)_{\vec{\mu}=\vec{B}=0} \tag{20.14}$$

After straightforward, but tedious algebra, this derivative is given by:[1)]

$$\sigma_{ab} = \left\langle E^{(a,b)} \right\rangle_0 \tag{20.15a}$$

$$-\frac{1}{kT}\left\langle E^{(0,b)}\, W^{(a,0)} \right\rangle_0 \tag{20.15b}$$

$$-\frac{1}{kT}\left\langle E^{(a,0)}\, W^{(0,b)} \right\rangle_0 \tag{20.15c}$$

$$-\frac{1}{kT}\left[\left\langle E^{(0,0)}\, W^{(a,b)} \right\rangle_0 - \left\langle E^{(0,0)} \right\rangle \left\langle W^{(a,b)} \right\rangle_0\right] \tag{20.15d}$$

$$+\frac{1}{(kT)^2}\left[\left\langle E^{(0,0)}\, W^{(a,0)}\, W^{(0,b)} \right\rangle_0 - \left\langle E^{(0,0)} \right\rangle \left\langle W^{(a,0)}\, W^{(0,b)} \right\rangle_0\right] \tag{20.15e}$$

In Eq. (20.15), the averages are taken in the absence of magnetic fields:

$$\langle X \rangle_0 = \frac{\sum_k X_k e^{-W_k^{(0,0)}/kT}}{\sum_k e^{-W_k^{(0,0)}/kT}} \tag{20.16}$$

The first term (20.15a) is simply the Boltzmann average of the familiar, orbital NMR shielding tensor. The second term (20.15b) describes the interaction of the nuclear magnetic moment with the average spin-density, induced by the orbital- and electron spin-Zeeman interactions. The remaining three terms (20.15c)–(20.15e) arise from the changes in the electronic state populations, induced by flipping the nuclear spin. Under the conditions where the nuclear relaxation time is sufficiently long to allow direct observation of the NMR transition, thermal populations of the electronic states are determined solely by the orbital and electron spin-Zeeman interactions [9–11], so that:

$$W^{(0,b)} = W^{(a,b)} = 0 \tag{20.17}$$

1) Formal differentiation of Eq. (20.14) leads to the following terms, in addition to the contributions shown in Eqs. (20.15a–e):

$$+\frac{1}{kT}\left\langle W^{(a,0)} \right\rangle_0 \left\langle E^{(0,b)} \right\rangle_0 + \frac{1}{kT}\left\langle W^{(0,b)} \right\rangle_0 \left\langle E^{(a,0)} \right\rangle_0$$
$$-\frac{1}{(kT)^2}\left\langle W^{(a,0)} \right\rangle_0 \left\langle E^{(0,0)}\, W^{(0,b)} \right\rangle_0 - \frac{1}{(kT)^2}\left\langle W^{(0,b)} \right\rangle_0 \left\langle E^{(0,0)}\, W^{(a,0)} \right\rangle_0$$
$$+\frac{2}{(kT)^2}\left\langle E^{(0,0)} \right\rangle_0 \left\langle W^{(a,0)} \right\rangle_0 \left\langle W^{(0,b)} \right\rangle_0$$

Symmetry with respect to time reversal guarantees that all states contributing to Eq. (20.16) are either: a) unchanged by the magnetic field to the first order; or b) appear in pairs, which are degenerate at the zero magnetic field. In the presence of the field, the energies of the latter (Kramers) pairs are shifted by equal amount, and in the opposite direction. As a result, the averages $\left\langle E^{(a,0)} \right\rangle_0$, $\left\langle W^{(a,0)} \right\rangle_0$, and $\left\langle E^{(0,0)}\, W^{(a,0)} \right\rangle_0$ must vanish, so that the terms above do not contribute to the final Eq. (20.15).

Finally, if the electron spin relaxation is faster than any spatial reorientation process (the so-called „solid state case" [9, 11]), derivatives of the Boltzmann energy factors and the electronic energy with respect to the external field strength coincide:

$$W^{(a,0)} = E^{(a,0)} \tag{20.18}$$

Substituting Eqs. (20.17) and (20.18) into Eq. (20.15), we obtain the working equation for the paramagnetic shielding tensor:

$$\sigma_{ab} = \left\langle E^{(a,b)} \right\rangle_0 - \frac{1}{kT} \left\langle E^{(0,b)} E^{(a,0)} \right\rangle_0 \tag{20.19}$$

In Eq. (20.19), the second term is equivalent to the general-case expression of Kurland and McGarvey [11]. The first term is the generalization of the orbital contribution of Rinkevicius et al. [20]. To the best of our knowledge, Eq. (20.19) represents the first complete, universal treatment of the paramagnetic shielding tensor.

Practical calculations of the paramagnetic shielding tensor can proceed as follows: First, energies and wavefunctions for all thermally accessible electronic states must be determined, in the absence of magnetic fields. For each of the states,[2)] the orbital NMR shielding tensor defines $E_k^{(a,b)}$. The EPR *g*-tensor determines $E_k^{(a,0)}$, while the hyperfine *A*-tensor leads to $E_k^{(0,b)}$. The Boltzmann averages in Eq. (20.19) then fully determine the paramagnetic NMR shielding tensor. Obviously, each of the ingredients in Eq. (20.19) can be treated independently, using the most suitable theoretical technique. A similar prescription was previously given by Lohr, Miller, and Sharp [16], within the ligand field theory.

20.3 Paramagnetic Shielding for an Isolated Kramers Doublet State

A doubly degenerate electronic ground state (S=1/2), with no thermally accessible electronically excited states, represents the simplest possible case for calculations of paramagnetic NMR shieldings. The structure of the energy levels for such system can be summarized by an effective spin Hamiltonian (see Chapter 4):

$$\hat{H} = -\vec{B} \cdot (1 - \boldsymbol{\sigma}^{orb}) \cdot \vec{\mu}_I + \beta_e \vec{B} \cdot \mathbf{g} \cdot \hat{S} + \frac{1}{g_I \beta_N} \vec{\mu}_I \cdot \mathbf{A} \cdot \hat{S} \tag{20.20}$$

The orbital nuclear shielding tensor $\boldsymbol{\sigma}^{orb}$, electronic paramagnetic resonance *g*-tensor, and the hyperfine coupling tensor *A* are discussed elsewhere in this book.

In the absence of nuclear magnetic moment ($\vec{\mu}_I$=0 in Eq. (20.20)), the energy levels of this Hamiltonian are given by Eq. 32.2 in Chapter 32. Differentiation with respect to the magnetic field strength gives:

2) For high-spin states with significant (compared to kT) zero-field splitting (ZFS), each degenerate subset has to be treated separately. For example, a triplet state can be treated as a combination of an effective doublet and an effective singlet (see Ref. 26).

$$E_m^{(a,0)} = m\beta_e\left(g_{ax}^2 + g_{ay}^2 + g_{az}^2\right)^{1/2} \tag{20.21}$$

In Eq. (20.21), the magnetic quantum number m can take values of ±1/2, while a specifies the direction of the external magnetic field (a=x, y, z).

The corresponding eigenvectors, for magnetic field applied in the direction $\vec{\xi}$ ($\vec{\xi} = \vec{B}/|B|$), can be obtained by diagonalizing the Hamiltonian matrix in the basis of the electronic α, β-spin functions. The resulting eigenvectors are given by [21]:

$$U(\vec{\xi}) = \left(U_{+1/2}, U_{-1/2}\right) = \begin{pmatrix} \cos\varphi & -\sin\varphi \cdot e^{-i\chi} \\ \sin\varphi \cdot e^{i\chi} & \cos\varphi \end{pmatrix} \tag{20.22}$$

where the angles φ and χ are defined as [21]:

$$\varphi = \frac{1}{2}\mathrm{atan}\left(\frac{\sqrt{G_x^2+G_y^2}}{G_z}\right) \tag{20.23}$$

$$\chi = \mathrm{atan}\left(\frac{G_y}{G_x}\right) \tag{20.24}$$

$$G_c = \left(\vec{\xi}\cdot\mathbf{g}\right)_c, \qquad c = x, y, z \tag{20.25}$$

The hyperfine contribution to the effective spin Hamiltonian, for nuclear magnetic moment oriented along the direction $\vec{\zeta}$ ($\vec{\zeta} = \vec{\mu}_I/|\mu_I|$) in the same α, β basis is given by:

$$\hat{H}_{hf} = \frac{\mu_I}{2g_I\beta_N}\begin{pmatrix} A_z & A_x - iA_y \\ A_x + iA_y & A_z \end{pmatrix} \tag{20.26}$$

$$A_c = \left(\vec{\zeta}\cdot\mathbf{A}\right)_c, \qquad c = x, y, z \tag{20.27}$$

Taking the expectation value of $\hat{H}_{hf}$ for the eigenfunctions of the g-only Hamiltonian (Eq. (20.22)), and differentiating with respect to the nuclear magnetic moment, we obtain the first-order hyperfine contributions as:

$$E_m^{(0,b)} = \frac{m}{g_I\beta_N}\frac{\left(A_{bx}g_{ax} + A_{by}g_{ay} + A_{bz}g_{az}\right)}{\sqrt{g_{ax}^2+g_{ay}^2+g_{az}^2}} \tag{20.28}$$

In Eq. (20.28), the external magnetic field is taken along axis a (a = x, y, z), thus defining the composition of the electronic eigenfunctions (Eq. (20.21)).

The final ingredient, required to evaluate the averages in Eq. (20.19), is the mixed derivative with respect to the magnetic field strength $\vec{B}$ and nuclear magnetic moment $\vec{\mu}_I$. This is given simply by:

$$E_m^{(a,b)} = \sigma_{ab}^{orb} \tag{20.29}$$

(We exclude the nuclear Zeeman contribution $-\vec{\mu}_I \cdot \vec{B}$, to be consistent with the definition of Eq. (20.6)). Both $m = 1/2$ and $m = -1/2$ states will lead to the same $E^{(a,b)}$ derivative.

In the absence of magnetic fields, the $m = \pm 1/2$ levels are exactly degenerate and must be taken with the same weight. Combining all contributions (Eqs. (20.21), (20.28) and (20.29), we finally obtain:

$$\boldsymbol{\sigma} = \boldsymbol{\sigma}^{orb} - \frac{\beta_e}{4kTg_I\beta_N}\mathbf{g}\cdot\mathbf{A}^T \tag{20.30}$$

where the superscript ^{T} denotes a matrix transpose. It is often useful to consider the isotropic and traceless parts of the *g* and *A* tensors separately:

$$g_{iso} = \frac{1}{3}Tr(\mathbf{g}) \tag{20.31}$$

$$\tilde{\mathbf{g}} = \mathbf{g} - g_{iso}\mathbf{1} \tag{20.32}$$

$$A_{iso} = \frac{1}{3}Tr(\mathbf{A}) \tag{20.33}$$

$$\mathbf{A}_{dip} = \mathbf{A} - A_{iso}\mathbf{1} \tag{20.34}$$

In this case, the PNMR shielding tensor is given by:

$$\boldsymbol{\sigma} = \boldsymbol{\sigma}^{orb} - \frac{\beta_e}{4kTg_I\beta_N}\left(g_{iso}A_{iso}\mathbf{1} + A_{iso}\tilde{\mathbf{g}} + g_{iso}\mathbf{A}_{dip}^T + \tilde{\mathbf{g}}\cdot\mathbf{A}_{dip}^T\right) \tag{20.35}$$

The first term in brackets is identical to the McConnell's contact shift (Eq. (20.2)). The next contribution represents the anisotropic part of the contact shift (already pointed out by McGarvey [14]). Both this and the third term ($g_{iso}\mathbf{A}_{dip}^T$) are traceless. Finally, the $\tilde{\mathbf{g}}\cdot\mathbf{A}_{dip}^T$ contribution arises due to the interaction between the anisotropic parts of the **g** and **A** tensors and can contain an isotropic part, the pseudocontact shift.

The isotropic PNMR shielding takes a particularly simple form in the coordinate system where **g** is diagonal, with the principal components given by g_1, g_2 and g_3:

$$\sigma_{iso} = \sigma_{iso}^{orb} - \frac{\beta_e}{4kTg_I\beta_N}g_{iso}A_{iso} - \frac{\beta_e}{12kTg_I\beta_N}\left(g_1A_{dip,11} + g_2A_{dip,22} + g_3A_{dip,33}\right) \tag{20.36}$$

where the first, second, and third terms represent the orbital, Fermi contact, and pseudocontact contributions. In Eq. (20.36), the traceless hyperfine tensor $\mathbf{A}_{dip}$ must be taken in the coordinate system diagonalizing the *g*-tensor, so that the diagonal components $\mathbf{A}_{dip,ii}$ may not coincide with the principal components of the $\mathbf{A}_{dip}$ tensor.

20.4
Practical Applications

Due to the complexity of the PNMR shielding tensor, most practical calculations of this property, traditionally rely on semi-quantitative approaches such as the ligand field theory [12, 14–16, 27, 28]. Such calculations give a minute understanding of the electronic structure [16], but require adjustable empirical parameters to reproduce the experimental results. Very recently, the first fully non-empirical calculations of the PNMR chemical shifts have been reported [17–20]. We will restrict ourselves just to these, first-principles techniques.

The implementation of Rinkevicius et al. [20] includes the σ_{iso}^{orb}, $g_{iso}A_{iso}$, and $g_{iso}\mathbf{A}_{dip}$ terms of Eq. (20.35). Moreover, it assumes that the deviation of the molecular g-value g_{iso}, from the free-electron g-factor g_e, is negligible. The orbital contribution σ_{iso}^{orb} is treated at the ROHF, MCSCF (implemented in DALTON [29]), and DFT (implemented in deMon-NMR [22, 30, 31]) levels. In the approach of Moon et al. [18, 19], all terms in Eq. (20.35) are considered. The orbital contribution is approximated at the DFT level, by quasi closed-shell NMR chemical shifts in a fictitious system, with half of an electron of α- and β-spin assigned to the SOMO. Calculation of NMR shielding tensors in such systems was previously implemented by Schreckenbach and Ziegler [32] in ADF [33]. The g-tensors, required for calculation of the pseudocontact term, are obtained with ADF [33] or deMon-EPR [31] codes. In both

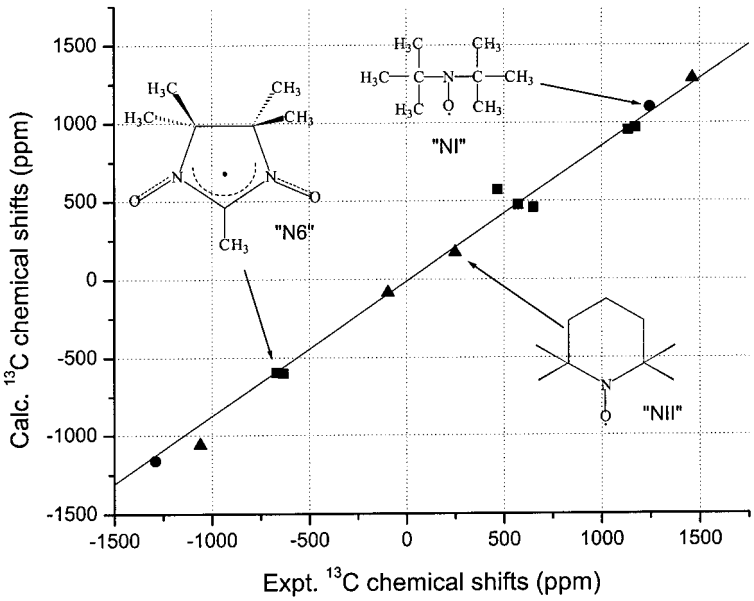

Figure 20.1 Correlation between the experimental and calculated paramagnetic ^{13}C NMR chemical shifts in substituted nitroxide radicals. Orbital and contact contributions were calculated using P86 [35,36] and B3LYP [37] exchange-correlation functionals ("P86m") respectively. Experimental and theoretical results are taken from Ref. [20].

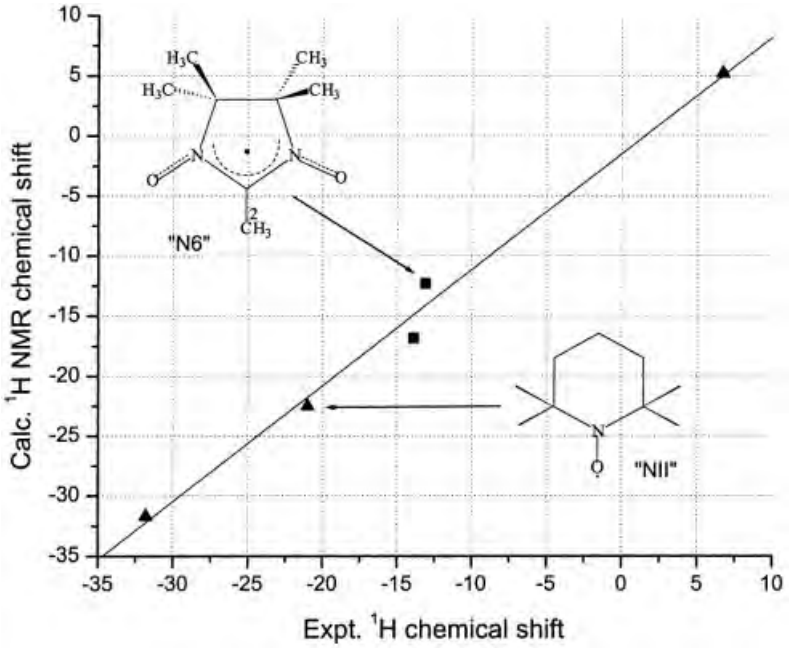

Figure 20.2 Correlation between the experimental and calculated paramagnetic NMR chemical shifts for ^{1}H nuclei in substituted nitroxide radicals. See Fig. 20.1 for details. Chemical shift of 2-CH_3 in "N6" is not shown (see text).

Rinkevicius' and Moon's approaches, the hyperfine tensors can be calculated using any available implementation, such as Gaussian [34], DALTON [29], deMon [22, 30, 31], or ADF [33].

The quality of DFT calculations of the ^{13}C PNMR chemical shifts is illustrated in Fig. 20.1, which is based on the results of Rinkevicius et al. [20] for simple nitroxide radicals. For ^{13}C chemical shifts, the root mean square error (RMSE) is 71.8 ppm, or 2.9% of the experimental range. The linear correlation slope is 0.893, with the intercept (at $\delta(^{13}C) = 0$ ppm) of –28.3 ppm. Given that neither the solvent effects, nor thermal vibrational motion are treated [20], this should be considered an excellent agreement with experiment.

For ^{1}H PNMR chemical shifts (Fig. 20.2), one calculated value (for 2-CH_3 of the "N6" radical) shows a significant deviation from experiment ("P86m": –329 ppm; expt.: –231 ppm [20]). If this outlier is excluded from statistics, the ^{1}H results are also in good agreement with experiment (RMSE 1.6 ppm; RMSE/range 5.3%; slope 0.968; intercept 5.1 ppm). The anomalous results for the 2-CH_3 protons are accompanied by strong dependence on the choice of the XC functional [20]. The latter often indicates a small HOMO–LUMO gap; the situation notoriously difficult for the prediction of magnetic properties in DFT.

We illustrate the relative importance of the different contributions to the PNMR chemical shieldings using an example of 2-methylphenyl-*tert*-butylnitroxide

Table 20.1 Calculated paramagnetic NMR chemical shifts relative to TMS (at 295 K, in ppm) of 2-methylphenyl-*tert*-butylnitroxide radical, in comparison with experiment.[a]

	DFT(BP86)				Expt.[b]
	δ^{orb}	δ^{FC}	δ^{PC}	δ^{total}	δ
t-bu-H	1.87	–14.26	–0.02	–12.41	–16.70
2-CH_3	2.46	22.72	0.08	25.26	19.14
3-H	7.55	51.14	0.01	58.70	52.44
4-H	7.36	–64.83	–0.01	–57.48	–23.44
5-H	7.38	53.19	0.00	60.57	60.02
6-H	7.46	–79.88	–0.04	–72.46	–55.45

a Paramagnetic NMR chemical shifts were calculated using Eq. (20.35), with TMS taken as a reference (σ^{ref}=32.04 ppm). Orbital contributions were determined with the ADF program [33], using an all-electron Slater-type basis set of TZP quality. Hyperfine and *g* tensors were calculated with the deMon program [22, 30, 31], using IGLO-III basis set [38]. Geometry was optimized at the B3LYP/6-311G(d,p) level, using Gaussian98 [34]. Further details are available elsewhere [18].

b Experimental results (CCl_4 solution) cited from Ref. [40].

(MPBN). In this radical, the Fermi contact term dominates ^{1}H chemical shifts, and determines all qualitative trends (Tab. 20.1). The orbital contribution $\delta^{orb}$is small, but not negligible ($\left|\delta^{orb}\middle/\delta^{FC}\right| \leq 15\,\%$). This term clearly brings the calculated values into a better numerical agreement with experiment. At the same time, it should be emphasized that the calculated orbital shifts are essentially identical to the NMR chemical shifts in similar, closed-shell environments. For example, experimental NMR chemical shifts of the aromatic hydrogens in aniline are in the range 6.7 to 7.2 ppm [39]. Calculated orbital contributions to the aromatic protons of MPBN are between 7.4 and 7.5 ppm. Similar results are seen for the 2-Me protons (2.4 ppm in toluene [39] vs. 2.5 ppm MPBN) and *tert*-butyl protons (0.9 ppm in neopentane [38] vs. 1.9 ppm in MPBN).

Finally, the pseudocontact shifts δ^{PC} are negligible in MPBN, and contribute less than 0.1 ppm to any of the ^{1}H shifts in Table 20.1. This is not surprising, given the small anisotropy of the *g*-tensor (g_{11} = 2.002, g_{22} = 2.008, g_{33} = 2.013) calculated for this radical. The pseudocontact contribution will become more important in transition metal complexes, which commonly exhibit anisotropic *g*-tensors. The presence of the occupied p and d orbitals at the NMR nucleus will also increase the δ^{PC} term, through a larger A_{dip} contribution.

The final practical point, which we would like to address, is the pronounced sensitivity of the PNMR chemical shifts to structural changes. The dependence of the calculated isotropic ^{1}H chemical shifts in MPBN on the orientation of the *tert*-BuN(O)- substituent is shown in the top panel of Fig. 20.3. When the radical centre is coplanar with the benzene ring ($\phi = 0°$), the spin density is delocalized to the aromatic system, leading to large contact shifts on the *ortho*- and *para*-hydrogens. The methyl substituent (2-Me) is also strongly affected through hyperconjugation with

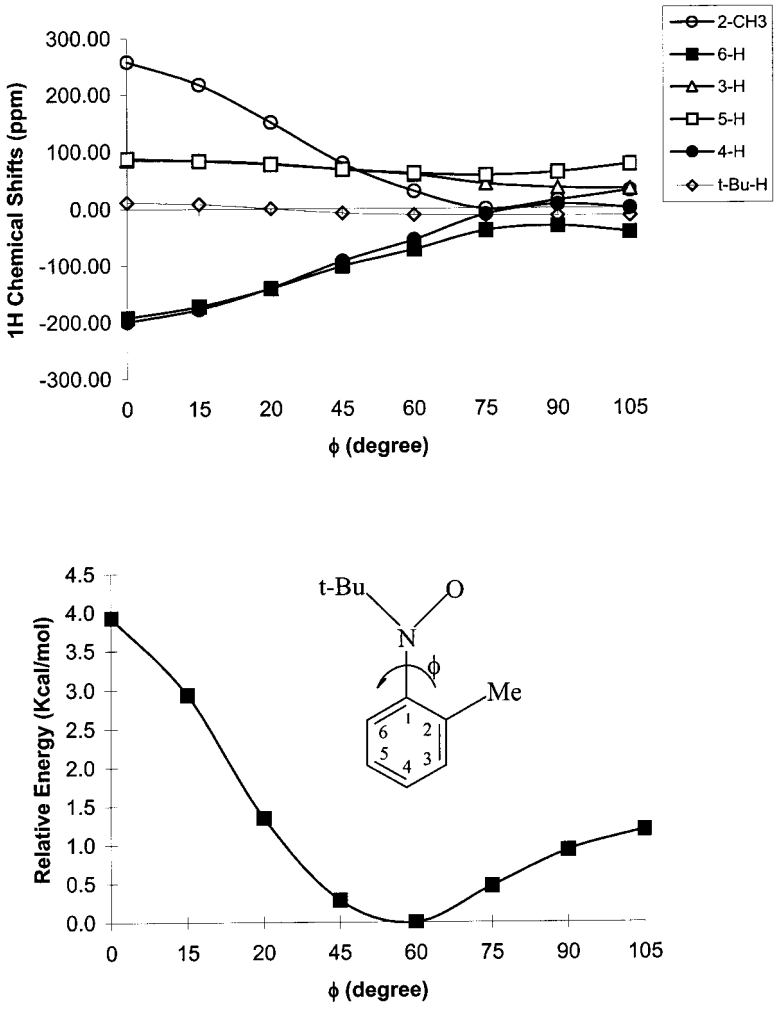

Figure 20.3 Structural dependence of the isotropic PNMR chemical shifts in 2-methylphenyl-*tert*-butylnitroxide (MPBN) radical, on the relative orientation of the *tert*-BuNO substituent and benzene ring. Parameter ϕ is the dihedral angle ONC_1C_2. Computational details are given in Table 20.1.

the aromatic system. Once the conjugation between the N(O) and the benzene π-system ring is interrupted ($\phi = 90°$), the magnitude of the contact shifts decreases. Given the soft potential energy surface for the ϕ rotation (see the lower panel of Fig. 20.3), thermal motion effects will be significant for this radical and may lead to a deviation from the T^{-1} Curie law dependence of the paramagnetic chemical shifts.

20.5 Conclusions

Unlike the closed-shell NMR shielding tensor, and many other NMR and EPR parameters, paramagnetic NMR shielding is an intrinsically statistical property, defined only as an ensemble average. Calculations of the PNMR shielding therefore require knowledge of magnetic parameters for thermally accessible excited states. In this chapter, we derive the first complete, general expression for the shielding tensor in open-shell species. The treatment considers all relevant contributions linear and bilinear in the external magnetic field and nuclear spin. Calculated values can therefore be compared directly to experiment.

In diamagnetic compounds, our expression reduces to the "standard" closed-shell NMR shielding tensor. For paramagnetic species, knowledge of the state energies in the absence of the field, together with the per-state orbital shieldings, hyperfine tensors, and EPR *g*-tensors, is sufficient to determine the paramagnetic shifts in the limit of fast electron spin relaxation. The theory takes a particularly simple form for an isolated Kramers doublet state, with no thermally accessible excited states. In the latter case, first-principles calculations show excellent agreement with experiment [20].

Paramagnetic NMR shifts can exhibit a strong dependence on structural parameters and so can be sensitive to thermal motion. Combined with the intrinsic temperature dependence of the PNMR shielding, this may complicate separation of the orbital and contact terms from temperature-dependent experimental spectra. Unraveling the individual contributions in such systems, required for determination of the electronic and molecular structure, may be simply impossible without theoretical input.

It is clear that the field of first-principles calculations of NMR chemical shifts in open-shell systems is only in its infancy. Nonetheless, all the ingredients required for accurate simulations of this property are already in place, and will lead to exciting new applications.

Acknowledgements

S. P. acknowledges John Tse for constant encouragement and support. S. M. is grateful to Dennis R. Salahub for his supervision, and acknowledges NSERC and CIPI for financial support.

References

1 I. Bertini, C. Luchinat, *NMR of Paramagnetic Molecules in Biological Systems*, Benjamin/Cummings, Menlo Park, CA **1986**.

2 I. Bertini, P. Turano, A. J. Vila, *Chem. Rev.* **1996**, *93*, 2833–2932.

3 I. Bertini, C. Luchinat, G. Parigi, *Solution NMR of Paramagnetic Molecules*, Elsevier, Amsterdam **2001**.

4 I. Bertini, C. Luchinat, M. Piccioli, *Methods Enzymol.* **2001**, *339*, 314–340.

5 I. Bertini, C. Luchinat, M. Piccioli, *Concepts Magn. Reson.* **2002**, *14*, 259–286.
6 M. Allegrozzi, I. Bertini, S.-N. Choi et al., *Eur. J. Inorg. Chem.* **2002**, 2121–2127.
7 G. N. La Mar, W. D. Horrocks, Jr., R. H. Holm, *NMR of Paramagnetic Molecules: Principles and Applications*, Academic Press, New York **1973**.
8 I. Bertini, C. Luchinat, in *Physical Methods for Chemists*, 2nd edition, ed. R. S. Drago, Harcourt Brace Jovanovich, **1992**, p. 500.
9 H. M. McConnell, D. B. Chesnut, *J. Chem. Phys.* **1958**, *28*, 107.
10 H. M. McConnell, R. E. Robertson, *J. Chem. Phys.* **1958**, *27*, 1361–1365.
11 R. J. Kurland, B. R. McGarvey, *J. Magn. Reson.* **1970**, *2*, 286–301.
12 B. Bleaney, *J. Magn. Reson.* **1972**, *8*, 91–100.
13 T. Helgaker, M. Jaszunski, K. Ruud, *Chem. Rev.* **1999**, *99*, 293–352.
14 B. R. McGarvey, *Inorg. Chem.* **1995**, *34*, 6000–6007.
15 B. R. McGarvey, N. C. Batista, C. W. B. Bezerra et al., *Inorg. Chem.* **1998**, *37*, 2865–2872.
16 L. L. Lohr, J. C. Miller, R. R. Sharp, *J. Chem. Phys.* **1999**, *111*, 10148–10158.
17 S. Moon, S. Patchkovskii, D. R. Salahub, *Quantum Mechanical Approaches for Paramagnetic NMR Shifts in Density Functional Theory*, CERMM Symposium, Montreal, Canada, **2002**; S. Moon, S. Patchkovskii, D. R. Salahub, *Prediction and Analysis of Paramagnetic NMR Shifts with Density Functional Theory: Applications to the Oxidized Blue Copper Systems*, deMon developers workshop, Geneva, Switzerland, **2002**.
18 S. Moon, Ph.D. Thesis, Université de Montréal, Canada, **2003**.
19 S. Moon, S. Patchkovskii, D. R. Salahub, in preparation.
20 Z. Rinkevicius, J. Vaara, L. Telyatnyk et al., *J. Chem. Phys.* **2003**, *118*, 2550.
21 J. E. Harriman, *Theoretical Foundations of Electron Spin Resonance*, Academic Press, New York **1978**.
22 V. G. Malkin, O. L. Malkina, L. A. Eriksson et al., in *Modern Density Functional Theory: A Tool for Chemistry*, eds. J. M. Seminario, P. Politzer, Vol. 2, Elsevier, Amsterdam **1995**.
23 J. Autschbach, T. Ziegler, *Coord. Chem. Rev.* **2003**, *238–239*, 83–126.
24 T. L. Hill, *An Introduction to Statistical Thermodynamics*, Dover, New York **1986**.
25 R. M. Lynden-Bell, in *Progress in Nuclear Magnetic Resonance Spectroscopy*, eds. J. W. Emsley, J. Feeney, L. H. Sutcliffe, Vol. 2, Pergamon Press, Oxford **1967**, pp. 163–204.
26 A. Abragam, B. Bleaney, *Electron Paramagnetic Resonance of Transition Ions*, Clarendon Press, Oxford **1970**.
27 J. Reuben, *J. Magn. Reson.* **1982**, *50*, 233–236.
28 I. Gattinger, M. A. Herker, W. Hiller et al., *Inorg. Chem.* **1999**, *38*, 2359–2368.
29 T. Helgaker, H. J. Aa. Jensen, P. Jørgensen et al., *DALTON, A Molecular Electronic Structure Program*, Release 1.2 (**2001**); also see http://www.kjemi.uio.no/software/dalton/dalton.html
30 D. R. Salahub, R. Fournier, P. Mlynarski et al., in *Density Functional Methods in Chemistry*, eds. J. K. Labanowski and J. Andzelm, Springer-Verlag, New York **1991**; A. St-Amant, D. R. Salahub, *Chem. Phys. Lett.* **1990**, *169*, 387–392; also see: http://www.deMon-software.com/
31 O. L. Malkina, J. Vaara, B. Schimmelpfennig et al., *J. Am. Chem. Soc.* **2000**, *122*, 9206–9218.
32 G. Schreckenbach, T. Ziegler, *J. Phys. Chem.* **1995**, *99*, 606–611.
33 E. J. Baerends, J. A. Autschbach, A. Bérces et al., *ADF 2003.2*, Scientific Computing and Modelling NV, Amsterdam, http://www.scm.com/
34 M. J. Frisch, G. W. Trucks, H. B. Schlegel et al., *Gaussian98, A.7*, Gaussian, Inc., Pittsburgh, PA, **1998**.
35 J. P. Perdew, Y. Wang, *Phys. Rev. B* **1986**, *33*, 8800–8802.
36 J. P. Perdew, *Phys. Rev. B* **1986**, *33*, 8822–8824.
37 A. D. Becke, *J. Chem. Phys.* **1993**, *98*, 5648–5652.
38 W. Kutzelnigg, U. Fleischer, M. Schindler, in *NMR Basic Principles and Progress*, eds. P. Diehl, E. Fluck, H. Günther, R. Kosfeld, Springer-Verlag, Heidelberg **1990**, Vol. 23, p. 165.
39 *Handbook of Proton-NMR Spectra and Data*, eds. Asahi Research Center, Academic Press, Tokyo **1987**.
40 A. Calder, A. R. Forrester, J. W. Emsley et al., *Mol. Phys.* **1970**, *18*, 481.

Part C
NMR Parameters, Applications

Calculation of NMR and EPR Parameters. Theory and Applications.
Edited by Martin Kaupp, Michael Bühl, Vladimir G. Malkin
Copyright © 2004 WILEY-VCH Verlag GmbH & Co. KGaA, Weinheim
ISBN: 3-527-30779-6

21
NMR Parameters in Proteins and Nucleic Acids

David A. Case

21.1
Introduction

The appearance of the one-dimensional proton NMR spectrum of an organic molecule is dominated by two key parameters, the chemical shifts (which determine the positions of the resonance lines) and the splittings of those lines caused by spin–spin interactions. Studies on biomolecules typically use multidimensional techniques and isotopic labeling to resolve and identify the large number of peaks present in the spectrum, but an understanding of how structure influences shifts and coupling constants is still of considerable importance in extracting information from NMR spectra. Since these two parameters depend upon electronic structure, it is appropriate to consider them in a book on the relationships between quantum chemistry and NMR.

In practice, however, quantum chemistry techniques are almost always applied to *fragments* of proteins and nucleic acids, and not to the macromolecules themselves, which in any event are studied in condensed phases whose effects are difficult to include in quantum chemistry calculations. Indirect spin–spin couplings are often mainly influenced by the local chemical structure, so that results on fragments can be applied directly to larger systems. This is much less true for chemical shifts, which often have significant contributions from longer-range interactions. For this reason, a common intermediate step is often used, in which quantum results on peptide or nucleotide fragments are fit to empirical models, and the latter are then applied to systems of more direct biological interest [1, 2].

Another feature that characterizes studies of chemical shifts in biomolecules is that the local chemical environments are quite limited; for example, there are just 20 amino acids, whose characteristic shifts (as measured in short peptides) are well known [3]. Hence, the primary focus is generally on the effects of rotations about carbon–carbon single bonds, and on contributions from the more distant chemical environment. This often means that one can use smaller basis sets than would generally be required for studies of more diverse chemical species [4], and that an understanding of non-covalent interactions (such as hydrogen-bond effects) will be an important component of such studies.

Calculation of NMR and EPR Parameters. Theory and Applications.
Edited by Martin Kaupp, Michael Bühl, Vladimir G. Malkin
Copyright © 2004 WILEY-VCH Verlag GmbH & Co. KGaA, Weinheim
ISBN: 3-527-30779-6

It is clearly not possible in a short article to provide any comprehensive account of calculations of NMR parameters of biomolecules. Instead, I shall try to provide a flavor of some approaches that appear promising for understanding the relationship between molecular structure and chemical shifts and spin–spin couplings. The quantum chemistry calculations cited here use the DFT model; this is often the only practical scheme for large fragments, but appears to give results of useful accuracy in many cases, at least when large basis sets are used.

21.2 Chemical Shifts, Classical Models

21.2.1 Group Susceptibility Effects

The most common model describing long-range effects on chemical shifts considers the case of remote functional groups with significant magnetic susceptibilities, generally characterized by "group susceptibilities." The interaction of these groups with the static spectrometer field induces local currents which, in turn, lead to local magnetic fields at probe nuclei in the vicinity of the functional group. This general model describes ring current shifts, pseudocontact shifts in paramagnetic systems, and a variety of other phenomena. The "McConnell equation" [5], gives the contribution to the shielding tensor arising from induced currents in a remote chemical group with magnetic susceptibility χ:

$$\boldsymbol{\sigma} = \frac{\chi}{r^3} - \frac{3\chi(\mathbf{r}\mathbf{r}^{\mathrm{T}})}{r^5} \tag{21.1}$$

Here $\mathbf{r}$ is the vector from the center of the remote group to the probe nucleus, and $\mathbf{r}\mathbf{r}^{\mathrm{T}}$ is the outer product of $\mathbf{r}$ with itself. (See Ref. [6] for a discussion of units and conversion between the SI and cgs systems.)

Eq. (21.1) has most often been used to compute contributions to isotropic shifts, which are –1/3 the trace of $\boldsymbol{\sigma}$. It is straightforward to show that the isotropic shift arises only from anisotropies in susceptibility tensors. For the case of an axially symmetric magnetic anisotropy, this becomes

$$\delta = (1/3)r^{-3}\Delta\chi(3\cos^2\theta - 1) \tag{21.2}$$

where θ is the angle between the vector $\mathbf{r}$ and the unique axis, and $\Delta\chi$ is the difference between magnetic susceptibilities along the unique axis and perpendicular to it. Hence the contribution to the isotropic shift vanishes when the susceptibility is isotropic, i.e. when $\Delta\chi = 0$. The use of this model to interpret chemical shift tensors is discussed elsewhere [6].

Semiempirical theories have been used for many years to generate atom- or group-based models for molecular magnetic susceptibilities [7]. More recently,

renewed attention has been paid to the ability of ab initio calculations to compute accurate susceptibility tensors. The Hartree–Fock limit (at least for hydrocarbons) can be reached with relatively small basis sets [8, 9], and correlation effects appear to be modest, tending to reduce Hartree–Fock values by 2–10% [10]. There is a long history, which I do not have space to review here, of attempts to fit group susceptibility tensors or ring-current "intensities" to observed shift data [11–14]. Calibration against quantum mechanical calculations can be done in a manner analogous to that commonly used to model charge distributions: parameters in group susceptibility models are determined by fits to grids of points surrounding the molecule [15].

Unpaired electrons, especially at transition metal sites, often make dominant contributions to magnetic susceptibilities. The contribution of this susceptibility to isotropic chemical shifts, is called the pseudo-contact term, and it can lead to large shifts if the unpaired electron distribution is especially anisotropic. This effect has been extensively studied in a variety of metalloproteins, and structure refinement methods have been developed to fit calculated and observed pseudocontact shifts [16]. The contribution of paramagnetic metal sites to chemical shift anisotropies also follows Eq. (21.1), and this has proved fruitful in extracting long-range geometric constraints for proteins [6, 17]. See also Chapter 20 by Moon and Patchkovskii.

21.2.2 Electric Field Effects

The susceptibility effect described above is "direct", in the sense that currents induced in neighboring groups give rise to secondary magnetic fields that contribute directly to the observed shielding at probe nuclei. A significant but more indirect contribution to chemical shifts arises from distant polar groups, which polarize the electron cloud around the probe nucleus and thereby increase or decrease the local shielding by electrons. The most significant term for protons is expected to be proportional to the projection of the local electric field onto the X–H bond vector, where X is the atom connected to H. The isotropic shift due to polarization effects is generally written as an expansion in the field strength:

$$\delta_{\mathrm{pol}} = A(\mathbf{E} \cdot \hat{\mathbf{r}}) + B\mathbf{E}^2 \tag{21.3}$$

where $\mathbf{E}$ is the electric field, $\hat{\mathbf{r}}$ is a unit vector along the bond direction, and A and B are proportionality constants specific to the X–H bond. Basically, fields that push electrons away from the H atom towards X (which have a positive projection on the X–H bond in the convention used here) will reduce the electron density near the H nucleus, tending to deshield it.

Modern quantum mechanical methods can be used to estimate the derivative of the proton shielding with respect to an external electric field. These calculations suggest a value of A close to 20 ppm $\text{Å}^2\,\text{e}^{-1}$ [15, 18–20]. For protons in methane, B has been estimated at –0.3 to -0.4×10^{-18} e.s.u^{-2} via shielding hyperpolarizability calcula-

tions [18, 21]. In most circumstances, estimated contributions from the second term in Eq. (21.3) are quite small compared to the first term.

Electric field effects on ^{13}C or ^{15}N are undoubtedly more complex to unravel, not least since these atoms are involved in more than one bond, so that a model of bond polarization is more difficult to apply. Furthermore, multi-configuration SCF results indicate that correlation effects can be quite important for ^{13}C, changing the shielding polarizabilities in methane, for example, by nearly a factor of two, compared to Hartree–Fock results [20]. This is in contrast to proton results, which show only small effects of correlation, and may make it more difficult to calibrate empirical theories against quantum calculations for these heavier nuclei. An empirical bond polarization model [22] gives a good account of many features of ^{13}C tensors in a variety of environments, and further work along these lines seems promising.

21.2.3
Close Contact and Solvent Effects

The study of close contact contributions to chemical shifts has a long and somewhat confusing history. At close proximity, London forces due to correlations of fluctuating dipoles can induce a buildup of electron density between molecules. The resultant loss of electron density near the nuclei is expected to decrease chemical shielding, by an amount that would be proportional to the mean square of the electric field, as in Eq. (21.3) [21, 23]. It is likely, however, that close-contact de-shielding effects also arise from exchange-repulsion effects that result from the electron reorganization required when the electron clouds of neighboring atoms begin to overlap. This can have a steep distance dependence that may be difficult to distinguish from the r^{-6} behavior predicted for dispersion. The general deshielding effect for protons has been fit to this sort of functional form for isotropic shifts computed for rare gas interactions with methane and *N*-Methylacetamide (NMA), and for a variety of small peptide models [1].

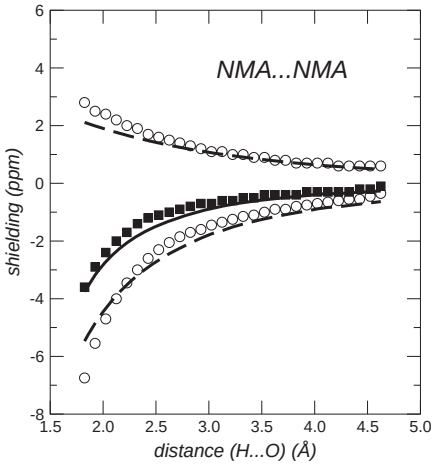

Figure 21.1 Shielding tensor for the hydrogen-bonding proton in a linear dimer of *N*-methylacetamide, as a function of H-bond distance. Central squares are computed results for the isotropic shielding; the upper curve shows the average tensor component perpendicular to the N–H bond, the lower circles are for the parallel component. Solid lines correspond to the empirical fit described in the text. Adapted from Ref. [1].

Realistic models for interactions in biomolecules involve a combination of susceptibility, bond polarization and close contact interactions. Figure 21.1 illustrates the application of all three terms discussed above to the amide proton shielding in an NMA dimer making a linear C=O ··· H–N hydrogen bond [6]. The solid lines show results from an empirical model based on shielding anisotropy, electric field, and close contact effects; squares and circles show results from DFT calculations. Although this is a very simple example of conformational analysis, we have shown elsewhere that similar models work for a variety of peptides [1], and these general ideas undergird many attempts to explain and predict shifts in biomolecules [2, 4, 24].

21.3 Chemical Shifts Calculations on Polypeptides and Proteins

Although the general subject has a long history, the use of quantum chemical calculations to interpret shifts in proteins really accelerated in the 1990s, with the development of efficient means of using gauge-including orbitals [25, 26], and the development of generalized-gradient DFT functionals. The group led by Oldfield was a leader in this "modern" era, showing how good results could be obtained from analysis of fragments of crystal structures [27–34], an idea that has been taken up by others [35]. Other groups have concentrated on studies of peptides, both as a function of the nature of the side chain and as a function of conformational parameters [1, 2, 4, 36–38]. Scaling these ideas up to full proteins is an active area of research; current models to predict shifts from structure capture much of the observed dispersion in proteins, but are far from accurate enough to be useful in assignment or even for most structural interpretations. A key current goal is to gain a better understanding of the effects of hydrogen bonding (and of other close contact interactions) on heavy atom (^{13}C and ^{15}N) shifts.

Interpreting chemical shift tensors in biomolecules (for example, by studying chemical shift anisotropy (CSA) relaxation) can also be a difficult task since the magnitudes and orientations of the shielding tensors are generally not known and since CSA relaxation competes with dipolar relaxation. Several groups have extracted CSA-related information for amide groups in proteins in liquids, both for ^{15}N [35, 39–44] and for protons [40, 45, 46]. The proton CSA appears to vary in a predictable way with hydrogen bond strength [6, 46, 47]. A key point that is not yet fully resolved is the extent to which the ^{15}N CSA in amides varies from one residue to another. The origins of this variability (as with the isotropic ^{15}N shift itself) have so far eluded generally applicable structural interpretations [35].

Carbon CSA effects are also receiving increasing attention in protein NMR. Experiments analogous to those described above for the amide N–H spin pair can also be used to probe CSA-dipolar cross-correlated relaxation along the C_α–H_α bond [48], or along C_α–C′ or H–C′, where C′ is the carbonyl carbon [49–51]. The C_α anisotropy probed by these experiments appears to be related to backbone torsional angles in a straightforward fashion that could be used for structure determination

or refinement [6]. Since the orientation of the carbonyl carbon shielding tensor is closely related to the direction of the C=O bond vector, it can provide information about the structure and dynamics of the peptide plane which can be difficult to obtain by other means [52, 53].

21.4 Chemical Shifts in Nucleic Acids

There have been fewer quantum chemical studies of shifts in nucleic acid fragments than in proteins, but this is likely to change as increased attention is paid to NMR studies of DNA and RNA and their complexes with proteins. The high charge density in nucleic acids makes it likely that careful attention to electrostatic effects (including solvent screening) will be required, and not just for ^{31}P shifts that are part of the formally-charged phosphate groups. This means that the conventional, gas-phase fragment approach that has proven so useful for peptides will probably have to be augmented by models that explicitly or implicitly take into account the effects of solvation and counterions. This may delay the application of quantum chemistry to these problems, but by no means represents an insuperable barrier.

Here we consider just a single example of how quantum calculations can yield insight into the relation between shifts and conformation. Figure 21.2 summarizes some recent computational results on a deoxythymidine model system [54]. Here the base is in the *anti* position, and the anisotropy of two of the sugar carbons is plotted against the pseudorotation phase. It is noteworthy that the C1′ and C3′ values clearly discriminate between N and S sugars (with P near 0° and 180°, respectively). The difference between these conformers is about 30 ppm, which is about 3–4 times larger than the changes seen in the isotropic shifts. These large predicted variations have been confirmed in subsequent experiments [55].

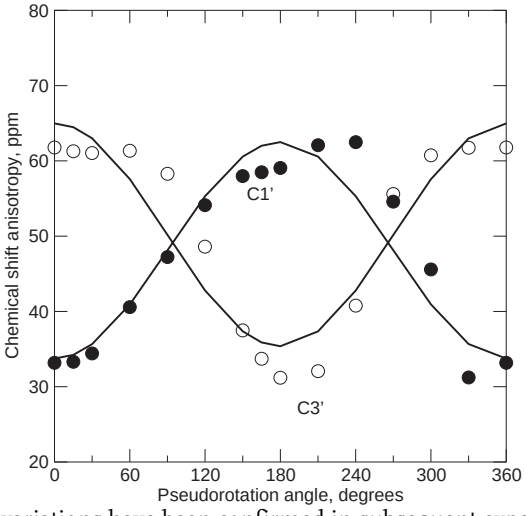

Figure 21.2 DFT predictions for the magnitude of the carbon CSA (projected along the C–H bond) for the C1′ (solid circles) and C3′ carbons (open circles) in a deoxyribose model. Solid lines show a simple dependence of the cosine of the pseudorotation angle. Adapted from Ref. [54].

21.5
Indirect Spin–Spin Couplings in Biomolecules

21.5.1
Dependence of Three-Bond Couplings on Torsion Angles

The "classic" application of coupling constants to conformation analysis uses three-bond coupling constants to infer information about the magnitude of the torsion angle that connects the two spins whose coupling is being monitored. The basic model for how these couplings should depend upon the intervening torsion was first worked out for proton–proton couplings about 40 years ago [56], and much has been learned from empirical modeling [57], but accurate quantum chemistry calculations are still very valuable, particularly in situations where it is difficult to prepare good model complexes for calibration.

Figure 21.3 shows a recent comparison between DFT results and empirical models for the six three-bond couplings that traverse the ϕ backbone dihedral in peptides. Just a few years ago, similar calculations gave very poor agreement with experiment [58], but more recent approaches that use gauge-including orbitals, density functional theory, and larger basis sets have yielded excellent results, often as

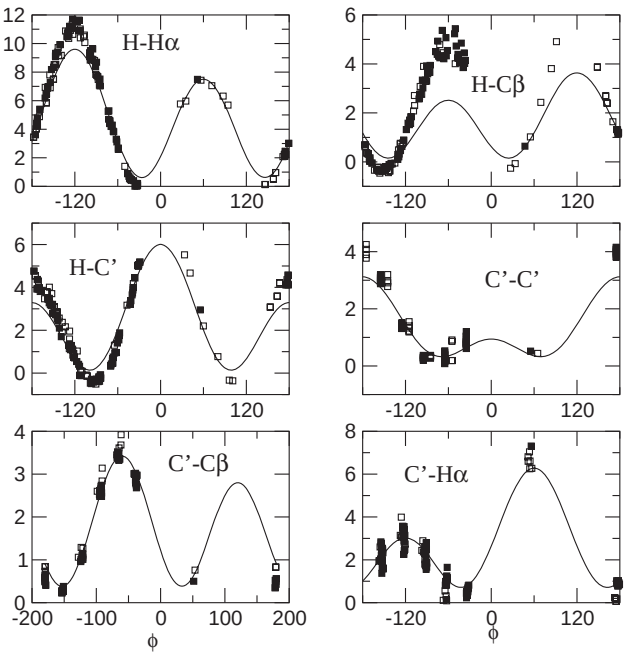

Figure 21.3 Three-bond couplings related to the ϕ backbone torsion in proteins. Solid lines represent empirical fits to flavodoxin, open and filled circles to density functional results. Adapted from Ref. [64].

good as or better than can be achieved with empirical fits. Among the many similar studies that could be cited, two recent analyses have yielded some surprising (yet experimentally verified) results for couplings about the glycosidic torsion in DNA [59], and about the C_α–C_β bond in peptides [60].

21.5.2 One-Bond Couplings

Recent experimental studies have also focused on the conformational dependence of one-bond spin–spin couplings. Traditionally, one-bond coupling constants have not been extensively studied in proteins, but this is now changing with the development of methods that produce a partial orientation of macromolecular systems [61]. In partially oriented systems, there are both direct and indirect contributions to the observed spin–spin couplings, and a measurement of the indirect contribution (usually under isotropic conditions) is required to extract the direct contribution by difference. Any local structural information that can be extracted from the indirect contribution would further increase the usefulness of these sorts of measurements.

A potentially important source of information about protein backbone conformations comes from one-bond C_α–H_α and C_α–C_β couplings [53, 62, 63]. These appear to be most sensitive to the ψ backbone angle, with the C_α–H_α coupling being largest near $\psi = -60°$ and the C_α–C_β coupling being large near $\psi = +60°$. These conformations are those where the C_α–H_α or C_α–C_β (respectively) are *syn* to the adjacent C=O bond [53]. In α_R regions, where both ϕ and ψ are positive, the C_α–H_α coupling is especially small, offering a useful way to observe this unusual conformation.

21.5.3 Couplings Across Hydrogen Bonds

Finally, it has recently been demonstrated that measurable spin–spin couplings can be observed for spins connected by hydrogen bonds as well as by covalent interactions. For peptides and proteins, the values which can potentially be measured are ^{2h}J(C′–H) and ^{3h}J(C′–N), where the "h" in the superscript indicates that one of the two or three bonds connected the nuclei is a hydrogen bond [65]. Although these couplings are rather small, they can provide key information, indicating not only the presence of a hydrogen bond (which might otherwise be inferred from chemical shift patterns) but also direct evidence about the partners involved in it, and in favorable cases, information about bond lengths as well [66]. Quantum calculations appear to be in generally good agreement with experiment, and indicate how the hydrogen bond angle as well as its length should influence the observed couplings [67, 68]. For example, Fig. 21.4 shows DFT results for the *N*-methylacetamide dimer as a function of H-bond distance. These indicate, somewhat surprisingly, that the ^{2h}J(C′–H) and ^{3h}J(C′–N) couplings should have (accidentally) about the same magnitude, and this prediction has subsequently been confirmed experimentally [69].

For nucleic acids, observations of internucleotide couplings can be used to securely identify hydrogen-bonded partners, which can be particularly important for

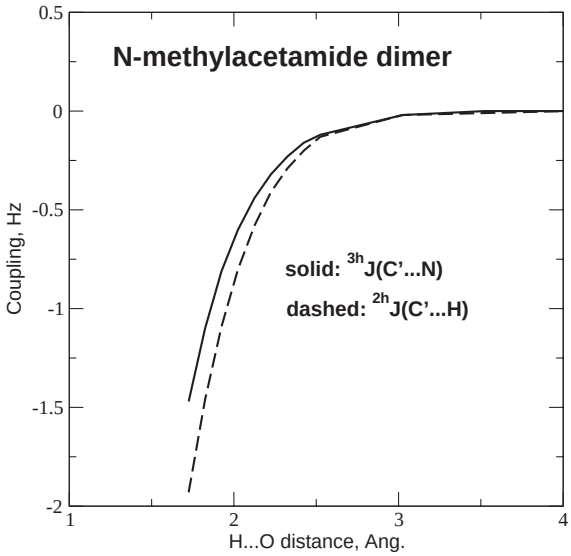

Figure 21.4 Calculated dependence of coupling constant on H-bond distance, from unpublished DFT calculations [B3LYP/ 6-311+G(2d,p)] by the author.

non-canonical patterns [65]. As in proteins, the general nature of the results appears to be in accord with results from density functional calculations [70, 71], a feature which may be of use in developing more elaborate interpretations of this sort of data. A surprising result is that the ^{2h}J(N,N) coupling is larger than ^{1h}J(N,H), even though the proton is a much more sensitive nucleus than ^{15}N. This can be rationalized in terms of a near cancellation in ^{1h}J(N,H) of two larger contributions of opposite sign, one arising from polarization of the N–H σ bond and the other from N lone pair to NH σ^* delocalization [72]. It seems likely that a more quantitative interpretation of these couplings (along with chemical shift trends) will be useful in characterizing the strength and directionality, as well as the existence, of these interesting hydrogen bonds. More insight into trans-H-bond couplings can be found in Chapter 22 by Del Bene.

21.6 Conclusions

This chapter could only touch the surface of this subject, and many interesting investigations have been passed over. This reflects to some extent a vibrant and active field. Although one always needs to carefully examine the accuracy and precision of quantum chemical calculations, it appears that many aspects of the conformational and environment dependence of shifts and spin–spin couplings are mod-

eled to useful accuracy by (large basis set) DFT calculations. As computer power increases, this opens the way for studies of molecular fragments that are increasingly realistic surrogates for biomolecules.

Acknowledgments

This work was supported by NIH grant GM45811. I thank Rafael Brüschweiler and Ad Bax for helpful discussions.

References

1 D. Sitkoff, D. A. Case, *J. Am. Chem. Soc.* **1997**, *119*, 12262–12273.
2 X.P. Xu, D. A. Case, *Biopolymers* **2002**, *65*, 408–423.
3 D. S. Wishart, D. A. Case, *Methods Enzymol.* **2001**, *338*, 3–34.
4 X. P. Xu, D. A. Case *J. Biomol. NMR* **2001**, *21*, 321–333.
5 H. M. McConnell. *J. Chem. Phys.* **1957**, *27*, 226–229.
6 D. Sitkoff, D. A. Case, *Prog. NMR Spectrosc.* **1998**, *32*, 165–190.
7 C. Giessner-Prettre, B. Pullman, *Q. Rev. Biophys.* **1987**, *20*, 113–172.
8 K. Ruud, T. Helgaker, K. L. Bak et al., *J. Chem. Phys.* **1993**, *99*, 3847.
9 K. Ruud, H. Skaane, T. Helgaker et al., *J. Am. Chem. Soc.* **1994**, *116*, 10135–10140.
10 K. Ruud, T. Helgaker, P. Jorgensen, *J. Chem. Phys.* **1997**, *107*, 10599–10606.
11 R. F. Zürcher, *Prog. NMR Spectrosc.* **1967**, *2*, 205–257.
12 W. H. Flygare, *Chem. Rev.* **1974**, *74*, 653–687.
13 P. Lazzeretti, *Prog. NMR Spectrosc.* **2000**, *36*, 1–88.
14 J. A. N. F. Gomes, R.B. Mallion, *Chem. Rev.* **2001**, *101*, 1349–1384.
15 D. A. Case, *J. Biomol. NMR* **1995**, *6*, 341–346.
16 I. Bertini, P. Turano, A.J. Vila, *Chem. Rev.* **1993**, *93*, 2833–2932.
17 J. Boisbouvier, P. Gans, M. Blackledge et al., *J. Am. Chem. Soc.* **1999**, *121*, 7700–7701.
18 J. D. Augspurger, C. E. Dykstra, *J. Phys. Chem.* **1991**, *95*, 9230–9238.
19 M. Grayson, W. T. Raynes, *Magn. Reson. Chem.* **1995**, *33*, 138–143.
20 S. Coriani, A. Rizzo, K. Ruud et al., *Mol. Phys.* **1996**, *88*, 931–947.
21 W. T. Raynes, in *Nuclear Magnetic Shieldings and Molecular Structure*, ed. J. A. Tossell, Kluwer, Dordrecht **1993**, pp. 401–420.
22 U. Sternberg, W. Priess, *J. Magn. Reson.* **1997**, *124*, 8–19.
23 C. J. Jameson, A. C. de Dios, *J. Chem. Phys.* **1992**, *97*, 417–434.
24 K. Ösapay, D. A. Case, *J. Am. Chem. Soc.* **1991**, *113*, 9436–9444.
25 K. Wolinski, J. F. Hinton, P. Pulay, *J. Am. Chem. Soc.* **1990**, *112*, 8324–8328.
26 K. Wolinski, R. Haacke, J. F. Hinton et al., *J. Comput. Chem.* **1997**, *18*, 816–825.
27 A. C. de Dios, E. Oldfield, *Chem. Phys. Lett.* **1993**, *205*, 108–116.
28 A. C. de Dios, J. G. Pearson, E. Oldfield *J. Am. Chem. Soc.* **1993**, *115*, 9768–9773.
29 A. C. de Dios, D. D. Laws, E. Oldfield, *J. Am. Chem. Soc.* **1994**, *116*, 7784–7786.
30 A. C. de Dios, E. Oldfield, *J. Am. Chem. Soc.* **1994**, *116*, 11485–11488.
31 J. G. Pearson, J.-F. Wang, J. L. Markley et al., *J. Am. Chem. Soc.* **1995**, *117*, 8823–8829.
32 H. Le, J. G. Pearson, A. C. de Dios, E. Oldfield, *J. Am. Chem. Soc.* **1995**, *117*, 3800–3807.
33 H. Le, E. Oldfield, *J. Phys. Chem.* **1996**, *100*, 16423–16428.
34 J. G. Pearson, H. Le, L. K. Sanders et al., *J. Am. Chem. Soc.* **1997**, *119*, 11941–11950.
35 C. Scheurer, N. Skrynnikov, S. F. Lienin et al., *J. Am. Chem. Soc.* **1999**, *121*, 4242–4251.
36 A. C. de Dios, J. L. Roach, A. E. Walling, in *Modeling NMR Chemical Shifts. Gaining Insights into Structure and*, eds. J. C. Facelli,

A. C. de Dios, American Chemical Society, Washington, DC **1999**, pp. 220–239.
37 B. Wang, J. F. Hinton, P. Pulay, *J. Comput. Chem.* **2002**, *23*, 492–497.
38 J. A. Vila, D. R. Ripoll, H. A. Baldoni et al., *J. Biomol. NMR* **2002**, *24*, 245–262.
39 N. Tjandra, A. Szabo, A. Bax *J. Am. Chem. Soc.* **1996**, *118*, 6986–6991.
40 N. Tjandra, A. Bax, *J. Am. Chem. Soc.* **1997**, *119*, 8076–8082.
41 D. Fushman, N. Tjandra, D. Cowburn, *J. Am. Chem. Soc.* **1998**, *120*, 10947–10952.
42 D. Fushman, N. Tjandra, D. Cowburn, *J. Am. Chem. Soc.* **1999**, *121*, 8577–8582.
43 C.D. Kroenke, M. Rance, A.G. Palmer, III, *J. Am. Chem. Soc.* **1999**, *121*, 10119–10125.
44 J. Boyd, C. Redfield, *J. Am. Chem. Soc.* **1999**, *121*, 7441–7442.
45 M. Tessari, F.A.A. Mulder, R. Boelens et al., *J. Magn. Reson.* **1997**, *127*, 128–133.
46 G. Wu, C. J. Freure, E. Verdurand, *J. Am. Chem. Soc.* **1998**, *120*, 13187–13193.
47 Y. Sharma, O. Y. Kwon, B. Brooks et al., *J. Am. Chem. Soc.* **2002**, *124*, 327–335.
48 N. Tjandra, A. Bax, *J. Am. Chem. Soc.* **1997**, *119*, 9576–9577.
49 M. W. Fischer, L. Zeng, A. Majumdar et al., *Proc. Natl. Acad. Sci. USA* **1998**, *95*, 8016–8019.
50 Y. Pang, L. Wang, M. Pellecchia et al., *J. Biomol. NMR* **1999**, *14*, 297–306.
51 T. Norwood, M. Tillett, L. Lian, *Chem. Phys. Lett.* **1999**, *300*, 429–434.
52 M. Pellecchia, Y. Pang, L. Wang et al., *J. Am. Chem. Soc.* **1999**, *121*, 9165–9170.
53 G. Cornilescu, A. Bax, D. A. Case, *J. Am. Chem. Soc.* **2000**, *122*, 2168–2171.
54 A. P. Dejaegere, D. A. Case, *J. Phys. Chem. A* **1998**, *102*, 5280–5289.
55 J. Boisbouvier, B. Brutscher, A. Pardi et al., *J. Am. Chem. Soc.* **2000**, *122*, 6779–6780.
56 M. Karplus, *J. Am. Chem. Soc.* **1963**, *85*, 2870–2871.
57 C. Altona, in *Encyclopedia of Nuclear Magnetic Resonance*, eds. D. M. Grant, R. K. Harris, John Wiley, London **1996**, pp. 4909–4922.
58 A. S. Edison, J. L. Markley, F. Weinhold, *J. Biomol. NMR* **1994**, *4*, 519–542.
59 M. L. Munzarová, V. Sklenár, *J. Am. Chem. Soc.* **2003**, *125*, 3649–3658.
60 J. J. Chou, R. Ishima, D. Torchia et al., *J. Am. Chem. Soc.* **2003**, in press.
61 N. Tjandra, A. Bax, *Science* **1997**, *278*, 1111–1114.
62 D. F. Mierke, S. G. Grdadolnik, H. Kessler, *J. Am. Chem. Soc.* **1992**, *114*, 8283–8284.
63 B. W. Vuister, F. Delaglio, A. Bax, *J. Biomol. NMR* **1993**, *3*, 67–80.
64 D. A. Case, C. Scheurer, R. Brüschweiler, *J. Am. Chem. Soc.* **2000**, *122*, 10390–10397.
65 S. Grzesiek, F. Cordier, A. J. Dingley, *Methods Enzymol.* **2001**, *338*, 111–133.
66 G. Cornilescu, B. E. Ramirez, M. K. Frank et al., *J. Am. Chem. Soc.* **1999**, *121*, 6275–6279.
67 C. Scheurer, R. Brüschweiler, *J. Am. Chem. Soc.* **1999**, *121*, 8661–8662.
68 M. Barfield, *J. Am. Chem. Soc.* **2002**, *124*, 4158–4168.
69 F. Cordier, M. Rogowski, S. Grzesiek et al., *J. Magn. Reson.* **1999**, *140*, 510–512.
70 A. J. Dingley, J. E. Masse, R. D. Peterson et al., *J. Am. Chem. Soc.* **1999**, *121*, 6019–6027.
71 M. Barfield, A. J. Dingley, J. Feigon et al., *J. Am. Chem. Soc.* **2001**, *123*, 4014–4022.
72 S. J. Wilkens, W. M. Westler, F. Weinhold et al., *J. Am. Chem. Soc.* **2002**, *124*, 1190–1191.

22
Characterizing Two-Bond NMR $^{13}C–^{15}N$, $^{15}N–^{15}N$, and $^{19}F–^{15}N$ Spin–Spin Coupling Constants across Hydrogen Bonds Using Ab Initio EOM-CCSD Calculations

Janet E. Del Bene

22.1
Introduction

Studies of the hydrogen bond have a long history, with the publication of the classic book "The Hydrogen Bond" by Pimentel and McClellan [1] signaling the beginning of an era of intense experimental research on this subject. However, it was not until the late sixties and early seventies that ab initio quantum chemical studies of hydrogen-bonded complexes were carried out in an effort to determine the structures and binding energies of these complexes from first-principles calculations. During the last 30 years of the twentieth century, developments in computational algorithms and their implementation in software packages, the advent of more powerful computing machines, and methodological improvements have had a dramatic impact on ab initio computational quantum chemistry. Computed structures, binding energies, and infrared (IR) vibrational spectral data, obtained at sophisticated levels of theory, have achieved an accuracy which makes them complementary to experimental data, and gives them predictive value in those cases for which experimental data are not available. Studies of hydrogen-bonded complexes carried out at these levels have led to a better understanding of the fundamental nature of the hydrogen bond.

In contrast, it was not until the last decade of the twentieth century that the first experimental measurements of NMR two-bond spin–spin coupling constants across hydrogen bonds were made. In a landmark paper [2], Dingley and Grzesiek reported two-bond $^{15}N–^{15}N$ spin–spin coupling constants across N–H...N hydrogen bonds in AU and GC pairs. This paper generated a great deal of interest and excitement in the chemical and biochemical communities, since it was suggested that such measurements might provide structural information about hydrogen-bonded complexes in solution. Subsequently, other experimental measurements of two-bond spin–spin coupling constants in hydrogen-bonded complexes have been made, and these are summarized in recent review articles by Elguero and Alkorta [3], and by Grzesiek, Cordier, and Dingley [4].

Just as there had been no experimental measurements of two-bond spin–spin coupling constants across hydrogen bonds until the end of the twentieth century, there were also no published ab initio calculations on this subject until that time. It would not be unreasonable to state that just a few years prior to the end of the cen-

Calculation of NMR and EPR Parameters. Theory and Applications.
Edited by Martin Kaupp, Michael Bühl, Vladimir G. Malkin
Copyright © 2004 WILEY-VCH Verlag GmbH & Co. KGaA, Weinheim
ISBN: 3-527-30779-6

tury, the data base of knowledge related to spin–spin coupling constants for a pair of hydrogen-bonded atoms based upon fundamental theoretical studies was comparable to the data base of knowledge of the structures, binding energies, and vibrational spectra of such complexes based on ab initio calculations in the early 1970s. Hence, investigations of two-bond spin–spin coupling constants across hydrogen bonds are a new and exciting area of experimental and theoretical research. From a computational viewpoint, there are many questions about spin–spin coupling constants across hydrogen bonds that need to be addressed at a level of theory capable of providing reliable answers. Among these questions are the following.

1. What is the relative importance of the paramagnetic spin–orbit, diamagnetic spin–orbit, Fermi-contact, and spin–dipole contributions to the total coupling constant?
2. How do spin–spin coupling constants vary with the nature of the atoms X and Y, and the hybridization and bonding of these atoms?
3. To what extent do spin–spin coupling constants depend on the structure of the hydrogen-bonded complex, particularly on the X–Y distance and the orientation of the hydrogen-bonded pair?
4. What is the dependence of the coupling constant on hydrogen bond type and on the charge on the complex?
5. What can spin–spin coupling constants reveal about the nature of the hydrogen bond?

This chapter contains a summary of the results of ab initio calculations carried out in this laboratory to determine $^{13}C–^{15}N$, $^{15}N–^{15}N$, and $^{19}F–^{15}N$ spin–spin coupling constants across C–H–N, N–H–N, and F–H–N hydrogen bonds, respectively, in both neutral and charged complexes. It is hoped that these results may provide some insights into the answers to the questions raised above.

22.2 Methods

Recent computational studies of spin–spin coupling constants across hydrogen bonds have been carried out using both DFT and ab initio methods. A review of these calculations has been given by Elguero and Alkorta [3], so the reader is referred to that paper for details. In this chapter the focus will be on studies carried out in this laboratory, using equation-of-motion coupled-cluster singles and doubles theory (EOM-CCSD).

The first step is to determine the optimized structures of the complexes at second-order perturbation theory (MP2) [5–8] with the 6-31+G(d,p) basis set [9–12]. This level of treatment employs an explicitly correlated wavefunction and a valence double-split basis set augmented with polarization functions on all atoms and diffuse functions on nonhydrogen atoms. It has been recommended as the level of theory required to provide reliable structures and vibrational frequency shifts (if the harmonic approximation is appropriate) at minimum computational expense [13].

Obtaining reliable energetics requires a larger basis set, such as Dunning's aug-cc-pVTZ basis [14, 15] without counterpoise corrections for binding energies [16].

Ab initio calculations to determine spin–spin coupling constants across hydrogen bonds have been carried out using the equation-of-motion coupled-cluster singles and doubles (EOM-CCSD) formalism in the CI-like approximation [17–20]. EOM-CCSD with the Ahlrichs (qzp, qz2p) basis set [21] gives good agreement between computed and experimental coupling constants in molecules [18], and good agreement with experimental data for hydrogen-bonded complexes when comparisons can be made. It is this level of theory which has been used for all of the studies that will be discussed below. Early calculations employed the qz2p basis set on all hydrogen atoms. However, subsequent studies indicated that replacing this basis set by Dunning's cc-pVDZ basis [14] on hydrogen atoms not involved in the hydrogen bond has little effect on computed X–Y coupling constants, but reduces the computational cost.

Two-bond X–Y spin–spin coupling constants across X–H–Y hydrogen bonds are designated $^{2h}J_{X-Y}$, where "2" indicates that the coupling is across two bonds, "h" indicates that the coupling is across a hydrogen bond, and "X–Y" are the hydrogen-bonded atoms that couple. In nonrelativistic theory, $^{2h}J_{X-Y}$ has four components: the paramagnetic spin–orbit (PSO), diamagnetic spin–orbit (DSO), Fermi-contact (FC), and spin–dipole (SD) terms. Because the calculation of spin–spin coupling constants across hydrogen bonds is a new area of research, we initially computed all terms that contribute to $^{2h}J_{X-Y}$ for a series of complexes in which X and Y are fixed, in order to evaluate the relative importance of each term for determining the X–Y coupling constant for a particular pair of hydrogen-bonded atoms.

22.3 Discussion

22.3.1 Hydrogen Bond Types and $^{2h}J_{X-Y}$

When examining both the IR and NMR spectral properties of hydrogen-bonded complexes, it is advantageous to classify X–H–Y hydrogen bonds into one of three types: traditional, proton-shared, or ion-pair [22–24]. A hydrogen bond is called traditional if the X–H bond of the proton-donor group remains intact in the complex, and the X–Y distance is normal (as opposed to short). The IR spectrum of such a complex is characterized by a strong X–H stretching band shifted to lower frequency relative to the X–H band in the monomer. The traditional hydrogen bond is by far the most common type found in uncharged complexes in the gas phase. Examples include $(H_2O)_2$, $(HF)_2$, $FH{:}NH_3$ and $ClH{:}NH_3$. In this chapter, a traditional hydrogen bond will be designated as X–H...Y.

In particular cases, the hydrogen-bonded proton can be transferred from X to Y, forming a hydrogen-bonded ion pair. In such a complex the X–Y distance is similar to the X–Y distance in a corresponding complex with a traditional hydrogen bond.

The Y–H distance is elongated relative to the corresponding isolated cation, and the IR spectrum exhibits a strong Y–H stretching band shifted to lower frequency relative to the cation. Such hydrogen bonds are depicted as $X^-...^+H–Y$. This type is not common in the gas phase, but can be formed if a very strong proton donor is complexed with a very basic proton acceptor. An ion-pair hydrogen bond stabilizes the complex formed between HBr and $N(CH_3)_3$ in the gas phase [25].

Intermediate between these two is the proton-shared hydrogen bond. A complex stabilized by such a hydrogen bond has a short X–Y distance, but long X–H and Y–H distances. The proton-stretching band is very intense and appears at a very low frequency. Other strong bands may be observed, depending on the nature of the complex. A hydrogen bond of this type is designated as X...H...Y. The complex between HCl and $N(CH_3)_3$ has a proton-shared hydrogen bond in the gas phase [25]. If in a proton-shared hydrogen bond the proton is shared equally between two equivalent atoms, the hydrogen bond is called symmetric. If the sharing is equal (as measured by the forces exerted by X and Y on H) but X and Y are different atoms, the hydrogen bond is referred to as a quasi-symmetric proton-shared hydrogen bond.

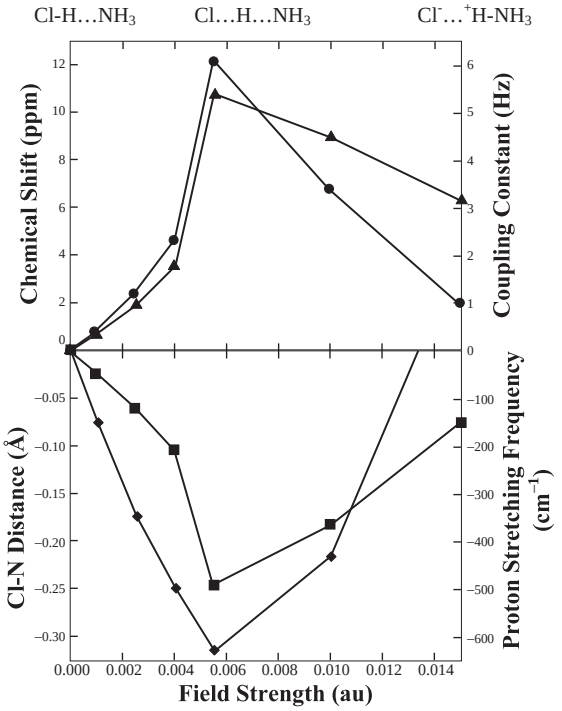

Figure 22.1 The two-bond Cl–N spin–spin coupling constant, the chemical shift of the hydrogen-bonded proton, the anharmonic proton-stretching frequency, and the Cl–N distance for $ClH:NH_3$ as a function of external field strength. Values are plotted relative to 0.0 for the zero-field values. Solid circle: coupling constant; solid triangle: chemical shift; solid diamond: proton-stretching frequency; solid square: Cl–N distance.

Research in enzyme kinetics has suggested that proton-shared hydrogen bonds (sometimes called "low-barrier" hydrogen bonds) may play an important role in determining reaction rates [26–32]. Could measurements of $^{2h}J_{X-Y}$ serve to prove the existence of such hydrogen bonds? We have addressed the relationship between $^{2h}J_{X-Y}$ and hydrogen bond type in a series of papers [22–24, 33–38]. We first recognized this relationship in a study of the $ClH{:}NH_3$ complex. Our interest in this and the related $BrH{:}NH_3$ complex [39] was originally stimulated by their unusual low-temperature Ar matrix vibrational spectra, and by the failure of the harmonic approximation to reproduce the large experimental low-frequency shifts of the Br–H and Cl–H stretching bands in these complexes [40]. In the course of our studies, we observed that an external electric field applied along the hydrogen-bonding axis was capable of mimicking the matrix environment of these and related complexes, inducing proton transfer, and thereby changing hydrogen bond type from traditional, to proton-shared, to ion-pair [39–41]. The $ClH{:}NH_3$ complex subsequently became our workhorse system, allowing for detailed studies of IR and NMR properties as a function of hydrogen bond type in a single chemical system. From such studies a rich harvest of information concerning the variation of these properties with hydrogen bond type has been obtained.

This variation is most succinctly illustrated in Fig. 22.1, which plots the equilibrium Cl–N distance, the two-bond spin–spin coupling constant ($^{2h}J_{Cl-N}$), the chemical shift of the hydrogen-bonded proton, and the two-dimensional anharmonic proton-stretching frequency as functions of increasing field strength and therefore changing hydrogen bond type. As is apparent from this figure, these properties are fingerprints of hydrogen bond type, exhibiting extremum values for a quasi-symmetric proton-shared hydrogen bond. The variation of $^{2h}J_{X-Y}$ with hydrogen bond type will be seen in the subsequent discussion of coupling constants across N–H–N, C–H–N, and F–H–N hydrogen bonds.

22.3.2
N–H–N Hydrogen Bonds

The experimental measurement of ^{15}N–^{15}N spin–spin coupling constants across the N–H...N hydrogen bonds in the AU and GC base pairs [2] generated a great deal of excitement. Hence, it seems fitting to begin this discussion of spin–spin coupling across hydrogen bonds by considering $^{2h}J_{N-N}$. Based on EOM-CCSD calculations for a series of complexes stabilized by N–H–N hydrogen bonds, we demonstrated that $^{2h}J_{N-N}$ is determined solely by the Fermi-contact (FC) term. This is not due to a cancellation of other terms, but arises because the FC term is more than an order of magnitude greater than any other term. Because the FC term approximates $^{2h}J_{N-N}$ so well, calculations of ^{15}N–^{15}N coupling constants are feasible in relatively large systems. Moreover, the Fermi-contact term and therefore total $^{2h}J_{N-N}$ are distance dependent, decreasing (in an absolute sense) with increasing N–N distance [34–36]. This suggests that it should be possible to obtain intermolecular N–N distances from experimentally measured N–N coupling constants. It was also our hope that

the innate simplicity of the Fermi-contact term might carry over and lead to general relationships between coupling constants and intermolecular distances.

Since the two-bond N–N coupling constant across an N–H...N hydrogen bond had been directly measured [2], we computed $^{2h}J_{N\text{-}N}$ for the CNH:NCH complex at an N–N distance of 2.90 Å, which corresponds to the N–N distance in the AU and GC pairs. The computed value is 7.2 Hz, in excellent agreement with the experimental value of about 7 Hz. This result was initially puzzling, since CNH:NCH would not be expected to be a good model for base pairs, and suggests that $^{2h}J_{N–N}$ is not very sensitive to the bonding at the nitrogens. Table 22.1 reports equilibrium N–N distances and $^{2h}J_{N–N}$ values computed at the equilibrium geometries of a series of neutral and cationic complexes with N–H–N hydrogen bonds [34–36]. The nitrogen atoms may be sp, sp^2, or sp^3 hybridized, although no cationic complexes with sp hybridized nitrogens as proton donors are included. The neutral complexes are stabilized by traditional hydrogen bonds, while the hydrogen bonds in the cationic complexes may be either traditional or proton-shared. Figure 22.2 shows a plot of $^{2h}J_{N–N}$ versus the N–N distance for these 13 complexes. The value of $^{2h}J_{N–N}$ at 2.90 Å obtained from this curve is 7.5 Hz, in agreement with the value of 7.2 Hz obtained for the CNH:NCH complex at the same N N distance, and with the experimental value of about 7 Hz for the AU and GC base pairs. These results suggest that two-bond $^{15}N–^{15}N$ spin–spin coupling constants across hydrogen bonds are insensitive to the nature of the hybridization of the nitrogens, the nature of the substituents bonded to nitrogens, and the presence or absence of a positive charge on the complex. However, it should be emphasized that there is an indirect dependence of $^{2h}J_{N–N}$ on the nature of the hybridization and bonding of the N atoms for a particular complex, since these properties determine the equilibrium N–N distance,

Table 22.1 N–N distances (Å) and $^{15}N–^{15}N$ spin–spin coupling constants ($^{2h}J_{N–N}$, Hz) in equilibrium structures of neutral and cationic complexes stabilized by N–H–N hydrogen bonds.

	***R*(N–N)**	**$^{2h}J_{N–N}$**
Neutral complexes		
CNH:pyridine	2.793	10.7
CNH:NCLi	2.833	9.6
CNH:NH_3	2.846	8.7
CNH:NCH	2.996	5.5
Pyrrole:NCH	3.164	3.0
Cationic complexes		
1,4-Diazinium:NCLi	2.633	16.5
NH_4^+:NCLi	2.634	16.1
Pyridinium:NCLi	2.673	14.4
NH_4^+:NH_3	2.705	12.9
NH_4^+:NCH	2.830	9.2
1,4-Diazinium:NCH	2.834	9.4
Pyridinium:NCH	2.872	8.2
NH_4^+:N_2	3.108	3.2

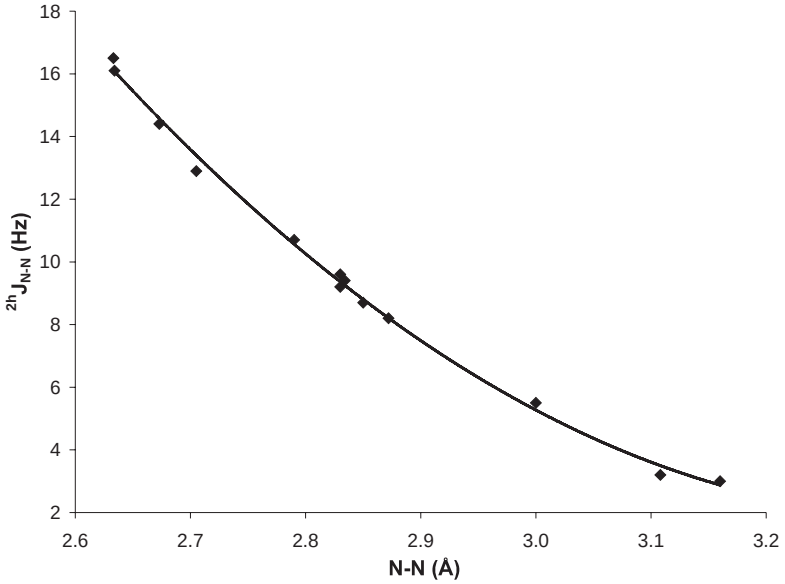

Figure 22.2 $^{2h}J_{N-N}$ versus the N–N distance for the equilibrium structures of neutral and cationic complexes with N–H–N hydrogen bonds.

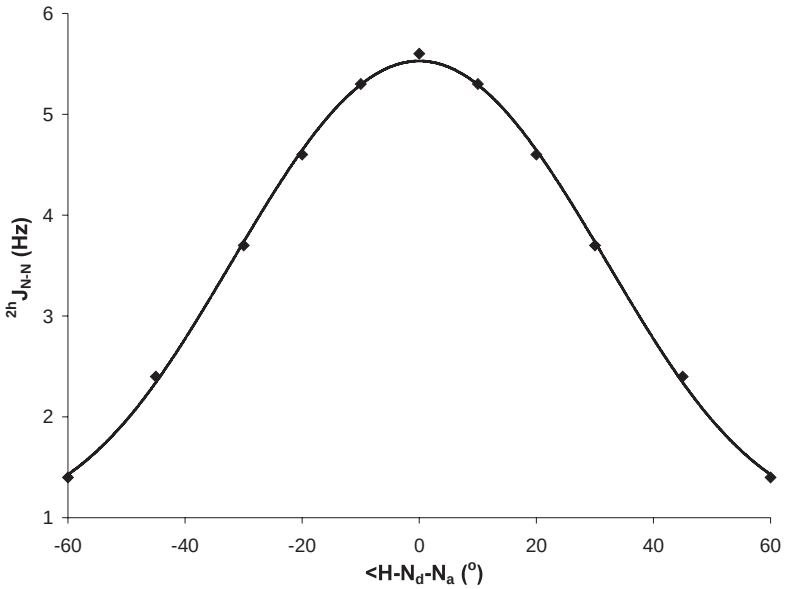

Figure 22.3 The variation of $^{2h}J_{N-N}$ as a function of the nonlinearity of the hydrogen bond in $CN_dH{:}N_aCH$. A value of $\angle$ H–N_d–N_a = 0.0° corresponds to a linear hydrogen bond.

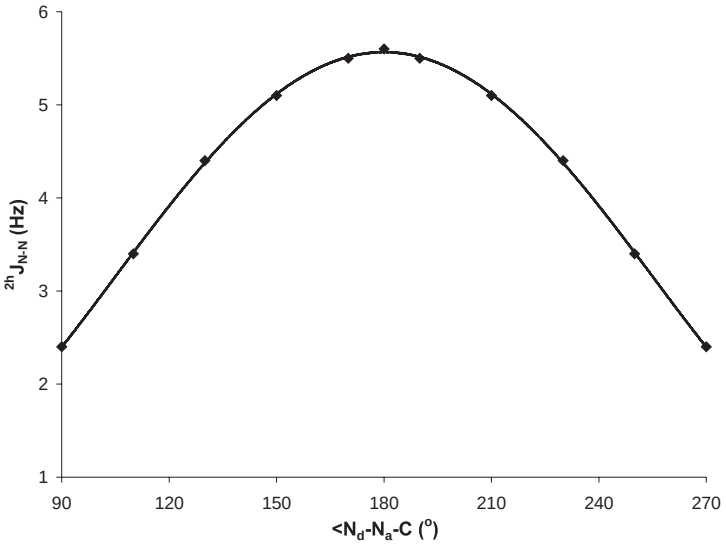

Figure 22.4 The dependence of $^{2h}J_{N-N}$ on the orientation of the lone pair on the proton-acceptor nitrogen in $CN_dH{:}N_aCH$. The lone pair is directed along the N_d–H–N_a axis when ∠ N_d–N_a–C = 180.0°.

which in turn, determines $^{2h}J_{N-N}$. Figure 22.2 should be useful for estimating N–N distances from experimental ^{15}N–^{15}N coupling constants, and for predicting $^{2h}J_{N-N}$ when experimental values are not available.

All of the complexes in Table 22.1 have linear hydrogen bonds formed with a directed lone pair of electrons on the proton-acceptor nitrogen atom. How does $^{2h}J_{N-N}$ change if the hydrogen bond becomes nonlinear, or if the directed lone pair is removed from the hydrogen bond? Figures 22.3 and 22.4 show the variation of $^{2h}J_{N-N}$ graphically as such changes occur in $CN_dH{:}N_aCH$. To obtain $^{2h}J_{N-N}$ as a function of the linearity of the hydrogen bond, a rotational axis was placed through N_d perpendicular to the N_d–N_a line, and CN_dH was rotated about this axis, keeping all other coordinates fixed. Similarly, to obtain the variation in $^{2h}J_{N-N}$ as the lone pair is removed from the hydrogen bond, an axis was placed through N_a perpendicular to the N_d–N_a line, and N_aCH was rotated about this axis, again keeping all other coordinates fixed. Figures 22.3 and 22.4 suggest that small perturbations which distort the hydrogen bond from linearity or displace the directed lone pair from the hydrogen bonding axis have relatively small effects on $^{2h}J_{N-N.}$ However, $^{2h}J_{N-N}$ decreases rapidly as these perturbations become larger.

22.3.3
C–H–N Hydrogen Bonds

In principle, it should be possible to measure spin–spin coupling constants across C–H–N hydrogen bonds. In anticipation of such experimental studies, we have car-

ried out systematic investigations of $^{13}C–^{15}N$ coupling constants in a series of neutral, cationic, and anionic complexes stabilized by C–H–N hydrogen bonds [42]. These complexes include C and N atoms that are sp, sp^2, and sp^3 hybridized. All of these complexes are stabilized by traditional hydrogen bonds in which a C–H group is the proton donor to N, except for pyridinium:CNH and NH_4^+:CNH, which are stabilized by traditional N–H^+...C hydrogen bonds.

C–N distances, the Fermi-contact term, and total $^{2h}J_{C–N}$ for the equilibrium structures of 23 complexes with C–H–N hydrogen bonds are reported in Table 22.2. The

Table 22.2 Equilibrium distances (Å) and the Fermi-contact term (FC) and $^{2h}J_{C–N}$ (Hz) for complexes with C–H–N hydrogen bonds.

	***R*(C–N)**	**FC**	$^{2h}J_{C–N}$
Neutral complexes			
HCCH...NCH	3.440	–5.24	–5.26
ClCCH...NCH	3.413	–6.03	–6.06
FCCH...NCH	3.412	–6.33	–6.35
NCH...NCH	3.316	–7.31	–7.34
HCCH...NCLi	3.303	–8.34	–8.37
FCCH...NCLi	3.272	–10.09	–10.09[a]
ClCCH...NCLi	3.268	–9.77	–9.77[a]
NCH...NCLi	3.160	–12.16	–12.21
NCH...pyridine	3.163	–12.66	–12.66[a]
HCCH...NH_3	3.327	–8.13	–8.14
ClCCH...NH_3	3.303	–9.26	–9.26
FCCH...NH_3	3.301	–9.73	–9.73[a]
NCH...NH_3	3.204	–10.95	–10.98
F(O)CH...NCH	3.466	–5.19	–5.19[a]
F(O)CH...NH_3	3.340	–8.39	–8.39[a]
F_3CH...NCH	3.456	–4.68	–4.68[a]
F_3CH...NH_3	3.341	–7.30	–7.30[a]
Cationic complexes			
Pyridine–H^+...CNH	2.974	–22.24	–22.24[a]
H_3NH^+...CNH	2.936	–26.40	–26.49
$HNCH^+$...NCH	2.832	–40.03	–40.13
Anionic complexes			
HCCH...NC^-	3.117	–16.19	–16.25
FCCH...NC^-	3.077	–20.09	–20.09[a]
NCH...NC^-	2.940	–24.66	–24.77

a Estimated from the Fermi-contact term.

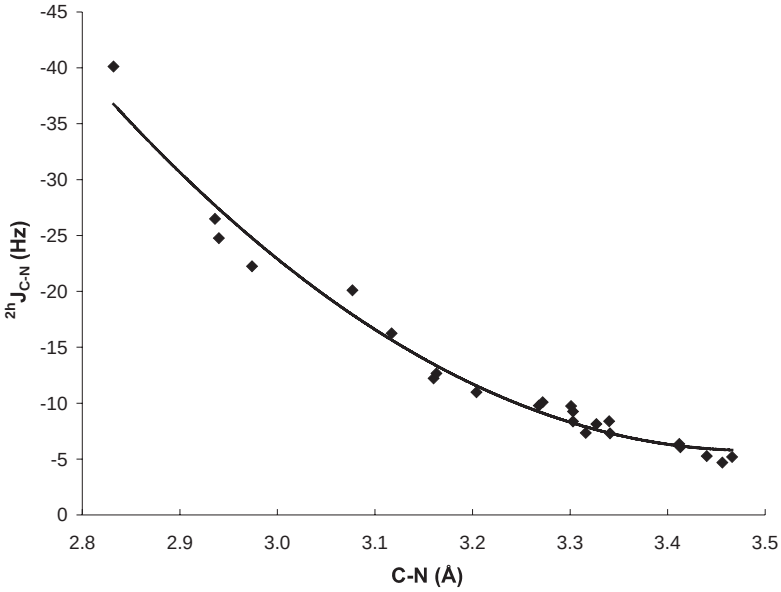

Figure 22.5 $^{2h}J_{C–N}$ versus the C–N distance for the equilibrium structures of neutral and charged complexes stabilized by C–H–N hydrogen bonds.

PSO, DSO, and SD terms make negligible contributions to the total coupling constant, and FC approximates $^{2h}J_{C–N}$ to 0.1 Hz in those complexes for which all terms were computed. Since the FC term is distance dependent, $^{2h}J_{C–N}$ also depends on the C–N distance. As evident from Table 22.2, the equilibrium distances in the charged complexes are relatively short compared to the neutral complexes, and the values of $^{2h}J_{C–N}$ are also greater.

$^{2h}J_{C–N}$ values for the entire set of 23 complexes have been plotted in Fig. 22.5 as a function of the C–N distance. There is some scatter in the data, as evident from Fig. 22.5 and the correlation coefficient of 0.97 for the best-fit quadratic curve. The scatter is due primarily to the dependence of $^{2h}J_{C–N}$ on the hybridization and bonding at the proton-donor C–H group [42]. Since $^{2h}J_{C–N}$ is also relatively insensitive to small deviations which perturb the linearity of the hydrogen bond, the curve presented in Fig. 22.5 should be useful for relating experimentally measured C–N coupling constants to C–N distances.

22.3.4
F–H–N Hydrogen Bonds

Experimental measurements of $^{19}F–^{15}N$ spin–spin coupling constants across F–H...N hydrogen bonds are available, due primarily to the work of Limbach and his associates [43, 44]. We have investigated F–N coupling constants for neutral complexes with F–H...N hydrogen bonds [45] and cationic complexes with $N–H^{+}$...F

hydrogen bonds [46]. Figure 22.6 presents $^{2h}J_{F-N}$ versus the F–N distance for the optimized structures of 13 neutral and 18 cationic complexes. The best-fit quadratic curve is not shown, but its low correlation coefficient of 0.62 is not unexpected given the scatter evident in these data. The scatter may be attributed primarily to the significantly greater values of coupling constants for cationic complexes compared to neutral complexes at the same F–N distance. This is apparent from Fig. 22.6, which shows that when $^{2h}J_{F-N}$ for neutral and cationic complexes are plotted separately against the F–N distance, improved correlations are found, although there is still some scatter. There are two obvious questions to be addressed.

1. What causes the scatter in the plots of $^{2h}J_{F-N}$ versus the F–N distance, particularly in the cationic complexes?
2. Why do the cationic complexes have larger coupling constants over the entire range of F–N distances?

Table 22.3 lists the F–N distances, PSO, DSO, FC, and SD terms, and $^{2h}J_{F-N}$ for complexes stabilized by F–H...N and N–H^+...F hydrogen bonds. The Fermi-contact term is again a good approximation to $^{2h}J_{F-N}$, although the differences between FC and $^{2h}J_{F-N}$ for the complexes of FH with ammonia and substituted amines are greater than observed previously for other complexes. For FH:NHF_2 and FH:NH_2F, FC underestimates (in an absolute sense) $^{2h}J_{F-N}$ primarily because of the contribution of the SD term. In contrast, for FH:NH_3 and FH:$NH_2(CH_3)$, FC overestimates $^{2h}J_{F-N}$ primarily because of the relatively large positive value of the PSO term.

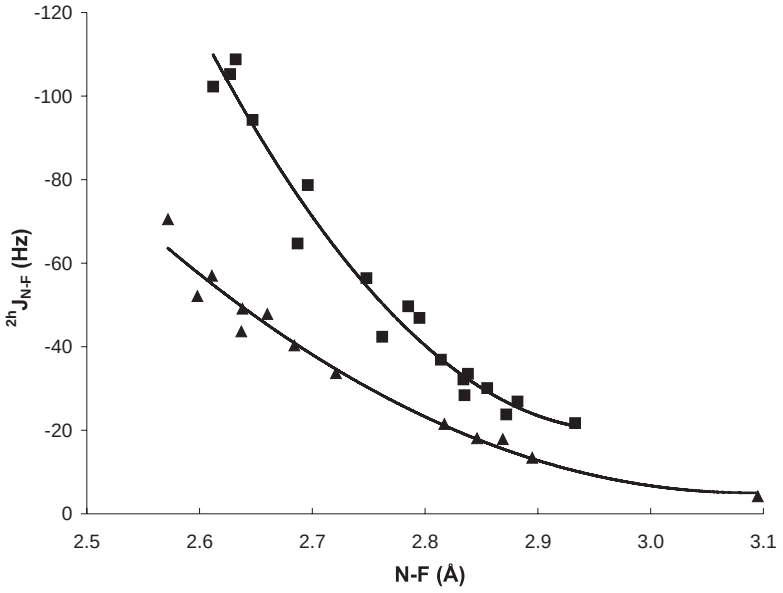

Figure 22.6 $^{2h}J_{F-N}$ versus the F–N distance for the optimized structures of neutral and cationic complexes stabilized by F–H–N hydrogen bonds. Solid square: cations; solid triangle: neutrals.

Table 22.3 Equilibrium distances (Å) and two-bond spin–spin coupling constants ($^{2h}J_{F-N}$) and components[a] of $^{2h}J_{F-N}$ (Hz) for complexes with F–H...N and N–H^+...F hydrogen bonds.

	F–N	PSO	DSO	FC	SD	$^{2h}J_{F-N}$
Neutral complexes						
FH:NF_3	3.095			–4.2		–4.2[b]
FH:NCCN	2.895	0.2	0.0	–13.1	–0.5	–13.4
FH:NHF_2	2.869	–0.5	–0.1	–16.1	–1.2	–17.9
FH:NCF	2.846	0.4	0.0	–18.1	–0.4	–18.1
FH:NCH	2.817	0.3	0.0	–21.2	–0.6	–21.5
FH:NH_2F	2.721	0.3	0.0	–32.4	–1.6	–33.7
FH:1,3,5-triazine	2.684			–40.3		–40.3[b]
FH:NCLi	2.660	0.6	0.0	–47.5	–0.9	–47.8
FH:1,4-diazine	2.638			–49.1		–49.1[b]
FH:NH_3	2.637	2.8	0.0	–45.2	–1.3	–43.7
FH:pyridine	2.611			–57.0		–57.0[b]
FH:$NH_2(CH_3)$	2.598	2.9	0.0	–53.3	–1.7	–52.1
FH:4-Li-pyridine	2.572			–70.5		–70.5[b]
Cationic complexes						
4-Li-Pyridinium:FH	2.933			–21.7		–21.7[b]
Pyridinium:FH	2.882			–26.9		–26.9[b]
$(CH_3)H_2NH^+$:FH	2.872			–23.8		–23.8[b]
1,4-Diazinium:FH	2.855			–30.1		–30.1[b]
$H_2C{=}NH_2^+$:FH	2.838			–33.5		–33.5[b]
H_3NH^+...FH	2.835	0.5	0.0	–28.7	–0.2	–28.4
1,3,5-Triazinium:FH	2.834			–32.2		–32.2[b]
$(F)HC{=}NH_2^+$:FH	2.814			–36.9		–36.9[b]
$LiCNH^+$:FH	2.795	0.4	–0.1	–47.1	–0.1	–46.9
1,2,4,6-Tetrazinium:FH	2.785			–49.7		–49.7[b]
F H_2NH^+:FH	2.762	0.3	–0.1	–42.3	–0.3	–42.4
$H_2C{=}N(F)H^+$:FH	2.748			–56.4		–56.4[b]
$(CH_3)CNH^+$:FH	2.696			–78.7		–78.7[b]
F_2HNH^+:FH	2.687	0.0	–0.1	–64.1	–0.5	–64.7
$HCNH^+$:FH	2.647	0.4	–0.1	–94.5	–0.2	–94.3
$FCNH^+$:FH	2.632	0.5	–0.1	–109.1	–0.1	–108.8
$NCCNH^+$:FH	2.627	0.4	–0.1	–105.4	–0.2	–105.3
F_3NH^+:FH	2.612			–102.3		–102.3[b]

a PSO = paramagnetic spin–orbit; DSO = diamagnetic spin–orbit; FC = Fermi-contact, SD = diamagnetic spin–orbit.
b Estimated from the Fermi-contact term.

The equilibrium structures of all of the neutral complexes have linear hydrogen bonds formed with directed lone pairs of electrons, while the equilibrium structures of the cationic complexes do not necessarily have this ideal structure. However, for comparison purposes, the structures of the cationic complexes were constrained during optimization so that N–H^+...F–H are collinear. These constraints are not

unreasonable, as discussed in detail in ref. 46. Although the quadratic correlation between $^{2h}J_{F-N}$ and the F–N distance for the neutral complexes is good, there is still some scatter in the data, as evident from Fig. 22.6. This scatter can be traced to the dependence of $^{2h}J_{F-N}$ on the hybridization of the nitrogen, as evident from Fig. 22.7. If the proton-acceptor molecules are grouped according to the nitrogen hybridization, excellent quadratic correlations between $^{2h}J_{F-N}$ and the F–N distance are found, with correlation coefficients between 0.99 and 1.00. Similarly, the greater scatter in the data for the cationic complexes can also be attributed to the hybridization of the nitrogen, as evident from Fig. 22.8. It is interesting to note that $^{2h}J_{F-N}$ for cationic complexes in which the proton donors are sp^3 hybridized have lower absolute values than $^{2h}J_{F-N}$ for complexes with sp and sp^2 nitrogens over the entire range of F–N distances.

It is also apparent from Fig. 22.6 that at a given F–N distance, $^{2h}J_{F-N}$ is significantly greater for a cationic complex, a reflection of its greater proton-shared character. One way to measure the degree of proton-sharing is to examine the difference between the F–H and N–H distances in a pair of neutral and cationic complexes that have similar F–N distances. (This comparison is not strictly valid, since the van der Waals radii for N and F are different. However, the radii are similar enough at 1.55 and 1.47 Å, respectively, to warrant such a comparison.) Table 22.4 presents data for three sets of neutral and cationic complexes that have similar N–F distances. It is evident from these data that the absolute value of the difference between the F–H and N–H distances is smaller in the cationic complexes, and these complexes

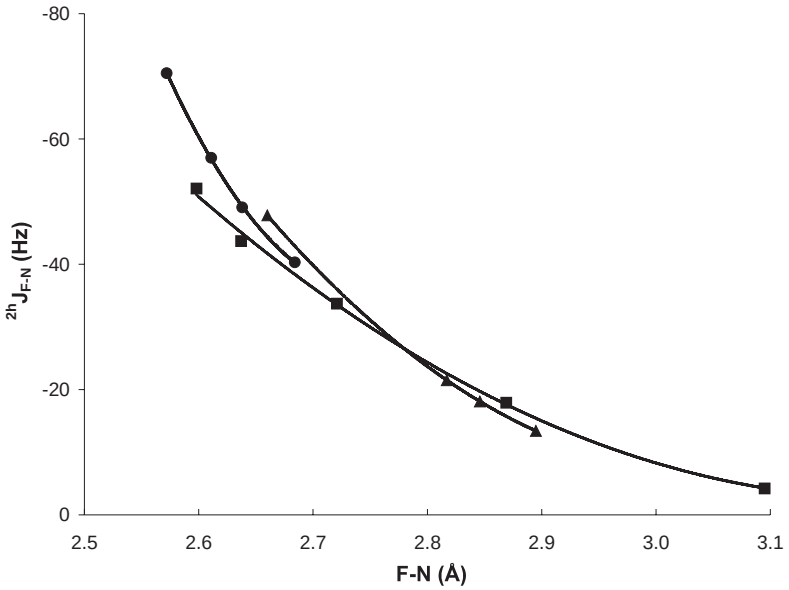

Figure 22.7 $^{2h}J_{F-N}$ versus the F–N distance for neutral complexes with F–H...N hydrogen bonds grouped according to the hybridization of the nitrogen. Solid triangle: sp; solid circle: sp^2 ; solid square: sp^3.

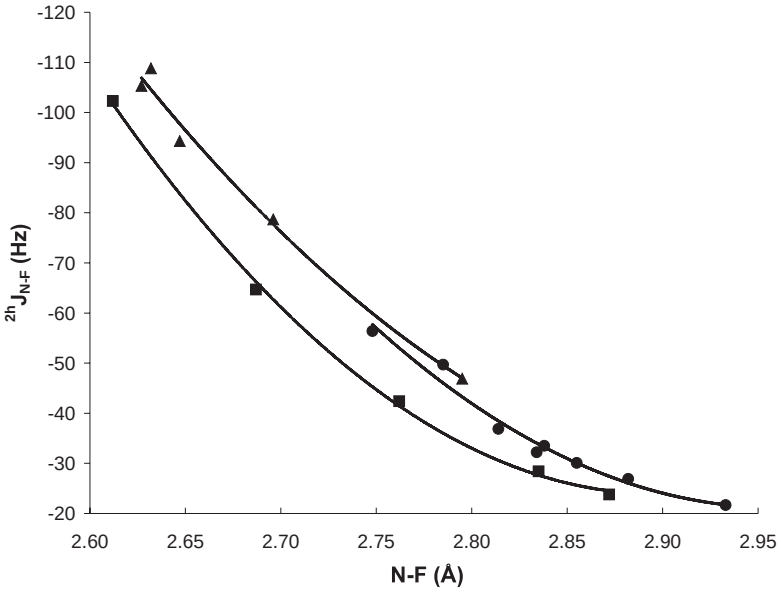

Figure 22.8 $^{2h}J_{F-N}$ versus the F–N distance for cationic complexes with N–H^+...F hydrogen bonds grouped according to the hybridization of the nitrogen. Solid triangle: sp; solid circle: sp^2; solid square: sp^3.

have significantly larger coupling constants. Perhaps an even more compelling argument can be made from the data in Table 22.4 that provide absolute values of the difference between the F–H and N–H distances for pairs of neutral and cationic complexes that have similar coupling constants but different F–N distances. It is evident from these data that when the degree of proton sharing is approximately the same (as measured by the difference between the F–H and N–H distances in the pair), then the coupling constants for the pair are very similar. Even though the hydrogen bonds in these complexes are traditional hydrogen bonds, they have a similar degree of proton-shared character.

Another feature of complexes with F–H–N hydrogen bonds is the very large values of F–N coupling constants. While the maximum N–N and C–N coupling constants computed are about 20 Hz and 45 Hz, respectively, F–N coupling constants can exceed 100 Hz. (Although reduced coupling constants $^{2h}K_{X-Y}$ should be used when comparing coupling constants for different atoms, it is $^{2h}J_{X-Y}$ that is measured experimentally, hence the large differences are significant.) An interesting consequence of the large range of values for N–F coupling constants is that a neutral and a cationic complex with similar F–N distances can have coupling constants that differ by more than 50 Hz!

In some recent experimental studies, Limbach and his associates investigated the temperature dependence of coupling constants across hydrogen bonds [43, 44, 47–49]. They observed that as a function of decreasing temperature, two-bond spin–spin coupling constants initially increase, exhibit a maximum absolute value, and

Table 22.4 $^{2h}J_{N-F}$ values (Hz) and differences between F–H and N–H distances (Å) for selected neutral and cationic complexes with F–H–N hydrogen bonds.

	R(N–F)	$\lvert R(N–H) - R(F–H)\rvert$	$^{2h}J_{N-F}$
Complexes with similar N–F distances			
FH:NCH	2.817	0.941	–21.5
(F)HC=NH_2^+:FH	2.814	0.767	–36.9
FH:1,3,5-triazine	2.684	0.778	–40.3
F_2HNH^+:FH	2.687	0.595	–64.7
FH:NH_3	2.637	0.711	–43.7
$FCNH^+$:FH	2.632	0.560	–108.8
Complexes with similar N–F coupling constants			
FH:pyridine	2.611	0.678	–57.0
H_2C=N(F)H^+:FH	2.748	0.683	–56.4
FH:1,4-diazine	2.638	0.718	–49.1
1,2,4,6-tetrazinium:FH	2.785	0.721	–49.7
FH:NCLi	2.660	0.750	–47.8
$LiCNH^+$:FH	2.795	0.763	–46.9
FH:NH_2F	2.721	0.824	–33.7
H_2C=NH_2^+:FH	2.838	0.792	–33.5
FH:NCH	2.817	0.941	–21.5
4-Li-pyridinium:FH	2.933	0.899	–21.7

then decrease. They interpreted their results in terms of solvent ordering and proton transfer. They suggested that as the temperature decreases, the type of hydrogen bond changes from traditional, to proton-shared, to ion-pair. Thus, they came to the same conclusions about the relationship between $^{2h}J_{X-Y}$ and hydrogen bond type based on experimental data as we did based on EOM-CCSD calculations. That reliable ab initio calculations can assist in the interpretation of experimental coupling constants for hydrogen-bonded complexes is illustrated below using the FH:collidine complex.

In a recent experimental study of the temperature dependence of $^{2h}J_{F-N}$ for the FH:collidine (FH:2,4,6-trimethylpyridine) complex between 100 and 200 K [43], Limbach and co-workers noted that as the temperature decreased, proton transfer occurred and hydrogen bond type changed from traditional, to proton-shared, to ion-pair. As the temperature decreased, they observed that the one-bond F–H coupling constant ($^1J_{F-H}$) decreased, the absolute value of the H–N coupling constant ($^{1h}J_{H-N}$) increased, but the two-bond F–N coupling constant remained essentially constant at –96 ± 5 Hz. This is puzzling, given their and our previous results. To

gain insight into these experimental results, we computed $^{1}J_{F-H}$, $^{1h}J_{H-N}$, and $^{2h}J_{F-N}$ in two model systems, FH:NH_3 and FH:pyridine [50]. For each system we systematically varied the F–H distance, optimized the complex at each distance, and then computed the coupling constant for each optimized structure. Figure 22.9 shows the variation of $^{1}J_{F-H}$, $^{1h}J_{H-N}$ and $^{2h}J_{F-N}$ as a function of the F–H distance, and therefore changing hydrogen bond type, for FH:pyridine. As the F–H distance increases, the F–N distance decreases to a minimum when the hydrogen bond is proton-shared, and then increases as the ion-pair hydrogen bond is formed. These distance changes are intimately related to the variation of $^{2h}J_{F-N}$ that is seen in Fig. 22.9. It should be noted that since collidine is a stronger base than pyridine, the equilibrium structure of FH:collidine has greater proton-shared character, even in the gas phase. Our data suggest that at the highest temperatures investigated experimentally in solution, the hydrogen bond in FH:collidine is proton-shared, being on the traditional side of quasi-symmetric. At the lowest temperature, the hydrogen bond is still proton-shared, but is now on the ion-pair side. Thus, the vertical bars in Fig. 22.9 are drawn to correspond to the region of the potential surface probed by the experiments. In this region, the potential surface for proton motion is relatively flat. This allows the proton to move freely while the F–N distance remains constant. It is the constancy of this distance that gives rise to the constancy of $^{2h}J_{F-N}$.

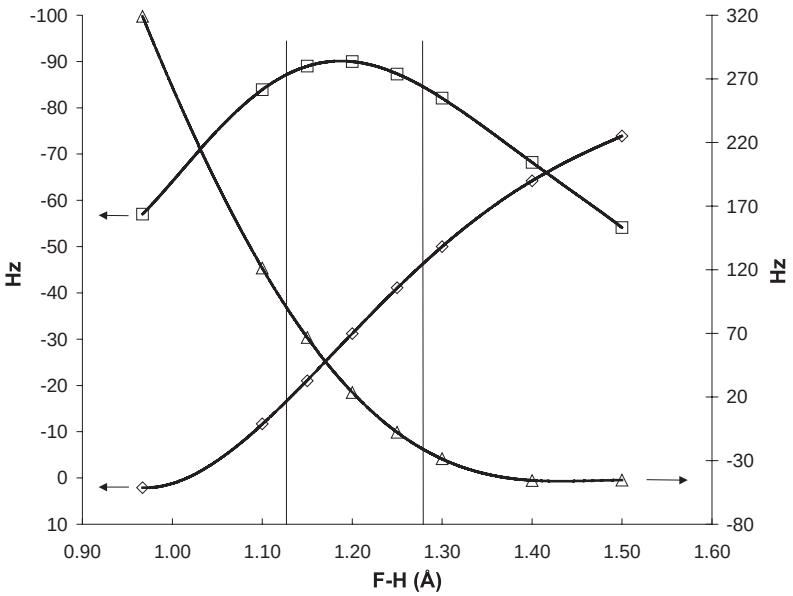

Figure 22.9 $^{2h}J_{F-N}$, $^{1h}J_{H-N}$, and $^{1}J_{F-H}$ for FH:pyridine as a function of the F–H distance. The values of the coupling constants (estimated from the FC terms) were computed for the optimized structures at these distances. Open square: F–N; open diamond: H–N; open triangle: F–H.

Table 22.5 NMR spin–spin coupling constants (Hz) for quasi-symmetric proton-shared hydrogen bonds in FH:collidine and FH:pyridine.

	FH:collidine Experimental	FH:pyridine EOM-CCSD[a]		
F–H (Å)		1.15	1.20	1.25
F–N (Å)		2.489	2.480	2.484
$^{2h}J_{F-N}$	–96	–89	–90	–87
$^{1}J_{F-H}$	30	68	24	–8
$^{1h}J_{H-N}$	–50	–21	–31	–41

a Estimated from the Fermi-contact term.

Although Limbach et al. were not able to specifically identify the temperature at which the complex is stabilized by a quasi-symmetric proton-shared hydrogen bond due to the constancy of $^{2h}J_{F-N}$, they presented their estimates of the values of F–H, F–N, and H–N coupling constants that might characterize such a complex. These are given in Table 22.5, along with our computed values for FH:pyridine in the proton-shared region. Given that pyridine is not as basic as collidine, and that $^{2h}J_{F-N}$ has been estimated only by the Fermi-contact term, the computed results are in good agreement with the experimental, and provide insight into the interpretation of the experimental findings.

22.4 Concluding Remarks

This chapter presents a summary of EOM-CCSD calculations carried out in this laboratory to characterize two-bond spin–spin coupling constants across N–H–N, C–H–N, and F–H–N hydrogen bonds in neutral and charged complexes. From the computed results, we have constructed curves for $^{2h}J_{X-Y}$ as a function of the X–Y distance for each set of hydrogen-bonded complexes. These curves are presented as tools for extracting X–Y distances from experimentally-measured coupling constants, and for predicting these constants in the absence of experimental data. The computed results have led to new insights into the factors that determine $^{2h}J_{X-Y.}$ Future work will expand on these results, with the aim of providing a systematic characterization of spin–spin coupling constants across various types of X–H–Y hydrogen bonds.

Acknowledgments

This work was supported by the National Science Foundation through NSF grant CHE-9873815. This support and that of the Ohio Supercomputer Center are gratefully acknowledged. It is a pleasure to acknowledge the many research collaborators who made important contributions to the work reported in this chapter.

References

1 G. C. Pimentel, A. L. McClellan, *The Hydrogen Bond*, Freeman, San Francisco **1960**.
2 A. J. Dingley, S. J. Grzesiek, *J. Am. Chem. Soc.* **1998**, *120*, 8293.
3 J. Elguero, I. Alkorta, *Int. J. Mol. Sci.* **2003**, *4*, 64.
4 S. Grzesiek, F. Cordier, A. J. Dingley, *Biol. Magn. Reson.* **2003**, *20*, 255.
5 R. J. Bartlett, D. M. Silver, *J. Chem. Phys.* **1975**, *62*, 3258.
6 R. J. Bartlett, G. D. Purvis, *Int. J. Quantum Chem.* **1978**, *14*, 561.
7 J. A. Pople, J. S. Binkley, R. Seeger, *Int. J. Quantum Chem. Quantum Chem. Symp.* **1976**, *10*, 1.
8 R. Krishnan, J. A. Pople, *Int. J. Quantum Chem.* **1978**, *14*, 91.
9 W. J. Hehre, R. Ditchfield, J. A. Pople, *J. Chem. Phys.* **1982**, *56*, 2257.
10 P. C. Hariharan, J. A. Pople, *Theor. Chim. Acta.* **1973**, *238*, 213.
11 G. W. Spitznagel, T. Clark, J. Chandrasekhar et al., *J. Comput. Chem.* **1983**, *3*, 3633.
12 T. Clark, J. Chandrasekhar, G. W. Spitznagel et al., *J. Comput. Chem.* **1983**, *4*, 294.
13 J. E. Del Bene, in *The Encyclopedia of Computational Chemistry*, eds. P. v. R. Schleyer, N. L. Allinger, T. Clark et al. John Wiley & Sons, Chichester **1998**, Vol. 2, pp. 1263–1271.
14 T. H. Dunning, Jr, *J. Chem. Phys.* **1989**, *90*, 1007.
15 D. E. Woon, T. H. Dunning, Jr., *J. Chem. Phys.* **1995**, *103*, 4572.
16 T. H. Dunning, Jr, *J. Am. Chem. Soc.* **2000**, *104*, 9062.
17 S. A. Perera, H. Sekino, R. J. Bartlett, *J. Chem. Phys.* **1994**, *101*, 2186.
18 S. A. Perera, M. Nooijen, R. J. Bartlett, *J. Chem. Phys.* **1996**, *104*, 3290.
19 S. A. Perera, R. J. Bartlett, *J. Am. Chem. Soc.* **1995**, *117*, 8476.
20 S. A. Perera, R. J. Bartlett, *J. Am. Chem. Soc.* **1996**, *118*, 7849.
21 A. Schäfer, H. Horn, R. Ahlrichs, *J. Chem. Phys.* **1992**, *97*, 2571.
22 J. E. Del Bene, M. J. T. Jordan, *J. Mol. Struct. (Theochem)* **2001**, *573*, 11.
23 K. Chapman, D. Crittenden, J. Bevitt et al., *J. Phys. Chem. A* **2001**, *105*, 5442.
24 J. E. Del Bene, S. A. Perera, R. J. Bartlett, *J. Am. Chem. Soc.* **2000**, *122*, 3560.
25 A. C. Legon, *Chem. Soc. Rev.* **1993**, *22*, 153.
26 J. A. Gerlt, M. M Kreevoy, W. W. Cleland et al., *Chem. Biol.* **1977**, *4*, 259.
27 W. W. Cleland, M. M. Kreevoy, *Science*, **1994**, *264*, 1927.
28 S. S. Marimanikkuppam, I.-S. Lee, D. A. Binder et al., *Croat. Chem. Acta* **1996**, *69*, 1661.
29 W. W. Cleland, *Biochemistry*, **1992**, *31*, 317.
30 J. P. Guthrie, R. Kluger, *J. Am. Chem. Soc.* **1993**, *115*, 11569.
31 J. P. Guthrie, *Chem. Biol.* **1996**, *3*, 163.
32 A. Warshel, A. Papazyan, *Proc. Natl. Acad. Sci.* **1996**, *93*, 13665.
33 J. E. Del Bene, M. J. T. Jordan, *J. Am. Chem. Soc.* **2000**, *122*, 4794.
34 J. E. Del Bene, R. J. Bartlett, *J. Am. Chem. Soc.* **2000**, *122*, 10480.
35 J. E. Del Bene, S. A. Perera, R. J. Bartlett, *J. Phys. Chem. A* **2001**, *105*, 930.
36 J. E. Del Bene, S. A. Perera, R. J. Bartlett, *Mag. Reson. Chem.* **2001**, *39*, S109.
37 J. Toh, M. J. T. Jordan, B. C. Husowitz et al., *J. Phys. Chem. A* **2001**, *105*, 10906.
38 J. E. Del Bene, M. J. T. Jordan, *J. Phys. Chem. A* **2002**, *106*, 5385.
39 J. E. Del Bene, M. J. T. Jordan, P. M. W. Gill et al., *Mol. Phys.* **1997**, *92*, 429.
40 J. E. Del Bene, M. J. T. Jordan, *J. Chem. Phys.* **1998**, *108*, 3205.
41 M. J. T. Jordan, J. E. Del Bene, *J. Am. Chem. Soc.* **2000**, *122*, 2101.
42 J. E. Del Bene, S. A. Perera, R. J. Bartlett et al., *J. Phys. Chem. A* **2003**, *107*, 3222.
43 I. G. Shenderovich, A. P. Burtsev, G. S. Denisov et al., *Magn. Reson. Chem.* **2001**, *39*, S91.
44 N. S. Golubev, I. G. Shenderovich, S. N. Smirnov et al., *Chem. Eur. J.* **1999**, *5*, 492.
45 J. E. Del Bene, S. A. Perera, R. J. Bartlett et al., *J. Phys. Chem. A* **2003**, *107*, 3121.
46 J. E. Del Bene, S. A. Perera, R. J. Bartlett et al., *J. Phys. Chem. A* **2003**, *107*, 3126.
47 S. N. Smirnov, N. S. Golubev, G. S. Denisov et al., *J. Am. Chem. Soc.* **1996**, *118*, 4094.
48 N. S. Golubev, S. N. Smirnov, V. A. Gindin et al., *J. Am. Chem. Soc.* **1994**, *116*, 12055.
49 H. Benedict, H-H. Limbach, M. Wehlan et al., *J. Am. Chem. Soc.* **1998**, *120*, 2939.
50 J. E. Del Bene, R. J. Bartlett, J. Elguero, *Magn. Reson. Chem.* **2002**, *40*, 767.

23
Calculation of NMR Parameters in Carbocation Chemistry

Hans-Ullrich Siehl and Valerije Vrček

23.1
Introduction

Carbocation chemistry is characterized by the fruitful interplay of experiment and theory. NMR spectroscopy has evolved as *the* important experimental method for the direct study of the structure and dynamics of carbocations in solution and, recently, also in the solid state. For general structure elucidation contemporary NMR techniques rival X-ray crystallography, which is particularly difficult for carbocations. Quantum chemical methods have developed as indispensable tools to complement experimental results. Despite great interest in ab initio calculation of experimentally observable molecular properties, calculations of NMR chemical shifts and coupling constants have become routine only recently. This chapter will review, in a non-comprehensive attempt, recent applications of quantum chemical calculations of NMR chemical shifts and spin–spin coupling constants in carbocation chemistry.

The IGLO method, an important breakthrough for the calculation of magnetic properties, was developed in the middle 1980s by Kutzelnigg , Fleischer and Schindler [1]. After some applications to carbocations were published in a landmark paper by Schindler [2] in 1987 the calculation of carbocations and related species rapidly developed into a flourishing field exploited by many research groups, especially Schleyer and collaborators [3, 4]. These early IGLO applications to carbocations were an important contribution to the recognition of NMR computations as a potential structural tool [5].

Further historical, methodological and practical aspects have been summarized and will not be considered in detail here [6]. Explanations for the acronyms and abbreviations used in theoretical chemistry and in this review are published by the IUPAC organization [7].

Recently the GIAO method for calculation of NMR chemical shifts has become the de facto standard and has been implemented in major quantum chemistry packages. The GIAO approach facilitates accurate NMR shift calculations via electron-correlated methods (see Chapter 8). GIAO-DFT methods have evolved as a standard tool, in particular for the calculation of shifts for larger molecules and transition metal complexes. DFT NMR results, however, for some types of carbocations are less satisfactory and lack possibilities for systematic improvements compared to

Calculation of NMR and EPR Parameters. Theory and Applications.
Edited by Martin Kaupp, Michael Bühl, Vladimir G. Malkin
Copyright © 2004 WILEY-VCH Verlag GmbH & Co. KGaA, Weinheim
ISBN: 3-527-30779-6

those obtained with the traditional methods for treating electron correlation. Calculations using the GIAO-MP2 approach have convincingly demonstrated the importance of electron correlation effects in NMR chemical shift calculations and could resolve a number of problems concerning the interpretation of experimental NMR spectra of carbocations [8–12].

However, GIAO-MP2 in certain cases tends to overestimate electron correlation effects on the absolute shielding constants [13]. The GIAO coupled cluster schemes provide shieldings with quantitative accuracy and CCSD(T) NMR calculations have been used extensively for benchmark calculations [14] and some challenging chemical shift problems in carbocation chemistry [15, 16].

It should be kept in mind that quantum chemical calculations of structures and magnetic properties generally are done for the isolated molecule or ensemble, without taking into account its environment and media effects such as solvent, site-specific solvation or counter ion effects. This is a critical point since NMR spectra of carbocations, with a few exceptions, are studied in superacid solutions, and properties calculated for the gas phase species are of little relevance if the electronic structure of the ion is strongly perturbed by solvent effects.

Another important point is whether disagreement between calculated and observed chemical shifts is due to an inadequate level used for the calculation of the geometry and/or a consequence of deficiencies in the model used for the calculation of NMR chemical shifts. Fortuitous error cancellation is ubiquitous in quantum chemistry at all levels of theory. Calculated relative NMR shifts are magnetic shielding differences and are thus prone to error cancellation effects. Provided that appropriate methods are used, and that the results for the geometry optimization and shielding tensors are sufficiently converged with respect to wave function model and basis set, the congruence of calculated and observed ^{13}C shifts would suggest that the geometry adopted by carbocations in superacid solution is similar to the gas-phase prediction and unperturbed by interaction with the environment. Such costly benchmark types of NMR calculations using the traditional methods for treating electron correlation, MP2, CCSD and CCSD(T), have been performed for very few carbocations, known to be particularly difficult cases for NMR chemical shift computations [15, 16].

23.2 Alkyl and Cycloalkyl Cations

CH_5^+ (protonated methane **1**) is considered as the parent of hypercoordinated carbocations containing a five-coordinated carbon atom. It has a fluxional structure as evident from infrared investigations and ab initio dynamic simulations [17]. For a C_s symmetrical structure of CH_5^+ a ^{13}C chemical shift of –11.5 ppm is calculated, which is 7.1 ppm more shielded than that of CH_4 at the GIAO-MP2 level [18]. The shielding effect in **1** is expected for such a hypercoordinated carbon [19].

The calculated parent six-coordinated dication **2**, diprotonated methane (CH_6^{2+}) has two 3c–2e bonding interactions in its minimum energy structure (C_{2v}). The cal-

culated ^{13}C NMR chemical shift of the dication is –25.7, 14.2 ppm more shielded than that of **1** [20]. The studies have been extended to hypercoordinated onium-carbonium dications of type **3** (X = NH_3, PH_3, H_2O, H_2S, HF, HCl, CO, N_2, CO_2 and CS_2) [21].

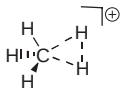

1

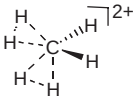

2

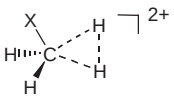

3

The prototypical primary ethyl cation, $C_2H_5^+$, is not stable enough to be observable directly in superacid media. Quantum chemical calculations predict the μ-hydrido-bridged form **5** to be 6–8 kcal mol^{-1} more stable than the "open" form **4**. NMR chemical shifts for both forms were calculated at the GIAO-MP2//CCSD level of theory [22]. The calculated ^{13}C chemical shifts of C1 and C2 in **4** were 361.17 and 73.96 ppm, respectively, while in the symmetrically bridged form **5** the calculated value for carbon atoms was 163.97 ppm. The chemical shift (-0.02 ppm) of the bridging hydrogen (H_b) is in accord with a 3c–2e bond in the bridged form. NMR spin–spin coupling constants were calculated with the EOM-CCSD method [23]. The small value calculated for $^1J(CH_b)$ of 13 Hz compared to $^1J(CH)$ = 125–250 Hz in hydrocarbons is diagnostic for such 1,2-hydrogen-bridged structures.

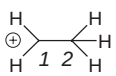

4

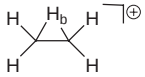

5

A systematic study of a set of 16 alkyl- and cycloalkyl cations (Scheme 23.1) was performed to investigate the performance of GIAO-B3LYP methods which require much less computational resources in terms of cpu time, memory, and temporary storage compared to GIAO-MP2 methods [24]. The chemical shifts of the carbons at positions most sensitive to the positive charge, i.e. C1, the formally positively charged carbon, and the α- and β-carbon atoms were investigated in detail. The structures were optimized at the B3LYP/6-31G(d) level and, for comparison, also at the MP2/6-31G(d) level. Chemical shift calculations were done at the GIAO-B3LYP/6-311G(d,p) level. Generally, the chemical shifts were calculated more downfield than the experimental shifts. This is due to deficiencies of the applied method, since GIAO-DFT calculations are known to overestimate the paramagnetic contributions to the chemical shielding, resulting in overly deshielded chemical shifts. The effect is, however, not uniform for all carbons. The slope and intercept for a correlation equation were determined separately for C^+ and the α- and β-carbon positions, and were found to be related to the mode of hyperconjugative charge delocalization in the particular carbocation structure. The chemical shifts calculated using the GIAO-

DFT method for MP2/6-31G(d) optimized structures are generally somewhat closer to the experimental values, however, at higher computational costs.

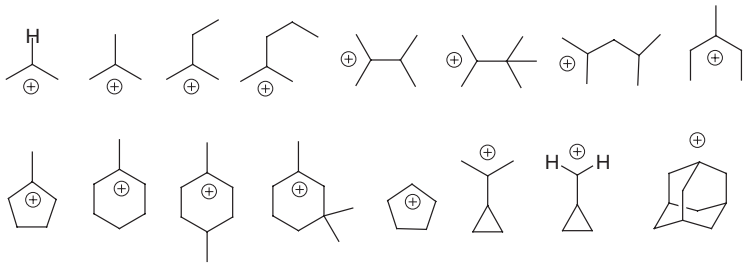

Scheme 23.1

The 2-propyl cation **6** has a C_2 symmetric structure which, at the MP2/6-311G(d,p) level, is the only open-chain minimum on the $C_3H_7^+$ potential energy surface [25]. IGLO-HF/II chemical shift calculations for this geometry agree reasonably well (deviation $\Delta = +4$ ppm) for the C^+ carbon (exp. 320.6 ppm), and slightly worse for the methyl carbons (exp. 51.5 ppm, $\Delta = -7$ ppm) [26]. At the GIAO-MP2/TZP/DZ level somewhat better agreement for the methyl groups was obtained [4]. The ^{13}C chemical shift tensors of the isopropyl cation were calculated at the GIAO-MP2/tzp/dz and GIAO-B3LYP/tzp/dz levels [27]. The principal component δ_{11} (coincident with the C–H bond along the C_2 axis of symmetry) was calculated to be 545 ppm, but the experimental value measured by CP MAS-NMR was only 497 ppm. The authors have considered the inclusion of counterions (FHF^- and SbF_6^-) to model the effect of the medium, but only modest improvements were obtained. The chemical shift tensors of the isopropyl cation in model ion pairs have also been calculated using GIAO-B3LYP//MP2/6-311G(d,p) and various basis sets [28].

The *tert*-butyl cation structure (**7**) with C_s symmetry is better suited for hyperconjugation than the C_{3h} form and is thus energetically slightly favored [29]. The IGLO/DZ//MPZ(full)/6-31G(d,p) calculated ^{13}C chemical shifts deviate by +11 ppm for the central carbon (exp. 335.2 ppm) and –1.3 ppm (averaged) for the CH_3-groups (exp. 45.6 ppm).

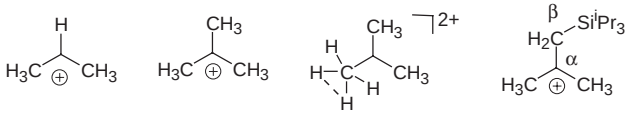

6 **7** **8** **9**

The ^{13}C chemical shift for the central carbon of the protio-*tert*-butyl dication (**8**) has been calculated as 327.5 ppm (IGLO/II//MP2/6-31G(d)) [30]. This value is shielded compared to the experimental and calculated shift of **7**. This was taken as evidence that the dication **8**, even in strong superacids, is only sparsely populated in the equilibrium with the *tert*-butyl cation.

The 2-methyl-1-triisopropylsilylpropyl-2-cation (**9**) is the first experimentally accessible β-silyl substituted alkyl cation [31, 32]. The GIAO-HF/tzp-dz//MP2/tzp calculated shifts show fortuitously small differences to the experimental shifts, even for the formally charged carbon (–7.3 ppm) and for silicon (+8.1 ppm). The large deviations of the GIAO-MP2 calculated shifts, in particular for those atoms involved in β-Si-hyperconjugation (C_α –28 ppm, C_β +15 ppm, ^{29}Si +35 ppm) can be rationalized assuming an overestimation of σ-delocalization effects. Further computational studies are in progress to clarify this point.

The 2-butyl cation is the smallest secondary cation that can be stabilized either by C–C or C–H hyperconjugation. Experimental results give evidence for two equilibrating isomers [33]. MP2/6-311G(d,p) calculations show that the symmetrically hydrido-bridged structure **11** is marginally more stable than the partially methyl bridged structure **10** [34, 35] NMR chemical shifts for **10** and **11** have been calculated using IGLO-HF, GIAO-HF and GIAO-MP2 methods and various basis sets [4]. As expected the chemical shifts for the C–C-hyperconjugatively stabilized structure is very sensitive towards the degree of bridging, which depends on the computational method used.

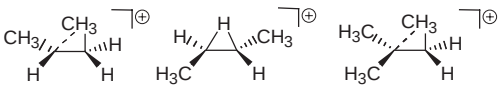

10 **11** **12**

The 2-methyl-2-butyl cation (**12**) is the smallest tertiary carbocation structurally suitable for stabilization through C–C hyperconjugation. A comparison of IGLO/DZ//MP2/6-31G(d) calculated and measured ^{13}C NMR chemical shifts demonstrates that the partially methyl bridged isomer is the preferred species [36]. It was demonstrated that the calculated ^{13}C chemical shifts are highly sensitive towards hyperconjugational distortion, i.e. the degree of bridging. (ca. 6 ppm degree^{-1} from 68° to 98°).

The experimental and computational study of the NMR spectra of *E*-1-cyclopropyl-2-(triisopropylsilyl)ethyl cation (**13**) (see Fig. 23.1) and its model structure *E*-1-cyclopropyl-2-(trimethylsilyl)ethyl cation demonstrates an application of calculations of ^{1}H and ^{13}C NMR chemical shifts and *J*(HH) spin spin coupling constants for the assignment of stereochemistry in this type of carbocation [37].

The 400 MHz ^{1}H NMR spectrum of **13** shows characteristic ^3J(HH) coupling constants for the non-equivalent *syn* and *anti* oriented β-CH_2-hydrogens to the α-methine-hydrogen. The spin–spin coupling constants were calculated using a finite perturbation level (FPT) [38], Perdew/III//MP2/6-31G(d), for both the *Z*- and the *E*-isomeric structures. The quite satisfactory agreement ($\Delta = 0.1$–1 Hz) of the calculated ^3J(HH) coupling constants for H_α H_β, and $H_{\beta'}$ for the *E*-isomer with the observed values, confirm the *trans* arrangement of H_α and H_β, the *syn*/*anti* assignment, and the *E*-conformation for the experimentally observed carbocation. The better agreement between experimental and GIAO-B3LYP/6-311G(d,p)//MP2/6-31G(d) calculated chemical shifts for the *E*-isomer (H_α $\Delta\delta$(exp.-calc.) = –0.5 ppm) than for

the *Z*-form (H_α $\Delta\delta = +1.05$ ppm) is in accord with the assignment to the *E*-configuration. In particular the large difference calculated for the Cγ' and Cγ'' carbons in the *Z*-isomer ($\Delta\delta C\gamma'/C\gamma'' = 21.76$ ppm), as compared to a calculated difference of $\Delta\delta C\gamma'/C\gamma'' = 2.79$ ppm for the *E*-isomer, is not in accord with the experimental shifts ($\Delta\delta C\gamma'/C\gamma'' = 1.92$ ppm).

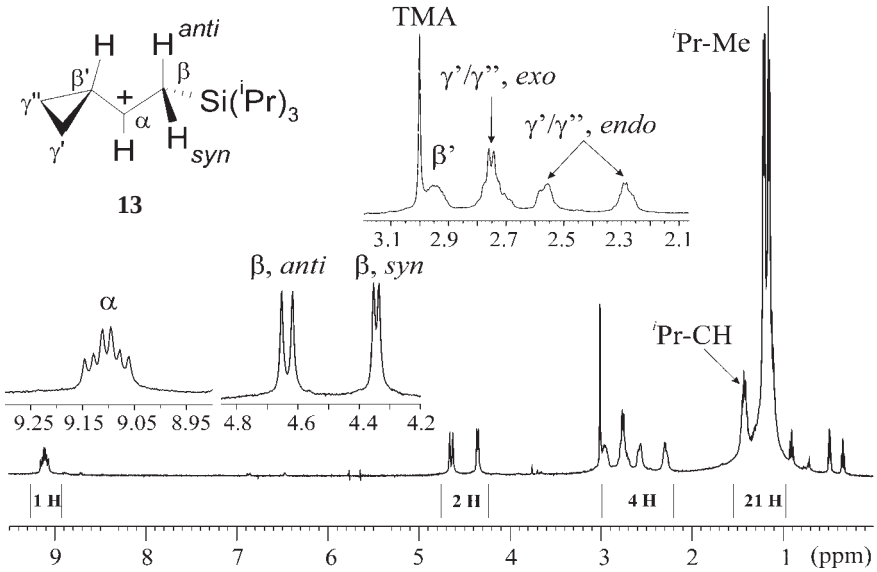

Figure 23.1 400 MHz ^{1}H-NMR spectrum of *E*-1-cyclopropyl-2-triisopropylsilyl-ethyl cation (**13**) at –105 °C in SO_2ClF/SO_2F_2 (taken from Ref. [37b]).

An experimental and calculational NMR investigation of dicyclopropyl substituted cyclobutylmethyl cation (**14**) [39] has shown that IGLO/DZ//B3LYP/6-31G(d) calculated ^{13}C NMR chemical shifts facilitate the assignment of the spectra.

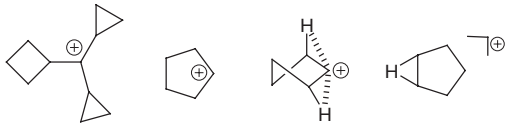

14 **15** **16** **17**

The cyclopentyl cation (**15**) undergoes a degenerate rearrangement which can be frozen out at cryogenic temperatures in the solid state CPMAS NMR spectrum. MP2/6-31G(d,p) calculations show that cyclopentyl cation has a twisted conformation (**16**) [40] in which the axial hydrogens bend toward the carbocation center because of pronounced hyperconjugational distortion expected for a secondary carbocation. IGLO-HF/DZ calculations of the ^{13}C NMR chemical shifts reveal that the chemical shifts are very sensitive to small changes in geometry and that an MP2/6-31G(d,p)

optimized geometry is required to obtain chemical shifts which are in agreement with the experimental data [4]. Earlier IGLO-HF/DZ calculations assuming a planar (C_{2v}) structure [2] or a symmetrically hydrido-bridged (C_s) structure **17** [41] lead to larger differences.

The nonamethylcyclopentyl cation (**18**) also undergoes a fast dynamic equilibrium process caused by circumambulatory *trans*-migrating methyl groups which lead to fast averaging of all quaternary carbons and dynamic line broadening of the methyl signals [42] B3LYP/6-31G(d) calculations show the structure to be a trivalent carbocation type with onset of bridging by the axial-oriented β-methyl groups because of hyperconjugative distortion. GIAO-DFT calculated ^{13}C NMR chemical shifts, empirically scaled using a linear correlation, [24] gave good agreement between the calculated averaged chemical shift for the ring carbons (108.5 ppm) and the experimental value (110.1 ppm).

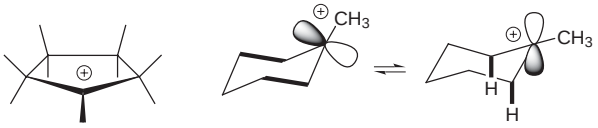

18 **19** **20**

The two chair conformations of tertiary methylcyclohexyl cation **19** and **20** are in rapid equilibrium. The two conformations are two isomers where the formally vacant p-orbital is either equatorially (**19**) or axially (**20**) oriented, interacting in **19** with the β-C–C bonds or, in **20**, with the β-C–H bonds, respectively. Experimental dynamic NMR measurements showed the C–C hyperconjugative isomer **19** to be marginally (1–3 kJ mol^{-1}) more stable [43]. The interpretation of the experimental data was confirmed by calculation of ^{13}C NMR chemical shifts of **19** and **20** [44]. The calculated shifts, in particular for those carbons involved in the hyperconjugative stabilization of the positive charge, are critically dependent on the level of theory used. For example, the β-carbon shift for the C–C hyperconjugatively stabilized isomer **19** calculated using IGLO-HF or GIAO-HF methods deviates from experiment by –20 ppm whereas GIAO-MP2 methods with dzp/dz (59.8 ppm) or tzp/dz basis sets (62.2 ppm), show good agreement with the experimental estimate of 60 ppm. Similarly, for the (2-propyl)-cyclohexyl cation β-C–C and β-C–H σ-bond hyperconjugatively stabilized isomers **21** and **22** have been characterized by experimental and computational NMR investigations [45].

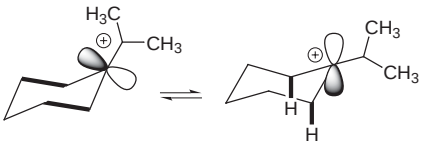

21 **22**

The experimentally observed ^{1}H and ^{13}C chemical shifts of the μ-hydrido-bridged [46] cyclooctyl cation (**23**) were reproduced reasonably well by IGLO-HF NMR chemical shift calculations for MP2/6-31G(d) geometries (C_s symmetry) except for a large deviation of the μ-hydrido bridged hydrogen (calc. –10.5 ppm, IGLO/II//MP2/6-31G(d)), exp. –7.7 ppm) [47]. CSGT-DFT NMR calculations on HF geometries have been performed for cyclooctyl (**23**), cyclononyl (**24**) and cyclodecyl (**25**) cations and overall somewhat better agreement compared to previous IGLO-HF calculations was obtained [48]. The chemical shift for the highly shielded μ-hydrogen in **23** was calculated to be –8.9 ppm. The shift for the bridgehead carbons deviates however by about +10 ppm, demonstrating again that HF and DFT levels are not appropriate to model geometries and chemical shifts for hydrido-bridged carbocations [4, 49] If electron correlation is taken into account using the GIAO-MP2 method, much better results are obtained including the shifts for the bridgehead carbons [50].

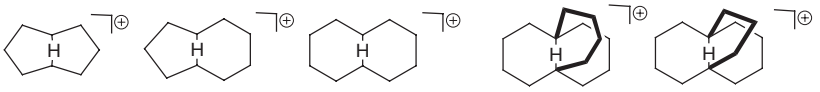

23 **24** **25** **26** **27**

A distinct upfield shift of the bridging hydrogen was also calculated for the *in*-bicyclo[4.4.4]tetradecyl cation (**26**) [51] using GIAO-HF methods, but the large discrepancy of about 6.5 ppm between theoretical and experimental δ ^{1}H values could not satisfactorily be explained at that time. A series of NMR calculations have been performed for **26**, where the μ-hydrogen was displaced in-plane and out-of-plane relative to the symmetric Born–Oppenheimer surface minimum [52]. The chemical shift of the μ-hydrogen did not change much. It was shown however, that electron correlation effects, for both the geometry optimization and the NMR calculations (GIAO-B3LYP/6-31G(d)//B3LYP/6-31G(d)), are required to reproduce the large upfield chemical shift of the bridging hydrogen. A large highfield shift (–12 ppm) for the μ-hydrogen was predicted for the experimentally elusive μ-hydrogen-bridged bicyclo[3.3.3]undecyl cation (**27**).

CSGT-DFT NMR calculations were also performed for some other types of cyclic and acyclic hydrido-bridged cations and dications [53]. Again, some discrepancies between experimental and theoretical results are apparent. For the triply-μ-hydrido-bridged carbodication **28**, a model for a 4c–2e bonding unit, which is not a minimum on the energy surface, a high-field bridging hydrogen (–9 ppm) and a low field shift for the bridgehead carbons (223 ppm) were calculated [54].

The unusual carbocation structure **29**, a linear 5-center 4-electron C–H–C–H–C array can be derived from three anthracenes "joined up" around a C–H–C–H–C core [55]. The GIAO-DFT computed ^{1}H and ^{13}C NMR shifts chemical for the bridging hydrogens (2.9 ppm) and carbons (112 and 182 ppm) of the 5-center array differ considerably from those found in typical 3-center 2-electron systems.

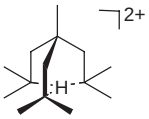

28

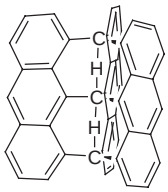

29

23.3 Bicyclic and Polycyclic Carbocations

The structure of the 2-norbornyl cation has been a focal point of controversy in physical organic chemistry. Experimental NMR spectroscopy and computational methods have been the most prominent tools, favoring the hypercoordinated symmetric bridged structure **30**, a protonated nortricyclane [56]. The tricoordinated 2-norbornyl cation **31** is not a local minimum on the energy surface [57].

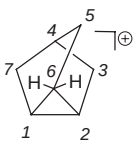

30

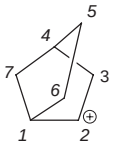

31

GIAO-MP2/TZP//MP2/6-31G(d) calculation of ^{13}C NMR chemical shifts (127.0 ppm C1, C2; 40.5 ppm C3, C7; 41.5 ppm C4; 23.5 ppm C5; 24.0 ppm C6) are, within +4 ppm, in agreement with the experimental chemical shifts measured at –158 °C (124.8 ppm C1, C2; 36.6 ppm C3, C7; 37.9 ppm C4; 20.2 ppm C5; 21.3 ppm C6) [4]. Similar ^{13}C NMR and ^{1}H NMR chemical shifts have been calculated using GIAO-MP2/DZP//MP2/DZP. The spin–spin coupling constants calculated for the same MP2/DZP geometry using an EOM-CCSD method [23] are in accord with the experimentally measured ones. The ^{1}J(C6C1) and the ^{1}J(C6C2) coupling constants of –5.6 Hz (which are not experimentally available) are particularly diagnostic for the nortricyclane framework of the hypercoordinated 2-norbornyl cation. The usual $^{1}J^{13}C^{13}C$ coupling constants are in the range 10–40 Hz and these small negative coupling constants are characteristic for small-ring bicyclic molecules and are often attributed to interference between one-bond and two-bond couplings in this type of small ring system [58].

NMR chemical shifts of 2-norbornyl cation related model structures, some with partly restricted geometries, have been calculated using the CSGT-B3LYP method [59]. As expected for σ-electron delocalized systems, the chemical shift for carbons C1, C2, and C6 involved in the hypercoordinative bonding was found to be very sensitive toward small geometrical changes and to vary greatly, whereas the shifts of carbons C3, C4, C5, and C7 are similar to the results obtained with more appropriate electron correlation methods such as GIAO-MP2.

2-methyl-2-norbornyl (**32**) and 1,2-dimethyl-2-norbornyl (**33**) cations have partially bridged structures. The IGLO-HF/DZ and the SOS-DFPT-IGLO/II calculated NMR chemical shifts using B3LYP/6-31G(d) optimized geometries agree well with the experimental values for both **32** and **33** [4]. A strong dependence of calculated chemical shifts on the extent of bridging was found for the camphenyl cation (**34**) using GIAO-DFT calculations [60]. For a B3LYP optimized geometry the ^{13}C NMR chemical shift for the C2 (C^+) carbon was 23 ppm too deshielded. Using the MP2 optimized structure the shift was 44 ppm too shielded, whereas the GIAO-B3LYP/6-31G(d)//MP4/6-31G(d) data gave the best agreement (266.8 ppm) with the experimental shift (261.9 ppm).

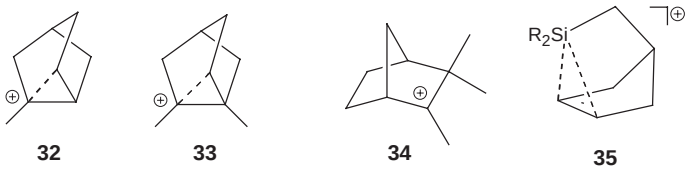

32 **33** **34** **35**

Silanorbornylcations **35** were characterized by experimental and computational ^{13}C and ^{29}Si NMR chemical shifts. ^{29}Si NMR chemical shift calculations at the B3LYP/6-311G(3d,p)//MP2/6-311G(d,p) level are in good agreement with the experimental data ($\Delta\delta = -3.8$ to -2.7 ppm). The calculated ^{13}C NMR chemical shifts deviate between +8.3 and 14.6 ppm [61].

Bridged cyclobutyl cations (bicyclobutonium ions) **36** have a pentacoordinated γ-carbon. Recent computational investigations, including IGLO-HF/DZ calculations, of the parent $[C_4H_7]^+$ cation show that the bicyclobutonium structure is preferred and the corresponding cyclopropylmethyl cation structure is a minor isomer marginally higher in energy. Experimental NMR spectra [62] are complicated because low barrier rearrangement processes give rise to averaged peaks. Two structurally different isomers are in fast equilibrium and each isomer undergoes a rapid threefold degenerate averaging process (Scheme 23.2, R = H). Analysis of the temperature dependence of solution NMR [63] and solid state CPMAS NMR spectra [64] and comparison with IGLO-HF and GIAO-MP2 computed chemical shifts of the two isomers confirm the evidence for the presence of two species [4].

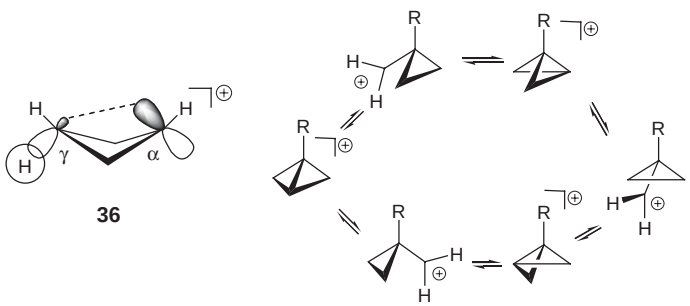

36

Scheme 23.2

The 1-methylbicyclobutonium ion and the 1-(trimethylsilyl)bicyclobutonium ion also undergo fast threefold methylene rearrangements (Scheme 23.2, R = CH_3 or $Si(CH_3)_3$). However, in contrast to the parent cation, the corresponding isomeric cyclopropylmethyl cation structures do not contribute to the averaged chemical shifts.

At the MP2/6-31G(d) level of theory the 1-silylcyclobutyl cation $[1\text{-}SiH_3\text{–}C_4H_6]^+$, which serves as a model compound for $[1\text{-}Si(CH_3)_3\text{–}C_4H_6]^+$, has a hypercoordinated puckered 1-silylbicyclobutonium structure (**37**), which is about 2.8 kcal mol^{-1} lower in energy than the (1′-silylcyclopropyl)methyl cation (**38**), which is a transition state [11, 65]. ^{13}C-NMR chemical shifts calculated (GIAO-MP2/tzpdz) for the MP2/6-31G(d) geometry of model cation **37** ($C_{\beta/\beta'}$: 79.6 ppm; C_γ: –14.5 ppm; => av. $C_\beta/C_{\beta'}/C_\gamma$ chemical shift: 48.2 ppm; C_α: 133.9 ppm) are in good agreement with the experimental values for the 1-trimethylsilyl substituted bicyclobutonium ion ($C_\beta/C_{\beta'}/C_\gamma$ av.: 48.9 ppm; C_α: 137.4 ppm), whereas the chemical shifts calculated for **38** are not in accord with experiment.

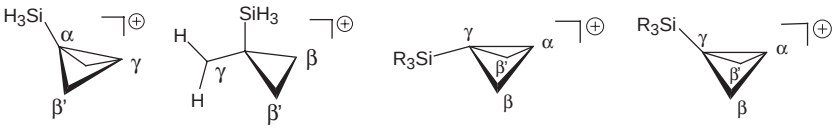

3-*endo*-Trialkylsilylbicyclobutonium ions **39** could be characterized by 1D- and 2D-NMR spectroscopy as static bicyclobutonium ions. The *endo* conformation was confirmed by comparison with calculated ^{13}C chemical shifts (GIAO-MP2/tzpdz) of model structures 3-*endo*- and 3-*exo*-SiH_3 substituted bicyclobutonium ions. The assignment was also confirmed by FPT (Perdew/III) calculation of the transannular $^3J(H_\alpha H_\gamma)$ spin spin coupling constant, which is 5.5 Hz measured experimentally and 5.9 Hz calculated for the *endo*-silyl isomer **39**, but is only 1.2 Hz calculated for the *exo*-silyl isomer **40** [65].

Similarly to the 2-norbornyl cation, the comparison of calculated (IGLO/DZ//MP2/6-31G(d)) and experimental ^{13}C NMR chemical shifts enables one to differentiate between the hypercoordinated **41** and the trivalent form **42** of the bicyclo[2.1.1.]-hexyl cation [66]. The experimental (157.8 ppm) and calculated (158.5 ppm) values for C1 and C2 (averaged signal) are nearly identical for the symmetrically bridged structure **41**, but do not correspond to the IGLO-HF/DZ chemical shift for classical structure **42** (207.4 ppm). On the basis of the calculated energies and the IGLO-HF results, it was concluded that the bicyclo[2.1.1.]hexyl cation prefers the symmetrically bridged to the trivalent structure.

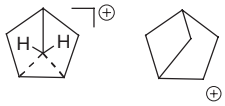

41 **42**

A series of hypercoordinated square-pyramidal carbocations were optimized at the MP2/6-31G(d) level and the ^{13}C NMR chemical shifts of the cations were calculated using IGLO-HF and GIAO-MP2 methods [67]. The parent square-pyramidal ion **43**, and the monomethyl-substituted analogs **44** and **45** with apical (**45**) and basal (**46**) substitution have not been observed experimentally. Good agreement between the calculated and experimental ^{13}C NMR chemical shifts was obtained for the 1,2-dimethyl-substituted analog **46** and the trimethyl-substituted analog **47**.

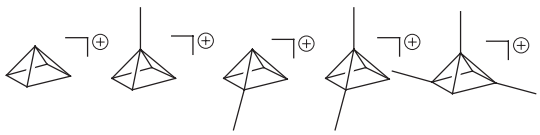

43 **44** **45** **46** **47**

The GIAO-MP2/dzp/dz calculated shift of the apical carbon (–17.3) for the bishomo square-pyramidal cations **48** agrees well with the experimental value of –17.2 ppm. The first chemical application of the IGLO-HF method has been the correct description of the unexpectedly small ^{13}C chemical shifts of the 1,3-dehydroadamantane-5,7-diyl-dication **49** [68].

48 **49**

23.4 Vinyl Cations

The parent vinyl cation has a hydrido-bridged structure **50** which is favored over the linear structure **51** both experimentally (6 kcal mol^{-1}) and computationally (3.8 kcal mol^{-1} at CCSD(T)) [69]. The chemical shifts were originally calculated using the IGLO-HF/DZ method [2]. The hydrido-bridged form **50** was characterized by an upfield shift (–2.6 ppm) for the bridging hydrogen, while the ^{13}C chemical shift for symmetrically bridged carbons was 104.3 ppm.

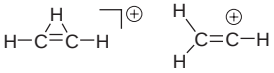

50 **51**

Experimental NMR spectra were reported for the α-cyclopropyl-cyclo-propylidene-methyl cation **52**, the only vinyl cation lacking π- or heteroatom stabilization which is accessible in superacid solution. Calculated chemical shifts at GIAO-HF levels showed large correlation errors of up to 45 ppm. GIAO-MP2 calculations using a tzp basis for carbon and dz for hydrogen yield reasonable results for all positions except the lowfield signal of the formally positively charged carbon, which is calculated 22 ppm shielded compared to the experimental shift [70]. The conspicuously selectively poor performance of the shift calculation for C_α at the MP2 level disappears when electron correlation effects are treated adequately. High-level coupled-cluster calculations (which were the first chemical application of these techniques) gave excellent agreement [15]. At the GIAO-CCSD(T) level, deviations between experiment and theory for the α-carbon are reduced to 1 ppm. The congruence of calculated and observed ^{13}C shifts suggests that the geometry adopted in superacid solution is similar to the gas-phase prediction. The effects of electron correlation, basis sets, and geometry on calculated NMR spectra of vinyl cations has subsequently also been studied in detail [71] for the parent vinyl cation in its linear form **51**, the cyclopropylidene-methyl cation (**53**), the α-cyclopropylvinyl cation (**54**), and the α-methylvinyl cation (**55**).

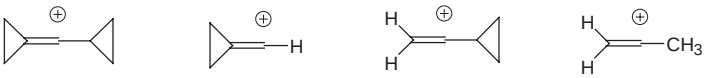

52 **53** **54** **55**

The allyl-resonance stabilized *E*- and *Z*-pent-1,3-dienyl-2-cations (**56** and **57**) are the smallest vinyl cations ever observed in superacid solutions [16]. A challenging task of quantum chemistry was to assign the NMR spectrum which exhibits pairs of signals which differ only by a few ppm to the chemical shifts for the carbon atoms of the *E*- and *Z*-isomers. HF-SCF NMR chemical shift calculations give poor agreement with experiment (the deviations are in the 40 ppm range). The basic HF-SCF treatment as well as DFT approaches [72] do not provide an adequate treatment, whereas inclusion of electron correlation, even at the modest MP2 level, improves the situation dramatically. MP2, CCSD and CCSD(T) levels calculations are in good agreement with experiment and allow an unequivocal assignment of the *Z*- and *E*-isomers. The mean deviation between experimental and calculated NMR chemical shifts at the CCSD(T) level is 1.8 and 2.0 ppm for *Z*- and *E*-isomers, respectively. It is noteworthy, but most likely fortuitous, that the lower level MP2 calculations give marginally better results. These results clearly demonstrate the degree of accuracy

provided by state-of-the-art coupled-cluster calculations of NMR chemical shifts, which allow unequivocal assignment of NMR signals that differ by only a few ppm.

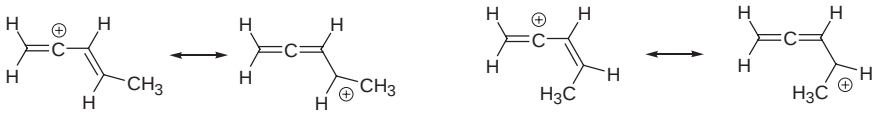

56 **57**

A β-silyl stabilized vinyl cation, the 1-bis(trimethylsilyl)methyl-2-bis(trimethylsilyl)ethenyl ion (**58**) was investigated by dynamic ^{13}C NMR spectroscopy [73]. The rotation around the C^+–$CH(SiMe_3)_2$ bond is controlled by strong hyperconjugation with the β-silyl groups. IGLO-HF/II calculations for model cations account for the strong shielding effect and confirm nicely the dihedral dependence of the β–silyl effect.

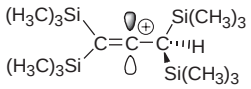

58

23.5 π-Stabilized Carbocations

Quantum chemical calculations at the MP4/6-31G(d)//HF/6-31G(d) level predict the puckered structures **59** of the cyclobutadienyl (R = H) and the tetramethylcyclobutadienyl ($R = CH_3$) dications to be more stable than the planar forms [74]. The IGLO-HF/DZ (209 and 18.7 ppm, respectively) and experimental (209.7 and 18.8 ppm) chemical shifts for the puckered geometry of the tetramethylcyclobutadienyl dication are nearly identical.

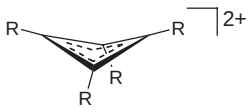

59

Arenium cations were the first carbocations investigated by correlated GIAO-MP2 NMR chemical shift calculations. A good agreement between experimental ^{13}C NMR chemical shifts of the 2,4-cyclohexadienyl cation **60** and the calculated values at the GIAO-MP2/tzp/dz//MP2/6-31G(d) level was obtained [8] whereas earlier

IGLO-HF/dz calculations for **60** and **61** deviated significantly from experiment [75]. On the basis of the observed ^{13}C NMR chemical shifts, the total chemical shift difference criteria, IGLO-HF/DZ chemical shift calculations, and comparison with the model spiro[2.5]oct-4-yl cation (**62**), it was concluded that the phenonium ion **61** is a spirocyclopropylbenzenium ion [76]. A linear correlation between calculated NPA charges and ^{13}C NMR chemical shifts was found for **60** and some methyl- and trifluoromethyl substituted homologues [77]. (Note, however, that interpretation of chemical shifts in terms of atomic charges is not generally appropriate, cf. Chapter 18 by Kaupp.)

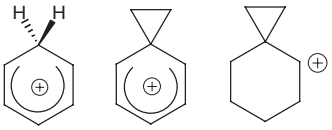

60 **61** **62**

IGLO-HF ^{29}Si NMR studies of silylated arenium ions **63** and **64** and comparison with experimental data have been reported [78, 79]. The results indicate that the formation of long-lived trimethyl substituted silyl cations, in the presence of aromatic solvents, as claimed by Lambert et al. [78, 79], is not feasible under these conditions. Persistent silicenium ions require sterically more shielding substituents at silicon or hypercoordinative stabilization [81–83].

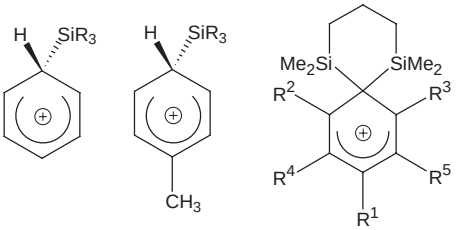

63 **64** **65**

^{13}C and ^{29}Si NMR chemical shifts were calculated for a series of disilylated arenium ions **65** at the DFT level of theory. The calculations predict consistently the unsaturated carbon atoms to be too deshielded by 8–15 ppm. Applying an empirical correction, the deviation between experiment and theory was reduced to –0.4 to –9.0 ppm, and the ^{13}C NMR chemical shift of the highly diagnostic C^{ipso} is reproduced by the calculations ($\Delta\delta = -3.8$ to -2.7 ppm) [84].

Below –120 °C the interconversion of the *anti* (**66**) and *syn* (**67**) 1-*p*-anisyl-2-triisopropylsilyl-ethyl-cation is slow on the NMR timescale [85]. Two sets of four lines are observed, one for the C2 and C6 *ortho* and C3 and C5 *meta* carbons in the *anti* iso-

mer, and another set with lower intensity for the C2′ and C6′ *ortho* and C3′ and C5′ *meta* carbons in the *syn* isomer. At higher temperatures kinetic line broadening and coalescence is observed. NMR chemical shift calculations were performed for the B3LYP/6-31G(d) optimized *anti* and *syn* isomeric structures of the analogous 1-*p*-anisyl-2-SiH_3 substituted ethyl cation which are close models for the experimentally observed cations. B3LYP/6-31G(d) calculated NMR chemical shifts for both the *anti* and *syn* isomer generally show deviations of more than 10 ppm and up to about 20 ppm for the SiR_3 substituted β-carbon (calc. R = H, exp. R = $CH(Me_2)$) compared to the experimental values. The deviations from experiment are smaller (< 8 ppm) when the 6-31G(d,p) basis set is used. SOS-DFPT-IGLO/III using the Perdew-Wang91 density functional yields the smallest deviations < 6 ppm (excluding the β-carbon chemical shift). The calculated differences between the chemical shifts for the two isomers allow, however, unequivocal assignment of the experimental signals at the lowest level of the calculations.

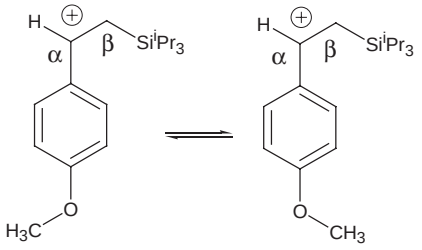

66 **67**

Substituted benzylic mono- and dications (**68** and **69**) were investigated by ^1H and ^{13}C NMR spectroscopy and IGLO-DFT calculations [86]. The results suggest that chinoid type structures are the predominant resonance contributors for **68**. The IGLO/DZ//3-21G calculated ^{13}C NMR chemical shifts of benzylic monocations **68** correlate reasonably well with the experimentally obtained data. The ^{13}C NMR chemical shifts of the carbocation centers (CH_2 carbon) are calculated 10.6–12.5 ppm too deshielded. Similar results were obtained for benzylic dications **69**.

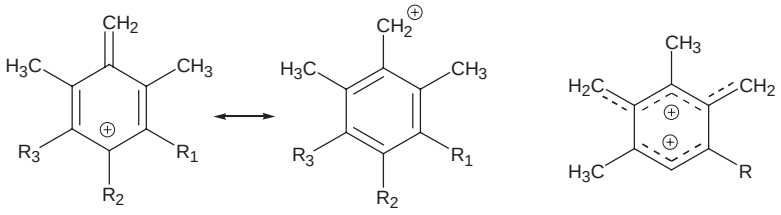

68 **69**

NMR chemical shifts of arenium ions derived from various classes of polycyclic aromatic hydrocarbons have been calculated using GIAO-DFT methods [87]. Generally,

for these arenium ions, the calculated ^{1}H NMR chemical shifts are overestimated whereas the ^{13}C NMR chemical shifts are in many cases underestimated.

In conjunction with the evaluation of ring current effects (NICS), (see Chapter 24 by Chen et al.), calculations of ^{1}H and ^{13}C NMR chemical shifts for a series of fluorenylidene dications were performed [88].

For some homoaromatic carbocations the magnetic criteria have been calculated [89, 90]. IGLO-HF and GIAO-MP2 calculated ^{13}C-NMR chemical shifts for bishomoaromatic 7-norbornenyl **70** and 7-norbornadienyl cation **71** have also been reported [91].

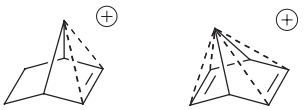

70 **71**

The cyclobutenyl cation (**72**) and the homotropylium cation, $C_8H_9^+$ (**73**), are both prototypes of homoaromatic systems. **72** is one of the first examples demonstrating that electron correlation is required both for geometry and NMR shift calculations [9]. The IGLO-HF/6-31G(d,p) calculated ^{13}C NMR chemical shifts of the planar form **74** clearly deviate from the experimental values (mean deviation $\Delta = 45.6$ ppm), which alternate in the seven-membered ring between 122 and 194 ppm, whereas those of the non-planar form **73** are in good agreement with the experiment (mean deviation $\Delta = 6.2$ ppm) [92].

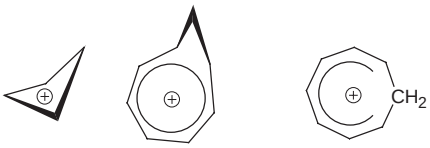

72 **73** **74**

DFT-calculated ^{13}C NMR chemical shifts for the pentamethylcyclopentadienyl cation and the $(CH_3)_5$-cyclopentenyl cation **77** provide conclusive evidence that the alleged synthesis and isolation of the potentially antiaromatic $(CH_3)_5$-cyclopentadienyl cation was not achieved [93]. Instead the allyl cation **77** was obtained. The reported experimental ^{13}C NMR data ($\delta^{13}C^{exp}$: $\delta = 250/243$, 153, 60) are in agreement with this structure, but differ significantly from the calculated ^{13}C NMR chemical shift for both Jahn–Teller distorted valence isomers of **75** and **76**.

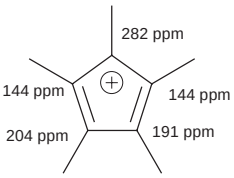

75

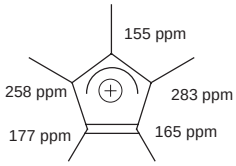

76

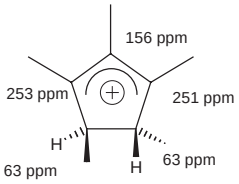

77

Carbocations have been generated in zeolites and were characterized by CPMAS ^{13}C NMR spectroscopy and accompanying quantum chemical calculations [94]. ^{13}C isotropic shifts calculated at the GIAO-MP2/tzp/dz level for the 1,3-dimethylcyclopentenyl (**78**) and 1,2,3-trimethylcyclopentenyl cations (**79**) [95] are in agreement with experimental spectra of the carbocations in the zeolite [96]. In both cases the calculated values are downfield of the experimental shifts (by ~ 5 ppm). It was suggested that the presence of the zeolite and motional averaging has some effect on the chemical shifts.

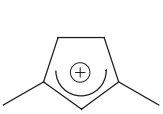

78

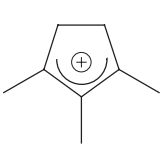

79

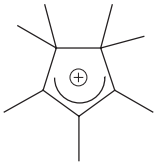

80

The heptamethylcyclopentenyl cation **80** was also characterized on zeolite [97]. ^{13}C NMR chemical shifts were calculated at the GIAO-MP2 using DFT geometries. Discrepancy levels of up to 17 ppm were suggested to result from geometrical distortions due to the zeolite cage. Other carbocations on zeolites, such as arenium [98] and 1,3-arylsubstituted allyl cations [99] have also been investigated by experimental and computational NMR methods.

23.6 Heteroatom Stabilized Carbocations

The experimental ^{13}C-NMR chemical shift of the simplest member of the acylium ions, the formyl cation HCO^+ was reported as $\delta = 139.5$ ppm (85 atm) which compares well with the GIAO-MP2 calculated shift of $\delta = 136$ ppm [100, 101]. The analogous fluoroformyl cation FCO^+ and protonated fluoroformic acid $[FC(OH)_2]^+$ were characterized experimentally [102] ($\delta^{13}C = 117.5$ ppm and $\delta^{13}C = 157.8$ ppm, respectively) as well as computationally ($\delta^{13}C = 118.6$ ppm and $\delta = 170.6$ ppm, respectively) [103].

A systematic study of experimental and calculated ^{13}C and ^{17}O NMR chemical shifts of oxonium, carboxonium [104], trifluoromethyl- [105] and trimethylsilyl- [106] substituted carboxonium ions and the corresponding acyl cations [107, 108] showed GIAO-MP2 to be superior to the IGLO-HF and GIAO-HF methods. Whereas for ^{13}C shifts tzp/dz basis sets are sufficient, qz2p/qz2p basis sets are required for an accurate prediction of ^{17}O chemical shifts.

The principal components of the ^{13}C chemical shift tensors for some acylium cations were determined by slow speed MAS NMR and quantum chemical methods [109]. A good agreement between the theoretical prediction and the experimental shift components of the acylium ions was found, which does not require inclusion of Lewis acid counteranions in the theoretical model, as was suggested for the isopropyl cation [27].

The ^{13}C and ^{19}F chemical shifts of a number of fluorocarbocations [110] and other halomethyl cations and their protonated forms have been studied experimentally and computationally [111]. It was shown by spin–orbit corrected IGLO-DFT calculations that for halomethyl cation CX_3 (X = F, Cl, Br, I) the experimentally observed decrease in the ^{13}C chemical shifts with increasing atomic number of X is due to spin–orbit coupling [112]. Previous explanations for this example of a 'normal halogen dependence' via electronegativity arguments were based on fortuitous empirical correlations. Comparison between IGLO-DFT, GIAO-HF and GIAO-MP2 results for these systems also demonstrates an increasing importance of electron correlation along the same series.

The ^{13}C, ^{15}N and ^{17}O NMR chemical shifts of some substituted methyl cations and the corresponding protonated dications were calculated by the GIAO-MP2 method on MP2/6-31G(d) geometries [113].

The *o*-, *m*- and *p*-phenylene bis(1,3-dioxolanium) dications **81** and the related tris(1,3-dioxolanium) trication have been prepared and the calculated ^{13}C and ^{17}O NMR chemical shifts (GIAO-DFT) closely match the experimental values [114]. The calculated ^{13}C chemical shift of the carbonyl carbon of monoprotonated benzaldehyde [115, 116] for the *E*-form **82** (205.5 ppm) and that for the *Z*-form **83** (207.4 ppm) agree well with the experimental shifts of 203.5 and 205.9 ppm, respectively. Protonation of α-substituted cinnamic acids such as **84** was studied by ^{13}C NMR spectroscopy and IGLO-HF computations [117].

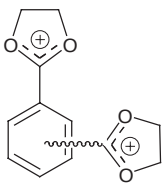

81

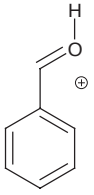

82

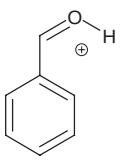

83

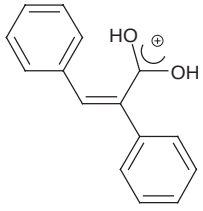

84

Protonated deltic acid (**85**) and related compounds [118, 119], as well as protonated urea **86** (X = O) [120] and thiourea **86** (X = S) [121] have been investigated by ^{13}C NMR spectroscopy and quantum chemical calculations [122]. GIAO-MP2 NMR results for DFT optimized geometries and comparison with experimental data were used to study the site of protonation of dimethyl sulfoxide [123]. The calculated ^{13}C chemical shift of O-protonated DMSO **87** (40.0 ppm) matches with the experimental value of 34.3 ppm. The calculated ^{13}C chemical shift of S-protonated DMSO **88** is 3 ppm deshielded compared to that calculated for **87**.

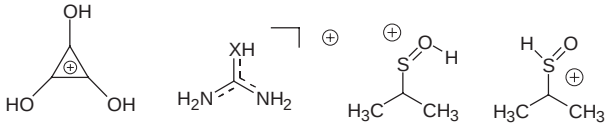

85 **86** **87** **88**

NMR chemical shifts of protonated carbonic acid **89** and **90** were investigated experimentally and computationally using IGLO-HF/II and MP2/6-31G(d) geometries [124]. The data indicate that in strong acidic solution H_2CO_3 may be in equilibrium with protonated carbonic acid. The structures of carbamic acid and its O- and N-protonated forms **91** and **92** were calculated at the MP2/6-31G(d) level [124]. The calculated ^{13}C and ^{15}N NMR chemical shifts, using the IGLO-HF and GIAO-MP2 methods, however, deviate substantially from the experimental results. This is in contrast with the previously reported results on protonated guanidines **93** and **94** [125] where GIAO-MP2 calculated ^{13}C and ^{15}N NMR chemical shifts were found to be in agreement with experiment. ^{13}C and ^{15}N NMR chemical shifts were calculated for protonated diazomethane $(CH_3N{\equiv}N)^+$ and the cyanodiazonium ion $(N{\equiv}CN{\equiv}N)^+$ [126]. For the C-protonated diazomethane, which is more stable than the N-protonated species, the IGLO-HF calculated ^{13}C chemical shift of 54.1 ppm agrees with the experimental value of 44.5 ppm. ^{15}N NMR chemical shifts were calculated as 237.9 and 379.9 ppm.

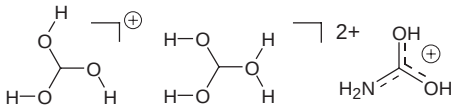

89 **90** **91**

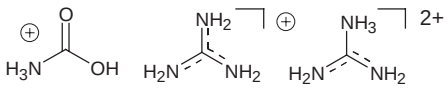

92 **93** **94**

The ^{1}H, ^{6}Li and ^{13}C NMR chemical shifts of the cyclopropenium cation and its lithium derivatives are calculated at both the GIAO-DFT and GIAO-HF levels using B3LYP optimized geometries [127]. It was shown that lithium is even more effective than the amino group in stabilizing the ethyl, vinyl, allenyl and cyclopropenium cations [128].

23.7 Conclusions

Calculation of NMR parameters such as chemical shift and spin–spin coupling constants have evolved into an important tool in carbocation chemistry, as well as in related fields such as silylenium ion and borane chemistry, which are not considered in this chapter. Computational NMR methods have provided detailed information on structures and stabilization modes of carbocations and deeper insights into intriguing questions and longstanding controversies in carbocation chemistry. The everlasting need for better tools and methods to explore the field has triggered the further development of NMR computational methods. Carbocation chemistry thus serves as a forerunner for a close integration of experimental and computational approaches in all areas of chemistry.

Acknowledgements

We acknowledge support by the Deutsche Forschungsgemeinschaft (DFG), the Fonds der Chemischen Industrie, the Alexander von Humboldt Foundation (AvH-Stiftung) and the Deutsche Akademische Austauschdienst (DAAD). Discussions and cooperation with Dr. Jürgen Gauss (University of Mainz) and Olga Malkina and Vladimir G. Malkin (Bratislava) are gratefully acknowledged.

References

1 W. Kutzelnigg, U. Fleischer, M. Schindler, in *NMR Basic Principles and Progress*, Vol. 23, Springer-Verlag, Berlin **1990**, p. 165.
2 M. Schindler, *J. Am. Chem. Soc.* **1987**, *109*, 1020.
3 P. Buzek, S. Sieber, P. v. R. Schleyer, *Chem. Uns. Zeit* **1992**, *26*, 116.
4 P. v. R. Schleyer, C. Maerker, P. Buzek et al., in *Stable Carbocation Chemistry*, eds. G. K. S. Prakash, P. v. R. Schleyer, John Wiley & Sons, New York **1997**, Ch. 2 and references therein.
5 M. Bühl, in *Encyclopedia of Computational Chemistry*, eds. P. v. R. Schleyer et al., Wiley, Chichester **1998**, p. 1835.
6 *Encyclopedia of Computational Chemistry*, eds. P. v. R. Schleyer et al., Wiley, Chichester **1998**.
7 a) R. D. Brown, J. E. Boggs, R. Hilderbrandt et al., *Pure Appl. Chem.* **1996**, *68*, 387; b) for an electronic version see the IUPAC web site: www.iupac.org/reports/1996/6802brown/index.html
8 S. Sieber, P. v. R. Schleyer, J. Gauss, *J. Am. Chem. Soc.* **1993**, *115*, 6987.

9 S. Sieber, P. v. R. Schleyer, A. H. Otto et al., *J. Phys. Org. Chem.* **1993**, *6*, 445.
10 P. Buzek, P. v. R. Schleyer, H. Vancik et al., *Angew. Chem. Int. Ed.* **1994**, *33*, 448.
11 H.-U. Siehl, M. Fuß, J. Gauss, *J. Am. Chem. Soc.* **1995**, *117*, 5983.
12 a) P. v. R. Schleyer, J. Gauss, M. Bühl et al., *J. Chem. Soc., Chem. Commun.* **1993**, 1766; b) M. Bühl, J. Gauss, M. Hofmann et al., *J. Am. Chem. Soc.* **1993**, *115*, 12385.
13 J. Gauss, *Chem. Phys. Lett.* **1994**, *229*, 198.
14 A. A. Auer, J. Gauss, J. F. Stanton, *J. Chem. Phys.* **2003**, *118*, 10407.
15 J. F. Stanton, J. Gauss, H.-U. Siehl, *Chem. Phys. Lett.* **1996**, *262*, 183.
16 H.-U. Siehl; T. Müller, J. Gauss, *J. Phys. Org. Chem.* **2003**; *16*, 577.
17 a) D. Marx and A. Savin, *Angew. Chem., Int. Ed. Engl.* **1997**, *36*, 2077; b) D. Marx and M. Parrinello, *Science*, **1999**, *284*, 59 and references therein; c) P. R. Schreiner, *Angew. Chem., Int. Ed. Engl.* **2000**, *39*, 3239 and references therein; (d) W. Klopper, W. Kutzelnigg, *J. Chem. Phys.* **1990**, *94*, 5256.
18 G. Rasul, G. K. S. Prakash, G. A. Olah, *Proc. Natl. Acad. Sci. USA* **1998**, *95*, 7257.
19 P. v. R. Schleyer, D. Lenoir, P. Mison et al., *J. Am. Chem. Soc.* **1980**, *102*, 683.
20 G. A. Olah, G. Rasul, *J. Am. Chem. Soc.* **1996**,*118*, 8503.
21 G. Rasul, G. K. S. Prakash, G. A. Olah, *Proc. Natl. Acad. Sci. USA* **2002**, *99*, 9635.
22 S. A. Perera, R. J. Bartlett, P. v. R. Schleyer, *J. Am. Chem. Soc.* **1995**, *117*, 8476.
23 S. A. Perera, H. Sekino, R. J. Bartlett, *J. Chem. Phys.* **1994**, *101*, 2186.
24 V. Vrcek, O. Kronja, H.-U. Siehl, *J. Chem. Soc., Perkin Trans. 2* **1999**, 1317
25 W. Koch, P. v. R. Schleyer, P. Buzek, B. Liu, *Croat. Chim. Acta* **1992**, *65*, 655.
26 P. v. R. Schleyer, W. Koch, B. Liu et al., *Chem. Commun.* **1989**, 1098.
27 J. B. Nicholas, T. Xu, D. H. Barich et al., *J. Am. Chem. Soc.* **1996**, *118, 4202.*
28 D. Farcasiu, D. Hâncu, J. F. Haw, *J. Phys. Chem. A* **1998**, *102*, 2493.
29 S. Sieber, P. Buzek, P. v. R. Schleyer et al., *J. Am. Chem Soc.* **1993**, *115*, 259.
30 G. A. Olah, N. Hartz, G. Rasul et al., *J. Am. Chem. Soc.* **1993**, *115*, 6985.
31 H.-U. Siehl, unpublished results; presented in part at the 6th WATOC, Lugano, **2002**, and the International Conference on Reaction Intermediates and Reaction Mechanisms, Ascona, **2002**.
32 C. Freudenberger, Ph.D. Thesis, University of Ulm, 2003.
33 M. Saunders, E. L. Hagen, J. Rosenfeld, *J. Am. Chem. Soc.* **1968**, *90*, 6882.
34 J. W. de M. Carneiro, P. v. R. Schleyer, W. Koch et al., *J. Am. Chem. Soc.* **1990**,*112*, 4064.
35 S. Sieber, P. Buzek, P. v. R. Schleyer et al., *J. Am. Chem. Soc.* **1993**, *115*, 259.
36 P. v. R. Schleyer, J. W. de M. Carneiro, W. Koch et al., *J. Am. Chem. Soc.* **1991**, *113*, 3990.
37 a) H.-U. Siehl, A. C. Backes, O. Malkina, in *Organosilicon Chemistry IV*, **1999**, p. 150; b) A. C. Backes, Ph.D. Thesis, University of Ulm, **1999**.
38 V. G. Malkin, O. L. Malkina, M. E. Casida et al., *J. Am. Chem. Soc.* **1994**, 116, 5898.
39 G. K. S. Prakash, V. P. Reddy, G. Rasul et al., *J. Am. Chem. Soc.* **1998**, *120*, 13362.
40 a) P. v. R. Schleyer, J. W. de M. Carneiro, W. Koch et al., *J. Am. Chem. Soc.* **1989**, *111*, 5475; b) J. H. Botkin, D. A. Forsyth, D. J. Sardella, *J. Am. Chem. Soc.* **1986**, 108, 2797.
41 P. C. Myhre, J. D. Kruger, B. L. Hammond et al., *J. Am. Chem. Soc.* **1984**, *106*, 6079.
42 O. Kronja, T.-P. Koehli, H. Mayr et al., *J. Am. Chem. Soc.* **2000**, *122*, 8067.
43 a) R. P. Kirchen, K. Ranganayakulu, T. S. Sorensen, *J. Am. Chem. Soc.*, **1987**, *109*, 7811; b) R. P. Kirchen, T. S. Sorensen, *J. Am. Chem. Soc.* **1978**, *100*, 1487.
44 a) A. Rauk , T. S. Sorensen, C. Maerker et al., *J. Am. Chem. Soc.* **1996**, *118*, 3761; b) A. Rauk, T. S. Sorensen, P. v. R. Schleyer *J. Chem. Soc., Perkin Trans. 2* **2001**, 869.
45 V. Vrcek, O. Kronja, H.-U. Siehl, *J. Chem. Soc., Perkin Trans. 2* **2002**, 106.
46 R. P. Kirchen, T. S. Sorensen, K. Wagstaff, *J. Am. Chem. Soc.* **1978**, *100*, 6761.
47 P. Buzek, P. v. R. Schleyer, H. Vancik et al., *Chem. Commun.* **1991**, 1538.
48 V. Galasso, *Int. J. Quantum Chem.* **1998**, *70*, 313.
49 a) I. Vinkovic-Vrcek, V. Vrcek, H.-U. Siehl, *J. Phys. Chem. A* **2002**, *106*, 1604; b) P. Buzek, P. v. R. Schleyer, S. Sieber et al., *Chem. Commun.* **1991**, 671
50 H.-U. Siehl, V. Vrcek, unpublished results.
51 J. Cioslowski, *J. Am. Chem. Soc.* **1993**, *115*, 5177.
52 C. Taeschler, T. S. Sorensen, *J. Mol. Model.* **2000**, *6*, 217.

53 V. Gallaso, *Chem. Phys.* **1999**, *241*, 247.
54 F. Sun, T. S. Sorensen, *J. Am. Chem. Soc.* **1993**, *115*, 77.
55 D. J. Tantillo, R. Hoffmann, *J. Am. Chem. Soc.* **2003**, *125*, 4042.
56 a) M. Saunders, M. H. Kates, *J. Am. Chem. Soc.* **1980**, *102*, 6867; b) C. W. Koch, B. Liu, D. J. de Frees, H. Vancik et al., *Angew. Chem., Int. Ed. Engl.* **1990**, *19*, 183; c) P. C. Myhre, G. G. Webb, C. S. Yannoni, *J. Am. Chem. Soc.* **1990**, *112*, 8991.
57 P. v. R. Schleyer, S. Sieber, *Angew. Chem., Int. Ed. Engl.* **1993**, *32*, 1606.
58 S. A. Perera, R. J. Bartlett, *J. Am. Chem. Soc.* **1996**, *118*, 7849.
59 N. H. Werstiuk, H. M. Muchall, *J. Phys. Chem. A* **2000**, *104*, 2054.
60 P. Brunelle, T. S. Sorensen, C. Taeschler, *J. Org. Chem.* **2001**, *66*, 7294.
61 T. Müller, C. Bauch, M. Ostermeier et al., *J. Am. Chem. Soc.* **2003**, *125*, 2158.
62 J. S. Staral, I. Yavari, J. D. Roberts et al., *J. Am. Chem. Soc.* **1978**, *100*, 8016.
63 a) M. Saunders, K. E. Laidig, K. B. Wiberg et al., *J. Am. Chem. Soc.* **1988**, *110*, 7625; b) W. Koch, B. Liu, D. J. DeFrees, *J. Am. Chem. Soc.* **1988**, *110*, 7325; c) M. L. McKee, *J. Phys. Chem.* **1986**, *90*, 4908.
64 P. C. Myhre, G. Webb, C. S. Yannoni, *J. Am. Chem. Soc.* **1990**, *112*, 8992.
65 M. Fuß, Ph.D. Thesis, Universität Tübingen, **1997**.
66 P. v. R. Schleyer, K. Laidig, K. B. Wiberg et al., *J. Am. Chem. Soc.* **1988**, *110*, 300.
67 G. K. S. Prakash, G. Rasul, G. A. Olah, *J. Phys. Chem. A* **1998**, *102*, 2579.
68 M. Bremer, P. v. R. Schleyer, K. Schötz et al., *Angew. Chem., Int. Ed. Engl.* **1987**, *26*, 761.
69 a) M. W. Crofton, M.-F. Jagod, B. D. Rehfus et al., *J. Chem. Phys.* **1989**, *91*, 5139; b) L. A. Curtiss, J. A. Pople, *J. Chem. Phys.* **1988**, *88*, 7405; c) C. Liang, T. P. Hamilton, H. F. Schaefer III, *J. Chem. Phys.* **1990**, *92*, 3653.
70 H.-U. Siehl, T. Müller, J. Gauss et al., *J. Am. Chem. Soc.* **1994**, *116*, 6384.
71 J. Gauss, J. F. Stanton, *J. Mol. Struct.* **1997**, *398*, 73.
72 H.-U. Siehl, S. Brixner, unpublished results.
73 H.-U. Siehl, F. P. Kaufmann, Y. Apeloig et al., *Angew. Chem. Int. Ed. Engl.* **1991**, *30*, 1479.
74 M. Bremer, P. v. R. Schleyer, U. Fleischer, *J. Am. Chem. Soc.* **1989**, *111*, 1147.
75 J. R. Cheeseman, G. W. Trucks, T. A. Keith et al., *J. Chem. Phys.* **1996**, *104*, 5497.
76 G. A. Olah, N. J. Head, G. Rasul et al., *J. Am. Chem. Soc.* **1995**, *117*, 875.
77 J. B. Levy, *Struct. Chem.* **1999**, *10*, 121.
78 P. v. R. Schleyer, P. Buzek, T. Müller et al., *Angew. Chem. Int. Ed. Engl.* **1993**, *32*, 1471.
79 G. A. Olah, G. Rasul, H. A. Buchholz et al., *Bull. Soc. Chim. Fr.* **1995**, *132*, 569.
80 a) J. B. Lambert, S. Zhang, C. L. Stern et al., *Science* **1993**, *260*, 1917; b) J. B. Lambert, S. Zhang, *J. Chem. Soc. Chem. Commun.* **1993**, 383.
81 J. B. Lambert, Y. Zhao, *Angew. Chem., Int. Ed. Engl.* **1997**, *36*, 400.
82 T. Müller, Y. Zhao, J. B. Lambert, *Organometallics* **1998**, *17*, 278. For similar results see a) D. Kraka, C. P. Sosa, D. Cremer, *Chem. Phys. Lett.* **1997**, *9*, 279; b) K.-C. Kim, C. A. Reed, D. W. Elliott et al., *Science* **2002**, *297*, 825.
83 T. Müller, *Angew. Chem. Int. Ed. Engl.* **2001**, *40*, 3033.
84 R. Meyer, K. Werner, T. Müller, *Chem. Eur. J.* **2002**, *8*, 1163.
85 H.-U. Siehl, B. Müller, O. Malkina, in *Organosilicon Chemistry III*, eds. N. Auner, J. Weiss, Wiley-VCH, Weinheim **1997**, p. 25.
86 G. A. Olah, T. Shamma, A. Burrichter et al., *J. Am. Chem. Soc.* **1997**, *119*, 12923.
87 a) K. K. Laali, S. Hollenstein, S. E. Galembeck et al., *J. Chem. Soc. Perkin Trans. 2* **1999**, 2129; b) K. K. Laali, T. Okazaki, S. E. Galembeck, *J. Chem. Soc. Perkin Trans. 2* **2002**, 621; c) K. K. Laali, S. Hollenstein, S. E. Galembeck et al., *J. Chem. Soc. Perkin Trans. 2* **2000**, 211; d) K. K. Laali, T. Okazaki, S. E. Galembeck et al., *J. Org. Chem.* **2001**, *66*, 8701.
88 a) N. S. Mills, M. A. Benish, C. Ybarra, *J. Org. Chem.* **2002**, *67*, 2003; b) N. S. Mills, *J. Org. Chem.* **2002**, 67, 7029; c) A. Levy, A. Rakowitz, N. S. Mills, *J. Org. Chem.* **2003**, *68*, 3990.
89 D. Cremer, P. Svensson, E. Kraka et al., *J. Am. Chem. Soc.* **1993**, *115*, 7445.
90 D. Cremer, P. Svensson, E. Kraka et al., *J. Am. Chem. Soc.* **1993**, *115*, 7457.
91 M. Bremer, K. Schötz, P. v. R. Schleyer et al., *Angew. Chem. Int. Ed. Engl.* **1989**, *28*, 1042.
92 D. Cremer, F. Reichel, E. Kraka, *J. Am. Chem. Soc.* **1991**, *113*, 9459.
93 a) J. B. Lambert, L. Lin, V. Rassolov, *Angew. Chem. Int. Ed. Engl.* **2002**, *41*, 1429;

b) T. Müller *Angew. Chem. Int. Ed. Engl.* **2002**, *41*, 2277; c) M. Otto, D. Scheschkewitz, T. Kato et al. *Angew. Chem. Int. Ed. Engl.* **2002**, *41*, 2275;
d) J. B. Lambert, *Angew. Chem. Int. Ed. Engl.* **2002** ,*41* , 2278.

94 J. F. Haw, J. B. Nicholas, T. Xu et al., *Acc. Chem. Res.* **1996**, *29*, 259.

95 a) J. F. Haw, J. B. Nicholas, W. Song et al., *J. Am. Chem. Soc.* **2000**, *122*, 4763; b) W. Song, J. B. Nicholas, J. F. Haw, *J. Am. Chem. Soc.* **2001**, *123*, 121.

96 T. Xu, J. F. Haw, *J. Am. Chem. Soc.* **1994**, *116*, 7753.

97 W. Song, J. B. Nicholas, J. F. Haw, *J. Chem. Phys. B* **2001**, *105*, 4317.

98 a) T. Xu, D. H. Barich, P. D. Torres et al., *J. Am. Chem. Soc.* **1997**, *119*, 406; b) T. Xu, D. H. Barich, P. W. Goguen et al., *J. Am. Chem. Soc.* **1998**, *120*, 4025; c) W. Song, J. B. Nicholas, A. Sassi et al., *Catal. Lett.* **2002**, *81*, 49.

99 L. Fernandez, V. Marti, H. Garcia, *Phys. Chem. Chem. Phys.* **1999**, *1*, 3689.

100 a) T. S. Sorensen, *Angew. Chem. Int. Ed. Engl.* **1998**, *37*, 603; b) P. J. F. de Rege, J. A. Gladysz, I. T. Horvath, *Science* **1997**, *276*, 776.

101 G. A. Olah, unpublished results.

102 G. A. Olah, A. Burrichter, T. Mathew et al., *Angew. Chem. Int. Ed. Engl.* **1997**, *36*, 1875.

103 K. O. Christe, B. Hoge, J. A. Boatz et al., *Inorg. Chem.* **1999**, *38*, 3132.

104 G. A. Olah, A. Burrichter, G. Rasul et al., *J. Am. Chem. Soc.* **1997**, *119*, 8035.

105 G. A. Olah, A. Burrichter, G. Rasul et al., *J. Org. Chem.* **1996**, *61*, 1934.

106 a) G. K. S. Prakash, Q. Wang et al., *J. Organomet. Chem.* **1998**, *550*, 119; b) G. K. S. Prakash, C. Bae, G. Rasul et al., *J. Org. Chem.* **2002**, *67*, 1297.

107 G. K. S. Prakash, G. Rasul, G. Liang et al., *J. Phys. Chem.* **1996**, *100*, 15805.

108 N. J. Head, G. Rasul, A. Mitra et al., *J. Am. Chem. Soc.* **1995**, *117*, 12107.

109 T. Xu, D. H. Barich, P. D. Torres et al., *J. Am. Chem. Soc.* **1997**, *119*, 396.

110 G. K. S. Prakash, G. Rasul, A. Burrichter et al., *J. Org. Chem.* **1996**, *61*, 9253.

111 a) G. A. Olah, G. Rasul, L. Heiliger et al., *J. Am. Chem. Soc.* **1996**, *118*, 3580; b) G. A. Olah, G. Rasul, A. K. Yudin et al., *J. Am. Chem. Soc.* **1996**, *118*, 1446.

112 M. Kaupp, O. L. Malkina, V. G. Malkin, *Chem. Phys. Lett.* **1997**, *265*, 55.

113 G. Rasul, G. K. S. Prakash, G. A. Olah, *J. Mol. Struct.* **1999**, *466*, 245.

114 V. P. Reddy, G. Rasul, G. K. S. Prakash et al., *J. Org. Chem.* **2003**, *68*, 3507.

115 G. A. Olah, G. Rasul, C. York et al., *J. Am. Chem. Soc.* **1995**, *117*, 11211.

116 G. A. Olah, M. Calin, D. H. O'Brien, *J. Am. Chem. Soc.* **1967**, *89*, 3582.

117 I. Pálinkó, A. Burrichter, G. Rasul et al., *J. Chem. Soc. Perkin Trans. 2* **1998**, 379.

118 G.K. S. Prakash, G. Rasul, G. A. Olah et al., *Can. J. Chem.* **1999**, *77*, 525.

119 G. A. Olah, J. Bausch, G. Rasul et al., *J. Am. Chem. Soc.* **1993**, *115*, 8060.

120 G. A. Olah, A. M. White, *J. Am. Chem. Soc.* **1968**, *90*, 6067.

121 G. A. Olah, A. M. White, D. H. O'Brien, *Chem. Rev.* **1970**, *70*, 561.

122 a) G. Rasul, G. K. S. Prakash, G. A. Olah, *J. Org. Chem.* **1994**, *59*, 2552; b) G. A. Olah, A. Burrichter, G. Rasul et al., *J. Am. Chem. Soc.* **1997**, *119*, 4345.

123 G. Rasul, G. K. S. Prakash, G. A. Olah, *J. Org. Chem.* **2000**, *65*, 8786.

124 a) G. A. Olah, T. Heiner, G. Rasul et al., *J. Org. Chem.* **1998**, *63*, 7993 b) G. Rasul, V. P. Reddy, L. Z. Zdunek, G. K. S. Prakash et al., *J. Am. Chem. Soc.* **1993**, *115*, 2236.

125 G. A. Olah, A. Burrichter, G. Rasul et al., *J. Am. Chem. Soc.* **1997**, *119*, 12929.

126 G. Rasul, G. K. S. Prakash, G. A. Olah, *J. Am. Chem. Soc.* **1994**, *116*, 8985.

127 E. D. Jemmis, G. Subramanian, A. J. Kos et al., *J. Am. Chem. Soc.* **1997**, *119*, 9504.

128 Y. Apeloig, P. v. R. Schleyer, J. A. Pople, *J. Am. Chem. Soc.* **1977**, *99*, 5901.

24
Aromaticity Indices from Magnetic Shieldings

Zhongfang Chen, Thomas Heine, Paul v. R. Schleyer, and Dage Sundholm

24.1
Introduction

Few concepts are as frequently used in the current chemical literature as aromaticity [1]. The traditional criteria for aromaticity include chemical behavior (lower reactivity), structural features (planarity and equal bond length tendencies), energetic (stability), and spectroscopic properties (UV, proton chemical shifts, magnetic susceptibility exaltation). A new magnetic criterion, nucleus-independent chemical shifts (NICS) [2], has proven to be a simple and efficient aromaticity probe, and is being employed with increasing frequency since its introduction in 1996, as shown by more than 490 citations till December 2003. Using this easily computable quantity, various long-standing chemical questions have been solved, and novel aromatics have been identified. Along with its ever wider application, the NICS method has also been enhanced and refined. This chapter gives an overview of NICS as well as the related aromatic ring-current shielding (ARCS) [3] method.

24.2
An Overview of Aromaticity Indices Based on Magnetic Shielding

Calculations of NMR chemical shifts at various levels of theory have become a standard tool in chemistry [4]. Because of the sensitivity to the electronic structure in their environment, magnetically active nuclei can be used to probe the near-by shielding influences. This is one of the reasons why NMR spectroscopy rivals X-ray diffraction as the best experimental method for characterizing molecular structure [5].

Schleyer et al. introduced nucleus-independent chemical shifts (NICS) in 1996 [2]. NICS indices are the negative value of the magnetic shielding computed at chosen points in the vicinity of molecules. They are typically computed at ring centers, at points above, and even on grids in and around the molecule. Significantly negative NICS values in interior positions of rings or cages indicate the presence of induced diatropic ring currents, interpreted as “aromaticity,” whereas positive values denote paratropic ring currents and “anti-aromaticity”.

Calculation of NMR and EPR Parameters. Theory and Applications.
Edited by Martin Kaupp, Michael Bühl, Vladimir G. Malkin
Copyright © 2004 WILEY-VCH Verlag GmbH & Co. KGaA, Weinheim
ISBN: 3-527-30779-6

Li^+ was the first computational aromaticity probe to sense electron-delocalization before the development of NICS [6], which led to the development of the NICS method. Because lithium bonding is primarily ionic and electrostatic, experimental Li chemical shifts generally show little variation. The exceptions involve aromatic (or anti-aromatic) compounds where Li^+ binds ca. 2 Å above π faces. At such distances, the shieldings (deshieldings) are still 5–10 ppm or more. However, the utility of Li^+ as a computational aromaticity probe was limited due to its influence on the studied system: unlike NICS, Li^+ cannot be placed in the center of arene rings. However, it could be computed, for example, in the center of fullerenes, and the first theoretical study of the magnetic properties of $^3He@C_{60}$ included $Li^+@C_{60}$ data [7]. Shifts of chemically inert ^3He and NICS values at fullerene centers are in very good agreement [8], and serve as an effective tool for characterizing fullerene structures (see also Chapter 25). Other possibilities to evaluate NICS experimentally include ^1H shifts of methane at places on top of aromatic rings, where the shielding cone of the ring strongly influences the chemical shift of the probe atom [9].

Being based directly on cyclic electron delocalization, the essence of aromaticity, NICS has the advantage over many other aromaticity criteria, in the sense of not requiring reference standards, increment schemes, or calibrating (homodesmotic) equations for evaluation. Actually, NICS can be related to the energetic, geometric, and other magnetic criteria of aromaticity [10]. However, NICS values do not depend purely on the delocalized electronic system, i.e. the π system, but also on other magnetic shielding contributions due to local circulations of electrons in bonds, lone pairs and atom cores. Thus, NICS approaches being an "absolute" measure of cyclic electron delocalization only when the radii of the systems are relative large, and hence the local shielding effects are negligible. For planar or nearly planar molecules, these complicating influences are reduced above ring centers. As the π orbitals have their maximum density in this area, NICS(1) values (i.e., at points 1 Å above the ring center) were recommended as being better measures of π effects than NICS(0) (i.e. at the ring center) [11].

The distribution of NICS values on grids around molecules has been studied in various cases [11b] and provides insight on diatropic and paratropic regions, as is illustrated for C_4H_4 and C_6H_6 in Fig. 24.1.

The shape of the magnetic shielding function also provides information about electron delocalization and molecular aromaticity [12]. Klod and Kleinpeter [12] deduced anisotropic effects by evaluating NICS in a three-dimensional grid. The direction and the size of the anisotropy effect of double or triple bonds, or of aromatic

Figure 24.1 NICS grid of benzene and cyclobutadiene. The red and green colors denote negative and positive NICS values, respectively.

rings, can be obtained by plotting iso-chemical-shielding surfaces (ICSS), which actually are isosurfaces of NICS values (see Fig. 24.2).

A NICS-related method, the aromatic ring-current shielding (ACRS), was introduced in 1999 by Jusélius and Sundholm [3]. In the ARCS method, the long-range part of the shielding function (e.g. 3–20 Å from the ring) is used to provide information about the induced ring current. A simple relation between the long-range behavior of the isotropic magnetic shielding function $\sigma(z)$ and the current susceptibility with respect to the applied magnetic field can be derived from Biot–Savart's law by assuming that the wire carrying the current is circular and infinitely thin. The ARCS expression relating the long-range part of the magnetic shielding function to the ring-current susceptibility and to the size of the aromatic pathway is then

$$\sigma(z) = -\frac{\mu_0}{2}\,\frac{\partial I_{\text{ring}}}{\partial B_{\text{ext}}}\,\frac{R^2}{(z^2 + R^2)^{3/2}} \tag{24.1}$$

where $\sigma(z)$ is the shielding function, z is the perpendicular distance from the center of the current loop, μ_0 is the vacuum permeability, $\partial I_{\text{ring}}/\partial B_{\text{ext}}$ is the current susceptibility, B_{ext} is the external magnetic field, and R is the radius of the current loop. The strength of the ring-current susceptibility can be defined as the ARCS aromaticity index. The current susceptibility can be obtained by calculating the shielding function at many NICS points along the z-axis and fitting them to Eq. (24.1). For planar molecules, the current is assumed to circulate in the molecular plane, whereas for non-planar homoaromatic molecules, the symmetry axis (z axis) is the one with the largest moment of inertia [3g]. The shielding contributions due to local currents around the nuclei and in the chemical bonds have small loop radii and decline fast with the distance from the molecule. For nonaromatic molecules, the shielding practically vanishes outside the electron density. As the effective current radius of aromatic rings is significantly larger, the long-range shielding is mainly due to electron delocalization i.e. the strength of the induced ring current. The size of the current loop and the ring-current susceptibility can be deduced from a logarithmic fit as shown in Fig. 24.3.

The center of the current loop used in the ARCS fit can be estimated from a plot of the ARCS function [3g]. For planar molecules, the ring center is the obvious

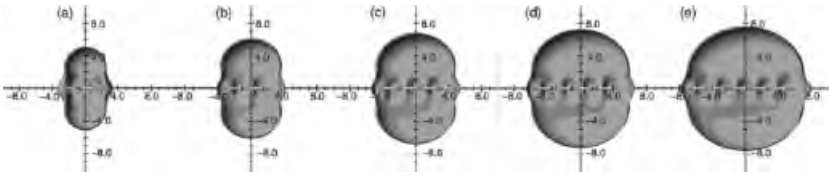

Figure 24.2 Comparison of the calculated 0.5 ppm shielding surface for annelated aromatic ring systems: (a) benzene, (b) naphthalene, (c) anthracene, (d) tetracene, (e) pentacene. View in the plane of the molecules. (Reproduced from Ref. [12a], by permission of The Royal Society of Chemistry.)

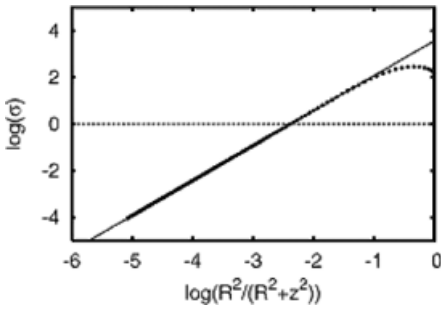

Figure 24.3 The ARCS fit for benzene. The long-range magnetic shielding function $\sigma(z)$ (in ppm) was calculated at the second order Møller–Plesset perturbation theory level.

ARCS origin, while for non-planar molecules, the choice of origin is somewhat arbitrary. However, the ARCS indices are found to be rather independent of the precise location of the ARCS origin.

The molecular aromaticity can be studied in more detail by employing orbital decomposition of the shieldings inherent in the IGLO (individual gauge for localized orbitals) method. Disturbing effects from the σ contribution can be removed by "dissected NICS" methods [11], in which only the part attributed to the π system is employed to characterize the aromaticity. The total shielding can be dissected into individual contributions from each localized molecular orbital (LMO) associated with bonds, lone-pairs and core electrons [13]. The LMOs can be constructed in several ways. The procedure proposed by Pipek and Mezey [14] has several advantages, which are important for such LMO-NICS computations. It separates σ and π systems by means of orbital symmetry when applied to planar molecules. Statistical analyses have indicated the π sums, $\sum NICS_\pi$, at the ring centers of related series of molecules to be an even better measure of aromaticity than NICS(0); NICS(1) also is often better than NICS(0) [10d]. The σ contributions, dissected in LMOs and corresponding to individual bonds, are also important for the interpretation. In many cases, $NICS(1)_\pi$ values are quite similar to $NICS(1)_{total}$, which reinforces the validity of the NICS(1) index.

However, the original LMO-NICS implementation necessarily has the limitations of the localization scheme. $NICS_\pi$ can also be obtained using other orbital representations such as natural bond orbitals (NBO) [15] and canonical orbitals [16]. In this approach, some individually selected orbitals are transformed to a localized set of orbitals. MO-NICS, a generalization of this method, distinguishes NICS contributions of the individual molecular orbitals. The GIAO (gauge-including atomic-orbitals) method [17] is applied and individual orbital contributions to the shielding tensor are given instead of LMOs or groups of orbitals [18]. $NICS_\pi$ indices can also be calculated using this method.

MO-NICS is based on the present implementations of the uncoupled form of current-density functional theory [19], and is restricted to 'pure' DFT calculations (i.e.

hybrid functionals cannot be used). The shielding tensor can then be written as a sum of orbital contributions, each of which can be very important for the interpretation. In annulenes, the lowest-energy π orbital gives the largest contribution to NICS. In the case of antiaromatic D_{2h} C_4H_4 the π contributions of the two orbitals nearly cancel (Fig. 24.4). In agreement with intuition and London–Hückel susceptibilities [20], the character and magnitude of the MO-NICS contribution depends on the number of nodes along the ring. The σ system is highly diatropic for low-energy

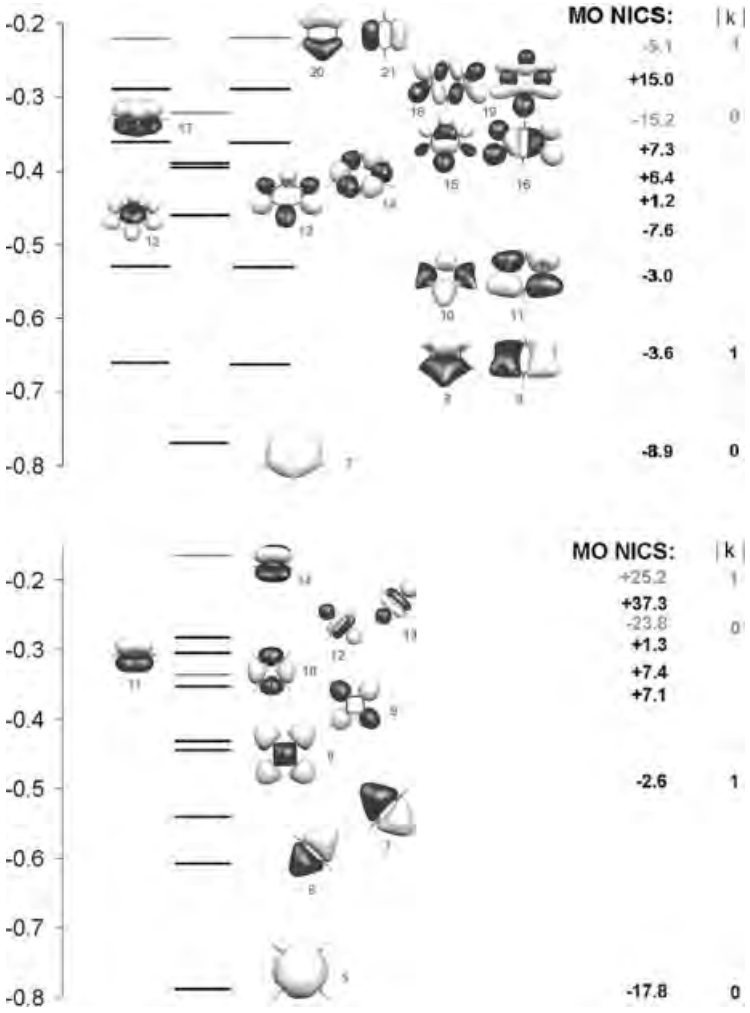

Figure 24.4 MO-NICS values of valence orbitals of D_{6h} C_6H_6 (top) and antiaromatic D_{2h} C_4H_4 (bottom). MO-NICS are given in ppm, the energy scale is in Hartrees. π orbital information is given in gray.

orbitals, but becomes highly paratropic for high-energy orbitals, since these contain many nodes around the ring not passing through atoms (see Fig. 24.4).

The ab initio ring-current [21] model was developed by Lazzeretti et al. starting in 1982 [22]. This model has been used frequently for plotting the ring current density, usually at one Bohr (a_0) above the ring plane. Steiner and Fowler extended this approach to molecular orbital dependent contributions [23]. The "anisotropy of the current-induced density" (ACID) [24] is a related method for visualizing the delocalization in aromatic and other molecules.

24.2.1 Comparison of NICS-Based Methods

Table 24.1 compares the performance of the NICS, $NICS_\pi$, MO-NICS and ARCS methods for a series of small molecules. The methods and their results are nicely complementary: All aromatic compounds exhibit negative NICS. However, according to NICS(0), the transition-metal complex $Cr(CO)_3C_6H_6$ is found to be more aromatic than benzene, and ARCS calculations on $Cr(CO)_3C_6H_6$ show that despite the fact that no satisfactory ARCS fit can be obtained for the whole range, the shielding at about 25 Å is significantly smaller than for a free benzene molecule, indicating that the large NICS indices are not due to induced ring currents. The $NICS_\pi$ index shows that the π systems of these two molecules are very similar. NICS, $NICS_\pi$ and ARCS agree that $C_5H_5^-$ is more and $C_7H_7^+$ is less aromatic than benzene. The ARCS method attributes this to the current radius, i.e, the ring size, which is smaller for $C_5H_5^-$ than for $C_7H_7^+$. MO-NICS shows that lowest-energy σ and π orbitals give diatropic contributions. The π contributions are dominated by the lowest-energy orbitals $NICS_{\pi 0}$, (i.e. the π orbitals without nodes in the *xy*-plane) in agreement with Hückel and London–Hückel computations [20]. These largest contributions to NICS arise from a nearly isotropic shielding tensor, whereas the contributions of the frontier orbitals are determined by the *zz*-component of the shielding tensor. This agrees with current density plots, which suggest that only the frontier orbitals exhibit a measurable ring current density [23]. NICS(1) is capable of removing σ and other complicating effects. For the transition metal-containing molecule, the falloff of the π contributions is much faster than for benzene itself. The homotropylium cation $C_8H_9^+$ is another non-planar molecule. The ARCS method shows that this molecule has a stronger diatropic ring current than even benzene. NICS confirms this observation. However, $NICS_\pi$ and MO-NICS show that the aromaticity is mainly caused by the σ framework of this molecule. $NICS_\pi$ is nearly zero, and the MO contributions of the π-like orbitals are very small. It is interesting to note that the $NICS_{\pi 0}$ orbital is paratropic. All π orbitals of this molecule have higher MO energies than the σ orbitals, which is different than for example in annulenes. As this nonplanar molecule does not have clearly separated σ and π MOs, the dissection into σ and π contributions is only qualitative. The mixing of the π contributions with the σ bonds contributes to the strongly diatropic character.

Table 24.1 The molecular radius R_{mol} (in Å), NICS, NICS$_\pi$, MO-NICS (σ and π contributions with 0 and 1 nodes along the ring, respectively, see Fig. 24.4). ARCS parameters include the ratio between ring current and molecular radius (R_I/R_{mol}) and ARCS susceptibilities ($\partial I/\partial B$ in nA T^{-1}).

		NICS(0)						NICS(1)		ARCS	
	R_{mol}	NICS	NICS$_\pi$	NICS$_{\sigma 0}$	NICS$_{\sigma 1}$	NICS$_{\pi 0}$	NICS$_{\pi 1}$	NICS	NICS$_\pi$	R_I/R_{mol}	$\frac{\partial I}{\partial B_{ext}}\left[\frac{nA}{T}\right]$
C_6H_6 (D_{6h})	1.386	–8.9	–20.7	–8.9	–15.2	–3.6	–5.1	–10.6	–9.7	0.88	8.0
C_4H_4 (D_{2h})	1.033	+21.5	+0.9	–17.8	–23.8	–2.6	+25.2	+13.3	+14.8	[b]	[b]
$Cr(CO)_3C_6H_6$ (C_{3v})	1.407	–24.2	–21.0					–12.0	–7.4	[b]	[b]
$C_5H_5^-$ (D_{5h})	1.204	–15.0	–22.1	–12.6	–18.9	–3.8	–3.4	–11.0	–6.6	0.64	18.1
$C_7H_7^+$ (D_{7h})	1.609	–6.7	–17.5	–6.1	–11.2	–3.6	–5.5	–9.5	–9.7	1.01	6.0
$C_8H_9^+$ (C_s)	1.718	–10.9	+1.3a	–6.7[a]	–4.2/–4.0[a]	+4.6	–3.2/–0.1[a]	–14.0	+0.5	0.61	14.7

Examples are taken from Ref. [11] and [3g]. All values at the IGLO-PW91/IGLOIII level, except MO-NICS at GIAO-PW91/IGLO-III level of theory, and ARCS for homotropylium $C_8H_9^+$ was studied at CHF/SVP, MO-NICS and NICS(1) calculations are carried out at the same level as for the other molecules.

a) For $C_8H_9^+$, a clear classification of σ and π contributions is impossible due to strong mixing of the contributions.

b) No ARCS fit possible.

In summary, we note the advantages of having different metrics, as no one of them provides all the information which can be deduced from the consistent picture given by all together.

24.3 Applications

The early theory of aromaticity was dominated by Hückel's rule stating that planar ring systems with $4n + 2\,\pi$ electrons are aromatic. This rule governs strictly only the aromaticity of two-dimensional systems. However, it can be extended to systems that deviate only modestly from planarity such as homoaromatic molecules, and even to some systems which are clearly "three dimensional" [25].

24.3.1 Möbius Aromaticity

In 1964 Heilbronner [26] predicted that singlet [4*n*]annulenes would be aromatic systems in twisted conformations where the p orbitals lie on the surface of a Möbius strip (Fig. 24.5). However, Möbius annulenes conforming to Heilbronner's original idea were not reported until 1998, when Schleyer et al. [27] first deduced that the most stable conformation of the known cyclic $C_9H_9^+$ 8π cation has C_2 symmetry (**1**, Fig. 24.6). This species sustains a diatropic ring current, quantified as a negative NICS value, and has a geometry consistent with significant Möbius aromaticity. Employing the NICS tool, Rzepa et al. [28] found that replacing a two-electron C=C

double bond in a planar $4n + 2$ Hückel aromatic ring with the four-electron allene unit (C=C=C) (as in **2**) induces modest $4n$ Möbius aromaticity and C_2-derived chirality in a variety of ring conjugated systems. Moreover, Möbius heteropines **3** [29] and carbeno[8]heteroannulenes **4** [30] with 8π electrons have also been confirmed as aromatic species. Most recently, Schleyer *et al.* [31] predicted Möbius local minima of [12]-, [16]- and [20]annulene; the aromaticity of these [$4n$]annulenes was demonstrated by NICS.

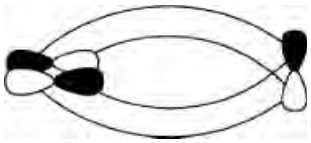

Figure 24.5 Schematic representation of the Möbius type overlapping π orbitals.

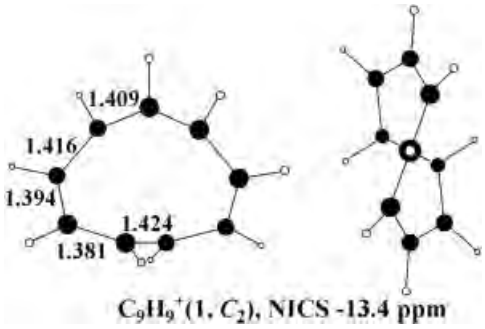

Figure 24.6 B3LYP/6-311+G** optimized structure of **1** and its NICS values.

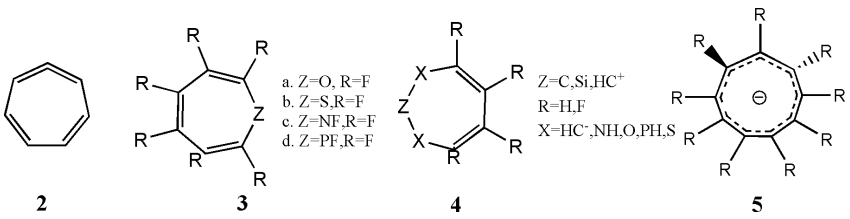

Scheme 24.1

24.3.2 Aromaticity of Triplet States

Aromaticity is not limited to singlet states. According to the Hückel MO theory, planar $4n$ π-electron annulenes in $D_{n\mathrm{h}}$ symmetry have degenerate ground states and should be non-aromatic. However, Baird concluded in 1972 that the rules for aroma-

ticity ($4n$+2) and antiaromaticity ($4n$) of annulenes are exactly reversed for the lowest triplet state [32]: the triplet $4n$ π-electron annulenes should be regarded as being aromatic rather than antiaromatic. This was confirmed by the comprehensive ab initio investigations on triplet C_4H_4, $C_5H_5^+$, $C_6H_6^{2+}$, $C_7H_7^-$, C_8H_8, and $C_9H_9^+$. [33] The triplet aromaticity in these annulenes with $4n$ π-electrons is not only documented by their negative NICS values, but also by structural, energetic and magnetic criteria such as planarity of near planarity, equalization of bond lengths, low-energy triplet states, appreciable aromatic stabilization energy, downfield ^{1}H NMR chemical shifts (when the paramagnetic effects of unpaired electrons are not included in the computations, see Chapter 20 by Moon and Patchkovskii for a full treatment), and significant diamagnetic susceptibility exaltations.

The triplet states of the Möbius conformations of annulenes can also be aromatic when $4n$+2 electrons participate in the electron delocalization. Rzepa et al. [30a] proposed the first formal example **5** in 2002.

24.3.3
Spherical Aromaticity

An important NICS application is the verification of the Hirsch $2(N+1)^2$ electron-counting rule for spherical aromaticity, proposed as the counterpart of the Hückel $4n$+2 rule for planar systems [34]. The $2(N+1)^2$ rule was initially applied to I_h-symmetrical fullerenes, i.e. C_{20}^{2+}, C_{60}^{10+} and C_{80}^{8+} that are exceptionally aromatic due to the complete filling of the electronic shell [35]. This rule also holds for other highly symmetrical systems belonging to T_d, O_h, and related point groups, e.g. inorganic clusters including the six- and twelve vertex *closo*-boranes, Zintl ions [36], and a few hydrogen and lithium clusters [35]. More importantly, a series of spherical homoaromatic systems have been designed on the basis of this rule, expanding the classical concept of homoaromaticity into three dimensions [37]. A more comprehensive review [38] on this topic has just appeared.

The π system of fullerenes covers the entire molecule, and is electronically important as HOMO and LUMO orbitals have π character. NICS computations give the local aromaticity of the π system in a given ring, and the endohedral NICS values give the shielding of the cage. Such NICS computations have been performed by Bühl for various fullerene cages [8]. These computations show that the pentagons of C_{60} are paratropic, while the hexagons have diatropic NICS values. Other fullerenes have also been studied, and in all cases the pentagons have been found to be much more strongly paratropic than the hexagons of the same cage. The shielding inside the fullerenes was related to projected ring currents on the fullerene surface in a similar way as in the ARCS method, and it was shown that the endohedral shielding originates from the induced currents in the surrounding carbon shell [8].

Integration of Eq. (24.1) also shows that the shielding is constant inside a spherical, infinitely thin and magnetically susceptible shell. ARCS functions calculated along the symmetry axes through the five- and six-membered rings of C_{60} are shown in Fig. 24.7. The shielding is almost constant inside the fullerene. The large change in the ARCS functions at the fullerene surface is due to the induced ring

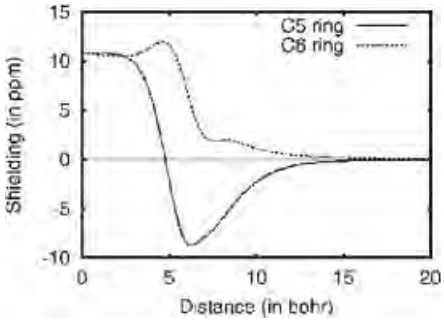

Figure 24.7 The magnetic shielding function (in ppm) along the symmetry axes through the five- and six-member rings of C_{60}.

currents in the carbon network. The sign change of the ARCS functions shows that the current in the five-membered rings is mainly paratropic and that the six-membered rings sustain diatropic currents [39]. As seen in Fig. 24.7, it is not easy to deduce an accurate value for the current susceptibility from the ARCS functions. However, the absolute value of the shielding at the maximum (and minimum) of the ARCS functions is about half the corresponding value for benzene, indicating that the current susceptibility for C_{60} is about half that of benzene.

24.3.4
Aromaticity of Pericyclic Reaction Transition Structures

As early as 1938, Evans and Warhurst recognized stabilization due to aromatic delocalization of the cyclic transition state of the Diels–Alder reaction of butadiene and ethylene [40]. Delocalization of the π electrons of the transition state (TS) was found to decrease the energy of the TS, thereby lowering its activation energy [41]. Employing NICS and other aromaticity probes, Jiao and Schleyer [42] confirmed the aromaticity of not only the Diels–Alder transition but also of many other thermally allowed pericyclic reactions, including acetylene trimerization to benzene and isomerization from diademane to triquinacene. Moreover, the in-plane aromatic transition states in 1,3-dipolar cycloaddition reactions have been analyzed in detail [43].

Geerlings et al. investigated the effect of the aromaticity on the path of the Diels–Alder reactions of various quinodimethanes with ethylene [44]. A progressive gain in aromaticity of both rings occurs during the reaction. The increase of aromaticity along the IRC is fully supported by NICS computations. However, more detailed MO-NICS analysis showed that the σ system influences the diatropic character of the TS to a large extent, and the transformation of the peripheral ring can be described correctly using ^{13}C and ^{1}H data and $NICS_{\pi}$, while NICS remains constant from TS to product [45]. The lowest barrier pathway and the most exothermic reactions are dictated by the high degree of aromaticity, in support of Evans's prescient

proposition. The same conclusions pertain to the Diels–Alder reactions between quinodimethanes with C_{60} [46].

24.3.5
σ-Aromaticity and σ-Antiaromaticity

Electron delocalization also exists in σ-systems. The σ-aromaticity of cyclopropane is now well established; the aromatic character of three-membered rings (3MR) in many compounds has been verified by NICS computations [47]. Most recently, LMO- and MO-NICS analyses of hydrocarbon rings and cage systems [48] have demonstrated the contrasting diatropic character of 3MR and 5MR on the one hand, and the paratropic 4MR behavior on the other. The archetypal aromatic shielding σ-framework of cyclopropane is magnified in tetrahedrane and other 3MR-containing cages. However, cyclobutane and related molecules with 4MRs (particularly cubane) have strongly deshielding CC(σ) bonds (i.e. σ-antiaromatic). Such electronic effects influence the strain energies: tetrahedrane is less strained and cubane more strained than expected on the basis of their angle deviations from tetrahedral.

The aromatic H_3^+ is the archetypal $4n+2$ σ-electron system, but larger, hypothetical D_{nh} symmetrical hydrogen rings also have been characterized as aromatic [49]. Experimental and theoretical evidence for a σ-aromatic bimetallic cluster Au_5Zn^+ has been presented [50]. The delocalization of the six σ-electrons in its planar geometry is consistent with its higher stability and abundance in gas phase experiments.

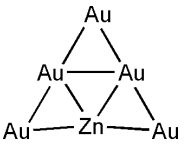

Figure 24.8 The sketch of the most stable isomer of Au_5Zn^+ (C_{2v}).

24.4
Outlook

Since its introduction in 1996, the NICS concept using computed magnetic shieldings as an aromaticity index has been refined and enhanced considerably. NICS is being used more and more widely, to characterize the aromaticity and antiaromaticity of not only rings, but also clusters, transition states, transition metal complexes etc.

The large flora of related methods to measure the molecular aromaticity from magnetic shieldings yields qualitatively the same aromaticity indices. The present indices highlight different aspects of magnetic aromaticity, such as the role of the σ and π systems, bond contributions, or projected ring currents. However, as the quantitative degree of aromaticity obtained using different approaches still differs

significantly, there is still a need for a more explicit way of determining the molecular aromaticity. Further developments, such as a method for explicit determination of induced ring currents using GIAO [51] and improvements and extensions of the NICS concept are in progress.

Acknowledgment

We thank the Deutsche Forschungsgemeinschaft (HE 3543/1), University of Georgia, the US National Science Foundation (Grant CHE-0209857), The Academy of Finland, and the Fonds der Chemischen Industrie for funding. ZC thanks Prof. Andreas Hirsch and Prof. Walter Thiel for support.

References

1 See reviews: a) V. I. Minkin, M. N. Glukhovtsev, B. Y. Simkin, *Aromaticity and Antiaromaticity*, John Wiley & Sons, New York **1994**; b) P. v. R. Schleyer, H. Jiao, *Pure Appl. Chem.* **1996**, *68*, 209; c) D. Lloyd, *J. Chem. Inf. Comput. Sci.* **1996**, *36*, 442; d) T. M. Krygowski, M. K. Cyranski, Z. Czarnocki et al., *Tetrahedron* **2000**, *56*, 1783; e) P. v. R. Schleyer (guest editor) *Chem. Rev.* Special Issue on Aromaticity, May **2001**.

2 P. v. R. Schleyer, C. Maerker, A. Dransfeld et al., *J. Am. Chem. Soc.* **1996**, *118*, 6317.

3 a) J. Jusélius, D. Sundholm, *Phys. Chem. Chem. Phys.* **1999**, *1*, 3429; b) J. Jusélius, D. Sundholm, *Phys. Chem. Chem. Phys.* **2000**, *2*, 2145; c) J. Jusélius, D. Sundholm, *J. Org. Chem.* **2000**, *65*, 5233; d) J. Jusélius, D. Sundholm, *Phys. Chem. Chem. Phys.* **2001**, *3*, 2433; e) J. Jusélius, M. Straka, D. Sundholm, *J. Phys. Chem. A* **2001**, *105*, 9939; (f) R. J. F. Berger, M. A. Schmidt, J. Jusélius et al., *Z. Naturforsch. B* **2001**, *56*, 979; (g) J. Jusélius, M. Patzschke, D. Sundholm, *Theochem.* **2003**, *622*, 123; (h) J. Jusélius, M.Sc. Thesis, Department of Chemistry, University of Helsinki, **2000**.

4 (a) M. Bühl, M. Kaupp, O. L. Malkina et al., *J. Comput. Chem.* **1999**, *20*, 91; (b) Z. Schreckenbach, T. Ziegler, *Theor. Chem. Acc.* **1998**, *99*, 71; (c) B. Wang, U. Fleischer, J. F. Hinton et al., *J. Comput. Chem.* **2001**, *22*, 1887.

5 H. Günther, *NMR Spectroscopy: Basic Principles, Concepts, and Applications in Chemistry*, 2nd edition, Wiley and Sons, New York **1995**.

6 a) L. A. Paquette, W. Bauer, M. R. Slivik et al., *J. Am. Chem. Soc.* **1990**, *112*, 8776; b) M. Bühl, N. J. R. van Eikema Hommes, P. v. R. Schleyer et al., *J. Am. Chem. Soc.* **1991**, *113*, 2459.

7 M. Bühl, W. Thiel, H. Jiao, P. v. R. Schleyer et al., *J. Am. Chem. Soc.* **1994**, *116*, 6005.

8 a) M. Bühl, *Chem. Eur. J.* **1998**, *4*, 734; b) M. Bühl, A. Hirsch, *Chem. Rev.* **2001**, *101*, 1153; c) G. Van. Lier, P. W. Fowler, F. De Proft et al., *J. Phys. Chem. A* **2002**, *106*, 5128.

9 R. V. Williams, J. R. Armantrout, B. Twamley et al., *J. Am. Chem. Soc.* **2002**, *124*, 13495.

10 a) L. Nyulaszi, P. v. R. Schleyer, *J. Am. Chem. Soc.* **1999**, *121*, 6872; b) I. Alkorta, J. Elguero, *New. J. Chem.* **1999**, *23*, 951; c) T. M. Krygowski, M. K. Cyranski, *Chem. Rev.* **2001**, *101*, 1385; d) M. K. Cyranski, T. M. Krygowski, A. R. Katritzky et al., *J. Org. Chem.* **2002**, *67*, 1333.

11 a) P. v. R. Schleyer, H. Jiao, N. J. R. van Eikema Hommes et al., *J. Am. Chem. Soc.* **1997**, *119*, 12669; b) P. v. R. Schleyer, M. Manoharan, Z. X. Wang et al., *Org. Lett.* **2001**, *3*, 2465.

12 a) S. Klod, E. Kleinpeter, *J. Chem. Soc., Perkin Trans. 2*, **2001**, 1893; (b) S. Klod, A. Koch, E. Kleinpeter, *J. Chem. Soc., Perkin Trans. 2* **2002**, 1506.

13 W. Kutzelnigg, *Isr. J. Chem.* **1980**, *19*, 193.

14 J. Pipek, P. G. Mezey, *J. Chem. Phys.* **1989**, *90*, 4916.

15 J. A. Bohmann, F. Weinhold, T. C. Farrar, *J. Chem. Phys.* **1997**, *107*, 1173.

16 C. Corminboeuf, T. Heine, J. Weber, *Phys. Chem. Chem. Phys.* **2003**, *5*, 246.

17 R. Ditchfield, *Mol. Phys.* **1974**, *27*, 789.

18 T. Heine, P. v. R. Schleyer, C. Corminboeuf et al., *J. Phys. Chem. A* **2003**, *107*, 6470.

19 a) W. Bieger, G. Seifert, H. Eschrig et al., *Chem. Phys. Lett.* **1985**, *115*, 275; b) K. Friedrich, G. Seifert, G. Grossmann, *Z. Phys. D: At. Mol. Clusters* **1990**, *17*, 45.

20 D. W. Davies, *The Theory of the Electric and Magnetic Properties of Molecules*, Wiley, London **1967**.

21 a) P. Lazzeretti, *Prog. NMR Spectrosc.* **2000**, *36*, 1; b) J. A. N. F. Gomes, R. B. Mallion, *Chem. Rev.* **2001**, *101*, 1349.

22 P. Lazzeretti, E. Rossi, R. Zanasi, *J. Chem. Phys.* **1982**, *77*, 3129.

23 a) E. Steiner, P. W. Fowler, *Chem. Commun.* **2001**, 2220; b) E. Steiner, P. W. Fowler, *J. Phys. Chem. A* **2001**, *105*, 9553; c) C. Corminboeuf, T. Heine, G. Seifert et al., *Phys. Chem. Chem. Phys.* **2004**, *6* (Advance article).

24 R. Herges, D. Geuenich, *J. Phys. Chem. A* **2001**, *105*, 3214.

25 E. D. Jemmis, P. v. R. Schleyer. *J. Am. Chem. Soc.* **1982**, *104*, 4781.

26 E. Heilbronner, *Tetrahedron Lett.* **1964**, 1923.

27 M. Mauksch, V. Gogonea, H. Jiao et al., *Angew. Chem. Int. Ed. Engl.* **1998**, *37*, 2395.

28 a) S. Martín-Santamaría, H. S. Rzepa, *Chem. Commun.* **2000**, 1089 ; b) S. Martín-Santamaría, H. S. Rzepa, *J. Chem. Soc., Perkin Trans.* 2 **2000**, 2372.

29 W. L. Karney, C. J. Kastrup, S. P. Oldfield et al., *J. Chem. Soc., Perkin Trans. 2* **2002**, 388.

30 a) C. J. Kastrup, S. P. Oldfield, H. S. Rzepa, *Chem. Commun.* **2002**, 642; b) C. J. Kastrup, S. P. Oldfield, H. S. Rzepa, *J. Chem. Soc., Dalton Trans.* **2002**, 2421.

31 C. Castro, C. M. Isborn, W. L. Karney et al., *Org. Lett.* **2002**, *4*, 3431.

32 N. C. Baird, *J. Am. Chem. Soc.* **1972**, *94*, 4941.

33 V. Gogonea, P. v. R. Schleyer, P. R. Schreiner, *Angew. Chem. Int. Ed. Engl.* **1998**, 37, 1945.

34 A. Hirsch, Z. Chen, H. Jiao, *Angew. Chem. Int. Ed. Engl.* **2000**, 39, 3915.

35 Z. Chen, H. Jiao, A. Hirsch et al., *J. Mol. Model.* **2001**, *7*, 161.

36 A. Hirsch, Z. Chen, H. Jiao, *Angew. Chem. Int. Ed. Engl.* **2001**, *40*, 2834.

37 Z. Chen, H. Jiao, A. Hirsch et al., *Angew. Chem. Int. Ed. Engl.* **2002**, *41*, 4309.

38 Z. Chen, H. Jiao, A. Hirsch, From Synthesis to Optoelectronic Applications, in *Fullerenes*, eds. D. M. Guldi, N. Martin, Kluwer, Dordrecht **2002**, pp. 121–135.

39 a) A. Pasquarello, M. Schlüter, R. C. Haddon, *Science* **1992**, *257*, 1660; b) R. Zanazi, P. W. Fowler, *Chem. Phys. Lett.* **1995**, *238*, 270.

40 M. G. Evans, E. Warhurst, *Trans. Faraday Soc.* **1938**, *34*, 614.

41 M. G. Evans, *Trans. Faraday Soc.* **1939**, *35*, 824.

42 H. Jiao, P. v. R. Schleyer, *J. Phys. Org. Chem.* **1998**, *11*, 655.

43 a) B. Lecea, I. Morao, F. P. Cossio, *J. Org. Chem.* **1997**, *62*, 7033; b) F. P. Cossio, I. Morao, H. Jiao et al., *J. Am. Chem. Soc.* **1999**, *121*, 6737.

44 M. Manoharan, F. De Proft, P. Geerlings, *J. Org. Chem.* **2000**, *65*, 7971.

45 C. Corminboeuf, T. Heine, J. Weber, *Org. Lett.* **2003**, *5*, 1127.

46 M. Manoharan, F. De Proft, P. Geerlings, *J. Org. Chem.* **2000**, *65*, 6132.

47 a) P. R. Sauers, *Tetrahedron* **1998**, 54, 337; b) K. Exner, P. v. R. Schleyer, *J. Phys. Chem. A* **2001**, *105*, 3407.

48 D. Moran, M. Manoharan, T. Heine, P. v. R. Schleyer, *Org. Lett.* **2003**, *5*, 23.

49 H. Jiao, P. v. R. Schleyer, M. N. Glukhovtsev, *J. Phys. Chem.* **1996**, *100*, 2299.

50 H. Tanaka, S. Neukermans, E. Janssens et al., *J. Am. Chem. Soc.* **2003**, *125*, 2862.

51 J. Jusélius, D. Sundholm, J. Gauss, in preparation.

25
Fullerenes

Thomas Heine

25.1
Introduction

^{13}C NMR measurements have always been extremely important in fullerene [1] chemistry. In the beginning, these molecules were detected in mass spectra only, and the structure for the first fullerene was a matter of much speculation. Cage structures have been suggested, and rationalised by the isolated-pentagon rule (IPR) [2, 3]: C_{60} is the first fullerene cage, containing only pentagons and hexagons, where all pentagons can be separated (for detailed discussion, see Ref. [4]). The first proof for the C_{60} structure was possible after the development of the Krätschmer–Huffman technique [5], which allowed the synthesis of larger quantities of fullerene material. In the same work, C_{60} was characterised for the first time using infrared spectroscopy, which showed a four-line spectrum, characteristic for the truncated icosahedron structure I_h C_{60}.

However, even more convincing was its ^{13}C NMR spectrum [6]. This spectrum contained a single peak at $\delta_{TMS} = 142.7$ ppm (NMR chemical shift with respect to tetramethylsilane), as expected for the highly symmetrical I_h structure in which all carbons are identical. This result eliminated planar graphite fragments and fullerenes of lower symmetry as possible structures for C_{60}. A sixty-membered polyalkyne ring would also be expected to exhibit one ^{13}C NMR signal, but the observed chemical shift position (142.7 ppm), ~15 ppm upfield from benzene, was inconsistent with this possibility: Alkyne carbons generally resonate between 50 and 100 ppm. Since that time, ^{13}C NMR, along with mass spectroscopy, has been the standard method for fullerene characterisation.

There was an immediate need for theoretical analysis of the experimental data, as direct structure analysis was generally not yet possible, especially for the higher fullerenes. In most cases, only ^{13}C NMR and mass spectroscopic data were available. Therefore, an important contribution from theoretical chemistry was the topological analysis of fullerene geometries [4, 7]. Using, for example, the spiral code [4], all possible fullerene isomer candidates of a given C_n could be created, their point group symmetries determined, and the number and intensities of ^{13}C NMR signals of each isomer provided. This information was sufficient for the structure determination of all experimentally synthesised IPR fullerene cages up to C_{78} and for C_{82}.

Calculation of NMR and EPR Parameters. Theory and Applications.
Edited by Martin Kaupp, Michael Bühl, Vladimir G. Malkin
Copyright © 2004 WILEY-VCH Verlag GmbH & Co. KGaA, Weinheim
ISBN: 3-527-30779-6

Topological analysis also showed that the number of isomers rises exponentially with the size of the cages [4]. Direct assignment of structures from topology becomes already impossible for C_{80} and for all fullerenes C_n $n \geq 84$, as several isomers with the same symmetry patterns as the experimental one are possible for these structures. Another outcome of the spiral code is a nomenclature for numbering fullerene isomers which has been accepted by the IUPAC [4], for example 60:1 denotes the I_h C_{60} molecule, as it is the first (and only) spiral for IPR C_{60}.

However, direct simulation of the ^{13}C NMR patterns, also for the lower IPR fullerenes, has been welcomed. In the early 1990s computations on fullerenes were, and still are, challenging tasks for quantum chemists. Fullerenes are large molecules. Even though their geometry can be optimised accurately at semi-empirical or tight-binding levels (see, for example, Ref. [8] for an overview), ^{13}C NMR calculations at decent accuracy were, except for cases of appreciable symmetry, impossible. In the new and exciting field of fullerene chemistry, ^{13}C NMR characterisation became the standard method in experiment. Quantum chemistry already had all the means of treating these systems except fast enough computers. This situation changed in the late 1990s, when implementations of computational methods further improved and computational equipment became elaborate enough to perform ^{13}C NMR calculations at reasonable accuracy and computational effort.

In 2002, Meier et al. summarised the need for quantitative ^{13}C NMR calculations [9]: 'NMR chemical shifts contain a great deal of information about the electronic structure of molecules. The primary tool for establishing structure in fullerene chemistry is ^{13}C NMR. However, ^{13}C NMR is often only used to establish the symmetry of a new fullerene derivative due to complexity of the spectra and the inherently low sensitivity of the method. The poor understanding of chemical shift dispersion in fullerenes prevents the effective use of the additional information present in the absolute chemical shifts'.

In the following, a technical introduction for efficient computation of NMR parameters of fullerenes and their derivatives is given. Then, quantum chemical computations of NMR parameters of fullerenes, endohedral fullerenes, isomeric fullerene addition compounds and dimer-like fullerenes are briefly reviewed, with the restriction of computations to those which supported structure assignment. Some parts, i.e. the computation of nucleus-independent chemical shifts (NICS), semi-empirical computations and endohedral ^3He chemical shifts, are discussed in Chapters 9 by Heine and Seifert and 24 by Chen et al.

25.2 Efficient Computation of NMR Parameters of Fullerenes and Their Derivatives

The first step for the computation of NMR parameters of fullerenes is to get information on the topology of the cages. Usually, a series of isomers are compatible with experimental ^{13}C NMR patterns, and in general all of these isomers have to be considered. The two most-widely used tools for creation of topological coordinates and their analysis are the spiral code, which is printed as hardcopy in 'An Atlas of

Fullerenes' [4], and the CaGe program, a complete algorithm for the generation of cages and other molecules, which can be downloaded from the world-wide-web [7]. Both programs allow one to restrict to IPR cages, to screen symmetries, and to obtain Cartesian coordinates of the generated structures. Fullerenes are usually labelled by the IUPAC convention, which is the spiral nomenclature [4]. Unfortunately, this nomenclature is not included in the CaGe program. When screening fullerenes by symmetry, the possibility of Jahn–Teller distortions needs to be considered, i.e. higher point groups can break down to smaller ones and also have to be considered as possible structural candidates.

In a next step, the geometry needs to be optimised. Most quantum mechanical methods, including semi-empirical Hamiltonians (for a review, see Ref. [10]), density-functional based tight-binding [11], DFT and ab inito methods give results in very good agreement with experimental data (for an overview, see, e.g. Ref. [8]). On the other hand, simple force fields failed in many cases to produce reasonable geometries [12].

The same holds for relative energies. No major discrepancies have been found for higher fullerenes (see the same works as above). However, it has been found that correlation is important for smaller fullerenes (see, e.g. Ref. [13]), and for the correct binding energy of fullerene dimers [14, 15]. Even though the structures have been found to be reasonable for most semiempirical Hamiltonians and LDA-DFT, the binding energies are often overestimated.

^{13}C NMR computations have been carried out with several methods, including the most-widely used gauge-including atomic orbitals (GIAO) [16] and individual-gauge for local orbital (IGLO) [17] approaches. The shielding constants depend strongly on the quality of the basis set [18, 19]; however, a large part of the error is systematic and disappears when computing chemical shifts taking C_{60} as a reference compound. Individual errors have been found for the most upfield signals with a value of ~2 ppm for chemical shifts at the GIAO-B3LYP/6-31G* level, which is a large value when taking into account that the whole span of the ^{13}C NMR scale is ~20 ppm in most cases [20]. The role of solvent effects has not been investigated yet, but the non-polar standard solvents are not expected to have a high and non-systematic contribution.

It was shown that computations at lower computational level can be very useful, and often sufficient for structure determination: Approximate schemes like IGLO-DFTB [21] and coupled Hartree–Fock (CHF) calculations with limited basis sets [22, 23] correctly reproduce characteristic features of the patterns (see below), and GIAO-MNDO was found to give good results for NICS at fullerene centres (see Ref. [10] and Chapter 9).

25.3 Classical IPR Fullerenes

Classical fullerenes are those with only pentagonal and hexagonal rings. So far, all experimental fullerenes are classical fullerenes, and all of them have been charac-

terised by mass spectrometry and, after extraction of the soot and HPLC separation, ^{13}C NMR spectroscopy. This technique has been applied to C_{60}, C_{70}, C_{76}, C_{78}, C_{80}, C_{82} and C_{84} (see Ref. [24] and references therein). In many cases a selection of isomers have been synthesised experimentally, with varying ratio. For example, in C_{78} three isomers have been isolated, and for C_{84} the major components of the fraction contain two isomers. More elaborate experimental techniques allow one to isolate minor isomers. For example, nine minor isomers of C_{84} have been isolated and characterised by various groups (see references in Refs. [25, 26]). Isolation of even larger fullerenes beyond C_{90} is possible, and their characterisation are in progress.

The first ^{13}C NMR quantum calculations for highly symmetric C_{60} were published by Fowler et al. in 1990 and 1991, at the coupled Hartree–Fock (CHF) level with different basis sets, ranging from STO-3G up to 6-31G* [18, 19]. They extrapolated the shielding constant of C_{60} to the basis set limit and found the principal components of the shielding tensor to be 179, 10 and –51 ppm [27]. The mean differs from the experimental shift by less than 4 ppm, but the tensor components showed larger deviations from the solid-state experiment [28, 29]. It was demonstrated that the shielding value for C_{60} at the CHF level has not yet converged at the 6-31G* basis set.

^{13}C NMR spectra of C_{70} were studied by Häser et al. as early as 1992 at the GIAO-CHF/DZP level [30]. Bühl et al. showed that DFT-NMR computations (GIAO-B88PW91/TZP//BP86/TZP) perform significantly better than CHF for C_{70} and other systems [31]. Heine et al. used an approximative tight-binding method [21] (see Chapter 9), which reproduced the ^{13}C NMR shifts of the major fullerenes C_{60}–C_{84} at reasonable accuracy. Sun and Kertesz [20, 32] employed the GIAO-B3LYP/6-31G* level of computation to study these fullerenes. At present, this is the most accurate study with largest individual errors of ~2 ppm.

In all these studies chemical shifts were computed using C_{60} as a reference and assigning $\delta_{TMS}(C_{60})$ to its experimental chemical shift. A systematic error of at least 5 ppm is removed in this procedure [20, 21].

^{13}C NMR computations led to the assignment of a series of higher fullerenes. Already in 1993 the main fraction of C_{84} was identified by the span of the ^{13}C NMR spectrum by Schneider et al. [33]. The patterns of the lower isomers of C_{84} have been predicted employing IGLO-DFTB [34] and final assignment of seven isomers could be achieved after simulating all patterns at the GIAO-B3LYP/6-31G* level [25].

The application of DFT-NMR computation led to the determination of a series of further fullerene isomers, namely the isomer of C_{82} [35], isomers of C_{86} [36] and C_{88} [37]. Structural assignment of fullerenes will become harder, but computationally feasible, for the higher fullerenes, and such studies are presently in progress [38].

Fullerene hexaanions of different sizes and shapes have been studied recently both by experiment and by theory [39]. Even though electrons were added to the cages they became deshielded. The existence of the anions was confirmed with the simulations of the barycentres of the patterns.

Schneider et al. [33] suggested to compare ^{13}C NMR chemical shifts of fullerenes with the local pyramidalisation of the carbon atoms, given by Haddon's π orbital axis vector (POAV) [40]. They found a poor correlation between these two quantities,

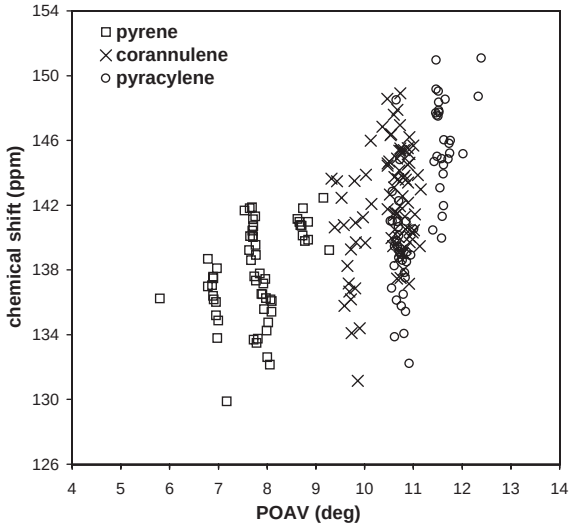

Figure 25.1 Theoretical ^{13}C NMR chemical shifts and POAV angles of isomers 4, 5, 11, 14, 16, 19, and 22–24 of fullerene C_{84} calculated by B3LYP/6-31G* (data from Ref. [25]). This figure was kindly provided by Dr. Guangyu Sun.

which excluded simple geometrical approaches to address ^{13}C NMR chemical shifts in an inexpensive way. This correlation was refined to include the chemical environment, i.e. pyrene, pyracylene and coronene sites, as suggested originally by Diederich and Whetten [41]. Again, different sites give shifts in different regions of the carbon NMR scale, but an accurate assignment was found to be impossible [21, 34, 20, 25] (see Fig. 25.1); sound quantum-chemical computations are necessary for correct assignments of fullerene isomers.

25.4 ^{13}C NMR Spectra of Isomeric Fullerene Addition Compounds

Fullerenes react readily with halogens, hydrogen, oxygen and other elements, to form exohedral addition compounds with characteristic addition patterns. Such compounds can be created from all fullerenes and, in all known cases, the cage structure is not destroyed in these reactions. The structures of the addition patterns are determined by steric hindrance of the additional atoms and by the stability of the modified π system. The structures of fullerene addition compounds, for example the benzyne adduct of C_{70}, indicate the aromatic character of fullerenes [42]. The aromatic character of fullerenes was investigated using magnetic criteria like nucleus independent chemical shifts in a series of computations which are reviewed in Chapters 9 and 24.

Structure determination and characterisation of these molecules was usually supported by two facts: (i) the underlying cage is known and (ii) the NMR pattern has been recorded. In addition, the 2D-NMR measurements often contributed to the structure determination and to the assignment of ^{13}C NMR signals to specific carbon atoms (see Ref. [9] and references therein). Fullerene addition compounds include sp^2 and sp^3 carbons and hence a much wider ^{13}C NMR shift range.

Quantum chemical computations of NMR chemical shifts of these compounds have been performed only on a few occasions to confirm the assignment of chemical shifts to atomic sites [9], but several studies of endohedral ^3He chemical shifts have been performed (see Section 25.5) for their characterisation. However, ^{13}C NMR computations are straight forward for such molecules if a relatively small set of isomer candidates has to be considered.

The situation is different for smaller fullerenes (below the C_{60} threshold). They are highly reactive and form fullerene hydrides and oxyhydrides during production, which means that the underlying cage is unknown. The most-widely studied example is $C_{36}H_x$, $x=4$, 6, which has been detected in the mass spectrum by several groups [43, 44, 45], but not yet fully characterized. The number of candidates for such systems is very large: If one takes only those cages with minimum number of pentagon adjacencies, 36:14 and 36:15, into account [4, 46, 13], ~250,000 isomer candidates for $C_{36}H_4$ and $C_{36}H_6$ are possible [47]. The ^{13}C NMR patterns of the 21 most stable candidates out of a complete scan of these isomers have been proposed and will assist in experimental assignment of the basis cage [48]. These ^{13}C NMR calculations gave very rich patterns, exhibiting isomer-dependent sp^3 peaks and an enlarged sp^2 region, ranging from δ_{TMS} ~110 to ~220 ppm. Parts of the patterns are characteristic for certain structural elements in the addition patterns themselves, as is shown in Fig. 25.2.

25.5 Endohedral Fullerenes

For the discussion of magnetic properties, endohedral fullerenes can be separated into three categories: (i) fullerenes with chemically inert endohedral atoms or molecules, as He and other noble gases, (ii) closed-shell fullerenes with active endohedral atoms or molecules, as for example transition metals, transition metals dimers and transition metal compounds Sc_3N, Sc_2 and others, or even with lanthanides or actinides, and (iii) open-shell isomers (including open-shell endohedral atoms or molecules) which are not interesting for NMR investigations, but provide interesting EPR parameters like g-tensors and hyperfine coupling constants. In this chapter, only categories (i) and parts of (ii) are discussed, as theoretical investigations on magnetic properties of molecules from category (iii) are in their infancy (see Chapter 20 by Moon and Patchkovskii).

The fundamental difference between categories (i) and (ii) is the influence of the endohedral species on the fullerene cage itself. Chemically inert molecules are trapped into the fullerene cage without having considerable influence on its struc-

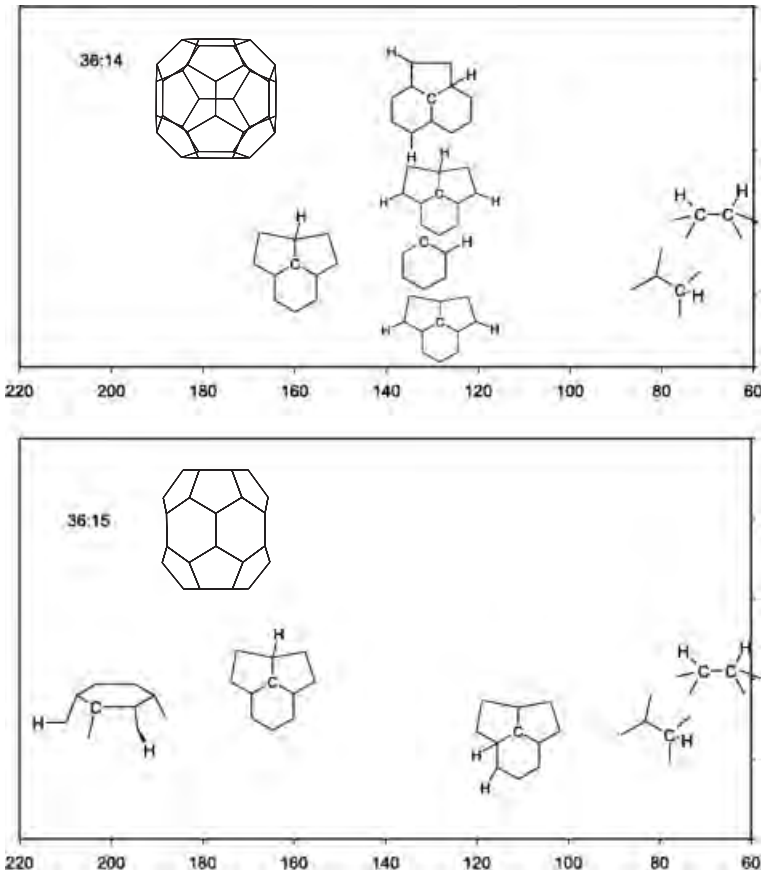

Figure 25.2 Interrelations between local structure and chemical shift. The ^{13}C NMR chemical shift regions for carbon sites in the different possible structural motifs of 36:14 and 36:15 are shown schematically.

ture. Thus, these species can be created for all 'standard' fullerenes. ^{3}He labelling and NMR technique provide a valuable characterization method for fullerenes, even though it is less informative than the ^{13}C NMR pattern. However, the presence of a single shift as a finger print of one fullerene, or even a fullerene addition or substitution compound, is very attractive, and this method was therefore applied in experiment and theory to a series of fullerenes [26, 49–52], and fullerene derivatives [53–55]. ^{3}He was used to address the shielding inside a fullerene, and fullerene anions have been found to provide a shielding of as much as –48.7 ppm with respect to free ^{3}He in solution [56]. However, the relatively small span of ^{3}He NMR shifts in IPR fullerene cages limits the applicability of this method for characterisation, and comparison to theoretical computations suffers the same intrinsic inaccuracies as

^{13}C NMR chemical shifts. However, ^{3}He labelling and NMR might be a valuable tool to identify fullerenes with the same symmetry but different endohedral shifts [26]. ^{3}He NMR is also a probe of the shielding inside the cage and is also discussed in Chapter 24.

On the other hand, molecules with valencies, often with large electronegativity, have been used as endohedral molecules. Experimentally, both the chemical shifts of the endohedral molecule and the chemical shift of the cage can be accessed.

NMR measurements and computations of these species meet the difficulty that the NMR time scale is very long, of the order of ns or even μs. Therefore, the NMR is a time-average of the structure over the whole measurement, and a static computation is not sufficient to reproduce the pattern. An example is Sc_3NC_{80} [57]. The I_h C_{80} molecule (80:1) was found to be one of the less stable isomer candidates. However, in the presence of Sc in the carbon rods and N_2 in the atmosphere of the arc discharge chamber $Sc_3N@C_{80}$ is formed. The NMR spectrum is of I_h symmetry, even though the symmetry of the system must be lower. This can only be explained by a nearly-free rotation of the Sc_3N molecule inside the fullerene, which leads to an averaged I_h NMR pattern. Indeed, molecular dynamics simulations demonstrated that Sc_3N is rotating [58]. The NMR pattern of such fullerenes should be reproducible by averaging snapshots of molecular dynamics simulations, as has been done earlier [60]. Such computations are feasible, but very expensive, at present.

25.6 Fullerene Dimers and Dimer-like Compounds

A major characteristic of fullerene dimer-like compounds is the presence of sp^3 carbon atoms. Structural identification is strongly supported by the fact that two regions, sp^3 and sp^2, can be compared, and often computations of quite low level are sufficient for this purpose. The number of sp^2 and sp^3 carbon atoms per molecule is essential information for structure determination and can be taken immediately from the experimental ^{13}C NMR pattern.

$(C_{60})_2$, was produced in quantities which allow X-ray spectroscopy and very clean ^{13}C NMR characterisation [61], and can therefore be taken as an ideal benchmark for calculations on this type of compound. The ^{13}C NMR pattern shows one signal corresponding to four sp^3-hybridized carbon atoms, indicating a cyclobutadiene [2+2] bridge between the fullerenes. For $(C_{70})_2$ (Fig. 25.3a) [62, 63], five stable isomer candidates are possible due to different bond types and orientations of C_{70}. Stability calculations showed that only two isomers are reasonable candidates, and that they are isoenergetic. They have a cyclobutadiene bridge between the closest-to-cap positions of the C_{70} monomers, and the symmetry of the ^{13}C NMR pattern was compatible with both candidates. However, the two candidates produce different ^{13}C NMR spectra, and its simulation has led to the identification of the cage [15].

An interesting odd-numbered fullerene, C_{119} (Fig. 25.3c), was created when C_{60} was treated with ozone [64]. Corresponding observations were made for a mixture of C_{60} and C_{70}, which can form C_{129} and C_{139}. The mechanism of these reactions was stud-

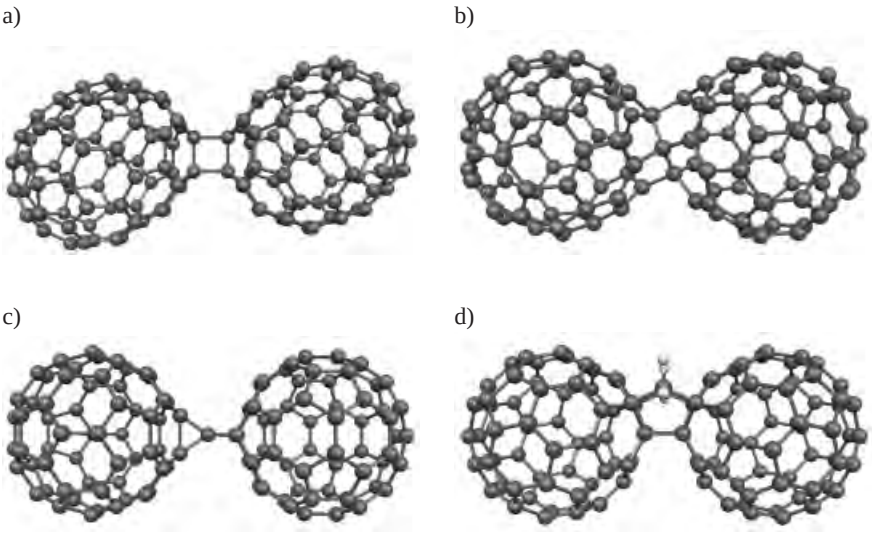

Figure 25.3 Structures of experimental fullerene dimers and dimer-like compounds as discussed in the text, a) $(C_{70})_2$, b) C_{119}, c) C_{121} and d) $C_{122}H_4$.

ied, and it was suggested that one carbon atom was removed from one C_{60} forming CO and a C_{59} radical, which reacts immediately with another C_{60} to form C_{119} [65]. The proposed mechanism leads to the most stable isomer of C_{119} candidates [66], and the ^{13}C NMR pattern was compatible with its point group symmetry (C_{2h}). However, there have been other, contradictory, propositions for the structure of C_{119} [67], and several isomer candidates exhibit C_{2h} symmetry. The final confirmation of the C_{119} structure and reaction mechanism was achieved by ^{13}C NMR experiment [68] and simulation at the IGLO-DFTB level [69].

The unsymmetrical bisfullerene C_{121} (Fig. 25.3c) was made, separated, characterised by vibrational and ^{13}C NMR spectroscopy, and compared with quantum calculations of structure, stability and ^{13}C NMR patterns [22, 70]. Computations were performed for all possible isomers of these species which can be created by two C_{60} linked by an additional carbon at the GIAO-HF/6-31G(d)//B3LYP/6-31G(d) level.

Similar studies have been performed on $C_{122}H_4$ (Fig. 25.3d), where two C_{60} are bridged by intercage bonds and extra-bonding CH_2 bridging moieties [23]. In both cases, there are several possibilities for the intercage bonds, some of them differ in symmetry or in the number of sp^3 carbon atoms, but can be unambiguously assigned by the simulation of the ^{13}C NMR pattern.

For the large bridged fullerene dimers, theoretical simulations have been performed on a pragmatic, quite low level of theory. However, these computations provide sufficient information for the assignment of these molecules, especially as the sp^3 regions are remarkably distinct. The sp^2 area differs strongly from experiment

and only minor information, such as the span and the barycentre, can be deduced from this part of the simulation.

25.7 Solid State NMR of Fullerenes

So far, solid state NMR has played only a minor role in fullerene science due to its poor resolution and the necessity for crystalline material. The first solid state NMR investigations were performed by Tycko et al. [71] and Yannoni et al. [29] on C_{60} powder. The shielding constant of these measurements agreed with measurements in solution [6, 28]. The first ab initio NMR calculations for gas-phase C_{60} at the CHF level of Fowler et al. [27] reproduced the solid-state chemical shift within 4 ppm, but its tensor components disagreed by more than 20 ppm.

Recent developments of fullerene solids constructed from smaller fullerenes [43, 72] and modern magic-angle spinning (MAS) NMR techniques indicate that solid state NMR may play a more important role in the future.

For the hypothetical C_{36} solid this technique of characterisation puts doubts on the existence of this species [43]: Solids, formed from smaller fullerenes, should always have sp^3 linking atoms between the cages. ^{13}C NMR signals of these atoms are in the typical sp^3 range of the pattern, as for example demonstrated for C_{60} dimer, or even for C_{36} dimer and $C_{36}H_6$ [21, 48, 61]. However, no sp^3 signals have been found in the powder spectrum of the alleged C_{36} solid [43].

Nevertheless, solid state ^{13}C NMR gives the sp^2:sp^3 ratio of the solid, which is important complementary information to TEM and electron diffraction measurements which are usually employed for information on fullerene polymers. Computational tools for the treatment of chemical shifts in infinite, periodic systems are available (see Chapter 16 by Mauri and Pickard).

25.8 Summary and Perspectives

NMR computational tools, especially at the DFT level, are nowadays implemented in most standard quantum chemistry codes and allow the simulation of ^{13}C NMR spectra of fullerenes and their derivatives with reasonable accuracy and at moderate computational cost. An accuracy of ~2 ppm for individual sites and better can be achieved in these computations. The signals of the high-field region suffer from the highest inaccuracies. The achieved accuracy was sufficient for the assignment of the fullerenes C_{60} to C_{86}. However, with increasing fullerene size the number of possible isomers will increase, and higher accuracy is necessary.

For the assignment of ^{13}C NMR signals to carbon atoms the same conclusion holds as above: For $C_{60}H_x$ the spectra can be assigned at a moderate computational level, but demands are already strongly increased for C_{70}. Simulations of higher accuracy will be appreciated in this field of theory. For endohedral fullerenes

dynamic averaging of a series of structures will be necessary for the accurate simulation of their ^{13}C NMR patterns. Experiences of ^{13}C NMR computations with fullerenes will be useful in other areas of chemistry, for example for dendrimers and supermolecules.

Acknowledgements

Financial support of DFG (HE 3543/1-1) is gratefully acknowledged.

References

1 H. W. Kroto, J. R. Heath, S. C. O'Brien et al., *Nature* **1985**, *318,* 162.
2 H. W. Kroto, *Nature* **1987**, *329,* 529.
3 T. G. Schmalz, W. A. Seitz, D. J. Klein et al., *J. Am. Chem. Soc.* **1988**, *110,* 1113.
4 P. W. Fowler, D. E. Manolopoulos, *An Atlas of Fullerenes,* Clarendon Press, Oxford 1995.
5 W. Krätschmer, L. D. Lamb, K. Fostiropoulos et. al., *Nature* **1990**, *347,* 354.
6 R. Taylor, J. P. Hare, A. K. Abdul-Sala et al., *J. Chem. Soc. Chem. Commun.* **1990**, 1423.
7 http://www.mathematik.uni-bielefeld.de/CaGe
8 J. Cioslowski, *Electronic Structure Calculations on Fullerenes and Their Derivatives,* Oxford University Press, Oxford **1995**.
9 M. S. Meier, H. P. Spielmann, R. G. Bergosh et al., *J. Am. Chem. Soc.* **2002**, *124,* 8090.
10 Z. Chen, W. Thiel, *Chem. Phys. Lett.* **2003**, *367,* 15.
11 D. Porezag, Th. Frauenheim, Th. Köhler et al., *Phys. Rev. B* **1995**, *51,* 12947.
12 E. Albertazzi, C. Domene, P. W. Fowler et al., *Phys. Chem. Chem. Phys.* **1999**, *1,* 2913.
13 P. W. Fowler, T. Heine, K. M. Rogers et al., *Chem. Phys. Lett.* **1999**, *300,* 369.
14 S. Patchkovskii, W. Thiel, *J. Am. Chem. Soc.* **1998**, *120,* 556.
15 T. Heine, F. Zerbetto, G. Seifert et al., *J. Phys. Chem. A* **2001**, *105,* 1140.
16 R. Ditchfield, *Mol. Phys.* **1974**, *27,* 789.
17 W. Kutzelnigg, *Isr. J. Chem.* **1980**, *19,* 193.
18 P. W. Fowler, P. Lazzeretti, R. Zanasi, *Chem. Phys. Lett.* **1990**, *165,* 79.
19 P. W. Fowler, P. Lazzeretti, M. Malagoli et al., *Chem. Phys. Lett.* **1991**, *179,* 174.
20 G. Sun, M. Kertesz, *J. Phys. Chem. A* **2000**, *104,* 7398.
21 T. Heine, G. Seifert, P. W. Fowler et al., *J. Phys. Chem. A* **1999**, *103,* 8738.
22 H. Shimotani, N. Dragoe, K. Kitazawa, *J. Phys. Chem. A* **2001**, *105,* 4980.
23 H. Shimotani, N. Dragoey K. Kitazawa, *Phys. Chem. Chem. Phys.* **2002**, *4,* 428.
24 C. Thilgen, F. Diederich, *Top. Curr. Chem.* **1999**, *199,* 135.
25 G. Sun, M. Kertesz, *J. Phys. Chem. A* **2001**, *105,* 5212.
26 Z. Chen, J. Cioslowski, N. Rao et al., *Theor. Chem. Acc.* **2001**, *106,* 364.
27 P. W. Fowler, P. Lazzeretti, M. Malagoli et al., *J. Phys. Chem.* **1991**, *95,* 6404.
28 D. S. Bethune, G. Meijer, W. C. Tang et al., *Chem. Phys. Lett.* **1990**, *174,* 219.
29 C. S. Yannoni, R. D. Johnson, G. Meijer et al., *J. Phys. Chem.* **1991**, *95,* 9.
30 M. Häser, R. Ahlrichs, H. P. Baron et al., *Theor. Chim. Acta* **1992**, *83,* 455.
31 M. Bühl, M. Kaupp, V. G. Malkin et al., *J. Comput. Chem.* **1999**, *20,* 91.
32 G. Sun, M. Kertesz, *Chem. Phys. Lett.* **2000**, *328,* 387.
33 U. Schneider, S. Richard, M. M. Kappes et al., *Chem. Phys. Lett.* **1993**, *210,* 165.
34 T. Heine, M. Bühl, P. W. Fowler et al., *Chem. Phys. Lett.* **2000**, *316,* 373.
35 G. Sun, M. Kertesz, *J. Phys. Chem. A* **2001**, *105,* 5468.
36 G. Sun, M. Kertesz, *Chem. Phys.* **2002**, *276,* 107.
37 G. Sun, *Chem. Phys. Lett.* **2003**, *367,* 26.
38 G. Sun, *Chem. Phys.* **2003**, *289,* 371.

39 T. Sternfeld, C. Thilgen, Z. Chen et al., *J. Org. Chem.* **2003**, *68,* 4850.

40 R. C. Haddon, L. T. Scott, *Pure Appl. Chem.* **1986**, *58,* 137.

41 F. Diederich, R. L. Whetten, *Acc. Chem. Res.* **1992**, *25,* 119.

42 M. S. Meier, G.-W. Wang, R. C. Haddon et al., *J. Am. Chem. Soc.* **1998**, *120,* 2337.

43 C. Piskoti, J. Yarger, A. Zettl, *Nature* **1998**, *393,* 771.

44 A. Koshio, M. Inakuma, Z. W. Wang et al., *J. Phys. Chem. B* **2000**, *104,* 7908.

45 A. Koshio, M. Inakuma, T. Sugai et al., *J. Am. Chem. Soc.* **2000**, *122,* 398.

46 J. C. Grossman, M. Coté, S. G. Louie et al., *Chem. Phys. Lett.* **1998**, *284,* 344.

47 T. Heine, P. W. Fowler, *J. Chem. Soc., Perkin Trans. 2* **2001**, 487.

48 C. Corminboeuf, P. W. Fowler, T. Heine, *Chem. Phys. Lett.* **2002**, *361,* 405.

49 M. Saunders, H. A. Jiménez-Vazquez, R. J. Cross et al., *J. Am. Chem. Soc.* **1995**, *117,* 9305.

50 E. Shabtai, A. Weitz, R. C. Haddon et al., *J. Am. Chem. Soc.* **1998**, *120,* 6389.

51 M. Bühl, S. Patchkovskii, W. Thiel, *Chem. Phys. Lett.* **1997**, *275,* 14.

52 M. Bühl, W. Thiel, *Chem. Phys. Lett.* **1995**, *233,* 585.

53 M. Bühl, W. Thiel, H. Jiao et al., *J. Am. Chem. Soc.* **1994**, *116,* 6005.

54 P. R. Birkett, M. Bühl, A. Khong et al., *J. Chem. Soc. Perkin Trans. 2* **1999**, 2037.

55 M. Bühl, W. Thiel, U. Schneider, *J. Am. Chem. Soc.* **1995**, *117,* 4623.

56 E. Shabtai, A. Weitz, R. C. Haddon et al., *J. Am. Chem. Soc.* **1998**, *120,* 6389.

57 S. Stevenson, G. Rice, T. Glass et al., *Nature* **1999**, *401,* 55.

58 M. Krause, H. Kuzmany, P. Georgi et al., *J. Chem. Phys.* **2001**, *115,* 6596.

59 K. Vietze, G. Seifert, in *Electronic Properties of Novel Materials. AIP Conference Proceedings 633*, eds. H. Kuzmany, J. Fink, M. Mehring et al., American Institute of Physics, New York **2002**, pp. 39–42.

60 C. Scheurer, N. R. Skrynnikov, S. F. Lienin et al., *J. Am. Chem. Soc.* **1999**, *121,* 4242; I. B. Woolf, V. G. Malkin; O. L. Malkina, B. Roux, *Chem. Phys. Lett.* **1995**, *239,* 186.

61 G.-W. Wang, K. Komatsu, Y. Murata et al., *Nature* **1997**, *387,* 583.

62 M. Ata, K. Kurihara, N. Takahashi, *J. Phys. Chem.* **1997**, *101,* 5.

63 S. Lebedkin, W. E. Hull, A. Soldatov et al., *J. Phys. Chem. B* **2000**, *104,* 4101.

64 R. S. W. McElvany, J. H. Callahan, L. D. Lamb et al., *Science* **1993**, *260,* 1632.

65 G. B. Adams, J. B. Page, M. O'Keeffe et al., *Chem. Phys. Lett.* **1994**, *228,* 485.

66 E. Albertazzi, F. Zerbetto, *J. Am. Chem. Soc.* **1996**, *118,* 2734.

67 R. Taylor, *J. Chem. Soc., Chem. Commun.* **1994**, 1629.

68 S. Lebedkin, H. Rietschel, G. B. Adams et al., *J. Chem. Phys.* **1999**, *24,* 11768.

69 T. Heine, F. Zerbetto, G. Seifert et al., *J. Phys. Chem. A* **2000**, *104,* 3865.

70 N. Dragoe, H. Shimotani, J. Wang et al., *J. Am. Chem. Soc.* **2001**, *123,* 1294.

71 R. Tycko, R. C. Haddon, G. Dabbagh et al., *J. Phys. Chem.* **1991**, *95,* 518.

72 Z. X. Wang, X. Z. Ke, Z. Y. Zhu et al., *Phys. Lett. A* **2001**, *280,* 351.

26
NMR of Transition Metal Compounds

Michael Bühl

26.1
Introduction

Transition metal complexes are ubiquitous in chemistry. For example, in almost every complex organic synthesis, one or more steps are mediated or catalyzed at a transition metal center. The study and development of such reagents are thus important research areas in modern chemistry. As with most new substances scrutinized by chemists, NMR and EPR spectroscopy are among the most important means of characterization for diamagnetic and paramagnetic transition metal complexes, respectively. Theoretical and computational contributions to NMR properties will be the topic of this account, whereas EPR applications to transition metal compounds will be covered elsewhere in this book (see Chapters 32 and 36 by Patchkovskii and Schreckenbach, and by Neese, respectively). Only NMR properties of diamagnetic species will be considered here; for NMR of paramagnetic compounds, see the corresponding Chapter 20 by Moon and Patchkovskii.

Reflecting the importance of NMR spectroscopy in chemistry, developments and applications of theoretical methods for the calculation of the salient parameters are reviewed regularly (for recent reviews see e.g. Refs. [1–5]). In some of these reviews, applications to transition metal compounds have been covered explicitly, and this aspect's state of the art has been summarized in the late 1990s [1–3]. The present account will emphasize more recent developments and applications, that is, from 1999 onwards.

Density functional theory (DFT) presents itself more than ever as the computational tool of choice to study geometries, energies, and properties of transition metal complexes [6, 7]. Note the following quote from the foreword by Davidson in the Special Edition: "Computational Transition Metal Chemistry" [6], "Computational transition metal chemistry today is almost synonymous with DFT for medium-sized molecules".

The finding that DFT-based methods are capable of reliably describing chemical shifts of transition metal complexes [8, 9], many of which pose excruciating problems to more traditional ab initio methods, has certainly contributed to the popularity of DFT. Consequently, the vast majority of examples cited in the present account are based on computations using this method. The particular choice of these exam-

Calculation of NMR and EPR Parameters. Theory and Applications.
Edited by Martin Kaupp, Michael Bühl, Vladimir G. Malkin
Copyright © 2004 WILEY-VCH Verlag GmbH & Co. KGaA, Weinheim
ISBN: 3-527-30779-6

ples is intended to be illustrative rather than exhaustive. This chapter is organized as follows: First, chemical shifts of ligands in the coordination sphere of transition metals are treated, followed by the chemical shifts of the metals themselves. Calculations of spin–spin coupling constants involving transition metal nuclei are presented thereafter. Finally, a few miscellaneous NMR-related applications are mentioned, and a brief summary concludes this chapter.

26.2 Ligand Chemical Shifts

26.2.1 Methodological Aspects

The quest for more accurate DFT-based chemical shifts contributes to the need for more accurate density functionals. Newly developed functionals are now often assessed in terms of their performance for computing ligand (and metal) chemical shifts [10]. Contrary to what is frequently found for the metal shifts (see below), "pure" GGA (generalized gradient approximation) functionals often afford ligand shifts similar in quality or even superior to those obtained with hybrid functionals. A highly parametrized GGA functional (termed HCTH) has shown promise in that area [10b]. As with the underlying density functionals, the effect of fundamental modifications to them, for instance the self-interaction correction [11a] is being tested by computations of ligand shifts, such as $\delta(^{31}P)$ in a transition metal complex [11b].

Current development of methods for chemical shift computations is mainly centered around appropriate description of relativistic effects when heavier nuclei are involved. Ligand shifts are an important testing ground in that area, in particular in complexes of 5d or f-block metals. How to include a major part of the relativistic effects on the ligand shifts has been known, almost from the onset, namely by means of relativistically adjusted effective core potentials (ECPs) on the heavy metal [9]. Further developments include other quasi-relativistic approaches such as DFT-ZORA (zero-order regular approximation) [12] and inclusion of spin–orbit coupling [13] (for more details the reader is referred to Chapter 6 by van Wüllen, Chapter 13 by Vaara et al., and Chapter 14 by Autschbach). Such relativistic effects have recently been shown to be important for $\delta(^{13}C)$ of some third-row transition metal carbonyls [14] and ^{17}O, ^{19}F, and ^{1}H chemical shifts of uranium compounds [15].

26.2.2 Isotropic and Anisotropic Ligand Chemical Shifts

With the implementation of DFT-NMR methods in popular quantum-chemical programs, chemical shift computations are now routinely possible. In many cases, experimental studies that report ligand chemical shifts in solution are being augmented by DFT computations of this property. Recent studies on isotropic $\delta(^{13}C)$

and $\delta(^1H)$ values of Ru [16], Nb [17], Pt [18], and Os [19] complexes may serve as representative examples. The implicit assumption is that when there is good accord between measured and computed shifts, the underlying molecular structure and assignments of the peaks are likely to be correct (see also below). In this context it may be noted that, in some cases, substituent effects on ligand shifts can also be reproduced at the Hartree–Fock level, for instance ring-current effects on $\delta(^1H)$ of metalloporphyrins [20] or $\delta(^{13}C)$ in a thiol adsorbed on small gold clusters [21].

Accurate description of the principal shielding tensor components is usually more demanding than that of isotropic shifts (see Chapter 27 by Wasylishen). One reason is that in the solid state, where measurements of shift tensors are usually carried out, intermolecular interactions tend to be more important than for solutes tumbling rapidly in a solvent. This is particularly true for ionic species, where larger fragments of the crystal, encompassing several cations and anions, have to be included in the NMR computation, a recent example being the computation of the ^{13}C chemical shift tensors in cadmium acetate [22]. Ligand shift tensors of neutral complexes, on the other hand, can also be well described using single molecules, that is, neglecting such intermolecular interactions. Good accord between theory and experiment has been achieved, for instance for ^{13}C, ^{15}N, and ^{17}O tensor components in iron porphyrins [23, 24], and for ^{13}C and ^{31}P tensors in metal carbonyl [25, 26] and ethylene complexes [27]. In the latter study, the calculations were also helpful in establishing the orientation of the principal axis system.

Breakdown of the computed shielding tensor into contributions from individual coupled pairs of MOs can often be useful for the rationalization of observed trends in ligand chemical shifts (see e.g. Refs. [28, 29] and Chapter 18 by Kaupp).

26.2.3
Structural Applications

Magnetic shieldings have been said to be "sensitive to everything" [15a]. For the experimental chemist, the prime interest is usually in the sensitivity towards structural details, such as configuration, conformation, or particular values of geometrical parameters. The combination of chemical shifts measured for a compound of uncertain structure with those computed for several alternative candidates for the latter can afford a powerful structural tool [30]: those isomers that give poor agreement between theoretical and experimental δ values can safely be excluded. In the following, several such theoretical structure refinements of transition metal complexes are highlighted.

Cationic zirconocene complexes bearing pendant aromatic groups, designed to model interactions between active olefin-polymerizing catalysts and aromatic solvents, have been suggested to possess an agostic interaction between Zr and a phenylic H-atom (as in **1a**, Chart 26.1). However, DFT calculations indicated that **1a** corresponds to a transition state for phenyl group rotation, rather than to a minimum. The lowest minimum (**1b**) shows η^1-coordination of the benzene moiety to the Zr center. While the ^1H and ^{13}C chemical shifts of **1b** can be reconciled with experimental data, those of **1a** cannot [31]. Agostic metal–hydrogen interactions

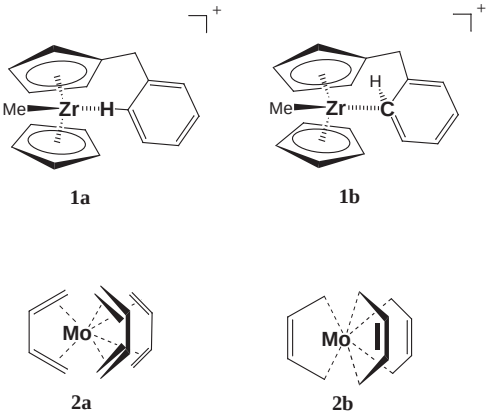

1a **1b** **2a** **2b**

Chart 26.1

have been found in [PdBr{P(*t*-Bu)$_2$(Adamantyl)}(C_6H_5)] complexes, and chemical shift calculations have been used to rationalize why these interactions do not show up in the ^{1}H NMR spectra [32].

An older X-ray crystallographic structure determination of [Mo(1,3-butadiene)$_3$] had afforded C–C distances indicative of almost undisturbed, coordinated olefins (as in **2a**, Chart 26.1). Redetermination of the structure with correction for previously undetected disorder in the crystal has yielded essentially equal C–C distances, as expected for significant metallacyclopentene character (viz. **2b**). The newly refined structure not only compares favorably to the DFT-optimized equilibrium geometry, but yields, when used as input in the NMR computation, $\delta(^{13}C)$ values in much better accord with experiment than those computed for the old X-ray-derived coordinates, for which deviations up to 20 ppm occur [33].

Theoretical ^{1}H and ^{13}C chemical shifts have been used to propose plausible structures for the reaction products between dimethylzirconocene and methylaluminoxane [34]. These results are an important step towards the identification and characterization of the dormant and active catalytic species involved in homogeneous olefin polymerization with these types of systems.

26.3 Metal Chemical Shifts

26.3.1 Nonrelativistic Computations

Metal shift calculations on nonrelativistic levels are only sensible for the 3d and 4d series. In the latter case, relativistic effects on absolute shieldings can be noticeable, but are usually similar for most compounds, so that they cancel to a large extent in the relative chemical shifts, δ. In many cases, the influence of the exchange-correlation functional on the δ values exceeds that of other sources, including relativity.

Hybrid functionals very often give results superior to those obtained with pure GGAs [35], and the reasons for the different performance of the different families of functionals have been analyzed [36]. As with the ligand shifts mentioned above, computed metal chemical shifts are being used to assess newly developed density functionals [10a].

A sizeable set of transition metal shifts has now been computed at a very uniform level of theory (i.e. B3LYP for GGA geometries), with the more recent extensions of this set encompassing ^{99}Ru [37], ^{55}Mn [38], and ^{49}Ti [39]. The overall performance of this particular combination of DFT methods is illustrated in Fig. 26.1. Except for $\delta(^{95}\text{Mo})$ [40], substituent effects on the metal shifts are captured very well, with an accuracy for each metal of typically a few percent of the respective chemical shift range. The reasons for the deviations for $\delta(^{95}\text{Mo})$ have not been analyzed yet; in this case, pure GGA functionals perform much better [40].

For $\delta(^{59}\text{Co})$ in metalloporphyrins and in aza-crown ether complexes, not only isotropic shifts, but also the principal tensor components are well described with the B3LYP functional [41, 42]. There have been attempts to compute metal chemical shifts using an ECP on the metal in the NMR calculation; despite the lack of theoretical justification for such a procedure, reasonably good correlations between calculated and experimental $\delta(^{183}\text{W})$ and $\delta(^{99}\text{Ru})$ values have been obtained [43]. With scale factors for the calculated shifts of the order of 10–20, however, the usefulness of this approach remains unclear.

A combination of experimental and theoretical ^{103}Rh chemical shifts has been used to discriminate between two coordination modes of a hemilabile ligand [44].

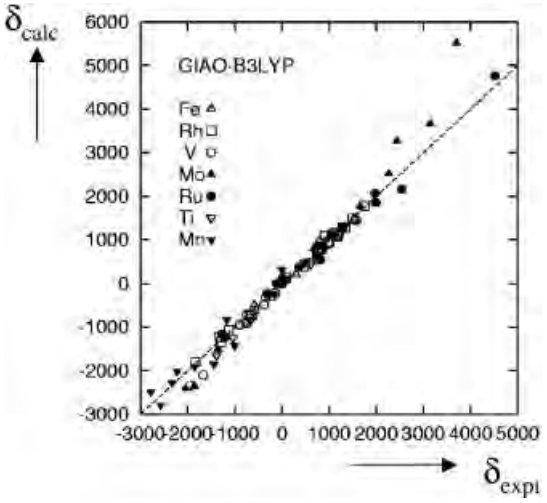

Figure 26.1 Plot of computed (B3LYP with gauge including atomic orbitals for GGA geometries) vs. experimental transition metal chemical shifts (data from Refs. [2, 35, 37–40]). The ideal line with slope 1 is shown (no fit); note that larger deviations occur only for ^{95}Mo [40].

Model calculations have shown that in Rh complexes with bidentate ligands, $\delta(^{103}\text{Rh})$ is governed by the Rh–ligand bond distance and not by the bite angle, as hitherto believed [45]. Plausible structures for vanadate–peptide complexes have been supported by reasonably good accord between computed and reported $\delta(^{51}\text{V})$ data [46]. DFT-derived ^{57}Fe chemical shifts have been used in the assessment of binding modes of CO, NO, and O_2 ligands in iron–porphyrin complexes, which serve as heme model compounds [47].

Following empirical precedence, theoretical metal shifts have been correlated with stabilities (i.e., computed reaction energies for ligand displacements) [48] or with reactivities (i.e., computed activation barriers for the key step in a catalytic cycle) [49–51]. Even though limited to specific families of compounds, such NMR/reactivity correlations could be useful in optimizing and designing new homogeneous catalytic systems.

More recently, a computational protocol based on molecular dynamics simulations has been applied to model thermal and solvent effects on transition metal chemical shifts (see Chapter 11 by Huber and Searles and Chapter 10 by Ruud). Variations of the order of a few dozen ppm, that is, small effects for a transition metal nucleus, have been noted for aqueous inorganic vanadate complexes [52] and for permanganate ion [53]. For $\delta(^{57}\text{Fe})$ of the highly charged $[\text{Fe}(\text{CN})_6]^{4-}$, however, much larger effects are found, exceeding 1000 ppm, due to the exceptional sensitivity of the iron shielding toward the metal–ligand bond distance, which is strongly affected by thermal averaging and by the interaction with the solvent, water [54]. The MD-derived, averaged shifts in water are in good agreement with experiment, suggesting that such simulations mimicking the actual conditions of the NMR experiment could be used to improve the accuracy of theoretical transition metal shifts in general.

26.3.2 Relativistic Computations

From the 5d series onwards, a proper treatment of relativistic effects (see Section 26.2.1) is also mandatory for the metal chemical shifts. When the leading terms, including spin–orbit coupling, are included, general trends in the δ values can be described at the Hartree–Fock level [55]. Relativistic DFT methods are promising for more quantitative agreement, and indeed, very good accord between experimental and DFT-ZORA chemical shifts has been obtained for ^{183}W [56, 57] and ^{195}Pt [58]. The latter nucleus is of particular importance due to its excellent experimental accessibility. For a set of Pt compounds covering a shift range of ca. 3500 ppm, the root mean square deviation between DFT and experimental δ values was found to be of the order of 300 ppm [58]. Remaining sources of error are probably shortcomings of the underlying density functional and the neglect of solvation effects (see spin–spin couplings below). Analysis of the theoretical results has afforded valuable insights into the mechanisms governing the trends in $\delta(^{195}\text{Pt})$: the latter emerges as a delicate balance between effects arising from spin–orbit contributions following Fermi contact mechanisms and the paramagnetic part of the magnetic shielding, which is

determined by the energetic separation and the degree of "orbital similarity" (i.e., overlap) of magnetically coupled pairs of occupied and virtual MOs [58].

The full ^{95}Mo shielding tensor of a piano stool complex, measured in the solid, has also been successfully reproduced at the DFT-ZORA level [25]. For the ^{235}U nucleus, where no experiments are available yet, a very large chemical shift range exceeding 20,000 ppm has been predicted computationally [15b]. For an analysis of the so-called normal vs. inverse halogen dependence of transition metal shifts, see Chapter 18 by Kaupp.

26.4 Spin–Spin Coupling Constants

Accurate nonempirical calculations of indirect spin–spin coupling constants, J (or, more specifically, of the reduced coupling constants, K), are still a challenge for theory, due to the high sensitivity of the results toward the approximations concerning the level of electron correlation and, for heavier nuclei, treatment of relativistic effects (see Chapters 14 and 15 by Autschbach and Ziegler, and by Malkina, respectively). That DFT-based methods can treat J values in transition metal complexes with about the same accuracy as those in main-group compounds, has been shown already in an early implementation [59]. Further validations involving a sizeable number of M–C, M–N, M–F, and M–P metal–ligand couplings have been given subsequently [60, 61]. The degree of accuracy that can be achieved with the DFT-ZORA method is illustrated in Fig. 26.2.

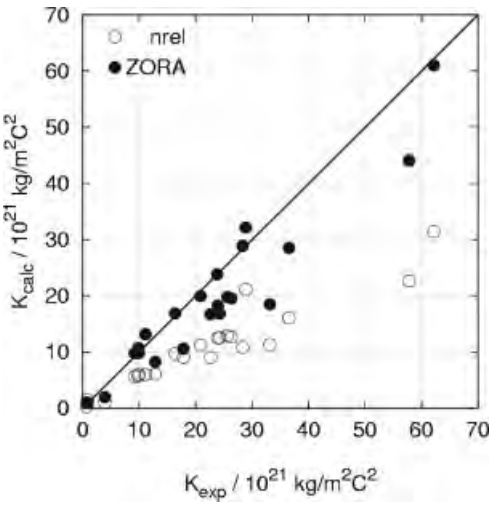

Figure 26.2 Plot of computed (ZORA = relativistic DFT-ZORA; nrel = non-relativistic) vs. experimental one-bond reduced spin–spin coupling constants ^1K involving W, Pt, and Hg (and Pb) nuclei (from Ref. [61]). The ideal line with slope 1 is shown (no fit). (Reprinted with permission from the American Institute of Physics).

For Hg and Pt complexes with, respectively, linear and planar coordination about the metal, agreement between theoretical and observed Hg–C and Pt–P couplings (including some of the outliers in Fig. 26.2) is improved when a limited number of solvent molecules ($CHCl_3$ or DMSO) are explicitly included in the computation [62]. The same has been found for ^1J(Pt,Tl) in $[(NC)_5Pt\text{-}Tl(CN)]^-$ (**3**) upon adding four water molecules to the coordinatively unsaturated Tl center [63], or for the very large ^1J(Hg,Hg) coupling in crown-ether complexes of Hg_2^{2+}, where the full coordination sphere (including one solvent molecule) has to be included [64].

The main applications of theoretical J (or K) values of transition metal complexes have, so far, concentrated on interpretations of observed magnitudes or trends by identifying and analyzing the molecular orbitals contributing to the coupling. Studies of this type comprise the connection between the *trans* influence and J values [60b] and an unusual spin–spin coupling pattern in **3** [63]. A qualitative pictorial rationalization has been given [65] of why the ^1J(Pt,Pt) values in related dinuclear complexes **4** and **5** differ by an order of magnitude (Chart 26.2): Contributions from Pt–Pt and axial Pt–ligand σ-bonds to ^1J(Pt,Pt) are both large, but have opposite signs; with the strongly interacting CO ligand both contributions are comparable in magnitude, thus resulting in the smaller net value for ^1J(Pt,Pt) in **4** [65].

DFT-ZORA ^1J(Ag,C) coupling constants have been used to assign ^{13}C NMR signals observed in solid silver cyanide to [···NC–Ag–CN···] and [···CN–Ag–CN···] sites in the polymeric chains [66].

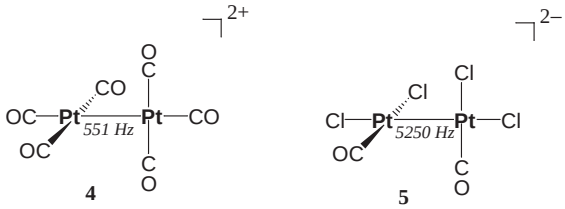

Chart 26.2.

26.5 Miscellaneous

A serious limitation in NMR spectroscopy of transition metal nuclei with spin $I > ½$ (i.e. the vast majority) is excessive line broadening due to quadrupolar relaxation. If that mechanism dominates relaxation, the NMR line width should be affected by the electric field gradient (EFG) at the metal. In keeping with this expectation, trends in ^{91}Zr [67], ^{99}Ru [37] and ^{59}Co line widths [68] have been rationalized in terms of variations in the computed EFGs. Quantitative prediction of line widths is difficult, however, because other factors are also crucial, such as reorientational mobility, and because accurate calculations of EFGs can be computationally quite demanding (see Chapter 17 by Schwerdtfeger et al. and Ref. [69] for recent applications to transition metal nuclei).

NMR chemical shift calculations as probes for aromaticity (see Chapter 24 by Chen et al.) have been applied to some transition metal complexes, namely Ni dithiolenes [70], Fe and Cr piano stool complexes [71], and tris(ethylene)nickel [72].

26.6 Conclusion and Outlook

The computation of NMR parameters has come of age, and applications to transition metal compounds with it. The palette of these applications ranges from guiding assignments and interpretations of experimental signals to furnishing quite detailed structural information. On the road to theoretical NMR spectra of transition metal complexes, DFT methods are currently without serious competition. Many computations of metal and ligand chemical shifts are now routinely possible and the treatment of relativistic effects and spin–spin coupling constants has blossomed recently. The growing body of experience with DFT-derived NMR parameters conveys the impression of very good overall performance and a certain reliability of these methods. Occasionally, however, larger errors can occur, and every new problem at hand usually entails the need for reassessment and validation of the methods. It can be envisaged that further theoretical developments, most notably in constructing and improving exchange-correlation functionals and, for heavier nuclei, refinement of relativistic approaches, will lead to increased accuracy of the calculated properties. The same is to be expected by mimicking the actual experimental conditions more realistically in the calculations, namely by taking thermal and solvent effects explicitly into account. With the concomitant, ever broader scope of possible applications in sight, the future of NMR calculations of transition metal compounds continues to be a promising one.

References

1 M. Kaupp, V. G. Malkin, O. L. Malkina, in *Encyclopedia of Computational Chemistry*, eds. P. v. R. Schleyer, N. L. Allinger, P. A. Kollman et al., Wiley, Chichester **1998**, Vol. 3, pp. 1857–1866.

2 G. Schreckenbach, T. Ziegler, *Theor. Chem. Acc.* **1998**, *99*, 71.

3 M. Bühl, M. Kaupp, V. G. Malkin, O. L. Malkina, *J. Comput. Chem.* **1999**, *20*, 91.

4 T. Helgaker, M. Jaszuński, K. Ruud, *Chem. Rev.* **1999**, *99*, *293*.

5 See also regular literature surveys, e.g.: C. J. Jameson, A. C. de Dios, in *NMR Spectroscopy, A Special Periodical Report, Vol. 31*, ed. G. A. Webb, The Royal Society of Chemistry, Cambridge **2002**, p. 48.

6 *Chem. Rev.* **2000**, *100*, 351–552.

7 W. Koch, M. C. Holthausen, *A Chemist's Guide to Density Functional Theory*, Wiley-VCH, Weinheim **2000**.

8 V. G. Malkin, O. L. Malkina, M. E. Casida et al., *J. Am. Chem. Soc.* **1994**, *116*, 5898.

9 a) M. Kaupp, V. G. Malkin, O. L. Malkina et al., *J. Am. Chem. Soc.* **1995**, *117*, 1851; b) M. Kaupp, V. G. Malkin, O. L. Malkina et al., *J. Am. Chem. Soc.* **1995**, *117*, 8492.

10 a) P. J. Wilson, R. D. Amos, N. C. Handy, *Chem. Phys. Lett.* **1999**, *312*, 475; b) P. J. Wilson, R. D. Amos, N. C. Handy, *Phys. Chem. Chem. Phys.* **2000**, *2*, 187.

11 a) S. Patchkovskii, J. Autschbach, T. Ziegler, *J. Chem. Phys.* **2001**, *115*, 26; b) S. Patchkovskii, T. Ziegler, *J. Phys. Chem. A* **2002**, *106*, 1088.

12 S. K. Wolff, T. Ziegler, E. van Lenthe et al., *J. Chem. Phys.* **1999**, *110*, 7689.
13 e.g. M. Kaupp, O. L. Malkina, P. Pyykkö, *Chem. Eur. J.* **1998**, *4*, 118.
14 J. Vaara, O. L. Malkina, H. Stoll et al., *J. Chem. Phys.* **2001**, *114*, 61.
15 a) G. Schreckenbach, S. K. Wolff, T. Ziegler, *J. Phys. Chem. A* **2000**, *104*, 8244; b) G. Schreckenbach, *Inorg. Chem.* **2002**, *41*, 6560.
16 J. A. Kintop, W. V. M. Machado, M. Franco et al., *Chem. Phys. Lett.* **1999**, *309*, 90.
17 E. Kolehmainen, K. Laihia, M. Nissinen et al., *J. Organomet. Chem.* **2000**, *613*, 7.
18 A. Knödler, W. Kaim, V. K. Jain et al., *J. Organomet. Chem.* **2002**, *655*, 218.
19 J. J. Carbó, P. Crochet, M. A. Esteruelas et al., *Organometallics* **2002**, *21*, 305.
20 R. M. Gomila, D. Quinonero, C. Garau et al., *Chem. Phys. Lett.* **2002**, *360*, 72.
21 A. D. de Dios, A. E. Abraham, *J. Mol. Struct.* **2002**, *602–603*, 209.
22 A. M. Orendt, J. C. Facelli, D. M. Grant, *Chem. Phys. Lett.* **1999**, *302*, 499.
23 a) R. Salzmann, M. T. McMahon, N. Godbout et al., *J. Am. Chem. Soc.* **1999**, *121*, 3818; b) N. Godbout, L. K. Sanders, R. Salzmann et al., *J. Am. Chem. Soc.* **1999**, *121*, 3829.
24 M. Kaupp, C. Rovira, M. Parrinello, *J. Phys. Chem.* B **2000**, *104*, 5200.
25 D. L. Bryce, R. E. Wasylishen, *Phys. Chem. Chem. Phys.* **2002**, *4*, 3591.
26 K. Eichele, R. E. Wasylishen, J. F. Corrigan et al., *J. Am. Chem. Soc.* **2002**, *124*, 1541.
27 G. M. Bernard, R. E. Wasylishen, A. D. Phillips, *J. Phys. Chem. A* **2000**, *104*, 8131.
28 M. Kaupp, V. G. Malkin, O. L. Malkina et al., *Chem. Eur. J.* **1996**, *2*, 24.
29 Y. Ruiz-Morales, T. Ziegler, *J. Phys. Chem. A* **1998**, *102*, 3970.
30 M. Bühl, in *Encyclopedia of Computational Chemistry*, eds. P. v. R. Schleyer, N. L. Allinger, P. A. Kollman et al., Wiley, Chichester **1998**, Vol. 3, pp. 1835–1845.
31 M. Bühl, J. Saßmannshausen, *J. Chem. Soc., Dalton Trans.* **2001**, 79.
32 J. P. Stambuli, M. Bühl, J. F. Hartwig, *J. Am. Chem. Soc.* **2002**, *124*, 9346.
33 M. Kaupp, T. Kopf, A. Murso et al., *Organometallics* **2002**, *21*, 5021.
34 E. Zurek, T. Ziegler, *Organometallics* **2002**, *21*, 83.
35 M. Bühl, *Chem. Phys. Lett.* **1997**, *267*, 251.
36 G. Schreckenbach, *J. Chem. Phys.* **1999**, *110*, 11936.
37 M. Bühl, S. Gaemers, C. J. Elsevier, *Chem. Eur. J.* **2000**, *6*, 3272.
38 M. Bühl, *Theor. Chem. Acc.* **2002**, *107*, 336.
39 F. T. Mauschick, Ph.D. Thesis, University of Wuppertal, **2003**.
40 M. Bühl, *Chem. Eur. J.* **1999**, *5*, 3515.
41 P. Zhou, S. C. F. Au-Yeung, X.-P. Xu, *J. Am. Chem. Soc.* **1999**, *121*, 1030.
42 X.-P. Xu, S. C. F. Au-Yeung, *J. Am. Chem. Soc.* **2000**, *122*, 6468.
43 a) A. Bagno, M. Bonchio, *Chem. Phys. Lett.* **2000**, *317*, 123; b) A. Bagno, M. Bonchio, *Eur. J. Inorg. Chem.* **2002**, 1475.
44 M. Bühl, W. Baumann, R. Kadyrov et al., *Helv. Chim. Acta* **1999**, *82*, 811.
45 a) W. Leitner, M. Bühl, R. Fornika et al., *Organometallics* **1999**, *18*, 1196; b) J. G. Donkervoort, M. Bühl, J. M. Ernsting et al., *Eur. J. Inorg. Chem.* **1999**, 27.
46 a) M. Bühl, *J. Comput. Chem.* **1999**, *20*, 1254; b) M. Bühl, *J. Inorg. Biochem.* **2000**, *80*, 137.
47 Review: L. K. Sanders, W. D. Arnold, E. Oldfield, *J. Porphyrins Phthalocyanines* **2001**, *5*, 323.
48 M. Bühl, M. Håkansson, A. H. Mahmoudkhani et al., *Organometallics* **2000**, *19*, 5589.
49 a) M. Bühl, *Angew. Chem. Int. Ed. Engl.* **1998**, *37*, 142; b) M. Bühl, *Organometallics* **1999**, *18*, 4894.
50 M. Bühl, F. T. Mauschick, *Organometallics* **2003**, *22*, 1422.
51 Overview: M. Bühl, in *Modeling NMR Chemical Shifts: Gaining Insights into Structure and Environment*, eds. J. C. Facelli. A. DeDios, ACS Symposium Series, Vol. 732, Washington DC **1999**, pp. 240–250.
52 M. Bühl, M. Parrinello, *Chem. Eur. J.* **2001**, *7*, 4487.
53 M. Bühl, *J. Phys. Chem. A.* **2002**, *106*, 10505.
54 a) M. Bühl, F. T. Mauschick, F. Terstegen et al., *Angew. Chem. Int. Ed. Engl.* **2002**, *41*, 2312; b) M. Bühl, F. T. Mauschick, *Phys. Chem. Chem. Phys.* **2002**, *4*, 5508.
55 a) J. Wan, R. Fukuda, M. Hada et al., *J. Phys. Chem. A* **2001**, *105*, 128; b) R. Fukuda, M. Hada, H. Nakatsuji, *J. Chem. Phys.* **2003**, *118*, 1027 and references cited therein.
56 A. Rodriguez-Fortea, P. Alemany, T. Ziegler, *J. Phys. Chem. A* **1999**, *103*, 8288.
57 R. Bouten, E. J. Baerends, E. van Lenthe et al., *J. Phys. Chem. A* **2000**, *104*, 5600.

58 T. M. Gilbert, T. Ziegler, *J. Phys. Chem. A* **1999**, *103*, 7535.

59 R. M. Dickson, T. Ziegler, *J. Phys. Chem.* **1996**, *100*, 5286.

60 a) J. Khandogin, T. Ziegler, *Spectrochim. Acta A* **1999**, *55*, 607; b) J. Khandogin, T. Ziegler, *J. Phys. Chem. A* **2000**, *104*, 113.

61 a) J. Autschbach, T. Ziegler, *J. Chem. Phys.* **2000**, *113*, 936; b) J. Autschbach, T. Ziegler, *J. Chem. Phys.* **2000**, *113*, 9410.

62 J. Autschbach, T. Ziegler, *J. Am. Chem. Soc.* **2001**, *123*, 3341.

63 J. Autschbach, T. Ziegler, *J. Am. Chem. Soc.* **2001**, *123*, 5320.

64 J. Autschbach, C. D. Igna, T. Ziegler, *J. Am. Chem. Soc.* **2003**, *125*, 4937.

65 J. Autschbach, C. D. Igna, T. Ziegler, *J. Am. Chem. Soc.* **2003**, *125*, 1028.

66 D. L. Bryce, R. E. Wasylishen, *Inorg. Chem.* **2002**, *41*, 4131.

67 M. Bühl, G. Hopp, W. v. Philipsborn et al., *Organometallics* **1996**, *15*, 778.

68 O. Q. Munro, S. C. Shabalala, N. C. Brown, *Inorg. Chem.* **2001**, *40*, 3303.

69 a) V. Kellö, A. J. Sadlej, P. Pyykkö, *Chem. Phys. Lett.* **2000**, *329*, 112; b) Y. Zhang, J. Mao, N. Godbout et al., *J. Am. Chem. Soc.* **2002**, *124*, 13921; c) R. Ida, G. Wu, *J. Phys. Chem. A* **2002**, *106*, 11234.

70 C. Lauterbach, J. Fabian, *Eur. J. Inorg. Chem.* **1999**, 1995.

71 a) P. v. R. Schleyer, B. Kiran, D. V. Simion et al., *J. Am. Chem. Soc.* **2000**, *122*, 510; b) C. Corminboeuf, T. Heine, J. Weber, *Phys. Chem. Chem. Phys.* **2003**, *5*, 246.

72 R. Herges, A. Papafilippopoulos, *Angew. Chem. Int. Ed. Engl.* **2001**, *40*, 4671.

27
Characterization of NMR Tensors via Experiment and Theory

Roderick E. Wasylishen

27.1
Introduction

Nuclear magnetic resonance (NMR) spectroscopy is arguably the most important general technique available for investigating molecular structure. What are the "observables" measured in an NMR experiment and how are these related to molecular structure? The purpose of this chapter is to briefly describe the most important parameters measured in an NMR experiment and to illustrate how modern computational chemistry is helping scientists to better understand the relationship between these parameters and molecular structure. Although most of the examples discussed here are from research carried out in my laboratory, I will also provide some key references to recent reviews of the experimental NMR literature.

Most NMR measurements are performed on samples that are either liquids or solutes dissolved in isotropic solvents [1–8]. In such media, molecules tumble rapidly and NMR experiments typically yield isotropic chemical shifts and so-called "scalar" spin–spin coupling constants. However, since the early 1950s, it has been recognized that second-rank tensors are required to fully characterize these NMR parameters [9–13]. In order to characterize parameters described by second-rank tensors experimentally, it is generally necessary to investigate the NMR spectra of molecules dissolved in partially ordered media (e.g., liquid-crystal solvents; see Ref. [14]) or in the solid state [15–18]. A general second-rank tensor is represented by a 3×3 matrix consisting of nine elements. Such a tensor may be written as a sum of a symmetric tensor with up to six unique elements and an antisymmetric tensor with up to three unique elements. To a very good approximation, NMR spectra are not influenced by that part of an interaction described by the first-rank antisymmetric tensor [15]. The frame of reference in which the symmetric part of the tensor is diagonal is known as the principal axis system (PAS). In the PAS, a second-rank tensor may be specified by its three principal components (the diagonal elements of the tensor) and three Euler angles describing the orientation of the PAS within an external frame. For an excellent general discussion of magnetic second-rank tensor quantities an early paper by Schneider is recommended [19]. Also, for an introduction to tensors, the text "Physical Properties of Crystals – Their Representation by Tensors and Matrices" by Nye is highly recommended [20].

Calculation of NMR and EPR Parameters. Theory and Applications.
Edited by Martin Kaupp, Michael Bühl, Vladimir G. Malkin
Copyright © 2004 WILEY-VCH Verlag GmbH & Co. KGaA, Weinheim
ISBN: 3-527-30779-6

This chapter is divided into three further sections. In the first, we describe how magnetic shielding tensors of a typical spin-1/2 nucleus, ^{31}P, are characterized in the solid state. The second deals with the measurement of spin–spin coupling tensors, specifically indirect spin–spin coupling tensors. The last section deals with NMR spectra of quadrupolar nuclei. The NMR spectra of these nuclei are generally dominated by the nuclear quadrupolar interaction which reflects the electric-field gradient (EFG) at the nucleus [21]. In each of the sections, an effort will be made to illustrate some of the important contributions of modern quantum chemistry computations. Although we emphasize the role that solid-state NMR is playing in characterizing shielding, spin–spin coupling and EFG tensors, it should be noted that other experimental techniques are also important. For example, NMR studies in liquid-crystal solvents [14], molecular beam and high-resolution microwave investigations (see Ref. [22] and references therein) and nuclear quadrupole resonance spectroscopy [21] are also used to characterize "NMR" tensors.

27.2 Magnetic Shielding and Chemical Shifts

27.2.1 Definitions and Conventions

In a typical NMR experiment involving solute molecules dissolved in an isotropic solvent one can, in principle, determine the isotropic chemical shift of each chemically distinct nucleus, *N*, in the sample. The chemical shift of nucleus *N* is defined by Eq. (27.1),

$$\delta_{iso}(N)_{sample} = \frac{\nu(N)_{sample} - \nu_{ref}}{\nu_{ref}} \tag{27.1}$$

where $\nu(N)_{sample}$ and ν_{ref} are the NMR resonance frequencies of the sample and a standard reference that contains the same isotope as the sample, respectively. In the case of ^{31}P NMR experiments, the accepted reference sample is 85% H_3PO_4 (aq) which is defined to have a chemical shift of 0.0 ppm. The isotropic chemical shift is related to a more fundamental parameter, the isotropic magnetic shielding constant, by Eq. (27.2),

$$\delta_{iso}(N)_{sample} = \frac{\sigma_{ref} - \sigma_{iso}(N)_{sample}}{1 - \sigma_{ref}} \tag{27.2}$$

In the case of phosphorus NMR, it has been established that the absolute shielding constant of 85% H_3PO_4 is 328.35 ppm [23]. That is, the ^{31}P nucleus of phosphoric acid is shielded by 328.35 ppm relative to a bare phosphorus nucleus. For isotopes of

the first- and second-row elements, σ_{ref} is typically much less than 10^{-3}; thus Eq. (27.2) reduces to

$$\delta_{iso}(N)_{sample} \cong \sigma_{ref} - \sigma_{iso}(N)_{sample} \tag{27.3}$$

Chemical shift reference samples for most NMR-active nuclei are compiled in a recent IUPAC document which has been published in numerous journals (for example see Ref. [24]). Absolute magnetic shielding constants are generally derived from accurate nuclear spin–rotation tensors measured using high-resolution microwave or molecular beam techniques (see Refs. [22, 25, 26]). In establishing an absolute shielding scale for phosphorus, the absolute magnetic shielding of ^{31}P in PH_3 was derived from the ^{31}P nuclear spin–rotation tensor in this same compound. The procedure for converting experimental spin–rotation tensors to magnetic shielding tensors involves careful consideration of rovibrational averaging effects as well as bulk magnetic susceptibility effects [27, 28]. Absolute magnetic shielding scales are available for numerous nuclei; however, it should be noted that in the case of heavier nuclei, where relativistic effects are important, the precise relationship between nuclear spin–rotation tensors and magnetic shielding tensors has not been established.

In the case of a solid sample where overall molecular tumbling does not occur, the magnetic shielding experienced by any nucleus, *N*, in the sample is generally dependent upon the orientation of the molecule in the applied magnetic field. For example, the phosphorus nuclei of solid tris(*p*-tolyl)phosphine reside on a crystallographic C_3-axis (space group *R*3; see Ref. [29]); hence the phosphorus magnetic shielding tensor must be axially symmetric. In such cases the orientation of the magnetic shielding tensor is completely specified. Experimentally, for a polycrystal-

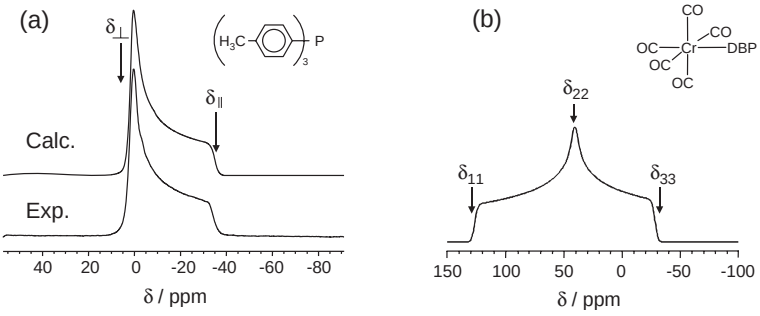

Figure 27.1 a) Example of an axially symmetric chemical shift tensor powder pattern. In this case the ^{31}P NMR spectrum of a stationary powder sample of tris(*p*-tolyl)phosphine.
b) Example of a non-axially symmetric chemical shift powder pattern. In this case the ^{31}P NMR spectrum of a stationary powder sample of (DBP)$Cr(CO)_5$. Adapted from Ref. [31].

line sample one observes a characteristic powder pattern with the unique component of the chemical shift tensor, $\delta_{||}$, corresponding to the unique symmetry axis of the molecule being parallel to the applied magnetic field (see Fig. 27.1a, also Ref. [30]). In the case of tris(*p*-tolyl)phosphine, $\delta_{||} = -35$ ppm and $\delta_{\perp} = 2.0$ ppm.

In the more general case where the nuclear site symmetry is insufficient to ensure an axially symmetric magnetic shielding tensor, one generally observes a non-axially symmetric powder pattern from which one can readily extract the three principal components of the chemical shift tensor. For example, consider the ^{31}P NMR spectrum of a polycrystalline sample of (phenyldibenzophosphole)chromium pentacarbonyl, (DBP)Cr(CO)$_5$, (see Fig. 27.1b, adapted from Ref. [31]). In this case, $\delta_{11} = 127$ ppm, $\delta_{22} = 41$ ppm and $\delta_{33} = -28$ ppm. The breadth of the powder pattern is often called the span, Ω, which is defined as $(\delta_{33} - \delta_{11})$, while the shape of the powder pattern is denoted by the skew, κ, which is $3(\delta_{22} - \delta_{iso})/\Omega$, where $\delta_{iso} = (\delta_{11} + \delta_{22} + \delta_{33})/3$. For the phosphorus chemical shift tensor of (DBP)Cr(CO)$_5$, $\delta_{iso} = 46.8$ ppm, $\Omega = 155$ ppm and $\kappa = -0.04$. In labelling the principal axes of the phosphorus chemical shift tensor we have adhered to the so-called Maryland convention, defining $\delta_{11} \geq \delta_{22} \geq \delta_{33}$ (see Ref. [32]). Another popular convention labels the axes such that: $|\delta_{33} - \delta_{iso}| \geq |\delta_{11} - \delta_{iso}| \geq |\delta_{22} - \delta_{iso}|$ and defines the shielding anisotropy, $\Delta = \delta_{33} - (\delta_{11} + \delta_{22})/2$, and the asymmetry, $\eta = (\delta_{22} - \delta_{11})/(\delta_{33} - \delta_{iso})$. Unfortunately, other definitions for anisotropy and asymmetry are also used, so when reading the literature it is essential to know what convention is being used. For an interesting debate concerning the conventions for tensor quantities used in NMR, see Harris [33] and Jameson [34].

Although one can obtain the three principal components of the CS tensor from NMR investigations of polycrystalline samples, information about the orientation of the CS tensor is not as readily available from such studies. If the nucleus of interest is spin–spin coupled via the dipolar interaction to a neighbouring nucleus, it is frequently possible to obtain some information about the orientation of the CS tensor [35]. However, if a "large" single crystal of the sample of interest can be grown, NMR investigations of the single crystal as a function of crystal orientation in the applied magnetic field will yield the most comprehensive characterization of magnetic shielding tensors [36, 37]. In cases where ambiguities arise, modern calculations can be of critical importance in helping experimentalists choose the correct orientation.

27.2.2
The Synergy of Theory and Experiment in Characterizing Chemical Shift Tensors: Two Examples

In the case of polycrystalline solids, NMR studies of isolated spin-pairs often provide information about the orientation of CS tensors. For example, the ^{31}P NMR spectrum of the ruthenium carbonyl phosphido cluster, $Ru_2(CO)_6(\mu_2\text{-}PPh_2)_2$, exhibits a powder pattern with some splittings that result from the ^{31}P,^{31}P dipolar interaction (see Fig. 3 of Ref. [38]). Qualitatively, the magnitude of these splittings allows one to obtain information about the orientation of the phosphorus CS-tensor with respect

to the ^{31}P–^{31}P "vector" [38]. Analysis of the powder spectrum leads to two possible orientations of δ_{11}, the least shielded component of the CS tensor (see Fig. 27.2). Calculations using both RHF and DFT methods with a variety of basis sets consistently support the assignment which indicates that δ_{11} is above the internuclear ^{31}P–^{31}P vector. Furthermore, the calculations allow one to systematically investigate how the phosphorus magnetic shielding tensor depends on subtle variations in molecular structure (for example, small systematic variations in the Ru–P–Ru bond angle).

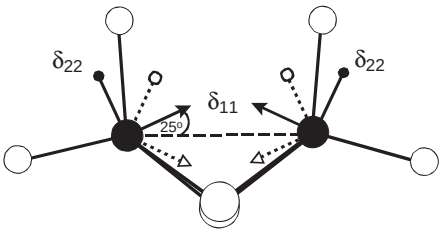

Figure 27.2 Analysis of the ^{31}P spectrum Ref. [38] results in two possible orientations of the phosphorus chemical shift tensor for $Ru_2(CO)_6(\mu_2\text{-}PPh_2)_2$. In both cases the component corresponding to greatest shielding, δ_{33}, is perpendicular to the plane of the page. The two assignments differ in that δ_{11} may either be 25° above or below the ^{31}P–^{31}P internuclear vector. Adapted from Ref. [38].

Several years ago, an experimental solid-state ^{31}P NMR study of analogous phosphido-bridging iron complexes led Carty and co-workers [39] to propose that the principal components of the phosphorus shielding tensor were exceedingly sensitive to the Fe–P–Fe bond angle. In particular, for compounds of the type $Fe_2(CO)_6(\mu_2\text{-}X)(\mu_2\text{-}PPh_2)$, δ_{11} was found to increase by more than 250 ppm as the Fe–P–Fe angle increases from 69° to 76°. Of course, in such an experimental study, isolating the effect of geometry variations from electronic effects due to changing the substituent X is impossible. Calculations for X = Cl support the trend observed but indicate that δ_{11} increases by approximately 100 ppm as the Fe–P–Fe angle increases from 69° to 76° [40]. Even for relatively large phosphido complexes it appears that present day computational methods are sufficiently reliable to make qualitative predictions on how magnetic shielding tensors depend on molecular geometry.

Isotropic ^{31}P NMR chemical shifts of the phosphinidene moiety, formally RP^{2-}, in transition metal complexes are often very large (i.e., the phosphorus nucleus is very deshielded). For example, the isotropic ^{31}P chemical shift of *nido*-$Ru_4(CO)_{13}(\mu_3\text{-}PPh)$ is 414 ppm [41]. Phosphorus-31 NMR spectra of a polycrystalline sample indicate that the principal components of the CS tensor are: $\delta_{11} = 890$ ppm, $\delta_{22} = 298$ ppm and $\delta_{33} = 53$ ppm [41]. What is the orientation of this highly anisotropic CS tensor? At the time we first asked this question (around 1990) we had little idea what to expect, so a single crystal was grown and examined by single-crystal NMR. The crystal belonged to the space group $P2_12_12_1$ and contained four molecules per unit cell.

After analysing the single-crystal NMR results, we were left with four possible ways to assign the chemical shift tensor to the four magnetically distinct sites. This is an inherent problem of single-crystal NMR investigations for systems containing more than one magnetically distinct site [41]. Fortunately, the orientation dependence of the $^{1}H,^{31}P$-dipolar interactions differed sufficiently for the four possible assignments and we were able to propose the assignment shown in Fig. 27.3 with a high-degree of confidence. Our proposed orientation was rationalized using extended Hückel molecular orbital calculations. More recent calculations [40, 42] confirm the orientation shown in Fig. 27.3. Kaupp discusses the interpretation of NMR chemical shifts in Chapter 18.

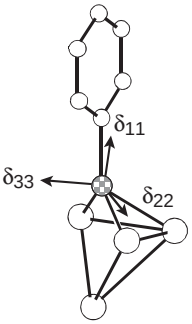

Figure 27.3 Orientation of the phosphorus chemical shift tensor for *nido*-$Ru_4(CO)_{13}(\mu_3\text{-PPh})$, as determined by single-crystal NMR. See Ref. [41] for details.

Although the two examples provided above have involved solid-state NMR measurements of phosphorus chemical shift tensors, considerable research has been carried out on other NMR-active nuclei. Duncan [43] has provided a useful compilation of experimental chemical shift tensor data prior to 1994. An annual survey of the literature prepared by Jameson and de Dios [44] is highly recommended. Several chapters in this text deal with the calculation of NMR chemical shifts (e.g., see Chapters 6, 8, 14, and 26).

As already mentioned, to a very good approximation NMR spectra are independent of antisymmetric tensor components. Recently Wi and Frydman [45] reported the first direct evidence that antisymmetric magnetic shielding tensor components influence NMR spectra. Their example involved ^{59}Co NMR spectra of solid cobalt (III)-tris(acetylacetonate).

Finally, it is important to mention that in comparing experimental magnetic shielding data with results from computational chemistry, one has always to be aware of intermolecular effects. Grant and co-workers [46, 47] have recently described an embedded ion method to account for intermolecular effects in "ionic" solids. Molecular dynamics simulations have been performed to deal with ions dissolved in aqueous solution (see Refs. [48] and [49] and references therein). In establishing the reliability of modern computational methods, there is an obvious need for accurate gas-phase NMR data (see e.g., Refs. [22, 26, 50, 51], also Chapter 8 by Gauss and Stanton).

27.3 Nuclear Spin–Spin Coupling

There are two fundamental mechanisms by which one nuclear spin interacts with another: the *direct* magnetic dipole–dipole interaction and the *indirect* spin–spin interaction. The direct dipolar interaction is a "through-space" interaction analogous to the classical dipolar coupling between two bar magnets. Hence, the magnitude of the direct dipolar coupling depends on the magnetic moments of the two nuclear spins and on the inverse cube of their separation. On the other hand, the indirect spin–spin coupling does not depend on internuclear separation in any simple way but may be thought of as a two-stage process whereby one nucleus perturbs "neighboring" electrons and these electrons in turn produce a small magnetic field at the other nucleus. Ramsey described three fundamental mechanisms by which the magnetic moment of the first nucleus, *N*, interacts with the electrons [11]. First, it may interact with the field produced by the orbital motion of the surrounding electrons; second, it may interact *via* the dipole–dipole interaction and finally *via* a contact coupling. Obtaining reliable first-principles calculations of indirect spin–spin coupling tensors (denoted **J**) in all but the simplest molecules has until recently been a challenge. It is also fair to add that the experimental characterization of **J**-tensors is difficult. In contrast, it is generally relatively straightforward to measure the magnitude of isotropic indirect spin–spin coupling constants, J_{iso} (i.e., one-third the trace of the **J** tensor).

Here, we will provide a brief discussion illustrating why it is difficult to characterize **J**-tensors experimentally. In spite of these difficulties, molecular beam, liquid-crystal and solid-state NMR techniques have yielded some reliable **J**-tensor data. We will also provide examples that illustrate how modern quantum chemical computations provide a better understanding of indirect spin–spin coupling tensors and how they act as a guide to the experimentalist. Introductory discussions of direct and indirect spin–spin coupling tensors may be found in the Encyclopedia of Nuclear Magnetic Resonance Spectroscopy [52, 53]. We have recently published a comprehensive review of indirect spin–spin coupling tensors, the interested reader should consult this resource for an overview and references to the original literature [54]. The calculation of indirect spin–spin coupling constants is discussed in several chapters of the present text (see e.g., Chapters 7, 15, and 19).

27.3.1 Inseparability of R_{DD} and ΔJ

The spin–spin coupling Hamiltonian describing an isolated pair of nuclear spins *N* and *M* may be represented by

$$\mathcal{H} = h\mathbf{I}_N \cdot (\mathbf{D} + \mathbf{J}) \cdot \mathbf{I}_M \tag{27.4}$$

where *h* is Planck's constant, $\mathbf{I}_N$ and $\mathbf{I}_M$ represent the nuclear spin angular momentum operators, **D** is the direct spin–spin coupling tensor and **J** is the indirect spin–

spin coupling tensor. While **D** is a traceless symmetric second-rank tensor, **J** is a general second-rank tensor with a non-zero trace. It is convenient to separate the isotropic portion of the indirect spin–spin coupling tensor from the traceless anisotropic portion, $\mathbf{J}_T$,

$$\mathcal{H} = hJ_{iso}\mathbf{I}_N \cdot \mathbf{I}_M + h\mathbf{I}_N \cdot (\mathbf{D} + \mathbf{J}_T) \cdot \mathbf{I}_M \tag{27.5}$$

Here, the antisymmetric portion of **J** is ignored. The isotropic nuclear spin–spin coupling constant is often called the scalar spin–spin coupling constant and may be either positive or negative. In the simplest case of a heteronuclear diatomic molecule, for example ^{127}I–^{19}F, where the PAS is defined by the C_∞ symmetry axis of the molecule, both the anisotropic **D** and $\mathbf{J}_T$ tensors take on a very simple form,

$$\mathbf{D} = R_{DD}\begin{bmatrix} 1 & 0 & 0 \\ 0 & 1 & 0 \\ 0 & 0 & -2 \end{bmatrix} \tag{27.6}$$

$$\mathbf{J}_T = -\frac{\Delta J}{3}\begin{bmatrix} 1 & 0 & 0 \\ 0 & 1 & 0 \\ 0 & 0 & -2 \end{bmatrix} \tag{27.7}$$

where the direct dipolar coupling constant, R_{DD}, defined by Eq. (27.8), depends on the inverse cube of the internuclear separation, r_{NM}:

$$R_{DD} = \frac{\mu_0}{4\pi}\frac{\hbar}{2\pi}\gamma_N\gamma_M\left\langle r_{NM}^{-3}\right\rangle \tag{27.8}$$

and, in the case of axial symmetry, the anisotropy in the indirect spin–spin coupling tensor, ΔJ, is $J_{||} - J_\perp$. Both R_{DD} and ΔJ are in frequency units, Hz, μ_0 is the permeability constant, $\hbar$ is Planck's constant divided by 2π, and γ_N and γ_M are the magnetogyric ratios of nuclei N and M, respectively. Equation (27.5) can be expressed as follows:

$$\mathcal{H}_{NM} = hJ_{iso}\mathbf{I}_N\mathbf{I}_M + hR_{eff}\mathbf{I}_N\begin{bmatrix} 1 & 0 & 0 \\ 0 & 1 & 0 \\ 0 & 0 & -2 \end{bmatrix}\mathbf{I}_M \tag{27.9}$$

where the effective dipolar coupling constant, R_{eff}, is $R_{DD} - \Delta J/3$. Equation (27.9) is general in that it demonstrates that one cannot measure R_{DD} and ΔJ separately. However, if one knows r_{NM} and can measure R_{eff}, then values of ΔJ can be obtained. In the following section, an example will be provided. Notice that in isotropic liquids where molecules rapidly tumble, the last term of Eq. (27.9) is zero (that is to say, the observed NMR spectrum to a first approximation will be independent of R_{eff}). Simi-

larly, for solids, it is easy to show that under conditions of rapid magic-angle spinning, the observed NMR spectrum will not be influenced directly by R_{eff}.

The inseparability of R_{DD} and ΔJ is often overlooked in the NMR literature. It is common practice in the literature to simply assume that the anisotropy in the indirect spin–spin coupling is negligible. While this may be a reasonable assumption for spin-pairs that only involve first-row nuclei, protons in particular, it is certainly not valid when heavier nuclei are involved (see e.g., Refs. [22, 54] and references therein). For example, in the case of the diatomic molecule, $^{127}I–^{19}F$, $J_{iso} = -5856$ Hz and $(\Delta J/R_{DD}) = -179\%$ [55].

27.3.2
Characterization of $\Delta J(^{77}Se, ^{31}P)$ for Trimethylphosphine Selenide

McFarlane and Rycroft [56, 57] used double resonance NMR experiments to determine the sign of $^1J(^{77}Se, ^{31}P)_{iso}$ for trimethylphosphine selenide. They concluded that the sign is negative and that the magnitude of this isotropic indirect spin–spin coupling constant is approximately 700 Hz. In 1980, Cogne et al. described the results of a ^{13}C and ^{31}P NMR study of $(^{13}CH_3)_3PSe$ dissolved in a nematic liquid crystal solvent [58]. When the data are analysed assuming the $\mathbf{J}(^{77}Se, ^{31}P)$ tensor is isotropic, an unrealistically long Se–P separation is obtained, $r_{Se,P} = 2.33 \pm 0.06$ Å. Using the experimental Se–P bond length from X-ray diffraction, 2.11 Å, allowed the authors to calculate the direct dipolar coupling constant and estimate the anisotropy in the indirect spin–spin coupling constant, $\Delta J = 680 \pm 180$ Hz [59]. In the original paper, ΔJ was reported as –680 Hz [58]; however, in a later review by two of the co-authors the sign was given as positive without comment (see Ref. [59]). For a detailed discussion of the procedure used to analyze the spectra, vibrational corrections, assumptions, etc., the reader should consult Ref. [58]. It is interesting to note that early relativistically parametrized extended Hückel calculations by Pyykkö and Wiesenfeld [60] predicted $\Delta J(^{77}Se, ^{31}P) = +265$ Hz.

More recently, Grossmann and co-workers [61] carried out both ^{31}P and ^{77}Se NMR studies on polycrystalline samples of trimethylphosphine selenide. They found $\Delta J(^{77}Se, ^{31}P)$ values of +640 ± 260 Hz and +550 ± 140 Hz from analyses of ^{31}P and ^{77}Se NMR spectra, respectively. The value of J_{iso} in the solid state was found to be –656 Hz. Using the X-ray structure, density functional calculations using the deMon-NMR code yielded $\Delta J(^{77}Se, ^{31}P)$ and $J(^{77}Se, ^{31}P)_{iso}$ values of +705 Hz and –820 Hz, respectively [61]. Similarly, using the ADF program and carrying out ZORA DFT calculations with the functionals described in Ref. [55], we obtain values of +610 Hz and –667 Hz, respectively, for these same parameters [62]. In summary, it appears that experiment and theory agree that the $\mathbf{J}(^{77}Se, ^{31}P)$ tensor for phosphine selenides exhibits significant anisotropy. While the example discussed here involves two spin–1/2 nuclei, it is important to recognize that in the solid state, quadrupolar nuclei have relatively long relaxation times so NMR techniques may be applied to spin-pairs consisting of one or two quadrupolar nuclei (see for example, Refs. [63–69]). In concluding this section on the measurement of anisotropies in indirect spin–spin coupling tensors, it is important to mention that librations of the

N–M vector in the solid state will lead to a reduced value of R_{eff} and that uncertainties in ($R_{eff} - R_{DD}$) are multiplied by a factor of 3 when one finally evaluates the uncertainty in ΔJ. Unfortunately there is no simple procedure for incorporating corrections due to motion in the solid state. In contrast, rovibrational corrections of high-resolution hyperfine parameters obtained from diatomic molecules in the gas phase are relatively straightforward [22, 26, 27, 28, 54, 70]. Of course one can also calculate rovibrationally averaged parameters using quantum chemistry computations [71]. See Chapter 10 by Ruden and Ruud for an excellent discussion of rovibrational corrections to NMR parameters.

27.3.3 Miscellaneous Applications of Computational Studies of J Tensors

In interpreting indirect spin–spin coupling data, researchers have commonly considered only the Fermi-contact mechanism. It appears that modern quantum chemistry computational techniques are sufficiently reliable to test this assumption. Furthermore, such calculations can provide convincing evidence about the absolute sign of indirect spin-spin coupling constants. For example, many years ago, an empirical correlation of $\delta_{iso}(^{19}F)$ versus $^{1}J_{iso}(^{129}Xe, ^{19}F)$ led Gillespie and Schrobilgen [72] to conclude that the sign of $^{1}J(^{129}Xe, F_{ax})$ for XeF_5^+ was opposite to that of most other $^{1}J(^{129}Xe, ^{19}F)$ values. From a recent review of the experimental NMR literature [73], it was concluded that most $^{1}J(^{129}Xe, ^{19}F)$ values are negative, with $^{1}J(^{129}Xe, ^{19}F_{ax})$ for XeF_5^+ being an exception. Recent relativistic density-functional calculations on XeF_5^+ confirm that indeed $^{1}J(^{129}Xe,^{19}F_{ax})$ is positive, +2190 Hz, and opposite to that of $^{1}J(^{129}Xe,^{19}F)$ in most other xenon fluorides [74]. In fact, the calculations indicate that $^{1}J(^{129}Xe, ^{19}F_{eq})$, for an isolated XeF_5^+ is negative, that is, –398 Hz. It is remarkable that in the sample molecule, two different one-bond $^{129}Xe, ^{19}F$ spin–spin coupling constants have opposite signs.

One of the most exciting observations involving indirect spin–spin coupling constants in the past decade was the report of significant $^{2h}J(^{15}N, ^{15}N)$ values (several Hz) across hydrogen bonds in biological macromolecules by Grzesiek and co-workers [75] (see Chapter 22 by DelBene). One of the advantages of computational chemistry is that one can construct models to investigate, for example, how such coupling constants depend on distance or a particular angle. In the case of the methyleneimine dimer, with angle N–H···N equal to 180°, we found $^{2h}J(^{15}N, ^{15}N)_{iso} = 9640 \exp(-2.73\, r_{NN})$, with r_{NN} in Å (see Ref. [76] for details).

Finally, while experiments to characterize the anti-symmetric components of the **J**-tensor have been proposed [54, 77], it appears that such experiments have been unsuccessful to date. Undoubtedly computational results may be useful in suggesting systems to investigate [78].

27.4
NMR Spectra of Quadrupolar Nuclei in Solids

More than 80% of the NMR accessible nuclei are quadrupolar nuclei (spin $I \geq 1$) and, with few exceptions, most of these have half-integer spin (that is, spin 3/2, 5/2, 7/2 or 9/2) [24]. For such nuclei, the +½ to –½ NMR transition is not perturbed by the first-order quadrupolar interaction [79]. This feature of non-integer quadrupolar nuclei makes it possible to study a wide range of quadrupolar nuclei in the solid state, particularly if the nuclear quadrupolar coupling constant, C_Q, is of the order of 10 MHz or less. With the availability of ultra-high magnetic fields [80, 81], NMR studies of these nuclei are being facilitated, in part, because the second-order quadrupolar broadening of the central transition depends on the inverse of the applied magnetic field strength. With the application of high applied fields, it is necessary for experimentalists to consider both the magnetic shielding tensor and the electric field gradient tensor at the nucleus being investigated (see e.g., Refs. [82, 83]).

The electric-field gradient tensor, **V**, is a traceless second-rank tensor [21, 79]. In its PAS, it is characterized by the largest component, V_{ZZ}, and asymmetry parameter, $\eta = (V_{XX} - V_{YY})/V_{ZZ}$, where $|V_{ZZ}| \geq |V_{YY}| \geq |V_{XX}|$. The nuclear quadrupolar coupling constant is defined by Eq. (27.10),

$$C_Q = eQV_{ZZ}/h = e^2 q_{ZZ} Q/h \tag{27.10}$$

where e is the charge of an electron, Q is the nuclear quadrupole moment, h is Planck's constant and $V_{ii} = eq_{ii}$. To fully characterize the nuclear EFG tensor, or the quadrupolar interaction tensor, one requires C_Q, η and the three Euler angles that define the orientation of the PAS of the EFG tensor with respect to the molecular frame.

Several excellent reviews concerning solid-state NMR studies of quadrupolar nuclei are available, (see for example, Refs. [84–87]); here we present an example from our laboratory that illustrates the strategy that may be used to investigate such nuclei. The study involved a ^{11}B NMR investigation of solid trimesitylborane and triphenyl borate [88]. Under conditions of rapid magic-angle spinning (MAS) the ^{11}B NMR spectra depend only on the values of C_Q, η and δ_{iso} (note that such spectra of effectively isolated spins do not depend on the sign of C_Q). Analysis of the MAS spectra indicated C_Q values of 4.75 MHz for the borane and 2.32 MHz for the borate. For both compounds, $\eta = 0.0$, indicating that the EFG tensor is axially symmetric, as expected from the local symmetry. The isotropic chemical shifts are significantly different, 77.4 ppm and 17.9 ppm, respectively, for the borane and borate. In the absence of MAS, the ^{11}B NMR spectra of the central transition depend on the boron chemical shift tensor, the EFG tensor at boron and the relative orientation of these two tensors. The ^{11}B NMR spectrum of trimesitylborane calculated at a field of 17.63 T assuming isotropic magnetic shielding is shown in Fig. 27.4.

In order to fit the experimental spectrum, a span of 121 ppm was required. Conversely, the span of the boron magnetic shielding tensor for the triphenyl borate was

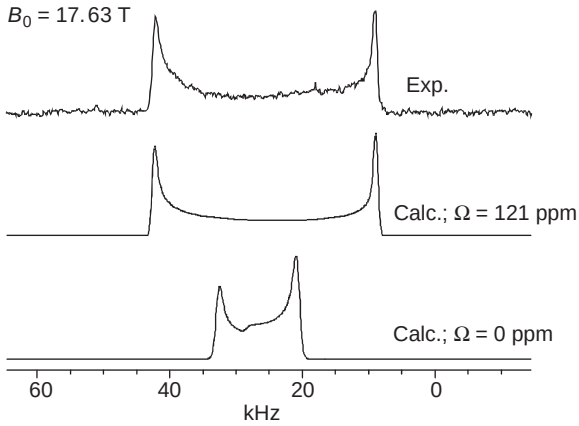

Figure 27.4 ^{11}B NMR spectrum of a stationary powder sample of trimesitylborane (top) along with the best-fit simulation (middle). The spectrum at the bottom is calculated assuming only the quadrupolar interaction (C_Q = 4.75 MHz and η = 0.0) contributes to the lineshape. In order to achieve agreement between the experimental and calculated spectra, it is necessary to include anisotropic magnetic shielding (i.e., a span of approximately 121 ppm is required). See Ref. [88] for details.

found to be less than 10 ppm. This study represents the first definitive experimental characterization of a boron shielding tensor [88]. Employing RHF and DFT calculations the different spans of the boron shielding tensors were rationalized. Furthermore, the calculations qualitatively reproduced the experimental EFG tensors. We have employed this same basic procedure to characterize some of the first measured magnetic shielding tensors for several other quadrupolar nuclei. In cases where the local symmetry does not fix the orientation of at least one of the principal components of the shielding and EFG tensors, variable-field measurements are essential and, in general, single-crystal NMR investigations are recommended.

In closing, it is important to note that even though the EFG is a first-order property, it is sometimes difficult to calculate reliable EFGs even for isolated molecules. For example, we have found that standard-reference *ab initio* calculations are unreliable for the nitrogen EFGs of nitrous oxide, N_2O. Similarly the calculation of an accurate EFG at the ^{27}Al nucleus of aluminum hydride appears challenging [89]. Finally, in the solid state one often has to consider lattice effects (that is, long-range effects) because the EFG does not readily converge. See Chapter 17 by Schwerdtfeger et al. for a discussion concerning the calculation of nuclear quadrupolar coupling constants.

27.5 Conclusions

I hope that this chapter has given the reader some sense of the tremendous advances in both experimental NMR and the computation of NMR parameters from

first principles. While most of the examples presented here are from our own research, I have attempted to refer to a number of recent reviews where the excellent work of many others is discussed. We have found "Nuclear Magnetic Resonance – a Specialist Periodic Report", published annually by the Royal Society of Chemistry, to be a valuable resource to the NMR literature. The contents of the present text provide a testimony to the success of modern computational methods in calculating NMR tensors.

Acknowledgements

Special thanks to Michelle A. M. Forgeron and Kirk Feindel who provided assistance in preparing this manuscipt. Most of the research described here would have been impossible without the efforts of a dedicated research group. I thank everyone in my group, past and present, for their contributions. Finally, our research would have been impossible without the financial assistance of the Natural Sciences and Engineering Research Council (NSERC) of Canada, the Province of Alberta, the Canada Research Chairs program and the University of Alberta.

References

1 *Multinuclear NMR*, ed. J. Mason, Plenum Press, New York **1987**.
2 S. Berger, H.-O. Kalinowski, S. Braun, *NMR Spectroscopy of the Non-Metallic Elements*, Wiley, New York **1986**.
3 H.-O. Kalinowski, S. Berger, S. Braun, *^{13}C-NMR Spectroscopy*, Wiley, New York **1988**.
4 *Phosphorus-31 NMR Spectroscopy in Stereochemical Analysis*, eds. J. G. Verkade, L. D. Quin, VCH, Deerfield Beach, FL **1987**.
5 *Transition Metal Nuclear Magnetic Resonance*, ed. P. S. Pregosin, Elsevier, Amsterdam **1991**.
6 J. W. Akitt, B. E. Mann, *NMR and Chemistry*, 4th edition, Stanley Thornes Ltd., Cheltenham, UK, **2002**.
7 K. Wüthrich, *NMR of Proteins and Nucleic Acids*, Wiley, New York **1986**.
8 J. H. Nelson, *Nuclear Magnetic Resonance Spectroscopy*, Prentice Hall, Upper Saddle River, NJ, **2003**.
9 N. F. Ramsey, *Phys. Rev.* **1950**, *78*, 699–703.
10 N. F. Ramsey, *Phys. Rev.* **1952**, *86*, 243–246.
11 N. F. Ramsey, *Phys. Rev.* **1953**, *91*, 303–307.
12 N. F. Ramsey, *Nuclear Moments*, Wiley, New York **1953**.
13 N. F. Ramsey, *Molecular Beams*, Oxford University Press, Oxford **1956**.
14 J. W. Emsley, J. C. Lindon, *NMR Spectroscopy Using Liquid Crystal Solvents*, Pergamon Press, Oxford **1975**.
15 U. Haeberlen, High Resolution NMR in Solids, in *Adv. Magn. Reson.*, Supplement 1, ed. J. S. Waugh, Academic Press, New York **1976**.
16 M. Mehring, *Principles of High Resolution NMR in Solids*, 2nd edition, Springer, Berlin 1983.
17 K. Schmidt-Rohr, H. W. Spiess, *Multidimensional Solid-State NMR and Polymers*, Academic Press, London **1994**.
18 *Solid-State NMR Spectroscopy*, ed. M. J. Duer, Blackwell Science, Oxford **2002**.
19 R. F. Schneider, *J. Chem. Phys.* **1968**, *48*, 4905–4909.
20 J. F. Nye, *Physical Properties of Crystals- Their Representation by Tensors and Matrices*, Oxford University Press, Oxford **1985**.
21 E. A. C. Lucken, *Nuclear Quadrupole Coupling Constants*, Academic Press, New York **1969**.
22 D. L. Bryce, R. E. Wasylishen, *Acc. Chem. Res.* **2003**, *36*, 327–334.
23 C. J. Jameson, A. de Dios, A. K. Jameson, *Chem. Phys. Lett.* **1990**, *167*, 575–582.
24 R. K. Harris, E. D. Becker, S. M. C. de Menezes et al., *Pure Appl. Chem.* **2001**, *73*, 1795–1818.

25 C. J. Jameson, in *Encyclopedia of NMR*, eds. D.M. Grant, R.K. Harris, Wiley, Chichester **1996**, pp. 1273–1281.
26 R. E. Wasylishen, D. L. Bryce, *J. Chem. Phys.* **2002**, *117*, 10061–10066.
27 D. K. Hindermann, C. D. Cornwell, *J. Chem. Phys.* **1968**, *48*, 4148–4154.
28 C. J. Jameson, A. K. Jameson, P. M. Burrell, *J. Chem. Phys.* **1980**, *73*, 6013–6020.
29 A. N. Sobolev, V. K. Bel'skii, I. P. Romm et al., *Zh. Strukt. Khim.* (*Russ. J. Struct. Chem.*) **1983**, *24*, 434–438.
30 G. H. Penner, R. E. Wasylishen, *Can. J. Chem.* **1989**, *67*, 1909–1913.
31 K. Eichele, R. E. Wasylishen, J. M. Kessler et al., *Inorg. Chem.* **1996**, *35*, 3904–3912.
32 J. Mason, *Solid State Nucl. Magn. Reson.* **1993**, *2*, 285–288.
33 R.K. Harris, *Solid State Nucl. Magn. Reson.* **1998**, *10*, 177–178.
34 C.J. Jameson, *Solid State Nucl. Magn. Reson.* **1998**, *11*, 265–268.
35 K. Eichele, R. E. Wasylishen, *J. Magn. Reson.* **1994**, *106A*, 46–56.
36 M. A. Kennedy, P. D. Ellis, *Concepts Magn. Reson.* **1989**, *1*, 35–47.
37 M. A. Kennedy, P. D. Ellis, *Concepts Magn. Reson.* **1989**, *1*, 109–129.
38 K. Eichele, R. E. Wasylishen, J. F. Corrigan et al., *J. Am. Chem. Soc.* **2002**, *124*, 1541–1552.
39 A. J. Carty, C. A. Fyfe, M. Lettinga et al., *Inorg. Chem.* **1989**, *28*, 4120–4124.
40 K.W. Feindel, R. E. Wasylishen, *Can. J. Chem.* **2004**, *82*, **27–44.**
41 K. Eichele, R. E. Wasylishen, J. F. Corrigan et al., *J. Am. Chem. Soc.* **1995**, *117*, 6961–6969.
42 M. Bühl, M. Kaupp, O. L. Malkina et al., *J. Comput. Chem.* **1999**, *20*, 91–105.
43 T. M. Duncan, *Principal Components of Chemical Shift Tensors: A Compilation*, 2nd edition, The Farragut Press, Chicago **1994**.
44 C. J. Jameson , A. C. de Dios, *Nuclear Magnetic Resonance – A Specialist Periodic Report*, ed. G. A. Webb, Royal Society of Chemistry, Cambridge **2003**, ch. 2.
45 S. Wi, L. Frydman, *J. Chem. Phys.* **2002**, *116*, 1551–1561.
46 D. Stueber, F. N. Guenneau, D. M. Grant, *J. Chem. Phys.* **2001**, *114*, 9236–9243.
47 D. Stueber, D. M. Grant, *Solid State Nucl. Magn. Reson.* **2002**, *22*, 439–457.
48 M. Gee, R. E. Wasylishen, A. Laaksonen, *J. Phys. Chem. A* **1999**, *103*, 10805–10812.
49 M. Bühl, *J. Phys. Chem. A* **2002**, *106*, 10505–10509.
50 A. A. Auer, J. Gauss, J. F. Stanton, *J. Chem. Phys.* **2003**, *118*, 10407–10417.
51 W. Makulski, K. Jackowski, *J. Mol. Struct.* **2003**, *651*, 265–269.
52 R. E. Wasylishen, in *Encyclopedia of Nuclear Magnetic Resonance Spectroscopy*, eds. D. M. Grant , R. K. Harris, Wiley, Chichester **1996**, Vol. 3, pp. 1685–1695.
53 R. E. Wasylishen, in *Encyclopedia of Nuclear Magnetic Resonance Spectroscopy*, eds. D. M. Grant, R. K. Harris, Wiley, Chichester **2002**, Supplement, Vol. 9, pp. 274–282.
54 J. Vaara, J. Jokisaari, R. E. Wasylishen et al., *Prog. Nucl. Magn. Reson. Spectrosc.* **2002**, *41*, 233–304.
55 D. L. Bryce, R. E. Wasylishen, J. Autschbach et al., *J. Am. Chem. Soc.* **2002**, *124*, 4894–4900.
56 W. McFarlane, D. S. Rycroft, *Chem. Commun.* **1972**, 902–903.
57 W. McFarlane, D. S. Rycroft, *J. Chem. Soc., Dalton Trans.* **1973**, 2162–2166.
58 A. Cogne, A. Grand, J. Laugier et al., *J. Am. Chem. Soc.* **1980**, *102*, 2238–2242.
59 J. B. Robert, L. Wiesenfeld, in *Phosphorus-31 NMR Spectroscopy in Stereochemical Analysis*, eds. J. G. Verkade, L. D. Quin, VCH, Deerfield Beach, FL **1987**, ch. 4.
60 P. Pyykkö, L. Wiesenfeld, *Mol. Phys.* **1981**, *43*, 557–580.
61 G. Grossmann, M. J. Potrzebowski, U. Fleischer et al., *Solid State Nucl. Magn. Reson.* **1998**, *13*, 71–85.
62 K. W. Feindel, R. E. Wasylishen, unpublished results.
63 R. E. Wasylishen, K. C. Wright, K. Eichele et al., *Inorg. Chem.* **1994**, *33*, 407–408.
64 S. Kroeker, J. V. Hanna, R. E. Wasylishen et al., *J. Magn. Reson.* **1998**, *135*, 208–215.
65 M. Tomaselli, D. deGraw, J. L. Yarger et al., *Phys. Rev. B* **1998**, *58*, 8627–8633.
66 G. Wu, K. Yamada, *Chem. Phys. Lett.* **1999**, *313*, 519–524.
67 S. Wi, V. Frydman, L. Frydman, *J. Chem. Phys.* **2001**, *114*, 8511–8519.
68 A. Jerschow, *Monatsh. Chem.* **2002**, *133*, 1481–1496.
69 G. Szalontai, *Monatsh. Chem.* **2002**, *133*, 1575–1586.
70 D. L. Bryce, R. E. Wasylishen, *J. Am. Chem. Soc.* **2000**, *122*, 3197–3205.

71 T. A. Ruden, O. Lutnæs, T. Helgaker et al., *J. Chem. Phys.* **2003**, *118*, 9572–9581.

72 R. J. Gillespie, G. J. Schrobilgen, *Inorg. Chem.* **1974**, *13*, 765–770.

73 M. Gerken, G. J. Schrobilgen, *Coord. Chem. Rev.* **2000**, *197*, 335–395.

74 D. L. Bryce, R. E. Wasylishen, *Inorg. Chem.* **2002**, *41*, 3091–3101.

75 A. J. Dingley, S. Grzesiek, *J. Am. Chem. Soc.* **1998**, *120*, 8293–8297.

76 D. L. Bryce, R. E. Wasylishen, *J. Biomol. NMR* **2001**, *19*, 371–375.

77 E. R. Andrew, *Prog. Nucl. Magn. Reson. Spectrosc.* **1972**, *8*, 1–39.

78 D. L. Bryce, R. E. Wasylishen, *J. Am. Chem. Soc.* **2000**, *122*, 11236–11237.

79 A. Abragam, *Principles of Nuclear Magnetism*, Oxford University Press, Oxford **1961**.

80 Z. Gan, P. Gor'kov, T. A. Cross et al., *J. Am. Chem. Soc.* **2002**, *124*, 5634–5635.

81 J. F. Stebbins, L-S. Du, S. Kroeker et al., *Solid State Nucl. Magn. Reson.* **2002**, *21*, 105–115.

82 R. W. Schurko, R. E. Wasylishen, A. D. Phillips, *J. Magn. Reson.* **1998**, *133*, 388–394.

83 A. S. Lipton, C. Bergquist, G. Parkin et al., *J. Am. Chem. Soc.* **2003**, *125*, 3768–3772.

84 A. P. M. Kentgens, *Geoderma* **1997**, *80*, 271–301.

85 M. E. Smith, E. R. H. van Eck, *Prog. Nucl. Magn. Reson. Spectrosc.* **1999**, *34*, 159–201.

86 L. Frydman, *Annu. Rev. Phys. Chem.* **2001**, *52*, 463–498.

87 M. J. Duer, I. Farnan, in *Solid-State NMR Spectroscopy*, ed. M. J. Duer, Blackwell Science, Oxford **2002**, ch. 4, pp. 179–215.

88 D. L. Bryce, R. E. Wasylishen, M. Gee, *J. Phys. Chem. A* **2001**, *105*, 3633–3640.

89 M. Gee, R. E. Wasylishen, *J. Mol. Spectrosc.* **2001**, *207*, 153–160.

28
Calculations of Nuclear Magnetic Resonance Parameters in Zeolites

Annick Goursot and Dorothée Berthomieu

28.1
Introduction

Zeolites are porous open-framework solids, built from corner-sharing SiO_4/AlO_4^- tetrahedra. These crystalline aluminosilicates contain regular arrangements of cages and mono-, bi- or tri-dimensional channels (Fig. 28.1). The empty volume (cages and channels) in these materials may reach 50% of the entire volume. This explains why, after dehydration, a large variety of gaseous organic or inorganic molecules may fill the intra-crystalline volume and adsorb on the large available internal surface (from 100 to $1000\,m^2\,g^{-1}$). Sorption in zeolites, also called molecular sieves because of this property, gives rise to commercial applications, such as drying of organics, separation of gas mixtures, removal of waste compounds from water, etc.

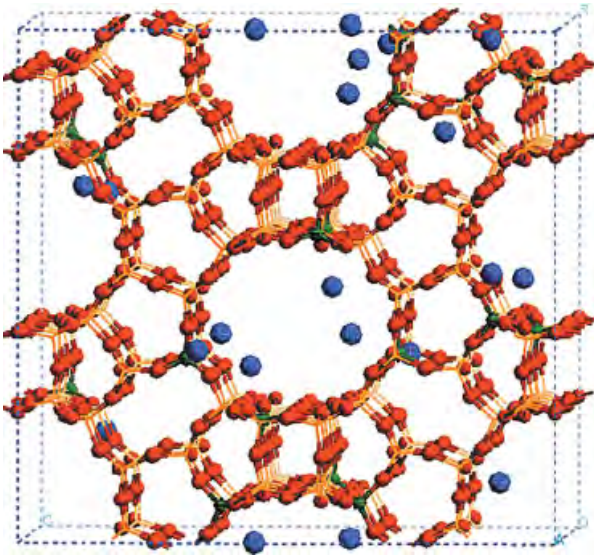

Figure 28.1 Zeolite β (4 unit cells) with Si/Al = 13; yellow sticks represent Si, green balls Al, red balls O, blue balls Na^+.

Calculation of NMR and EPR Parameters. Theory and Applications.
Edited by Martin Kaupp, Michael Bühl, Vladimir G. Malkin
Copyright © 2004 WILEY-VCH Verlag GmbH & Co. KGaA, Weinheim
ISBN: 3-527-30779-6

The zeolite framework bears a net negative charge equal to the number of Al atoms, which is balanced by the total positive charge of exchangeable cations M^{n+}, also called extra-framework cations. The global formula for a zeolite is $M_{x/n}$ $(AlO_2)_x$ $(SiO_2)_y \cdot mH_2O$, with $y \geq x$. According to the so-called Loewenstein rule [1], two Al tetrahedra cannot be next neighbours. Natural and synthetic zeolites, which represent more than 160 structures, display a wide range of possible Si/Al (y/x) ratios, with much larger values (more Si) for the synthetic ones. Moreover, other elements, such as Ga, Ge, B, Fe, P etc., can be substituted into the framework.

Despite the fact that the Si/Al ratio is controlled by synthesis, the distribution of Al in the framework is not known (except for Si/Al = 1). Indeed, the scattering factors of Si and Al are too similar in X-ray diffraction and only average coordination and geometries can be obtained from experimental techniques. In the same way, the distribution of the extra-framework cations is not known, except if their occupation in a specific site is 100%. Indeed, although the occupancies of the various cationic sites are obtained from X-ray or neutron diffractions, the actual positions of the cations, which are located at partially occupied sites, are not defined.

Apart from sorbing properties, and cation exchange, zeolites are well-known for their broad spectrum of catalytic properties. When the organic or alkali metal cations used in the synthesis are exchanged with protons by hydrothermal treatment, acid catalysts are obtained, which are used in numerous industrial applications, such as cracking, hydrocracking, isomerization of hydrocarbons, etc. When alkali metal cations are exchanged with transition metal ions, the zeolites act as oxido-reductive catalysts, mainly used in environmental chemistry.

The development of high resolution solid-state NMR techniques, such as magic angle spinning (MAS), has been of great importance in many domains of zeolite chemistry: (i) ^{29}Si, ^{27}Al, ^{23}Na MAS NMR for the characterization of solids (structure, Si/Al ordering, assignment of crystallographically non-equivalent sites, substitution by other elements); (ii) ^{1}H MAS NMR for the study of Brønsted sites (use of probe molecules); ^{1}H, ^{13}C, ^{15}N MAS NMR in situ spectra for insight into catalytic reactions [2–4].

^{29}Si, ^{27}Al, ^{23}Na, ^{17}O, ^{31}P elements of zeolitic frameworks have been studied by MAS NMR. ^{29}Si spectra have been particularly rich in information thanks to the wide range of ^{29}Si chemical shifts, which are very sensitive to the local geometry and electronic structure of the nearest neighbours [5–7]. ^{29}Si signals produced by crystallographically non-equivalent silicons can be obtained, as demonstrated in the pioneering work on a highly siliceous silicalite [8, 9] showing up to 20 well-resolved lines for the 24 sites. The study of ^{27}Al NMR spectra is less easy, due to its quadrupolar nucleus, leading to broadening and shifting of the signals. These effects, combined with the weaker sensitivity of ^{27}Al chemical shifts to the environment (compared with Si) have hindered quantitative structural studies of the Al sites. However, ^{27}Al NMR studies have been used to analyse dealumination and realumination processes [10], as well as Al coordination [11]. More recently, measurements of ^{27}Al quadrupole coupling constants [12–15], which are directly related to the electric field gradient at the Al nuclei, have provided information about the local structure around the Al tetrahedra, in particular in acidic zeolites (see Section 28.4). In spite of their

narrow range of variation, a very large amount of studies have been devoted to ^{1}H NMR shifts of the bridged (Si–OH–Al) acidic hydroxy groups (see Section 28.4).

Despite the remarkable sensitivity of NMR techniques to very small changes in atomic positions (changes in Al content, temperature effects, adsorption of molecules etc.), they have two main limitations in the study of structures and reactions: (i) the timescale of NMR prevents the characterization of transition states or short-lived intermediates; (ii) the difficulty in using chemical shifts to determine specific structures unequivocally.

Moreover, the structural information contained in the values of the shielding tensor components is missing for zeolite framework elements. The small size of the zeolite crystals is probably the reason why the principal components of ^{29}Si shielding tensors are not measured, as is done for solid silicates [16–18]. Actually, these components are obtained for ^{13}C or ^{15}N nuclei of guest molecules in strong interaction with the zeolite cavities, eventually protonated long-lived organic cations such as substituted acetonitrile [19], acetone [20, 21], arenes [22, 23], halopropanes [24, 25]. In these in situ experiments, the information about the shielding tensor anisotropy is extracted from the intensity of spinning sidebands of the isotropic signal [26].

Theoretical calculations in synergy with NMR experiments can help to overcome the methodological limits. Models of active sites are built and comparison of their magnetic properties with experiment leads to helpful information about the structures [23–26].

Quantum mechanical (QM) calculations of NMR parameters in zeolites have appeared in the last decade. Indeed, modelling NMR shifts of large systems (50–100 atoms) has become more and more feasible, due to the development of faster methods and computers. Success in simulating NMR properties of zeolites has interesting consequences: (i) the assignment of MAS NMR signals to crystallographically distinct Si or Al sites; (ii) the correlation between observed changes in the NMR spectra and structural modifications, including zeolite–adsorbent interactions; (iii) the easier prediction of in situ reaction mechanisms.

The remainder of this chapter is organized into four sections. First, a brief summary of QM methods used to calculate NMR properties will be reported in Section 28.2. Then, Section 28.3 will be devoted to calculations of NMR chemical shifts of framework elements, in relation with structure characterization. Section 28.4 will deal with the NMR studies of Brønsted sites and Section 28.5 reports NMR calculations of guest organic molecules.

28.2 Theoretical Methods

Ab initio calculations of NMR shielding constants are presently performed in the framework of two main theories: Hartree–Fock (HF), by far the earlier, and density functional theory (DFT), which was developed later.

The *ab initio* theoretical predictions of NMR properties started with the early work of Ditchfield [31], who proposed the GIAO method, later implemented in Hartree–Fock (CPHF) [32–34] and post-Hartree–Fock (MP2) calculations [35, 36]. Although this method has been applied to predict chemical shifts of organic compounds, its application to zeolites has begun only recently. CPHF-GIAO is presently the most commonly used method to calculate chemical shifts in zeolites. GIAO-MP2 is generally chosen for molecules in zeolites. The programs TURBOMOLE, TURBONMR [32, 34] and GAUSSIAN [37] propose adequate modules.

Studies performed with CPHF-GIAO have used double zeta plus polarization (DZP) bases for ^{29}Si and TZP for ^{1}H, ^{17}O and ^{27}Al, ^{13}C and ^{15}N [38].

The sum-over-states density functional perturbation theory (SOS-DFPT) approach has been proposed by Malkin et al. [39], associated with individual gauge for localized orbitals (IGLO) [40]. This method has proven its validity for a broad range of compounds, including organics, zeolites (vide infra), metal complexes, etc. deMon programs generate data for the associated magnetic properties program [41, 42].

Very recently, a new method based on DFT has been developed to calculate NMR shieldings within periodic boundary conditions and a pseudopotential approach [43, 44]. The gauge-including projector augmented wave (GIPAW) method, derived from the work of Blöchl [45], is used to reconstruct the all-electron induced current from the pseudo-wavefunctions [44]. This methodology is available in the PARATEC code [46].

The programs mentioned above can also evaluate electric field gradients at the nucleus, and thus quadrupolar coupling constants (C_q) for nuclei with spin values larger than ½, such as ^{17}O, ^{27}Al, ^{23}Na, etc.

From experimental and theoretical studies, it appears that NMR can be considered as a local property in zeolitic systems. Indeed, as reported in Section 28.3, the experimental ^{29}Si spectra of various zeolites have been reproduced using clusters including 2–3 shells of neighbours around the studied nucleus, oxygens being the first shell, silicons the second, etc. Moreover, experimentalists have evaluated, for a long time, the Al bulk composition of a zeolite using a formula which relates the NMR ^{29}Si peaks areas of the SiO_4(*n*Al) (n= 0 to 4) units to the global Si/Al ratio [47, 48]. This means that the composition in Si/Al of the second shell of neighbours determines the ^{29}Si MAS NMR chemical shifts (assuming that there are no Al–O–Al linkages, according to the Löwenstein rule). These results show that, in these solids, the response of the density to the external magnetic field remains centered around the nuclei.

Periodic plane-wave based codes are now starting to be used for the evaluation of chemical shifts of zeolites. This methodology will certainly be more extensively used in the near future. However, the large size of most unit-cells of aluminated zeolites, associated with the randomness of the Al distribution, will remain limitations for such calculations in zeolites with a substantial Al content.

28.3
NMR of Framework Elements: Structure Characterization

Following the development of MAS NMR, extensive studies of the composition and structure of zeolite frameworks have appeared. The assignment of ^{29}Si NMR spectra of zeolites was based essentially on empirical formulae derived from the relations between geometry and observed chemical shifts [48–52]. The analysis of the deshielding effects, due to the presence of Al neighbours, has led to linear relationships between ^{29}Si chemical shifts and the number of Al [53]. These empirical predictions have been very useful in determining the distribution of Al in the framework (number of Al neighbours per Si) in faujasites at different Si/Al ratios [48]. However, their use is more problematic when signals from non-equivalent Si atoms in Si(nAl) units overlap.

These empirical correlations can now be replaced by quantum mechanical calculations, with a similar or better precision, but with the advantage of a direct assignment of the spectra. Calculations of ^{29}Si, ^{27}Al and ^{17}O shielding constants of framework zeolite elements have been performed with the aim of assigning the different NMR signals to specific sites.

A good prediction of the NMR spectra of framework elements necessitates having a good framework structure and giving a precise evaluation of the NMR shifts of the nonequivalent sites. In fact, these studies demonstrate how NMR signals are strongly dependent on the local geometries, even on very small variations of bond lengths and angles.

Bussemer et al. [54] have reported the calculated ^{29}Si spectra (CPHF-GIAO method) of all-silica ZSM-5, ZSM-18, ZSM-12, theta-1 and faujasite, based on evaluations involving 29 clusters to represent all the crystallographic sites of these zeolites. They demonstrate that the size of the model clusters necessary to obtain converged NMR ^{29}Si chemical shifts is reached when three shells of neighbours surround the studied nucleus.

Moreover, they compare the chemical shifts calculated using the experimental geometries with those calculated using structures predicted from lattice energy minimization based on inter-atomic potential functions [55] and with chemical shifts established using empirical formulae [56]. Comparison between observed and predicted values shows that chemical shifts calculated with experimental geometries display a regular low-field shift of about 4 ppm with respect to experimental values, whereas those calculated with predicted geometries are shifted by about –0.5 ppm (2.78 ppm of average deviation). The difference of 4.5 ppm between both sets of predicted chemical shifts is comparable with the difference of ^{29}Si chemical shifts of α-quartz evaluated using clusters with three and with four shells of neighbours, or with four and five shells. This demonstrates that the precision of the structural parameters is critical for quantitative evaluation of the NMR shifts.

The locality of the ^{29}Si NMR shielding in zeolites could be the reason why the MAS NMR spectrum of zeolite-β can be deconvoluted into nine distinct signals, in spite of the stacking disorder of this solid. This spectrum has been calculated using the SOS-DFPT method and the signals assigned to the various crystallographic sites

[57]. In this work, as well as in the study of the zeolite mazzite [58], the calculated and experimental chemical shifts are shown to obey a linear relationship with respect to the average <Si–O–Si> bond angle at each site. A quantitative prediction of the ^{29}Si chemical shifts (1 ppm) is obtained using the average value calculated with four octamer models (2 Si sites per model).

Moreover, as shown in Fig. 28.2, different frameworks such as mazzite and zeolite-β follow the same linear relation between δ and the <Si–O–Si> bond angles. Figure 28.2 allows one also to compare SOS-DFPT (IGLO) and CPHF (GIAO) results obtained with the same clusters representing zeolite-β, namely one site- (1T) and two site- (2T) models [59]. Both methods reproduce the same trend for ^{29}Si δ versus the average <Si–O–Si> bond angles. The absolute values for 1T models obtained with the CPHF method display a slightly larger downfield shift than those obtained with SOS-DFPT. Moreover, the improvement provided by increasing the cluster size shown by SOS-DFPT for sites 1, 3 and 8 (including respectively 0, 1 and 2 four-membered rings) is not really reproduced with CPHF, showing that these two methods behave differently with the cluster size.

Substitution of Si by Al induces a substantial variation of the local geometry: Al–O bonds are about 0.1 Å larger than Si–O bonds whereas TOT bond angles decrease. This geometric effect, associated with electronic effects, strongly decreases the chemical shifts of the next Si neighbours. These variations have been quantitatively reproduced and analysed by theoretical calculations of the ^{29}Si and ^{27}Al spectra of zeolite-β and mazzite [57, 58].

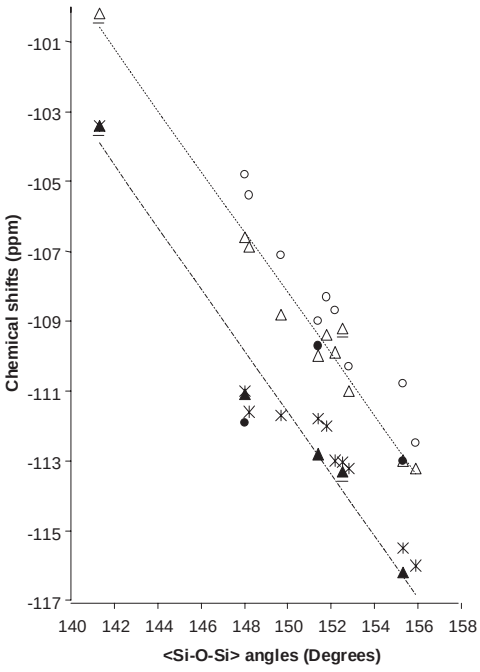

Figure 28.2 ^{29}Si chemical shifts in zeolite β (9 sites) and mazzite (2 sites) as a function of the average <SiOSi> angle: DFT results are indicated by white triangles (1T) and black triangles (2T) for zeolite β, the same symbols are underlined for mazzite; HF results are indicated by white circles (1T) and black circles (2T); experimental results are represented by stars.

In conjunction with molecular dynamics energy minimization, NMR calculations have also been used to propose positions for framework aluminum and Na^{+} cations in a Na-Y zeolite, with Si/Al ratio of 2.43 [60].

Replacement of Al by Ga gives only a small decrease in the average <TOT> angle of the next Si, correlated with a small downfield shift (1 ppm) of the ^{29}Si NMR signal, reproduced by calculation (CPHF) [61]. In contrast, substitution of Si by B (associated with Na^{+} counterions) does not produce a large change in the TOT angles around the next Si neighbours but a substantial decrease in the average B–Si distances [62]. In agreement with experimental results measured in various zeolites, the chemical shift calculated for a ^{29}Si next to B(Na^{+}) is intermediate between that of a non-substituted Si and that of a Si next to Al(Na^{+}). The replacement of Na^{+} by H^{+} induces B–O bond breaking and the formation of a silanol [62].

Recently, ^{17}O NMR chemical shifts and quadrupolar parameters have been investigated for the fully siliceous zeolites faujasite and ferrierite, with different methodologies, such as CPHF-GIAO using four shell clusters [63, 64] and the GIPAW method with periodic boundary conditions [65]. In the former studies, the faujasite structure was optimized and two experimental structures of ferrierite were compared, whereas in the latter study, the choice was the opposite, i.e. to optimize the ferrierite structure and use the experimental faujasite geometry. It appears that the quality of the NMR spectra and also of the quadrupole coupling constants is superior when calculated with the DFT-based GIPAW method which takes account of the full solid. However, it must be stressed that the ^{17}O NMR parameters are extremely sensitive to the geometry, more than the X-Ray diffraction patterns [65]. As suggested by Bull et al. [64], the vibrational amplitudes of the bridging oxygens are larger than those of the silicons and should be introduced in the evaluation of average oxygen properties. More work is certainly necessary to understand why the geometry of the full solid is much more important for a good description of the NMR properties of ^{17}O than for those of ^{29}Si.

28.4
^{1}H NMR: Acidity and Proton Transfer

Zeolites are inorganic solid acids where the framework aluminums are compensated by protons (Brønsted acid sites). The nature of their acid sites, their physicochemical properties and catalytic activity have been widely studied [29, 66].

Zeolites have been considered for a long time as superacids supposed to transfer their protons easily to reactants and generate high-energy cationic species. However, extensive experimental NMR studies brought evidence that the reaction intermediates were not unstable cations but rather species covalently bound to the zeolite framework, leading to rescaling the zeolite acid strength to much lower values [28, 66, 67]. Actually, the acid strength of the sites depends on the geometry, on their distribution and density. It is a specific property of the zeolite, which correlates with the presence of a base. NMR experiments and modeling have been used to study the

proton transfer from the Brønsted sites to the base. Both ^{1}H and ^{27}Al NMR spectra have been used for this purpose.

Attempts to correlate ^{1}H chemical shifts and deprotonation energies, i.e. the acid strength of the sites, have been made for faujasite clusters with one and two Al sites in a four-membered ring (protons at O_1 and O_3) and for different Al environments [68]. As expected, the two oxygen sites having different geometries, the related ^{1}H chemical shifts show a non-negligible difference for an all-silicon environment (their calculated and experimental difference are 0.5 and 0.7 ppm, respectively). The presence of other Al in the next shells also induces substantial variations of the ^{1}H chemical shifts. Interestingly, these models show that there is no relationship between ^{1}H chemical shifts and site acidity.

The interaction of the Brønsted protons with molecules, such as H_2O, NH_3, CH_3OH etc. leads to changes in the ^{1}H NMR spectrum, which can be used to evaluate the degree of proton transfer from the Brønsted site to the molecule [69–71]. Indeed, the two structures, i.e. the neutral complex formed by the hydrogen bonded molecule and the zeolite, or the ion pair formed by the zeolite anion and the protonated base, display different ^{1}H NMR signals. Comparison with experimental chemical shifts allows one thus to determine to what extent the acidic proton is transferred to the adsorbed molecule. There is no doubt that NH_4^+ is formed by interaction of one NH_3 molecule with the acidic site and the calculated ^{1}H chemical shift of the NH_4^+-zeolite ion pair agrees well with experiment in different zeolites (6.0–7.0 ppm) [69]. For H_2O and CH_3OH, theoretical calculations show that the results are dependent on the loading in molecules. For one molecule adsorbed per acidic site, the difference in chemical shift between the neutral complex and the ion pair is substantial (about 7 ppm) which rules out, by comparison with experiment, the existence of protonated forms [69, 70]. At larger loading (2 molecules per site), the ion pair becomes more stable than the hydrogen bonded system and the difference in the ^{1}H chemical shifts of both forms is reduced from about 7 ppm (low loading) to about 2–3 ppm, with an ion pair ^{1}H average signal at 9–10 ppm [71], which correlates with an experimental value of 9.1 ppm [72]. However, experimental results are not all concordant, and a clear conclusion cannot be drawn for high loadings.

Theoretical ^{27}Al chemical shifts and nuclear quadrupolar coupling constants (NQCC) have also been used recently to analyse the transfer of the zeolite proton to an adsorbed base [73, 74]. For nuclei with spin values larger than 1/2, the NQCC values reflect the importance of the electric field gradient generated at the nucleus by the surrounding electron distribution. Detailed information on NQCC calculations can be found in Chapter 17 by Schwerdtfeger, Pernpointner and Nazarewicz. Large electric field gradients are obtained for zeolite acid sites because of the large perturbation of the Al coordination due to the presence of the proton (weakening of the Al–OH bond, strengthening of the three other bonds). Actually, recent calculations have shown that a linear correlation exists between the calculated NQCC and Al–O bond orders [73]. Interaction of the zeolite proton with a molecule weakens the zeolite oxygen–proton bond order, decreasing the NQCC value, which can thus be used as a measure of the strength of the zeolite acid–base interaction [73]. As a consequence, ^{27}Al NMR signals are much broader (larger NQCC) for the acidic zeo-

lite alone, i.e. without any loading, in particular, for dehydrated zeolites. Upon adsorption of one methanol molecule per acid site a NQCC value of about 8 MHz is observed, i.e. half the value obtained without methanol. This decrease, which could be due to the protonation of methanol [73], has been attributed to dynamic effects, in order to keep consistency with the ^{1}H NMR results mentioned above [29].

Very recently, a combined theoretical and experimental study of ^{27}Al NMR shifts and line shapes has been performed for CH_3NO_2, CH_3COCH_3, pyridine and $P(CH_3)_3$ adsorbed in HZSM-5 [75]. These results have shown that the ^{27}Al chemical shift is not sensitive to the transfer of the proton to an adsorbed base. In contrast, the NQCC value is very sensitive, which demonstrates how the MAS NMR line width of the central $(1/2 \Leftrightarrow -1/2)$ transition is correlated to the occurrences of proton transfer.

28.5 NMR Studies of Guest Molecules in Zeolites: in situ NMR

Rare gas atoms inside zeolite cavities have been widely used as probes of the structures of zeolites. In particular, due to its high sensitivity to the environment, ^{129}Xe NMR spectroscopy has been applied to a large variety of investigations, including the estimate of the pore sizes and the cation distribution [76]. Theoretical investigations on model clusters with various numbers and positions of Al have shown that the rare gas chemical shift (^{39}Ar) is higher for a greater Al content [77].

In the last few years, theoretical calculations have been used in conjunction with in situ NMR to establish the structures of guest molecules or intermediate species in zeolites. The strategy employed was to propose possible models from the study of the experimental spectrum, optimize their structures and calculate their related NMR spectra. Comparison with experimental NMR values leads then to more ascertained assignments.

Using this methodology, the problem of the existence of carbenium ions in zeolite has been revisited [28, 66, 75], and the differences between zeolites and true solid superacids, such as $AlBr_3$, have been underlined. In situ ^{13}C MAS NMR spectra of propene-2 in HZSM-5 have been recorded at various temperatures, showing unambiguously that the isopropyl cation is not formed. Instead, two species are generated, i.e. a π complex with the acid site and a covalent bonded isopropoxy species, which is proposed as an intermediate in the ^{13}C $1 \Leftrightarrow 3$ scrambling observed for propene. The calculated ^{13}C chemical shifts of the π complex (119.5, 150.6 and 20.6 ppm) are in agreement with the experimental values (116, 146, 18 ppm) and, in the isopropoxy species, the ^{13}C chemical shifts of C_2 and C_3 are strongly decreased (the C_2 signal only, calculated at 94.2 ppm, can be compared with the experimental value of 88 ppm) [75].

The interaction of CH_3CN and HZSM-5 has also been studied, using ^{1}H and ^{13}C NMR [78] or ^{13}C NMR [79]. The most stable structure was found to be the acetonitrile–zeolite hydrogen bonded complex. Since the experimental results were suggesting a progressive proton transfer to acetonitrile with increasing temperatures, con-

straints were imposed to the models to reduce progressively the distance between CH_3CN and the zeolite, mimicking the effect of higher temperatures [78]. Only acetonitrile bent structures could account for the experimental ^{13}C NMR shifts (shifted about 10 ppm downfield with respect to isolated acetonitrile), whereas the ^{1}H NMR values for the acidic proton reproduce the experimental trend observed with increasing temperature [78]. The combination of theory and experiment has thus led to a different view of the acetonitrile protonation, better described as a concerted process, where the changes in the structure of the base drive proton transfer along the reaction coordinate.

Following the same spirit, Nicholas has used coupled theoretical and experimental approaches to demonstrate the coadsorption effect of nitromethane on the protonation of acetone [30]. The presence of nitromethane interacting with acetone generates a downfield shift of 1.2 ppm of the zeolite proton chemical shift, which is predicted to be 1.3 ppm by the calculations.

The behavior of the ^{13}C chemical shift of the carbonyl of acetone also reflects the cooperative effect of the nitromethane molecule.

Comparison of the reaction of benzene with excess methanol in HZSM-5 and zeolite-β showed that two different intermediate carbenium ions were formed in these zeolites: pentamethylbenzenium ion in the former and heptamethylbenzenium ion in the latter, these assignments being confirmed by in situ NMR associated with theoretical calculations of the ^{13}C NMR shifts [80, 81]. These examples demonstrate how different zeolite topologies can control the substitution pattern of persistent carbenium ions, which certainly play a role in the methanol to olefin conversion. Theoretical calculations of ^{13}C and ^{15}N NMR tensors, combined with in situ NMR with the pulse-quench reactor have also been devoted to the study of the reaction of acetonitrile with *tert*-butyl alcohol in HZSM-5, showing the formation of *N-tert*-butylacetonitrilium as the intermediate species [19]. The presence of this intermediate cation is ascertained by the good correlation between the theoretical and experimental values of the principal components of the ^{13}C and ^{15}N shielding tensors. The GIAO-MP2 method [35] used in this study seems to be more adequate for the treatment of ^{13}C NMR shifts than for those of ^{15}N. The authors suggest that better values of the ^{15}N chemical shifts could be obtained using extensions of the GIAO method to MP4 [82] and coupled cluster treatments [83], necessary for a better account of electron correlation.

The diffusion and adsorption of ethane, propane and isobutane in HZSM-5 and silicalite have been investigated by classical methods, Monte Carlo and molecular dynamics, on large clusters containing four unit cells [84]. The interaction of these molecules with HZSM-5 and their paths to dehydrogenation were then studied on cluster models cut in the structures using a DFT-based methodology. Alkoxide products were proposed for ethane and propane but not for isobutane which would better convert to isobutene. This conclusion is supported by the calculated ^{13}C NMR shifts of the corresponding alkoxides, which fall in the range 80–100 ppm, as observed for the primary alkanes.

28.6 Conclusions

In the last decade, NMR predictions in zeolites have started to become a new powerful tool, which, in conjunction with experimental MAS NMR techniques, contributes to the characterization of these solids and to the understanding of their behavior with respect to incoming reactants. Obviously, the next necessary step in the theoretical contributions will be to take into account the dynamics of the interaction between the zeolite and the guest molecule or the solvent. Indeed, recent works on water [85–87] or molecules in water [88] have demonstrated the effect of the solvent on NMR shielding values. Moreover, ab initio MD studies can provide, in addition, a correlation between the shielding values and the structures (see also Chapter 11 by Searles and Huber). In fact, the dynamical aspect of the zeolite–molecule hydrogen bonding is certainly an important factor in order to get a realistic description of the structure, reactivity and magnetic properties of these complex systems.

References

1 W. Loewenstein, *Am. Mineral.* **1954**, *39*, 92.
2 J. Klinowski, *Chem. Rev.* **1991**, *91*, 1459.
3 G. Engelhardt, D. Michel, *High-Resolution Solid-State NMR of Silicates and Zeolites*, Wiley, Chichester **1987**.
4 A. V. Mc Cormick, A.T. Bell, *Catal. Rev. Sci. Eng.* **1989**, *31*, 97.
5 D. G. Hay, H. Jaeger, G. W. West, *J. Phys. Chem.* **1985**, *89*, 107.
6 J. Klinowski, T. A. Carpenter, T. A. Gladden, *Zeolites* **1987**, *7*, 73.
7 H. Strobl, C. A. Fyfe, G. T. Kokotailo et al., *J. Am. Chem. Soc.* **1987**, *109*, 4733.
8 C. A. Fyfe, G. C. Gobbi, J. Klinowski et al., *Nature* **1982**, *296*, 530.
9 C. A. Fyfe, J. H. O'Brien, H. Strobl, *Nature* **1987**, *326*, 281.
10 J. Perez-Pariente, J. Sanz, V. Fornes et al., *J. Catal.* **1990**, *124*, 217.
11 E. Bourgeat-Lami, P. Massiani, F. Di Renzo et al., *Appl. Catal.* **1991**, *72*, 139.
12 V. Bosacek, D. Freude, T. Fröhlich et al., *J. Colloid. Interface Sci.* **1982**, *85*, 502.
13 D. Freude, T. Fröhlich, H. Pfeifer et al., *Zeolites* **1983**, *3*, 171.
14 H. Ernst, D. Freude, I. Wolf, *Chem. Phys. Lett.* **1993**, *212*, 588.
15 A. Medek, J. S. Harwood, L. Frydman, *J. Am. Chem. Soc.* **1995**, *117*, 12779.
16 R. Radeglia, A. R. Grimmer, *Z. Phys. Chem. Leipzig* **1981**, *262*, 718.
17 A. R. Grimmer, *Chem. Phys. Lett.* **1985**, *119*, 416.
18 M. Backer, A. R. Grimmer, N. Auner et al., *Solid State Nucl. Magn. Res.* **1997**, *9*, 241.
19 D. H. Barich, T. Xu, W. Song et al., *J. Phys. Chem.* **1998**, *102*, 7163.
20 J. Sepa, C. Lee, R. J. Gorte et al., *J. Phys. Chem.* **1996**, *100*, 18515.
21 D. H. Barich, J. B. Nicholas, T. Xu et al., *J. Am. Chem. Soc.* **1998**, *120*, 12342.
22 T. Xu, J. F. Haw, *J. Am. Chem. Soc.* **1994**, *116*, 10188.
23 T. Xu, D. H. Barich, P. D. Torres et al., *J. Am. Chem. Soc.* **1997**, *119*, 406.
24 J. B. Nicholas, T. Xu, D. H. Barich et al., *J. Am. Chem. Soc.* **1996**, *118*, 4202.
25 T. Xu, D. H. Barich, P. D. Torres et al., *J. Am. Chem. Soc.* **1997**, *119*, 396.
26 J. Herzfeld, A. E. Berger, *J. Chem. Phys.* **1980**, *73*, 6021.
27 J. F. Haw, M. B. Hall, A. E. Alvarado-Swaisgood et al., *J. Am. Chem. Soc.* **1994**, *116*, 7308.
28 J. F. Haw, J. B. Nicholas, T. Xu et al., *Acc. Chem. Res.* **1996**, *29*, 259.
29 H. Koller, G. Engelhardt, R. A. van Santen, *Top. Catal.* **1999**, *9*, 163.
30 J. B. Nicholas, *Top. Catal.* **1999**, *9*, 181.
31 R. Ditchfield, *Mol. Phys.* **1974**, *27*, 789.
32 R. Ahlrichs, M. Bär, M. Häser et al., *Chem. Phys. Lett.* **1989**, *154*, 165.
33 K. Wolinski, J. F. Hinton, P. Pulay, *J. Am. Chem. Soc.* **1990**, *112*, 8251.
34 M. Häser, R. Ahlrichs, H. P. Baron et al., *Theor. Chim. Acta* **1992**, *83*, 455.

35 J. Gauss, *Chem. Phys. Lett.* **1992**, *191*, 614.
36 J. Gauss, *J. Chem. Phys.* **1993**, *99*, 3629.
37 M. J. Frisch, G. W. Trucks, H. B. Schlegel et al., *Gaussian98, Revision A.9*, Gaussian Inc., Pittsburgh PA **1998**.
38 A. Schäfer, H. Horn, R. Ahlrichs, *J. Phys. Chem.* **1992**, *97*, 2571.
39 V. G. Malkin, O. L. Malkina, M. E. Casida et al., *J. Am. Chem. Soc.* **1994**, *116*, 5898.
40 W. Kutzelnigg, U. Fleischer, M. Schindler, *NMR-Basic Principles and Progress*, Springer-Verlag, Heidelberg **1990**, Vol. 23, p. 165.
41 A. St-Amant, D. R. Salahub, *Chem. Phys. Lett.* **1990**, *169*, 387.
42 M. E. Casida, C. D. Daul, A. Goursot et al., *deMon Software–deMonKS3 Module*, Université de Montréal, **1996**.
43 F. Mauri, B. G. Pfrommer, S. G. Louie, *Phys. Rev. Lett.* **1996**, *77*, 5300.
44 C. J. Pickard, F. Mauri, *Phys. Rev. B* **2001**, *63*, 245101.
45 P. E. Blöchl, *Phys. Rev. B* **1994**, *50*, 17953.
46 B. Pfrommer, D. Raczkowski, A. Canning et al., *PARATEC* (*PARAllel Total Energy Code*); Lawrence Berkeley National Laboratory, (with contributions from F. Mauri, M. Cote, Y. Yoon et al.).
47 G. Engelhardt, U. Lohse, E. Lippmaa et al., *Z. Anorg. Allg. Chem.* **1981**, *482*, 49.
48 J. M. Thomas, C. A. Fyfe, S. Ramdas et al., *J. Phys. Chem.* **1982**, *86*, 3061.
49 J.V. Smith, C. S. Blackwell, *Nature* **1982**, *302*, 223.
50 R. Radeglia, G. Engelhardt, *Chem. Phys. Lett.* **1985**, *114*, 28.
51 J. M. Newsam, *J. Phys. Chem.* **1987**, *91*, 1259.
52 C. A. Fyfe, H. Grondey, Y. Feng et al., *J. Am. Chem. Soc.* **1990**, *112*, 8812.
53 J. M. Newsam, *J. Phys. Chem.* **1985**, *89*, 2002.
54 B. Bussemer, K. P. Schröder, J. Sauer, *Solid State Nucl. Magn. Reson.* **1997**, *9*, 155.
55 K. P. Schröder, J. Sauer, *J. Phys. Chem.* **1996**, *100*, 11053.
56 G. Engelhardt, R. Radeglia, *Chem. Phys. Lett.* **1984**, *271*, 108.
57 G. Valerio, A. Goursot, R. Vetrivel et al., *J. Am. Chem. Soc.* **1998**, *120*, 11426.
58 G. Valerio, A. Goursot, *J. Phys. Chem.* **1999**, *103*, 51.
59 P. Pullumbi, A. Goursot, unpublished results.
60 H. Himei, M. Yamadaya, Y. Oumi et al., *Microporous Mater.* **1996**, 235.
61 K. J. Chao, S. P. Sheu, L. H. Lin et al., *Zeolites* **1997**, *18*, 18.
62 G. Valerio, J. Plévert, F. Di Renzo et al., *Phys. Chem. Chem. Phys.* **2000**, *2*, 1091.
63 L. M. Bull, A. K. Cheetham, T. Anupold et al., *J. Am. Chem. Soc.* **1998**, *120*, 3510.
64 L. M. Bull, B. Bussemer, T. Anupold et al., *J. Am. Chem. Soc.* **2000**, *122*, 4948.
65 M. Profeta, F. Mauri, C. J. Pickard, *J. Am. Chem. Soc.* **2002**, *125*, 541.
66 A. Corma, *Chem. Rev.* **1995**, *95*, 559.
67 J. F. Haw, *Phys. Chem. Chem. Phys.* **2002**, *4*, 5431.
68 M. Sierka, U. Eichler, J. Datka et al., *J. Phys. Chem. B* **1998**, *102*, 6387.
69 F. Haase, J. Sauer, *J. Phys. Chem.* **1994**, *98*, 3083.
70 F. Haase, J. Sauer, *J. Am. Chem. Soc.* **1995**, *117*, 3780.
71 M. Krossner, J. Sauer, *J. Phys. Chem.* **1996**, *100*, 6199.
72 Z. Luz, A. J. Vega, *J. Phys. Chem.* **1987**, *91*, 374.
73 H. Koller, E. L. Meijer, R.A. van Santen, *Solid State NMR* **1997**, *9*, 167.
74 J. O. Ehresmann, W. Wang, B. Herreros et al., *J. Am. Chem. Soc.* **2002**, *124*, 10868.
75 J. B. Nicholas, T. Xu, J. F. Haw, *Top. Catal.* **1998**, *6*, 141.
76 M. Stöcker, *Stud. Surf. Sci. Catal.* **1994**, *85*, 429.
77 C. J. Jameson, H. M. Lim, *J. Chem. Phys.* **1995**, *103*, 3885.
78 J. F. Haw , M. B. Hall, A. E. Alvarado-Swaisgood et al., *J. Am. Chem. Soc.* **1994**, *116*, 7308.
79 J. Sepa, R. J. Gorte, D. White et al., *Chem. Phys. Lett.* **1996**, *262*, 321.
80 T. Xu, D. H. Barich, P. W. Goguen et al., *J. Am. Chem. Soc.* **1998**, *120*, 4025.
81 W. Song, J. B. Nicholas, A. Sassi et al., *Catal. Lett.* **2002**, *81*, 49.
82 J. Gauss, *Chem. Phys. Lett.* **1994**, *229*, 198.
83 J. Gauss, J. F. Stanton, *J. Chem. Phys.* **1995**, *103*, 3561.
84 E. A. Furtado, I. Milas, J. O. Milam de Albuquerque Lins et al., *Phys. Status Solidi* **2001**, *187*, 275.
85 V. G. Malkin, O. L. Malkina, G. Steinebrunner et al., *Chem. Eur. J.* **1996**, *2*, 452.
86 B. G. Pfrommer, F. Mauri, S. G. Louie, *J. Am. Chem. Soc.* **2000**, *122*, 123.
87 D. Sebastiani, M. Parrinello, *Chem. Phys. Chem.* **2002**, *3*, 675.
88 S. Krishnamurty, T. Heine, A. Goursot, *J. Phys. Chem. B* **2003**, *107*, 5728–5732.

Part D
EPR Parameters, Methodological Aspects

Calculation of NMR and EPR Parameters. Theory and Applications.
Edited by Martin Kaupp, Michael Bühl, Vladimir G. Malkin
Copyright © 2004 WILEY-VCH Verlag GmbH & Co. KGaA, Weinheim
ISBN: 3-527-30779-6

29
DFT Calculations of EPR Hyperfine Coupling Tensors

Markéta L. Munzarová

29.1
Introduction

The history of *ab initio* quantum chemical studies of hyperfine coupling constants (HFCCs) goes back to the pioneering work of Meyer in the late 1960s [1]. The significant deviations of the early Hartree–Fock results from experiment (see Chapter 3 by Neese and Munzarová) indicated that an account of electron correlation is mandatory for quantitative HFCC calculations. Theoretical predictions of high accuracy became possible with the development of MCSCF, MRCI and CC methods; compare Chapter 30 by Engels. However, applications of these post-Hartree–Fock approaches concentrated mainly on small organic radicals or on other light main group systems. Larger radicals or transition metal complexes, which have been and still are of significant experimental interest, remain computationally too demanding to be treated at highly correlated *ab initio* levels of theory.

An alternative has been provided by recent advances in density functional theory (DFT). DFT includes electron correlation approximately, at moderate computational cost. Preceded by a number of X_α-computations of HFCCs [2], the development of gradient-corrected and hybrid DFT schemes in the late 1980s and early 1990s gave rise to numerous validation and application studies, examined in several excellent reviews. Malkin and coworkers [3] discussed the use of DFT for parameters of EPR and NMR spectroscopy, while the review of Barone [4] concentrates on the performance of DFT for structure, magnetic properties and reactivities of open-shell systems. Engels et al. [5] reviewed radical HFCC calculations from the DFT and configuration interaction perspectives. A very brief account of hyperfine coupling is provided also in the DFT monograph of Koch and Holthausen [6], including some results of an extended, critical validation of DFT and CC approaches for HFCCs of transition metal complexes [7].

On purely theoretical grounds, it is not obvious which of the gradient corrections should be the most appropriate to use in HFCC calculations. Thus the choice of a functional along with a basis set has to be based on its behavior for the given class of systems. The aim of this chapter is to provide the reader with a feeling for the performance of representative state-of-the-art density functionals, based on the comparison of DFT results with reliable experimental and high-level *ab initio* data. The

Calculation of NMR and EPR Parameters. Theory and Applications.
Edited by Martin Kaupp, Michael Bühl, Vladimir G. Malkin
Copyright © 2004 WILEY-VCH Verlag GmbH & Co. KGaA, Weinheim
ISBN: 3-527-30779-6

discussion is organized by system type but, whenever possible, an attempt is made to point out the general behavior of a functional across wider sets of compounds, as well as the physical background of the observed performance.

29.2 Theoretical Background

29.2.1 The Hyperfine Coupling Tensor

The hyperfine coupling parameters describe the interactions of unpaired electrons with magnetic nuclei. The 3×3 hyperfine interaction tensor A can be separated into its isotropic and anisotropic (dipolar) components. In the first-order approximation, isotropic hyperfine splittings $A_{\mathrm{iso}}(N)$ are equal to the Fermi-contact term and they are related to the spin densities $\rho^{\alpha-\beta}(R_N)$ at the corresponding nuclei by

$$A_{\mathrm{iso}}(N) = \frac{4\pi}{3}\beta_{\mathrm{e}}\beta_{\mathrm{N}}g_{\mathrm{e}}g_{\mathrm{N}}\langle S_{\mathrm{Z}}\rangle^{-1}\rho_N^{\alpha-\beta} \tag{29.1}$$

Here β_{e} is the Bohr magneton, β_{N} the nuclear magneton, g_{e} the free-electron g-value (2.002 319 31), g_{N} the nuclear g-value, $\langle S_Z\rangle$ the expectation value of the z-component of total electronic spin, and $\rho_N^{\alpha-\beta}$ the spin density at the position of nucleus N ($\mathbf{R}_N$). The components T_{kl} of the anisotropic tensor are, in the first-order approximation, given by

$$T_{kl}(N) = \frac{1}{2}\beta_{\mathrm{e}}\beta_{\mathrm{N}}g_{\mathrm{e}}g_{\mathrm{N}}\langle S_Z\rangle^{-1}\sum_{\mu,\nu}P_{\mu,\nu}^{\alpha-\beta}\left\langle\phi_\mu\left|\mathbf{r}_N^{-5}\left(\mathbf{r}_N^2\delta_{kl}-3r_{N,k}r_{N,l}\right)\right|\phi_\nu\right\rangle \tag{29.2}$$

where $\mathbf{r}_N = \mathbf{r} - \mathbf{R}_N$, and $P_{\mu,\nu}^{\alpha-\beta}$ is the spin density matrix. T is always traceless and may be brought to diagonal form. For magnetic nuclei located on an at least threefold symmetry axis, it adopts the form ($-A_{\mathrm{dip}}$, $-A_{\mathrm{dip}}$, $2A_{\mathrm{dip}}$), where A_{dip} is the so-called dipolar coupling constant.

29.2.2 The Exchange-Correlation Functionals

The principles of DFT were formulated almost 40 years ago by Hohenberg and Kohn who proved that the full many-particle ground state is a unique functional of the density (ρ) that minimizes the total energy [8]. The form of the exact functional is unknown, however, and the way towards practical applications of DFT has been opened only by the ingenious idea of Kohn and Sham to construct a noninteracting reference system having the same density as the real system [9]. By this method, a

major part of the unknown functional can be expressed exactly, leaving only a small part of the total energy to be approximated. This so-called exchange-correlation energy (E_{xc}) contains non-classical contributions to the potential energy, as well as the difference between the kinetic energy of the noninteracting reference system and that of the real interacting system. The most basic approximation to E_{xc} is the local density approximation (LDA)

$$E_{xc}^{LDA}\left[\rho_\alpha, \rho_\beta\right] = \int \rho(\mathbf{r}) \varepsilon_{xc}\left(\rho_\alpha(\mathbf{r}), \rho_\beta(\mathbf{r})\right) \mathrm{d}\mathbf{r} \tag{29.3}$$

where ε_{xc} denotes the one-particle exchange-correlation energy in a uniform electron gas and ρ_α, ρ_β are the spin densities. The most common form of LDA is the Slater exchange term (S) [10] together with the Vosko, Wilk and Nusair parametrization (VWN) of the exact uniform electron gas model for the correlation part [11].

To improve upon this rather crude approximation, the most widely used corrections are the so-called generalized gradient approximations (GGA) that employ not only the density but also its gradient

$$E_{xc}^{GGA}\left[\rho_\alpha, \rho_\beta\right] = \int f\left(\rho_\alpha(\mathbf{r}), \rho_\beta(\mathbf{r}), \nabla\rho_\alpha, \nabla\rho_\beta\right) \mathrm{d}\mathbf{r} \tag{29.4}$$

The main correlation corrections commonly in use are by Perdew (P86) [12], by Lee, Yang and Parr (LYP) [13], and by Perdew and Wang (PW91) [14]. Of the corrections to the exchange energy, the most common forms are those by Perdew and Wang (PW and PW91) [15,16], and by Becke (B) [17]. From the more recently introduced exchange functionals, we discuss in the following the modified Perdew–Wang (*m*PW) [18] and the Gill 1996 (G96) [19] functionals. Recently, the so-called meta-GGA functionals have been developed, in which the gradient of the electronic density is augmented by some additional parameter(s) of inhomogeneity: either the Laplacian of the density, the local kinetic energy density, or both (for a brief review and references see Ref. [20]). Another class of functionals, "hybrid functionals", introduced by Becke, uses a linear combination of Hartree–Fock, LDA, and B88 exchange contributions. Becke's so-called three-parameter hybrid functional (B3) [21] includes ca. 20% of exact HF exchange, while the "half-and-half" hybrid functional (BH) [22] incorporates as much as 50% exact exchange. More recently, one-parameter hybrid functionals based on B88 exchange (B1) [23], and the "modified Perdew–Wang" exchange functional (*m*PW1) [18] have been introduced. In the following, exchange-correlation potentials v_{xc} will be denoted by the usual combination of labels for the exchange and correlation functionals, like BP86 or B3LYP. The combination of PW91 exchange and PW91 correlation will be denoted PW91. Finally, the recently developed hybrid functional due to Adamo and Barone [25] based on the PBE GGA by Perdew, Burke and Ernzerhof [26] is discussed in the following as PBE0.

29.2.3 Basis Sets

Within the standard delta-function formulation, the isotropic HFCCs depend on the local quality of the wavefunction at the nuclei, suggesting that Slater-type orbitals (STOs) should be preferred, as they fulfill the correct cusp condition. However, the majority of studies employ Gaussian-type orbitals (GTOs) based on existing evidence [1] that the cusp problem can be overcome by adding very tight *s* functions to standard basis sets (see Chapter 31 by Rassolov and Chipman for another possibility to improve basis-set convergence). A lucid discussion by Barone [4] compares a number of GTO sets to a benchmark basis (referred to as EXT) of 18s13p4d3f composition for first-row atoms and of 9s4p3d composition for hydrogen. While conventional DZP bases are not sufficiently accurate to generate satisfactory HFCCs [5, 27], they can give reliable results if uncontracted in the outer core-, inner valence region. An example is the 5s2p1d basis set (3s1p for hydrogen) of Barone called EPR-II that provides HFCC results comparable to much more extensive sets, except for isolated atoms. Larger basis sets have been built with the aim of using the same method to optimize and determine spectroscopic properties. The conventional TZP basis gives reasonable but slightly too large isotropic couplings. Of the partially uncontracted triple-ζ-polarized basis sets tested, the 7s6p2d (4s2p for hydrogen) set known as IGLO-III is considered highly suitable for molecular HFCC calculations [5, 27]. It should be noted, however, that the IGLO-III basis is not saturated with respect to hydrogen hyperfine couplings. The latter are underestimated for certain radicals. In contrast, the so-called TZ2P' basis of Barone for hydrogen improves the results significantly [4]. Results of IGLO-III quality are also obtained using the van Duijneveldt series, contracted and augmented by a double set of polarization functions to 8s5p2d (7s2p for hydrogen) [28]. Finally, the 7s4p2d basis (6s2p for hydrogen) known as EPR-III has been purposely tailored by Barone for reliable evaluation of DFT magnetic properties [4].

Basis set studies for transition metal complexes are much less abundant. For several 3d-metal systems, a large uncontracted 21s15p10d3f basis has been compared to a medium-sized basis in a (15s11p6d)/[9s7p4d] contraction [7]. As found analogously for main-group compounds, decontraction of the outermost core *s*-functions on the transition metal influences hyperfine couplings significantly. Due to systematic error compensation, the 9s7p4d basis simulates the 21s15p10d3f basis quite well and can be considered a decent medium-sized basis set for use in larger systems. Examination of the effect of the ligand basis on the isotropic HFCCs indicates that the IGLO-III basis set is rather well converged relative to a larger benchmark 8s6p3d1f basis [7].

DFT calculations of HFCCs employing STO basis sets are scarce but provide very interesting results. Ishii and Shimizu have employed several Slater-type basis sets along with the LDA and BP86 functionals to calculate isotropic HFCCs in main-group systems [29–31]. STO bases consisting of 6s5p4d sets for main group atoms and a 5s3p set for hydrogen along with BP86 yielded most encouraging results and outperformed conventional GTO basis sets significantly for "difficult" mono- and

biatomic radicals. Also in the case of the methyl radical (see below), the results of Belanzoni et al. [32] demonstrated that LDA and BP86 spin densities on C, H computed using STO bases are, in absolute values, larger and closer to experiment than their counterparts with GTO bases. The origin of the better behavior of the LDA and BP86 functionals when combined with STOs is as yet unclear. On the one hand, the GTO basis sets studied are considered converged (see above) and are expected to simulate the cusp at the point of the nucleus sufficiently well. The STO basis sets studied were necessarily smaller in size, which might indicate a fortuitous error cancellation when combining BP86 along with STOs. On the other hand, only in the case of STOs is the crucial cusp condition at the nucleus exactly fulfilled. Systems, whose HFCCs are represented well with STOs cover a relatively wide range of electronic structures. The different results with STOs vs. GTOs regarding the performance of different functionals are certainly worth a deeper theoretical analysis.

In the case of transition metal complexes, different metal and ligand STO basis sets have been studied on the TiF_3 system by Belanzoni, Baerends, and coworkers [32, 33]. The "best" Ti basis set employed, of triple-ζ quality augmented with extra core and diffuse s and p functions, provided BP86 results very close to the above-mentioned 9s7p4d GTO basis [7]. Likewise, the LDA, PW91 and PW86 functionals when used with all-electron STO basis sets provide results similar to BP86 (–233 to –246 MHz) [32].

29.3 The Performance of the Model

29.3.1 Main Group Atoms

Table 29.1 documents the dependence of HFC tensors on ν_{xc} and on basis set for first-row atoms in comparison to experimental reference data. The results reveal some general features that are also found with polyatomic radicals, as well as with transition metal complexes: (i) Anisotropic coupling constants are much less sensitive to ν_{xc} and basis set than isotropic ones, and essentially all of the results are in semiquantitative agreement with the CCSD(T) reference. (ii) For isotropic coupling, the requirements for basis set and ν_{xc} are much less stringent if the unpaired spin populates s-type orbitals (^{7}Li) rather than p-type (and d-type, see Section 29.3.5) orbitals. The transfer of unpaired spin from p- or d-orbitals to the magnetic nuclei takes place exclusively via the spin-polarization mechanism, the description of which represents the major challenge of HFC calculations. Basis sets of very good quality along with a high-level treatment of electron correlation are thus mandatory in order to obtain accurate results. This is particularly highlighted in the case of atomic calculations, while for other systems (e.g. organic π-radicals, Section 29.3.2) the description appears less critical and less method dependent. Another problem specific to computations on atomic systems is the handling of their spherical symmetry [4].

Table 29.1 Isotropic and dipolar hyperfine splitting of second row atoms (in MHz) computed using different basis sets and density functionals, compared to experiment and CCSD(T) data.

Method	Basis	^{7}Li(^{2}S)	^{11}B(^{2}P)	^{13}C(^{3}P)	^{14}N(^{4}S)	^{17}O(^{3}P)	^{19}F(^{2}P)
A_{iso}							
LDA[a]	GTO-EXT	399.5	–8.3	–6.1	–1.9	5.7	–62.4
BP86[a]	GTO-EXT	388.4	–16.4	–6.1	–0.3	–2.3	7.5
BLYP[a]	GTO-EXT	460.2	16.2	21.1	7.9	–20.2	145.1
B3LYP[a]	GTO-EXT	453.3	18.6	25.1	10.0	–26.4	213.6
B3LYP[a]	6–31(d,p)	373.3	–4.1	5.4	7.3	–30.2	227.3
B3LYP[a]	EPR-II		10.9	14.9	5.2	–11.8	139.4
B3LYP[a]	IGLO-III	449.2	17.1	23.8	9.5	–25.5	207.0
B3LYP[a]	EPR-III	449.2	18.0	24.2	9.7	–25.5	210.2
BP86[b]	STO-6s5p4d		1.4	19.6	11.8	–32.5	305.5
CCSD(T)[c]	23s12p10d4f2g		10.3	21.4	11.0	–33.2	302.9
Exp[d]		401.8	11.5,18.7	19.6,22.5	10.4	–34.5	301.7
A_{dip}							
LDA[a]	GTO-EXT		59.9	99.4		149.6	1628.2
BP86[a]	GTO-EXT		59.9	99.1		153.7	1650.9
BLYP[a]	GTO-EXT		62.0	101.0		153.9	1655.1
B3LYP[a]	GTO-EXT		61.2	100.1		152.2	1641.9
B3LYP [a]	6–31G(d,p)		53.6	87.7		135.1	1473.0
B3LYP[a]	EPR-II		54.3	91.0		141.0	1536.2
B3LYP[a]	IGLO-III		60.7	98.9		148.5	1601.8
B3LYP[a]	EPR-III		59.9	98.3		148.5	1605.5
CCSD(T)[c]	23s12p10d4f2g		55.1	93.8		150.4	1575.0

a) Ref. [4].
b) Ref. [31].
c) Ref. [64].
d) Ref. [65] for ^{7}Li, Refs. [66, 67] for ^{11}B, Refs. [66, 68, 69] for ^{13}C, Refs. [70, 71] for ^{14}N, and Ref. [72] for ^{17}O and ^{19}F.

Looking at the data in Table 29.1 in somewhat more detail, we conclude that all presented results for A_{dip} fall within ca. 10% of the reference CCSD(T) values, and that all A_{iso} results for ^{7}Li(^{2}S) lie within 15% of the experiment. In particular, ^{7}Li is the only system where LDA along with the EXT basis set of Barone provides reasonable results for the isotropic coupling, while for all other atoms even the sign of $\rho_N^{\alpha-\beta}$ comes out wrong. The BP86/EXT level of calculation corrects the LDA spin density in the wrong direction for ^{11}B(^{2}P), leaves it unchanged for ^{13}C(^{3}P), while improving it slightly for ^{14}N(^{4}S), ^{17}O(^{3}P), and ^{19}F(^{2}P). The BLYP gradient correction already provides a significant improvement over LDA, but the best results with the EXT basis are provided by the B3LYP method. The B3LYP-based validation of various GTO bases reveals that the 6-31G and EPR-II basis sets are much too small for A_{iso} calculations on atoms, whereas EPR-II appears sufficient in the case of polyatomic main-group radicals (see below). Both EPR-III and IGLO-III sets give results comparable to the EXT basis and along with the B3LYP functional represent an effi-

cient tool for isotropic HFC calculations for first-row atoms. With the exception of ^{11}B results, the BP86/STO-6s5p4d isotropic hyperfine couplings are in excellent agreement with experiment.

Concerning the performance of DFT for second-row atoms (and further below), available studies concentrated on alkali metal and alkaline earth metal atomic radicals, where good agreement has been obtained between the PWP86 calculations and experiment [34]. Although encouraging results have been obtained for HFCCs in molecular phosphorus and sulfur centered radicals [35, 36], the higher sensitivity of atomic radicals to theoretical treatment suggests that 3p atom hyperfine parameters might turn out more challenging.

29.3.2
Methyl, Vinyl and Allyl Radicals

We proceed now by studying the performance of DFT approaches for three typical hydrocarbon radicals: a nonconjugated π radical (methyl, CH_3), a conjugated π radical (allyl, C_3H_5), and an unsaturated σ radical (vinyl, C_2H_3). Table 29.2 summarizes selected A_{iso} data obtained with conventional GTO and STO basis sets along with the local density approximation, three gradient-corrected and two hybrid functionals. The body of data available in the literature has been augmented by additional calculations of the author in order to complete the picture.

The equilibrium D_{3h} geometry of the methyl radical, a species well characterized by EPR, possesses little resistance to pyramidalization in the symmetric ν_2 "umbrella" vibrational mode. This motion influences significantly the isotropic couplings. In Table 29.2, data computed for the hypothetical nonvibrating planar radical are compared to experimental HFCCs with vibrational contributions subtracted, as estimated by Chipman [37]. In addition, a direct comparison is made between experimental data and Barone's DFT results accounting for the vibrational averaging.

For any of these two comparisons, LDA with GTO bases underestimates spin densities at C and H significantly in absolute value, whereas BP86 does this less so. The isotropic carbon splitting is already improved notably at the PWP86 level and the result closest to experiment is obtained at the BLYP level. The hybrid B3LYP and PBE0 functionals slightly overestimate carbon spin densities but provide the best agreement with experiment in the case of hydrogen spin densities. One of the motivations for the use of hybrid functionals has been the hope of obtaining simultaneously good results for spectroscopic parameters and structures at the same level of theory. Indeed, Table 29.2 shows that B3LYP and PBE0 provide C–H bond lengths closest to experiment. The LDA and BP86 spin densities at C and H computed with STO bases are significantly more negative than their counterparts with GTO bases, and the BP86/STO-6s4p2d results already compare well to experiment [32]. The PWP86/STO-6s4p2d level describes C coupling correctly but underestimates H coupling. The lack of data does not allow any conclusions about the behavior of other ν_{xc} when combined with STO bases (no implementations of hybrid functionals are available with STO basis sets).

Table 29.2 Isotropic hyperfine splitting of methyl, vinyl and allyl radicals (in MHz) computed using different basis sets and density functionals, compared with experiment and coupled-cluster results.[a]

$^2CH_3$								
HFCC	**LDA / TZ2P′**	**BP86 / TZ2P′**	**PWP86 / EPR-II**	**BLYP / TZ2P′**	**B3LYP / TZ2P′**	**PBE0 / EPR-III**	**CCSD(T) / Chipman**	**exp.**
Structure	LDA	BP86	PWP86	BLYP	B3LYP	PBE0	exp	
r(CH) (in Å)	1.088	1.087	1.091	1.085	1.079	1.078	1.079	1.079
A_{iso}(C)[b]	30.5	64.5	75.0	76.3	83.4	81.8	79.7	76
A_{iso}(H)[b]	–50.7	–64.0	–61.5	–60.8	–65.4	–73.1	–72.6	–70
$\langle A_{iso}(C)\rangle$[c]	58.2	92.2		104.0	111.0			107.3
$\langle A_{iso}(H)\rangle$[c]	–45.1	–58.4		–55.2	–59.8			–64.7
Ref.	73	73	74	73	73	75	64, 76	77
HFCC	**LDA / STO-6s4p2d**	**BP86 / STO-6s4p2d**	**PWP86 / STO-6s4p2d**				**CCSD (T) / Chipman**	**exp.**
Structure	BP86	BP86	BP86				exp	
r(CH) (in Å)	1.090	1.090	1.090				1.079	1.079
A_{iso}(C)[b]	45.9	81.8	76.7				79.7	76
A_{iso}(H)[b]	–53.9	–67.0	–59.0				–72.6	–70
Ref.	32	32	32				76	77
$^2C_2H_3$								
HFCC	**LDA / EPR-III**	**BP86 / STO-6s5p4d**	**PWP86 / EPR-II**	**BLYP / EPR-III**	**B3LYP / EPR-III**	**PBE0 / EPR-III**	**CCSD(T) / Chipman**	**exp.**
Structure	LDA	BP86	PWP86	BLYP	B3LYP	PBE0	Ref. 78	
$A_{iso}(C^{\alpha})$	233.2	313.9	283.9	292.9	316.9	308.8	328.7	301.5
$A_{iso}(C^{\beta})$	–6.4	–12.3	–11.2	–10.8	–16.3	–19.3	–17.1	–24.1
$A_{iso}(H^{\alpha})$	45.4	46.2	45.4	55.1	49.9	37.3	33.3	38.7
$A_{iso}(H^{\beta}_a)$[d]	182.3	186.4	169.3	195.6	183.8	174.3	143.8	184.7
$A_{iso}(H^{\beta}_s)$[d]	124.2	118.3	101.5	122.0	117.4	112.7	82.0	111.0
Ref.	79	30	4	79	75	75	83	77a,b
$^2C_3H_5$								
HFCC	**LDA / GTO-7s6p2d**	**BP86 / GTO-7s6p2d**	**PWP86 / GTO-7s6p2d**	**BLYP / EPR-III**	**B3LYP / EPR-III**	**PBE0 / EPR-III**	**CCSD(T) / Chipman**	**exp.**
Structure	LDA	LDA	LDA	BLYP	B3LYP	PBE0	Ref. 80	
$A_{iso}(H^{\alpha})$	2.1	8.3	8.6	10.4	12.3	15.7	13.3	11.8
$A_{iso}(H^{\beta 1})$	–28.7	–38.7	–36.5	–39.9	–43.4	–48.5	–48.3	–39.0
$A_{iso}(H^{\beta 2})$	–27.6	–37.9	–34.7	–37.6	–40.9	–45.7	–50.4	–41.5
$A_{iso}(C^{\alpha})$	–31.6	–39.5	–40.9	–38.1	–45.4	–51.8	–63.5	–48.2
$A_{iso}(C^{\beta})$	15.4	36.4	56.0	45.9	51.8	53.8	59.3	61.4
Ref.	38	38	38	79	75	75	76, 81	82, 83

a) Data given for the ^1H and ^{13}C isotopes.
b) Data for the hypothetical planar nonvibrating radical.
c) Vibrationally averaged values.
d) H^{β}_a (H^{β}_s) proton oriented *anti* (*syn*) with respect to the singly occupied hybrid AO

The allyl radical is well-investigated spectroscopically. It is also of particular theoretical interest as a small molecule which exhibits the phenomenon of doublet instability. The DFT results available in the literature for A_{iso} do not allow the validation of all ν_{xc} examined in Table 29.2 at a uniform level for both structures and basis sets. We note, however, that the effect of using a PWP86-optimized or experimental geometry instead of the LDA one has been estimated by Eriksson et al. to be small, and that both the 7s6p2d/3s2p and the EPR-III basis sets are supposed to provide converged results [24, 38]. LDA underestimates in absolute value the spin densities at all nuclei. BP86, PWP86 and BLYP gradient corrections bring A_{iso} to within 10–15% of experiment for β-hydrogens but not for α-hydrogens and carbons. The best overall agreement with experiment (10% for all couplings) is obtained using the B3LYP/EPR-III level of calculation. PBE0 gives the highest absolute values for $\rho_N^{\alpha-\beta}$ at all centers and provides thus the best results for C^{β}(supposedly due to the remarkable accuracy of PBE0 structures) but overestimates somewhat A_{iso}(H).

The calculation of HFCCs of unsaturated σ radicals is particularly difficult for conventional HF-based methods. This makes the vinyl radical a suitable benchmark for the performance of DFT approaches. PBE0 appears to be most successful. It provides A_{iso} within 10% (C^{α}, H^{α}, H^{β}) to 20% (C^{β}) of experiment. The GGA functionals (including BP86/STO-6s5p4d) along with B3LYP provide isotropic couplings within 10% of the experiment for C^{α} and H^{β} but too positive spin densities at C^{β} and H^{α}, apparently due to an insufficient description of spin polarization.

In summary, with GTO basis sets, the most accurate A_{iso} for hydrocarbon radicals are obtained with B3LYP and PBE0 functionals: Except for some C^{β} and H^{α} couplings, all results are within 10% of experiment. In the case of CH_3, results of the same quality are provided by the BP86/STO-6s4p2d level of calculation.

29.3.3
π-Radicals Involving Heteroatoms

Proceeding now to oxygen-centered radicals, we point out additional difficulties in HFCC calculations for systems where the constituent atoms possess significantly different electronegativities [4]. The three examples examined in Table 29.3, OH, H_2O^+, and H_2CO^+, represent a diatomic π-radical, an out-of-plane π-radical, and an in-plane π-radical, respectively. The scatter in computed isotropic HFCCs increases in the order H < C < O and is significantly larger than in the case of hydrocarbon radicals. The BP86/IGLO-III approach provided $A_{iso}(C^{\alpha})$ for the latter species within 15–20% of experiment (Tab. 29.2). It now underestimates spin densities at oxygen by more than 50% (Tab. 29.3). We see the best performance with GTO basis sets for the PWP86 and B3LYP functionals.

The hydroxyl radical, OH, represents one of the smallest systems for which accurate experimental isotropic ^{17}O couplings exist [39a] and, in contrast to the homologous CH and NH radicals [4, 28], it is a particular challenge for current quantum chemical methods [40]. With the IGLO-III basis set, B3LYP is the only functional tested that provides A_{iso}(O, H) couplings within 15% of experiment. The problem of

Table 29.3 Isotropic and dipolar HFCCs of main-group radicals (in MHz) computed using different basis sets and density functionals, compared to experiment and to coupled-cluster results.[a] Unless stated otherwise, calculations have been performed on experimental structures: in ^2OH, r(O–H) = 0.969 Å; in $^2H_2O^+$, r(O–H)=0.999 Å, ∠HOH = 110.5°.

^2OH								
HFCC	**BVWN / IGLO-III**	**BP86 / IGLO-III**	**PWP86 / IGLO-III**	**PW91 / IGLO-III**	**BLYP / IGLO-III**	**B3LYP / IGLO-III**	**CCSD(T) / 11s7p2d**	**exp.**
A_{iso}(O)	–31.3	–19.4	–49.9	–14.2	–35.0	–43.9	–46.5	–51.3
A_{iso}(H)	–52.0	–54.6	–58.3	–53.1	–56.9	–61.2	–71.7	–73.1
A_{dip}(O)	145.2	143.3	145.7	–140.4	144.1	142.8		125.0
A_{dip}(H)	44.1	43.9	43.7	44.2	44.5	45.1		49.9
Ref.	4	4	27	79	4	4	84	39
HFCC		**BP86 / STO-6s5p4d**			**BLYP / GTO-8s5p2d / 7s2p**	**B3LYP / GTO-18s13p4d 3f/11s4p**	**CCSD(T) / 11s7p2d**	**exp.**
A_{iso}(O)		–47.1			–34	–65.9[b]	–46.5	–51.3
A_{iso}(H)		–65.3			–62	–66.4[b]	–71.7	–73.1
Ref.		31			28	85	84	39
$^2H_2O^+$								
HFCC	**BVWN / IGLO-III**	**BP86 / IGLO-III**	**PWP86 / IGLO-III**	**PW91 / IGLO-III**	**BLYP / IGLO-III**	**B3LYP / IGLO-III**		**exp.**
A_{iso}(O)	–47.4	–35.3	–68.9	–37.1	–50.9	–64.7		–83.2
A_{iso}(H)	–54.5	–57.6	–61.9	–59.8	–60.6	–65.0		–73.1
Ref.	4	4	27	79	4	4		86
HFCC	**BVWN / EPR-III**	**BP86 / EPR-III**			**BLYP / EPR-III**	**B3LYP / EPR-III**		**exp.**
A_{iso}(O)	–47.8	–36.5			–50.9	–66.1		–83.2
A_{iso}(H)	–60.2	–63.7			–66.7	–72.3		–73.1
Ref.	79	79			79	79		86
$^2H_2CO^+$								
HFCC	**BVWN / Chipman**	**BP86 / IGLO-III**	**PWP86 / IGLO-III**	**PW91 / IGLO-III**	**BLYP / IGLO-III**	**B3LYP / EPR-III**		**exp.**
Structure	QCISD(T)	BP86	PW86	PW91	BLYP	B3LYP		
A_{iso}(C)	–62	–81	–89	–85.1	–87	–93.9	–108.7	109
A_{iso}(H)	325	364	374	369.1	384.0	365.2	300.4	373
A_{iso}(O)	–22	–17	–35.3	–16.9	–28	–43.2	–56.9	
Ref.	28	28	27	79	28	75	87	88
HFCC	**BVWN / STO-6s6p4d**	**BP86 / STO-6s6p4d**			**BLYP / IGLO-III**			**exp.**
Structure	MCSCF	MCSCF			QCISD(T)			
A_{iso}(C)	–68.4	–83.8			–78		–108.7	109
A_{iso}(H)	359.5	368.5			328		300.4	373
A_{iso}(O)	–16.5	–31.7			–36		–56.9	
Ref.	29, 89	29, 89			28		87	88

a) Data for the ^1H, ^{13}C and ^{17}O isotopes.
b) A B3LYP bond length of 0.974 Å has been employed.

the DFT description appears to arise from insufficient delocalization of the unpaired spin from O to H (cf. O, H dipolar and H isotropic couplings) and insufficient spin polarization of oxygen 1s and 2s orbitals (cf. O isotropic coupling). While the use of more extensive basis sets improves the spin density at hydrogen (compare BLYP, B3LYP results in Tab. 29.3), $\rho_N^{\alpha-\beta}$ at oxygen is either unchanged (BLYP) or overestimated (B3LYP). On the other hand, the BP86 functional, that provided very poor results with GTO bases, gives the best overall results for A_{iso} (10% agreement for C, H) when the STO-6s5p4d basis is used instead.

The DFT spin densities at O and H nuclei are, in general, also below experiment in the case of the water cation, H_2O^+. The A_{iso}(O,H) results closest to experiment (within 15–20 %) are those obtained with the PWP86/IGLO-III and B3LYP/EPR-III levels of calculation. Note that with any v_{xc}, the change from IGLO-III to EPR-III basis sets increases A_{iso}(H) by ca. 6 Hz but leaves A_{iso}(O) almost unchanged. This trend corresponds to Barone's observation that the IGLO-III basis is not converged for hydrogen in molecular HFCC calculations [4]. Too low heavy-atom isotropic coupling has also been reported for the isoelectronic radical NH_2, where most of the conventional DFT or *ab initio* techniques appear to recover only 70–90% of $A_{iso}(^{14}N)$. Apparently, the description of electron correlation effects on the spin density at the nuclei seems particularly difficult in the case of nitrogen and oxygen [41], and even more so for fluorine [42]. Increasing difficulties along the series H, C, N, O and F have been encountered in a related problem of one-bond spin–spin coupling constants. They were first reported by Malkin et al. [43] who suggested that the ability of the current exchange-correlation functionals to describe spin-density distribution depends on the number of lone pairs at the nucleus in question. For more information on DFT performance in calculations of NMR spin-spin coupling, see Chapter 7 of Helgaker and Peal.

Turning to H_2CO^+, the best performance is again found for PWP86 and B3LYP/IGLO-III levels of calculation (for the latter, A_{iso}(C, H) are within 15% of experiment, and A_{iso}(O) is within 25% of the CC results). As in the previous cases, the description of A_{iso}(O) by BP86 changes strongly when going to an STO basis. A detailed discussion of hyperfine parameters of H_2CO^+ as compared to isoelectronic H_2CN is given in Ref [5].

29.3.4
Further Main-Group Systems

In numerous cases problems with a quantitative reproduction of HFCCs are related to difficulties in determining the structure of the radical. A well-known example is the F_2^- radical, where the hyperfine parameters are highly sensitive to changes in the F–F bond length [44], and at the same time there is an unusually large disagreement in predicted bond lengths between different theoretical methods. As a two-center-three-electron system, F_2^- is highly susceptible to the self-interaction energy error which makes the DFT-optimized bond length too large [45]. Using instead the more accurate MRCI F–F distance, the HFCCs at DFT level exhibit perfect agreement with experiment and with high level *ab initio* methods [27]. Difficulties related

to structure may represent the major obstacle in quantitative HFCC calculations, yet in other cases the major challenge appears the description of spin-density distribution, and sometimes both problems are coupled. A good example is provided by the two inorganic peroxides HOO and FOO, where a debate persists in the literature as to what are the correct equilibrium structures, and which structures correspond to the observed HFCCs [42]. In the case of HOO, high-level QCISD results for the isotropic couplings are in much closer agreement with experimental data (for related small peroxide radicals) than the B3LYP results, in spite of very similar geometrical structures [46]. In the case of FOO, very good agreement exists between QCISD/6-311+G(2d) calculations of HFCCs done on the QCISD optimized structure and experiment. At the same time, B3LYP calculations yield significantly different HFCCs when working with both the much larger B3LYP F–O bond length and with the QCISD structure [42].

The above examples indicate the type of accuracy we may expect from DFT approaches. However, small gas-phase radicals are not very realistic systems from a chemical point of view. In the remainder of this section we will instead focus on the major strength of the DFT approach, the possibility of treating large radicals, including their interactions with the surroundings. An extensively explored class of paramagnetic systems are large organic π-radicals of more or less direct biophysical importance. Existing studies conclude that the PWP86 and B3LYP approaches along with basis sets of extended TZ quality (IGLO-III, EPR-III, partially decontracted bases of the 6-311G(2df,p) family) can provide reasonable HFCC data for most nuclei in these systems [47–49]. As shown by Barone and coworkers, dynamical and solvent effects are in general important in EPR calculations of organic radicals and can be successfully reproduced by current theoretical approaches [50–52]. An overview of the models to include solvent effects is provided in Chapter 12 by Ciofini. Let us finally turn to systems containing metals: Eriksson has shown that the PWP86/IGLO-III approach is well-suited for relatively large clusters of main-group metal atoms. Good performance for isotropic hyperfine couplings was found for both s (Li, Na, K, Mg) and p (Al) valence metals. Furthermore, the DFT approach successfully mimics the effects of Ne, Ar, and zeolite matrices on metal radical hyperfine structures [49].

29.3.5
Transition Metal Complexes

The variable performance of different functionals for different systems is particularly pronounced for the group of transition metal complexes. Figure 29.1 illustrates the ν_{xc} dependence of metal spin densities for (a) complexes with a singly occupied MO (SOMO) composed mainly of the metal 4s orbital (ScO, TiN, TiO, VN) and for (b) compounds where SOMO is dominated by the metal $3d_z^2$ orbital with some 4s character mixed in (TiF_3, MnO_3). The results taken from a recent validation study [7] (see also Tab. 29.4) clearly show that while the ν_c dependence can be considered dominant for ScO, TiN or TiO, it is the ν_x dependence that is crucial for TiF_3 and especially for MnO_3.

For the first group of complexes, metal isotropic hyperfine couplings closest to experiment are obtained with the BPW91 and B3PW91 functionals. Yet all computed values were within 5% (ScO, TiN) to 10% (TiO) of the very precise gas-phase

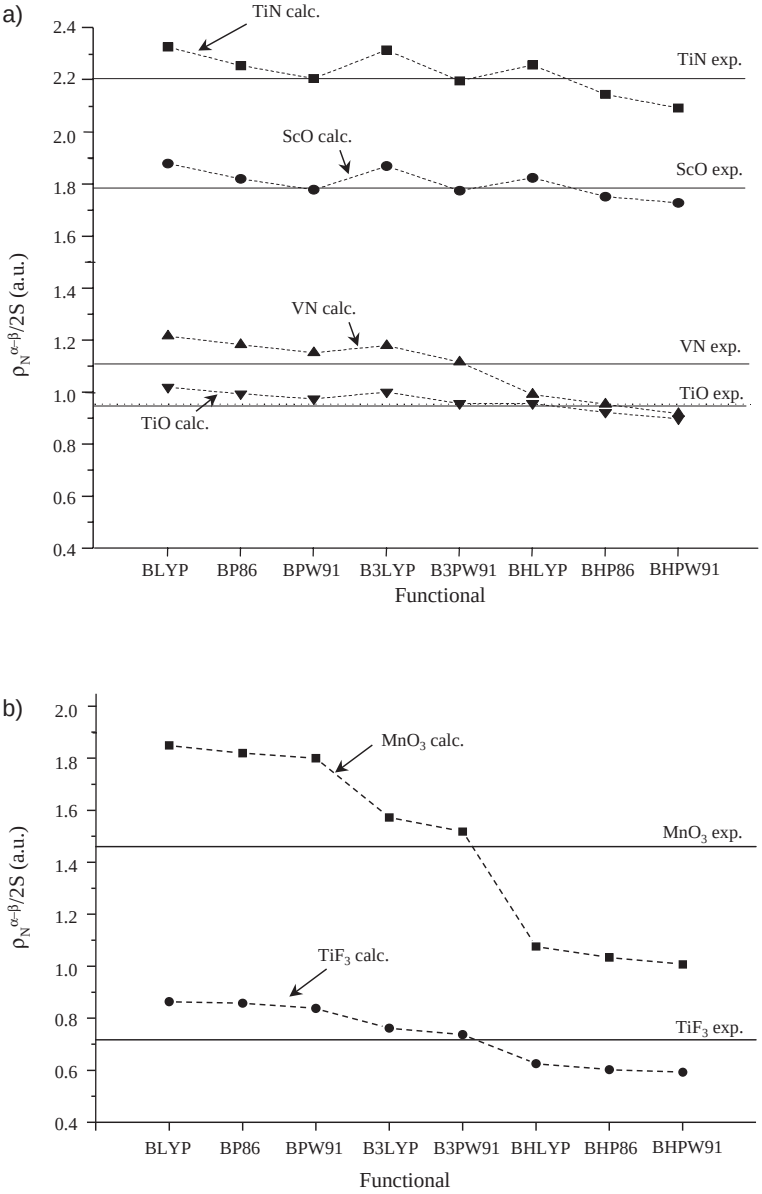

Figure 29.1 Spin density $\rho_N^{\alpha-\beta}$ at their metal nuclei in (a) ^{2}ScO, ^{3}TiO, ^{2}TiN, ^{3}VN, and (b) $^2TiF_3$, $^2MnO_3$, normalized to the number of unpaired electrons. Dependence on v_{xc}.

experimental data. In the case of VN, pure DFT and B3- functionals behave analogously to isoelectronic TiO. However, BH-type functionals underestimate appreciably the spin density at vanadium, due to a significant spin contamination ($<S^2> \sim 2.5$, nominal triplet-state $<S^2> = 2.0$) causing a large negative contribution to $\rho_N^{\alpha-\beta}$. In the cases of ScO and TiN, spin densities are determined mainly by the contribution from the singly occupied metal 4s orbital, since 3d spin population as well as spin polarization contributions are negligibly small. Metal hyperfine couplings thus reflect the composition of the singly occupied orbital that becomes more diffuse along the series LYP < P86 < PW91 as well as upon the addition of an exact exchange. TiO and VN have in addition one $3d_\sigma$-type SOMO, inducing a negative spin-polarization contribution to $\rho_N^{\alpha-\beta}$. While the direct 4s contribution again dominates the metal HFCCs, the dramatic onset of spin contamination found for VN (contrary to isoelectronic TiO!) leads to a much larger dependence on ν_x and the deterioration of the results with the BH-hybrid functionals.

The metal isotropic HFCCs of the trigonally planar complexes TiF_3 and MnO_3 again reveal a considerable direct contribution making $\rho_N^{\alpha-\beta}$ at the metal positive, but spin polarization is very important as well. The sensitivity to ν_x is already significant for TiF_3 with results closest to experiment given by the B3-type hybrid functionals, but all ν_{xc} do still give results within ca. 15% of the measured value. For MnO_3, the ν_x dependence is particularly pronounced and is complicated by significant spin contamination (cf. Tab. 29.4). The results for MnO_3 exemplify a dilemma that arises also in other cases [7]: While some admixture of exact exchange increases spin polarization and thus may improve the agreement with experiment relative to the "pure" GGA results, it may lead at the same time to considerable spin contamination. The more covalent, highly oxidized MnO_3 turns out to be much more sensitive to spin contamination than the isoelectronic TiF_3. While the B3-type functionals provide A_{iso}(Mn) closest to the experimental and CC results, the large variations of A_{dip} (Mn) from the reference data suggest that the overall description of spin density distribution deteriorates rather than improves when exact exchange is introduced.

The exact-exchange mixing is thus in general problematic, especially for systems with low-lying virtual orbitals that significantly overlap with the SOMO and may give rise to spin contamination. Yet for many, especially high-spin, systems, the spin contamination problem is not encountered and the hybrid functionals provide most encouraging results. An example is given by the $[Cr(CO)_4]^+$ complex where, due to the high T_d symmetry, all of the five metal-centered singly occupied orbitals contain only Cr 3d and no Cr 4s contributions. The spin density at the metal thus arises exclusively due to spin polarization. It is negative, in absolute value considerably smaller than in the previous complexes, and very sensitive to ν_{xc}. As illustrated by the results in Tab. 29.4, the β spin density at Cr is enhanced considerably with the admixture of exact exchange. A_{iso} of both Cr and C closest to experiment are those obtained with ν_x containing as much as 50% of the HF exchange.

Unfortunately, the success of hybrid functionals is not universal and the spin-polarization vs. spin-contamination dilemma remains a challenge for the DFT description of open-shell transition metal complexes. This holds not only for HFCCs but also for other properties like *g*-tensors [20]. Table 29.5 examines the behavior of five

Table 29.4 Metal and ligand isotropic and dipolar hyperfine splitting (in MHz) of selected transition metal complexes computed using various density functionals, compared to experiment and coupled-cluster results.[a]

	BLYP	BP86	BPW91	B3LYP	B3PW91	BHPW91	UCCSD	exp.
^{2}ScO								
A_{iso}(Sc)	2043.5	1979.6	1933.5	2032.3	1930.2	1847.7	1823.1	1947.3
A_{dip}(Sc)	17.1	17.5	17.3	18.7	18.7	21.0	23.1	24.8
A_{iso}(O)	–22.8	–21.3	–19.8	–19.9	–17.0	–11.6	–17.4	–20.3, –18.9
A_{dip}(O)	0.2	–0.2	–0.2	0.6	0.2	0.7	0.4	0.4, 0.7
$<S^2>$	0.751	0.752	0.752	0.751	0.752	0.753	0.751	0.750
$^2TiF_3$								
A_{iso}(Ti)	–218.0	–216.6	–211.6	–192.2	–186.1	–149.4	–170.5	–184.8, –177.1
A_{dip}(Ti)	–9.9	–9.2	–9.1	–10.1	–9.5	–9.3	–7.5	–6.6, –8.1
A_{iso}(F)	8.7	5.0	1.7	–5.6	–12.9	–24.3	–35.1	8.3, 8.0
T_{11}	20.9	26.9	29.7	19.4	25.2	21.6	18.7	
T_{22}	–0.2	5.0	6.4	–0.4	4.8	2.8	5.9	
T_{33} (F)	–20.7	–31.9	–35.8	–19.0	–30.0	–24.4	–24.6	
$<S^2>$	0.752	0.752	0.753	0.752	0.753	0.753	0.750	0.750
$^2MnO_3$								
A_{iso}(Mn)	2042.4	2009.3	1987.2	1735.5	1675.9	1111.7	1511.3	1613
A_{dip}(Mn)	95.9	95.1	95.5	124.5	125.9	171.4	101.5[b]	81
A_{iso} (O)	–5.1	–4.1	–3.5	2.6	2.6	19.0	7.8	
T_{11}	–23.9	–24.2	–24.7	–34.7	–55.3	–61.5	–27.0	
T_{22}	3.0	2.0	1.5	–14.9	18.1	–57.8	–35.8	
T_{33} (O)	20.9	22.2	23.2	49.6	37.2	119.3	62.8	
$<S^2>$	0.765	0.768	0.770	0.880	0.914	2.054	1.068	0.750
$^6[Cr(CO)_4]^+$								
A_{iso}(Cr)	21.9	23.8	25.2	26.9	30.8	40.4		41.5
A_{dip}(Cr)	0	0	0	0	0	0		0[c]
A_{iso}(C)	–5.0	–9.2	–11.5	–8.4	–13.4	–15.4		–13.5
A_{dip}(C)	1.1	1.1	0.8	1.4	1.1	1.4		1.0
A_{iso}(O)	–1.6	–1.2	–1.1	–1.8	–1.4	–1.6		
A_{dip}(O)	1.0	0.8	1.0	0.9	0.9	0.8		
$<S^2>$	8.757	8.761	8.762	8.759	8.764	8.765		8.750

a) All results have been taken from Ref. [7]; for structures, bases and references to experimental works see therein. Data given are for the most abundant magnetic isotopes.

b) A strongly asymmetric tensor has been obtained. The value reported represents 1/2 of the maximum element of the tensor.

c) Determined by the molecular symmetry.

more recently introduced functionals (three gradient corrected and two hybrid ones) for MnO_3 and $[Mn(CN)_4]^{2-}$, the latter complex being isoelectronic with $[Cr(CO)_4]^+$. While for $[Mn(CN)_4]^{2-}$ inclusion of exact exchange seems advisable and problem-free, for MnO_3 the spin-contamination problem remains. A recent study of meta-GGA and model exchange-correlation potentials reported no improvement over the previously validated v_{xc} [20].

The results presented above have been obtained in nonrelativistic KS-DFT calculations and the comparison of theoretical and experimental HFCCs was based on the

assumption of negligible spin–orbit (SO) and scalar relativistic (SR) contributions. Accordingly, systems were considered for which relativistic contributions to HFCCs

Table 29.5 Metal isotropic and dipolar hyperfine splitting of MnO_3 and $[Mn(CN)_4]^{2-}$ (in MHz) computed using several more recently implemented density functionals, compared coupled-cluster results and experiment.[a]

	PW91[b] PW91[c]	mPW[b] PW91[c]	G96[b] PW91[c]	mPW1[b] PW91[c]	B1[b] LYP[c]	RCCSD	UCCSD	exp./ nominal $<S^2>$
$^2MnO_3$								
A_{iso}(Mn)	1996.6	1994.3	1983.5	1689.8	1747.6	1492.0	1511.3	1613
A_{dip}(Mn)	95.3	95.4	97.1	112.9	112.5	94.7	101.5	81(3)
$<S^2>$	0.767	0.768	0.770	0.816	0.801	0.771	1.068	0.750
$^6[Mn(CN)_4]^{2-}$								
A_{iso}(Mn)	–104.7	–104.2	–113.0	–140.5	–121.8			–199
$<S^2>$	8.764	8.745	8.766	8.766	8.763			8.750

a) Structures and basis sets have been taken from Ref. [7]; for references to experimental data see therein. Data given are for the most abundant magnetic isotopes.
b) Exchange potential.
c) Correlation potential.

have been estimated or at least can be expected to be relatively small (see below). In general, relativistic effects on HFCCs are important for transition metal complexes, and an increasing number of recent studies has been devoted to this issue. A second-order perturbation treatment of spin–orbit coupling for TiF_3 due to Belanzoni et al. [33] along with the BP86 functional gave very small positive spin–orbit (pseudocontact) contribution to A_{iso} (Ti) (ca. 3–6 MHz). SO contributions to A_{dip} were estimated negative (–2.3 to –2.8 MHz) and large compared to the small dipolar coupling.

A more rigorous treatment of SO effects is due to van Lenthe et al. who derived expressions for molecular hyperfine interactions within the zeroth-order regular approximation (ZORA) to the Dirac equation [54]. ZORA results for TiF_3 [54] have been found to be in nice agreement with the perturbation treatment due to Belanzoni et al. [33]. The performance of the DFT-ZORA approach for the HFCC calculations has been validated for a set of 22 small metal compounds by Belanzoni et al. [55] including the ScO complex for which very small relativistic contributions have been found. This was expected since the *g*-value of ScO is very close to the free-electron *g*-value g_e [55, 56]; for the same reason we also expect small SO effects for the other complexes discussed above. On the other hand, substantial SO effects were found especially for late 3d elements like Ni [57].

A limitation of the ZORA formalism is that spin polarization and SO coupling currently cannot be introduced at the same time, and the formalism has been worked out only for a single unpaired electron. Both restrictions are absent in the coupled-perturbed Kohn–Sham implementation of SO contributions to HFCCs due to Neese [58]. Validation calculations on a set of 3d transition metal complexes

HFCCs have been found in reasonable to good agreement with the experimental data, with the main error being probably due to the Fermi contact term [58]. For systems involving still heavier elements, besides SO coupling scalar relativistic contributions also become of importance, as shown in a systematic study for a series of 4s, 5s, and 6s radicals by Belanzoni et al. [55]. Very recently, the calculation of HFCCs withthin the four-component formulation of the Dirac–Hartree–Fock (DHF) approximation has been implemented and validated by Quiney and Belanzoni [59]. Results for a test set of transition metal compounds are in good agreement with experiment; the existing discrepancies are attributed to the neglect of higher-order core polarization effects as well as to the lack of electron correlation.

Calculations of EPR parameters for transition metal complexes are now becoming increasingly important in studies of biological systems. A lucid discussion of the applications can be found in a recent review by Neese [60], as well as in Chapter 36 by the same author.

29.4 Concluding Remarks

Judging the performance of DFT in calculations of HFCCs from the perspective of transition metal HFCCs, unfortunately none of the v_{xc} tested so far provides acceptable results for all compounds considered. Moreover, for some particularly difficult systems, essentially none of the functionals has been found to be truly appropriate. The core of the problem seems to be in the spin-polarization vs. spin-contamination dilemma that is a challenge to a single-determinant description of HFCCs. On the other hand, for a significant number of transition metal complexes, a 10–15% agreement with experiment may be obtained with a wide class of functionals along with appropriate but not necessarily very large basis sets. For other subsets of complexes, a qualitative electronic structure analysis may suggest a pragmatic choice of the range of functionals (like the B3-type or BH-type hybrids) appropriate for HFCC calculations. It should also be noted that reproducing trends in HFCCs as functions of structural/electronegativity parameters appears much easier than matching their absolute values. Such correlations may often be achieved with a wide range of functionals [61–63].

For many light main-group radicals, DFT methods provide isotropic and dipolar HFCCs as good as high-level MRCI or CCSD(T) results. This may be partly due to favorable error cancellation. It is in any case necessary to select an appropriate functional. The most recommended candidates are PWP86 within the GGA family, and B3LYP or PBE0 among the hybrid functionals. The results provided by other GGA functionals deviate usually more from the reference data for heavier atoms than for hydrogen. The deviations turn out to be relatively small for hydrocarbon π-radicals and larger for systems containing electronegative elements like N, O and F. Calculations on isolated atoms are most demanding regarding both the requirements on functional and on basis set. All of these conclusions are based on validation studies performed using GTO basis sets. A few studies on a limited class of systems with

STO basis sets reveal a much better performance of the BP86 GGA functional than found with GTOs, providing HFCCs close to the best PWP86 or B3LYP results. In order to understand the better performance of the BP86/STO calculations compared to the available BP86/GTO studies, the results should be analyzed and studied in terms of their basis-set convergence. It would also be highly interesting to explore the performance of further functionals in calculations with STOs. Finally, it is important to note that the DFT results for HFCCs of light main group systems come very close to the most accurate *ab initio* calculations only in cases where the HF configuration dominates for the latter. Where large MRCI calculations with many reference determinants are required to get highly accurate data, DFT also fails and predicts HFCCs with a quality between single-reference CISD, QCISD(T), or CCSD(T) [49]. Such "difficult systems" remain a challenge and a stimulation for new developments in density functional theory.

Acknowledgment

This work was supported by grant LN00A016 from the Ministry of Education of the Czech Republic.

References

1 W. Meyer, *J. Chem. Phys.* **1969**, *51*, 5149.
2 a) D. A. Case, M. Karplus, *J. Am. Chem. Soc.* **1977**, *99*, 6182; b) P. J. M. Geurts, P. C. P. Bouten, A. van der Avoird, *J. Chem. Phys* **1980**, *73*, 1306; c) J. Weber, A. Goursot, E. Pénigault et al. *J. Am. Chem. Soc.* **1982**, *104*, 1491.
3 V. G. Malkin, O. L. Malkina, L. A. Eriksson et al. in *Theoretical and Computational Chemistry, Vol. 1, Density Functional Calculations*, eds. Seminario, J. M.; Politzer, P., Elsevier, Amsterdam **1995**, pp. 273–347.
4 V. Barone, in *Recent Advances in Density Functional Methods, Part 1*, ed. D. P. Chong, World Scientific, Singapore 1995, p. 287.
5 B. Engels, L. A. Eriksson, S. Lunell, *Adv. Quantum Chem.* **1996**, *27*, 297.
6 W. Koch, M. Holthausen, *A Chemist's Guide to Density Functional Theory*, Wiley-VCH, Weinheim **2000**, p. 209.
7 M. Munzarová, M. Kaupp, *J. Phys. Chem. A* **1999**, *48*, 9966.
8 P. Hohenberg, W. Kohn, *Phys. Rev. B* **1964**, *136*, 864.
9 W. Kohn, L. J. Sham, *Phys. Rev. A* **1965**, *140*, 1133.
10 J. C. Slater, *Quantum Theory of Molecules and Solids, Vol. 4: The Self-Consistent Field for Molecules and Solids*, McGraw-Hill, New York **1974**.
11 S. H. Vosko, L. Wilk, M. Nusair, *Can. J. Phys.* **1980**, *58*, 1200.
12 J. P. Perdew, Y. Wang, *Phys. Rev. B* **1986**, *33*, 8822; J. P. Perdew, Y. Wang, *Phys. Rev. B* **1986**, *34*, 7406.
13 C. Lee, W. Yang, G. R. Parr, *Phys, Rev. B* **1988**, *37*, 785; B. Miehlich, A. Savin, H. Stoll et al. *Chem. Phys. Lett.* **1989**, *157*, 200.
14 J. P. Perdew, *Physica B* **1992**, *172*, 1; J. P. Perdew, in *Electronic Structure of Solids '91*, eds. P. Ziesche, H. Eschring, Akademie Verlag, Berlin 1991; J. P. Perdew, Y. Wang, *Phys. Rev. B* **1992**, *45*, 13244.
15 J. P.Perdew, Y. Wang, *Phys. Rev. B* **1986**, *33*, 8800.
16 J. P. Perdew, in *Electronic Structure of Solids*, eds. P. Ziesche, H. Eschrig, Akademie Verlag, Berlin **1991**.
17 A. D. Becke, *Phys. Rev. A* **1988**, *38*, 3098.

18 C. Adamo, V. Barone, *J. Chem. Phys.* **1998**, *108*, 664.
19 P. M. W. Gill, R. D. Adamson, *Chem. Phys. Lett.* **1996**, *261*, 105.
20 A. V. Arbouznikov, M. Kaupp, V. G. Malkin et al. *Phys. Chem. Chem. Phys.* **2002**, *4*, 5467.
21 A. D. Becke, *J. Chem. Phys.* **1993**, *98*, 5648.
22 A. D. Becke, *J. Chem. Phys.* **1993**, *98*, 1372.
23 A. D. Becke, *J. Chem. Phys.* **1996**, *104*, 1040.
24 C. Adamo, V. Barone, *J. Chem. Phys.* **1998**, *108*, 664.
25 C. Adamo, V. Barone, *J. Chem. Phys.* **1999**, *110*, 6158.
26 J. P. Perdew, K. Burke, M. Ernzerhof, *Phys. Rev. Lett.* **1996**, *77*, 3865; J. P. Perdew, K. Burke, M. Ernzerhof, *Phys. Rev. Lett.* **1997**, *78*, 1396.
27 L. A. Eriksson, O. L. Malkina, V. G. Malkin et al., *J. Chem. Phys.* **1994**, *100*, 5066.
28 H. U. Suter, V. Pless, M. Ernzerhof et al., *Chem. Phys. Lett.* **1994**, *230*, 398.
29 N. Ishii, T. Shimizu, *Phys. Rev. A* **1993**, *48*, 1691.
30 N. Ishii, T. Shimitzu, *Chem. Phys. Lett.* **1994**, *225*, 462.
31 I. Ishii, T. Shimitzu, *Chem. Phys. Lett.* **1995**, *235*, 614.
32 P. Belanzoni, E. J. Baerends, M. Gribnau, *J. Phys. Chem. A* **1999**, *103*, 3732.
33 P. Belanzoni, E. J. Baerends, S. van Asselt et al., *J. Phys. Chem.* **1995**, *99*, 13094.
34 F. Himo, L. A. Eriksson, *J. Chem. Soc., Faraday Trans.* **1995**, *91*, 4343.
35 M. T. Nguyen, S. Creve, L. C. Vanquickenborne, *J. Phys. Chem. A* **1997**, *101*, 3174.
36 M. Engström, O. Vahtras, H. Ågren, *Chem. Phys. Lett.* **2000**, *328*, 483.
37 D. M. Chipman, *J. Chem. Phys.* **1983**, *78*, 3112.
38 L. A. Eriksson, V. G. Malkin, O. L. Malkina et al., *Int. J. Quantum Chem.* **1994**, *52*, 879.
39 a) K. R. Leopold, K. M. Evenson, E. R. Comben et al., *J. Mol. Spectrosc.* **1997**, *122*, 440; b) J. A. Coxon, K. V. L. N. Sastry, J. A. Austin et al., *Can. J. Phys.* **1979**, *57*, 619.
40 S. D. Wetmore, L. A. Eriksson, R. J. Boyd, *J. Chem. Phys.* **1998**, *109*, 9451.
41 D. Feller, E. D. Glendening, E. A. McCullogh, Jr., et al., *J. Chem. Phys.* **1993**, *99*, 2829.
42 L. A. Eriksson, A. Laakonsen, in *Recent Research Developments in Physical Chemistry, Vol. 2*, 1998, ed. S. G. Pandalai, Transworld Research Network, Trivandrum **1998**, p. 369.
43 V. G. Malkin, O. L. Malkina, D. R. Salahub, *Chem. Phys. Lett.* **1994**, *221*, 91.
44 D. Feller, *J. Chem. Phys.* **1990**, *93*, 579.
45 H. Chermette, I. Ciofini, F. Mariotti et al., *J. Chem. Phys. 2001*, **115**, 11068.
46 S. D. Wetmore, R. J. Boyd, L. A. Eriksson, *J. Chem. Phys.* **1997**, *106*, 7738.
47 L. A. Eriksson, F. Himo, *Trends in Phys. Chem.* **1997**, *6*, 153.
48 C. Adamo, V. Barone, A. Fortunelli, *J. Chem. Phys.* **1995**, *102*, 384.
49 L. A. Eriksson, in *Density-functional Methods in Chemistry and Materials Science*, ed. M. Springborg, Wiley & Sons, New York **1997**, p. 125.
50 V. Barone, *Chem. Phys. Lett.* **1996**, *262*, 201.
51 V. Barone, A. Bencini, I. Ciofini et al., *J. Phys. Chem. A* **1999**, *103*, 4275.
52 G. A. A. Saracino, A. Tedeschi, G. D'Errico et al., *J. Phys. Chem. A* **2002**, *106*, 10700.
53 A. V. Arbouznikov, M. Kaupp, V. G. Malkin et al., *Phys. Chem. Chem. Phys.* **2002**, *4*, 5467.
54 E. van Lenthe, A. van der Avoird, P. E. S. Wormer, *J. Chem. Phys.* **1998**, *108*, 4783.
55 P. Belanzoni, E. van Lenthe, E. J. Baerends, *J. Chem. Phys.* **2001**, *114*, 4421.
56 A. Abragam, B. Bleaney, *Electron Paramagnetic Resonance of Transition Ions*, Clarendon Press, Oxford **1970**.
57 M. Stein, E. van Lenthe, E. J. Baerends et al., *J. Phys. Chem. A* **2001**, *105*, 416.
58 F. Neese, *J. Chem. Phys.* **2003**, *118*, 3939.
59 H. M. Quiney, P. Belanzoni, *Chem. Phys. Lett.* **2002**, *353*, 253.
60 F. Neese, *Curr. Opin. Chem. Biol.* **2003**, *7*, 125.
61 M. L. Munzarová, M. Kaupp, *J. Phys. Chem. B* **2001**, 105, 12644.
62 a) P. J. Carl, S. L. Isley, S. Larsen, *J. Phys. Chem. A* **2001**, *105*, 4563; b) A. C. Saladino, S. C. Larsen, *J. Phys. Chem. A* **2002**, *106*, 10444.
63 J. Swann, T. D. Westmoreland, *Inorg. Chem.* **1997**, *36*, 5348.
64 S. A. Perera, J. D. Watts, R. J. Bartlett *J. Chem. Phys.* **1994**, *100*, 1425.
65 F. W.King, *Phys. Rev. A* **1989**, *40*, 1735.
66 J. S. M. Harvey, L. Evans, H. Lew, *Can. J. Phys.* **1972**, *50*, 1719.
67 W. R. M. Graham, W. Weltner, Jr., *J. Chem. Phys.* **1976**, *65*, 1516.
68 G. Wolber, H. Figger, R. A. Haberstroh et al., *Z. Physik* **1970**, *236*, 337.
69 J. R. Macdonald, R. M. Golding, *Theoret. Chim. Acta* **1978**, *47*, 1.

70 J. M. Hirsch, G. H. Zimmerman III, D. J. Larson et al., *Phys. Rev. A*. **1977**, *16*, 484.

71 W. W. Holloway, Jr., E. Lüscher, R. Novick, *Phys. Rev.* **1962**, *126*, 2109.

72 J. S. M. Harvey, *Proc. R. Soc. London, Ser. A* **1965**, *285*, 581.

73 C. Adamo, V. Barone, A. Fortunelli, *J. Chem. Phys.* **1995**, *102*, 384.

74 C. Adamo, V. Barone, A. Fortunelli, *J. Phys. Chem.* **1994**, *98*, 8648.

75 C. Adamo, M. Cossi, V. Barone, *J. Mol. Struct. Theochem.* **1999**, *493*, 145.

76 S. A. Perera, L. M. Salemi, R. Bartlett, *J. Chem. Phys.* **1997**, *106*, 4061.

77 Experimental A_{iso}: a) R. W. Fessenden, R. H. Schuler, *J. Chem. Phys.* **1963**, *39*, 2147; b) R. W. Fessenden, *J. Phys. Chem.* **1967**, *71*, 74; c) W. Weltner, Jr., *Magnetic Atoms and Molecules*, Dover Publications, Mineola, NY **1983**. The observed isotropic values have been corrected (Ref. [37]) to remove the large effect of ν_2 vibrational averaging. Experimental bond length: d) E. Hirota, C. Yamada, *J. Mol. Spectrosc.* **1985**, *96*, 175 and references therein.

78 a) P. Millie, G. Berthier, *Int. J. Quantum Chem. Symp.* **1968**, *2*, 67; b) P. Millie, B. Levy, G. Berthier, *Int. J. Quantum Chem.* **1972**, *6*, 155.

79 M. L. Munzarová, unpublished results using the Gaussian 98 DFT-implementation of EPR HFCCs. For geometry optimizations, the 6-311G(d,p) basis set has been employed.

80 D. M. Chipman, personal communication to S. A. Perera, L. M. Salemi and R. J. Bartlett (see Ref. 76).

81 H. J. McManus, R. W. Fessenden, D. M. Chipman, *J. Phys. Chem.* **1988**, *92*, 3778.

82 E. Hirota, C. Yamada, M. Okunishi, *J. Chem. Phys.* **1992**, *97*, 2963.

83 H. Sekino, R. J. Bartlett, *J. Chem. Phys.* **1985**, *82*, 4225.

84 S. D. Wetmore, L. A. Eriksson, R. J. Boyd, *J. Chem. Phys.* **1998**, *109*, 9451.

85 a) V. Barone, *J. Chem. Phys.* **1994**, *101*, 6834; b) V. Barone, *Chem. Phys. Lett.* **1994**, *226*, 392.

86 L. B. Knight, J. Steadman, *J. Chem. Phys.* **1983**, *78*, 5940.

87 V. Barone, *Theor. Chim. Acta* **1995**, 91, 113.

88 L. B. Knight, J. Steadman, *J. Chem. Phys.* **1984** *80*, 1018.

89 D. Feller, E. R. Davidson, *Theor. Chim. Acta* **1985**, *68*, 57.

30
Ab Initio Post-Hartree–Fock Calculations of Hyperfine Coupling Tensors and Their Comparison with DFT Approaches

Bernd Engels

30.1
Introduction

The measurement of the hyperfine interaction offers information about the electronic structure of radicals since the associated hyperfine coupling constants (HFCCs) provide a map of the spin distribution in the systems [1, 2]. The isotropic HFCC [3]

$$A_{\mathrm{iso}}(N) = \frac{4}{3}\beta_{\mathrm{e}}\beta_{\mathrm{N}}g_{\mathrm{e}}g_{\mathrm{N}}\langle S_Z\rangle^{-1}\langle\Psi|\delta(r_N)S_Z|\Psi\rangle \tag{30.1}$$

gives the spin density at each nucleus N. It is also termed the Fermi contact term or simply contact interaction. In Eq. (30.1) β_{e} is the Bohr magneton, β_{N} is the nuclear magneton, g_{e} is the free-electron g-value (2.002 319 31), g_{N} is the nuclear g-value, and $\langle S_Z\rangle$ is the expectation value of the z-component of the total electronic spin. Finally, $\delta(r_N)$ is the Dirac delta function which picks out the value of the wavefunction at r_N so that $\langle\Psi|\delta(r_N)S_Z|\Psi\rangle$ gives the spin density at the position of nucleus N.

The anisotropic HFCCs in Cartesian coordinates k, l are given as [3]

$$A_{kl}(N) = \beta_{\mathrm{e}}\beta_{\mathrm{N}}g_{\mathrm{e}}g_{\mathrm{N}}\langle S_Z\rangle^{-1}\left\langle\Psi\left|\mathbf{r}_N^{-5}\left(\mathbf{r}_N^2\delta_{kl} - 3r_{N,k}r_{N,l}\right)S_Z\right|\Psi\right\rangle \tag{30.2}$$

They contain information about the spin density in the environment of the nuclei. In ab initio calculations for main group elements it is found that anisotropic HFCCs mainly depend on the quality of the atomic orbital (AO) basis set, while they are quite insensitive to the theoretical approach used for the calculation. The isotropic HFCC A_{iso} depends strongly on the chosen basis set *and* on the theoretical method if the unpaired electrons occupy orbitals which have π character within the vicinity of the nuclei under consideration [4–8]. For such systems the isotropic HFCC vanishes at the restricted Hartree–Fock (RHF) level since the value of such an

Calculation of NMR and EPR Parameters. Theory and Applications.
Edited by Martin Kaupp, Michael Bühl, Vladimir G. Malkin
Copyright © 2004 WILEY-VCH Verlag GmbH & Co. KGaA, Weinheim
ISBN: 3-527-30779-6

orbital at the nucleus is zero and RHF does not describe spin polarization[1)] by which spin density could be transferred to orbitals with s-character (which can contribute to A_{iso}). The unrestricted Hartree–Fock approach (UHF) allows for such spin polarization but largely overestimates the effects (and tends to lead to spin contamination). The computation of A_{iso} is further complicated by the fact that for atoms of the second row of the Periodic Table the contributions to A_{iso} arising from the spin polarization of the 1s and 2s shells are similar in magnitude but possess opposite signs [10]. For radicals with open shell σ orbitals the computation of the isotropic HFCC is much easier since spin polarization effects only contribute about 10–20% of the total value so that RHF already provides reasonable values [4, 8, 11–13].

To some extent the difficulties connected with reliable computations of A_{iso} can also be traced back to the fact that the Dirac delta function $\delta(r_N)$ evaluates the wavefunction only at a single point. As a consequence no error cancellation, which often takes place for other one-electron properties, can occur. Operator expressions that compute A_{iso} by integrating over parts of the wavefunction are discussed in Chapter 31 by Rassolov and Chipman. They seem to depend less on the theoretical approach. In the present chapter A_{iso} is computed from the trace of the tensor of the anisotropic HFCCs expressed in cartesian coordinates.

Currently, most theoretical investigations employ DFT approaches to compute the HFCCs as described in Chapter 29 by Munzarová. The reason is that current functionals provide astonishingly good isotropic HFCCs for a large variety of systems, while approaches based on the wavefunction, such as multi-reference configuration interaction (MR-CI) or coupled cluster (CC) approaches, show a slow convergence with respect to the level of sophistication [11, 12]. However, the tremendous success of DFT quite often seems to result from fortuitous error cancellation. In some cases the cancellation does not work so that large residual errors are found. Therefore, ab initio approaches are still of interest for benchmark calculations and for a better understanding of the error cancellations in DFT. The latter is important to foresee the cases where the error cancellation breaks down. In the present chapter we will focus on problems which arise for MR-CI approaches since they also provide an insight into the effects responsible for the difficulties of other methods, e.g. for the coupled cluster approach. Finally, we use the ground state of H_2CN ($^2B_2$) to discuss error compensations in DFT.

1) Spin polarization comprises the effects which result because the interaction between electrons with equal spins are slightly different from the interaction between electrons possessing opposite spin. As a consequence, in a system with an unpaired electron, two paired electrons of a doubly occupied orbital interact somewhat differently with the unpaired electron. In the unrestricted Hartree–Fock approach (UHF), which allows different radial expansions for the two paired electrons, this effect is considered. Since the restricted Hartree–Fock (RHF) approach forces both spatial expansions to be equal, the effect cannot be considered. Consequently, in the RHF method, spin polarization effects appear as correlation effects but in UHF they are already included in the orbitals. A nice phenomenological explanation can be found in Ref. [3]. A description of the more technical differences in UHF and RHF can be taken from Ref. [9].

30.2 Problems Appearing in MR-CI Computations of A_{iso}

After various investigations it became clear that reliable ab initio computations of the isotropic hyperfine interaction require the consideration of higher than double excitations [4–8, 10, 11, 14]. As a consequence, multi-reference configuration interaction (MR-CI) approaches need large reference spaces. With individually selecting CI approaches, in which the configurations are selected due to their importance for the energy, nearly all configurations have to be considered to obtain accurate isotropic HFCCs. This represents a much stronger dependence than found for other one-electron properties. In coupled cluster approaches quite often the CCSD level is already accurate[2)] but sometimes also triple substitutions (CCSD(T)-approach) have to be included. It is quite intriguing that a CI treatment which considers only all single excitations (S-CI[3)]) as used by Chipman [15] gives isotropic HFCCs which are in excellent agreement with experiment [8]. Computations for the ground state of the CH molecule ($X\ ^2\Pi$) show that this results from an error cancellation [15, 16]. For the carbon center the S-CI approach gives an isotropic HFCC of about 41 MHz. It is in good agreement with the experimental value of 46.7 MHz ±2 MHz. However, if the wavefunction is improved by including all double excitations with respect to the RHF configuration the value drops to about 30 MHz. A nearly converged value of about 45 MHz is only found if all triple excitations are also taken into consideration.

Computations for the boron atom (^2P_u) and the nitrogen atom (^4S_u) provide more insight into the various effects. Second-row atoms turned out to be quite troublesome (also for DFT computations) and were used as test systems by some groups [5, 6, 14, 15, 17]. The AO basis sets used for the present study consist of a 13s8p basis contracted to an [8s5p] set. They were augmented by two d functions (boron: 0.2 / 0.8; carbon: 0.318 / 1.097; nitrogen: 0.5 / 1.9) [6, 18]. The basis sets were chosen to include the most important features necessary for the computation of HFCCs [7, 10], while keeping the cost of the calculations reasonable. All calculations were performed employing natural orbitals (NO) as underlying one-particle basis.

Table 30.1 summarizes the computed values of A_{iso} for the two systems as a function of the CI treatment. The RHF treatment (not given) gives zero for all systems since the singly occupied p orbitals vanish at the position of the nuclei. Consequently, only spin polarization effects can contribute. Taking the nitrogen system as an example it is seen that the agreement with the experimental value gets worse as we go from the S-CI treatment to a SD-CI treatment. An improvement is found if

2) It is important to note that within the framework of the coupled cluster approach higher excitations are always taken into account. As a consequence CCSD already includes, e.g., the influence of higher excitations on the coefficients of single substitutions.

3) In the present paper the expression "excitation" is used for a replacement at the spatial orbital level as used, e.g., by Chipman [15]. In the case of a single excitation at the spatial orbital level, it has to be kept in mind that for an open shell system at least one of the arising determinants represents a higher than single excitation with respect to the RHF determinant. More information can be found in Refs. [12, 15].

triple excitations are taken into account. The influence of further quadruple excitations seems to be small which can be seen if the MR-CI value is compared with the SDT-CI result. The remaining differences with respect to the experimental results are due to basis set deficiencies [5–7, 20]. Similar behavior is found for the carbon system (not given) [12, 17]. For boron, SD-CI shows an improvement with respect to S-CI but both approaches even predict the wrong sign of the isotropic HFCCs. Again a real improvement is only found if triple substitutions are considered.

To understand the variations as a function of wavefunction quality, the influence of the different excitations on A_{iso} is important. Going from an S-CI to an SD-CI treatment, two effects of the double excitations exist [17]. A *direct effect* arises from the double excitations themselves. Furthermore, since within the SD-CI treatment the coefficients of the single excitations are optimized considering their interactions with the double excitations, their values in the S-CI wavefunction are different compared to their values in the SD-CI wavefunction. These alterations also influence the value of A_{iso}. In the following this effect will be called *indirect effect*. Both effects can be separated. The indirect effect can be computed if one projects the configurations of the S-CI out of the SD-CI wavefunction and renormalizes. The indirect effect then is the difference between the values obtained with the S-CI and the projected wavefunction. Please note that the renormalization has only minor effects.

The size of the indirect effect of the double, triple and even higher excitations on the coefficients of the single excitations can be taken from Table 30.2. If the coefficients of the single excitations are taken from the S-CI wavefunction (S-WF, S-CI in Table 30.2) for the ^2P_u state of the boron atom, a value of -3.2 MHz is computed. If the coefficients are projected out of an SD-CI wavefunction (S-WF from SD-CI in Table 30.2), the value drops to –20.5 MHz showing that the indirect influence of the doubly excited configurations leads to a change in A_{iso} of about –17 MHz. Taking the coefficients of the singly excited configurations from an SDT-CI the isotropic HFCC of the boron atom is predicted to be –15.2 MHz. This shows that due to the interaction with triple excitations the coefficients of the single substitutions also change considerably. It is unclear whether this effect results from a direct interaction between the single and triple excitations or whether it is indirectly induced via

Table 30.1 Isotropic hyperfine coupling constants for the ground states of the boron atom (^2P_u) and nitrogen atom (^4S_g) using different levels of the CI treatment.

CI-Treatment	A_{iso} (in MHz)	
	B (^2P_u)	N (^4S_g)
S-CI	–3.2	5.4
SD-CI	–1.3	3.9
SDT-CI	5.2	7.8
MR-CI	6.5	7.8
Exp	11.6[a]	10.4[b]

a) Ref. [14].
b) Ref. [18].

the double excitations. This consideration also shows that a wavefunction-based method can only be reliable for computations of isotropic HFCCs if it provides accurate coefficients for the singly excited configurations.

A similar discussion to that for the singly excited configurations could also be applied for the other excitation classes, however, a separation of the various effects becomes more complicated. Such information can be obtained if the various contributions of the excitation classes to A_{iso} are considered. Since A_{iso} is a one-electron property, it can be written as a sum over matrix elements between configurations belonging to the same excitation class or differing by one excitation:

$$\begin{aligned}\left\langle A_{\mathrm{iso}}\right\rangle \sim & \sum_{i,r} c_0 c_i^r \langle i|\delta(r-r_N)S_z|r\rangle \\ & + \sum_{i,r} c_i^r c_i^r \sum_a \langle a|\delta(r-r_N)S_z|a\rangle \\ & + \sum_{i,r<s} c_i^r c_i^s \langle r|\delta(r-r_N)S_z|s\rangle \\ & + \sum_{i<j,r} c_i^r c_j^r \langle i|\delta(r-r_N)S_z|j\rangle \\ & + \sum_{i<j,r<s} c_i^r c_{ij}^{rs} \langle j|\delta(r-r_N)S_z|s\rangle \\ & + \cdots\end{aligned} \tag{30.3}$$

In Eq. (30.3) *i, j* and *r, s* indicate the orbitals involved in the excitations. The first term in Eq. (30.3) gives the contribution arising from matrix elements between the RHF determinant and the single excitation (singles-RHF), while the following three terms contain the contributions resulting from matrix elements between single excitations amongst themselves (singles–singles). The last term gives the singles–doubles contributions. Further contributions arising from doubles–doubles, doubles–triples, etc. are straightforward. It should be kept in mind that the contribution from the diagonal matrix element of the RHF determinant in the cases considered in the present work is zero.

Table 30.2 Indirect influence of double and triple excitations on A_{iso} for the ground states of the boron and the nitrogen atom. All values were obtained with a wavefunction including the RHF determinant and all single excitations. They were projected out of the wavefunction obtained by different CI treatments.

CI-treatment for Coefficients	A_{iso} (in MHz)	
	B (^2P_u)	N (^4S_u)
S-CI	–3.2	5.4
SD-CI	–20.5	–3.2
SDT-CI	–15.2	–0.3
MR-CI	–14.9	–0.2

Table 30.3 summarizes the size of the various contributions obtained with different wavefunctions. The indirect influence of the doubles and of the triples on the coefficients of the singles, which we already discussed above, can be seen from the variations of the terms singles–RHF and singles–singles depending on the wavefunction. It is seen that mainly the contribution from the singles–RHF matrix elements changes. It varies from –11.4 MHz (S-CI) to –29.1 MHz (SD-CI) to –24.7 MHz (SDT-CI) while the contribution from the single–single matrix elements stays more or less constant. Since the coefficients of the single excitations appear in both terms the variations in the singles–singles contribution arising due to the variations in the coefficients either average out or are too small. This may arise since for the singles–singles contributions two small coefficients are always multiplied while for the singles-RHF matrix elements the small coefficients of the single excitations are multiplied by the large coefficient of the RHF configuration.

The direct contribution of the double excitations (sum of doubles–singles and doubles–doubles) is around 19 MHz. It does not change much if one takes the coefficients from an SD-CI or an SDT-CI calculation. This shows that the indirect influence of the triples on the doubles is quite small. However, we cannot rule out that cancellation effects also occur here. Table 30.3 also shows that the direct contribution of the triples (triples–doubles and triples–triples) can be neglected. As discussed previously, the influence of even higher excitations can also be neglected.

In summary a wavefunction-based method designed to give accurate isotropic HFCCs must be able to provide very accurate coefficients for the singly and doubly

Table 30.3 Decomposition of the various contributions to A_{iso} of the boron and nitrogen atoms.

	A_{iso} [MHz]	
Approach/Contribution	B (^2P_u)	N (^4S_u)
S-CI	–3.2	5.4
singles–RHF[a]	–11.4	1.1
singles–singles	8.2	4.3
SD-CI	–1.3	3.9
singles–RHF	–29.1	–6.6
singles–singles	8.6	3.3
doubles–singles	6.3	3.3
SDT-CI	5.2	7.7
singles–RHF	–24.7	–4.1
singles–singles	9.5	3.7
doubles–singles	7.6	3.7
doubles–doubles	13.3	4.2
triples–doubles	–0.7	0.2
triples–triples	0.2	0.1

a) Singles-RHF summarizes all contributions to A_{iso} arising from the first term of Eq. (30.3), while singles–singles gives the contribution due to the second term and so on.

Table 30.4 Theoretical HFCCs (in MHz) for the ground state of CCO ($^3\Sigma_u^-$). ($A_\perp = A_{iso} + A_{zz}$, $A_{||} = -1/2\, A_{zz}$).

$C_\alpha C_\beta O$		C_α			C_β			O	
	A_{iso}	$A_\perp$	$A_{||}$	A_{iso}	$A_\perp$	$A_{||}$	A_{iso}	$A_\perp$	$A_{||}$
S-CI	17.3	43.7	−35.5	−33.8	−32.4	−36.6	−26.6	−43.3	6.8
SD-CI	−8.0	17.9	−59.7	−34.8	−32.0	−40.2	−5.2	−17.7	19.8
MRD-CI	−7.8	17.9	−59.3	−34.0	−31.7	−38.7	−12.7	−26.8	15.7
MRD-CI/B_K	30.7	56.3	−20.7	−30.7	−29.6	−32.9	−23.8	−41.3	11.2
Exp.		57(3)	−17(3)		−26(3)	−32 (3)	–	–	–

excited determinants. The direct contribution of triples and even higher excitations can be neglected but the influence of these excitations on the coefficients of the single excitations is necessary. Such a method is the MRD-B_K method [16, 21]. In a first step, an individually selecting MR-CI is used to select an appropriate CI wavefunction out of the full MR-CI space. In the second step, the B_K method [22] is used to correct the coefficients of this wavefunction by considering the indirect influence of the neglected configurations. With this approach it is possible to predict very accurate values for A_{iso} with quite compact wavefunctions including only up to 3×10^4 configuration state functions. In most applications the accuracy of this approach was found to be comparable to that of the CCSD(T) or QCISD(T) approach [12, 16, 21, 23]. A description of the underlying theory can be found elsewhere [12, 16, 21]. As an example for the accuracy of the MRD-CI/B_K method, Table 30.4 gives the HFCCs of the CCO molecule in its $^3\Sigma_u^-$ groundstate [24]. Other examples can be taken from the literature [12, 25]. Table 30.4 again reflects the error compensations found within a S-CI, which brings the values into a much better agreement with the experimental values than the computed values of a SD-CI. However, it is also obvious that the error compensation is not sufficient in this case. Similar behavior was also found for other triplet molecules [24].

30.3 Error Cancellations in Computations of A_{iso} with DFT

As already mentioned, DFT quite often predicts very accurate isotropic HFCCs which is quite astonishing taking into account the problems found for wavefunction-based methods. It is even stranger that DFT predicts especially accurate proton HFCCs which are very problematic for wavefunction-based methods [12]. This is a very valuable feature for DFT since in most cases only the isotropic HFCCs of the protons are known. Table 30.5 summarizes results for H_2CN as an example. It shows that both RHF and UHF fail completely. The GGA functionals BLYP and BP86 predict the proton couplings extremely accurately but are not able to provide good coupling constants for the heavier atoms. For the heavier centers their accuracy is only comparable to the MRD-CI approach which possesses large errors for all centers. If the wavefunction is corrected by the MRD-CI/B_K approach, the predicted isotropic HFCCs

for the heavier centers are in very good agreement with experiment but for the proton couplings still larger errors are found. To get a feeling for the differences it is important to distinguish between contributions arising directly from the singly occupied orbital (SOMO) and those resulting from spin polarization effects. In H_2CN the SOMO is mainly centered at the nitrogen atom and represents a $\pi_{\text{in plane}}$ orbital i.e. it vanishes at the position of both heavier centers but not at the position of both protons. As a consequence the isotropic HFCCs of the heavier centers are solely determined by spin polarization effects, while contributions from the SOMO and from spin polarization effects are important for the hydrogen nuclei. The direct contributions from the SOMO are also given in Table 30.5 (H^{SOMO}, right-hand side). Comparing both contributions to the HFCCs of the hydrogen centers it is obvious that in comparison to MRD-CI/B_K both DFT approaches possess much higher contributions from the SOMO but considerably lower contributions due to spin polarization effects. A definite statement on which approach is right is not possible since for the isotropic HFCCs of the hydrogen atoms only the sum of both contributions represents a measurable quantity. However, some insight can be gained from the isotropic HFCCs of the heavier centers. Here the direct contribution vanishes so that the strength of the spin polarization is directly measurable. The fact that for the heavier centers the spin polarization effects of the MRD-CI/B_K method are also much larger than those described by DFT, might point to a deficiency of the current functionals. For the hydrogen centers, this is canceled by an overestimation of the contributions from the SOMO. Taking into account that the spin polarization effects at the heavier centers arise due to non-local interaction their underestimation is in line with the well known difficulties of DFT in describing such interactions [28].

Two other error compensations which appear quite often in DFT should also be addressed. One is connected with properties of the UHF approach. From Table 30.5 it is seen that the UHF approach largely overestimates all isotropic HFCCs. From this it is obvious (see also the discussion in Chapter 29 by Munzarová) why hybrid functionals (e.g. B3LYP), which are obtained from a combination of a pure GGA

Table 30.5 Isotropic HFCCs of H_2CN ($^2B_2$). For all computations we used the MCSCF-ACPF/Duij geometry described in Ref. [26]. All values given in G. All calculations were performed with an AO basis optimized for the computation of isotropic HFCCs [6, 7, 10, 18]. The experimental values are taken from Ref. [27].

Approach	C	N	H	$H^{SOMO\ a}$
ROHF	0	0	31	31
UHF	–69	26	102	83
BLYP	–21	7	84	63
BP86	–19	4	80	63
MRD–CI	–20	4	61	41
MRD–CI/B_k	–28	9	74	41
Exp.	–29	9	83	–

a) Contribution from the singly occupied orbital (SOMO).

functional (e.g. BLYP) with UHF, in most cases exhibit much higher spin polarization effects than pure GGA functionals. However, in our opinion, this also represents an error compensation since the underestimation of the GGA is coupled with the overestimation of the UHF. Finally, as discussed in some length in Refs. [12, 29], it is found that DFT predictions of isotropic HFCCs are even better if the underlying geometry is not taken from a high level *ab initio* approach but optimized using the DFT method itself. However, as already discussed in Ref. [30], very often these geometries are not as good as the *ab initio* data.

30.4 Concluding Remarks

In the present chapter we have discussed problems which appear within MR-CI computations of isotropic HFCCs, A_{iso}. We focused on the MR-CI method since its problems also provide insight into effects responsible for difficulties of other wavefunction-based methods. We have shown that wavefunction-based methods designed to give accurate isotropic HFCCs must be able to provide very accurate coefficients for the determinants representing single and double excitations with respect to the RHF determinant. Higher excitations (triples, etc.) do not contribute directly to A_{iso} but are only important since they indirectly influence the coefficients of the single excitations within the MR-CI treatment. As a consequence, approaches which take such effects into account but neglect the higher excitations within the wavefunction already give very accurate predictions for A_{iso}. As an example we discussed results given by the MRD-CI/B_K approach. This finding also explains why CCSD approaches give very accurate results for A_{iso} in most cases while the CISD method fails in nearly all cases. We also discussed the error compensations appearing in an S-CI approach.

In the second part of the paper we discussed error cancellations appearing in DFT approaches. Results for the H_2CN molecule indicate that the current functionals underestimate spin polarization effects. However, for protons in a β position with respect to the radical center, this error is often compensated by higher direct contributions from the singly occupied orbital. The orbital provided by DFT seems to be somewhat more compact than the corresponding orbitals obtained from ab initio methods (e.g. Hartree–Fock, natural or CASSCF orbitals). Additional error compensation arising from geometrical parameters or with hybrid functionals were also addressed. Nevertheless, we would like to state that, despite all of these deficiencies, DFT has proven to be extremely valuable for the interpretation of experimental spectra since it is sometimes more helpful for the experimentalists to get right results for the wrong reasons than wrong results for the right reasons.

References

1 W.Weltner, *Magnetic Atoms and Molecules,* Scientific and Academic Editions, **1983**.
2 *Radical Ionic Systems. Properties in Condensed Phase,* eds. A. Lund, M. Shiotani, Kluwer, Dordrecht **1991**.
3 J. E. Harriman, *Theoretical Foundations of Electron Spin Resonance,* Academic Press, New York **1978**. Please note that the expression given by Munzarová in Chapter 29 differs from the one given here. While we formulate the constants as expectation values of a wavefunction, Munzarová gives them as a product of the spin density matrix and the corresponding integrals. Clearly both expressions are equivalent, but from the latter expression the influences of parts of the wavefunctions cannot be taken.
4 D. Feller, E. R. Davidson, *Theor. Chim. Acta* **1985**, *68*, 57.
5 B. Engels, S. D. Peyerimhoff, E. R. Davidson, *Mol. Phys.* **1987**, *62*, 109.
6 C. W. Bauschlicher Jr., S. R. Langhoff, H. Partridge et al., *J. Chem. Phys.* **1988**, *89*, 2985.
7 I. Carmichael, *J. Chem. Phys.* **1989**, *91*, 1072.
8 D. M. Chipman, Magnetic Coupling Constants in Free Radicals, in *Quantum Mechanical Electronic Structure Calculations with Chemical Accuracy,* ed. S. R. Langhoff, Kluwer, Dordrecht **1995**.
9 A. Szabo, N. S. Ostlund *Modern Quantum Chemistry,* Dover Publications, **1996**.
10 B. Engels, S. D. Peyerimhoff, *J. Phys. B: At. Mol. Opt. Phys.* **1988,** *21*, 3459.
11 B. Engels, S. D. Peyerimhoff, S. P. Karna et al., *Chem. Phys. Lett.* **1988**, *152*, 397.
12 B. Engels, L. Eriksson S. Lunell, *Adv. Quantum Chem.* **1996**, *27*, 297.
13 V. Barone, in *Recent Advances in Density Functional Methods, Part 1*, ed. D. P. Chong, World Scientific, Singapore **1996**.
14 D. Feller, E. R. Davidson, *J. Chem. Phys.* **1988**, *88*, 7580.
15 D.M. Chipman, *Theor. Chim. Acta* **1992**, *82*, 93 and references cited therein.
16 B. Engels, *J. Chem. Phys.* **1994**, *100*, 1380.
17 B. Engels, *Theor. Chim. Acta* **1993**, *86*, 429.
18 K. Funken, B. Engels, S. D. Peyerimhoff et al., *Chem. Phys. Lett.* **1990**, *172*, 180.
19 W. W. Holloway Jr., E. Lüscher, R. Novick, *Phys. Rev.* **1962**, *162*, 2109.
20 I. Carmichael, *J. Phys. Chem.* **1989**, *93*, 190.
21 B. Engels, *Chem. Phys. Lett.* **1991**, *179*, 398.
22 Z. Geshgorn, I. Shavitt, *Int. J. Quantum Chem.* **1968**, *2*, 751.
23 H. U. Suter, B. Engels, *Chem. Phys. Lett.* **1996**, *261*, 644.
24 H. U. Suter, M.-B. Huang, B. Engels, *J. Chem. Phys.* **1994**, *101*, 7686.
25 B. Engels, *Acta Chem Scand.* **1997**, *51*, 199.
26 H. U. Suter, B. Engels, *J. Chem. Phys.* **1994**, *100*, 2936.
27 S. Yamamoto, S. Saito, *J. Chem. Phys.* **1992**, *96*, 1457.
28 J. P. Perdew, *Int. J. Quantum Chem., Quantum Chem. Symp.* **1993**, *27*, 93.
29 H. U. Suter, V. Pleß, M. Ernzerhof et al., *Chem. Phys. Lett.* **1996**, *261*, 644.
30 L. A. Eriksson, O. L. Malkina, V.G. Malkin et al., *J. Chem. Phys.* **1994**, *100*, 5066.

31
Alternative Fermi Contact Operators for EPR and NMR

Vitaly A. Rassolov and Daniel M. Chipman

31.1
Introduction

Fermi contact interactions determine important parameters characterizing magnetic resonance spectra. The EPR isotropic hyperfine coupling constant observed at magnetic nucleus A in a free radical is given by known constants times $\langle \Psi_0 \mid \delta_A \, 2 \, \hat{S}_z \mid \Psi_0 \rangle$, which is the electronic spin density evaluated at point A as expressed by an expectation value over the ground state electronic wavefunction Ψ_0 of the delta function operator $\delta_A 2\hat{S}_z \equiv \sum_i^{\text{electrons}} \delta^3 \, (\mathbf{r}_i - \mathbf{R}_A) 2\hat{S}_{zi}$ (see Chapter 29 by Munzarová). A major contribution to the NMR indirect spin–spin coupling constant between magnetic nuclei A and B in a molecule is given by known constants times $\sum_{n \neq 0} \langle \Psi_0 \mid \delta_A \hat{\mathbf{S}} \mid \Psi_n \rangle \cdot \langle \Psi_n \mid \delta_B \hat{\mathbf{S}} \mid \Psi_0 \rangle \, / \, (E_n - E_0)$, which is a sum-over-states expression involving off-diagonal matrix elements of delta function operators between the ground state and all excited electronic wavefunctions Ψ_n (see Chapter 7 by Helgaker and Pecul).

These Fermi contact properties are difficult to calculate accurately because of their high sensitivity to the quality of the wavefunction at the nucleus that is picked out by the delta function operator. Most electronic wavefunctions are determined by some kind of global energy-based optimization procedure, and may admit large errors at a single point in space. Furthermore, the Gaussian basis sets used in most molecular calculations are especially deficient at nuclei. To obtain accurate results, it is usually necessary to use very large Gaussian basis sets that are designed for these particular properties.

Promising alternative approaches for Fermi contact interactions are possible by substituting the delta function operators with more global operators that are less sensitive to local errors in the wavefunctions. It is possible to find alternative global operators that would lead to exactly the same results as the delta function operators if exact wavefunctions were utilized. With approximate wavefunctions they generally give different results, and may in fact be preferable in practice to the delta function operators.

An alternative operator of this type was first proposed by Hiller, Sucher and Feinberg [1] (HSF), analyzed by Sucher and Drachman [2], and later extended by Harriman [3] to spin density calculation. Cioslowski and Challacombe [4] have shown that

Calculation of NMR and EPR Parameters. Theory and Applications.
Edited by Martin Kaupp, Michael Bühl, Vladimir G. Malkin
Copyright © 2004 WILEY-VCH Verlag GmbH & Co. KGaA, Weinheim
ISBN: 3-527-30779-6

the HSF operator provides a density possessing a cusp at the nucleus, even with Gaussian basis sets, although the form of the cusp differs from the exact condition obtained by Kato [5]. However, it was also formally shown [6] that with most approximate wavefunctions the HSF operator leads to incorrect long-range asymptotic behavior of the density.

Numerical studies have been made of both charge and spin densities with the HSF operator [7–13]. These reveal that, despite its promise, the HSF formulation is advantageous to the usual delta function formulation only with relatively large basis sets. The incorrect long-range asymptotic behavior of HSF causes it to give inaccurate values of charge densities at light atoms in the vicinity of heavy ones [9], and similarly limits the accuracy of spin density calculations [13]. An additional very serious problem for implementation of the HSF operator in systems of practical interest is that the calculations may require more computer resources than it takes for determination of the wavefunction.

We have developed a new class of alternative operators [14–16] that are free of many of the drawbacks of both the delta function and the HSF formulations. The alternative operators are derived in Section 31.2 and their formal properties are presented in Section 31.3. Selected numerical results from the literature are given for EPR applications in Section 31.4 and for NMR applications in Section 31.5. Finally, a conclusion is provided in Section 31.6.

We consider in this work only nonrelativistic stationary-state real normalized electronic wavefunctions of atoms and molecules obtained under the approximation of clamped nuclei. Atomic units (au) are used throughout, unless specifically noted otherwise.

31.2
Derivation of New Alternative Operators

The alternative operators of interest here can be obtained from the hypervirial theorem [17], which states that the commutator $\hat{H}\hat{W}-\hat{W}\hat{H}$ of a Hamiltonian $\hat{H}$ with an arbitrary operator $\hat{W}$ has vanishing expectation value when taken over an eigenfunction Ψ_0:

$$\langle\Psi_0|\hat{H}\hat{W} - \hat{W}\hat{H}|\Psi_0\rangle = 0\,. \tag{31.1}$$

This is immediately seen to be true by making use of the eigenvalue relation $\hat{H}\Psi_0 = E_0\Psi_0$ and the hermitian nature of the Hamiltonian. We have further proved [11] that the hypervirial relation holds if $\hat{W}$ is any one-electron operator and Ψ_0 is any fully optimized MCSCF wavefunction. The hypervirial relation provides many interesting results when considering operators $\hat{W}$ that do not commute with $\hat{H}$. For example, the well-known quantum mechanical virial theorem [18] is obtained by putting $\hat{W} = \sum_i r_i \partial/\partial r_i$.

The simple concept underlying the alternative operators can be illustrated by first treating a single-electron system, placing the nucleus of interest at the origin. Consider the antihermitian generating operator[1)]

$$\hat{W} = F(r)\left(\frac{\partial}{\partial r} + \frac{1}{r}\right) + \frac{1}{2}F'(r)\,, \tag{31.2}$$

where $F(r)$ is an arbitrary weight function, except that it should be well-behaved and not vanish at the origin, and the prime notation indicates differentiation with respect to r. The electronic Hamiltonian is $\hat{H} = \hat{T} + U$ with kinetic energy operator $\hat{T} = -\nabla_r^2/2 + \hat{L}^2/2r^2$, where $\nabla_r^2 = \partial^2/\partial r^2 + (2/r)\partial/\partial r$ and $\hat{L}^2$ represents electronic angular momentum, and U is a one-electron potential energy function that need not be explicitly specified. A delta function arises in working out the relevant commutator, from a term involving $\nabla_r^2(1/r) = -4\pi\delta^3(\mathbf{r})$. The final result of the hypervirial theorem in this example then turns out to be

$$\langle\Psi_0|\delta|\Psi_0\rangle = \langle\Psi_0|\hat{\boldsymbol{d}}|\Psi_0\rangle\ ,$$

where $\hat{\boldsymbol{d}}$ is a hermitian operator given by

$$\hat{\boldsymbol{d}} = \frac{1}{2\pi F(0)}\left[F(r)\left(-\frac{\hat{L}^2}{r^3} + \frac{\partial U}{\partial r}\right) + F'(r)\left(\frac{\partial^2}{\partial r^2} + \frac{2}{r}\frac{\partial}{\partial r}\right)\right.$$
$$\left. + F''(r)\left(\frac{\partial}{\partial r} + \frac{1}{r}\right) + \frac{1}{4}F'''(r)\right] \tag{31.3}$$

In words, with an exact wavefunction the expectation value of a delta function operator at the nucleus is equal to the expectation value of a global operator $\hat{\boldsymbol{d}}$.

For the electronic charge density at nucleus A in a many-electron molecule we use a generating operator $\hat{W}_A$ that is a sum of one-electron terms, each term given by $\hat{W}$ as defined above and referred to origin at A, to obtain

$$\langle\Psi_0|\delta_A|\Psi_0\rangle = \langle\Psi_0|\hat{D}_A|\Psi_0\rangle\ . \tag{31.4}$$

Here $\delta_A \equiv \sum_i \delta^3(\mathbf{r}_i - \mathbf{R}_A)$ is a sum of one-electron operators. The operator $\hat{D}_A \equiv \sum_i \hat{\boldsymbol{d}}_i$ also involves a sum over individual electrons i, with each term $\hat{\boldsymbol{d}}_i$ being

1) Originally [14, 15] we considered the simpler nonhermitian generating operator $F(r)\partial/\partial r$. That approach leads to a nonhermitian alternative to the delta function, which in practice necessitates symmetrization of all integrals over basis functions with respect to the basis function indices. The version given here that leads to a hermitian alternative to the delta function was reported later [16].

implicitly referred to an origin at nucleus *A*. The Hamiltonian potential energy function must now be represented as $U+V$, which has both one-electron terms U and two-electron terms V. Consequently, the commutator of ∇_i^2 with the potential energy function produces contributions to $\hat{\boldsymbol{d}}_i$ from both a one-electron term involving $\partial U/\partial r_i$ and also a two-electron term involving $\partial V/\partial r_i$. Similarly, the electronic spin density at nucleus *A* that determines the EPR isotropic hyperfine coupling constant in a many-electron molecule can be expressed as

$$\langle\Psi_0|\delta_A 2\hat{S}_z|\Psi_0\rangle = \langle\Psi_0|\hat{D}_A 2\hat{S}_z|\Psi_0\rangle \ , \tag{31.5}$$

where $\delta_A 2\hat{S}_z \equiv \sum_i \delta^3(\mathbf{r}_i - \mathbf{R}_A)2\hat{S}_{zi}$ is a sum of spin-dependent one-electron operators and $\hat{D}_A 2\hat{S}_z \equiv \sum_i \hat{\boldsymbol{d}}_i 2\hat{S}_{zi}$ contains both one- and two-electron spin-dependent operators. It is shown in Section 31.3 that, in practice, all two-electron contributions can be made negligible.

Treatment of the NMR indirect spin–spin coupling constant is more difficult because off-diagonal matrix elements of the delta function are involved. There is no analog of the hypervirial relation that would allow each matrix element over a delta function operator to be equated with one over an alternative global operator. Nevertheless, useful results can still be obtained for the property of interest here, because it involves a sum of matrix elements over all excited states, making possible use of the completeness of the set of all hamiltonian eigenfunctions as expressed by $\sum_{n\neq 0}|\Psi_n\rangle\langle\Psi_n| = 1 - |\Psi_0\rangle\langle\Psi_0|$. We refer to the original work [16] for all detailed arguments, and quote here just the final result of

$$\sum_{n\neq 0}\frac{\langle\Psi_0|\delta_A\hat{\mathbf{S}}|\Psi_n\rangle\cdot\langle\Psi_n|\delta_B\hat{\mathbf{S}}|\Psi_0\rangle}{E_n - E_0} = \sum_{n\neq 0}\frac{\langle\Psi_0|\hat{D}_A\hat{\mathbf{S}}|\Psi_n\rangle\cdot\langle\Psi_n|\hat{D}_B\hat{\mathbf{S}}|\Psi_0\rangle}{E_n - E_0}$$

$$-\frac{1}{4\pi F_A(0)}\langle\Psi_0|\hat{\mathbf{W}}_A\hat{\mathbf{S}}\cdot(\delta_B + \hat{D}_B)\hat{\mathbf{S}}|\Psi_0\rangle + \frac{1}{4\pi F_B(0)}\langle\Psi_0|(\delta_A + \hat{D}_A)\hat{\mathbf{S}}\cdot\hat{\mathbf{W}}_B\hat{\mathbf{S}}|\Psi_0\rangle \tag{31.6}$$

This effectively replaces delta functions by alternative operators in the off-diagonal matrix elements, at the price of introducing ground state expectation value terms. It is described in Section 31.5 how, in practice, the ground state expectation value terms can be made negligible.

31.3
Formal Properties of Short-Range Alternative Operators

In this section we consider specific choices for the weighting function $F(r)$, with r being the radial distance from a nucleus located at the origin. We have studied [14] two possibilities for $F(r)$. One choice is the Heaviside step function defined by

$$F^{\Theta}(r) = \begin{cases} 1 & \text{if } r \le r_0 \\ 0 & \text{otherwise} \end{cases} , \tag{31.7}$$

and the other choice is a Gaussian function defined by

$$F^{G}(r) = \mathrm{e}^{-r^2/r_0^2}, \tag{31.8}$$

both operators being governed by a range parameter r_0. Through the hypervirial theorem, these lead to alternative operators $\hat{\boldsymbol{d}}^{\Theta}$ and $\hat{\boldsymbol{d}}^{G}$, respectively.

Results equivalent to the delta function are reached by either new alternative operator in the limit of $r_0 \to 0$. Results equivalent to the HSF operator, which corresponds to the choice $F(r) = 1$, are reached by either alternative operator in the limit of $r_0 \to \infty$. Thus, by changing the value of the range parameter r_0 the alternative operators can interpolate between delta function and HSF results. The alternative operators turn out to be most useful when the range parameter r_0 is chosen to be small but nonzero, which effectively limits the integration region to the near vicinity of the nucleus while still allowing for a region of space over which some averaging of wavefunction errors may take place.

Formal properties of these short-range alternative operators can be analyzed by expanding all relevant quantities as power series in r_0 and working out the coefficients of the lowest few terms. The Heaviside weighting happens to be most convenient for such analysis, and was used [14] to establish most of the results reported in this section. It can be expected that the formal properties of the Gaussian-weighted operator are essentially the same as for the Heaviside-weighted operator. Indeed, by utilizing numerical grid methods to effectively generate complete basis set results, this expectation has been fully confirmed by calculations of charge and spin densities in first-row atoms and in first-row diatomic hydrides [15].

In principle, the alternative operators can be used to evaluate charge and spin densities from an approximate wavefunction at any point in space. We have shown [14] that at a point far from any nucleus the charge and spin density evaluated from the alternative operators differ negligibly from the corresponding delta function charge and spin density, as long as r_0 is chosen to be small. The new alternative operators therefore do not suffer from the incorrect long-range asymptotic behavior that plagues the HSF operator.

For evaluation of Fermi-contact interactions in EPR and NMR the main interest lies in the behavior of the alternative operators when evaluated at a nucleus. Several very interesting properties can be analytically derived in this situation, as we now demonstrate.

Any exact wavefunction Ψ satisfies a cusp condition when one electron approaches a nucleus. We focus on a nucleus of charge Z at the origin and an electron lying a small distance r away, while suppressing the coordinates of all other particles. Per-

forming an average over a small sphere about $r=0$ (as indicated by an overhead tilde notation) and expanding in a Taylor series about this point we have

$$\tilde{\Psi}(r) = \Psi(0) + r\Psi'(0) + r^2\Psi''(0)/2 + r^3\Psi'''(0)/6 + \mathcal{O}(r^4). \tag{31.9}$$

Kato [5] proved that

$$\Psi'(0) = -Z\Psi(0), \tag{31.10}$$

showing that the first derivative is nonzero and is completely determined in terms of the amplitude. Making use of the Heaviside-weighted alternative operator [16], and later verifying the results by independent methods [19], we have further proven that

$$\Psi'''(0) = Z^3\Psi(0) - 2Z\Psi''(0), \tag{31.11}$$

giving the third derivative in terms of lower ones. Thus, the singular coulomb potential produced by a nucleus governs the behavior of the exact electronic wavefunction out to larger distance than was previously appreciated. These same cusp relations also hold for any Hartree–Fock or MCSCF s-orbital that is obtained exactly within a complete basis set. Analogous results have also been obtained for electron-electron cusps [19].

The alternative operators show a remarkable behavior for the density near a nucleus. The exact charge density $\rho(\mathbf{r})$ satisfies the cusp condition [20]

$$\tilde{\rho}(r) = \rho(0) - 2Zr\rho(0) + \mathcal{O}(r^2), \tag{31.12}$$

where again the nonzero first derivative is determined by the amplitude. With an approximate wavefunction, the delta function charge density $\rho^{\delta}(\mathbf{r})$ will generally not satisfy this condition unless specifically constrained to do so. Nevertheless, we have proved [14] that

$$\tilde{\rho}^{\delta}(r_0) = \rho^{\Theta}(0) - 2Zr_0\rho^{\delta}(0) + \mathcal{O}(r_0^2) \tag{31.13}$$

for any general approximate wavefunction. Thus, the alternative operator produces a density $\rho^{\Theta}(0)$ having a cusp at the nucleus, which coincides with the exact cusp condition at the particular distance r_0, even if the underlying wavefunction from which it is evaluated has no cusp at all! The analogous result also holds for the spin density, and this property significantly improves the evaluation of EPR and NMR Fermi contact interactions with the alternative operators when constructing wavefunctions from Gaussian basis sets that preclude any cusp-like behavior of the delta function

density. To use the words of Pyykkö in a comment made at the International Conference on Quantum Chemical Calculations of NMR and EPR Parameters held in the Slovak Republic on September 14–18, 1998, the alternative operators "show how to put a pointed hat on a round head".

Efficiency of calculations is also an important concern. Two-electron contributions to the alternative operators would require considerable computer resources to evaluate in many-electron systems. This drawback seriously limits interest in the HSF operator, but is not a problem for our new alternative operators because of a formal demonstration [14] that two-electron terms do not begin to contribute until $\mathcal{O}(r_0^4)$ and higher, and so are negligible in comparison to one-electron terms when r_0 is small. EPR and NMR Fermi contact interactions can be therefore be obtained with the new alternative operators from one-electron integrals that require only modest computer resources to evaluate, comparable to calculation of the usual one-electron integrals needed for energy evaluation.

EPR and NMR calculations have been carried out [15, 16] to examine how results change as r_0 is varied in the new alternative operators. Basis sets of at least double-zeta quality (with splitting of both core and valence orbitals) are necessary to describe important spin polarization effects in the wavefunction, otherwise qualitatively incorrect results are usually obtained no matter what operator is used. Starting from the delta function result at $r_0 = 0$, it is generally found with double zeta and larger basis sets that the results initially change quickly as r_0 increases, and then level off to a flat plateau where the results are insensitive to the particular value chosen for r_0. As r_0 becomes still larger a point is eventually reached where neglected two-electron contributions cause the results to again change rapidly and become nonsensical. The optimum value of r_0 corresponds to a balance between the competing desires of making it as large as possible to provide significant averaging of wavefunction errors, while still keeping it small enough to allow neglect of two-electron contributions.

31.4 EPR Calculations

As an example, we report selected numerical results for spin densities of π-radicals from the first-row diatomic hydrides CH ($X^2\Pi$), NH ($X^3\Sigma^-$), and OH ($X^2\Pi$). In few-electron systems the Heaviside-weighted operator sometimes [15, 16] produces oscillations in the results as a function of the range parameter r_0, while the Gaussian-weighted operator generally leads to smooth behavior, and we therefore show here results only from the Gaussian-weighted operator. Interested readers can consult the original publications [15, 16] for detailed comparisons of numerical results from both new alternative operators, and from the HSF operator as well, for hydrogen, first-row atoms, and first-row diatomic hydrides.

In practical applications, it is helpful to determine the dependence of the range parameter r_0 on the charge Z of the nucleus under consideration. For this, we note that both Kato's cusp condition [5] and its extension to higher order [14, 19] show

that in the vicinity of a nucleus the wavefunction depends on a scaled variable Zr. Thus, with small r_0 the optimum value of Zr_0 should be roughly constant for different nuclei. In a comprehensive study of first-row atoms [15] we carefully estimated that two-electron contributions to the spin density per unpaired electron remain below 0.0002 au whenever Zr_0 is about 0.25 a_0 or smaller. This rather conservative criterion is adopted for the results to be reported here, although in low accuracy calculations even higher values of Zr_0 would be acceptable.

We adopt SP-MCSCF (spin-polarization multiconfiguration self-consistent-field) wavefunctions. In this context, spin-polarization configurations are those spin-adapted single excitation configurations that are connected by nonzero matrix elements to the dominant spin-restricted configuration in the Hamiltonian matrix. All orbitals are variationally optimized within a given basis set. Seminumerical grid calculations are also obtained with high enough precision to effectively correspond to use of a complete basis set.

The most proper theoretical comparison for present purposes is that of finite basis set results to the limiting seminumerical grid results, with a fixed wavefunction model. Even so, it is naturally of interest to inquire how well the given wavefunction model is capable of matching experiment. Comparing the seminumerical grid results to experimental values in Tab. 31.1 shows that the SP-MCSCF model gives quite good agreement with experiment in this example. That happens frequently for spin densities of π-radicals, but is probably fortuitous [21, 22] owing to an accidental cancellation of significant contributions from doubly-excited configurations that describe dynamic electron correlations with certain triply-excited configurations that describe spin-polarization of the important doubles (see Chapter 30 by Engels). It is fully expected that the new alternative operators examined here will be just as valuable in studies that include dynamic electron correlation effects as they are in the simpler studies made so far.

Table 31.1 Electronic spin densities in au at the nuclei in CH, NH, and OH radicals as calculated with SP-MCSCF wavefunctions. Results from the δ operator and the $\hat{d}^G$ alternative operator with $r_0 = 0.25/Z\ a_0$ are compared with different basis sets, with seminumerical calculations corresponding to the complete basis set limit, and with experiment.

		[4 2|2]	[6 3 1|4 1]	[6↑4↑2|4↑1]	Limit	Experiment
C	δ	0.0343	0.0351	0.0405	0.0393	0.042
	$\hat{d}^G$	0.0406	0.0377	0.0414	0.0393	
N	δ	0.0455	0.0521	0.0588	0.0596	0.061
	$\hat{d}^G$	0.0549	0.0565	0.0608	0.0596	
O	δ	0.0495	0.0593	0.0662	0.0706	0.084
	$\hat{d}^G$	0.0625	0.0657	0.0700	0.0706	
H(CH)	δ	–0.0152	–0.0125	–0.0128	–0.0137	–0.0129
	$\hat{d}^G$	–0.0165	–0.0132	–0.0134	–0.0137	
H(NH)	δ	–0.0167	–0.0141	–0.0142	–0.0148	–0.0148
	$\hat{d}^G$	–0.0181	–0.0147	–0.0146	–0.0148	
H(OH)	δ	–0.0176	–0.0154	–0.0154	–0.0158	–0.0164
	$\hat{d}^G$	–0.0191	–0.0158	–0.0157	–0.0158	

Several basis sets of increasing size and complexity are considered. Comparing the smallest [42|2] double zeta set [23, 24] results to the limiting seminumerical grid results in Tab. 31.1 shows that $\hat{d}^G$ performs much better than δ at the heavy atoms, although not quite as well at the hydrogens. Uncontracting the outermost primitive s member from the innermost contraction group and adding diffuse *s* and *p* functions as well as polarization functions gives a [631|41] basis especially designed for spin density calculations [25]. With this basis both operators give notably better results than with [42|2], and $\hat{d}^G$ performs much better than δ at all nuclei. For quantitative calculations it is further necessary to add functions that are highly peaked near the nuclei. The [$6^{\dagger}4^{\dagger}2|4^{\dagger}1$] basis [13] includes very high exponent *s* and *p* functions at the heavy atom and *s* function at hydrogen, and also somewhat uncontracts the *p* space and adds an additional *d* shell at the heavy atom. The dagger implies that the extra tight functions are contracted into the existing innermost groups. Both operators show improved results with this basis, and are both now close to the limiting numerical values.

It can be concluded that with small basis sets the new alternative Gaussian-weighted operator gives substantially better spin density results than the delta function, and also converges more rapidly with increasing basis set size to the limiting results that both operators ultimately attain with very large basis sets. The Gaussian-weighted operator has also been found [15] to give much more dramatic improvement over other operators for the total charge density at a nucleus. The less dramatic, but still substantial, improvement found for spin density at a nucleus is attributed to the loss of significant figures occurring when subtracting two large alpha and beta densities of nearly equal magnitude.

The new Gaussian-weighted alternative operator with small r_0 has also been used [26] in spin density calculations based on density functional theory (DFT). To simplify evaluation of basis function integrals over the alternative operator, an ad hoc assumption was made that contributions from Coulomb and exchange-correlation terms could be neglected, which is analogous to our analytic demonstration that two-electron contributions can be neglected in ab initio approaches. First-row atoms, first-row diatomic hydrides, and several small polyatomic radicals were considered. With first-row atoms it was found that the best DFT results are obtained with a value of $0.35\,a_0$ for Zr_0, which is a little larger than the $0.25\,a_0$ value we recommend for ab initio studies. The study concluded that with moderate-sized and carefully selected Gaussian basis sets, the new operator combined with DFT has clear advantage for the calculation of nuclear spin densities in molecules.

31.5 NMR Calculations

The only NMR application of the new alternative operators to date is our study [16] of indirect nuclear spin–spin coupling in the HD molecule. It treats only the Fermi contact contribution at the equilibrium bond distance, for which limiting results corresponding to complete basis set calculations have been estimated [16] from litera-

ture studies [27, 28] as 53.23 Hz for coupled Hartree–Fock (CHF) and 40.13 Hz for full configuration interaction (FCI). The latter value accounts for about 93% of the experimental result of 43.11 Hz, with the remainder [27, 28] coming from averaging the Fermi contact contribution over nuclear motions and also, to a lesser extent, from non-Fermi contact contributions arising from spin dipole, paramagnetic spin–orbit, and diamagnetic spin–orbit interactions.

Optimum values of r_0 obtained from EPR experience need not carry over to NMR. Indeed, two-electron contributions to the spin–spin coupling in HD begin to be noticeable [16] at r_0 of about $0.10\,a_0$, which is significantly shorter than found in spin density explorations. We use $r_{0H} = r_{0D} = 0.10\,a_0$ to evaluate spin–spin coupling in HD, and neglect all two-electron contributions. These r_0 values are much shorter than the internuclear distance, making the overlap of the weighting functions on the two centers very small. Consequently, it is also permissible to neglect the ground state expectation value terms. The remaining sum-over-states expression was indirectly evaluated by a finite-field method [29, 30].

Selected results are given in Tab. 31.2. We use medium to large basis sets that show a flat plateau region where the results are not very sensitive to r_0. Very small basis sets do not show a plateau region, making them unsuitable for the alternative operators in this problem.

The [41] and [4†1] contracted basis sets are the same as described above in Section 31.4. With the [41] basis δ shows significant errors while $\hat{\boldsymbol{d}}^G$ performs well. The [4†1] basis produces considerable improvement with δ and some improvement with $\hat{\boldsymbol{d}}^G$. Moving to a large uncontracted (10 5 2) basis taken from the literature [27], δ is a little worse while $\hat{\boldsymbol{d}}^G$ is again improved. After further augmentation with four more tight *s*-functions to produce the (14 5 2) basis that effectively saturates the *s* space [28], the errors are finally small with δ while unchanged with $\hat{\boldsymbol{d}}^G$. This independence of the $\hat{\boldsymbol{d}}^G$ results to addition of very tight *s*-functions clearly illustrates the improved behavior in the cusp region produced by the new operators. The lack of complete convergence with $\hat{\boldsymbol{d}}^G$ to the exact limiting result suggests some lingering small deficiency in the basis, quite possibly in the tight regions of the *p* space.

It may be concluded that the $\hat{\boldsymbol{d}}^G$ operator performs somewhat better than δ for calculation of the indirect spin–spin coupling constant in HD, both with CHF and FCI wavefunctions.

Table 31.2 Fermi contact contribution in Hz to the indirect nuclear spin–spin coupling constant in the HD molecule as calculated with CHF and FCI wavefunctions. Results from the δ operator and the $\hat{\boldsymbol{d}}^G$ alternative operator with $r_0 = 0.10\,a_0$ are compared with different basis sets and with the estimated complete basis set limit.

		[4 1]	[4†1]	(10 5 2)	(14 5 2)	Limit
CHF	δ	48.10	51.80	51.98	53.19	53.23
	$\hat{\boldsymbol{d}}^G$	53.99	53.55	53.42	53.42	53.23
FCI	δ	36.58	39.39	39.20	40.10	40.13
	$\hat{\boldsymbol{d}}^G$	41.08	40.75	40.30	40.30	40.13

31.6 Conclusions

For calculations of Fermi contact interactions, the delta function operator is "too local." It is sensitive to significant errors often found at the nuclei in molecular wavefunctions. On the other hand, the HSF operator is "too global." An inexact description of the wavefunction far from the point of interest contributes to error in the HSF results.

The new alternative operators achieve accuracy by averaging wavefunction errors over a vicinity around the nucleus, and by providing a density cusp at the nucleus even when the wavefunction itself is cuspless. It is also possible to easily and efficiently compute results with the alternative operators, whereas the HSF formulation is very complicated and expensive.

To date, only a few studies have been reported with the new alternative operators. The Heaviside-weighted operator has been most useful for proving formal properties, while the Gaussian-weighted operator performs a little better in numerical calculations. Further detailed investigations should be made to gain more practical experience. EPR hyperfine coupling constant calculations should be carried out with highly correlated wavefunctions to see if the alternative operators work as well there as with the simple spin-polarization wavefunctions studied so far. Also, the optimum value of the range parameter r_0 should be examined in more systems, especially in connection with NMR spin–spin coupling constants.

From the studies made so far, it can be concluded that the new alternative operators are useful in providing improved values of Fermi contact interactions. They are a very promising tool and are recommended for more widespread use in both EPR and NMR applications.

Acknowledgements

The research described herein was supported by the Office of Basic Energy Sciences of the Department of Energy. This is Contribution No. NDRL-4451 from the Notre Dame Radiation Laboratory

References

1 J. Hiller, J. Sucher, G. Feinberg, *Phys. Rev. A* **1978**, *18*, 2399.
2 J. Sucher, R. J. Drachman, *Phys. Rev. A* **1979**, *20*, 424.
3 J. E. Harriman, *Int. J. Quantum Chem.* **1980**, *17*, 689.
4 J. Cioslowski, M. Challacombe, *Chem. Phys. Lett.* **1994**, *224*, 175.
5 T. Kato, *Commun. Pure Appl. Math.* **1957**, *10*, 151.
6 J. Cioslowski, M. Challacombe, *Theor. Chim. Acta* **1992**, *83*, 185.
7 S. Larsson, *Chem. Phys. Lett.* **1981**, *77*, 176.
8 K. Ishida, *Int. J. Quantum Chem.* **1986**, *30*, 543; erratum **1988**, *34*, 195.

9 M. Challacombe, J. Cioslowski, *Mol. Phys.* **1994**, *83*, 397.
10 V. A. Rassolov, D. M. Chipman, *Theor. Chim Acta* **1994**, *88*, 329.
11 V. A. Rassolov, D. M. Chipman, *Theor. Chim. Acta* **1995**, *91*, 1.
12 D. Sundholm, *J. Chem. Phys.* **1995**, *102*, 4895.
13 V. A. Rassolov, D. M. Chipman, *J. Chem. Phys.* **1995**, *103*, 10058.
14 V. A. Rassolov, D. M. Chipman, *J. Chem. Phys.* **1996**, *105*, 1470.
15 V. A. Rassolov, D. M. Chipman, *J. Chem. Phys.* **1996**, *105*, 1479.
16 D. M. Chipman, V. A. Rassolov, *J. Chem. Phys.* **1997**, *107*, 5488.
17 J. O. Hirschfelder, *J. Chem. Phys.* **1960**, *33*, 1462.
18 F. L. Pilar, *Elementary Quantum Chemistry*, McGraw-Hill, New York **1968**.
19 V. A. Rassolov, D. M. Chipman, *J. Chem. Phys.* **1996**, *104*, 9008.
20 E. Steiner, *J. Chem. Phys.* **1963**, *39*, 2365.
21 D. M. Chipman, *Theor. Chim. Acta* **1992**, *82*, 93.
22 D. M. Chipman, Magnetic Hyperfine Coupling Constants in Free Radicals, *in Quantum Mechanical Electronic Structure Calculations with Chemical Accuracy*, ed. S. R. Langhoff, Kluwer, Dordrecht **1995**.
23 S. Huzinaga, *J. Chem. Phys.* **1965**, *42*, 1293.
24 T. H. Dunning, *J. Chem. Phys.* **1970**, *53*, 2823.
25 D. M. Chipman, *J. Chem. Phys.* **1989**, *91*, 5455.
26 B. Wang, J. Baker, P. Pulay, *Phys. Chem. Chem. Phys.* **2000**, *2*, 2131.
27 J. Oddershede, J. Geertsen, G. E. Scuseria, *J. Phys. Chem.* **1988**, *92*, 3056.
29 O. Vahtras, H. Ågren, P. Jørgensen, et al., *J. Chem. Phys.* **1992**, *96*, 6120.
29 J. A. Pople, J. W. McIver, Jr., N. S. Ostlund, *J. Chem. Phys.* **1968**, *49*, 2965.
30 J. Kowalewski, A. Laaksonen, B. Roos et al., *J. Chem. Phys.* **1979**, *71*, 2896.

32
Calculation of EPR g-Tensors with Density Functional Theory

Serguei Patchkovskii and Georg Schreckenbach

32.1
Introduction

Applications of density functional theory [1, 2] to calculations of EPR **g** tensors [3–5] have a long and distinguished history (See Refs. [6–10], and references therein). Used together with semiempirical spin–orbit coupling operators and approximate perturbation theory expressions, early DFT techniques have proven successful in gaining a qualitative understanding of the experimental results [9]. In the last few years, the remarkable success of DFT in calculations of the NMR shielding tensors (See Chapters 6 by van Wüllen; 14 by Autschbach; 18 by Kaupp) has led to a renewed interest in DFT approaches to the closely related [11] **g**-tensors. These developments were also spurred by the seminal *ab initio* work of Lushington and Grein [12–14], and other recent *ab initio* techniques [15–17] (also see Chapter 33 by Lushington). Following the first modern DFT implementation of the EPR **g**-tensors by Schreckenbach and Ziegler in 1996 [18, 19], a number of density functional approaches to this property have been implemented [20–26]. More than 50 application papers using these techniques have appeared in print so far. Some of the applications of these techniques are reviewed later in this volume, as well as elsewhere [11, 27–30].

Although some fundamental, unresolved problems remain (see below), density functional calculations of EPR **g**-tensors are clearly entering the age of maturity. Nonetheless, gaining understanding of the unique strengths and weaknesses of any given implementation[1)] can be a daunting task, not least because the original research publications [18–26] tend to emphasize the differences rather than the essential affinity between these techniques. Therefore, the goal of this chapter is to provide a bird's eye view of the existing DFT approaches to **g**-tensor calculations, which is then used as a basis for a better understanding of their individual quirks.

The rest of this chapter is organized as follows. Section 32.2 briefly summarizes the physical origin of the **g**-tensor, as far as is necessary for defining the **g**-tensor

1) The authors are aware of seven independent implementations of the EPR **g**-tensors, in six different DFT codes.

Calculation of NMR and EPR Parameters. Theory and Applications.
Edited by Martin Kaupp, Michael Bühl, Vladimir G. Malkin
Copyright © 2004 WILEY-VCH Verlag GmbH & Co. KGaA, Weinheim
ISBN: 3-527-30779-6

expressions. Section 32.3 introduces the first- and second-order approaches to **g**-tensor calculations, and discusses the issues arising in the treatment of the spin–orbit coupling operator. It also briefly summarizes the features of published DFT implementations. Section 32.4 provides an overview of the factors affecting the accuracy of practical **g**-tensor calculations. Finally, Section 32.5 gives the conclusions, and outlines possible directions of future development.

32.2
The Physical Origin of the g-Tensor

The **g** tensor, together with the zero-field splitting tensor **D** (covered in Chapter 34 by Neese), serves as a convenient summary of the electronic transitions in experimental electron paramagnetic resonance (EPR) spectra. To a good approximation, the observed energies and intensities of such transitions can be reproduced by an effective Hamiltonian [3–5] (See also Chapter 4 by Lushington), expressed in terms of a fictitious, *effective spin* operator $\tilde{\mathbf{S}}$ (atomic units):

$$\tilde{H} = \frac{1}{2c}\vec{B}\cdot\mathbf{g}\cdot\tilde{\mathbf{S}} + \tilde{\mathbf{S}}\cdot\mathbf{D}\cdot\tilde{\mathbf{S}} \tag{32.1}$$

In Eq. (32.1), c is the speed of light (≈137.04), and $\vec{B}$ is the magnetic field. The total effective spin is chosen to reproduce the experimental $(2\tilde{S}+1)$-level multiplet structure. For effective doublet radicals ($\tilde{S} = 1/2$), as well as high-spin radicals in the strong field limit, the eigenvalues of this Hamiltonian are given by [3]:

$$E_k = k\frac{B}{2c}\left(\vec{\xi}^{\mathrm{T}}\cdot\mathbf{g}\cdot\mathbf{g}^{\mathrm{T}}\cdot\vec{\xi}\right)^{1/2} \tag{32.2}$$

In Eq. (32.2), k varies between $-\tilde{S}$ and $\tilde{S}$, in integer increments, while $\vec{\xi}$ specifies the direction of the magnetic field ($\vec{\xi} = \vec{B}/B$). When the deviation $\Delta\mathbf{g}$ ($\Delta\mathbf{g} = \mathbf{g} - g_e\,\mathbf{1}$, $\mathbf{1}$ being the 3×3 unit matrix) from the free electron g-value g_e ($g_e \approx 2.002\,319\,277\,8$) is small, Eq. (32.2) can be expanded to first order in $\Delta\mathbf{g}$, giving:

$$E_k = k\frac{B}{2c}\left(g_e + \vec{\xi}^{\mathrm{T}}\cdot\Delta\mathbf{g}\cdot\vec{\xi} + \mathrm{O}\left(\Delta\mathbf{g}^2\right)\right) \tag{32.3}$$

Any theoretical treatment of the **g** tensor employs a physical, *microscopic* Hamiltonian to determine the magnetic field-induced splitting of two convenient electronic energy levels. This energy separation, calculated for different orientations of the magnetic field, is then matched to the individual components of the **g** tensor above.

The simplest non-relativistic microscopic Hamiltonian, which can qualitatively account for the deviation of **g**-tensors from the free-electron value g_e, must include at least the one-electron spin Zeeman ($\hat{H}_{\mathrm{Z}}$), orbital Zeeman ($\hat{H}_{\mathrm{L}}$), and nuclear spin–orbit (SO) coupling ($\hat{H}_{\mathrm{SO(N)}}$) operators [4, 31]:

$$\tilde{H}_{\mathrm{Z}} = \sum_j \hat{h}_Z^j = \sum_j \frac{g_e}{2c}\,\vec{B}\cdot\hat{\mathbf{s}}_j \tag{32.4}$$

$$\tilde{H}_{\mathrm{L}} = \sum_j \hat{h}_L^j = \sum_j \frac{1}{2c}\,\vec{B}\cdot\left(\vec{r}_j\times\hat{\boldsymbol{p}}_j\right) \tag{32.5}$$

$$\tilde{H}_{\mathrm{SO(N)}} = \sum_j \hat{h}_{SO(N)}^j = \sum_j \frac{g'}{4c^2}\sum_A Z_A\hat{\mathbf{s}}_j\cdot\frac{\left(\vec{r}_j-\vec{R}_A\right)\times\hat{\boldsymbol{p}}_j}{\left|\vec{r}_j-\vec{R}_A\right|^3} \tag{32.6}$$

In Eqs. (32.4) – (32.6), the summation runs over all electrons (j) and nuclei (A). Position, momentum and spin operators of an electron j are given by $\vec{r}_j$, $\hat{\boldsymbol{p}}_j$, and $\hat{\mathbf{s}}_j$, respectively. The symbols $\vec{R}_A$ and Z_A refer to the positions and nuclear charges of a (fixed) nucleus A. The spin–orbit g'-factor g is given by [4]:

$$g' = 2g_e - 2 \tag{32.7}$$

The spin Zeeman operator manifests itself in the diagonal, free-electron contribution to the **g**-tensor. The interplay between $\hat{H}_{\mathrm{L}}$ and $\hat{H}_{\mathrm{SO(N)}}$ is responsible for the leading contribution to $\Delta\mathbf{g}$. Qualitatively similar, but mathematically more involved operators will appear in relativistic two- [4, 20, 26] and four- [4, 32] component approaches.

Additionally, calculations aiming for quantitative agreement with experiment will need to consider [4, 12, 13] two-electron (2e) contributions to the spin–orbit coupling operator (2e spin–orbit $\hat{H}_{\mathrm{SO(2e)}}$, and spin–other-orbit $\hat{H}_{\mathrm{SOO}}$), as well as the spin Zeeman kinetic energy correction $\hat{H}_{\mathrm{ZKE}}$:

$$\hat{H}_{\mathrm{SO(2e)}} = \sum_j\sum_{k\neq j} -\frac{g'}{4c^2}\hat{\mathbf{s}}_j\cdot\frac{\left(\vec{r}_j-\vec{r}_k\right)\times\hat{\boldsymbol{p}}_j}{\left|\vec{r}_j-\vec{r}_k\right|^3} \tag{32.8}$$

$$\hat{H}_{\mathrm{SOO}} = \sum_j\sum_{k\neq j} -\frac{1}{c^2}\hat{\mathbf{s}}_j\cdot\frac{\left(\vec{r}_k-\vec{r}_j\right)\times\hat{\boldsymbol{p}}_k}{\left|\vec{r}_k-\vec{r}_j\right|^3} \tag{32.9}$$

$$\hat{H}_{\mathrm{ZKE}} = \sum_j -\frac{g_e}{4c^3}\hat{\boldsymbol{p}}_j^2\,\vec{B}\cdot\hat{\mathbf{s}}_j \tag{32.10}$$

Finally, in order to obtain gauge-invariant results, "gauge correction" operators (nuclear spin–orbit $\hat{H}^{\mathrm{dia}}_{\mathrm{SO(N)}}$, 2–e SO $\hat{H}^{\mathrm{dia}}_{\mathrm{SO(2e)}}$, and 2–e SOO $\hat{H}^{\mathrm{dia}}_{\mathrm{SOO}}$) must also be included. These terms are sometimes called "diamagnetic" contributions, following the convention used in NMR literature [19]. The explicit form of the diamagnetic operators can be obtained by replacing the electron momentum operator ($\hat{\boldsymbol{p}}_j$) in

field-free SO operators (32.6), (32.8), and (32.9) by the vector potential contribution due to the magnetic field (minimal coupling [33]):

$$\hat{p}_j \rightarrow \frac{1}{c}\vec{A}\left(\vec{r}_j\right) = \frac{1}{2c}\vec{B}\times\vec{r}_j \tag{32.11}$$

where the Coulomb gauge has been used for the magnetic field.

A succinct physical interpretation of Eqs. (32.6) – (32.10) was given by Pickard and Mauri [25]: *"The spin–other-orbit correction ... describes the screening of the external field B by the induced electronic currents, as experienced by the unpaired electron. The unpaired electron itself is not at rest and in the reference frame of the unpaired electron the electric field due to the ions and to the other electrons is Lorentz transformed so as to appear as a magnetic field. The interaction between the spin of the unpaired electron and this magnetic field results in the spin–orbit correction ... Finally, the electron Zeeman kinetic energy correction ... is a purely kinematic relativistic correction."*

The four one-electron operators ($\hat{H}_Z$, $\hat{H}_L$, $\hat{H}_{SO(N)}$, and $\hat{H}^{dia}_{SO(N)}$) do not present any special difficulty in the context of density functional theory. However, a direct evaluation of the matrix elements of the two-electron $\hat{H}_{SO(2e)}$ and $\hat{H}_{SOO}$ operators (and their diamagnetic counterparts $\hat{H}^{dia}_{SO(2e)}$, $\hat{H}^{dia}_{SOO}$) requires knowledge of the two-particle density matrix [31], not available in Kohn–Sham DFT [1]. In all practical DFT calculations, these terms are therefore either neglected, or treated approximately (see Section 32.3.3).

32.3 DFT Expressions for g-Tensors of Isolated Molecules

In the Kohn–Sham formulation of one- (non-relativistic) and two-component (relativistic[2]) density functional theory, the total energy expression is given by [1, 2]:

$$E^{KS} = \sum_i \left\langle \psi_i | \hat{f} | \psi_i \right\rangle - \frac{1}{2}\int v_{ee}(\vec{r})\rho(\vec{r})d\vec{r} - \int v_{xc}(\vec{r})\rho(\vec{r})d\vec{r} + E_{xc} \tag{32.12}$$

In Eq. (32.12), index i runs over all occupied Kohn–Sham (KS) one-particle spin-orbitals ψ_i, which are obtained as self-consistent solutions of the eigenequations:

$$\hat{f}\psi_i = \varepsilon_i\psi_i \tag{32.13}$$

The Kohn–Sham–Fock operator $\hat{f}$, including the principal terms relevant for the **g**-tensor calculations, is given by:

2) Although four-component Dirac–Hartree–Fock calculations of **g**-tensors of atoms and molecules have been reported [32, 34], we are not aware of any four-component molecular DFT calculations of this property. Therefore, we will not consider four-component density functional theory approaches presently. Because spin–orbit coupling is an integral part of the Dirac equation, the **g**-tensor will appear as a first-order perturbation with respect to the magnetic field [26, 32], similar to the two-component techniques.

$$\hat{f} = \hat{T} + v_{\text{ext}} + v_{\text{ee}} + v_{\text{xc}} + \hat{h}_{\text{SO}} + \hat{h}_Z + \hat{h}_L + \hat{h}_{\text{SO}}^{\text{dia}} \tag{32.14}$$

The terms $\hat{h}_Z$ and $\hat{h}_L$ are the one-electron spin- and orbital- Zeeman operators, respectively (see Eqs. (32.4) and (32.5)). The functionals E_{xc} and v_{xc} are, respectively, the exchange-correlation (XC) energy and XC potential. At least in principle [2], these functionals may incorporate the dependence on spin-densities ρ_σ, spin-current densities $\vec{j}_\sigma$, and KS orbitals (for "exact exchange" [35] and "τ-dependent" [36] functionals). Operators $\hat{h}_{\text{SO}}$ and $\hat{h}_{\text{SO}}^{\text{dia}}$ are effective, one-electron operators, intended to represent the spin–orbit coupling and the SO gauge correction. Their explicit form will be given in Section 32.3.3.

In the familiar, non-relativistic case, the non-interacting kinetic energy operator $\hat{T}$ is given by:

$$\hat{T}^{\text{NR}} = \frac{1}{2}\hat{p}^2 \tag{32.15.1}$$

For the zeroth order regular approximation (ZORA) [37–39] it is:

$$\hat{T}^{\text{ZORA}} = \hat{p} \cdot \frac{c^2}{2c^2 - v_{\text{eff}}}\hat{p} \tag{32.15.2}$$

where v_{eff} is the effective one-electron potential. Finally, for the two-component Douglas–Kroll (DK) method [40–42], the non-interacting kinetic energy is given by:

$$\hat{T}^{\text{DK}} = c\left(\hat{p}^2 + m^2c^2\right)^{1/2} \tag{32.15.3}$$

In the non-relativistic case, and for the existing ZORA implementations, the external scalar potential v_{ext} and electron–electron interaction potentials v_{ee} are given by the Coulomb law expressions:

$$v_{\text{ext}}(\vec{r}) = -\sum_A \frac{Z_A}{\left|\vec{r} - \vec{R}_A\right|} \tag{32.16}$$

$$v_{\text{ee}}(\vec{r}) = \int \frac{\rho(\vec{r}')}{\left|\vec{r} - \vec{r}'\right|} \mathrm{d}\,\vec{r}' \tag{32.17}$$

In the Douglas–Kroll approach, v_{ext} is replaced by a rather complicated expression [40], which is beyond the scope of this review. (See Ref. [43] for a critical comparison of ZORA, DK, and other relativistic approaches).

Because of the small energy scale of the EPR transitions (even in the high-field, 150 GHz F-band spectra, typical separation between EPR energy levels is below 0.001 eV [3]), the field-dependent terms are best treated as a perturbation. For the spin–orbit coupling, the situation is less clear. For light nuclei, the spin–orbit coupling is quite weak (e.g. the $^3P_2$ and $^3P_1$ levels in atomic oxygen are split by only

0.02 eV), which appears to indicate perturbative treatment (however, also see Section 32.4.2). Already for copper, spin–orbit splitting becomes comparable to two-electron interaction (in free Cu^{+2} ion, the $^2D_{5/2}$ and $^2D_{3/2}$ levels are split by 0.26 eV). The SO splittings increase by another order of magnitude for 5d transition metals, and heavier elements, making the perturbational treatment of the SO operators in such systems questionable.

As a result, two distinct approaches to the calculation of **g**-tensors have emerged: in two-component approaches, the spin–orbit coupling is treated variationally, with the **g**-tensor calculated as a first derivative of the energy. In one-component methods, both the magnetic field and the SO coupling are treated as perturbations, leading to a second-order **g**-tensor expression. The conceptually simpler first-order approach will be examined first, followed by the mathematically more involved second-order method.

32.3.1
EPR g-Tensor as a First-Order Property (Two-Component Methods)

A two-component **g**-tensor treatment is not new in DFT. The **g**-tensor was already calculated as a first-order property of a two-component, spin–orbit coupled DFT wavefunction by Case back in 1985 [8, 44]. More recently, it has been implemented in ADF [45, 46] by van Lenthe et al. [20] and in PARAGAUSS [47] by Neyman et al. [26]. Perhaps the clearest exposition of this technique was given by Jayatilaka [15], although not in the context of density functional theory.

In molecular, two-component relativistic DFT calculations, Kohn–Sham orbitals are given by the expansion over basis functions:

$$\psi_i = \psi_i^{\alpha}|\alpha\rangle + \psi_i^{\beta}|\beta\rangle \tag{32.18}$$

$$\psi_i^{\alpha} = \sum_{\mu} C_{\mu i}^{\alpha}\chi_{\mu} \tag{32.19}$$

$$\psi_i^{\beta} = \sum_{\mu} C_{\mu i}^{\beta}\chi_{\mu} \tag{32.20}$$

where the coefficients $C_{\mu i}^{\alpha}$ and $C_{\mu i}^{\beta}$ (and therefore the spatial parts ψ_i^{α} and ψ_i^{β}, associated with $|\alpha\rangle$ – and $|\beta\rangle$ –spin components) are allowed to become complex. These coefficients are determined through a self-consistent solution of the eigenequations:

$$\begin{pmatrix} \mathbf{F}^{\alpha\alpha} & \mathbf{F}^{\alpha\beta} \\ \mathbf{F}^{\beta\alpha} & \mathbf{F}^{\beta\beta} \end{pmatrix} \begin{pmatrix} \mathbf{C}_i^{\alpha} \\ \mathbf{C}_i^{\beta} \end{pmatrix} = \varepsilon_i \begin{pmatrix} \mathbf{S} & 0 \\ 0 & \mathbf{S} \end{pmatrix} \begin{pmatrix} \mathbf{C}_i^{\alpha} \\ \mathbf{C}_i^{\beta} \end{pmatrix} \tag{32.21}$$

where **S** is the matrix of overlap integrals between the basis functions, and **F** are the matrix elements of the Kohn–Sham–Fock operator (Eq. (32.14)), calculated in the absence of the magnetic field. For field-independent basis functions, the derivative

of the total energy with respect to magnetic field strength can then be calculated using the Hellmann–Feynman theorem [15]:

$$\sum_{i}^{\mathrm{occ}} \left\langle \psi_i \middle| \frac{\partial}{\partial B} \left(\hat{h}_{\mathrm{Z}} + \hat{h}_{\mathrm{L}} + \hat{h}_{\mathrm{SO}}^{\mathrm{dia}} \right) \middle| \psi_i \right\rangle = \frac{\partial E}{\partial B} = \frac{\tilde{S}}{2c} \left(\vec{\xi} \cdot G \cdot \vec{\xi} \right)^{1/2} \tag{32.22}$$

(The factor c^{-1} on the right-hand side of Eq. (32.22) is often absorbed in the definition of the Zeeman operators $\hat{h}_{\mathrm{Z}}$and $\hat{h}_{\mathrm{L}}$). In the absence of symmetry, the derivative has to be evaluated at six different orientations of the magnetic field [15]. This fully determines the symmetric tensor $\mathbf{G} = \mathbf{g} \cdot \mathbf{g}^{\mathrm{T}}$ (see Eq. (32.2)).

Evaluation of the derivative in Eq. (32.22) requires that the Kohn–Sham orbitals are perturbation-adapted[3)] [15], which does not place any restrictions on the form of the wavefunction, but may require several, independent SCF calculations, one for each orientation of the magnetic field. While this is straightforward to achieve in *ab initio* calculations, a peculiar practical complication arises in spin-density functional theory. In the two-component approach, spatial components of the spin operator do not commute with the Hamiltonian. Therefore, if the spin-density is defined in analogy to one-component techniques (the so-called "collinear" approach [48, 49]), by:

$$\rho_{\alpha-\beta} = 2 \sum_{i}^{\mathrm{occ}} \psi_i^* \hat{s}_z \psi_i \tag{32.23}$$

the spin-densities, and hence the exchange-correlation potential, become orientation-dependent. In turn, this leads to orientational dependence of the total energy, of the order of $0.05\,\mathrm{eV\,atom^{-1}}$ [48], so that Eq. (32.22) can no longer be applied with confidence.

The problem can be overcome within the "non-collinear" spin-density functional theory, which arises naturally within relativistic DFT [50] (Also see Ref. [49] for a recent review). In the non-collinear approach, the spin-density is defined as the magnitude of the local magnetization vector:

$$\rho_{\alpha-\beta}^2 = \sum_{\sigma=x,y,z} \left(2 \sum_{i}^{\mathrm{occ}} \psi_i^* \hat{s}_\sigma \psi_i \right)^2 \tag{32.24}$$

Definition of Eq. (32.24) is rigorously rotationally invariant, and thus presents no difficulties with Eq. (32.22).

Practical implementation of Eq. (32.24) requires somewhat tedious algebra, particularly if gradient or higher terms are included in the exchange-correlation potential [48]. Instead, a constraint is commonly placed on the spatial part of the Kohn–Sham orbitals, by requiring that the orbitals appear in conjugate pairs, connected by time-reversal symmetry (Kramers pairs) [20, 26]:

3) A simple way to guarantee that the final SCF orbitals are perturbation-adapted is to perform the SCF procedure in the presence of a weak magnetic field, which is gradually switched off as convergence is approached [15].

$$\begin{aligned}\psi_{i,1} &= \overset{\alpha}{\psi}_i |\alpha\rangle + \overset{\beta}{\psi}_i |\beta\rangle \\ \psi_{i,2} &= -\left(\overset{\beta}{\psi}_i\right)^* |\alpha\rangle + \left(\overset{\alpha}{\psi}_i\right)^* |\beta\rangle\end{aligned} \tag{32.25}$$

Contributions to Eq. (32.22) from fully occupied Kramers pairs will vanish, so that only the singly occupied molecular orbital (SOMO) will appear on the left-hand side of Eq. (32.22). For a spin-restricted calculation with one unpaired electron ($\tilde{S} = 1/2$), the requirement of perturbation-adapted orbitals can be removed, by treating the singly occupied Kramers pair with degenerate perturbation theory [31]. To first order in the magnetic field, the Hamiltonian matrix within the degenerate subspace can be written as [20, 26]:

$$\mathbf{\Phi} = \begin{pmatrix} \vec{B}\cdot\mathbf{\Phi}_{11} & \vec{B}\cdot\mathbf{\Phi}_{12} \\ \vec{B}\cdot\mathbf{\Phi}_{21} & \vec{B}\cdot\mathbf{\Phi}_{22} \end{pmatrix} = \sum_{a=x,y,z} B_a \begin{pmatrix} \mathbf{\Phi}^a_{11} & \mathbf{\Phi}^a_{12} \\ \mathbf{\Phi}^a_{21} & \mathbf{\Phi}^a_{22} \end{pmatrix} \tag{32.26}$$

where matrix elements $\mathbf{\Phi}$ are given by the first derivative of the orbital-, spin-Zeeman, and diamagnetic spin-orbit integrals over the SOMO Kramers pair, with respect to the magnetic field:

$$\mathbf{\Phi}_{ab} = \left(\mathbf{\Phi}^x_{ab},\ \mathbf{\Phi}^y_{ab},\ \mathbf{\Phi}^z_{ab}\right) \tag{32.27}$$

$$\mathbf{\Phi}^c_{ab} = \left\langle \psi_{\mathrm{SOMO},a} \middle| \frac{\partial}{\partial B_c}\left(\hat{h}_{\mathrm{Z}} + \hat{h}_{\mathrm{L}} + \hat{h}^{\mathrm{dia}}_{\mathrm{SO}}\right) \middle| \psi_{\mathrm{SOMO},b} \right\rangle \tag{32.28}$$

After writing the effective Hamiltonian of Eq. (32.1) in terms of Pauli matrices σ [31, 33]:

$$H = \frac{1}{4c}\vec{B}\cdot(\mathbf{g}\cdot\vec{\sigma}) = \frac{1}{4c}\sum_{a=x,y,z} B_a \begin{pmatrix} g_{az} & g_{ax} - ig_{ay} \\ g_{ax} + ig_{ay} & -g_{az} \end{pmatrix} \tag{32.29}$$

term-by-term comparison of Eqs. (32.26) and (32.29), for different orientations of the magnetic field, leads to the final expressions for the **g**-tensor components [20]:

$$\begin{aligned} g_{kx} &= 4c\mathrm{Re}\left(\mathbf{\Phi}^k_{21}\right) = 4c\mathrm{Re}\left(\mathbf{\Phi}^k_{12}\right) \\ g_{ky} &= 4c\mathrm{Im}\left(\mathbf{\Phi}^k_{21}\right) = -4c\mathrm{Im}\left(\mathbf{\Phi}^k_{12}\right) \\ g_{kz} &= 4c\mathrm{Re}\left(\mathbf{\Phi}^k_{11}\right) = 4c\mathrm{Re}\left(\mathbf{\Phi}^k_{22}\right) \end{aligned} \tag{32.30}$$

It should be emphasized that, unlike the general result of Eq. (32.22), these expressions are valid only for the case of an effective spin-doublet, treated in the spin-restricted approximation.

32.3.2
EPR g-Tensor as a Second-Order Property (One-Component Methods)

In the second-order treatment of the **g**-tensor, both the magnetic field and spin–orbit coupling operators are treated as perturbations. With a few exceptions [8, 15, 32], this is the approach taken by most *ab initio* studies [12–14, 16, 17], and many early DFT implementations [6, 7, 9, 10]. In a second-order approach, it is sufficient to determine the electronic structure up to the first order in either spin–orbit coupling, or the magnetic field (orbital Zeeman operator $\hat{h}_{\mathrm{L}}$). For practical reasons [19], the magnetic field is usually chosen as the first perturbation [19, 21–25]. In the simplest case (all-electron calculation with single gauge origin, no relativistic effects beyond $\hat{h}_{\mathrm{SO}}$, no current dependence in the exchange-correlation functional, and no admixture of the exact exchange), the **g**-tensor is then given by [19, 21–25]:

$$g_{\mathrm{st}} = g_{\mathrm{e}}\delta_{\mathrm{st}} + \Delta g^{\mathrm{d}}_{\mathrm{st}} + \Delta g^{\mathrm{p}}_{\mathrm{st}} \tag{32.31}$$

$$\Delta g^{\mathrm{d}}_{\mathrm{st}} = \frac{2c}{\tilde{S}} \sum_{\sigma i}^{\mathrm{occ}} \left\langle \psi_{\sigma i} \middle| \hat{h}^{\mathrm{dia}}_{\mathrm{SO,\,st}} \middle| \psi_{\sigma i} \right\rangle \tag{32.32}$$

$$\Delta g^{\mathrm{p}}_{\mathrm{st}} = \frac{2c}{\tilde{S}} \sum_{\sigma} \sum_{i}^{\mathrm{occ}} \sum_{a}^{\mathrm{virt}} u_{ai}^{\sigma,s} \left\langle \psi_{\sigma i} \middle| \frac{1}{i}\, \hat{h}_{\mathrm{SO,\,t}} \middle| \psi_{\sigma a} \right\rangle \tag{32.33}$$

In Eqs. (32.32) and (32.33), σ refers to electron spin ($\sigma = \alpha, \beta$), while indices i and a run over occupied and virtual KS MOs, respectively. Additional, small terms will appear if further relativistic corrections are considered, or gauge-dependent orbitals are introduced. The free-electron contribution $g_{\mathrm{e}}\,\delta_{\mathrm{st}}$ arises from the spin-Zeeman term in the Hamiltonian (which commutes with the zeroth-order Hamiltonian in this approximation.)

The coefficients $u_{ai}^{\sigma,s}$ describe the mixing between occupied and virtual Kohn–Sham MOs, induced by the *s*-component of the magnetic field. Under the same assumptions as Eqs. (32.31) – (32.33), they are given by:

$$u_{ai}^{\sigma,s} = \frac{1}{\varepsilon_{\sigma a} - \varepsilon_{\sigma i}} \left\langle \psi_{\sigma a} \middle| \frac{1}{i} \frac{\partial \hat{h}_L}{\partial B_s} \middle| \psi_{\sigma i} \right\rangle \tag{32.34}$$

(The factor $1/i$ in Eqs. (32.33) and (32.34) appears to ensure that all quantities and operators are real.) For current-dependent functionals, or for exact-exchange functionals [35], additional terms, dependent on the first-order change in density matrix, will appear in Eq. (32.34). In the latter case, orbital mixing coefficients have to be determined as solutions of coupled-perturbed Kohn–Sham (CPKS) equations [22, 24]. Most of the mathematical aspects, involved in the derivation of the

Eqs. (32.31) – (32.34) are shared with the DFT approaches to the NMR shielding tensors, which are discussed in Chapter 6.

Equations (32.32) and (32.33) are derived in the assumption that the operators $\hat{h}_{\mathrm{SO,t}}$ and $\hat{h}^{\mathrm{dia}}_{\mathrm{SO,st}}$ do not couple spin-orbitals $\psi_{\sigma i}$ from different spin spaces. Satisfying this assumption requires special treatment of the spin–orbit coupling. The operators $\hat{h}_{\mathrm{SO,t}}$ and $\hat{h}^{\mathrm{dia}}_{\mathrm{SO,st}}$ are commonly written as:

$$\hat{h}^{\mathrm{dia}}_{\mathrm{SO,st}} = \left.\frac{\partial^2 \hat{h}^{\mathrm{dia}}_{\mathrm{SO}}}{\partial B_s \partial \hat{s}_t}\right|_{s=0,\ \vec{B}=0} \tag{32.35}$$

$$\hat{h}_{\mathrm{SO,t}} = \left.\frac{\partial \hat{h}_{\mathrm{SO}}}{\partial \hat{s}_t}\right|_{s=0} \tag{32.36}$$

In this case, the "derivatives" with respect to the spin operators, which appear in Eqs. (32.35) and (32.36) are nothing more than a shorthand notation for the spin-field reduction procedure, where the axis of spin quantization is chosen to coincide with each component of the spin operator ($\hat{s}_x$, $\hat{s}_y$, $\hat{s}_z$) in turn. Given this choice (which is possible because the zeroth order Hamiltonian in one-component approaches commutes with the one-electron spin operator), the spin-orbitals are automatically perturbation-adapted.

For example, the components of the one-electron nuclear spin–orbit coupling operator $\hat{h}_{\mathrm{SO(N),}t}$ ($t = x, y, z$):

$$\hat{h}_{\mathrm{SO(N),t}} = \frac{g'}{2c^2} \sum_A Z_A \hat{s}_q \left|\vec{r} - \vec{R}_A\right|^{-3} \left\{\left(\vec{r} - \vec{R}_A\right) \times \hat{p}\right\}_t \tag{32.37}$$

are given in terms of the spin operator $\hat{s}_q = \hat{s}_z$ (corresponding to the direction of spin quantization), rather than operators $\hat{s}_x$, and $\hat{s}_y$, as might have been naïvely expected from the component-by-component expansion of Eq. (32.6)[4].

The paramagnetic contribution Δg^p_{st} can be re-cast in a physically more transparent [25, 31, 51] form in terms of spin-currents $\vec{j}^s_\alpha$ and $\vec{j}^s_\beta$, induced by a unit magnetic field applied along the direction s:

$$\Delta g^{\mathrm{p}}_{\mathrm{st}} = \frac{2c}{\tilde{S}} \left[\int \hat{g}_{\mathrm{SO}} \times \left(\vec{j}^s_\alpha - \vec{j}^s_\beta\right) \mathrm{d}\vec{r}\right]_t \tag{32.38}$$

4) It would have been possible to use the straightforward expansion of Eq. (32.6) as well, giving the alternative form of the spin –orbit coupling operators

$$\tilde{h}_{\mathrm{SO(N),t}} = \frac{g'}{2c^2} \sum Z_A \hat{s}_t \left|\vec{r} - \vec{R}_A\right|^{-3} \left\{\left(\vec{r} - \vec{R}_A\right) \times \hat{p}\right\}_t .$$

For the components $t = x$ and y, the alternative SO operators will couple the α- and β-spin KS orbitals, contrary to the assumptions made in deriving Eqs. (32.32)–(32.34). In the *spin-restricted* approach, this mixing can be accommodated by treating each pair of α/β-spin orbitals sharing the same spatial part with degenerate perturbation theory. The final working expressions are then identical to Eqs. (32.31)–(32.37). It is far from clear how the alternative SO coupling operators could be treated perturbationally in the *spin-unrestricted* approximation.

$$\vec{j}_{\sigma}^{s} = \sum_{i}^{\text{occ}} \sum_{a}^{\text{virt}} u_{ai}^{\sigma,s} \left(\psi_{\sigma i} \vec{\nabla} \psi_{\sigma a} - \psi_{\sigma a} \vec{\nabla} \psi_{\sigma i} \right) \tag{32.39}$$

The total spin-current is given by $\vec{j}_{\sigma} = \vec{B} \cdot \left(\vec{j}_{\sigma}^{x}, \vec{j}_{\sigma}^{y}, \vec{j}_{\sigma}^{z} \right)$. The operator $\hat{g}_{\text{SO, t}}$ is obtained from the corresponding spin–orbit coupling operator $\hat{h}_{\text{SO, t}}$, by removing the electron momentum operator (which is transferred to the spin-current expression (32.39)) and replacing spin operator $\hat{s}_z$ with ½. For example, for $\hat{g}_{\text{SO(N)}}$:

$$\hat{g}_{\text{SO(N)}} = \frac{g'}{4c^2} \sum_{A} Z_A \left| \vec{r} - \vec{R}_A \right|^{-3} \left(\vec{r} - \vec{R}_A \right) \tag{32.40}$$

It should be emphasized that despite the formal similarity to the classical perturbation theory result [12, 52], derivation of Eqs. (32.31) – (32.40) does not rely on summation over excited states. Their justification is found entirely within the current-density functional theory (CDFT) [53].

32.3.3
Treatment of the Spin–Orbit Coupling Operator

In a purist view of non-relativistic DFT, both two-electron contributions to the spin–orbit coupling operator ($\hat{H}_{\text{SO(2e)}}$ and $\hat{H}_{\text{SOO}}$) would belong to the exchange-correlation functional, with the spin–other-orbit term $\hat{H}_{\text{SOO}}$ appearing as current dependence of the exchange-correlation potential. Because no sufficiently accurate functionals of this kind have been developed so far (See Ref. [54], and references therein), practical **g**-tensor calculations are left with the task of choosing an approximate one-electron operator $\hat{h}_{\text{SO}}$, suitable for use in Eq. (32.33) (one-component methods), or within the zeroth-order Hamiltonian (two-component methods).

The simplest approach, widely used in early DFT calculations [6, 9, 10] is to approximate the total spin–orbit coupling by a modified nuclear spin–orbit operator:

$$\hat{h}_{\text{SO}} = \sum_{A} \xi_A \left(\left| \vec{r} - \vec{R}_A \right| \right) \hat{\mathbf{s}} \cdot \left(\vec{r} - \vec{R}_A \right) \times \hat{p} \tag{32.41}$$

with the atomic factors $\xi_A(r)$ designed to mimic the screening effect of the core electrons. A common choice of $\xi_A(r)$ (used by Ref. [22]) is simply:

$$\xi_A(r) = \frac{g'}{4c^2} \frac{Z_{A,\,\text{eff}}}{r^3} \tag{32.42}$$

The effective nuclear charges $Z_{A,\,\text{eff}}$ are then adjusted to reproduce experimental spin–orbit term splittings [55]. Relativistic spin–orbit effective core potentials [56] can be used to a similar effect [21, 25]. These approximations are justified by the fact

that the spin–orbit coupling is nearsighted, and is dominated by regions of space close to the nuclei.

A more sophisticated approach based on the same effective-potential idea, makes use of the observation that the $\vec{r}/r^3$ terms in the nuclear and 2e SO Hamiltonians (Eqs. (32.6) and (32.8)) are simply the derivatives of the corresponding electron–nuclear and electron–electron interaction potentials. In the one-electron Kohn–Sham–Fock eigenequations (Eq. (32.13)), these interactions are represented by an effective one-electron potential:

$$v_{\text{eff}} = v_{\text{ext}} + v_{\text{ee}} + v_{\text{xc}} \tag{32.43}$$

Therefore, the same substitution appears to be justified in the SO coupling operator, giving:

$$\hat{h}_{\text{SO}} = \frac{g'}{4c^2}\ \hat{s} \cdot \left(\frac{\partial v_{\text{eff}}}{\partial \vec{r}} \times \hat{p} \right) \tag{32.44}$$

This approximation is used by several implementations [19, 20, 25, 26] and is expected to give a faithful description of the nuclear and 2e spin–orbit coupling. By design, it neglects the $\hat{H}_{\text{SOO}}$ contribution in the many-electron Hamiltonian, which is often small, compared to $\hat{H}_{\text{SO(N)}} + \hat{H}_{\text{SO(2e)}}$ [21, 25] (See Section 32.4.3 and Tab. 32.5 below).

An ingenious suggestion for an approximate treatment of the spin–other orbit contribution to the **g**-tensor was given by Pickard and Mauri [25]:

$$\Delta g_{st}^{\text{SOO}} = \frac{1}{\tilde{S}} \int B_t^{1,s}(\vec{r}) \left[\rho_\alpha(\vec{r}) - \rho_\beta(\vec{r}) \right] \mathrm{d}\vec{r} \tag{32.45}$$

where $\vec{B}^{1,s}$ is the magnetic field due to the induced current, arising from unit magnetic field applied in direction s ($s = x, y, z$):

$$\vec{B}^{1,s}(\vec{r}) = \frac{1}{c} \int \left[\left(\vec{j}_\alpha^{\,s}(\vec{r}) + \vec{j}_\beta^{\,s}(\vec{r}) \right) - \frac{1}{2\tilde{S}} \left(\vec{j}_\alpha^{\,s}(\vec{r}) - \vec{j}_\beta^{\,s}(\vec{r}) \right) \right] \times \frac{\vec{r} - \vec{r}'}{|\vec{r} - \vec{r}'|^3} \mathrm{d}\vec{r}' \tag{32.46}$$

The $\left(\vec{j}_\alpha^{\,s} - \vec{j}_\beta^{\,s} \right)$ term in Eq. (32.46) is intended as a self-interaction correction, preventing the unpaired electron from "feeling" its own magnetic field. It still remains to be seen how this prescription fares in practical calculations in molecules.

Yet another approach to treating the two-electron SO coupling operators is taken by Malkina and coworkers [21, 24, 57], who step outside density functional theory and approximate the one-electron matrix elements in Eq. (32.33) by matrix elements of the two-electron operators $\hat{H}_{\text{SO(2e)}}$ and $\hat{H}_{\text{SOO}}$, taken between the non-interacting Kohn–Sham reference wavefunction Ψ_{ref}, and a single-determinantal wavefunction

$\Psi_{\mathrm{ref}}^{i\to a}$ obtained by promoting an electron from an occupied KS orbital i to a virtual orbital a[5]:

$$\left\langle \psi_{\sigma i}\middle|\hat{\boldsymbol{h}}_{\mathrm{SO}}\middle|\psi_{\sigma a}\right\rangle \approx \left\langle \Psi_{\mathrm{ref}}\middle|\hat{H}_{\mathrm{SO(N)}}+\hat{H}_{\mathrm{SO(2e)}}+\hat{H}_{\mathrm{SOO}}\middle|\Psi_{\mathrm{ref}}^{i\to a}\right\rangle \tag{32.47}$$

The underlying assumption of this approach is that Ψ_{ref} is a good approximation to the (unknown) wavefunction Ψ_{true} of the interacting system. Direct evaluation of the right-hand side of Eq. (32.47) can be computationally very demanding [21]. Very similar results can be obtained by exploiting the locality of the SO operators, using the atomic mean field approximation (AMFI) introduced by Hess et al. [59] and popularized by Schimmelpfennig [60].

32.3.4
Gauge Invariance of the g-Tensor

The dependence of magnetic operators on the choice of the origin of the coordinate system (or more generally, on the gauge of the vector-potential) is often the major stumbling block in calculations of magnetic properties [61]. Practical experience with ab initio and DFT calculations so far [12, 14, 15, 20] indicates that the gauge dependence of the **g**-tensors is usually small, so that the common prescription [62] of placing the gauge origin at the centroid of the electron charge is sufficient to obtain accurate results in small molecules. As noted by Kaupp and co-workers [63], an exception to this rule of thumb can occur in situations where a delocalized radical exhibits a **g**-tensor with two similar principal components. In this case, the orientation (but not the magnitude) of the principal components becomes quite sensitive to the choice of the coordinate origin, making a gauge-independent treatment mandatory.

In larger systems, all common approaches to mitigation of the gauge dependence (gauge-including atomic orbitals, GIAOs [19, 20, 63]; individual gauge origin for localized orbitals, IGLO [21], and gauge-including projector-augmented waves, GIPAW [25, 64]) give very similar results for the **g**-tensors. At the same time, the individual implementations vary greatly, depending on the choice of zeroth-order Hamiltonian and treatment of the spin–orbit operators. These details can be found in the original publications [19–21, 24, 25] and need not be discussed here (also see Chapter 6 by van Wüllen). On aesthetical grounds, the rigorously gauge invariant GIAO and GIPAW approaches are to be preferred over IGLO, which may suffer

5) The original publications by Malkina and coworkers [21, 57] give the 2-electron SO interaction integrals as "$\langle\Psi_{\sigma,i}|\,\hat{H}_{\mathrm{SO(2e)}}+\hat{H}_{\mathrm{SOO}}\,|\Psi_{\sigma,a}\rangle$", with $\Psi_{\sigma,i}$ and $\Psi_{\sigma,a}$ defined as *one-electron* Kohn–Sham orbitals, and *N-electron* operators $\hat{H}_{\mathrm{SO-e}}$, $\hat{H}_{\mathrm{SOO}}$ given by Eqs. (32.8) and (32.9). The integration over the remaining (N-1) electronic coordinates is thus left unspecified. From the close agreement of the results of ref. [21] to other DFT and ab initio implementations, as well as from the approximate AMFI expressions, given in Refs. [57, 58], Eq. (32.47) appears to be the only reasonable interpretation of the formula above.

from artifacts, introduced due to arbitrariness of the underlying localization procedure.

32.3.5 Practical Implementations

A number of DFT **g**-tensor implementations have been reported in the literature [19–25]. The salient features of these implementations are summarized in Table 32.1. The implementations fall into two major classes. Two-component codes (using ZORA in ADF [20] and Douglas-Kroll in PARAGAUSS [26]) include spin–orbit coupling effects to all orders, and can be applied to studies of radicals with arbitrarily large Δg shifts. However, both the ADF and PARAGAUSS implementations invoke the spin-restricted approximation (Eq. (32.30)), which reduces their usefulness in cases where spin-polarization is important. In their current form, two-component techniques are also limited to treating effective doublet states, and are somewhat restricted in the choice of the XC functionals.

One-component methods, on the other hand, can treat radicals of arbitrary multiplicity (even if not "officially" implemented, the required change to the code is trivial [22, 23]). Due to the incorporation of spin-polarization terms, these methods tend to be more accurate for radicals with small Δg values. At the same time, truncation of the SO contributions at the first order leads to some qualitative failures (See Section 32.4). One- and two- component approaches are therefore complementary. In this respect, the ADF [45, 46] program package, which incorporates both one- [19, 23] and two- component [20] implementations is particularly attractive for practical applications.

The implementation of Pickard and Mauri [25] also deserves a special mention. This is the first, and so far the only, **g**-tensor program, which supports calculations on defects in periodic solids. In principle, **g**-tensors of solid defects can also be modeled with cluster models, using standard molecular codes [67]. However, the cluster size dependence of the calculated **g**-tensors is usually severe [67, 68], which makes it difficult to obtain converged results. This is also one of the only two implementations to treat the spin–orbit coupling operator completely, including spin–other-orbit terms. (The first complete implementation was by Malkina et al. [21, 24]). Unfortunately, Pickard and Mauri did not publish any results including the Δg_{SOO} correction for small radicals, making comparison of the two approaches impossible.

Table 32.1 Comparison of published DFT implementations of the EPR **g**-tensors.

	ADF (A)[a]	ADF (B)[b]	deMon-EPR[c]	ReSpect[d]	ORCA[e]	PARAGAUSS[f]	GIPAW[g]
Molecular/ periodic	molecular	molecular	molecular	molecular	molecular	molecular	periodic
One or two-component[h]	1	2	1	1	1	2	1
Treatment of $\hat{h}_{SO}$	effective (Eq. (32.44))	effective (Eq. (32.44))	Ψ_{ref} (Eq. (32.47)); AMFI; effective (SO-ECP, Eq. (32.41))	Ψ_{ref} (Eq. (32.47)); AMFI; effective (SO-ECP, Eq. (32.41))	effective (Eqs. (32.41) and (32.42))	effective	effective, including SOO (Eqs. (32.44) and (32.45))
Treatment of the gauge dependence	GIAO	GIAO, common	IGLO, common	IGLO, GIAO, common	common	common	GIPAW, CSGT
Radical type	high-spin[i]	doublet[j]	high-spin[k]	high-spin[k]	high-spin[i]	doublet[j]	high-spin[k]
Scalar relativity	yes (Breit–Pauli)	yes (ZORA)	yes (ECPs)	yes (ECPs)	no	yes (Douglas–Kroll)	yes (relativistic pseudo-potentials)
Basis set	STO, L=spdf	STO, L=spdf	GTO, L=spd	GTO, any L	GTO	GTO	augmented plane wave
Functionals	LDA, GGA, SIC[l]	LDA, GGA	LDA, GGA	LDA, GGA, hybrid, meta-GGA	LDA, GGA, hybrid	LDA, GGA	LDA, GGA

a) Refs. [19, 23].
b) Ref. [20].
c) Ref. [21].
d) Refs. [24, 63].
e) Ref. [22].
f) Ref. [26].
g) Ref. [25].
h) All 2-component methods in this table are limited to the spin-restricted treatment (RKS). All one-component approaches support both spin-restricted and spin-unrestricted calculations.
i) Spatially non-degenerate radicals of arbitrary multiplicity are supported.
j) Spatially non-degenerate doublets are supported.
k) Published formulation and results are for doublet radicals only. However, high-spin **g**-tensors can be added with a trivial code modification [22, 23].
l) Self-interaction corrected functionals [66], both for LDA and GGA.

32.4
Numerical Performance of the DFT Approaches

Before briefly examining the factors affecting the accuracy of DFT **g**-tensors, it is instructive to see how DFT fares under the *optimal* circumstances: for light main group radicals with no close-lying excited states. This situation is illustrated by the DFT results for the g-shift component perpendicular to the main symmetry axis ($\Delta g_\perp$) in ten high-spin, diatomic radicals ($^3\Sigma$ ground state), which are collected in Table 32.2. Highly accurate, *ab initio* results for this set were previously obtained by Engstrom et al., using correlated CASSCF wavefunctions [16]. Experimental estimates of the gas-phase $\Delta g_\perp$ values are available from the rotational spectra, using Curl's relation [5]. These values are compared with the DFT and ab initio results in Fig. 32.1. With the exception of the three sulfur-containing radicals (SO, SH^+, S_2), DFT results are in admirable agreement with experiment. Even for the more difficult sulfur radicals, DFT agrees with experiment to within 20%, the accuracy expected from Curl's relation [5]. At least in this case, DFT is clearly competitive with much more laborious CASSCF calculations.

Table 32.2 Comparison of DFT and CASSCF results for $\Delta g_\perp$ tensor components (in parts per thousand, ppt), in diatomic main-group radicals with $^3\Sigma$ ground states.

Radical	Experiment[a]	CASSCF[b]	DFT[c]
O_2	2.9	2.8	3.3
SO	3.6	4.1	4.8
S_2	14.5	11.2	12.6
NH	1.7	1.4	1.9
NF	2.0	1.9	2.2
NCl	5.4	4.1	5.6
PH	4.5	4.0	4.8
PF	–1.6	–0.6	–1.0
OH^+	4.4	4.0	5.0
SH^+	9.0	7.8	11.2
Correlation coefficient		0.993	0.974
Correlation slope		0.749	0.909
Correlation intercept		0.6	0.8
RMS error		1.3	1.0

a) Experimental values are estimated from gas-phase spin-rotational constants given in Ref. [16].
b) CASSCF results for the large "CAS2" active space and TZ2P-quality basis set are cited from Ref. [16].
c) DFT results for the VWN LDA functional and TZP-quality basis set are cited from Ref. [23]. For PF, OH^+, and SH^+, which were not treated in Ref. [23], **g**-tensors were calculated using the program of Refs. [19,23], VWN functional, and an all-electron Slater-type TZ2P basis set.

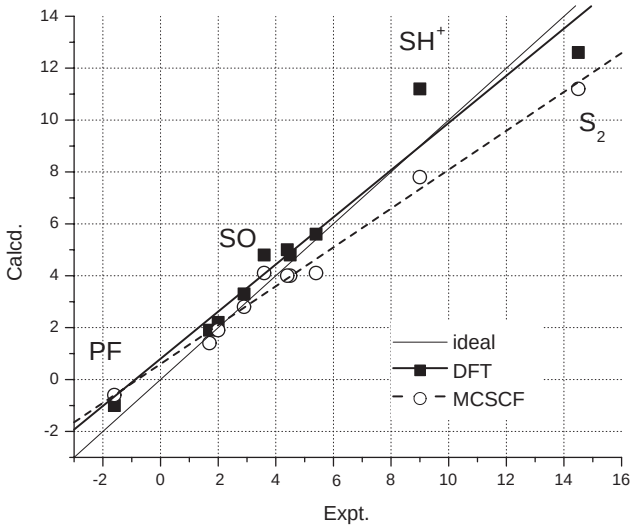

Figure 32.1 Comparison of the DFT and MCSCF $\Delta g_{\perp}$ results (in ppt) for diatomic $^3\Sigma$ radicals. All values are from Table 32.2.

32.4.1
Exchange-Correlation Functionals and Basis Sets

For many magnetic properties, calculated values are rather sensitive to the choice of the basis set [61], either in the vicinity of the nuclei [69], or in the diffuse region [70]. Happily, the **g**-tensor is essentially a valence and semi-core property [18, 27], and is relatively insensitive to the choice of the basis set [19, 21, 23]. Quite modest split-valence basis sets, with one polarization function in the valence region, already produce reasonable results, with polarized triple-ζ basis sets being close to saturation [19, 21], both for the Slater and Gaussian-type basis sets. Any improvements from further expansion of the basis set appear to be swamped by the residual errors due to other approximations (see below). In d-block transition metal compounds, addition of f-type polarization functions appears unnecessary as well [23]. This weak dependence of the calculated Δg values on the basis set choice is illustrated in Fig. 32.2.

A cautionary note applies to elements with large semi-cores [71]. In this case, an adequate description of the core polarization is essential for obtaining reliable results. For example, freezing the 2p shell of the Al atom in aluminum oxide AlO ($^2\Sigma$), leads to $\Delta g_{\perp}$ value of –0.1 parts per thousand (ppt), completely out of line with the experiment (–2.2 ppt). Unfreezing the 2p shell leads to a much more reasonable value of –2.1 ppt.

The influence of the exchange-correlation functional on the calculated **g**-tensor components has received a great deal of attention [21–24, 51, 65]. A particularly impressive study, covering all major classes of functionals, was undertaken by Arbuznikov et al. [65]. In principle, due to the close analogy that exists between the

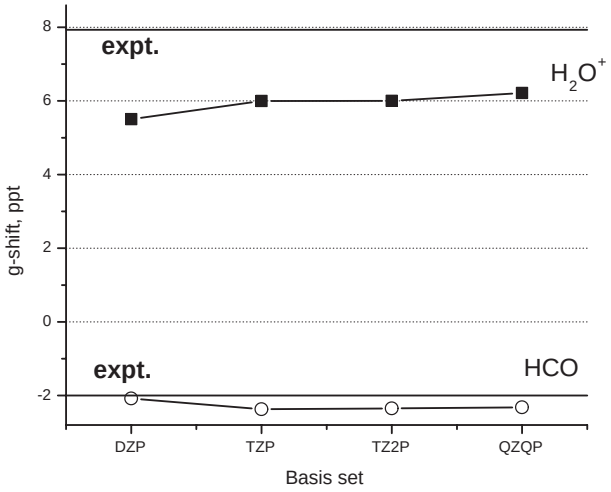

Figure 32.2 Dependence of the calculated isotropic Δg shifts (in ppt) on the choice of the basis set. Corresponding experimental values are shown as solid lines. (Data from Ref. [19]).

NMR shielding tensors and **g**-tensors [11, 19], many of the observations on the functional dependence of the former [11, 72, 73] also apply to the latter [27]. In particular, **g**-tensors of main-group radicals are, by and large, insensitive to the choice of the XC functional. In such radicals, common gradient-corrected functionals perform identically [21, 23], and do not represent a major improvement over the local density approximation (LDA) results [21–24]. For example, for a set of 19 high-spin, main group radicals [23], BP86 and RPBE functionals lead to root-mean-square (RMS) deviations from experimental $\Delta g_\perp$ values of, respectively, 6.2 and 6.3 ppt. Main-group results obtained with hybrid [22, 24, 65], meta-GGA [65], or model potential [65] functionals are also similar. For the main-group test set of Arbuznikov et al. [65], all functionals led to standard deviation from experiment of ≈0.5 ppt, and identical correlation coefficients (0.993–0.994). As usual, an exception is furnished by radicals with close-lying excited states (such as H_2O^+), which do show a significant dependence on the choice of the exchange-correlation functional. The latter example has been analyzed in detail by Kaupp et al. [24].

In transition metal radicals, the differences between functionals become more pronounced, but are still rather small compared to deviations from the experiment [21–24, 51, 65]. The huge variety in the electronic structure and bonding situation in transition metal complexes also means that the choice of the "best" functional is strongly system-dependent. For example, Patchkovskii and Ziegler found essentially no difference between LDA and GGA functionals for 15 small nd^1 (n=3,4,5) complexes [51] (RMS error of 56 ppt for VWN LDA, vs. 57 ppt for BP86 GGA), or for 28 high-spin diatomic radicals [23]. Kaupp and co-workers [24], studying a more diverse set of twelve 3d transition metal complexes, concluded that GGA functionals are some-

Table 32.3 Influence of the exchange-correlation functional, spin–orbit coupling, and spin polarization treatment on the calculated **g**-tensor components (in ppt) for a representative transition metal complex (TiF_3).

	$\hat{h}_{SO}$ Treatment	Program	$\Delta g_{\|\|}$	$\Delta g_{\perp}$	Ref.
Expt.[a]			–3.7	–123.7	
	Spin-restricted approaches				
LDA (VWN)	2-component, effective (Eq. (32.44))	ADF	–1.4	–84.8	[20]
GGA (BP86)	2-component, effective (Eq. (32.44))	ADF	–1.0	–79.7	[20]
GGA (BP86)	1-component, effective (Eq. (32.44))	ADF	+0.1	–73.3	[20]
GGA (BP86)	2-component, effective	PARAGAUSS	–0.3	–45.3	[26][6)]
	One-component, spin-unrestricted approaches				
LDA (VWN)	effective (Eq. (32.44))	ADF	–1.6	–60.7	[66]
LDA (VWN)	AMFI	ReSpect	–1.2	–50.9	[24]
GGA (BP86)	effective (Eq. (32.44))	ADF	–1.7	–42.8	[20]
GGA (BP86)	AMFI	deMon-EPR[b]	–1.1	–26.6	[21]
GGA (BP86)	AMFI	ReSpect	–1.3	–36.0	[24]
GGA (BP86)	effective (Eqs. (32.41), (32.42))	ORCA	–0.9	–30.7	[22]
meta-GGA (FT98)	AMFI	ReSpect	–1.2	–31.2	[65]
meta-GGA (PKZB)	AMFI	ReSpect	–1.3	–29.1	[65]
hybrid (B3LYP)	effective (Eqs. (32.41), (32.42))	ORCA	–1.1	–41.8	[22]
hybrid (B3PW91)	AMFI	ReSpect	–1.4	–48.8	[24]
hybrid (BHPW91)	AMFI	ReSpect	–1.4	–71.4	[24]
SIC-VWN[c]	effective (Eq. (32.44))	ADF	–1.9	–123.5	[66]
SIC-revPBE[c]	effective (Eq. (32.44))	ADF	–1.2	–71.4	[66]

a) In neon matrix; cited from Ref. [20].
b) The large difference in the calculated value $\Delta g_{\perp}$, compared to later AMFI calculations [24], arises from the use of an inadequate fitting set [24].

what more reliable (correlation coefficient of 0.972 for GGA, vs. 0.963 for LDA). The hybrid functionals were found to give the best results (correlation coefficient of 0.981 for B3PW91). A similar conclusion was reached by Neese [22], who examined

6) The PARAGAUSS result, obtained in the spin-restricted approximation, is not consistent with other spin-restricted values for this radical. Because the DK treatment [26] is closely related to the ZORA approach [20], and produces similar results in all other cases, this likely indicates an unnoticed technical problem with the Douglas–Kroll calculation of the TiF_3 **g**-tensor in Ref. [26].

B3LYP and PBE0 hybrid functionals. Somewhat disappointingly, in transition metal complexes meta-GGA functionals appear to be inferior to both hybrids and standard GGA functionals [65].

A stark example of the sensitivity of transition metal radicals to the choice of the exchange-correlation functional and treatment of spin-polarization is given by one of the most studied transition metal radicals, TiF_3 [10, 20–22, 24, 26, 65, 66]. The **g**-tensor components, calculated for this radical with different XC functionals, are summarized in Table 32.3. From the results of spin-restricted calculations [10, 20], it may appear that this radical is, at least qualitatively, well described by density functional theory. Spin-restricted LDA recovers about 2/3 of the experimental $\Delta g_\perp$ shift (–85 ppt vs. –124 ppt in experiment). However, this is an artifact of the spin-restricted treatment. Removing the spin-polarization constraint leads to an LDA $\Delta g_\perp$ shift of only half of the experimental value. Adding gradient, laplacian, or kinetic energy corrections deteriorates the result even further, so that BP86 (gradient-corrected), FT98 (laplacian meta-GGA), and PKZB (kinetic energy density meta-GGA) functionals all recover only about one third of the experimental $\Delta g_\perp$ value (ca. –30 ppt) [65]. Adding an admixture of the exact exchange improves the result to about the spin-unrestricted LDA level (B3PW91: –49 ppt; BHPW91: –71 ppt). At the same time, functionals with a high exact exchange fraction (BHPW91) begin to suffer from spin contamination, which significantly deteriorates the overall correlation with experiment [24]. A ray of hope for such cases is provided by the recently introduced self-interaction corrected functionals [74]. These functionals appear to be at least as successful in reproducing "difficult" **g**-tensors as hybrid functionals [66], without suffering from the undesirable spin-contamination effects.

32.4.2 Relativity and Spin-Polarization

An unpleasant dilemma, currently faced by all practical DFT calculations of the **g**-tensors, is that spin-polarization and high-order spin–orbit coupling effects cannot be treated at the same time. The problem is not new [8], and is closely related to the fundamental difficulty in defining spin-density in two-component approaches (see Section 32.3.1). While the issue is widely recognized and acknowledged [20, 23, 26, 27], we believe that its practical consequences have received much less attention than they deserve.

Table 32.4 collects calculated **g**-tensor components ($\Delta g_{||}$ and $\Delta g_\perp$) for 21 linear radicals with $^2\Sigma$ ground states, obtained with one- [19] and two-component [20] approaches. Because we used the same geometries, same functional, same approximation for the spin–orbit coupling operator, and basis sets similar to the original two-component ZORA study of this series [75], all major differences are expected to come from the treatment of spin polarization and high-order SO coupling effects.

For the parallel component $\Delta g_{||}$, the qualitative difference of the two approaches can be clearly seen in Fig. 32.3. While the two-component ZORA calculations are reasonably successful in reproducing experimental trends (correlation slope of 0.918, with root of the mean square error of 5 ppt), one-component results bear no

Table 32.4 Performance of one- and two-component DFT methods for the Δg tensor components (in ppt) for diatomic $^2\Sigma$ radicals, in comparison with experiment and four-component Dirac–Hartree–Fock calculations.

Radical	Experiment[a]		ZORA[a]		SZ[b]		DHF[c]	
	$\Delta g_{\parallel}$	$\Delta g_{\perp}$	$\Delta g_{\parallel}$	$\Delta g_{\perp}$	$\Delta g_{\parallel}$	$\Delta g_{\perp}$	$\Delta g_{\parallel}$	$\Delta g_{\perp}$
ZnH	–2.0	–17.1	–0.4	–24.9	–0.0	–19.7	–2.1	–1.8
CdH	–5.3	–49.9	–2.4	–71.7	–0.1	–55.9	–0.3	–17.2
HgH	–26.3	–174.3	–30.0	–251.8	–0.1	–158.9		
ZnF	–0.3	–6.3	–0.3	–6.8	–0.1	–6.3	–0.4	–43.7
CdF	–1.3	–17.3	–0.9	–21.4	–0.1	–20.0		
HgF	–9.3	–41.3	–14.0	–66.1	–0.2	–30.1		
ZnAg	0.2	–11.8	–0.3	–21.8	–0.0	–16.7		
CdAg	–0.9	–31.2	–1.3	–51.3	–0.0	–40.3		
HgAg	–6.5	–88.7	–10.4	–143.8	–0.1	–93.8		
CdCN		–34.2	–1.5	–40.4	–0.1	–36.7		
HgCN		–123.4	–18.4	–137.2	–0.2	–86.9		
ScO	–0.5	–0.5	–0.1	0.1	–0.0	–0.8	0.0	–0.5
YO	–0.7	–0.2	–0.2	0.6	–0.0	1.0	–0.2	–1.8
LaO	–2.3	–3.3	–0.7	–6.3	–0.0	–3.3	–0.2	–1.7
BO	–0.3	–1.7	–0.1	–2.5	–0.0	–2.2	–0.1	–1.4
AlO	–0.3	–2.2	–0.3	0.8	–0.1	–2.1[d]		
GaO	–3.3	–34.3	–6.0	–88.4	–0.2	–37.4		
InO	–27.3	–192.3	–45.3	–277.5	–0.2	–121.9		
BS	–0.7	–8.1	–0.5	–12.4	–0.1	–9.9	–0.1	–7.5
PdH	–37.3	290.9	–27.7	294.8	–0.2	248.3	–64.6	595.0
RhC	1.6	51.8	–2.0	50.3	–0.1	49.8		
Data points (All values)			19	21	19	21	9	9
Correlation coefficient			0.918	0.985	0.590	0.987	0.991	0.988
Correlation slope			1.067	1.193	0.004	0.822	1.763	1.961
RMS error			5.1	31.8	12.5	20.3	9.3	102.9
Data points ($\lvert\Delta g_{\perp}\rvert$ <100 ppt)[e]				17		17		8
Correlation coefficient				0.965		0.991		0.235
Correlation slope				1.459		1.023		0.210
RMS error				21.2		4.4		18.4

a) Experimental and two-component ZORA results, obtained with the BP86 exchange-correlation functional and all-electron QZP basis set, are cited from [75].

b) Ref. [19] and this work. One-component DFT results for the BP86 exchange-correlation functional were calculated using the program of Ref. [19], and geometries of Ref. [75]. Standard ADF basis set of TZ2P quality was used on hydrogen through gallium. Heavier nuclei were treated using TZP basis set. Frozen cores were used on Sc and Zn (2p), Ga (3p), Y through Cd (3d), In (4p), La and Hg (4d). Scalar Pauli relativistic corrections were applied self-consistently.

c) Four-component Dirac–Hartree–Fock results, using basis sets of double-ζ quality, are cited from Ref. [32].

d) A different $\Delta g_{\perp}$ value of –0.1 ppt, calculated using the same approach, was reported previously [19]. The discrepancy arises from the use of an excessively large 2p core in Ref. [19].

e) Data points restricted to the range of $\Delta g_{\perp}$ values where the first-order treatment of spin–order coupling operator may be expected to be adequate.

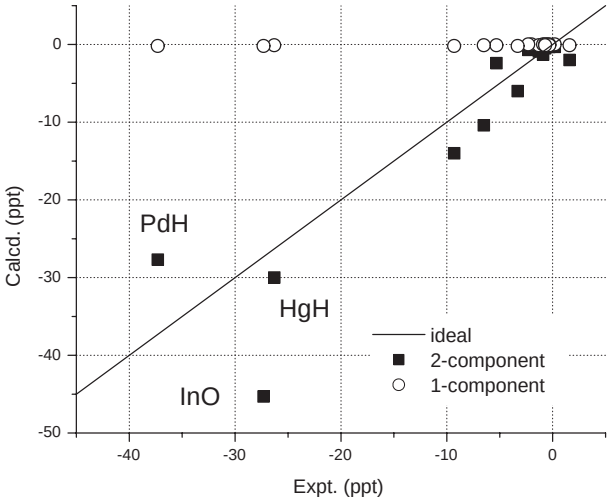

Figure 32.3 Calculated $\Delta g_{||}$ tensor components (in ppt) for linear $^2\Sigma$ radicals: one- and two-component results, in comparison with experiment.

relation to experiment at all (slope: 0.004, RMSE: 13 ppt). The reason for this failure is qualitatively simple [5, 75]. In a sum-over states model using a one-component reference, $\Delta g_{||}$ is given by [5]:

$$g_{||} = g_e - 2\xi \sum_n \frac{\langle 0|\hat{L}_z|n\rangle\langle n|\hat{L}_z|0\rangle}{E_n - E_0} - 2\xi^2 \sum_n \frac{\left|\langle 0|\hat{L}_x|n\rangle\right|^2}{(E_n - E_0)^2} + \ldots \qquad (32.48)$$

where $\hat{L}_z$ is the angular momentum operator, ξ is the effective spin–orbit coupling constant (compare Eq. (32.42)), and summation is over all electronically excited states.

For radicals with an $^n\Sigma$ ground state, $\hat{L}_z|0\rangle$ vanishes, so that the term in the first order of ξ is zero. Because this is the only contribution that is treated in one-component approaches, these methods give zero for $\Delta g_{||}$ in $^2\Sigma$ radicals. (In practice, small non-zero contributions will still arise from Zeeman kinetic energy correction and gauge terms. These terms are of no practical consequence in this case.) On the other hand, the two-component methods, which treat the spin–orbit coupling operator variationally, include all terms in Eq. (32.48), and thus lead to a qualitatively correct result for $\Delta g_{||}$.

A similar correlation plot for the perpendicular component $\Delta g_\perp$ is given in Fig. 32.4. In this case, the leading contribution to Δg is in the first order in spin–orbit coupling and is treated by both approaches. Consequently, both methods show a reasonable agreement with experimental values. At the same time, the spin-polarized, one-component results (corr.: 0.987; RMSE: 20 ppt) are clearly superior to the two-component values (corr.: 0.985; RMSE: 32 ppt). The difference is particularly

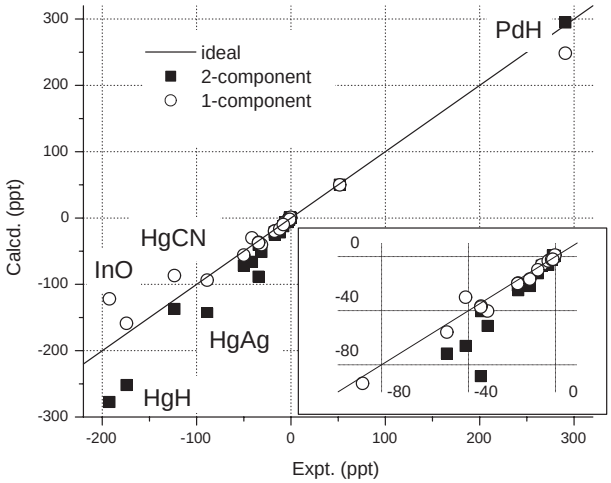

Figure 32.4 Calculated $\Delta g_\perp$ tensor components (in ppt) for linear $^2\Sigma$ radicals: one- and two-component results, in comparison with experiment. The insert shows the part of the data set for small $\Delta g_\perp$ shifts ($|\Delta g_\perp|$ <100 ppt) where the first-order treatment of the spin–orbit coupling operator is expected to be adequate

pronounced for the small $\Delta g_\perp$ shifts ($|\Delta g_\perp| < 100$ ppt), where one-component numbers are in quantitative agreement with experiment (RMSE: 4 ppt), while the two-component results show significant scatter (RMSE: 21 ppt), and systematically overestimate the shifts (correlation slope 1.46, vs. 1.02 in the one-component treatment). For larger g shifts, higher-order spin–orbit contributions are expected to become more important, so that one-component results start to deteriorate. Therefore, it appears that both spin-polarization and high-order spin–orbit terms are important and must be considered simultaneously, in order to obtain accurate results.

In passing, we also note that treatment of the electron correlation effects is essential for obtaining qualitatively correct g shifts in these radicals. Consider the four-component Dirac–Hartree–Fock (DHF) results, which are available for nine radicals in this series [32] (Tab. 32.4). Once the extreme outlier PdH (expt. $\Delta g_\perp$ 291 ppt; DHF: 595 ppt) is excluded from the statistics, the DHF results for this data set are uncorrelated with the experimental values (correlation coefficient of 0.235), and have no predictive power.

32.4.3
Approximations Used for the Spin–Orbit Coupling Operator

The final issue we would like to consider in this chapter is the dependence of the calculated **g**-tensor components on the choice of the approximate treatment of the spin–orbit coupling operator. A certain controversy [21, 23, 24] exists on the subject of the best approximation for this operator. Rather than going into the detailed argu-

ments in favour of the effective potential [23] or Ψ_{ref}/AMFI [21, 24] approaches, we will simply examine the results, obtained with three different approximations for the spin–orbit coupling operator [19, 22, 24] for a number of small radicals (Table 32.5).

Despite the small differences in the calculated **g**-tensor components, which may favor one of the methods over the other, the calculated **g**-tensor components are of roughly the same quality. For this set of radicals, the AMFI approach of Malkina et al. [21, 24] and the empirically parametrized SO operator used by Neese [22] are clearly superior to the effective potential approach of Schreckenbach and Ziegler. The likely reason is the inclusion of the spin–other-orbit terms, either explicitly [21, 24] or through the empirical parameters [22, 55]. This drawback of the non-empirical effective potential approach may disappear if the simple Δg_{SOO} correction of Pickard and Mauri [25] (Eq. 32.45) is included.

Compared to the remaining deviations from experiment, the differences between the approaches to the SO coupling operator become even less significant for radicals containing heavier nuclei, and particularly transition metal complexes. This is illustrated in Table 32.6, using the example of the d^1 $CrOCl_4^-$ radical. In this system, the effective potential [19] and AMFI [21, 24] results for $\Delta g_{\|}$ differ by 0.4 ppt, compared to 28 ppt deviation from the experimental value. The $\Delta g_{\perp}$ components agree to with-

Table 32.5 Influence of the spin–orbit coupling treatment on calculated Δg values (in ppt) in light main-group radicals. All calculated values use BP86 GGA functional.

Radical	Δg component	Effective[a]	Effective[b]	AMFI[c]	Expt.[d]
H_2O^+	Δg_{xx}	0.1	–0.1	–0.2	0.2
	Δg_{yy}	13.8	10.2	10.9	18.8
	Δg_{zz}	5.1	3.7	3.8	4.2
HCO	Δg_{xx}	2.7	2.2	2.3	+1.5
	Δg_{yy}	–0.3	–0.2	–0.2	0.0
	Δg_{zz}	–9.5	–7.4	–7.7	–7.5
C_3H_5	Δg_{xx}	–0.1	–0.0	–0.0	0.0
	Δg_{yy}	0.7	0.5	0.5	0.4
	Δg_{zz}	0.8	0.6	0.6	0.8
NO_2	Δg_{xx}	4.2	3.4	3.6	3.9
	Δg_{yy}	–13.7	–11.2	–11.4	–11.3
	Δg_{zz}	–0.8	–0.7	–0.6	–0.3
NF_2	Δg_{xx}	–0.7	–0.6	–0.5	–0.1
	Δg_{yy}	7.6	6.2	6.5	6.2
	Δg_{zz}	4.7	3.9	5.1	2.8

a) Ref. [19], using Eq. (32.44).
b) Ref. [22], using Eqs. (32.41), (32.42).
c) Ref. [24]. Somewhat different results have been reported for the same SO treatment earlier [21].
d) Experimental values cited from Refs. [19, 24]. For NO_2, Δg_{xx} values from +3.2 to + 3.8; Δg_{yy} values from –9.1 to –11.7, and Δg_{zz} values from –2.7 to +0.7 were also reported, see Ref. [19] for the references.

in 2.7 ppt, compared to 3.0 ppt (effective) or 5.7 ppt (AMFI) deviation from experiment. The individual g-tensor contributions in this molecule are also in reasonable agreement. In fact, some of the more spectacular examples [21] of the differences between the Ψ_{ref}/AMFI and the effective potential approaches seem to arise from the use of an inadequate auxiliary fitting set in the original publication [24]. Thus, the original AMFI results for $CrOF_4^-$ ($\Delta g_{\parallel} = -13.6$ ppt; $\Delta g_{\perp} = -21.8$ ppt [21]) were later corrected [24] to $\Delta g_{\parallel} = -17.1$ ppt, $\Delta g_{\perp} = -25.8$ ppt, bringing them into better agreement with the effective potential **g**-tensor ($\Delta g_{\parallel} = -19$ ppt; $\Delta g_{\perp} = -29$ ppt [47]), and a somewhat better agreement with experiment ($\Delta g_{\parallel} = -43$ ppt; $\Delta g_{\perp} = -34$ ppt [47]). A similar correction has also been made for TiF_3 (see Tab. 32.3).

Table 32.6 Dependence of the individual contributions to the calculated Δg tensor (in ppt) in $CrOCl_4^-$ on the treatment of the SO coupling operator.

Contribution	$\Delta g_{\parallel}$		$\Delta g_{\perp}$	
	Effective[a]	AMFI[b]	Effective[a]	AMFI[b]
$\Delta g_{GC(1e)}$[c]	+0.6	+0.5	+0.5	+0.5
$\Delta g_{GC(2e)}$[d]	–0.4	n/c	–0.3	n/c
Δg_{RMC}[e]	–0.6	–0.7	–0.6	–0.7
$\Delta g_{SO\text{-}N}$[f]	+15.9	+20.9	–34.0	–32.8
$\Delta g_{SO\text{-}2e}$[g]	+3.1	–0.3	+12.5	+13.4
Δg_{SOO}[h]	n/c	–0.1	n/c	+1.6
Total	+18.6	+20.3[i]	–22.0	–18.1[i]
Expt.	–10.0		–25.0	

a) Calculated using program of Schreckenbach and Ziegler [19] using all-electron Slater-type basis of TZP quality, at optimized VWN geometry [51].
b) Cited from Ref. [21].
c) 1-electron gauge correction terms.
d) 2-electron gauge correction terms.
e) Contributions due to relativistic Zeeman mass correction term (Eq. (32.10)).
f) Contributions due to nuclear spin–orbit coupling operator (Eq. (32.6)).
g) Contributions due to two-electron spin–same orbit coupling operator (Eq. (32.8)).
h) Contributions due to two-electron spin–other orbit coupling operator (Eq. (32.9)). This contribution is not included in program of Ref. [19].
i) Calculations using the same functional and SO treatment in ReSpect give: $\Delta g_{\parallel} = +18.2$ ppt, $\Delta g_{\perp} = -19.3$ ppt [24], in significantly better agreement with the results of effective potential treatment.

32.5 Summary and Outlook

We have examined density functional theory approaches to calculation of the EPR **g**-tensors, trying to emphasize that the existing techniques are fundamentally much the same. Moreover, we have attempted to underscore the physical meaning of the resulting expressions. In the process, we have scrutinized the critical approximations, which have to be made to obtain a computationally useful theory.

Further, we have illustrated the utility of the DFT techniques for both the "best-case" applications (main group radicals), where DFT is competitive with high-level ab initio approaches, and for the more challenging transition metal radicals. For the latter systems, DFT is, at present, the only practical choice for large-scale calculations. In many transition metal complexes, the absolute values of the DFT **g**-tensors suffer from the approximations made in most XC functionals. However, trends in related systems can be predicted with much better accuracy.

We have given a dramatic example of a simple, *qualitative* failure of one-component approaches, in radicals where the first-order spin–orbit contribution vanishes. Furthermore, we have examined three common approximations for the spin–orbit coupling operator, using a selection of main-group and transition metal radicals. Despite the drastically different approach to the SO coupling operator, these approximations lead to calculated **g**-tensors of similar quality, thus underlining the essential robustness of all three approximations.

We have also provided a glimpse of possible future developments of density functional theory approaches to **g**-tensors. The most obvious improvement involves combining treatments of spin-polarization effects and higher-order spin–orbit coupling terms in a single method. One possibility for such a technique is given by Eq. (32.22), closely related to the GUHF method of Jayatilaka [15], which could be implemented using the non-collinear two-component treatment of spin densities (Eq. (32.24)) [26, 48]. Another likely development involves introduction of new exchange-correlation functionals [66], which show promise for correcting some of the known deficiencies in the existing techniques. A third area where future developments are called for is related to the DFT treatment of the **g**-tensors for degenerate and quasi-degenerate ground states. This is closely related to the issue of achieving a qualitatively correct description of degenerate multiplet states, which is one of the big unsolved problems in approximate DFT [76].

Altogether, we believe that the next few years promise to be rather exciting for DFT approaches to **g**-tensors, both in terms of the theoretical development and for the practical application of the DFT techniques to problems in chemistry, solid-state physics, and biochemistry.

Acknowledgements

We would like to thank Martin Kaupp for giving us access to Ref. [27] prior to publication. S. P. would like to acknowledge interesting and useful discussions with

Dennis Klug, Seongho Moon, and Sergey Yurchenko. Comments and suggestions from Martin Kaupp, Vladimir Malkin, and Frank Neese are also gratefully acknowledged.

References

1 R. G. Parr, W. Yang, *Density Functional Theory of Atoms and Molecules,* Oxford University Press, Oxford **1989**.
2 W. Koch, M. C. Holthausen, *A Chemist's Guide to Density Functional Theory,* 2nd edition, Wiley-VCH, Weinheim **2001**.
3 A. Abragam, B. Bleaney, *Electron Paramagnetic Resonance of Transition Ions*, Clarendon Press, Oxford **1970**.
4 J. E. Harriman, *Theoretical Foundations of Electron Spin Resonance*, Academic Press, New York **1978**.
5 W. Weltner Jr., *Magnetic Atoms and Molecules*, Dover, New York **1983**.
6 P. J. M. Geurts, P. C. P. Bouten, A. van der Avoird, *J. Chem. Phys.* **1980**, *73*, 1306–1312.
7 L. Noodleman, E. J. Baerends, *J. Am. Chem. Soc.* **1984**, *106*, 2316–2327.
8 D. A. Case, *J. Chem. Phys.* **1985**, *83*, 5792–5796.
9 E. I. Solomon, M. J. Baldwin, *Chem. Rev.* **1992**, *92*, 521–542.
10 P. Belanzoni, E. J. Baerends, S. van Asselt, P. B. Langewen, *J. Phys. Chem.* **1995**, *99*, 13094–13102.
11 G. Schreckenbach, T. Ziegler, *Theor. Chem. Acc.* **1998**, *99*, 71–82.
12 G. H. Lushington, P. Bündgen, F. Grein, **1995**, *55*, 377.
13 G. H. Lushington, F. Grein, *Int. J. Quantum Chem.* **1996**, *60*, 1679–1684.
14 G. H. Lushington, *J. Phys. Chem. A* **2000**, *104*, 2969.
15 D. Jayatilaka, *J. Chem. Phys.* **1998**, *108*, 7587–7594.
16 M. Engstrom, B. Minaev, O. Vahtras et al., *Chem. Phys.* **1998**, *237*, 149–158.
17 O. Vahtras, M. Engstrom, B. Schimmelpfennig, *Chem. Phys. Lett.* **2002**, *351*, 424–430.
18 H. G. Schreckenbach, Ph.D. thesis, University of Calgary, Calgary **1996**.
19 G. Schreckenbach, T. Ziegler, *J. Phys. Chem. A* **1997**, *101*, 3388–3399.
20 E. van Lenthe, P. E. S. Wormer, A. van der Avoird, *J. Chem. Phys.* **1997**, *107*, 2488–2498.
21 O. L. Malkina, J. Vaara, B. Schimmelpfennig et al., *J. Am. Chem. Soc.* **2000**, *122*, 9206–9218.
22 F. Neese, *J. Chem. Phys.* **2001**, *115*, 11080–11096.
23 S. Patchkovskii, T. Ziegler, *J. Phys. Chem. A* **2001**, *105*, 5490–5497.
24 M. Kaupp, R. Reviakine, O. L. Malkina et al., *J. Comput. Chem.* **2002**, *23*, 794–803.
25 C. J. Pickard, F. Mauri, *Phys. Rev. Lett.* **2002**, *88*, 086403.
26 K. M. Neyman, D. I. Ganyushin, A. V. Matveev et al., *J. Phys. Chem. A* **2002**, *106*, 5022–5030.
27 M. Kaupp, in *EPR Spectroscopy of Free Radicals in Solids. Trends in Methods and Applications,* eds.A. Lund, M. Shiotani, Kluwer, Dordrecht **2003**.
28 F. Neese, *Curr. Opin. Chem. Biol.* **2003**, *7*, 125–135.
29 F. Neese, E.I. Solomon, in *Magnetoscience – From Molecules to Materials,* Vol. IV, eds. J. S. Miller, M. Drillon, Wiley, **2003**.
30 J. Autschbach, T. Ziegler, *Coord. Chem. Rev.* **2003**, *238–239*, 83–126.
31 R. McWeeny, *Methods of Molecular Quantum Mechanics,* 2nd edition, Academic Press, London **1978**.
32 H. M. Quiney, P. Belanzoni, *Chem. Phys. Lett.* **2002**, *253–258*.
33 L. D. Landau, E. M. Lifshitz, *Quantum Mechanics (Non-relativistic Theory),* 3rd edition, Pergamon Press, Oxford **1977**.
34 E. van Lenthe, A. van der Avoird, P. E. S. Wormer, *J. Chem. Phys.* **1998**, *108*, 4783–4796.
35 A. D. Becke, *J. Chem. Phys.* **1993**, *98*, 5648–5652.
36 A. D. Becke, M. R. Roussel, *Phys. Rev. A* **1989**, *39*, 3761–3767.
37 C. Chang, M. Pélissier, P. Durand, *Phys. Scr.* **1986**, *34*, 394.
38 E. van Lenthe, E. J. Baerends, J. G. Snijders, *J. Chem. Phys.* **1993**, *99*, 4597–4610.

39 E. van Lenthe, E. J. Baerends, J. G. Snijders, *J. Chem. Phys.* **1994**, *101*, 9783–9792.
40 P. Knappe, N. Rösch, *J. Chem. Phys.* **1990**, *92*, 1153–1162.
41 O. D. Häberlen, N. Rösch, *Chem. Phys. Lett.* **1992**, *199*, 491–496.
42 M. Mayer, S. Krüger, N. Rösch, *J. Chem. Phys.* **2001**, *115*, 4411–4423.
43 C. van Wüllen, *J. Comput. Chem.* **1999**, *20*, 51–62.
44 R. Arratia-Perez, D. A. Case, *J. Chem. Phys.* **1983**, *79*, 4939–4949.
45 G. te Velde, F. M. Bickelhaupt, E. J. Baerends et al., *J. Comput. Chem.* **2001**, *22*, 931–967.
46 E. J. Baerends, J. Autschbach, A. Berces et al., *ADF 2003.2*, Scientific Computing and Modelling NV, Amsterdam, http://www.scm.com/
47 T. Belling, T. Grauschopf, S. Krüger et al., *PARAGAUSS 2.2*, Munich Technical University, Munich, http://theo1.theochem.tu-muenchen.de/ParaGauss.html
48 C. van Wüllen, *J. Comput. Chem.* **2002**, *23*, 779–785.
49 L.M. Sandratskii, *Adv. Phys.* **1998**, *47*, 91–160.
50 M.V. Ramana, A.K. Rajagopal, *J. Phys. C* **1981**, *14*, 4291–4302.
51 S. Patchkovskii, T. Ziegler, *J. Chem. Phys.* **1999**, *111*, 5730–5740.
52 A. J. Stone, *Proc. R. Soc. London Ser. A* **1963**, *271*, 424–434.
53 G. Vignale, M. Rasolt, *Phys. Rev. Lett.* **1987**, *59*, 2360–2363.
54 E. Engel, S. Keller, R. M. Dreizler, in *Electronic Density Functional Theory: Recent Progress and New Directions*, eds. J. F. Dobson, G. Vignale, M. P. Das, Plenum, New York **1997**, p. 149.
55 S. Koseki, M. W. Schmidt, M. S. Gordon, *J. Phys. Chem.* **1992**, *96, 10768–10772.*
56 R. M. Pitzer, N. W. Winter, *J. Phys. Chem.* **1988**, *92*, 3061.
57 J. Vaara, O. L. Malkina, H. Stoll et al., *J. Chem. Phys.* **2001**, *114*, 61–71.
58 O. L. Malkina, B. Schimmelpfennig, M. Kaupp et al., *Chem. Phys. Lett.* **1998**, *296*, 93–104.
59 B. A. Heß, C. M. Marian, U. Wahlgren et al., *Chem. Phys. Lett.* **1996**, *251*, 365–371.
60 B. Schimmelpfennig, AMFI, an *Atomic Mean-field Spin–Orbit Integral Program*, University of Stockholm, **1996**.
61 T. Helgaker, M. Jaszuński, K. Ruud, *Chem. Rev.* **1999**, *99*, 293–352.
62 A. V. Luzanov, E. N. Babich, V. V. Ivanov, *J. Mol. Struct. THEOCHEM* **1994**, *311*, 211–220.
63 M. Kaupp, T. Gress, R. Reviakine et al., *J. Phys. Chem. B* **2003**, *107*, 331–337.
64 C. J. Pickard, F. Mauri, *Phys. Rev. B* **2001**, *63*, 245101.
65 A. V. Arbuznikov, M. Kaupp, V. G. Malkin et al., *Phys. Chem. Chem. Phys.* **2002**, *4*, 5467–5474.
66 S. Patchkovskii, manuscript in preparation.
67 F. Stevens, H. Vrielinck, F. Callens et al., *Phys. Rev. B*. **2002**, *66*, 134104.
68 S. Patchkovskii, T. Ziegler, unpublished results.
69 J. Autschbach, T. Ziegler, *J. Chem. Phys.* **2000**, *113*, 936–947.
70 J. Autschbach, T. Ziegler, S. J. A. van Gisbergen et al., *J. Chem. Phys.* **2002**, *116*, 6930–6940.
71 G. Schreckenbach, T. Ziegler, *Int. J. Quantum Chem.* **1996**, *60*, 753–766.
72 V. G. Malkin, O. L. Malkina, L. A. Eriksson et al., in *Modern Density Functional Theory*: A Tool for Chemistry, Vol. 2, eds. J. M. Seminario, P. Politzer, Elsevier, Amsterdam **1995**.
73 M. Bühl, M. Kaupp, O. L. Malkina et al., *J. Comput. Chem.* **1999**, *20*, 91–105.
74 S. Patchkovskii, T. Ziegler, *J. Phys. Chem. A*, **2002**, *106*, 1088–1099.
75 P. Belanzoni, E. van Lenthe, E. J. Baerends, *J. Chem. Phys.* **2001**, *114*, 4421–4433.
76 M. Filatov, S. Shaik, *J. Phys. Chem. A.* **2000**, *104*, 6628–6636.

33
Ab Initio Calculations of *g*-Tensors

Gerald H. Lushington

As has been noted frequently throughout this book, EPR spectroscopy is a valuable analytical tool not only for the unique molecular fingerprints it provides, but also for the detailed structural insight that it can convey. Although hyperfine interactions are often considered first when extracting structural information, the *g*-tensor can be of substantial analytical value as well. From the discussions of Atkins [1], one sees how anisotropic shifts in *g*-tensor values (*g*-shifts) relative to the free-electron *g*-value can yield significant information about the bound state environment of unpaired electrons, their interactions with the external magnetic field, and the magnetic properties of low-lying excited states. However, from Chapter 4 by Lushington one recalls that the electronic Zeeman effect in a bound state arises as a sum of different concurrent electromagnetic interactions of both collaborative and competitive natures. Without some prior estimate of the ratios for these different contributions, it can be difficult to infer much from EPR peak positions beyond the fact that a molecule resonates at a given magnetic field strength and frequency of incident radiation.

Devising a fully general formalism for predicting *g*-tensors for bound molecular environments requires accounting for all major electromagnetic contributions present in the full phenomenological spin Hamiltonian described for the electronic Zeeman effect in Chapter 4. In practice this can be a challenge, but offers rich analytical rewards in that detailed expansion of *g*-tensors as a sum of physically intuitive contributions quantifies the aforementioned ratios between the different electromagnetic effects underlying magnetic resonance. Given high quality theoretical *g*-tensor predictions (i.e., at a level of theory that has been consistently shown to give fairly close agreement with experiment), it is thus possible to confidently deconstruct the implications behind the *g*-shifts and make sophisticated inferences about molecule structure in accordance with Atkins' principles. This ability to deconvolute the interactions underlying *g*-shifts has thus been a major motivation for development of reliable ab initio *g*-tensor prediction methods.

Despite obvious motivations for developing advanced *g*-tensor prediction methods, such tools have proven quite elusive until fairly recently. In fact, although interest in the field dates from the early days of quantum mechanics, practical and broadly available ab initio methods have only existed for theoretical *g*-tensor prediction since 1996. Tremendous recent progress has been made however: High accu-

Calculation of NMR and EPR Parameters. Theory and Applications.
Edited by Martin Kaupp, Michael Bühl, Vladimir G. Malkin
Copyright © 2004 WILEY-VCH Verlag GmbH & Co. KGaA, Weinheim
ISBN: 3-527-30779-6

racy implementations now exist and are widely available as part of popular computational chemistry software. Among these are ab initio models described in this chapter, and DFT methods discussed in Chapter 32 by Patchkovskii and Schreckenbach.

Two important measures of the usefulness of a *g*-tensor prediction scheme are: (1) the ability to properly and accurately represent the Zeeman effect for a broad range of different molecular systems, and (2) the efficiency in handling specific cases. These goals are often at odds. From symmetry arguments, one finds that the choice of spin Hamiltonian operators depends on the complexity of the molecule; thus the pursuit of broad generality demands rigorous inclusion of the full spin Hamiltonian in order to properly represent disparate cases. However, such rigor may prove needlessly complex when applied to simple molecules wherein many operators may be superfluous. Ab initio *g*-tensor method development has paid heed alternately to both of these competing considerations, and this chapter explores the gradual evolution of a balance between the two goals.

The first known ab initio *g*-tensor calculations, dating to the early 1970s, were highly simplistic and efficient models for special cases such as hydrogen atoms [2], and H_2^+ [3]. With computational resources being a limiting factor, simple cases like atoms, diatomics and linear polyatomics would remain especially popular for the next decade. A 1972 paper by Hayden and McCain reporting Hartree–Fock / STO-3G level *g*-tensors for the isoelectronic species O_3^-, NO_2^{2-} and NF_3 [4] was likely the first published attempt to extend ab initio methodology to nonlinear polyatomics. Their method was limited in that it did not include any first-order *g*-tensor correction terms such as the relativistic mass correction or the one- and two-electron spin–orbit Zeeman gauge corrections. In retrospect, their work can also be viewed as heavily empirical and, in fact, rather flawed methodologically. Based on a formulation by Atkins and Symons [5], their method approximated sum-over-state magnetic response contributions in following fashion:

$$\langle \Psi_i | H_{SO} | \Psi_0 \rangle \langle \Psi_0 | L | \Psi_i \rangle \approx \lambda \langle \Psi_i | L | \Psi_0 \rangle \langle \Psi_0 | L | \Psi_i \rangle \tag{33.1}$$

where λ is the spin–orbit coupling constant of the molecule, estimated empirically as a sum of experimental atomic spin–orbit coupling constants. This approximation of λ is questionable as spin–orbit coupling is a property of the whole molecule and is not validly expressed as a sum of atom components, but the predicted values seem empirically reasonable. Any attempt to decouple λ from the molecular spin–orbit operator to isolate a magnetic dipole moment operator, L, however, is not. From Eqs. (4.26), (4.27) in Chapter 4, one recalls that the orbital moment in H_{SO} is defined via sums over charged centers (nuclei and electrons), while for the orbital Zeeman term (Eq. (4.25) in Chapter 4), it is defined relative to an unspecified gauge origin: a critical difference. It is difficult even to find an empirical justification for doing so. Equation (33.1) implies that for a particular molecule, the H_{SO} and L transition moments for all states Ψ_i coupled with the ground state Ψ_0 should exhibit roughly constant ratios (H_{SO} / L) approximately equal to λ. Experience has shown us, in fact, that decomposition of sample sum-over-states expansions completely

refutes this assumption of consistency. For example, in the case of the $\Delta g_{\perp}$ component of CO^{+} [6], one finds that the ratio of H_{SO} and L transition moments varies dramatically in both sign (five of the first nine states have a negative ratio, four have a positive one) and magnitude (e.g., the seventh state has a ratio nearly 3000 times larger than that of the third). Although this misleading formulation has been propagated to numerous subsequent papers, most recently a 1996 multi-reference configuration interaction level *g*-tensor study by Tachikawa [7], it is not an empirical approximation that is particularly defensible.

Overlooking the dubious contribution of Hayden and McCain, a landmark 1973 paper of Moores and McWeeny [8] appears to be the first published demonstration of fully ab initio and broadly general (i.e., suitable for nonlinear polyatomics) *g*-tensor calculations. The paper treated NO_2 and CN at the ROHF / STO-4G level via a spin Hamiltonian adhering to the full extent to the Stone formula for *g*-tensor evaluation [9], thus significantly exceeding the representation used by Hayden and McCain. Moores and McWeeny rigorously included not just the second-order magnetic response expansion, but also first-order spin–orbit Zeeman gauge corrections, and explicitly treated both the one- and two-electron contributions to both of these terms in an ab initio fashion. Without explanation, they did omit the spin-Zeeman relativistic mass correction term, an apparent oversight given its relative ease of computation (all required integrals are available within a standard Fock matrix) and given the prior knowledge of its importance to the Zeeman effect [10]. Regardless, their work stands as a major milestone in the development of ab initio *g*-tensor theory, and the rigorous nature of their method yielded quantitatively reasonable reproduction of CN *g*-shift magnitudes, and excellent agreement with experimental parameters for NO_2. The biggest shortcoming in their work was that it did not continue: the 1973 paper was apparently their last in the field, and more than 20 years would pass before others achieved similar rigor and accuracy.

Although theoretical g-tensor research during the years 1974–1995 represented a step back from the ambitious work of Moores and McWeeny, it did include some important developments. Atomic *g*-factor prediction was pursued vigorously by a number of groups, including the simple Hartree–Fock level studies of Hegstrom (e.g., Ref. [11]), the subsequent large basis set Hartree–Fock calculations of Veseth (e.g. Ref. [12] and references therein), the relativistic Dirac–Fock calculations of Marketos [13] and a correlated (coupled cluster singles and doubles) relativistic treatment of Lindroth and Ynnerman [14]. Interestingly, these relativistic studies did not expose significant deviations in atomic *g*-values relative to nonrelativistic treatment (even for atoms as heavy as Rb [13, 14]). Very recent work has, however, demonstrated this to be largely a function of the subject choice (i.e., atoms as opposed to molecules). Specifically, the magnetic response effects that are a major component of the molecular Zeeman effect but not the atomic one, have been found to exhibit substantial dependence on the relativistic nature of the wavefunctions used (see Ref. [15], plus a more thorough discussion of DFT methods in Chapter 32), whereas the first-order corrections examined in the atomic formulations of Marketos [13], and Lindroth and Ynnerman [14] displayed only a modest effect. While it would be some time before the importance of relativistic theory in reproducing *g*-tensors for mole-

cules containing heavy atoms was definitively established, this earlier work did still set an important precedent for the use of multi-component wavefunctions for *g*-shift prediction.

During the 1973–1995 period, ab initio level *g*-tensor calculations on molecules were rather sparse. Veseth and coworkers published numerous high-level theoretical predictions of Zeeman parameters for diatomic systems (see Ref. [16] and references therein); however their analysis did not elucidate *g*-tensors per se. Their work focused on a quantity, g_s, that is mathematically equivalent to a sum of the first-order *g*-tensor corrections, and is experimentally tractable via fitting analysis of EPR spectra of linear molecules, but did not include the second-order magnetic response term, and thus could not be generalized to the case of nonlinear polyatomics. Conversely, a 1991 paper of Ishii et al. did pursue ab initio *g*-tensor calculations that included the appropriate magnetic response effects for a series of nonlinear polyatomics; however their formulation neglected all first-order correction terms [17]. This latter work is nonetheless noteworthy for an important methodological development therein: the magnetic response was evaluated via finite perturbation theory (closely analogous to the Hartree–Fock perturbation theory methods recently reported by Mustafaev et al. [18] and by Angstl for INDO level *g*-tensor calculations [19]) rather than the cumbersome sum-over-states expansion. This afforded significantly improved accuracy at negligible added computational cost and, as we shall see later in this chapter, would serve as a useful model for future schemes.

Prior to 1996, a common thread in all ab initio *g*-tensor studies was the use of an incomplete spin Hamiltonian. To this point, there had been only one attempt to even empirically account for all of the first-order plus magnetic response terms relevant to description of nonlinear polyatomics: the aforementioned INDO paper by Angstl [19]. Angstl's paper explicitly treated the relativistic mass correction term, plus the one-electron contributions to the spin–orbit Zeeman gauge correction and the magnetic response, but accounted for all two-electron contributions empirically by scaling the effective nuclear charges to mimic the screening effects of electron–electron interactions. The first truly ab initio treatment to rigorously treat the complete-to-second-order spin Hamiltonian was that of Lushington and Grein [20], who reported ROHF level calculations for NO_2, CO^+ and H_2O^+ over a variety of basis sets ranging from minimal (STO-4G) to the triple-zeta-valence polarized sets of Sadlej [21]. Their minimal basis set results for NO_2 afforded the first independent theoretical validation of the 1973 calculations by Moores and McWeeny [8]. In the absence of the relative mass correction term (omitted by Moores and McWeeny) very close agreement was found, with the minor deviations (several hundred parts per million for the g_x- and g_z-shifts, and less than 10% of the value of the large g_y-shift) likely being attributable to slight differences in molecular geometry and to neglect of multi-center integrals in the 1973 paper. For both of these papers, the ROHF/STO-4G results for NO_2 enjoyed rather astonishing agreement with experiment. Augmenting the results with the relativistic mass correction term brought the apparent accuracy to nearly within the experimental uncertainty range. Each improvement in basis set quality beyond the minimal STO-4G led to a decline in quantitative agreement relative to experiment, however. Thus, while the triple-zeta polarized treat-

ment still reproduced basic qualitative trends (large positive g_x-shift, large negative g_y-shift, small g_z-shift), errors of 50% or more in shift magnitude were observed. Large basis set results for the other two molecules studied (CO^+ and H_2O^+) were comparably mediocre, leading to the inescapable conclusions: (1) *g*-tensor calculations apparently exhibit significant basis set dependence, (2) the tantalizing quantitative agreement between experiment and the ROHF / STO-4G level treatment of NO_2 was likely a product of fortuitous cancellation of errors, and (3) the ROHF level of treatment, although adequate for general qualitative predictions, was apparently insufficient for quantitative *g*-shift prediction. Lushington and Grein would later demonstrate that the shortcomings in large basis set ROHF calculations were directly attributable to the absence of electron correlation, and that rigorously correlated models obtained by a multi-reference configuration interaction (MRCI) level representation of the relevant excited-state matrix elements in the magnetic response term could consistently achieve excellent results for moderate to large basis set representations [6].

Although responsible for providing some of the most accurate representations of electromagnetic response type properties in the current literature, MRCI methods quickly become computationally unwieldy for increasingly large or complex molecules, scale poorly with basis set size, and require substantial user expertise for even fairly simple systems. Given the EPR community's substantial interest in complex molecules (e.g., proteins and other biomolecules) and materials (e.g., crystal defects, disordered media, etc.), the practical limitations of MRCI-based methodologies are unrealistically inhibiting. Fortunately, new developments since 1997 have been helping to close the gap between the computationally demanding expert-driven *g*-tensor prediction methods that had been developed and a need for more efficient, user-friendly formalisms. The DFT-based methods discussed in Chapter 32 have become especially prominent, demonstrating great efficacy for handling the bulkier, more disordered molecular systems of broad general interest. Ab initio techniques, with their inherent capacity for systematic improvement will, however, likely remain a gold standard to which new DFT implementations are benchmarked. It is also fairly certain that the value of ab initio theory will persist for high accuracy prediction of small molecule magnetic parameters of interest to the matrix isolation EPR and (via the Curl relationship [22]) gas phase ultraviolet / visible spectroscopy communities. Ab initio method development and refinement has thus continued, leading to important new publications from several different sources, including Lushington [23], Jayatilaka [24], Neese [25] and Vahtras et al. [26, 27].

Lushington's most recent work in the field explored a simplified configuration interaction methodology whose restriction of the configuration space to magnetically relevant (i.e., single electron) excitations [23] permitted effective representation of the magnetic response contributions via modest-sized sum-over-states expansions. The benefits of this approach were two-fold: the computational expense was reduced to a level comparable to the underlying ROHF treatment, and the resulting sum-over-states expansion is small enough to be readily amenable to treatment in a complete, closed form, thus avoiding the truncation errors in the MRCI formalism associated with the eventual necessity for terminating the discrete sum-over-states

expansion. Although each individual state is not resolved with the full precision available in the MRCI method, the closed-form CI expansion still seems capable of achieving much of the accuracy level of complex MRCI calculations. The method allows for much of the calculation to be effectively automated and should thus prove significantly easier for non-expert users to assemble; however some expert intervention is still required in order to scale the excited state energy manifold to account for the uncorrelated ground state energy.

Employing a significantly different tack, Jayatilaka's *General Hartree–Fock* technique [24] avoided explicit sum-over-states perturbative expansions (and their various pitfalls) by relying on a coupled two-component unrestricted Hartree–Fock formalism with spin–orbit coupling explicitly included in the Hamiltonian. Field-dependent terms were also included, albeit only to fix the orientation of the spin. Net first-order contributions were approximated via explicit inclusion of the relativistic mass correction. Using triple zeta polarized basis sets of Sadlej [21], Jayatilaka was able to predict *g*-tensors of an accuracy level comparable to (arguably better than) the best DFT results of the time [28], and approaching that of MRCI level treatments [6, 29]. The method omitted one- and two-electron spin–orbit Zeeman gauge corrections, arguing that except for very small molecules, ab initio calculations consistently show that one- and two-electron gauge correction terms largely cancel, leaving residues that are generally small relative to experimental uncertainty (see e.g., Refs. [6, 16, 20] and references therein). The large computational expense of treating the two-electron first-order correction term renders this a pragmatic omission. Such a variational Hartree–Fock method has recently been extended by Neese [25], who treated the *g*-tensor as a mixed second derivative property with respect to the applied field and the electron magnetic moment. Neese's method allowed for direct inclusion of spin-polarization effects, enhancing generality across different spin states. It also proved amenable to both HF and density functional theory, allowing implementation for hydrid functionals [25].

The final methodological developments of note, those of Vahtras et al., may hold the greatest promise for a future of accurate and efficient ab initio *g*-tensor predictions. Like Jayatilaka, the method of Vahtras et al. circumvented the sum-over-states expansion, this time in favor of a second-order polarization propagator formalism applied rigorously at the multi-configurational SCF level. Benchmarks relative to other ab initio calculations do not appear in the literature; however the combination of a non-perturbative representation of the magnetic response effect and a correlated level of theory suggests an accuracy level that should exceed uncorrelated methods such as the General Hartree–Fock, and likely approach the MRCI. Indeed, rigorous multi-configurational response calculations appear to frequently yield *g*-shift predictions within 10% of experiment [26], a precision comparable to the MRCI results [6, 29], in spite of the fact that Vahtras et al. have not addressed any of the first-order contributions in their work. More recent work by this group explores a reworking of this scheme, aimed at rendering it amenable to molecules containing heavy (second and third row) atoms [27]. Taking a lead from an earlier DFT level *g*-tensor treatment [30], they noted a declining importance in the two-electron contributions to the magnetic response contribution for systems with heavy atoms, and thus have applied

the atomic mean field approximation (AMFI) to the spin–orbit Hamiltonian [31], a scheme that more rigorously implements the Z-screening concept used much earlier by Angstl [19] and others. In general, the AMFI leads to results of modest accuracy relative to the rigorous all-electron treatment for first-row molecules (differing by upwards of 20% in *g*-shift values), but exhibits dramatically improved performance for molecules containing second- and third-row atoms (e.g., SiH_3, GeH_3) where the difference is rarely more than 1% relative to the all-electron formulation, while computational savings are frequently of the order of 90% for the *g*-tensor prediction portion of the calculation.

Assessing these recent theoretical developments, two distinct but complementary foci are apparent: (1) a desire to devise more accurate and rigorous methodologies, and (2) a goal of selectively simplifying these advanced new methods so as to balance accuracy with computational viability in the case of large, complex molecules. Both objectives are important to the theoretical EPR community; hand in hand, they can be expected to enhance the scientific maturity of the field and strengthen the analytical relevance of theoretical *g*-tensor predictions to the experimental community.

At this point it bears asking where ab initio *g*-tensor prediction methods stand with respect to maturity and analytical relevance? Significant achievements have been clearly effected on the latter. Detailed studies by Bruna et al., for example, have applied Atkins-type arguments to the analysis of correlations between observed *g*-shifts and other physical effects such as excited state properties and electron spin localization (see, e.g., Refs. [32–34] and references therein), while Kiljunen et al. [35] performed the first explicit ab initio study on the physical effects of rare gas matrices on electronic *g*-tensors. If the true test of maturity is the ability to pinpoint and correct potential errors in experimental analysis, then theory is probably getting quite close. Bruna et al. [34], for example, exposed an obvious inconsistency with an unusual spectrum whose EPR activity had been implausibly attributed to H_2^- trapped in a matrix of solid hydrogen [36]. Significant amounts of validation clearly must still be done, but evidence is growing that viable, useful ab initio *g*-tensor methods have indeed arrived.

References

1 P.W. Atkins, *Molecular Quantum Mechanics,* Oxford University Press, New York **1983**.
2 H. Grotch, *Phys. Rev. Lett.* **1970**, *24*, 39.
3 P. de Montgolfier, J. E. Harriman, *J. Chem. Phys.* **1971**, *55*, 5262.
4 D. W. Hayden, D. C. McCain, *J. Chem. Phys.* **1972**, *57*, 171.
5 P. W. Atkins, M. C. R. Symons, *The Structure of Inorganic Radicals,* Elsevier, New York **1967**.
6 G. H. Lushington, F. Grein, *J. Chem. Phys.* **1997**, *106*, 3292.
7 H. Tachikawa, *Chem. Phys. Lett.* **1996**, *260*, 582.
8 W. H. Moores, R. McWeeny, *Proc. R. Soc. London, Ser. A* **1973**, *332*, 365.
9 A.J. Stone, *Proc. R. Soc. London, Ser. A* **1963**, *271*, 424.
10 P.W. Atkins, A. M. Jamieson, *Mol. Phys.* **1967**, *14*, 425.
11 R. A. Hegstrom, *Phys. Rev. A* **1975**, *11*, 421.
12 L. Veseth, *J. Phys. B* **1987**, *20*, L73.
13 P. Marketos, *Z. Phys. D* **1993**, *27*, 219.
14 E. Lindroth, A. Ynnerman, *Phys. Rev. A* **1993**, *47*, 961.
15 K. M. Neyman, D. I. Ganyushin, A. V. Matveev et al., *J. Phys. Chem. A* **2002**, *106*, 5022–5030.

16 H. Christensen, L. Veseth, *J. Mol. Spectrosc.* **1978**, *72*, 438.
17 M. Ishii, K. Morihashi, O. Kikuchi, *J. Mol. Struct.* (THEOCHEM) **1991**, *325*, 39.
18 S. A. Mustafaev, V. G. Malkin, P. V. Schastnev, *Z. Strukt. Khimii* **1987**, *28*, 41.
19 R. Angstl, *Chem. Phys.* **1990**, *145*, 413.
20 G. H. Lushington, F. Grein, *Theor. Chim. Acta* **1996**, *93*, 259.
21 A. J. Sadlej, *Coll. Czech. Chem. Commun.* **1988**, *53*, 1995.
22 R. F. Curl, *Mol. Phys.* **1965**, *9*, 585.
23 G. H. Lushington, *J. Phys. Chem. A* **2000**, *104*, 2969.
24 D. Jayatilaka, *J. Chem. Phys.* **1998**, *108*, 7587.
25 F. Neese, *J. Chem. Phys.* **2001**, *115*, 11080.
26 O. Vahtras, B. Minaev, H. Ågren, *Chem. Phys. Lett.* **1997**, *281*, 186.
27 O. Vahtras, M. Engström, B. Schimmelpfennig, *Chem. Phys. Lett.* **2002**, *351*, 424.
28 G. Schreckenbach, T. Ziegler, *J. Phys. Chem. A* **1997**, *101*, 388.
29 G. H. Lushington, F. Grein, *Int. J. Quantum Chem.* **1996**, *60*, 467–472.
30 O. L. Malkina, J. Vaara, B. Schimmelpfennig et al., *J. Am. Chem. Soc.* **2000**, *122*, 9206.
31 B. A. Hess, C. Marian, U. Wahlgren et al., *Chem. Phys. Lett.* **1996**, *251*, 365.
32 P. J. Bruna, F. Grein, *Mol. Phys.* **2002**, *100*, 1681.
33 P. J. Bruna, F. Grein, *J. Phys. Chem. A* **1999**, *103*, 3294.
34 P. J. Bruna, G. H. Lushington, F. Grein, *Chem. Phys. Lett.* **1996**, *258*, 427.
35 T. Kiljunen, J. Eloranta, J. Ahokas et al., *J. Chem. Phys.* **2001**, *114*, 7144.
36 T. Miyazaki, K. Yamamoto, Y. Aratono, *Chem. Phys. Lett.* **1995**, *232*, 229.

34
Zero-Field Splitting

Frank Neese

34.1
Introduction

Systems with more than one unpaired electron do frequently occur in nature. In particular they are commonplace in transition metal chemistry where many d^N configurations give rise to ground state multiplicities with $S > 1/2$ [1–3]. In organic molecules systems of higher spin are usually limited to triplet states, i.e. $S = 1$ [4, 5]. These occur in organic biradicals, in short lived excited triplet states or reaction intermediates when bonds are broken. Most prominently such charge separation occurs in the light reactions of the photosystems [6]. If the states are sufficiently long-lived they can be studied by a variety of experimental techniques including EPR spectroscopy and its high-resolution extensions, optically detected magnetic resonance (ODMR) or magnetic circular dichroism (MCD). In addition, the net magnetic moments of molecules with high-spin ground states can be conveniently and accurately measured with SQUID devices which gives rise to the vast field of molecular magnetism [7, 8]. This field has recently received much attention due to the desire to construct single-molecule magnets [9, 10].

In all of these cases the analysis of the experimental data requires additions to the spin-Hamiltonian (SH) of a $S = 1/2$ system in order to describe the additional splittings that arise within the $2S+1$ magnetic sublevels. The leading term that must be added to the electronic Zeeman term (H_{Ze}) is the so-called zero-field splitting (ZFS) term H_{ZFS}. In the absence of nuclear spins and exchange interactions, the SH up to terms bilinear in the effective (fictitious) spin is usually written [1]:

$$\begin{aligned} \hat{H}_{\mathrm{spin}} &= \hat{H}_{\mathrm{Ze}} + \hat{H}_{\mathrm{ZFS}} \\ &= \beta_{\mathrm{B}} \vec{B}\mathbf{g}\vec{S} + \vec{S}\mathbf{D}\vec{S} \end{aligned} \tag{34.1}$$

where β_{B} is the Bohr magneton, $\vec{B}$ is the magnetic flux density, $\vec{S}$ is the operator for the effective spin and **g** and **D** are the **g**-matrix and the ZFS-tensor respectively. $\hat{H}_{\mathrm{spin}}$ acts on the basis functions $|SM\rangle$ with $M = S, S-1, .., -S$. If a coordinate system is chosen that diagonalizes **D**, $\hat{H}_{\mathrm{ZFS}}$ can be rewritten:

Calculation of NMR and EPR Parameters. Theory and Applications.
Edited by Martin Kaupp, Michael Bühl, Vladimir G. Malkin
Copyright © 2004 WILEY-VCH Verlag GmbH & Co. KGaA, Weinheim
ISBN: 3-527-30779-6

$$H_{\mathrm{ZFS}} = D\left[S_z^2 - \frac{1}{3}S(S+1)\right] + E\left[S_x^2 - S_y^2\right] \tag{34.2}$$

$$D = D_{zz} - \frac{1}{2}\left(D_{xx} + D_{yy}\right); \quad E = \frac{1}{2}\left(D_{xx} - D_{yy}\right) \tag{34.3}$$

Note that a constant $1/3\ (D_{xx} + D_{yy} + D_{zz})\ S(S+1)$ has been dropped because it shifts all levels equally and the factor $-1/3\ DS(S+1)$ is introduced for convenience. In a so-called 'proper coordinate system' x, y and z are chosen such that $0 \leq E/D \leq 1/3$ [11]. Note that in general $D_{xx} + D_{yy} + D_{zz} \neq 0$; i.e. the **D**-tensor is not necessarily traceless, as is frequently stated. Thus, the ZFS has the appearance of a 'spin–spin interaction' since it is bilinear in the fictitious electron spin $\vec{S}$. Higher order terms that contain higher than the second power of the electron spin are also known and sometimes used to interpret measurements. However, their physical origin is not exceedingly well understood and precise experimental values are rare for molecular systems. Consequently these terms will not be considered in this chapter.

A rigorous discussion of the origin of ZFS effects has been given in the monograph of Harriman [12]. However, as has been pointed out in the literature [13, 14], the ZFS is the least studied SH parameter from a theoretical point of view. There are a few ab initio and semiempirical calculations available on organic [15–25] and inorganic [13, 26–34] molecules. Most recently this field has been revived by Vahtras et al. [14, 35] who presented a modern and promising implementation. In the transition metal field, the ZFS is up to now a domain of ligand field theory (LFT) which has been extensively reviewed [2, 3, 36–38]. However, as we have discussed several times, LFT is not reliable for the interpretation of ZFSs and more rigorous approaches are necessary [13, 38]. While some progress in this direction has been made, much more work is required to reach the level of sophistication that has been reached for example in the calculation of g-values and HFCs which are described elsewhere in this volume (Chapter 33 by Lushington, Chapter 32 by Patchkovskii and Schreckenbach, Chapter 29 by Munzarová and Chapter 30 by Engels). However, as will become evident below, the ZFS is a very complicated property to model by quantum chemical methods.

In this brief review an overview is given of ZFS effects in EPR spectroscopy and available quantum chemical approaches to calculate this quantity with a focus of the treatments in Refs. [14, 35] and [13]. In addition a few examples of ZFS calculations will be given and future directions will be indicated. Biological examples of ZFS calculations will be dealt with in Chapter 36 by Neese.

34.2
Zero-Field Splittings in EPR Spectroscopy

In systems with $S > 1/2$ the ZFS usually strongly dominates the spectral shape. It is therefore important to understand the basic ZFS effects in the following limiting cases: (1) the weak field case, in which $\beta_B B \ll D$, (2) the high-field case in which

$\beta_B B \gg D$ and (3) the intermediate case where $\beta_B B \approx D$. In the weak field case it is furthermore necessary to distinguish between Kramers systems with a half-integer spin S and non-Kramers systems with an integer spin S. This is necessary because of Kramers time-reversal invariance theorem which has the consequence that in the absence of a magnetic field the degeneracy of the M_S levels of a given multiplet cannot be completely lifted if the system contains an odd number of electrons [39]. The remaining doubly degenerate levels are commonly referred to as 'Kramers doublets'. For an even electron system the situation is different and, in general, no degeneracy remains, even in the absence of a magnetic field.

34.2.1
Kramers Systems in the Weak Field Regime

This case is frequently realized in transition metal complexes, where D is commonly of the order of several wavenumbers, which is large compared to the commonly employed resonance energy at X-band frequency ($h\nu = g\beta_B B \approx 0.3\,\mathrm{cm}^{-1}$). The degeneracy of the $S + 1/2$ Kramers doublets is lifted by the application of a homogenous external magnetic field and resonances can always be observed. Since the inter-doublet spacing is larger than the microwave frequency, in this regime, only transitions within each Kramers doublet can be observed by EPR techniques. The transition energies can be modeled conveniently by using the so-called 'rhombogram method' [40]. In this method, each Kramers doublet is regarded as an effective $S' = 1/2$ system with an 'effective g-matrix' $\boldsymbol{g}_{\mathrm{eff}}$ which is different for each doublet. The effective g-values then only depend on the value of E/D and the true g-values $\boldsymbol{g}$. If these are taken to be close to 2.00, as is most often the case, a single parameter, namely E/D, determines the resonance positions in the EPR experiment. In addition, the different Kramers doublets will be populated according to Boltzmann statistics, which means that an estimate of the inter-doublet spacing and therefore D and E/D can be obtained from variable temperature measurements. The transition probability can be calculated by diagonalizing the SH at each resonance field and evaluating the magnetic transition dipole moment for a microwave magnetic field which is polarized perpendicularly to the static magnetic field (or parallel in a so-called parallel mode experiment, vide infra) [41].

As an example consider the case of $S = 5/2$ which is frequently met in transition metal complexes of the Fe(III) ion. As indicated in Fig. 34.1B, an axial ZFS leads to a splitting of the six levels of the ferric ion into three Kramers doublets. Introduction of a static magnetic field lifts the degeneracies of the three doublets and gives rise to the possibility of inducing intra-doublet EPR transitions. For a positive D, the transitions observed for a sample with randomly oriented molecules arise from the lowest Kramers doublet as indicated in Fig. 34.1A, whereas they arise from the middle Kramers doublet in a completely rhombic system with $E/D = 1/3$. The effective g-values found from the relation $g_{\mathrm{eff}} = h\nu / B_{\mathrm{res}}\beta_B$ are plotted in Fig. 34.1C. It is clear from this figure that the origin of a given observed transition can be clearly traced back to an individual Kramers doublet and that the value of E/D can be uniquely determined from the spectrum with little effort.

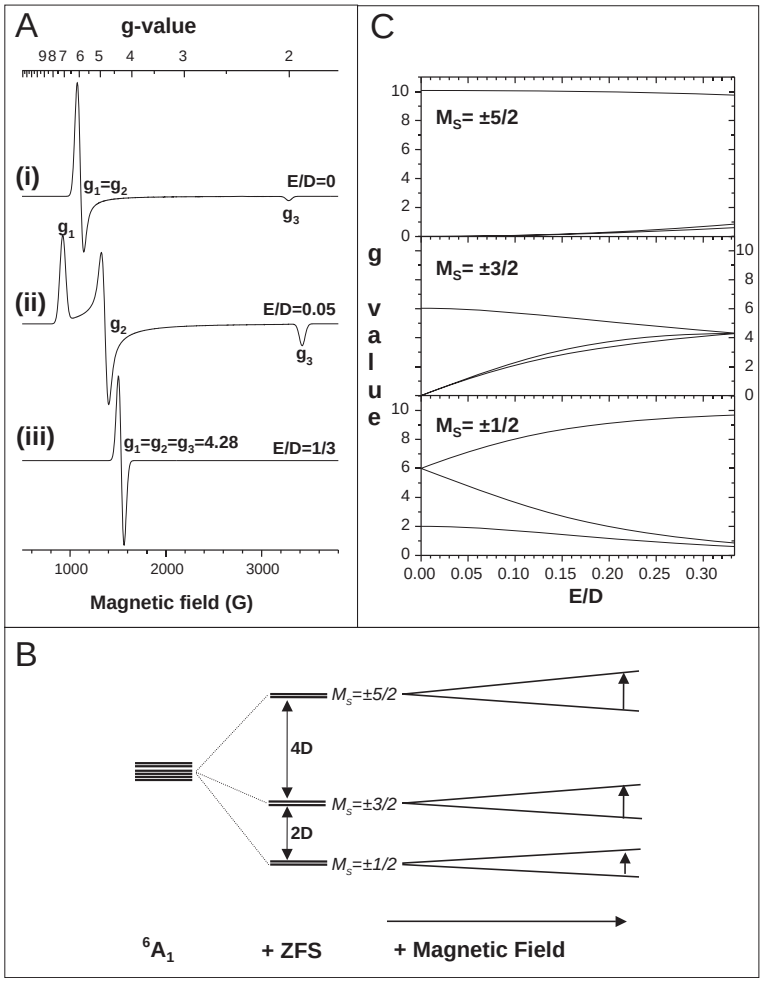

Figure 34.1 Zero-field splitting effects in S=5/2 systems with a D parameter that is large compared to the microwave frequency. (A) Appearance of powder spectra for three different values of E/D, (B) Level splittings caused by the ZFS and indication of intra-doublet transitions observed in an EPR experiment, (C) Rhombogram for $S = 5/2$ showing the effective g-value as a function of the rhombicity E/D.

The rhombogram method is a convenient way to obtain systematic information about the observed transitions, to identify the relevant spin system and to obtain a reliable value of E/D. However, it does not lead to a unique determination of the sign and magnitude of the D parameter. This can be done by simply recording the spectrum as a function of temperature and observing the population and depopulation of the individual Kramers doublets. The case of the complex $[Fe(EDTA)(O_2)]^{3-}$ is shown in Fig. 34.2 [31]. The spectrum in Fig. 34.2A shows a large signal around $g_{eff} = 4.3$ which is, however, anisotropic, as well as two small but sharp peaks around

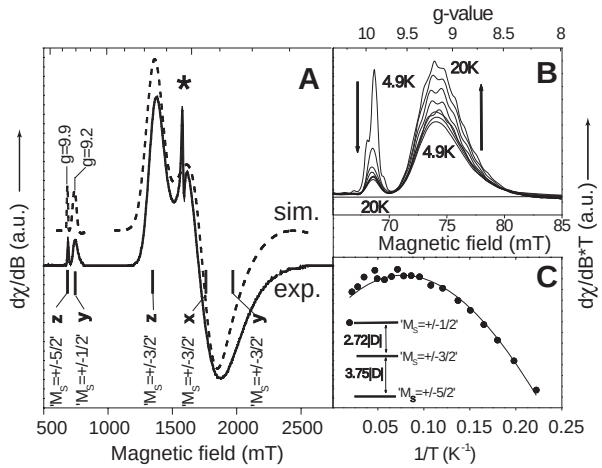

Figure 34.2 Determination of the sign and magnitude of D from variable temperature EPR measurements. (A) the EPR spectrum (measured at ~10 K) and the assignment of individual peaks to transitions between Kramers doublets. (B) the temperature variation of the high g_{eff}-peaks. (C) Boltzmann fit to the temperature variation of the intense middle peak around $g = 4.3$. (Reprinted with permission from Ref. [31]).

$g_{eff} = 9$–10. From the rhombogram an assignment of these transitions is readily possible and also indicated in Fig. 34.2A which leads to $E/D = 0.21$. From this assignment, the peak at $g_{eff} = 9.9$ must come from the $M_S = \pm 5/2$ doublet, while the $g_{eff} = 9.2$ peak must come from the $M_S = \pm 1/2$ doublet. The temperature variation of the two small peaks shown in Fig. 34.2B shows that the intensity of the $M_S = \pm 5/2$ transition decreases with increasing temperature while that of the $M_S = \pm 1/2$ transition increases. Consequently, the $M_S = \pm 1/2$ is a 'hot' transition and the $M_S = \pm 5/2$ transition is a 'cold' transition. This leads to the conclusion that the sign of D must be negative, which means that the $M_S = \pm 5/2$ doublet is lowest in energy. At $E/D = 0.21$ the two Kramers doublets are split by $2.72|D|$ and $3.75|D|$ as shown in Fig. 34.2C. Consequently, a Boltzmann fit to variable temperature data yields the magnitude of D, which amounts to $-1 \pm 0.1\,cm^{-1}$ in the case of $[Fe(EDTA)(O_2)]^{3-}$. This analysis is typical for ZFS effects in transition metal EPR and is widely used. It is also clear that the accuracy obtained from the Boltzmann fits is limited and typically not better than a few tenths of a wavenumber.

As an alternative to the use of Boltzmann fits the use of microwave power saturation studies has also been advocated to obtain information about ZFSs in transition metal complexes with apparently similar accuracy [42].

34.2.2
Non-Kramers's Systems in the Weak Field Regime

In the case of non-Kramers ions the ZFS already removes all degeneracies even at zero-field. The best understood example is the $S = 2$ configuration, which is fre-

quently met in high-spin Fe(II) sites. High-spin Fe(II) has an $S=2$ non-Kramers ground state that can split into five components even in the absence of a magnetic field. Using the standard SH, Eq. (34.1), the following eigenfunctions and energies can be derived in zero magnetic field [43]:

$$\left|2^s\right\rangle = a^+\left(|+2\rangle + |-2\rangle\right)/2^{1/2} + a^-|0\rangle \qquad E_{2s} = 2\sqrt{D^2+3E^2} \tag{34.4}$$

$$\left|2^a\right\rangle = \left(|+2\rangle - |-2\rangle\right)/2^{1/2} \qquad E_{2a} = 2D \tag{34.5}$$

$$\left|1^s\right\rangle = \left(|+1\rangle + |-1\rangle\right)/2^{1/2} \qquad E_{1s} = -D+3E \tag{34.6}$$

$$\left|1^a\right\rangle = \left(|+1\rangle - |-1\rangle\right)/2^{1/2} \qquad E_{1a} = -D-3E \tag{34.7}$$

$$|0'\rangle = a^-\left(|+2\rangle + |-2\rangle\right)/2^{1/2} - a^+|0\rangle \qquad E_{0'} = -2\sqrt{D^2+3E^2} \tag{34.8}$$

where $a^{\pm} = \sqrt{1/2\left(1 \pm D/\sqrt{D^2+3E^2}\right)}$.

In the case where E is zero and $|D|$ is large ($|D| \gg h\nu_j$ the normal case for high-spin Fe(II)) the level scheme consists of the isolated state $|0'\rangle$ and two pairwise degenerate non-Kramers doublets. In this case the energy of the microwave is not sufficient to induce a transition between states that belong to two different of the

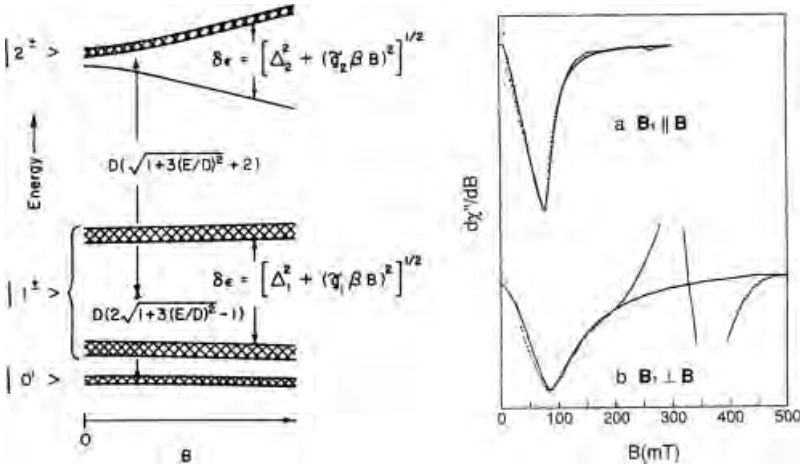

Figure 34.3 Schematic description of a parallel mode EPR experiment for a $S=2$ system. Left panel: level scheme showing the relevant splittings in zero field and with applied field. Right panel: Experimental data and computer simulations for $[Fe(H_2O)_6]^{2+}$ (reprinted with permission from Ref. [43]).

three sets. In addition, the transitions within the $|1^{s,a}\rangle$ and $|2^{s,a}\rangle$ non-Kramers doublets are forbidden in standard EPR and therefore no transition can be detected. In the more general case of $E \neq 0$, intra-doublet splittings $\Delta_{1,2}$ are already present. If these splittings are smaller or equal to the microwave energy, EPR resonances are, in principle, detectable. The resonance condition in this case reads:

$$(h\nu)^2 = \Delta_k^2 + \left(g^{(k)}\beta B\right)^2 \tag{34.9}$$

where $g^{(k)}$ is an effective g-value for the kth doublet. However, in a standard EPR experiment the transition probability for both intra-doublet transitions is zero along the principal axes. Therefore it is convenient to employ a parallel mode cavity (microwave magnetic field $\mathbf{B_1}$ oriented parallel to the static field $\mathbf{B_0}$ instead of perpendicular as in a standard EPR experiment; see Figure 34.3). In such an experiment, the selection rules change from $\Delta M_S = \pm 1$ to $\Delta M_S = 0$. Using this methodology, EPR analysis of a wide variety of Fe(II), Mn(III), Co(II) centers as well as spin-coupled oligonuclear complexes became possible [44–56].

34.2.3
Paramagnets in the High Field Regime

The high field regime is frequently met for organic triplets and biradicals, where the ZFS is usually much smaller than in transition metal complexes [5]. The most common case is $S = 1$. In this case, the ZFS gives rise to a so-called fine structure and it is appropriately treated by perturbation theory within the SH formalism.

The principle of spectrum analysis for a spin triplet with isotropic g-factor is shown in Fig. 34.4A. In the axial case ($E/D = 0$) the eigenenergies with the magnetic field oriented along the molecular z-axis are given by:

$$E(|0\rangle) = -\frac{2}{3}D \tag{34.10}$$

$$E(|\pm 1\rangle) = \frac{1}{3}D \pm g\beta_B B \tag{34.11}$$

For the field in the x,y-plane one has:

$$E(|0\rangle) = \frac{1}{3}D \tag{34.12}$$

$$E(|\pm 1\rangle) = -\frac{1}{6}D \pm \frac{1}{2}\sqrt{D^2 + 4\left(g\beta_B B\right)^2} \tag{34.13}$$

where $|M_S\rangle$ is an abbreviation for the magnetic sublevels of the electronic ground state ($|0SM_S\rangle$) but with the quantization axis chosen along the external magnetic field for the convenience of labeling. For such a level scheme one observes five

peaks in an EPR spectrum taken on randomly oriented molecules but with fixed orientation such as in a frozen solution.

The lowest transition is situated at $g_{\text{eff}} = 4$ and is called 'half-field' transition since it occurs at $2g\beta_B B$. It formally corresponds to a $\Delta M_S = 2$ transition which is forbid-

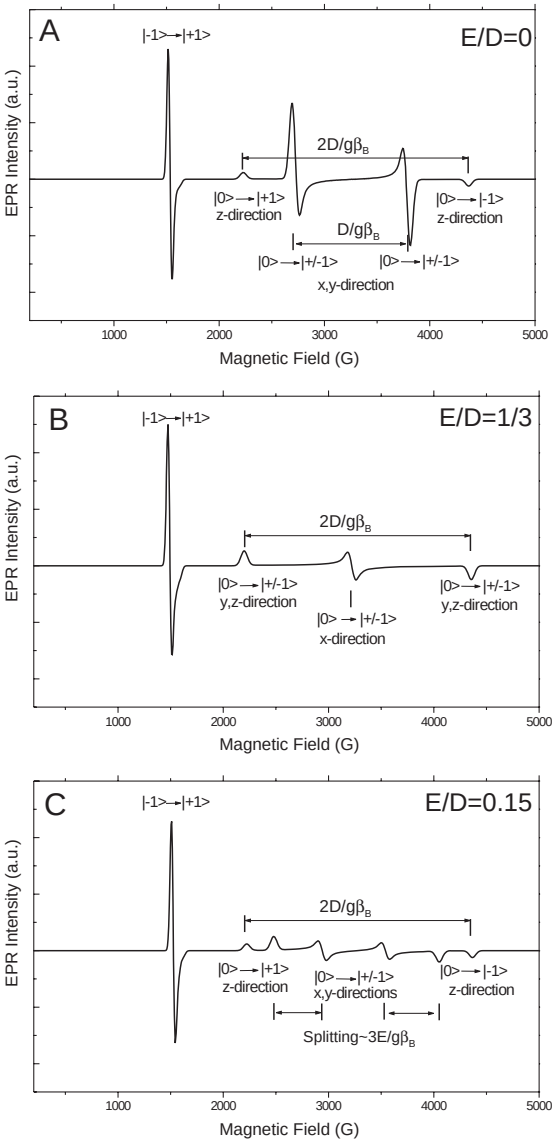

Figure 34.4 Simulated continuous wave X-band EPR spectra of spin triplets in the strong field regime (here $\nu = 9.25$ GHz, $D = 0.1\ \text{cm}^{-1}$ and $T = 4.2$ K). (A) $E/D = 0$, (B) $E/D = 1/3$ and (C) $E/D = 0.15$

den under the standard EPR selection rule $\Delta M_S = 1$. However, it gains intensity in the *x*- and *y*-directions due to mixing of the $|\pm 1\rangle$ and $|0\rangle$ sublevels by the Zeeman operator. In addition, as long as the *g*-matrix is isotropic, the transition is also isotropic and therefore can be observed with finite intensity unless *D* becomes zero. The second pair of transitions is symmetrically split by $2D/g\beta_B$ around the hypothetical center transition at $B_{res} = h\nu/g\beta_B$ where ν is the spectrometer frequency. The intensity of these transitions arises from molecules oriented with their *z*-axis along the static magnetic field. The third pair of transitions arises from molecules oriented with their *x*- and *y*-axes along the static magnetic field and is seen to be split by $D/g\beta_B$.

The situation is only slightly more complicated in the completely rhombic case ($E/D = 1/3$) shown in Fig. 34.4B. Here one still observes a half field transition and a pair of transitions split by $2D/g\beta_B$ as in the axial case. However, the third pair of transitions coalesces into a single transition observed at $B_{res} = h\nu/g\beta_B$.

For intermediate E/D values the spectrum becomes fairly complicated (Fig. 34.4C) but is easily understood with reference to the axial case. The main change is that the third pair of transitions splits into two transitions each due to the inequality of the molecular *x*- and *y*-axes. The energies of the three magnetic sublevels are given by:

Field along molecular *z*-axis:

$$E(|0\rangle) = -\frac{2}{3}D \tag{34.14}$$

$$E(|\pm 1\rangle) = \frac{1}{3}D \pm \sqrt{E^2 + \left(g\beta_B B\right)^2} \tag{34.15}$$

Field along molecular *x*-axis:

$$E(|0\rangle) = \frac{1}{3}D - E \tag{34.16}$$

$$E(|\pm 1\rangle) = -\frac{1}{6}D + \frac{1}{2}E \pm \frac{1}{2}\sqrt{(D+E)^2 + 4\left(g\beta_B B\right)^2} \tag{34.17}$$

Field along molecular *y*-axis:

$$E(|0\rangle) = \frac{1}{3}D + E \tag{34.18}$$

$$E(|\pm 1\rangle) = -\frac{1}{6}D - \frac{1}{2}E \pm \frac{1}{2}\sqrt{(D-E)^2 + 4\left(g\beta_B B\right)^2} \tag{34.19}$$

From which it follows that the splitting of the *x*,*y*-transitions on a magnetic field scale is approximately given by:

$$\Delta B_{res} \cong \frac{E}{g\beta_B}\left(3 \pm \frac{D}{\sqrt{E^2 + 4\left(g\beta_B B_{res}\right)^2}}\right) \tag{34.20}$$

where B_{res} is the transition field for the case where $E = 0$; the positive sign holds for the higher field pair and the negative sign for the lower field pair of transitions.

From this discussion it is evident that the spectral analysis for spin triplets in the strong field regime yields the values of D and E/D directly and to high accuracy.

A spectacular example of such a spin triplet species is the observation of a triplet state of the primary donor, $^3P_{680}$, in photosystem II by Lubitz and co-workers [6]. This state can be generated under certain conditions by charge recombination from the primary radical pair formed in photosynthesis. If the recombination takes place in the presence of a magnetic field selective population of only one of the three magnetic sublevels is obtained which leads to strong absorption and emission peaks in the observed EPR spectra (Fig. 34.5). Straightforward analysis of these spectra directly yields accurate values for $D = 0.00287\,cm^{-1}$ and $E = 0.00043\,cm^{-1}$ [6].

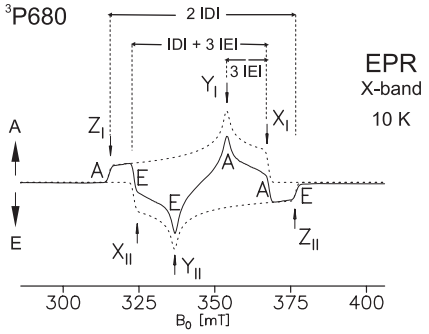

Figure 34.5 Transient EPR of the spin-polarized triplet state $^3P_{680}$ of a frozen solution of photosystem II particles. The spectral components (X,Y,Z) in the powder pattern of the emissive (E) and absorptive (A) branch are indicated together with the determination of the D and E parameters from this data. (Reprinted with permission from Ref. [6]).

34.2.4 The Intermediate Regime

In the regime where the ZFS is comparable to the microwave frequency the spectra take a rather complicated appearance and require detailed computer simulations in order to obtain the D and E/D values. However, the values extracted from such simulations tend to be accurate since they are not based on a Boltzmann fit as is the only choice in the weak field regime. An exciting recent development is the advent of high-field EPR spectrometers which operate at frequencies up to ~550 GHz which leads to resonance energies up to $\sim 18\,cm^{-1}$. Thus, by changing to a high-field spectrometer one can step outside the weak field regime and measure large ZFSs much more accurately than with conventional spectrometers.

An example is provided by a recent study of Mn(III) in *trans*-[Mn(cyclam)I_2] by Mossin, Weihe and Barra [57]. This complex, unexpectedly, has a positive ZFS $D = 0.604\,cm^{-1}$ with an $E/D = 0.034\,cm^{-1}$ which would have made its study by con-

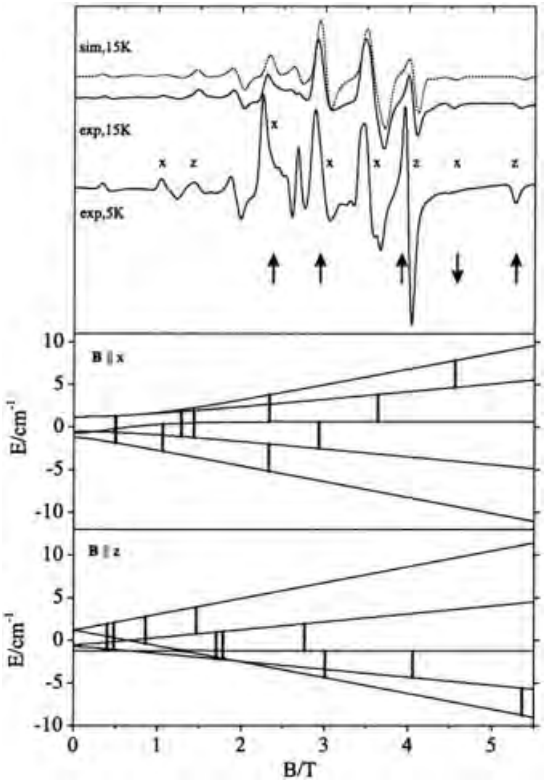

Figure 34.6 High-Field EPR Spectra on *trans*-[Mn^{III}(cylcam)I_2]. Top panel: experimental data taken at 95 GHz recorded at 5 K and 15 K respectively and computer simulation. Bottom panel: assignment of transitions based on the diagonalization of the spin-Hamilton operator as a function of magnetic field orientation and strength. (Reprinted with permission from Ref. [57]).

ventional X-band EPR spectroscopy difficult. However, the 95 GHZ spectra shown in Fig. 34.6 show a rich structure and computer simulation of the spectra leads to accurate values of D and E/D. A number of similar high-field EPR studies on first-row transition metal sites with significant ZFS interactions have appeared over the years [57–78], starting with the pioneering work of Freed and co-workers [79].

34.2.5
Other Methods for Measuring ZFSs

While EPR in most circumstances is the method of choice, ZFS effects are ubiquitous in many physical methods including magnetic susceptibility [7], magnetic circular dichroism [80–82], optically detected magnetic resonance [4, 83–87], inelastic

neutron scattering [88, 89], far-infrared spectroscopy [90–95], magnetic torque magnetometry [96] and Mössbauer spectroscopy [97].

34.3 Theory of Zero-Field Splittings

From a quantum chemical perspective, the calculation of ZFSs needs to deal with two basic contributions: (1) the contribution from the direct spin–spin coupling of the unpaired electrons and (2) the contribution from the spin–orbit coupling (SOC) [12]. The first contribution most frequently dominates the ZFSs of organic molecules since these are made from atoms with small SOC constants. The SOC contribution is believed to commonly dominate in the case of transition metal complexes. Both contributions are challenging from a theoretical point of view since: (1) they involve matrix elements of spin-dependent two-electron operators that are not diagonal in the total spin and consequently require the inclusion of several spin states in the calculations and (2) the integrals involved in the calculation are fairly complicated.

In order to arrive at a theoretical equation for the ZFS it is convenient to start from an effective-Hamiltonian treatment. In this treatment one defines a zeroth order model space that already contains the main physics of the problem. Then an effective Hamiltonian is set up in this basis that approximately incorporates the effects of the additional terms in the Hamiltonian [98]. This effective Hamiltonian is then compared term by term to the matrix of the spin-Hamiltonian and in this way the SH parameters are defined in terms of matrix elements of the perturbing operators over zeroth order (non-relativistic) wavefunctions.

The treatment starts by assuming that the Hamiltonian can be divided into a major part and a perturbation:

$$\hat{H} = \hat{H}_0 + \hat{H}_1 \tag{34.21}$$

where in the present case $\hat{H} = \hat{H}_{\mathrm{BO}}$ (the Born–Oppenheimer Hamiltonian) and $\hat{H}_1$ represents the sum of the various magnetic operators to be described below. The full set of states $\{|\alpha SM\rangle\}$ is divided into two sets: (i) the "a" set $\{|0S_0M\rangle\}$ of the $2S+1$ functions which make up the orbitally nondegenerate electronic ground state and (ii) the "b" set $\{|\alpha SM\rangle,\ \alpha = 1,2...\}$ of excited state wavefunctions. Any wavefunction can then be represented as a linear combination of the form:

$$\Psi = \sum_M c^a_M \left|0S_0M\right\rangle + \sum_{\alpha SM} c^b_{\alpha SM} \left|\alpha S_\alpha M_\alpha\right\rangle \tag{34.22}$$

The secular equations arising from the variation principle can be set up in matrix form like:

$$\mathbf{Hc} = E\mathbf{c} \tag{34.23}$$

where **c** is the vector that collects the expansion coefficients and **H** is the matrix of the complete Hamiltonian with elements:

$$H_{\alpha SM,\alpha' S' M'} = \left\langle \alpha SM \middle| \hat{H} \middle| \alpha' S' M' \right\rangle \tag{34.24}$$

Applying the partitioning into "a" and "b" sets Eq. (34.23) can be written in the partitioned form:

$$\begin{pmatrix} \mathbf{H}_{aa} & \mathbf{H}_{ab} \\ \mathbf{H}_{ba} & \mathbf{H}_{bb} \end{pmatrix} \begin{pmatrix} \mathbf{c}^a \\ \mathbf{c}^b \end{pmatrix} = E \begin{pmatrix} \mathbf{c}^a \\ \mathbf{c}^b \end{pmatrix} \tag{34.25}$$

The second equation can formally be solved for $\mathbf{c}^b$ to give:

$$\mathbf{c}^b = -\left(\mathbf{H}_{bb} - \mathbf{I}E\right)^{-1} \mathbf{H}_{ba} \mathbf{c}^a \tag{34.26}$$

If this is inserted into the first set of equations one obtains:

$$\mathbf{H}_{aa}\mathbf{c}^a - \mathbf{H}_{ab}\left(\mathbf{H}_{bb} - \mathbf{I}E\right)^{-1} \mathbf{H}_{ba}\mathbf{c}^a = E\mathbf{c}^a \tag{34.27}$$

which is equivalent to the matrix eigenvalue equation of an effective Hamiltonian:

$$\mathbf{H}_{eff}\mathbf{c}^a = E\mathbf{c}^a \tag{34.28}$$

with

$$\mathbf{H}_{eff} = \mathbf{H}_{aa} - \mathbf{H}_{ab}\left(\mathbf{H}_{bb} - \mathbf{I}E\right)^{-1} \mathbf{H}_{ba} \tag{34.29}$$

Since we are dealing with small splittings of the electronic ground state, the value of E in Eq. (34.29) can, to a first approximation, be set equal to the unperturbed energy of the ground state E_0 [98]. If it is assumed that the basic set of states, $\{|\alpha SM\rangle\}$, diagonalizes $\hat{H}_0$ we have for the matrix inverse term in Eq. (34.29) the equation $(\mathbf{H}_{bb} - \mathbf{I}E_0)^{-1}_{\alpha\alpha} = (E_\alpha - E_0)^{-1} \equiv \Delta_\alpha^{-1}$ which means that the effective Hamiltonian assumes the simple form:

$$\left\langle 0SM \middle| \hat{H}_{eff} \middle| 0SM' \right\rangle$$

$$= E_0\delta_{MM'} + \left\langle 0SM \middle| \hat{H}_1 \middle| 0SM' \right\rangle - \sum_{\alpha S'M''} \Delta_\alpha^{-1} \left\langle 0SM \middle| \hat{H}_1 \middle| \alpha S'M'' \right\rangle \left\langle \alpha S'M'' \middle| \hat{H}_1 \middle| 0SM' \right\rangle \tag{34.30}$$

The matrix of the Hamiltonian is of the same dimension as the matrix of the SH. As perturbing operators one has to choose those terms that give contributions that are bilinear in the electron spin operators [12, 98, 99]. The first perturbing operator is the direct dipolar spin–spin interaction:

$$\hat{H}_{SS} = \frac{\alpha^2}{2} \sum_i \sum_{j \neq i} \frac{\mathbf{s}_i \mathbf{s}_j}{r_{ij}^3} - 3 \frac{\left(\mathbf{s}_i \mathbf{r}_{ij}\right)\left(\mathbf{s}_j \mathbf{r}_{ij}\right)}{r_{ij}^5} \tag{34.31}$$

where $\mathbf{r}_{ij} = \mathbf{r}_i - \mathbf{r}_j$ and i and j sum over electrons. $\mathbf{s}_i$ is the spin operator for the *i*'th electron at position $\mathbf{r}_i$.

The second perturbing operator is the SOC. In the Breit–Pauli approximation the SOC operator is [100]:

$$\hat{H}_{SO} = \hat{H}_{SO}^{(1)} + \hat{H}_{SO}^{(2)} \tag{34.32}$$

The one-electron part, $\hat{H}_{SO}^{(1)}$, is given by:

$$\hat{H}_{SO}^{(1)} = \frac{\alpha^2}{2} \sum_A \sum_i \frac{Z_A}{\left|\mathbf{R}_A - \mathbf{r}_i\right|^3} \mathbf{l}_i^A \mathbf{s}_i \tag{34.33}$$

where $\mathbf{l}_i^A$ is the angular momentum of the *i*th electron relative to nucleus *A* at position $\mathbf{R}_A$

$$\mathbf{l}_i^A = (\mathbf{r}_i - \mathbf{R}_A) \times \mathbf{p}_i \tag{34.34}$$

and $\mathbf{p}_i$ is the linear momentum operator for the *i*'th electron. The two electron part consists of two terms and is given by:

$$\hat{H}_{SO}^{(2)} = -\frac{\alpha^2}{2} \sum_i \mathbf{s}_i \sum_{j \neq i} \frac{1}{\left|\vec{r}_i - \vec{r}_j\right|^3} \left\{ \mathbf{l}_i^j + 2\mathbf{l}_j^i \right\} \tag{34.35}$$

where $\mathbf{l}_i^j$ is the angular momentum of electron *i* relative to electron *j*.

$$\mathbf{l}_i^j = \left(\mathbf{r}_i - \mathbf{r}_j\right) \times \mathbf{p}_i \tag{34.36}$$

This form of the spin–orbit coupling was derived by Bethe and Salpeter [100] from the Breit equation [101–103] and with classical arguments by Slater [104]. The first term in $\hat{H}_{SO}^{(2)}$ arises from the movement of electron *i* in the Coulomb field of electron *j* and the second term describes the coupling of the spin magnetic moment of electron *i* with the orbital current of electron *j* (the spin–other orbit, SOO, contribution). The one-electron term $\hat{H}_{SO}^{(1)}$ has the familiar interpretation as described in popular textbooks (i.e. Ref [105], p. 1215).

The first order contribution to the **D**-tensor follows from the derivations described by Harriman [12] and reads (μ,ν = x,y,z):

$$D_{\mu\nu}^{(SS)} = \frac{1}{2} \frac{\alpha^2}{S(2S-1)} \left\langle 0SS \middle| \sum_i \sum_{j \neq i} \frac{r_{ij}^2 \delta_{\mu\nu} - 3\left(\mathbf{r}_{ij}\right)_\mu \left(\mathbf{r}_{ij}\right)_\nu}{r_{ij}^5} \left\{ 2s_{zi}s_{zj} - s_{xi}s_{xj} - s_{yi}s_{yj} \right\} \middle| 0SS \right\rangle \tag{34.37}$$

This contribution is symmetric and traceless as expected for a dipolar interaction. Recently, Vahtras et al. have worked out an elegant ab initio formalism to deal with the complicated Eq. (34.37) and applied it to the calculation of triplet state ZFSs in organic molecules [14]. In their notation, the **D**-tensor takes the form:

$$D_{\mu\nu}^{(SS)} = \sum_{p,q,r,s} d_{pqrs}^{\mu\nu} q_{pqrs} \tag{34.38}$$

where q_{pqrs} is a 'quintet density' (p,q,r,s label MOs):

$$q_{pqrs} = \frac{\left\langle 0SS \middle| \left(2s_z s_z - s_x s_x - s_y s_y\right)_{pqrs} \middle| 0SS \right\rangle}{3S^2 - S(S+1)} \tag{34.39}$$

with the second quantized operators $\hat{s}_{\mu,pq} = \sum_{\sigma_p,\sigma_q} \langle \sigma_p | s_\mu | \sigma_q \rangle a^+_{p,\sigma_p} a_{q,\sigma_q} (\sigma_p, \sigma_q = \alpha, \beta)$. As shown by Vahtras et al. [14], the operator in Eq. (34.39) can be written in a more convenient form which uses unitary group generators [106] as:

$$\left(2s_z s_z - s_x s_x - s_y s_y\right)_{pqrs} = \frac{1}{2} e^-_{pqrs} + \frac{1}{4}\left[e^+_{psrq} - e^-_{psrq}\right] \tag{34.40}$$

where

$$e^\pm_{pqrs} = E^\pm_{pq} E^\pm_{rs} - E^\pm_{ps}\delta_{rq} \tag{34.41}$$

$$E^\pm_{pq} = a^+_{p\alpha} a_{q\alpha} \pm a^+_{p\beta} a_{q\beta} \tag{34.42}$$

The matrix elements of the generators over configuration state functions can be very efficiently generated using the sophisticated algorithms that are based on the symmetric group or graphical unitary groups approaches [107–109].

The integrals $d_{pqrs}^{\mu\nu}$ are given by:

$$d_{pqrs}^{\mu\nu} = \frac{\alpha^2}{2} \int\int \psi_p(r_1)\psi_q(r_2) \left[\frac{\vec{r}_{1\mu}\vec{r}_{2\nu} - 3\vec{r}_1\vec{r}_2}{r_{12}^5}\right] \psi_r(r_1)\psi_s(r_2) \mathrm{d}\vec{r}_1 \mathrm{d}\vec{r}_2 \tag{34.43}$$

Using one of the modern algorithms for the calculations of one- and two-electron integrals over gaussian basis functions, these integrals can be reduced to linear combinations of geometric second derivative integrals (i.e. Helgaker and Taylor [110]).

Physically, the dipole–dipole contribution is readily interpreted as the interaction between two "smeared out" magnetic dipoles where the "smearing" is determined from the second-order reduced spin density matrix of the state under consideration.

In the simplest possible approach this distribution reflects the shapes of the squares of the two singly occupied MOs of the system.

The summation over a four-indexed quantity in the MO basis implies either the transformation of the two electron integrals to the MO basis ($d^{\mu\nu}_{abcd} \rightarrow d^{\mu\nu}_{pqrs}$, a,b,c,d label AOs) or of the two electron quintet density matrix to the AO basis ($q_{pqrs} \rightarrow q_{abcd}$) both of which are potentially time consuming for large molecules. However, Vahtras et al. have shown that within the MC-SCF approximation, the range of the indices is restricted to the orbitals in the active space (typically not more than 14) which makes the computations quite feasible and the transformation of the density the method of choice.

The contributions from the SOC arise in second order. However, these contributions are complicated since they do not automatically yield a ZFS tensor in the standard form **SDS**. This arises because the perturbation calculation involves matrix elements between states of different total spin. The precise form that the *D*-tensor takes can be obtained from the evaluation of the second order part of Eq. 34.30) by using the Wigner–Ekhard theorem [111] to simplify summations over M_S components as far as possible. We will not repeat the detailed derivation here [13] but only quote the final results which show that the SOC contribution to the ZFS can be written as a sum of three terms that come from excited states with S, $S-1$ and $S+1$.

$$D^{\mathrm{SOC}-(0)}_{\mu\nu} = -\frac{1}{S^2} \sum_{b(S_b=S)} \Delta_b^{-1} \left\langle 0SS \middle| \sum_i h^{\mathrm{SO}}_{\mu}(i) s_{i,z} \middle| bSS \right\rangle \left\langle bSS \middle| \sum_i h^{\mathrm{SO}}_{\nu}(i) s_{i,z} \middle| 0SS \right\rangle \tag{34.44}$$

$$D^{\mathrm{SOC}-(-1)}_{\mu\nu} = -\frac{1}{S(2S-1)} \sum_{b(S_b=S-1)} \Delta_b^{-1} \left\langle 0SS \middle| \sum_i h^{\mathrm{SO}}_{\mu}(i) s_{i,+1} \middle| bS-1S-1 \right\rangle \left\langle bS-1S-1 \middle| \sum_i h^{\mathrm{SO}}_{\nu}(i) s_{i,-1} \middle| 0SS \right\rangle \tag{34.45}$$

$$D^{\mathrm{SOC}-(+1)}_{\mu\nu} = -\frac{1}{(S+1)(2S+1)} \sum_{b(S_b=S+1)} \Delta_b^{-1} \left\langle 0SS \middle| \sum_i h^{\mathrm{SO}}_{\mu}(i) s_{i,-1} \middle| bS+1S+1 \right\rangle \left\langle bS+1S+1 \middle| \sum_i h^{\mathrm{SO}}_{\nu}(i) s_{i,+1} \middle| 0SS \right\rangle \tag{34.46}$$

where S+1 and S–1 are components of the standard spin vector operators [111].

For convenience we have assumed an effective one-electron SOC operator. One of the simplest possible choices is the operator which has been used by Koseki et al. [112–114], where:

$$h_{\mu}^{\mathrm{SO}}(i) = \sum_{A} \xi(r_{iA}) l_{\mu}^{A}(i) \tag{34.47}$$

where $l_{\mu}^{A}(i)$ is the μth component of the orbital angular momentum operator relative to center A and $\xi(r_{iA})$ is a suitable radial operator, i.e.:

$$\xi(r_{iA}) = \frac{\alpha^2}{2} \frac{Z_A^{\mathrm{eff}}}{\left|\vec{r}_i - \vec{R}_A\right|^3} \tag{34.48}$$

where Z_A^{eff} is an effective charge for center A situated at point $\vec{R}_A$ and $\vec{r}_i$ is the position operator of the ith electron. More sophisticated effective SOC operators are certainly feasible and have been discussed in the literature [22, 115–117]. In all cases the necessary integrals over gaussian functions can be reduced to combinations of geometric derivative integrals such that few technical difficulties arise [110].

It is evident from the formal apparatus developed above that the SOC contribution to the ZFS arises from *differences* in orbital motions. The physical picture may be interpreted as follows: the SOC introduces some nonzero angular momentum into the orbitally nondegenerate electronic ground state wavefunction. The associated orbital motion can be regarded as a current, which according to the laws of electromagnetism gives rise to a magnetic dipole moment perpendicular to the current. The total net magnetic dipole moment of the current distributions then interacts with the total spin angular momentum. The interaction energy then depends on the relative orientations of the two magnetic dipole moments. A zero observable effect arises if the orbital motion is isotropic, since in this case the orientation of the spin angular momentum is energetically equivalent in all directions. Consequently, it is the *anisotropic* orbital motion that gives rise to the observable SOC contribution to the ZFS.

34.4 Calculation of Zero-Field Splittings

Ab initio calculations of ZFSs are relatively scarce in the literature. Most of the older calculations are of limited reliability due to the technical and software limitations at the time. While there are some reports on ab initio calculations of ZFSs it is only recently that Vahtras et al. have developed and implemented a general methodology which is compatible with mainstream quantum chemistry [14, 35]. Promising results have been obtained with this method for a number of small and organic molecules in triplet states [35]. These papers also provide pointers to the older literature on the subject. For the first excited triplet state of benzene Vahtras et al. find that

the SOC contribution to the ZFS is very small ($\sim 10^{-5}\,cm^{-1}$) which confirms the notion that the ZFS in organic molecules is usually dominated by the direct spin–spin interaction. With a basis set of DZP quality and an active CASSCF space of 6 electrons in 6 orbitals, Vahtras et al. report a calculated D of $0.1583\,cm^{-1}$ which is surprisingly close to the experimental value of $0.159\,cm^{-1}$. This result is remarkable in view of the fact that the direct spin–spin coupling depends on the inverse third power of the interelectronic distance. However, the mean interelectronic distance is only crudely modeled in the slowly converging expansions based on orbital products. Thus, one would expect difficulties in the calculations of two electron observables of the type of the spin–spin coupling and indeed, Kutzelnigg in his textbook has termed the computation of such quantities 'almost hopeless' [118]. However, since the good results obtained by Vahtras et al. also extend to more complicated molecules like naphthalene to pentacene, the situation may not be as severe as assumed. It is to be expected that, now that the technical difficulties have been essentially overcome, more experience on the typical and obtainable accuracy using CASSCF wavefunctions will be gained in the near future.

Calculations of the spin–spin dipolar part of the ZFS on the basis of DFT calculations has been reported recently [119]. At the B3LYP level with the EPR-II basis for carbon and EPR-III for hydrogen a value of $D = 0.897\,cm^{-1}$ was obtained for CH_2 in its lowest triplet state, in fair agreement with the experimental value of $D = 0.7567\,cm^{-1}$. Note that in the evaluation of the expectation value of a two electron operator within DFT the assumption is made that the unknown many electron wavefunction can be replaced by the Kohn–Sham reference determinant for the fictitious noninteracting system.

Ab initio calculations of the ZFS in transition metal complexes are even more elusive. A recent study by Ribbing et al. [28–30] addresses the (dominant) SOC contributions to the ZFS in $[Cr^{III}(1,3\text{-propanedionato})_3]$ using a CI approach. In this method, the SOC operator is diagonalized in the basis of a (small) number of eigenvectors of the CI matrix. Note that this requires all M_S components of all configuration state functions with spin S to be included. The D-value is found a posteriori from the small splittings of the ground state multiplet [28–30]. An effective charge model has been used to represent the SOC operator and only the SOC within the Cr(III) d-shell has been considered. Importantly, both quartet and doublet states were included in the CI calculations. Excellent agreement with the experimental value of $D = 1.2\,cm^{-1}$ has been obtained by this approach, the calculations predicting values of $D = 1.0$–$1.2\,cm^{-1}$ [30].

The calculation of the SOC contribution to the ZFS within a DFT framework has recently been reported [120]. The calculations showed fair agreement with experimental data for large magnetic clusters such as $[Mn_{12}O_{12}(RCOO)_{16}(H_2O)_4]$ [120, 121]. However, details of how to extract the D-tensor from these calculations and a discussion of the multiplet problem within DFT approaches to the ZFS has not been given. In addition, it would be interesting to apply this method to well characterized transition metal complexes with a single magnetic center where the intricate problem of how to properly treat the spin coupling between magnetic ions does not occur.

The final two examples of ZFS calculations are taken from our own work and are designed to show the principal challenges involved in calculating ZFSs of transition metal complexes. The computational level in these calculations is the semiempirical INDO/S method with single excitations on top of a multireference reference space and (configuration averaged) ROHF orbitals. Despite its simplicity this method has proven to be effective for the prediction of the excited states of transition metal complexes, which is crucial for the reliable prediction of ZFSs. A more systematic discussion of the ZFSs of transition metal complexes is outside the scope of this chapter and the reader is referred to a recent review which deals with the EPR properties of transition metal complexes in d^N configurations in detail [38].

Consider a high-spin Fe(III) center with $S = 5/2$ in a distorted tetrahedral environment. In the ligand field approximation, the high-spin d^5 configuration with 5 electrons in 5 orbitals gives rise to only a single sextet term ($^6A_1$) which is the ground state. Consequently, the relevant low-lying d–d excited states are all of quartet multiplicity and will give rise to an important part of the ZFS. In addition, there will be sextet excited states of charge-transfer nature which will also contribute to the observable ZFS (see Figure 34.7).

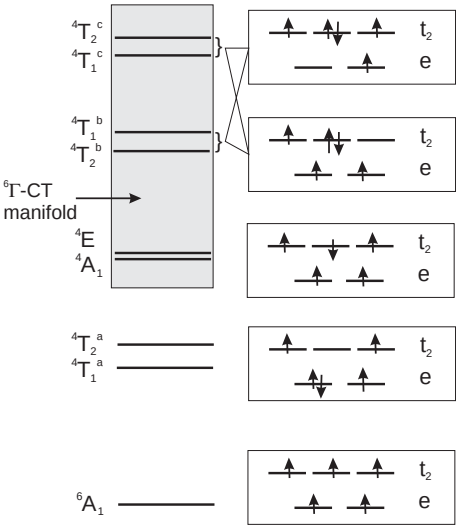

Figure 34.7 Many electron terms arising from the d^5 configuration in a tetrahedral environment and indication of their one-electron nature. (Reprinted with permission from Ref. [13]).

In order to appreciate the subtlety of the problem we first consider the contribution of the first relevant quartet state ($^4T_1{}^a$) to the ZFS (from group theoretical selection rules it follows that only states of T_1 symmetry can have non-zero SOC with the $^6A_1$ ground state). With perfectly cubic symmetry the ZFS is precisely zero, since it only arises if the three Cartesian directions are inequivalent. Thus, nonzero ZFS is only possible for a distortion of the tetrahedron which we take as either a flattening or

compression. If only one-center SOC terms at the iron center are taken into account and the metal–ligand overlap is neglected one gets the simple expression for the SOC contribution of the first quartet state to the *D*-value as indicated in Fig. 34.8 [13].

In this figure, the metal-based MOs have been simply approximated as covalently "diluted" metal d-orbitals ("L" refers to an appropriate ligand group orbital α^2, β_1^2 and γ^2 is the fractional metal character in the indicated MO and ζ_{Fe} is the one-electron SOC constant of the ferric ion). The distortion of the tetrahedron leads to a splitting Δ_{t_2} between the σ-antibonding t_2 orbitals while the splitting due to the distortion is much smaller for the e-set. Note that Δ_{t_2} is negative if the d_{xy} orbital is energetically above the $d_{xz,yz}$ orbitals. E_0 denotes the energy of the $^4T_1$ term over the $^6A_1$ ground state in perfectly tetrahedral symmetry. The important point is, that the expression for the *D*-value has two main contributions: (1) the contribution of the differential covalency (β_1^2 versus γ^2 in the numerator) and (2) the contribution due to the geometric distortion ($E_0 \pm \Delta_{t_2}$ in the denominator). If one considers a flattening of the tetrahedron then Δ_{t_2} will be negative and $\beta_1^2 < \gamma^2$ since the d_{xy}-based MO will become more antibonding then the $d_{xz,yz}$-based MOs. Thus, the numerators will tend to make the *D*-parameter negative while the denominators will tend to make the *D*-parameter positive. Similar considerations apply to the contributions from the other quartet states. Consequently, the *D*-value arises from a fine balance between geometric distortion and differential covalency effects. Treatment of only one of them, as in ligand field theory, which only treats the geometric distortion

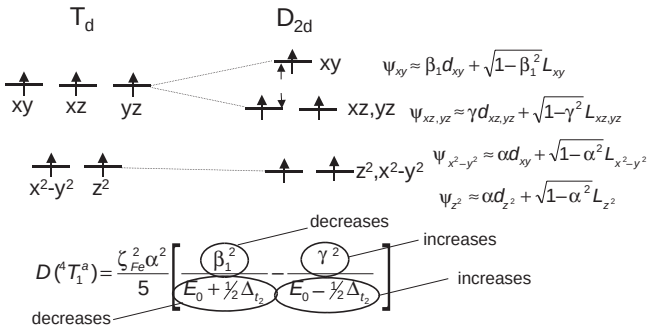

Figure 34.8 Contribution of the first quartet excited state to the ZFS in distorted tetrahedral Fe(III) sites with sextet ground state multiplicity.

effect, is therefore inappropriate. Experimentally, the *D*-value in $FeCl_4^-$ is negative which indicates that the differential covalency prevails over the geometric distortion contribution. These relationships were first worked out by Solomon and co-workers [122, 123].

A full calculation of all quartet and sextet contributions to the ZFS in $FeCl_4^-$ has been done at the INDO/S-CIS level [13] with the result shown in Fig. 34.9. It is apparent from this figure that the sextet charge-transfer and quartet ligand field contributions are of the same sign and similar magnitude. The calculations also cor-

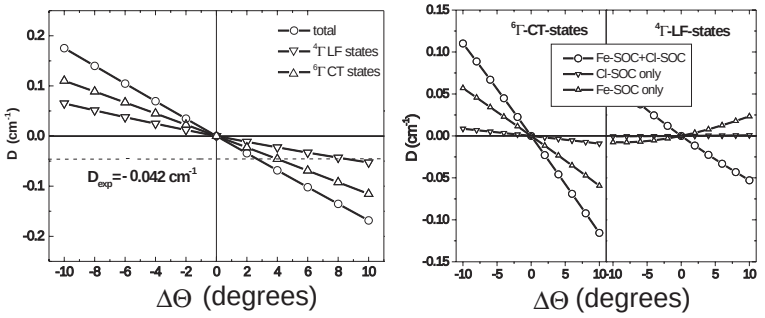

Figure 34.9 Contributions to the *D*-value in $FeCl_4^-$ as a function of geometric distortion. Left panel: contributions from the sextet and the quartet states to the total *D*-value. Right panel: contributions from the iron and chlorine SOC to the total *D*-value. ($\Delta\theta$ is the deviation in degrees of the Cl–Fe–Cl angle from the ideal tetrahedral value 109.4712°) (Reprinted with permission from Ref. [13])

rectly predict a negative *D*-value for a flattened tetrahedron. The distortion angle (Cl–Fe–Cl) at which the experimental value of $-0.042\,cm^{-1}$ is reached is within 2 degrees of experiment, which is considered satisfactory given the approximate nature of the calculations and the smallness of *D*. In addition, the contributions from the iron and chlorine SOC have been analyzed. The result in Fig. 34.9 shows that the chlorine contribution to the quartet state *D*-value is negligible, while it becomes significant for the sextet states. However, the contributions are not simply additive as terms that are proportional to $\zeta_{Fe}\,\zeta_{Cl}$ do also contribute to the final *D*-value. A full discussion is given in Ref. [13].

A more recent example of a larger system is given by the Mn(III) complex $[Mn(salen)(H_2O)_2]^+$ with a $S = 2$ ground state [124]. This system has been of interest in catalytic reactions. The *D*-value has been experimentally determined to be $\sim -2\,cm^{-1}$ [56] which is well reproduced by INDO/S-CIS calculations that include the full quintet and triplet manifolds. Interestingly, in this case the quintets account for only $-0.3\,cm^{-1}$ while the triplets account for as much as $-1.7\,cm^{-1}$ of the total calculated *D*-value of $-2.00\,cm^{-1}$. This is in strong contrast to the usual ligand field models for Mn(III) which attribute the entire ZFS to the quintet states alone and adjust ligand-field parameters up to the point where this result is reproduced. Thus, one can conclude that spin-flip ligand-field excited states are, in general, of crucial importance for a correct interpretation of the ZFS in transition metal complexes. A number of similar studies on metalloprotein active sites and model complexes thereof have been reported [31–34].

34.5 Conclusions

In conclusion we hope that it has become obvious that ZFS effects are crucial for understanding the physical properties of open shell molecules with more than one

unpaired electron and that the effects can be studied by a wide variety of experimental methods. It hopefully also became evident that the quantum chemical calculation of ZFSs is a challenging area of research which is, despite recent progress, still in its infancy. However, in our opinion, there are good reasons to be optimistic that much further progress will be made in the foreseeable future and that this will lead to more reliable interpretations of the now rapidly emerging accurate experimental data.

Acknowledgements

Our research on spin-Hamiltonian parameters is financially supported by the Deutsche Forschungsgemeinschaft within the priority program "Molecular Magnetism" which is gratefully acknowledged. It is a pleasure to acknowledge Dr. Eckhard Bill and Prof. Wolfgang Lubitz for sharing their expertise in EPR spectroscopy with me.

References

1 A. Abragam, B. Bleaney, *Electron Paramagnetic Resonance of Transition Ions*, Clarendon Press, Oxford **1970**.
2 A. Benchini, D. Gatteschi, *Transition Met. Chem.* **1979**, *8*, 1.
3 B. R. McGarvey, *Transition Met. Chem.* **1966**, *3*, 89.
4 S. McGlynn, T. Azumi, M. Kinoshita, *Molecular Spectroscopy of the Triplet State*, Prentice-Hall, Englewood Cliffs, New Jersey **1969**.
5 N. M. Atherton, *Principles of Electron Spin Resonance*, 2nd edition, Ellis Horwood, Prentice-Hall, New York **1993**.
6 W. Lubitz, *Phys. Chem. Chem. Phys.* **2002**, *4*, 5539.
7 O. Kahn, *Molecular Magnetism*, VCH, New York 1993.
8 J. S. Miller, M. Drillon, Wiley-VCH, Weinheim **2001–2003**.
9 D. Gatteschi, A. Caneschi, L. Pardi, S. R., *Science* **1994**, *265*, 1054.
10 W. Wernsdorfer, R. Sessoli, *Science* **1999**, *284*, 133.
11 W. E. Blumberg, in *Magnetic Resonance in Biological Systems*, eds. A. Ehrenberg, B. Malmström, Pergamon Press, Oxford **1967**, p. 110.
12 J. E. Harriman, *Theoretical Foundations of Electron Spin Resonance*, Academic Press, New York **1978**.
13 F. Neese, E. I. Solomon, *Inorg. Chem.* **1998**, *37*, 6568.
14 O. Vahtras, O. Loboda, B. Minaev et al., *Chem. Phys.* **2002**, *279*, 133.
15 H. Hameka, *J. Chem. Phys.* **1959**, *31*, 315.
16 S. A. Boorstein, M. Gouterman, *J. Chem. Phys.* **1963**, *39*, 2443.
17 A. Pullmann, E. Kochanski, *Int. J. Quantum Chem.* **1967**, *IS*, 251.
18 R. P. Pritchard, C. W. Kern, O. Zamani-Khamiri et al., *J. Chem. Phys.* **1972**, *56*, 5744.
19 S. R. Langhoff, *J. Chem. Phys.* **1974**, *61*, 1708.
20 E. R. Davidson, J. C. Ellenbogen, S. R. Langhoff, *J. Chem. Phys.* **1980**, *73*, 865.
21 B. A. Hess, R. J. Buenker, C. M. Marian et al., *Chem. Phys.* **1982**, *71*, 79.
22 B. A. Hess, C. M. Marian, S. D. Peyerimhoff, in *Modern Electronic Structure Theory*, ed. D. R. Yarkony, World Scientific, Singapore **1995**, p. 152.
23 P. R. Surjan, K. Nemeth, M. Bennati et al., *Chem. Phys. Lett.* **1996**, *251*, 115.
24 B. Bomfleur, M. Sironi, M. Raimondi et al., *J. Chem. Phys.* **2000**, *112*, 1066.
25 J. Mählmann, M. Klessinger, *Int. J. Quantum Chem.* **2000**, *77*, 446.
26 L. L. Lohr, W. N. Lipscomb, *J. Chem. Phys.* **1963**, *38*, 1607.

27 B. R. McGarvey, *J. Chem. Phys.* **1964**, *41*, 3743.
28 C. Ribbing, M. Odelius, A. Laaksonen et al., *Int. J. Quantum Chem. Symp. Ser.* **1990**, *24*, 295.
29 C. Ribbing, M. Odelius, *Mol. Phys.* **1993**, *78*, 1259.
30 C. Ribbing, K. Pierloot, A. Ceulemans, *Inorg. Chem.* **1998**, *37*, 5227.
31 F. Neese, E. I. Solomon, *J. Am. Chem. Soc.* **1998**, *120*, 12829.
32 M. I. Davis, A. M. Orville, F. Neese et al., *J. Am. Chem. Soc.* **2002**, *124*, 602.
33 T. A. Jackson, J. Xie, E. Yikilmaz et al., *J. Am. Chem. Soc.* **2002**, *124*, 10833.
34 T. A. Jackson, E. Yikilmaz, A.-F. Miller et al., *J. Am. Chem. Soc.* **2003**, *125*, 8348.
35 O. Loboda, B. Minaev, O. Vahtras et al., *Chem. Phys.* **2003**, *286*, 127.
36 A. Bencini, C. Benelli, D. Gateschi, *Coord. Chem. Rev.* **1984**, *60*, 131.
37 D. Gatteschi, L. Sorace, *J. Solid. State Chem.* **2001**, *159*, 253.
38 F. Neese, E. I. Solomon, in *Magnetism: Molecules to Materials IV*, eds. J. S. Miller, M. Drillon, Wiley-VCH, Weinheim **2003**, pp. 345.
39 See for example the discussion in Ch. 6 of P. Strange, *Relativistic Quantum Mechanics*, Cambridge University Press, Cambridge **1998**.
40 W. R. Hagen, *Adv. Inorg. Chem.* **1992**, *38*, 165.
41 B. J. Gaffney, H. J. Silverstone, in *EMR of Paramagnetic Molecules*, eds. L. J. Berliner, J. Reuben, Plenum Press, New York **1993**, p. 1.
42 M. B. Yim, L. C. Kuo, M. W. Makinen, *J. Magn. Reson.* **1982**, *46*, 247.
43 M. P. Hendrich, P. G. Debrunner, *Biophys. J.* **1989**, *56*, 489.
44 W. R. Hagen, *Biochim. Biophys. Acta* **1982**, *708*, 82.
45 M. P. Hendrich, E. Munck, B. G. Fox et al., *J. Am. Chem. Soc.* **1990**, *112*, 5861.
46 T. R. Holman, K. A. Andersen, O. P. Anderson et al., *Angew. Chem. Int. Ed. Engl.* **1990**, *29*, 921.
47 M. P. Hendrich, L. L. Pearce, L. Que et al., *J. Am. Chem. Soc.* **1991**, *113*, 3039.
48 K. K. Surerus, M. P. Hendrich, P. D. Christie et al., *J. Am. Chem. Soc.* **1992**, *114*, 8579.
49 B. G. Fox, M. P. Hendrich, K. K. Surerus et al., *J. Am. Chem. Soc.* **1993**, *115*, 3688.
50 T. Matsukawa, H. Mino, D. Yoneda et al., *Biochemistry* **1999**, *38*, 4072.
51 S. J. Yoo, H. C. Angove, B. K. Burgess et al., *J. Am. Chem. Soc.* **1999**, *121*, 2534.
52 K. R. Strand, S. Karlsen, K. K. Andersson, *J. Biol. Chem.* **2002**, *277*, 34229.
53 H. Andres, E. L. Bominaar, J. M. Smith et al., *J. Am. Chem. Soc.* **2002**, *124*, 3012.
54 K. A. Campbell, D. A. Force, P. J. Nixon et al., *J. Am. Chem. Soc.* **2000**, *122*, 3754.
55 D. Burdinski, E. Bill, F. Birkelbach et al., *Inorg. Chem.* **2001**, *40*, 1160.
56 K. A. Campbell, M. R. Lashley, J. K. Wyatt et al., *J. Am. Chem. Soc.* **2001**, *123*, 5710.
57 S. Mossin, H. Weihe, A. L. Barra, *J. Am. Chem. Soc.* **2002**, *124*, 8764.
58 K. K. Andersson, A. L. Barra, *Spectrochim. Acta A* **2002**, *58*, 1101.
59 J. Krzystek, J. H. Park, M. W. Meisel et al., *Inorg. Chem.* **2002**, *41*, 4478.
60 A. Bencini, E. Berti, A. Caneschi et al., *Chem.-Eur. J.* **2002**, *8*, 3660.
61 J. Yoo, A. Yamaguchi, M. Nakano et al., *Inorg. Chem.* **2001**, *40*, 4604.
62 J. Limburg, J. S. Vrettos, R. H. Crabtree et al., *Inorg. Chem.* **2001**, *40*, 1698.
63 J. Mrozinski, A. Skorupa, A. Pochaba et al., *J. Mol. Struct.* **2001**, *559*, 107.
64 S. Un, P. Dorlet, G. Voyard et al., *J. Am. Chem. Soc.* **2001**, *123*, 10123.
65 J. Krzystek, J. Telser, B. M. Hoffman et al., *J. Am. Chem. Soc.* **2001**, *123*, 7890.
66 C. Duboc-Toia, H. Hummel, E. Bill et al., *Angew. Chem. Int. Ed. Engl.* **2000**, *39*, 2888.
67 J. Telser, L. A. Pardi, J. Krzystek et al., *Inorg. Chem.* **2000**, *39*, 1834.
68 L. A. Pardi, A. K. Hassan, F. B. Hulsbergen et al., *Inorg. Chem.* **2000**, *39*, 159.
69 M. J. Knapp, J. Krzystek, L. C. Brunel et al., *Inorg. Chem.* **2000**, *39*, 281.
70 W. R. Hagen, *Coord. Chem. Rev.* **1999**, *192*, 209.
71 R. M. Wood, D. M. Stucker, L. M. Jones et al., *Inorg. Chem.* **1999**, *38*, 5384.
72 P. Tregenna-Piggott, H. Weihe, J. Bendix et al., *Inorg. Chem.* **1999**, *38*, 5928.
73 M. J. Knapp, J. Krzystek, L. C. Brunel et al., *Inorg. Chem.* **1999**, *38*, 3321.
74 A. L. Barra, A. Caneschi, A. Cornia et al., *J. Am. Chem. Soc.* **1999**, *121*, 5302.
75 C. Policar, M. Knupling, Y. M. Frapart et al., *J. Phys. Chem. B* **1998**, *102*, 10391.
76 J. Telser, L. A. Pardi, J. Krzystek et al., *Inorg. Chem.* **1998**, *37*, 5769.
77 S. M. J. Aubin, N. R. Dilley, L. Pardi et al., *J. Am. Chem. Soc.* **1998**, *120*, 4991.

78 D. P. Goldberg, J. Telser, J. Krzystek et al., *J. Am. Chem. Soc.* **1997**, *119*, 8722.
79 W. B. Lynch, R. S. Boorse, J. H. Freed, *J. Am. Chem. Soc.* **1993**, *115*, 10909.
80 W. R. Browett, A. F. Fucaloro, T. V. Morgan et al., *J. Am. Chem. Soc.* **1983**, *105*, 1868.
81 V. S. Oganesyan, S. J. George, M. R. Cheesman et al., *J. Chem. Phys.* **1999**, *110*, 762.
82 F. Neese, E. I. Solomon, *Inorg. Chem.* **1999**, *38*, 1847.
83 S. J. Bingham, J. J. Davies, D. Wolverson, *Phys. Rev. B* **2002**, *65*, art. no. 155301.
84 B. Borger, J. Gutschank, D. Suter et al., *J. Am. Chem. Soc.* **2001**, *123*, 2334.
85 S. J. Bingham, J. Gutschank, B. Borger et al., *J. Chem. Phys.* **2000**, *113*, 4331.
86 B. Borger, S. J. Bingham, J. Gutschank et al., *J. Chem. Phys.* **1999**, *111*, 8565.
87 S. J. Bingham, D. Suter, A. Schweiger et al., *Chem. Phys. Lett.* **1997**, *266*, 543.
88 R. Basler, P. Tregenna-Piggott, H. Andres et al., *J. Am. Chem. Soc.* **2001**, *123*, 3377.
89 C. Dobe, H. P. Andres, P. Tregenna-Piggott et al., *Chem. Phys. Lett.* **2002**, *362*, 387.
90 R. R. Joyce, P. L. Richards, *Phys. Rev.* **1969**, *179*, 375.
91 G. C. Bracket, P. L. Richards, W. S. Caughey, *J. Chem. Phys.* **1971**, *54*, 4383.
92 P. M. Champion, A. J. Sievers, *J. Chem. Phys.* **1977**, *66*, 1819.
93 P. M. Champion, A. J. Sievers, *J. Chem. Phys.* **1980**, *72*, 1569.
94 W. Weltner, R. J. Van Zee, S. Li, *J. Phys. Chem.* **1995**, *99*, 6277.
95 S. Vongtragool, B. Gorshunov, M. Dressel et al., *Inorg. Chem.* **2003**, *42*, 1788.
96 A. Cornia, D. Gatteschi, R. Sessoli, *Coord. Chem. Rev.* **2001**, *219*, 573.
97 P. Gütlich, R. Link, A. Trautwein, *Mössbauer Spectroscopy and Transition Metal Chemistry*, Springer, Heidelberg **1978**.
98 R. McWeeny, *Methods of Molecular Quantum Mechanics*, Academic Press, London **1992**.
99 R. McWeeny, *Spins in Chemistry*, Academic Press, New York **1970**.
100 H. Bethe, E. Salpeter, *Quantum Mechanics of One- and Two-Electron Atoms*, Springer, Berlin **1957**.
101 G. Breit, *Phys. Rev.* **1929**, *34*, 553.
102 G. Breit, *Phys. Rev.* **1930**, *36*, 363.
103 G. Breit, *Phys. Rev.* **1932**, *39*, 616.
104 J. C. Slater, *The Quantum Theory of Atomic Structure. Vol II*, McGraw-Hill, New York **1960**.
105 C. Cohen Tanudji, B. Diu, F. Laloe, *Quantum Mechanics. Vol. 2*, Wiley, Paris **1977**.
106 J. Olsen, in *Lecture Notes in Quantum Chemistry*, ed. B. O. Roos, Springer, Berlin **1992**, p. 37.
107 M. A. Robb, U. Niazi, *Comput. Phys. Rep.* **1984**, *1*, 129.
108 W. Duch, J. Karwowski, *Comput. Phys. Rep.* **1985**, *2*, 93.
109 R. Pauncz, *The Symmetric Group in Quantum Chemistry*, CRC Press, Boca Raton 1995.
110 T. Helgaker, P. R. Taylor, in *Modern Electronic Structure Theory*, ed. D. Yarkony, World Scientific, Singapore **1995**, p. 725.
111 M. E. Rose, *Elementary Theory of Angular Momentum*, Wiley, New York **1957**.
112 S. Koseki, M. W. Schmidt, M. S. Gordon, *J. Chem. Phys.* **1992**, *96*, 10768.
113 S. Koseki, M. S. Gordon, M. W. Schmidt et al., *J. Phys. Chem.* **1995**, *99*, 12764.
114 S. Koseki, M. W. Schmidt, M. S. Gordon, *J. Phys. Chem. A.* **1998**, *102*, 10430.
115 B. A. Hess, C. M. Marian, U. Wahlgren et al., *Chem. Phys. Lett.* **1996**, *251*, 365.
116 B. A. Hess, C. M. Marian, in *Computational Molecular Spectroscopy*, eds. P. Jensen, P. R. Bunker, John Wiley & Sons, New York **2000**, p. 169 ff.
117 B. Schimmelpfennig, AMFI program, University of Stockholm, Stockholm, Sweden, **1996**.
118 W. Kutzelnigg, *Einführung in die Theoretische Chemie. Band 2*, VCH, Weinheim **1994**.
119 T. T. Petrenko, T. L. Petrenko, V. Y. Bratus, *J. Phys: Condens. Matter* **2002**, *14*, 12433.
120 M. R. Pederson, S. N. Khanna, *Phys. Rev. B.* **1999**, *60*, 9566.
121 J. Kortus, *Phys. Rev. B.* **2002**, *66*, 092403.
122 J. C. Deaton, M. S. Gebhard, E. I. Solomon, *Inorg. Chem.* **1989**, *28*, 877.
123 M. S. Gebhard, J. C. Deaton, S. A. Koch et al., *J. Am. Chem. Soc.* **1990**, *112*, 2217.
124 F. Neese, T. Glaser, in preparation.

Part E
EPR Parameters, Applications

Calculation of NMR and EPR Parameters. Theory and Applications.
Edited by Martin Kaupp, Michael Bühl, Vladimir G. Malkin
Copyright © 2004 WILEY-VCH Verlag GmbH & Co. KGaA, Weinheim
ISBN: 3-527-30779-6

35
Computation of Hyperfine Coupling Tensors to Complement EPR Experiments

Fuqiang Ban, James W. Gauld, and Russell J. Boyd

35.1
Introduction

Radicals, species with at least one unpaired electron, have long been of interest. This interest has grown tremendously with our ever-increasing understanding of their role in biological systems [1–3]. For example, they are known to play central roles in the aging process and the effects of radiation exposure [4]. Furthermore, radical species are now known to play important roles in an increasing number of biological enzymes, either as an integral part of the enzyme or as transient intermediates.

Experimentally, important and powerful tools for the study of such species are electron paramagnetic resonance (EPR) spectroscopy and related techniques [5–7]. These techniques take advantage of the fact that in a radical the unpaired electron(s) is delocalized and thus, there is a non-zero probability that the unpaired electron exists at each nucleus. The interaction of the spin of the unpaired electron with the magnetic moment of each nucleus gives rise to a hyperfine structure which is fully described by its hyperfine tensor measured by EPR spectroscopy. The hyperfine coupling tensor of a given nucleus in a free radical is highly sensitive to its chemical environment and hence, can be used not only to determine the spin density distribution of the radical, but also to deduce valuable information about the identity and structure of the radical. It can be separated into an isotropic hyperfine coupling constant (HFCC) A_{iso} and three anisotropic coupling constants, T_{xx}, T_{yy} and T_{zz}, where $T_{xx} + T_{yy} + T_{zz} = 0$.

Currently, computational chemistry has become an attractive, alternative approach to complement EPR spectroscopic techniques, since transient radicals are equally amenable to computational investigation as stable long-lived species. However, such investigations do have their own inherent difficulties, in particular, determining a suitable computational method for reliably and accurately determining the hyperfine coupling tensors of interest. Indeed, the insight gained from calculated HFCCs has been found to be highly dependent on the level of theory being applied. As a result, great effort has been made to understand the requirements of theory for the accurate prediction of HFCCs [8, 9].

Calculation of NMR and EPR Parameters. Theory and Applications.
Edited by Martin Kaupp, Michael Bühl, Vladimir G. Malkin
Copyright © 2004 WILEY-VCH Verlag GmbH & Co. KGaA, Weinheim
ISBN: 3-527-30779-6

There are a few recent reviews on computational strategies for computational studies of biological systems in condensed phases [10] and on theoretical calculations of DNA base-derived radicals [11], amino acid-derived radicals [12], and quinoidal radicals [13]. This chapter extends our earlier review [12] on the computation of the hyperfine coupling tensors of biological radicals with updated literature. It summarizes the understanding of HFCCs from a theoretical perspective, providing a survey of methods that are suitable for the calculation of HFCCs and guidelines for selecting an appropriate computational scheme for predicting HFCCs. Difficulties in modelling radical species in matrices, and trends in treating environmental effects, are discussed.

35.2
Insight Gained from a Conventional Ab Initio Approach

Isotropic HFCCs are related to the spin density at the nucleus. From a theoretical point of view, the origin of the spin density at a nucleus plays a key role in understanding the mechanisms of hyperfine coupling [14]. In the 1980s, the reliable prediction of HFCCs presented a challenging computational problem. The Hartree–Fock method, which does not incorporate electron correlation, in combination with the use of static gas-phase structures, generally predicted highly erroneous coupling constants. Essentially, the inclusion of single, double and triple excitations at the MRCI, QCI or CC levels of theory is necessary for obtaining accurate spin densities at the nuclei for isotropic HFCCs. Good results obtained at lower levels of theory are due to cancellation of errors (for a detailed analysis, see Chapter 30 by Engels).

35.3
Benchmark Results Using Conventional Methods on Static Gas-phase Structures

The establishment of calculated benchmark values for a given property, those that set standards of accuracy and reliability within a set of well-defined conditions, has long been a desirable goal in computational chemistry. Such results serve not only to define the accuracy achievable by the current computational methods thus enhancing their use as a predictive tool, but also enable greater insight into the problem at hand, due in part to the explicit defining of conditions included or omitted from the calculations. In computational chemistry, standard geometry optimizations on a molecule effectively correspond to the molecule being isolated at a temperature of 0 K, i.e., static, in the gas phase without any external environmental effects, i.e., in a field-free vacuum. Thus, 'standard' benchmark calculations are typically based on the use of such structures.

The simplest chemical species are the atomic elements themselves. Thorough investigations of the role of electron correlation and basis set effects were published by Feller and Davidson in their classic paper entitled, "A multireference CI determination of the isotropic hyperfine constants for the first-row atoms B–F" [15]. Similar-

ly, Perera et al. [16] reported benchmark calculations on the atoms B–F at the highly-correlated CCSD(T) level, employing very extensive basis sets (see Table 35.1). Although the first-row atoms are simple atomic radicals, their high symmetry makes it difficult to calculate their isotropic HFCCs accurately. From such studies it was found that a more complete consideration of electron correlation and the use of uncontracted s-orbital functions were essential for obtaining accurate values [15]. Excellent comments on the performance of various levels of theory on such radicals have been previously made by Perera et al. [16].

Molecular radicals introduced researchers to the consequences of differences between computationally optimized and experimentally observed vibrationally averaged structures, as a factor that affects HFCCs. An inherent assumption of the use of static structures is that the effects of vibrational motion are negligible. For molecules for which this assumption is acceptable, e.g., NH_2, the MRCI method has been found to behave quite well [23, 24]. The ideal optimized geometry should be the converged result, i.e., increasing the level of theory has little or no further effect on the optimized structure. However, the empirical choice of method for geometry optimizations is often at fairly modest and less expensive levels at which reliable geometries can generally be obtained. Since reliable HFCC predictions demand a higher level of theory, a common approach for HFCC calculations is to employ a computational scheme involving single-point calculations at a high level of theory, based on structures obtained at a considerably lower level of theory. When no experimental structural data is available for comparison, the choice of method and basis set for obtaining optimized structures of the radical of interest is critical, and often other criteria for determining the suitability of a particular method must be used, e.g., performance of a method for related radicals [25]. In addition, the use of geometries that minimize errors in the calculated HFCCs, has been employed in examinations of the performance of single-point HFCC calculations [26].

Benchmark results obtained using highly correlated methods in combination with large uncontracted basis sets, highlight the capability of computational chemistry for predicting accurate HFCCs. However, such approaches are generally too

Table 35.1 Benchmark HFCC (in MHz) predictions of first-row atoms.

Method	$^{11}B(^2P)$	$^{13}C(^3P)$	$^{14}N(^4S)$	$^{17}O(^3P)$	$^{19}F(^2P)$
CCSD(T) /[23.12.10.4.2][a b]	8.19	19.38	10.4	–31.77	300.18
CCSD(T) / [23.12.10.4.2][c]	10.25	21.42	11.00	–33.16	302.87
Exptl.	11.6[d]	21.4[e]	10.4[f]	34.5[g]	301.7[g]
	18.7[h]	22.5[d]			

a) Based on a UHF reference determinant.
b) Ref. [17].
c) Based on a ROHF reference determinant.
d) Ref. [18].
e) Ref. [19].
f) Ref. [20].
g) Ref. [21].
h) Ref. [22].

costly for moderate-size radicals and therefore are not practically feasible and are inappropriate for common use. When the CCSD(T) level of theory with large basis sets (such as aug-cc-pVQZ with s- and p-functions uncontracted) appears to be less accurate when compared with experimental values, than when a smaller basis set (such as DZP) is used, the effects of vibrational averaging have been considered responsible for the results. The same is also said to be the case when the B3LYP method in combination with a large basis set, is employed. This is illustrated by the results of Petraco et al. [27] for the thioformyl radical (Tab. 35.2).

Table 35.2 Benchmark HFCC (MHz) predictions for HCS radical.

Method	^{1}H	^{13}C
CCSD(T)/aug-cc-pVQT// CCSD(T)/cc-pVQT	121.06	274.7
B3LYP/aug-cc-pVQT// CCSD(T)/cc-pVQT	127.35	281.85
CCSD(T)/DZP// CCSD(T)/cc-pVQT	120.06	304.51
Exptl.[a]	127.43	287.90

a) Ref. [28, 29].

Because investigation of the temperature and environmental effects is technically more difficult and expensive, such effects have not been included in the above results. However, predictions of HFCCs for the first-row magnetic nuclei are very reliable when vibrational averaging, solvent or matrix, spin–orbit coupling and relativistic effects are negligible.

35.4 The Performance of Contracted Pople Basis Sets for Small Radicals Consisting Only of First-Row Atoms

The HFCCs of small radicals, in particular those containing three or fewer heavier-than-hydrogen atoms, have been extensively studied using computational methods. This is due in part to their small size which, as a result, has enabled the broadest range of methods to be applied. Such studies have shown that HFCCs are quite sensitive to the extent of consideration of electron correlation and to the basis set used. To expand the limits of a computational approach beyond those imposed by the use of very large fully-uncontracted basis sets, the potential of more computationally tractable contracted or partially uncontracted (s- and/or p-functions uncontracted) Pople basis sets has been assessed with a variety of methods. Table 35.3 shows the single-point calculation performance of Pople basis sets with the QCISD and B3LYP methods for a range of small radicals, employing optimized geometries obtained at the QCISD/6-31G(d) level.

As can be seen, for carbon and oxygen, at the QCISD level, the 6-311+G(d,p) and 6-311+G(2df,p) basis sets give the most reliable results. In contrast, the isotropic HFCCs of H and N are reasonably reproduced with all basis sets listed in Table 35.3.

Table 35.3 Effect of basis set on QCISD and B3LYP calculated A_{iso} values (in MHz) for the OH, H_2O^+, CN, and HCN^- radicals [26] using QCISD/6-31G(d) geometries.

Method	Basis Set	OH		H_2O^+		CN		HCN^-		
		H	O	H	O	C	N	H	C	N
QCISD(T)	6-31G(d)	–83.8	–59.1	–84.4	–109.0	561.6	–9.0	410.6	340.2	19.3
	6-31G(d,p)	–82.1	–59.1	–84.4	–108.7	561.6	–9.0	399.1	349.5	19.3
	6-311G(d,p)	–80.7	–42.9	–83.8	–78.5	585.2	–5.9	359.6	310.2	15.7
	6-311+G(d,p)	–80.4	–46.2	–83.5	–77.1	602.0	–6.7	350.3	210.7	20.7
	6-311G(df,p)	–75.7	–41.5	–79.0	–76.2	574.2	–7.3	360.7	308.3	14.6
	6-311G(2df,p)	–74.8	–45.4	–77.1	–79.0	595.5	–9.2	366.0	303.2	16.5
	6-311+G(2df,p)	–74.8	–48.5	–77.1	–78.5	603.7	–9.8	354.2	213.6	20.5
B3LYP	6-311+G(2df,p)	–63.9	–31.9	–68.1	–52.1	524.9	–19.3	346.4	241.9	15.4
	usp-6-311+G(2df,p)	–63.6	–44.0	–67.8	–65.6	518.5	–16.0	346.4	240.5	17.7
	Exptl.[a]	–73.4	–51.3	–73.1	–83.2	588.5	–12.6	384.5	211.3	19.9

a) Ref. [30–32].

This also highlights one of the unfortunate challenges for calculating HFCCs of polyatomic molecules: not all atoms are necessarily treated equally well by a given basis set.

35.5
Density Functional Theory: An Alternative to a Conventional Ab Initio Approach

Density functional theory (DFT) offers an attractive alternative approach to conventional electron correlation procedures because it incorporates the effects of electron correlation more cheaply, and thus has the potential to be applied to considerably larger systems. However, this does necessarily depend on the correct choice of DFT method and basis set for the molecule and property of interest. This is also true for HFCCs. Despite the fact that several extensive assessments of DFT calculations on HFCCs have appeared in the literature, a well-defined standard test set of radicals for validating a particular computational model has not yet been established. It should be noted that the remarkable performance of a particular DFT method does depend to a certain extent on the fortuitous cancellation of errors due to incomplete electron correlation and contracted basis set effects (see Chapter 30 by Engels and Chapter 29 by Munzarová).

However, promising results have been obtained using PBE0/EPR-III on CH_3 and H_2CO^+ radicals [10], B3LYP/EPR-III on first-row atoms and HOO [33], PWP86/IGLO-III on OH, CH_3, CN, NO_2, H_2O^+, H_2CO^+, HCO, FCO, HCN^-, FCN^- and F_2^- [34] and NO_2 and NO_3 [35], PWP86/6-311G(2d,p) proton HFCCs on 22 substituted benzene radicals [36] and B3LYP/6-311+G(2df,p) on OH, H_2O^+, CN and HCN^- [26]. The above calculations suggested that combinations of certain gradient-corrected functionals with appropriate basis sets can provide reasonably accurate results for radicals containing only hydrogen and first-row atoms. Furthermore, as noted pre-

viously, the HFCCs for different atoms exhibit different basis set dependences. For example, for the B3LYP method, the H HFCCs are not sensitive to uncontraction of the s- and p-basis functions in the 6-311+G(2df,p) basis set. However, the corresponding basis set in which they are uncontracted, usp-6-311+G(2df,p), gives much better oxygen HFCCs with little change in the H HFCCs, see Table 35.3.

Recently, extensive DFT HFCC calculations have been performed for radicals containing second-row atoms, in particular sulfur and phosphorus, and shown that such methods can provide reliable HFCCs [37–41]. For example, for the $H_2C_2S_2N$ radical, the B3LYP/6-31G(df,p)//B3LYP/6-31G(d) method gave ^{1}H, ^{14}N and ^{33}S HFCCs in good agreement with the experimental values [39]. In addition, investigations on a series of six neutral mono-, bi- and tri-cyclic dithiazole radicals, found that the B1LYP/(EPR-III for H, C, N and 6-31G(df) for S) method using structures obtained experimentally by X-ray crystal structure determinations or optimized at the B3LYP/6-31G(d) level, gave ^{1}H, ^{14}N *and* ^{33}S HFCCs that were in quantitative agreement with experimental data [37]. For the calculation of the ^{31}P HFCC in phosphorus radicals, a B3LYP/TZVP//MP2/6-31(d,p) scheme is recommended on the basis of an assessment of 35 P-containing radicals [41].

In addition to the development of methods for the study of organic radicals, tremendous progress has also been made in the study of transition metal complexes [42, 43]. It has been found that the performance of a given functional is very different for different classes of metal complexes. This behavior arises because present functionals have difficulty in accurately describing core–shell spin polarization while avoiding deterioration due to spin contamination [42]. Thus, the choice of DFT method to be employed for a particular transition metal complex should be guided by the electronic structure of the metal complex (see Section 29.3.5 in Chapter 29). Neese has developed a method to calculate spin–orbit coupling contributions to the hyperfine coupling and has shown that B3LYP, in the majority of cases, is more accurate than other functionals [44, 45].

35.6 Consideration of Environmental Effects

A common feature of all the calculations discussed above, is that they neglect the effects on HFCCs arising from external sources, e.g., a solid matrix. However, it is known that when free radical systems are studied in a crystalline or aqueous environment, the particular environment can have significant effects on their structures and HFCCs [46–49]. Accounting for and describing such effects have always been difficult tasks for computational chemists. However, tremendous progress in developing strategies for including the environmental effects on molecular structures and hyperfine couplings has been made [47–51].

The most direct approach for including environmental effects is to use the *supermolecular model* approach in which a unit cell, or a sufficient number of the environment molecules centered around the target radical, is explicitly included in the calculation. An advantage of this approach is that electrostatic effects arising from the

surrounding media *as well as* explicit interactions between the target radical and molecules of the surrounding environment are included. For example, Pauwels and co-workers have built two cluster models that include 6 and 14 L-α-alanine molecules, respectively, around a zwitterionic alanine radical $H_3N^+C(CH_3)COO^-$ [52, 53]. For such calculations, they employed an ONIOM approach in order to reduce the computational cost for geometry optimization of such a large cluster.

An alternative approach is the use of periodic boundary conditions (PBC). For example, Imptota and co-workers [54] have applied such an approach to the study of molecular crystals of stable nitroxides, species whose magnetic properties are strongly dependent on the hydrogen-bond network within the crystals. In particular, they found that the use of the PBE/6-31G(d) method performs remarkably well for the crystals of three nitroxide derivatives: 2,2,6,6-tetramethylpiperidin-1-oxyl (TEMPO) and its 4-hydroxy and 4-hydroxyimino derivatives [54]. The calculated geometries, spin populations and the HFCCs are in agreement with the available experimental results, highlighting the complementtary nature of computational and experimental investigations for designing new organomagnets.

The most common and widely used approach is the use of a self-consistent reaction field (SCRF) to model the general electrostatic effects arising from the radical environment (see Chapter 12 by Ciofini). This can then be applied directly to the radical, i.e., complete neglect of explicit radical–environment interactions [55], or by applying to small cluster-systems consisting of a few surrounding molecules that directly interact with the target radical; in effect a simplified *supermolecular model* approach [48, 56, 57]. Rega et al. have provided a very comprehensive analysis of solvent effects on the HFCCs of the glycine anion radical $H_2NCHCOO^-$ in aqueous solution [49].

SCRF methods include the Onsager model and the polarizable continuum models (PCM, IPCM, SCIPCM and CPCM) [58]. The applicability of the SCRF methods is well illustrated by the numerous computational investigations on a diverse variety of biological radicals in solution or matrices, that have appeared in the literature [46–48, 56, 57, 59–67]. For instance, SCRF calculations have appeared on the tyrosyl dipeptide radical and analogues [65], 4-amino-2,2,6,6-tetramethylpiperidine-1-oxyl-4-carboxylic acid and analogue radicals [62], glycine amino acid radicals [56, 57, 61], 1,2- and 1,4-benzosemiquinone radicals [66], cytosine radicals [59], and the radical anions of the nucleobases uracil, thymine, and various methylated deriviatives [47, 48]. In general, the best approach for choosing a suitable SCRF-based method for the radical and environment of interest, is to first test on a related radical for which experimental HFCCs are available. For example, Langella et al. have shown that the CPCM-PBE0/EPR-II//CPCM-PBE0/6-31G(d) method is sufficient to describe solvent effects on the hyperfine couplings of a tyrosyl dipeptide radical and analogues [65]. (The SCRF-method notation denotes that the calculation has been performed using the given method and applying the given SCRF procedure.) In contrast, for zwitterionic radicals of amino acids in matrices it has been shown that the PWP86/6-311G(2d,p)//Onsager-B3LYP/6-31+G(d,p) method can provide accurate proton HFCCs [46, 60, 61]. While the comparatively straightforward Onsager-B3LYP/6-31G(d) method has been shown to give HFCCs in good agreement with experi-

ment for uracil, thymine and cytosine, and various methylated derivatives [47], it should be noted that a systematic basis set and SCRF model investigation suggested that the CPCM-B3LYP/6-31G(d) and CPCM-B3LYP/6-31G(d,p)//CPCM-B3LYP/6-311+G(d,p) methods gave the best agreement with experiment for the radical anions of uracil, thymine and their methylated deriviatives, although this is most likely due to fortuitous cancellation of errors [48]. The SCRF method IPCM has also been employed, with the critical effects of aprotic and protic solvents on the HFCCs of 1,2- and 1,4-benzosemiquinone being successfully interpreted using the IPCM-B3LYP/D95//B3LYP/D95 method [66].

It should be noted that in some of the above cases, structures were optimized within an SCRF method to give structures that reflect the effect of the surrounding dielectric continuum (e.g., those described above for the zwitterionic amino acid radicals) while in other cases, the gas-phase structures were simply used (e.g., those described above using the IPCM method). In the former case, zwitterionic amino acids do not correspond to energy minima in the gas-phase but do in solution, hence the need to optimize using an SCRF method.

35.7
Illustration of the Applications of DFT Methods to Biological Radicals

There are numerous ways in which computational investigations can be used to complement experimental studies, particularly for biological radicals. Indeed, there are many good examples of such studies in the literature. For this present brief review, we have chosen to simply highlight a couple of ways in which DFT calculations have been applied to biological radicals, and how they have complemented experimental investigations.

35.7.1
DFT Investigations on Amino Acid Radicals Generated in an Irradiated Crystal

In 1997, Brustolon et al. investigated radicals arising from irradiation of amino acid crystals, and assigned three newly observed hyperfine coupling tensors to the radical NH_2CH_2 [68]. In 1998, Sanderud et al. showed this to be incorrect and proposed that the radical was $NH_2CHCOOH$, i.e., the radical formed by homolytic cleavage of a C–H bond in the $–CH_2–$ group [69]. In addition, they assigned three more observed hyperfine couplings to another conformer of $NH_2CHCOOH$. The two experimentally observed conformers of $NH_2CHCOOH$ are denoted hereafter as $R^{\#}$ and R^{*}. The H_α isotropic HFCCs of $R^{\#}$ (–30.15 MHz) and R^{*} (–24.62 MHz) differ significantly. Based on the McConnell relation and the Gordy–Bernhard method, the smaller absolute isotropic HFCC for the proposed R^{*}, was ascribed to non-planarity of the radical center in the glycine crystal. Furthermore, experimental data suggested a twist angle of 24.2° between the OCO and CCN planes in R^{*}.

When $NH_2CHCOOH$ was optimized in the gas-phase at the B3LYP/6-31+G(d,p) level, it was found to have four possible conformations, shown in Fig. 35.1 [61]. The

computed HFCCs in for the four radical conformers R-I, R-II, R-III and R-IV, and the experimental HFCCs of $R^{\#}$ and R^{*} are listed in Table 35.4.

From careful comparison of the calculated HFCCs for the four conformers of $NH_2CHCOOH$, they can be divided into two groups, with R-I in one group and the rest in a second group. The isotropic HFCCs of H_α in R-II, R-III and R-IV are all in similar agreement with the experimental value of $R^{\#}$ (within 6–8 MHz), however, they differ significantly from the experimental value of R^{*} by at least 12 MHz. The anisotropic components of the H_α hyperfine coupling tensors for the above conformers are all in similar agreement with the experimental values of both $R^{\#}$ and R^{*}. Except for the isotropic HFCC of H_2 in R-IV, the isotropic HFCCs and anisotropic components of the two amino protons of R-II, R-III and R-IV are in good agreement with the corresponding experimental values of both $R^{\#}$ and R^{*}, which are themselves very similar. Larger deviations are found between the calculated isotropic and anisotropic HFCCs of H_α and the experimental values of $R^{\#}$ or R^{*} in R-I than in R-II to R-IV. In addition, the computed amino-proton isotropic H_1 HFCCs (25.03 MHz) in R-I and the experimental values $R^{\#}$ and R^{*} (–18.05 and –16.87 MHz,

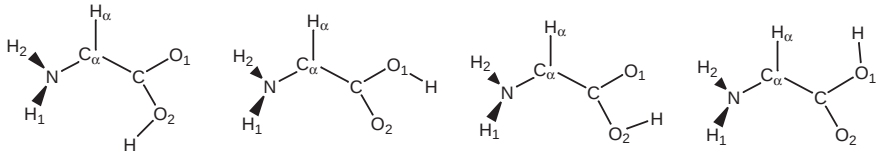

Figure 35.1 Four conformers of $NH_2CHCOOH$.

Table 35.4 PWP86/6-311G(2d,p)//B3LYP/6-31+G(d,p) calculated HFCCs [61] (MHz) of R-I, R-II, R-III, R-IV and the experimental values of $R^{\#}$ and R^{*}.

Tensor		R-I	R-II	R-III	R-IV	Exptl.[a]	
						($R^{\#}$)	(R^{*})
H_α	A_{iso}	–40.41	–36.10	–38.03	–37.61	–30.15	–24.62
	T_{xx}	–24.95	–22.26	–22.36	–23.47	–17.24	–16.22
	T_{yy}	–2.04	–2.14	–2.06	–1.38	–0.19	–1.54
	T_{zz}	26.99	24.40	24.42	24.85	17.48	17.77
H_1	A_{iso}	25.04	–17.01	–16.39	–16.02	–18.05	–16.87
	T_{xx}	–12.60	–16.08	–15.81	–14.96	–16.00	–17.25
	T_{yy}	–5.52	–6.45	–5.04	–5.74	–4.18	–4.37
	T_{zz}	18.12	22.53	20.85	20.70	20.28	21.62
H_2	A_{iso}	–12.78	–14.27	–14.78	–10.70	–16.79	–15.46
	T_{xx}	–13.99	–19.26	–17.60	–18.02	–15.39	–16.42
	T_{yy}	–4.83	–5.42	–4.54	–4.65	–2.94	–3.99
	T_{zz}	18.82	24.67	22.15	22.67	18.34	20.40

a) Ref. [69].

respectively) are of the same magnitude, however, their signs are opposite. Thus, R-I can be neither $R^{\#}$ nor R^{*}. Although the above calculations using gas-phase optimized structures of R could not distinguish between $R^{\#}$ and R^{*}, it was concluded that the experimentally observed signals assigned to $R^{\#}$ can be due to one conformer, or a mixture of the R-II, R-III and R-IV conformers.

In addition, it was noted that the calculated H_α isotropic HFCCs of R-II, R-III and R-IV are in closer agreement with the experimental isotropic HFCCs (33.0 MHz) of $NH_2CHCOOH$ in solution [70]. Hence, it was suggested that the deviation of the calculated H_α isotropic HFCCs of R-II to R-IV from the experimental values of $R^{\#}$ is likely due to crystal-packing effects, which were not taken into account by the above calculations.

An experimentally suggested twist angle of 24.2° between the $NC_\alpha C_1$ and $O_1C_1O_2$ planes in R^{*} implies that the two amino protons and the two carboxylic oxygens are constrained by intermolecular hydrogen bonding. The effect of the two-plane twist on the H_α, H_1 and H_2 HFCCs of $R^{\#}$ was investigated by re-optimizing only H_α related geometrical parameters, i.e., H_α–C_α, $\angle H_\alpha C_\alpha C_1$, and $\angle H_\alpha C_\alpha C_1 N$ in R-II, R-III and R-IV. The twisting of the $NC_\alpha C_1$ plane with respect to the $O_1C_1O_2$ plane was carried out by incrementally increasing the absolute value of $\angle O_2C_1C_\alpha N$ by 10° from 0°. The variation of the isotropic HFCCs of H_α, H_1 and H_2 in R-II with respect to the twist angle is shown in Fig. 35.2.

The corresponding plots for R-III and R-IV exhibit the same pattern. The absolute isotropic HFCC of H_α decreases as the twist angle increases in R-II, R-III and R-IV. The isotropic HFCC of one amino proton (H_1) increases as the isotropic HFCC of the other amino proton (H_2) decreases in R-II, R-III and R-IV. As the isotropic HFCCs of H_1 and H_2 become equal (see Fig. 35.2), the average ($H_{1,2}^{ave}$) of the isotropic HFCCs of H_1 and H_2 decreases slightly. However, the $H_{1,2}^{ave}$ values are all very close to the average of the experimental H_1 and H_2 isotropic couplings in R^{*}

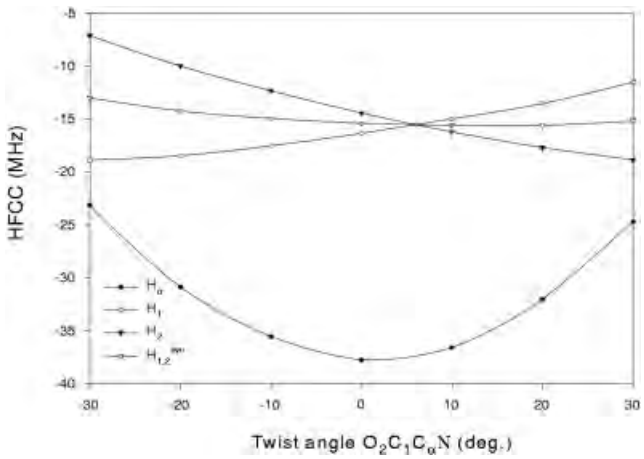

Figure 35.2 Variation of H_α, H_1, H_2, and $H_{1,2}^{ave}$ isotropic HFCCs in R-II.

(16.16 MHz). It should be noted that by varying the twist angle, one is able to produce changes in the calculated H_α and $H_{1,2}{}^{ave}$ HFCCs, similar to the experimentally observed differences between $R^{\#}$ and R^{*} (see Tab. 35.4). Thus, although the calculations are unable to determine the conformation of R^{*}, it does support the experimental conclusion that R^{*} is only a twisted configuration of $R^{\#}$ fixed by intermolecular hydrogen bonding in glycine crystals.

35.7.2
Compromise Computational Scheme for Treating Fairly Large Radicals

The diverse array of radicals of biological or chemical interest is far more than those few mentioned briefly above. A majority of biological radicals are rather big, such as the bacteriochlorophyll *a* radical cation (Fig. 35.3). For molecules of this size, it is usually possible to optimize their structures with a DFT method, such as B3LYP, in combination with the modest 6-31G(d) basis set; an approach that generally provides reliable geometries. However, the existence of substituents on a core model chemical structure, such as the groups peripheral to the main aromatic system in chlorophyll *a* radical cation, can give rise to many possible conformations of the same system. A complete conformational search using a DFT approach is often too expensive for present computational resources. Thus, for fairly large radical systems, a compromise has often to be made by using a model radical system and reasonably cheap basis sets for a meaningful description of the experimental system in question. The common practice is to simplify the chemical system by replacing those unnecessary substituents with hydrogens. For example, the model I (Fig. 35.3b) and model II (Fig. 35.3c) chemical systems have been used by O'Malley et al. [71] and Sinnecker et al. [72], respectively, to model the real bacteriochlorophyll *a* radical cation (Fig. 35.3a). Indeed, they found that use of the B3LYP/6-31G(d)//B3LYP/6-31G(d) and B3LYP/EPR-II//BLYP/DZVP methods respectively, produced ^{14}N and ^{25}Mg isotropic hyperfine couplings for the bacteriochlorophyll *a* radical in excellent agreement with those reported for bacteriochlorophyll *a* in aqueous solution [71].

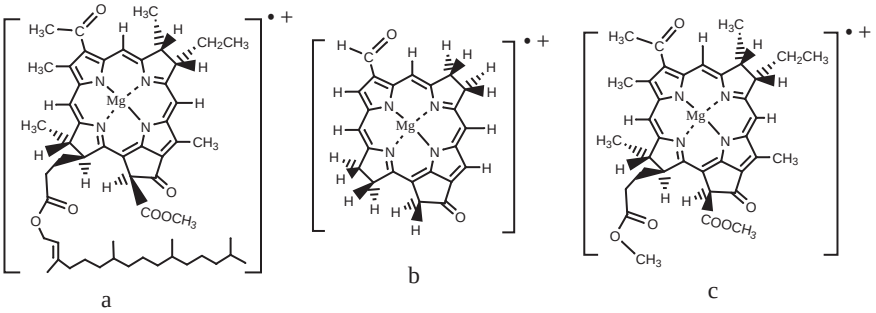

Figure 35.3 (a) Bacteriochlorophyll *a* radical cation, (b) model I and (c) model II bacteriochlorophyll *a* radical cation.

A similar computational scheme to those illustrated above has provided good HFCCs for the chlorophyll radical cation and anion [71, 73, 74], bacteriopheophytin *a* radical anion [75–77], and bacteriochlorophyll radical cation and anion [71, 72].

For accurate prediction of the HFCCs of particular atoms within a portion of a moderate size radical, D'Amore et al. have applied an ONIOM-like strategy in which the whole biological radical is used: the entire radical is treated with the PBE0 functional, while the target portion of the radical is treated at a considerably higher level of theory, QCISD. In effect, this approach is similar to those previously discussed for inclusion of environmental effects. Their "ONIOM-like strategy" HFCC calculations for the nitrogen in a 4-amino-2,2,6,6-tetramethylpiperidine-1-oxyl-4-carboxylic acid analogue provide a possible avenue for correcting, or improving, DFT results when needed [62].

35.8 Summary

In the last few decades, the HFCC property of free radicals has been well understood through complementary computational and experimental investigations. In general, CCSD(T) or QCISD(T) levels of theory in conjunction with appropriate basis sets are the preferred choices for calculating accurate HFCCs for small radicals. Indeed, such methods, when feasible, provide benchmark results. The DFT functionals B3LYP, PWP86, PBE and BLYP, in combination with appropriate well-balanced basis sets, have been shown to provide comparable results or even better than CCSD(T) or QCISD(T), due in the most part to fortuitous cancellation of errors. For DFT methods, many radical systems do not show strong basis set dependence. This allows large biological and chemical radicals to be investigated. In particular, it is now feasible to computationally tackle the HFCCs of radicals within environments of experimental relevance. Using the state-of-the-art SCRF models in combination with small cluster models to consider the bulky and explicit solvent effects, it is possible to interpret many observed hyperfine couplings of radicals that gas phase calculations cannot explain.

Acknowledgements

We gratefully acknowledge the Natural Sciences and Engineering Research Council of Canada (NSERC) and the Killam Trusts for financial support.

References

1 J. Stubbe, W. A. van der Donk, *Chem. Rev.* **1998**, *98*, 705–762.
2 W. M. Garrison, *Chem. Rev.* **1987**, *87*, 381–398.
3 W. K. Pogozelski, T. D. Tullius, *Chem. Rev.* **1998**, *98*, 1089–1107.
4 B. Halliwell, J. M. C. Gutteridge, *Free Radicals in Biology and Medicine*; Oxford University Press, New York **1999**.
5 N. M. Atherton, *Principles of Electron Spin Resonance*; Ellis Horwood, Chichester **1993**.
6 J. A. Weil, J. R. Bolton, J. E. Wertz, *Electron Paramagnetic Resonance (Elementary Theory and Practical Applications)*, John Wiley & Sons, Chichester **1994**.
7 W. Weltner, Jr., *Magnetic Atoms and Molecules*; Van Nostrand, New York **1983**.
8 I. Carmichael, *J. Phys. Chem.* **1991**, *95*, 6198–6201.
9 I. Carmichael, *J. Chem. Phys.* **1989**, *91*, 1072–1078.
10 C. Adamo, M. Cossi, N. Rega, V. Barone et al., *Theoretical Biochemistry-Processes and Properties of Biological Systems*, ed. L. A. Eriksson, Elsevier, Amsterdam **2001**, pp. 467–532.
11 S. D. Wetmore, L. A. Eriksson, R. J. Boyd, *Theoretical Biochemistry-Processes and Properties of Biological Systems*; ed. L. A. Eriksson, Elsevier, Amsterdam **2001**, pp. 409–458.
12 F. Ban, J. W. Gauld, S. D. Wetmore et al., *EPR of Free Radicals in Solids: Trends in Methods and Applications*, eds. A. Lund, M. Shiotani, Kluwer, Dordrecht **2003**.
13 R. A. Wheeler, *Theoretical Biochemistry-Processes and Properties of Biological Systems*, ed. L. A. Eriksson, Elsevier, Amsterdam **2001**, pp. 655–685.
14 D. M. Chipman, *Theor. Chim. Acta*. **1992**, *82*, 93–115.
15 D. Feller, E. R. Davidson, *J. Chem. Phys.* **1988**, *88*, 7580–7587.
16 S. A. Perera, J. D. Watts, R. J. Bartlett, *J. Chem. Phys.* **1994**, *100*, 1425–1434.
17 M. W. Schmidt, K. Ruedenberg, *J. Chem. Phys.* **1979**, *71*, 3951–3962.
18 J. S. M. Harvey, L. Evans, H. Lew, *Can. J. Phys.* **1972**, *50*, 1719–1727.
19 J. R. Macdonald, R. M. Golding, *Theor. Chim. Acta*. **1978**, *47*, 1–16.
20 W. W. Holloway, Jr., E. Luscher, R. Novick, *Phys. Rev.* **1962**, *126*, 2109–2115.
21 J. S. M. Harvey, *Proc. R. Soc. London, Ser. A* **1965**, *285*, 581.
22 W. R. M. Graham, W. Weltner, Jr., *J. Chem. Phys.* **1976**, *65*, 1516–1521.
23 J. Kong, R. J. Boyd, L. A. Eriksson, *J. Chem. Phys.* **1995**, *102*, 3674–3678.
24 K. Funken, B. Engels, S. D. Peyerimhoff et al., *Chem. Phys. Lett.* **1990**, *172*, 180–186.
25 M. Guerra, *J. Phys. Chem. A* **1999**, *103*, 5983–5988.
26 J. W. Gauld, L. A. Eriksson, L. Radom, *J. Phys. Chem. A* **1997**, *101*, 1352–1359.
27 N. D. K. Petraco, S. S. Wesolowski, M. L. Leininger et al., *J. Chem. Phys.* **2000**, *112*, 6245–6254.
28 H. Habara, S. Yamamoto, C. Ochsenfeld et al., *J. Chem. Phys.* **1998**, *108*, 8859–8863.
29 H. Habara, S. Yamamoto, *J. Mol. Spectrosc.* **2003**, *219*, 30–36.
30 L. B.Knight, Jr., J. Steadman, *J. Chem. Phys.* **1983**, *78*, 5940–5945.
31 E. L. Cochran, F. J. Adrian, V. A. Bowers, *J. Chem. Phys.* **1962**, *36*, 1938–1942.
32 W. C. Easley, W. Weltner, Jr., *J. Chem. Phys.* **1970**, *52*, 197–205.
33 V. Barone, *Recent Advances in Density Functional Methods Part I*, ed. D. P. Chong, World Scientific, Singapore **1996**, p. 287.
34 L. A. Eriksson, O. L. Malkina, V. G. Malkin et al., *J. Chem. Phys.* **1994**, *100*, 5066–5075.
35 L. A. Eriksson, J. Wang, R. J. Boyd et al., *J. Phys. Chem.* **1994**, *98*, 792–799.
36 L. A. Eriksson, *Mol. Phys.* **1997**, *91*, 827–833.
37 S. M.Mattar, A. D. Stephens, *Chem. Phys. Lett.* **2000**, *327*, 409–419.
38 S. M. Mattar, A. D. Stephens, *J. Phys. Chem. A* **2000**, *104*, 3718–3732.
39 S. M. Mattar, *Chem. Phys. Lett.* **1999**, *300*, 545–552.
40 C. Adamo, R. Arnaud, G. Scalmani et al., *J. Phys. Chem. B* **1999**, *103*, 6863–6869.
41 M. T. Nguyen, S. Creve, L. G. Vanquickenborne, *J. Phys. Chem. A* **1997**, *101*, 3174–3181.
42 M. Munzarová, M. Kaupp, *J. Phys. Chem. A* **1999**, *103*, 9966–9983.
43 M. L. Munzarová, P. Kubáček, M. Kaupp, *J. Am. Chem. Soc.* **2000**, *122*, 11900–11913.
44 F. Neese, *J. Chem. Phys.* **2001**, *115*, 11080–11096.
45 F. Neese, *J. Chem. Phys.* **2003**, *118*, 3939–3948.

46 F. Ban, S. D. Wetmore, R. J. Boyd, *J. Phys. Chem. A* **1999**, *103*, 4303–4308.
47 S. Naumov, A. Barthel, J. Reinhold et al., *Phys. Chem. Chem. Phys.* **2000**, *2*, 4207–4211.
48 S. Naumov, J. Reinhold, D. Beckert, *Phys. Chem. Chem. Phys.* **2003**, *5*, 64–72.
49 N. Rega, M. Cossi, V. Barone, *J. Am. Chem. Soc.* **1998**, *120*, 5723–5732.
50 V. Barone, A. Bencini, M. Cossi et al., *J. Am. Chem. Soc.* **1998**, *120*, 7069–7078.
51 V. Barone, A. Bencini, A. di Matteo, *J. Am. Chem. Soc.* **1997**, *119*, 10831–10837.
52 E. Pauwels, V. Van Speybroeck, P. Lahorte et al., *J. Phys. Chem. A* **2001**, *105*, 8794–8804.
53 E. Pauwels, V. Van Speybroeck, M. Waroquier, *Int. J. Quantum Chem.* **2003**, *91*, 511–516.
54 R. Improta, K. N. Kudin, G. E. Scuseria et al., *J. Am. Chem. Soc.* **2002**, *124*, 113–120.
55 J. B. Foresman, A. Frisch, *Exploring Chemistry with Electronic Structure Methods*, Gaussian Inc., Pittsburgh, PA **1996**.
56 N. Rega, M. Cossi, V. Barone, *J. Am. Chem. Soc.* **1997**, *119*, 12962–12967.
57 N. Rega, M. Cossi, V. Barone, *J. Am. Chem. Soc.* **1998**, *120*, 5723–5732.
58 A. Frisch, M. J. Frisch, *Gaussian 98 User's Reference*, Gaussian, Inc., Pittsburgh, PA **1998**, p. 161.
59 C. Adamo, M. Heitzmann, F. Meilleur et al., *J. Am. Chem. Soc.* **2001**, *123*, 7113–7117.
60 F. Ban, J. W. Gauld, R. J. Boyd, *J. Phys. Chem. A* **2000**, *104*, 8583–8592.
61 F. Ban, J. W. Gauld, R. J. Boyd, *J. Phys. Chem. A* **2000**, *104*, 5080–5086.
62 M. D'Amore, R. Improta, V. Barone, *J. Phys. Chem. A* **2003**, *107*, 6264–6269.
63 V. Gomzi, J. N. Herak, *THEOCHEM* **2003**, *629*, 71–76.
64 R. Improta, A. di Matteo, V. Barone, *Theor Chem Acc* **2000**, *104*, 273–279.
65 E. Langella, R. Improta, V. Barone, *J. Am. Chem. Soc.* **2002**, *124*, 11531–11540.
66 M. Langgard, J. Spanget-Larsen, *THEOCHEM* **1998**, *431*, 173–180.
67 S. Weber, G. Richter, E. Schleicher et al., *Biophys. J.* **2001**, *81*, 1195–1204.
68 M. Brustolon, V. Chis, A. L. Maniero et al., *J. Phys. Chem. A* **1997**, *101*, 4887–4892.
69 A. Sanderud, E. Sagstuen, *J. Phys. Chem. B* **1998**, *102*, 9353–9361.
70 P. Neta, R. W. Fessenden, *J. Phys. Chem. 75*, 738–748.
71 P. J. O'Malley, S. J. Collins, *J. Am. Chem. Soc.* **2001**, *123*, 11042–11046.
72 S. Sinnecker, W. Koch, W. Lubitz, *Phys. Chem. Chem. Phys.* **2000**, *2*, 4772–4778.
73 P. J. O'Malley, *J. Am. Chem. Soc.* **2000**, *122*, 7798–7801.
74 S. Sinnecker, W. Koch, W. Lubitz, *J. Phys. Chem. B* **2002**, *106*, 5281–5288.
75 P. J. O'Malley, *J. Comp. Chem.* **1999**, *20*, 1292–1298.
76 P. J. O'Malley, *J. Am. Chem. Soc.* **1999**, *121*, 3185–3192.
77 P. J. O'Malley, *Chem. Phys. Lett.* **2000**, *325*, 69–72.

36
Applications to EPR in Bioinorganic Chemistry

Frank Neese

36.1
Introduction

Transition metal ions are essential for all forms of life. They are found in the active sites of metalloproteins which constitute about 40% of all known enzymes. Many of these active sites feature ions in open-shell situations. Consequently the array of experimental techniques that probe the paramagnetic properties of the active sites (EPR, ENDOR, ESEEM, MCD and Mössbauer spectroscopy) are among the most frequently used in the study of these proteins. These techniques yield the ground state spin-Hamiltonian (SH) parameters of the active sites that must subsequently be interpreted in order to obtain reliable molecular level information. This process may be significantly facilitated by combining the experimental studies with results from quantum chemical calculations of spectral parameters that are the subject of this book. However, while the number of studies that report calculations of SH parameters for radicals of biological significance is substantial and rapidly growing, the number of studies that attempt the calculation of SH parameters of biological transition metal active sites is limited. We will give a brief summary of calculations that have been done on actual enzyme active sites, model complexes thereof and some molecules that have served to calibrate theoretical approaches (for other reviews see Refs. [1, 2]).

A few (perhaps too) general statements about the reliability of the various theoretical approaches appear appropriate: in general high level ab initio methods with large basis sets that take account of static and dynamic correlation are the most reliable but most of them are not yet applicable to large paramagnetic transition metal complexes (see Chapter 33 by Lushington). The Hartree–Fock method itself is significantly inferior to DFT approaches for all EPR properties. Modern DFT methods (hybrid and GGA functionals) combined with basis sets of at least double-zeta plus polarization quality give relatively reliable results (within ~10% of experiment) for a range of properties including quadrupole couplings and ligand hyperfine couplings. Quantitative accuracy for metal hyperfine couplings and *g*-tensors has not yet been achieved with these methods and errors of a factor of ~2 are not uncommon (see Chapters 32 by Patchkovskii and Schreckenbach and 29 by Munzarová). Older DFT methods such as the X_α-scattered wave (X_α-SW) formalism suffer from the severe

Calculation of NMR and EPR Parameters. Theory and Applications.
Edited by Martin Kaupp, Michael Bühl, Vladimir G. Malkin
Copyright © 2004 WILEY-VCH Verlag GmbH & Co. KGaA, Weinheim
ISBN: 3-527-30779-6

approximations made in the muffin tin potential and need extensive semiempirical adjustments in order to achieve agreement with experiment. The only semiempirical method that has been successfully applied to open shell transition metal spectroscopy is the INDO/S method. It typically gives results for *g*-tensors in transition metal complexes that are as good or better than DFT values. It is presently the only alternative to ligand-field theory (LFT) in approaching the zero-field-splitting (ZFS) of transition metal complexes. The method appears to predict the sign of the ZFS correctly in most cases and the magnitude typically within a factor of ~2. Hyperfine couplings predicted by INDO/S are restricted to ligand nuclei and are, at most, of qualitative significance. Furthermore the semiempirical approaches typically show a larger scatter than first principles methods due to the crude approximation made and the minimal valence basis sets assumed (see also Chapter 34 by Neese). They are nevertheless several orders of magnitude faster than ab initio or DFT methods. Approaches of the extended Hückel type are only of historical value.

36.2 Biological Metal Sites

36.2.1 Iron

36.2.1.1 Iron–Sulfur Sites

Iron–sulfur sites are ubiquitous in biology and are mainly involved in transferring electrons. They exist in mononuclear centers of the rubredoxin type with $[Fe(S_{Cys})_4]^{1-,2-}$ coordination and in higher nuclearity clusters with bridging sulfido ions of the type $[Fe_2S_2]^{2+,1+}$, $[Fe_3S_4]^{1+,0}$, $[Fe_4S_4]^{3+,2+,1+}$. Most of the common oxidation states can be probed with EPR which provides invaluable information [3, 4]. Computationally, the paramagnetic properties of the oxidized rubredoxin site were perhaps first studied by Loew with the iterative extended Hückel method [5]. Since the method already included spin–orbit coupling (SOC) between the sextet ground state and the ligand field excited quartet and doublet states, a correct interpretation of the zero-field splitting (ZFS), the effective *g*-values and the magnetic moment was possible [5]. Much more recently the paramagnetically shifted NMR signals (proportional to the Fermi contact interaction) of the same system were studied by hybrid density functional theory (DFT) employing a large 104 atom model and the 6-311G** basis set [6] (for a general discussion about paramagnetic NMR see Chapter 20 by Moon and Patchkovskii). Fairly good agreement with experiment was obtained, the slope of the correlation line being 0.93–0.96 for protons and 0.85–0.94 for ^{15}N nuclei. Partial geometry optimization improved the agreement with experiment [6]. Pioneering work on the interpretation of the ZFS in the reduced and oxidized active sites in terms of anisotropic covalency and geometric distortion (see Chapter 34 by Neese) was done by Solomon and co-workers [7–9] and used a combination of experiment and adjusted X_α-SW calculations. The reduced site in rubredoxin was recently studied in detail with DFT methods and in conjunction with ligand field arguments by

Vrajmasu et al. [10]. The authors estimated the relative contributions to the ZFS parameter (see Chapter 34 by Neese) to be: 51% from the spin quintets, 42% from the spin triplets and 7% from the direct spin–spin interaction. The importance of the S–C–Fe torsion angles for the paramagnetic properties of the reduced active site was stressed [10].

The DFT analysis of higher nuclearity clusters was pioneered by Noodleman in the early 1980s [11–16] using the broken symmetry (BS) methodology [17] to overcome the restrictions of a mono-determinantal approach in DFT. Using the methodology of Geurts et al. [18], Noodleman already provided DFT predictions for the antiferromagnetically coupled $[Fe_2S_2]^{1+}$ core with $S_t = 1/2$[1)] and was able to rationalize many of the experimental findings [11]. This work was later continued by Mouesca, Noodleman and co-workers who interpreted the hyperfine properties of the higher nuclearity clusters on the basis of BS-DFT results and in combination with high-resolution spectroscopic data [19–24].

36.2.1.2 Hemoproteins

The second ubiquitous form of iron in nature is in the active sites of hemoproteins. While these systems have been extensively studied with quantum chemical methods for at least four decades, high level calculations of magnetic resonance properties have only emerged more recently. The *g*-tensor of low-spin ferric hemes has been used for a long time to extract crystal field parameters in terms of a ligand field model (for reviews see Refs. [2, 25]). The computational challenge in predicting the *g*-tensor with quantum chemistry is the near orbital degeneracy of the low-symmetry split $^2T_{2g}$ ground term which makes perturbational approaches unstable. The method of choice is therefore to include the SOC variationally and extract the *g*-tensor with first order perturbation theory with respect to the Zeeman interaction. This approach has been taken by van Lenthe et al. [26] who arrived at promising results with the relativistic two component ZORA method and the BP86 functional [27].

Another "trademark" EPR signal arises from the binding of the NO radical to low-spin Fe^{II} hemes, which gives rise to a characteristic rhombic EPR signal with observed nitrogen hyperfine structure in the g_{mid} region [25]. This signal has been widely used to probe ferrous active sites in hemoproteins but the interpretation has always been difficult. A recent detailed study by Patchkovskii and Ziegler used double perturbation theory to study the *g*-tensor of these nitrosyl porphyrins [28]. The quantitative agreement with experiment was not entirely satisfactory but the orientation of the *g*-tensor was in agreement with the experimental findings and overall the calculations gave much insight into the EPR properties of nitrosyl porphyrins. A second paper by the same authors dealt with d^1 metal porphyrins [29]. The paramagnetically shifted NMR signals of hemoproteins have recently been studied by Oldfield and co-workers with DFT methods [30].

1) S_t is used throughout this chapter to denote the total ground state electronic spin quantum number as opposed to site-spins in spin-coupled systems.

36.2.1.3 Non-Heme Iron

A large class of iron proteins contains mono or dinuclear iron sites which perform a wide variety of chemical reactions [31]. Since the ligands to these sites are typically of the weak-field type, the majority of these sites exist in high-spin states ($S_t = 5/2$ for Fe(III) and $S_t = 2$ for Fe(II)). Thus, the main EPR property of interest in these systems is the ZFS. Using the INDO/S-CI methodology described in Chapter 34 [32], a variety of these sites were recently studied in combination with MCD spectroscopy [33–36]. The combination of ZFS calculations with variable-temperature, variable-field (VTVH) MCD measurements allows the polarization of the observed electronic transitions to be determined from randomly oriented molecules in frozen solutions [37]. This ultimately leads to a high-resolution, experimentally calibrated binding picture of the active sites. The first application was to the model system $[Fe(EDTA)(O_2)]^{3-}$ where the methodology gave insight into the nature of the side-on $Fe^{III}–O_2^{2-}$ bond and its covalency [34]. An enzyme study along these lines was reported for the active site of 3,4-protocatechoate dioxygenase (3,4 PCD) where the anisotropic covalency of two coordinating tyrosine residues and their relation to catalysis was the focus of interest [36]. More recently, Brunold and co-workers have used the same methodology with good success. In a study of manganese and iron-superoxide dismutases (MnSOD and FeSOD) the combined approach led to insight into the nature of active site protonation/deprotonation events which turned out to arise in the second coordination sphere and to be crucial for catalysis [33]. A second study addressed the binding of the substrate-analogue azide to the active site of FeSOD and could resolve some puzzling old observations that turned out to be related to the coordinative flexibility of the coordinating azide ion [38]. A third study was related to NO binding to FeSOD. In this case a $S_t = 3/2$ $\{FeNO\}^7$ site is formed (the superscript seven refers to the number of metal d plus NO-π^* electrons). Again, the calculations provided insight into the origin of the two different species observed in the experiments which, according to the analysis, differ by the FeNO bond angle [39]. In addition, the INDO/S-CI calculations were able to correctly predict the complicated ordering of multideterminantal spin states and confirmed the broken-symmetry DFT prediction [40] of antiferromagnetic coupling between a high-spin Fe^{III} ($S_{Fe} = 5/2$) and an NO^- ($S_{NO} = 1$) to give the observed $S_t = 3/2$ [39].

Low-spin iron-ions exist in a few non-heme iron sites. Most notably, the anticancer drug bleomycin features a unique ligand field which involves modified histidine and pyrimidine residues. The EPR *g*-tensor and the ^{17}O hyperfine coupling (HFC) in 'activated bleomycin' (ABLM, a low-spin $Fe^{III}–^{-}OOH$ complex) together with optical and Mössbauer spectra were studied using the INDO/S-CI methodology [35]. The importance of third order corrections for the *g*-values of low-spin ferric sites was pointed out. The crucial intra-$^2T_{2g}$ transitions were experimentally observed for the first time and validated the popular ligand field model for the *g*-tensor arising from the $^2T_{2g}$ configuration. However, even in this orbitally almost degenerate case the multiplets arising from $t_{2g} \rightarrow e_g$ excitations play a non-negligible role for the *g*-shift [35].

Low-spin ferrous nitrosyls with $S_t = 1/2$ are not restricted to porpyhyrins but also occur in model systems with suitable ligands. The EPR properties of the complexes

$[M(CN)_5(NO)]^{3-}$ (M = Fe, Ru, Os) were calculated with the two-component ZORA method [41]. A second study addressed the question of iron valencies in the series $[Fe(CN)_5(NO)]^{2-,3-,4-}$ and concluded that the redox steps are mainly ligand centered [42]. Another study addressed the question of bonding and EPR properties of iron nitrosyls in the complexes $[Fe(pyS_4)(NO)]^{0,+1}$ [43]. The conclusion was reached, again, that the reduction is essentially ligand centered and that the EPR properties are best interpreted in terms of backbonding between a central low-spin Fe^{II} and a neutral $NO^{\bullet}$ ligand. EPR parameters calculated with coupled perturbed Kohn–Sham theory and the BP86 and B3LYP functionals successfully reproduced the experimental data and supported this interpretation [43].

36.2.2 Copper

36.2.2.1 Blue Copper Sites

The mononuclear blue copper site in small electron transfer proteins like plastocyanin and azurin became a trademark of bioinorganic chemistry and many original concepts have been worked out by studying these centers. The copper ion is situated in a distorted tetrahedral environment with two 'normal' Cu–His bonds and an extremely short $Cu–S_{cys}$ bond in an almost trigonal arrangement, as well as a methionine at much larger distances. The first correct interpretation of the electronic structure, EPR properties and optical spectra of the species was provided in the work of Solomon and co-workers [44–52]. At the time, the scattered-wave X_α method was used to study the spectroscopic properties of the site. EPR *g*-values, second-order HFCs as well as absorption and MCD spectra were calculated by diagonalizing a simplified SOC operator in the basis of $S_t = 1/2$ configurations formed from the X_α-SW orbitals [45, 48]. After adjusting the atomic sphere sizes to compensate for the tendency of DFT methods to produce too covalent bonding (which was perhaps realized for the first time in this work), fairly good agreement with experiment was obtained. The results showed that the blue copper site features an extremely covalent $Cu–S_{cys}$ bond with only ~38% copper 3d-character in the singly-occupied MO in the ground state [45, 48]. The present consensus appears to be that the tendency for overly covalent bonds in DFT is an artifact caused by the self-interaction error in present day DFT functionals, most importantly in the exchange part (e.g. Ref. [53]). Numerous theoretical studies were reported for the blue-copper site but few have directly calculated EPR parameters. An exception is the work of van Gastel et al. who used a multireference CI (MR-CI) method and successfully predicted *g*-values and nitrogen HFCs of the blue-copper site [54]. The INDO/S method was also used in combination with a spin–orbit coupled CI implementation for the prediction of the *g*-values [55]. A complete study of the proton and nitrogen couplings in blue copper centers based on the hybrid B1LYP functional was reported and showed reasonable agreement with experiment for most couplings but with a tendency to overestimate dipolar HFCs [56].

36.2.2.2 Cu_A

The Cu_A site is a fascinating mixed-valence system that features two copper ions of formal valence $Cu^{1.5}$ which are bridged by two cysteine thiolates and are capped by two histidine nitrogens and two weaker coordinating ligands at longer distances. This arrangement gives rise to the complete delocalization of the single unpaired electron over both coppers and the thiolate sulfurs, as becomes evident in a seven line hyperfine pattern in the EPR spectra of Cu_A centers [57, 58]. The site was extensively studied with advanced EPR methods as well as electronic structure calculations. A combination of INDO/S-CI and BP86 DFT calculations was used to successfully interpret the EPR *g*-tensor, hyperfine couplings and optical spectra of Cu_A [57–59]. A significant number of theoretical studies using DFT methods have later been performed on Cu_A but no other calculations of EPR parameters have been reported to date.

36.2.2.3 Model Complexes

The EPR properties of the Cu^{II} ion have been studied fairly extensively in different Werner-type coordination environments with quantum chemical methods. In all of these studies it became evident that the Cu^{II} ion, despite its formally simple d^9 electron configuration is a difficult case. On top of the increasing importance of SOC and scalar relativistic effects as well as the large dynamic correlation in the 'crowded' metal d-shell, an important point is that the singly occupied MO is strongly σ-antibonding with the ligands and thus, any shortcoming of the theoretical method in the description of the metal–ligand covalency shows up directly as a significant error in the calculated properties. Thus, Hartree–Fock based methods have a rather strong bias towards too ionic bonding while DFT methods tend to give exaggerated covalencies [60, 61]. In particular, *g*-value predictions with DFT methods have been particularly difficult and large errors have been observed for the g_{max} shift in all studies [62, 63]. These were attributed to both, exaggerated metal–ligand covalencies and too large d–d- excitation energies in Ref. [64]. Although not in a biological context, the work of Pierloot et al. should be mentioned; this demonstrated that fairly good *g*-value predictions can be obtained under some simplifying assumptions with a sum-over-states-like CASPT2 method [65]. In addition, the INDO/S-MR-CI method was fairly successful in predicting the *g*-values of a series of model complexes, thus lending credence to the bonding descriptions derived from these simple calculations [66]. It is well known since the first days of ligand field theory that ^{63,65}Cu HFCs contain large contributions from the Fermi contact term, the spin-dipolar contribution and the SOC, which makes their prediction very challenging. Reasonable results have been recently obtained with a coupled-perturbed Kohn–Sham procedure and hybrid functionals but the good agreement was argued to be partially fortuitous due to partial cancellation of large errors [67]. Ligand-HFCs in Cu^{II} complexes have also been studied in some detail with DFT methods, with the result that the overall agreement between theory and experiment is fairly good [68]. However, there is a systematic overestimation of the spin-dipolar contribution which was attributed to an underestimation of the valence-shell spin-polarization [68]. In this context hybrid functionals perform better than GGA functionals and the effect of SOC was

found to be negligible [68]. A recent DFT study by Deeth on the EPR parameters of $[Cu(dien)_2]^{2+}$ noted the same shortcomings of too-low *g*-values and too-high d–d excitation energies and tried to overcome these effects by using a modified nuclear charge of 28.2 on the copper center, thus making it less electron attracting [69]. A similar approach has been taken in the thesis work by Swart which discusses, in detail, DFT calculations on copper protein active sites and model complexes including their EPR properties on the basis of scalar relativistic and spin–orbit corrected ZORA calculations in conjunction with a variety of non-hybrid functionals [70].

36.2.3 Manganese

Very few first principles quantum chemical results are available for the EPR parameters of biologically relevant manganese centers. Most recently, a DFT study [71] addressed the *g*-values, Mn-HFCs and quadrupole couplings as well as ligand HFCs in a dimeric $Mn^{III}Mn^{IV}$ complex for which high-quality experimental data are available [72]. In the theoretical work, a BS-DFT methodology was worked out which allowed the prediction of the *g*-tensor of the spin-coupled system. Reasonable agreement was found for all magnetic properties with the B3LYP DFT method except for the ^{55}Mn-HFC which, as expected from the work of Munzarová and Kaupp [73], came out significantly too small in magnitude [71]. Still, the trends predicted by the DFT calculations were correct and a scaling factor of 1.5 was proposed by comparison with the results on mononuclear manganese complexes [71]. On the semiempirical side the study of Jackson et al. used the INDO/S-CI methodology to successfully calculate the ZFS in MnSOD in the trivalent state [33].

36.2.4 Nickel

36.2.4.1 Model Complexes

A number of DFT studies are available that discuss the EPR properties of Ni in model complexes which are related to the active site of NiFe-hydrogenases. Results are available for hyperfine couplings and the *g*-values in $[Ni(mnt)_2]^-$ with the two component and scalar relativistic ZORA methods together with the BP86 functional by Stein et al. [74] and Stadler et al. [75] as well as with coupled perturbed Kohn–Sham methodology in conjunction with the BP86 and B3LYP functionals [64, 67]. Both sets of calculations lead to reasonable results but with the B3LYP results being overall the most accurate for *g*-values, ^{61}Ni-HFCs and ligand HFCs. In addition the ligand HFCs in this system where studied with the B3LYP method by Hayes [76]. An interesting set of Ni-dithiolene complexes were studied successfully with the two component ZORA method and the BP86 functional by Formitchev et al. [77]. Most recently, Craft et al. reported a spectroscopic and combined INDO/S-CI and DFT theoretical study on a model complex for the Acetyl–CoA Syntase active site with emphasis on Ni^I–CO bonding [78].

36.2.4.2 Nickel–Iron Hydrogenase

NiFe hydrogenase is a fascinating enzyme which catalyzes the reversible splitting of the H–H bond in H_2 to $2H^+$ and $2e^-$. Several paramagnetic intermediates exist in the reaction cycle of this enzyme and have been extensively probed with high-level EPR spectroscopy on single crystals of the enzyme [74, 75, 79–88]. A substantial number of DFT studies have been reported for this enzyme. However, only two groups reported the detailed calculation of magnetic resonance parameters at the two component and scalar relativistic ZORA/BP86 levels [82–87]. The complicated details of these studies are outside the scope of this review and the reader is referred to a recent review [87]. It appears that a full consensus about the individual structures and reaction steps has not yet been reached and therefore the mechanism of NiFe hydrogenases will remain a challenging target for theoretical studies. The importance of obtaining simultaneous agreement with all available experimental data at a consistent level of theory and the judgment of the computational data with respect to the known systematic deficiencies of methods used can hardly be overemphasized.

36.2.5 Vanadium

Vanadium occurs in a number of enzymes, perhaps most prominently in alternative nitrogenases. However, no high-level studies on the EPR properties of enzyme active sites appear to have been published. A number of DFT results are available from model and calibration studies. Munzarová and Kaupp have studied the EPR properties of Schiff-base complexes of $(VO)^{2+}$ in detail with DFT methods. The emphasis was on the validation of the methodology and the interpretation of the changes that occur in the EPR spectra with respect to structural distortions away from a regular square pyramid [89]. The dependence of nitrogen HFCs on the orientation of imidazole ligands to vanadyl complexes has been studied for the prototypical complex $[VO(H_2O)_4(\text{imidazole})]^{2+}$ with the scalar relativistic ZORA methodology and good qualitative agreement with the experimentally deduced orientation dependence has been found [90]. Fairly good results for quadrupole couplings of $(VO)^{2+}$-containing systems as predicted by the B3LYP functional were reported [91]. A ^{51}V solid state NMR study on V(V) complexes mimicking the active sites of haloperoxidases together with DFT calculations at the B3LYP level gave good agreement with experiment for the ^{51}V quadrupole interaction and magnetic shielding anisotropy [92]. The complex $[VO(H_2O)_5]^{2+}$ has received some attention and results of two component and scalar relativistic ZORA/BP86 calculations [93] as well as BP86 and B3LYP coupled-perturbed Kohn–Sham calculations are available [67].

36.2.6 Molybdenum

Despite its biological importance few first principles studies on the EPR parameters of Mo^V have been reported. Westmoreland and co-workers used DFT calculations

together with ligand field arguments and single-crystal EPR to discuss *g*-values, ^{95,97}Mo-HFCs as well as metal-ligand covalencies in some Mo^{V} species [94]. Two conference reports have appeared; the prediction of *g*-values of some larger Mo^{V} species with modern DFT methods by Patchkovskii and Ziegler [95] and a calibration study of EPR properties of Mo^{V} species by Fritscher et al. [96]. In both cases the agreement achieved with experiment was qualitative. Peng et al. successfully used the INDO/S-CI methodology to compute the *g*-tensors of a series of Mo^{V} model complexes [97]. Most recently, a combination of single-crystal EPR and INDO/S-CI calculations showed, despite the lack of molecular symmetry, very good agreement with experiment for the principal values and the orientation of the *g*-tensor in some model complexes for the sulfite oxidase active site [98].

36.3 Concluding Remark

The transition metal sites occurring in metalloproteins are a vast playground for theoretical methods aimed at predicting EPR properties. Using these methods important contributions to the understanding of the structure and function of active sites can be made. It has probably become evident in this short review that the amount of work that has been done is still limited. However, given the ready availability of efficient and user-friendly program packages it appears safe to predict that a rapid increase in the number of publications that use quantum chemical calculations in conjunction with EPR spectroscopy will occur in the near future.

Acknowledgement

Our research on spin-Hamilton parameters is supported by the Deutsche Forschungsgemeinschaft within the priority program 'Molecular Magnetism' which is gratefully acknowledged.

References

1 F. Neese, *Curr. Opin. Chem. Biol.* **2003**, *7*, 125.
2 F. Neese, E. I. Solomon, in *Magnetism: Molecules to Materials IV*, eds. J. S. Miller, M. Drillon, Wiley-VCH, Weinheim **2003**, p. 345.
3 W. R. Hagen, *Adv. Inorg. Chem.* **1992**, *38*, 165.
4 B. Guigliarelli, P. Bertrand, *Adv. Inorg. Chem.* **1999**, *47*, 421.
5 G. H. Loew, M. Chadwick, D. Lo, *Theor. Chim. Acta.* **1974**, *33*, 147.
6 S. J. Wilkens, B. Xia, F. Weinhold et al. *J. Am. Chem. Soc.* **1998**, *120*, 4806.
7 J. C. Deaton, M. S. Gebhard, S. A. Koch et al., *J. Am. Chem. Soc.* **1988**, *110*, 6241.
8 J. C. Deaton, M. S. Gebhard, E. I. Solomon, *Inorg. Chem.* **1989**, *28*, 877.
9 M. S. Gebhard, J. C. Deaton, S. A. Koch et al. *J. Am. Chem. Soc.* **1990**, *112*, 2217.
10 V. V. Vrjamasu, E. L. Bominaar, J. Meyer et al., *Inorg. Chem.* **2002**, *41*, 6358.
11 L. Noodleman, E. J. Baerends, *J. Am. Chem. Soc.* **1984**, *106*, 2316.
12 L. Noodleman, J. G. Norman, J. H. Osborne et al., *J. Am. Chem. Soc.* **1985**, *107*, 3418.
13 L. Noodleman, E. R. Davidson, *Chem. Phys.* **1986**, *109*, 131.

14 L. Noodleman, D. A. Case, A. Aizman, *J. Am. Chem. Soc.* **1988**, *110*, 1001.
15 L. Noodleman, C. Y. Peng, D. A. Case et al., *Coord. Chem. Rev.* **1995**, *144*, 199.
16 L. Noodleman, D. A. Case, J. M. Mouesca et al., *J. Biol. Inorg. Chem.* **1996**, *1*, 177.
17 L. Noodleman, *J. Chem. Phys.* **1981**, *74*, 5737.
18 P. J. M. Geurts, P. C. P. Bouten, A. van der Avoird, *J. Chem. Phys.* **1980**, *73*, 1306.
19 L. LePape, B. Lamotte, J. M. Mouesca et al., *J. Am. Chem. Soc.* **1997**, *119*, 9757.
20 L. LePape, B. Lamotte, J. M. Mouesca et al., *J. Am. Chem. Soc.* **1997**, *119*, 9771.
21 J. M. Mouesca, G. Rius, B. Lamotte, *J. Am. Chem. Soc.* **1993**, *115*, 4714.
22 J. M. Mouesca, L. Noodleman, D. A. Case, *Inorg. Chem.* **1994**, *33*, 4819.
23 J. M. Mouesca, L. Noodleman, D. A. Case, *Int. J. Quant. Chem.* **1995**, 95.
24 J. M. Mouesca, L. Noodleman, D. A. Case et al., *Inorg. Chem.* **1995**, *34*, 4347.
25 G. Palmer, in *The Porphyrins. Vol. 2,* eds. A. B. P. Lever, H. B. Gray, Addison-Wesley, London **1983**, p. 43.
26 E. van Lenthe, A. van der Avoird, W. R. Hagen et al., *J. Phys. Chem. A* **2000**, *104*, 2070.
27 E. van Lenthe, J. G. Snijders, E. J. Baerends, *J. Chem. Phys.* **1996**, *105*, 6505.
28 S. Patchkovskii, T. Ziegler, *Inorg. Chem.* **2000**, *39*, 5354.
29 S. Patchkovskii, T. Ziegler, *J. Am. Chem. Soc.* **2000**, *122*, 3506.
30 J. H. Mao, Y. Zhang, E. Oldfield, *J. Am. Chem. Soc.* **2002**, *124*, 13911.
31 E. I. Solomon, T. C. Brunold, M. I. Davis et al., *Chem. Rev.* **2000**, *100*, 235.
32 F. Neese, E. I. Solomon, *Inorg. Chem.* **1998**, *37*, 6568.
33 T. A. Jackson, J. Xie, E. Yikilmaz et al., *J. Am. Chem. Soc.* **2002**, *124*, 10833.
34 F. Neese, E. I. Solomon, *J. Am. Chem. Soc.* **1998**, *120*, 12829.
35 F. Neese, J. M. Zaleski, K. L. Zaleski et al., *J. Am. Chem. Soc.* **2000**, *122*, 11703.
36 M. I. Davis, A. M. Orville, F. Neese et al., *J. Am. Chem. Soc.* **2002**, *124*, 602.
37 F. Neese, E. I. Solomon, *Inorg. Chem.* **1999**, *38*, 1847.
38 J. Xie, E. Yikilmaz, A. F. Miller et al., *J. Am. Chem. Soc.* **2002**, *124*, 3769.
39 T. A. Jackson, E. Yikilmaz, A.-F. Miller et al., *J. Am. Chem. Soc.* **2003**, *125*, 8348.
40 C. A. Brown, M. A. Pavlosky, T. E. Westre et al., *J. Am. Chem. Soc.* **1995**, *117*, 715.
41 M. Wanner, T. Scheiring, W. Kaim et al., *Inorg. Chem.* **2001**, *40*, 5704.
42 M. Lebrero, D. Scherlis, G. Estiu et al., *Inorg. Chem.* **2001**, *40*, 4127.
43 M. Li, D. Bonnet, E. Bill et al., *Inorg. Chem.* **2002**, *41*, 3444.
44 A. A. Gewirth, S. L. Cohen, H. J. Schugar et al., *Inorg. Chem.* **1987**, *26*, 1133.
45 A. A. Gewirth, E. I. Solomon, *J. Am. Chem. Soc* **1988**, *110*, 3811.
46 L. B. LaCroix, S. E. Shadle, Y. Wang et al., *J Am. Chem. Soc.* **1996**, *118*, 7755.
47 K. W. Penfield, R. R. Gay, R. S. Himmelwright et al., *J. Am. Chem. Soc.* **1981**, *103*, 4382.
48 K. W. Penfield, A. A. Gewirth, E. I. Solomon, *J. Am. Chem. Soc.* **1985**, *107*, 4519.
49 S. E. Shadle, J. E. Penner-Hahn, H. J. Schugar et al., *J. Am. Chem. Soc.* **1993**, *115*, 767.
50 E. I. Solomon, A. A. Gewirth, T. D. Westmoreland, in *Advanced EPR. Applications in Biology and Biochemistry.* ed. A. J. Hoff, Elsevier, Amsterdam **1989**, p. 865.
51 E. I. Solomon, M. J. Baldwin, M. D. Lowery, *Chem. Rev.* **1992**, *92*, 521.
52 E. I. Solomon, M. D. Lowery, in *The Chemistry of Copper and Zinc Triads,* eds. A. J. Welch, S. K. Chapman, Royal Society of Chemistry, Cambridge **1993**, p. 12.
53 S. Patchkovskii, J. Autschbach, T. Ziegler, *J. Chem. Phys.* **2001**, *115*, 26.
54 M. van Gastel, J. W. A. Coremans, H. Sommerdijk et al., *J. Am. Chem. Soc.* **2002**, *124*, 2035.
55 F. Neese, Ph.D. Thesis, Universität Konstanz (Konstanz), **1997**.
56 A. R. Jaszewski, J. Jezierska, *Chem. Phys. Lett.* **2001**, *343*, 571.
57 F. Neese, W. G. Zumft, W. E. Antholine et al., *J. Am. Chem. Soc.* **1996**, *118*, 8692.
58 F. Neese, R. Kappl, J. Huttermann et al., *J. Biol. Inorg. Chem.* **1998**, *3*, 53.
59 J. Farrar, F. Neese, P. Lappalainen et al., *J. Am. Chem. Soc.* **1996**, *118*, 11501.
60 E. I. Solomon, M. J. Baldwin, M. D. Lowery, *Chem. Rev.* **1992**, *92*, 521.
61 R. Szylagi, E. I. Solomon, *J. Phys. Chem. A,* **2001**, *106*, 2994.
62 O. L. Malkina, J. Vaara, B. Schimmelpfenning et al., *J. Am. Chem. Soc.* **2000**, *122*, 9206.
63 F. Neese, *J. Chem. Phys.* **2001**, *115*, 11080.

64 F. Neese, *J. Inorg. Biochem.* **2001**, *86*, 357.
65 K. Pierloot, A. Delabie, M. H. Groothaert et al., *Phys .Chem. Chem. Phys.* **2001**, *3*, 2174.
66 F. Neese, *Int. J. Quantum Chem.* **2001**, *83*, 104.
67 F. Neese, *J. Chem. Phys.* **2003**, *118*, 3939.
68 F. Neese, *J. Phys. Chem. A* **2001**, *105*, 4290.
69 R. J. Deeth, *J. Chem. Soc. Dalton* **2001**, 664.
70 M. Swart, Ph.D. Thesis, Rijksuniversiteit Groningen (Groningen), **2002**. http://www.scm.com/Doc/publist.html
71 S. Sinnecker, F. Neese, L. Noodleman et al., *J. Am. Chem. Soc.* **2004**, in press.
72 K. O. Schäfer, R. Bittl, F. Lendzian et al., *J. Phys. Chem. B* **2003**, *107*, 1242.
73 M. Munzarová, M. Kaupp, *J. Phys. Chem. A* **1999**, *103*, 9966.
74 M. Stein, E. van Lenthe, E. J. Baerends et al., *J. Phys. Chem. A* **2001**, *105*, 416.
75 C. Stadler, A. L. de Lacey, B. Hernandez et al., *Inorg. Chem.* **2002**, *41*, 4417.
76 R. G. Hayes, *Inorg. Chem.* **2000**, *39*, 156.
77 D. V. Fomitchev, B. S. Lim, R. H. Holm, *Inorg. Chem.* **2001**, *40*, 645.
78 J. L. Craft, B. S. Mandinutsira, K. Fujita et al., *Inorg. Chem.* **2003**, *42*, 859.
79 W. Lubitz, M. Stein, M. Brecht et al., *Biophys. J.* **2000**, *78*, 1660.
80 O. Trofanchuk, M. Stein, C. Gessner et al., *J. Biol. Inorg. Chem.* **2000**, *5*, 36.
81 W. Lubitz, M. Stein, M. Brecht et al., *Biophys. J.* **2000**, *78*, 1660.
82 M. Stein, W. Lubitz, *Phys .Chem. Chem. Phys.* **2001**, *3*, 5115.
83 M. Stein, W. Lubitz, *J. Inorg. Biochem.* **2001**, *86*, 442.
84 M. Stein, W. Lubitz, *Phys .Chem. Chem. Phys.* **2001**, *3*, 2668.
85 M. Stein, E. van Lenthe, E. J. Baerends et al., *J. Am. Chem. Soc.* **2001**, *123*, 5839.
86 C. Stadler, A. L. Lacey, Y. Montet et al., *Inorg. Chem.* **2002**, *41*, 4424.
87 M. Stein, W. Lubitz, *Curr. Opin. Chem. Biol.* **2002**, *6*, 243.
88 S. Foerster, M. Stein, M. Brecht et al., *J. Am. Chem. Soc.* **2003**, *125*, 83.
89 M. L. Munzarová, M. Kaupp, *J. Phys. Chem. B* **2001**, *105*, 12644.
90 A. C. Saladino, S. C. Larsen, *J. Phys. Chem. A* **2002**, *106*, 10444.
91 C. V. Grant, W. Cope, J. A. Ball et al., *J. Phys. Chem. B* **1999**, *103*, 10627.
92 N. Pooransingh, E. Pomerantseva, M. Ebel et al., *Inorg. Chem.* **2003**, *42*, 1256.
93 S. C. Larsen, *J. Phys. Chem. A* **2001**, *105*, 8333.
94 C. Balagopalakrishna, J. T. Kimbrough, T. D. Westmoreland, *Inorg. Chem.* **1996**, *35*, 7758.
95 S. Patchkovskii, T. Ziegler, Canadian Society for Chemistry (Toronto), **1999**.
96 J. Fritscher, T. F. Prisner, M. Kaupp, Abstract for EURBIC 6 (Lund,Sweden), **2002**.
97 G. Peng, J. Nichols, E. A. McCullough et al., *Inorg. Chem.* **1994**, *33*, 2857.
98 M. Mader Cosper, F. Neese, A. V. Astashkin et al., *J. Am. Chem. Soc* **2003**, submitted.

Index

a

absolute shielding scale 13
acetonitrile
– gas-to-liquid change in chemical shift 182
– N chemical shift 185
agostic interactions 423
alkoxides 458
alkyl cations 372 ff
– β-silyl 375
all-electron current reconstruction from pseudopotential calculation 270
allyl cation 389
alternative hyperfine operator 493 ff
AMFI see atomic mean field approximation
amino acid radicals 574 ff
amino acids (zwitterionic radicals of) 573
anharmonicity 155
anisotropy effects 396
anisotropy of spin–spin coupling 259, 261 ff
anomalous Zeeman effect 78
antiaromaticity 148, 394
σ-antiaromaticity 405
apparent surface charge methods 193 ff
ARCS see aromatic ring-current shielding
arenium cations 385 ff
aromaticity 148, 394 ff
– spherical 403
– of transition states 404
– of triplet states 402
σ-aromaticity 405
aromatic ring-current shielding 397
asymmetry parameter 281
atomic charge (correlation of chemical shift with) 293
atomic mean field approximation for spin–orbit coupling 220, 517, 528 ff, 538
atoms-in-molecules approach 321
Au_5Zn^+ cluster 405
average energy approximation 9

b

bacteriochlorophyll radical ions 577 ff
basis set 14, 89
– for calculations of hyperfine coupling 466, 501 ff
– influence on g-tensor 521 ff
basis set superposition error 271
benzene
– ARCS fit for 398
– MO-NICS 399
– NICS grid 396
benzylic cations 388
BH molecule 299 ff
bicyclic carbocations 380 ff
bicyclobutonium ion 382
bioinorganic chemistry, EPR in 581 ff
biomolecules 341
– chemical shift tensor in 345
– spin–spin couplings in 347
Biot-Savart law 85, 142, 397
bleomycin 584
blue copper sites, EPR parameters of 585
body-fixed coordinate system 282 ff
Bohr magneton 311
Boltzmann averaging method 181
Born–Oppenheimer molecular dynamics 176
boron carbide 273
Breit interaction 55, 76
Breit–Pauli Hamiltonian 27, 39, 209 ff, 232
Breit–Pauli level 302
$BrH{:}NH_3$ complex 357
broken symmetry methodology 583
2-butyl cation 375
tert-butyl cation 374

Calculation of NMR and EPR Parameters. Theory and Applications.
Edited by Martin Kaupp, Michael Bühl, Vladimir G. Malkin
Copyright © 2004 WILEY-VCH Verlag GmbH & Co. KGaA, Weinheim
ISBN: 3-527-30779-6

c
C_{36} 418
C_{60}
– ^{13}C shielding tensor 412, 418
– ARCS calculation for 403 ff
– as reference for fullerene chemical shift 411
C_{70} 412
C_{119} 149 ff, 416 ff
C_{121} 417
$C_{122}H_4$ 417
canonical orbitals 91 ff, 94, 297, 314
carbenium ions 458
carbocations
– heteroatom stabilized 391 ff
– μ-hydrogen bridged 379
– in zeolites 390
– NMR parameters of 371 ff
Car–Parrinello molecular dynamics 176
Cartesian matrix 36
CASPT2 see complete active space perturbation theory
cavity solute 180, 192 ff
CCSD see coupled cluster method
centrifugal distortion 161 ff
CH_4 gauge dependence of shielding constants 90
chemical shift 11 ff, 227 ff, 325 ff, 426, 434
– aluminium 453 ff
– close-contact effects on 344
– electric field effects on 343, 356
– heavy-atom 12
– helium 396, 414 ff
– interpretation of 293 ff
– iron 178, 426
– isotropic, definition of 434
– lithium, as aromaticity probe 396
– long-range magnetic susceptibility effects on 342
– mercury 239 ff
– normal halogen dependence of 303
– in nucleic acids 346
– oxygen 453 ff
– polypeptides 345
– proteins 345
– proton 234 ff, 455 ff
– reference samples for 435
– relativistic effects on 422
– semiempirical models 12
– silicon 453 ff
– solvent effect 178
– solvent induced 197 ff
– spin–orbit effect on 12
– tellurium 241
– temperature dependence 181
– transition metal complexes 421 ff
– transition metals 178, 184, 239, 424 ff
– transition metals, correlation with reactivity 426
– transition metals, relativistic effects on 426 ff
– transition metals, thermal and solvent effects on 426
– vanadium 184
– see also spin–orbit chemical shift
chemical shift tensor 423
– anisotropy 436
– antisymmetric contributions 438
– asymmetry 436
– in biomolecules 345
– breadth 436
– for cobalt 425
– compilations of 438
– Maryland convention 436
– orientation 435 ff
– phosphorus 437 ff
– powder pattern 435 ff
– skew 436
– structural dependence 437 ff
ClF ^{19}F shielding 300 ff
$ClH{:}NH_3$ complex 356 ff
cluster approximation 265
cluster method 176, 185
CNDO see complete neglect of differential overlap
complete active space perturbation theory 586
complete neglect of differential overlap 26, 141
computational transition metal chemistry 421
condensed phase calculations 265
configuration interaction method 25, 316
contact shift 325 ff
continuous set of gauge transformations 96, 124, 127, 271
continuum solvent model 180 ff, 191 ff
copper model complexes, EPR parameters of 586
copper protein sites, EPR parameters of 585
core-polarization 521
correction factors, multiplicative, on hyperfine integrals 10
correlation effects 239 ff
Coulomb force 44
Coulomb gauge 46, 52

coupled cluster method 87 ff, 124, 128, 484 ff
– with gauge-including orbital, for chemical shift 133
coupled Hartree–Fock equation 91, 94
– within semiempirical methods 144
coupled perturbed Hartree–Fock method 11, 65, 319, 452 ff
coupled multi-configuration Hartree–Fock method 65
coupling deformation density 321 ff
coupling energy density 320 ff
CPMD see molecular dynamics simulations
$Cr(CO)_3(C_6H_6)$ 400
crystal-field theory 23 ff
– for chemical shift 12
CSGT see continuous set of gauge transformations
Cu_A protein sites, EPR parameters of 586
current density 44, 72, 85 ff, 95, 97, 142, 296, 298, 319
– diamagnetic part 88, 93, 96
– paramagnetic part 88, 96, 298
current density functional theory 97
current density plot 298 ff
cut-off energy of plane wave basis set 271
cycloalkyl cations 372 ff, 378 ff
cyclobutadiene
– MO-NICS 399
– NICS grid 396
cyclobutadienyl dication 385
cyclobutyl cations bridged 382
cyclobutylmethyl cation 377
cyclopentyl cation 377
cyclopropane aromatic shielding 405
cyclopropenium cation 393
cyclopropyl methyl cation 376, 382
cyclopropylvinyl cations 384 ff

d

Dalgarno exchange theorem 65, 76
Darwin term 75, 211
defect structure of boron carbide 273
1,3-dehydroadamantane-5,7-diyl dication 384
delocalization 204
ΔE model 144
delta function operator 493 ff
density functional theory 258 ff, 332 ff, 505 ff
density-functional tight binding method 146 ff
– for chemical shift 146 ff
– with individual gauge for localized orbitals, for chemical shift 142
density matrix 105 ff, 129
deoxyribose model chemical shift anisotropy in 346
DFT see density functional theory
DFTB see density-functional tight binding method
diamagnetic contribution in operators 507
– to energy 70
– to nuclear shielding 231, 252
– see also current density and nuclear shielding
diamagnetic part in semiempirical methods 151
diamagnetic spin–orbit term 102 ff, 212, 307 ff
diamagnetism 66
diazine 200
Diels–Alder reaction (transition state) 404
differential overlap
– neglect of 141, 145
– see also complete neglect, intermediate neglect, and modified neglect of differential overlap
dimethyl sulfoxide 185
Dirac delta function 483 ff
Dirac equation 22, 39, 56, 69 ff
Dirac–Hartree–Fock method 209 ff, 286, 479
Dirac operator 54 ff
– unitary transformation of 71 ff
Dirac vector model 319
– of spin–spin coupling 309 ff
Dirac wavefunction 11
direct perturbation theory 72 ff, 210
disilenes ^{29}Si shifts 301 ff
double bonds anisotropy effects 396
Douglas–Kroll approach 233 ff, 238 ff, 286 ff, 509 ff, 518
Douglas–Kroll–Hess approach see Douglas–Kroll approach
Douglas–Kroll transformation 209 ff
DSO term see diamagnetic spin–orbit term
dynamic nuclear polarization 39

e

effective core potential see pseudopotential
effective geometry 158
effective-Hamiltonian 552 ff
effective potential, one-electron 516
effective spin Hamiltonian 23 ff, 27, 33 ff, 331
effective spin operator 506
EFG see electric field gradient

electric field, external, (effect on spin–spin coupling constants and chemical shift 356 ff
electric field effects on chemical shift 343
electric field gradient 178 ff, 185, 272, 279 ff
– relation to line widths 428
electric field gradient tensor 443 ff
electrodynamic potentials 45
electron correlation 123, 127 ff, 132 ff, 239 ff, 256 ff
– dynamic 127
– for nuclear shielding constant 123 ff
– static 127
electron localization function 321
electron-nuclear double resonance 22, 38
electron spin echo envelope modulation 39
electrostatic effects 266
endohedral fullerenes 414
energy denominator 98
– averaged 144
– for nuclear shieldings 298, 301
– for spin–spin coupling 311
energy level diagrams of spin–spin coupling 309
environmental effects 191
EOM-CCSD see equations of motion coupled cluster method
equations of motion
– Car-Parrinello 176
– Newton 176
equations of motion coupled cluster method 354
escaped charge 192
ethyl cation 373
Euler-Lagrange equations 47
exact exchange 92, 98 ff
exchange-correlation functional 107, 464
– current-dependent terms 97
– influence on g-tensor 521 ff
exchange interaction 25
experimental techniques in EPR, development of 21 ff
extended-Hückel method, relativistic 11, 254

f

F_2 shielding constant 98
FC term see Fermi contact term
Fermi contact interaction 22 ff, 493 ff
Fermi contact operator 213, 327, 493 ff
– kinetic energy correction 215
Fermi contact term 54, 63 ff, 69, 102 ff, 251 ff, 303, 307 ff, 316, 464, 479, 483 ff
– distance dependence 357, 362
ferrierite 274 ff
FH:pyridine complex 368 ff
finite perturbation theory 9, 113, 309, 317
– double 320 ff
– single 313
first-order orbitals 89 ff, 93
first-order property 510 ff
first-order response 129
fluctuation potential 131
fluorine shielding constant 98
force field 158
formyl cation 391
four-component computations 232 ff
four-component formalism 252 ff
four-component methods 255 ff
four-component picture 231
frozen-core method 222
fullerene addition compounds 413 ff
fullerene dimers 416
fullerenes 409 ff
– ^{13}C chemical shift of 147, 149, 409 ff
– endohedral 414
– ^{3}He chemical shift 148
– isomers 412
– NICS values 403, 411
– POAV and ^{13}C NMR 412 ff
– topological analysis of geometries 409 ff

g

Galileo transformation 48
gauge of vector potential 45
gauge correction spin–orbit Zeeman 40
gauge-correction operator 507
gauge dependence 88 ff
– basis set effects 89, 126
gauge-including atomic orbitals 13 ff, 67 ff, 92, 95, 123 ff, 141 ff, 269, 398, 517
– with coupled cluster method, for chemical shift 133
– with local MP2 method, for chemical shift 134
– with MNDO method, for chemical shift 142 ff
– with MP2 method, for chemical shift 133
– with multi-configurational Hartree–Fock method, for chemical shift 133
gauge-including projector augmented wave method 269 ff, 275, 452, 455, 517
gauge invariance 269, 517 ff
gauge origin 53, 66 ff, 86 ff, 218
– distributed 92, 96
gauge term 93
gauge transformation 52 ff, 56, 87, 96, 151

Gaussian-type orbitals GTOs 466
Gaussian-weighted operator 499 ff
geminal spin–spin coupling 316
generalized gradient approximation 107, 110, 114, 465
g-factor quantum-electrodynamic corrections 63
GGA see generalized gradient approximation
GIAO see gauge-including atomic orbitals
GIPAW see gauge-including projector augmented wave method
Gordon decomposition 72
group susceptibility effects on chemical shift 342
g-tensor 24, 28, 37, 203 ff, 275, 330 ff, 505 ff, 533 ff, 581 ff
– ab initio calculation of 28
– with continuum models 201
– basis set effects 521 ff
– density functional calculation of 28 ff
– paramagnetic contributions 514
– solvent effect on 204
guest molecule NMR of 457

h

HAHA effect see heavy-atom effect (on heavy atom)
HALA effect see heavy-atom effect (on light atom)
halomethyl cations 391
Hamiltonian, electronic 326
harmonic oscillator 155
Hartree–Fock method
– restricted, for open shells 484 ff, 537
– unrestricted, for open shells 25 ff, 484 ff
Hartree–Fock orbitals 88
HCS radical hyperfine coupling constant 570
heavy-atom effect 294
– on heavy atom 222, 228 ff, 236 ff, 250
– on light atom 222, 228, 235 ff, 250, 254, 302
Heaviside-weighted operator 498 ff
^{3}He chemical shift in endohedral fullerene compounds 148
hemoproteins, EPR parameters of 583
Hessian electronic 109 ff
highest occupied molecular orbital (HOMO) 205
high-field NMR 443
high field regime 547
Hiller–Sucher–Feinberg HSF) operator 494
HIV-1 protease 184
homoaromatic carbocations 389
Hückel molecular orbital theory 23, 26
Hückel's rule 401
Hund's rule 310
hybrid functionals 92, 98 ff, 465
hydrogen bond 348, 353 ff
– C-H-N hydrogen bond 361 ff
– direction of lone pair 360
– F-H-N hydrogen bond 363 ff
– ion-pair 355
– N-H-N hydrogen bond 357 ff
– proton-shared 355
– spin–spin coupling across 442
hydrogen bonding 201 ff
– effect on chemical shift 345
hydrogen halides 234 ff
hyperconjugation 315, 375, 385
hyperconjugative charge delocalization 373
hyperconjugative effects 204
hyperfine coupling 21, 63 ff, 77, 325, 567, 581 ff
– anisotropic 567
– basis set effects 570 ff
– basis sets for calculation of 466, 501 ff
– in biological systems 568, 574 ff
– cusp condition for 466 ff
– DFT methods 571 ff
– dipolar 464, 483
– effect of vibrational correction 568 ff
– electron correlation effects 570 ff
– environmental effects 572 ff
– error cancellation in DFT calculations of 480, 489
– of first-row atoms 568 ff
– isotropic 25, 27, 464, 483, 567
– isotropic, with continuum models 201
– of main group atoms 467 ff
– matrix effects 474
– organic radicals 469 ff
– P-containing radicals 572
– π-radicals with heteroatoms 470 ff
– S-containing radicals 570, 572
– solvent effect 178
– spin–orbit corrections to 478 ff, 572, 586 ff
– spin–orbit effects on 28
– spin polarization mechanism 467 ff, 476 ff, 484 ff
– structural dependence 474
– transition metal 25
– transition metal complexes 475 ff
hyperfine coupling for cusp condition 466 ff, 498 ff
hyperfine coupling tensor 24, 37 ff, 330 ff, 463 ff, 567 ff

– excitation contributions to 485 ff
– post-Hartree–Fock calculations of 483 ff
hyperfine integrals 252 ff
hyperfine structure 279 ff
Hypervirial theorem 494 ff
HZSM-5 zeolite 458

i
IGAIM see individual gauge for atoms in molecules
IGLO see individual gauge for localized orbitals
individual gauge for atoms in molecules 97, 269, 302
individual gauge for localized orbitals 14, 67 ff, 92 ff, 517
– application to carbocations 371
– density functional calculations 94
– with density-functional tight binding method 142, 146 ff
– multi-configuration Hartree–Fock 94, 124
– orbital decomposition 398
INDO see intermediate neglect of differential overlap
integral-direct techniques 133
interbond bond order 309, 312
intermediate neglect of differential overlap 26, 141, 145
– INDO/S method 559 ff, 582 ff
intermolecular interactions 191
internal coordinates 160
intrinsic quadrupole moment 282 ff
iron-sulfur protein sites, EPR parameters of 582 ff
isopropyl cation 374
isotope effects 159 ff
– on magnetic shielding tensor 13
– on nuclear shielding constants 167
– on spin–spin coupling 170
isotopomer 159 ff

k
Karplus–Fraenkel equation 26
Karplus relation 9, 117, 303, 313 ff
kinetic energy correction to spin Zeeman, Fermi contact, and spin-dipolar hyperfine operators 215
Kirkwood-Onsager model 194
Knight shift see paramagnetic shift
Kohn–Sham energy 107
Kohn–Sham orbitals 88
Kramers doublet 329, 330, 333, 511 ff, 543
Kramers pair see Kramers doublet
Kramers-systems 543
k-vector 267

l
laboratory-system model 284
Lagrangean 46 ff, 50
$\mathcal{A}$-equations 129
Lamb term 67
lanthanide shift reagent 12
LCAO see linear combination of atomic orbitals
LDA see local density approximation
Legendre transformations 47, 50
Levy–Leblond equation 55, 57 ff
ligand field theory 542, 582
ligands of transition metals, chemical shift of 422 ff
linear combination of atomic orbitals 143, 310 ff
linear response theory 88, 108
linear scaling 133
liquid crystal NMR 441
liquids
– magnetic susceptibility in 187
– NMR properties of 175
– spin–spin coupling 187
local correlation methods 133 ff
local density approximation 107, 110, 114, 465
localized molecular orbitals 94
– contributions from 398
localized orbital/local origin second-order 123
Lorentz force 44
Lorentz gauge 46
Lorentz invariance 50
Lorentz transformation 48
LORG see localized orbital/local origin

m
magic angle spinning NMR 441
magnetic field, local 85
magnetic shielding see nuclear shielding
magnetic susceptibility 66, 187
– long range effects on chemical shift 342
magnetic susceptibility tensors 343
magnetizability tensor 60 ff, 65 ff
Malkin correction 99
manganese complexes, EPR parameters of 587
mass-velocity term 75
Maxwell equations 44 ff

mazzite 454
McConnell equation 25 ff, 342
MCSCF see multi-configuration Hartree–Fock method
mean-field model 284
mechanics, classical 50
meta-GGA functionals 465
metalloporphyrins 423, 425 ff
metalloproteins, EPR parameters of 581 ff
methane gauge dependence of shielding constants 90
method 258 ff
minimal coupling 508
MNDO see modified neglect of differential overlap
modified neglect of differential overlap 145
– with gauge-including orbitals, for chemical shift 142
Möbius aromaticity 401 ff
molecular dynamics simulations 164, 175 ff, 198 ff
– Born–Oppenheimer 176
– Car–Parrinello 176
molecular orbital
– canonical 91 ff, 94, 297, 314
– highest occupied 317
– localized 297, 314, 316
– lowest unoccupied 205, 317
Møller–Plesset perturbation theory 124, 128
– local, with gauge-including orbitals, for chemical shift 134
– with gauge-including orbitals, for chemical shift 133
molybdenum complexes, EPR parameters off 588 ff
momentum
– canonical 47
– kinematical 47
Monte Carlo simulations 176
MO theory, qualitative 24
MP2 see Møller–Plesset perturbation theory
multi-configuration Hartree–Fock method 114, 124, 128, 195, 332
– coupled 65
– with gauge-including orbitals for chemical shift 133
– with individual gauge for localized orbitals, for chemical shift 94, 124
multipole expansion methods 193 ff
multi-reference configuration interaction method 484 ff, 489, 537 ff

n

N_2 correlation effects on shielding constant 134
natural bond orbital 297, 314 ff, 317
natural chemical shielding analysis 297
natural J-coupling analysis 314 ff
natural localized molecular orbital 314 ff, 317
$NH_2CHCOOH$ 574 ff
nickel complexes, EPR parameters of 587 ff
nickel-iron hydrogenases, EPR parameters of 588
NICS see nucleus-independent chemical shift
nitrosyl porphyrins, EPR parameters of 583
nitroxides hyperfine coupling 573
N-methylacetamide dimer 344, 348
N-methylformamide ^{17}O chemical shift 182, 185
NMR tensors 433 ff
2-nobornyl cation 380 ff
no-core shell model 283 ff
non-collinear spin density functional approach 511
non-heme iron protein sites, EPR parameters of 584
non-Kramers system 543, 545
nonrelativistic limit 43, 48 ff, 70 ff
normal coordinates 160 ff
normal halogen dependence 391
– of chemical shift 303
nuclear acids NMR parameters in 341 ff
nuclear deformation 279 ff
nuclear quadrupole coupling 24, 178, 272, 279 ff, 443 ff, 581 ff
– aluminium 456
– ammonia 185
– deuterium in water 177, 185
– ^{17}O in CO_2 185
– tensor 37 ff
nuclear quadrupole resonance 37
nuclear shielding 65, 67 ff, 153 ff, 209 ff
– with continuum models 195 ff
– diamagnetic contribution 130, 231
– diamagnetic part 14, 201
– diamagnetic term 252, 295
– MO contributions to 296
– paramagnetic contribution 131
– paramagnetic part 14, 201
– paramagnetic term 295
– scalar relativistic effects 304
– semiempirical methods 141, 143
– SO effect on 79 ff
nuclear shielding constant 86, 90
– electron-correlation effects 135

– halides 236
– isotope effects 167
– solvent effects 175
– spin–orbit effects 166
– vibrational corrections 165
– of W, Pt, Pb, U 242
nuclear shielding density 298 ff
nuclear shielding tensor 36, 229 ff, 328, 330
– boron 443 ff
– components 95
– isotope effect on 13
– orbital 329 ff
– paramagnetic part 330
– relativistic effects 218, 220
– symmetry of 13
nuclear Zeeman interaction 24
nuclear Zeeman term 332
nucleic acids chemical shift in 346
nucleus-independent chemical shift 86, 147 ff, 394 ff, 398
– comparison of methods based on 400
– dissected 398
– for fullerenes 148
– isosurfaces 397
– using GIAO-MNDO 148 ff

o

one-component method 508 ff, 518 ff
one-electron systems 44
optical excitation energies correlation of chemical shift with 294
orbital shift 325 ff
orbital Zeeman interaction 212
orbital Zeeman term 295
ozone electron-correlation effects on shielding constants 135 ff

p

pair-additivity 179, 185
paramagnetic contribution to energy 70
paramagnetic current 299
paramagnetic NMR 325 ff, 582
paramagnetic part in semiempirical methods 151
paramagnetic shift 36
paramagnetic spin–orbit term 102 ff, 212, 295, 307 ff
paramagnetism 63, 66
Pauli equation 57
Pauli matrix 56
Pauli principle 310
Pauli spin matrices 211
Penney–Dirac bond order 312
pentadienyl cation 389
peptides three-bond coupling in 347
pericyclic reactions transition states 404
periodic boundary conditions 177, 179, 265
periodic treatments 179
perturbational methods 257
perturbation operators, magnetic 229 ff
perturbation theory 35, 58 ff, 88, 103, 209 ff
– degenerate 60, 75
– multiple 59
– quasidegenerate 78
– third order 218
picture change effects 230
π-radical 25
π-stabilized carbocations 385
plane wave basis set 269, 271 ff, 274
Poisson–Boltzmann equation 193
Poisson equation 193
polarizable continuum model 181, 194 ff
– for hyperfine coupling 573
polarization functions 89
polarization-propagator method (second-order) 131
polycyclic carbocations 380 ff
polypeptides chemical shift calculations on 345
position operator 268
principal axis system of NMR tensors 433 ff
projector augmented wave method 269
property density 318 ff, 320 ff
property derivatives 159 ff
property surfaces 178
2-propyl cation 374
proteins
– chemical shift calculations on 345
– NMR parameters in 341 ff
protonated carbonic acid 392
protonated diazomethane 392
protonated methane 372
protonated urea 392
proton transfer 455 ff
pseudocontact shift 325 ff, 343
pseudopotential 209, 222, 228 ff, 268, 272, 528 ff
pseudopotential calculation reconstruction of all-electron current from 270
pyridine N chemical shift 185

q

QCE method see quantum cluster equilibrium method

quadrupolar interaction
– first-order 443
– second-order 443
quantum cluster equilibrium method 181
– results for liquid water 183
quantum confinement effects 266
quantum electrodynamics 49, 55, 77, 209, 231
quantum mechanical spin Hamiltonian 33 ff
quantum Monte-Carlo simulation secondary isotope effect 164

r
Ramsey equation 295, 309
– relativistic analog 10, 13
Ramsey, Norman F 7 ff
Ramsey term 67
random-phase approximation 131
reaction field 180 ff
real-space function of spin–spin coupling 317
reduced spin–spin coupling constant 310
reference interaction site model 181
reference shift see orbital shift
relativistic calculations 249 ff
relativistic corrections 61, 65, 74, 257
relativistic DFT 508 ff
relativistic effects 44, 166, 209 ff, 217 ff, 272, 513 ff
– active terms 221
– on nuclear shielding 218, 220
– on nuclear shieldings, interpretation of 302
– passive terms 222
– on spin–spin coupling 10, 118, 219, 221
relativistic kinematic effects 213
relativistic mass-correction term 534, 536, 538
relativistic methods 227, 286 ff
relativistic scaling factor 253 ff
relativistic theory 43
relativity principles 48
relaxation quadrupolar 179, 185
relaxation time 178, 185
resolution of the identity 133
response equations 111
response theory 103 ff
– first-order 129
– second order 125
restricted open-shell Hartree–Fock method 332
REX see extended-Hückel method
ring current 298, 343, 394 ff
– diamagnetic part 298 ff
– density 400
– susceptibility 397
RISM see reference interaction site model
rotational state 162 ff
ro-vibrational correction see vibrational corrections
rubredoxin 582
$2(N+1)^2$ rule 403

s
Sc_3NC_{80} 416
scalar relativistic effects 239 ff, 256 ff
– on nuclear shielding 304
s-character of bond or molecular orbital 312
Schrödinger equation 57 ff
Schrödinger Hamiltonian 50
SCRF see self-consistent reaction field
SD term see spin-dipolar term
secondary isotope effect 159 ff, 167, 170
second derivatives analytic 124, 129 ff
second-order property 123, 513 ff
second-order response 125
selection rules for magnetic-dipole allowed couplings 296
self-consistent reaction field for hyperfine coupling 573
self-coupling effects 11
self-interaction 99
self-interaction correction 99, 422
self-interaction error, in DFT 585
semiempirical methods 141 ff, 254
– limitations for NMR parameters 151
semiempirical models of chemical shift 12
semiquinone 203 ff
shielding anisotropies 243 ff
shielding constant see nuclear shielding
shielding hyperpolarizability 343
shielding tensor see nuclear shielding tensor
short-range alternative operator 497
SIC see self-interaction correction
silanorbornyl cations 381
β-silyl effect 385
singly occupied molecular orbital SOMO 475, 490
Slater-type orbitals STOs 466
snapshot 177
SOLO see localized orbital/local origin (second order)
solute-solvent interactions 191 ff
– direct 198
– indirect 198
– specific 198

solvation, free energy of 193 ff
solvent effect 239 ff
– electrostatic 178
– on hyperfine coupling 178
– on nuclear shielding constants 175, 178
– on spin–spin coupling 118, 175, 178
SOPPA see polarization-propagator method, second-order
SOS see sum-over-states theory
spherical aromaticity 403
spin contamination 476 ff
spin-current 515
spin density 105 ff, 252 ff, 314, 317
spin-dipolar hyperfine operator kinetic energy correction 215
spin-dipolar operator 213
spin-dipolar term 66, 69, 102 ff, 251 ff, 307 ff
spin-Hamiltonian 541 ff
spin–orbit chemical shift 12, 303
– analogy with spin–spin coupling 303
spin–orbit core potential, relativistic 515
spin–orbit coupling 37 ff, 44, 62, 65 ff, 75 ff, 78 ff, 211, 216 ff, 235 ff, 276, 302 ff, 507 ff, 552 ff
– operators 40, 515 ff
spin–orbit effects 239 ff, 256 ff, 286 ff
– on chemical shift 12, 303
– on hyperfine coupling 28
– on nuclear shieldings 166 ff, 301
spin–orbit operator 233, 507 ff
– approximations 527 ff
– effective 557
– empirically parametrized 528
spin-other-orbit operator 507 ff, 528
spin polarization 25 ff, 303, 309, 317, 524 ff
spin quantization direction 514
spin-restricted approach 512, 518, 524
spin–spin coupling 9 ff, 61, 68 ff, 101 ff, 153 ff, 209 ff, 249 ff, 307 ff, 439, 439 ff, 496
– ^{19}F-^{15}N across F-H-N hydrogen bond 363 ff
– ^{13}C-^{15}N across C-H-N hydrogen bond 361 ff
– across hydrogen bonds 348 ff, 353 ff, 357 ff, 442
– across hydrogen bonds, temperature dependence 367
– anisotropy of 261
– in biomolecules 347
– through bond 308, 310, 313, 319 ff
– with continuum models 195 ff
– with DFT methods 101 ff
– diamagnetic orbital terms 251 ff
– dipolar 36
– effects of electric fields 356
– geminal 115
– with Hartree–Fock methods 101 ff
– indirect 36
– isotope effects 170
– in liquids 187
– one-bond, conformational dependence of 348
– paramagnetic orbital terms 251 ff
– Ramsey mechanisms 439
– reduced coupling constant 310
– relativistic effects 10, 118, 219, 221
– scalar quantum exchange 164
– sign of 442
– solvent effects 118, 175, 178
– through space 308, 310, 313, 319 ff
– spin orbit effect on 79 ff
– three-bond, in peptides 347
– in transition-metal complexes 187, 427
– vibrational corrections 116, 118, 168
– vicinal 118
– visualization of 317
spin–spin coupling density 319
spin–spin coupling pathways 308
spin–spin coupling tensor 102 ff, 112, 439 ff
– antisymmetric contributions 442
– magnetic dipole-dipole interaction 439
– principal axis system for 440
– for trimethylphosphine 441
– vibrational corrections 442
spin–spin interaction, direct dipolar 553
spin-Zeeman interaction 211, 213, 221
spin-Zeeman operator kinetic energy correction 215
spiral code 409
Stone's theory 28
sum-over-states density functional perturbation theory 452 ff
sum-over-states perturbation theory 9, 27, 309 ff, 316
sum-over-states theory 92, 98, 103, 125, 131, 144, 295, 537 ff
– expansion of third order relativistic terms 302
super-cell 267
supermolecular model 572 ff
superoxide dismutase 584

t

temperature effects 161 ff, 165
TEMPO radical 573

tensor ranks of 213
tetrahedrane aromatic shielding 405
tetrazole 197
thioformyl radical hyperfine coupling constant 570
Thomson radius 49
through-bond coupling spin–spin 308, 310, 313, 319 ff
through-space coupling spin–spin 308, 310, 313, 319 ff
tight binding method 142, 146
time-correlation functions 179
trajectory 176
transferability of MO contributions 300
trans influence 428
transition metal carbonyl clusters 300
transition metal chemical shift 178, 184, 424, 426
transition metal complexes
– aromaticity of 400, 429
– spin–spin coupling 187, 427 ff
– structural refinement 423
transition metal compounds 288
– NMR of 421
transition metal hydrides (1H shieldings) 301
transition metal nuclei 183
transition metal oxo complexes (^{17}O shieldings) 300
transition metal phosphine complexes (^{31}P coordination shifts) 301
transition states aromaticity of 404
translational symmetry 267
trimethylphosphine spin–spin coupling tensor for 441
triple bonds anisotropy effects 396
triplet states aromaticity of 402
tunneling 164
two-component method 232 ff, 252 ff, 508 ff, 518 ff, 538

u

uncoupled DFT method 92, 296
units
– atomic 51, 55, 85
– atomic, SI-based 211
– for magnetic properties 45
unrestricted approach 538

v

valence-bond theory 25
vanadium complexes 183
– EPR parameters of 588
Van–Vleck paramagnetism 299
variable-field NMR 443 ff
vector potential 45, 53, 86
vibrational averaging 202 ff
vibrational corrections 153 ff, 154, 163, 202 ff
– to hyperfine coupling 569
– to nuclear shielding constants 165
– to spin–spin coupling 116, 118, 168
– to spin–spin coupling tensor 442
vibrational wavefunction 159 ff
vicinal spin–spin coupling 118, 316
vinyl cations 384 ff

w

water
– chemical shift 177, 179 ff
– chemical shift anisotropies 183
– deuterium quadrupole coupling constant 177, 185
– gas-to-liquid change in chemical shift 183
– magnetic susceptibility 187
– supercritical 187
wave function spatial 35
weak field regime 543, 545

x

X-α scattered wave method 581, 585

z

Zeeman effect 62 ff, 533 ff
– anomalous 78
Zeeman gauge diamagnetic correction 327
Zeeman kinetic energy correction, spin 507
Zeeman operator
– electron spin 327 ff
– nuclear spin–orbit coupling 506
– one-electron spin 506
– orbital 327 ff, 506
Zeeman splitting 77 ff
Zeeman term, nuclear 332
– spin–orbit gauge correction 534
zeolites 271, 274 ff, 449 ff, 454, 458
– carbocations in 390
– cation positions in 455
zero-field splitting 24, 38, 78, 541 ff, 582 ff
– theory 552
zero-field splitting tensor 506
zero-order regular approximation 209 ff, 233 ff, 238 ff, 258 ff, 272, 479, 509, 518
zero-point vibrational corrections 154 ff, 166
ZFS see zero-field splitting
ZORA see zero-order regular approximation
Z-vector method 129